Mathematical Problems in Engineering

Control Problems of Nonlinear Systems with Applications 2020

Lead Guest Editor: Rongwei Guo
Guest Editors: Yi Qi, Ping Zhao, and Cuimei Jiang

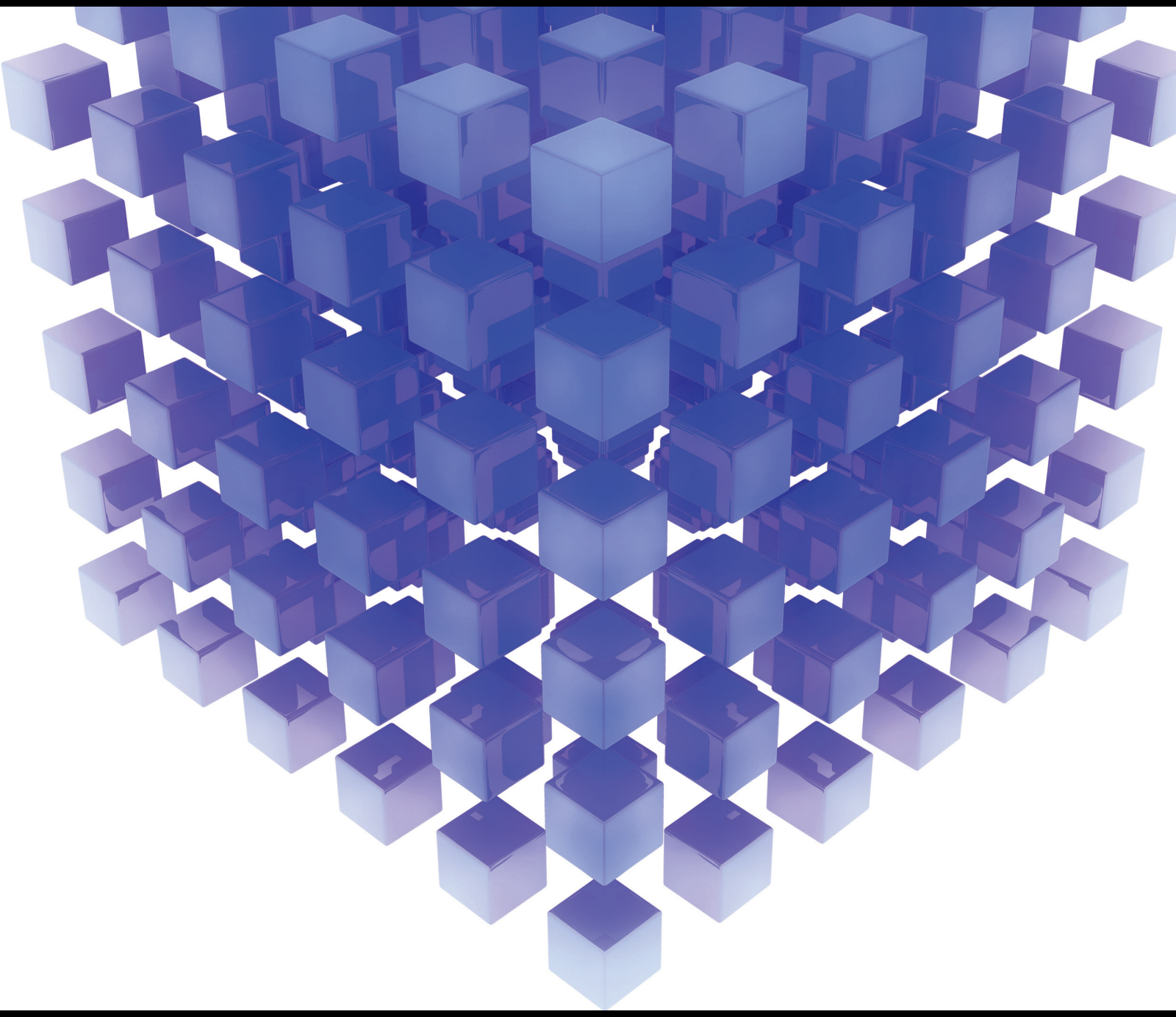

Control Problems of Nonlinear Systems with Applications 2020

Mathematical Problems in Engineering

Control Problems of Nonlinear Systems with Applications 2020

Lead Guest Editor: Rongwei Guo
Guest Editors: Yi Qi, Ping Zhao, and Cuimei Jiang

Contents

Contents

Contents

Hindawi
Mathematical Problems in Engineering
Volume 2021, Article ID 5084693, 8 pages
https://doi.org/10.1155/2021/5084693

Research Article

Synchronization of a Class of Chaotic Systems with Both Uncertainty and Disturbance by the UDE-Based Control Method

Zuoxun Wang [1,2] **and Hongsheng Sha** [1]

[1] *School of Electrical Engineering and Automation, Qilu University of Technology (Shandong Academy of Sciences), Jinan 250353, China*
[2] *High-Tech Industrial (Pilot) Base, Shandong Academy of Sciences, Jinan 250014, China*

Correspondence should be addressed to Zuoxun Wang; wangzuoxun@126.com

Received 2 April 2020; Accepted 24 January 2021; Published 13 February 2021

Academic Editor: Luigi Rodino

In this paper, chaotic synchronization with uncertainties and disturbances is studied. Firstly, a new control method based on UDE control is proposed, which is composed of two controllers: one is the stabilization controller in order to realize the stabilization of nominal system without uncertainties and disturbances and the other is the UDE controller in order to deal with the given controlled system with both uncertainties and disturbances. Then, two examples are studied by the above method. Finally, the correctness and effectiveness of the method are verified by numerical simulation.

1. Introduction

The chaotic synchronization phenomenon that caused great sensation in the academic world was first discovered by Pecora and Carrol in 1990 [1]. They realized the chaotic synchronization of the two same systems with different initial conditions in the electronics experiment. Decades later, they reviewed the literature on chaotic synchronization again [2]. Chaotic synchronization refers to the fact that the unstable motion controlled by the chaotic system tends to move in angular phase or amplitude with a similar rhythm through a certain coupling relationship and it has a wide range of applications in communications encryption, information science, chaotic generator design, and chemical reactions [3–8], etc. In recent years, scholars had proposed a variety of control methods to realize the synchronization between the same chaotic systems or the different chaotic systems with different initial conditions (refer to [9–20]). Among many control methods, the adaptive feedback control method [20] has a wide range of applications due to its simple design and easy implementation.

As far as we know, for chaotic synchronization, most of the existing control methods [9–13] only deal with the chaotic systems whose systems do not include model uncertainty and external disturbance and even if some methods can be used to cancel the uncertainty and disturbance, but the uncertainty and the disturbance are assumed bounded. As a matter of fact, uncertainty and the disturbance of such systems cannot be avoided and are often very large. Therefore, to investigate chaotic synchronization of the systems with both model uncertainty and disturbance is not only necessary, but also meaningful.

In order to solve this problem, the UDE controller [21–23], with its high bandwidth filter, can effectively remove the interference outside the system and it did have been widely used in the field of nonlinear control [22, 24]. However, this control method has some limitations in applications; for example, the controller's design is too complex to be realized in applications, which partly motivates our present work. Based on this, a new adaptive feedback control method based on UDE control is proposed by combining the adaptive feedback controller with the UDE controller to deal with synchronization problems of given chaotic system with both uncertainty and disturbance.

The remainder content of this paper is as follows: first of all, an adaptive feedback control method is given to solve the

synchronization of given chaotic systems without uncertainty and disturbance. Then, the adaptive feedback controller is combined with the UDE controller to deal with synchronization problems of given chaotic system with both uncertainty and disturbance. At last, the simulation results verify the effectiveness and feasibility of the proposed control method.

The main structure of the following article is divided into three parts:

(1) Firstly, an adaptive feedback control method is given to solve the synchronization of given chaotic systems without uncertainty and disturbance

(2) Secondly, the adaptive feedback controller is combined with the UDE controller to deal with synchronization problems of given chaotic system with both uncertainty and disturbance

(3) Finally, the simulation results verify the effectiveness and feasibility of the proposed control method

2. Preliminary

2.1. Adaptive Feedback Control Method. Consider the following nonlinear system

$$\dot{w} = g(w), \tag{1}$$

where $w \in R^n$ is the state vector and $g(w)$ is a continuous function.

Let system (1) be the master system, then the corresponding controlled slave system is given as follows:

$$\dot{v} = g(v) + Nu, \tag{2}$$

where $v \in R^n$ is the state vector, $N \in R^{n\times r}$, $r \geq 1$, and u is the designed controller.

Let $q = v - w$, the controlled error system can be written as follows:

$$\dot{q} = g(v) - g(w) + Nu. \tag{3}$$

Definition 1. Consider system (3). If $\lim_{t\longrightarrow\infty}\|q(t)\| = 0$, the master system (1) will synchronize the slave system (2) by the controller u.

Next, according to the existing result [20], let us briefly introduce the adaptive feedback controller.

$$u_s = Kq, \tag{4}$$

where $K = m(t)N^T$, and

$$\dot{m}(t) = -o\|q(t)\|^2, \tag{5}$$

where $o > 0$ is a constant.

Lemma 1. *(see [20]). Consider the controlled error system (3), if $N = (N_{ij})_{n\times r}$ and $N_{ij} = 0$ or $N_{ij} = 1$, $i = 1, 2, \ldots, n$ and $j = 1, 2, \ldots, r$, and $(g(v) - g(w), N)$ is controllable, then an adaptive controller u_s is obtained as follows:*

2.2. The UDE Controller. Since the UDE controller [22] is suitable for linear and nonlinear systems with uncertainties and perturbations, it is used by us to solve the problems of system uncertainty and perturbation. The following is a brief introduction of this control method.

Consider the following nonlinear system

$$\dot{w} = h(w) + \Delta h(w) + Nu + D(t), \tag{6}$$

and $w \in R^n$ is the state vector, $N \in R^{n\times r}$ is a constant matrix, $\Delta h(w) \in R^n$ is the model uncertainty, and $D(t) \in R^n$ represents the external disturbance.

The stable linear reference model is described as follows:

$$\dot{w}_m = Z_m w_m + N_m C, \tag{7}$$

where $w_m \in R^n$ is the reference state vector, $Z_m \in R^{n\times n}$ is Hurwitz, $N_m \in R^{n\times r}$, and $C \in R^{r\times 1}$ is continuously consistent and bounded instructions for the system.

Lemma 2. *(see [23]). Consider system (6), the designed filter $g_A(t)$ should satisfy*

$$\tilde{u}_d = \hat{u}_d - u_d \longrightarrow 0, \quad t \longrightarrow \infty, \tag{8}$$

where $\hat{u}_d = (\dot{w} - h(w) - Nu) * s_f(t)$ and $u_d = \Delta h(w) + D(t)$, and then, the UDE controller u is designed as follows:

$$\begin{aligned} u = {} & N^+\left\{\ell^{-1}\left[\frac{1}{1 - J_f(s)}\right] * \left(Z_m w + N_m C - Kq\right)\right\} \\ & - N^+\left\{h(w) + \ell^{-1}\left[\frac{sJ_f(s)}{1 - J_f(s)}\right] * w(t)\right\}, \end{aligned} \tag{9}$$

where ℓ^{-1} denotes the inverse Laplace transform operator, $N^+ = (N^T N)^{-1} N^T$, $*$ is the convolution operator, and $J_f(s) = \ell[g_f(t)]$.

Remark 1. According to the existing result [22], the following two filters are often used in applications.

One is

$$J_f(s) = \frac{1}{\tau s + 1}, \tag{10}$$

in general, $\tau = 0.001$.

And the other is

$$J_f(s) = \frac{as + b - w_0^2}{s^2 + as + b}, \tag{11}$$

where $w_0 = 4\pi$, $a = 10w_0$, and $b = 100w_0$.

3. Main Results

Consider the advantages of the adaptive control method and UDE control method, a new result of the combination of UDE controller and adaptive feedback controller is proposed.

Consider the following master chaotic system with both uncertainty and disturbance

$$\dot{w} = A(w) + \Delta A(w) + D(t), \tag{12}$$

where $w \in R^n$, $\Delta A(w)$ denotes system model uncertainty, and $D(t)$ is external disturbance.

Then, the slave system is shown as follows:

$$\dot{v} = A(v) + Nu, \tag{13}$$

where $v \in R^n$ is the state vector, $N = (b_{ij})_{n\times r}$ and $b_{ij} = 0$ or $b_{ij} = 1$, $i = 1, 2, \ldots, n$, $j = 1, 2, \ldots, r$, and u is the controller to be designed.

Let $q = v - w$, the error system is represented as follows:

$$\dot{q} = A(v) - A(w) + \Delta A(w) + D(t) + Nu, \tag{14}$$

where $q \in R^n$ and $(A(v) - A(w), N)$ is controllable.

Then, we propose a conclusion.where $F(w, q) = A(v) - A(w) + Nu_s$.

Theorem 1. *Consider the error system (14), if the designed filter $g_A(t)$ satisfies the following condition:*

$$\tilde{u}_d = \hat{u}_d - u_d, \quad t \longrightarrow \infty, \tag{15}$$

where $\hat{u}_d = (\dot{x} - A(w) - u_d) * g_f(t)$ and $u_d = \Delta A(w) + D(t)$; and then, the UDE-based controller u is shown as follows:

$$u = u_s + u_{ude}, \tag{16}$$

where $u_s = Kq$, $K = m(t)N^T$, and

$$\dot{m}(t) = -o\|e(t)\|^2, \tag{17}$$

$$\begin{aligned} u_{ude} = {} & N^+\left\{\ell^{-1}\left[\frac{J_f}{1 - J_f(s)}\right] * F(w, q)\right\} \\ & - N^+\left\{\ell^{-1}\left[\frac{sJ_f(s)}{1 - J_A(s)}\right] * q(t)\right\}, \end{aligned} \tag{18}$$

Proof. Substituting u in (16) to the error system (14), it results in $\dot{q} = A(v) - A(w) + Nu_s + Nu_{ude} - u_d = F(w, q) + Nu_{ude} - u_d$.

According to (15), it can be calculated as $Bu_{ude} = \hat{u}_d$, and according to Lemma 1, it can be concluded that the system $\dot{q} = F(w, q)$ is globally asymptotically stable. Thus, the conclusion is established. □

4. Illustrative Examples with Numerical Simulation

In this section, the three-dimensional Lorenz chaotic system and 4D hyperchaotic system are taken as examples, respectively.

$$\dot{w} = A(w) + \Delta A(w) + D(t), \tag{19}$$

where $w = (w_1, w_2, w_3)^T$, $\Delta A(w)$ denotes system model uncertainty, and $D(t)$ is external disturbance, i.e.,

$$A(w) = \begin{pmatrix} A_1(w) \\ A_2(w) \\ A_3(w) \end{pmatrix} = \begin{pmatrix} 10(w_2 - w_1), \\ 28w_1 - w_2 - w_1w_3 \\ -\frac{8}{3}w_3 + w_1w_2, \end{pmatrix} \tag{20}$$

$$\begin{aligned} \Delta A(w) &= \begin{pmatrix} 0, \\ -0.1w_1^2, \\ 0, \end{pmatrix} \\ D(t) &= \begin{pmatrix} 0, \\ 0.1\sin(t) \\ 0, \end{pmatrix} \end{aligned} \tag{21}$$

Example 1. Consider the following master chaotic system with both uncertainty and disturbance

Then, the slave system is shown as follows:

$$\dot{v} = A(v) + Nu, \tag{22}$$

where $v = (v_1, v_2, v_3)^T$ and $(A(v) - A(v), N)$ is controllable, i.e.,

$$A(v) = \begin{pmatrix} A_1(v) \\ A_2(v) \\ A_3(v) \end{pmatrix} = \begin{pmatrix} 10(v_2 - v_1), \\ 28v_1 - v_2 - v_1v_3, \\ -\frac{8}{3}v_3 + v_1v_2, \end{pmatrix} \tag{23}$$

$$N = \begin{pmatrix} 0 \\ 1 \\ 0 \end{pmatrix}. \tag{24}$$

Let $q = v - w$, the error system is shown as follows:

$$\dot{q} = A(v) - A(w) + Nu - \Delta A(w) - D(t), \tag{25}$$

where $q = v - w \in R^3$ and $u = u_s + u_{ude}$ is the controller to be designed. Our goal is to design a controller $u = u_s + u_{ude}$ to stabilize system (25) with two control steps.

In the first step, the controller u_s is to be designed as follows. By observing (20) and (23), if $q_2 = 0$, the following two-dimensional system

$$\begin{aligned} \dot{q}_1 &= -28q_1, \\ \dot{q}_3 &= -\frac{8}{3}q_3 + w_2q_1 \end{aligned} \tag{26}$$

is globally asymptotically stable.

According to Lemma 2, the controller u_s can be designed as follows:

$$u_s = m(t)N^Tq = m(t)(010)^Tq, \tag{27}$$

and the feedback gain $m(t)$ is updated by the update law (17). Next, the numerical simulation is carried out with the initial conditions (for the convenience of the reader, we replace $w(.)$ with $x(.)$, $v(.)$ with $y(.)$, and $m(.)$ with $k(.)$, and the specific initial values are shown as follows: $x_1(0) = 0.1, x_2(0) = \quad 0.2, x_3(0) = 0.3, y_1(0) = 1, y_2(0) = 2, y_3(0) = 3, k(0) = -1$); then, the numerical simulation results are shown as follows.

Figure 1 shows that the error system is asymptotically stable, and Figure 2 shows that the feedback gain $k(t)$ converges to a negative constant.

The second step is to design the UDE controller u_{ude}. Let $u_d = \Delta A(w) + D(t)$, $F(x) = A(v) - A(w) + Nu_s$, and system (25) is rewritten as follows:

$$\dot{w} = F(w) + Nu_{ude} - u_d. \tag{28}$$

According to Lemma 2, the controller u_{ude} is designed as

$$u_{ude} = N^{+}(\dot{w} - A(w)) * g_f(t). \tag{29}$$

Thus, the controller $u = u_s + u_{ude}$ is completely designed. In the following, the simulation results is carried out as follows.

Figure 3 shows that the error system is also asymptotically stable, Figure 4 shows that the states x_1, x_2, x_3 synchronize the states y_1, y_2, y_3, respectively, Figure 5 shows that the feedback gain $k(t)$ converges to a negative constant, and Figure 6 shows that $\hat{u}_d$ tends to u_d as $t \longrightarrow \infty$.

Example 2. Consider the controlled 4D hyperchaotic system with both uncertainty and disturbance as follows:

$$\dot{w} = A(w) + \Delta A(w) + D(t), \tag{30}$$

where $w = (w_1, w_2, w_3, w_4)^T$.

$$A(w) = \begin{pmatrix} A_1(w) \\ A_2(w) \\ A_3(w) \\ A_4(w) \end{pmatrix} = \begin{pmatrix} 15(w_2 - w_1), \\ 10w_2 - w_1w_3 + w_4, \\ w_1w_2 - 5w_3, \\ w_3 - w_4, \end{pmatrix}$$

$$\Delta A(w) = \begin{pmatrix} 0, \\ -0.1w_1^2, \\ 0, \\ 0, \end{pmatrix} \tag{31}$$

$$D(t) = \begin{pmatrix} 0, \\ 0.1\sin(t), \\ 0, \\ 0, \end{pmatrix}$$

Let system (30) be the master system, then the slave system is given as follows:

$$\dot{v} = f(v) + Nu, \tag{32}$$

where $v = (v_1, v_2, v_3, v_4)^T$.

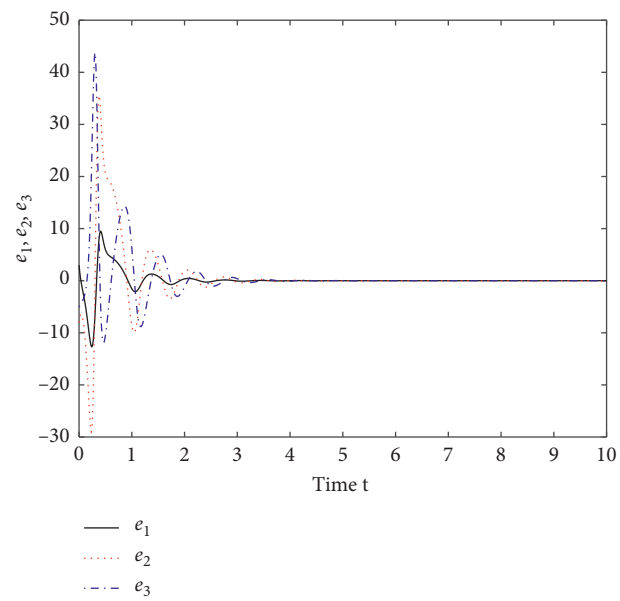

Figure 1: The error system is asymptotically stable.

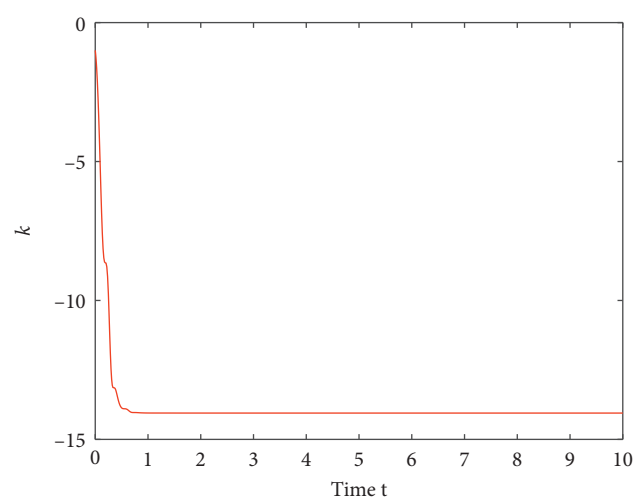

Figure 2: The feedback gain $k(t)$ converges to a negative constant.

$$A(v) = \begin{pmatrix} A_1(v) \\ A_2(v) \\ A_3(v) \\ A_4(v) \end{pmatrix} = \begin{pmatrix} 15(v_2 - v_1) \\ 10v_2 - v_1v_3 + v_4 \\ v_1v_2 - 5v_3 \\ v_3 - v_4 \end{pmatrix},$$

$$N = \begin{pmatrix} 0 & 0 \\ 1 & 0 \\ 0 & 1 \\ 0 & 0 \end{pmatrix}. \tag{33}$$

Let $q = v - w$, the error system is represented as follows:

$$\dot{q} = f(v) - f(w) + Nu - \Delta A(w) - D(t), \tag{34}$$

where $u = u_s + u_{ude}$ is the controller to be designed.

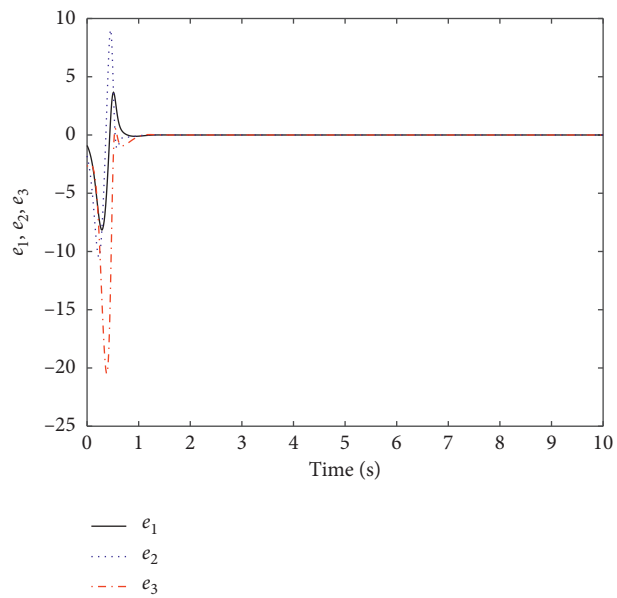

Figure 3: The error system is also asymptotically stable.

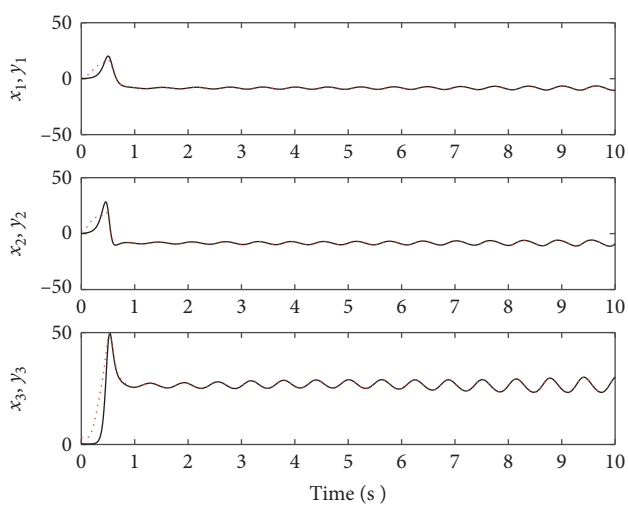

Figure 4: The states x_1, x_2, x_3 synchronize the states y_1, y_2, y_3, respectively.

Our goal is to design a controller $u = u_s + u_{ude}$ to stabilize system (34) with two control steps.

In the first step, the controller u_s is to be designed as follows.

By observing the error system (34), i.e.,

$$\begin{aligned} \dot{q}_1 &= 15(q_2 - q_1), \\ \dot{q}_2 &= 10q_2 - q_1q_3 + q_4 - w_3q_1 - w_1q_3, \\ \dot{q}_3 &= q_1q_2 - 5q_3 + w_1q_2 + w_2q_1, \\ \dot{q}_4 &= q_3 - q_4. \end{aligned} \tag{35}$$

By observing the conclusion results of (35), we note that, if $q_2 = 0, q_3 = 0$, then the following subsystem

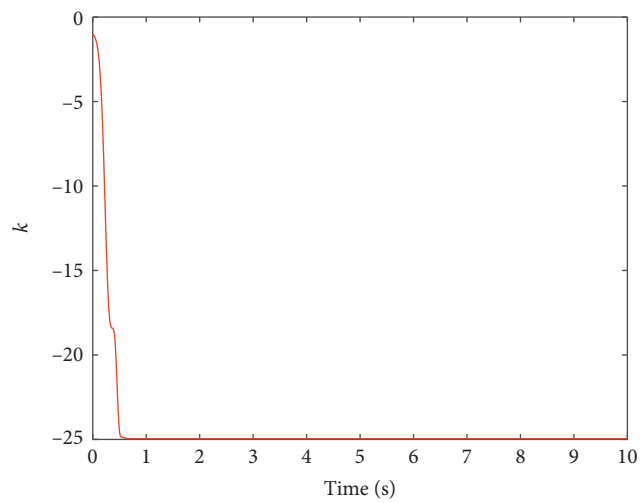

Figure 5: The feedback gain $k(t)$ converges to a negative constant.

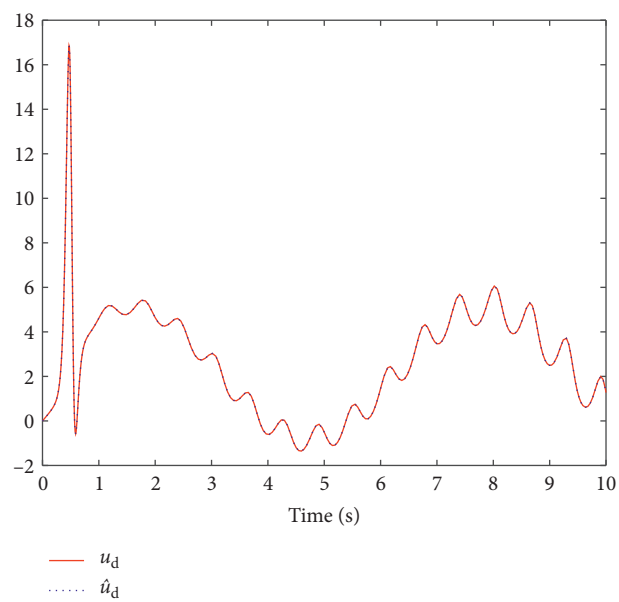

Figure 6: $\hat{u}_d$ tends to u_d as $t \longrightarrow \infty$.

$$\begin{aligned} \dot{q}_1 &= -15q_1, \\ \dot{q}_4 &= -q_4 \end{aligned} \tag{36}$$

is globally asymptotically stable.

Therefore, according to Lemma 1, the controller u_s can be designed as follows:

$$u_s = m(t)N^T q = m(t)\begin{pmatrix} 0 & 1 & 0 & 0 \\ 0 & 0 & 1 & 0 \end{pmatrix} q, \tag{37}$$

and the feedback gain $m(t)$ is updated by the update law (17).

Then, the simulation result is carried out with the initial condition (for the convenience of the reader, we replace $w(.)$ with $x(.)$, $v(.)$ with $y(.)$, and $m(.)$ with $k(.)$: $x_1(0) = 1, x_2(0) = -2, x_3(0) = 3, x_4(0) = -4, y_1(0) = 5, y_2(0) = -6, y_3(0) = 7, y_4(0) = -8, k_0 = -1$).

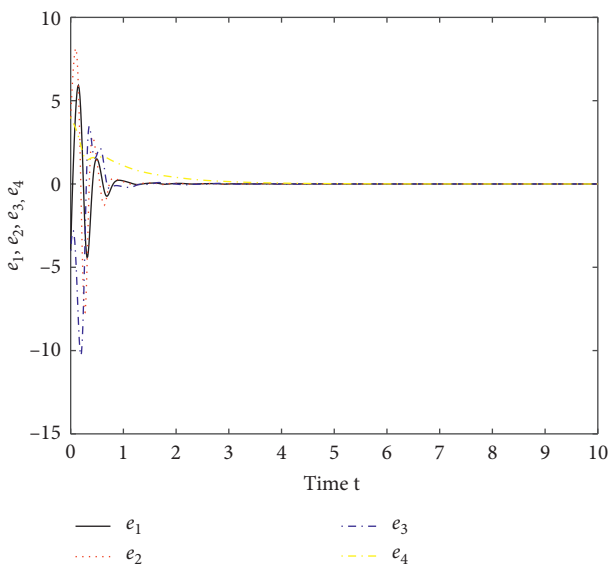

FIGURE 7: The error system is asymptotically stable.

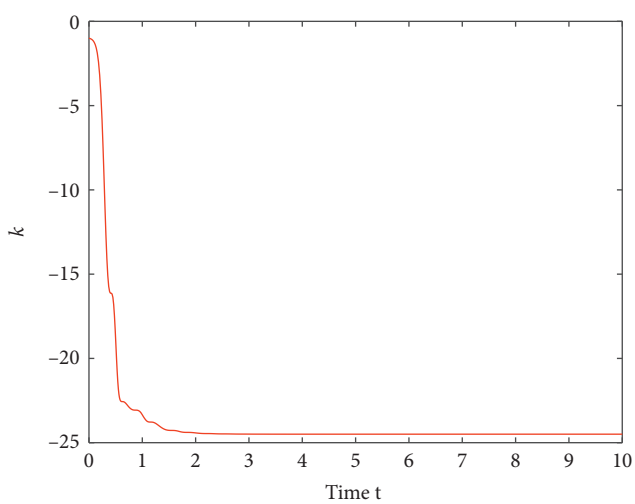

FIGURE 8: The feedback gain $k(t)$ converges to a negative constant.

Figure 7 shows that the error system is asymptotically stable, and Figure 8 shows that the feedback gain $k(t)$ converges to a negative constant.

In the second step, the controller u_{ude} is designed as follows. Let $u_d = \Delta A(w) + D(t), F(w) = A(v) - A(w) + Nu_s$, system (30) is rewritten as follows:

$$\dot{w} = F(w) + Nu_{ude} - u_d. \tag{38}$$

According to Lemma 2, the controller u_{ude} can be designed as follows:

$$\begin{aligned} u_{ude} = {} & N^{+}\left\{\ell^{-1}\left[\frac{J_A(s)}{1-J_A(s)}\right] * F(w,q)\right\} \\ & - N^{+}\left\{\ell^{-1}\left[\frac{sJ_A(s)}{1-J_A(s)}\right] * q(t)\right\}, \end{aligned} \tag{39}$$

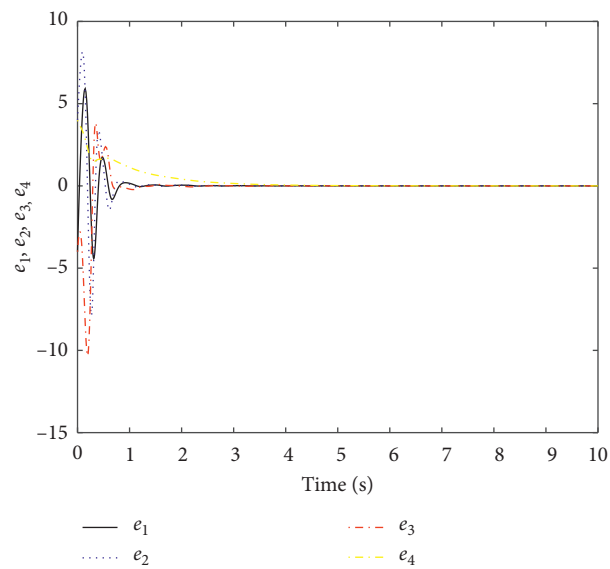

FIGURE 9: The error is also asymptotically stable.

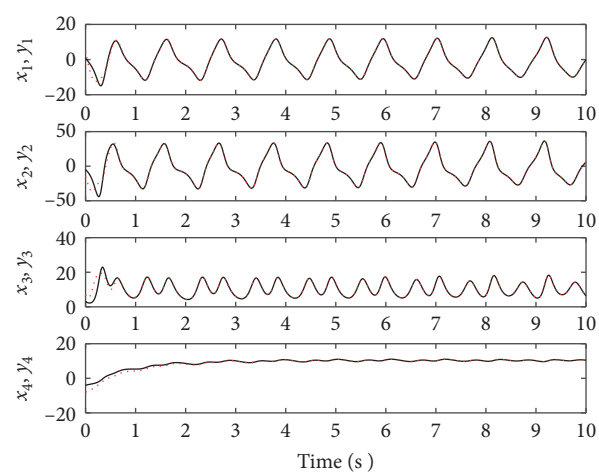

FIGURE 10: The states x_1, x_2, x_3, x_4 synchronize the states y_1, y_2, y_3, y_4, respectively.

where ℓ^{-1} denotes the inverse Laplace transform operator, $N^{+} = (N^T N)^{-1} N^T$, $*$ is the convolution operator, and $J_A(s) = \ell[g_A(t)]$. Thus, the controller $u = u_s + u_{ude}$ is completely designed. Next, the simulation is carried out with the initial condition (for the convenience of the reader, we replace $w(.)$ with $x(.)$, $v(.)$ with $y(.)$, and $m(.)$ with $k(.)$: $x_1(0) = 1, x_2(0) = -2, x_3(0) = 3, x_4(0) = -4, y_1(0) = 5, y_2(0) = -6, y_3(0) = 7, y_4(0) = -8, k_0 = -1$), and the numerical simulation results are shown in Figure 9–12.

Figure 9 shows that the error system is also asymptotically stable, Figure 10 shows that the states x_1, x_2, x_3 synchronize the states y_1, y_2, y_3, respectively, Figure 11 shows that the feedback gain $k(t)$ converges to a negative constant, and Figure 12 shows that $\hat{u}_d$ tends to u_d as $t \longrightarrow \infty$.

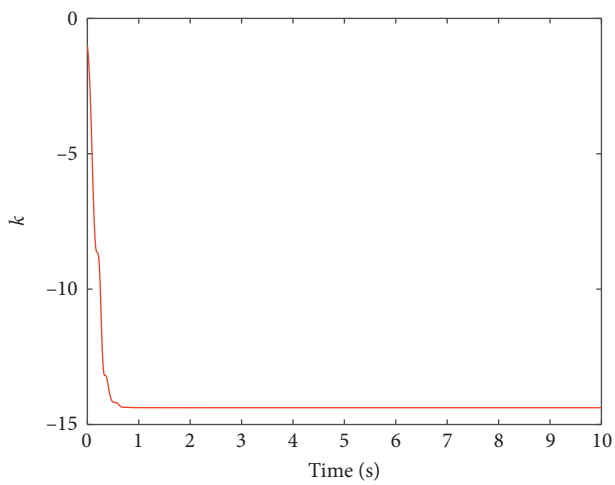

Figure 11: The feedback gain $k(t)$ converges to a negative constant.

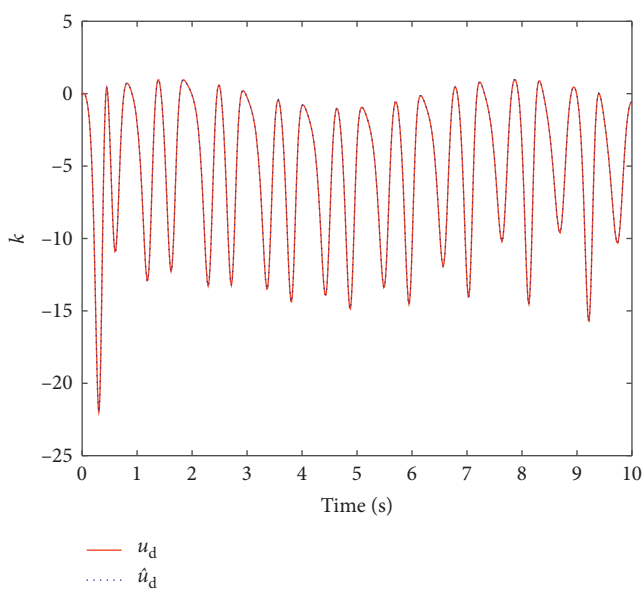

Figure 12: $\hat{u}_d$ tends to u_d as $t \longrightarrow \infty$.

5. Conclusion

In this paper, synchronization of chaotic systems with both uncertainty and disturbance has been investigated. Firstly, a new UDE-based control method has been presented, which is composed of two controllers: one is the stabilization controller and the other is the UDE controller. Secondly, two examples have been studied by the above methods. Finally, numerical simulations have verified the effectiveness and correctness of the theoretical results.

Data Availability

No data were used in this paper.

Conflicts of Interest

The authors declare that they have no financial and personal relationships with other people or organizations that can inappropriately influence our work, and there is no professional or other personal interest of any nature or kind in any product, service, and/or company that could be construed as influencing the position presented in, or the review.

Acknowledgments

This work was supported by Science, Education, and Industry Integration Innovation Pilot Project of Qilu University of Technology (Shandong Academy of Sciences) (2020KJC-ZD04).

References

[1] L. M. Pecora and T. L. Carroll, "Synchronization in chaotic systems," *Physical Review Letters*, vol. 64, no. 8, pp. 821–824, 1990.

[2] L. M. Pecora and T. L. Carroll, "Synchronization of chaotic systems," *Chaos*, vol. 25, no. 9, pp. 097–611, 2015.

[3] S. Bowong, "Stability analysis for the synchronization of chaotic systems with different order: application to secure communications," *Physics Letter A*, vol. 326, no. 2, pp. 102–113, 2004.

[4] R. R. Ojalvo, "Spatiotemporal communication with synchronized optical chaos," *Physical Review Letter*, vol. 86, no. 28, p. 5204, 2001.

[5] K. Murali and M. Lakshmanan, "Drive-response scenario of chaos synchronization in identical nonlinear systems," *Physical Review E*, vol. 49, no. 6, p. 4882, 1994.

[6] K. Murali and M. Lakshmanan, "Impulsive stabilization for control and synchronization of chaotic systems: theory and application to secure communication," *Physical Review E*, vol. 44, no. 10, pp. 976–988, 1997.

[7] Z.-L. Wang and X.-R. Shi, "Anti-synchronization of Liu system and Lorenz system with known or unknown parameters," *Nonlinear Dynamics*, vol. 57, no. 3, pp. 425–430, 2009.

[8] R. Guo, "Projective synchronization of a class of chaotic systems by dynamic feedback control method," *Nonlinear Dynamics*, vol. 90, no. 1, pp. 53–64, 2017.

[9] A. Yang, L. Li, Z. Wang, and R. Guo, "Tracking control of a class of chaotic systems," *Symmetry*, vol. 11, no. 4, p. 568, 2019.

[10] Z. Wang and R. Guo, "Hybrid synchronization problem of a class of chaotic systems by an universal control method," *Symmetry*, vol. 10, no. 11, p. 552, 2018.

[11] D. B. Huang, "Simple adaptive-feedback controller for identical chaos synchronization," *Physical Review E*, vol. 71, no. 3, pp. 037–203, 2005.

[12] D. B. Huang, "Adaptive-feedback control algorithm," *Physical Review E*, vol. 73, no. 6, pp. 066–204, 2006.

[13] D. B. Huang, "Synchronization in adaptive weighted networks," *Physical Review E*, vol. 74, no. 4, pp. 046–208, 2006.

[14] H. G. Zhang, Y. H. Xie, Z. L. Wang, and C. D. Zheng, "Adaptive synchronization between two different chaotic neural networks with time delay," *IEEE Transaction on Network*, vol. 18, no. 6, pp. 1841–1845, 2007.

[15] T. Yang and L. O. Chua, "Impulsive stabilization for control and synchronization of chaotic systems: theory and application to secure communication," *IEEE Transations on Circuits Systems*, vol. 44, no. 10, pp. 976–988, 1997.

[16] M. Chen, Q. Wu, and C. Jiang, "Disturbance-observer-based robust synchronization control of uncertain chaotic systems," *Nonlinear Dynamics*, vol. 70, no. 4, pp. 2421–2432, 2012.

[17] T. Hou, Y. Liu, and F. Deng, "Finite horizon H2/H∞ control for SDEs with infinite Markovian jumps," *Nonlinear Analysis: Hybrid Systems*, vol. 34, pp. 108–120, 2019.

[18] H. Chen, J. Chang, J. Yan, and T. Liao, "EP-based PID control design for chaotic synchronization with application in secure communication," *Expert Systems with Applications*, vol. 34, no. 2, pp. 1169–1177, 2008.

[19] R. Xu and F. Zhang, "ϵ-Nash mean-field games for general linear-quadratic systems with applications," *Automatica*, vol. 114, Article ID 108835, 2020.

[20] L. Liu, B. Li, and R. Guo, "Consensus control for networked manipulators with switched parameters and topologies," *IEEE Access*, vol. 9, p. 9209, 2021.

[21] B. Ren, Q.-C. Zhong, and J. Dai, "Asymptotic reference tracking and disturbance rejection of UDE-based robust control," *IEEE Transactions on Industrial Electronics*, vol. 64, no. 4, pp. 3166–3176, 2017.

[22] B. B. Ren, Q. C. Zhong, and J. H. Jinhao, "Robust control for a class of nonaffine nonlinear systems based on the uncertainty and disturbance estimator," *IEEE Transactions on Industrial Electronics*, vol. 62, no. 9, pp. 0278–0046, 2015.

[23] Q.-C. Zhong and D. Rees, "Control of uncertain LTI systems based on an uncertainty and disturbance estimator," *Journal of Dynamic Systems, Measurement, and Control*, vol. 126, no. 4, pp. 905–910, 2004.

[24] A. Kuperman and Q.-C. Zhong, "UDE-based linear robust control for a class of nonlinear systems with application to wing rock motion stabilization," *Nonlinear Dynamics*, vol. 81, no. 1-2, pp. 789–799, 2015.

Hindawi
Mathematical Problems in Engineering
Volume 2021, Article ID 5082947, 5 pages
https://doi.org/10.1155/2021/5082947

Research Article

A Decomposability Property to the Weighted Myerson Value and the Weighted Position Value

Guangming Wang[1,2] **and Erfang Shan**[1]

[1]*School of Management, Shanghai University, Shanghai 200444, China*
[2]*School of Mathematical Sciences, University of Jinan, Jinan 250022, China*

Correspondence should be addressed to Guangming Wang; ss_wanggm@ujn.edu.cn

Received 3 April 2020; Accepted 19 January 2021; Published 3 February 2021

Academic Editor: Libor Pekař

Myerson value and position value are important values in a cooperative game with a graph structure. Usually, due to the differences of players in the game, the weighted Myerson value and weighted position value are more widely used in practical situations. This article offers a new calculation approach of the weighted Myerson value and weighted position value. Instead of using induced games (point game and edge game), we prove that the weighted Myerson value and weighted position value meet decomposability property.

1. Introduction

Transferable utility game (TU game) [1] usually assumes that a viable alliance can be formed between any players in the game. However, due to the influence of different cultures and backgrounds as well as social classes, hierarchies, organization structure, or communication technology constraints, alliance cannot be formed between any players in the game. In order to solve it, some efforts have been made to deal with this problem. Myerson firstly introduced Myerson value and proposed the method of graph-restricted game (point game), where the points in the graph represent the players in the game, and the edges represent the cooperative relationship between the players [2]. Myerson value is a kind of Shapley value depended on graph [3]. Later, Myerson, Slikker, and van den Nouweland studied other axiomatic characterizations of Myerson value, respectively, see Refs. [4, 5]. From then on, an increasing interest has been devoted to the study of Myerson value. Li and Shan studied Myerson value on local structures of coalitions and Myerson value for directed graph games, see Refs [6–8]. In addition, van den Nouweland et al. extended the idea initiated by Myerson to hypergraph games and stable system games, respectively, see Refs. [9, 10]. Motivated by point game, Borm et al. proposed the edge game by using the Shapley value of the edge to obtain the position value [11]. Meessen extended position value on the acyclic graph and axiomatic characterizations of position value [12]. Later, Slikker obtained a complete characterization of the position value on any graph game [13]. Li and Shan studied position value of the structures of graphs [14]. Shan and Zhang investigated position value and the Myerson value for hypergraph [15].

However, in many practical situations, a player in the game has many differences, such as different bargaining powers; it is necessary to give a corresponding weight to each player in the game. Haeringer proposed the weighted Myerson value, that is, the weighted Shapley value of the restricted game [16]. Later, Slikker and van den Nouweland extended the weighted Myerson value to layer structure based on the weight systems of Kalai et al. [17–19]. Xu et al. studied weighted harmonic game and matrix expression of Shapley value [20–23]. To calculate the Myerson value and the position value, we usually need to obtain the corresponding induced game firstly: the point game for the Myerson value and the edge game for the position value. However, induced game is too complex in most cases both in generation and follow-up calculation. Motivated by the above discussion, we investigate an approach that allows us

to calculate the Myerson value or the position value in a similar way.

The rest of this paper is organized as follows. In Section 2, we provide some preliminaries on TU games, the weighted graph allocation rule, and the decomposability property. In Section 3, we prove that both weighted Myerson value and weighted position value can be calculated uniformly using the decomposability principle. Section 4 gives conclusions with some remarks.

2. Preliminaries

2.1. TU Games. A cooperative game with characteristic function is often referred to as transferable utility game (TU game) [1], represented by a pair (N, v), where v: $2^N \longrightarrow \mathbb{R}$ is a characteristic function with $v(\varnothing) = 0$. A value or an allocation rule is a function about the payoff of player in a cooperative game. A very famous allocation rule is the Shapley value:

$$\mathrm{Sh}_i(v) = \sum_{S \subseteq N} \frac{(|N| - |S|)!\,(|S| - 1)!}{|N|!}(v(S) - v(S \setminus \{i\})), \quad i \in N. \tag{1}$$

2.2. Smallest Connected Set. The triple (N, v, L) represents a graph game, which is composed of two parts: the TU game (N, v) and the graph structure (N, L), $L \subseteq \{\{i, j\} \in N \times N\colon i \neq j\}$. Let $L_i = \{\{i, j\} \in L\colon j \in N\}$ be the set of edges in the graph L containing point $i \in N$. The dissimilarity points $(i_1, i_2, \ldots, i_k)$ are called a path of L. If there is a path between two points i, j, then i and j are connection. If S is connection in (N, L^S) and not connection in (N, A) for any $A \subset L^S$, $A \neq L^S$, then we denote by $MC_L^e(S)$ the smallest connected (edge) set $L^S \subset L$ in (N, L).

2.3. The Weighted Graph Allocation Rule and Decomposability Property

(a) The weighted graph allocation rule of the point game:

$$c_i^{r^\theta}(N, L) = \frac{\theta_i \delta_i(N, D(L))}{\sum_{j \in D(L)} \theta_j}, \quad i \in N, \tag{2}$$

where θ_i represents the weight of i and $D(L)$ represents the set of nonisolated points in the graph (N, L). In particular, $c_i^{r^\theta}(N, L) = ((\delta_i(N, D(L)))/(|D(L)|))$, if $\theta_i = \theta_j$ for any $i, j \in N$.

(b) The weighted graph allocation rule of the edge game:

$$d_i^{r^\theta}(N, L) = \frac{\sum_{ih \in L_i} (\theta_i / (\theta_i + \theta_h))}{|L|}, \quad i \in N, \tag{3}$$

where θ_i represents the weight of i and $D(L)$ represents the set of nonisolated points in the graph (N, L). In particular, $d_i^{r^\theta}(N, L) = ((d_i(N, L))/(2|L|))$, if $\theta_i = \theta_j$ for any $i, j \in N$, where $d_i(N, L)$ represents the degree of the i in the graph.

(c) For any (N, u_S, L), $S \subset N$, $|S| \geq 2$, $MC_L^e(S) = \{L_k^S\}_{k=1}^{r(S)} \neq \phi\gamma(N, u_S, L) = \sum_{k=1} r(S) h(N, L_k^S) - \sum_{k \neq m} h(N, L_k^S \cup L_m^S) + \cdots + (-1)^{r(S)+1} h(N, \cup_{k=1}^{r(S)} L_k^S)$. We will say that γ meets decomposability property.

3. The Decomposability Property of the Weighted Values

In this section, we calculate the weighted Myerson value and weight position value using the weighted graph allocation rule. It is proved that both weighted Myerson value and weighted position value can be calculated uniformly using the decomposability principle.

Firstly, we introduce the existing approach [11] as follows.

Lemma 1. *If* $(N, u_S, L) \in CS^N$, $|S| \geq 2$, $MC_L^e(S) = \{L_k^S\}_{k=1}^{r(S)}$, *then characteristic function of point game* (N, u_S^L) *is*

$$u_S^L = \begin{cases} 1 - \prod_{k=1}^{r(S)} \left[1 - u_{D(L_k^S)}\right], MC_L^e(S) \neq \phi, 0, MC_L^e(S) = \phi. \end{cases} \tag{4}$$

Lemma 2. *If* $(N, u_S, L) \in CS_0^N$, $|S| \geq 2$, $MC_L^e(S) = \{L_k^S\}_{k=1}^{r(S)}$, *then characteristic function of edge game* $(L, r_L^{u_S})$ *is*

$$r_L^{u_S} = \begin{cases} 1 - \prod_{k=1}^{r(S)} \left[1 - u_{L_k^S}\right], MC_L^e(S) \neq \phi, 0, MC_L^e(S) = \phi. \end{cases} \tag{5}$$

Theorem 1. *The weighted Myerson value meets the decomposability property.*

Proof. If $(N, u_S, L) \in CS^N, |S| \geq 2, MC_L^e(S) = \{L_K^S\}_{k=1}^{r(S)}$, according to Lemma 1,

$$\begin{aligned} \mu^\theta(N, u_S, L) &= \varphi^\theta(u_S^L) = \varphi^\theta\left(1 - \prod_{k=1}^{r(S)}\left[1 - u_{D(L_k^S)}\right]\right), \\ 1 - \prod_{k=1}^{r(S)}\left[1 - u_{D(L_K^S)}\right] &= \sum_{k=1}^{r(S)} u_{D(L_k^S)} - \sum_{k \neq m} u_{D(L_k^S) \cup D(L_m^S)} \\ &\quad + \cdots + (-1)^{r(S)+1} u_{\cup_{k=1}^{r(S)} D(L_k^S)}. \end{aligned} \tag{6}$$

For any $L_1, L_2 \subset L, D(L_1 \cup L_2) = D(L_1) \cup D(L_2)$, we have

$$\begin{aligned} \mu^\theta(N, u_S, L) &= \sum_{k=1}^{r(S)} \varphi^\theta\left(u_{D(L_k^S)}\right) - \sum_{k \neq m} \varphi^\theta\left(u_{D(L_K^S \cup L_m^S)}\right) \\ &\quad + \cdots + (-1)^{r(S)+1} \varphi^\theta\left(u_{D(\cup_{k=1}^{r(S)} L_k^S)}\right). \end{aligned} \tag{7}$$

Using expression in (2), it results in

$$\mu^{\theta}(N,u_S,L)=\sum_{k=1}^{r(S)}c^{r^{\theta}}\left(N,L_k^S\right)-\sum_{k\neq m}c^{r^{\theta}}\left(N,L_k^S\cup L_m^S\right)+\cdots+(-1)^{r(S)+1}c^{r^{\theta}}\left(N,\cup_{k=1}^{r(S)}L_k^S\right). \tag{8}$$

Therefore, the weighted Myerson value meets the decomposability property. □

Theorem 2. *The weighted position value meets the decomposability property.*

Proof. For any $i\in N$,

$$\begin{aligned}\pi_i^{\theta}(N,u_S,L)&=\sum_{ih\in L_i}\frac{\theta_i}{\theta_i+\theta_h}\varphi_{ih}\left(r_L^{u_S}\right)\\&=\sum_{jh\in L}\frac{\theta_j}{\theta_j+\theta_h}\delta_{jh}(L,L_i)\varphi_{jh}\left(r_L^{u_S}\right).\end{aligned} \tag{9}$$

For any $jh\in L,\varphi_{jh}(r_L^{u_S})=\varphi_{jh}(1-\prod_{k=1}^{r(S)}(1-u_{L_k^S}))$, according to Lemma 2, we have

$$\varphi_{jh}\left(r_L^{u_S}\right)=\sum_{k=1}^{r(S)}\varphi_{jh}\left(u_{L_k^S}\right)-\sum_{k\neq m}\varphi_{jh}\left(u_{L_k^S\cup L_m^S}\right)+\cdots+(-1)^{r(S)+1}\varphi_{jh}\left(u_{\cup_{k=1}^{r(S)}L_k^S}\right). \tag{10}$$

Moreover, we get

$$\varphi_{jh}\left(r_L^{u_S}\right)=\sum_{k=1}^{r(S)}\frac{\delta_{jh}\left(L,L_k^S\right)}{\left|L_k^S\right|}-\sum_{k\neq m}\frac{\delta_{jh}\left(L,L_k^S\cup L_m^S\right)}{\left|L_k^S\cup L_m^S\right|}+\cdots+(-1)^{r(S)+1}\frac{\delta_{jh}\left(L,\cup_{k=1}^{r(S)}L_k^S\right)}{\left|\cup_{k=1}^{r(S)}L_k^S\right|}, \tag{11}$$

and then, it results in

$$\begin{aligned}\pi_i^{\theta}(N,u_S,L)&=\sum_{jh\in L}\frac{\theta_j}{\theta_j+\theta_h}\delta_{jh}(L,L_i)\sum_{k=1}^{r(S)}\frac{\delta_{jh}\left(L,L_k^S\right)}{\left|L_k^S\right|}-\sum_{jh\in L}\frac{\theta_j}{\theta_j+\theta_h}\delta_{jh}(L,L_i)\sum_{k\neq m}\frac{\delta_{jh}\left(L,L_k^S\cup L_m^S\right)}{\left|L_k^S\cup L_m^S\right|}\\&\quad+\cdots+(-1)^{r(S)+1}\sum_{jh\in L}\frac{\theta_j}{\theta_j+\theta_h}\delta_{jh}(L,L_i)\frac{\delta_{jh}\left(L,\cup_{k=1}^{r(S)}L_k^S\right)}{\left|\cup_{k=1}^{r(S)}L_k^S\right|}\\&=\sum_{jh\in L}\frac{\theta_j}{\theta_j+\theta_h}\sum_{k=1}^{r(S)}\frac{\delta_{jh}\left(L,L_i\cap L_k^S\right)}{\left|L_k^S\right|}-\sum_{jh\in L}\frac{\theta_j}{\theta_j+\theta_h}\sum_{k\neq m}\frac{\delta_{jh}\left(L,L_i\cap\left(L_k^S\cup L_m^S\right)\right)}{\left|L_k^S\cup L_m^S\right|}\\&\quad+\cdots+(-1)^{r(S)+1}\sum_{jh\in L}\frac{\theta_j}{\theta_j+\theta_h}\frac{\delta_{jh}\left(L,L_i\cap\left(\cup_{k=1}^{r(S)}L_k^S\right)\right)}{\left|\cup_{k=1}^{r(S)}L_k^S\right|}\\&=\sum_{k=1}^{r(S)}\sum_{jh\in L}\frac{\theta_j}{\theta_j+\theta_h}\frac{\delta_{jh}\left(L,L_i\cap L_k^S\right)}{\left|L_k^S\right|}-\sum_{k\neq m}\sum_{jh\in L}\frac{\theta_j}{\theta_j+\theta_h}\frac{\delta_{jh}\left(L,L_i\cap\left(L_k^S\cup L_m^S\right)\right)}{\left|L_k^S\cup L_m^S\right|}\\&\quad+\cdots+(-1)^{r(S)+1}\sum_{jh\in L}\frac{\theta_j}{\theta_j+\theta_h}\frac{\delta_{jh}\left(L,L_i\cap\left(\cup_{k=1}^{r(S)}L_k^S\right)\right)}{\left|\cup_{k=1}^{r(S)}L_k^S\right|}\\&=\sum_{k=1}^{r(S)}\sum_{ih\in L_k^S}\frac{\theta_i}{\theta_i+\theta_h}\frac{1}{\left|L_k^S\right|}-\sum_{k\neq m}\sum_{ih\in L_k^S\cup L_m^S}\frac{\theta_i}{\theta_i+\theta_h}\frac{1}{\left|L_k^S\cup L_m^S\right|}\\&\quad+\cdots+(-1)^{r(S)+1}\sum_{ih\in\cup_{k=1}^{r(S)}L_k^S}\frac{\theta_i}{\theta_i+\theta_h}\frac{1}{\left|\cup_{k=1}^{r(S)}L_k^S\right|}\\&=\sum_{k=1}^{r(S)}\frac{\sum_{ih\in L_k^S}\left(\theta_i/\left(\theta_i+\theta_h\right)\right)}{\left|L_k^S\right|}-\sum_{k\neq m}\frac{\sum_{ih\in L_k^S\cup L_m^S}\left(\theta_i/\left(\theta_i+\theta_h\right)\right)}{\left|L_k^S\cup L_m^S\right|}+\cdots+(-1)^{r(S)+1}\frac{\sum_{ih\in\cup_{k=1}^{r(S)}L_k^S}\left(\theta_i/\left(\theta_i+\theta_h\right)\right)}{\left|\cup_{k=1}^{r(S)}L_k^S\right|}.\end{aligned} \tag{12}$$

Therefore, the weighted position value meets the decomposability property, which completes the proof. □

Example 1. Let (N,u_s,L) be a communication situation game with Figure 1,

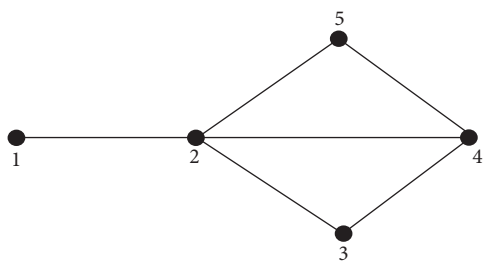

Figure 1: (N, L).

$$\begin{aligned} N &= \{1,2,3,4,5\}, \\ L &= \{\{1,2\},\{2,3\},\{2,4\},\{2,5\},\{3,4\},\{4,5\}\}, \\ S &= \{1,4\}, \\ \theta_i &= i, \\ i &= 1,2,\ldots,5, \end{aligned} \tag{13}$$

then

$$\begin{aligned} MC_L^e &= \left\{L_1^S, L_2^S, L_3^S\right\}, \\ L_1^S &= \{\{1,2\}\}\{2,3\},\{3,4\}\}, \\ L_2^S &= \{\{1,2\},\{2,4\}\}, \\ L_3^S &= \{\{1,2\},\{2,5\},\{4,5\}\}. \end{aligned} \tag{14}$$

If the distribution rule γ^θ is the weight Myerson value or weight position value, then

$$\begin{aligned} \gamma^\theta\left(N, u_{\{1,4\}}, L\right) = {} & h^\theta\left(N, L_1^S\right) + h^\theta\left(N, L_2^S\right) + h^\theta\left(N, L_3^S\right) \\ & - h^\theta\left(N, L_1^S \cup L_2^S\right) - h^\theta\left(N, L_1^S \cup L_3^S\right) \\ & - h^\theta\left(N, L_2^S \cup L_3^S\right) + h^\theta\left(N, L_1^S \cup L_2^S \cup L_3^S\right). \end{aligned} \tag{15}$$

If $h^\theta = c^{r^\theta}$, the weighted Myerson value can be obtained as follows:

$$\begin{aligned} \mu^\theta\left(N, u_{\{1,4\}}, L\right) = {} & \left(\frac{1}{10}, \frac{2}{10}, \frac{3}{10}, \frac{4}{10}, 0\right) + \left(\frac{1}{7}, \frac{2}{7}, 0, \frac{4}{7}, 0\right) \\ & + \left(\frac{1}{12}, \frac{2}{12}, 0, \frac{4}{12}, \frac{5}{12}\right) - \left(\frac{1}{10}, \frac{2}{10}, \frac{3}{10}, \frac{4}{10}, 0\right) \\ & - \left(\frac{1}{15}, \frac{2}{15}, \frac{3}{15}, \frac{4}{15}, \frac{5}{15}\right) - \left(\frac{1}{12}, \frac{2}{12}, 0, \frac{4}{12}, \frac{5}{12}\right) \\ & + \left(\frac{1}{15}, \frac{2}{15}, \frac{3}{15}, \frac{4}{15}, \frac{5}{15}\right) \\ = {} & \left(\frac{1}{7}, \frac{2}{7}, 0, \frac{4}{7}, 0\right). \end{aligned} \tag{16}$$

If $h_\theta = d^{r^\theta}$, the weighted position value can be obtained as follows:

$$\begin{aligned} \pi^w\left(N, u_{\{1,4\}}, L\right) = {} & \frac{(1/3, 2/3 + 2/5, 3/5 + 3/7, 4/7, 0)}{3} + \frac{(1/3, 2/3 + 2/6, 0, 4/6, 0)}{2} \\ & + \frac{(1/3, 2/3 + 2/7, 0, 4/9, 5/7 + 5/9)}{3} - \frac{(1/3, 2/3 + 2/5 + 2/6, 3/5 + 3/7, 4/6 + 4/7, 0)}{4} \\ & - \frac{(1/3, 2/3 + 2/5 + 2/7, 3/5 + 3/7, 4/7, 5/7 + 5/9)}{5} \\ & - \frac{(1/3, 2/3 + 2/6 + 2/7, 0, 4/6 + 4/9, 5/7 + 5/9)}{4} \\ & + \frac{(1/3, 2/3 + 2/5 + 2/6 + 2/7, 3/5 + 3/7, 4/6 + 4/7 + 4/9, 5/7 + 5/9)}{6} \\ = {} & \left(\frac{19}{90}, \frac{1613}{3150}, \frac{9}{175}, \frac{17}{105}, \frac{4}{63}\right). \end{aligned} \tag{17}$$

In particular, if $S = \{1,4\}, \theta_i = 1, i = 1,2,\ldots,5,$ the weighted Myerson value and the weighted position value are Myerson value and position value, respectively, the following calculation can be obtained:

$$\begin{aligned} \mu\left(N, u_{\{1,4\}}, L\right) &= \left(\frac{1}{3}, \frac{1}{3}, 0, \frac{1}{3}, 0\right), \pi\left(N, u_{\{1,4\}}, L\right) \\ &= \left(\frac{19}{60}, \frac{9}{20}, \frac{1}{20}, \frac{2}{15}, \frac{1}{20}\right). \end{aligned} \tag{18}$$

4. Conclusion

In this paper, a simpler weighted graph allocation rule which is used to calculate the weighted values has been investigated. Without the induced games, the weighted Myerson value and weight position value have been calculated by using the weighted graph allocation rule. It has been proved that both the weighted values can be calculated uniformly using the decomposability principle. In addition, it should be pointed out that the obtained results can be

extended to the future research about Myerson with edge weight and point-edge mixed weight.

Data Availability

No data were used to support this study. In this paper, the authors only use MATLAB for calculation.

Conflicts of Interest

The authors declare that they have no conflicts of interest.

References

[1] R. Branzei, D. Dimitrov, and S. Tijs, *Models in Cooperative Game Theory*, Springer, Berlin, Germany, 2008.

[2] R. B. Myerson, "Graphs and cooperation in games," *Mathematics of Operations Research*, vol. 2, no. 3, pp. 225–229, 1977.

[3] L. S. Shapley, "A value for n-person games," in *Contributions to the Theory of Games II*, pp. 307–317, Princeton University Press, Princeton, NJ, USA, 1953.

[4] R. B. Myerson, "Conference structures and fair allocation rules," *International Journal of Game Theory*, vol. 9, no. 3, pp. 169–182, 1980.

[5] M. Slikker and A. van den Nouweland, *Social and Economic Networks in Cooperative Game Theory*, Kluwer Academic Publishers, Boston, MA, USA

[6] D. L. Li and E.-F. Shan, "The Myerson value on local structures of coalitions," *Journal of the Operations Research Society of China*, vol. 7, no. 3, pp. 461–473, 2019.

[7] D. Li and E. Shan, "The Myerson value for directed graph games," *Operations Research Letters*, vol. 48, pp. 42–46, 2020.

[8] E. Shan, J. Han, and J. Shi, "The efficient proportional Myerson values," *Operations Research Letters*, vol. 47, no. 6, pp. 574–578, 2019.

[9] A. van den Nouweland, P. Borm, and S. Tijs, "Allocation rules for hypergraph communication situations," *International Journal of Game Theory*, vol. 20, no. 3, pp. 255–268, 1992.

[10] E. Algaba, J. M. Bilbao, P. Borm, and J. J. López, "The Myerson value for union stable structures," *Mathematical Methods of Operations Research*, vol. 54, no. 3, pp. 359–371, 2001.

[11] P. Borm, G. Owen, and S. Tijs, "On the position value for communication situations," *Siam Journal on Discrete Mathematics*, vol. 5, no. 3, pp. 305–320, 1992.

[12] R. Meessen, "Communication games," Master's thesis, Department of Mathematics, University of Nijmegen, Nijmegen, The Netherlands, 1988, in Dutch.

[13] M. Slikker, "A characterization of the position value," *International Journal of Game Theory*, vol. 33, no. 4, pp. 505–514, 2005.

[14] D. L. Li and E. Shan, "The position value and the structures of graphs," *Applied Mathematics and Computation*, vol. 356, pp. 190–197, 2019.

[15] E. Shan and G. Zhang, "The position value and the Myerson value for hypergraph communication situations," *Static & Dynamic Game Theory: Foundations & Applications*, pp. 237–250, 2018.

[16] G. Haeringer, "Weighted Myerson value," *International Game Theory Review*, vol. 2, no. 2, pp. 187–192, 1999.

[17] M. Slikker and A. van den Nouweland, "Communication situations with asymmetric players," *Mathematical Methods of Operations Research (ZOR)*, vol. 52, no. 1, pp. 39–56, 2000.

[18] E. Kalai and D. Samet, "On weighted Shapley values," *International Journal of Game Theory*, vol. 16, no. 3, pp. 205–222, 1987.

[19] A. Ghintran, "Weighted position values," *Mathematical Social Sciences*, vol. 65, no. 3, pp. 157–163, 2013.

[20] R. Xu and F. Zhang, "ϵ-nash mean-field games for general linear-quadratic systems with applications," *Automatica*, vol. 114, pp. 108835-108836, 2020.

[21] Y. Wang, T. Liu, and D. Cheng, "From weighted potential game to weighted harmonic game," *IET Control Theory & Applications*, vol. 11, no. 13, pp. 2161–2169, 2017.

[22] L. Liu, B. Li, and R. Guo, "Consensus control for networked manipulators with switched parameters and topologies," *IEEE Access*, vol. 9, p. 9209, 2021.

[23] X. Yi, R. Guo, and Y. Qi, "Stabilization of chaotic systems with both uncertainty and disturbance by the UDE-based control method," *IEEE Access*, vol. 8, no. 1, pp. 62471–62477, 2020.

Hindawi
Mathematical Problems in Engineering
Volume 2020, Article ID 9543928, 13 pages
https://doi.org/10.1155/2020/9543928

Research Article

Model Predictive Control Based on Parametric Disturbance Compensation

Lingliang Xu,[1] **Guiming Chen**,[1] **Guangshuai Li**,[2] **and Qiaoyang Li**[1]

[1]*College of Combat Support, Xi'an Research Institute of High-Tech, Xi'an 710025, China*
[2]*College of Nuclear Engineering, Xi'an Research Institute of High-Tech, Xi'an 710025, China*

Correspondence should be addressed to Guiming Chen; 792757066@qq.com

Received 16 March 2020; Revised 26 April 2020; Accepted 19 September 2020; Published 7 October 2020

Academic Editor: Jose Vicente Salcedo

Model predictive control (MPC) has been widely implemented in the motor because of its simple control design and good results. However, MPC relies on the permanent magnet synchronous motor (PMSM) system model. With the operation of the motor, parameter drift will occur due to temperature rise and flux saturation, resulting in model mismatch, which will seriously affect the control accuracy of the motor. This paper proposes a model predictive control based on parameter disturbance compensation that monitors system disturbances caused by motor parameter drift and performs real-time parameter disturbance compensation. And the frequency-domain method was used to analyze the convergence and filterability of the model. The Bode diagram of measurement error and input disturbance was studied when the parameters were underdamped, critically damped, and overdamped. Guidelines for parameter selection are given. Simulation results show that the proposed method has good dynamic performance, anti-interference ability, and parameter robustness, which effectively avoids the current static difference and oscillation problems caused by parameter changes.

1. Introduction

Since the discovery of electromagnetic induction by Faraday in 1831, scholars around the world have been exploring new areas of application, among which electromagnetic launch technology is one of the newer fields. As a driving device of electromagnetic launch technology, electric motors play an important role. The permanent magnet synchronous motor (PMSM) has the obvious advantages of small size, low power consumption, high transmission efficiency, and high power-weight ratio [1], making it the first choice in the electromagnetic launch research field.

PMSM is a complex system with multiple variables, strong coupling, nonlinearity, and variable parameters, hence the need for the adoption of a reasonable control method to control it [2]. Traditional control methods include vector control and direct torque control.

The vector control technology is based on the idea that the armature current and the excitation current of the direct current (DC) motor are perpendicular to each other without coupling and independent control. Based on coordinate transformation, the size and direction of the stator current in the synchronous rotating coordinate system are controlled to achieve decoupling. The purpose is to realize the decoupling of magnetic field and torque. But in the vector control module, there are many intermediate variables involved in the design of the parameter setting method of the speed loop PI regulator, and in many cases are approximate results obtained based on assumptions. To overcome the shortcomings, Singh et al. [3] discussed the changes of various parameters. The effect on the output and torque of the PI regulator exposed the limitations of PI control. Templos-Santos et al. [4] evaluated the efficiency of five bionic optimization algorithms by introducing two reference speed profiles and finally selected the free radical algorithm to adjust PI control device parameters.

Direct torque control (DTC) utilizes bang-bang control to generate pulse width modulation (PWM) signals and optimally control the inverter switches to obtain high dynamic performance of torque. DTC solves some of the problems in vector

control, such as the complexity of calculation and the large error caused by model mismatch. However, the torque and magnetic flux pulsation generated by DTC are large, and the switching frequency is variable [5–7]. In order to overcome the shortcomings of large torque and magnetic flux pulsations, Zhang and Zhu [8] used an appropriate permutation vector sequence and adopted the amplitude and phase compensation voltage model of the low-pass filter to obtain an accurate stator flux linkage estimation to reduce smaller pulsation. Zhang and Zhu [9] established a unified switch table and performed three-vector selection instead of the traditional two-vector selection to obtain smaller torque and flux ripple.

To further improve the control performance of the PMSM and solve the problems of motor control under complex conditions, various control methods such as sliding mode control of variable structure, modern intelligent control, and model predictive control (MPC) have been proposed. MPC occupies an important position due to its multiobjective, multivariable, and multiconstraint control characteristics, as well as its intuitive and simple design methods [10, 11].

MPC discretizes the mathematical model of PMSM to obtain the control vector for the next period. Therefore, MPC depends on the PMSM system model, but as the motor runs, the motor parameters will be affected by factors such as temperature, motor operating state, and magnetic field saturation. Parameter drift occurs, model mismatch occurs, and then reusing the marked parameters on the motor nameplate will cause greater errors, which will reduce the control accuracy of the PMSM system [12]. Young et al. [13] carried out an experimental evaluation of the model mismatch caused by changes in load parameters and analyzed that the steady-state performance and transient performance of PMSM were greatly affected by the model error. In order to reduce the control deterioration due to model mismatch, Xia et al. [14] estimated the model uncertainty by minimizing the error between the measured current and the model current, but this method focuses more on the uncertainty of the converter than the model parameters. Antoniewicz and Kazmierkowski [15] proposed an improved direct power prediction algorithm to minimize the difference between instantaneous power and reactive power and avoid the impact of inductance changes.

With the operation of the motor, motor parameters will be affected by factors such as temperature, motor operating state, magnetic field saturation, various disturbances, and so on, resulting in parameter drift and model mismatch and severely affecting the stability of PMSM. This paper analyzes the effects of model mismatch caused by changes in parameter resistance, inductance, and magnetic flux. Aiming at the disturbance caused by parameter drift, external input deviation, and measurement error during the operation of the motor, an expanded state observer is designed to monitor the disturbance in real time and perform disturbance compensation to improve the system's robust performance [16–21]. In view of the problem of gain parameters in the extended state observer, the frequency-domain analysis method is used to determine the appropriate parameters to improve the stability of the motor operation. Simulation results show that the model established has good parameter robustness and avoids current static differences and oscillation problems caused by parameter drift. Under actual production conditions, this control method is helpful to solve the model mismatch problem that occurs during the operation of the motor, which is conducive to the smooth operation of the motor without large fluctuations, and the production process is not interrupted and the production operations are carried out in an orderly manner.

The structure of this paper is as follows. Section 2 describes the PMSM mathematical model and analyzes the model mismatch caused by parameter changes. Section 3 discretizes the mismatched mathematical model and obtains the control vector for the next period. Considering the influence of parameter changes, an extended state observer is constructed. In Section 4, we consider the one-shot delay of the digital control system and perform control delay compensation. In Section 5, the frequency-domain analysis method is used to analyze the convergence and filtering of the model. Section 6 gives the simulation results. Section 7 concludes the paper.

2. Model Mismatch Analysis

The mathematical model of PMSM [22] under the d-q axis of the rotating coordinate system is

$$\begin{cases} u_d = R_0 i_d + \dfrac{\mathrm{d}\psi_d}{\mathrm{d}t} - \omega\psi_q, \\ u_q = R_0 i_q + \dfrac{\mathrm{d}\psi_q}{\mathrm{d}t} + \omega\psi_d, \end{cases} \tag{1}$$

$$\begin{cases} \psi_d = L_d i_d + \psi_{f0}, \\ \psi_q = L_q i_q. \end{cases} \tag{2}$$

Substitute formula (2) into formula (1) to get

$$\begin{cases} u_d = R_0 i_d + L_d \dfrac{\mathrm{d}i_d}{\mathrm{d}t} - \omega L_q i_q, \\ u_q = R_0 i_q + L_q \dfrac{\mathrm{d}i_q}{\mathrm{d}t} + \omega L_d i_d + \omega\psi_{f0}. \end{cases} \tag{3}$$

Among them, u_d and u_q are the stator d-q axis voltage components, Ψ_d and Ψ_q are the d-q axis components of the stator flux linkage, R_0 is the stator resistance, L_d and L_q are inductances of d-q axis, respectively. For a surface-mounted PMSM (SPMSM) control, the stator inductance meets $L_d = L_q = L_0$. i_d and i_q are, respectively, the stator d-q axis current components, Ψ_{f0} is the permanent magnet flux, p is the number of pole pairs, ω is the motor speed, and T_e is the electromagnetic torque.

Selecting the stator current as the state variable, according to formula (3), the following can be obtained:

$$\begin{cases} \dot{i}_d = \dfrac{u_d}{L_0} - \dfrac{R_0 i_d}{L_0} + \dfrac{\omega L_0 i_q}{L_0}, \\ \dot{i}_q = \dfrac{u_q}{L_0} - \dfrac{R_0 i_q}{L_0} + \omega i_d + \dfrac{\omega\psi_{f0}}{L_0}, \end{cases} \tag{4}$$

$$\dot{i} = Ai + Bu + d, \tag{5}$$

where

$$i = \begin{bmatrix} i_d \\ i_q \end{bmatrix}, \quad u = \begin{bmatrix} u_d \\ u_q \end{bmatrix}, \quad d = \begin{bmatrix} 0 \\ \dfrac{-\omega\psi_{f0}}{L} \end{bmatrix}, \quad A_0 = \begin{bmatrix} \dfrac{-R_0}{L_0} & \omega \\ \omega & \dfrac{-R_0}{L_0} \end{bmatrix}, \quad B_0 = \begin{bmatrix} \dfrac{1}{L_0} & \omega \\ \omega & \dfrac{1}{L_0} \end{bmatrix}. \tag{6}$$

The continuous time model (formula (5)) was discretized to obtain the state space model of the discrete time system:

$$i(k+1) = Ai(k) + Bu(k) + T_s d(k), \tag{7}$$

where

$$\begin{cases} A = e^{A_0 T_s} = 1 + A_0 T_s, \\ B = \displaystyle\int_0^{T_s} e^{A_c \tau} \mathrm{d}\tau \times B_0. \end{cases} \tag{8}$$

In the actual algorithm, the parameters used in the model are nominal values on the nameplate of the motor, and the predicted current is

$$\begin{cases} i_{d0}(k+1) = \left(1 - \dfrac{R_0}{L_0} T_s\right) i_d(k) + \dfrac{T_s}{L_0} u_{d0}(k) + T_s \omega i_q(k), \\ i_{q0}(k+1) = \left(1 - \dfrac{R_0}{L_0} T_s\right) i_q(k) + \dfrac{T_s}{L_0} u_{q0}(k) + \omega T_s i_d(k) - T_s \dfrac{\omega\psi_{f0}}{L_0}. \end{cases} \tag{9}$$

The values of the parameters R_0, L_0, and Ψ_{f0} are the standard values on the motor nameplate.

However, in the actual control process, with the motor running, the parameters of the motor will change, and the predicted current is

$$\begin{cases} i_d(k+1) = \left(1 - \dfrac{R}{L} T_s\right) i_d(k) + \dfrac{T_s}{L} u_d(k) + T_s \omega i_q(k), \\ i_q(k+1) = \left(1 - \dfrac{R}{L} T_s\right) i_q(k) + \dfrac{T_s}{L} u_q(k) + \omega T_s i_d(k) - T_s \dfrac{\omega\psi_f}{L}. \end{cases} \tag{10}$$

The values of the parameters R, L, Ψ_f are the actual values of the motor.

Due to the influence of temperature rise, flux saturation, and other factors, the nominal value on the nameplate of the motor will produce an error with the actual value. We make the control voltage equal and get the relationship between the actual predicted current and the ideal predicted current:

$$\begin{cases} u_d(k) = u_{d0}(k), \\ u_q(k) = u_{q0}(k). \end{cases} \tag{11}$$

Then,

$$\begin{cases} i_d(k+1) = \dfrac{L_0}{L} i_{d0}(k+1) + \dfrac{\Delta L - RT_s}{L} i_d(k) + \dfrac{\Delta L}{L} T_s \omega i_q(k), \\ i_q(k+1) = \dfrac{L_0}{L} i_{q0}(k+1) + \dfrac{\Delta L - \Delta R T_s}{L} i_q(k) - \dfrac{\Delta L}{L} T_s \omega i_d(k) - \dfrac{\Delta\psi_f}{L} T_s \omega, \end{cases} \tag{12}$$

where $\Delta L = L - L_0$, $\Delta R = R - R_0$, and $\Delta\Psi_f = \Psi_f - \Psi_{f0}$. Because the sampling time T_s is small enough and $i_d = 0$, the Z transform of equation (12) can be used to obtain the following equation:

$$\begin{cases} z \times i_d(z) = z \dfrac{L_0}{L} i_{d0}(z) + \dfrac{\Delta L}{L} i_d(z), \\ z \times i_q(k+1) = z \dfrac{L_0}{L} i_{q0}(z) + \dfrac{\Delta L}{L} i_q(k). \end{cases} \tag{13}$$

Therefore, the transfer function between the actual value of current prediction and the nominal value is obtained as

$$\frac{i_{d,q}(z)}{i_{d0,q0}(z)} = \frac{(L_0/L) \times z}{z + ((L_0/L) - 1)}. \tag{14}$$

To maintain the stability of the discrete system, the poles of the discrete system are located in the unit circle, that is, $|(L_0/L) - 1| \le 1$; when $0 \le L_0 \le 2L$, the system is in a stable state, and when the inductance value on the nameplate of the motor is

greater than twice the actual inductance value, the system will be unstable, resulting in oscillation and current static difference.

3. Mathematical Model of PMSM Based on Parameter Disturbance

When parameter perturbation is considered, the PMSM mathematical model changes from formula (1) to

$$\begin{cases} u_d = (R_0 + \Delta R)i_d + (L_0 + \Delta L)\dfrac{\mathrm{d}i_d}{\mathrm{d}t} - \omega(L_0 + \Delta L)i_q, \\ u_q = (R_0 + \Delta R)i_q + (L_0 + \Delta L)\dfrac{\mathrm{d}i_q}{\mathrm{d}t} + \omega(L_0 + \Delta L)i_d + \omega(\psi_{f0} + \Delta\psi_f), \end{cases} \tag{15}$$

where R_0, L_0, and Ψ_{f0}, respectively, correspond to the motor nameplate resistance, inductance, and magnetic flux calibration values and ΔR, ΔL, and $\Delta\Psi_f$ are parameter change values. Formula (15) simplifies to

$$\begin{cases} \dfrac{\mathrm{d}i_d}{\mathrm{d}t} = \dfrac{u_d}{L_0} + \left(-\dfrac{\Delta L}{L_0}\dfrac{\mathrm{d}i_d}{\mathrm{d}t} - \dfrac{(R_0 + \Delta R)i_d}{L_0} + \dfrac{\omega(L_0 + \Delta L)i_q}{L_0}\right), \\ \dfrac{\mathrm{d}i_q}{\mathrm{d}t} = \dfrac{u_q}{L_0} + \left(-\dfrac{\Delta L}{L_0}\dfrac{\mathrm{d}i_q}{\mathrm{d}t} - \dfrac{(R_0 + \Delta R)i_q}{L_0} + \dfrac{\omega(L_0 + \Delta L)i_d}{L_0} + \dfrac{\omega(\psi_{f0} + \Delta\psi_f)}{L_0}\right), \end{cases} \tag{16}$$

where the d-q axis current is the state variable and the d-q axis voltage is the control variable. If the remaining parameter variation terms, which correspond to the total disturbance of parameter changes, are expressed as E_d and E_q, formula (16) can be simplified into

$$\begin{cases} \dfrac{\mathrm{d}i_d}{\mathrm{d}t} = \dfrac{u_d}{L_0} + E_d, \\ \dfrac{\mathrm{d}i_q}{\mathrm{d}t} = \dfrac{u_q}{L_0} + E_q, \end{cases} \tag{17}$$

where

$$\begin{cases} E_d = -\dfrac{\Delta L}{L_0}\dfrac{\mathrm{d}i_d}{\mathrm{d}t} - \dfrac{(R_0 + \Delta R)i_d}{L_0} + \dfrac{\omega(L_0 + \Delta L)i_q}{L_0}, \\ E_q = -\dfrac{\Delta L}{L_0}\dfrac{\mathrm{d}i_q}{\mathrm{d}t} - \dfrac{(R_0 + \Delta R)i_q}{L_0} + \dfrac{\omega(L_0 + \Delta L)i_d}{L_0} + \dfrac{\omega(\psi_{f0} + \Delta\psi_f)}{L_0}. \end{cases} \tag{18}$$

Taking the d-axis as an example, an extended state observer is established [23–25], and its state space equation is

$$\begin{cases} \Delta m_d = z_{1d} - i_d, \\ \dot{z}_{1d} = z_{2d} + bu_d - \beta_{1d}\Delta m_d, \\ \dot{z}_{2d} = -\beta_{2d}\Delta m_d, \end{cases} \tag{19}$$

where z_{1d} is the observed value of i_d, z_{2d} is the observed value of E_d, and β_{1d} and β_{2d} are the gains of each state observer, respectively.

To enhance the antidisturbance ability of the system and neutralize the interference caused by the uncertain factors of the system, a nonlinear error feedback control rate is designed:

$$\begin{cases} u_0 = \beta_{3d}(i_d^* - i_d), \\ u_d = \dfrac{u_0 - z_{2d}}{b}, \end{cases} \tag{20}$$

where β_{3d} represents the system's unknown interference gain.

Consistent with the discretization method of formula (5), discretization is carried out in formula (19) to obtain the discretization state space equation as

$$\begin{cases} \Delta m_d(k) = z_{1d}(k) - i_d(k), \\ z_{1d}(k+1) = z_{1d}(k) + T_s \times \{z_{2d}(k) + bu_d(k) - \beta_{1d}\Delta m_d(k)\}, \\ z_{2d}(k+1) = z_{2d}(k) - T_s\beta_{2d}\Delta m_d(k). \end{cases} \tag{21}$$

Applying the Z transformation to formula (21) yields

$$\begin{cases} \Delta m_d(z) = z_{1d}(z) - i_d(z), \\ z \cdot z_{1d}(z) = z_{1d}(z) + T_s \times \{z_{2d}(z) + bu_d(z) - \beta_{1d}\Delta m_d(z)\}, \\ z \cdot z_{2d}(z) = z_{2d}(z) - T_s\beta_{2d}\Delta m_d(z). \end{cases} \tag{22}$$

Then, the transfer function of the discrete system is

$$G_1(z) = \frac{z_{1d}(z)}{i_d(z)} = \frac{\beta_1 z + \beta_2 T_s - \beta_1}{(z-1)^2 + \beta_1 z + \beta_2 T_s - \beta_1}. \tag{23}$$

where $\beta_1 = \beta_{1d}T_s$ and $\beta_2 = \beta_{2d}T_s$.

To maintain the stability of the discrete system, the poles of the discrete system should be located in the unit circle, and hence the characteristic equation can be obtained as

$$(z-1)^2+\beta_1 z+\beta_2 T_s-\beta_1=0. \tag{24}$$

To apply the Routh–Hurwitz criterion, let $z=((\lambda+1)/(\lambda-1))$, thus yielding the characteristic equation of λ domain as

$$\beta_2 T_s\lambda^2+2(\beta_1-\beta_2 T_s)\lambda+(4+\beta_2 T_s-\beta_1)=0. \tag{25}$$

According to the Rolls-Helvitz criterion, each coefficient of the order equation is greater than 0, and the range of gain coefficients is obtained by

$$\begin{cases}\beta_2 T_s<\beta_1<4+\beta_2 T_s,\\ \beta_2>0.\end{cases} \tag{26}$$

The total perturbation observations z_{2d} and z_{2q} of parameter changes are substituted into formula (17) and discretized to obtain the predicted current value based on parameter perturbations, that is,

$$\begin{cases} i_d(k+1)=i_d(k)+\dfrac{T_s}{L_0}u_d(k)+T_s z_{2d},\\ i_q(k+1)=i_q(k)+\dfrac{T_s}{L_0}u_q(k)+T_s z_{2q}.\end{cases} \tag{27}$$

Then, according to formula (27), the required d-q control voltage is obtained as

$$\begin{cases} u_d(k)=\dfrac{L_0}{T_s}\{i_d(k+1)-i_d(k)\}-L_0 z_{2d},\\ u_q(k)=\dfrac{L_0}{T_s}\{i_q(k+1)-i_q(k)\}-L_0 z_{2q}.\end{cases} \tag{28}$$

When $i_d(k+1)=i_d^*$ and $i_q(k+1)=i_q^*$, where i_d^* and i_q^* are the output currents of the PMSM speed ring, for the control needed when the current values i_d^* and i_q^* are output, the voltage is obtained by

$$\begin{cases} u_d^*=\dfrac{L_0}{T_s}\{i_d^*-i_d(k)\}-L_0 z_{2d},\\ u_q^*=\dfrac{L_0}{T_s}\{i_q^*-i_q(k)\}-L_0 z_{2q}.\end{cases} \tag{29}$$

The optimal basic voltage is finally obtained.

The MPC based on parametric disturbance compensation is shown in Figure 1.

4. Control Delay Compensation

In the process of digital system control, there is a beat delay between the actual output instruction and the control instruction; therefore, the model prediction method was used to compensate this delay [26]. The specific method is given as follows: firstly, $u_d(k)$ and $u_q(k)$ were used to calculate the prediction current $i_d(k+1)$ and $i_q(k+1)$ at the next moment of the d-q axis. Using (29), $i_d(k)$ and $i_q(k)$ were replaced in $i_d(k+1)$ and $i_q(k+1)$, respectively, and u_d^* and u_q^* were obtained. The algorithm flow of the proposed method is shown in Figure 2.

5. Analysis of PMSM Model Based on the Frequency-Domain Method

5.1. Convergence Analysis of PMSM Model. According to formulas (17) and (19),

$$\Delta\dot{m}_d=\dot{z}_{1d}-\dot{i}_d=z_{2d}-\beta_{1d}\Delta m_d-E_d. \tag{30}$$

Consistent with the discretization method of formula (5), the discretized state space equation of formula (30) is

$$\Delta m_d(k+1)=(1-\beta_{1d}T_s)\Delta m_d(k)+T_s(z_{2d}-E_d). \tag{31}$$

Formula (31) is transformed by Z:

$$z\cdot\Delta m_d(z)=(1-\beta_{1d}T_s)\Delta m_d(z)+T_s\{z_{2d}(z)-E_d(z)\}. \tag{32}$$

Combined with formula (22), the closed-loop transfer function can be obtained as

$$G_2(z)=\frac{z_{2d}(z)}{E_d(z)}=\frac{\beta_2 T_s}{(z-1)^2+\beta_1 z+\beta_2 T_s-\beta_1}. \tag{33}$$

Substituting $z=j\omega$ into formulas (23) and (33) yields

$$\begin{cases} G_1(j\omega)=\dfrac{z_{1d}(j\omega)}{i_d(j\omega)}=\dfrac{j\beta_1\omega+\beta_2 T_s-\beta_1}{(j\omega-1)^2+j\beta_1\omega+\beta_2 T_s-\beta_1}=\dfrac{(j\omega-1)\beta_1}{(1-\omega^2-2j\omega)+\beta_2 T_s+(j\omega-1)\beta_1},\\ G_2(j\omega)=\dfrac{z_{2d}(j\omega)}{E_d(j\omega)}=\dfrac{\beta_2 T_s}{(j\omega-1)^2+j\beta_1\omega+\beta_2 T_s-\beta_1}=\dfrac{\beta_2 T_s}{(1-\omega^2-2j\omega)+\beta_2 T_s+(j\omega-1)\beta_1}.\end{cases} \tag{34}$$

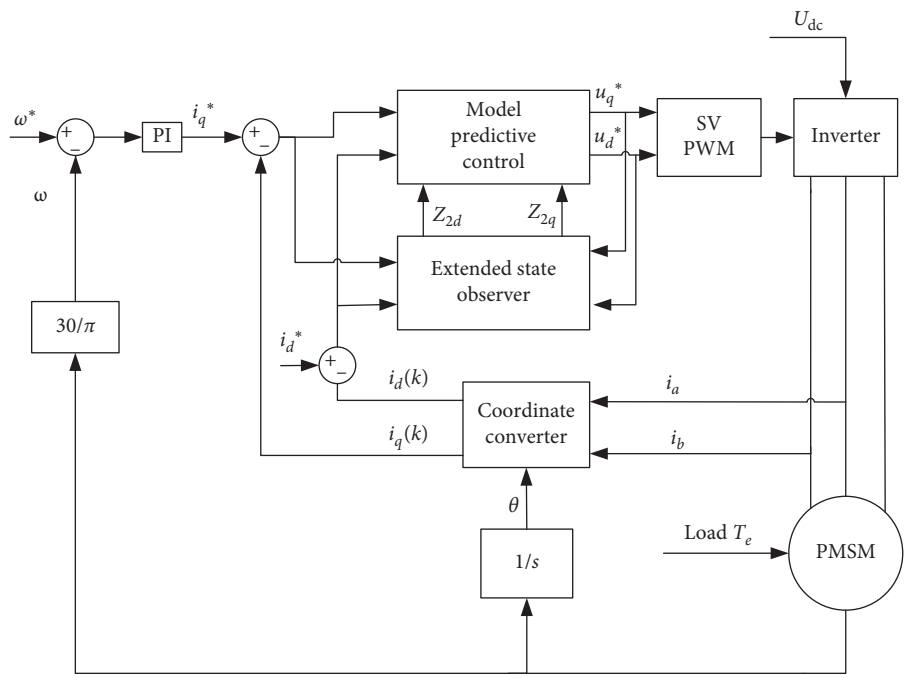

Figure 1: MPC based on parametric disturbance compensation.

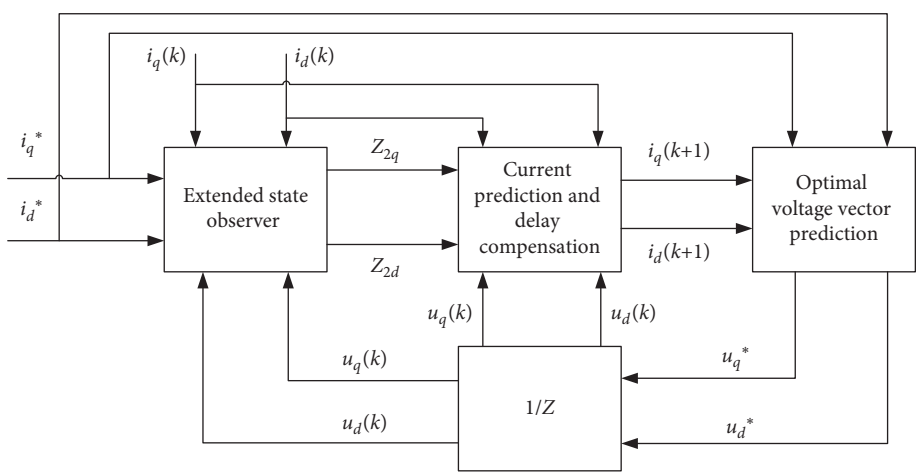

Figure 2: Flowchart of control delay compensation method.

According to the knowledge of classical control theory, when the maximum cutoff frequency of $\omega_{\max}$ at the i-th channel in the control system and the gain parameters β_1 and β_2 satisfy $\min\{\beta_1, \beta_2\} \gg \omega_{\max}$, then under the condition $\omega \leq \omega_{\max}$, the system transfer function is

$$\begin{cases} G_1(j\omega) \approx 1, \\ G_2(j\omega) \approx 1. \end{cases} \tag{35}$$

It can be observed from formula (35) that the control system converges and is stable at this time, $z_{1d} \longrightarrow i_d$, $z_{2d} \longrightarrow E_d$. This shows that the observed values obtained by the constructed system model reflect the true values more accurately.

In the PMSM motion control system, the speed control loop is used as the outer loop and the current control loop is used as the inner loop. The purpose of the speed control loop is to control the speed of the motor so that it can both regulate and stabilize the speed. The purpose of the current control loop is to focus on the dynamic adjustment process of the control system so that the stator current can track the given current vector more accurately and quickly. To achieve a good control effect, the current inner loop control cycle should generally be short, the bandwidth should be high, and the speed outer loop bandwidth should be low. The common PMSM has a current loop bandwidth of 2.5 kHz and a speed loop bandwidth of 400 Hz. According to the analysis of the actual situation, the proposed model is feasible and meets the convergence requirement.

5.2. Filtering Performance Analysis of PMSM Model. During the operation of the motor, the parameter drift and the disturbance of external noise will cause the model

mismatch of the motor model established above, hence the need to analyze the filterability and robustness of the established PMSM model. According to formula (19),

$$\begin{cases} z_{1d} \cdot s = -s^{-1}\beta_{2d} \cdot z_{1d} + s^{-1}\beta_{2d} \cdot i_d + bu_d - \beta_{1d} \cdot z_{1d} + \beta_{1d} \cdot i_d, \\ z_{2d} \cdot s = -\beta_{2d} \cdot z_{1d} + \beta_{2d} \cdot i_d. \end{cases} \tag{36}$$

This can be further simplified to

$$\begin{cases} z_{1d} = \dfrac{\beta_{1d} \cdot s + \beta_{2d}}{s^2 + \beta_{1d} \cdot s + \beta_{2d}} i_d + \dfrac{bs}{s^2 + \beta_{1d} \cdot s + \beta_{2d}} u_d, \\ z_{2d} = \dfrac{\beta_{2d} \cdot s}{s^2 + \beta_{1d} \cdot s + \beta_{2d}} i_d - \dfrac{b\beta_{2d}}{s^2 + \beta_{1d} \cdot s + \beta_{2d}} u_d. \end{cases} \tag{37}$$

It can be seen from formula (37) that the state observers z_{1d} and z_{2d} are related to the measured value i_d and the input value u_d. Because this paper focuses on the analysis of model mismatch caused by parameter disturbance, the filter and robustness of the parameter disturbance observer will be analyzed next.

Characterize the transfer function of the state observer z_{2d} as

$$\begin{cases} f_{2d1} = \dfrac{\beta_{2d} \cdot s}{s^2 + \beta_{1d} \cdot s + \beta_{2d}}, \\ f_{2d2} = \dfrac{b\beta_{2d}}{s^2 + \beta_{1d} \cdot s + \beta_{2d}}. \end{cases} \tag{38}$$

The characteristic equations of f_{2d1} and f_{2d2} transfer functions are

$$s^2 + \beta_{1d} \cdot s + \beta_{2d} = 0. \tag{39}$$

According to the classical control theory, the speed of convergence of the observer for z_{2d} estimation is directly related to the characteristic equation. Define the damping ratio ξ as

$$\xi = \frac{\beta_{1d}}{2\sqrt{\beta_{2d}}}. \tag{40}$$

The damping ratio ξ is divided into three states: underdamping, critical damping, and overdamping. The transfer function of the observer z_{2d} operates in these three states, as shown in the amplitude-frequency characteristics and phase-frequency characteristics of its Bode diagram. By fixing $\beta_{1d} = 10$, ξ becomes equal to 0.707, 1, and 1.770, corresponding to the three states of the damping ratio. At this time, using formula (40) can yield $\beta_{2d} = 50.015$, 25, and 7.980.

The Bode diagram of the measurement error transfer function f_{2d1} due to the measurement value i_d is shown in Figure 3.

Because the noise signal is generally a high-frequency signal, the amplitude of the logarithmic amplitude frequency of the system transfer function in the high-frequency band directly reflects the suppression effect of the system on the high-frequency noise signal. Lower amplitudes correspond to an increased ability of the system to suppress higher-frequency noise signals. The characteristics near the cutoff frequency determine the stability of the dynamic response of the system, and the size of the cutoff frequency determines the fast response. With the decrease in the β_{2d} value, the system operates under the three states: underdamping, critical damping, and overdamping. These three states change little in the low-frequency band. In contrast, the amplitude gradually decreases in the high-frequency band, which means that the attenuation characteristics increase, thus increasing its ability to suppress high-frequency noise. However, the cutoff frequency of the system decreases in turn, so the rapidity of the system's dynamic response gradually decreases. In the overdamped state, the system's ability to suppress high-frequency noise is enhanced, and the anti-interference ability is enhanced as well; however, the dynamic response characteristics are slower, and the stability is poor, while in the underdamped state, the system's anti-interference ability and robustness are reduced, and the dynamic response is faster. Therefore, according to the research needs, appropriate parameters can be debugged to obtain the desired anti-interference ability and dynamic response speed.

Input perturbations caused by the input value u_d. By observing the molecules of its characteristic function f_{2d2}, the transition frequency of the transfer function f_{2d2}, namely, $\sqrt{b\beta_{2d}}$, will not change and the low-frequency and high-frequency characteristics of the system are directly related to this transition frequency. Therefore, the low-frequency and high-frequency characteristics of the system are unchanged. However, when β_{1d} is fixed and different β_{2d} values are selected, different system characteristics will be obtained. It can be seen from Figure 4 that with the decrease of β_{2d}, the system operates in the three states: underdamping, critical damping, and overdamping in turn. The system is in a low-frequency band, and its characteristics are unchanged, similar to a low-pass filter. Compared with the underdamped state, the overdamped state has a higher amplitude in the high-frequency range, but the cutoff frequency is larger; therefore, the system has a stronger anti-interference ability in the overdamped state.

5.3. Selection of Gain Parameters. According to the above analysis, the anti-interference ability of the system and the its dynamic response speed are not only related to β_{1d} and β_{2d} parameter values but also to the relationship between them. When the system's damping ratio is in different states, different system characteristics will be obtained. The bandwidth of the observer and the bandwidth of the controller can be used to set the parameters. When the natural frequency ω_0 of the system channel is known and the system satisfies formula (35), the system converges. To improve the stability of the system, $\beta_{2d} = \omega_0^2$ is selected. Taking the underdamped system as an example, let $\xi = 0.707$, we can obtain β_{1d} from equation (40). Under this condition, the system is underdamped, and the dynamic response speed is fast, but the anti-interference

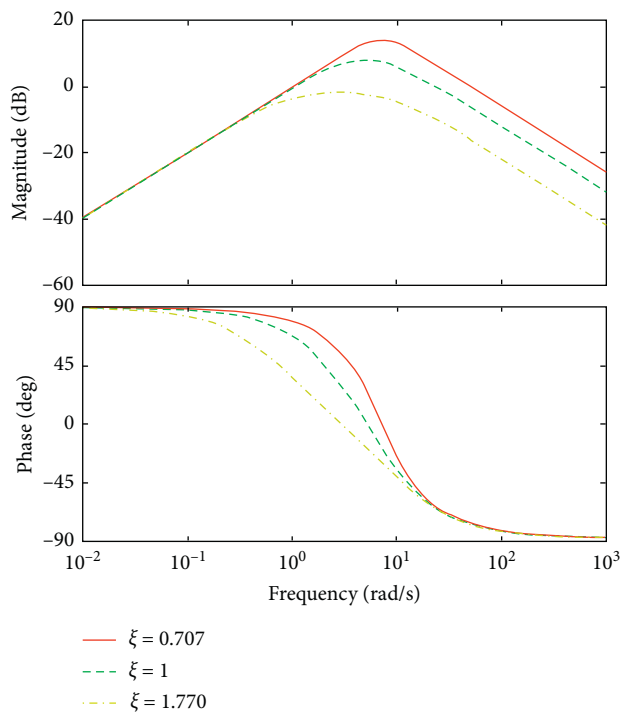

Figure 3: The noise frequency characteristics measured under different ξ conditions.

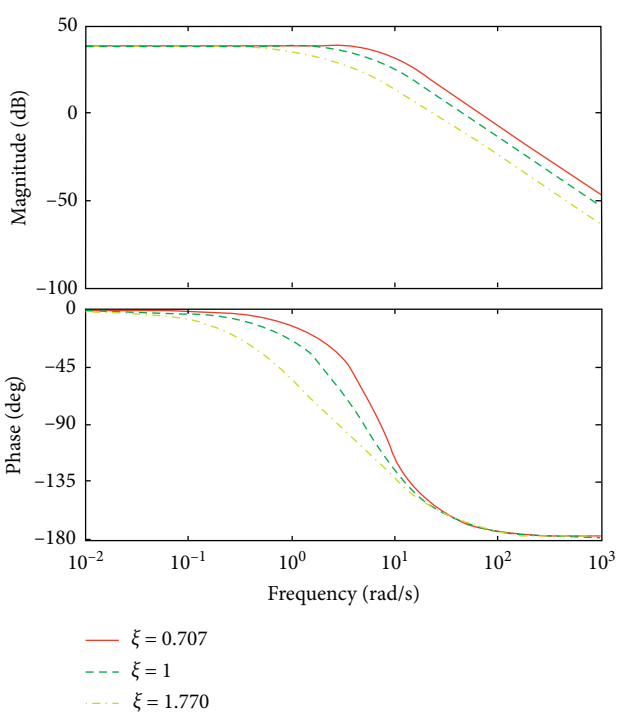

Figure 4: Input disturbance frequency characteristics under different ξ conditions.

ability and robustness are poor. Therefore, according to the requirements, the amplitude-frequency characteristics and phase-frequency characteristics should be analyzed before changing the parameters to achieve a balanced compromise.

6. Simulation Verification

To verify the effectiveness of the method proposed in this paper, MATLAB/Simulink simulation software was used for the simulation experiment. The simulation experiment parameters are listed in Table 1. The inductance disturbance was set as a straight slope from $0.5L_0$ to $2.5L_0$ during a time interval from 0.1 s to 0.3 s.

First, only continuous inductance disturbance was considered in a no-load scenario. As can be seen from Figure 5, due to the influence of the inductance disturbance, the traditional vector control method showed a large ripple in the motor speed, electromagnetic torque, and d-q axis current, which is not conducive to the stable control of the motor. The method presented in this paper shows good tracking, smoothness, and stability of the running curve. As shown in Figure 5(a), the rated speed set by the motor was 1000 rad/s. During the period of inductance disturbance, the method proposed in this paper maintained stable rated speed and the motor ran smoothly.

The method presented in this paper has better dynamic characteristics than the vector control method in a no-load condition. To better verify the method proposed in this paper, under the condition of continuous inductance disturbance, load torque was added.

According to the simulation results, as shown in Figure 6(a), under the continuous inductance disturbance, the dynamic curve proposed in this paper has better tracking, stability, and smaller pulsation than the vector control method. When load torque was added at $t = 0.2$ s, although both methods show a decrease in speed, the method proposed in this paper has a small decrease and a

Table 1: Simulation parameters.

Symbol	Quantity	Numerical value
T_s	Sampling period	100 μs
p	Number of pole pairs	4
R_0	Stator resistance	0.958 Ω
Ψ_{f0}	Permanent magnet flux	0.1827 Wb
L_0	Electrical inductance	12 mH
J	Rotational inertia	0.003 kg·m^2
U_{dc}	DC bus voltage	311 V
Ω	Motor speed	1000 rad/s

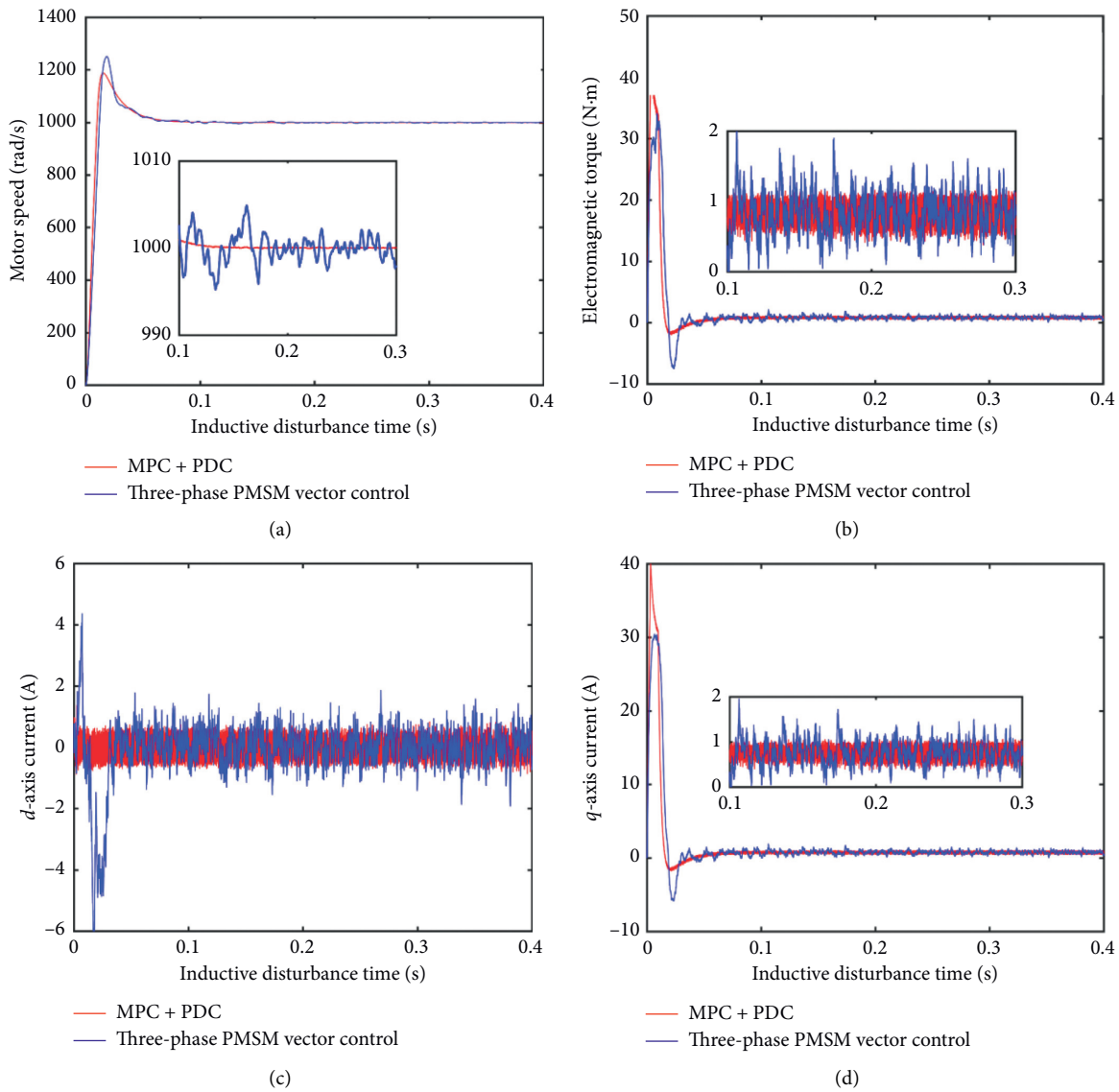

Figure 5: The motor response waveforms of the two proposed methods: (a) motor speed; (b) electromagnetic torque; (c) d-axis current; (d) q-axis current.

fast dynamic response, which allows the system to recover the rated speed quickly, indicating that the proposed method has a good dynamic performance and anti-interference ability. In Figure 6(b): electromagnetic torque dynamic curve, the method proposed in this paper shows good stability. It follows the load torque after approximately 0.02 s and has a fast response speed. However, in both methods, the load torque of $T_L = 10$ N·m shows a slight overshoot. In Figure 6(c): measurement of d-axis current, the method proposed in this paper shows a small ripple and relatively

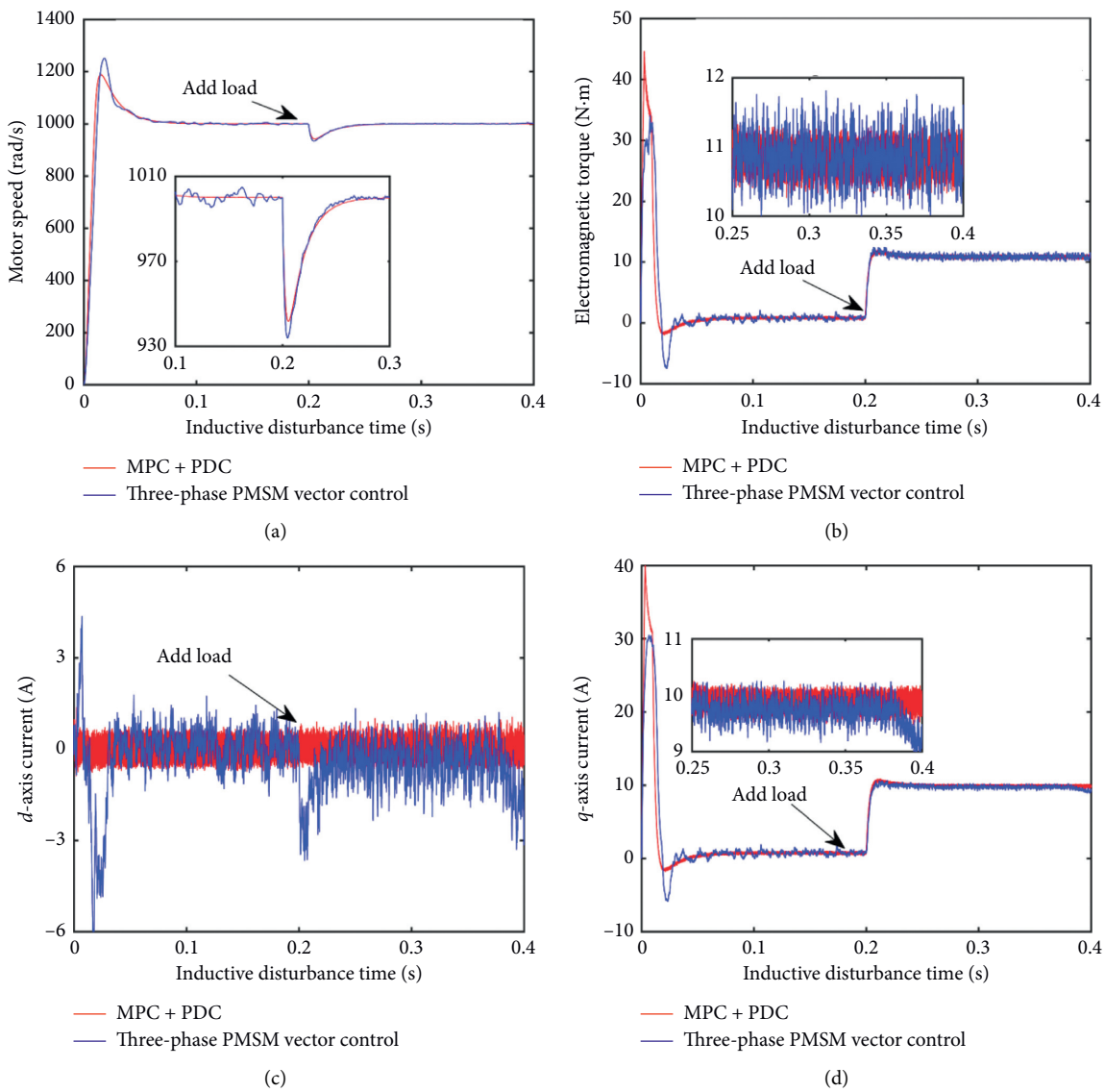

Figure 6: The motor response waveform of the two methods when load is added: (a) motor speed; (b) electromagnetic torque; (c) d-axis current; (d) q-axis current.

stable current following the rated d-axis. When $t = 0.2$ s and load torque is added, the method presented in this paper shows better stability, can maintain the rated current, and has better anti-interference ability and dynamic performance. However, the traditional vector control method has a large imbalance and takes a long time to return to the rated current. As for Figure 6(d), the method proposed in this paper has better overall stability; after adding load, the method proposed in this paper has a small overshoot and can quickly recover to the rated state.

The drift of the parameter inductance and the magnet flux linkage leads to the model mismatch, which has a greater impact on the control performance of the motor, while the mismatch of the stator resistance has a small impact on the control performance of the motor, which is almost negligible [27]. Figure 7 shows the robustness and anti-interference ability of the method proposed in this paper in the case of magnet flux linkage mismatch and external load disturbance. The magnet flux linkage disturbance was set as a straight slope from $0.5\psi_{f0}$ to $2.5\psi_{f0}$ during a time interval from 0.1 s to 0.3 s. In Figure 7(a), under the continuous disturbance of the magnet flux linkage, the vector control shows large speed pulsation, while the MPC + PDC method has a smooth operating curve without large pulsation. In Figure 7(b), the vector control method produces larger torque ripple, while the MPC + PDC method has less torque ripple. When external load disturbances are added, it can quickly track and maintain smooth operation. In Figures 7(c) and 7(d), the vector control

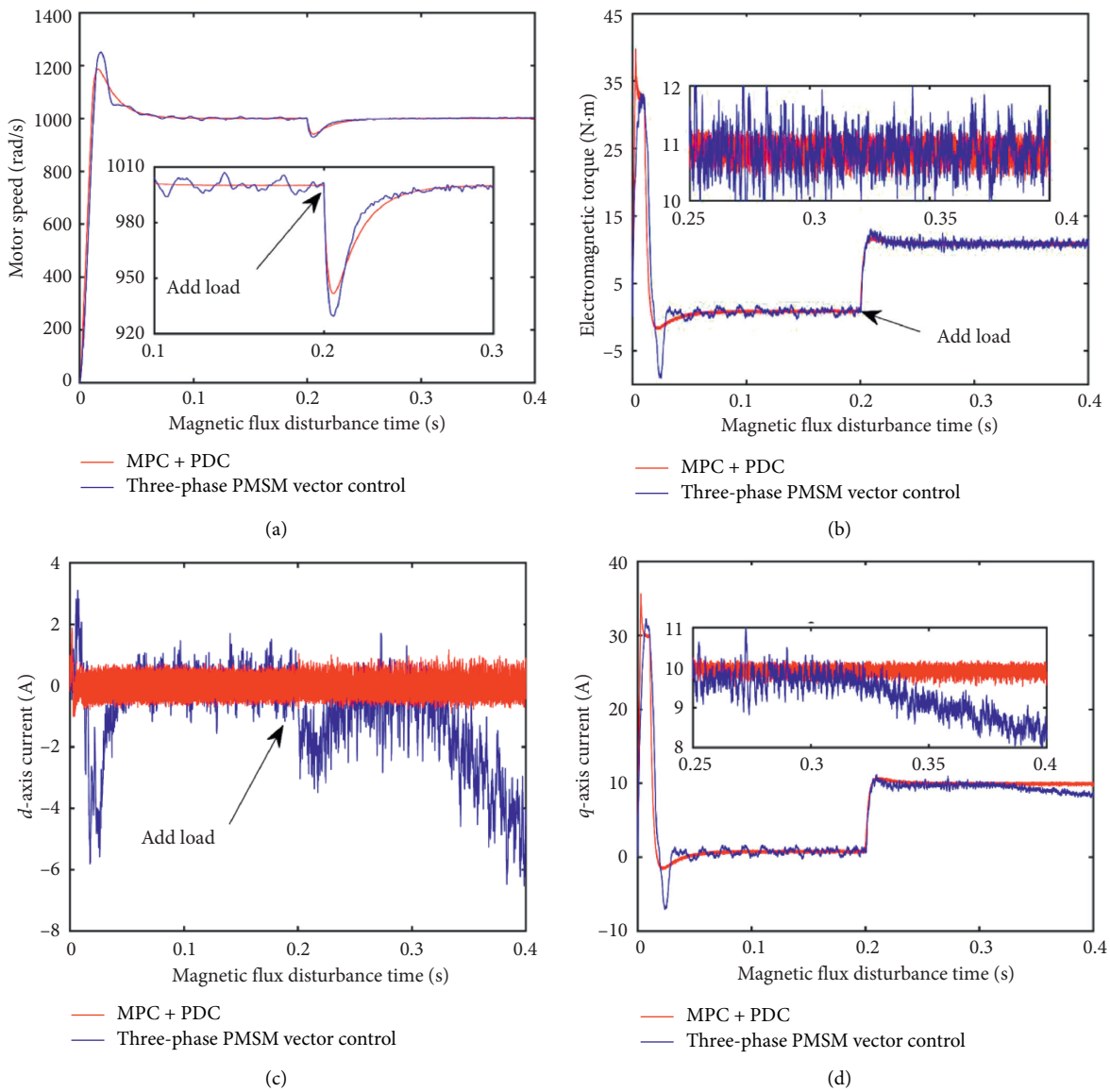

Figure 7: The motor response waveform of the two methods when load is added: (a) motor speed; (b) electromagnetic torque; (c) d-axis current; (d) q-axis current.

method produces a larger current ripple, and the current tracking effect is poor. The d-q axis current cannot accurately track the rated current under the disturbance of the magnet flux linkage and external load disturbance, and the stability is poor. However, the MPC + PDC method does not produce large current ripples under interference, maintains a good tracking effect, and has strong robustness and anti-interference ability.

Figure 8 shows the comparison between the MPC method and the MPC + PDC method proposed in this paper under the condition of model mismatch and external load disturbance. In the motor starting phase, the MPC method produces a large overshoot, which is not conducive to the smooth operation of the motor. In the working phase, he MPC method produces large torque ripples and current ripples, with low robustness and anti-interference ability, while MPC + PDC runs relatively smoothly, with better tracking effect, strong robustness, and anti-interference ability.

The simulation results show that MPC based on parametric disturbance compensation has good stability and followability under the interference of continuous inductance and can maintain good performance when adding load, showing good anti-interference ability and fast dynamic response.

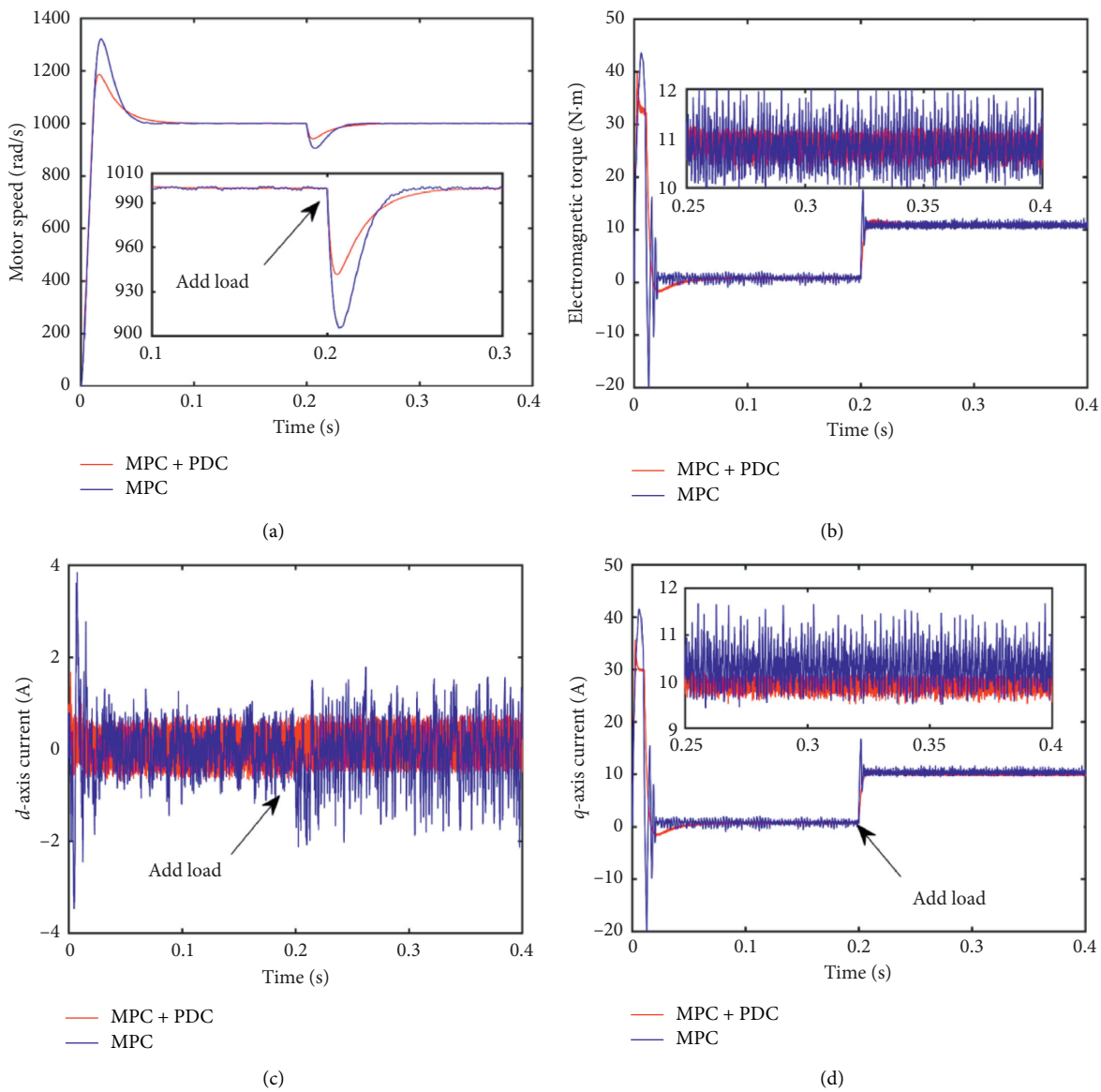

Figure 8: Comparison of MPC and MPC + PDC methods: (a) motor speed; (b) electromagnetic torque; (c) d-axis current; (d) q-axis current.

7. Conclusion

This paper presents MPC based on the parametric disturbance compensation method. By observing the parameter disturbance during the operation of the motor, this paper proposes a model predictive control based on parameter disturbance compensation, and through the frequency domain method, it gives the parameter tuning steps, analyzes the convergence, filtering, and parameter robustness of the model under different parameter selection states. This method has better parameter robustness and effectively avoids current static difference and oscillation problems caused by parameter changes. Under parameter changes and load conditions, the method showed strong robustness and anti-interference performance, obtained a good tracking effect, effectively reduced the speed and current ripples, and suppressed chattering.

Data Availability

The data used to support the findings of this study are included within the article.

Conflicts of Interest

The authors declare that they have no conflicts of interest.

Acknowledgments

This research was funded by the National Natural Science Foundation of China (no. 71601180).

References

[1] F. Deng and Y. Guan, "PMSM vector control based on improved ADRC," in *Proceedings of the 2018 IEEE International*

Conference of Intelligent Robotic and Control Engineering (IRCE), Lanzhou, China, August 2018.

[2] X. Liu, H. Yu, J. Yu, and L. Zhao, "Combined speed and current terminal sliding mode control with nonlinear disturbance observer for PMSM drive," *IEEE Access*, vol. 6, pp. 29594–29601, 2018.

[3] A. K. Singh, R. Raja, T. Sebastian, and A. Ali, "Limitations of the PI control with respect to parameter variation in PMSM motor drive systems," in *Proeedings of the 2019 IEEE International Electric Machines & Drives Conference (IEMDC)*, San Diego, CA, USA, May 2019.

[4] J. Templos-Santos, O. Aguilar-Mejia, E. Peralta-Sanchez, and R. Sosa-Cortez, "Parameter tuning of PI control for speed regulation of a PMSM using bio-inspired algorithms," *Algorithms*, vol. 12, no. 3, 2019.

[5] T. Inoue, Y. Inoue, S. Morimoto, and M. Sanada, "Maximum torque per ampere control of a direct torque controlled PMSM in a stator flux linkage synchronous frame," *IEEE Transactions on Industry Applications*, vol. 52, no. 3, pp. 2360–2367, 2016.

[6] D. Casadei, F. Profumo, G. Serra, and A. Tani, "FOC and DTC :two viable schemes for induction motors torque control," *Converter Technology & Electric Traction*, vol. 17, no. 5, pp. 779–787, 2004.

[7] L. Zhong, M. F. Rahman, W. Y. Hu, and K. W. Lim, "Analysis of direct torque control in permanent magnet synchronous motor drives," *IEEE Transactions on Power Electronics*, vol. 12, no. 3, pp. 528–536, 1997.

[8] Y. Zhang and J. Zhu, "Direct torque control of permanent magnet synchronous motor with reduced torque ripple and commutation frequency," *IEEE Transactions on Power Electronics*, vol. 26, no. 1, pp. 235–248, 2011.

[9] Y. Zhang and J. Zhu, "A novel duty cycle control strategy to reduce both torque and flux ripples for DTC of permanent magnet synchronous motor drives with switching frequency reduction," *IEEE Transactions on Power Electronics*, vol. 26, no. 10, pp. 3055–3067, 2011.

[10] C. He, J. Hu, and X. Ran, "Finite control set model predictive current control for PMSM based on extended state observer," in *Proceedings of the 2019 14th IEEE Conference on Industrial Electronics and Applications (ICIEA)*, Xi'an, China, June 2019.

[11] Z. Zhang, Z. Zhang, C. Garcia, J. Rodríguez, W. Huang, and R. Kennel, "Discussion on control methods with finite-control-set concept for PMSM drives," in *Proceedings of the 2019 IEEE international electric machines & drives conference (IEMDC)*, San Diego, CA, USA, May 2019.

[12] X. Zhang, L. Zhang, and Y. Zhang, "Model predictive current control for PMSM drives with parameter robustness improvement," *IEEE Transactions on Power Electronics*, vol. 34, no. 2, pp. 1645–1657, 2018.

[13] H. A. Young, M. A. Perez, and J. Rodriguez, "Analysis of finite-control-set model predictive current control with model parameter mismatch in a three-phase inverter," *IEEE Transactions on Industrial Electronics*, vol. 63, no. 5, p. 1, 2016.

[14] C. Xia, M. Wang, Z. Song, and T. Liu, "Robust model predictive current control of three-phase voltage source PWM rectifier with online disturbance observation," *IEEE Transactions on Industrial Informatics*, vol. 8, no. 3, pp. 459–471, 2012.

[15] P. Antoniewicz and M. P. Kazmierkowski, "Virtual-flux-based predictive direct power control of AC/DC converters with online inductance estimation," *IEEE Transactions on Industrial Electronics*, vol. 55, no. 12, pp. 4381–4390, 2009.

[16] W. H. Chen, J. Yang, L. Guo, and S. Li, "Disturbance observer-based control and related methods: an overview," *IEEE Transactions on Industrial Electronics*, vol. 63, no. 2, p. 1, 2015.

[17] L. Xin and B. Z. Sensorless, "Adaptive sliding mode FCS-MPC using extended state observer for PMSM system," in *Proceedings of the 2018 IEEE International Conference of Intelligent Robotic and Control Engineering (IRCE)*, Lanzhou, China, August 2018.

[18] Y. Zhao, X. Liu, and Q. Zhang, "Predictive speed-control algorithm based on a novel extended-state observer for PMSM drives," *Applied Sciences*, vol. 9, no. 12, 2019.

[19] Y.-j. Wu and G.-f. Li, "Adaptive disturbance compensation finite control set optimal control for PMSM systems based on sliding mode extended state observer," *Mechanical Systems and Signal Processing*, vol. 98, pp. 402–414, 2018.

[20] R. Guo, "Projective synchronization of a class of chaotic systems by dynamic feedback control method," *Nonlinear Dynamics*, vol. 90, pp. 53–64, 2017.

[21] R. Xu and F. Zhang, "ϵ-Nash mean-field games for general linear-quadratic systems with applications," *Automatica*, vol. 114, Article ID 108835, 2020.

[22] W. Yao, Y. Hai Tao, G. Rong, and L. D. Yang, "Fuzzy adaptive sliding mode control of PMSM based on extended state observer," *International Journal of Applied Electromagnetics and Mechanics*, vol. 63, no. 3, pp. 391–407, 2020.

[23] H. Liu and S. Li, "Speed control for PMSM servo system using predictive functional control and extended state observer," *IEEE Transactions on Industrial Electronics*, vol. 59, no. 2, pp. 1171–1183, 2012.

[24] A. Gonzalez, V. Balaguer, P. Garcia, and A. Cuenca, "Gain-scheduled predictive extended state observer for time-varying delays systems with mismatched disturbances," *ISA Transactions*, vol. 84, pp. 206–213, 2019.

[25] Y. Deng, J. Wang, H. Li, J. Liu, and D. Tian, "Adaptive sliding mode current control with sliding mode disturbance observer for PMSM drives," *ISA Transactions*, vol. 88, pp. 113–126, 2019.

[26] Y. Zhang, D. Xu, J. Liu, S. Gao, and W. Xu, "Performance improvement of model predictive current control of permanent magnet synchronous motor drives," *IEEE Transactions on Industry Applications*, vol. 53, no. 4, pp. 3683–3695, 2017.

[27] Y. Zhang, J. Jin, and L. Huang, "Model-free predictive current control of PMSM drives based on extended state observer using ultra-local model," *IEEE Transactions on Industrial Electronics*, p. 1, 2020.

Hindawi
Mathematical Problems in Engineering
Volume 2020, Article ID 8428762, 10 pages
https://doi.org/10.1155/2020/8428762

Research Article

Thermophoresis and Brownian Model of Pseudo-Plastic Nanofluid Flow over a Vertical Slender Cylinder

Faizan Hussain,[1] **Azad Hussain**,[1] **and Sohail Nadeem**[2]

[1]*Department of Mathematics, University of Gujrat, Gujrat 50700, Pakistan*
[2]*Department of Mathematics, Quaid-I-Azam University, Islamabad 44000, Pakistan*

Correspondence should be addressed to Faizan Hussain; hussainfaizan8@gmail.com

Received 20 April 2020; Revised 2 July 2020; Accepted 24 July 2020; Published 14 August 2020

Guest Editor: Cuimei Jiang

This study focuses on the industrial and engineering interest quantities, such as drag force and rate of transmission of heat, for pseudo-plastic nanofluid flow. The attributes of natural convection of the pseudo-plastic nanofluid flow model over a vertical slender cylinder are explored. The pseudo-plastic flow is studied under the influence of concentration of nanoparticles, rate of heat transmission, and drag force. For the first time, the pseudo-plastic nanofluid flow model has been implemented over a vertical slender cylinder which is not yet investigated. The acquired model is based on thermophoresis and Brownian motion mechanisms. The governing equations of pseudo-plastic nanofluid in cylindrical coordinates are modelled. The developed system of nonlinear equations is tackled by boundary layer assumptions and similarity transformations. Moreover, the solution of the acquired system exhibited by using a new powerful numerical technique. A comprehensive debate on drag force and transmission of heat under the influence of various emerging parameters is illustrated in the table. Furthermore, the effects of dimensionless parameters over the velocity profile, temperature profile, and concentration of nanoparticle profile have been exhibited graphically.

1. Introduction

Investigation of the non-Newtonian fluids gains prodigious attention of researchers over a half-century because naturally, most of the fluids used in the industrial applications are non-Newtonian fluids. This is the main cause of increased applications of non-Newtonian fluids in the industrial field and engineering such as petroleum production, molten plastics, food engineering, automobiles, polymer solution industry, chemical engineering, and power engineering. A solitary established equations cannot pronounce the attributes of such non-Newtonian fluids because these kinds of fluids have a nonlinear relationship among the rate of stress and strain. Therefore, several scientists and engineers have pronounced models for non-Newtonian fluids [1–10]. Ellahi et al. [11] explored thermally charged MHD biphase flow coating with non-Newtonian nanofluid over the slippery walls. The sustainable features of MHD Jaffrey fluid for bio-bi-phase flow are carried out by Zeeshan et al. [12]. Rehman et al. [13] examined MHD flow of the nanoparticle influenced near a stagnation point over an exponential stretched surface. Parand et al. [14] described the boundary layer flow of Powell–Eyring fluid for a stretching sheet. Generation/absorption of heat through the flow of axisymmetric Casson fluid over a stretched cylinder is addressed by Javed et al. [15]. Additional appropriate studies in this way are in [16, 17].

Over the last few years, we have adopted a pioneering procedure for refining the transmission of heat by utilizing ultrafine solid particles in the fluids, and these particles have been used widely called as nanofluid. The label "nanofluid" was used for the first time in 1995 by Choi and Eastman [18]. He cited that it is conceivable to boost convection of transmission of heat and thermal conductivity efficiency by using nanofluids. To handle nanofluids, Buongiorno [19] introduced a mathematical model and explored numerous transport mechanisms and applications about the nanofluids. Miscellaneous purposes of nanofluids have been

uncovered by Das et al. [20]. Zhang et al. [21] scrutinized the nanofluid for MHD radiative flow over a variable heat flux and chemical reaction surface. Transport of heat for the ferromagnetic fluid with thermal stratification over a stretching sheet was examined by Muhammad et al. [22]. Saini and Sharma [23] extended the application of nanofluids through the investigation of double-diffusive bioconvection. Further extensive research and applications of nanofluids across numerous fields are heat transmission, energy, microequipment, and boiling applications [24–28].

Williamson's fluid model has non-Newtonian behaviour in nature like pseudo-plastic fluid which defines the flow of shear thinning. The industrial, engineering, and biological fluids which observe as Williamson's fluid are blood, glue, paint, ketchup, polymer solutions, and nail polish. Williamson [29] who discovered the model to communicate pseudo-plastic attributes along with features of extreme points of viscosity. Due to this invention, innovated researchers are motivated to discover more upfront classifications of non-Newtonian fluid. Ramzan et al. [30] analyzed the numerical solution of MHD flow over a stretched surface with convective boundary conditions using the shooting method. Two-dimensional flow of Williamson's fluid film with heat diffusion under the influence of thermal radiation was inspected via an optimal approach by Shah et al. [31].

Rate of transmission of heat, the transmission of mass rate, and skin friction coefficient play a dynamic character during coating of wires or polymer fibre coating. As wires have a thin cylindrical shape, miscellaneous researchers have launched several mathematical models. In axial incompressible flow, Seban and Bond [32] premeditated the attributes of drag force and rate of transmission of heat for a cylinder in 1951. Under the uniform surface heat flux, Mucoglu and Chen [33], for the first time, scrutinized the slender cylinder with the help of mixed convection regime. Nadeem et al. [34] analyzed the boundary layer flow and transmission of heat of a nanofluid in a vertical slender cylinder. Patil et al. [35] examined the mixed convection nanofluid boundary layer flow under the effect of surface roughness with a moving slender cylinder. Reddy et al. [36] explored the natural convection for the Casson fluid flow past over a hollow slender cylinder. With the help of Bejan's heat function concept, Reddy et al. [37] investigated the unsteady MHD micropolar fluid flow in a homogeneously thermal radiative hollow slender cylinder with the radiative transmission of heat effect. Further latest stimulating work in this area can be found in [38–42].

The literature review replicates that, generally, the researchers engaged themselves to study non-Newtonian fluids' behaviour by assuming different effects. The attributes of natural convection of Williamson's nanofluid model over a vertical slender cylinder are not explored until now. Therefore, the developed model is simplified by the boundary layer approximation and similarity transformations. The governing coupled nonlinear system of equations is then solved by a new powerful numerical technique. Furthermore, physical behaviour for the industrial interests of the fluid will be examined through the table.

2. Analysis of Flow and Mathematical Formulation

Suppose an incompressible Williamson's nanofluid flow along with a permeable vertical slender cylinder with radius a having uniform ambient temperature T_∞. The coordinates (x, r) are used, whereas x is acting along the surface of the cylinder and r along the radial direction. The velocity profile, temperature profile, and concentration profile are as follows:

$$\begin{aligned} V(x,r) &= (w, 0, u), \\ T &= T(x,r), \\ \phi &= \phi(x,r), \end{aligned} \tag{1}$$

where $(w(x,r), u(x,r))$ are velocity components along the surface and radial direction. The boundary layer equations of motion, energy, and the nanoparticle concentration are

$$\frac{\partial}{\partial r}(rw) + r\frac{\partial u}{\partial x} = 0, \tag{2}$$

$$\begin{aligned} u\frac{\partial u}{\partial x} + w\frac{\partial u}{\partial r} = -\frac{1}{\rho}\frac{\partial p}{\partial x} + \upsilon\Bigg(\frac{\partial^2 u}{\partial r^2} + \frac{1}{r}\frac{\partial u}{\partial r} + \Gamma\frac{1}{r\sqrt{2}}\left(\frac{\partial u}{\partial r}\right)^2 \\ + \sqrt{2}\,\Gamma\frac{\partial^2 u}{\partial r^2}\frac{\partial u}{\partial r}\Bigg) + \Bigg(\frac{(\rho^* - \rho)(\phi - \phi_\infty)}{\rho} \\ + (1 - \phi_\infty)(T - T_\infty)\beta_{\text{th}}\Bigg)g_{\text{gr}}, \end{aligned} \tag{3}$$

$$\begin{aligned} w\frac{\partial T}{\partial r} + u\frac{\partial T}{\partial x} = \alpha\left(\frac{\partial^2 T}{\partial r^2} + \frac{1}{r}\frac{\partial T}{\partial r}\right) + \frac{\rho^* c_p^*}{\rho c_p}\Bigg(D_B\frac{\partial \phi}{\partial r}\frac{\partial T}{\partial r} \\ + \frac{D_T}{T_\infty}\left(\frac{\partial T}{\partial r}\right)^2\Bigg), \end{aligned} \tag{4}$$

$$w\frac{\partial \phi}{\partial r} + u\frac{\partial \phi}{\partial x} = D_B\left(\frac{\partial^2 \phi}{\partial r^2} + \frac{1}{r}\frac{\partial \phi}{\partial r}\right) + \frac{D_T}{T_\infty}\left(\frac{\partial^2 T}{\partial r^2} + \frac{1}{r}\frac{\partial T}{\partial r}\right). \tag{5}$$

The accompanied boundary conditions are

$$\begin{aligned} u(x,a) &= 0, \\ T(x,a) &= T_w(x), \end{aligned} \tag{6}$$

$$\begin{aligned} u(x,r) &\longrightarrow U(x), \quad \text{as } r \longrightarrow \infty, \\ T(x,r) &\longrightarrow T_\infty, \quad \text{as } r \longrightarrow \infty, \end{aligned} \tag{7}$$

$$\begin{aligned} \phi(x,a) &= \phi_w(x), \\ \phi(x,r) &\longrightarrow \phi_\infty, \quad \text{as } r \longrightarrow \infty. \end{aligned} \tag{8}$$

Here, $U(x) = (x/l)U_\infty$ is the mainstream velocity, υ is called kinematic viscosity and is defined as $\upsilon = (\mu/\rho)$, $\Gamma > 0$ articulated the material constant for Williamson's fluid, and ρ denotes the density of the fluid. Now, the nondimensional variables and similarity transformations are defined as follows:

$$u = U_\infty\left(\frac{x}{l}\right)f'(\eta),$$
$$w = -\frac{a}{r}\left(\frac{\upsilon U_\infty}{l}\right)^{(1/2)} f(\eta),$$
$$\theta = \frac{T - T_\infty}{T_w - T_\infty}, \tag{9}$$
$$\psi = \frac{\phi - \phi_\infty}{\phi_w - \phi_\infty},$$
$$\eta = \frac{r^2 - a^2}{2a}\left(\frac{U_\infty}{\upsilon l}\right)^{(1/2)},$$

in which $T_w - T_\infty = \Delta T(x/l)$ and $\phi_w - \phi_\infty = \Delta\phi(x/l)$ operated for the characteristic temperature ΔT and nanoparticle concentration $\Delta\phi$. By using the above transformations, equation (2) is identically satisfied, and equations (3)–(5) will be articulated as

$$\begin{aligned}&(2\eta\gamma_c + 1)f''' + 2\gamma_c f'' + 3\lambda\gamma_c(2\eta\gamma_c + 1)^{(1/2)} f''^2\\&+ 2\lambda(2\eta\gamma_c + 1)^{(3/2)} f''f''' + ff'' - f'^2\\&+ \lambda_N(1 - \phi_\infty)(\theta + N_r\psi) + 1 = 0,\end{aligned} \tag{10}$$

$$\begin{aligned}&(2\eta\gamma_c + 1)\theta'' + 2\gamma_c\theta' + \Pr(f\theta' + f'\theta) + (2\eta\gamma_c + 1)\\&\cdot\left(T_p\theta'^2 + B_p\theta'\psi'\right) = 0,\end{aligned} \tag{11}$$

$$\begin{aligned}&(2\eta\gamma_c + 1)\psi'' + 2\gamma_c\psi' + \mathrm{PrLe}(f\psi' - f'\psi) + \frac{T_p}{B_p}\\&\cdot\left[(2\eta\gamma_c + 1)\theta'' + 2\gamma_c\theta a'\right] = 0.\end{aligned} \tag{12}$$

Dimensionless attached boundary conditions are

$$\begin{aligned}&f(0) = c_0,\\&f'(0) = 0,\\&f' \longrightarrow 1, \quad \text{as } \eta \longrightarrow \infty,\end{aligned} \tag{13}$$

$$\begin{aligned}&\theta(0) = 1,\\&\psi(0) = 1,\\&\theta \longrightarrow 0,\\&\psi \longrightarrow 0, \quad \text{as } \eta \longrightarrow \infty,\end{aligned} \tag{14}$$

where $\gamma_c = \sqrt{\upsilon l/U_\infty a^2}$ illustrates the curvature parameter, $\lambda = (\Gamma x U^{(3/2)})/(\sqrt{2\upsilon}\, l^{(3/2)})$ symbolizes Williamson's dimensionless parameter, $\lambda_N = (l\Delta T g_{gr}\beta_{th})/U_\infty^2$ pronounces as the parameter of natural convection, $N_r = ((\phi_w - \phi_\infty)(\rho^* - \rho))/(\rho\beta_{th}(1 - \phi_\infty)(T_w - T_\infty))$ means the buoyancy ratio, $\Pr = \upsilon/\alpha$ is identified as the Prandtl number, $B_p = (\rho^* c_p^* D_B(\phi_w - \phi_\infty))/(\rho c_p \alpha)$ stands for the Brownian motion parameter, $T_p = (\rho^* c_p^* D_T(T_w - T_\infty))/(\alpha T_\infty \rho c_p)$ corresponds to the thermophoresis parameter, and $\mathrm{Le} = \alpha/D_B$ is known as the Lewis number.

3. Physical Quantities of the Industrial Interest

For the industrial interest, the physical quantities, i.e., drag force and transmission of heat, are stated as

$$C_f = \frac{s_w}{(1/2)\rho U^2},$$
$$\mathrm{Nu} = \frac{x q_w}{\alpha_\infty(T_w - T_\infty)}, \tag{15}$$

where s_w stands for the shear stress tensor over the surface of the slender cylinder, while q_w is called wall heat flux. These physical quantities can be articulated as

$$s_w = \mu\left(\frac{\partial u}{\partial r} + \frac{\Gamma}{\sqrt{2}}\left(\frac{\partial u}{\partial r}\right)^2\right)_{r=a},$$
$$q_w = -\alpha_\infty\left(\frac{\partial T}{\partial r}\right)_{r=a}. \tag{16}$$

According to similarity transformation, equation (15) is transformed as

$$\frac{1}{2}C_f \mathrm{Re}^{(1/2)} = f''(0) + \lambda f''(0)^2,$$
$$\mathrm{Nu}\mathrm{Re}^{-(1/2)} = -\theta'(0). \tag{17}$$

4. Numerical Solution

The solution of the nonlinear system of ODEs (10)–(12) over the accompanied condition equations (13) and (14) is tackled through the numerical algorithm of MATLAB inherent scheme bvp4c. In order to apply this scheme, first of all, higher-order differential equations are transformed into first-order ODEs. The procedure is as follows.

Let us suppose that

$$\begin{aligned}f(\eta) &= y_1(x),\\f'(\eta) &= y_2(x),\\f''(\eta) &= y_3(x),\\f'''(\eta) &= y_3'(x),\\\theta(\eta) &= y_4(x),\\\theta'(\eta) &= y_5(x),\\\theta''(\eta) &= y_5'(x),\\\psi(\eta) &= y_6(x),\\\psi'(\eta) &= y_7(x),\\\psi''(\eta) &= y_7'(x).\end{aligned} \tag{18}$$

Therefore, equations (10)–(14) are transformed as follows:

$$y_3'(x) = \frac{\left(-2\gamma_c y_3 - 3\lambda\gamma_c\left(1+2x\gamma_c\right)^{(1/2)}\left(y_3\right)^2 - y_1 y_3 + \left(y_2\right)^2 - \lambda_N\left(1-\phi_\infty\right)\left(y_4 + N_r y_6\right) - 1\right)}{\left(1+2x\gamma_c\right) + 2\lambda\left(1+2x\gamma_c\right)^{3/2} y_3(x)},$$

$$y_5'(x) = \frac{-2\gamma_c y_5 - \Pr\left(y_1 y_5 + y_2 y_4\right) - \left(1+2x\gamma_c\right)\left(B_p y_5 y_7 + T_p y_5^2\right)}{\left(1+2x\gamma_c\right)}, \tag{19}$$

$$y_7'(x) = -2\gamma_c y_7 - \mathrm{LePr}\left(y_1 y_7 - y_2 y_6\right) - \left(\frac{T_p/B_c)\left[\left(1+2x\gamma_c\right)y_5' + 2\gamma_c y_5\right]}{\left(1+2x\gamma_c\right)},$$

with conditions

$$\begin{aligned} y_1(0) - c_0 &= 0, \\ y_2(0) &= 0, \\ y_2(\infty) - 1 &= 0, \\ y_4(0) - 1 &= 0, \\ y_5(\infty) &= 0, \\ y_6(0) - 1 &= 0, \\ y_7(\infty) &= 0. \end{aligned} \tag{20}$$

5. Discussion

Natural convection of Williamson's nanofluid over a slender cylinder has been analyzed. Numerical solution is obtained by using MATLAB scheme bvp4c. Physical properties of the nanofluid are portrayed by using the Buongiorno model. Likewise, transmission of heat and mass is differentiated by means of assorted parameters.

5.1. Velocity Profiles

5.1.1. Attributes of γ_c and λ for $f'(\eta)$. Figures (1) and (2) show the attributes of curvature parameter γ_c and Williamson's dimensionless parameter λ for $f'(\eta)$. It is well defined from Figures (1) and (2) that intensifying the values of γ_c tends to devalue $f'(\eta)$; however, equivalent behaviour is anticipated for Williamson's parameter λ. This is because after intensifying the curvature parameter γ_c, the radius of the cylinder with the fluid declines. Similarly, after intensifying Williamson's parameter λ which will cause a decline in velocity because fluid opposes more resistance.

5.1.2. Attributes of λ_N and N_r for $f'(\eta)$. The attribution of λ_N and N_r is shown in Figures (3) and (4). From Figures (3) and (4), it defines that, by intensifying natural convection λ_N and buoyancy ratio N_r, the buoyancy force will cause the higher velocity attained by the fluid.

5.2. Temperature Profiles

5.2.1. Attributes of γ_c and Pr *for $\theta(\eta)$.* The behaviour of temperature profile $\theta(\eta)$ for distinct values of curvature parameter γ_c and Prandtl number is reported in Figures (5) and (6). Evidently, from Figure 5, it can be described that enhancement in the curvature parameter yields intensifying in $\theta(\eta)$. Moreover, in Figure 6, the temperature profile and the boundary layer thickness decrease due to enhancement in Prandtl number (Pr). Which uncovers the truth that, enlarging in Pr cause the reduction in the thermal diffusivity of the fluids accordingly.

5.2.2. Attributes of T_p and B_p for $\theta(\eta)$. The contribution of thermophoresis parameter T_p and Brownian motion B_p is described in Figures (7) and (8). Evidently, larger T_p and B_p produce higher $\theta(\eta)$. Practically, movement of a small number of particles from higher temperature to the lower one is defined as the thermophoresis phenomenon. Hence, a greater number of nanoparticles are shifted from the hot region which raises the fluid temperature. However, due to the increase in Brownian motion parameter B_p in the result, random motion of the nanoparticles will be raised which causes intensifying in the temperature of the fluid.

5.3. Concentration Profiles

5.3.1. Attributes of $\psi(\eta)$ on γ_c. Figure 9 exhibits the consequences of curvature parameter γ_c on nanoparticle concentration $\psi(\eta)$. It is clear from the figure that intensifying curvature parameter γ_c diminishes the nanoparticle concentration of the fluid. According to the industrial view, after increase in the curvature parameter, it caused the reduction in the radius of the slender cylinder; hence, concentration of nanoparticles also reduced.

5.3.2. Attributes of Lewis Number Le and Prandtl Number on $\psi(\eta)$. The behaviour of Lewis number Le is depicted for $\psi(\eta)$ through Figure 10. It is scrutinized that $\psi(\eta)$ is diminished by increasing Lewis number Le. Physically, due to the levitation of diffusivity of heat and mass, nanoparticle concentration $\psi(\eta)$ diminished. Furthermore, scrutinization of the attribution of Prandtl number Pr for $\psi(\eta)$ is portrayed through Figure 11. Physically, intensifying in Prandtl number will cause the more heat convection occur because thickness of the thermal boundary layer is greater than the velocity boundary layer. Hence, nanoparticle concentration diminished.

5.3.3. Attributes of T_p and B_p on $\psi(\eta)$. The impact of thermophoresis parameter T_p and Brownian motion parameter B_p on $\psi(\eta)$ is depicted in Figures (12) and (13). Due

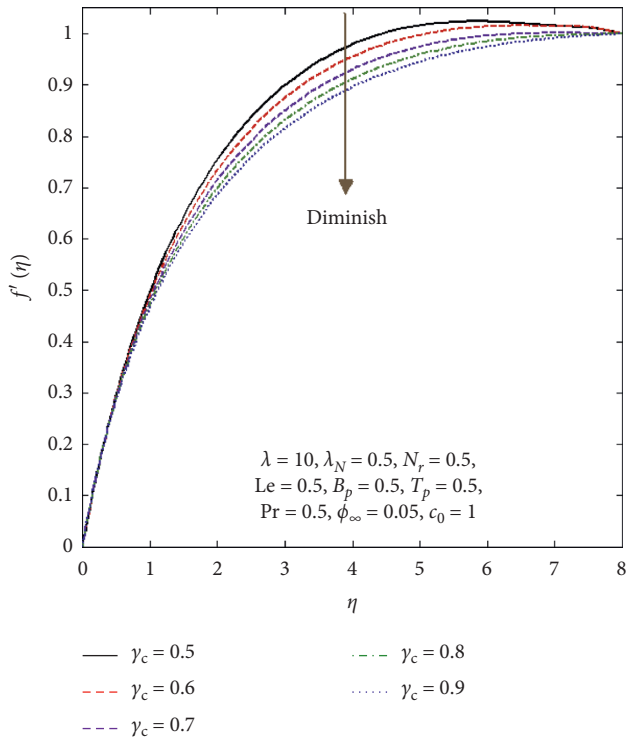

Figure 1: Consequences for γ_c on $f'(\eta)$.

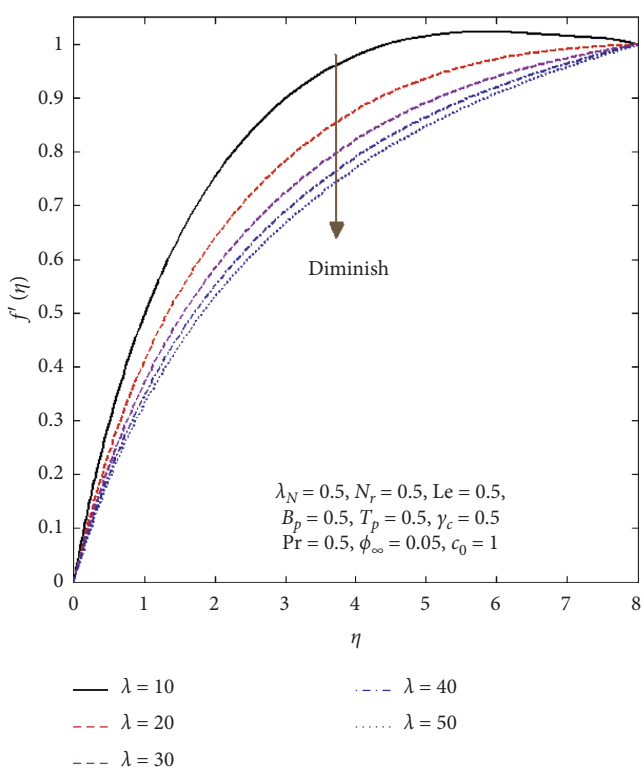

Figure 2: Consequences for λ on $f'(\eta)$.

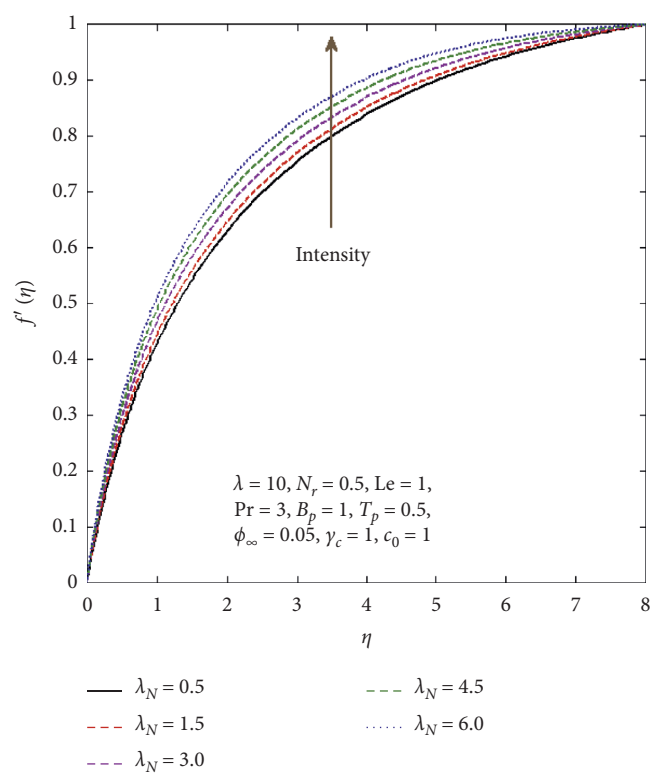

Figure 3: Consequences for λ_N on $f'(\eta)$.

to the increase of T_p, boundary layer thickness of nanoparticle concentration intensified. As a matter of fact, thermophoresis force increases for higher estimation of T_p, which yields nanoparticle relocations from higher to lower temperature; hence, $\psi(\eta)$ intensifies (see Figure 12). However, $\psi(\eta)$ and its concentration boundary layer diminish when B_p is amplified (see Figure 13).

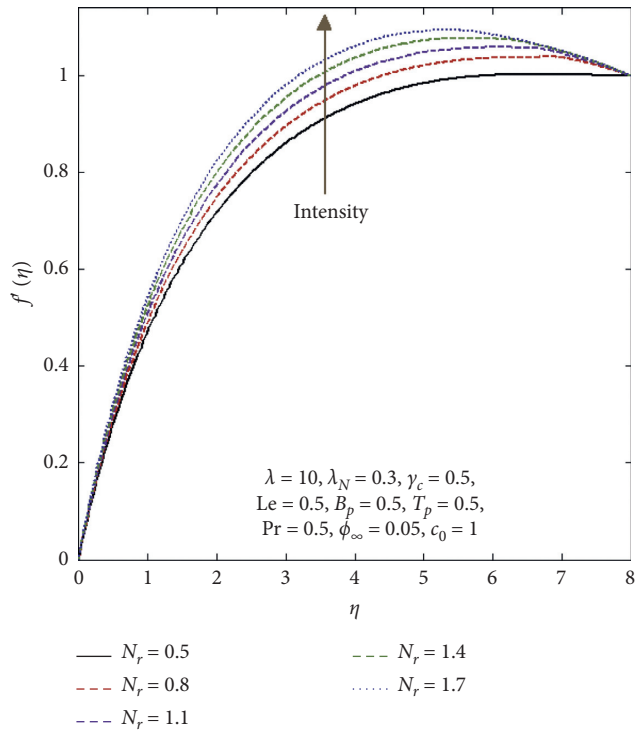

Figure 4: Consequences for N_r on $f'(\eta)$.

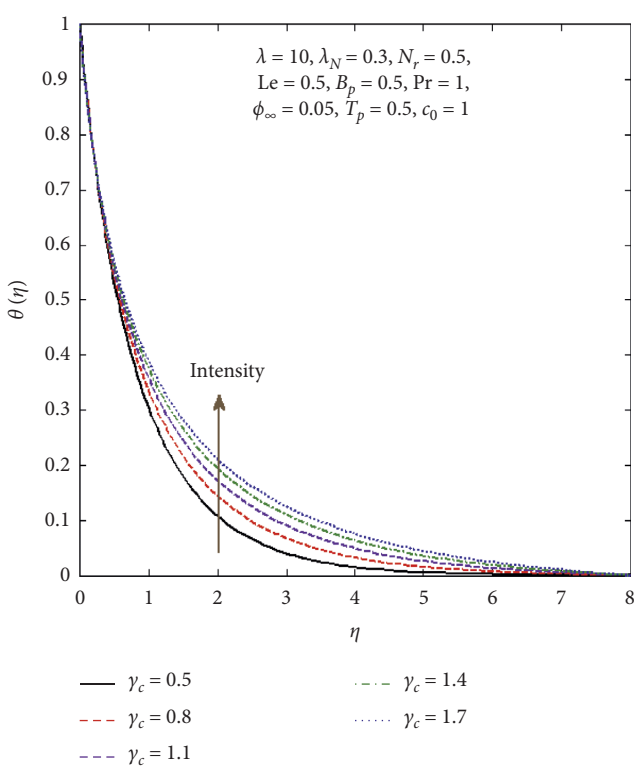

Figure 5: Consequences for γ_c on $\theta(\eta)$.

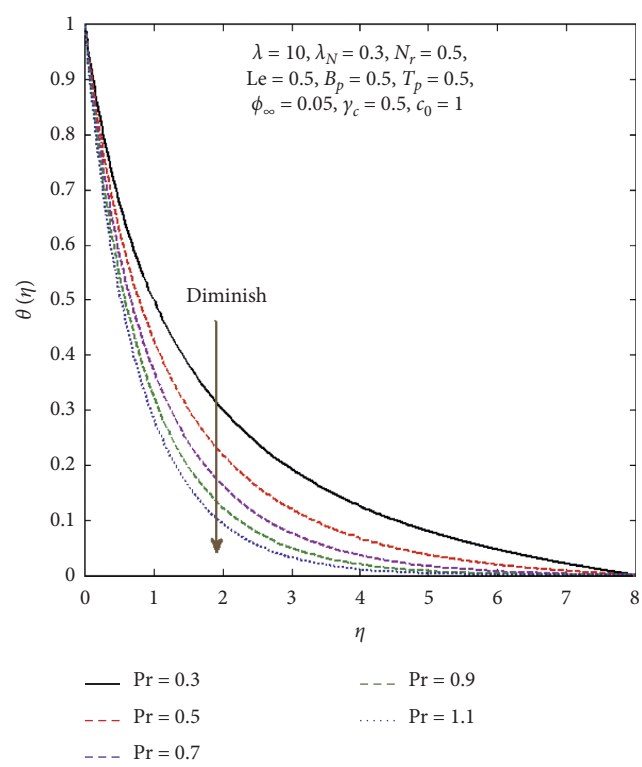

Figure 6: Consequences for Pr on $\theta(\eta)$.

5.4. Attributes of Drag Force and Rate of Transmission of Heat. The attributes of physical parameters such as curvature parameter γ_c, Williamson's parameter λ, natural convection λ_N, and buoyancy ratio N_r on drag force are exhibited in Table 1. It is evidently clear from the table that drag force is intensified by enhancing γ_c, λ, λ_N, and N_r. Table 2 expresses the behaviour of physical parameters on the rate of

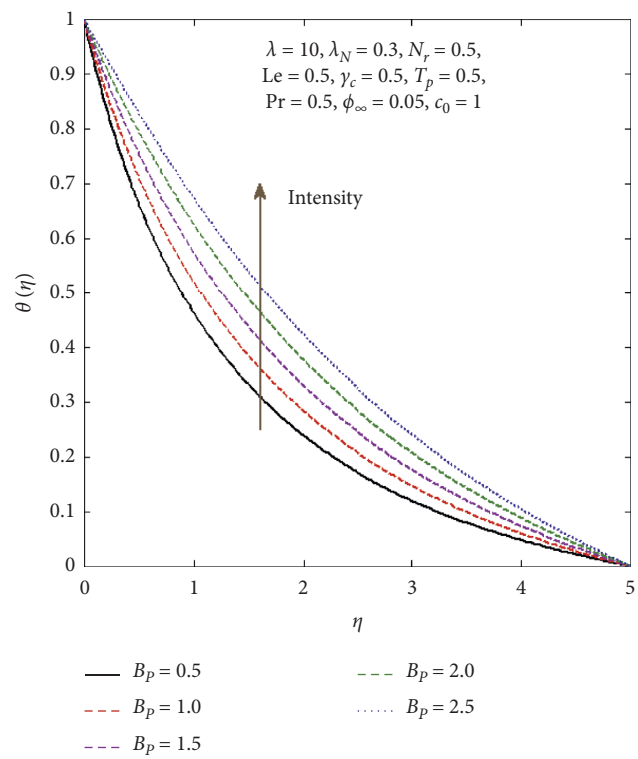

Figure 7: Consequences for T_p on $\theta(\eta)$.

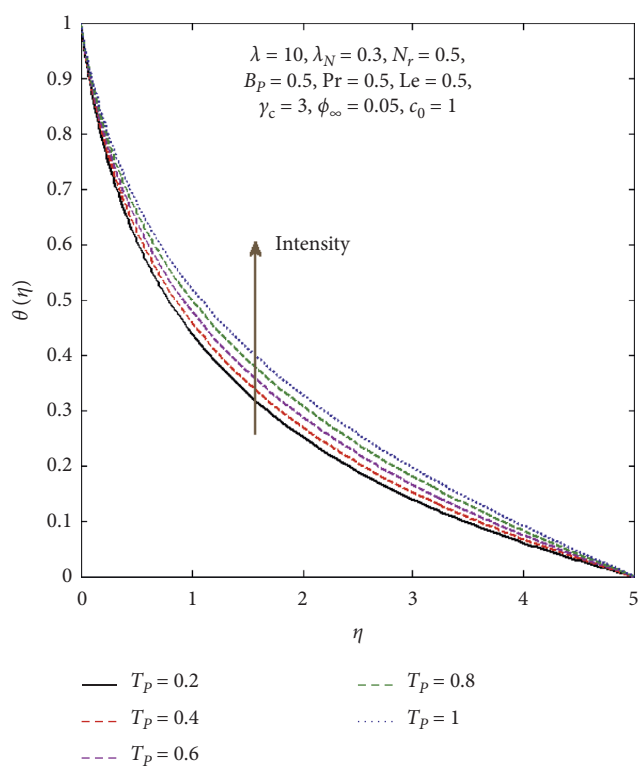

Figure 8: Consequences for B_p on $\theta(\eta)$.

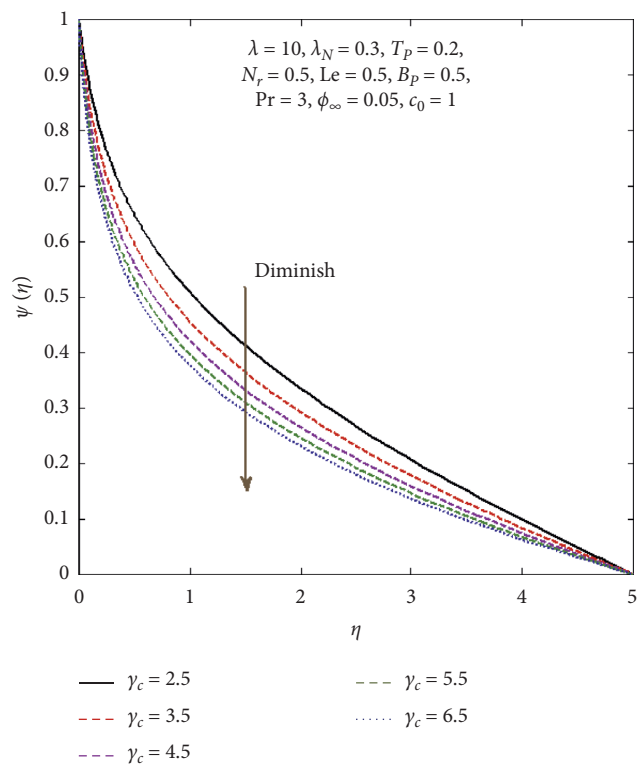

Figure 9: Consequences for γ_c on $\psi(\eta)$.

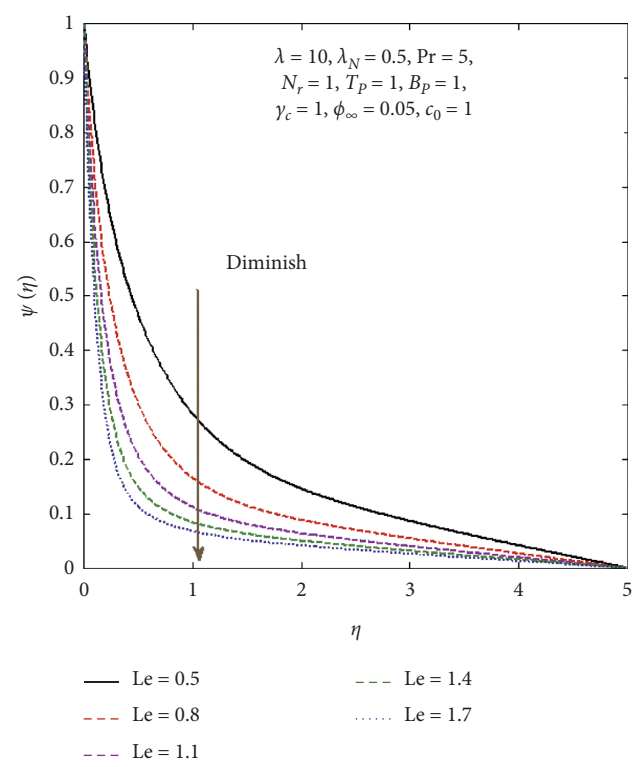

Figure 10: Consequences of Lewis number Le.

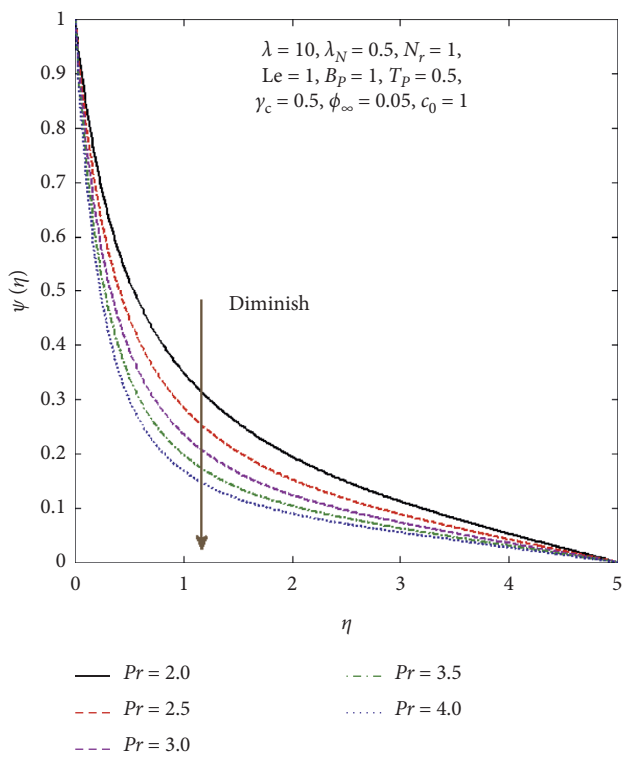

Figure 11: Consequences of Prandtl number Pr.

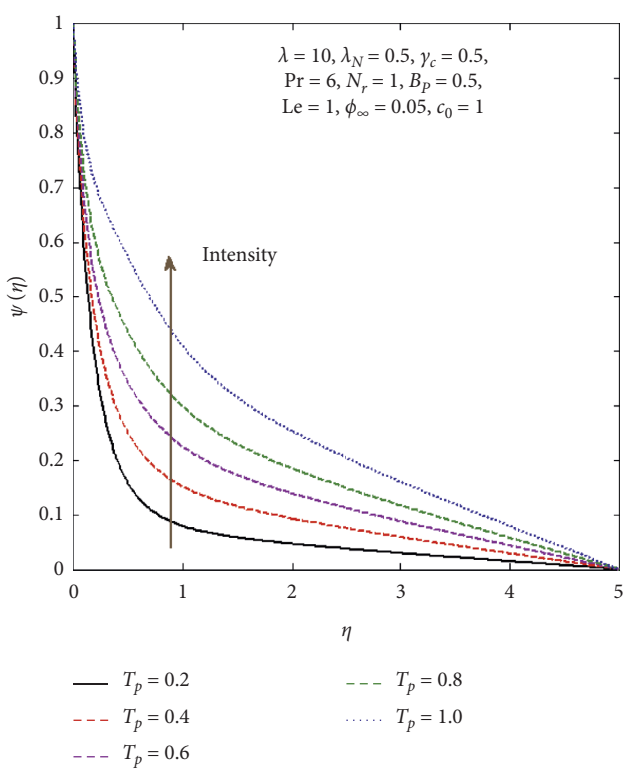

Figure 12: Consequences of T_p on $\psi(\eta)$.

transmission of heat. It is inspected that the rate of transmission of heat enhances by increasing γ_c, T_p, and Pr, while it declines for inclination of λ, B_p, and Le.

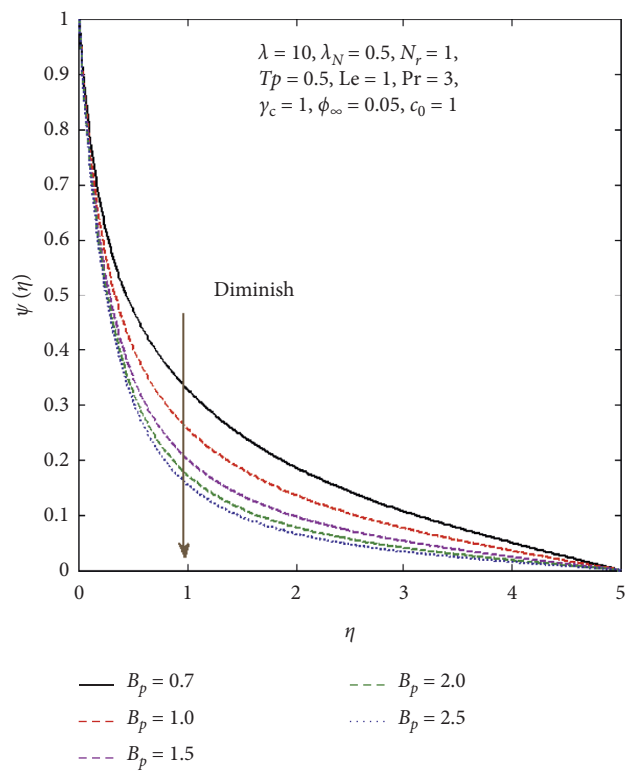

Figure 13: Consequences of B_p on $\psi(\eta)$.

Table 1: Numerical values of drag forces $(1/2)C_f\mathrm{Re}^{(1/2)}$.

γ_c	λ	λ_N	N_r	$f''(0)$	$(1/2)C_f\mathrm{Re}^{(1/2)}$
0.1	0.1	0.1	0.1	1.7290	2.0279
0.2	—	—	—	1.7670	2.0792
0.3	—	—	—	1.8030	2.1281
0.4	—	—	—	1.8390	2.1772
—	1	—	—	1.1340	2.4200
—	2	—	—	0.9252	2.6372
—	3	—	—	0.8488	3.0102
—	4	—	—	0.7853	3.2521
—	1	0.1	—	1.2290	2.7394
—	—	0.2	—	1.2430	2.7880
—	—	0.4	—	1.2860	2.9398
—	—	0.7	—	1.3510	3.1762
0.5	3	0.1	0.1	0.9011	3.3370
—	—	—	0.2	0.9031	3.3499
—	—	—	0.4	0.9067	3.3730
—	—	—	0.7	0.9070	3.3749

6. Final Remarks

This exploration scrutinized the natural convection of Williamson's nanofluid for boundary-layer stagnation point flow over a vertical slender cylinder. Hence, thermophoresis, Brownian motion, natural convection, Williamson's parameter, and curvature parameter are utilized for modelling and analysis. The governing coupled nonlinear ODEs are then solved numerically by using MATLAB technique bvp4c. This research reveals the following outcomes:

Table 2: Numerical values of the rate of transmission of heat $Nu/Re^{1/2}$.

γ_c	λ	T_p	B_p	Pr	Le	$Nu/Re^{(1/2)}$
0.1	0.1	0.1	0.1	0.3	0.4	0.8118
0.2	—	—	—	—	—	0.8446
0.3	—	—	—	—	—	0.8739
—	0.5	—	—	—	—	1.1190
—	0.7	—	—	—	—	0.9200
—	0.9	—	—	—	—	0.8702
—	—	0.3	—	—	—	1.0120
—	—	0.5	—	—	—	1.1430
—	—	0.7	—	—	—	0.7092
—	—	0.1	0.3	—	—	0.8221
—	—	—	0.5	—	—	0.7641
—	—	—	0.7	—	—	0.7092
—	—	—	0.1	0.5	—	1.1140
—	—	—	-	0.7	—	1.3200
—	—	—	—	0.9	—	1.5120
—	—	—	—	0.3	0.5	0.8764
—	—	—	—	—	0.6	0.8700
—	—	—	—	—	0.8	0.8589

(i) The velocity profile is declining due to upsurge in the curvature parameter and Williamson's parameter

(ii) Inclination of the Prandtl number and curvature parameter causes decline in the temperature profile, whereas it is intensified by increments in γ_c, B_p, and T_p

(iii) The concentration of nanoparticles is dropped via amplifying Le, Pr, and B_p

(iv) The greater value of Williamson's parameter and curvature parameter causes the drag force to increase

(v) Rate of transmission of heat is reduced for larger Williamson's parameter

Data Availability

The data used to support the findings of this study are included within the article.

Conflicts of Interest

The authors declare that they have no conflicts of interest.

References

[1] S. Nadeem, S. Ahmad, N. Muhammad, and M. T. Mustafa, "Chemically reactive species in the flow of a Maxwell fluid," *Results in Physics*, vol. 7, pp. 2607–2613, 2017.

[2] K. U. Rehman, A. Qaiser, M. Y. Malik, and U. Ali, "Numerical communication for MHD thermally stratified dual convection flow of Casson fluid yields by stretching cylinder," *Chinese Journal of Physics*, vol. 55, no. 4, pp. 1605–1614, 2017.

[3] M. Hassan, R. Ellahi, A. Zeeshan, and M. M. Bhatti, "Analysis of natural convective flow of non-Newtonian fluid under the effects of nanoparticles of different materials," *Proceedings of the Institution of Mechanical Engineers, Part E: Journal of Process Mechanical Engineering*, vol. 233, no. 3, pp. 643–652, 2019.

[4] S. Nadeem, S. Ahmad, and N. Muhammad, "Cattaneo-Christov flux in the flow of a viscoelastic fluid in the presence of Newtonian heating," *Journal of Molecular Liquids*, vol. 237, pp. 180–184, 2017.

[5] R. U. Haq, S. Nadeem, N. S. Akbar, and Z. H. Khan, "Buoyancy and radiation effect on stagnation point flow of micropolar nanofluid along a vertically convective stretching surface," *IEEE Transactions on Nanotechnology*, vol. 14, no. 1, pp. 42–50, 2014.

[6] Z. Ahmed, S. Nadeem, S. Saleem, and R. Ellahi, "Numerical study of unsteady flow and heat transfer CNT-based MHD nanofluid with variable viscosity over a permeable shrinking surface," *International Journal of Numerical Methods for Heat & Fluid Flow*, vol. 29, no. 12, pp. 4607–4623, 2019.

[7] M. M. Bhatti, A. Zeeshan, R. Ellahi, O. A. Bég, and A. Kadir, "Effects of coagulation on the two-phase peristaltic pumping of magnetized Prandtl biofluid through an endoscopic annular geometry containing a porous medium," *Chinese Journal of Physics*, vol. 58, pp. 222–234, 2019.

[8] M. Sheikholeslami, Z. Li, and A. Shafee, "Lorentz forces effect on NEPCM heat transfer during solidification in a porous energy storage system," *International Journal of Heat and Mass Transfer*, vol. 127, pp. 665–674, 2018.

[9] N. Ijaz, M. Bhatti, and A. Zeeshan, "Heat transfer analysis in magnetohydrodynamic flow of solid particles in non-Newtonian ree-eyring fluid due to peristaltic wave in a channel," *Thermal Science*, vol. 23, no. 2, pp. 1017–1026, 2019.

[10] N. S. Akbar, S. Nadeem, R. Ul Haq, and Z. H. Khan, "Radiation effects on MHD stagnation point flow of nano fluid towards a stretching surface with convective boundary condition," *Chinese Journal of Aeronautics*, vol. 26, no. 6, pp. 1389–1397, 2013.

[11] R. Ellahi, A. Zeeshan, F. Hussain, and T. Abbas, "Thermally charged MHD bi-phase flow coatings with non-Newtonian nanofluid and hafnium particles along slippery walls," *Coatings*, vol. 9, no. 5, p. 300, 2019.

[12] A. Zeeshan, N. Ijaz, T. Abbas, and R. Ellahi, "The sustainable characteristic of bio-bi-phase flow of peristaltic transport of MHD Jeffrey fluid in the human body," *Sustainability*, vol. 10, no. 8, p. 2671, 2018.

[13] F. U. Rehman, S. Nadeem, H. U. Rehman, and R. U. Haq, "Thermophysical analysis for three-dimensional MHD stagnation-point flow of nanomaterial influenced by an exponential stretching surface," *Results in Physics*, vol. 8, pp. 316–323, 2018.

[14] K. Parand, M. Fotouhifar, H. Yousefi, and M. Delkhosh, "A rational approximation to the boundary layer flow of a non-Newtonian fluid," *Journal of the Brazilian Society of Mechanical Sciences and Engineering*, vol. 41, no. 3, p. 125, 2019.

[15] M. F. Javed, M. I. Khan, N. B. Khan et al., "Axisymmetric flow of Casson fluid by a swirling cylinder," *Results in Physics*, vol. 9, pp. 1250–1255, 2018.

[16] A. Rehman, S. Nadeem, and M. Y. Malik, "Boundary layer stagnation-point flow of a third grade fluid over an exponentially stretching sheet," *Brazilian Journal of Chemical Engineering*, vol. 30, no. 3, pp. 611–618, 2013.

[17] M. Y. Malik, M. Bibi, F. Khan, and T. Salahuddin, "Numerical solution of Williamson fluid flow past a stretching cylinder and heat transfer with variable thermal conductivity and heat generation/absorption," *AIP Advances*, vol. 6, no. 3, Article ID 035101, 2016.

[18] S. U. Choi and J. A. Eastman, "Enhancing Thermal Conductivity of Fluids with Nanoparticles," Argonne National Lab., Lemont, IL, USA, No. ANL/MSD/CP-84938; CONF-951135-29, 1995.

[19] J. Buongiorno, "Convective transport in nanofluids," 2006.

[20] S. K. Das, S. U. Choi, W. Yu, and T. Pradeep, *Nanofluids: Science and Technology*, John Wiley & Sons, Hoboken, NJ, USA, 2007.

[21] C. Zhang, L. Zheng, X. Zhang, and G. Chen, "MHD flow and radiation heat transfer of nanofluids in porous media with variable surface heat flux and chemical reaction," *Applied Mathematical Modelling*, vol. 39, no. 1, pp. 165–181, 2015.

[22] N. Muhammad, S. Nadeem, and R. U. Haq, "Heat transport phenomenon in the ferromagnetic fluid over a stretching sheet with thermal stratification," *Results in Physics*, vol. 7, pp. 854–861, 2017.

[23] S. Saini and Y. D. Sharma, "Double-diffusive bioconvection in a suspension of gyrotactic microorganisms saturated by nanofluid," *Journal of Applied Fluid Mechanics*, vol. 12, no. 1, 2019.

[24] M. Safaei, G. Ahmadi, M. Goodarzi, M. Safdari Shadloo, H. Goshayeshi, and M. Dahari, "Heat transfer and pressure drop in fully developed turbulent flows of graphene nanoplatelets-silver/water nanofluids," *Fluids*, vol. 1, no. 3, p. 20, 2016.

[25] M. M. Rashidi, M. Nasiri, M. S. Shadloo, and Z. Yang, "Entropy generation in a circular tube heat exchanger using nanofluids: effects of different modeling approaches," *Heat Transfer Engineering*, vol. 38, no. 9, pp. 853–866, 2017.

[26] M. Goodarzi, A. Amiri, M. S. Goodarzi et al., "Investigation of heat transfer and pressure drop of a counter flow corrugated plate heat exchanger using MWCNT based nanofluids," *International Communications in Heat and Mass Transfer*, vol. 66, pp. 172–179, 2015.

[27] E. Abedini, T. Zarei, H. Rajabnia, R. Kalbasi, and M. Afrand, "Numerical investigation of vapor volume fraction in subcooled flow boiling of a nanofluid," *Journal of Molecular Liquids*, vol. 238, pp. 281–289, 2017.

[28] M. Afrand, E. Abedini, and H. Teimouri, "Experimental investigation and simulation of flow boiling of nanofluids in different flow directions," *Physica E: Low-Dimensional Systems and Nanostructures*, vol. 87, pp. 248–253, 2017.

[29] R. V. Williamson, "The flow of pseudoplastic materials," *Industrial & Engineering Chemistry*, vol. 21, no. 11, pp. 1108–1111, 1929.

[30] M. Ramzan, M. Bilal, and J. D. Chung, "MHD stagnation point Cattaneo-Christov heat flux in Williamson fluid flow with homogeneous-heterogeneous reactions and convective boundary condition-a numerical approach," *Journal of Molecular Liquids*, vol. 225, pp. 856–862, 2017.

[31] Z. Shah, E. Bonyah, S. Islam, W. Khan, and M. Ishaq, "Radiative MHD thin film flow of Williamson fluid over an unsteady permeable stretching sheet," *Heliyon*, vol. 4, no. 10, e00825 pages, 2018.

[32] R. A. Seban and R. Bond, "Skin-friction and heat-transfer characteristics of a laminar boundary layer on a cylinder in axial incompressible flow," *Journal of the Aeronautical Sciences*, vol. 18, no. 10, pp. 671–675, 1951.

[33] A. Mucoglu and T. S. Chen, "Buoyancy effects on forced convection along a vertical cylinder with uniform surface heat flux," *Journal of Heat Transfer*, vol. 98, no. 3, pp. 523–525, 1976.

[34] S. Nadeem, A. Rehman, and M. E. Ali, "The boundary layer flow and heat transfer of a nanofluid over a vertical, slender cylinder," *Proceedings of the Institution of Mechanical Engineers, Part N: Journal of Nanoengineering and Nanosystems*, vol. 226, no. 4, pp. 165–173, 2012.

[35] P. M. Patil, A. Shashikant, and P. S. Hiremath, "Effects of surface roughness on mixed convection nanoliquid flow over slender cylinder with liquid hydrogen diffusion," *International Journal of Hydrogen Energy*, vol. 44, no. 21, pp. 11121–11133, 2019.

[36] G. J. Reddy, B. Kethireddy, J. C. Umavathi, and M. A. Sheremet, "Heat flow visualization for unsteady Casson fluid past a vertical slender hollow cylinder," *Thermal Science and Engineering Progress*, vol. 5, pp. 172–181, 2018.

[37] G. J. Reddy, B. Kethireddy, and O. A. Beg, "Flow visualization using heat lines for unsteady radiative hydromagnetic micropolar convection from a vertical slender hollow cylinder," *International Journal of Mechanical Sciences*, vol. 140, pp. 493–505, 2018.

[38] B. Mallikarjuna, A. M. Rashad, A. Chamkha, and M. M. M. Abdou, "Mixed bioconvection flow of a nanofluid containing gyrotactic microorganisms past a vertical slender cylinder," *Frontiers in Heat and Mass Transfer (FHMT)*, vol. 10, 2018.

[39] G. J. Reddy, B. Kethireddy, M. Kumar, and H. P. Rani, "Entropy generation for transient Casson fluid past a vertical cylinder with Bejan's flow visualization," *International Journal for Computational Methods in Engineering Science and Mechanics*, vol. 20, no. 3, pp. 175–200, 2019.

[40] W. Xu, A. Cheng, Y. Ma, and X. Gao, "Multi-mode flow-induced vibrations of two side-by-side slender flexible cylinders in a uniform flow," *Marine Structures*, vol. 57, pp. 219–236, 2018.

[41] T. Li, N. Pintus, and G. Viglialoro, "Properties of solutions to porous medium problems with different sources and boundary conditions," *Zeitschrift für angewandte Mathematik und Physik*, vol. 70, no. 3, p. 86, 2019.

[42] R. Shah and T. Li, "The thermal and laminar boundary layer flow over prolate and oblate spheroids," *International Journal of Heat and Mass Transfer*, vol. 121, pp. 607–619, 2018.

Hindawi
Mathematical Problems in Engineering
Volume 2020, Article ID 4651823, 12 pages
https://doi.org/10.1155/2020/4651823

Research Article

An Improved MPC-Based SVPWM Mechanism for NPC Three-Level Z-Source Converters

Wenbao Hou,[1,2,3] **Guojun Tan**,[1] **and Delu Li**[2]

[1]*School of Electrical and Power Engineering, China University of Mining and Technology, Xuzhou, China*
[2]*JiangSu Vocational Institute of Architectural Technology, Xuzhou, China*
[3]*JiangSu Collaborative Innovation Center for Building Energy Saving and Construction Technology, Xuzhou, China*

Correspondence should be addressed to Guojun Tan; gjtan_cumt@163.com

Received 14 April 2020; Accepted 22 June 2020; Published 12 August 2020

Guest Editor: Yi Qi

Model predictive control (MPC) method has been widely used to reduce the computational complexity of the traditional space vector pulse width modulation (SVPWM). However, for a neutral-point clamped three-level Z-source converter, the performance of the normal MPC strategy would highly depend on the computation processing rate because of the multiple times optimization calculation. In this paper, an improved MPC strategy has been developed, with a voltage prediction being designed to replace the current prediction, the calculation of the roll optimization could be effectively simplified significantly, and then the digital execution efficiency would be improved. Besides, in order to obtain a fixed output harmonic frequency, a combination of this improved MPC and SVPWM has been studied and the shoot-through state insertion for the Z-source also has been analyzed in detail. Lastly, comparison experiments have been carried out to make verification of this improved modulation mechanism.

1. Introduction

NPC three-level converters have significant advantages, e.g., smaller device pressure, lower dv/dt, and better harmonic distortion in the output [1, 2]. With a Z-source network, this NPC three-level converters would have a wide range of adjustable voltage, some allowed shoot-through states and better harmonic distortion in the output, and have been widely used in the photovoltaic(PV) grid-connecting system and the ac drive field [3–8]. For example, a switched quasi-Z-source DC-DC inverter has been used for PV Systems [9], and a novel Z-source three-level four-leg inverter has been researched to reduce the leakage current for three-phase PV inverters [10]. Nevertheless, the control difficulty, e.g., modulation method and stability assurance, would also increase because of the existing of Z-source network.

In terms of modulation, many improved algorithms have been proposed, e.g., in [6], the space vectors pulse width modulation along with the shoot-through insertions were introduced to the single Z-source NPC three-level inverters. A pulse width modulation (PWM) based on the stage-space averaging model was researched in [11] for a novel quasi-Z-source inverter topology. In [12], a new modulation strategy was studied in detail to reduce the leakage current for the Z-source four-leg inverters. In [13], a hybrid switching method with the combination of the PWM and pulse amplitude modulation (PAM) was proposed in details, which might result in a complicated computation and a high switching frequency and a switching loss reduction method based on a modified space vector modulation strategy [14].

In the past few years, the finite control set model predictive control (FCS-MPC) has been widely used in the modern power electrical areas for its fast response and being suitable for the multivariable and nonlinear systems [1, 15, 16]. In [17], the high performance MPC method has been used for the quasi-impedance source inverter and a FCS-MPC method was studied in [18]for the quasi-Z-source four-leg inverters with the consideration of an unbalanced load

condition. In [19, 20], model predictive control based on the discrete models were also presented. In [21], the MPC strategy with a ripple power compensation structure was presented for the Z-source converters, and the corresponding output harmonic distortions were random which were unsuitable for the filtering.

Unfortunately, when the MPC method was used for the NPC three-level converters, the control performance could be influenced because of the excessive optimization calculations, and for these NPC three-level converters, which combined with the Z-source network, how to make insertions for the shoot-through states is also one of the difficulties. In [22], a modified MPC method by using a novel voltage prediction has been studied for the grid-connected T-type inverter, which could improve the execution efficiency.

In order to solve the above problems and develop an efficient modulation approach for the NPC three-level ZSC to simplify the control complexity, an improved MPC-based SVPWM mechanism has been presented in this paper. In detail, a voltage prediction was designed instead of the normal current prediction, and the calculation of the roll optimization could be simplified significantly although the optimization times are the same. Besides, in order to obtain a relative fixed output harmonic frequency, the optimized voltage vector resulted from the improved MPC method then was generated by the basic vectors of the normal SVPWM and the insertions of the shoot-through states also have been studied in detail.

This study is organized into five sections. Following the introduction, the operation principle of the NPC three-level ZSC is explained in Section 2. In Section 3, this improved MPC-based SVPWM mechanism has been introduced in detail with the comparison to the traditional MPC method. Section 4 illustrates the experimental results with the performance comparisons between the traditional SVPWM strategy. Finally, some conclusions are drawn in Section 5.

2. Operation Principle of the NPC Three-Level Z-Source Converters

The NPC three-level ZSC researched in this paper is shown in Figure 1, containing two independent DC-power supplies. The connection point O of supplies is also regarded as the zero potential linking with the clamped point.

If the three up switches turn on (e.g., SA_1, SA_2, and SA_3), it is called upper shoot-through (UST) status being denoted as status "U." On the contrary, if the three down switches turn on, it is called down shoot-through status (DST), which is represented as status "D." The different states of this topology is summarized in Table 1.

Hypothesis $C_1 = C_2$ and $L_1 = L_2$ (means $V_{C1} = V_{C2} = V_C$ and $V_{L1} = V_{L2} = V_L$). All the different states described in Table 1 can be summarized as three kinds of working conditions: nonshoot-through, UST, and DST. They are shown in Figures 2(a)–2(c), respectively. From Figure 2(a), several equations can be derived as follows:

$$\begin{cases} V_C = 2V_{dc} - V_L, \\ V_i = V_C - V_L, \\ V_P = \dfrac{V_i}{2}, \\ V_O = 0, \\ V_N = -\dfrac{V_i}{2}. \end{cases} \tag{1}$$

Similarly, the equations derived from Figures 2(b) and 2(c) are as follows:

$$\begin{cases} V_L = V_{dc}, \\ V_i = V_C - V_L, \\ V_P = V_O = 0, \\ V_N = -V_i. \end{cases} \tag{2}$$

$$\begin{cases} V_L = V_{dc}, \\ V_i = V_C - V_L, \\ V_P = V_i, \\ V_N = V_O = 0. \end{cases} \tag{3}$$

Here, the time duration of UST status is denoted as T_{sh_U} and T_{sh_D} for DST status. Normally, T_{sh_U} should be equal to T_{sh_D} in order to reduce the output voltage harmonic components, which means

$$T_{sh\_U} = T_{sh\_U} = T_{sh}. \tag{4}$$

At the steady state, the average voltages across L_1 and L_2 keep zero over the sampling period T_S, and the following equation could be derived from equations (1)–(3):

$$2V_{dc} \cdot T_{sh} + (2V_{dc} - V_c) \cdot (T_S - 2T_{sh}) = 0. \tag{5}$$

$$\begin{aligned} V_C &= \frac{T_S - T_{sh}}{T_S - 2T_{sh}} \cdot 2V_{dc} = \frac{(1 - T_{sh}/T_S)}{(1 - 2T_{sh}/T_S)} \cdot 2V_{dc} \\ &= \frac{1 - D}{1 - 2D} \cdot 2V_{dc}, \end{aligned} \tag{6}$$

where $D = (T_{sh}/T_S)$ is defined as the duty ratio of the shoot-through states.

According to equations (1) and (6), for the nonshoot-through state, the output voltage V_i could be obtained as

$$\begin{aligned} V_i &= V_C - V_L = 2(V_C - V_{dc}), \\ &= 2\left(\frac{1 - D}{1 - 2D} 2V_{dc} - V_{dc}\right) = \frac{1}{1 - 2D} 2V_{dc}. \end{aligned} \tag{7}$$

For the Up or Down shoot-through states, the output voltage V_i could be obtained according to equations (2), (3), and (6):

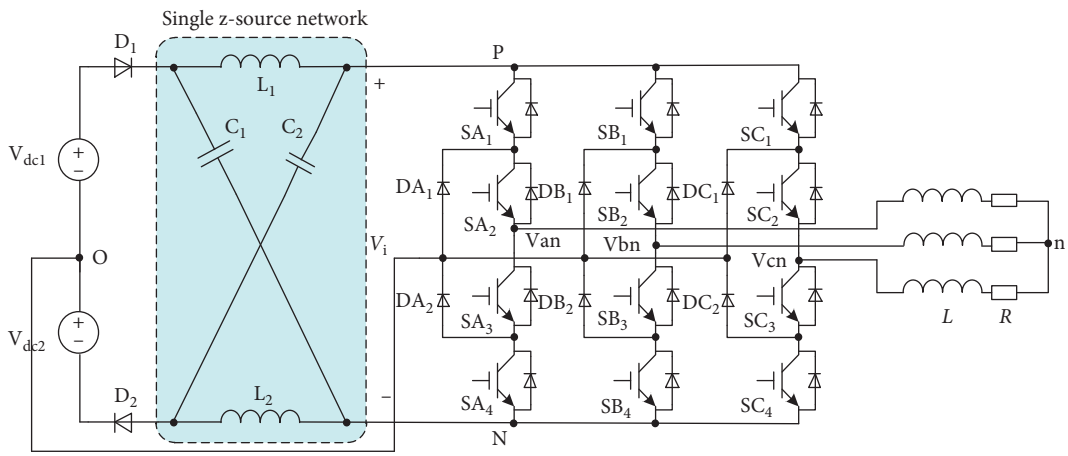

Figure 1: Topology of the NPC three-level ZSC.

Table 1: Different states and output voltage.

Mode	Turn-on switches	Output voltage
1	SX_1, SX_2, D_1, D_2	$V_i/2$
0	SX_2, SX_3, D_1, D_2	0
−1	SX_3, SX_4, D_1, D_2	$-V_i/2$
U	SX_1, SX_2, SX_3, D_1	0 or $-V_i$
D	SX_2, SX_3, SX_4, D_2	0 or V_i

Here, $X = A$, B, or C.

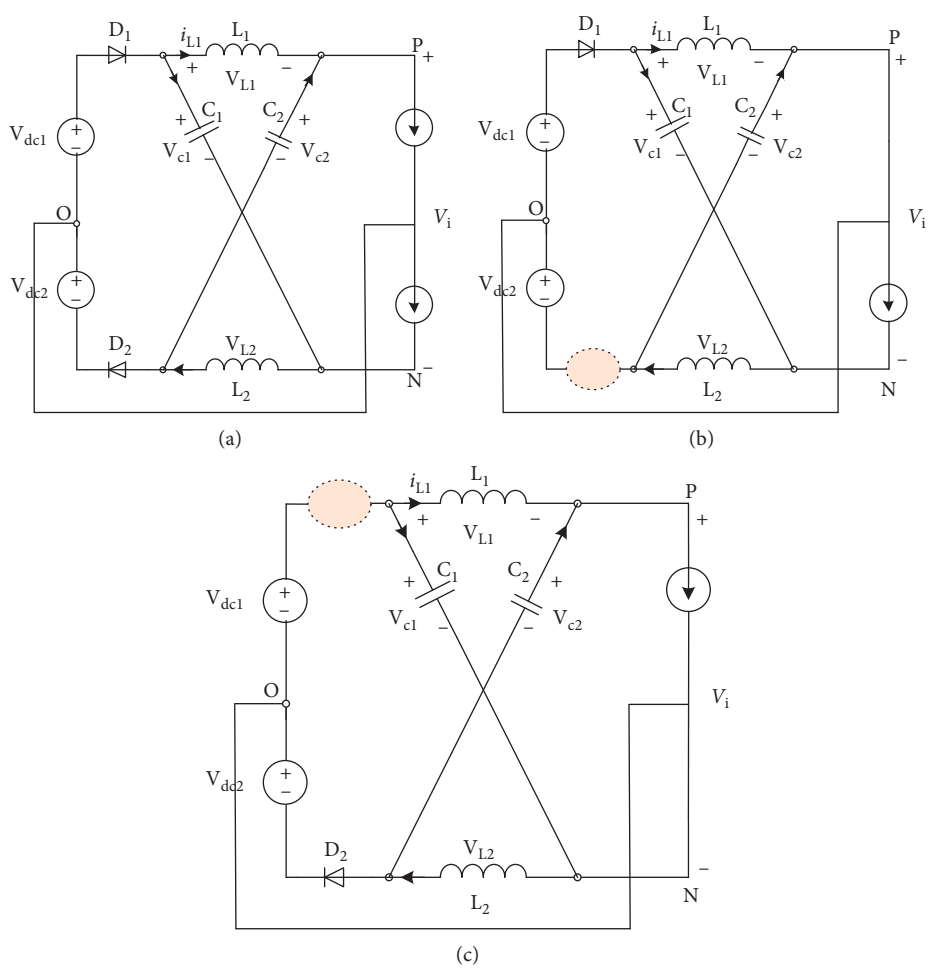

Figure 2: Equivalent circuits of the different states. (a) Nonshoot-through (b) Up shoot-through. (c) Down shoot-through.

$$V_{\mathrm{i}} = V_{\mathrm{C}} - V_{\mathrm{L}} = V_{\mathrm{C}} - V_{\mathrm{dc}},$$
$$= \frac{1-D}{1-2D} 2V_{\mathrm{dc}} - V_{\mathrm{dc}} = \frac{1}{1-2D} V_{\mathrm{dc}}. \tag{8}$$

Now, the three output voltages could also be represented as

$$V_{\mathrm{P}} = \frac{V_{\mathrm{dc}}}{1-2D},$$
$$V_{\mathrm{O}} = 0, \tag{9}$$
$$V_{\mathrm{N}} = -\frac{V_{\mathrm{dc}}}{1-2D}.$$

And the output phase voltage U_x could be derived as

$$U_x = M \cdot \frac{V_{\mathrm{dc}}}{1-2D} = MH \cdot V_{\mathrm{dc}}, \quad x = a, b, c, \tag{10}$$

where M is the modulation coefficient and $H = 1/(1\text{-}2D)$ represents the booster ratio.

3. An Improved MPC-Based SVPWM Mechanism

3.1. Traditional MPC. The mathematical model of the NPC three-level ZSC in $\alpha\beta$ coordinates can be given as

$$u_{\alpha,\beta} = L\frac{\mathrm{d}i_{\alpha,\beta}}{\mathrm{d}t} + Ri_{\alpha,\beta}, \tag{11}$$

where R and L are the load resistance and inductance, respectively.

By using the Euler approximation for a sampling time T_{s} (shown in equation (12)), equation (10) is discretized as in equation (13):

$$\frac{\mathrm{d}x(t)}{\mathrm{d}t} = \frac{x(k+1) - x(k)}{T_s}, \tag{12}$$

$$i_{\alpha,\beta}(k+1) = \left[1 - \frac{T_s R}{L}\right] i_{\alpha,\beta}(k) + \frac{T_s}{L} u_{\alpha,\beta}(k), \tag{13}$$

where $i_{\alpha,\beta}$ is the output current in $\alpha\beta$ coordinates, $u_{\alpha,\beta}$ stands for the output voltage also in $\alpha\beta$ coordinates, which is determined by the 27 switching states of the NPC three-level ZSC, and k is the kth sampling period.

From this mathematical model, the predictive output current at $(k+1)$th could be derived as

$$i^P_{\alpha,\beta}(k+1) = \left[1 - \frac{T_s R}{L}\right] i_{\alpha,\beta}(k) + \frac{T_s}{L} u_{\alpha,\beta}(k). \tag{14}$$

For the traditional MPC strategy, a roll optimization of objective function could be set, as shown in equation (15), for the current trajectory control:

$$g = \left|i^*_\alpha(k+1) - i^P_\alpha(k+1)\right| + \left|i^*_\beta(k+1) - i^P_\beta(k+1)\right|, \tag{15}$$

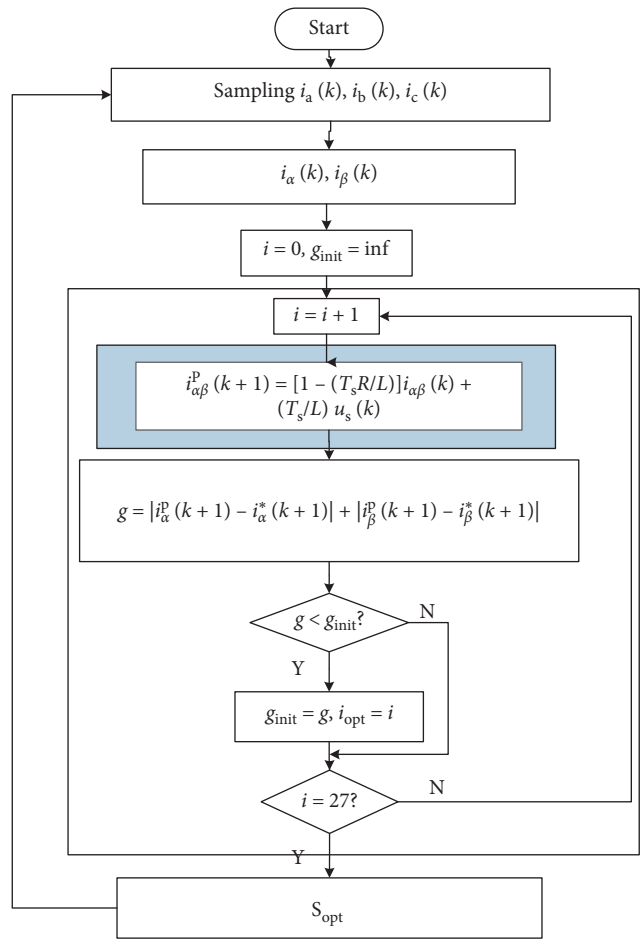

Figure 3: Implementation flow chart of the traditional MPC.

where $i^*_\alpha(k+1)$ and $i^*_\beta(k+1)$ are the given current components, respectively, and $i^{\mathrm{P}}_\alpha(k+1)$ and $i^{\mathrm{P}}_\beta(k+1)$ are the predictive current components from equation (14).

Obviously, for this traditional method, 27 cycles of optimization should be conducted to obtain the smallest g and the corresponding optimal switching state, in which equation (13) need to be also calculated 27 times in order to obtain the current components with different input voltages, which significantly increases the computation consumption. The implementation flow chart of the traditional MPC strategy is shown in Figure 3.

3.2. Improved MPC. For equation (14), the input voltage can be represented as

$$u_{\alpha,\beta}(k) = \frac{L}{T_s}\left[i^P_{\alpha,\beta}(k+1) - i_{\alpha,\beta}\right] + Ri_{\alpha,\beta}(k). \tag{16}$$

Assume that the predictive output current in equation (15) equals the given current components in ideal condition, which means

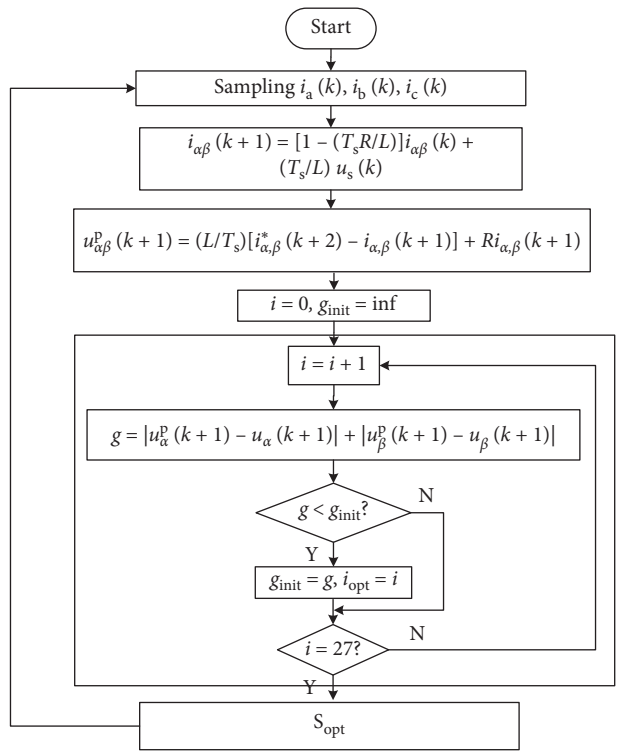

Figure 4: Implementation flow chart of the improved MPC.

$$i^*_{\alpha,\beta}(k+1) = i^p_{\alpha,\beta}(k+1). \tag{17}$$

With the combination of equations (16) and (17), the predictive voltage components $u^p_{\alpha,\beta}(k)$ could be obtained as

$$u^p_{\alpha,\beta}(k) = \frac{L}{T_s}\left(i^*_{\alpha,\beta}(k+1) - i_{\alpha,\beta}(k)\right) + Ri_{\alpha,\beta}(k), \tag{18}$$

where superscript "p" means the expected value and $i^*_{\alpha,\beta}(k+1)$ is the reference current at $(k+1)$th sampling, while the $i_{\alpha,\beta}(k)$ is the actual current at kth sampling.

For the improved MPC strategy, the roll optimization of objective function was set as

$$g = \left|u^p_\alpha(k) - u_\alpha(k)\right| + \left|u^p_\beta(k) - u_\beta(k)\right|. \tag{19}$$

In order to make compensation of the time delay, equations (18) and (19) are shifted one step forward. Thus, the predictive voltage components and the objective function at $(k+1)$th could be derived as equations (20) and (21):

$$u^p_{\alpha,\beta}(k+1) = \frac{L}{T_s}\left(i^*_{\alpha,\beta}(k+2) - i_{\alpha,\beta}(k+1)\right) + Ri_{\alpha,\beta}(k+1), \tag{20}$$

$$g = \left|u^p_\alpha(k+1) - u_\alpha(k+1)\right| + \left|u^p_\beta(k+1) - u_\beta(k+1)\right|. \tag{21}$$

The implementation flow chart of this improved MPC strategy then could be derived, as shown in Figure 4.

It is obvious that, for the improved MPC, the current calculation within the roll optimization has been omitted, which could improve the execution efficiency to a great degree.

On the other aspect, for the prediction accuracy, the predictive voltage error could be derived with equations (16) and (18):

$$\begin{aligned}\left|u^p_{\alpha\beta}(k) - u_{\alpha\beta}(k)\right| &= \left|\left\{\frac{L}{T_s}\left(i^*_{\alpha,\beta}(k+1) - i_{\alpha,\beta}(k)\right) + Ri_{\alpha,\beta}(k)\right\}\right. \\ &\quad \left. - \left\{\frac{L}{T_s}\left(i^p_{\alpha,\beta}(k+1) - i_{\alpha,\beta}(k)\right) + Ri_{\alpha,\beta}(k)\right\}\right|, \\ &= \frac{L}{T_s}\left|i^*_{\alpha,\beta}(k+1) - i^p_{\alpha,\beta}(k+1)\right|.\end{aligned} \tag{22}$$

From (22), it can be seen that the voltage tracking performance is consistent with the current, which provides the validation of the proposed improved MPC strategy.

3.3. Insertion of the Shoot-Through States. For both the traditional and improved MPC strategies, their output frequency is a varying variable, which is unsuitable for the filtering design. Here, the optimized voltage $u_{opt}(k)$ (the corresponding switch state is S_{opt}) has been implemented by the basic space voltage vectors and based on which the shoot-through states of the Z-source are inserted to ensure the boost performance. The MPC-based SVPWM mechanism is shown in Figure 5.

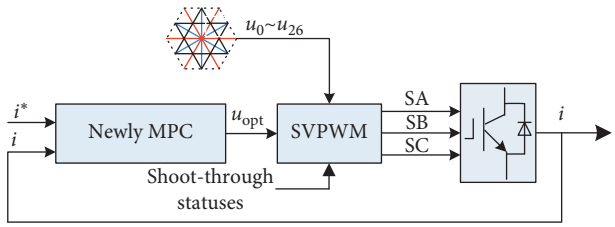

Figure 5: MPC-based SVPWM mechanism.

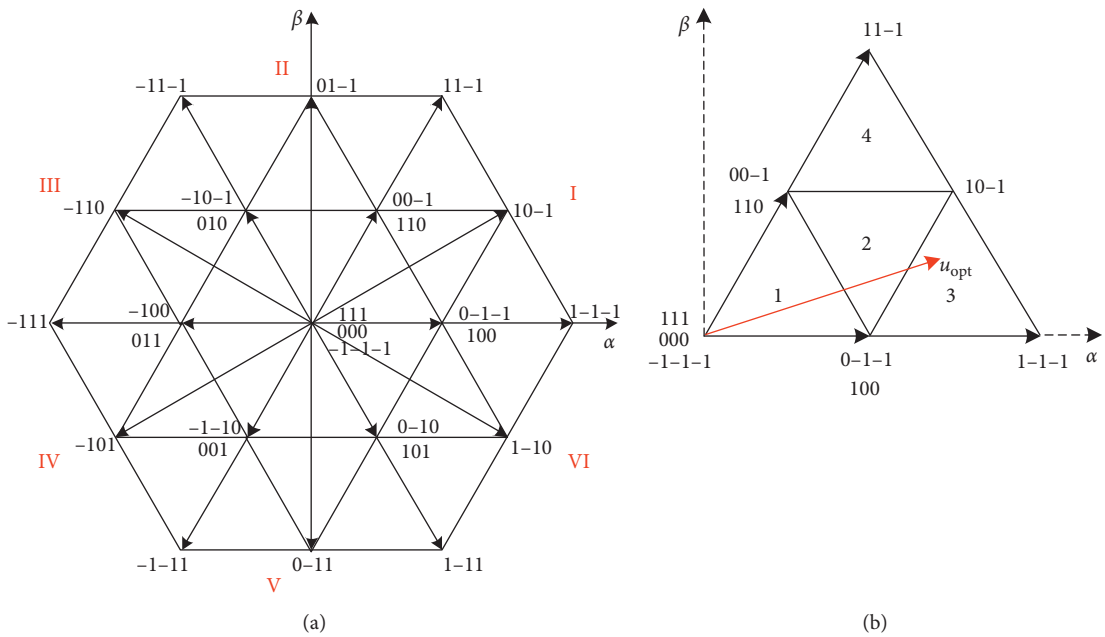

Figure 6: Space voltage vectors of the NPC three-level converter. (a) Space voltage vectors. (b) Space voltage vectors in Zone I.

Shoot-trough states' insertion not only determines the boost performance but also affects the output harmonic distortion and the switch losses. For the space voltage vectors shown in Figure 6(a), it is being taken as an example that the obtained optimized voltage u_{opt} locates in Zone I and triangle 3, as shown in Figure 6(b).

Assume that the initial switch state is "0 −1 −1," which means SA2, SA3, SB3, SB4, SC3, and SC4 are turned ON:

(1) At $t = t1$, state "0 −1 −1" should be switched to "1 −1 −1" (for phase A, SA is changed from "0" to "1"), and the UST could be inserted in phase A by previously turning on the switch "SA1," as shown in Figure 7 (SA1, SA2, and SA3 are ON while SA4 are OFF). During this insertion, the switch states for phases B and C remain unchanged, which satisfy the "volt-second" principle.

(2) At $t = t2$, state "1 −1 −1" should be switched to "1 0 −1" (for phase B, SB is changed from "−1" to "0"). If the UST is previously inserted in phase B, the switch state of phase A could be kept as "1," while the switch state of phase C should be clamped from "−1" to "0," which means the "volt-second" state would be destroyed so this insertion should be omitted.

(3) At $t = t3$, state "1 0−1" should be switched to "1 0 0" (for phase C, SC is changed from "−1" to "0"). The DST could be inserted in phase C by persistently turning on the switch "SC4," as shown in Figure 7 (SC2, SC3, and SC4 are ON while SC1 are OFF). During this insertion, the switch states for phases A and B remain unchanged, which satisfy the "volt-second" principle.

Obviously, when the reference vector is located in Zone I and triangle 3, the UST and DST can be inserted in the interaction range of the equivalent zero vector. Thus, the condition of $T_{sh\_U} = T_{sh\_D}$ can ensure the balance of the UST status and the DST status.

From Figure 7, it could be easily seen that both the up and down shoot-through states would increase the output voltage (comparing Ref.Va(SA') and Ref.Va(SA) and Ref.Vc(SC') and Ref.Vc(SC)).

4. Experimental Results

In this paper, the effectiveness of the proposed improved MPC-based SVPWM mechanism is verified via an

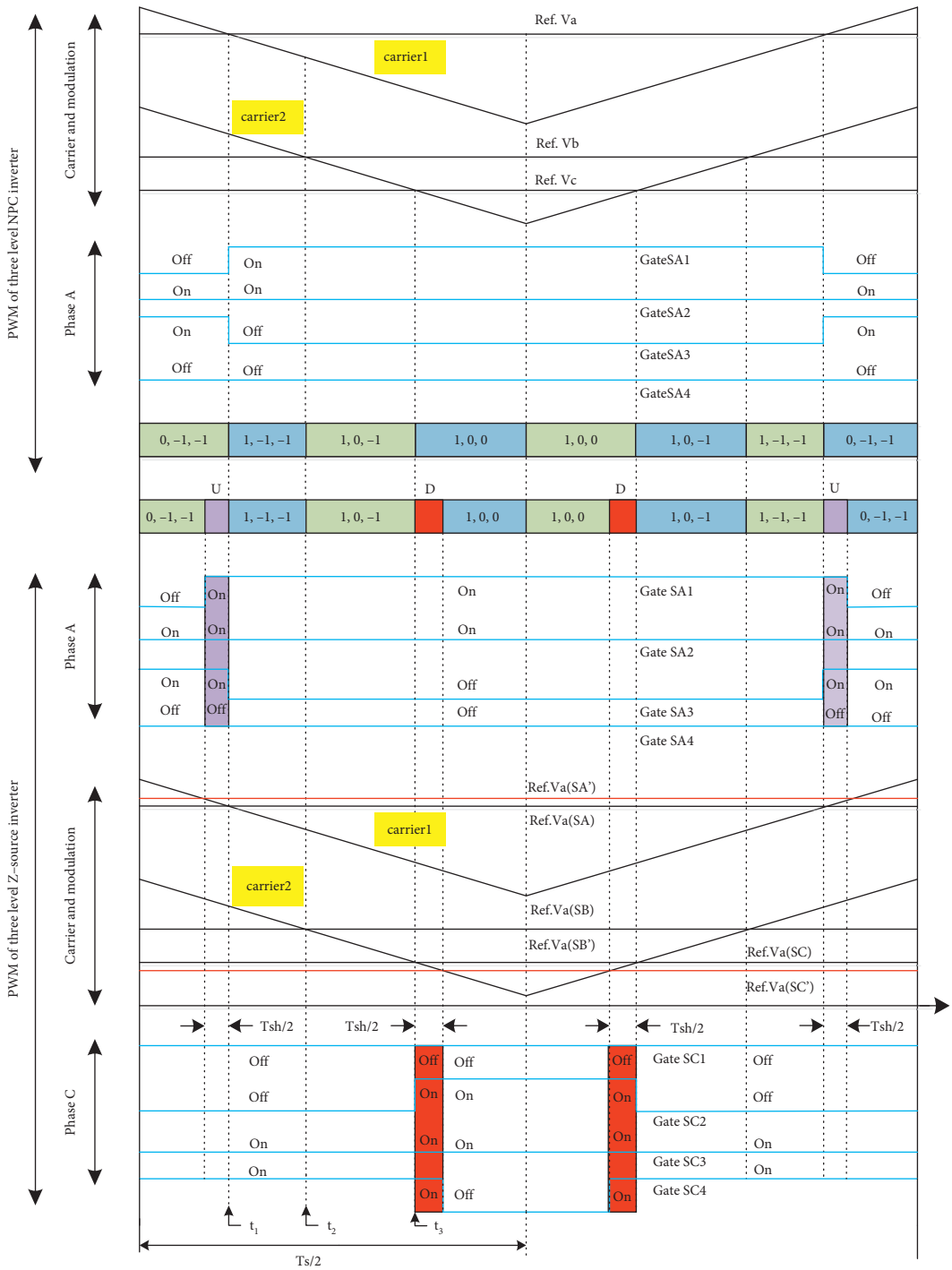

Figure 7: Insertion strategy (Zone I and triangle 3).

established experimental platform, as shown in Figure 8, along with the deep comparisons with the traditional SVPWM method. The detailed parameters are listed in Table 2. The control algorithm is implemented on a TMS320F28335 DSP with floating-point arithmetic.

Firstly, when the input voltage V_{dc} changes from 100 V to 200 V ($V_{dc1} = V_{dc2}$ change from 50 V to 100 V), the corresponding dynamical line and phase voltages of the improved strategy are shown in Figure 9.

However, because of the voltage prediction error shown in Figure 10, there is some voltage ripple existing in the DC-link voltage.

When the duty ratio D changes from 0 to 0.3, which means the output voltage of the Z-source topology V_i could be 2.5 times as much as the input voltage V_{dc} (according to equation (7)), the dynamical output line and phase voltages u_{ab} and u_a from the traditional SVPWM method and the improved proposed MPC-based

Figure 8: Experimental platform.

Table 2: Platform parameters.

Parameters	Value
DC-link voltage ($V_{dc1} = V_{dc2}$) (V)	50
Inductance of Z-source ($L_1 = L_2$) (mH)	2
Capacitance of Z-source ($C_1 = C_2$) (μF)	100
Load inductance (mH)	5
Load resistance (Ω)	10
Sampling frequency (Hz)	10 k
Reference current's amplitude (A)	10
Duty ratio(D)	0->0.3

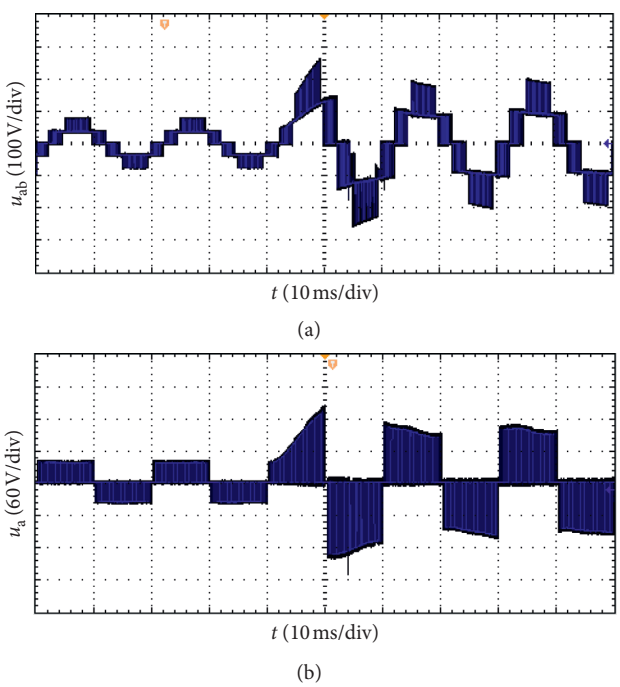

Figure 9: Dynamical line and phase voltages of the improved MPC-based SVPWM mechanism. (a) Line voltage u_{ab}. (b) Phase voltage u_a.

SVPWM mechanism are shown in Figures 11 and 12, respectively.

Correspondingly, the output voltage V_i and the capacitors' voltages V_{c1} and V_{c2} are shown in Figures 13 and 14. It is obvious that V_i changes from 100 V to about 250 V and the

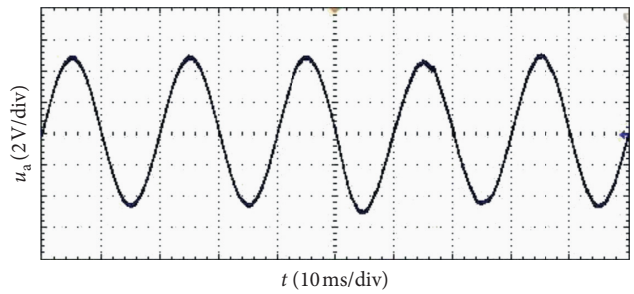

Figure 10: Voltage prediction error.

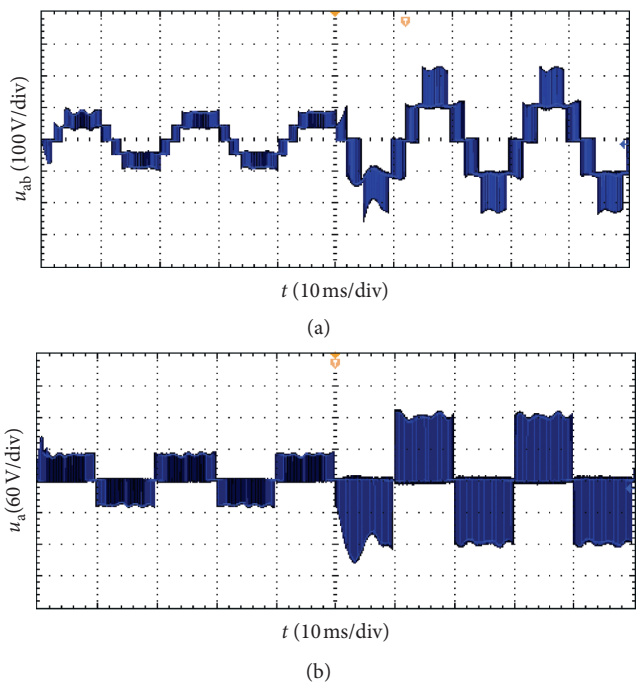

Figure 11: (a) Line voltage u_{ab} and (b) Phase voltage u_a of the traditional SVPWM.

capacitors' voltages are basically guaranteed to be in equilibrium.

For the output current, the dynamic comparisons are shown in Figures 15 and 16 along with the harmonic distortion analysis by taking a-phase current as an example.

From Figures 15 and 16, it can be seen that the harmonic distortion changes from 3.69% to 2.11% for the traditional and improved methods without the booster function ($D = 0$), while from 4.20% to 3.53% with the insertion of the shoot-through states ($D = 0.3$), which could make verification of the improved mechanism studied in this paper. Besides, with the improved MPC-based SVPWM mechanism, the harmonic frequency is a relative fixed value, which is suitable for the filter designing. Besides, after the dynamic change, the restability time is about half an cycle for this improved MPC-based SVPWM, which is faster than the traditional SVPWM method (about one cycle).

In order to exhibit the superior property of the improved MPC-based SVPWM mechanism. The execution

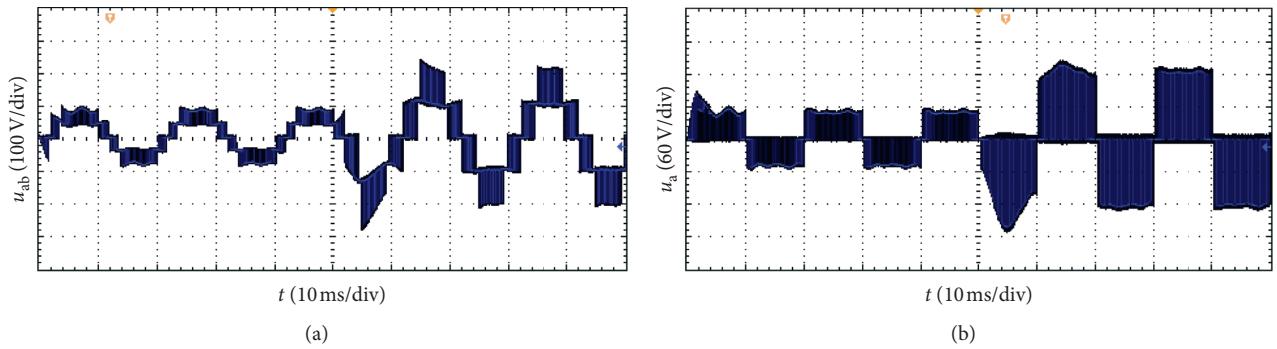

Figure 12: (a) Line voltage u_{ab}. (b) Phase voltage u_a of the improved strategy.

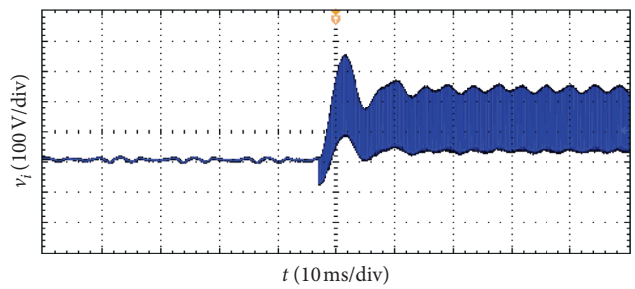

Figure 13: Output voltage V_i.

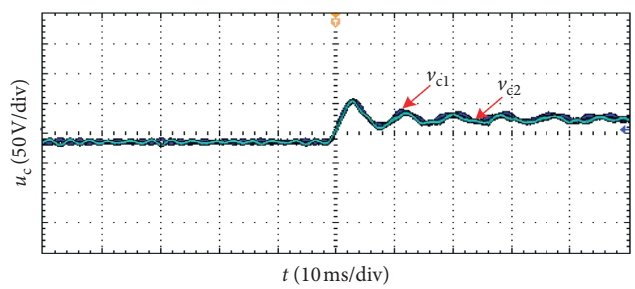

Figure 14: Capacitors' voltages V_{C1} and V_{C2}.

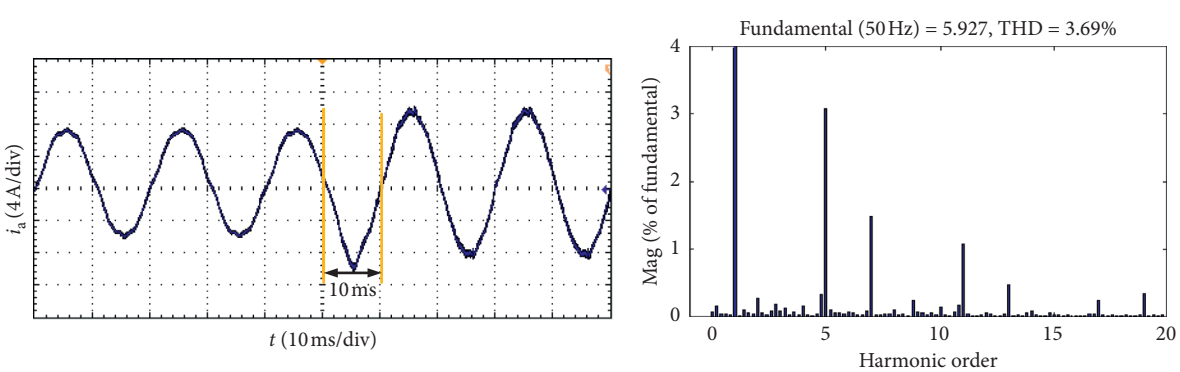

Figure 15: Continued.

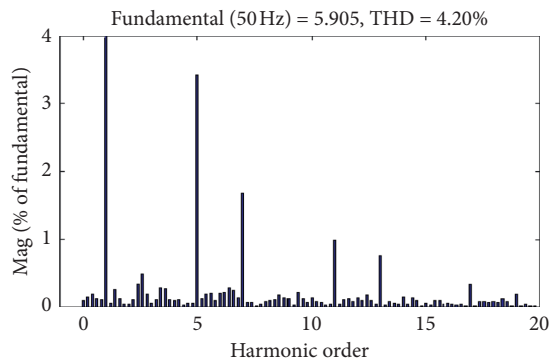

(c)

Figure 15: Dynamic current waveform and the corresponding THD analysis of the traditional SVPWM method. (a) Dynamic a-phase current i_a. (b) THD of i_a when $D = 0$. (c) THD of i_a when $D = 0.3$.

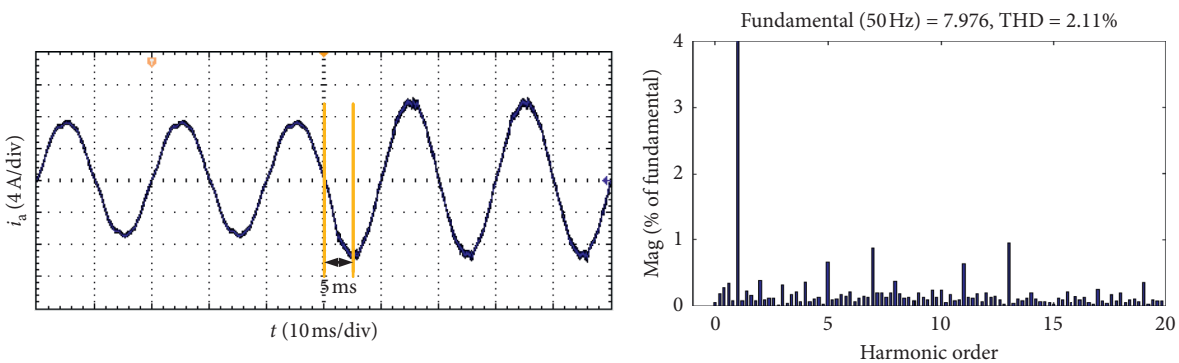

(a) (b)

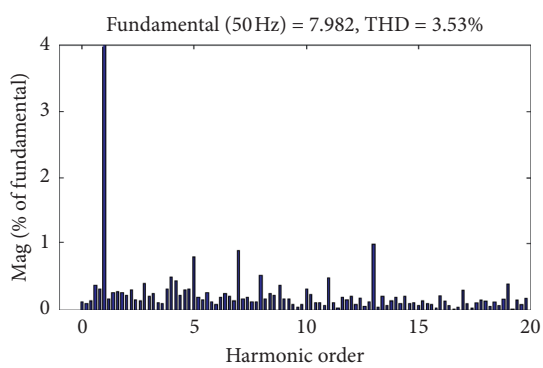

(c)

Figure 16: Dynamic current waveform and the corresponding THD analysis of the improved MPC-based SVPWM mechanism. (a) Dynamic a-phase current i_a. (b) THD of i_a when (D) = 0. (c) THD of i_a when (D) = 0.3.

time comparisons between the proposed method, the traditional SVPWM, and the normal MPC-based SVPWM are summarized in Table 3, where the execution time is calculated by averaging ten-time measured results when $D = 0$ and $D = 0.3$ and the sampling frequency is 10 kHz.

For the normal MPC-based SVPWM method, it has 10.03% and 13.91% time savings than the traditional SVPWM for the complicated trigonometric calculations has been omitted. Similarly, for the calculation reduction in the roll optimization, the improved scheme has over 26.25% and 19.25% time saving improvements than the traditional SVPWM and the normal MPC-based SVPWM when $D = 0$, while 28.78% and 17.27% when $D = 0.3$.

Table 3: Execution time comparisons.

	Traditional SVPWM (μs)	Normal MPC-based SVPWM (μs)	Improved MPC-based SVPWM (μs)
$D = 0$	18.13	16.31	13.37
$D = 0.3$	19.91	17.14	14.18

5. Conclusions

In this paper an improved MPC-based SVPWM mechanism has been proposed for the NPC three-level ZSC. Firstly, in order to improve the execution efficiency, a novel voltage prediction has been derived based on the mathematical models to replace the normal current prediction, by which the optimization could be effectively simplified along with a relative nice performance. Besides, with the combination of the improved MPC and SVPWM, the harmonic frequency of the output current could be kept relatively fixed to be suitable for the filtering design and the shoot-through states insertions have been also studied to realize the voltage boosting. Lastly, comparison experiments have been carried out to make verification of this improved MPC-based SVPWM mechanism. In particular, this improved method has a similar static performance to the traditional SVPWM with a better dynamic performance, while for the execution efficiency, it has over 26.25% and 19.25% time saving improvements than the traditional SVPWM and the normal MPC-based SVPWM when $D = 0$, while 28.78% and 17.27% when $D = 0.3$, which is suitable for the digital implementation.

Data Availability

The processed data required to reproduce these findings cannot be shared at this time as the data also forms part of an ongoing study.

Conflicts of Interest

The authors declare that they have no conflicts of interest.

Acknowledgments

This work was supported by Research Foundation of JiangSu Collaborative Innovation Center for Building Energy Saving and Construction Technology (no. SJXTBS1704); Jiangsu University Natural Science Research Project (No. 18KJB470024).

References

[1] Q. Yuan, J. Qian, H. Wu, W. Yin, and Q. Jiang, "Stator current harmonic elimination control for the high-power synchronous motors with online implementation," *IET Power Electronics*, vol. 12, no. 4, pp. 801–809, 2019.

[2] R. Vargas, P. Cortés, U. Ammann, J. Rodriguez, and J. Pontt, "Predictive control of a three-phase neutral-point-clamped inverter," *IEEE Transactions on Industrial Electronics*, vol. 54, no. 5, pp. 2697–2705, 2007.

[3] Z. Fang, "Z-source inverter," *IEEE Transactions On Industry Applications*, vol. 39, no. 2, pp. 504–510, 2003.

[4] Y. Zhang, C. Fu, M. Sumner, and P. Wang, "A wide input-voltage range quasi-Z-source boost DC-DC converter with high-voltage gain for fuel cell vehicles," *IEEE Transactions on Industrial Electronics*, vol. 65, no. 6, pp. 5201–5212, 2018.

[5] F. Z. Peng, M. Shen, and K. Holland, "Application of Z-source inverter for traction drive of fuel cell-battery hybrid electric vehicles," *IEEE Transactions on Power Electronics*, vol. 22, no. 3, pp. 1054–1061, 2007.

[6] P. C. Loh, F. Gao, F. Blaabjerg, and S. W. Lim, "Operational analysis and modulation control of three-level Z-source inverters with enhanced output waveform quality," *IEEE Transactions on Power Electronics*, vol. 24, no. 7, pp. 1767–1775, 2009.

[7] X. Guo, Y. Yang, and T. Zhu, "ESI: a novel three-phase inverter with leakage current attenuation for transformerless PV systems," *IEEE Transactions on Industrial Electronics*, vol. 65, no. 4, pp. 2967–2974, 2018.

[8] F. Gao, P. C. Loh, F. Blaabjerg, and D. M. Vilathgamuwa, "Performance evaluation of three-level Z-source inverters under semiconductor-failure conditions," *IEEE Transactions on Industry Applications*, vol. 45, no. 3, pp. 971–981, May. 2009.

[9] J. Liu, J. Wu, J. Qiu, and J. Zeng, "Switched Z-source/quasi-Z-source DC-DC converters with reduced passive components for photovoltaic systems," *IEEE Access*, vol. 7, pp. 40893–40903, 2019.

[10] X. Zeng, Y. Yang, B. Wang, and F. Blaabjerg, "Leakage current reduction of three-phase Z-source three-level four-leg inverter for transformerless PV system," *IEEE Transactions on Power Electronics*, vol. 34, no. 7, pp. 6299–6308, 2019.

[11] A. Blaabjerg, E.-H. Miliani, S. Pierfederici, and F. Meibody-Tabar, "A novel quasi-Z-source inverter topology with special coupled inductors for input current ripples cancellation," *IEEE Transactions on Power Electronics*, vol. 31, no. 3, pp. 2409–2416, Mar. 2016.

[12] X. Guo, Y. Yang, R. He, B. Wang, and F. Blaabjerg, "Transformerless Z-source four-leg PV inverter with leakage current reduction," *IEEE Transactions on Power Electronics*, vol. 34, no. 5, pp. 4343–4352, May. 2019.

[13] M. Wang, J. S. Moghani, and J. Milimonfared, "A novel dual switching frequency modulation for Z-source and quasi-Z-source inverters," *IEEE Transactions on Industrial Electronics*, vol. 65, no. 6, pp. 5167–5176, 2018.

[14] A. Abdelhakim, P. Davari, F. Blaabjerg, and P. Mattavelli, "Switching loss reduction in the three-phase quasi-Z-source inverters utilizing modified space vector modulation strategies," *IEEE Transactions on Power Electronics*, vol. 33, no. 5, pp. 4045–4060, 2018.

[15] X. Mattavelli, J. Zou, J. Zhao et al., "A novel model predictive control strategy to eliminate zero-sequence circulating current in paralleled three-level inverters," *IEEE Journal of Emerging and Selected Topics in Power Electronics*, vol. 7, no. 1, pp. 309–320, Mar. 2019.

[16] B. Hu, L. Kang, J. Liu, J. Zeng, S. Wang, and Z. Zhang, "Model predictive direct power control with fixed switching frequency and computational amount reduction," *IEEE Journal of Emerging and Selected Topics in Power Electronics*, vol. 7, no. 2, pp. 956–966, Jun. 2019.

[17] M. Mosa, R. S. Balog, and H. Abu-Rub, "High-performance predictive control of quasi-impedance source inverter," *IEEE Transactions on Power Electronics*, vol. 32, no. 4, pp. 3251–3262, 2017.

[18] S. Bayhan, M. Trabelsi, H. Abu-Rub, and M. Malinowski, "Finite-control-set model-predictive control for a quasi-Z-source four-leg inverter under unbalanced load condition," *IEEE Transactions on Industrial Electronics*, vol. 64, no. 4, pp. 2560–2569, Apr. 2017.

[19] A. Ayad, P. Karamanakos, and R. Kennel, "Direct model predictive current control strategy of quasi-Z-source

inverters," *IEEE Transactions on Power Electronics*, vol. 32, no. 7, pp. 5786–5801, 2017.

[20] Y. Liu, H. Abu-Rub, Y. Xue, and F. Tao, "A discrete-time average model-based predictive control for a quasi-Z-source inverter," *IEEE Transactions on Industrial Electronics*, vol. 65, no. 8, pp. 6044–6054, 2018.

[21] L. He, J. Nai, and J. Zhang, "Single-phase safe-commutation trans-Z-source AC-AC converter with continuous input current," *IEEE Transactions on Industrial Electronics*, vol. 65, no. 6, pp. 5135–5145, 2018.

[22] V.-Q.-B. Ngo, M.-K. Nguyen, and T.-T. Tran, "A modified model predictive power control for grid-connected T-Type inverter with reduced computational complexity," *Electronics*, vol. 8, no. 2, 2019.

Hindawi
Mathematical Problems in Engineering
Volume 2020, Article ID 7417314, 11 pages
https://doi.org/10.1155/2020/7417314

Research Article

Robust Model-Free Control for Robot Manipulator under Actuator Dynamics

Dorsaf Elleuch and Tarak Damak

University of Sfax, National Engineering School of Sfax (ENIS), Laboratory of Sciences and Techniques of Automatic Control & Computer Engineering (Lab-STA), Tunisia B. P. 1173, 3038 Sfax, Tunisia

Correspondence should be addressed to Dorsaf Elleuch; dorsafelleuch@yahoo.fr

Received 26 April 2020; Revised 12 July 2020; Accepted 17 July 2020; Published 3 August 2020

Guest Editor: Cuimei Jiang

An intelligent proportional-derivative sliding mode controller (i-PDSMC) is presented to overcome the unmodeled complexity of the robot manipulator under an actuator. i-PDSMC is a free model intelligent control based on the ultralocal, sliding mode, and PD control structure. A stability condition is determined by the Lyapunov theory. A comparative study between a classical PD, an intelligent PD control, and i-PDSMC is done through a robot manipulator under actuators. The simulation results prove that the proposed controller is more robust to trajectory tracking under parameter variations and external disturbances.

1. Introduction

Disturbance and uncertainty are the major problems of the robot manipulator control. In the literature, many model-based controls have shown a robustness to overcome uncertainty such as the sliding mode control, but the chattering phenomenon is still its major problem, or the backstepping control, which is limited for strict feedback nonlinear systems. Researchers take more interest in PD control because of its rapidity and its steady-state tracking error which is imposed.

Because of the sliding mode control robustness, in [1–4], the authors have developed a sliding mode control in which the equivalent control term is the PD control and the sliding surface is of the PD form. In this controller, named PD-SMC, only a measured feedback is considered. The proposed PD-SMC applied to a robot manipulator proved a better performance than the classical SMC in reducing tracking errors. In [1], a comparative study is done between PD, SMC, and PD-SMC in which the last controller showed the best performance under parameter variations. However, the PD-SMC parameters must be carefully chosen due to the significant and complicate effect on the tracking error. In [4], the authors proposed an adaptive PD-SMC (APD-SMC) scheme in which the discontinuous term is obtained by an adaptation law. The APD-SMC performances are tested and validated through a 4 DOF SCARA robotic manipulator.

Formerly, the model complication was removed, and a nonmodel or free model control was introduced. This control, named model-free control (MFC), does not need a model to determine the control law. It is based on an ultralocal model, a PID control, and a compensate term. The ultralocal model is online estimated using input and output measurements. This MFC is called an intelligent PID (i-PID) control. In [5, 6], the authors prove that i-PID is robust to trajectory tracking than the classical PID. Also, the intelligent PI (i-PI) [7, 8] and the intelligent PD (i-PD) [9–11] are studied in the literature. Both controllers, which are validated on complex nonlinear systems, show the best performance compared to other different model-based controls. The advantages of MFC have attracted many researchers to develop a new control form. For that, a partial MFC in which the control law depends on a part of

the model (input matrix) and the controller gains are optimized using a linear quadratic regulator (LQR) is proposed in [12]. The partial MFC performances are proved through a helicopter system. In [13–15], the authors have developed a robust MFC based on the sliding mode technique for a multilink flexible robot-based energy relationship of the system.

Sometimes a control-based observer or state estimation is named as the model-free control [16, 17]. But, this method still depends totally or partially on the model structure to build an estimator or an observer. In [16], the authors proposed a model-free filtered backstepping control for marine power systems. The estimated dynamic model converges slowly to its real value. In [17], a terminal sliding mode controller combined with a nonlinear disturbance observer is proposed. The observer is based on the model dynamic system part, and the control results did not have a well performance.

A model-free sliding mode controller can be a more attractive approach. In [18, 19], the control law was designed using only the measured state and the previous control input. A nonlinear second-order system is considered to show the proposed controller performance under measured noise and parameter variations. These results were extended to multi-input multioutput systems [20, 21]. The MFC sliding mode control (MFC-SMC) is developed based on a PI control. The designed control is validated on a twin-rotor aerodynamic system (TRAS), and it is implemented as two SISO control loops. The corresponding simulation and experimental results show a good performance of the MFC-SMC compared to an i-PI controller.

To overcome the control problem of robot manipulators under unmodeled actuator dynamics and control complexity, many controller algorithms are proposed in the literature. In [22], the authors proposed an intelligent control which is compared to a PD and a sliding mode controller. The proposed control did not prove a well performance under uncertainty. Besides, it is difficult to implement the intelligent control.

To benefit the i-PD and SMC advantages, an i-PDSMC is proposed in this paper. A basic SMC form is used when the 1st SMC term is an i-PD controller and the 2nd term is a classical discontinuous form. The proposed controller is compared to a classical PD controller and an i-PD controller, and robustness under parameter variations and external disturbance is validated using a robot manipulator under actuator dynamics. The rest of the paper is organized as follows.

Firstly, a robot manipulator under actuator dynamics is presented. Next, a brief description of a classical PD control is introduced. In Section 4, a model-free control is presented, and i-PD and i-PDSM control laws are defined. i-PDSMC stability to the trajectory tracking problem is proved. In the last section, the three previous controllers are applied to the robot manipulator, and simulation results under parameter variation and external disturbance are presented.

1.1. Robot Manipulator under Actuator Dynamics. In Lagrange form, an n–link interconnected to an n robot manipulator model is expressed as follows [22]:

$$M(q)\ddot{q} + C(q,\dot{q})\dot{q} + G(q) + N = \tau, \tag{1}$$

in which $M(q)$ is the inertia matrix, $C(q,\dot{q})$ is the centripetal and Coriolis forces, $G(q)$ is the gravity vector, N is the external disturbance τ_l + friction term $f(\dot{q})$ + unmodeled dynamics, τ is the torque control, q is the vector of the joint position, $\dot{q}$ is the joint velocity, and $\ddot{q}$ is the acceleration vector.

Recently, an actuator dynamic related to the robot manipulator model effect is considered in many interesting research studies. Considering an armature DC-servo motor as an actuator in each joint, it can be expressed as follows:

$$\tau_e = K_T I_a, \tag{2}$$

$$\tau_e = J_m\ddot{\theta}_m + B_m\dot{\theta}_m + \tau_m, \tag{3}$$

$$u = R_a I_a + L_a\dot{I}_a + K_E\dot{\theta}_m. \tag{4}$$

The gear ratio g_r, relating the joint position q and a motor shaft position θ_m, is expressed as

$$g_r = \frac{\theta_m}{q} = \frac{\tau}{\tau_m}, \tag{5}$$

where τ_e is the electromagnetic torque, K_T is the diagonal matrix of motor torque, I_a is the armature currents, J_m is the diagonal matrix of the moment inertia, B_m is the diagonal matrix of torsional damping coefficients, τ_m is the load torque vector, R_a is the diagonal matrix of armature resistance, L_a is the diagonal matrix of armature inductance, K_E is the diagonal matrix of the feedback electromotive force (EMF) coefficients, θ_m is the vector of motor shaft position, $\dot{\theta}_m$ is the velocity of the motor shaft, and $\ddot{\theta}_m$ is the acceleration of the motor shaft.

Considering (2), (3), and (5), the armature input voltage could be rewritten as

$$u = L_n\dot{\tau} + R_n\tau + L_nJ_n\ddot{q} + (R_nJ_n + L_nB_n)\ddot{q} + (R_nB_n + K_{En})\dot{q}, \tag{6}$$

where $L_n = L_a(g_rK_T)^{-1}$, $R_n = R_a(g_rK_T)^{-1}$, $J_n = g_r^2J_m$, $B_n = g_r^2B_m$, and $K_{En} = K_Eg_r$.

Including the actuator dynamic expression (6), the model expression (1) will be rewritten as

$$M^*\ddot{q} + D(q,\dot{q},\ddot{q}) + d = u. \tag{7}$$

Noting

$$M(q) = M_n + M_\theta(q), \tag{8}$$

$$M^* = L_n[M_n + J_n], \tag{9}$$

$$D(q,\dot{q},q) = \left\{L_n\left[\dot{M}_\theta(q,\dot{q}) + C(q,\dot{q}) + B_n\right] + R_n\left[M(q) + J_n\right]\right\}\ddot{q} + \left[L_n\dot{C}(q,\dot{q},\ddot{q})\dot{q} + R_nC(q,\dot{q})\dot{q} + R_nB_n\dot{q} + K_{En}\dot{q} + L_n\dot{G}(q,\dot{q}) + R_nG(q)\right], \tag{10}$$

$$d = L_nM_\theta(q)\dddot{q} + L_n\dot{N} + R_nN, \tag{11}$$

in which d is the dynamic uncertainty and u is the control effort vector, i.e., armature input voltages.

The elements $M, M^*, M_n, M_\theta, C, G, N, L_n$, and J_n are defined in [22].

Model (7) will be applied to the controller defined in the following to test its performance under uncertainty.

2. Classical PD Controller

Widely employed to the robotic control, the PD control is robust to trajectory tracking. In a closed loop system, the PD controller is a fast controller, besides its derivative action, and improves the rise time and oscillation effect, but the steady state performance is decreased.

A PD controller has the following form:

$$\tau = K_pe + K_D\dot{e}, \tag{12}$$

where e is the tracking error defined as $e = y - y_d$.

The PD controller inconvenience is the vibration problem caused by a measured noise due its high control gain. To improve controller performance, recently, many researchers have shown interest in an intelligent PD controller.

3. Model-Free Control

Without the differential equation model, a model-free control is a nonlinear control developed recently in [1, 4]. Then, an ultralocal model replaces the unknown mathematical model:

$$y^{(\vartheta)} = F + \alpha u, \tag{13}$$

where

(i) $\alpha \in \mathbb{R}$ is a constant parameter chosen arbitrary such that $y^{(\vartheta)}$ and αu have the same magnitude.

(ii) $y^{(\vartheta)}$ is the derivative of y at ϑ order, where $\vartheta \geq 1$. In practice, ϑ is chosen equal to 1 or 2 and does not have connection with the system order.

(iii) F is the unknown plant and any uncertainty, and it is estimated in real time through the input and output information measured system behavior.

The estimate of F is defined as follows:

$$\widehat{F} = \widehat{y}^{(\vartheta)} - \alpha\widehat{u}, \tag{14}$$

where

(i) $\widehat{y}^{(\vartheta)}$ is the estimate of $y^{(\vartheta)}$. Diverse estimation methods are used to estimate $y^{(\vartheta)}$, like algebraic methods [4], a low-pass filter. To avoid the algebraic loop problem, $\widehat{y}^{(\vartheta)}$ is generated by a first-order derivative plus the low-pass filter with the transfer function:

$$H_{\text{lpf}} = \left(\frac{K_{\text{lpf}}s}{T_{\text{lpf}}s + 1}\right)^{\vartheta}. \tag{15}$$

(ii) $\widehat{u}$ is the estimate of u. It is chosen as a past value of u to avoid algebraic loops in the controllers such that $\widehat{u} = u(t-1)$.

Then, the model-free controller is as follows:

$$u = \frac{1}{\alpha}\left(\widehat{y}_d^{(\vartheta)} - \widehat{F} - \Lambda e^{\langle -\xi,\zeta\rangle}\right), \tag{16}$$

in which Λ is a function set to $\mathbb{R}^{\xi+\zeta+1} \longrightarrow \mathbb{R}$. The dynamical error described by $e^{(\vartheta)} = \Lambda(e^{-\xi,\zeta})$ is asymptotically stable.

Remark 1. $e^{-\xi,\zeta} = (\int^{\xi} e, \int^{\xi-1} e, \ldots, e, \dot{e}, \ldots, e^{(\zeta)})$; $\xi, \zeta \in [0, \vartheta]$; $\int^k$ is the k iterative integral.

3.1. Intelligent PD (i-PD). The derivative order ϑ is generally equal to 1 or 2, yielding the intelligent PID (i-PID).

If $\vartheta = 2$,

$$u = \frac{1}{\alpha}\left(\ddot{\widehat{y}}_d - \widehat{F} - K_pe - K_I\int e - K_D\dot{e}\right). \tag{17}$$

Then, if $K_I = 0$, the controller becomes an i-PD controller, and the control input of the feedback is expressed as

$$u = \frac{1}{\alpha}\left(\ddot{\widehat{y}}_d - \widehat{F} - K_pe - K_D\dot{e}\right), \tag{18}$$

where K_p and K_D are the proportional and derivative gains.

3.2. Intelligent i-PD Sliding Mode Control (i-PDSMC). A general classical sliding mode control form is

$$u_{SM} = u_{\text{eq}} + u_{\text{dis}}, \tag{19}$$

where u_{eq} depends on the system mathematical model and u_{dis} is a discontinuous control.

In this study, an i-PD sliding mode control is introduced by choosing the equivalent control u_{eq} such that

$$u_{\text{eq}} = \frac{1}{\alpha}\left(\ddot{\widehat{y}}_d - \widehat{F} - K_pe - K_D\dot{e}\right). \tag{20}$$

The system model (7) is written as an interconnected SISO nonlinear system. Then, the discontinuous control is considered as follows:

$$u_{\text{dis}} = -KS - \mu sign(S), \tag{21}$$

in which S is the sliding surface verifying Filippov theory, and it is chosen as

$$S = \dot{e} + \lambda e. \tag{22}$$

i-PDSMC has the following form:

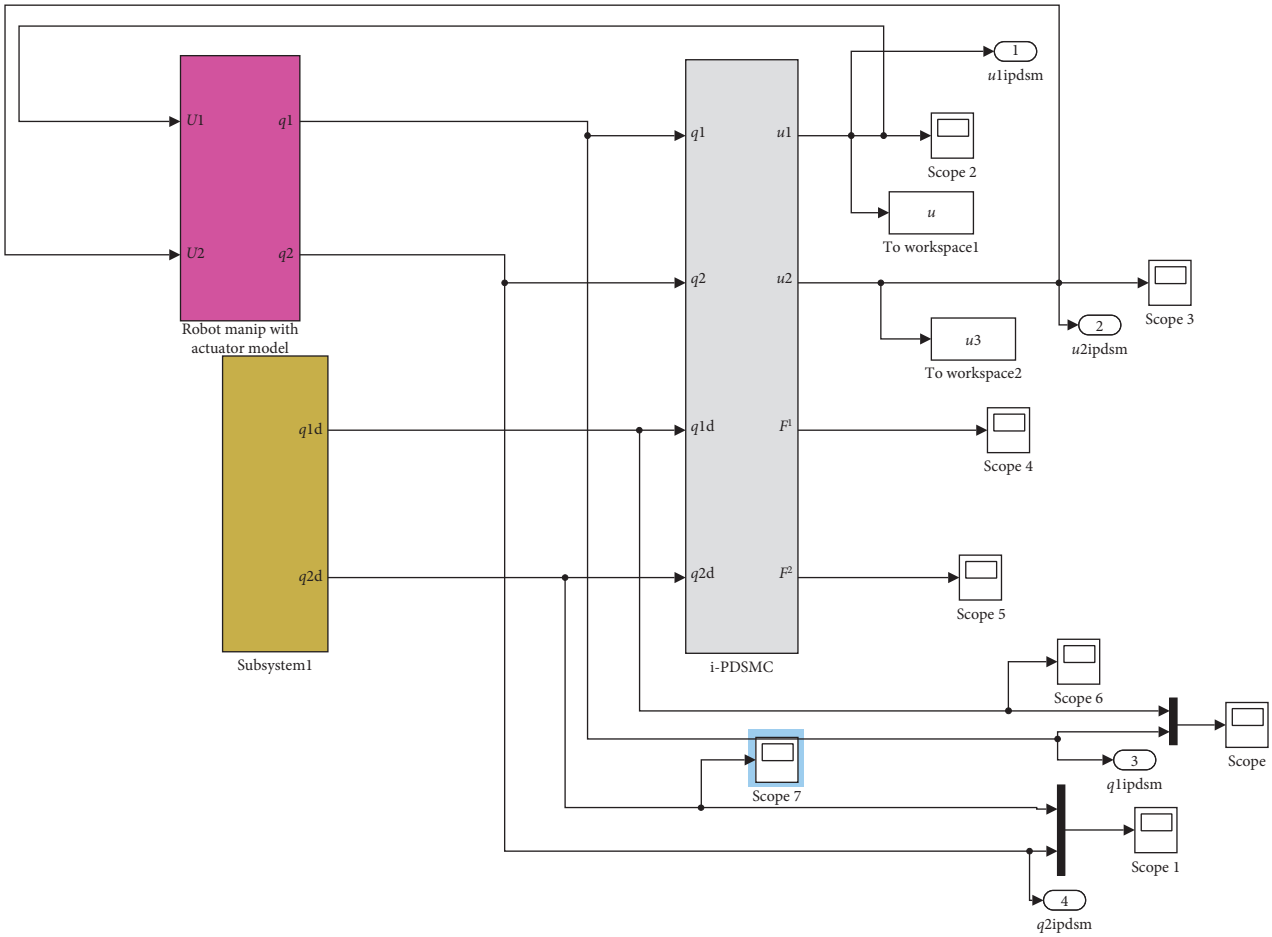

(a)

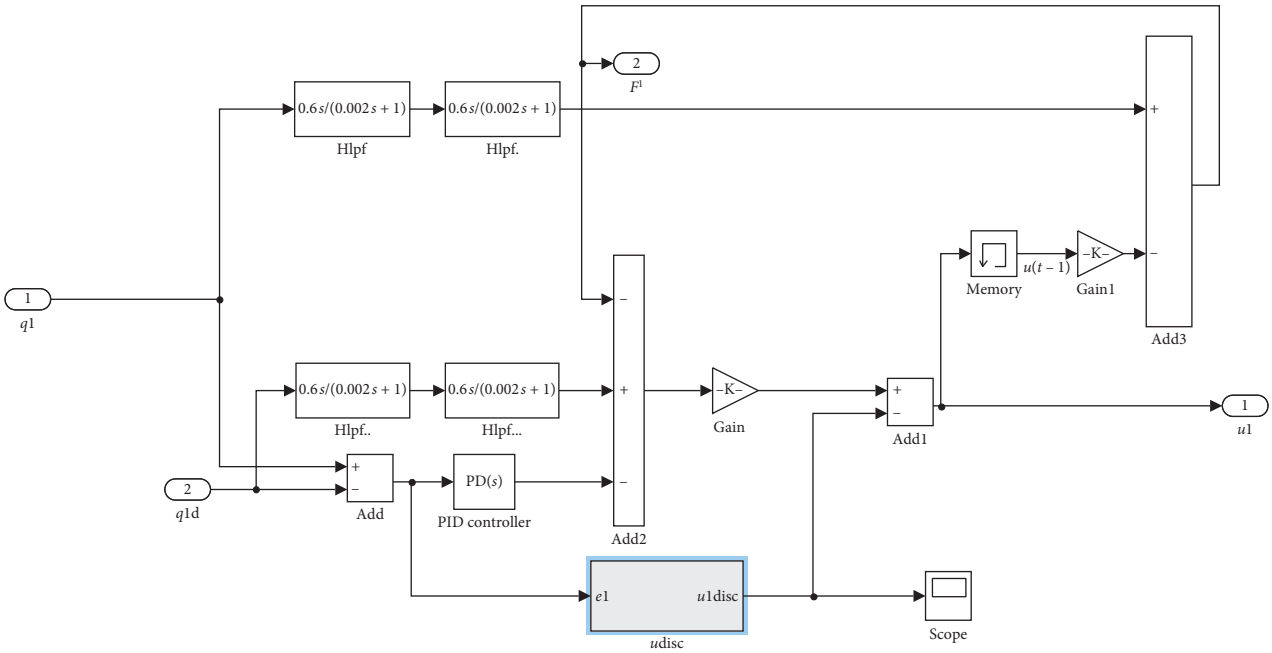

(b)

Figure 1: Continued.

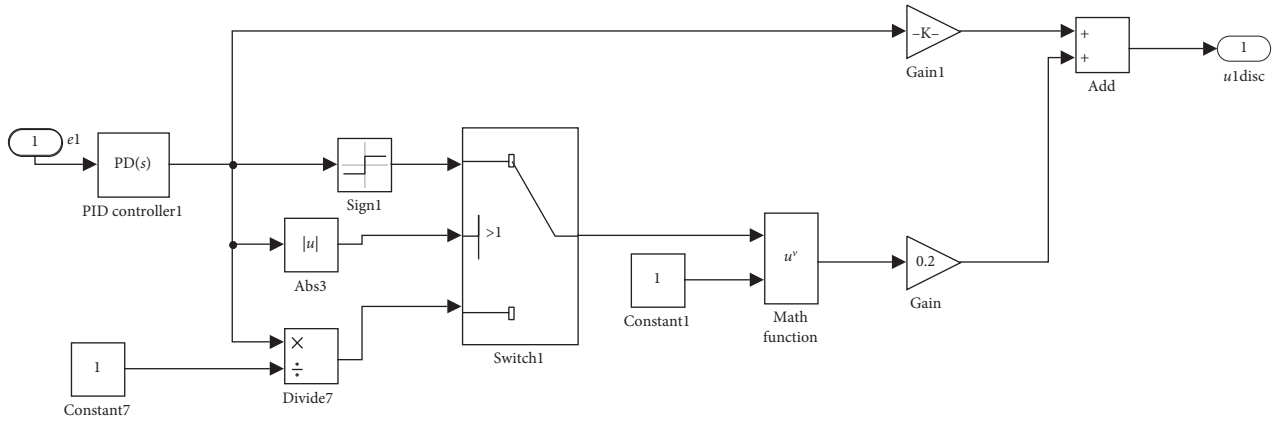

(c)

Figure 1: Block diagram of the i-PDSMC. (a) Block diagram of the i-PDSMC system. (b) Block diagram of the i-PDSMC structure. (c) Block diagram of the i-PDSMC discontinuous term.

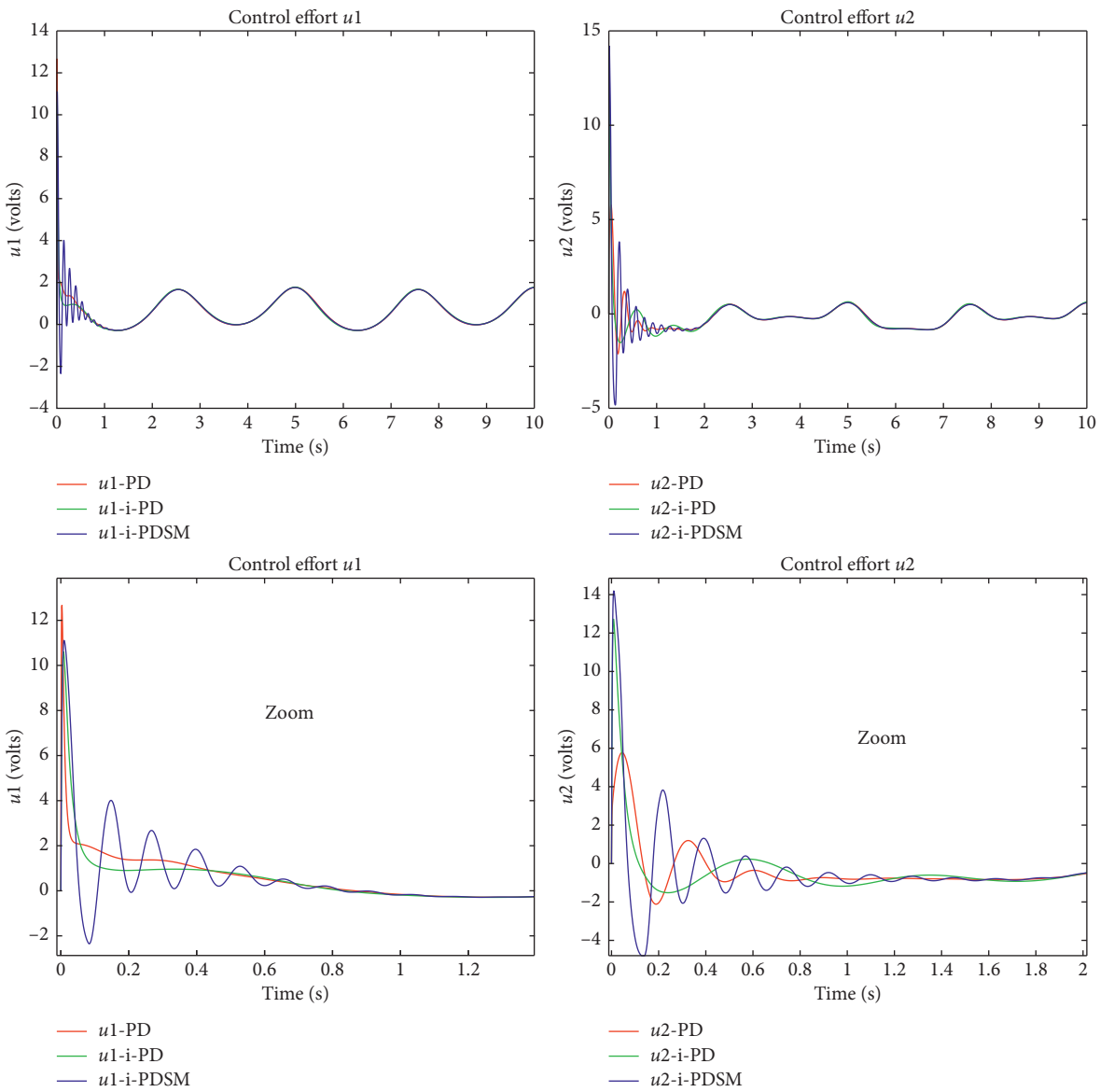

(a)

Figure 2: Continued.

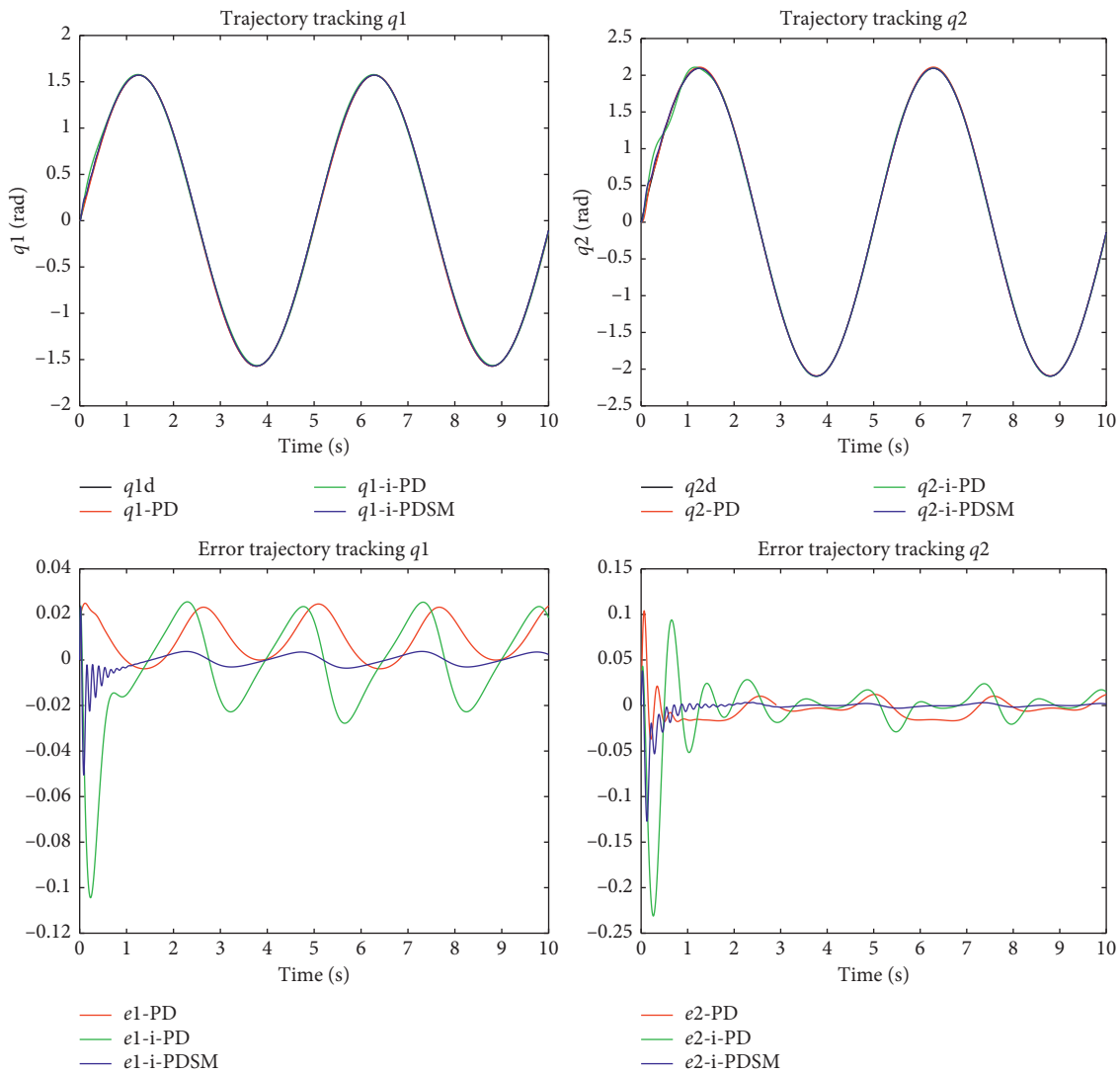

(b)

FIGURE 2: 1st case: nominal situation. (a) The control input at the nominal situation. (b) Tracking trajectory and error tracking trajectory to q_1 and q_2 at the nominal situation.

$$u_{SM} = \frac{1}{\alpha}\left(\ddot{\hat{y}}_d - \hat{F} - K_p e - K_D \dot{e}\right) - KS - \mu sat\left(S, \varepsilon\right), \quad (23)$$

in which $sat\left(S, \varepsilon\right) = \begin{cases} -1 & \text{if } S < -\varepsilon \\ S/\varepsilon & \text{if } |S| \le \varepsilon \\ 1 & \text{if } S > \varepsilon \end{cases}$ and $\varepsilon > 0$ is the boundary layer thickness.

Theorem 1. *The i-PDSM control (23) is stable if and only if the control gains verify the following equalities:* $K_p > 0$; $\lambda > K_D$; $\alpha \neq 0$; $k > -(\mu/\varepsilon)$; $\forall \alpha, \mu > 0 x_2 > (K_p x_1)/(\lambda - K_D)$.

3.2.1. i-PDSMC Stability Analysis. Introducing a state variable error such as

$$\begin{cases} x_1 = e, \\ x_2 = \dot{e}. \end{cases} \quad (24)$$

The sliding surface is rewritten using the new state variables:

$$S = x_2 + \lambda x_1. \quad (25)$$

So, $\dot{x}_2 = \ddot{y} - \ddot{y}_d$.

An estimate error e_{est} is considered such that

$$e_{\text{est}} = F - \hat{F} = \ddot{y} - \ddot{\hat{y}} = \ddot{y}_d - \ddot{\hat{y}}_d. \quad (26)$$

Let $\vartheta = 2$, then

$$\ddot{y} = F + \alpha u_{SM}. \quad (27)$$

Introducing (23) in (27), we have

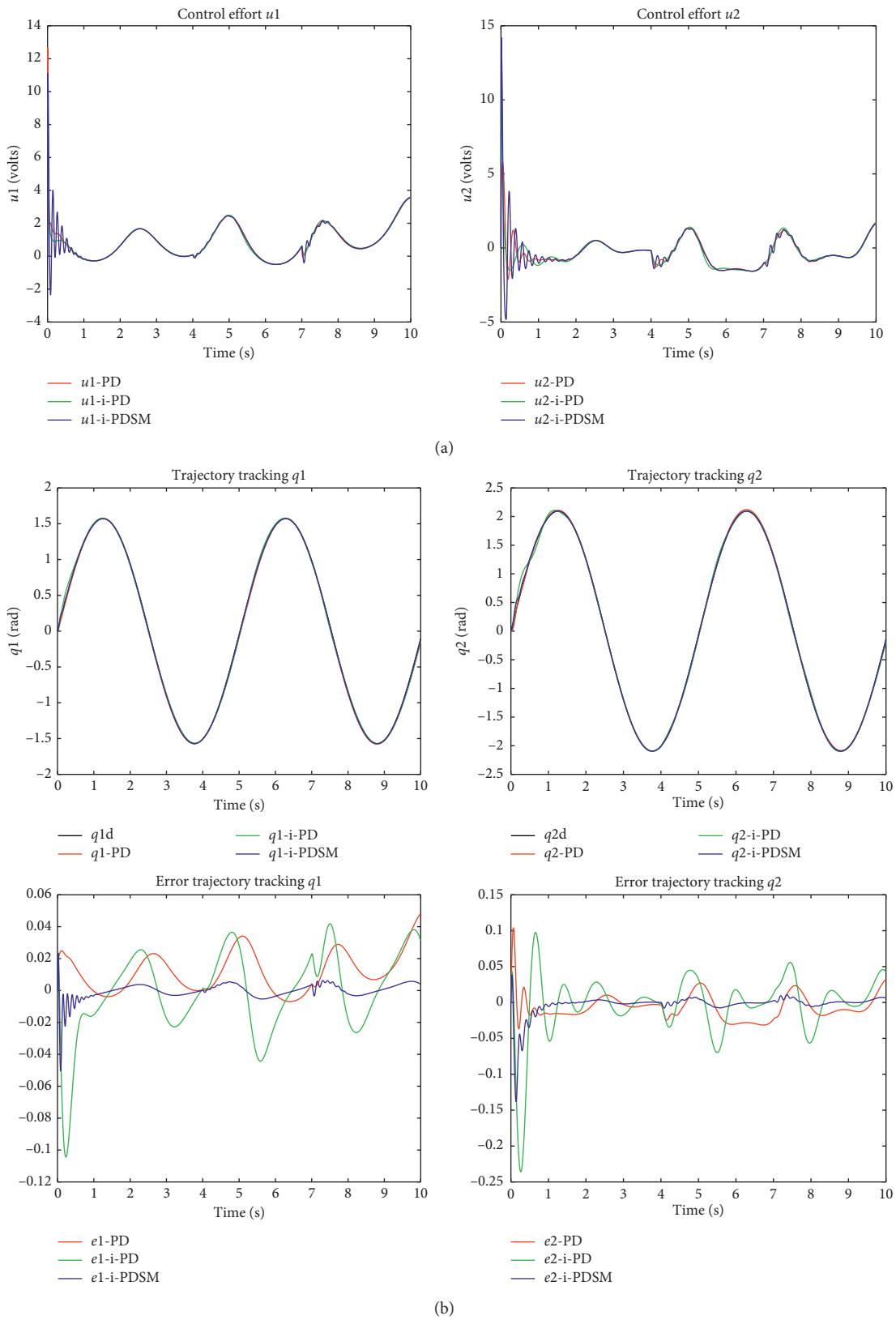

FIGURE 3: 2nd case: presence of parameter variation and external disturbance. (a) The control input: parameter variation and an external disturbance is injected. (b) Tracking trajectory q_1 and q_2: parameter variation and an external disturbance is injected.

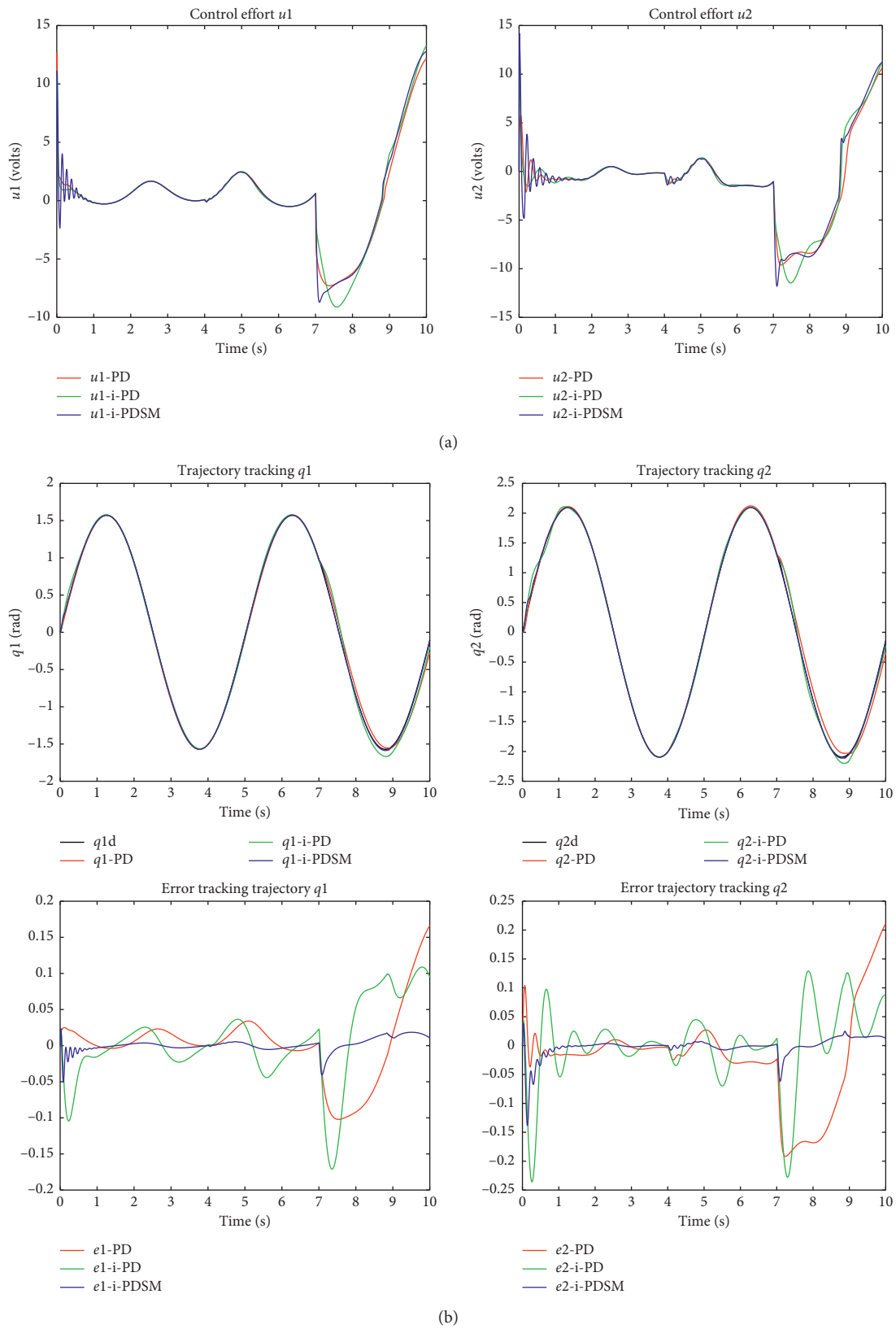

FIGURE 4: 3rd case: presence of parameter variation, external disturbance, and friction force. (a) The control input: parameter variation and an external disturbance is injected adding a friction force at $t = 7$s. (b) Tracking trajectory q_1 and q_2: parameter variation and an external disturbance is injected adding a friction force at $t = 7$s.

$$\ddot{y} = F + \alpha\left(\frac{1}{\alpha}\left(\ddot{\hat{y}}_d - \hat{F} - K_p e - K_D \dot{e}\right) - KS - \mu sat(S,\varepsilon)\right). \tag{28}$$

So, $\dot{x}_2 = \ddot{y} - \ddot{y}_d = F - \hat{F} - (\ddot{y}_d - \ddot{\hat{y}}_d) - K_p e - K_D \dot{e} - \alpha(KS + \mu sat(S,\varepsilon))$,

$$\begin{aligned} \dot{x}_2 &= -K_p e - K_D \dot{e} - \alpha(KS + \mu sat(S,\varepsilon)), \\ \dot{x}_2 &= -K_p x_1 - K_D x_2 - \alpha(KS + \mu sat(S,\varepsilon)). \end{aligned} \tag{29}$$

The sliding surface derivative is $\dot{S} = \dot{x}_2 + \lambda \dot{x}_1 = \dot{x}_2 + \lambda x_2$. Then, $\dot{S} = -K_p x_1 - K_D x_2 - \alpha(KS + \mu sat(S,\varepsilon)) + \lambda x_2$. Considering the following Lyapunov function:

$$V = \frac{1}{2}S^2. \tag{30}$$

Its derivative is

$$\begin{aligned} \dot{V} &= S\dot{S}, \\ \dot{V} &= S\left(-K_p x_1 - K_D x_2 - \alpha(KS + \mu sat(S,\varepsilon)) + \lambda x_2\right). \end{aligned} \tag{31}$$

If $|S| \le \varepsilon$, then

$$\begin{aligned} \dot{V} &\le S\left(-K_p x_1 - K_D x_2 - \alpha KS - \alpha\mu \frac{S}{\varepsilon} + \lambda x_2\right), \\ \Rightarrow \dot{V} &\le -\alpha\left(k + \frac{\mu}{\varepsilon}\right)S^2, \end{aligned} \tag{32}$$

$$-K_p x_1 - (K_D - \lambda)x_2 = 0. \tag{33}$$

Equation (33) is implying that $x_1 = e^{-(K_p/\lambda - K_D)t}$. When $t \longrightarrow \infty, x_1 \longrightarrow 0$ if only if $(K_p/\lambda - K_D) > 0$. Then, $K_p > 0$ and $\lambda > K_D$.

To guarantee stability, the term $\alpha(k + (\mu/\varepsilon))$ is positive. For that, α must be different to zeros and $k > -(\mu/\varepsilon)$.

If $|S| > \varepsilon$, then the Lyapunov derivative function becomes

$$\begin{aligned} \dot{V} &\le S\left(-K_p x_1 - K_D x_2 - \alpha KS - \alpha\mu + \lambda x_2\right), \\ \dot{V} &\le -\alpha KS^2. \end{aligned} \tag{34}$$

And, $-K_p x_1 - K_D x_2 - \alpha\mu + \lambda x_2 = 0$; then, $K_p x_1 = (\lambda - K_D)x_2 - \alpha\mu$:

$$\Rightarrow x_2 = \frac{K_p x_1 + \alpha\mu}{\lambda - K_D}. \tag{35}$$

Then, $\lambda \ne K_D$ and $\forall \alpha, \mu > 0$, $x_2 > (K_p x_1)/\lambda - K_D$.

3.3. Simulation Results. To verify the robustness, the previously defined controls are applied to a robot manipulator under actuator dynamics described in (7). The current voltage u is the control input.

The parameters of the robot manipulator are considered as follows:

$$\begin{aligned} J_{m1} &= 3.7 \times 10^{-5}\,\mathrm{kg \cdot m^2}, \\ J_{m2} &= 1.47 \times 10^{-4}\,\mathrm{kg \cdot m^2}, \\ R_{a1} &= 2.8\,\Omega, \\ R_{a2} &= 4.8\,\Omega, \\ l_1 &= 205\,\mathrm{mm}, \\ l_2 &= 210\,\mathrm{mm}, \\ l_{c1} &= 154.8\,\mathrm{mm}, \\ l_{c2} &= 105\,\mathrm{mm}, \\ m_1 &= 3.55\,\mathrm{kg}, \\ m_2 &= 0.75\,\mathrm{kg}, \\ B_{m1} &= 1.3 \times 10^{-5}\,\mathrm{N \cdot m/s}, \\ B_{m2} &= 2 \times 10^{-5}\,\mathrm{N \cdot m/s}, \\ K_{T1} &= 0.21\,\mathrm{N \cdot m/A}, \\ K_{T2} &= 0.23\,\mathrm{N \cdot m/A}, \\ L_{a1} &= 3\,\mathrm{mH}, \\ L_{a2} &= 2.4\,\mathrm{mH}, \\ K_{E1} &= 2.42 \times 10^{-4}\,\mathrm{s/rad \cdot V}, \\ K_{E2} &= 2.18 \times 10^{-4}\,\mathrm{s/rad \cdot V}, \\ g &= 9.8\,\mathrm{m/s^2}, \\ g_{r1} &= 60, \\ g_{r2} &= 30. \end{aligned} \tag{36}$$

The control robustness is studied under the following three cases:

(i) 1st case: at nominal situation (without disturbance $(N = 0)$)

(ii) 2nd case: a parameter variation appears at $t = 4$s in which 1kg is added to link 2 masses (m_2 becomes 0.75kg + 1kg), and an external disturbance $N = \tau_l = [\,5\sin(5t)\ \ 0.5\sin(5t)\,]^T$ is occurred at $t = 7$s

(iii) 3rd case: added to the 2nd case, a friction force is injected at $t = 7$s, having the following form:

$$f(\dot{q}) = [\,20\dot{q}_1 + 1.6\mathrm{sgn}(\dot{q}_1)\ \ 4\dot{q}_2 + 3.2\mathrm{sgn}(\dot{q}_2)\,]^T. \tag{37}$$

Then, the external disturbance becomes $N = \tau_l + f(\dot{q})$.

3.3.1. The Control Simulation Parameters. Error tracking trajectory: $e = y - y_d$, where $y = [q_1 q_2]^T$:

(i) PD control: $u_{pd} = K_a e + K_b \dot{e}$

$$K_a = \begin{bmatrix} 70 & 0 \\ 0 & 50 \end{bmatrix}; K_b = \begin{bmatrix} 7 & 0 \\ 0 & 1 \end{bmatrix}.$$

(ii) i-PD control: $u_{ipd} = (1/\alpha)(-\widehat{F} + \ddot{\hat{y}}_d - K_p e - K_D \dot{e})$, where $\widehat{F} = \ddot{\hat{y}} - \alpha u(t-1)$; $\ddot{\hat{y}} = ((K_{\text{lfp}} s)/T_{\text{lfp}} s + 1)^2 y$; $\ddot{\hat{y}}_d = ((K_{\text{lfp}} s)/T_{\text{lfp}} s + 1)^2 y_d$ $K_p = \begin{bmatrix} 15 & 0 \\ 0 & 20 \end{bmatrix}$; $K_D = \begin{bmatrix} 3 & 0 \\ 0 & 2 \end{bmatrix}$; $K_{\text{lfp}} = \begin{bmatrix} 0.6 \\ 0.6 \end{bmatrix}$; $T_{\text{lfp}} = \begin{bmatrix} 0.002 \\ 0.002 \end{bmatrix}$; $\alpha = \begin{bmatrix} 90 \\ 100 \end{bmatrix}$.

(iii) i-PDSM control: $u_{ipd} = (1/\alpha)(-\widehat{F} + \ddot{y}_d - K_p e - K_D \dot{e}) - (KS + \mu sign(S))$, where $S = \dot{e} + \lambda e$; $\ddot{\hat{y}} = ((K_{\text{lfp}} s)/T_{\text{lfp}} s + 1)^2 y$; $\ddot{\hat{y}}_d = ((K_{\text{lfp}} s)/T_{\text{lfp}} s + 1)^2 y_d$; $K_p = \begin{bmatrix} 15 & 0 \\ 0 & 20 \end{bmatrix}$; $K_D = \begin{bmatrix} 3 & 0 \\ 0 & 2 \end{bmatrix}$; $K_{\text{lfp}} = \begin{bmatrix} 0.6 \\ 0.6 \end{bmatrix}$; $K_{\text{lfp}} = \begin{bmatrix} 0.002 \\ 0.002 \end{bmatrix}$; $\alpha = \begin{bmatrix} 100 \\ 100 \end{bmatrix}$; $\lambda = \begin{bmatrix} 4 \\ 4 \end{bmatrix}$; $K = \begin{bmatrix} 0.04 \\ 0.004 \end{bmatrix}$; $\mu = \begin{bmatrix} 0.2 \\ 0.2 \end{bmatrix}$.

The block diagram of the i-PDSMC is presented in Figure 1. All controller terms are developed in Figures 1(a)–1(c). The control law is implemented using the MATLAB program.

In the first case, the simulation results show that the PD control has an important impulse at the control effort u_1 in the initial instant, but, in the control effort u_2, the i-PDSM control has a higher impulse than PD and i-PD controllers (Figure 2(a)).

The PD and i-PD controls have a transition phase smoother than the i-PDSM one. In the steady state, all the controllers have the same performances. But, the i-PDSM control has a lower error to tracking trajectory than the others (Figure 2(b)).

For the 2nd case, the PD, i-PD, and i-PDSM controls keep their control effort robustness (Figure 3(a)).

At $t = 7$s, i-PDSMC is more robust to tracking trajectory, and this is due to the sliding mode capability to reject uncertainty and disturbance; however, the PD and i-PD controllers lose their performance (Figure 3(b)).

In the 3rd case, the PD and i-PD controls lose their performances to tracking trajectory under external disturbance, while the i-PDSM control is still robust in the steady state (Figure 4). To tracking trajectory, the i-PDSM control converges more rapidly than the other controllers.

4. Conclusion

In this work, an intelligent sliding mode controller is defined based on an intelligent PD controller as an equivalent control term and a classical discontinuous control term. It is called as i-PDSMC. The stability of i-PDSMC is studied, and a sufficient condition to guarantee tracking trajectory robustness is determined. The proposed controller is compared to a classical PD and an intelligent PD (i-PD) controller. These controllers are applied to a robot manipulator under actuators to test their performances in the presence of parameter variations and external disturbances. The simulation results prove that the proposed i-PDSMC is robust than PD and i-PD controllers under uncertainties.

Data Availability

No data were used to support this study.

Conflicts of Interest

The authors declare that they have no conflicts of interest.

References

[1] P. R. Ouyang, J. Acob, and V. Pano, "PD with sliding mode control for trajectory tracking of robotic system," *Robotics and Computer-Integrated Manufacturing*, vol. 30, no. 2, pp. 189–200, 2014.

[2] P. R. Ouyang, J. Tang, W. H. Yue, and S. Jayasinghe, "Adaptive PD plus sliding mode control for robotic manipulator," in *Proceedings of the 2016 IEEE International Conference on Advanced Intelligent Mechatronics (AIM)*, Banff, Canada, July 2016.

[3] J. Sangrok, B. Jeongae, K. Jongwon, S. TaeWon, and S. K. Hwa, "Switching PD-based sliding mode control for hovering of a tilting-thruster under water robot," *PLoS One*, vol. 13, no. 3, Article ID e0194427, 2018.

[4] T. Kara and A. H. Mary, "Adaptive PD-SMC for nonlinear robotic manipulator tracking control," *Studies in Informatics and Control*, vol. 26, no. 1, 2017.

[5] M. Fliess and C. Join, "Model-free control and intelligent PID controllers: towards a possible Trivialization of nonlinear control?" in *Proceedings of the 15th IFAC Symposium on System Identification*, Saint-Malo, France, July 2009.

[6] M. Fliess and C. Join, "Model-free control," *International Journal of Control, Taylor & Francis*, vol. 86, no. 12, pp. 2228–2252, 2013.

[7] F. Lafont, N. Pessel, J. F. Balmat, and M. Fliess, "On the model-free control of an experimental greenhouse," in *Proceedings of the World Congress on Engineering and Computer Science, WCECS 2013*, pp. 23–25, San Francisco, CA, USA, October 2013.

[8] Y. Liu, W. Yan, D. Xu, W. Yang, and W. Zhang, "Direct torque control of PMSM based on model free iPI controller," in *Proceedings of the 7th Data Driven Control and Learning Systems Conference*, Enshi, China, May 2018.

[9] M. Ticherfatine and Z. Qidan, "Model-free approach based on intelligent PD controller for vertical motion reduction in fast ferries," *Turkish Journal of Electrical Engineering & Computer Sciences*, vol. 26, pp. 393–406, 2018.

[10] H. Wang, X. Ye, Y. Tian, and N. Christov, "Attitude control of a quadrotor using model free based sliding model controller," in *Proceedings of the 20th International Conference on Control Systems and Sciences*, Bucharest, Romania, May 2015.

[11] M. Ticherfatine and Z. Qidan, "Fast ferry smoothing motion via intelligent PD controller," *Journal of Marine Science and Application*, vol. 17, no. 2, pp. 273–279, 2018.

[12] Y. Xin, Z. C. Qin, W. G. Wu, and J. Q. Sun, "Partial model-free control of a 2-input and 2-output helicopter system," in *Proceedings of the ENOC*, Budapest, Hungary, June 2017.

[13] T. H. Lee, S. S. Ge, and Z. P. Wang, "Adaptive robust controller design for multi-link flexible robots," *Mechatronics*, vol. 11, no. 8, pp. 951–967, 2001.

[14] S. S. Ge, T. H. Lee, and G. Zhu, "Energy-based robust controller design for multi-link flexible robots," *Mechatronics*, vol. 6, no. 7, pp. 779–798, 1996.

[15] C. K. Pang, G. Dai, T. H. Lee, and M. Nagashima, "Adaptive non-model-based vibration control of critical flexible modes inMechatronic systems," in *Proceedings of the 18th World Congressthe International Federation of Automatic Control*, Milano, Italy, August 2011.

[16] H. Zhou, D. Xu, and B. Jiang, "Model free command filtered backstepping control for marine power systems," *Mathematical Problems in Engineering*, vol. 2015, Article ID 619430, 8 pages, 2015.

[17] X. Liu, H. Yu, J. Yu, and L. Zhao, "Combined speed and current terminal sliding mode control with nonlineardisturbance observer for PMSM drive," *IEEE Access*, vol. 6, pp. 29594–29601, 2018.

[18] A. Crassidis and A. Mizov, "A model-free control algorithm derived using the sliding mode control method," in *Proceedings of the 2nd International Conference of Control, Dynamic Systems, and Robotics*, Ottawa, Canada, May 2015.

[19] A. Crassidis and R. M. Reis, "Model-free sliding mode control method," in *Proceedings of the 3rd International Conference on Control, Dynamic Systems, and Robotics (CDSR'16)*, Ottawa, Canada, May 2016.

[20] R.-E. Precup, M.-B. Radac, R.-C. Roman, and E. M. Petriu, "Model-free sliding mode control of nonlinear systems: algorithms and experiments," *Information Sciences*, vol. 381, pp. 176–192, 2017.

[21] R. M. Reis, "A new model-free sliding mode control method with estimation of control input error," Rochester Institute of Technology, Rochester, NY, USA, 2016.

[22] R.-J. Wai and P.-C. Chen, "Robust neural fuzzy network control for robot manipulator including actuator dynamics," *IEEE Transactions on Industrial Electronics*, vol. 53, no. 4, pp. 1328–1349, 2006.

Hindawi
Mathematical Problems in Engineering
Volume 2020, Article ID 6082586, 8 pages
https://doi.org/10.1155/2020/6082586

Research Article

Control Based on Linear Algebra for Trajectory Tracking and Positioning of Second-Order Chained Form System

Leandro Rodriguez,[1] Emanuel Serrano,[1] Mabel Cristina Sánchez,[2] and Gustavo Scaglia[1]

[1]*National Council of Scientific and Technological Research (CONICET), Instituto de Ingeniería Química, Universidad Nacional de San Juan, Av. Libertador San Martín Oeste, 1109 San Juan, Argentina*
[2]*Departamento de Ingeniería Química, Universidad Nacional del Sur (UNS), Planta Piloto de Ingeniería Química (PLAPIQUI) (UNS-CONICET), Bahía Blanca 8000, Argentina*

Correspondence should be addressed to Gustavo Scaglia; gscaglia@unsj.edu.ar

Received 22 April 2020; Revised 27 June 2020; Accepted 14 July 2020; Published 1 August 2020

Guest Editor: Yi Qi

The development of controllers for underactuated systems with nonholonomic constraints has been a topic of significant interest for many researchers in recent years. These systems are hard to control because their linearization transform them into uncontrollable systems. The proposed approaches involve the use of a permanent excitation in the reference trajectory; coordinate transformation; discontinuities; or complex calculations. This paper proposes the design of the controller of the second-order chained form system for trajectory tracking by using a simpler approach based on linear algebra. Up to the present time, no controllers based on this approach have been designed for that system. The control problem is solved by setting two of the three systems variables as a reference, while the remaining variable is calculated imposing the condition that the equations system has an exact solution to ensure that tracking errors go to zero. The stability of the proposed controller is theoretically demonstrated, and simulations results show a suitable control system performance. Also, no coordinate transformation is necessary.

1. Introduction

In recent years, the interest in the control of underactuated systems with nonholonomic constraints has increased [1]. Underactuated systems are mechanical systems with fewer control inputs than degrees of freedom and nonintegrable acceleration constraints [2]. This paper considers the control for trajectory tracking and positioning of second-order chained form systems. These are hard to control because their linearization transform them into uncontrollable systems. The well-known paper of Brockett highlights the difficulty of solving these problems [3].

Several articles addressed the control of underactuated systems with nonholonomic constraints. Aneke et al. [4, 5] resolved the problem of trajectory tracking by using a three-stage method. In the first step, they transformed the original system into an extended chained form system with a cascade arrangement. They applied a linear feedback controller to the first subsystem. After that, the second subsystem is exponentially stabilized by employing a backstepping procedure. In the third step, they showed the closed-loop tracking dynamics stability of the system. More recently, other authors used the backstepping procedure to develop control methodologies for trajectory tracking [6, 7]. A permanent excitation in the reference trajectory is also necessary for system stability. This implies that the signals must not converge to zero, limiting their applications.

Also, in [8], smooth time-varying controllers are proposed to address the exponential tracking of second-order nonholonomic systems. These techniques use coordinate transformation based on time-varying dilation with a cascade-design strategy. In contrast to the previous approach, it does not require the excitation condition in the reference trajectory. This kind of control laws frequently involves

complex calculations; their design is not intuitive and only applies for special nonholonomic systems. Another method used a discontinuous coordinate transformation to map the initial system into the space of discontinuous nonholonomic systems. In this new space, the control problem can be solved [9, 10].

An adaptive dynamic sliding mode controller with integrator was also found in the literature to control nonholonomic systems [11]. This scheme uses a modified backstepping kinematic controller for generating the kinematic trajectories and the velocity errors to drive the sliding surface. The normalized least-square mean was used to control the switching of a sliding mode controller in the presence of uncertainties and parameter variations. Also, other authors developed sliding mode control methodologies for trajectory tracking and positioning of nonholonomic second-order chained form systems [12–14]. Sarfraz and ur Rehman [15] addressed the positioning problem of a particular nonholonomic planar underactuated mechanical system using adaptive sliding mode control. The control law assures the derivative of a suitable Lyapunov function becomes strictly negative.

The aforementioned controllers use a permanent excitation in the reference trajectory [4, 5]; coordinate transformation [8]; discontinuities [9, 10]; and high computational load calculations [11–15] to solve the trajectory tracking problem. To overcome these drawbacks, this paper aims to solve the problem of trajectory tracking of a second-order chained form system with nonholonomic constraints by using a novel control law inspired by the design method Linear Algebra-Based Controller (LABC) [16]. This technique computes the control actions by solving a system of linear equations and has been applied to different nonlinear systems [17–23].

Until now, LABC has not been applied to second-order chained form systems with nonholonomic constraints in the space of the original variables. For this reason, the major contribution of this work is to extend the LABC technique to solve the tracking and positioning problem for these systems. The system should follow the reference coordinates of two of three variables while the other one is unknown. The key point of this strategy is to find the conditions for which the system of linear equations has an exact solution, ensuring the calculus of the remaining variable, named sacrificed variable. In this way, the reference trajectories of the selected variables and the sacrificed one form an admissible trajectory of the system and the tracking error goes to zero [16].

This paper is organized as follows. The Materials and Methods section describes the second-order chained form system with nonholonomic constraints and solves the problem of trajectory tracking and positioning using a controller based on linear algebra. The stability of the closed-loop system is demonstrated by applying the Khalil lemma. In the Results and Discussion section, simulation results show the effectiveness of the proposed controllers. Conclusions are given at the end of this manuscript.

2. Materials and Methods

2.1. Problem Formulation. This section presents the special canonical form of an underactuated system with nonholonomic constraints. The control of this system remains a problem under study [1]. One of the most important issues is the transformation to a chained form.

Consider the second-order chained form system, S_ξ, given by following set of equations:

$$\ddot{\xi}_1 = u_1, \tag{1}$$

$$\ddot{\xi}_2 = u_2, \tag{2}$$

$$\ddot{\xi}_3 = \xi_2 u_1, \tag{3}$$

where $\xi = [\xi_1; \xi_2; \xi_3]^T \in R^3$ are the generalized coordinates of the second-order chained form system and $\mathbf{u} = [u_1 u_2]^T$ represents the inputs such that $u_1 \in R$ and $u_2 \in R$. Also, the reference trajectory is $\Phi_\xi = [\xi_{1,\mathrm{ref}}; \xi_{2,\mathrm{ref}}; \xi_{3,\mathrm{ref}}]$.

The tracking errors $\mathbf{e} = [e_1; e_2; e_3]^T \in R^3$ are the differences between the reference paths and the variables:

$$\begin{aligned} e_1 &= \xi_{1,\mathrm{ref}} - \xi_1, \\ e_2 &= \xi_{2,\mathrm{ref}} - \xi_2, \\ e_3 &= \xi_{3,\mathrm{ref}} - \xi_3. \end{aligned} \tag{4}$$

This work proposes the design of a controller for trajectory tracking and positioning of a second-order nonholonomic system represented by (1)–(3).

2.2. Problem 1: Trajectory Tracking. Given the system S_ξ, the trajectory tracking control problem is solvable if it is possible to design an appropriate controller of the form

$$u_1 = u_1\left(t, \boldsymbol{\xi}, \boldsymbol{\Phi}_\xi\right), \tag{5}$$

$$u_2 = u_2\left(t, \boldsymbol{\xi}, \boldsymbol{\Phi}_\xi\right), \tag{6}$$

such that the closed-loop system constituted by (1)–(3) and the control actions (5) and (6) is globally uniformly asymptotically stable.

2.3. Problem 2: Positioning. Given the system S_ξ, the positioning control problem is solvable if it is possible to design an appropriate controller of the form

$$u_1 = u_1\left(t, \boldsymbol{\xi}, \boldsymbol{\Phi}_\xi\right), \tag{7}$$

$$u_2 = u_2\left(t, \boldsymbol{\xi}, \boldsymbol{\Phi}_\xi\right), \tag{8}$$

such that the closed-loop system constituted by (1)–(3) and the control actions (7) and (8) is globally uniformly and asymptotically stable. Here, the reference trajectory Φ_ξ is zero.

To the best of our knowledge, LABC technique has not been applied directly to systems of second-order equations without considering a model in state variables; therefore, we extend its use to these systems. The control method is based on determining the conditions for which the system has an exact solution. Knowing the system model, it is only necessary to fix the desired trajectory of ξ_1 ($\xi_{1,\mathrm{ref}}$) and ξ_3 ($\xi_{3,\mathrm{ref}}$) to find the solution [16].

2.4. Controller Design for Trajectory Tracking. Given an initial state $\xi(0)$, the system represented by (1)–(3), S_ξ, should follow the desired trajectory Φ_ξ with a low tracking error. Therefore, it is necessary to find a control law capable of generating a signal $\mathbf{u} = [u_1 u_2]^T$ such that it satisfies this objective.

The system S_ξ is expressed in matrix form as follows:

$$\begin{bmatrix} 1 & 0 \\ 0 & 1 \\ \xi_2 & 0 \end{bmatrix} \begin{bmatrix} u_1 \\ u_2 \end{bmatrix} = \begin{bmatrix} \ddot{\xi}_1 \\ \ddot{\xi}_2 \\ \ddot{\xi}_3 \end{bmatrix}. \tag{9}$$

To calculate the control actions u_1 and u_2, (9) should have an exact solution, that is,

$$u_2 = \ddot{\xi}_2, \tag{10}$$

$$\begin{bmatrix} 1 \\ \xi_2 \end{bmatrix} u_1 = \begin{bmatrix} \ddot{\xi}_1 \\ \ddot{\xi}_3 \end{bmatrix}. \tag{11}$$

If a proportional control approach is assumed, the tracking errors are the differences between the reference and real trajectories. Thus, the second-order derivatives of the variables ξ_1 and ξ_3, i.e., $\ddot{\xi}_1$ and $\ddot{\xi}_3$, are $\ddot{\xi}_1 = \ddot{\xi}_{1,\text{ref}} + k_{11}(\dot{\xi}_{1,\text{ref}} - \dot{\xi}_1) + k_{10}(\xi_{1,\text{ref}} - \xi_1)$ and $\ddot{\xi}_3 = \ddot{\xi}_{3,\text{ref}} + k_{31}(\dot{\xi}_{3,\text{ref}} - \dot{\xi}_3) + k_{30}(\xi_{3,\text{ref}} - \xi_3)$, respectively [16].

If the internal variable $\xi_{2,\text{ez}}$ is set to the value of ξ_2 for which the above system has an exact solution, then (11) is rewritten as

$$\begin{bmatrix} 1 \\ \xi_{2,\text{ez}} \end{bmatrix} u_1 = \begin{bmatrix} \ddot{\xi}_{1,\text{ref}} + k_{11}\left(\dot{\xi}_{1,\text{ref}} - \dot{\xi}_1\right) + k_{10}\left(\xi_{1,\text{ref}} - \xi_1\right) \\ \ddot{\xi}_{3,\text{ref}} + k_{31}\left(\dot{\xi}_{3,\text{ref}} - \dot{\xi}_3\right) + k_{30}\left(\xi_{3,\text{ref}} - \xi_3\right) \end{bmatrix}, \tag{12}$$

and the tracking errors in variables 1 and 3 tend to zero.

Variable $\xi_{2,\text{ez}}$ is computed according to

$$\xi_{2,\text{ez}} = \frac{\ddot{\xi}_{3,\text{ref}} + k_{31}\left(\dot{\xi}_{3,\text{ref}} - \dot{\xi}_3\right) + k_{30}\left(\xi_{3,\text{ref}} - \xi_3\right)}{\ddot{\xi}_{1,\text{ref}} + k_{11}\left(\dot{\xi}_{1,\text{ref}} - \dot{\xi}_1\right) + k_{10}\left(\xi_{1,\text{ref}} - \xi_1\right)}. \tag{13}$$

Remark 1. Variable ξ_2 follows $\xi_{2,\text{ez}}$ and this one tracks $\xi_{2,\text{ref}}$.

The first-order derivatives of the tracking errors are $\dot{e}_1 = \dot{\xi}_{1,\text{ref}} - \dot{\xi}_1$ and $\dot{e}_3 = \dot{\xi}_{3,\text{ref}} - \dot{\xi}_3$, and the control action u_1 is obtained using the linear least-squares approximation method to (12) is

$$u_1 = \frac{\ddot{\xi}_{1,\text{ref}} + k_{11}\dot{e}_1 + k_{10}e_1 + \xi_{2,\text{ez}}\left(\ddot{\xi}_{3,\text{ref}} + k_{31}\dot{e}_3 + k_{30}e_3\right)}{1 + {\xi_{2,\text{ez}}}^2}. \tag{14}$$

We can write the second-order derivative of the variable ξ_2 ($\ddot{\xi}_2$) as a function of the sacrificed variable $\xi_{2,\text{ez}}$:

$$\ddot{\xi}_2 = \ddot{\xi}_{2,\text{ez}} + k_{21}\left(\dot{\xi}_{2,\text{ez}} - \dot{\xi}_2\right) + k_{20}\left(\xi_{2,\text{ez}} - \xi_2\right). \tag{15}$$

Furthermore, the first-order derivative of the tracking error of variable 2 is $\dot{e}_2 = \dot{\xi}_{2,\text{ez}} - \dot{\xi}_2$, and the control action u_2 is

$$u_2 = \ddot{\xi}_{2,\text{ez}} + k_{21}\dot{e}_2 + k_{20}e_2. \tag{16}$$

Remark 2. If the numerator and denominator of (13) tend to zero simultaneously, the division is undetermined and $\xi_{2,\text{ez}}$ cannot be calculated. To avoid this problem, it is necessary to choose adequately the coefficients k_{11}, k_{10}, k_{31}, and k_{30} forcing the errors e_3 and $\dot{e}_3$ to go to zero more quickly than e_1 and $\dot{e}_1$. This avoids that $\xi_{2,\text{ez}}$ tends to infinity following trajectories whose second derivatives are zero (linear and constant reference trajectories).

2.5. Stability of the Tracking Error Dynamics: Trajectory Tracking Case. In this section, the stability of the closed-loop system [(1)–(3), (14)–(16)] is demonstrated.

Theorem 1. *Given the second-order chained form system S_ξ, expressed in (1)–(3), and the control actions u_1 and u_2 formulated by (14)–(16), $\sqrt{e_1^2 + e_2^2 + e_3^2} \longrightarrow 0$ when $t \longrightarrow \infty$.*

Proof. The following steps are proposed to prove Theorem 1.

Step 1

Variable $\xi_{2,\text{ez}}$ is substituted in (14), and after performing algebraic manipulations, u_1 is obtained:

$$u_1 = \frac{\left(\left(\ddot{\xi}_{1,\text{ref}} + k_{11}\dot{e}_1 + k_{10}e_1\right)^2 + \left(\ddot{\xi}_{3,\text{ref}} + k_{31}\dot{e}_3 + k_{30}e_3\right)^2\right) / \left(\ddot{\xi}_{1,\text{ref}} + k_{11}\dot{e}_1 + k_{10}e_1\right)}{\left(\left(\ddot{\xi}_{1,\text{ref}} + k_{11}\dot{e}_1 + k_{10}e_1\right)^2 + \left(\ddot{\xi}_{3,\text{ref}} + k_{31}\dot{e}_3 + k_{30}e_3\right)^2\right) / \left(\ddot{\xi}_{1,\text{ref}} + k_{11}\dot{e}_1 + k_{10}e_1\right)^2}, \tag{17}$$

$$u_1 = \ddot{\xi}_{1,\text{ref}} + k_{11}\dot{e}_1 + k_{10}e_1. \tag{18}$$

From (1), $u_1 = \ddot{\xi}_1$, also we define the second-order derivative of the tracking error of variable 1 as $\ddot{e}_1 = (\ddot{\xi}_{1,\text{ref}} - \ddot{\xi}_1)$; in consequence, (18) is rewritten as follows:

$$0 = \ddot{e}_1 + k_{11}\dot{e}_1 + k_{10}e_1. \tag{19}$$

Step 2

Replacing (16) with (10),

$$0 = \ddot{\xi}_{2,\mathrm{ez}} - \ddot{\xi}_2 + k_{21}\dot{e}_2 + k_{20}e_2, \tag{20}$$

and defining the second-order derivative of the tracking error of variable 2 as $\ddot{e}_2 = (\ddot{\xi}_{2,\mathrm{ez}} - \ddot{\xi}_2)$, the following equation arises:

$$0 = \ddot{e}_2 + k_{21}\dot{e}_2 + k_{20}e_2. \tag{21}$$

Step 3

Given that $\xi_2 = (\xi_{2,\mathrm{ez}} - e_2)$, the algebraic manipulation of (3) gives

$$\ddot{\xi}_3 = \left(\xi_{2,\mathrm{ez}} - e_2\right)u_1. \tag{22}$$

Furthermore, from (13) and (14), the following expression is obtained: $\xi_{2,\mathrm{ez}}u_1 = \ddot{\xi}_{3,\mathrm{ref}} + k_{31}(\dot{\xi}_{3,\mathrm{ref}} - \dot{\xi}_3) + k_{30}(\xi_{3,\mathrm{ref}} - \xi_3)$. We define the second-order derivative of the tracking error of variable 3 as $\ddot{e}_3 = \ddot{\xi}_3 - \ddot{\xi}_{3,\mathrm{ref}}$ and rewrite (22) as

$$0 = \ddot{e}_3 + k_{31}\left(\dot{\xi}_{3,\mathrm{ref}} - \dot{\xi}_3\right) + k_{30}\left(\xi_{3,\mathrm{ref}} - \xi_3\right) - e_2u_1. \tag{23}$$

By replacing the control action $u_1 = \ddot{\xi}_{1,\mathrm{ref}} + k_{11}\dot{e}_1 + k_{10}e_1$ in the above equation, the following second-order equation arises:

$$\begin{aligned} 0 = {} & \ddot{e}_3 + k_{31}\left(\dot{\xi}_{3,\mathrm{ref}} - \dot{\xi}_3\right) + k_{30}\left(\xi_{3,\mathrm{ref}} - \xi_3\right) \\ & - e_2\left(\ddot{\xi}_{1,\mathrm{ref}} + k_{11}\dot{e}_1 + k_{10}e_1\right). \end{aligned} \tag{24}$$

Then, (19), (21), and (24) are rewritten according to (5.32) and (5.33) on page 221 of [24], where $\dot{x}_1 = f_1(t, x_1, x_2)$ and $\dot{x}_2 = f_1(t, x_2)$, being $\mathbf{x}_1 = \{\dot{\xi}_1; \xi_1; \dot{\xi}_3; \xi_3\}$ and $\mathbf{x}_2 = \{\dot{\xi}_2; \xi_2\}$. By defining $x_{11} = e_1$; $x_{12} = \dot{e}_1$; $x_{21} = e_2$; $x_{22} = \dot{e}_2$; $x_{13} = e_3$; $x_{14} = \dot{e}_3$, the following system of equations is obtained:

$$\begin{aligned} \begin{bmatrix} \dot{x}_{11} \\ \dot{x}_{12} \\ \dot{x}_{13} \\ \dot{x}_{14} \end{bmatrix} &= \begin{bmatrix} 0 & 1 & 0 & 0 \\ -k_{10} & -k_{11} & 0 & 0 \\ 0 & 0 & 0 & 1 \\ 0 & 0 & -k_{30} & -k_{31} \end{bmatrix} \begin{bmatrix} x_{11} \\ x_{12} \\ x_{13} \\ x_{14} \end{bmatrix} \\ & - x_{21} \begin{bmatrix} 0 \\ 0 \\ 0 \\ \ddot{\xi}_{1,\mathrm{ref}} + k_{11}\dot{e}_1 + k_{10}e_1 \end{bmatrix}, \\ \begin{bmatrix} \dot{x}_{21} \\ \dot{x}_{22} \end{bmatrix} &= \begin{bmatrix} 0 & 1 \\ -k_{20} & -k_{21} \end{bmatrix} \begin{bmatrix} x_{21} \\ x_{22} \end{bmatrix}. \end{aligned} \tag{25}$$

Finally, by applying Lemma 5.6 of Khalil, the system is globally uniformly asymptotically stable and satisfies the condition $\sqrt{e_1^2 + e_2^2 + e_3^2} \longrightarrow 0$ when $\longrightarrow \infty$. □

Remark 3. If the controller parameters are adjusted such that the roots of the polynomial (19), $\ddot{e}_1 + k_{11}\dot{e}_1 + k_{10}e_1 = 0$, have a negative real part closer to the imaginary axis than the roots of the polynomial (24), $\ddot{e}_3 + k_{31}\dot{e}_3 + k_{30}e_3 = 0$, then e_3 will go to zero faster than e_1 and $\xi_{2,\mathrm{ez}}$ does not go to infinity.

2.6. Controller Design for Positioning. The positioning problem for the system, S_ξ, consists in computing the control inputs, $u_1 = u_1(t, \xi, \Phi_\xi)$ and $u_2 = u_2(t, \xi, \Phi_\xi)$, such that the origin of the system is stable for any initial state $\xi(0)$. Positioning is a particular case of trajectory tracking, where $\dot{\xi}_{1,\mathrm{ref}}$, $\dot{\xi}_{3,\mathrm{ref}}$, $\ddot{\xi}_{1,\mathrm{ref}}$, and $\ddot{\xi}_{3,\mathrm{ref}}$ are zero, and $\xi_{2,\mathrm{ez}}$ is the sacrificed variable.

The system S_ξ is expressed in matrix form as follows:

$$\begin{bmatrix} 1 & 0 \\ 0 & 1 \\ \xi_2 & 0 \end{bmatrix} \begin{bmatrix} u_1 \\ u_2 \end{bmatrix} = \begin{bmatrix} \ddot{\xi}_1 \\ \ddot{\xi}_2 \\ \ddot{\xi}_3 \end{bmatrix}. \tag{26}$$

To calculate the control actions u_1 and u_2, (26) should have an exact solution; that is,

$$\begin{gathered} u_2 = \ddot{\xi}_2, \\ \begin{bmatrix} 1 \\ \xi_2 \end{bmatrix} u_1 = \begin{bmatrix} \ddot{\xi}_1 \\ \ddot{\xi}_3 \end{bmatrix}. \end{gathered} \tag{27}$$

If a proportional control approach is assumed, the tracking errors are the differences between the reference (zero) and real trajectories. Thus, the variables $\ddot{\xi}_1$ and $\ddot{\xi}_3$ are $\ddot{\xi}_1 = -k_{11}\dot{\xi}_1 + k_{10}e_1$ and $\ddot{\xi}_3 = -k_{31}\dot{\xi}_3 + k_{30}e_3$.

If $\xi_{2,\mathrm{ez}}$ is the value of ξ_2 for which the above system has an exact solution, then

$$\begin{bmatrix} 1 \\ \xi_{2,\mathrm{ez}} \end{bmatrix} u_1 = \begin{bmatrix} -k_{11}\dot{\xi}_1 + k_{10}e_1 \\ -k_{31}\dot{\xi}_3 + k_{30}e_3 \end{bmatrix}, \tag{28}$$

and the tracking errors in variables 1 and 3 tend to zero.

Variable $\xi_{2,\mathrm{ez}}$ is computed according to

$$\xi_{2,\mathrm{ez}} = \frac{-k_{31}\dot{\xi}_3 + k_{30}e_3}{-k_{11}\dot{\xi}_1 + k_{10}e_1}. \tag{29}$$

Remark 4. Variable ξ_2 follows $\xi_{2,\mathrm{ez}}$ and this one tracks $\xi_{2,\mathrm{ref}}$.

The control action u_1 obtained using linear least-squares approximation method to (28) is

$$u_1 = \frac{-k_{11}\dot{\xi}_1 + k_{10}e_1 + \xi_{2,\mathrm{ez}}\left(-k_{31}\dot{\xi}_3 + k_{30}e_3\right)}{1 + \xi_{2,\mathrm{ez}}^{\ 2}}. \tag{30}$$

Furthermore, the control action u_2 is a function of variables $\ddot{\xi}_{2,\mathrm{ez}}$, $\dot{e}_2$, and e_2:

$$u_2 = \ddot{\xi}_{2,\mathrm{ez}} + k_{21}\dot{e}_2 + k_{20}e_2. \tag{31}$$

Remark 5. Equations (30) and (31) for positioning are a particular case of (13) and (14) for trajectory tracking of the system, S_{ξ}.

2.7. Stability of the Tracking Error Dynamics: Positioning Case. In this section, the stability of the closed-loop system [(1)–(3) and (29)–(31)] is demonstrated.

Theorem 2. *Given the second-order chained form system (1)–(3), and the control actions u_1 and u_2 formulated in (29)–(31), the variables ξ_1, ξ_2, $\xi_3 \longrightarrow 0$ and $\xi_{2,ez}$, $\dot{\xi}_{2,ez}$, $\ddot{\xi}_{2,ez} \longrightarrow 0$ when $t \longrightarrow \infty$.*

Proof. The following steps are proposed to prove Theorem 2:

Step 1

Variable $\xi_{2,\mathrm{ez}}$ is substituted in (30), and after doing algebraic manipulations, u_1 is obtained:

$$u_1 = -k_{11}\dot{\xi}_1 + k_{10}e_1. \tag{32}$$

From (1), $u_1 = \ddot{\xi}_1$. Then, (32) is rewritten as follows:

$$0 = -\ddot{\xi}_1 - k_{11}\dot{\xi}_1 + k_{10}e_1. \tag{33}$$

Step 2

Substituting (31) with (10), and given that $\ddot{e}_2 = (\ddot{\xi}_{2,\mathrm{ez}} - \ddot{\xi}_2)$, the following equation arises:

$$0 = \ddot{e}_2 + k_{21}\dot{e}_2 + k_{20}e_2. \tag{34}$$

Equation (34) for positioning is coincident with (21) for trajectory tracking.

Step 3

Given that $\xi_2 = (\xi_{2,\mathrm{ez}} - e_2)$, the algebraic manipulation of (3) gives

$$\ddot{\xi}_3 = \left(\xi_{2,\mathrm{ez}} - e_2\right)u_1. \tag{35}$$

Furthermore, from (29) and (30), the following expression is obtained: $\xi_{2,ez}u_1 = -k_{31}\dot{\xi}_3 - k_{30}\xi_3$. We rewrite (35) as

$$0 = \ddot{\xi}_3 - k_{31}\dot{\xi}_3 - k_{30}\xi_3 - e_2\left(-k_{11}\dot{\xi}_1 + k_{10}e_1\right). \tag{36}$$

Then, (33), (34), and (36) for positioning are rewritten according to (5.32) and (5.33) of [24] where $\dot{\xi}_{1,\mathrm{ref}} = 0$; $\dot{\xi}_{3,\mathrm{ref}} = 0$; $\ddot{\xi}_{1,\mathrm{ref}} = 0$; and $\ddot{\xi}_{3,\mathrm{ref}} = 0$; $\dot{e}_1 = -\dot{\xi}_1$; $\dot{e}_3 = -\dot{\xi}_3$; $\ddot{e}_1 = -\ddot{\xi}_1$ and $\ddot{e}_3 = -\ddot{\xi}_3$, being $\mathbf{x}_1 = \left\{\xi_1; \dot{\xi}_1; \dot{\xi}_3; \xi_3\right\}$ and $\mathbf{x}_2 = \left\{\xi_2; \dot{\xi}_2\right\}$. By defining $x_{11} = e_1$; $x_{12} = \dot{e}_1$; $x_{21} = e_2$; $x_{22} = \dot{e}_2$; $x_{13} = e_3$; and $x_{14} = \dot{e}_3$, the following equations arise:

$$\begin{bmatrix} \dot{x}_{11} \\ \dot{x}_{12} \\ \dot{x}_{13} \\ \dot{x}_{14} \end{bmatrix} = \begin{bmatrix} 0 & 1 & 0 & 0 \\ -k_{10} & -k_{11} & 0 & 0 \\ 0 & 0 & 0 & 1 \\ 0 & 0 & -k_{30} & -k_{31} \end{bmatrix} \begin{bmatrix} x_{11} \\ x_{12} \\ x_{13} \\ x_{14} \end{bmatrix} - x_{21} \begin{bmatrix} 0 \\ 0 \\ 0 \\ k_{11}\dot{e}_1 + k_{10}e_1 \end{bmatrix}, \tag{37}$$

$$\begin{bmatrix} \dot{x}_{21} \\ \dot{x}_{22} \end{bmatrix} = \begin{bmatrix} 0 & 1 \\ -k_{20} & -k_{21} \end{bmatrix} \begin{bmatrix} x_{21} \\ x_{22} \end{bmatrix}.$$

Finally, according to the stability lemma of Khalil [24], the system is globally uniformly asymptotically stable and verifies the conditions (ξ_1, ξ_2, $\xi_3 \longrightarrow 0$) and ($\xi_{2,\mathrm{ez}}$, $\dot{\xi}_{2,\mathrm{ez}}$, $\ddot{\xi}_{2,\mathrm{ez}} \longrightarrow 0$) when $t \longrightarrow \infty$. □

Remark 6. By adjusting the controller parameters in such a way the roots of the polynomial (33) have a negative real part closer to the imaginary axis than the roots of the polynomial (36), the tracking error e_3 will go to zero faster than e_1 and $\xi_{2,\mathrm{ez}}$ will not tend to infinity.

3. Results and Discussion

The closed-loop system (1)–(3) and (13), (14), (16) for trajectory tracking is simulated and analyzed in the first test. In the same way, the closed-loop system (1)–(3) and (29)–(31) for positioning is simulated, and the results are discussed in the second test.

3.1. Trajectory Tracking Test. The aim of this section is to show that given a reference trajectory, the proposed controller can calculate a control law that allows following effectively. The reference trajectories of ξ_1; ξ_2; and ξ_3 are simulated considering $\xi_1(0) = 40$ and $\xi_2(0) = \xi_3(0) = 0$ as the initial state of the system, and $\xi_{1,\mathrm{ref}}$ and $\xi_{3,\mathrm{ref}}$ follow a parabolic path, while $\xi_{2,\mathrm{ref}}$ follows an ascending sine wave. The controller parameters, set by trial and error, are $k_{10} = 0.72$; $k_{11} = 0.72$; $k_{20} = 0.55$; $k_{21} = 0.55$; $k_{30} = 0.90$; and $k_{31} = 0.90$. With these values, ξ_1; ξ_2; and ξ_3 converge satisfactorily to the reference trajectory. Figure 1 shows the trajectory of variable 1. Variable ξ_1 (blue line) initially fluctuates around its reference $\xi_{1,\mathrm{ref}}$ (red-dashed line) reaching it after 40 seconds.

The trajectories of ξ_2(blue solid line); $\xi_{2,\mathrm{ez}}$ (green solid line); and $\xi_{2,\mathrm{ref}}$ (red dashed line) are shown in Figure 2. Variable ξ_2 follows the sacrificed variable $\xi_{2,\mathrm{ez}}$, and after 60 seconds, both variables follow the reference $\xi_{2,\mathrm{ref}}$. In this way, the tracking errors e_1 and e_3 tend to zero. This remarks the performance of the proposed controller.

Figure 3 shows the trajectory of variable 3. Variable ξ_3 (blue line) perfectly follows $\xi_{3,\mathrm{ref}}$ (red-dashed line) without undesirable oscillations.

Figures 4 and 5 present the control actions u_1 and u_2, respectively. Its initial values are $u_1(0) = u_2(0) = 0$,

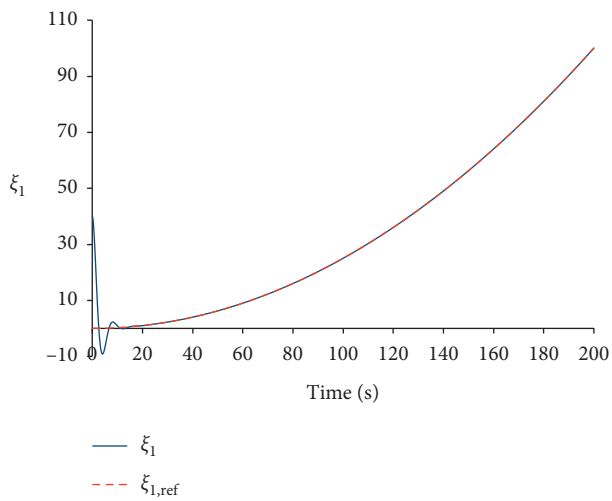

Figure 1: Trajectory tracking of ξ_1.

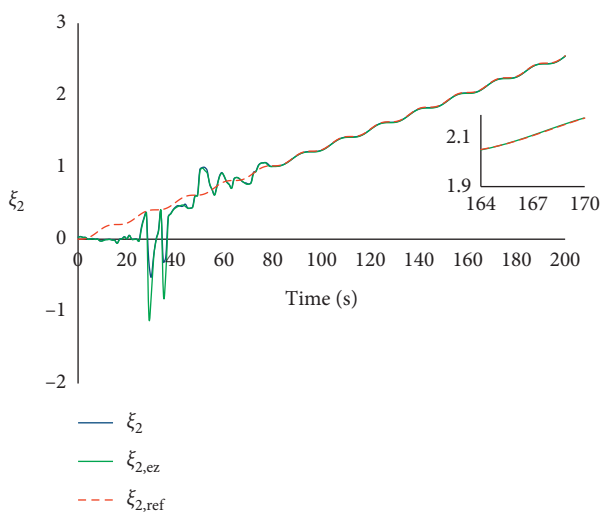

Figure 2: Trajectory tracking of ξ_2.

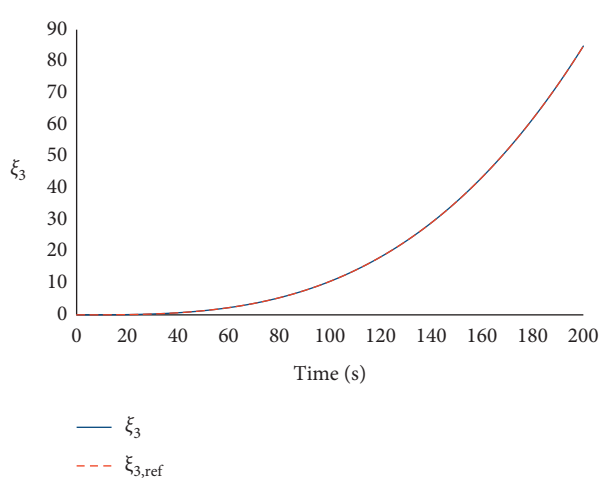

Figure 3: Trajectory tracking of ξ_3.

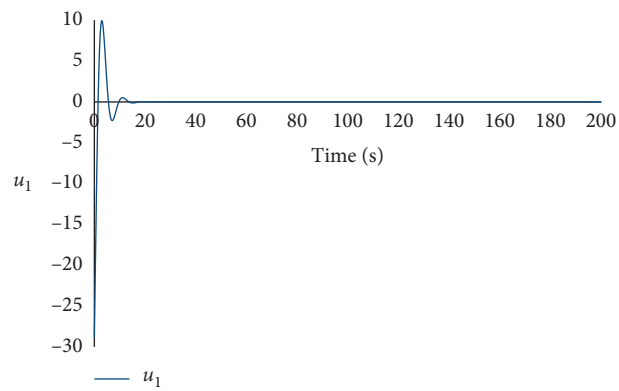

Figure 4: Control action u_1.

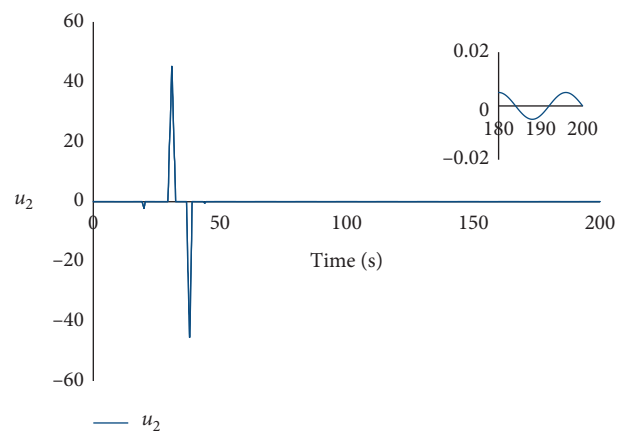

Figure 5: Control action u_2.

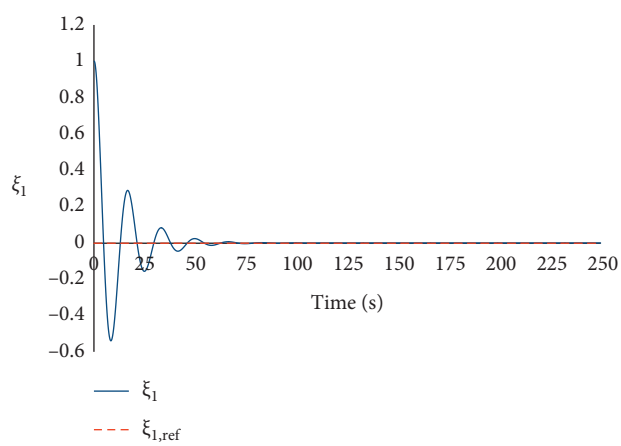

Figure 6: Trajectory of ξ_1.

respectively. The first one, u_1, evolves quickly from 0 to 10^{-4} remaining constant. The second one, u_2, follows a sine wave path with mean 0, amplitude 0.8, and frequency $1/8\pi$.

3.2. Positioning Test. The closed-loop system (1)–(3) and (29)–(31) is simulated considering $\xi_1(0) = 1$; $\xi_2(0) = 0$; and $\xi_3(0) = 10^{-3}$ as the initial state. The controller parameters are $k_{10} = 0.15$; $k_{11} = 0.15$; $k_{20} = 0.45$; $k_{21} = 0.45$; $k_{30} = 0.95$;

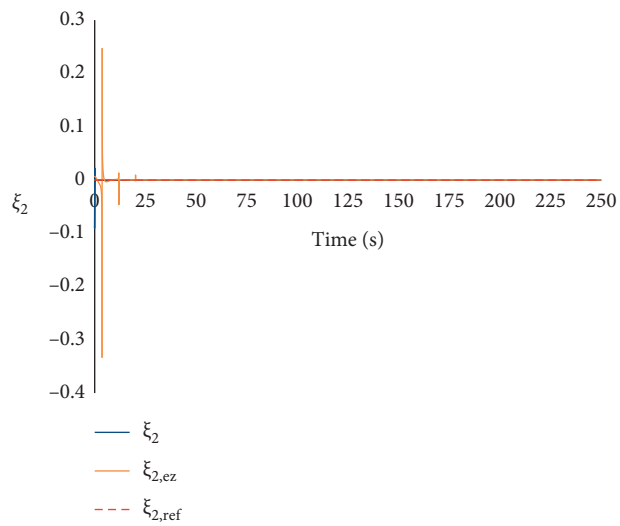

Figure 7: Trajectory of ξ_3.

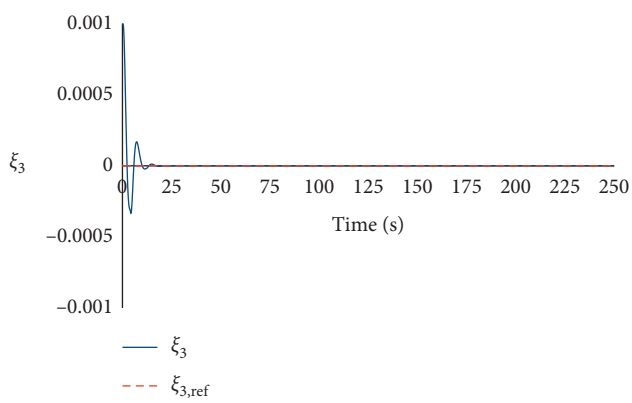

Figure 8: Control action u_1.

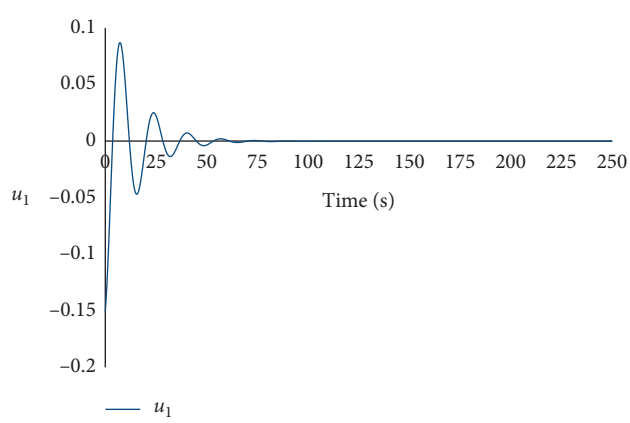

Figure 9: Trajectory of ξ_2.

and $k_{31} = 0.95$. Figures 6 and 7 show the trajectories of system variables ξ_1 and ξ_3 (blue solid lines). The red and magenta dashed lines indicate the zero reference. Figure 8 presents the control action u_1, calculated by (30). In Figure 9, variables ξ_2 and $\xi_{2,ez}$ are represented by a blue and orange solid lines, respectively. Finally, Figure 10 displays the trajectory of the control action u_2 calculated by (31).

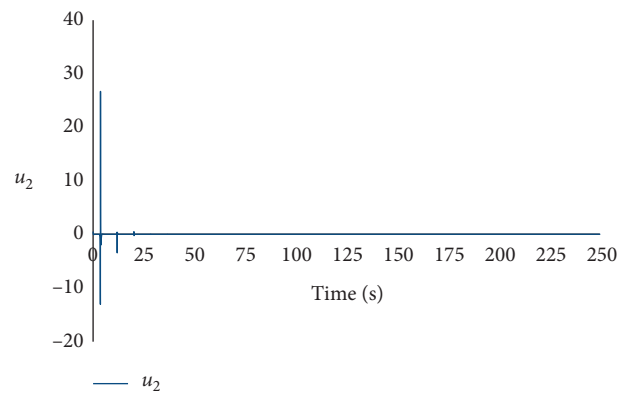

Figure 10: Control action u_2.

4. Conclusion

The major contribution of this paper is to extend the LABC technique for trajectory tracking and positioning of a second-order nonholonomic system. This controller is based on determining the conditions for which the system model has an exact solution. Knowing the model equations, it is necessary only to fix the desired trajectory to find the control action. Variables 1 and 3 were set as references, while variable 2 is the sacrificed one to ensure that the tracking errors go to zero. An important advantage of the proposed controller is the low computational load of the required mathematical operations. The stability of the system is demonstrated by applying the Khalil lemma [24].

Simulation results show the performance of the proposed control algorithm. The controller parameters were empirically tuned. For trajectory tracking, these parameters ensure that the system variables quickly reach the reference and follow it without undesirable oscillations. In the case of the positioning problem, these parameters were tuned in such a way variable ξ_3 goes to zero more quickly than ξ_1.

Data Availability

The data used to support the finding of this study are included within the article.

Conflicts of Interest

The authors declare that there are no conflicts of interest regarding the publication of this paper.

Acknowledgments

The authors thank the Institute of Chemical Engineering of the National University of San Juan, Argentina, Planta Piloto de Ingeniería Química (PLAPIQUI-National University of the South), Argentina, and Consejo Nacional de Investigaciones Científicas y Técnicas (CONICET, National Council for Scientific Research), Argentina. This work was partially funded by Consejo Nacional de Investigaciones

Científicas y Técnicas (CONICET), Universidad Nacional de San Juan (UNSJ), and Universidad Nacional del Sur (UNS), Argentina.

References

[1] G. He, C. Zhang, W. Sun, and Z. Geng, "Stabilizing the second-order nonholonomic systems with chained form by finite-time stabilizing controllers," *Robotica*, vol. 34, no. 10, pp. 2344–2367, 2016.

[2] N. P. I. Aneke, *Control of underactuated mechanical systems*, Ph.D. dissertation, Department of Mechanical Engineering, Eindhoven University of Technology, Eindhoven, The Netherlands, 2003.

[3] R. W. Brockett, R. S. Millman, and H. J. Sussmann, "Asymptotic stability and feedback stabilization," in *Differential Geometric Control Theory*, pp. 2961–2963, Birkhäuser, Basel, Switzerland, 1983.

[4] N. P. I. Aneke, H. Nijmeijer, and A. G. de Jager, "Trajectory tracking by cascaded backstepping control for a second-order non-holonomic mechanical system,"," in *Nonlinear Control in the Year 2000. Lecture Notes in Control and Information Sciences*, A. Isidori, F. Lamnabhi-Lagarrigue, and W. Respondek, Eds., vol. 258, pp. 35–49, Springer, Paris, France, 2000.

[5] N. P. I. Aneke, H. Nijmeijer, and A. G. de Jager, "Tracking control of second-order chained form systems by cascaded backstepping," *International Journal of Robust and Nonlinear Control*, vol. 13, no. 2, pp. 95–115, 2003.

[6] Z. P. Yuan, Z. P. Wang, and Q. J. Chen, "Trajectory tracking control of a nonholonomic mobile robot," in *Proceedings of the IEEE ICCA 2010*, pp. 2207–2211, Xiamen, China, June 2010.

[7] N. Adhikary and C. Mahanta, "Integral backstepping sliding mode control for underactuated systems: swing-up and stabilization of the cart-pendulum system," *ISA Transactions*, vol. 52, no. 6, pp. 870–880, 2013.

[8] Y.-P. Tian and K.-C. Cao, "Time-varying linear controllers for exponential tracking of non-holonomic systems in chained form," *International Journal of Robust and Nonlinear Control*, vol. 17, no. 7, pp. 631–647, 2007.

[9] A. Astolfi, "Discontinuous control of nonholonomic systems," *Systems & Control Letters*, vol. 27, no. 1, pp. 37–45, 1996.

[10] Y. Nakamura and R. Mukherjee, "Nonholonomic path planning of space robots via a bidirectional approach," *IEEE Transactions on Robotics and Automation*, vol. 7, no. 4, pp. 500–514, 1991.

[11] M. Asif, M. J. Khan, and N. Cai, "Adaptive sliding mode dynamic controller with integrator in the loop for nonholonomic wheeled mobile robot trajectory tracking," *International Journal of Control*, vol. 87, no. 5, pp. 964–975, 2014.

[12] L. Yang and J. Y. Yang, "Stabilization for a class of nonholonomic perturbed systems via robust adaptive sliding mode control," in *Proceedings of the American Control Conference*, pp. 1178–1183, Baltimore, MD, USA, June 2010.

[13] N. Chen, F. Song, G. Li, X. Sun, and C. Ai, "An adaptive sliding mode backstepping control for the mobile manipulator with nonholonomic constraints," *Communications in Nonlinear Science and Numerical Simulation*, vol. 18, no. 10, pp. 2885–2899, 2013.

[14] M. A. Fairus, Z. Mohamed, M. N. Ahmad, and W. S. Loi, "LMI-based multi objective integral sliding mode control for rotary inverted pendulum system under load variations," *Journal Teknologi*, vol. 73, pp. 125–137, 2015.

[15] M. Sarfraz and F. ur Rehman, "Adaptive sliding mode control for a second order nonholonomic planar four-link UMS," in *Proceedings of the 2017 13th International Conference on Emerging Technologies (ICET)*, pp. 1–6, Islamabad, Pakistan, July 2017.

[16] S. Gustavo, S. M. Emanuel, and A. Pedro, *Linear Algebra Based Controller - Design and Applications*, Springer International Publishing, Cham, Switzerland, 2020.

[17] G. Scaglia, E. Serrano, A. Rosales, and P. Albertos, "Tracking control design in nonlinear multivariable systems: robotic applications," *Mathematical Problems in Engineering*, vol. 2019, Article ID 8643515, 15 pages, 2019.

[18] G. Scaglia, V. Mut, A. Rosales, and O. Quintero, "Tracking control of a mobile robot using linear interpolation," *IMAACA07*, vol. 1, pp. 11–15, 2007.

[19] A. Rosales, G. Scaglia, V. Mut, and F. Di Sciascio, "Trajectory tracking of mobile robots in dynamic environments-a linear algebra approach," *Robotica*, vol. 27, no. 7, pp. 981–997, 2009.

[20] M. E. Serrano, S. A. Godoy, L. Quintero, and G. J. Scaglia, "Interpolation based controller for trajectory tracking in mobile robots," *Journal of Intelligent & Robotic Systems*, vol. 86, no. 3-4, pp. 569–581, 2017.

[21] M. E. Serrano, G. J. E. Scaglia, S. A. Godoy, V. Mut, and O. A. Ortiz, "Trajectory tracking of underactuated surface vessels: a linear algebra approach," *IEEE Transactions on Control Systems Technology*, vol. 22, no. 3, pp. 1103–1111, 2014.

[22] M. E. Serrano, G. J. E. Scaglia, F. A. Cheein, V. Mut, and O. A. Ortiz, "Trajectory-tracking controller design with constraints in the control signals: a case study in mobile robots," *Robotica*, vol. 33, no. 10, pp. 2186–2203, 2015.

[23] G. Scaglia, P. M. Aballay, M. E. Serrano, O. A. Ortiz, M. Jordan, and M. D. Vallejo, "Linear algebra based controller design applied to a bench-scale oenological alcoholic fermentation," *Control Engineering Practice*, vol. 25, pp. 66–74, 2014.

[24] H. K. Khalil, *Nonlinear Systems*, Prentice-Hall, Upper Saddle River, NJ, USA, 2nd edition, 1996.

Hindawi
Mathematical Problems in Engineering
Volume 2020, Article ID 4632434, 11 pages
https://doi.org/10.1155/2020/4632434

Research Article

Soliton Solutions and Collisions for the Multicomponent Gross–Pitaevskii Equation in Spinor Bose–Einstein Condensates

Ming Wang and Guo-Liang He

School of Mathematics and Information Science, Zhengzhou University of Light Industry, Zhengzhou, Henan 450002, China

Correspondence should be addressed to Ming Wang; hsxh1943@126.com

Received 29 March 2020; Revised 1 June 2020; Accepted 23 June 2020; Published 31 July 2020

Guest Editor: Cuimei Jiang

In this paper, we investigate a five-component Gross–Pitaevskii equation, which is demonstrated to describe the dynamics of an $F = 2$ spinor Bose–Einstein condensate in one dimension. By employing the Hirota method with an auxiliary function, we obtain the explicit bright one- and two-soliton solutions for the equation via symbolic computation. With the choice of polarization parameter and spin density, the one-soliton solutions are divided into four types: one-peak solitons in the ferromagnetic and cyclic states and one- and two-peak solitons in the polar states. For the former two, solitons share the similar shape of one peak in all components. Solitons in the polar states have the one- or two-peak profiles, and the separated distance between two peaks is inversely proportional to the value of polarization parameter. Based on the asymptotic analysis, we analyze the collisions between two solitons in the same and different states.

1. Introduction

Bose–Einstein condensates (BECs) of the alkali-metal-atom gases have attracted certain attention in both experimental [1, 2] and theoretical studies [3–5]. BECs can have the internal degrees of freedom associated with the hyperfine spin and such condensates are usually called the spinor BECs [6]. The spinor BECs are classified according to the relative values of certain characteristic scattering lengths [7]. For the spinor BEC with the hyperfine spin $F = 1$, the condensate can have either ferromagnetic state and polar state, such as ^{87}Rb and ^{23}Na, respectively, and the corresponding ground-state structure and dynamical properties of those two cases are distinct [8]. In the description of [7, 8], a spinor condensate with the spin $F = 2$ bosons in an optical trap can be one of the three types: ferromagnetic, polar, and cyclic. Dynamics of the spinor BEC have been addressed in [9–14].

The dynamics of nonlinear phenomena can be analyzed by means of the corresponding nonlinear evolution equations. There has been considerable work carried out on the control problem of nonlinear systems, such as those in chaotic and stochastic systems [15–19]. Solitons, resulted from the balance between the effects of nonlinearity and dispersion [20], have been studied in fields such as nonlinear optics, plasma physics, and condensed matter physics [3, 21–23]. In addition, breathers and rogue waves have been concerned in recent research [24, 25]. In the spinor BECs, matter-wave solitons are thought to be useful for their application in the atom laser, atom interferometry, and coherent atom transport, which can contribute to the realization of quantum information processors or computation [26]. The dynamics of magnetic soliton, dark soliton, and dark-bright vector soliton in spinor Bose–Einstein condensates have been investigated [27–30]. A frontier is the model extension from the single-component condensate to the multicomponent, which opens up new fields for the study of quantum matter waves and fluids [11]. The spinor BECs with spin F is described by a $(2F + 1)$-component mean-field wave function [31].

In this paper, we will consider a five-component Gross–Pitaevskii (GP) equation for the dynamics of an $F = 2$ spinor BEC in one dimension [32]:

$$i\partial_t\Phi_{\pm2} + \partial_x^2\Phi_{\pm2} + 2n\Phi_{\pm2} - \Theta\Phi_{\mp2}^* = 0, \tag{1a}$$

$$i\partial_t\Phi_{\pm1} + \partial_x^2\Phi_{\pm1} + 2n\Phi_{\pm1} + \Theta\Phi_{\mp1}^* = 0, \tag{1b}$$

$$i\partial_t\Phi_0 + \partial_x^2\Phi_0 + 2n\Phi_0 - \Theta\Phi_0^* = 0, \tag{1c}$$

where $\Phi_{\pm j}$'s $(j = 0, 1, 2)$ are the wave functions of the five spin components, t and x, respectively, denote the time and spatial co-ordinate, and the asterisk represents the complex conjugation, while the number density n and singlet-pair amplitude Θ are defined by [10, 33]

$$\begin{aligned} n &= \sum_{k=-2}^{2} \Phi_k\Phi_k^*, \\ \Theta &= 2\Phi_2\Phi_{-2} - 2\Phi_1\Phi_{-1} + \Phi_0^2. \end{aligned} \tag{2}$$

Equation (1) is the integrable version of the multi-component GP equation mentioned in [31] and simplified under the condition $2m = 1$, $\hbar = 1$, $c_2 = 0$, $c_4 = 1$, and $c_0 = -2 < 0$, which corresponds to the attractive interaction. Due to the integrability, equation (1) has the infinite conservation laws, which restricts the dynamics of the system in an important way. The normalization is imposed as $\int dx\, n = N_T$, where N_T is the total number of atoms. For equation (1), bright one- and two-soliton solutions have been given via the Zakharov–Shabat dressing [32]. However, the solitons are not classified according to the forms of the solutions and then the properties of soliton collisions are not clearly analyzed, that is the aim of this paper.

In this paper, we will concentrate on the soliton types and collisions in the same and different states in an $F = 2$ spinor BEC. For equation (1), we will present the Hirota form with an auxiliary function and explicit one- and two-soliton solutions. With symbolic computation [34, 35], this paper will be organized as follows. In Section 2, the Hirota bilinearization procedure for equation (1) will be presented. In Section 3, based on the bilinear form, we will obtain and analyze the one-soliton solutions, which reveal the one- or two-peak solitons in three different states. In Section 4, making the asymptotic analysis on the obtained two-soliton solutions, we will discuss the soliton collisions in the same and different states. Section 5 will be our conclusions.

2. Hirota Bilinearization Method for Equation (1)

In order to understand the dynamics of equation (1), it is essential to obtain the soliton solutions. The Hirota bilinear method is a tool to construct the soliton solutions for certain nonlinear evolution equations [36]. For equation (1), we will utilize the Hirota method with an auxiliary function to obtain the one- and two-soliton solutions. The procedure can be extended to obtain N-soliton solutions [37].

To begin with, equation (1) can be expressed in the bilinear form:

$$\left(iD_t + D_x^2\right)\left(G_{\pm2}\cdot F\right) = SG_{\mp2}^*, \tag{3a}$$

$$\left(iD_t + D_x^2\right)\left(G_{\pm1}\cdot F\right) = -SG_{\mp1}^*, \tag{3b}$$

$$\left(iD_t + D_x^2\right)\left(G_0\cdot F\right) = SG_0^*, \tag{3c}$$

$$D_x^2(F\cdot F) = 2\sum_{k=-2}^{2} G_kG_k^*, \tag{3d}$$

$$SF = 2G_2G_{-2} - 2G_1G_{-1} + G_0^2, \tag{3e}$$

with an auxiliary function S and the following transformations:

$$\Phi_{\pm j} = \frac{G_{\pm j}}{F}, \quad \text{for } j = 0, 1, 2, \tag{4}$$

where G_j's are the complex functions of t and x and F is a real one. D_x and D_t are the bilinear differential operators [36] defined by

$$D_x^lD_t^m(f\cdot g) = \left(\frac{\partial}{\partial x} - \frac{\partial}{\partial x'}\right)^l\left(\frac{\partial}{\partial t} - \frac{\partial}{\partial t'}\right)^m f(x,t)g(x',t')|_{x'=x,t'=t}. \tag{5}$$

where l and m are the positive integers and x' and t' are the formal variables. Multisoliton solutions for equation (1) can be generated by solving equation (3) with the following power series expansions as

$$\begin{aligned} G_{\pm j} &= \varepsilon g_{\pm j}^{(1)} + \varepsilon^3 g_{\pm j}^{(3)} + \varepsilon^5 g_{\pm j}^{(5)} + \cdots, \\ F &= 1 + \varepsilon^2 f_2 + \varepsilon^4 f_4 + \varepsilon^6 f_6 + \cdots, \\ S &= \varepsilon^2 s_2 + \varepsilon^4 s_4 + \varepsilon^6 s_6 + \cdots, \end{aligned} \tag{6}$$

where ε is the formal parameter, $g_{\pm j}^{(l)}$'s $(l = 1, 3, 5, \cdots)$ are the complex functions of t and x, and f_m's $(m = 2, 4, 6, \cdots)$ are the real ones which will be determined later.

3. Bright One-Soliton Solutions

In order to obtain one-soliton solutions for equation (1), the power series expansions for $G_{\pm j}$, F, and S are terminated as

$$\begin{aligned} G_{\pm j} &= \varepsilon g_{\pm j}^{(1)} + \varepsilon^3 g_{\pm j}^{(3)}, \\ S &= \varepsilon^2 S_2, \\ F &= 1 + \varepsilon^2 f_2 + \varepsilon^4 f_4. \end{aligned} \tag{7}$$

It is noted that equation (7) are usually taken to obtain the two-soliton solutions. Substituting equation (7) into equation (3) and collecting the terms with the same power of ε, we obtain the one-soliton solutions for equation (1):

$$\Phi_{\pm j} = \frac{b_1^{(\pm j)}e^{\theta_1} + e^{2\theta_1+\theta_1^*+d_1^{(\pm j)}}}{1 + e^{\theta_1+\theta_1^*+l_1} + e^{2\theta_1+2\theta_1^*+c_{11}}}, \tag{8}$$

and the auxiliary function S given as

$$S = \Lambda_1 e^{2\theta_1}, \tag{9}$$

with

$$\begin{aligned}
\theta_1 &= k_1 x + i k_1^2 t,\\
e^{d_1^{(\pm j)}} &= \frac{\delta(j) b_1^{(\mp j)^*} \Lambda_1}{2\left(k_1 + k_1^*\right)^2},\\
\delta(j) &= \begin{cases} -1 & j = 1\\ 1 & j = 0, 2,\end{cases}\\
e^{l_1} &= \frac{\sum_{k=0}^{2} \left|b_1^{(\pm k)}\right|^2}{\left(k_1 + k_1^*\right)^2},\\
e^{c_{11}} &= \frac{\left|\Lambda_1\right|^2}{4\left(k_1 + k_1^*\right)^4},\\
\Lambda_1 &= 2 b_1^{(+1)} b_1^{(-1)} + \left(b_1^{(0)}\right)^2 - 2 b_1^{(+2)} b_1^{(-2)},
\end{aligned} \tag{10}$$

where $b_1^{(\pm j)}$'s and k_1 are all complex constants. Here, we give the spin densities $f = (f^x, f^y, f^z)$ with [32]

$$\begin{aligned}
f^x &= 2\left[\Phi_{-2}\Phi_{-1}^* + \frac{\sqrt{6}}{2}\Phi_0^*\left(\Phi_{+1} + \Phi_{-1}\right) + \Phi_2\Phi_1^*\right]_R,\\
f^y &= 2i\left[\Phi_{-2}\Phi_{-1}^* + \frac{\sqrt{6}}{2}\Phi_0^*\Phi_{-1} + \frac{\sqrt{6}}{2}\Phi_0\Phi_1^* + \Phi_1\Phi_2^*\right]_I,\\
f^z &= 2\left|\Phi_{-2}\right|^2 + \left|\Phi_{-1}\right|^2 - \left|\Phi_1\right|^2 - 2\left|\Phi_2\right|^2,
\end{aligned} \tag{11}$$

where the subscripts R and I, respectively, denote the real and imaginary parts and the total spin can be given with $\int dx\, f = F_T$. For equation (1), there exist different types of solitons according to the values of Λ_1. When $\Lambda_1 = 0$, equation (8) admit the one-peak solitons in the ferromagnetic and cyclic states corresponding to the spin densities $|f| > 0$ and $f = 0$, respectively. For the case of $\Lambda_1 \neq 0$, we can find the one- and two-peak solitons in the polar state, while only the two-peak soliton in the polar state for the $F = 1$ spinor BECs [38].

3.1. One-Peak Solitons in the Ferromagnetic and Cyclic States. When $\Lambda_1 = 0$, equation (9) can be expressed as

$$\Phi_{\pm j} = A_{\pm j} e^{i\theta_{1I}} \operatorname{sech}\left(\theta_{1R} + \frac{l_1}{2}\right), \tag{12}$$

with

$$\begin{aligned}
A_{\pm j} &= \frac{1}{2} b_1^{(\pm j)} e^{-(l_1/2)},\\
k_1 &= k_{1R} + i k_{1I},\\
\theta_{1R} &= k_{1R}\left(x - 2k_{1I} t\right),\\
\theta_{1I} &= k_{1I} x + \left(k_{1R}^2 - k_{1I}^2\right) t.
\end{aligned} \tag{13}$$

Here, $A_{\pm j}$, $2k_I$, and $l_1/2k_R$, respectively, characterize the amplitude, velocity, and initial phase of the soliton. For $|f| > 0$, it corresponds to the one-peak soliton in the ferromagnetic state [31]. When choosing suitable parameters to make $f = 0$, we find that the soliton is in the cyclic state. Those two types of solitons posses the similar intensity profile of one peak in all components, as shown in Figures 1 and 2. For simplicity, we choose the parameters to make $|\Phi_{+j}| = |\Phi_{-j}|$ in Figure 1. It is noted that the auxiliary function S vanishes in this case, as given in equation (12).

3.2. One- and Two-Peak Solitons in the Polar State. For the case $\Lambda_1 \neq 0$, equation (8) can be expressed as

$$\Phi_{\pm j} = A_{\pm j} e^{i\theta_{1I}} \frac{\cosh\left(\theta_{1R} + \left(c_{11}/4\right) + P_{\pm j}\right)}{4\cosh^2\left(\theta_{1R} + \left(c_{11}/4\right)\right) + L}, \tag{14}$$

where $A_{\pm j} = 2e^{(d_1^{(\pm j)} + \ln b_1^{(\pm j)} - c_{11})/2}$, $L = e^{(l_1 - (c_{11}/2))} - 2$, and $P_{\pm j} = e^{(2d_1^{(\pm j)} - 2\ln b_1^{(\pm j)} - c_{11})/4}$. The form of equation (14) will be of use in the following asymptotic analysis of the two-soliton solutions. When $f = 0$ under certain constraint, equation (14) depicts the one-peak soliton in the polar state, as the short dashed lines shown in Figure 3. When $f \neq 0$ but the spin $F = \int f \mathrm{d}x = 0$, we can observe the two-peak soliton in the polar state, as the solid lines shown in Figure 3. In addition, as the value of Λ_1 decreases, the separated distance between two peaks increases, and it looks like that there exist two ferromagnetic solitons traveling parallel in the same velocity and amplitudes as Λ_1 approaches to zero, as the long dashed lines shown in Figure 3.

4. Two-Soliton Solutions and Soliton Collisions

In this paper, we will concentrate on the two-soliton solutions and analyze the collisions between two solitons. Employing the following expansions,

$$\begin{aligned}
G_{\pm j} &= \varepsilon g_{\pm j}^{(1)} + \varepsilon^3 g_{\pm j}^{(3)} + \varepsilon^5 g_{\pm j}^{(5)} + \varepsilon^7 g_{\pm j}^{(7)},\\
S &= \varepsilon^2 s_2 + \varepsilon^4 s_4 + \varepsilon^6 s_6,\\
F &= 1 + \varepsilon^2 f_2 + \varepsilon^4 f_4 + \varepsilon^6 f_6 + \varepsilon^8 f_8.
\end{aligned} \tag{15}$$

We obtain the two-soliton solutions for equation (1) in the form of

$$\Phi_{\pm j} = \frac{G_{\pm j}}{F}, \quad j = 0, 1, 2, \tag{16}$$

where the functions $G_{\pm j}$ and F are expressed as

$$\begin{aligned}G_{\pm j} = {} & b_1^{(\pm j)}e^{\theta_1} + b_2^{(\pm j)}e^{\theta_2} + e^{2\theta_1+\theta_1^*+d_1^{(\pm j)}} + e^{2\theta_1+\theta_2^*+d_{12}^{(\pm j)}} + e^{2\theta_2+\theta_1^*+d_{21}^{(\pm j)}} \\ & + e^{2\theta_2+\theta_2^*+d_2^{(\pm j)}} + e^{\theta_1+\theta_1^*+\theta_2+D_{12}^{(\pm j)}} + e^{\theta_2+\theta_2^*+\theta_1+D_{21}^{(\pm j)}} + e^{2\theta_1+2\theta_1^*+\theta_2+h_{12}^{(\pm j)}} + e^{2\theta_2+2\theta_2^*+\theta_1+h_{21}^{(\pm j)}} + e^{2\theta_2+2\theta_1^*+\theta_1+H_{12}^{(\pm j)}} \\ & + e^{2\theta_1+2\theta_2^*+\theta_2+H_{21}^{(\pm j)}} + e^{2\theta_1+\theta_1^*+\theta_2+\theta_2^*+w_{12}^{(\pm j)}} + e^{2\theta_2+\theta_2^*+\theta_1+\theta_1^*+w_{21}^{(\pm j)}} + e^{2\theta_1+2\theta_1^*+2\theta_2+\theta_2^*+W_{12}^{(\pm j)}} + e^{2\theta_1+2\theta_2+2\theta_2^*+\theta_1^*+W_{21}^{(\pm j)}},\end{aligned} \tag{17}$$

$$\begin{aligned}F = {} & 1 + e^{\theta_1+\theta_1^*+l_1} + e^{\theta_1+\theta_2^*+l_0} + e^{\theta_2+\theta_1^*+l_0^*} + e^{\theta_2+\theta_2^*+l_2} + e^{2\theta_1+2\theta_1^*+c_{11}} + e^{2\theta_1+2\theta_2^*+c_{12}} + e^{2\theta_2+2\theta_1^*+c_{12}^*} + e^{2\theta_2+2\theta_2^*+c_{22}} \\ & + e^{2\theta_1+\theta_1^*+\theta_2^*+l_{12}} + e^{2\theta_1^*+\theta_1+\theta_2+l_{12}^*} + e^{2\theta_2+\theta_1^*+\theta_2^*+l_{21}} + e^{2\theta_2^*+\theta_1+\theta_2+l_{21}^*} + e^{\theta_1+\theta_1^*+\theta_2+\theta_2^*+l_3} + e^{2\theta_1+2\theta_1^*+\theta_2+\theta_2^*+L_{12}} \\ & + e^{2\theta_2+2\theta_2^*+\theta_1+\theta_1^*+L_{21}} + e^{2\theta_1+2\theta_2^*+\theta_2+\theta_1^*+l_4} + e^{2\theta_2+2\theta_1^*+\theta_1+\theta_2^*+l_4^*} + e^{2\theta_1+2\theta_1^*+2\theta_2+2\theta_2^*+l_5},\end{aligned} \tag{18}$$

and the auxiliary function S takes the form

$$\begin{aligned}S = {} & \Lambda_1 e^{2\theta_1} + \Lambda_2 e^{2\theta_2} + e^{\theta_1+\theta_2+r_1} + e^{\theta_1+\theta_1^*+2\theta_2+r_{21}} + e^{\theta_2+\theta_2^*+2\theta_1+r_{12}} \\ & + e^{\theta_1+\theta_2^*+2\theta_2+R_{21}} + e^{\theta_2+\theta_1^*+2\theta_1+R_{12}} + e^{2\theta_1+2\theta_1^*+2\theta_2+r_3} \\ & + e^{2\theta_1+2\theta_2+2\theta_2^*+r_4} + e^{2\theta_1+\theta_1^*+2\theta_2+\theta_2^*+r_5},\end{aligned} \tag{19}$$

with

$$\theta_m = k_m x + i k_m^2 t,$$

$$\Lambda_m = 2b_m^{(+1)}b_m^{(-1)} + \left(b_m^{(0)}\right)^2 - 2b_m^{(+2)}b_m^{(-2)},$$

$$m = 1, 2,$$

$$e^{d_m^{(\pm j)}} = \frac{\delta(j) b_m^{(\mp j)*}\Lambda_m}{2\left(k_m + k_m^*\right)^2},$$

$$e^{d_{lm}^{(\pm j)}} = \frac{\delta(j) b_l^{(\mp j)*}\Lambda_m}{\left(k_m + k_l^*\right)^2},$$

$$l = 1, 2, m \neq l, \delta(j) = \begin{cases} -1, & j = 1, \\ 1, & j = 0, 2, \end{cases}$$

$$\begin{aligned}e^{D_{lm}^{(\pm j)}} = {} & \frac{1}{\left(k_m + k_m^*\right)^2\left(k_l + k_m^*\right)^2}\left\{2\left(k_m - k_l\right)\left[b_m^{(\pm j)}\left(k_m + k_m^*\right)\sum_{k=0}^{2} b_m^{(\pm k)*}b_l^{(\pm k)} - b_l^{(\pm j)}\left(k_l + k_m^*\right)\sum_{k=0}^{2}\delta(k)\left|b_m^{(\pm k)}\right|^2\right]\right. \\ & \left. + \delta(j) b_m^{(\mp j)*}\left(k_m + k_m^*\right)\left(k_l + k_m^*\right)\sum_{k=0}^{2}\delta(k) b_m^{(\pm k)} b_l^{(\pm k)}\right\},\end{aligned}$$

$$e^{h_{lm}^{(\pm j)}} = \frac{b_l^{(\pm j)}\left|\Lambda_m\right|^2\left(k_m^* - k_l^*\right)^2}{4\left(k_m + k_m^*\right)^4\left(k_l + k_m^*\right)^2},$$

$$e^{H_{lm}^{(\pm j)}} = \frac{b_m^{(\mp j)*}\Lambda_m\Lambda_l^*\left(k_m^* - k_l^*\right)^2}{4\left(k_m + k_m^*\right)^2\left(k_m + k_l^*\right)^4},$$

$$
\begin{aligned}
e^{w_{lm}^{(\pm j)}} &= \frac{\Lambda_m (k_m - k_l)^2}{2(k_m + k_m^*)^2 |k_m + k_l^*|^4 (k_l + k_l^*)^2} \left\{ b_l^{(\pm j)} (k_l + k_l^*)(k_l + k_m^*) \sum_{k=0}^{2} \delta(k) b_m^{(\mp k)*} b_l^{(\pm k)*} + \delta(j)(k_m^* - k_l^*) \right. \\
&\quad \left. \left[b_m^{(\mp j)*} (k_l + k_m^*) \sum_{k=0}^{2} \left| b_l^{(\pm k)} \right|^2 - b_l^{(\mp j)*} (k_l + k_l^*) \sum_{k=0}^{2} b_m^{(\pm k)*} b_l^{(\pm k)} \right] \right\}, \\
e^{W_{lm}^{(\pm j)}} &= \frac{\delta(j) b_l^{(\mp j)*} |\Lambda_m|^2 \Lambda_l (k_m - k_l)^4 (k_m^* - k_l^*)^2}{8(k_m + k_m^*)^4 (k_l + k_m^*)^4 (k_m + k_l^*)^2 (k_l + k_l^*)^2}, \\
e^{l_0} &= \frac{\sum_{k=0}^{2} b_1^{(\pm k)} b_2^{(\pm k)*}}{(k_1 + k_2^*)^2}, \\
e^{l_m} &= \frac{\sum_{k=0}^{2} \left| b_m^{(\pm k)} \right|^2}{(k_m + k_m^*)^2}, \\
e^{c_{lm}} &= \frac{\Lambda_m \Lambda_l^*}{4(k_m + k_l^*)^4}, \\
e^{l_3} &= \frac{2}{(k_1 + k_1^* + k_2 + k_2^*)^2} \left[\left(|k_1|^2 + |k_2|^2 - 2k_1^* k_2 \right) \left(\left| e^{c_0} \right|^2 - e^{c_1} e^{c_2} \right) - \left(k_1^2 + k_2^2 - 2k_1 k_2 \right) \left(\left| e^{c_0} \right|^2 + e^{c_1} e^{c_2} \right) - 2 \sum_{m,l=1, m \neq l}^{2} \sum_{k=0}^{2} b_m^{(\pm k)*} e^{D_{lm}^{(\pm k)}} \right]_R, \\
e^{l_{lm}} &= \frac{\Lambda_m \sum_{k=0}^{2} \delta(k) b_1^{(\mp k)*} b_2^{(\pm k)*}}{2(k_m + k_m^*)^2 (k_m + k_l^*)^2}, \\
e^{L_{lm}} &= \frac{|\Lambda_m|^2 \sum_{k=0}^{2} \left| b_l^{(\pm k)} \right|^2 |k_1 - k_2|^4}{4(k_m + k_m^*)^4 |k_m + k_l|^4 (k_l + k_l^*)^2}, \\
e^{l_4} &= \frac{\Lambda_1 \Lambda_2^* \sum_{k=0}^{2} b_2^{(\pm k)} b_1^{(\pm k)*} |k_1 - k_2|^4}{4(k_1 + k_1^*)^2 |k_1 + k_2|^4 (k_1 + k_2^*)^2 (k_2 + k_2^*)^2}, \\
e^{m_5} &= \frac{|\Lambda_1|^2 |\Lambda_2|^2 |k_1 - k_2|^8}{16(k_1 + k_1^*)^4 |k_1 + k_2^*|^8 (k_2 + k_2^*)^4}, \\
e^{r_1} &= 2 \sum_{k=0}^{2} \delta(k) b_1^{(\mp k)} b_2^{(\pm k)}, \\
e^{r_{lm}} &= \frac{\Lambda_m \sum_{k=0}^{2} \left| b_l^{(\pm k)} \right|^2 (k_m - k_l)^2}{(k_m + k_l^*)^2 (k_l + k_l^*)^2}, \\
e^{R_{lm}} &= \frac{\Lambda_m \sum_{k=0}^{2} b_l^{(\pm k)} b_m^{(\pm k)*} (k_1 - k_2)^2}{(k_l + k_m^*)^2 (k_m + k_m^*)^2}, \\
e^{r_3} &= \frac{\Lambda_2 |\Lambda_1|^2 (k_1 - k_2)^4}{4(k_1 + k_1^*)^4 (k_2 + k_1^*)^4}, \\
e^{r_4} &= \frac{\Lambda_1 |\Lambda_2|^2 (k_1 - k_2)^4}{4(k_2 + k_2^*)^4 (k_1 + k_2^*)^4}, \\
e^{r_5} &= \frac{\Lambda_1 \Lambda_2 \sum_{k=0}^{2} \delta(k) b_1^{(\mp k)*} b_2^{(\pm k)*} (k_1 - k_2)^4}{2(k_1 + k_1^*)^2 |k_1 + k_2^*|^4 (k_2 + k_2^*)^2},
\end{aligned}
\tag{20}
$$

where k_1, k_2, $b_1^{(\pm j)}$'s, and $b_2^{(\pm j)}$'s are all complex constants. To understand the collision property of solitons in the $F = 2$ spinor BEC, we will make the asymptotic analysis on two-soliton solution (16) as $t \longrightarrow \mp\infty$, which are associated with the initial and final state, respectively. Without loss of generality, we set

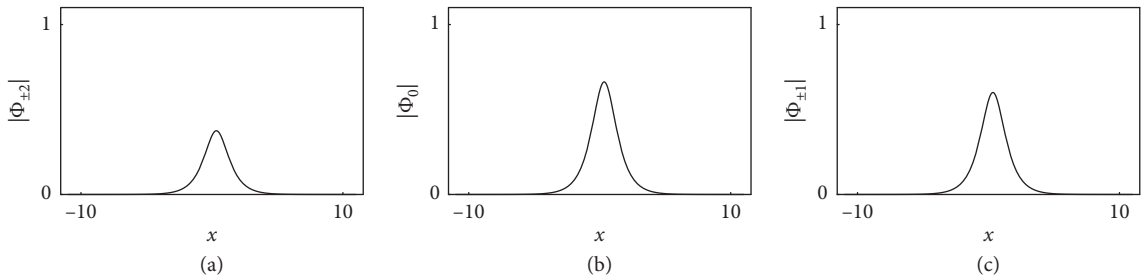

Figure 1: Intensity plots of the one soliton in the ferromagnetic state for the components $\Phi_{\pm j}$ via solution (8). Parameters are $k_1 = 1.2 + i$, $b_1^{(\pm 2)} = 0.5$, $b_1^{(0)} = 0.5$, and $b_1^{(\pm 1)} = \sqrt{0.78}$.

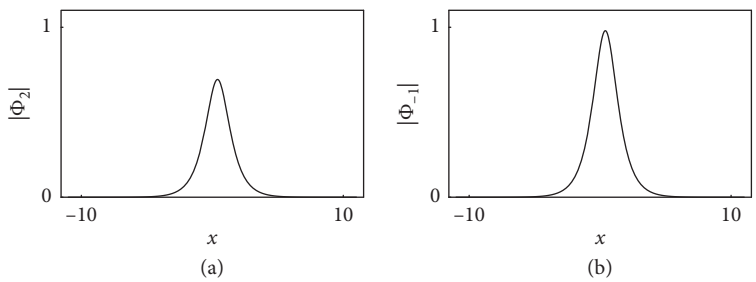

Figure 2: Intensity plots of the one soliton in the cyclic state for the components Φ_2 and Ψ_{-1} via solution (8). Parameters are $k_1 = 1.2 + i$, $b_1^{(2)} = 0.5 + 0.7i$, $b_1^{(-2)} = b_1^{(0)} = b_1^{(1)} = 0$, and $b_1^{(-1)} = \sqrt{2}\,(0.5 - 0.7i)$.

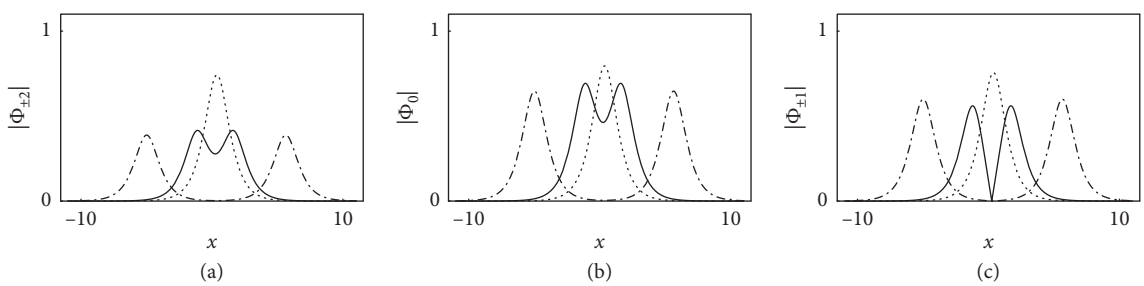

Figure 3: Intensity plots of the one soliton in the polar state for the components $\Phi_{\pm j}$ via Solutions (8). Parameters are $k_1 = 1.2 + i$ with (1) $b_1^{(2)} = b_1^{(-2)*} = 0.5 + 0.8i$, $b_1^{(0)} = 1.01$, and $b_1^{(1)} = -b_1^{(-1)*} = 0.75 + 0.6i$, short dashed lines; (2) $b_1^{(\pm 2)} = 0.6$, $b_1^{(0)} = 1$, and $b_1^{(\pm 1)} = \sqrt{0.75}$, solid lines; (3) $b_1^{(\pm 2)} = 0.6$, $b_1^{(0)} = 1$, and $b_1^{(\pm 1)} = \sqrt{0.85999}$, long dashed lines.

$$\begin{aligned} k_{1R} &> 0, \\ k_{1I} &> 0, \\ k_{2R} &> 0, \\ k_{2I} &< 0. \end{aligned} \tag{21}$$

Following the classification on the one-soliton solutions, we naturally consider the collisions between the same and different types of solitons, which are determined by Λ_m and f. Since the one-peak soliton in the cyclic state is obtained under certain strong restriction, its collisions with other types of soliton are omitted here.

4.1. Collisions between Two Solitons in the Ferromagnetic State. At first, we will consider the collision between two solitons in the ferromagnetic state. Under the condition $\Lambda_m = 0$, the asymptotic forms for equation (16) are given as follows:

(A) Before the collision ($t \longrightarrow -\infty$).

(1) SolitonS^{1-} ($\theta_{1R} \sim 0, \theta_{2R} \longrightarrow -\infty$):

$$\Phi_{\pm j} \longrightarrow A_{\pm j}^{1-} e^{i\theta_{1I}} \operatorname{sech}\left(\theta_{1R} + \frac{l_1}{2}\right). \tag{22}$$

(2) Soliton S^{2-} ($\theta_{2R} \sim 0, \theta_{1R} \longrightarrow \infty$):

$$\Phi_{\pm j} \longrightarrow A_{\pm j}^{2-} e^{i\theta_{2I}} \operatorname{sech}\left(\theta_{2R} + \frac{l_3 - l_1}{2}\right). \tag{23}$$

(B) After the collision ($t \longrightarrow +\infty$).

(1) SolitonS^{1+} ($\theta_{1R} \sim 0, \theta_{2R} \longrightarrow \infty$):

$$\Phi_{\pm j} \longrightarrow A_{\pm j}^{1+} e^{i\theta_{1I}} \operatorname{sech}\left(\theta_{1R} + \frac{l_3 - l_2}{2}\right). \tag{24}$$

(2) Soliton S^{2+} ($\theta_{2R} \sim 0, \theta_{1R} \longrightarrow -\infty$):

$$\Phi_{\pm j} \longrightarrow A_{\pm j}^{2+} e^{i\theta_{2I}} \operatorname{sech}\left(\theta_{2R} + \frac{l_2}{2}\right), \tag{25}$$

with

$$\begin{aligned} A_{\pm j}^{1-} &= \frac{b_1^{(\pm j)}}{2} e^{-(l_1/2)}, \\ A_{\pm j}^{2-} &= \frac{1}{2} e^{\left(\left(D_{12}^{(\pm j)} - l_2 - l_3\right)/2\right)}, \\ A_{\pm j}^{1+} &= \frac{1}{2} e^{\left(\left(D_{21}^{(\pm j)} - l_2 - l_3\right)/2\right)}, \\ A_{\pm j}^{2+} &= \frac{b_2^{(\pm j)}}{2} e^{-(l_2/2)}. \end{aligned} \tag{26}$$

The superscripts $m\pm$ ($m = 1, 2$) represent the solitons indicated as S_1 and S_2 at $t \longrightarrow \pm\infty$. Setting $b_1^{(\pm j)}/b_2^{(\pm j)} =$ constant, we find that the amplitudes $A_{\pm j}^{m\pm}$ before and after the collision can be related through $A_{\pm j}^{1+} = (A_{\pm j}^{1-}(k_1 - k_2)(k_1^* + k_2))/((k_1^* - k_2^*)(k_1 + k_2^*))$ and $A_{\pm j}^{2+} = (A_{\pm j}^{2-}(k_1^* - k_2^*)(k_1^* + k_2))/((k_1 - k_2)(k_1 + k_2^*))$, namely, $|A_{\pm j}^{m+}| = |A_{\pm j}^{m-}|$, which means that the collision is elastic in this case. Besides, the solitons S_1 and S_2, respectively, experience a phase shift of $\eta_1 = (l_3 - l_1 - l_2)/4k_{1R} = \ln[(k_1 - k_2)(k_1^* - k_2^*)/(k_1^* + k_2)(k_1 + k_2^*)]/k_{1R}$ and $\eta_2 = -\eta_1 k_{1R}/k_{2R}$ during the collision. For other choices of $b_m^{(\pm j)}$ satisfying $\Lambda_m = 0$, we will take an example and give Figure 4. The intensity of soliton S_2 in component Φ_0 decreases while those of S_2 in components $\Phi_{\pm 1}$ increase after the collision, as shown in Figures 4(b) and 4(c). This process might be of value for the realization of soliton switching devices [39]. The similar changes of soliton intensities can be observed for soliton S_1. For this case, the collision is similar to that with an intensity redistribution among all components of each soliton in the multicomponent NLS equation [40].

4.2. Collisions between Soliton in the Ferromagnetic State and Solitons in the Polar State. We will analyze the collisions between soliton in the ferromagnetic state and one- and two-peak solitons in the polar state. Here, we choose S_1 to be the soliton in the ferromagnetic state ($\Lambda_1 = 0$), and S_2 to be the soliton in the polar state corresponding to the condition $\Lambda_2 \neq 0$. The asymptotic forms of solitons S_1 and S_2 are given as follows:

(A) Before the collision.

(1) SolitonS^{1-}:

$$\Phi_{\pm j} \longrightarrow A_{\pm j}^{1-} e^{i\theta_{1I}} \operatorname{sech}\left(\theta_{1R} + \frac{l_1}{2}\right), \tag{27}$$

where $A_{\pm j}^{1-} = (1/2) b_1^{(\pm j)} e^{-(l_1/2)}$.

(2) Soliton S^{2-}:

$$\Phi_{\pm j} \longrightarrow A_{\pm j}^{2-} e^{i\theta_{2I}} \frac{\cosh\left(\theta_{2R}^- + P_{\pm j}^{2-}\right)}{4\cosh^2\left(\theta_{2R}^-\right) + L^{2-}}, \tag{28}$$

where $A_{\pm j}^{2-} = 2e^{(W_{21}^{(\pm j)} + D_{12}^{(\pm j)} - L_{21} - l_1)/2}$, $L^{2-} = e^{(l_3 - ((L_{21} + l_1)/2))} - 2$, $P_{\pm j}^{2-} = e^{(2W_{21}^{(\pm j)} - 2D_{12}^{(\pm j)} - L_{21} + l_1)/4}$, and $\theta_{2R}^- = \theta_{2R} + ((L_{21} - l_1)/4)$, with

$$\begin{aligned} k_2 &= k_{2R} + ik_{2I}, \\ \theta_{2I} &= k_{2I}x + \left(k_{2R}^2 - k_{2I}^2\right)t, \\ \theta_{2R} &= k_{2R}x - 2k_{2R}k_{2I}t. \end{aligned} \tag{29}$$

(B) After the collision.

(1) Soliton S^{1+}:

$$\Phi_{\pm j} \longrightarrow A_{\pm j}^{1+} e^{i\theta_{1I}} \operatorname{sech}\left(\theta_{1R} + \frac{L_{12} - c_{22}}{2}\right), \tag{30}$$

where $A_{\pm j}^{1+} = (1/2) e^{(2h_{12}^{(\pm j)} - L_{12} - c_{22})/2}$.

(2) Soliton S^{2+}:

$$\Phi_{\pm j} \longrightarrow A_{\pm j}^{2+} e^{i\theta_{2I}} \frac{\cosh\left(\theta_{2R}^+ + P_{\pm j}^{2+}\right)}{4\cosh^2\left(\theta_{2R}^+\right) + L^{2+}}, \tag{31}$$

where $A_{\pm j}^{2-} = 2e^{(d_2^{(\pm j)} + \ln b_2^{(\pm j)} - c_{22})/2}$, $L^{2-} = e^{(l_2 - c_{22})/2} - 2$, $P_{\pm j}^{2-} = e^{(2d_2^{(\pm j)} - 2\ln b_2^{(\pm j)} - c_{22})/4}$, and $\theta_{2R}^- = \theta_{2R} + (c_{22}/4)$. It is noted that equations (32) and (34) have the similar forms as equation (14). Choosing suitable parameters, we give Figure 5 illustrating the collision between one-peak solitons in the ferromagnetic and polar states. The solitons S_1 in the ferromagnetic state retain their shapes invariant after the collision, and only has a phase shift at the moment of collision in all components, due to the total spin conservation. However, the amplitudes of one-peak soliton S_2 in the polar state increase in components $\Phi_{\pm 2}$ after the collision, accompanied by the decrease of amplitude for S_2 in component Φ_0. For the case of collision between one-peak soliton in the ferromagnetic state and two-peak soliton in the polar state, the collision occurs without change of intensities for the solitons in the ferromagnetic state, while with an intensity redistribution among the two-peak solitons in the polar state in all components, as shown in Figure 6. Therefore, we can conclude that there exists no mixing collision in the internal states for the solitons in the ferromagnetic state outside the collision region.

4.3. Collisions between Two Solitons in the Polar State. In this section, we will consider the collisions between the solitons

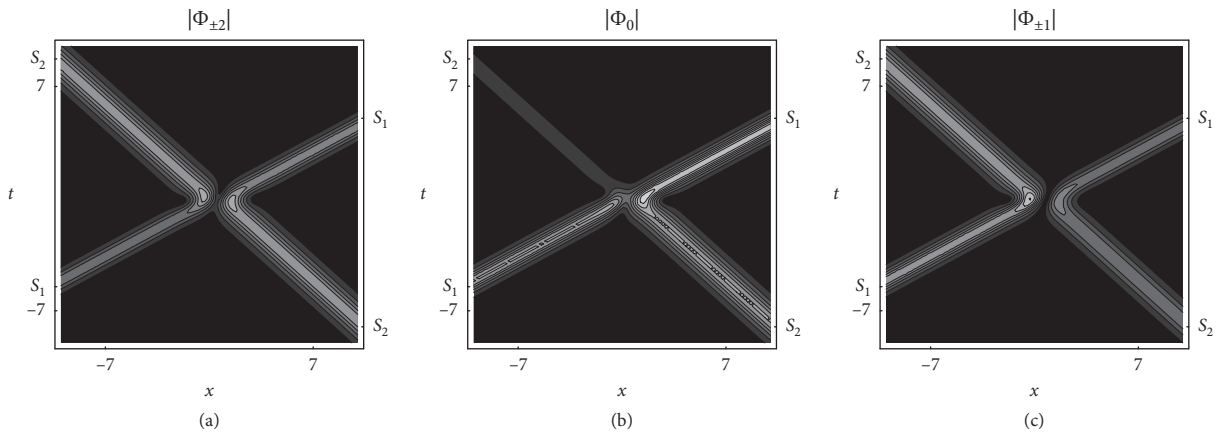

Figure 4: Collision between two solitons in the ferromagnetic state for the components $\Phi_{\pm j}$ via solution (16). Parameters are $k_1 = 1.2 + i$, $k_2 = 1.2 - 0.6i$, $b_1^{(\pm 2)} = 0.6$, $b_1^{(0)} = \sqrt{0.9}$, $b_1^{(\pm 1)} = 0.9$, $b_2^{(\pm 2)} = 1.1$, $b_2^{(0)} = \sqrt{0.08}$, and $b_2^{(\pm 1)} = \sqrt{1.25}$.

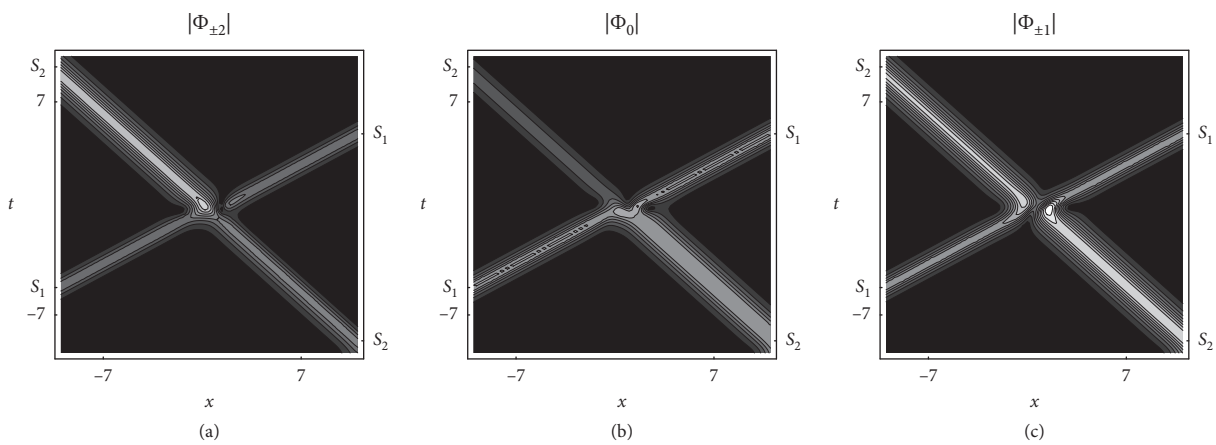

Figure 5: Collision between one-peak solitons in the ferromagnetic and polar states for the components $\Phi_{\pm j}$ via solution (16). Parameters are the same as those in Figure 4 except $b_2^{(2)} = b_2^{(-2)*} = 0.8 + 0.5i$, $b_2^{(0)} = 0.3$, and $b_2^{(1)} = -b_2^{(-1)*} = 0.4 - 0.9i$.

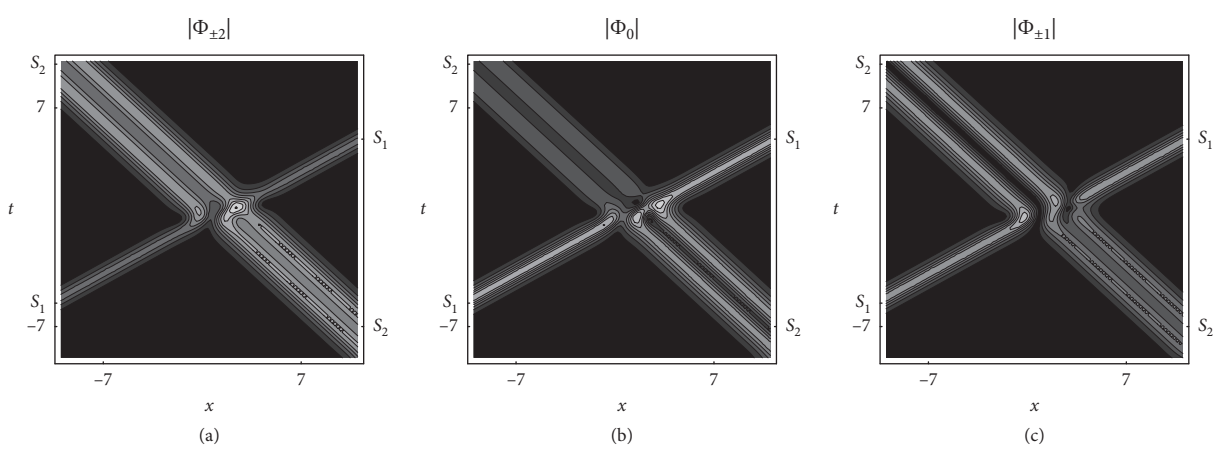

Figure 6: Collision between one-peak soliton in the ferromagnetic state and two-peak soliton in the polar state for the components $\Phi_{\pm j}$ via solutions (16). Parameters are $k_1 = 1.2 + i$, $k_2 = 1.2 - 0.6i$, $b_1^{(\pm 2)} = 0.5$, $b_1^{(0)} = 1$, $b_1^{(\pm 1)} = \sqrt{0.75}$, $b_2^{(\pm 2)} = 0.8$, $b_2^{(0)} = 0.4$, and $b_2^{(\pm 1)} = \sqrt{0.65}$.

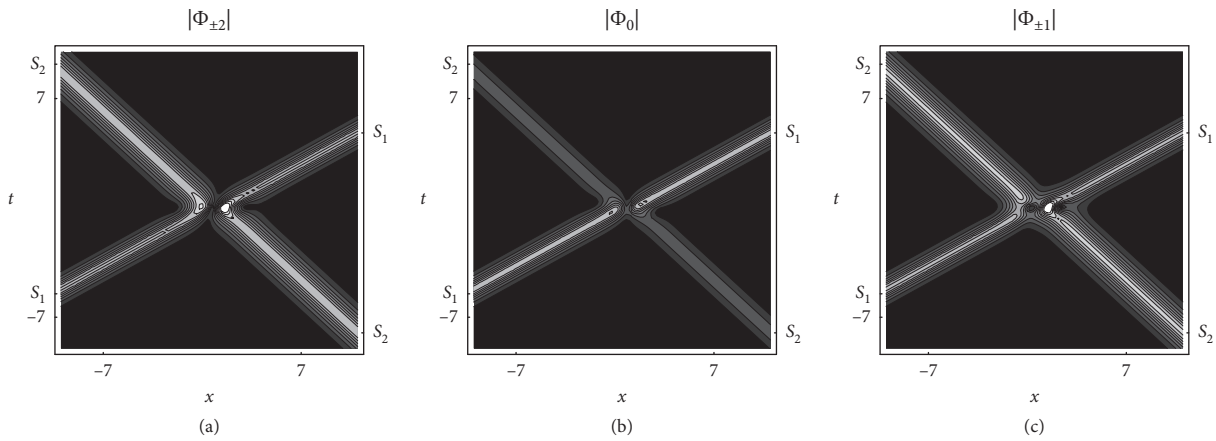

Figure 7: Collision between one-peak solitons in the polar state for the components $\Phi_{\pm j}$ via solution (16). Parameters are $k_1 = 1.2 + i$, $k_2 = 1.2 - 0.6i$, $b_1^{(2)} = b_1^{(-2)*} = 0.5 + 0.8i$, $b_1^{(0)} = 1.01$, $b_1^{(1)} = -b_1^{(-1)*} = 0.75 - 0.6i$, $b_2^{(2)} = b_2^{(-2)*} = 0.8 + 0.5i$, $b_2^{(0)} = 0.3$, and $b_2^{(1)} = -b_2^{(-1)*} = 0.4 - 0.9i$.

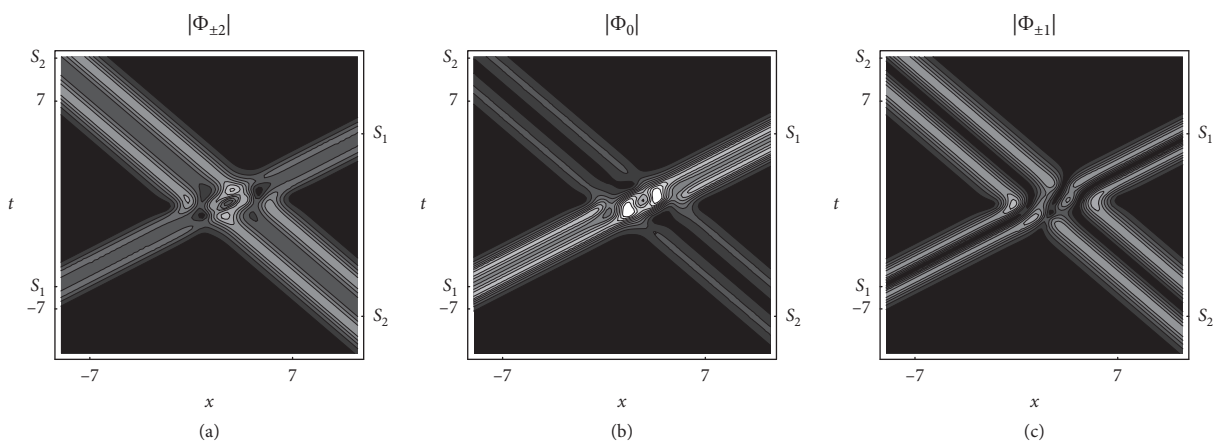

Figure 8: Collision between two-peak solitons in the polar state for the components $\Phi_{\pm j}$ via solution (16). Parameters are $k_1 = 1.2 + i$, $k_2 = 1.2 - 0.6i$, $b_1^{(\pm 2)} = 0.5$, $b_1^{(0)} = 1.1$, $b_1^{(\pm 1)} = \sqrt{0.75}$, $b_2^{(\pm 2)} = 0.8$, $b_2^{(0)} = 0.3$, and $b_2^{(\pm 1)} = \sqrt{0.66}$.

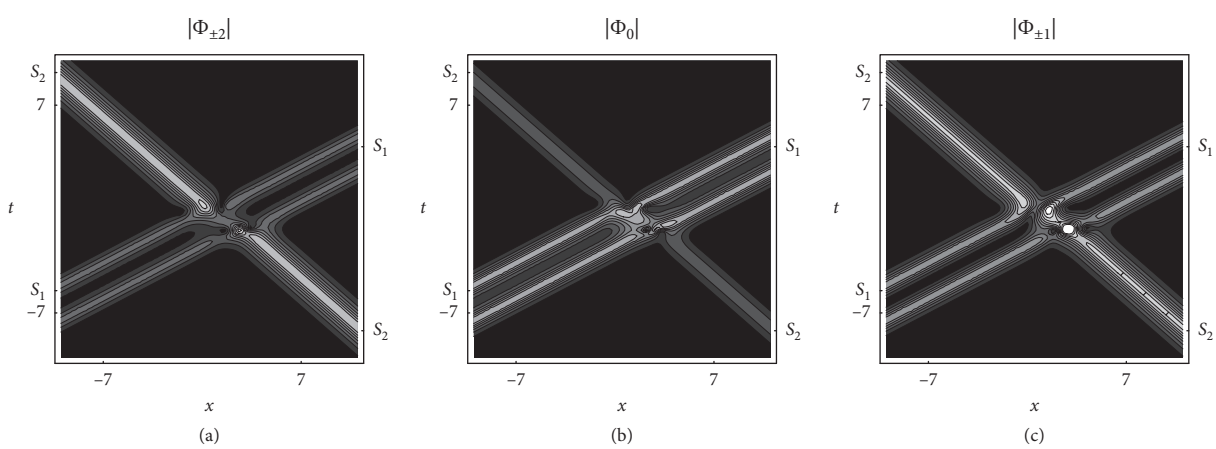

Figure 9: Collision between one- and two-peak solitons in the polar state for the components $\Phi_{\pm j}$ via solution (16). Parameters are the same as those in Figure 7 except $b_1^{(\pm 2)} = 0.5$, $b_1^{(0)} = 1.01$, and $b_1^{(\pm 1)} = \sqrt{0.75}$.

in the polar state ($\Lambda_m \neq 0$). In this case, the asymptotic forms are given as

(A) Before the collision.

(1) Soliton S^{1-}:

$$\Phi_{\pm j} \longrightarrow A_{\pm j}^{1-} e^{i\theta_{1I}} \frac{\cosh\left(\theta_{1R}^{-} + P_{\pm j}^{1-}\right)}{4\cosh^2\left(\theta_{1R}^{-}\right) + L^{1-}}, \tag{32}$$

where $A_{\pm j}^{1-} = 2e^{(d_1^{(\pm j)} + \ln b_1^{(\pm j)} - c_{11})/2}$, $L^{1-} = e^{(l_1 - (c_{11}/2))} - 2$, $P_{\pm j}^{1-} = e^{(2d_1^{(\pm j)} - 2\ln b_1^{(\pm j)} - c_{11})/4}$, and $\theta_{1R}^{-} = \theta_{1R} + (c_{11}/4)$.

(2) Soliton S^{2-}:

$$\Phi_{\pm j} \longrightarrow 2A_{\pm j}^{2-} e^{i\theta_{2I}} \frac{\cosh\left(\theta_{2R}^{-} + P_{\pm j}^{2-}\right)}{4\cosh^2\left(\theta_{2R}^{-}\right) + L^{2-}}, \tag{33}$$

where $A_{\pm j}^{2-} = 2e^{(W_{12}^{(\pm j)} + h_{12}^{(\pm j)} - l_5 - c_{11})/2}$, $L^{2-} = e^{(L_{12} - (l_5 + c_{11}/2))} - 2$, $P_{\pm j}^{2-} = e^{(2W_{12}^{(\pm j)} - 2h_{12}^{(\pm j)} - l_5 + c_{11})/4}$, and $\theta_{2R}^{-} = \theta_{2R} + ((l_5 - c_{11})/4)$.

(B) After the collision.

(1) Soliton S^{1+}:

$$\Phi_{\pm j} \longrightarrow 2A_{\pm j}^{1+} e^{i\theta_{1I}} \frac{\cosh\left(\theta_{1R}^{+} + P_{\pm j}^{1+}\right)}{4\cosh^2\left(\theta_{1R}^{+}\right) + L^{1+}}, \tag{34}$$

where $A_{\pm j}^{1+} = 2e^{(W_{21}^{(\pm j)} + h_{21}^{(\pm j)} - l_5 - c_{22})/2} = (((k_1 - k_2)(k_1^* + k_2))/((k_1^* - k_2^*)(k_1 + k_2^*)))A_{\pm j}^{1-}$, $L^{1+} = e^{L_{21} - ((l_5 + c_{22})/2)} - 2$, $\theta_{1R}^{+} = \theta_{1R} + ((l_5 - c_{22})/4)$, and $P_{\pm j}^{1+} = e^{(2W_{21}^{(\pm j)} - 2h_{21}^{(\pm j)} - l_5 + c_{22})/4}$.

(2) Soliton S^{2+}:

$$\Phi_{\pm j} \longrightarrow 2A_{\pm j}^{2+} e^{i\theta_{2I}} \frac{\cosh\left(\theta_{2R}^{+} + P_{\pm j}^{2+}\right)}{4\cosh^2\left(\theta_{2R}^{+}\right) + L^{2+}}, \tag{35}$$

where $A_{\pm j}^{2+} = 2e^{(d_2^{(\pm j)} + \ln b_2^{(\pm j)} - c_{22})/2} = (((k_1^* - k_2^*)(k_1^* + k_2))/(k_1 - k_2)(k_1 + k_2^*))A_{\pm j}^{2-}$, $L^{2+} = e^{(l_2 - (c_{22}/2))} - 2$, $P_{\pm j}^{2+} = e^{(2d_2^{(\pm j)} - 2\ln b_2^{(\pm j)} - c_{22})/4}$, and $\theta_{2R}^{+} = \theta_{2R} + (c_{22}/4)$. Figures 7–9, respectively, describe the collisions between two one-peak solitons, two two-peak solitons, and one-peak and two-peak solitons in the polar state. From equations (32)–(35), one can find that the collisions are elastic in this case. As shown in Figures 7–9, solitons with one or two peaks collide with each other and the intensity and shape of each soliton keeps invariant after the collision.

5. Conclusions

In this paper, we have investigated the solitons and their collisions for the five-component GP equations, i.e., equation (1), which can describe the dynamics of an $F = 2$ spinor BECs in one dimension. Through the Hirota method and symbolic computation, we have derived one-soliton solutions (8) and two-soliton solutions (16) for equation (1). With different polarization parameters and spin densities, one-soliton solutions (8) have been classified as (a) the one-peak soliton in the ferromagnetic and cyclic states (as seen in Figures 1 and 2); (b) one- and two-peak solitons in the polar state (as seen in Figure 3). For the two-peak soliton in the polar state, the distance between the two peaks increases inversely with the polarization parameter Λ_1 (as seen in Figure 3). Performing the asymptotic analysis on two-soliton solutions (16), we have analyzed the collisions between two solitons in the same and different states. For the collisions between two solitons in the ferromagnetic state, we have shown the constrained condition, under which the collision is elastic. In addition, we have given the example of the inelastic collision with intensity redistribution (as seen in Figure 4), and it is feasible to exploit the inelastic collision in the design of soliton switching architectures. For the collisions between soliton in the ferromagnetic state and solitons in the polar state, the solitons in the ferromagnetic state keep their characteristics invariant while the shapes and intensities change for those in the polar state after the collision (as seen in Figures 5 and 6). For the collisions between two solitons in the polar state, the procedure occurs only with a phase shift for each soliton at the moment of collision, and the collisions are inelastic (as seen in Figures 7–9). We hope that the results given in this paper will be of value for the applications in the atom laser and coherent atom transport, which can contribute to the realization of quantum information processors or computation.

Data Availability

The data used to support the findings of this study are available from the corresponding author upon request.

Conflicts of Interest

The authors declare that they have no conflicts of interest.

Acknowledgments

This work was supported by the National Natural Science Foundation of China under Grant nos. 11501526 and 11871232, Key Projects of Science and Technology Research of the Henan Education Department, (No. 17A110035), and Doctoral Research Fund of Zhengzhou University of Light Industry.

References

[1] K. E. Strecker, G. B. Partridge, A. G. Truscott, and R. G. Hulet, "Formation and propagation of matter-wave soliton trains," *Nature*, vol. 417, no. 6885, pp. 150–153, 2002.

[2] L. Khaykovich, F. Schreck, G. Ferrari et al., "Formation of a matter-wave bright soliton," *Science*, vol. 296, p. 1290, 2002.

[3] C. J. Pethick and H. Smith, *Bose-Einstein Condensation in Dilute Gases*, Cambridge University, Cambridge, UK, 2008.

[4] P. G. Kevrekidis, D. J. Frantzeskakis, and R. Carretero-González, *Emergent Nolinear Phenomena in Bose-Einstein Condensates: Theory and Experiment*, Springer, Berlin, Germany, 2008.

[5] B. Xiong and J. B. Gong, "Dynamical creation of complex vector solitons in spinor Bose-Einstein condensates," *Physical Review A*, vol. 81, p. 033618, 2010.

[6] E. V. Doktorov, V. M. Rothos, and Y. S. Kivshar, "Full-time dynamics of modulational instability in spinor Bose-Einstein condensates," *Physical Review A*, vol. 76, p. 013626, 2007.

[7] T.-L. Ho, "Spinor Bose condensates in optical traps," *Physical Review Letters*, vol. 81, no. 4, pp. 742–745, 1998.

[8] T. Ohmi and K. Machida, "Bose-Einstein condensation with internal degrees of freedom in alkali atom gases," *Journal of the Physical Society of Japan*, vol. 67, p. 1882, 1998.

[9] J. Stenger, S. Inouye, D. M. Stamper-Kurn, H.-J. Miesner, A. P. Chikkatur, and W. Ketterle, "Spin domains in ground-state Bose-Einstein condensates," *Nature*, vol. 396, no. 6709, pp. 345–348, 1998.

[10] M. Ueda and M. Koashi, "Theory of spin-2 Bose-Einstein condensates: spin correlations, magnetic response, and excitation spectra," *Physical Review A*, vol. 65, p. 063602, 2002.

[11] M.-S. Chang, C. D. Hamley, M. D. Barrett et al., "Observation of spinor dynamics in optically trapped Rb87 Bose-Einstein condensates," *Physical Review Letters*, vol. 92, p. 140403, 2004.

[12] H. Schmaljohann, M. Erhard, J. Kronjäger et al., "Dynamics of $F=2$ spinor Bose-Einstein condensates," *Physical Review Letters*, vol. 92, p. 040402, 2004.

[13] P. Rosenbusch, V. Bretin, and J. Dalibard, "Dynamics of a single vortex line in a Bose-Einstein condensate," *Physical Review Letters*, vol. 89, p. 200403, 2002.

[14] L. D. Carr and J. Brand, "Spontaneous soliton formation and modulational instability in Bose-Einstein condensates," *Physical Review Letters*, vol. 92, p. 040401, 2004.

[15] C. M. Jiang, A. Zada, T. Senel, and T. X. Li, "Synchronization of bidirectional N-coupled fractional-order chaotic systems with ring connection based on antisymmetric structure," *Advances in Difference Equations*, vol. 2019, 456, 2019.

[16] A. Yang, L. Li, Z. Wang, and R. Guo, "Tracking control of a class of chaotic systems," *Symmetry*, vol. 11, no. 4, p. 568, 2019.

[17] R. Gao, J. Xu, and H. Zhang, "Receding horizon control for multiplicative noise stochastic systems with input delay," *Automatica*, vol. 81, pp. 390–396, 2017.

[18] R. Gao, J. Xu, W. Li, and X. Liu, "A necessary and sufficient RHC stabilizability condition for stochastic control with delayed input," *Applied Mathematics and Computation*, vol. 360, pp. 122–130, 2019.

[19] R. Gao, X. Liu, and H. Zhang, "Receding horizon control for discrete-time multiple input delay systems," *Optimal Control Applications and Methods*, vol. 38, no. 6, pp. 1187–1192, 2017.

[20] A. Hasegawa and F. Tappert, "Transmission of stationary nonlinear optical pulses in dispersive dielectric fibers. I. Anomalous dispersion," *Applied Physics Letters*, vol. 23, no. 3, pp. 142–144, 1973.

[21] A. Hasegawa and M. Matsumoto, *Optical Solitons in Fibers*, Springer, Berlin, Germany, 2003.

[22] K. E. Lonngren, "Soliton experiments in plasmas," *Plasma Physics*, vol. 25, no. 9, pp. 943–982, 1983.

[23] L. Li, Z. Li, B. A. Malomed, D. Mihalache, and W. M. Liu, "Exact soliton solutions and nonlinear modulation instability in spinor Bose-Einstein condensates," *Physical Review A*, vol. 72, p. 033611, 2005.

[24] Z. D. Li, Q. Y. Li, L. Li, and W. M. Liu, "Soliton solution for the spin current in a ferromagnetic nanowire," *Physical Review E*, vol. 76, p. 026605, 2007.

[25] Z. D. Li, Q. Y. Li, T. F. Xu, and P. B. He, "Publisher's Note: breathers and rogue waves excited by all-magnonic spin-transfer torque [Phys. Rev. E 94, 042220 (2016)]," *Physical Review E*, vol. 94, p. 042220, 2016.

[26] P. Meystre, *Atom Optics*, Springer, Berlin, Germany, 2001.

[27] Z. D. Li, P. B. He, L. Li, J. Q. Liang, and W. M. Liu, "Magnetic soliton and soliton collisions of spinor Bose-Einstein condensates in an optical lattice," *Physical Review A*, vol. 71, p. 053611, 2005.

[28] T. F. Xu, W. L. Li, Z.-D. Li, and C. Zhang, "Phase diagram and dynamics of dark-bright vector solitons in spin-orbit-coupled Bose-Einstein condensate," *Chaos, Solitons & Fractals*, vol. 111, pp. 62–67, 2018.

[29] Z.-D. Li and Q.-Y. Li, "Dark soliton interaction of spinor Bose-Einstein condensates in an optical lattice," *Annals of Physics*, vol. 322, no. 8, pp. 1961–1971, 2007.

[30] Z.-D. Li, Q.-Y. Li, X.-H. Hu, Z.-X. Zheng, and Y. Sun, "Hirota method for the nonlinear Schrödinger equation with an arbitrary linear time-dependent potential," *Annals of Physics*, vol. 322, no. 11, pp. 2545–2553, 2007.

[31] M. Uchiyama, J. i. Ieda, and M. Wadati, "Multicomponent bright solitons in $F=2$ spinor bose-einstein condensates," *Journal of the Physical Society of Japan*, vol. 76, no. 7, p. 074005, 2007.

[32] V. S. Gerdjikov, N. A. Kostov, and T. I. Valchev, "Solutions of multi-component NLS models and Spinor Bose-Einstein condensates," *Physica D: Nonlinear Phenomena*, vol. 238, no. 15, pp. 1306–1310, 2009.

[33] C. V. Ciobanu, S.-K. Yip, and T.-L. Ho, "Phase diagrams of $F=2$ spinor Bose-Einstein condensates," *Physical Review A*, vol. 61, p. 033607, 2000.

[34] B. Tian, Y.-T. Gao, and H.-W. Zhu, "Variable-coefficient higher-order nonlinear Schrödinger model in optical fibers: variable-coefficient bilinear form, Bäcklund transformation, brightons and symbolic computation," *Physics Letters A*, vol. 366, no. 3, pp. 223–229, 2007.

[35] B. Tian and Y.-T. Gao, "Variable-coefficient higher-order nonlinear Schrödinger model in optical fibers: new transformation with burstons, brightons and symbolic computation," *Physics Letters A*, vol. 359, no. 3, pp. 241–248, 2006.

[36] R. Hirota, *The Direct Method in Soliton Theory*, Cambridge University, Cambridge, UK, 2004.

[37] R. Hirota, "Exact envelope–soliton solutions of a nonlinear wave equation," *Journal of Mathematical Physics*, vol. 14, no. 7, pp. 805–809, 1973.

[38] J. Ieda, T. Miyakawa, and M. Wadati, "Exact analysis of soliton dynamics in spinor Bose-Einstein condensates," *Physical Review Letters*, vol. 93, p. 194102, 2004.

[39] J. Babarro, M. J. Paz-Alonso, H. Michinel, J. R. Salgueiro, and D. N. Olivieri, "Controllable scattering of vector Bose-Einstein solitons," *Physical Review A*, vol. 71, p. 043608, 2005.

[40] H. Q. Zhang, X. H. Meng, T. Xu, L. L. Li, and B. Tian, "Integrability of an N-coupled nonlinear Schrödinger system for polarized optical waves in an isotropic medium via symbolic computation," *Physical Review E*, vol. 77, p. 026605, 2008.

Hindawi
Mathematical Problems in Engineering
Volume 2020, Article ID 2314356, 8 pages
https://doi.org/10.1155/2020/2314356

Research Article

Real-Time Hovering Control of Unmanned Aerial Vehicles

Cuauhtémoc Acosta Lúa,[1,2] **Claudia Carolina Vaca García**,[1] **Stefano Di Gennaro**,[2,3] **B. Castillo-Toledo**,[2,4] **and María Eugenia Sánchez Morales**[1]

[1]*Technological Sciences Department, La Cienega University Center, University of Guadalajara, Av. Universidad 1115, Ocotlán, Jalisco CP 47820, Mexico*
[2]*Center of Excellence DEWS (Design Methodologies of Embedded Controllers, Wireless Interconnect and Systems-on-chip), University of L'Aquila, Via Vetoio, Loc. Coppito, L'Aquila 67100, Italy*
[3]*Department of Information Engineering, Computer Science and Mathematics, University of L'Aquila, Via Vetoio, Loc. Coppito, L'Aquila 67100, Italy*
[4]*Center for Research and Advanced Studies, Campus Guadalajara, Av. del Bosque 1145 Col. El Bajío, Zapopan CP 45019, Mexico*

Correspondence should be addressed to Cuauhtémoc Acosta Lúa; cuauhtemoc.acosta@cuci.udg.mx

Received 24 April 2020; Accepted 4 June 2020; Published 27 July 2020

Guest Editor: Yi Qi

In this paper, the design of a controller for the altitude and rotational dynamics is presented. In particular, the control problem is to maintain a desired altitude in a fixed position. The unmanned aerial vehicle dynamics are described by nonlinear equations, derived using the Newton–Euler approach. The control problem is solved imposing the stability of the error dynamics with respect to desired position and angular references. The performance and effectiveness of the proposed control are tested, first, via numerical simulations, using the Pixhawk Pilot Support Package simulator provided by Mathworks. Then, the controller is tested via a real-time implementation, using a quadrotor Aircraft F-450.

1. Introduction

Quadrotors have recently attracted the attention of many researchers due to their interesting applications. As a matter of fact, the potential applications of such devices are countless. Examples of such applications include searching and surveillance, monitoring, and rescuing tasks. From a methodological point of view, the interest relies on the fact that a quadrotor is a complex underactuated system with high nonlinearities and strong dynamical couplings. Furthermore, it is affected by aerodynamic disturbances, unmodeled dynamics, and parametric uncertainties. Therefore, the quadrotors represent an interesting testbed for testing new control techniques.

There are a large number of works dealing with quadrotors. As far as the mathematical model is concerned, in Bouabdallah et al. [1], Zeng and Zhao [2], and Nagaty et al. [3], a Newton–Euler model was presented. Furthermore, Magnussen et al. [4] and Valenti et al. [5] considered quaternions to describe the angular kinematics, whilst Antonio-Toledo et al. [6] applied the Euler–Lagrange equations to obtain the whole quadrotor mathematical model. Regarding the control of quadrotors, many control techniques have been proposed. In Panomruttanarug et al. [7] and Pounds et al. [8], the linear quadratic regulator control and the proportional integral derivative control, respectively, were exploited to design a control law. However, these controllers ensure only local stability. In order to enlarge the basin of attraction, nonlinear control techniques have also been considered. Examples are sliding model control Luque–Vega et al. [9], backstepping Bouabdallah and Siegwart [10], and adaptive control Matouk et al. [11]. Moreover, a global fast dynamic terminal sliding mode control method was proposed for position and attitude tracking control in Xiong and Zhang [12]. An adaptive command filtered backstepping control law was designed for trajectory tracking in Choi and Ahn [13]. In Liu et al. [14], a robust adaptive attitude tracking control for a quadrotor with an unknown inertia matrix and bounded external disturbances was proposed. A command filtered

implementation of an adaptive backstepping was proposed in Dong et al. [15], and the stability of the closed loop system was proved via the Lyapunov direct method. Finally, in Islam et al. [16], an observer-based adaptive fuzzy backstepping controller was designed for trajectory tracking, in the case of a quadrotor undergoing wind gusts and with parametric uncertainties. All these aforementioned methods provide good dynamic performance and robust stability and are tested mainly considering numerical simulations.

The main contribution of this paper is the design of a controller for the attitude and altitude of a quadrotor helicopter. This controller has been designed using the backstepping technique and has been tested using numerical simulations and real-time experimentation. In particular, the focus of this paper is to obtain a controller ensuring hovering so that

(1) The reference attitude is zero for the Euler angles describing the quadrotor angular position

(2) The reference altitude is a constant value

The performance and effectiveness of the proposed controller has been first tested with numerical simulations using the Pixhawk Pilot Support Package (PSP). Then, the real-time implementation has been performed implementing the proposed controller on a real F-450 quadrotor equipped of a Pixhawk and tested under environmental perturbations.

The paper is organized as follows. Section 2 introduces the description and the mathematical model of the quadrotor. In Section 3, the control problem is solved. In Section 4, numerical simulations and real-time tests are provided to show the effectiveness of the proposed controller. Finally, some concluding remarks are commented in Section 5.

2. Mathematical Model

The quadrotor considered in this work consists of a rigid frame equipped with four rotors. The rotors generate the propeller force $F_i = b\omega_{p,i}^2$, proportional to the propeller angular velocity $\omega_{p,i}$, $i = 1, 2, 3, 4$. The propellers 1 and 3 rotate counterclockwise, and the propellers 2 and 4 rotate clockwise.

Denote $\mathrm{RC}(O, e_1, e_2, e_3)$ and $\mathrm{R\Gamma}(\Omega, \varepsilon_1, \varepsilon_2, \varepsilon_3)$ as the frames fixed with the Earth and the quadrotor, respectively, with Ω coincident with the center of mass of the quadrotor (see Figure 1). The quadrotor absolute position in RC is described by $p = (x, y, z)^T$, whereas its attitude is described by the Euler angles $\alpha = (\phi, \theta, \psi)^T$, where $\phi, \theta, \psi \in (-\pi/2n, q\pi h/2)$ are the pitch, roll, and yaw angles, respectively. The sequence 3–2–1 has been considered by Huges [17]. Moreover, $v = (v_1, v_2, v_3)^T$ and $\omega = (\omega_1, \omega_2, \omega_3)^T$ are the linear and angular velocities of the center of mass of the quadrotor, expressed in RC and in RΓ, respectively.

The translation dynamics (in RC) and rotation dynamics (in the RΓ) of the quadrotor are

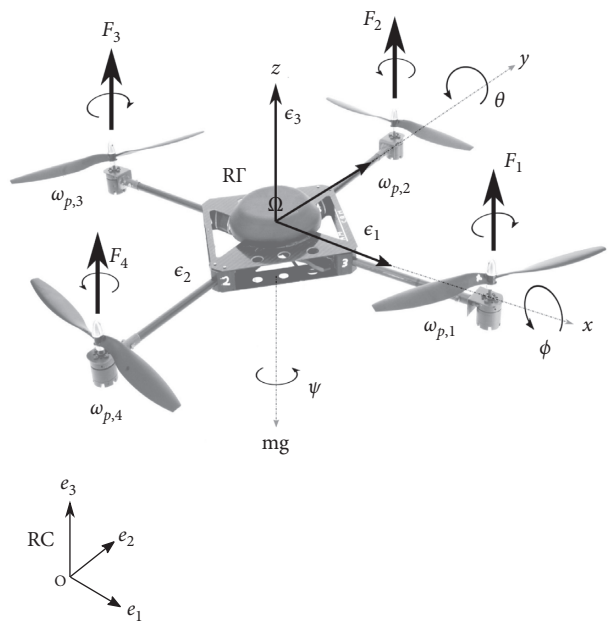

Figure 1: Quadrotor orientation using Euler angles.

$$\begin{aligned}
\dot{p} &= v,\\
\dot{v} &= \frac{1}{m}\mathscr{R}(\alpha)F_{\text{prop}} + \frac{1}{m}F_{\text{grav}} + \frac{1}{m}F_d,\\
\dot{\alpha} &= M(\alpha)\omega,\\
\dot{\omega} &= J^{-1}\left(-\tilde{\omega}J\omega + \tau_{\text{prop}} - \tau_{\text{gyro}} + M_d\right),
\end{aligned} \tag{1}$$

where m is the mass of the quadrotor, J is the inertia matrix of the quadrotor, and $J = \operatorname{diag}\{J_x, J_y, J_z\}$ (expressed in RΓ), and

$$\tilde{\omega} = \begin{pmatrix} 0 & -\omega_3 & \omega_2 \\ \omega_3 & 0 & -\omega_1 \\ -\omega_2 & \omega_1 & 0 \end{pmatrix}, \tag{2}$$

is the so-called dyadic representation of ω,

$$\begin{aligned}
F_{\text{prop}} &= \begin{pmatrix} 0 \\ 0 \\ \sum_{i=1}^{4} F_i \end{pmatrix},\\
\tau_{\text{prop}} &= \begin{pmatrix} \tau_1 \\ \tau_2 \\ \tau_3 \end{pmatrix} = \begin{pmatrix} l(F_2 - F_4) \\ l(F_3 - F_1) \\ c(F_1 - F_2 + F_3 - F_4) \end{pmatrix},
\end{aligned} \tag{3}$$

are the forces and moments produced by the propellers (inputs), with l as the distance between the center of mass to the rotor shaft. Moreover, $F_{\text{grav}} = \begin{pmatrix} 0 & 0 & -\text{mg} \end{pmatrix}^T$ is the force due to the gravity expressed in RC.

The vectors expressed in RΓ are transformed into vectors in RC by the rotation matrix:

$$\mathscr{R}(\alpha)=\begin{pmatrix} c_\theta c_\psi & s_\phi s_\theta c_\psi - c_\phi s_\psi & c_\phi s_\theta c_\psi + s_\phi s_\psi \\ c_\theta s_\psi & s_\phi s_\theta s_\psi + c_\phi c_\psi & c_\phi s_\theta s_\psi - s_\phi c_\psi \\ -s_\theta & s_\phi c_\theta & c_\phi c_\theta \end{pmatrix}, \tag{4}$$

with $c_\gamma = \cos(\gamma)$, $s_\gamma = \sin(\gamma)$, and $\gamma = \phi, \theta, \psi$. The angular velocity dynamics are expressed using the matrix:

$$M(\alpha)=\begin{pmatrix} 1 & s_\phi tg_\theta & c_\phi tg_\theta \\ 0 & c_\phi & -s_\phi \\ 0 & s_\phi sc_\theta & c_\phi sc_\theta \end{pmatrix}, \tag{5}$$

with $tg_\gamma = \tan(\gamma)$ and $sc_\gamma = \sec(\gamma)$.

The rolling torque τ_1 is produced by the forces F_2 and F_4. Similarly, the pitching torque τ_2 is produced by the forces F_1 and F_3. Due to Newton's third law, the propellers produce a yawing torque τ_3 on the body of the quadrotor, in the opposite direction of the propeller rotation. Moreover,

$$\tau_{\text{gyro}} = \sum_{i=1}^{4} (-1)^{i+1} J_p \omega_p \tilde{\omega} \varepsilon_3, \tag{6}$$

is the gyroscopic torque due to the propeller rotations, with J_p the propeller moment of inertia with respect to its rotation axis. Finally, F_d and M_d are the forces and torques due to the external disturbances, which are assumed negligible here.

Under the assumption of small angles, matrix $M(\alpha)$ reduces to the identity matrix. This assumption is justified by the fact that the control objective is to maintain the quadrotor in an hover position Nagaty et al. [3]. This leads to a simplified mathematical model of the quadrotor given by

$$\begin{aligned} \ddot{x} &= \frac{1}{m}\left(c_\phi s_\theta c_\psi + s_\phi s_\psi\right)u_1, \\ \ddot{y} &= \frac{1}{m}\left(c_\phi s_\theta s_\psi - s_\phi c_\psi\right)u_1, \\ \ddot{z} &= \frac{1}{m} c_\phi c_\theta u_1 - g, \\ \ddot{\phi} &= \frac{J_y - J_z}{J_x}\dot{\theta}\dot{\psi} - \frac{J_p}{J_x}\omega_p \dot{\theta} + \frac{l}{J_x}\tau_1, \\ \ddot{\theta} &= \frac{J_z - J_x}{J_y}\dot{\phi}\dot{\psi} + \frac{J_p}{J_y}\omega_p \dot{\phi} + \frac{l}{J_y}\tau_2, \\ \ddot{\psi} &= \frac{J_x - J_y}{J_z}\dot{\phi}\dot{\theta} + \frac{1}{J_z}\tau_3, \end{aligned} \tag{7}$$

where the control variables are defined as

$$\begin{aligned} u_1 &= \sum_{i=1}^{4} F_i, \\ \tau_1 &= l\left(F_2 - F_4\right), \\ \tau_2 &= l\left(F_3 - F_1\right), \\ \tau_3 &= c\left(F_1 + F_3 - F_2 - F_4\right), \end{aligned} \tag{8}$$

where l is the distance of the center of mass to the rotor shaft, c is the drag factor, and $\omega_p = \omega_{p,1} - \omega_{p,2} + \omega_{p,3} - \omega_{p,4}$ is the so-called rotor relative speed. The parameters used in (7) and their values are defined in Table 1.

3. Control Design

3.1. Attitude Control. To design the attitude control law, let us define the following variables:

$$\begin{aligned} \phi &= \phi_1, \\ \theta &= \theta_1, \\ \psi &= \psi_1, \\ \dot{\phi} &= \phi_2, \\ \dot{\theta} &= \theta_2, \\ \dot{\psi} &= \psi_2, \end{aligned} \tag{9}$$

so that system (7) can be rewritten as

$$\begin{aligned} \dot{\phi}_1 &= \phi_2, \\ \dot{\phi}_2 &= \frac{J_y - J_z}{J_x}\theta_2\psi_2 - \frac{J_p}{J_x}\omega_p\theta_2 + \frac{l}{J_x}\tau_1, \\ \dot{\theta}_1 &= \theta_2, \\ \dot{\theta}_2 &= \frac{J_z - J_x}{J_y}\phi_2\psi_2 + \frac{J_p}{J_y}\omega_p\phi_2 + \frac{l}{J_y}\tau_2, \\ \dot{\psi}_1 &= \psi_2, \\ \dot{\psi}_2 &= \frac{J_x - J_y}{J_z}\phi_2\theta_2 + \frac{1}{J_z}\tau_3, \end{aligned} \tag{10}$$

where $X = (\phi_1, \phi_2, \theta_1, \theta_2, \psi_1, \psi_2)$ are the measured signals. The control objective is to match the UAV attitude X to a desired reference:

$$X_{\text{ref}} = \left(\phi_{1,\text{ref}}, \phi_{2,\text{ref}}, \theta_{1,\text{ref}}, \theta_{2,\text{ref}}, \psi_{1,\text{ref}}, \psi_{2,\text{ref}}\right). \tag{11}$$

To this aim, let us define the tracking errors as

$$\begin{aligned} e_{\phi,1} &= \phi_1 - \phi_{1,\text{ref}}, \\ e_{\phi,2} &= \phi_2 - \phi_{2,\text{ref}} + k_1 e_{\phi,1}, \\ e_{\theta,1} &= \theta_1 - \theta_{1,\text{ref}}, \\ e_{\theta,2} &= \theta_2 - \theta_{2,\text{ref}} + k_3 e_{\theta,1}, \\ e_{\psi,1} &= \psi_1 - \psi_{1,\text{ref}}, \\ e_{\psi,2} &= \psi_2 - \psi_{2,\text{ref}} + k_5 e_{\psi,1}, \end{aligned} \tag{12}$$

with $k_1, k_3, k_5 > 0$. Note that $e_{j,1} = 0$ implies $e_{j,2} = 0$, $j = \phi, \theta, \psi$. Deriving the error system (12) with respect to (10) is possible to calculate the error dynamics:

Table 1: Quadrotor parameters.

m	Mass of the airframe	1.1 kg
l	Distance of the center of mass to the rotor shaft	0.223 m
J_x	Inertia in the x-axis	6.825×10^{-3} kg m^2
J_y	Inertia in the y-axis	6.825×10^{-3} kg m^2
J_z	Inertia in the z-axis	12.39×10^{-3} kg m^2
J_p	Inertia of the propellers	6×10^{-5} kg m^2
g	Gravity acceleration	9.81 m/s^2
b	Thrust factor	54.2×10^{-6}
c	Drag factor	1.1×10^{-6} N s^2 rad^{-2}
ϕ	Roll angle	deg
θ	Pitch angle	deg
ψ	Yaw angle	deg
z_1	z-position	m

$$\begin{aligned}
\dot{e}_{\phi,1} &= e_{\phi,2} - k_1 e_{\phi,1} - \dot{\phi}_{1,\mathrm{ref}} + \phi_{2,\mathrm{ref}},\\
\dot{e}_{\phi,2} &= \frac{J_y - J_z}{J_x}\theta_2\psi_2 - \frac{J_p}{J_x}\omega_p\theta_2 + \frac{l}{J_x}\tau_1,\\
&\quad - \dot{\phi}_{2,\mathrm{ref}} + k_1\left(e_{\phi,2} - k_1 e_{\phi,1} + \phi_{2,\mathrm{ref}} - \dot{\phi}_{1,\mathrm{ref}}\right),\\
\dot{e}_{\theta,1} &= e_{\theta,2} - k_3 e_{\theta,1} - \dot{\theta}_{1,\mathrm{ref}} + \theta_{2,\mathrm{ref}} = e_{\theta,2} - k_3 e_{\theta,1}\\
&\quad - \dot{\theta}_{1,\mathrm{ref}} + \theta_{2,\mathrm{ref}},\\
\dot{e}_{\theta,2} &= \frac{J_z - J_x}{J_y}\phi_2\psi_2 + \frac{J_p}{J_y}\omega_p\phi_2 + \frac{l}{J_y}\tau_2,\\
&\quad - \dot{\theta}_{2,\mathrm{ref}} + k_3\left(e_{\theta,2} - k_3 e_{\theta,1} + \theta_{2,\mathrm{ref}} - \dot{\theta}_{1,\mathrm{ref}}\right),\\
\dot{e}_{\psi,1} &= e_{\psi,2} - k_5 e_{\psi,2} - \dot{\psi}_{1,\mathrm{ref}} + \psi_{2,\mathrm{ref}},\\
\dot{e}_{\psi,2} &= \frac{J_x - J_y}{J_z}\phi_2\theta_2 + \frac{1}{J_z}\tau_3 - \dot{\psi}_{2,\mathrm{ref}}\\
&\quad + k_5\left(e_{\psi,2} - k_5 e_{\psi,1} + \psi_{2,\mathrm{ref}} - \dot{\psi}_{1,\mathrm{ref}}\right).
\end{aligned} \tag{13}$$

Using the following control law [18],

$$\begin{aligned}
\tau_1 &= \frac{J_x}{l}\left(-\frac{J_y - J_z}{J_x}\theta_2\psi_2 + \frac{J_p}{J_x}\omega_p\theta_2 + \dot{\phi}_{2,\mathrm{ref}} - k_1\left(e_{\phi,2} - k_1 e_{\phi,1}\right.\right.\\
&\quad \left.\left. + \phi_{2,\mathrm{ref}} - \dot{\phi}_{1,\mathrm{ref}}\right) - k_2 e_{\phi,2}\right),\\
\tau_2 &= \frac{J_y}{l}\left(-\frac{J_z - J_x}{J_y}\phi_2\psi_2 - \frac{J_p}{J_y}\omega_p\phi_2 + \dot{\theta}_{2,\mathrm{ref}} - k_3\left(e_{\theta,2} - k_3 e_{\theta,1}\right.\right.\\
&\quad \left.\left. + \theta_{2,\mathrm{ref}} - \dot{\theta}_{1,\mathrm{ref}}\right) - k_4 e_{\theta,2}\right),\\
\tau_3 &= J_z\left(-\frac{J_x - J_y}{J_z}\phi_2\theta_2 + \dot{\psi}_{2,\mathrm{ref}} - k_5\left(e_{\psi,2} - k_5 e_{\psi,1} + \psi_{2,\mathrm{ref}}\right.\right.\\
&\quad \left.\left. - \dot{\psi}_{1,\mathrm{ref}}\right) - k_6 e_{\psi,2}\right),
\end{aligned} \tag{14}$$

with gains $k_i > 0$, $i = 2, 4, 6$ in (13), the tracking error dynamics become

$$\begin{aligned}
\dot{e}_X &= \begin{pmatrix} \dot{e}_{\phi,1}\\ \dot{e}_{\phi,2}\\ \dot{e}_{\theta,1}\\ \dot{e}_{\theta,2}\\ \dot{e}_{\psi,1}\\ \dot{e}_{\psi,2}\end{pmatrix} = \begin{pmatrix} -k_1 & 1 & 0 & 0 & 0 & 0\\ 0 & -k_2 & 0 & 0 & 0 & 0\\ 0 & 0 & -k_3 & 1 & 0 & 0\\ 0 & 0 & 0 & -k_4 & 0 & 0\\ 0 & 0 & 0 & 0 & -k_5 & 1\\ 0 & 0 & 0 & 0 & 0 & -k_6\end{pmatrix}\begin{pmatrix} e_{\phi_1}\\ e_{\phi_2}\\ e_{\theta_1}\\ e_{\theta_2}\\ e_{\psi_1}\\ e_{\psi_2}\end{pmatrix}\\
&= A_X e_X,
\end{aligned} \tag{15}$$

where $e_X = \left(e_{\phi_1}\ e_{\phi_2}\ e_{\theta_1}\ e_{\theta_2}\ e_{\psi_1}\ e_{\psi_2}\right)^T$, which converge exponentially to zero. In fact, considering the Lyapunov candidate

$$V_X(t, e_X) = \frac{1}{2}e_X^T P_X e_X, \tag{16}$$

and differentiating along the error dynamics (15), one obtains

$$\begin{aligned}
\dot{V}_X(t, e_X) &= e_X^T\left(A_X^T P_X + P_X A_X\right)e_X = -e_X^T Q_X e_X\\
&\le -\lambda_{\min}^{Q_X}\|e_X\|^2 \le -\alpha V_X(t, e_X), \quad \alpha = \frac{2\lambda_{\min}^{Q_X}}{\lambda_{\min}^{Q_X}} > 0,
\end{aligned} \tag{17}$$

with P_X solution of the equation $A_X^T P_X + P_X A_X = -Q_X$ for a fixed matrix $Q_X = Q_X^T > 0$. Therefore,

$$V_X(t, e_X) \le e^{-\alpha t} V(0, e_X(0)), \tag{18}$$

so that the tracking error converges globally exponentially to zero [19].

3.2. Altitude Control. For the altitude control, let us consider the altitude dynamics:

$$\begin{aligned}
\dot{z}_1 &= z_2,\\
\dot{z}_2 &= g + c_{\phi_1}c_{\theta_1}\frac{1}{m}u_1.
\end{aligned} \tag{19}$$

The control problem is to maintain the quadrotor at a desired constant altitude $z_{1,\mathrm{ref}}$, $z_{2,\mathrm{ref}} = 0$. The tracking errors are defined as

$$e_{z,1} = z_1 - z_{1,\text{ref}},$$
$$e_{z,2} = z_2 - z_{2,\text{ref}}. \tag{20}$$

Choosing

$$u_1 = \frac{m}{c_{\phi_1} c_{\theta_1}} \left(g + \dot{z}_{2,\text{ref}} - k_{z,1} e_{z,1} - k_{z,2} e_{z,2} \right), \tag{21}$$

with $k_{z,1}, k_{z,2} > 0$, we obtain

$$\dot{e}_z = A_z e_z, \tag{22}$$

where $e_z = (e_{z,1}, e_{z.2})^T$ and

$$A_z = \begin{pmatrix} 0 & 1 \\ -k_{z,1} & -k_{z,2} \end{pmatrix}. \tag{23}$$

The stability proof is similar to that of the previous section.

4. Simulation and Experimental Results

In this section, the performance of the attitude and altitude controllers (14) and (21) is tested considering an F-450 quadrotor. First, numerical simulations are carried out. Then, real-time experimental tests are performed, showing the effectiveness of the control design.

4.1. Simulation Results. For the numerical simulations, the quadrotor model provided by the Pixhawk PSP, in Simulink, has been used. This model contains the attitude and altitude flight control model called px4 demo attitude control, which shows a good performance in predicting the dynamic quadrotor behavior, very close to the real drone dynamics.

Controllers (14) and (21) use the nominal values of Table 1 and the gains of Table 2. The simulations have been performed in two steps. In the first one, the quadrotor is stabilized in altitude. In Figure 2, the altitude z is shown. In the second step, the quadrotor is stabilized in attitude. The pitch, roll, and yaw angles are shown in Figure 3. The initial conditions considered are $z(0) = 0$, $\phi(0) = -5.73^\circ$, $\theta(0) = 5.73^\circ$, and $\psi(0) = 5.73^\circ$. The reference values are $z_{\text{ref}} = 2$ m and $\phi_{\text{ref}} = \theta_{\text{ref}} = \psi_{\text{ref}} = 0$.

4.2. Experimental Results. In this section, we describe the physical setting of the embedded control that allows stabilizing the quadrotor. An embedded control system generally consists of three elements: sensors, actuators, and a microcontroller. The microcontroller interacts with the continuous dynamics of the plant via the sensors and actuators, and its major function is to compute and generate control commands for the actuators that are based on sensor measurements. The onboard electronic system consists of a flight controller, a hardware setup, and some ultrasonic sensors.

4.2.1. Flight Controller. The 3DR-PIXHAWK is a high-performance autopilot-on-module suitable for fixed wing, multi rotors, helicopters, cars, boats, and other mobile robotic platforms. Its processor can run to 168 MHz/252 MIPS Cortex-M4F with 256 KB in RAM and 2 MB flash and has 14 PWM/Servo outputs and abundant connectivity options for additional peripherals, such as 5x UART (serial ports), one high-power capable, 2x with HW flow control, 2x CAN, Spektrum DSM/DSM2/DSM–X® Satellite compatible input, PPM sum signal input, RSSI (PWM or voltage) input, I2C, SPI, 3.3 and 6.6 V ADC input. Moreover, the 3DR-Pixhawk has different sensors, such as ST Micro L3GD20H 16 bit gyroscopes, ST Micro LSM303D 14 bit accelerometers/magnetometers, Invensense MPU 6000 3-axis accelerometers/gyroscopes, and MEAS MS5611 barometers.

Table 2: Gain values.

$k_{p,1} = 46$	$k_{d,1} = 35$	$k_{i,1} = 28$
$k_{p,2} = 4.3$	$k_{d,2} = 9$	$k_{i,2} = 0.2$
$k_{p,3} = 4.5$	$k_{d,3} = 7$	$k_{i,3} = 0.2$
$k_{p,4} = 7$	$k_{d,4} = 19$	$k_{i,4} = 0.1$

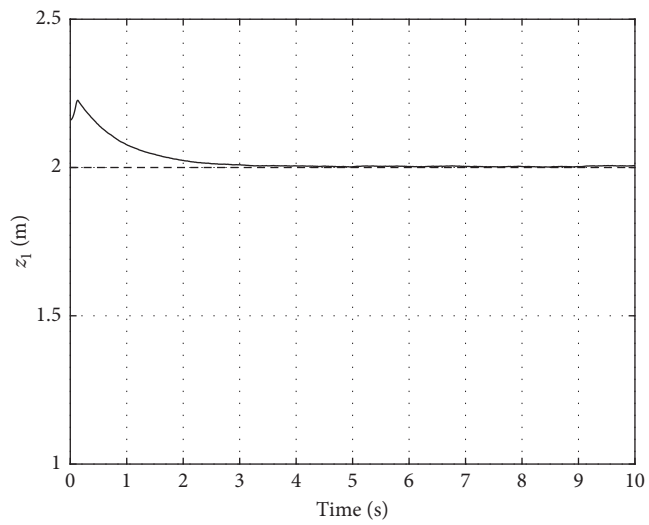

Figure 2: Numerical simulation: quadrotor's altitude z_1 (solid) and altitude reference $z_{1,\text{ref}}$ (dash).

4.2.2. Hardware Setup. The structure of the quadrotor is composed by an F-450 frame with integrated PCB wiring, whereas the rotors are brushless motors manufactured by E–max, with 935 rpm/V and a $10 \times 4.5''$ propellers. Turnigy speed drivers (ESC) are BHC type at 18 A max. The battery used in this setup is a 3S, 2800 mAh, 25C. The radio-transmitter is a Turnigy with 9 PPM channels working at 2.4 GHz.

An LV-MaxSonar-EZ4 sensor with a resolution of 2.54 cm, 20 Hz reading rate, 42 kHz ultrasonic sensor measures, a maximum Range of 645 cm, operating in the range of 2.5–5.5 VDC was used to measure the altitude.

For the real-time running, the same parameter values and gains shown in Table 2 were used. The initial condition for the altitude was $z(0) = 2.16$ m. For the pitch, roll, and yaw angles, the initial condition were chosen at $\phi_1(0) = 1.6^\circ$, $\theta_1(0) = 0.9^\circ$, and $\psi_1(0) = -1.6^\circ$. Figures 4 and 5 show the dynamic behavior of the altitude and the pitch, roll, and yaw angles, respectively. It is worth noticing that these

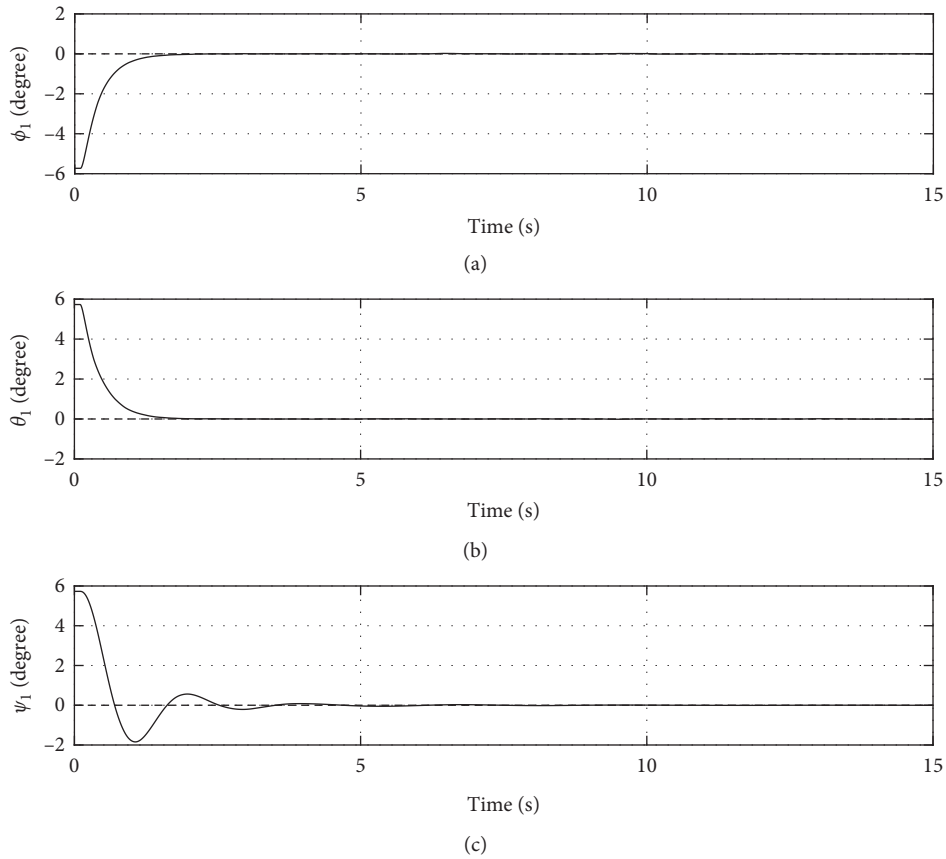

Figure 3: Numerical simulation: (a) roll angle ϕ_1 (solid) and roll angle reference $\phi_{1,\mathrm{ref}}$ (dash); (b) pitch angle θ_1 (solid) and pitch angle reference $\theta_{1,\mathrm{ref}}$ (dash); (c) yaw angle ψ_1 (solid) and yaw angle reference $\psi_{1,\mathrm{ref}}$ (dash).

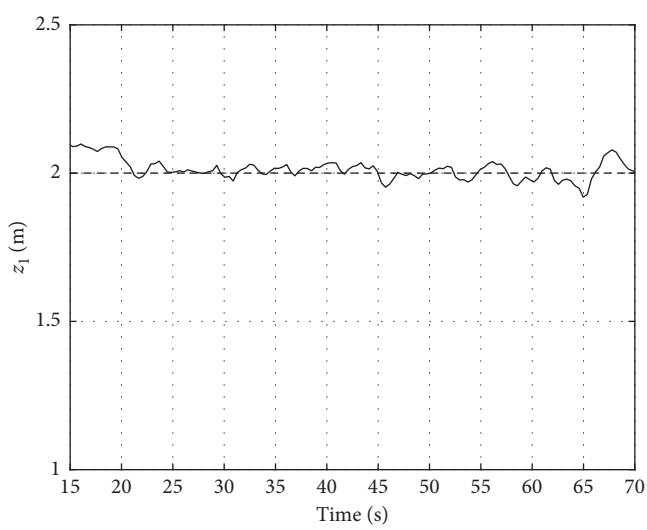

Figure 4: Experimental implementation: quadrotor's altitude z_1 (solid) and altitude reference $z_{1,\mathrm{ref}}$ (dash).

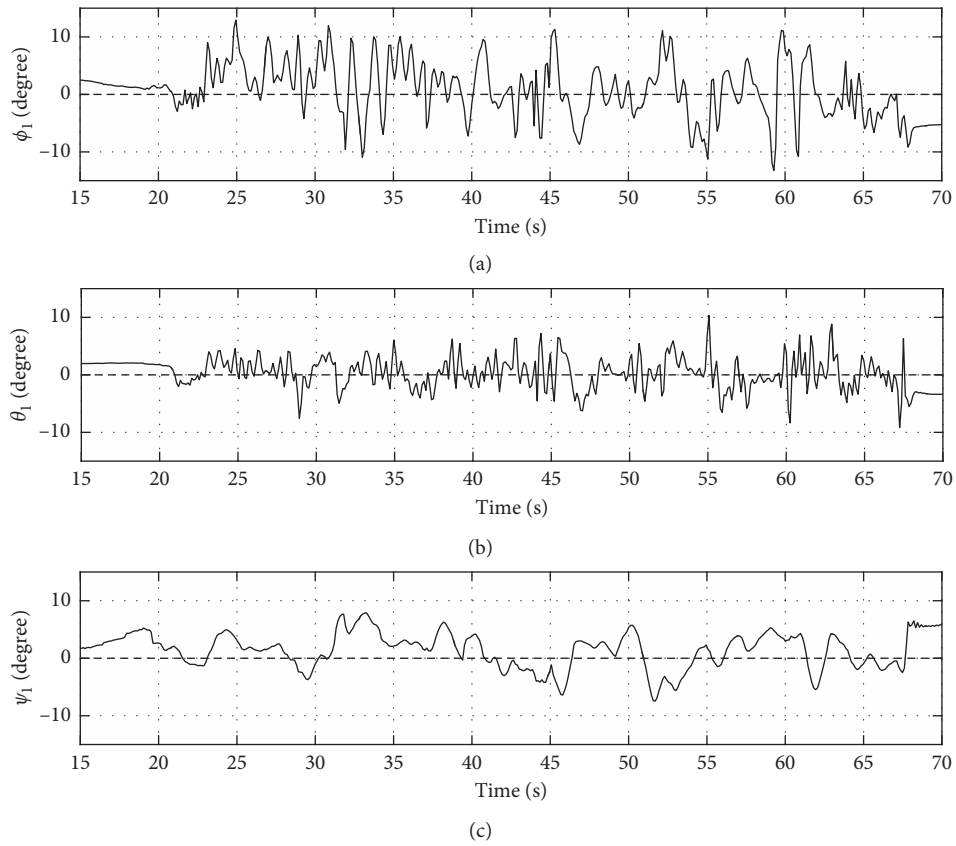

Figure 5: Experimental simulation: (a) roll angle ϕ_1 (solid) and roll angle reference $\phi_{1,\text{ref}}$ (dash) (degree vs. s); (b) pitch angle θ_1 (solid) and pitch angle reference $\theta_{1,\text{ref}}$ (dash) (degree vs. s); (c) yaw angle ψ_1 (solid) and yaw angle reference $\psi_{1,\text{ref}}$ (dash).

experimental tests were performed in an outdoor environment, without using the GPS sensor.

5. Conclusions

In this paper, a controller based on the stabilization technique for the altitude and attitude error has been proposed for a quadrotor. The simulation results have been performed using the Pixhawk PSP. Then, the controller has been implemented on a laboratory quadrotor. The simulation and experimental results show a good performance, even in outdoor environment, showing some degree of robustness in the presence of environmental disturbances.

Data Availability

The figures, tables, and other data used to support this study are included within the article.

Conflicts of Interest

The authors declare that there are no conflicts of interest regarding the publication of this paper.

Acknowledgments

This paper has been partially supported by the European Project ECSEL–JU RIA–2018 "Comp4Drones" and project "Coordination of autonomous unmanned vehicles for highly complex performances," Executive Program of Scientific and Technological Agreement between Italy (Ministry of Foreign Affairs and International Cooperation, Italy) and Mexico (Mexican International Cooperation Agency for the Development), SAAP3.

References

[1] S. Bouabdallah, P. Murrieri, and R. Siegwart, "Design and control of an indoor Micro quadrotor," in *Proceedings of the IEEE International Conference on Robotics and Automation*, pp. 1–6, New Orleans, LA, USA, April-May 2004.

[2] Y. Zeng and L. Zhao, "Parameter identification for unmanned four–rotor helicopter with nonlinear model," in *Proceedings of the 2014 IEEE Chinese Guidance, Navigation and Control Conference*, pp. 922–926, Yantai, China, August 2014.

[3] A. Nagaty, S. Saeedi, C. Thibault, M. Seto, and H. Li, "Control and navigation framework for quadrotor helicopters," *Journal of Intelligent & Robotic Systems*, vol. 70, no. 1–4, pp. 1–12, 2013.

[4] O. Magnussen, M. Ottestad, and G. Hovland, "Experimental validation of a quaternion–based attitude estimation with direct input to a quadcopter control system," in *Proceedings of the International Conference on Unmanned Aircraft Systems (ICUAS)*, pp. 48–485, Atlanta, GA, USA, May 2013.

[5] R. Valenti, I. Dryanovski, and J. Xiao, "Keeping a good attitude: a quaternion-based orientation filter for IMUs and MARGs," *Sensors*, vol. 15, no. 8, pp. 19302–19330, 2015.

[6] M. Elena Antonio–Toledo, A. Y. Alanis, and E. N. Sanchez, "Robust neural decentralized control for a quadrotor UAV," in *Proceedings of the International Joint Conference on Neural Networks (IJCNN)*, pp. 714–719, Vancouver, Canada, July 2016.

[7] B. Panomruttanarug, K. Higuchi, and F. Mora-Camino, "Attitude control of a quadrotor aircraft using LQR state feedback controller with full order state observer," in *Proceeding of the International Conference on Instrumentation, Control and Information Technology (SICE)*, pp. 2041–2046, Konya, Turkey, June 2013.

[8] P. E. I. Pounds, D. R. Bersak, and A. M. Dollar, "Stability of small-scale UAV helicopters and quadrotors with added payload mass under PID control," *Autonomous Robots*, vol. 33, no. 1-2, pp. 129–142, 2012.

[9] L. Luque–Vega, B. Castillo–Toledo, and A. G. Loukianov, "Robust block second order sliding mode control for a quadrotor," *Journal of the Franklin Institute*, vol. 349, no. 2, pp. 719–739, 2012.

[10] S. Bouabdallah and R. Siegwart, "Backstepping and sliding-mode techniques applied to an indoor Micro quadrotor," in *Proceedings of the 2005 IEEE International Conference on Robotics and Automation*, Barcelona, Spain, April 2005.

[11] D. Matouk, O. Gherouat, F. Abdessemed, and A. Hassam, "Quadrotor position and attitude control via backstepping approach," in *Proceedings of the 8th International Conference on Modelling, Identification and Control (ICMI)*, pp. 73–79, Algiers, Algeria, November 2016.

[12] J.-J. Xiong and G.-B. Zhang, "Global fast dynamic terminal sliding mode control for a quadrotor UAV," *ISA Transactions*, vol. 66, pp. 233–240, 2017.

[13] Y. C. Choi and H. S. Ahn, "Nonlinear control of quadrotor for point tracking: actual implementation and experimental tests," *IEEE/ASME Transactions on Mechatronics*, vol. 20, no. 3, pp. 1179–1192, 2015.

[14] Y.-C. Liu, J. Zhang, T. Zhang, and J.-Y. Song, "Robust adaptive spacecraft attitude tracking control based on similar skew-symmetric structure," *Computers & Electrical Engineering*, vol. 56, pp. 784–794, 2016.

[15] W. Dong, J. A. Farrell, M. M. Polycarpou, V. Djapic, and M. Sharma, "Command filtered adaptive backstepping," *IEEE Transactions on Control Systems Technology*, vol. 20, no. 3, pp. 566–580, 2012.

[16] S. Islam, J. Dias, and L. D. Seneviratne, "Adaptive output feedback control for miniature unmanned aerial vehicle," in *Proceedings IEEE International Conference on Advanced Intelligent Mechatronics, AIM*, pp. 318–322, Banff, Canada, July 2016.

[17] P. C. Hughes, *Spacecraft Attitude Dynamics*, Dover Publications, Inc., Mineola, NY, USA, 1986.

[18] A. Isidori, *Nonlinear Control Systems*, Springer-Verlag, Berlin, Germany, 3rd edition, 1995.

[19] H. K. Khalil, *Nonlinear Systems*, Prentice-Hall, Upper Saddle River, NJ, USA, 2002.

Hindawi
Mathematical Problems in Engineering
Volume 2020, Article ID 4517969, 14 pages
https://doi.org/10.1155/2020/4517969

Research Article

Stability Analysis for Milling Process with Variable Pitch and Variable Helix Tools by High-Order Full-Discretization Methods

Yang Zhang, Kenan Liu, Wuyun Zhao, Wei Zhang, and Fei Dai

Mechanical and Electrical Engineering College, Gansu Agricultural University, Lanzhou 730070, China

Correspondence should be addressed to Kenan Liu; 85263795@qq.com

Received 12 April 2020; Revised 23 June 2020; Accepted 4 July 2020; Published 26 July 2020

Guest Editor: Cuimei Jiang

Chatter is one of the significant limitations in the milling process, which may cause poor surface quality, reduced productivity, and accelerated tool wear. Variable pitch and variable helix tools can be used to suppress regenerative chatter. This study extends the high-order full-discretization methods (FDMs) to predict the stability of milling with variable pitch and variable helix tools. The time-periodic delay-differential equation (DDE) with multiple delays is used to model the milling process using variable pitch and variable helix tools. Then, the DDE with multiple delays is reexpressed by the state-space equation. Meanwhile, the spindle rotational period is divided into many small-time intervals, and the state space equation is integrated on the small-time interval. Then, the high-order interpolation polynomials are used to approximate the state term, and the weights related to the time delay are employed to approximate the time-delay term. The second-order, third-order, and fourth-order extended FDMs (2nd EFDM, 3rd EFDM, and 4th EFDM) are compared with the benchmark in terms of the rate of convergence. It is found that the 2nd EFDM, 3rd EFDM, and 4th EFDM converge faster than the benchmark method. The difference between the curves obtained by different EFDMs and the reference curve is very small. There is no need to extend hypersecond FDMs to analyze the stability of milling with variable pitch and variable helix tools.

1. Introduction

High precision products machined by using high-speed milling technology have an increasing demand in various industries. Chatter is one of the significant limitations in the milling process, which may cause poor surface quality, reduced productivity, and accelerated tool wear. Therefore, a great deal of effort has been made to develop chatter avoidance methods. The stability lobe diagram (SLD) is an effective way to predict the stability in the milling process.

In the milling process, regenerative chatter can be modeled by time-periodic DDE. The mapping relations of the dynamic responses between two consecutive periods can be obtained by solving the DDE. Then, the stability lobe diagrams can be determined according to the obtained mapping relations. Until now, different methods for calculating stability lobe diagrams have been reported. Altintas and Budak [1] developed a famous and efficient zeroth-order approximation (ZOA) method that determines the stability lobe diagram in the frequency domain. In this method, the time-varying cutting force coefficients are approximated by their Fourier series components. However, this method cannot accurately predict the stability lobes at low radial immersion milling operations. Hence, Merdol and Altintas [2] presented a so-called multifrequency method. This method can be used to accurately predict the milling stability under low radial immersion conditions in the frequency domain. After that, many time-domain methods have been developed to predict the stability in milling. Bayly et al. [3] proposed a temporal finite element analysis method, Butcher et al. [4] presented a Chebyshev collocation method, and Insperger and Stépán reported the updated semi-discretization method (SDM) [5] and first-order semi-discretization method (1st SDM) [6]. The abovementioned time-domain methods can be used to predict the stability of milling accurately; however, their computational efficiency should be further improved. To improve computational efficiency, Ding et al. [7] presented a full-discretization

method (FDM) based on the direct integration scheme. Then, on the framework of FDM, Ding et al. [8] introduced the second-order FDM (2nd FDM), Guo et al. [9] proposed the third-order FDM (3rd FDM), and Ozoegwu reported the least squares approximation methods [10] and hyper-third-order full-discretization methods [11]. Besides, the numerical integration method [12] and differential quadrature method [13] developed by Ding and his coworkers, the Runge–Kutta-based methods proposed by Niu et al. [14], the improved precise integration method proposed by Li et al. [15], the Simpson-based method presented by Zhang et al. [16], numerical differentiation method reported by Zhang et al. [17], and so on are proposed for the stability prediction in the milling process. More recently, Olvera et al. [18] presented the stability analysis for a single degree of freedom down-milling operation in a thin-walled workpiece by using the enhanced multistage homotopy perturbation (EMHP) method.

The above works mainly studied the chatter avoidance methods by using stability lobe diagrams. However, chatter suppression is also a critical issue for the study of stability in milling. It is well known that variable pitch and variable helix (nonuniform) milling tools can be used to suppress regenerative chatter by disturbing the regeneration mechanism. Many studies on the stability analysis in milling with variable pitch and variable helix tools have been reported. Based on the ZOA method, Altintas et al. [19] presented an analytical model for stability prediction in milling with variable pitch cutters. Based on this model, a method for selecting optimal pitch angles is also presented. Sims et al. [20] utilized the semidiscretization method, time-averaged semidiscretization method, and temporal finite element method to predict the chatter stability for variable pitch and variable helix milling tools. Sellmeier and Denkena [21] proposed a method based on Ackermann's approach for investigating the stability of an unequally pitched end mill. Compeán et al. [22] suggested the enhanced multistage homotopy perturbation method (EMHPM) to predict the stability of a multivariable milling tool. Wan et al. [23] presented a unified method for predicting the stability lobes of the milling process with multiple delays. Jin et al. [24] proposed a frequency-domain solution for efficient stability prediction of variable helix cutters milling. After that, Jin et al. [25] extended the semidiscretization method to predict the stability of the variable pitch and variable helix milling cutter. Guo et al. [26] proposed a new variable interpolation method to predict the stability of milling with multidelays combining the effect of the cutter's variable-helix angle's effect. Sims [27] described a new formulation for predicting the chatter stability of variable helix tools based on Laplace formulation. Wang et al. [28] proposed an improved semidiscretization algorithm (ISDA) for modeling and simulation with variable pitch and variable helix milling tools. Niu et al. [29] studied the mechanics and multiregenerative stability of variable pitch and variable helix milling tools considering runout. Huang et al. [30] developed the robust active chatter control for milling processes with variable pitch cutters whose dynamics are governed by multidelay nonlinear differential equations. Stepan et al. [31] presented the achievable upper and lower capability bounds by introducing so-called stabilizability diagrams of a hypothetical variable pitch milling cutter that is tuned continuously along the stability boundaries. Huang et al. [32] presented a stability analysis method for milling system with variable pitch cutters under variable speed. Regarding the mechanics model for nonuniform milling tools, Chen et al. [33] proposed a unified analytical cutting force model based on a predictive machining theory for variable helix end mill considering cutter runout. Otto et al. [34] derived a dynamic process model for milling with nonuniform pitch and variable helix tools. In this model, the nonlinear cutting force behavior and the effect of runout are included. Guo et al. [35] presented a compensated-chip thickness-based cutting force model for nonuniform helix tools in the five-axis milling process. Cai et al. [36] proposed an integrated process-machine model based on the computer graphics method for simulating the milling process of a variable pitch cutter. Additionally, the stability lobe diagrams are usually considered in the design process of the nonuniform milling tools. Regarding the milling tool design with consideration of stability, Budak [37, 38] presented a design method for optimizing the pitch angles of the milling tool. Yusoff and Sims [39] proposed a semidiscretization method combined with differential evolution to predict milling stability as well as optimize variable helix end milling tools. Comak and Budak [40] presented a practical but accurate design method for the selection of the best variation combination to maximize chatter-free material removal rate without using time-consuming computer simulations. Mei et al. [41] proposed an analytical method for designing milling cutters with alternating variable pitches. Guo et al. [42] proposed an effective optimization method for variable helix cutter by introducing an index called "suppression factor" to measure stability quantitatively. Moreover, serrated milling tools can also be employed to suppress chatter in the milling process. Merdol and Altintas [43, 44] analyzed the mechanics and dynamics of milling with serrated cutters, where the periodic serrations ground on the helical flutes are modeled by fitting a cubic spline on the design profile. Dombovari et al. [45, 46] presented the stability model of serrated cutters in analytical semidiscrete time domain. Hosseini et al. [47] proposed mechanistic modeling for cutting with serrated end mills using a parametric representation approach. Tehranizadeh and Budak [48] presented the methods for designing optimum serration shapes. In their methods, the effects of serration shapes on the mechanics of milling are investigated. Guo et al. [49] presented a mechanistic cutting force model of the serrated end mill to predict cutting forces. Bari et al. [50] presented an improved chip thickness model for serrated end mills that account for the actual trochoidal path traced by the tooth. Tehranizadeh et al. [51] investigated the effects of different waveforms on the mechanics of process. In their work, the effects of phase shift direction and local cutting angles on milling forces are also experimentally verified. Pelayo et al. [52] studied the mechanics of the milling system with serrated end mills using force and surface topography models. In their study, a stationary milling force model is developed including the main

geometric parameters of the serrated profile, and a surface topography model is developed to predict the resulting machined surfaces.

In the literature [11], Ozoegwu et al. pointed out that the accuracy of stability result rises with the order of full-discretization method peaking at fourth order and then declined at the fifth order. That is, in the hyper-fourth-order full-discretization methods, the accuracy of the stability results may be affected by the Runge phenomenon. Although it is indicated from the literature [11] that the fourth-order FDM is the best for a uniform pitch and uniform helix tool, whether it is the best for a variable pitch and variable helix cutter is also worthy of study. In this study, the high-order FDMs which are proposed for the analysis of milling with uniform tools are extended to analyze the stability of milling with variable pitch and variable helix tools, and the performances of extended FDMs are also evaluated.

This paper is organized as follows: in Section 2, the mathematical model of milling dynamics is introduced; in Section 3, the high-order FDMs are extended to predict the stability of milling with variable pitch and variable helix tools; in Section 4, the rates of convergence of the extended FDMs are analyzed, and the stability lobe diagrams for different conditions are obtained; and conclusions are drawn in Section 5.

2. Mathematical Model of Milling Dynamics

In the process of modeling the dynamics of the milling process with variable pitch and variable helix tools, the axial depth of cut a_p is equally discretized into L axial layers with the thickness of Δz; thus, $\Delta z = a_p/L$.

2.1. Angular Position. The angular position of the jth tooth on the lth $(1 \le l \le L)$ axial layer $\varphi_{l,j}(t)$ is represented as

$$\varphi_{l,j}(t) = \begin{cases} \dfrac{2\pi\Omega}{60}t - \dfrac{a_p(l-1/2)\tan\beta_j}{RL}, & \text{if } j = 1, \\ \dfrac{2\pi\Omega}{60}t + \displaystyle\sum_{j=2}^{j} P_j - \dfrac{a_p(l-1/2)\tan\beta_j}{RL}, & \text{if } 1 < j \le N, \end{cases} \tag{1}$$

where Ω is the spindle speed in rpm, a_p is the axial depth of cut, β_j is the helix angle of the jth tooth, R is the radius of the tool shank envelope, P_j is the pitch angle between the jth tooth and (j-1)th tooth, and N is the number of cutter tooth.

2.2. The Dynamic Chip Thickness. The dynamic chip thickness caused by regenerative effect, $d_{l,j}(t)$, can be given by

$$\begin{aligned} d_{l,j}(t) = {} & \left(x(t) - x\left(t - \tau_{l,j}\right)\right)\sin\left(\varphi_{l,j}(t)\right) \\ & + \left(y(t) - y\left(t - \tau_{l,j}\right)\right)\cos\left(\varphi_{l,j}(t)\right), \end{aligned} \tag{2}$$

where $x(t)$ and $y(t)$ are the displacements of the current tooth in the X and Y directions, respectively; $x(t - \tau_{l,j})$ and $y(t - \tau_{l,j})$ are the displacements of the previous tooth in the X and Y directions, respectively; and the time delay $\tau_{l,j}$ depends on the separation angle between the jth tooth and (j−1)th tooth on the lth layer, $\Delta\varphi_{l,j}$. Thus, the time delay $\tau_{l,j}$ can be given by

$$\tau_{l,j} = T\frac{\Delta\varphi_{l,j}}{2\pi}, \tag{3}$$

where the period T is equal to the spindle rotational period, namely, $T = 60/\Omega$. The separation angle $\Delta\varphi_{l,j}$ can be expressed as follows [24, 29]:

$$\Delta\varphi_{l,j} = \begin{cases} P_j + \dfrac{(l-1/2)\left(\tan\beta_j - \tan\beta_N\right)}{LR}, & \text{if } j = 1, \\ P_j + \dfrac{(l-1/2)\left(\tan\beta_j - \tan\beta_{j-1}\right)}{LR}, & \text{if } 1 < j \le N. \end{cases} \tag{4}$$

2.3. Milling Dynamics. The governing equation of milling dynamics for a two-degree-of-freedom milling system can be written as follows [5]:

$$\begin{aligned} & \begin{pmatrix} \ddot{x}(t) \\ \ddot{y}(t) \end{pmatrix} + \begin{pmatrix} 2\zeta_x\omega_{nx} & 0 \\ 0 & 2\zeta_y\omega_{ny} \end{pmatrix}\begin{pmatrix} \dot{x}(t) \\ \dot{y}(t) \end{pmatrix} + \begin{pmatrix} \omega_{nx}^2 & 0 \\ 0 & \omega_{ny}^2 \end{pmatrix}\begin{pmatrix} x(t) \\ y(t) \end{pmatrix} \\ & = \sum_{j=1}^{N}\sum_{l=1}^{L}\begin{pmatrix} \dfrac{-h_{xx}(t)}{m_x} & \dfrac{-h_{xy}(t)}{m_x} \\ \dfrac{-h_{yx}(t)}{m_y} & \dfrac{-h_{yy}(t)}{m_y} \end{pmatrix}\begin{pmatrix} x(t) - x\left(t - \tau_{l,j}\right) \\ y(t) - y\left(t - \tau_{l,j}\right) \end{pmatrix}, \end{aligned} \tag{5}$$

where ζ_x, ω_{nx}, and m_x are the damping ratio, angular natural frequency, and modal mass of the milling system in the X direction, respectively; and ζ_y, ω_{ny}, and m_y are the damping ratio, angular natural frequency, and modal mass of the milling system in the Y direction, respectively. The specific cutting force coefficients $h_{xx}(t)$, $h_{xy}(t)$, $h_{yx}(t)$, and $h_{yy}(t)$ are given as follows:

$$\begin{aligned} h_{xx}(t) &= g\left(\varphi_{l,j}(t)\right)\sin\left(\varphi_{l,j}(t)\right)\left(K_t\cos\left(\varphi_{l,j}(t)\right) + K_n\sin\left(\varphi_{l,j}(t)\right)\right)\Delta z, \\ h_{xy}(t) &= g\left(\varphi_{l,j}(t)\right)\cos\left(\varphi_{l,j}(t)\right)\left(K_t\cos\left(\varphi_{l,j}(t)\right) + K_n\sin\left(\varphi_{l,j}(t)\right)\right)\Delta z, \\ h_{yx}(t) &= g\left(\varphi_{l,j}(t)\right)\sin\left(\varphi_{l,j}(t)\right)\left(-K_t\sin\left(\varphi_{l,j}(t)\right) + K_n\cos\left(\varphi_{l,j}(t)\right)\right)\Delta z, \\ h_{yy}(t) &= g\left(\varphi_{l,j}(t)\right)\cos\left(\varphi_{l,j}(t)\right)\left(-K_t\sin\left(\varphi_{l,j}(t)\right) + K_n\cos\left(\varphi_{l,j}(t)\right)\right)\Delta z, \end{aligned} \tag{6}$$

where K_t and K_n are the tangential and normal cutting coefficients, respectively. The window function $g(\varphi_{l,j}(t))$ is used to determine whether the tooth is in or out of cut [5].

3. The Proposed Methods

Let $\mathbf{u}(t) = [x(t)y(t)\dot{x}(t)\dot{y}(t)]^T$, and equation (5) can be represented in state-space form as follows:

$$\dot{\mathbf{u}}(t) = \mathbf{A}\mathbf{u}(t) + \sum_{j=1}^{N}\sum_{l=1}^{L}\mathbf{B}_{l,j}(t)\left(\mathbf{u}(t) - \mathbf{u}\left(t - \tau_{l,j}\right)\right), \tag{7}$$

where

$$\mathbf{A} = \begin{bmatrix} 0 & 0 & 1 & 0 \\ 0 & 0 & 0 & 1 \\ -\omega_{nx}^2 & 0 & -2\zeta_x\omega_{nx} & 0 \\ 0 & -\omega_{ny}^2 & 0 & -2\zeta_y\omega_{ny} \end{bmatrix},$$

$$\mathbf{B}_{l,j}(t) = \begin{bmatrix} 0 & 0 & 0 & 0 \\ 0 & 0 & 0 & 0 \\ \dfrac{-h_{xx}}{m_x} & \dfrac{-h_{xy}}{m_x} & 0 & 0 \\ \dfrac{-h_{yx}}{m_y} & \dfrac{-h_{yy}}{m_y} & 0 & 0 \end{bmatrix}. \tag{8}$$

To solve equation (7) numerically, the period T is equally divided into k small-time intervals firstly; thus, $T = k\Delta t$, where k is an integer and Δt is the length of the small-time interval. The integer $k_{l,j}$ related to the time delay $\tau_{l,j}$ can be expressed as

$$k_{l,j} = \mathrm{int}\left(\frac{\tau_{l,j} + \Delta t/2}{\Delta t}\right), \tag{9}$$

where int (*) is the function that rounds positive numbers towards zero.

Then, equation (7) is integrated on the ith small-time interval $[t_i, t_{i+1}]$ resulting in

$$\begin{aligned} \mathrm{u}(t) = e^{\mathbf{A}(t-t_i)}\mathbf{u}(t_i) + \int_{t_i}^{t} e^{\mathbf{A}(t-\xi)}\sum_{j=1}^{N}\sum_{l=1}^{L}\Big(&\mathbf{B}_{l,j}(\xi)\mathbf{u}(\xi) \\ &- \mathbf{B}_{l,j}(\xi)\mathbf{u}\left(\xi - \tau_{l,j}\right)\Big)d\xi. \end{aligned} \tag{10}$$

Equation (10) can be equivalently written as follows [7]:

$$\begin{aligned} u_{i+1} = e^{\mathbf{A}\Delta t}\mathbf{u}_i + \int_{t_i}^{t_{i+1}} e^{\mathbf{A}(\mathbf{t}_{i+1}-\xi)}\sum_{j=1}^{N}\sum_{l=1}^{L}\Big(&\mathbf{B}_{l,j}(\xi)\mathbf{u}(\xi) \\ &- \mathbf{B}_{l,j}(\xi)\mathbf{u}\left(\xi - \tau_{l,j}\right)\Big)d\xi. \end{aligned} \tag{11}$$

In equation (11), $\mathbf{u}_{i+1}$ and $\mathbf{u}_i$ denote $\mathbf{u}(t_{i+1})$ and $\mathbf{u}(t_i)$, respectively.

In this work, the existing 2nd FDM, 3rd FDM, and 4th FDM are all extended to analyze the stability of milling with variable pitch and variable helix tools, and the corresponding extended methods are denoted as 2nd EFDM, 3rd EFDM, and 4th EFDM. In the 2nd EFDM, 3rd EFDM, and 4th EFDM, the second-, third-, and fourth-order interpolation polynomials are used to approximate the state term $\mathbf{u}(\xi)$, respectively. The periodic coefficient term $\mathbf{B}_{l,j}(\xi)$ is approximated by first-order interpolation polynomial, and the time-delay term $\mathbf{u}(\xi - \tau_{l,j})$ is approximated by using the weights related to time delay. Since the derivation processes of the 2nd EFDM, 3rd EFDM, and 4th EFDM are similar, to avoid repetitive work, only the detailed derivation process of the 4th EFDM is given in this work.

In the 4th EFDM, the state term $\mathbf{u}(\xi)$ and the periodic coefficient term $\mathbf{B}_{l,j}(\xi)$ can be, respectively, approximated by the fourth-order and first-order interpolation polynomials using the Lagrange interpolation scheme. In the calculation process, the interpolation nodes $t_{i-3}, t_{i-2}, t_{i-1}, t_i, t_{i+1}$ and the corresponding node values $\mathbf{u}_{i-3}$, $\mathbf{u}_{i-2}$, $\mathbf{u}_{i-1}$, $\mathbf{u}_i$, $\mathbf{u}_{i+1}$ are employed to approximate the state term. Meanwhile, the interpolation nodes t_i, t_{i+1} and the node values $\mathbf{B}_i$, $\mathbf{B}_{i+1}$ are employed to approximate the periodic coefficient term. Then, the state term $\mathbf{u}(\xi)$ and the periodic coefficient term $\mathbf{B}_{l,j}(\xi)$ can be expressed as follows:

$$\begin{aligned} \mathbf{u}(\xi) = &\left(\frac{\xi^4}{24(\Delta t)^4} + \frac{\xi^3}{12(\Delta t)^3} - \frac{\xi^2}{24(\Delta t)^2} - \frac{\xi}{12(\Delta t)}\right) \\ &\mathbf{u}_{i-3} + \left(\frac{-\xi^4}{6(\Delta t)^4} - \frac{\xi^3}{2(\Delta t)^3} + \frac{\xi^2}{6(\Delta t)^2} + \frac{\xi}{2(\Delta t)}\right) \\ &\mathbf{u}_{i-2} + \left(\frac{\xi^4}{4(\Delta t)^4} + \frac{\xi^3}{(\Delta t)^3} + \frac{\xi^2}{4(\Delta t)^2} - \frac{3\xi}{2(\Delta t)}\right) \\ &\mathbf{u}_{i-1} + \left(\frac{-\xi^4}{6(\Delta t)^4} - \frac{5\xi^3}{6(\Delta t)^3} - \frac{5\xi^2}{6(\Delta t)^2} + \frac{5\xi}{6(\Delta t)} + 1\right) \\ &\mathbf{u}_i + \left(\frac{\xi^4}{24(\Delta t)^4} + \frac{\xi^3}{4(\Delta t)^3} + \frac{11\xi^2}{24(\Delta t)^2} + \frac{\xi}{4(\Delta t)}\right)\mathbf{u}_{i+1}, \end{aligned} \tag{12}$$

$$\mathbf{B}_{l,j}(\xi) = \frac{\Delta t - \xi}{\Delta t}\mathbf{B}_i^{\langle l,j\rangle} + \frac{\xi}{\Delta t}\mathbf{B}_{i+1}^{\langle l,j\rangle}. \tag{13}$$

The time-delay term $\mathbf{u}(\xi - \tau_{l,j})$ is approximated by using the weights $\omega_a^{\langle l,j\rangle}$ and $\omega_b^{\langle l,j\rangle}$, which can be written as

$$\mathbf{u}\left(\xi - \tau_{l,j}\right) = \left(\omega_b^{\langle l,j\rangle} - \frac{\xi}{\Delta t}\right)\mathbf{u}_{i-k_{l,j}+1} + \left(\omega_a^{\langle l,j\rangle} + \frac{\xi}{\Delta t}\right)\mathbf{u}_{i-k_{l,j}}, \tag{14}$$

where the weights $\omega_a^{\langle l,j\rangle}$ and $\omega_b^{\langle l,j\rangle}$ are calculated as follows:

$$\omega_a^{\langle l,j\rangle} = \frac{k_{l,j}\Delta t + \Delta t/2 - \tau_{l,j}}{\Delta t}, \tag{15}$$

$$\omega_b^{\langle l,j\rangle} = \frac{\tau_{l,j} + \Delta t/2 - k_{l,j}\Delta t}{\Delta t} = 1 - \omega_a^{\langle l,j\rangle}. \tag{16}$$

Substituting equations (12)–(16) into equation (11) yields

$$\mathrm{u}_{i+1} = \mathbf{P}_i \begin{bmatrix} \left(\mathrm{F}_0 + \sum_{j=1}^{N}\sum_{l=1}^{L}\left(\mathrm{G}_{17}\mathbf{B}_i^{\langle l,j\rangle} + \mathrm{G}_{18}\mathbf{B}_{i+1}^{\langle l,j\rangle}\right)\right)\mathrm{u}_i + \sum_{j=1}^{N}\sum_{l=1}^{L}\left(\mathrm{G}_{15}\mathbf{B}_i^{\langle l,j\rangle} + \mathrm{G}_{16}\mathbf{B}_{i+1}^{\langle l,j\rangle}\right)\mathrm{u}_{i-1} \\ + \sum_{j=1}^{N}\sum_{l=1}^{L}\left(\mathrm{G}_{13}\mathbf{B}_i^{\langle l,j\rangle} + \mathrm{G}_{14}\mathbf{B}_{i+1}^{\langle l,j\rangle}\right)\mathrm{u}_{i-2} + \sum_{j=1}^{N}\sum_{l=1}^{L}\left(\mathrm{G}_{11}\mathbf{B}_i^{\langle l,j\rangle} + \mathrm{G}_{12}\mathbf{B}_{i+1}^{\langle l,j\rangle}\right)\mathrm{u}_{i-3} \\ - \sum_{j=1}^{N}\sum_{l=1}^{L}\left(\mathrm{G}_{23}\mathbf{B}_i^{\langle l,j\rangle} + \mathrm{G}_{24}\mathbf{B}_{i+1}^{\langle l,j\rangle}\right)\mathrm{u}_{i-k_{l,j}+1} - \sum_{j=1}^{N}\sum_{l=1}^{L}\left(\mathrm{G}_{21}\mathbf{B}_i^{\langle l,j\rangle} + \mathrm{G}_{22}\mathbf{B}_{i+1}^{\langle l,j\rangle}\right)\mathrm{u}_{i-k_{l,j}} \end{bmatrix}, \tag{17}$$

where

$$\mathbf{G}_{11} = -\frac{\mathbf{F}_6}{24(\Delta t)^5} - \frac{\mathbf{F}_5}{24(\Delta t)^4} + \frac{\mathbf{F}_4}{8(\Delta t)^3} + \frac{\mathbf{F}_3}{24(\Delta t)^2} - \frac{\mathbf{F}_2}{12\Delta t},$$

$$\mathbf{G}_{12} = \frac{\mathbf{F}_6}{24(\Delta t)^5} + \frac{\mathbf{F}_5}{12(\Delta t)^4} - \frac{\mathbf{F}_4}{24(\Delta t)^3} - \frac{\mathbf{F}_3}{12(\Delta t)^2},$$

$$\mathbf{G}_{13} = \frac{\mathbf{F}_6}{6(\Delta t)^5} + \frac{\mathbf{F}_5}{3(\Delta t)^4} - \frac{2\mathbf{F}_4}{3(\Delta t)^3} - \frac{\mathbf{F}_3}{3(\Delta t)^2} + \frac{\mathbf{F}_2}{2\Delta t},$$

$$\mathbf{G}_{14} = -\frac{\mathbf{F}_6}{6(\Delta t)^5} - \frac{\mathbf{F}_5}{2(\Delta t)^4} + \frac{\mathbf{F}_4}{6(\Delta t)^3} + \frac{\mathbf{F}_3}{2(\Delta t)^2},$$

$$\mathbf{G}_{15} = -\frac{\mathbf{F}_6}{4(\Delta t)^5} - \frac{3\mathbf{F}_5}{4(\Delta t)^4} + \frac{3\mathbf{F}_4}{4(\Delta t)^3} + \frac{7\mathbf{F}_3}{4(\Delta t)^2} - \frac{3\mathbf{F}_2}{2\Delta t},$$

$$\mathbf{G}_{16} = \frac{\mathbf{F}_6}{4(\Delta t)^5} + \frac{\mathbf{F}_5}{(\Delta t)^4} + \frac{\mathbf{F}_4}{4(\Delta t)^3} - \frac{3\mathbf{F}_3}{2(\Delta t)^2},$$

$$\mathbf{G}_{17} = \frac{\mathbf{F}_6}{6(\Delta t)^5} + \frac{2\mathbf{F}_5}{3(\Delta t)^4} - \frac{5\mathbf{F}_3}{3(\Delta t)^3} - \frac{\mathbf{F}_2}{6(\Delta t)^2} + \mathbf{F}_1,$$

$$\mathbf{G}_{18} = -\frac{\mathbf{F}_6}{6(\Delta t)^5} - \frac{5\mathbf{F}_5}{6(\Delta t)^4} - \frac{5\mathbf{F}_4}{6(\Delta t)^3} + \frac{5\mathbf{F}_3}{6(\Delta t)^2} + \frac{\mathbf{F}_2}{\Delta t},$$

$$\mathbf{G}_{19} = -\frac{\mathbf{F}_6}{24(\Delta t)^5} - \frac{5\mathbf{F}_5}{24(\Delta t)^4} - \frac{5\mathbf{F}_4}{24(\Delta t)^3} + \frac{5\mathbf{F}_3}{24(\Delta t)^2} + \frac{\mathbf{F}_2}{4\Delta t},$$

$$\mathbf{G}_{110} = \frac{\mathbf{F}_6}{24(\Delta t)^5} + \frac{\mathbf{F}_5}{4(\Delta t)^4} + \frac{11\mathbf{F}_4}{24(\Delta t)^3} + \frac{\mathbf{F}_3}{4(\Delta t)^2},$$

$$\mathbf{G}_{21} = \frac{\mathbf{F}_3}{\Delta t^2} + \frac{\omega_a^{\langle l,j\rangle} - 2}{\Delta t}\mathbf{F}_2 + \left(1 - \omega_a^{\langle l,j\rangle}\right)\mathbf{F}_1,$$

$$\mathbf{G}_{22} = \frac{-\mathbf{F}_3}{\Delta t^2} + \frac{1 - \omega_a^{\langle l,j\rangle}}{\Delta t}\mathbf{F}_2,$$

$$\mathbf{G}_{23} = \frac{-\mathbf{F}_3}{\Delta t^2} + \frac{1 - \omega_a^{\langle l,j\rangle}}{\Delta t}\mathbf{F}_2 + \omega_a^{\langle l,j\rangle}\mathbf{F}_1,$$

$$\mathbf{G}_{24} = \frac{\mathbf{F}_3}{\Delta t^2} + \frac{\omega_a^{\langle l,j\rangle}}{\Delta t}\mathbf{F}_2,$$

$$\mathbf{P}_i = \left[\mathbf{I} - \sum_{j=1}^{N}\sum_{l=1}^{L}\left(\mathbf{G}_{19}\mathbf{B}_i^{\langle l,j\rangle} + \mathbf{G}_{20}\mathbf{B}_{i+1}^{\langle l,j\rangle}\right)\right]^{-1}, \tag{18}$$

where $\mathbf{I}$ denotes the identity matrix and the matrixes $\mathbf{F}_1$–$\mathbf{F}_6$ can be expressed as follows:

$$\begin{aligned} \mathbf{F}_0 &= e^{\mathbf{A}\Delta t}, \\ \mathbf{F}_1 &= (\mathbf{F}_0 - \mathbf{I})\mathbf{A}^{-1}, \\ \mathbf{F}_2 &= (\mathbf{F}_1 - (\Delta t)\mathbf{I})\mathbf{A}^{-1}, \\ \mathbf{F}_3 &= \left(2\mathbf{F}_2 - (\Delta t)^2\mathbf{I}\right)\mathbf{A}^{-1}, \\ \mathbf{F}_4 &= \left(3\mathbf{F}_3 - (\Delta t)^3\mathbf{I}\right)\mathbf{A}^{-1}, \\ \mathbf{F}_5 &= \left(4\mathbf{F}_4 - (\Delta t)^4\mathbf{I}\right)\mathbf{A}^{-1}, \\ \mathbf{F}_6 &= \left(5\mathbf{F}_5 - (\Delta t)^5\mathbf{I}\right)\mathbf{A}^{-1}. \end{aligned} \tag{19}$$

According to equation (17), the following local discrete map can be obtained:

$$\begin{bmatrix} \mathbf{u}_{i+1} \\ \mathbf{u}_i \\ \mathbf{u}_{i-1} \\ \vdots \\ \mathbf{u}_{i+1-k_{\max}} \end{bmatrix} = \mathbf{D}_i \begin{bmatrix} \mathbf{u}_i \\ \mathbf{u}_{i-1} \\ \mathbf{u}_{i-2} \\ \vdots \\ \mathbf{u}_{i-k_{\max}} \end{bmatrix}, \tag{20}$$

where $k_{\max}$ denotes the maximum value of $k_{l,j}$, and matrix $\mathbf{D}_i$ can be expressed as follows:

$$\mathbf{D}_i = \begin{bmatrix} \mathbf{M}_{11}^i & \mathbf{M}_{12}^i & \mathbf{M}_{13}^i & \mathbf{M}_{14}^i & \cdots & 0 & 0 & 0 \\ \mathbf{I} & 0 & 0 & 0 & \cdots & 0 & 0 & 0 \\ 0 & \mathbf{I} & 0 & 0 & \cdots & 0 & 0 & 0 \\ \vdots & \vdots & \vdots & \vdots & \vdots & \vdots & \vdots & \vdots \\ 0 & 0 & 0 & 0 & 0 & 0 & \mathbf{I} & 0 \end{bmatrix} + \sum_{j=1}^{N}\sum_{l=1}^{L}\begin{bmatrix} 0 & \cdots & \mathbf{M}_{1,k_{l,j}}^i & \mathbf{M}_{1,k_{l,j}+1}^i & \cdots & 0 \\ 0 & \cdots & 0 & 0 & 0 & 0 \\ 0 & \cdots & 0 & 0 & 0 & 0 \\ \vdots & \vdots & \vdots & \vdots & \vdots & \vdots \\ 0 & \cdots & 0 & 0 & \cdots & 0 \end{bmatrix}, \tag{21}$$

where

$$\begin{aligned}
\mathbf{M}_{11}^{i} &= \mathbf{P}_i\left(\mathbf{F}_0 + \sum_{j=1}^{N}\sum_{l=1}^{L}\left(\mathbf{G}_{17}\mathbf{B}_i^{\langle l,j\rangle} + \mathbf{G}_{18}\mathbf{B}_{i+1}^{\langle l,j\rangle}\right)\right),\\
\mathbf{M}_{12}^{i} &= \mathbf{P}_i\left(\sum_{j=1}^{N}\sum_{l=1}^{L}\left(\mathbf{G}_{15}\mathbf{B}_i^{\langle l,j\rangle} + \mathbf{G}_{16}\mathbf{B}_{i+1}^{\langle l,j\rangle}\right)\right),\\
\mathbf{M}_{13}^{i} &= \mathbf{P}_i\left(\sum_{j=1}^{N}\sum_{l=1}^{L}\left(\mathbf{G}_{13}\mathbf{B}_i^{\langle l,j\rangle} + \mathbf{G}_{14}\mathbf{B}_{i+1}^{\langle l,j\rangle}\right)\right),\\
\mathbf{M}_{14}^{i} &= \mathbf{P}_i\left(\sum_{j=1}^{N}\sum_{l=1}^{L}\left(\mathbf{G}_{11}\mathbf{B}_i^{\langle l,j\rangle} + \mathbf{G}_{12}\mathbf{B}_{i+1}^{\langle l,j\rangle}\right)\right),\\
\mathbf{M}_{1,k_{l,j}}^{i} &= -\mathbf{P}_i\left(\mathbf{G}_{23}\mathbf{B}_i^{\langle l,j\rangle} + \mathbf{G}_{24}\mathbf{B}_{i+1}^{\langle l,j\rangle}\right),\\
\mathbf{M}_{1,k_{l,j}+1}^{i} &= -\mathbf{P}_i\left(\mathbf{G}_{21}\mathbf{B}_i^{\langle l,j\rangle} + \mathbf{G}_{22}\mathbf{B}_{i+1}^{\langle l,j\rangle}\right).
\end{aligned} \tag{22}$$

The positions of the matrices $\mathbf{M}_{1,k_{l,j}}^{i}$ and $\mathbf{M}_{1,k_{l,j}+1}^{i}$ in equation (21) depend on the value of $k_{l,j}$ related to the time delay $\tau_{l,j}$. As for the two-degree-of-freedom milling system, the matrix $\mathbf{M}_{1,k_{l,j}}^{i}$ is located in columns $(4k_{l,j}-3)$ to $(4k_{l,j})$ of the matrix $\mathbf{D}_i$, and the matrix $\mathbf{M}_{1,k_{l,j}+1}^{i}$ is located in columns $(4k_{l,j}+1)$ to $(4k_{l,j}+4)$ of the matrix $\mathbf{D}_i$. Additionally, the dimension of the matrix $\mathbf{D}_i$ depends on the value of $k_{\max}$.

Then, the Floquet state transition matrix $\boldsymbol{\psi}$ is obtained as

$$\boldsymbol{\psi} = \mathbf{D}_{k-1}\mathbf{D}_{k-2}\ldots\mathbf{D}_0. \tag{23}$$

According to Floquet theory, the stability of the milling system can be determined using the criterion expressed by equation (24). The Matlab code for the stability analysis by using the 4th EFDM is in Appendix:

$$\max\left(|\mathrm{eig}(\boldsymbol{\psi})|\right)\begin{cases} < 1, & \text{stable},\\ = 1, & \text{critical stable},\\ > 1, & \text{unstable}.\end{cases} \tag{24}$$

4. Stability Analysis

The two-degree-of-freedom milling system is employed for verifying the accuracy and efficiency of the extended FDMs. The rate of convergence and computational time are analyzed for the study of accuracy and efficiency, respectively. The parameters are chosen as the same as those used in the literature [28]. The detailed parameters are as follows: the number of cutter teeth is $N = 4$, the diameter of the cutter is 19.05 mm, the modal masses are $m_x = 1.4986$ kg and $m_y = 1.199$ kg, the damping ratios are $\zeta_x = 0.055801$ and $\zeta_y = 0.025004$, the angular natural frequencies are $\omega_{nx} = 3540.89$ rad/s and $\omega_{ny} = 3243.44$ rad/s, and the tangential and the normal cutting force coefficients are $K_t = 697$ MPa and $K_n = 256$ MPa, down-milling.

4.1. Rate of Convergence. The rate of convergence is used to estimate the local error between the absolute value of the maximum-magnitude eigenvalue of the system $|\mu(k)|$ and the reference eigenvalue μ_0. In this section, the parameter combinations ($\Omega = 6000$ rpm, $a_p = 0.5$ mm) and ($\Omega = 7000$ rpm, $a_p = 2$ mm) are employed to analyze the rates of convergence of the extended FDMs. The radial immersion ratio is set as $a/D = 1$, the pitch angle combination of the cutter is $\mathbf{P} = [70^\circ, 110^\circ, 70^\circ, 110^\circ]$, and the corresponding helix angle combination is $\boldsymbol{\beta} = [30^\circ, 35^\circ, 30^\circ, 35^\circ]$. The axial depth of cut is discretized into 20 axial layers, that is, $L = 20$. To determine the reference eigenvalues for the adopted parameter combinations, the convergences of the eigenvalues obtained by different methods are studied, as shown in Figure 1.

It is seen from Figure 1 that the ISDA, 2nd EFDM, 3rd EFDM, and 4th EFDM all converge to the same reference value when the parameter k reaches 800. In this study, the reference eigenvalue μ_0 is determined by using the 2nd EFDM with $k = 800$. It should be noted that the reference eigenvalue μ_0 can also be determined by using the ISDA, 3rd EFDM, and 4th EFDM since all methods converge to the same reference value. After calculation, the reference eigenvalues for the parameter combinations ($\Omega = 6000$ rpm and $a_p = 0.5$ mm) and ($\Omega = 7000$ rpm and $a_p = 2$ mm) are 0.483935 and 0.955073, respectively.

In practice, the calculation burden will increase severely when the parameter k is chosen as a very large value. Therefore, the parameter k is usually smaller than that used to determine the value of μ_0. With the aim of estimating the rate of convergence of the extended FDMs, the rate of convergence of the improved semidiscretization algorithm (ISDA) [28] is taken as the benchmark. Figure 2 illustrates the rates of convergence of the ISDA, 2nd EFDM, 3rd EFDM, and 4th EFDM with different values of parameter k.

From Figure 2, it is found that the difference between the approximated eigenvalues and the ideals ones calculated by the ISDA has more significant fluctuation than that calculated by the 2nd EFDM, 3rd EFDM, and 4th EFDM. Besides, the eigenvalues obtained by the 2nd EFDM, 3rd EFDM, and 4th EFDM converge to a constant when the parameter k is equal to 300, while the eigenvalues obtained by the ISDA do not converge to a constant under the same condition. It is also seen from Figure 2 that the 2nd EFDM, 3rd EFDM, and 4th EFDM converge faster than the ISDA. The analysis results indicate that the 2nd EFDM, 3rd EFDM, and 4th EFDM are more robust and accurate than the benchmark method.

According to Figure 2, it is also indicated that there is no significant difference between the 2nd EFDM, 3rd EFDM, and 4th EFDM in terms of the rate of convergence. It is difficult to evaluate the accuracy of different extended FDMs by using the rates of convergence of limited parameter combinations. In the following section, the accuracy of different extended FDMs is further studied by taking the stability lobe diagrams into consideration.

4.2. Stability Lobe Diagrams. To verify the effectiveness of the 2nd EFDM, 3rd EFDM, and 4th EFDM, the time-averaged SDM suggested by Sims et al. [20] and the extended SDM suggested by Jin et al. [25] are taken for comparison. The parameters derived from the literature [20] are used for

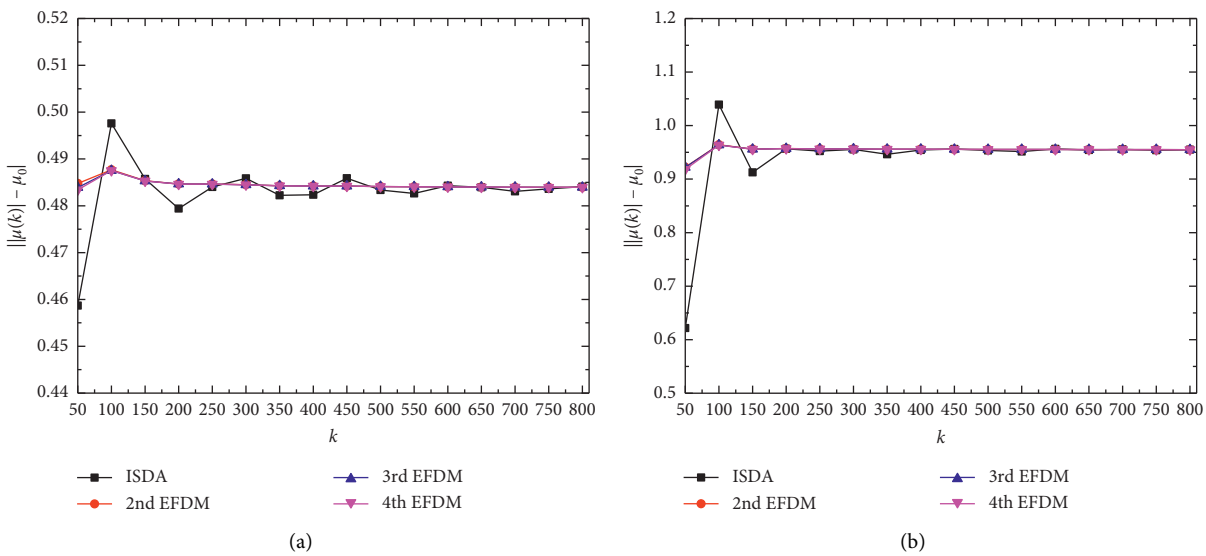

Figure 1: The convergences of the eigenvalues obtained by ISDA, 2nd EFDM, 3rd EFDM, and 4th EFDM: (a) $\Omega = 6000$ rpm and $a_p = 0.5$ mm; (b) $\Omega = 7000$ rpm and $a_p = 2.0$ mm.

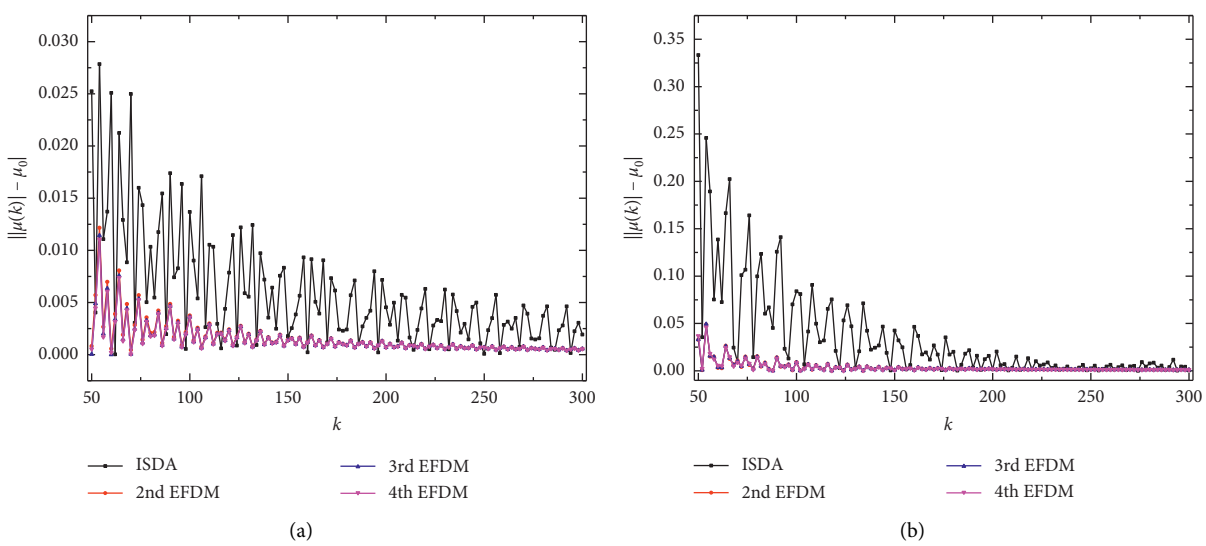

Figure 2: Rates of convergence of the ISDA, 2nd EFDM, 3rd EFDM, and 4th EFDM: (a) $a_p = 0.5$ mm, $\Omega = 6000$ rpm, and $|\mu_0| = 0.483935$; (b) $a_p = 2$ mm, $\Omega = 7000$ rpm, and $|\mu_0| = 0.955073$.

analysis. The stability lobe diagrams obtained by the time-averaged SDM, the extended SDM, the 2nd EFDM, 3rd EFDM, and 4th EFDM are described in Figure 3.

As shown in Figure 3, the parameter combinations A ($\Omega = 8500$ rpm and $a_p = 5$ mm) and B ($\Omega = 8500$ rpm and $a_p = 7$ mm) are considered. In the literature [21], the parameter combinations A and B are proved to be a stable case and an unstable case through time-domain simulations, respectively. However, in the stability lobe diagram obtained by the time-averaged SDM, the parameter combination A corresponds to an unstable situation. That is, the time-averaged SDM cannot predict the stability correctly when the spindle speed ranges from 8000 rpm to 9000 rpm. It is seen from Figure 3 that the stabilities of parameter combinations A and B are correctly predicted in the stability lobe diagrams obtained by the 2nd EFDM, 3rd EFDM, and 4th EFDM. Additionally, the stability lobe diagrams obtained by the extended FDMs agree well with that obtained by the extended SDM [25]. Therefore, the 2nd EFDM, 3rd EFDM, and 4th EFDM are proved to be effective methods.

The computational time consumed by the 2nd EFDM, 3rd EFDM, and 4th EFDM is compared with that consumed by enhanced multistage homotopy perturbation method (EMHPM) [22] and to illustrate the efficiencies of the extended FDMs. In the calculation process, the pitch angle combination of the cutter is $\mathbf{P} = [70^\circ, 110^\circ, 70^\circ, 110^\circ]$, and the corresponding helix angle combination is $\boldsymbol{\beta} = [30^\circ, 35^\circ, 30^\circ, 35^\circ]$. The parameter plane, which includes the parameter combinations of spindle speed and axial depth

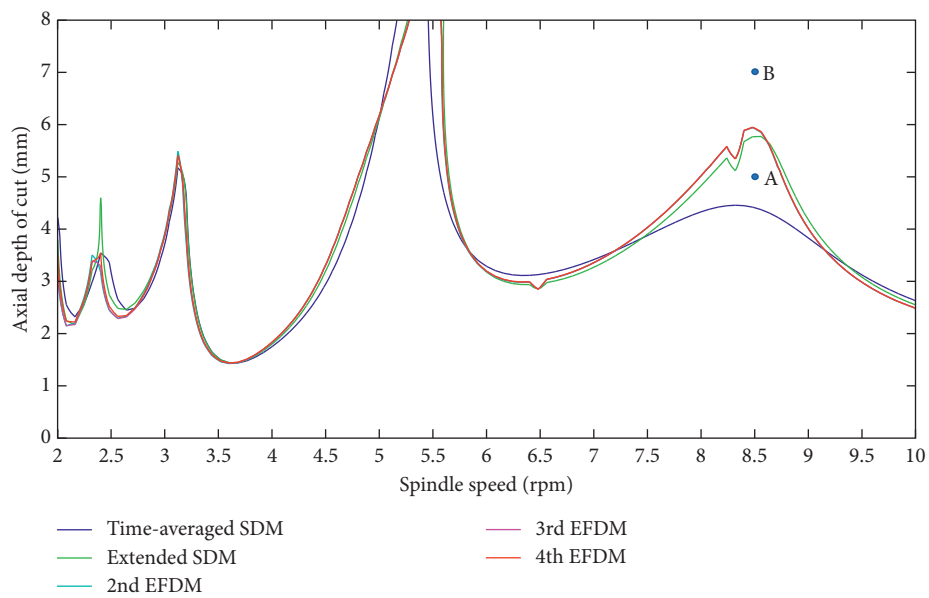

Figure 3: Stability lobe diagrams obtained by the time-averaged SDM [20], the extended SDM [25], and the 2nd EFDM, 3rd EFDM, and 4th EFDM.

Table 1: Stability lobe diagrams obtained by the EMHPM, 2nd EFDM, 3rd EFDM, and 4th EFDM under full immersion condition ($a/D = 1$).

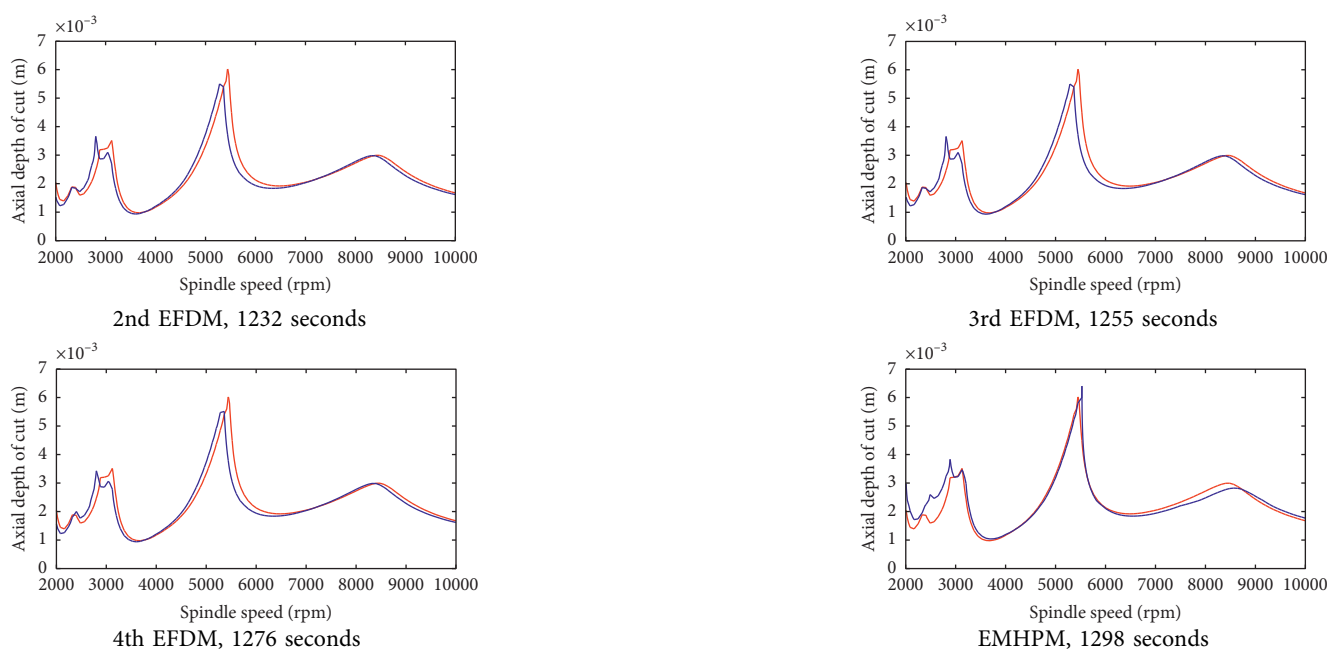

of cut, is divided into a 100×100 size grid. The spindle speed ranges from 2×10^3 rpm to 10×10^3 rpm, and the axial depth of cut ranges from 0 mm to 20 mm. The parameter k is chosen as 80, and the axial depth of cut is discretized into 10 axial layers, that is, $L = 10$. The referenced stability lobe diagrams denoted by the red line are obtained by the 2nd EFDM with $k = 300$. The stability lobe diagrams obtained by the EMHPM, 2nd EFDM, 3rd EFDM, and 4th EFDM as well as the corresponding computational time under full immersion condition ($a/D = 1$) are shown in Table 1.

It is seen from Table 1 that the stability lobe diagrams calculated by the EMHPM, 2nd EFDM, 3rd EFDM, and 4th EFDM are consistent with the referenced ones. The results

Table 2: Stability lobe diagrams obtained by the 2nd EFDM, 3rd EFDM, and 4th EFDM under half immersion ($a/D = 0.5$) and low immersion ($a/D = 0.1$) conditions.

	$a/D = 0.5$	$a/D = 0.1$
2nd EFDM	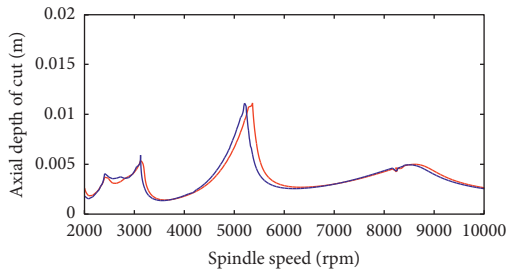	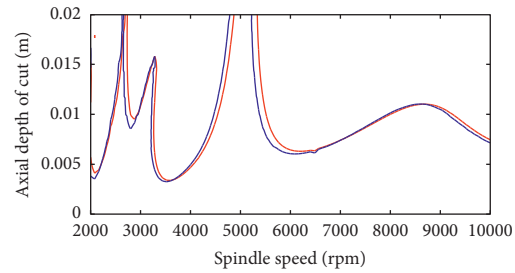
3rd EFDM	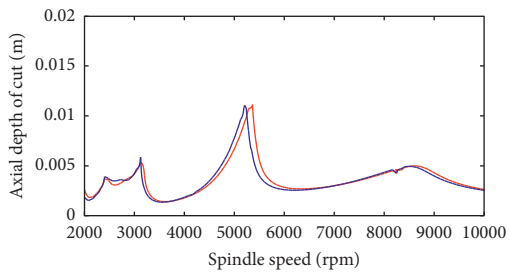	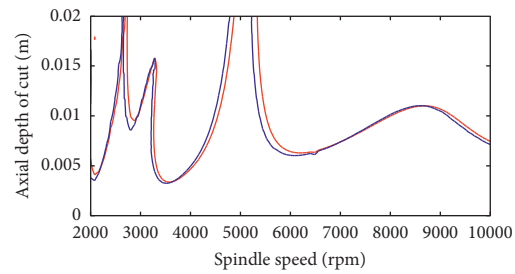
4th EFDM	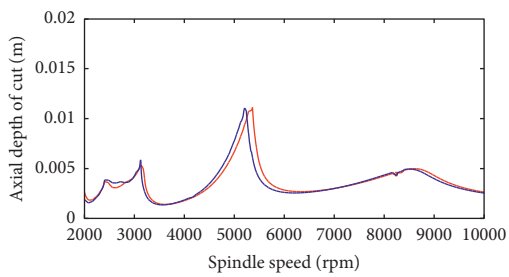	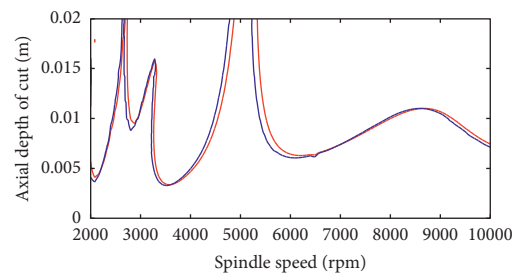

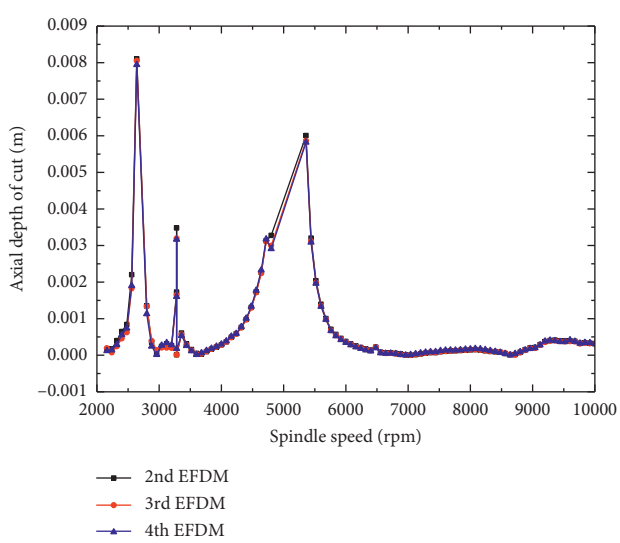

(a)

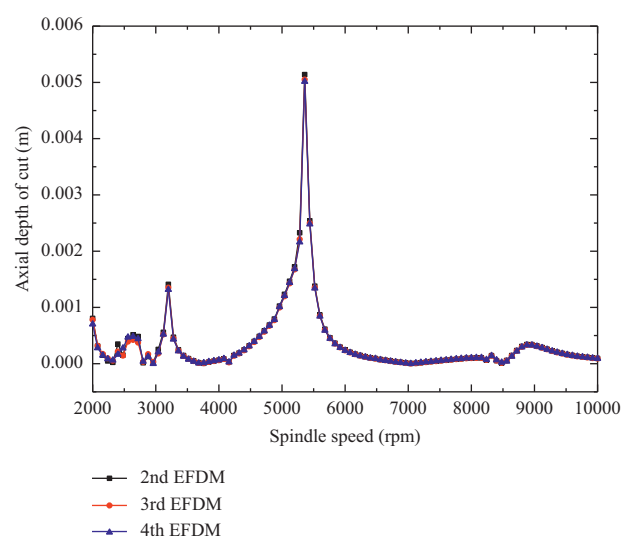

(b)

Figure 4: Continued.

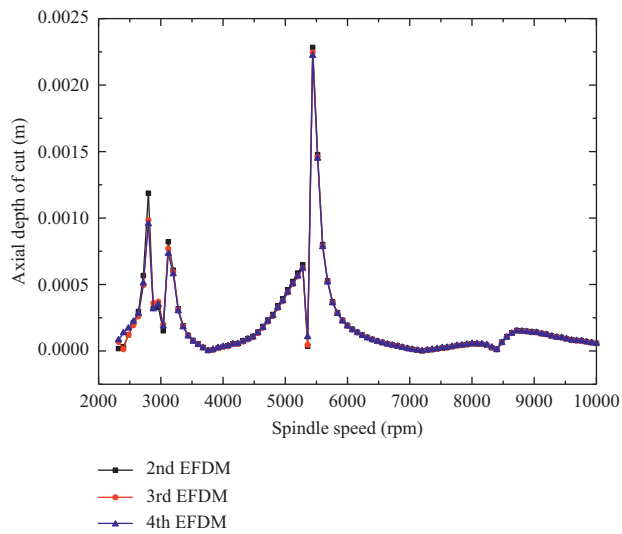

(c)

Figure 4: Difference between the curves obtained by different EFDMs and the reference curve: (a) $a/D = 0.1$; (b) $a/D = 0.5$; (c) $a/D = 1.0$.

indicate that all these methods are effective in predicting the stability of milling with variable pitch and variable helix cutters. As for the computational time, it is seen from Table 1 that the 4th EFDM takes more time than the 2nd EFDM and 3rd EFDM to obtain stability lobe diagrams. The calculation time depends on the number of matrices. More computing time is needed for calculating more matrices. The higher the order of the method is, the more the matrixes there are. Therefore, 4th EFDM takes more time than the other extended methods.

The computational time consumed by extended FDMs is also compared with that consumed by the enhanced multistage homotopy perturbation method (EMHPM). Although more matrixes need to be calculated in the 4th EFDM, one more calculation cycle related to expansion order needs to be calculated in the EMHPM. Generally, the EMHPM takes a little more time to obtain stability lobe diagrams.

To further evaluate the different EFDMs, the stability lobe diagrams under low immersion condition ($a/D = 0.1$) and half immersion ($a/D = 0.5$) are also obtained, as shown in Table 2.

For comparison, the difference between the curves obtained by different EFDMs and the reference curve is also presented, as shown in Figure 4.

As shown in Figure 4, it can be seen that the difference between the curves obtained by different EFDMs and the reference curve is very small. This result is consistent with the conclusion mentioned above that there is no significant difference between the 2nd EFDM, 3rd EFDM, and 4th EFDM in terms of convergence rate. Therefore, there is no need to extend hypersecond FDMs to analyze the stability in milling with variable pitch and variable helix tools. Besides, higher-order methods require a more computational cost.

5. Conclusions

In this work, the high-order full-discretization methods are extended for stability analysis of milling with variable pitch and variable helix tools. The two-degree-of-freedom milling system is employed to validate the extended methods. The following conclusions can be drawn:

(1) The 2nd EFDM, 3rd EFDM, and 4th EFDM are compared with the benchmark method in terms of the rate of convergence. It is found that the 2nd EFDM, 3rd EFDM, and 4th EFDM converge faster than the benchmark method.

(2) The 4th EFDM takes more time than the 2nd EFDM and 3rd EFDM to obtain stability lobe diagrams. Besides, the EMHPM takes a little more time than the 4th EFDM to obtain stability lobe diagrams.

(3) The difference between the curves obtained by different EFDMs and the reference curve is very small. There is no need to extend hypersecond FDMs to analyze the stability of milling with variable pitch and variable helix tools.

Appendix

Matlab code for the stability analysis by using the 4th EFDM.

```
close all; clear all; clc
N = 4; % number of tool teeth
R = 0.009525; % radius (m)
P = [70*pi/180,110*pi/180,70*pi/180,110*pi/180]; % pitch angle combination
beta = [30*pi/180,35*pi/180,30*pi/180,35*pi/180]; % helix angle combination
aD = 1.0; % radial immersion ratio a/D
Kt = 6.97e8; % tangential cutting force coefficient (N/m^2)
Kn = 2.56e8; % normal cutting force coefficient (N/m^2)
```

```
wnx = 563.55*2*pi; % angular natural frequency (rad/s)
wny = 516.21*2*pi; % angular natural frequency (rad/s)
m_tx = 1.4986; % mass in x direction (kg)
m_ty = 1.199; % mass in y direction (kg)
zeta_x = 0.055801; % relative damping in x direction
zeta_y = 0.025004; % relative damping in y direction
up_or_down = −1; % l:up-milling, −l:down-milling
if up_or_down = = 1 % up-milling
   fist = 0; % start angle
   fiex = acos(1−2*aD); % exit angle
elseif up_or_down = = −1% down-milling
   fist = acos(2*aD−1); % start angle
   fiex = pi; % exit angle
end
stx = 100; % steps of spindle speed
sty = 100; % steps of depth of cut
w_st = 0e-3; % starting depth of cut (m)
w_fi = 20e-3; % final depth of cut (m)
o_st = 2e3; % starting spindle speed (m)
o_fi = 10e3; % final spindle speed (rpm)
k = 100; % discrete number for spindle speed
L = 10; % discrete number for axial depth of cut
dtr = 2*pi/k;
intk = 10;
for y = 1:sty + 1
   w(y) = w_st + (y−1)*(w_fi-w_st)/sty;
   for i = 1:k + 1
      h2xx(y, i) = 0;
      h2xy(y, i) = 0;
      h2yx(y,i) = 0;
      h2yy(y,i) = 0;
      ti = i*dtr;
      pitch = 0;
      for j = 1 : N
         h1xx(y,i,j) = 0;
         h1xy(y,i,j) = 0;
         h1yx(y,i,j) = 0;
         h1yy(y,i,j) = 0;
         if j = = 1
            pitch = 0;
         else
            pitch = pitch + P(j);
         end
         for n = 1 : L
            hxx(y,i,j,n) = 0;
            hxy(y,i,j,n) = 0;
            hyx(y,i,j,n) = 0;
            hyy(y,i,j,n) = 0;
            if j = = 1
               dt_helix = (n−1/2)*(w(y)/L)*(tan(beta(j))−
tan(beta(N)))/R;
else
dt_helix=(n−1/2)*(w(y)/L)*(tan(beta(j))−
tan(beta(j−1)))/R;
end
dt_phi(y,j,n) = P(j) + dt_helix;
l_max = fix((max(max(max(dt_phi)))+dtr/2)/dtr);
for hh = 1:intk
   fi = ti-pitch-(n−1)*(w(y)/L)*tan(beta(j))/R + hh*dtr/
intk;
   fi = mod(fi,2*pi);
   if (fi ≥ fist)*(fi ≤ fiex)
      g = 1;
   else
      g = 0;
end
hxx(y,i,j,n) = hxx(y,i,j,n) + g*(Kt*cos(fi) + Kn*sin(fi))*
sin(fi)*(w(y)/L)/intk;
hxy(y,i,j,n) = hxy(y,i,j,n) + g*(Kt*cos(fi) + Kn*sin(fi))*
cos(fi)*(w(y)/L)/intk;
hyx(y,i,j,n) = hyx(y,i,j,n) + g*(−Kt*sin(fi) + Kn*cos(fi))*
sin(fi)*(w(y)/L)/intk;
hyy(y,i,j,n) = hyy(y,i,j,n) + g*(−Kt*sin(fi) + Kn*cos(fi))*
cos(fi)*(w(y)/L)/intk;
end
h1xx(y,i,j) = h1xx(y,i,j) + hxx(y,i,j,n);
h1xy(y,i,j) = h1xy(y,i,j) + hxy(y,i,j,n);
h1yx(y,i,j) = h1yx(y,i,j) + hyx(y,i,j,n);
h1yy(y,i,j) = h1yy(y,i,j) + hyy(y,i,j,n);
end
h2xx(y,i) = h2xx(y,i) + h1xx(y,i,j);
h2xy(y,i) = h2xy(y,i) + h1xy(y,i,j);
h2yx(y,i) = h2yx(y,i) + h1yx(y,i,j);
h2yy(y,i) = h2yy(y,i) + h1yy(y,i,j);
      end
   end
end
A = [0 0 1 0; 0 0 0 1; −wnx^2 0−2*zeta_x*wnx 0; 0 −wny^2
0−2*zeta_y*wny];
invA = inv(A);
I = eye(4,4);
for x = 1:stx + 1
   o = o_st + (x−1)*(o_fi-o_st)/stx;
   T = 60/o; % spindle rotational period
   dt = T/k; % time step
```

```
F0 = expm(A*dt);
F1 = (F0–I)*invA;
F2 = (F1–dt*I)*invA;
F3 = (2*F2–df2*I)*invA;
F4 = (3*F3–df3*I)*invA;
F5 = (4*F4–df4*I)*invA;
F6 = (5*F5–df5*I)*invA;
G11 = (–1/24)/(df5)*F6–1/(24*df4)*F5 + 1/(8*df3)*F4 + 1/(24*df2)*F3–1/(12*dt)*F2;
G12 = (1/24)/(df5)*F6 + 1/(12*df4)*F5–1/(24*df3)*F4–1/(12*df2)*F3;
G13 = (1/6)/(df5)*F6 + 1/(3*df4)*F5–2/(3*df3)*F4–1/(3*df2)*F3 + 1/(2*dt)*F2;
G14 = (–1/6)/(df5)*F6–1/(2*df4)*F5 + 1/(6*df3)*F4 + 1/(2*df2)*F3;
G15 = (–1/4)/(df5)*F6–3/(4*df4)*F5 + 3/(4*df3)*F4 + 7/(4*df2)*F3–3/(2*dt)*F2;
G16 = (1/4)/(df5)*F6 + 1/(df4)*F5 + 1/(4*df3)*F4–3/(2*df2)*F3;
G17 = (1/6)/(df5)*F6 + 2/(3*df4)*F5–5/(3*df2)*F3–1/(6*dt)*F2 + F1;
G18 = (–1/6)/(df5)*F6–5/(6*df4)*F5–5/(6*df3)*F4 + 5/(6*df2)*F3 + 1/(dt)*F2;
G19 = (–1/24)/(df5)*F6–5/(24*df4)*F5–5/(24*df3)*F4 + 5/(24*df2)*F3 + 1/(4*dt)*F2;
G110 = (1/24)/(df5)*F6 + 1/(4*df4)*F5 + 11/(24*df3)*F4 + 1/(4*df2)*F3;
for y = 1 : sty + 1 % sweeping depth of cuts
  FFi = eye(4*l_max + 4,4*l_max + 4); % construct transition matrix FFi
  for i = 1 : k
    Ai = [0,0,0,0; 0,0,0,0; -h2xx(y,i)/m_tx,-h2xy(y,i)/m_tx,0,0; -h2yx(y,i)/m_ty,-h2yy(y,i)/m_ty,0,0];
    Aii = [0,0,0,0; 0,0,0,0; -h2xx(y,i + 1)/m_tx,-h2xy(y,i + 1)/m_tx,0,0; -h2yx(y,i + 1)/m_ty,-h2yy(y,i + 1)/m_ty,0,0];
    Pi = inv(I–G110*Aii–G19*Ai); %x(i + 1)
    M11 = Pi*(F0 + G18*Aii + G17*Ai); % X(i)
    M12 = Pi*(G16*Aii + G15*Ai); % X(i–1)
    M13 = Pi*(G14*Aii + G13*Ai); % X(i–2)
    M14 = Pi*(G12*Aii + G11*Ai); % X(i–3)
    D1 = zeros(4*l_max + 4,4*l_max+4);
    vlow1 = ones(4*l_max,1);
    D1 = D1 + diag(vlow1,–4);
    D1(1 : 4,1 : 4) = M11;
    D1(1 : 4,5 : 8) = M12;
    D1(1 : 4,9 : 12) = M13;
    D1(1 : 4,13 : 16) = M14;
    M2 = zeros(4∗l_max + 4,4 l_max + 4);
    for j = 1 : N
  D2 = zeros(4*l_max + 4,4*l_max + 4);
  for n = 1 : L
    Bi = [0,0,0,0; 0,0,0,0; -hxx(y,i,j,n)/m_tx,-hxy(y,i,j,n)/m_tx,0,0; -hyx(y,i,j,n)/m_ty,-hyy(y,i,j,n)/m_ty,0,0];
    Bii = [0,0,0,0; 0,0,0,0; -hxx(y,i + 1,j,n)/m_tx,-hxy(y,i + 1,j,n)/m_tx,0,0; -hyx(y,i + 1,j,n)/m_ty,-hyy(y,i + 1,j,n)/m_ty,0,0];
    D3 = zeros(4*l_max + 4,4*l_max + 4);
    s = fix((dt_phi(y,j,n) + 0.5*dtr)/dtr);
    w_a = (s*dtr + 0.5*dtr-dt_phi(y,j,n))/dtr;
    G21 = F3/(df2) + (–2/dt + w_a/dt)*F2 + (–w_a+1)*F1; %x(i–k)B(i)
    G22 = –F3/(df2) + (1/dt–w_a/dt)*F2; %x(i–k)B(i + 1)
    G23 = –F3/(df2) + (1/dt–w_a/dt)*F2 + w_a*F1; %x(i–k + 1)B(i)
    G24 = F3/(df2) + (w_a/dt)*F2; %x(i–k + 1)(i + 1)
    Fi_lj = G21*Bi + G22*Bii;
    Pi_lj = G23*Bi + G24*Bii;
    D3(1 : 4,(4*s-3):4*s) = –Pi*Pi_lj;
    D3(1 : 4,(4*s + 1):4*s + 4) = –Pi*Fi_lj;
    D2 = D2 + D3;
  end
  M2 = M2 + D2;
    end
    D = D1 + M2;
    FFi = D*FFi;
  end
  ss(x,y) = o; % matrix of spindle speeds
  dc(x,y) = w(y); % matrix of depth of cuts
  ei(x,y) = max(abs(eig(FFi))); % matrix of eigenvalues
 end % End of sweeping depth of cuts
 stx + 1–x
end
figure;
contour (ss,dc,ei, [1,1], "k"), xlabel("(rmp)"), ylabel("w(m)")
```

Data Availability

The data used to support the findings of this study are included within the article.

Conflicts of Interest

The authors declare that they have no conflicts of interest.

Acknowledgments

This research was funded by the Special Fund for Talents of Gansu Agricultural University (Grant nos. GAU-KYQD-2018-29, 2017RCZX-21, and 2017RCZX-35).

References

[1] Y. Altintas and E. Budak, "Analytical prediction of stability lobes in milling," *CIRP Annals-Manufacturing Technology*, vol. 44, no. 1, pp. 357–362, 1995.

[2] S. D. Merdol and Y. Altintas, "Multi frequency solution of chatter stability for low immersion milling," *Journal of Manufacturing Science and Engineering*, vol. 126, no. 3, pp. 459–466, 2004.

[3] P. V. Bayly, J. E. Halley, B. P. Mann, and M. A. Davies, "Stability of interrupted cutting by temporal finite element analysis," *Journal of Manufacturing Science and Engineering*, vol. 125, no. 2, pp. 220–225, 2003.

[4] E. A. Butcher, O. A. Bobrenkov, E. Bueler, and P. Nindujarla, "Analysis of milling stability by the Chebyshev collocation method: algorithm and optimal stable immersion levels," *Journal of Computational and Nonlinear Dynamics*, vol. 4, no. 3, Article ID 031003, 2009.

[5] T. Insperger and G. Stépán, "Updated semi-discretization method for periodic delay-differential equations with discrete delay," *International Journal for Numerical Methods in Engineering*, vol. 61, no. 1, pp. 117–141, 2004.

[6] T. Insperger, G. Stépán, and J. Turi, "On the higher-order semi-discretizations for periodic delayed systems," *Journal of Sound and Vibration*, vol. 313, no. 1-2, pp. 334–341, 2008.

[7] Y. Ding, L. Zhu, X. Zhang, and H. Ding, "A full-discretization method for prediction of milling stability," *International Journal of Machine Tools and Manufacture*, vol. 50, no. 5, pp. 502–509, 2010.

[8] Y. Ding, L. Zhu, X. Zhang, and H. Ding, "Second-order full-discretization method for milling stability prediction," *International Journal of Machine Tools and Manufacture*, vol. 50, no. 10, pp. 926–932, 2010.

[9] Q. Guo, Y. Sun, and Y. Jiang, "On the accurate calculation of milling stability limits using third-order full-discretization method," *International Journal of Machine Tools and Manufacture*, vol. 62, pp. 61–66, 2012.

[10] C. G. Ozoegwu, "Least squares approximated stability boundaries of milling process," *International Journal of Machine Tools and Manufacture*, vol. 79, pp. 24–30, 2014.

[11] C. G. Ozoegwu, S. N. Omenyi, and S. M. Ofochebe, "Hyper-third order full-discretization methods in milling stability prediction," *International Journal of Machine Tools and Manufacture*, vol. 92, pp. 1–9, 2015.

[12] Y. Ding, L. M. Zhu, X. J. Zhang, and H. Ding, "Numerical integration method for prediction of milling stability," *Journal of Manufacturing Science and Engineering*, vol. 133, no. 3, Article ID 031005, 2011.

[13] Y. Ding, L. M. Zhu, X. J. Zhang, and H. Ding, "Stability analysis of milling via the differential quadrature method," *Journal of Manufacturing Science and Engineering*, vol. 135, no. 4, Article ID 044502, 2013.

[14] J. Niu, Y. Ding, L. Zhu, and H. Ding, "Runge-Kutta methods for a semi-analytical prediction of milling stability," *Nonlinear Dynamics*, vol. 76, no. 1, pp. 289–304, 2014.

[15] H. Li, Y. Dai, and Z. Fan, "Improved precise integration method for chatter stability prediction of two-DOF milling system," *The International Journal of Advanced Manufacturing Technology*, vol. 101, no. 5-8, pp. 1235–1246, 2019.

[16] Z. Zhang, H. Li, G. Meng, and C. Liu, "A novel approach for the prediction of the milling stability based on the Simpson method," *International Journal of Machine Tools and Manufacture*, vol. 99, pp. 43–47, 2015.

[17] X. Zhang, C. Xiong, Y. Ding, and H. Ding, "Prediction of chatter stability in high speed milling using the numerical differentiation method," *The International Journal of Advanced Manufacturing Technology*, vol. 89, no. 9-12, pp. 2535–2544, 2017.

[18] D. Olvera, G. Urbikain, A. Elías-Zuñiga, and L. López de Lacalle, "Improving stability prediction in peripheral milling of Al7075T6," *Applied Sciences*, vol. 8, no. 8, p. 1316, 2018.

[19] Y. Altıntas, S. Engin, and E. Budak, "Analytical stability prediction and design of variable pitch cutters," *Journal of Manufacturing Science and Engineering*, vol. 121, no. 2, pp. 173–178, 1999.

[20] N. D. Sims, B. Mann, and S. Huyanan, "Analytical prediction of chatter stability for variable pitch and variable helix milling tools," *Journal of Sound and Vibration*, vol. 317, no. 3-5, pp. 664–686, 2008.

[21] V. Sellmeier and B. Denkena, "Stable islands in the stability chart of milling processes due to unequal tooth pitch," *International Journal of Machine Tools and Manufacture*, vol. 51, no. 2, pp. 152–164, 2011.

[22] F. I. Compeán, D. Olvera, F. J. Campa, L. N. López de Lacalle, A. Elías-Zúñiga, and C. A. Rodríguez, "Characterization and stability analysis of a multivariable milling tool by the enhanced multistage homotopy perturbation method," *International Journal of Machine Tools and Manufacture*, vol. 57, pp. 27–33, 2012.

[23] M. Wan, W.-H. Zhang, J.-W. Dang, and Y. Yang, "A unified stability prediction method for milling process with multiple delays," *International Journal of Machine Tools and Manufacture*, vol. 50, no. 1, pp. 29–41, 2010.

[24] G. Jin, Q. Zhang, H. Qi, and B. Yan, "A frequency-domain solution for efficient stability prediction of variable helix cutters milling," *Proceedings of the Institution of Mechanical Engineers, Part C: Journal of Mechanical Engineering Science*, vol. 228, no. 15, pp. 2702–2710, 2014.

[25] G. Jin, Q. Zhang, S. Hao, and Q. Xie, "Stability prediction of milling process with variable pitch and variable helix cutters," *Proceedings of the Institution of Mechanical Engineers, Part C: Journal of Mechanical Engineering Science*, vol. 228, no. 2, pp. 281–293, 2014.

[26] Q. Guo, Y. Jiang, B. Zhao, and P. Ming, "Chatter modeling and stability lobes predicting for non-uniform helix tools," *The International Journal of Advanced Manufacturing Technology*, vol. 87, no. 1-4, pp. 251–266, 2016.

[27] N. D. Sims, "Fast chatter stability prediction for variable helix milling tools," *Proceedings of the Institution of Mechanical Engineers, Part C: Journal of Mechanical Engineering Science*, vol. 230, no. 1, pp. 133–144, 2016.

[28] Y. Wang, T. Wang, Z. Yu, Y. Zhang, Y. Wang, and H. Liu, "Chatter prediction for variable pitch and variable helix milling," *Shock and Vibration*, vol. 2015, Article ID 419172, 9 pages, 2015.

[29] J. Niu, Y. Ding, L. Zhu, and H. Ding, "Mechanics and multi-regenerative stability of variable pitch and variable helix milling tools considering runout," *International Journal of Machine Tools and Manufacture*, vol. 123, pp. 129–145, 2017.

[30] T. Huang, L. Zhu, S. Du, Z. Chen, and H. Ding, "Robust active chatter control in milling processes with variable pitch cutters," *Journal of Manufacturing Science and Engineering*, vol. 140, Article ID 101005, 2018.

[31] G. Stepan, D. Hajdu, A. Iglesias, D. Takacs, and Z. Dombovari, "Ultimate capability of variable pitch milling cutters," *CIRP Annals*, vol. 67, no. 1, pp. 373–376, 2018.

[32] J. Huang, P. Deng, H. Li, and B. Wen, "Stability analysis for milling system with variable pitch cutters under variable speed," *Journal of Vibroengineering*, vol. 21, no. 2, pp. 331–347, 2019.

[33] D. Chen, X. Zhang, Y. Xie, X. Zhang, and H. Ding, "A unified analytical cutting force model for variable helix end mills," *The International Journal of Advanced Manufacturing Technology*, vol. 92, no. 9-12, pp. 3167–3185, 2017.

[34] A. Otto, S. Rauh, S. Ihlenfeldt, and G. Radons, "Stability of milling with non-uniform pitch and variable helix tools," *The International Journal of Advanced Manufacturing Technology*, vol. 89, no. 9-12, pp. 2613–2625, 2017.

[35] Q. Guo, B. Zhao, Y. Jiang, and W. Zhao, "Cutting force modeling for non-uniform helix tools based on compensated chip thickness in five-axis flank milling process," *Precision Engineering*, vol. 51, pp. 659–681, 2018.

[36] S. Cai, B. Yao, W. Feng, Z. Cai, B. Chen, and Z. He, "Milling process simulation for the variable pitch cutter based on an integrated process-machine model," *The International Journal of Advanced Manufacturing Technology*, vol. 106, no. 7-8, pp. 2779–2791, 2020.

[37] E. Budak, "An analytical design method for milling cutters with nonconstant pitch to increase stability, part I: theory," *Journal of Manufacturing Science and Engineering*, vol. 125, no. 1, pp. 29–34, 2003.

[38] E. Budak, "An analytical design method for milling cutters with nonconstant pitch to increase stability, part 2: application," *Journal of Manufacturing Science and Engineering*, vol. 125, no. 1, pp. 35–38, 2003.

[39] A. R. Yusoff and N. D. Sims, "Optimisation of variable helix tool geometry for regenerative chatter mitigation," *International Journal of Machine Tools and Manufacture*, vol. 51, no. 2, pp. 133–141, 2011.

[40] A. Comak and E. Budak, "Modeling dynamics and stability of variable pitch and helix milling tools for development of a design method to maximize chatter stability," *Precision Engineering*, vol. 47, pp. 459–468, 2017.

[41] J. Mei, M. Luo, J. Guo, H. Li, and D. Zhang, "Analytical modeling, design and performance evaluation of chatter-free milling cutter with alternating pitch variations," *IEEE Access*, vol. 6, pp. 32367–32375, 2018.

[42] Y. Guo, B. Lin, and W. Wang, "Optimization of variable helix cutter for improving chatter stability," *The International Journal of Advanced Manufacturing Technology*, vol. 104, no. 5-8, pp. 2553–2565, 2019.

[43] S. D. Merdol and Y. Altintas, "Mechanics and dynamics of serrated end mills," in *Proceedings of the ASME 2002 International Mechanical Engineering Congress and Exposition*, pp. 337–342, New Orleans, LA, USA, November 2002.

[44] S. D. Merdol and Y. Altintas, "Mechanics and dynamics of serrated cylindrical and tapered end mills," *Journal of Manufacturing Science and Engineering*, vol. 126, no. 2, pp. 317–326, 2004.

[45] Z. Dombovari, Y. Altintas, and G. Stepan, "Stability of serrated milling cutters," in *Proceedings of the 12th CIRP Conference on Modelling of Machining Operations*, pp. 873–878, Mondragon, Spain, 2009.

[46] Z. Dombovari, Y. Altintas, and G. Stepan, "The effect of serration on mechanics and stability of milling cutters," *International Journal of Machine Tools and Manufacture*, vol. 50, no. 6, pp. 511–520, 2010.

[47] A. Hosseini, B. Moetakef-Imani, and H. A. Kishawy, "Mechanistic modelling for cutting with serrated end mills—a parametric representation approach," *Proceedings of the Institution of Mechanical Engineers, Part B: Journal of Engineering Manufacture*, vol. 225, no. 7, pp. 1019–1032, 2011.

[48] F. Tehranizadeh and E. Budak, "Design of serrated end mills for improved productivity," *Procedia CIRP*, vol. 58, pp. 493–498, 2017.

[49] Y. Guo, B. Lin, and W. Wang, "Modeling of cutting forces with a serrated end mill," *Mathematical Problems in Engineering*, vol. 2019, Article ID 1796926, 13 pages, 2019.

[50] P. Bari, M. Law, and P. Wahi, "Improved chip thickness model for serrated end milling," *CIRP Journal of Manufacturing Science and Technology*, vol. 25, pp. 36–49, 2019.

[51] F. Tehranizadeh, R. Koca, and E. Budak, "Investigating effects of serration geometry on milling forces and chatter stability for their optimal selection," *International Journal of Machine Tools and Manufacture*, vol. 144, p. 103425, 2019.

[52] G. U. Pelayo and D. O. Trejo, "Model-based phase shift optimization of serrated end mills: minimizing forces and surface location error," *Mechanical Systems and Signal Processing*, vol. 144, p. 106860, 2020.

Hindawi
Mathematical Problems in Engineering
Volume 2020, Article ID 2350431, 9 pages
https://doi.org/10.1155/2020/2350431

Research Article

Fully Distributed Event-Triggered Containment Control of Uncertain Multiagent Systems

Zhaodong Liu,[1] Zhi Liu,[1] Xuewu Qian,[1] Ancai Zhang,[1] and Zhenxing Li[1,2]

[1]*Department of Automation, Linyi University, Linyi 276000, China*
[2]*School of Mathematics, Southeast University, Nanjing 210096, China*

Correspondence should be addressed to Zhenxing Li; zhxingli@gmail.com

Received 23 April 2020; Accepted 30 June 2020; Published 26 July 2020

Guest Editor: Rongwei Guo

This paper investigates the event-triggered containment control problem of a class of uncertain nonlinear multiagent systems (MASs). By employing the local relative information, we design an adaptive event-triggered containment algorithm. The proposed containment algorithm can cope with the unavailability of global topology information and uncertain dynamics of follower agents. Therefore, the presented containment algorithm is free of global topology information, i.e., the designed algorithm is fully distributed. In addition, it is proved that Zeno behavior will not occur. At last, a numerical example is given to verify our event-triggered containment algorithm.

1. Introduction

During past two decades, cooperative control of MASs has been a hot research field for the reason of broad engineering applications, such as formation control [1], attitude alignment [2], mobile sensor networks [3], multirobot systems [4], and so forth [5, 6]. In practice, MASs are composed of mobile units, such as UAVs and robots, which are equipped with embedded control chips and limited energy supply. To extend the working hours of MASs, researchers developed various cooperative algorithms. Event-triggered cooperative algorithms can effectively reduce communications among neighbor agents and have gained extensive attention.

MASs can be divided into three cases, i.e., leaderless MASs, leader-follower MASs, and multileader MASs. The control objectives of those three kinds of MASs are consensus control, tracking control, and containment control, respectively. Consensus control and tracking control have been widely studied, from linear MASs [1, 7, 8] to nonlinear MASs [9–11]. Event-triggered control technique is also employed to design consensus and tracking controllers for various kinds of MASs [12–16]. Unlike consensus and tracking control, the objective of containment control is that each follower agent enters into the convex hull spanned by leader agents. In papers [2, 17–19], containment control problems of different kinds of MASs were studied. Event-triggered containment problems are also considered by researchers [20–24]. Miao studied the event-triggered containment control for first/second-order MASs with constant time delay in [20]. Event-triggered containment control of second-order MASs with sampled position data and time-varying input delays are considered in [21, 22]. Rong and her coauthors studied the event-triggered containment control problem for general MIMO linear MASs in [23]. Xu studied the event-triggered containment problem of Euler–Lagrange MASs in [24].

Cooperative algorithms of MASs use the local information to achieve global control tasks. However, most of the existing control algorithms of MASs need the information of Laplacian which is a global information. Control algorithms that do not need any global information are said to be fully distributed. Many researchers devoted to develop the fully distributed algorithms for MASs. Papers [25–28] presented some typical works of fully distributed algorithms. Recently, some researchers studied the fully distributed control problems of MASs via event-triggered approach as well. Zhu and Cheng studied the fully distributed event-triggered control problems for linear MASs in [29, 30]. Li and his

coauthors investigated both event-triggered consensus and tracking problems of second-order nonlinear MASs in [31]. Apart from Euler–Lagrange MASs in [24], event-triggered containment problem of multiple leaders MASs was seldom considered.

Inspired by the above papers, we study the fully distributed event-triggered containment problem of a class of uncertain MASs. Not only the Laplacian of MASs but also the dynamics of follower agents are unavailable to design the containment controllers. To deal with these two unknown data, adaptive techniques are used to design event-triggered containment controllers. The main contributions of this paper are listed as follows: (i) our containment algorithm is fully distributed and does not use any global information of MASs; (ii) our containment algorithm is robust and still works when the dynamics of follower agent is uncertain; and (iii) our presented event-triggered algorithm is free of Zeno behavior.

2. Problem Statement and Preliminaries

Notations. Let $I_N \in R^{N\times N}$ be the N-dimensional identity matrix, $1_N \in R^N$ be a vector with each entry being 1, $\|\cdot\|$ be the Euclidean norm (2-norm), $\otimes$ be the Kronecker product, and $\mathrm{diag}\{a_1,\ldots,a_N\}$ be a diagonal matrix. We use $\lambda_{1A}\le\lambda_{2A}\le\ldots\le\lambda_{NA}$, to denote N eigenvalues of a symmetric matrix $A\in R^{N\times N}$. $\|A\|_F=\sqrt{tr\{A^TA\}}$ denotes the Frobenius norm of matrix A.

2.1. Preliminaries. In this paper, there are $N+M$ agents in the considered MASs. The communication topology among those $N+M$ agents is depicted by a graph $\mathscr{G}=\{\mathscr{V},\mathscr{E},\mathscr{A}\}$, where $\mathscr{V}=\{1,\ldots,N+M\}$, $\mathscr{E}=\mathscr{V}\times\mathscr{V}$, and $\mathscr{A}=[a_{ij}]\in\mathbb{R}^{(N+M)\times(N+M)}$ are the agent set, edge set, and adjacency matrix, respectively. $(i,j)\in\mathscr{E}$ denotes a directed edge from agent j to agent i and the associated weighing factor $a_{ij}>0$; otherwise, $a_{ij}=0$. If $a_{ij}=a_{ji}>0$, then there is an undirected edge between agent i and agent j. We assume that there is no self-loop edge, i.e., $a_{ii}=0,\forall i\in\mathscr{V}$. Edge sequence $(i_2,i_1)(i_3,i_2),\ldots,(i_k,i_{k-1})$ denotes a directed path from agent i_1 to agent i_k. $L=[l_{ij}]\in\mathbb{R}^{(N+M)\times(N+M)}$ denotes the Laplacian matrix of graph $\mathscr{G}$, with $l_{ii}=\sum_{j=1}^{N+M}a_{ij}$ and $l_{ij}=-a_{ij}$. Suppose that there are N follower agents and M leader agents in the considered MASs. For simplicity, we assume that agents indexed by $1,\ldots,N$ are the followers, and agents indexed by $N+1,\ldots,N+M$ are the leaders. In practice, the desired trajectories of followers are generated by leaders. Hence, we assume that each leader is not influenced by other agents, that is, $a_{ij}=0, i=N+1,\ldots,N+M$. For brevity, we use $\mathscr{F}=\{1,\ldots,N\}$ and $\mathscr{L}=\{N+1,\ldots,N+M\}$ to denote the follower set and leader set, respectively.

For the topology of MASs, we have the following assumption.

Assumption 1. For every follower agent $i\in\mathscr{F}$, there exists at least a leader agent $j\in\mathscr{L}$ that has a path to follower agent i.

Assumption 2. The induced subgraph of follower agents is an undirected graph.

Since each leader agent is not influenced by other agents, the associated Laplacian matrix can be partitioned as follows:

$$L=\begin{bmatrix} L_1 & L_2\\ 0_{M\times N} & 0_{M\times M}\end{bmatrix}, L_1\in\mathbb{R}^{N\times N},\ L_2\in\mathbb{R}^{N\times M}. \tag{1}$$

Lemma 1 (see [19]). *If Assumptions 1 and 2 hold, L_1 is positive definite, each entry of $-L_1^{-1}L_2$ is nonnegative and the sum of each row of $-L_1^{-1}L_2$ equals one.*

Definition 1 (see [32]). A set $\mathscr{C}\subseteq\mathbb{R}^n$ is convex if $(1-\lambda)x+\lambda y\in\mathscr{C}$, for any $x,y\in\mathscr{C}$ and any $\lambda\in[0,1]$. The convex hull $Co(X)$ of a finite set of points $X=\{x_1,x_2,\ldots,x_q\}$ is the minimal convex set containing all points in X. That is, $Co(X)=\{\sum_{i=1}^q\lambda_ix_i\mid x_i\in X,\quad \lambda_i\ge0,\sum_{i=1}^q\lambda_i=1\}$.

2.2. Problem Statement. In this paper, we study event-triggered containment control problem of uncertain MASs without using any global topology information.

Consider a network system of $N+M$ agents with the following dynamics:

$$\dot{x}_i(t)=Ax_i(t)+B[f_i(x_i(t))+u_i(t)],\quad i\in\mathscr{F}, \tag{2}$$

$$\dot{x}_i(t)=Ax_i(t)+Bu_i(t),\quad i\in\mathscr{L}, \tag{3}$$

where $A\in\mathbb{R}^{n\times n}$, $B\in\mathbb{R}^{n\times m}$, $x_i(t)\in\mathbb{R}^n$, and $u_i(t)\in\mathbb{R}^m$ are the system matrix, input matrix, state vector, and control input of agent i, respectively; input nonlinearity $f_i(x_i(t))$ is an unknown smooth function.

Based on the fact that $f_i(x_i(t))$ is smooth and Stone–Weierstrass approximation theory [33], the unknown nonlinear function $f_i(x_i(t))$ can be approximated by

$$f_i(x_i(t))=W_i^T\phi_i(x_i(t))+\varepsilon_i,\forall x_i(t)\in\Pi, \tag{4}$$

with $\phi_i(\cdot)\colon\mathbb{R}^n\longrightarrow\mathbb{R}^s$ being a known basis function, $W_i\in\mathbb{R}^{s\times m}$ being the neural network (NN) weight matrix, $\Pi\subset\mathbb{R}^m$ being a compact set, and $\varepsilon_i\in\mathbb{R}^m$ being the approximation error such that

$$\|\varepsilon_i\|_\infty\le\varepsilon_M,\quad\forall i\in\mathscr{F}. \tag{5}$$

Suppose that both $\max_{x_i(t)\in\Pi}\{\|\phi_i(x_i(t))\|\}$ and $\|W_i\|_F$ are bounded, i.e., there exist nonnegative numbers $\phi_M,W_M\ge0$ such that

$$\max_{x_i(t)\in\Pi}\|\phi_i(x_i(t))\|\le\phi_M,\|W_i\|_F\le W_M,i\in\mathscr{F}. \tag{6}$$

For the control input of each leader, we assume that $u_i(t)$ satisfies the following assumption, $i\in\mathscr{L}$.

Assumption 3. $u_i(t)$ is bounded by a nonnegative constant τ, that is, $\|u_i(t)\|\le\tau,\forall i\in\mathscr{L}$.

The control objective of MASs (2) and (3) is to design event-triggered controllers $u_i, i\in\mathscr{F}$ for follower agents such that the states of follower agents enter into the convex hull spanned by leaders' states, that is, $\lim_{t\longrightarrow\infty}\mathrm{dist}(x_i(t),Co(\mathscr{L}))=0$, where $Co(\mathscr{L})=Co(x_{N+1}(t),\ldots,x_{N+M}(t))$.

3. Adaptive Event-Triggered Containment Algorithm

In this section, we will give an adaptive event-triggered algorithm to solve the containment problem of MASs (2) and (3).

Let

$$x_f(t) = \left[x_1^T(t), \ldots, x_N^T(t)\right]^T, x_l(t) = \left[x_{N+1}^T(t), \ldots, x_{N+M}^T(t)\right]^T,$$
$$\gamma(t) = \left[\gamma_1^T(t), \ldots, \gamma_N^T(t)\right]^T = -\left(L_1^{-1}L_2 \otimes I_n\right)x_l(t). \tag{7}$$

From Lemma 1, we know that $\gamma_i(t), i \in \mathscr{F}$, is a convex combination of states of leader agents. If follower agent i can track $\gamma_i(t)$, then $x_i(t)$ enters into $Co(\mathscr{L})$, $i \in \mathscr{F}$. We call $\gamma_i(t)$ the target state trajectory of follower agent $i, i \in \mathscr{F}$.

Denote $\delta_i(t) = x_i(t) - \gamma_i(t)$ as the tracking error of follower agent i and $\delta(t) = [\delta_1^T(t), \ldots, \delta_N^T(t)]^T$. Then, we have

$$\begin{aligned}\dot{\delta}((t) &= \dot{x}_f(t) + \left(L_1^{-1}L_2 \otimes I_n\right)\dot{x}_l(t)\\ &= (I_N \otimes A)x_f(t) + (I_N \otimes B)\left(F\left(x_f(t)\right) + u_f(t)\right)\\ &\quad + \left(L_1^{-1}L_2 \otimes I_n\right)\left[(I_M \otimes A)x_l(t) + (I_M \otimes B)u_l(t)\right]\\ &= (I_N \otimes A)\delta(t) + (I_N \otimes B)\left(F\left(x_f(t)\right) + u_f(t)\right)\\ &\quad + \left(L_1^{-1}L_2 \otimes B\right)u_l(t),\end{aligned} \tag{8}$$

where

$$\begin{aligned}F\left(x_f(t)\right) &= \left[f_1^T(x_1(t)), \ldots, f_N^T(x_N(t))\right]^T,\\ u_f(t) &= \left[u_1^T(t), \ldots, u_N^T(t)\right]^T,\\ u_l(t) &= \left[u_{N+1}^T(t), \ldots, u_{N+M}^T(t)\right]^T.\end{aligned} \tag{9}$$

Let $\xi_i(t) = \sum_{j=1}^{N+M} a_{ij}(x_i(t) - x_j(t))$ be the local relative state of follower agent $i, i \in \mathscr{F}$. $\xi_i(t_k^i)$ denotes the sample value of $\xi_i(t)$ at sample instant t_k^i, and $e_i(t)$ denotes sample error of $\xi_i(t_k^i)$, i.e.,

$$e_i(t) = \xi_i\left(t_k^i\right) - \xi_i(t), t \in \left[t_k^i, t_{k+1}^i\right), i \in \mathscr{F}. \tag{10}$$

By using $\xi_i(t_k^i)$, we give the following dynamical containment controller for each follower agent:

$$\begin{aligned}u_i(t) &= -c_i B^T P \xi_i\left(t_k^i\right) - \widehat{W}_i^T \phi_i(x_i(t)) - \alpha h\left(B^T P \xi_i\left(t_k^i\right)\right),\\ \dot{c}_i(t) &= \frac{1}{\eta}\left(\left(1 - \frac{\beta_1}{2}\right)\xi_i^T\left(t_k^i\right)PBB^TP\xi_i\left(t_k^i\right) - \sigma\left(c_i(t) - 1\right)\right),\\ \dot{\widehat{W}}_i(t) &= \phi_i(x_i(t))\xi_i^T\left(t_k^i\right)PB - \rho\widehat{W}_i(t), \quad t \in \left[t_k^i, t_{k+1}^i\right), i \in \mathscr{F},\end{aligned} \tag{11}$$

where $c_i(t)$ is the dynamical gain of $u_i(t)$ with $c_i(0) \geq 1$, $\alpha \geq \varepsilon_M + \tau$ is a positive constant, $\beta_1 \in (0, 2)$ is a constant, $\widehat{W}_i(t)$ is the dynamical estimation of W_i with $\widehat{W}_i(0) = 0$, $\sigma > 0$ and $\rho > 0$ are the turning scalars, and $P > 0$ is the unique solution of the following Riccati equation:

$$PA + A^TP - PBB^TP + I_n = 0, \tag{12}$$

and $h_i(\cdot)$ is a discontinuous function such that, for $z \in \mathbb{R}^m$,

$$h(z) = \begin{cases} \dfrac{z}{\|z\|}, & \text{if } \|z\| \neq 0,\\ 0, & \text{if } \|z\| = 0.\end{cases} \tag{13}$$

The trigger function for adaptive controller (11) is given as

$$f_i(t) = k_{i1}e_i^T(t)PBB^TPe_i(t) - k_{i2}\xi_i^T\left(t_k^i\right)PBB^TP\xi_i\left(t_k^i\right) - r, \tag{14}$$

where

$$\begin{aligned}k_{i1} &= \mu\left(c_i(t) + \phi_M + \alpha\right) + \frac{(2 - \beta_1)(1 - \beta_4)\beta_5}{2\beta_4}, \quad r > 0\\ k_{i2} &= \frac{(2 - \beta_1)(1 - \beta_5)}{2}, \quad \mu > 0, \beta_4 \in (0, 1), \beta_5 \in (0, 1).\end{aligned} \tag{15}$$

Remark 1. Usually, the feedback gain of a consensus controller depends on the eigenvalues of the Laplacian matrix, which are the global topology information. Since adaptive gains $c_i(t)$ can be adjusted by $\xi_i(t_k^i)$ automatically, adaptive controller (11) does not rely on any global topology information.

Remark 2. Trigger function (14) is a hybrid trigger function. Unlike trigger functions in other papers, we use a positive constant r to replace the exponential decay term. The exponential decay term only guarantees that there is no Zeno behavior for finite time t. By choosing a relative small r, a satisfactory tracking error $\delta(t)$ and a lower bound of $t_{k+1}^i - t_k^i$ can be guaranteed.

Remark 3. In the design of dynamical controller (11), we use the σ-modification technique. Containment controller (11) and trigger function (14) only guarantee that tracking error $\delta(t)$ is uniformly ultimately bounded. If we do not employ the σ-modification technique, the dynamical gains $c_i(t)$ and estimation parameters $\widehat{W}_i(t)$ may increase unboundedly. To ensure the boundedness of $c_i(t)$ and $\widehat{W}_i(t)$, we use σ-modification technique to adjust the dynamical parameters.

Denote

$$\begin{aligned}\xi(t) &= \left[\xi_1^T(t), \ldots, \xi_N^T(t)\right]^T, \xi(t_k) = \left[\xi_1^T\left(t_k^1\right), \ldots, \xi_N^T\left(t_k^N\right)\right]^T,\\ c(t) &= \operatorname{diag}\{c_1(t), \ldots, c_N(t)\}, \varepsilon = \left[\varepsilon_1^T, \ldots, \varepsilon_N^T\right]^T,\\ \widetilde{W}_i(t) &= W_i - \widehat{W}_i(t), \widetilde{W} = diag\{\widetilde{W}_1(t), \ldots, \widetilde{W}_N(t)\},\\ \phi\left(x_f(t)\right) &= \left[\phi_1^T(x_1(t)), \ldots, \phi_N^T(x_N(t))\right]^T,\\ H(\xi(t_k)) &= \left[h^T\left(B^TP\xi_1\left(t_k^1\right)\right), \ldots, h^T\left(B^TP\xi_N\left(t_k^N\right)\right)\right]^T.\end{aligned} \tag{16}$$

Then, combining (4), (8), and (11), we have, for $t \in [t_k^i, t_{k+1}^i)$,

$$\begin{aligned}\dot{\delta}(t) &= (I_N \otimes A)\delta(t) - \left(c(t) \otimes BB^T P\right)\xi(t_k) \\ &\quad + (I_N \otimes B)\left(\widetilde{W}^T(t)\phi\left(x_f(t)\right) + (I_N \otimes B)\varepsilon\right. \\ &\quad - \alpha(I_N \otimes B)H(\xi(t_k))) - \left(-L_1^{-1}L_2 \otimes B\right)u_l(t).\end{aligned} \tag{17}$$

Theorem 1. *Suppose that Assumptions 1 and 2 hold, containment problem of MASs (2) and (3) will be solved by dynamical controller (11). The tracking errors $\delta_i(t)$ and adaptive parameters $c_i(t)$ and $\widehat{W}_i(t)$ are uniformly ultimately bounded (UUB). Furthermore, controller (11) does not exist Zeno behavior.*

Proof. Take Lyapunov function candidate as

$$\begin{aligned}V &= \frac{1}{2}\delta^T(t)(L_1 \otimes P)\delta(t) + \sum_{i=1}^{N}\frac{\eta}{2}\widetilde{c}_i^2(t) \\ &\quad + \sum_{i=1}^{N}\frac{1}{2}tr\left\{\widetilde{W}_i^T(t)\widetilde{W}_i(t)\right\},\end{aligned} \tag{18}$$

where $\widetilde{c}_i(t) = c_i(t) - \overline{c}$ with $\overline{c}$ being a constant to be determined later.

Along with (11 and 17), we compute $\dot{V}$ as follows:

$$\begin{aligned}\dot{V} &= \delta^T(t)(L_1 \otimes PA)\delta(t) - \delta^T(t)\left(L_1 c(t) \otimes PBB^T P\right)\xi(t_k) \\ &\quad + \delta^T(t)(L_1 \otimes PB)\widetilde{W}^T(t)\phi\left(x_f(t)\right) + \delta^T(t)(L_1 \otimes PB)\varepsilon \\ &\quad - \alpha\delta^T(t)(L_1 \otimes PB)H(\xi(t_k)) + \sum_{i=1}^{N}\eta\widetilde{c}_i(t)\dot{\widetilde{c}}_i(t) \\ &\quad - \delta^T(t)\left(-L_1L_1^{-1}L_2 \otimes PB\right)u_l(t) + \sum_{i=1}^{N}tr\left\{\widetilde{W}_i^T(t)\dot{\widetilde{W}}_i(t)\right\}.\end{aligned} \tag{19}$$

From the definition of $\xi_i(t)$, one obtains

$$\begin{aligned}\xi(t) &= (L_1 \otimes I_n)x_f(t) + (L_2 \otimes I_n)x_l(t) \\ &= (L_1 \otimes I_n)\left(x_f(t) - \left(-L_1^{-1}L_2 \otimes I_n\right)x_l(t)\right) \\ &= (L_1 \otimes I_n)\delta(t).\end{aligned} \tag{20}$$

Hence, we get

$$\begin{aligned}\dot{V} &= \delta^T(t)(L_1 \otimes PA)\delta(t) - \xi^T(t)\left(c(t) \otimes PBB^T P\right)\xi(t_k) \\ &\quad + \xi^T(t)(I_N \otimes PB)\widetilde{W}^T(t)\phi\left(x_f(t)\right) + \xi^T(t)(I_N \otimes PB) \\ &\quad \times \varepsilon - \alpha\xi^T(t)(I_N \otimes PB)H(\xi(t_k)) + \sum_{i=1}^{N}\eta\widetilde{c}_i(t)\dot{\widetilde{c}}_i(t) - \xi^T(t) \\ &\quad .\left(-L_1^{-1}L_2 \otimes PB\right)u_l(t) + \sum_{i=1}^{N}\mathrm{tr}\left\{\widetilde{W}_i^T(t)\dot{\widetilde{W}}_i(t)\right\} \\ &\quad - \sum_{i=1}^{N}\alpha\xi_i^T(t)PBh\left(B^T P\xi_i\left(t_k^i\right)\right) - \sum_{i=1}^{N}\xi_i^T(t)PBu_{il}(t) \\ &= \delta^T(t)(L_1 \otimes PA)\delta(t) - \xi^T(t)\left(c(t) \otimes PBB^T P\right)\xi(t_k) \\ &\quad + \sum_{i=1}^{N}\xi_i^T(t)PB\widetilde{W}_i^T(t)\phi_i(x_i(t)) + \sum_{i=1}^{N}\xi_i^T(t)PB\varepsilon_i \\ &\quad + \sum_{i=1}^{N}\eta\widetilde{c}_i(t)\dot{\widetilde{c}}_i(t) + \sum_{i=1}^{N}\mathrm{tr}\left\{\widetilde{W}_i^T(t)\dot{\widetilde{W}}_i(t)\right\},\end{aligned} \tag{21}$$

where $u_{il}(t)$ are convex combinations of leaders' inputs with $[u_{1l}^T(t), \ldots, u_{Nl}^T(t)]^T = (-L_1^{-1}L_2 \otimes I_m)u_l(t)$. Since the sum of each row of $-L_1^{-1}L_2$ is equal to 1, one has

$$\left\|u_{il}(t)\right\| \le \tau, \quad i \in \mathscr{F}. \tag{22}$$

Denote $e(t) = [e_1^T(t), \ldots, e_N^T(t)]^T$. Since $\xi(t) = \xi(t_k) - e(t)$, one gets

$$\begin{aligned}&- \xi^T(t)\left(c(t) \otimes PBB^T P\right)\xi(t_k) \\ &= -\xi^T(t_k)\left(c(t) \otimes PBB^T P\right)\xi(t_k) \\ &\quad + e^T(t)\left(c(t) \otimes PBB^T P\right)\xi(t_k) \\ &\le -\left(1 - \frac{\beta_1}{2}\right)\xi^T(t_k)\left(c(t) \otimes PBB^T P\right)\xi(t_k) \\ &\quad + \sum_{i=1}^{N}\frac{c_i(t)}{2\beta_1}e_i^T(t)PBB^T Pe_i(t),\end{aligned} \tag{23}$$

where $\beta_1 \in (0, 2)$.

For the third term of $\dot{V}$ (21), one has

$$\begin{aligned}&\xi_i^T(t)PB\widetilde{W}_i^T(t)\phi_i(x_i(t)) \\ &\quad = \xi_i^T\left(t_k^i\right)PB\widetilde{W}_i^T(t)\phi_i(x_i(t)) - e_i^T(t)PB\widetilde{W}_i^T(t)\phi_i(x_i(t)).\end{aligned} \tag{24}$$

Note that

$$\xi_i^T\left(t_k^i\right)PB\widetilde{W}_i^T(t)\phi_i(x_i(t)) = tr\left\{\widetilde{W}_i^T(t)\phi_i(x_i(t))\xi_i^T\left(t_k^i\right)PB\right\}, \tag{25}$$

$$\begin{aligned}&- e_i^T(t)PB\widetilde{W}_i^T(t)\phi_i(x_i(t)) \\ &= -tr\left\{\widetilde{W}_i^T(t)\phi_i(x_i(t))e_i^T(t)PB\right\} \\ &\le \phi_M\left\|\widetilde{W}_i(t)\right\|_F\left\|B^T Pe_i(t)\right\| \\ &\le \frac{\beta_2\phi_M}{2}\left\|\widetilde{W}_i(t)\right\|_F^2 + \frac{\phi_M}{2\beta_2}e_i^T(t)PBB^T Pe_i(t),\end{aligned} \tag{26}$$

where $\beta_2 \in (0, \rho/2\phi_M)$.

For the fourth, fifth, and sixth terms, one obtains

$$\begin{aligned}\xi_i^T(t)PB\varepsilon_i &= \xi_i^T\left(t_k^i\right)PB\varepsilon_i - e_i^T(t)PB\varepsilon_i \\ &\le \varepsilon_M\left\|B^TP\xi_i\left(t_k^i\right)\right\| + \varepsilon_M\left\|B^TPe_i(t)\right\|, \\ &\quad - \alpha\xi_i^T(t)PBh\left(B^TP\xi_i\left(t_k^i\right)\right) \\ &\le -\alpha\left\|B^TP\xi_i\left(t_k^i\right)\right\| + \alpha\left\|B^TPe_i(t)\right\|,\end{aligned} \tag{27}$$

$$-\xi_i^T(t)PBu_{il}(t) \le \tau\left\|B^TP\xi_i\left(t_k^i\right)\right\| + \tau\left\|B^TPe_i(t)\right\|. \tag{28}$$

Hence, we have

$$\begin{aligned}&\sum_{i=1}^N\left(\xi_i^T(t)PB\varepsilon_i - \alpha\xi_i^T(t)PBh\left(B^TP\xi_i\left(t_k^i\right)\right) - \xi_i^T(t)PBu_{il}(t)\right) \\ &\le \sum_{i=1}^N 2\alpha\left\|B^TPe_i(t)\right\| \le \sum_{i=1}^N\left(\alpha\beta_3 + \frac{\alpha}{\beta_3}e_i^T(t)PBB^TPe_i(t)\right),\end{aligned} \tag{29}$$

where $\beta_3 > 0$ is a real constant. From (11), we have

$$\begin{aligned}&\sum_{i=1}^N \eta\tilde{c}_i(t)\dot{c}_i(t) \\ &= \left(1 - \frac{\beta_1}{2}\right)\xi^T(t_k)\left(c(t)\otimes PBB^TP\right)\xi(t_k) \\ &\quad - \bar{c}\left(1 - \frac{\beta_1}{2}\right)\xi^T(t_k)\left(I_N\otimes PBB^TP\right)\xi(t_k) \\ &\quad - \sum_{i=1}^N \sigma\tilde{c}_i(t)\left(c_i(t) - 1\right),\end{aligned} \tag{30}$$

$$\begin{aligned}&tr\left\{\tilde{W}_i^T(t)\dot{\tilde{W}}_i(t)\right\} \\ &= -tr\left\{\tilde{W}_i^T(t)\phi_i(x_i(t))\xi_i^T\left(t_k^i\right)PB\right\} + \rho tr\left\{\tilde{W}_i^T(t)\hat{W}_i(t)\right\}.\end{aligned} \tag{31}$$

Substituting (23)–(31) into (21), we obtain

$$\begin{aligned}\dot{V} &\le \delta^T(t)\left(L_1\otimes PA\right)\delta(t) + \sum_{i=1}^N\frac{\beta_2\phi_M}{2}\left\|\tilde{W}_i(t)\right\|_F^2 \\ &\quad - \bar{c}\left(1 - \frac{\beta_1}{2}\right)\xi^T(t_k)\left(I_N\otimes PBB^TP\right)\xi(t_k) \\ &\quad - \sum_{i=1}^N \sigma\tilde{c}_i(t)\left(c_i(t) - 1\right) + \sum_{i=1}^N \rho tr\left\{\tilde{W}_i^T(t)\hat{W}_i(t)\right\} \\ &\quad + \sum_{i=1}^N\left(\frac{c_i(t)}{2\beta_1} + \frac{\phi_M}{2\beta_2} + \frac{\alpha}{\beta_3}\right)e_i^T(t)PBB^TPe_i(t) + N\alpha\beta_3.\end{aligned} \tag{32}$$

Note that

$$\begin{aligned}&-\xi^T(t_k)\left(I_N\otimes PBB^TP\right)\xi(t_k) \\ &= -\xi^T(t)\left(I_N\otimes PBB^TP\right)\xi(t) - 2\xi^T(t)\left(I_N\otimes PBB^TP\right)e(t) \\ &- e^T(t)\left(I_N\otimes PBB^TP\right)e(t),\end{aligned} \tag{33}$$

$$\begin{aligned}&-2\xi^T(t)\left(I_N\otimes PBB^TP\right)e(t) \\ &\le \beta_4\xi^T(t)\left(I_N\otimes PBB^TP\right)\xi(t) + \sum_{i=1}^N\frac{1}{\beta_4}e_i^T(t)PBB^TPe_i(t),\end{aligned} \tag{34}$$

where $\beta_4 \in (0,1)$. Since $\xi(t) = (L_1\otimes I_n)\delta(t)$ and L_1 is positive definite, we have the following inequalities:

$$\begin{aligned}\xi^T(t)\left(I_N\otimes PBB^TP\right)\xi(t) &= \delta^T(t)\left(L_1^2\otimes PBB^TP\right)\delta(t), \\ &\ge \frac{\underline{\lambda}_{L_1}^2}{\overline{\lambda}_{L_1}}\delta^T(t)\left(L_1\otimes PBB^TP\right)\delta(t),\end{aligned} \tag{35}$$

where $\underline{\lambda}_{L_1}$ and $\overline{\lambda}_{L_1}$ are the smallest and largest eigenvalues of L_1, respectively.

Combining (32)–(35), one has

$$\begin{aligned}\dot{V} &\le \delta^T(t)\left(L_1\otimes PA\right)\delta(t) + \sum_{i=1}^N\frac{\beta_2\phi_M}{2}\left\|\tilde{W}_i(t)\right\|_F^2 \\ &\quad - \bar{c}\left(1 - \frac{\beta_1}{2}\right)(1-\beta_4)\beta_5\frac{\underline{\lambda}_{L_1}^2}{\overline{\lambda}_{L_1}}\delta^T(t)\left(L_1\otimes PBB^TP\right) \\ &\quad \times \delta(t) - \sum_{i=1}^N \sigma\tilde{c}_i(t)\left(c_i(t) - 1\right) + \sum_{i=1}^N \rho tr\left\{\tilde{W}_i^T(t)\hat{W}_i(t)\right\} \\ &\quad + \sum_{i=1}^N\left(\frac{c_i(t)}{2\beta_1} + \frac{\phi_M}{2\beta_2} + \frac{\alpha}{\beta_3} + \bar{c}\frac{(2-\beta_1)}{2}\frac{(1-\beta_4)}{\beta_4}\beta_5\right) \\ &\quad \times e_i^T(t)PBB^TPe_i(t) - \sum_{i=1}^N\bar{c}\left(1 - \frac{\beta_1}{2}\right)(1-\beta_5) \\ &\quad \times \xi_i^T\left(t_k^i\right)PBB^TP\xi_i\left(t_k^i\right) + N\alpha\beta_3,\end{aligned} \tag{36}$$

where $\beta_5 \in (0,1)$ is a constant.

Choosing enough large $\bar{c}$ such that

$$\begin{aligned}&\bar{c} \ge \frac{\overline{\lambda}_{L_1}}{(2-\beta_1)(1-\beta_4)\beta_5\underline{\lambda}_{L_1}^2}, \\ &\bar{c} \ge \frac{1}{2\beta_1\mu}, \bar{c} \ge \frac{1}{2\beta_2\mu}, \bar{c} \ge \frac{1}{\beta_3\mu}.\end{aligned} \tag{37}$$

Then, Riccati equation (12) and trigger function (14) guarantee that

$$\dot{V} \le -\frac{1}{2}\delta^T(t)(L_1 \otimes I_n)\delta(t) + \sum_{i=1}^{N}\frac{\beta_2\phi_M}{2}\|\widetilde{W}_i(t)\|_F^2 + Nr - \sum_{i=1}^{N}\sigma\widetilde{c}_i(t)(c_i(t)-1) + \sum_{i=1}^{N}\rho tr\left\{\widetilde{W}_i^T(t)\widehat{W}_i(t)\right\} + N\alpha\beta_3. \tag{38}$$

Since $c_i(t) = \widetilde{c}_i(t) + \overline{c}$ and $\widehat{W}_i(t) = W_i - \widetilde{W}_i(t)$, one gets

$$\begin{aligned} -\sigma\widetilde{c}_i(t)(c_i(t)-1) &= -\sigma\widetilde{c}_i(t)(\widetilde{c}_i(t)+\overline{c}-1) \\ &= -\sigma\widetilde{c}_i^2(t) - \sigma\widetilde{c}_i(t)(\overline{c}-1) \\ &\le -\frac{\sigma}{2}\widetilde{c}_i^2(t) + \frac{\sigma}{2}(\overline{c}-1)^2, \end{aligned} \tag{39}$$

$$\begin{aligned} \mathrm{tr}\left\{\widetilde{W}_i^T(t)\widehat{W}_i(t)\right\} &= tr\left\{\widetilde{W}_i^T(t)(W_i - \widetilde{W}_i(t))\right\} \\ &\le W_M\|\widetilde{W}_i(t)\|_F - \|\widetilde{W}_i(t)\|_F^2 \\ &\le -\left(1 - \frac{\beta_6}{2}W_M\right)\|\widetilde{W}_i(t)\|_F^2 + \frac{W_M}{2\beta_6}, \end{aligned} \tag{40}$$

where $\beta_6 \in (0, 1/2W_M)$ is a constant.

Combining (38)–(40) yields

$$\begin{aligned} \dot{V} \le& -\frac{1}{2}\delta^T(t)(L_1 \otimes I_n)\delta(t) - \sum_{i=1}^{N}\frac{\sigma}{2}\widetilde{c}_i^2(t) \\ &- \sum_{i=1}^{N}\left(\rho\left(1 - \frac{\beta_6}{2}W_M\right) - \frac{\beta_2}{2}\phi_M\right)\|\widetilde{W}_i(t)\|_F^2 + \varsigma, \end{aligned} \tag{41}$$

where $\varsigma = N\alpha\beta_3 + N\sigma/2(\overline{c}-1)^2 + NW_M/2\beta_6 + Nr$. Since $\beta_2 \in (0, \rho/2\phi_M)$ and $\beta_6 \in (0, 1/2W_M)$, we get

$$\begin{aligned} \dot{V} \le& -\frac{1}{2}\delta^T(t)(L_1 \otimes I_n)\delta(t) - \sum_{i=1}^{N}\frac{\sigma}{2}\widetilde{c}_i^2(t) \\ &- \sum_{i=1}^{N}\frac{\rho}{2}\|\widetilde{W}_i(t)\|_F^2 + \varsigma \\ \le& -\kappa V + \varsigma, \end{aligned} \tag{42}$$

where $\kappa = \min\left\{1/\overline{\lambda}_p, \sigma/\eta, \rho\right\}$ with $\overline{\lambda}_p$ being the largest eigenvalue of P.

After simple calculations, we have

$$V(t) \le \left(V(0) - \frac{\varsigma}{\kappa}\right)e^{-\kappa t} + \frac{\varsigma}{\kappa}, \tag{43}$$

which indicates that tracking error $\delta(t)$, dynamical gains $c_i(t)$, and $\widehat{W}_i(t)$ are UUB.

In the last step, we prove that event-triggered controller (11) does not exist Zeno behavior.

When $t = t_k^i$, sample error $e_i(t)$ will be set to zero. Dini derivative will be used to analyze $e_i(t)$, and we get

$$D^+\|e_i(t)\| = \frac{d}{dt}\sqrt{e_i^T(t)e_i(t)} \le \|\dot{e}_i(t)\|. \tag{44}$$

Since $e_i(t) = \xi_i(t_k^i) - \xi_i(t)$, for $t \in [t_k^i, t_{k+1}^i]$, we have

$$\begin{aligned} \dot{e}_i(t) = -\dot{\xi}_i(t) &= -A\xi_i(t) - \sum_{j=1}^{N}a_{ij}B\left[f_i(x_i(t)) - f_j(x_j(t))\right] - \sum_{j=1}^{N+M}a_{ij}(u_i(t) - u_j(t)) \\ &= Ae_i(t) - A\xi_i(t_k^i) - \sum_{j=1}^{N}a_{ij}B\left[f_i(x_i(t)) - f_j(x_j(t))\right] - \sum_{j=1}^{N+M}a_{ij}(u_i(t) - u_j(t)). \end{aligned} \tag{45}$$

Denote

$$\varphi_k^i = \max_{t\in[t_k^i, t_{k+1}^i]}\left\|A\xi_i(t_k^i) + \sum_{j=1}^{N}a_{ij}B\left[f_i(x_i(t)) - f_j(x_j(t))\right] + \sum_{j=1}^{N+M}a_{ij}(u_i(t) - u_j(t))\right\|. \tag{46}$$

And, one gets

$$D^+\|e_i(t)\| \le \|A\| \cdot \|e_i(t)\| + \varphi_k^i. \tag{47}$$

Notice that $e_i(t_k^i) = 0$. Hence, for $t \in [t_k^i, t_{k+1}^i]$, $\|e_i(t)\|$ satisfies following inequality:

$$\|e_i(t)\| \le \frac{1}{\|A\|}\varphi_k^i\left(e^{\|A\|(t-t_k^i)} - 1\right). \tag{48}$$

Let $\psi_k^i(t) = \sqrt{k_{i2}/k_{i1}\xi_i^T(t_k^i)PBB^TP\xi_i(t_k^i) + r/k_{i1}}$. From trigger function (14), we know that the $(k+1)$th event of agent i will not be triggered unless $\|B^TPe_i(t)\|$ exceeds $\psi_k^i(t)\|$, i.e.,

$$\begin{aligned} &\|B^TPe_i(t)\| \le \psi_k^i(t), \forall t \in \left[t_k^i, t_{k+1}^i\right), \\ &\lim_{t\longrightarrow t_{k+1}^i}\|B^TPe_i(t)\| = \psi_k^i. \end{aligned} \tag{49}$$

Because $\|B^TPe_i(t) \le \|B^TP\| \cdot \|e_i(t)\|$, one has

$$\lim_{t\longrightarrow t_{k+1}^i}\|e_i(t)\| \ge \frac{\psi_k^i(t)}{\|B^TP\|}. \tag{50}$$

By (48) and (50), one obtains the interinterval satisfying

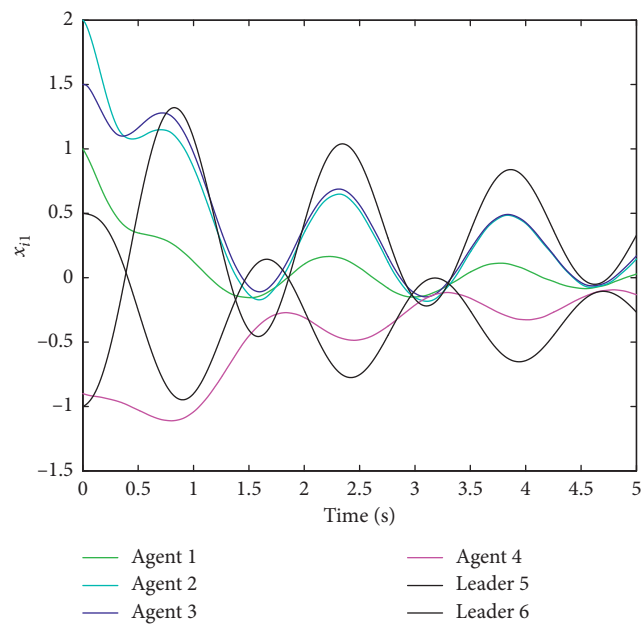

FIGURE 1: $x_{i1}(t)$ trajectories of each agent.

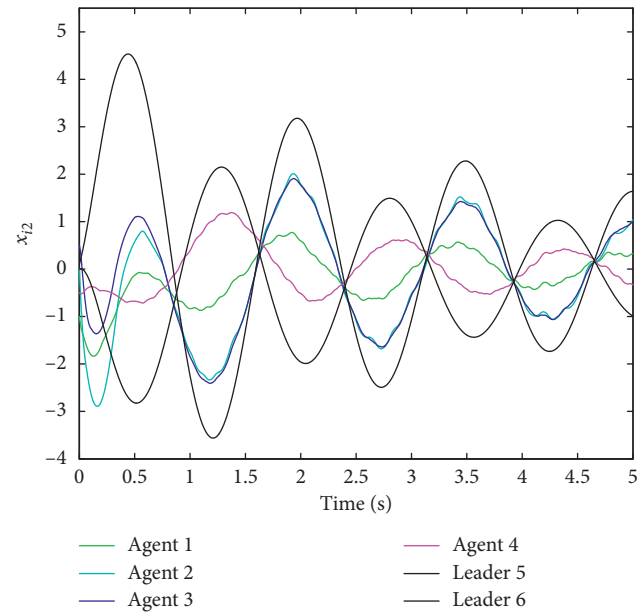

FIGURE 2: $x_{i2}(t)$ trajectories of each agent.

$$t_{k+1}^{i} - t_{k}^{i} \geq \frac{1}{\|A\|} \ln\left(\frac{\|A\|\psi_{k}^{i}(t)}{\|B^{T}P\|\varphi_{k}^{i}} + 1\right). \tag{51}$$

Due to the existence of positive real $r > 0$, $\psi_{k}^{i}(t)$ is greater than zero for any given $t > 0$. That means $t_{k+1}^{i} - t_{k}^{i}$ is strictly positive.

4. Simulations

One numerical example is given in this section to verify the adaptive event-triggered containment controller (11) developed in this paper.

Consider a leader-follower multiagent system with four follower agents and two leader agents. The Laplacian matrix associated with topology is given as follows:

$$L = \begin{bmatrix} 2 & 0 & -1 & -1 & 0 & 0 \\ 0 & 1 & -1 & 0 & 0 & 0 \\ -1 & -1 & 3 & 0 & -1 & 0 \\ -1 & 0 & 0 & 2 & 0 & -1 \\ 0 & 0 & 0 & 0 & 0 & 0 \\ 0 & 0 & 0 & 0 & 0 & 0 \end{bmatrix}. \tag{52}$$

The dynamics of leaders is depicted by the linearized model of the longitudinal dynamics of an aircraft [34], described by (3) with

$$A = \begin{bmatrix} -0.2770 & 1.0000 & -0.0002 \\ -17.1000 & -0.1780 & -12.2000 \\ 0 & 0 & -6.6700 \end{bmatrix}, B = \begin{bmatrix} 0 \\ 0 \\ 6.67 \end{bmatrix}. \tag{53}$$

$x_i(t) = [x_{i1}(t), x_{i2}(t), x_{i3}(t)]^T$ denotes the state of each agent with $x_{i1}(t)$ being the angle of attack, $x_{i2}(t)$ being the pitch rate, and $x_{i3}(t)$ being the elevator angle. From

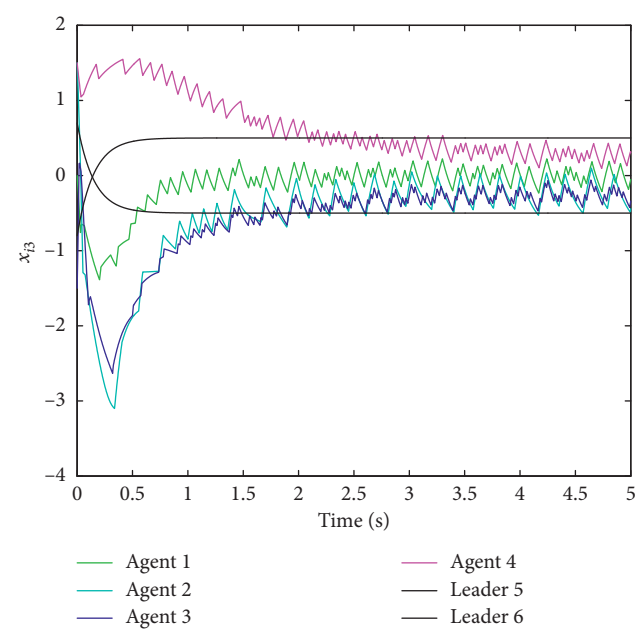

FIGURE 3: $x_{i3}(t)$ trajectories of each agent.

Stone–Weierstrass approximation theory, the approximation error ε_i can be arbitrarily selected. We set $\phi_i(x_i(t)) = [4x_{i1}\sin(x_{i1}(t)), 2\cos(x_{i2}(t))]^T$ and $\varepsilon_M = 0.01$. The initial conditions of follower agents are given as $x_1(0) = [1, -1, 0]^T$, $x_2(0) = [2, 0, 1.5]^T$, $x_3(0) = [1.5, 0.5, -1.5]^T$, and $x_4(0) = [-0.9, -0.5, 1.5]$. We choose control inputs of leader agents as $u_5(t) = -0.5$ and $u_6(t) = 0.5$ and initial conditions as $x_5(0) = [-1, 0.1, 0.7]^T$ and $x_6(0) = [0.5, 0, -0.8]^T$.

We set the initial values of adaptive gains $c_i(t)$ and $\widehat{W}_i(t)$ as $c_i(0) = 1$ and $\widehat{W}_i(0) = [0, 0]^T$. By solving Riccati equation (12), we get $B^T P = [1.2566, -0.9116, 1.3097]^T$. According to

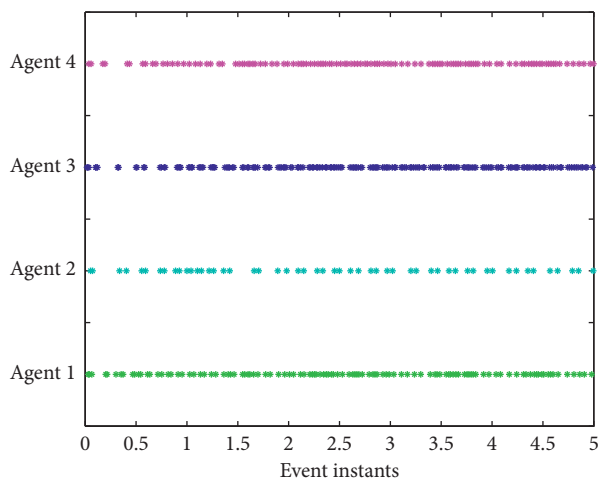

Figure 4: Triggering instants of each follower agent.

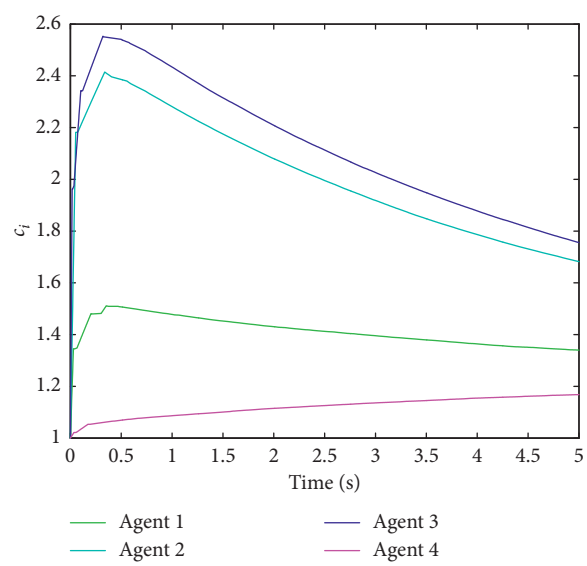

Figure 5: Adaptive gains $c_i(t)$.

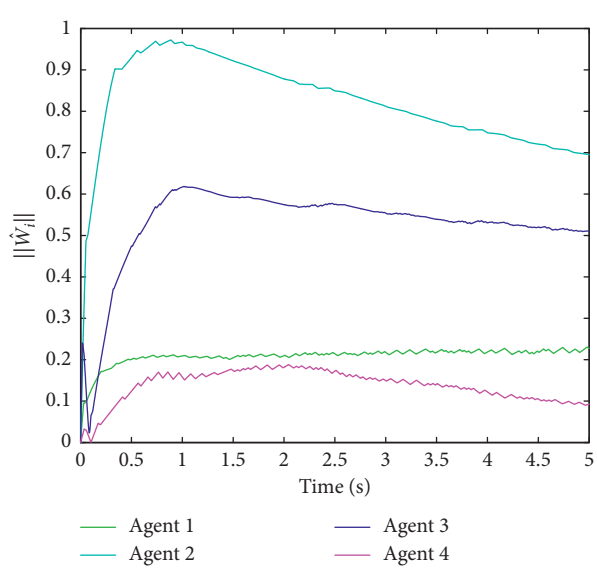

Figure 6: Norms of $\widehat{W}_i(t)$.

controller design (11), we set $\beta_1 = 0.2, \beta_4 = 0.5, \beta_5 = 0.2, \eta = 1, \sigma = 0.2, \rho = 0.1, \mu = 0.2$, and $\alpha = 0.51$.

The simulation results are presented in Figures 1–6. Figures 1 and 3 show the trajectories of follower agents and leader agents. The black lines denote the trajectories of leader agents which indicate that the states of follower agents enter into the convex hull spanned by leaders' states. Figure 4 displays the triggering instants of each agent. Figure 5 displays the adaptive gains $c_i(t)$. Figure 6 presents the norms of estimation coefficients $\widehat{W}_i(t)$.

5. Conclusions

In this paper, we have studied the event-triggered containment problem of a class of uncertain MASs. The global topology information is unavailable, and parameters of follower agents are uncertain. Based on adaptive control technique, we have proposed an event-triggered containment controller which does not rely on any global topology information and can estimate the uncertain parameters. Under this containment algorithm, follower agents enter into the convex hull of leader agents. Moreover, the proposed algorithm has no Zeno behavior. In the future, we will concentrate our study on event-triggered consensus problem of MAS with unknown control directions.

Data Availability

The simulation data used to support the findings of this study are included within the article.

Conflicts of Interest

The authors declare that they have no conflicts of interest.

Acknowledgments

This work was supported by the National Natural Science Foundation of China under Grant nos. 61803193, 61803194, and 61773193, the Postdoctoral Scientific Foundation of China under Grant 2017M620183, and Jiangsu Planned Projects for Postdoctoral Research Funds under Grant 1701077B.

References

[1] W. Ren and E. Atkins, "Distributed multi-vehicle coordinated control via local information exchange," *International Journal of Robust and Nonlinear Control*, vol. 17, no. 10-11, pp. 1002–1033, 2007.

[2] Z. Meng, W. Ren, and Z. You, "Distributed finite-time attitude containment control for multiple rigid bodies," *Automatica*, vol. 46, no. 12, pp. 2092–2099, 2010.

[3] H. Su, X. Chen, M. Z. Q. Chen, and L. Wang, "Distributed estimation and control for mobile sensor networks with coupling delays," *ISA Transactions*, vol. 64, pp. 141–150, 2016.

[4] L. Consolini, F. Morbidi, D. Prattichizzo, and M. Tosques, "Leader-follower formation control of nonholonomic mobile robots with input constraints," *Automatica*, vol. 44, no. 5, pp. 1343–1349, 2008.

[5] G. Zhao, Y. Wang, and H. Li, "A matrix approach to the modeling and analysis of networked evolutionary games with time delays," *IEEE/CAA Journal of Automatica Sinica*, vol. 5, no. 4, pp. 56–64, 2018.

[6] G. Zhao, H. Li, W. Sun, and F. E. Alsaadi, "Modelling and strategy consensus for a class of networked evolutionary games," *International Journal of Systems Science*, vol. 49, no. 12, pp. 2548–2557, 2018.

[7] R. Olfati-Saber and R. M. Murray, "Consensus problems in networks of agents with switching topology and time-delays," *IEEE Transactions on Automatic Control*, vol. 49, no. 9, pp. 1520–1533, 2004.

[8] F. Borreli and T. Keviczky, "Distributed LQR design for identical dynamically decoupled systems," *IEEE Transactions on Automatic Control*, vol. 53, no. 8, pp. 1901–1912, 2008.

[9] A. Das and F. L. Lewis, "Distributed adaptive control for synchronization of unknown nonlinear networked systems," *Automatica*, vol. 46, no. 12, pp. 2014–2021, 2010.

[10] Z. Li and H. Ji, "Distributed consensus and tracking control of second-order time-varying nonlinear multi-agent systems," *International Journal of Robust and Nonlinear Control*, vol. 27, pp. 3549–3563, 2017.

[11] Z. Li and H. Ji, "Finite-time consensus and tracking control of a class of nonlinear multiagent systems," *IEEE Transactions on Automatic Control*, vol. 63, no. 12, pp. 4413–4420, 2018.

[12] D. V. Dimarogonas, E. Frazzoli, and K. H. Johansson, "Distributed event-triggered control for multi-agent systems," *IEEE Transactions on Automatic Control*, vol. 57, no. 5, pp. 1291–1297, 2012.

[13] M. Cao, F. Xiao, and L. Wang, "Event-based second-order consensus control for multi-agent systems via synchronous periodic event detection," *IEEE Transactions on Automatic Control*, vol. 60, no. 9, pp. 2452–2457, 2015.

[14] E. Garcia, Y. Cao, and D. W. Casbeer, "Decentralized event-triggered consensus with general linear dynamics," *Automatica*, vol. 50, no. 10, pp. 2633–2640, 2014.

[15] D. Liuzza, D. V. Dimarogonas, M. Di Bernardo, and K. H. Johansson, "Distributed model based event-triggered control for synchronization of multi-agent systems," *Automatica*, vol. 73, pp. 1–7, 2016.

[16] Z. Li, J. Yan, W. Yu, and J. Qiu, "Event-triggered control for a class of nonlinear multiagent systems with directed graph," *IEEE Transactions on Systems, Man, and Cybernetics: Systems*, 2020.

[17] Y. Zheng and L. Wang, "Containment control of heterogeneous multi-agent systems," *International Journal of Control*, vol. 87, no. 1, pp. 1–8, 2014.

[18] S. J. Yoo, "Distributed adaptive containment control of uncertain nonlinear multi-agent systems in strict-feedback form," *Automatica*, vol. 49, no. 7, pp. 2145–2153, 2013.

[19] Z. Li and H. Ji, "Containment control of a class of heterogeneous nonlinear multi-agent systems," *International Journal of Control*, vol. 90, no. 9, pp. 2020–2030, 2017.

[20] G. Miao, J. Cao, A. Alsaedi, and F. E. Alsaadi, "Event-triggered containment control for multi-agent systems with constant time delays," *Journal of the Franklin Institute*, vol. 354, no. 15, pp. 6956–6977, 2017.

[21] H. Xia, W. X. Zheng, and J. Shao, "Event-triggered containment control for second-order multi-agent systems with sampled position data," *ISA Transactions*, vol. 73, pp. 91–99, 2018.

[22] T. Li, Z. Li, S. Fei, and Z. Ding, "Second-order event-triggered adaptive containment control for a class of multi-agent systems," *ISA Transactions*, vol. 96, pp. 132–142, 2020.

[23] L. Rong, Y. Hua, G. P. Jiang, and S. Xu, "Distributed event—triggered containment control for dynamical multiagent networks," *International Journal of Robust and Nonlinear Control*, vol. 29, no. 7, pp. 2223–2235, 2019.

[24] T. Xu, Y. Hao, and Z. Duan, "Fully distributed containment control for multiple Euler-Lagrange systems over directed graphs: an event-triggered approach," *IEEE Transactions on Circuits and Systems I*, vol. 67, no. 6, pp. 2078–2090, 2019.

[25] W. Yu, W. Ren, W. X. Zheng, G. Chen, and J. Lü, "Distributed control gains design for consensus in multi-agent systems with second-order nonlinear dynamics," *Automatica*, vol. 49, no. 7, pp. 2107–2115, 2013.

[26] C. Wang and H. Ji, "Leader-following consensus of multi-agent systems under directed communication topology via distributed adaptive nonlinear protocol," *Systems & Control Letters*, vol. 70, pp. 23–29, 2014.

[27] C. Wang, X. Wang, and H. Ji, "Leader-following consensus for a class of second-order nonlinear multi-agent systems," *Systems & Control Letters*, vol. 89, pp. 61–65, 2016.

[28] Z. Liu, A. Zhang, Z. Liu, and Z. Li, "Fully distributed tracking control of high-order nonlinear multi-agent systems," *IEEE Access*, vol. 7, pp. 141594–141601, 2019.

[29] W. Zhu, Q. Zhou, and D. Wang, "Consensus of linear multi-agent systems via adaptive event-based protocols," *Neurocomputing*, vol. 318, pp. 175–181, 2018.

[30] B. Cheng and Z. Li, "Fully distributed event-triggered protocols for linear multiagent networks," *IEEE Transactions on Automatic Control*, vol. 64, no. 4, pp. 1655–1662, 2019.

[31] Z. Li, J. Yan, W. Yu, and J. Qiu, "Adaptive event-triggered control for unknown second-order nonlinear multiagent systems," *IEEE Transactions on Cybernetics*, 2020.

[32] R. T. Rockafellar, *Convex Analysis*, Princeton University Press, Princeton, NJ, USA, 1972.

[33] M. H. Stone, "The generalized Weierstrass approximation theorem," *Mathematics Magazine*, vol. 21, no. 5, pp. 237–254, 1948.

[34] G. Wen, P. Wang, T. Huang, W. Yu, and J. Sun, "Robust neuro-adaptive containment of multileader multiagent systems with uncertain dynamics," *IEEE Transactions on Systems, Man, and Cybernetics: Systems*, vol. 49, no. 2, pp. 406–417, 2019.

Hindawi
Mathematical Problems in Engineering
Volume 2020, Article ID 1982363, 9 pages
https://doi.org/10.1155/2020/1982363

Research Article

Stability Analysis Method for Periodic Delay Differential Equations with Multiple Distributed and Time-Varying Delays

Gang Jin,[1] Xinyu Zhang,[1] Kaifei Zhang,[2] Hua Li,[3] Zhanjie Li,[1] Jianxin Han,[1] and Houjun Qi[1]

[1]*Tianjin Key Laboratory of High Speed Cutting and Precision Machining, Tianjin University of Technology and Education, Tianjin 300222, China*
[2]*College of Mechanical and Electrical Engineering, Henan Agricultural University, Zhengzhou 450002, China*
[3]*Tianjin Jinhang Institute of Technical Physical, Tianjin 300000, China*

Correspondence should be addressed to Kaifei Zhang; kaifeizhang@126.com

Received 20 April 2020; Revised 23 June 2020; Accepted 29 June 2020; Published 25 July 2020

Guest Editor: Cuimei Jiang

Dynamic stability problems leading to delay differential equations (DDEs) are found in many different fields of science and engineering. In this paper, a method for stability analysis of periodic DDEs with multiple distributed and time-varying delays is proposed, based on the well-known semidiscretization method. In order to verify the correctness of the proposed method, two typical application examples, i.e., milling process with a variable helix cutter and milling process with variable spindle speed, which can be, respectively, described by DDEs with the multidistributed and time-varying delays are considered. Then, comparisons with prior methods for stability prediction are made to verify the accuracy and efficiency of the proposed approach. As far as the milling process is concerned, the proposed method supplies a generalized algorithm to analyze the stability of the single milling systems associated with variable pith cutter, variable helix cutter, or variable spindle speed; it also can be utilized to analyze the combined systems of the aforementioned cases.

1. Introduction

Time-delay systems, where rate of change of state is determined by both present and past state variables, are encountered in many different fields of science and engineering, such as machining processes, chemical processes, wheel dynamics, feedback controller dynamics, and population dynamics. However, time delays are frequently a source of system instability, thus may lead to poor performance, unpleasant noise and sound, or other potential damage for the engineering practice. Therefore, the study of dynamical systems with time delays has received considerable attention in the past decades.

Stability charts are a useful tool for studying dynamic problems in engineering because they can present the stability of the linearized system in the plane of the system parameters. As a result of the time delays, the study of stability of the systems becomes an infinite-dimensional problem and the governing equations are delay differential equations (DDEs) rather than the traditional ordinary differential equations. For simple time-delay systems, the stability charts can be derived analytically; however, only numerical techniques can be used for complex systems. Around the dynamic analysis for such systems, a lot of research has been carried out by the scientists and mathematicians committed themselves in the past, and many methods including analytical, semianalytical, and numerical ones have been proposed, such as D-subdivision [1], cluster treatment method [2], Galerkin projection [3], harmonic balance [4], Chebyshev collocation method [5], Lambert W function-based method [6], temporal finite element analysis [7], semidiscretization method (SDM) [8–10], full-discretization method [11], and spectral element method [12, 13].

Moreover, many scholars are also committed to dealing with DDEs with various types of time delays caused by more complex engineering practice [14–16]. Taking the typical application of time-delay system, stability of the machining process, as an example, the corresponding model of the turning process is an autonomous DDE, while the milling

operation can be described by DDEs with time-periodic coefficients. The associated delays originate from the surface regeneration, which is caused by the current and previous positions of the tool and the workpiece [17]. For some special cases, e.g., the utilization of the unconventional tools or spindle speed, the time delays may be in various forms as well. For the milling cases of variable pitch cutter or cutter runout, they can be characterized by multiple time delays. The frequency-domain model [18, 19], cluster treatment of characteristic roots [20], unified SDM [21], improved FDM [22], and improved SDM [23–25] are utilized to analyze their dynamics. Also, Turner et al. [26], Dombovari et al. [27], Dombovari and Stepan [28], Sims et al. [29], Yusoff and Sims [30], and Jin et al. [31, 32] modeled and analyzed the milling stability for special serrated tools or variable helix tools, where the distributed time delays exist. Besides, DDEs with time-varying time delays corresponding to variable spindle speed milling [33, 34] and that with state-dependent ones associated with the trochoidal path of the teeth [35] are also analyzed by SDM effectively.

It should be noted that although the methods in [18–33, 35] have been proved to be effective for the cases with time-varying, multiple or distributed delays, they can only be effective in one or two forms of time delay. For the method in [34], it can be utilized to deal with the DDEs with time-varying and multiple delays; however, it is incapable of solving the distributed delay problem. Obviously, the scope of application of the aforementioned methods is limited. From the point of view of the convenience of calculation and the collaborative optimization of the related parameters, it is necessary to propose a generalized stability solution method.

With the aforementioned issue in mind, in this paper, a generalized method is proposed to obtain the stability chart for the periodic DDEs with multiple distributed time-varying delays. The focus of the current work is to present a method which has a greater scope of application. As far as the practical application of milling process is concerned, the method is applicable not only to the stability prediction of variable pitch, variable helix, or variable speed systems but also to the stability analysis of combined systems of variable pitch angle and speed or variable helix angle and speed. The structure of the paper is as follows. In Section 2, the mathematical model is introduced. In Section 3, two typical examples are used to verify the effectiveness of the proposed method. In Section 4, conclusions with a brief discussion are presented.

2. Mathematical Model

Without loss of generality, n-dimensional linear, time-periodic DDEs with multiple distributed and time-varying delays can be expressed by the following state-space form:

$$\begin{aligned}\dot{\mathbf{y}}(t) &= \mathbf{A}_0\mathbf{y}(t) + \mathbf{A}(t)\mathbf{y}(t) \\ &\quad + \sum_{j=1}^{N}\int_{\alpha_1}^{\alpha_2}\mathbf{B}_j(t,\phi)\mathbf{u}\big(t-\tau_j(t,\phi)\big)\mathrm{d}\phi, \\ \mathbf{u}(t) &= \mathbf{D}\mathbf{y}(t),\end{aligned} \tag{1}$$

where $\mathbf{y}(t) \in \mathbb{R}^n$is the state, $\mathbf{u}(t) \in \mathbb{R}^m$is the input, $\mathbf{A}_0$ is a constant matrix, $\mathbf{A}(t)$ and $\mathbf{B}_j(t,\phi)$, respectively, are $n \times n$ and $n \times m$ periodic coefficient matrices that satisfy $\mathbf{A}(t) = \mathbf{A}(t+T)$and $\mathbf{B}_j(t,\phi) = \mathbf{B}_j(t+T,\phi)$, $j = 1, 2, \ldots, N$, and $\tau_j(t,\phi) = \tau_j(t+T,\phi) > 0$, T is the time period, and N is the number of time delay. Considering the idea in [10] and defining $\mathbf{C}_j(t,\phi) = \mathbf{B}_j(t,\phi)D$, equation (1) can be written in the following form:

$$\dot{\mathbf{y}}(t) = \mathbf{A}_0\mathbf{y}(t) + \mathbf{A}(t)\mathbf{y}(t) + \sum_{j=1}^{N}\sum_{k=1}^{f}\widetilde{\mathbf{C}}_{j,k}(t)\mathbf{y}\big(t-\widetilde{\tau}_{j,k}(t)\big), \tag{2}$$

where

$$\widetilde{\mathbf{C}}_{j,k}(t) = \begin{cases}\displaystyle\int_{\alpha_1}^{\alpha_1+kh} C_j(t,\phi)d\phi, & k = 1,2,\ldots,f-1, \\ \displaystyle\int_{\alpha_1+(f-1)h}^{\alpha_2} C_j(t,\phi)d\phi, & k = f.\end{cases}$$

$$\widetilde{\tau}_{j,k}(t) = \begin{cases}\tau_j\left(t,\left(k-\dfrac{1}{2}\right)h\right), & k = 1,2,\ldots,f-1, \\ \tau_j\left(t,\dfrac{(\alpha_2+fh-h}{2}\right), & k = f.\end{cases} \tag{3}$$

$f = \mathrm{ceil}((\alpha_2-\alpha_1)/h)$, with ceil being the ceiling function (i.e., ceil (x) is the smallest integer not less than x) and $h$defines the discretization step for integral interval $[\alpha_1, \alpha_2]$. Then, equation (2) is approximated [10, 11] in interval $[t_i, t_{i+1}]$ by

$$\dot{\mathbf{y}}(t) = \mathbf{A}_0\mathbf{y}(t) + \widetilde{\mathbf{A}}(t)\widetilde{\mathbf{y}}(t) + \sum_{j=1}^{N}\sum_{k=1}^{f}\widetilde{\mathbf{C}}_{j,k}(t)\mathbf{y}\big(t-\widetilde{\tau}_{j,k,i}\big), \tag{4}$$

where

$$\begin{aligned}\widetilde{\mathbf{A}}(t) &= \mathbf{A}_i + \frac{\mathbf{A}_{i+1}-\mathbf{A}_i}{\Delta t}(t-t_i), \\ \widetilde{\mathbf{y}}(t) &= \mathbf{y}_i + \frac{\mathbf{y}_{i+1}-\mathbf{y}_i}{\Delta t}(t-t_i), \\ \widetilde{\mathbf{C}}_{j,k}(t) &= \mathbf{C}_{j,k,i} + \frac{\mathbf{C}_{j,k,i+1}-\mathbf{C}_{j,k,i}}{\Delta t}(t-t_i), \\ \mathbf{y}\big(t-\widetilde{\tau}_{j,k,i}\big) &= \mathbf{y}_{i-m_{j,k,i}} + \frac{\mathbf{y}_{i+1-m_{j,k,i}}-\mathbf{y}_{i-m_{j,k,i}}}{\Delta t}(t-t_i), \\ \widetilde{\tau}_{j,k,i} &= \frac{1}{\Delta t}\int_{t_i}^{t_{i+1}}\widetilde{\tau}_{j,k}(t)\mathrm{d}t, \\ m_{j,k,i} &= \mathrm{int}\left(\frac{\widetilde{\tau}_{j,k,i}+(\Delta t/2)}{\Delta t}\right).\end{aligned} \tag{5}$$

Substituting equation (5) into equation (4) leads to

$$\mathbf{y}_{i+1} = \mathbf{H}_i\mathbf{y}_i + \mathbf{J}_i \sum_{j=1}^{N}\sum_{k=1}^{f}\left(\mathbf{R}_{j,k,i}\mathbf{y}_{i-m_{j,k,i}} + \mathbf{S}_{j,k,i}\mathbf{y}_{i+1-m_{j,k,i}}\right), \quad (6)$$

where

$$\begin{aligned}
\mathbf{H}_i &= \mathbf{J}_i\left(\Phi_0 + \mathbf{F}_i\right),\\
\mathbf{J}_i &= \left(\mathbf{I} - \mathbf{P}_i\right)^{-1},\\
\mathbf{F}_i &= \left(\Phi_1 - \frac{2}{\Delta t}\Phi_2 + \frac{1}{\Delta t^2}\Phi_3\right)\mathbf{A}_i + \left(\frac{1}{\Delta t}\Phi_2 - \frac{1}{\Delta t^2}\Phi_3\right)\mathbf{A}_{i+1},\\
\mathbf{P}_i &= \left(\frac{1}{\Delta t}\Phi_2 - \frac{1}{\Delta t^2}\Phi_3\right)\mathbf{A}_i + \left(\frac{1}{\Delta t^2}\Phi_3\right)\mathbf{A}_{i+1},\\
\mathbf{R}_{j,k,i} &= \left(\Phi_1 - \frac{2}{\Delta t}\Phi_2 + \frac{1}{\Delta t^2}\Phi_3\right)\mathbf{C}_{j,k,i} + \left(\frac{1}{\Delta t}\Phi_2 - \frac{1}{\Delta t^2}\Phi_3\right)\mathbf{C}_{j,k,i+1},\\
\mathbf{S}_{j,k,i} &= \left(\frac{1}{\Delta t}\Phi_2 - \frac{1}{\Delta t^2}\Phi_3\right)\mathbf{C}_{j,k,i} + \left(\frac{1}{\Delta t^2}\Phi_3\right)\mathbf{C}_{j,k,i+1}.
\end{aligned} \quad (7)$$

Clearly, Φ_0, Φ_1, Φ_2, and Φ_3 can be expressed as follows:

$$\begin{aligned}
\Phi_0 &= e^{A_0\Delta t},\\
\Phi_1 &= \int_0^{\Delta t} e^{A_0(\Delta t - s)}\mathrm{d}s = \mathbf{A}_0^{-1}\left(\Phi_0 - \mathbf{I}\right),\\
\Phi_2 &= \int_0^{\Delta t} s e^{A_0(\Delta t - s)}\mathrm{d}s = \mathbf{A}_0^{-1}\left(\Phi_1 - \Delta t\mathbf{I}\right),\\
\Phi_3 &= \int_0^{\Delta t} s^2 e^{A_0(\Delta t - s)}\mathrm{d}s = \mathbf{A}_0^{-1}\left(2\Phi_2 - \Delta t^2\mathbf{I}\right),
\end{aligned} \quad (8)$$

where $\mathbf{I}$ denotes the identity matrix. Let $M = \max\left\{m_{j,k,i}\right\}$ and

$$\mathbf{Z}_i = \mathrm{col}\left(\mathbf{y}_i, \mathbf{y}_{i-1}, \ldots, \mathbf{y}_{i-M}\right). \quad (9)$$

Then, combining equation (6) with (9), one can recast it into a discrete map as

$$\mathbf{Z}_{i+1} = \mathbf{D}_i\mathbf{Z}_i, \quad (10)$$

where each $\mathbf{D}_i$ matrix is given by

$$\begin{aligned}
\mathbf{D}_i = &\begin{bmatrix} \mathbf{H}_i & 0 & \cdots & 0 & 0 & 0\\ \mathbf{I} & 0 & \cdots & 0 & 0 & 0\\ 0 & \mathbf{I} & \cdots & 0 & 0 & 0\\ \vdots & \vdots & \ddots & \vdots & \vdots & \vdots\\ 0 & 0 & \cdots & \mathbf{I} & 0 & 0\\ 0 & 0 & \cdots & 0 & \mathbf{I} & 0 \end{bmatrix}\\
&+ \sum_{j=1}^{N}\sum_{k=1}^{f}\begin{bmatrix} 0 & \cdots & \mathbf{J}_i\mathbf{R}_{j,k,i} & \mathbf{J}_i\mathbf{S}_{j,k,i} & \cdots & 0\\ 0 & \cdots & 0 & 0 & \cdots & 0\\ 0 & \cdots & 0 & 0 & \cdots & 0\\ \vdots & \ddots & \vdots & \vdots & \ddots & \vdots\\ 0 & \cdots & 0 & 0 & \cdots & 0\\ 0 & \cdots & 0 & 0 & \cdots & 0 \end{bmatrix}.
\end{aligned} \quad (11)$$

It should be noted that the horizontal position of the discrete input matrices $\mathbf{J}_i\mathbf{R}_{j,k,i}$ and $\mathbf{J}_i\mathbf{S}_{j,k,i}$ in equation (11) depends on the value of $m_{j,k,i}$corresponding to $\tilde{\tau}_{j,k,i}$ in equation (5) and, respectively, begins from the column of $2m_{j,k,i} - 1$ and $2m_{j,k,i} + 1$ for a single degree of freedom (DOF) system ($4m_{j,k,i} - 3$ and $4m_{j,k,i} + 1$ for a two-DOF system).

Then, the approximate Floquet transition matrix is obtained as $\Phi = \mathbf{D}_{k-1}\mathbf{D}_{k-2}\cdots\mathbf{D}_1\mathbf{D}_0$. Now according to Floquet theory, the stability of the system can be determined: if the moduli of all the eigenvalues of the transition matrix Φ are less than unity, the system is stable; otherwise, it is unstable.

3. Verification of the Method

In this section, two typical applications of periodic DDEs associated with milling operations are chosen and analyzed. One is the dynamics of milling process with a variable helix cutter, characterized by multiple distributed time delays [29–32], whereas the other is corresponding to variable spindle speed where multiple time-varying delays exist [33, 34].

3.1. Milling with Variable Helix Cutter

3.1.1. Dynamic Model. The two-DOF mathematical model for the milling process with a variable helix cutter [32], as shown in Figure 1, can be written as

$$\begin{aligned}
&\begin{bmatrix} m_x & 0\\ 0 & m_y \end{bmatrix}\begin{bmatrix} \ddot{x}(t)\\ \ddot{y}(t) \end{bmatrix} + \begin{bmatrix} c_x & 0\\ 0 & c_y \end{bmatrix}\begin{bmatrix} \dot{x}(t)\\ \dot{y}(t) \end{bmatrix} + \begin{bmatrix} k_x & 0\\ 0 & k_y \end{bmatrix}\begin{bmatrix} x(t)\\ y(t) \end{bmatrix}\\
&= \sum_{j=1}^{N}\int_0^{a_p}\begin{bmatrix} -h_{xx,j}(t,z) & -h_{xy,j}(t,z)\\ -h_{yx,j}(t,z) & -h_{yy,j}(t,z) \end{bmatrix}\begin{bmatrix} x(t) - x\left(t - \tau_j(z)\right)\\ y(t) - y\left(t - \tau_j(z)\right) \end{bmatrix}\mathrm{d}z,
\end{aligned} \quad (12)$$

with the modal mass $m_{(\bullet)}$, the spring stiffness $k_{(\bullet)} = 2m_{(\bullet)}\zeta_{(\bullet)}\omega_{(\bullet)}$, and the damping coefficient $c_{(\bullet)} = m_{(\bullet)}\omega_{(\bullet)}^2$, where $(\bullet) = x$ and y, $\zeta_{(\bullet)}$are the damping ratios, and $\omega_{(\bullet)}$are the natural frequencies. $h_{j,xx}(t,z)$, $h_{j,xy}(t,z)$, $h_{j,yx}(t,z)$, and $h_{j,yy}(t,z)$are the cutting force coefficients for the jth tooth, which can be defined as

$$\begin{aligned}
h_{xx,j}(t,z) &= g\left(\phi_j(t,z)\right)\left(K_t\cos\phi_j(t,z)\right.\\
&\quad\left.+ K_r\sin\phi_j(t,z)\right)\sin\phi_j(t,z),\\
h_{xy,j}(t,z) &= g\left(\phi_j(t,z)\right)\left(K_t\cos\phi_j(t,z)\right.\\
&\quad\left.+ K_r\sin\left(\phi_j(t,z)\right)\cos\phi_j(t,z)\right.,\\
h_{yx,j}(t,z) &= g\left(\phi_j(t,z)\right)\left(-K_t\sin\phi_j(t,z)\right.\\
&\quad\left.+ K_r\cos\phi_j(t,z)\right)\sin\phi_j(t,z),\\
h_{yy,j}(t,z) &= g\left(\phi_j(t,z)\right)\left(-K_t\sin\phi_j(t,z)\right.\\
&\quad\left.+ K_r\cos\phi_j(t,z)\right)\cos\phi_j(t,z),
\end{aligned} \quad (13)$$

where g is a unit step function that determines whether the tooth is in or out of cut, K_t and K_r are the tangential and the radial cutting force coefficients, respectively, and $\phi_j(t,z)$ is the angular position of the jth tooth defined by

$$\phi_j(t,z) = \Omega t + \sum_{i=1}^{j-1}\frac{2\pi\psi_i}{360} - z\gamma, \quad (14)$$

and the delay $\tau_j(z)$ can be derived from pitch angle ψ_j and helix angles β_j as

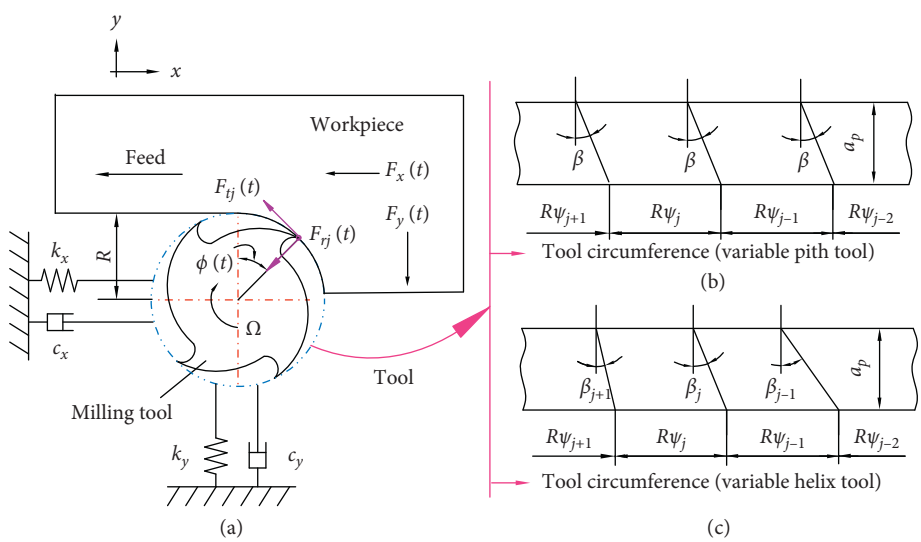

Figure 1: Schematic mechanical model of a two-DOF milling system with variable pitch/helix tool.

$$\tau_j(z) = \frac{30\psi_j}{\pi\Omega} - \frac{30z\gamma_j}{\pi R\Omega}, \tag{15}$$

where $\gamma_j = \begin{cases} \tan\beta_{j-1} - \tan\beta_j & 1 < j \le N \\ \tan\beta_N - \tan\beta_1 & j = 1 \end{cases}$, Ω is the spindle speed in rpm, and R is the cutter radius.

Denoting $M = \begin{bmatrix} m_x & 0 \\ 0 & m_y \end{bmatrix}$, $C = \begin{bmatrix} c_x & 0 \\ 0 & c_y \end{bmatrix}$, $K = \begin{bmatrix} k_x & 0 \\ 0 & k_y \end{bmatrix}$, $q(t) = \begin{bmatrix} x(t) \\ y(t) \end{bmatrix}$, $p(t) = M\dot{q} + cq/2$, and $x(t) = [q(t) \;\; p(t)]^{\mathrm{T}}$, the two-DOF milling model in equation (12) can be represented as

$$\dot{\mathbf{y}}(t) = \mathbf{A}_0\mathbf{y}(t) + \mathbf{A}(t)\mathbf{y}(t) + \sum_{j=1}^{N}\int_0^{a_p} \mathbf{C}_j(t,z)\mathbf{y}\big(t - \tau_j(t,z)\big)\mathrm{d}z, \tag{16}$$

where

$$\mathbf{A}_0 = \begin{bmatrix} \dfrac{-M^{-1}C}{2} & M^{-1} \\ \dfrac{CM^{-1}C}{4-K} & \dfrac{-CM^{-1}}{2} \end{bmatrix},$$

$$\mathbf{A}(t) = \begin{bmatrix} 0 & 0 & 0 & 0 \\ 0 & 0 & 0 & 0 \\ -\sum_{j=1}^{N}\int_0^{a_p} h_{xx,j}(t,z)\mathrm{d}z & -\sum_{j=1}^{N}\int_0^{a_p} h_{xy,j}(t,z)\mathrm{d}z & 0 & 0 \\ -\sum_{j=1}^{N}\int_0^{a_p} h_{yx,j}(t,z)\mathrm{d}z & -\sum_{j=1}^{N}\int_0^{a_p} h_{yy,j}(t,z)\mathrm{d}z & 0 & 0 \end{bmatrix},$$

$$\mathbf{C}_j(t,z) = \begin{bmatrix} 0 & 0 & 0 & 0 \\ 0 & 0 & 0 & 0 \\ h_{xx,j}(t,z) & h_{xy,j}(t,z) & 0 & 0 \\ h_{yx,j}(t,z) & h_{yy,j}(t,z) & 0 & 0 \end{bmatrix}. \tag{17}$$

Here, it should be noted that the value of h in equation (3) can be determined by helix angle β, cutter radius R, and discrete number of time period k and is equal to $2\pi R/\tan\beta/k$.

3.1.2. Verification of the Proposed Method. To illustrate the performance of the proposed approach for the milling process with a variable helix cutter, the related studies [29, 32] are considered firstly. Based on the proposed approach and the methods in [29, 32], the stability charts are, respectively, calculated in cases of four types of milling cutters with different combinations of pitch angles ψ and helix angles β (see Table 1) and are plotted in Figure 2. The main parameters are as follows: down milling, the cutting-force coefficients $K_t = 679 \times 10^6\ \mathrm{N/m^2}$and $K_r = 256 \times 10^6\ \mathrm{N/m^2}$, the mode masses $m_x = 1.4986\,\mathrm{kg}$ and $m_y = 1.199\,\mathrm{kg}$, the natural frequencies $\omega_x = 563.6\,\mathrm{Hz}$ and $\omega_y = 516.21\,\mathrm{Hz}$, the damping ratios $\zeta_x = 0.0558$ and $\zeta_y = 0.025$, the number of the cutter teeth $N = 4$, and the tool radius $R = 9.525 \times 10^{-3} m$.

It can be seen from Figure 2 that the results obtained via the proposed method in this paper are in basic agreement with those by the methods in [29, 32]. This indicates that the proposed method is effective. On the other hand, there are also some little differences among the three results. This is mainly attributed to the discrepancies in the method themselves or the selection of discrete parameters.

3.1.3. Comparisons of Methods. In Figure 2, three typical methods are utilized to analyze the stability of milling with variable pith/helix cutters. In the following, the analysis of

Table 1: Tool parameters.

Number	Tool types	Pitch angles ψ	Helix angles β
1	Variable pitch	(70, 110, 70, 110)°	(30, 30, 30, 30)°
2	Variable helix 1	(90, 90, 90, 90)°	(30, 35, 30, 35)°
3	Variable helix 2	(70, 110, 70, 110)°	(30, 35, 30, 35)°
4	Variable helix 3	(70, 110, 70, 110)°	(35, 30, 35, 30)°

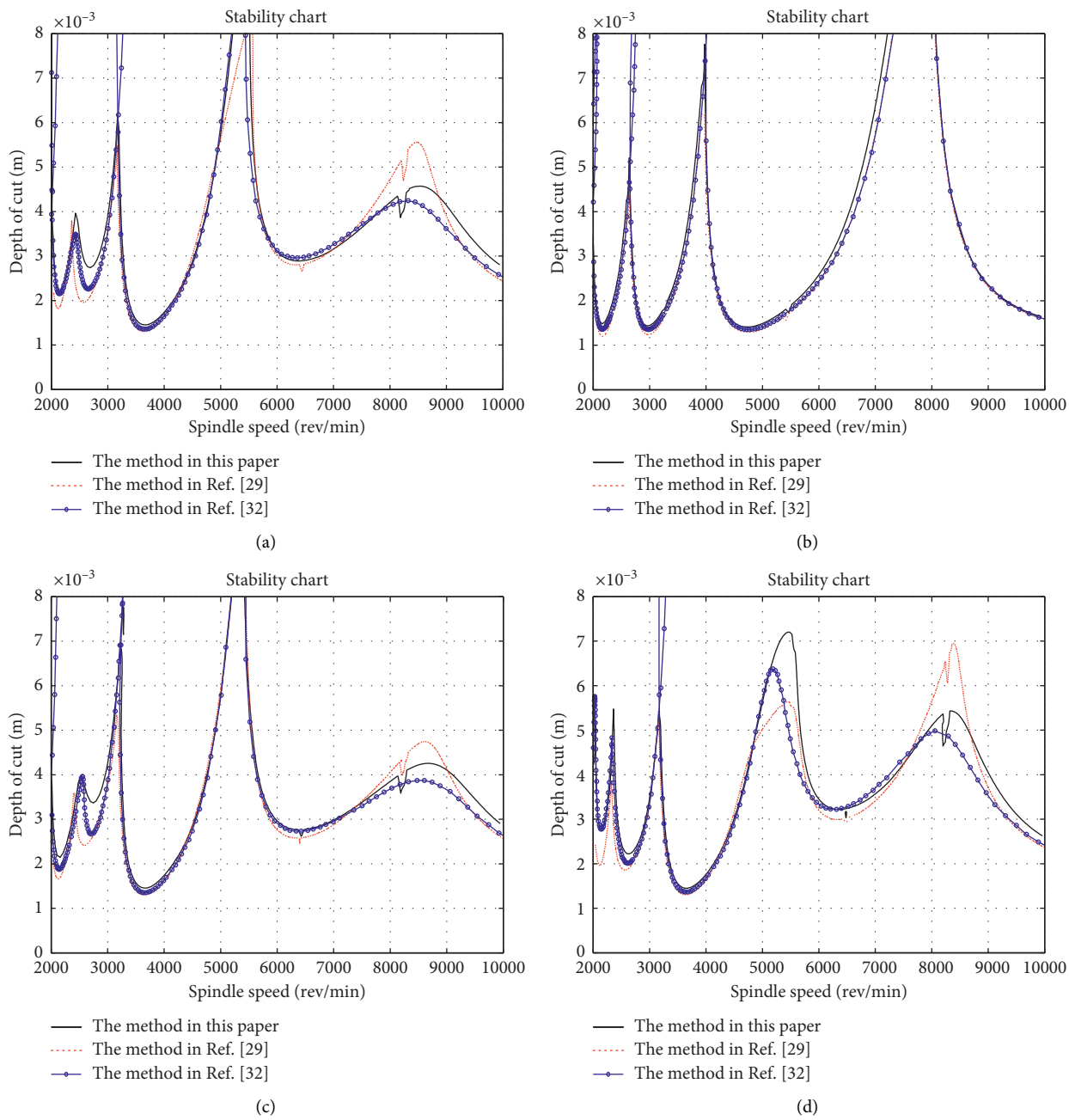

Figure 2: The stability charts for 50% radial immersion down milling with different combinations of variable helix angle. (a) $\psi = (70, 110, 70, 110)^\circ$ and $\beta = (30, 30, 30, 30)^\circ$; (b) $\psi = (90, 90, 90, 90)^\circ$ and $\beta = (30, 35, 30, 35)^\circ$; (c) $\psi = (70, 110, 70, 110)^\circ$ and $\beta = (30, 35, 30, 35)^\circ$; (d) $\psi = (70, 110, 70, 110)^\circ$ and $\beta = (35, 30, 35, 30)^\circ$.

the aforementioned methods will be carried out through comparisons.

(1) The proposed method and the method in [32]:

(i) The proposed method is a numerical one as opposed to the frequency-domain one in [32] that is on the basis of the well-known zeroth-order approximation method [14]. Thus, compared with the method in [32], the proposed method has worse computational efficiency to predict stability charts naturally.

(ii) However, for a traditional milling, the method in [32] cannot accurately predict the stability lobes under small axial depth of cut because of the replacement of time-varying system matrices with time-averaged ones [14]. Moreover, if the nature corresponding to variable pith/helix cutter is also considered, the prediction error may be bigger regardless of low and high radial immersion due to the more markedly time-varying character [24, 25]. Fortunately, the aforementioned problems do not exist in the proposed method. In other words, the proposed method has a much better ability to accurately predict milling stability.

(2) The proposed method and the method in [29]:

(i) Both methods are motivated by the work in [10].

(ii) The method in [29] is on the basis of a new semidiscretization formulation that performs spatial and temporal discretization of the tool, but the proposed one is based on the work of Ding et al. [11], where one utilizes a different concept in the discretization scheme compared with SDM.

(iii) The rates of convergence of both methods are different. In [31], authors presented an updated SDM and pointed out that their method converges much faster than that in [29]. Actually, the method in [31] is a zeroth-SDM, which has similar rate of convergence to the basic algorithm of the proposed method, as known from [36]. By a comprehensive comparison, one can say that the proposed method has better rates of convergence than the method in [29].

In addition, the biggest advantage of this method is that besides the aforementioned case related to distributed time delay, it is also effective to deal with the problem with regard to varying time delay, such as the variable spindle speed milling, that will be analyzed in the next section.

3.2. Milling with Varying Spindle Speed

3.2.1. Dynamic Model. Based on the nonlinear force model in [10], the one-DOF mathematical model for milling processes with spindle speed variation considering helix angles, as shown in Figure 3, can be written as

$$\begin{aligned} m_x\ddot{x}(t) + c_x\dot{x}(t) + k_x x(t) \\ = -\sum_{j=1}^{N}\int_0^{a_p} h_j(z,t)\big(x(t) - x\big(t-\tau_j(t)\big)\big)\mathrm{d}z, \end{aligned} \tag{18}$$

where $h_j(t,z)$ are the cutting force coefficients for the jth tooth defined as

$$\begin{aligned} h_j(t,z) = a_p q f_z^{q-1} g_j(t,z)\sin^q\phi_j(t,z) \\ \cdot\big(K_t\cos\phi_j(t,z) + K_r\sin\phi_j(t,z)\big), \end{aligned} \tag{19}$$

where q is the nonlinear parameter in cutting force, and the angular position of tooth j is

$$\phi_j(t,z) = \frac{2\pi}{60}\int_0^t \Omega(s)\mathrm{d}s + j\frac{2\pi}{N} - z\gamma, \tag{20}$$

where $\Omega(s)$is the spindle speed and is assumed to change in the form of a sinusoidal wave [10], which is periodic at a time period $T = 60/\Omega_0/\mathrm{RVF}$, with a nominal value, Ω_0, and an amplitude, $\Omega_1 = \mathrm{RVA}\times\Omega_0$, as shown in Figure 3. For this sinusoidal modulation, the shape function is modeled as

$$\begin{aligned} \Omega(t) &= \Omega_0 + \Omega_1\sin\left(\frac{2\pi}{T}t\right) \\ &= \Omega_0\left[1 + \mathrm{RVA}\cdot\sin\left(\mathrm{RVF}\cdot\frac{2\pi}{60}\Omega_0 t\right)\right], \end{aligned} \tag{21}$$

where $\mathrm{RVA} = \Omega_1/\Omega_0$ is the ratio of the speed variation amplitude to the nominal spindle speed and $\mathrm{RVF} = 60/(\Omega_0 T)$ is the ratio of the speed variation frequency to the nominal spindle speed. Under these circumstances, the time delay $\tau_j(t)$ can be obtained in the following relationship:

$$\tau_j(t) = \frac{\psi_j}{\kappa/6}, \tag{22}$$

where $\kappa = \Omega_0 + \Omega_1\sin(\omega_m t)$.

Let $y(t) = m_x\dot{x}(t) + m_x\zeta_x\omega_x x(t)$ and $x(t) = [\,x(t)\ y(t)]^{\mathrm{T}}$, then equation (18) can be represented as

$$\dot{\mathbf{y}}(t) = \mathbf{A}_0\mathbf{y}(t) + \mathbf{A}(t)\mathbf{y}(t) + \sum_{j=1}^{N}\int_0^{a_p}\mathbf{C}_j(t,z)\mathbf{y}\big(t-\tau_j(t)\big)\mathrm{d}z, \tag{23}$$

where

$$\begin{aligned} \mathbf{A}_0 &= \begin{bmatrix} -\zeta_x\omega_x & \dfrac{1}{m_x} \\ m_x(\zeta\omega_x)^2 - m_x\omega_x^2 & -\zeta_x\omega_x \end{bmatrix}, \\ \mathbf{A}(t) &= \begin{bmatrix} 0 & 0 \\ -\dfrac{1}{m_x}\displaystyle\sum_{j=1}^{N}\int_0^{a_p} h_j(t,z)\mathrm{d}z & 0 \end{bmatrix}, \\ \mathbf{C}_j(t,z) &= \begin{bmatrix} 0 & 0 \\ \dfrac{1}{m_x}h_j(t,z) & 0 \end{bmatrix}. \end{aligned} \tag{24}$$

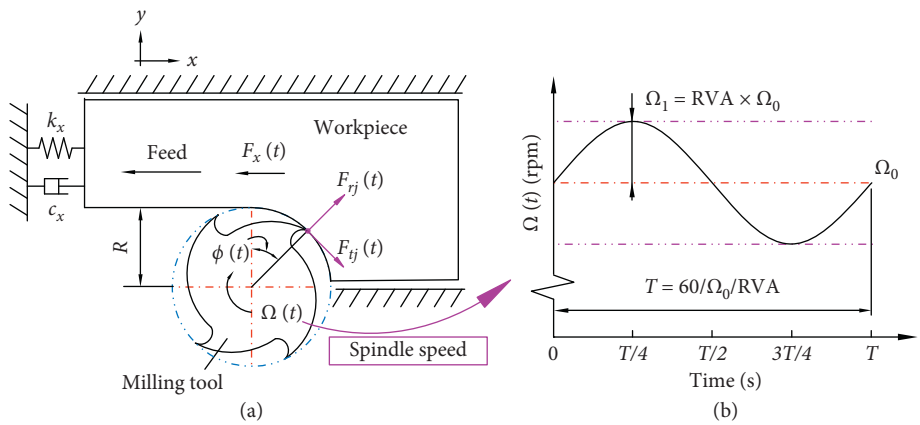

Figure 3: Schematic mechanical model of the one-DOF milling system with variable spindle speed.

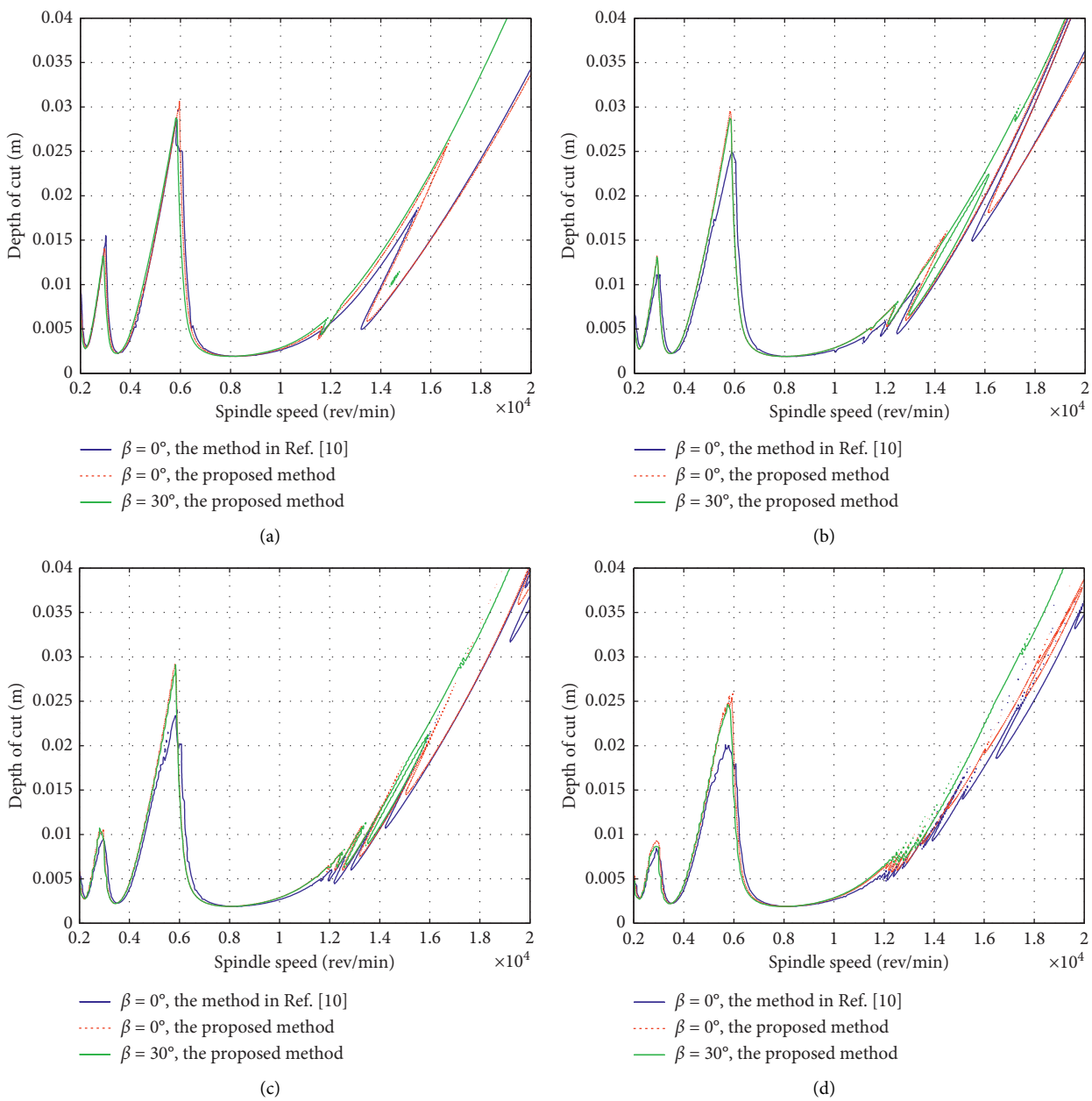

Figure 4: Comparison of stability charts for milling processes with sinusoidal spindle speed modulation with RVA = 0.1 in the high-speed domain: (a) RVF = 0.5; (b) RVF = 0.2; (c) RVF = 0.1; (d) RVF = 0.05.

3.2.2. Results and Discussion. To illustrate the effectiveness of the proposed method for milling process with variable spindle speed, the method and results in [10] are taken into consideration. The stability charts corresponding to the milling processes for RVA = 0.1 and for four different RVF values are calculated using the proposed method and the method in [10] and plotted in Figure 4. The main calculation parameters are as follows: up milling, the cutting-force exponent $q = 0.75$, the cutting-force coefficients $k_t = 107 \times 10^6\ \mathrm{N/m^{1+q}}$ and $k_r = 40 \times 10^6\ \mathrm{N/m^{1+q}}$, the mode mass $m_x = 3.1663$ kg, the natural frequency $\omega_x = 400$ Hz, damping ratios $\zeta_x = 0.02$, the number of the cutter teeth $N = 4$, the tool radius $R = 9.525 \times 10^{-3}$ m, and the feed per tooth $f_z = 0.1$ mm/tooth. It can be seen from Figure 4 that the results obtained via the above two methods are in close agreement with each other. This indicates the effectiveness of the proposed method for the case of variable spindle speed.

Moreover, because the proposed method is based on the ones in [23, 31, 34], but suitable for variable spindle speed with helix angle, the stability charts associated with helix angle $\beta = 30^\circ$ are also plotted in Figure 4 for comparison. It can be seen that the effect of helix angle is mainly reflected in the high-speed region (e.g., among 12000–18000 rpm in every graphic of Figure 4), whereas this effect is relatively small for the low-speed region. The results are consistent with the conclusion in [33], where the effective suppression of period double chatter is investigated in the high-speed region for variable spindle speed milling.

In addition, two points about the above two methods have to be emphasized here. First, they utilize different policies in the process of equation approximations. For the method in [10], the delayed term is approximated by a linear function of time and the periodic coefficient is approximated by a piecewise constant function. However, the delayed term $\mathbf{y}(t - \tilde{\tau}_{j,k}(t))$, the state term $\mathbf{y}(t)$, and the periodic terms $\mathbf{A}(t)$ and $\tilde{\mathbf{C}}_{j,k}(t)$ in equation (2) are all discretized by linear interpolation for the proposed method. Second, the matrices Φ_0, Φ_1, Φ_2, and Φ_3 in equation (8) are dependent on spindle speed but on depth of cut; thus, the calculation time in the process of sweeping the range of the depth of cut will be decreased consequently [11].

4. Conclusion

In this work, an improved semidiscretization method for stability analysis of periodic DDEs with multiple distributed time-periodic delays is proposed. Then, two typical application examples, i.e., variable spindle speed milling system associated with time-varying delays and variable helix cutter milling system associated with multiple distributed delays, are utilized to demonstrate the effectiveness of the proposed algorithm. Through comparison with prior works, it is found that the results obtained by the presented method are in close agreement with those by the prior methods.

Furthermore, for the milling process, the proposed method actually provides a generalized algorithm, which can be utilized to predict stability not only for the single milling process with variable pitch cutter, variable helix cutter, or variable spindle speed but also for combined processes, such as variable pitch angle and variable speed, variable helix angle and variable speed. Meanwhile, the application scope of the existing methods, e.g., the ones in [24, 31, 34], has been expanded to a certain extent.

Data Availability

The MATLAB data used to support the findings of this study have been deposited in the "Baidu online disk" repository (https://pan.baidu.com/s/10mA5uypwbzUd2QGIO8drlA, extraction code: aakg).

Conflicts of Interest

The authors declare that there are no conflicts of interest regarding the publication of this paper.

Acknowledgments

This work was supported by the National Natural Science Foundation of China (11702192 and 51405343), Tianjin Science and Technology Planning Project (18JCZDJC10050), School Project of Tianjin Vocational and Technical Normal University (KJ1909), and Innovation Team Training Plan of Tianjin Universities and Colleges (TD13-5096).

References

[1] S. J. Bhatt and C. S. Hsu, "Stability criteria for second-order dynamical systems with time lag," *Journal of Applied Mechanics*, vol. 33, no. 1, pp. 113–118, 1966.

[2] N. Olgac, A. F. Ergenc, and R. Sipahi, ""Delay scheduling": a new concept for stabilization in multiple delay systems," *Journal of Vibration and Control*, vol. 11, no. 9, pp. 1159–1172, 2005.

[3] P. Wahi and A. Chatterjee, "Galerkin projections for delay differential equations," *Journal of Dynamic Systems, Measurement, and Control*, vol. 127, no. 1, pp. 80–87, 2005.

[4] L. Liu and T. Kalmar-Nagy, "High dimensional harmonic balance analysis for second-order delay-differential equations," *Journal of Vibration and Control*, vol. 16, no. 7-8, pp. 1189–1208, 2010.

[5] E. A. Butcher, H. Ma, E. Bueler, V. Averina, and Z. Szabo, "Stability of linear time-periodic delay-differential equations via Chebyshev polynomials," *International Journal for Numerical Methods in Engineering*, vol. 59, no. 7, pp. 895–922, 2004.

[6] S. Yi, P. Nelson, and A. G. Ulsoy, "Delay differential equations via the matrix Lambert W function and bifurcation analysis: application to machine tool chatter," *Mathematical Biosciences and Engineering : MBE*, vol. 4, no. 2, pp. 355–368, 2007.

[7] P. V. Bayly, J. E. Halley, B. P. Mann, and M. A. Davies, "Stability of interrupted cutting by temporal finite element analysis," *Journal of Manufacturing Science and Engineering*, vol. 125, no. 2, pp. 220–225, 2003.

[8] T. Insperger and G. Stépán, "Semi-discretization method for delayed systems," *International Journal for Numerical Methods in Engineering*, vol. 55, no. 5, pp. 503–518, 2002.

[9] T. Insperger and G. Stepan, "Updated semi-discretization method for periodic delay-differential equations with discrete delay," *International Journal for Numerical Methods in Engineering*, vol. 61, pp. 114–141, 2004.

[10] T. Insperger and G. Stepan, *Semi-Discretization for Time-Delay Systems Stability and Engineering Applications (Applied Mathematical Sciences)*, Springer-Verlag, New York, NY, USA, 1 edition, 2011.

[11] Y. Ding, L. Zhu, X. Zhang, and H. Ding, "A full-discretization method for prediction of milling stability," *International Journal of Machine Tools and Manufacture*, vol. 50, no. 5, pp. 502–509, 2010.

[12] F. A. Khasawneh and B. P. Mann, "Stability of delay integro-differential equations using a spectral element method," *Mathematical and Computer Modelling*, vol. 54, no. 9-10, pp. 2493–2503, 2011.

[13] D. Lehotzky, T. Inspergera, and G. Stepan, "Extension of the spectral element method for stability analysis of time-periodic delay-differential equations with multiple and distributed delays," *Communications in Nonlinear Science and Numerical Simulation*, vol. 35, pp. 177–189, 2016.

[14] W. Chartbupapan, O. Bagdasar, and K. Mukdasai, "A novel delay-dependent asymptotic stability conditions for differential and riemann-liouville fractional differential neutral systems with constant delays and nonlinear perturbation," *Mathematics*, vol. 8, no. 1, pp. 1–10, 2020.

[15] P. Singkibud, L. T. Hiep, P. Niamsup, T. Botmart, and K. Mukdasai, "Delay-dependent robust H_∞ performance for uncertain neutral systems with mixed time-varying delays and nonlinear perturbations," *Mathematical Problems in Engineering*, vol. 2018, Article ID 5721695, 16 pages, 2018.

[16] W. Chartbupapan, T. Botmart, K. Mukdasai, and N. Kaewbanjak, "Non-differentiable delay-interval-dependent exponentially passive conditions for neutral integro-differential equations with time-varying delays," *Thai Journal of Mathematics*, vol. 18, pp. 232–250, 2020.

[17] Y. Altintas, *Manufacturing Automation*, Cambridge University Press, New York, NY, USA, 2012.

[18] Y. Altintas, S. Engin, and E. Budak, "Analytical stability prediction and design of variable pitch cutters," *Journal of Manufacturing Science and Engineering-Transactions of the ASME*, vol. 121, no. 2, pp. 173–179, 1999.

[19] E. Budak, "An analytical design method for milling cutters with nonconstant pitch to increase stability, part I: theory," *Journal of Manufacturing Science and Engineering*, vol. 125, no. 1, pp. 29–34, 2003.

[20] N. Olgac and R. Sipahi, "Dynamics and stability of variable-pitch milling," *Journal of Vibration and Control*, vol. 13, no. 7, pp. 1031–1043, 2007.

[21] M. Wan, W.-H. Zhang, J.-W. Dang, and Y. Yang, "A unified stability prediction method for milling process with multiple delays," *International Journal of Machine Tools and Manufacture*, vol. 50, no. 1, pp. 29–41, 2010.

[22] X. Zhang, C. Xiong, Y. Ding, and Y. Xiong, "Variable-step integration method for milling chatter stability prediction with multiple delays," *Science China Technological Sciences*, vol. 54, no. 12, pp. 3137–3154, 2011.

[23] G. Jin, H. Qi, Y. Cai, and Q. Zhang, "Stability prediction for milling process with multiple delays using an improved semi-discretization method," *Mathematical Methods in the Applied Sciences*, vol. 39, no. 4, pp. 949–958, 2016.

[24] G. Jin, H. Qi, Z. Li, J. Han, and H. Li, "A method for stability analysis of periodic delay differential equations with multiple time-periodic delays," *Mathematical Problems in Engineering*, vol. 2017, Article ID 9490142, 8 pages, 2017.

[25] V. Sellmeier and B. Denkena, "Stable islands in the stability chart of milling processes due to unequal tooth pitch," *International Journal of Machine Tools and Manufacture*, vol. 51, no. 2, pp. 152–164, 2011.

[26] S. Turner, D. Merdol, Y. Altintas, and K. Ridgway, "Modelling of the stability of variable helix end mills," *International Journal of Machine Tools and Manufacture*, vol. 47, no. 9, pp. 1410–1416, 2007.

[27] Z. Dombovari, Y. Altintas, and G. Stepan, "The effect of serration on mechanics and stability of milling cutters," *International Journal of Machine Tools and Manufacture*, vol. 50, no. 6, pp. 511–520, 2010.

[28] Z. Dombovari and G. Stepan, "The effect of helix angle variation on milling stability," *Journal of Manufacturing Science and Engineering*, vol. 134, no. 5, Article ID 051015, 2012.

[29] N. D. Sims, B. Mann, and S. Huyanan, "Analytical prediction of chatter stability for variable pitch and variable helix milling tools," *Journal of Sound and Vibration*, vol. 317, no. 3–5, pp. 664–686, 2008.

[30] A. R. Yusoff and N. D. Sims, "Optimisation of variable helix tool geometry for regenerative chatter mitigation," *International Journal of Machine Tools and Manufacture*, vol. 51, no. 2, pp. 133–141, 2011.

[31] G. Jin, Q. Zhang, S. Hao, and Q. Xie, "Stability prediction of milling process with variable pitch and variable helix cutters," *Proceedings of the Institution of Mechanical Engineers, Part C: Journal of Mechanical Engineering Science*, vol. 228, no. 2, pp. 281–293, 2014.

[32] G. Jin, Q. Zhang, H. Qi, and B. Yan, "A frequency-domain solution for efficient stability prediction of variable helix cutters milling," *Proceedings of the Institution of Mechanical Engineers, Part C: Journal of Mechanical Engineering Science*, vol. 228, no. 15, pp. 2702–2710, 2014.

[33] S. Seguy, T. Insperger, L. Arnaud, G. Dessein, and G. Peign, "On the stability of high-speed milling with spindle speed variation," *The International Journal of Advanced Manufacturing Technology*, vol. 48, no. 9–12, pp. 883–895, 2010.

[34] G. Jin, H. Qi, Z. Li, and J. Han, "Dynamic modeling and stability analysis for the combined milling system with variable pitch cutter and spindle speed variation," *Communications in Nonlinear Science and Numerical Simulation*, vol. 63, pp. 38–56, 2018.

[35] T. Insperger, G. Stepan, F. Hartung, and J. Turi, "State dependent regenerative delay in milling processes," in *Proceedings of the ASME 2005: International Design Engineering Technical Conferences and Computers and Information in Engineering Conference*, pp. 955–964, Long Beach, CA, USA, September 2005.

[36] T. Insperger, "Full-discretization and semi-discretization for milling stability prediction: some comments," *International Journal of Machine Tools and Manufacture*, vol. 50, no. 7, pp. 658–662, 2010.

Hindawi
Mathematical Problems in Engineering
Volume 2020, Article ID 3961287, 8 pages
https://doi.org/10.1155/2020/3961287

Research Article

Simultaneity of Synchronization and Antisynchronization in a Class of Chaotic Systems

Zhi Liu,[1] Rongwei Guo,[2] Yi Qi,[3] and Cuimei Jiang[2]

[1]*School of Information Engineering, Key Laboratory of TCM Data Cloud Service in Universities of Shandong, Shandong Management University, Jinan 250357, China*
[2]*School of Mathematics and Statistics, Qilu University of Technology (Shandong Academy of Sciences), Jinan 250353, China*
[3]*Texas South University, Houston 250061, USA*

Correspondence should be addressed to Rongwei Guo; rongwei_guo@163.com

Received 11 April 2020; Revised 26 June 2020; Accepted 2 July 2020; Published 22 July 2020

Academic Editor: Alessio Gizzi

In this paper, a new synchronization phenomenon, that is, the simultaneity of synchronization and antisynchronization, is investigated for a class of chaotic systems. First, for a given chaotic system, necessary and sufficient conditions for the simultaneity of synchronization and antisynchronization are proved. Then, based on these conditions, all solutions of such synchronization phenomenon for a given chaotic system are derived. After that, physical controllers that are not only simple but also implementable are designed to realize the simultaneity of synchronization and antisynchronization in the above system. Finally, illustrative examples based on numerical simulations are used to verify the validity and effectiveness of the above theoretical results.

1. Introduction

Lorenz firstly proposed the famous Lorenz chaotic system in 1963. From then on, many researchers are stimulated to investigate the chaotic phenomena, and lots of chaotic systems and hyperchaotic systems are obtained. Since Pecora and Carroll first proposed the chaos synchronization method [1], meanwhile Ott et al. first obtained the chaos control method [2] in 1990, chaotic systems and their control problems have attracted significant attention and have been investigated extensively [3–17]. However, most of the existing works focus on investigating the same kind of synchronization in a given system, i.e., all the states of the master system have the same kind of synchronization with the corresponding states of the slave system. For example, when two systems are referred to as completely synchronized with each other, it means that each pair of the states between the interactive systems is completely synchronous.

In general, coexistence problem is very common, see [18–22] and the references therein. Recently, a new synchronization phenomenon, that is, the simultaneity of synchronization and antisynchronization, was firstly found in the generalized Lorenz system [23]. In this system, the variables x_1, x_2 of the master system antisynchronize the variables y_1, y_2 of the slave system, while the variable x_3 of the master system synchronizes the variable y_3 of the slave system. This new synchronization phenomenon is very interesting not only in applications but also in theory. The existence of the simultaneity of synchronization and antisynchronization problem is a basis for designing a physical controller. Zhang et al. [23] found this new synchronization phenomenon, but they did not address some critical theoretical questions. For instance, for a given chaotic system, how to prove the existence of the simultaneity of synchronization and antisynchronization? In addition, if such new synchronization phenomenon exists, how many solutions can be derived. Therefore, for a given chaotic system, it is critical to have a systematic method that can be used for proving the simultaneity of synchronization and antisynchronization, deriving all solutions for this type of synchronization phenomenon and then designing the corresponding physical controller. To address this critical problem, this study is to develop such a systematic method that can be applied to a class of chaotic systems.

To realize the simultaneity of synchronization and antisynchronization in a chaotic system, many methods can be used, including the linear feedback control method, nonlinear feedback control method, and dynamic feedback control method. Among those methods, the dynamic feedback control method has been widely applied and was adopted by this study.

In this paper, we investigated the simultaneity of synchronization and antisynchronization problem in a class of chaotic systems by using the dynamic feedback control method. At first, the existence of the simultaneity of synchronization and antisynchronization problem of such system is proved. Then, physical controllers were designed to realize the simultaneity of synchronization and antisynchronization in such system. After that, numerical simulations were conducted to verify the validity and correctness of the obtained theoretical results.

2. Preliminary

Consider the following chaotic system:

$$\dot{X} = F(X), \tag{1}$$

where $X \in R^n$ is the state, $F(X) \in R^n$ is a continuous vector function, i.e.,

$$X = \begin{pmatrix} X^E \\ X^e \end{pmatrix}, \quad F(X) = \begin{pmatrix} F^E(X) \\ F^e(X) \end{pmatrix} = \begin{pmatrix} F^E(X^E, X^e) \\ F^e(X^E, X^e) \end{pmatrix}, \tag{2}$$

$X^E \in R^m, X^e \in R^{n-m}, \quad m \geq 1, \quad F^E(X) \in R^m$, and $F^e(X) \in R^{n-m}$.

For system (1), the slave system can be described as

$$\dot{Y} = F(Y) + Bu, \tag{3}$$

where $Y \in R^n$ is the state, $F(Y) \in R^n$ is a continuous vector function, $B \in R^{n\times r}$ is a constant matrix, $r \geq 1$, and $u \in R^r$ is the controller to be designed, i.e.,

$$Y = \begin{pmatrix} Y^E \\ Y^e \end{pmatrix}, \quad B = \begin{pmatrix} B^E \\ B^e \end{pmatrix}, \tag{4}$$

$$F(Y) = \begin{pmatrix} F^E(Y) \\ F^e(Y) \end{pmatrix} = \begin{pmatrix} F^E(Y^E, Y^e) \\ F^e(Y^E, Y^e) \end{pmatrix}, \tag{5}$$

where $Y^E \in R^m$, $Y^e \in R^{n-m}$, $m \geq 1$, $F^E(Y) \in R^m$, and $F^e(Y) \in R^{n-m}$.

Let $E^E = X^E + Y^E$ and $E^e = Y^e - X^e$, then the sum and error system can be described as follows:

$$\dot{E} = G(X, Y, E) + Bu, \tag{6}$$

where $E \in R^n$ is the state:

$$E = \begin{pmatrix} E^E \\ E^e \end{pmatrix}, \tag{7}$$

$$G(X, Y, E) = \begin{pmatrix} G^E(X, Y, E) \\ G^e(X, Y, E) \end{pmatrix} = \begin{pmatrix} F^E(Y^E, Y^e) + F^E(X^E, X^e) \\ F^e(Y^E, Y^e) - F^e(X^E, X^e) \end{pmatrix}, \tag{8}$$

$$\dot{E}^E = F^E(Y^E, Y^e) + F^E(X^E, X^e) + B^E u, \tag{9}$$

$$\dot{E}^e = F^e(Y^E, Y^e) - F^e(X^E, X^e) + B^e u, \tag{10}$$

where B is given by equation (4).

Next, a definition is presented as follows.

Definition 1. Consider the sum system (9) and the error system (10). If $\lim_{t\longrightarrow\infty}\|E^E(t)\| = 0$ and $\lim_{t\longrightarrow\infty}\|E^e(t)\| = 0$, then the master system (1) and the slave system (3) are called to achieve the simultaneity of synchronization and antisynchronization.

To present the proposed method, a lemma is introduced at first.

Lemma 1 (see [17]). *Consider the following system:*

$$\dot{x} = h(x) + bu, \tag{11}$$

where $x \in R^n$ is the state, $h(x) \in R^n$ is a vector function, $b \in R^{n\times l}$ is a constant matrix, $l \geq 1$, and $u \in R^l$ is the controller to be designed. If $(h(x), b)$ can be stabilized, then a dynamic feedback controller u is designed as follows:

$$u = Kx, \tag{12}$$

where $K = k(t)b^T$, and the feedback gain $k(t)$ is updated by the following law:

$$\dot{k}(t) = -\|x(t)\|^2. \tag{13}$$

3. Problem Formulation

Consider the following chaotic system:

$$\dot{x} = f(x), \tag{14}$$

where $x \in R^n$ is the state and $f(x) \in R^n$ is a vector function.

The main goal of this paper is to investigate the simultaneity of synchronization and antisynchronization for the given chaotic system (14) in the following three aspects:

(1) The existence of the simultaneity of synchronization and antisynchronization.

(2) The solutions of the simultaneity of synchronization and antisynchronization for this chaotic system.

(3) The implementation of the simultaneity of synchronization and antisynchronization. A simple and physically implementable controller is designed for such a problem.

4. Main Result

4.1. Existence of the Simultaneity of Synchronization and Antisynchronization. In this section, the necessary and sufficient conditions for the existence of the simultaneity of synchronization and antisynchronization are proved for two given chaotic systems.

Theorem 1. *Consider the chaotic system (1). Its existence of the simultaneity of synchronization and antisynchronization can be realized by the controllers in the following form:*

$$\begin{aligned} u &= H\left(E^E, E^e, X\right), \\ H(0,0,X) &= 0, \end{aligned} \tag{15}$$

if and only if

$$F^E\left(X^E, X^e\right) = -F^E\left(-X^E, X^e\right), \tag{16}$$

$$F^e\left(X^E, X^e\right) = F^E\left(-X^E, X^e\right). \tag{17}$$

Proof (necessity). According to the nonlinear control theorem, $E^E = 0$ and $E^e = 0$ should be the equilibria of the following systems:

$$\begin{aligned} \dot{E}^E &= F^E\left(Y^E, Y^e\right) + F^E\left(X^E, X^e\right) \\ &= F^E\left(E^E - X^E, E^e + X^e\right) + F^E\left(X^E, X^e\right), \end{aligned} \tag{18}$$

$$\begin{aligned} \dot{E}^e &= F^e\left(Y^E, Y^e\right) - F^e\left(X^E, X^e\right) \\ &= F^e\left(E^E - X^E, E^e + X^e\right) - F^E\left(X^E, X^e\right), \end{aligned} \tag{19}$$

respectively.

It results in

$$\begin{aligned} F^E\left(-X^E, X^e\right) + F^E\left(X^E, X^e\right) &= 0, \\ F^e\left(-X^E, X^e\right) - F^E\left(X^E, X^e\right) &= 0, \end{aligned} \tag{20}$$

i.e., equations (16) and (17) hold. □

Proof (sufficiency). If equations (16) and (17) hold, which implies that $E^E = 0$ and $E^e = 0$ are the equilibria of systems (18) and (19), respectively. Thus, the simultaneity of synchronization and antisynchronization for the given chaotic system can be realized by the controller u given in equation (15).

Especially, if

$$F(X) = \begin{pmatrix} F^E\left(X^E, X^e\right) \\ F^e\left(X^E, X^e\right) \end{pmatrix} = \begin{pmatrix} M\left(X^e\right)X^E \\ N\left(X^E\right)X^e \end{pmatrix}, \tag{21}$$

where $N(-X^E) = N(X^E)$, system (1) becomes

$$\begin{aligned} \dot{X}^E &= M\left(X^e\right)X^E, \\ \dot{X}^e &= N\left(X^E\right)X^e, \end{aligned} \tag{22}$$

and the simultaneity of synchronization and antisynchronization of system (22) holds. □

Theorem 2. *Consider the chaotic system (14). Its existence of the simultaneity of synchronization and antisynchronization if and only the following algebraic equation about α*

$$\begin{cases} f_1(\alpha x) & \equiv & \alpha_1 f_1(x), \\ f_2(\alpha x) & \equiv & \alpha_2 f_2(x), \\ \vdots & \equiv & \vdots \\ f_n(\alpha x) & \equiv & \alpha_n f_n(x), \end{cases} \tag{23}$$

has a solution in the following form:

$$\beta^{(s)} = \begin{pmatrix} \alpha_{i_1} \\ \vdots \\ \alpha_{i_{s-1}} \\ \alpha_{i_s} \\ \alpha_{i_{s+1}} \\ \vdots \\ \alpha_{i_n} \end{pmatrix} = \begin{pmatrix} -1 \\ -1 \\ \vdots \\ -1 \\ 1 \\ \vdots \\ 1 \end{pmatrix} \leftarrow s, \tag{24}$$

where $s \geq 1$ is the number of $\alpha_{i_j} = -1$, $i_j \in \Lambda = \{1, 2, \ldots, n\}$, $j = 1, 2, \ldots, n$, and α is given as follows:

$$\alpha = \begin{pmatrix} \alpha_1 & 0 & 0 & \cdots & 0 \\ 0 & \alpha_2 & 0 & \cdots & 0 \\ 0 & 0 & \alpha_3 & \cdots & 0 \\ \vdots & \vdots & \vdots & \vdots & \vdots \\ 0 & 0 & 0 & \cdots & \alpha_n \end{pmatrix}, \tag{25}$$

$$\left|\alpha_i\right| = 1, \quad i \in \Lambda. \tag{26}$$

Proof. For system (14), the uncontrolled slave system is given as

$$\dot{y} = f(y), \tag{27}$$

where $y \in R^n$ is the state.

Let $e = y - \alpha x$, where α is given in (25), then the sum and error system is

$$\dot{e} = f(y) - \alpha f(x), \tag{28}$$

where $e \in R^n$ is the state.

Then, the existence of the simultaneity of synchronization and antisynchronization in system (14) if and only if $e = 0$ is the equilibrium point of system (28), i.e.,

$$f(y) - \alpha f(x) = f(\alpha x) - \alpha f(x) \equiv 0, \tag{29}$$

which completes the proof. □

4.2. Solutions of the Simultaneity of Synchronization and Antisynchronization. We can obtain all solutions of the simultaneity of synchronization and antisynchronization in the given chaotic system (14) by solving equation (23).

After proving the existence of the simultaneity of synchronization and antisynchronization in a given chaotic

system (1), the question about how to find a nonsingular transformation matrix T to transfer system (14) into system (1) will be raised naturally.

In general, according to the solutions of the algebraic equation (23), we can find the matrix T by the following algorithm:

Algorithm 1. $k = 1$; let s be the number of $\alpha_j = -1,\ j \in \Lambda$,

$$\min\left\{j \mid \alpha_j = -1,\ j \in \Lambda\right\} \triangleq i_k, \tag{30}$$

while $k \le s$ do

$$k = k + 1, \tag{31}$$

$$\min_{j\in\Lambda}\left\{\alpha_j = -1,\ j \ne i_1, i_2, \ldots, i_{k-1}\right\} \triangleq i_k. \tag{32}$$

Then, let

$$X^E = \begin{pmatrix} X_1^E \\ X_2^E \\ \vdots \\ X_s^E \end{pmatrix} = \begin{pmatrix} x_{i_1} \\ x_{i_2} \\ \vdots \\ x_{i_s} \end{pmatrix}. \tag{33}$$

Next,

$$k = s + 1, \tag{34}$$

$$\min\left\{j \mid \alpha_j = 1,\ j \in \Lambda\right\} \triangleq i_k. \tag{35}$$

while $k \le n$ do

$$k = k + 1, \tag{36}$$

$$\min\left\{\alpha_j = 1,\ j \ne i_{s+1}, i_{s+2}, \ldots, i_{k-1},\ j \in \Lambda\right\} \triangleq i_k. \tag{37}$$

Then, let

$$X^e = \begin{pmatrix} X_{s+1}^e \\ X_{s+2}^e \\ \vdots \\ X_n^e \end{pmatrix} = \begin{pmatrix} x_{i_{s+1}} \\ x_{i_{s+2}} \\ \vdots \\ x_{i_n} \end{pmatrix}. \tag{38}$$

By Algorithm 1, the nonsingular transform matrix T can be obtained as follows:

$$T = \begin{pmatrix} \delta_n^{i_1} \\ \vdots \\ \delta_n^{i_s} \\ \vdots \\ \delta_n^{i_n} \end{pmatrix}, \tag{39}$$

$$\delta_n^{i_1} = \begin{pmatrix} 0 & \cdots & 0 & 1 & 0 & \cdots & 0 \\ & & & \uparrow & & & \\ & & & i_1 & & & \end{pmatrix} \in R^n, \tag{40}$$

where $i_j \in \Lambda,\ j = 1, 2, \ldots, n$.

For example, for the chaotic system, $\dot{x} = f(x)$, $x \in R^3$, and $f(x) \in R^3$. If $\alpha_1 = -1$, $\alpha_2 = 1$, and $\alpha_3 = -1$, then $s = 2$, $i_1 = 1$, $i_2 = 3$, and $i_3 = 2$. By Algorithm 1, we obtain

$$T = \begin{pmatrix} \delta_3^{i_1} \\ \delta_3^{i_2} \\ \delta_3^{i_3} \end{pmatrix} = \begin{pmatrix} \delta_3^{1} \\ \delta_3^{3} \\ \delta_3^{2} \end{pmatrix} = \begin{pmatrix} 1 & 0 & 0 \\ 0 & 0 & 1 \\ 0 & 1 & 0 \end{pmatrix}. \tag{41}$$

By T, the system $\dot{x} = f(x)$ is transferred into the following system:

$$\dot{X} = F(X), \tag{42}$$

$$\begin{aligned} X &= \begin{pmatrix} X_1 \\ X_2 \\ X_3 \end{pmatrix} = \begin{pmatrix} X^E \\ X^e \end{pmatrix} = Tx = \begin{pmatrix} x_1 \\ x_3 \\ x_2 \end{pmatrix}, \\ F(X) &= \begin{pmatrix} F_1(X) \\ F_2(X) \\ F_3(X) \end{pmatrix} = \begin{pmatrix} F^E(X^E, X^e) \\ F^e(X^E, X^e) \end{pmatrix} \\ &= Tf(x) = \begin{pmatrix} f_1(x) \\ f_3(x) \\ f_2(x) \end{pmatrix}. \end{aligned} \tag{43}$$

4.3. Implementation of the Simultaneity of Synchronization and Antisynchronization. In this section, a simple and physically implementable controller is designed for the implementation of the simultaneity of synchronization and antisynchronization.

According to the results in [16], we propose the following theorem.

Theorem 3. *Consider the sum system (9) and error system (10).*

If $(G(X, Y, E), B)$ can be stabilized, then the controller u is designed as follows:

$$u = KE, \tag{44}$$

where $K = k(t)B^T$, and $k(t)$ is updated by the following update law:

$$\dot{k} = -\gamma\|E\|^2, \tag{45}$$

and $\gamma > 0$, which implies that the master system (1) and the slave system (3) reach the simultaneity of synchronization and antisynchronization.

Proof. Since $(G(X, Y, E), B)$ can be stabilized, according to Lemma 1, the controller u is designed as equation (44). □

5. Illustrative Examples Based on Numerical Simulations

In this section, two examples based on numerical simulations are used to demonstrate the validity and effectiveness of the derived theoretical results.

Example 1. The Lorenz system [24]:

$$\dot{x} = f(x) = \begin{pmatrix} f_1(x) \\ f_2(x) \\ f_3(x) \end{pmatrix} = \begin{pmatrix} 10(x_2 - x_1) \\ 28x_1 - x_2 - x_1x_3 \\ -\frac{8}{3}x_3 + x_1x_2 \end{pmatrix}. \quad (46)$$

According to the algebraic equation (24),

$$\begin{cases} f_1(\alpha x) - \alpha_1 f_1(\alpha x) = 10(\alpha_2 - \alpha_1)x_2 \equiv 0, \\ f_2(\alpha x) - \alpha_2 f_2(\alpha x) = 28(\alpha_1 - \alpha_2)x_1 - (\alpha_1\alpha_3 - \alpha_2)x_1x_3 \equiv 0, \\ f_3(\alpha x) - \alpha_3 f_3(\alpha x) = (\alpha_1\alpha_2 - \alpha_3)x_1x_2 \equiv 0, \end{cases} \quad (47)$$

and it results in

$$\begin{cases} \alpha_2 = \alpha_1, \\ \alpha_1\alpha_3 = \alpha_2, \\ \alpha_1\alpha_2 = \alpha_2. \end{cases} \quad (48)$$

By solving equation (48), a solo solution can be obtained:

$$\beta^{(2)} = \begin{pmatrix} \alpha_{i_1} \\ \alpha_{i_2} \\ \alpha_{i_3} \end{pmatrix} = \begin{pmatrix} \alpha_1 \\ \alpha_2 \\ \alpha_3 \end{pmatrix} = \begin{pmatrix} -1 \\ -1 \\ 1 \end{pmatrix}. \quad (49)$$

By Algorithm 1, it results in

$$T = \begin{pmatrix} \delta_3^{i_1} \\ \delta_3^{i_2} \\ \delta_3^{i_3} \end{pmatrix} = \begin{pmatrix} \delta_3^1 \\ \delta_3^2 \\ \delta_3^2 \end{pmatrix} = \begin{pmatrix} 1 & 0 & 0 \\ 0 & 1 & 0 \\ 0 & 0 & 1 \end{pmatrix}. \quad (50)$$

Thus, let $X^E = (x_1, x_2)^T$ and $X^e = x_3$; the Lorenz system (46) is rewritten as follows:

$$\begin{aligned} \dot{X}^E &= F^E(X), \\ \dot{X}^e &= F^e(X), \end{aligned} \quad (51)$$

$$F^E(X) = M(X^e)X^E, \quad (52)$$

$$M(X^e) = \begin{pmatrix} -10 & 10 \\ 28 - X^e & -1 \end{pmatrix}, \quad (53)$$

$$F^e(X) = -\frac{8}{3}X^e + X_1^E X_2^E. \quad (54)$$

Then, the slave Lorenz system is given as

$$\dot{Y} = F(Y) + Bu, \quad (55)$$

$$\begin{aligned} Y &= \begin{pmatrix} Y^E \\ Y^e \end{pmatrix}, \\ F(Y) &= \begin{pmatrix} F^E(Y) \\ F^e(Y) \end{pmatrix}, \end{aligned} \quad (56)$$

$$F^E(Y) = M(Y^e)Y^E, \quad (57)$$

$$M(Y^e) = \begin{pmatrix} -10 & 10 \\ 28 - Y^e & -1 \end{pmatrix}, \quad (58)$$

$$F^e(Y) = -\frac{8}{3}Y^e + Y_1^E Y_2^E, \quad (59)$$

$$\begin{aligned} B &= \begin{pmatrix} B^E \\ B^e \end{pmatrix} = \begin{pmatrix} B^E \\ 0 \end{pmatrix}, \\ B^E &= \begin{pmatrix} 0 \\ 1 \end{pmatrix}. \end{aligned} \quad (60)$$

Let $E^E = X^E + Y^E$ and $E^e = Y^E - X^e$; then, the sum and error system is given as

$$\dot{E} = G(X, Y, E) + Bu, \quad (61)$$

$$E = \begin{pmatrix} E^E \\ E^e \end{pmatrix}, \quad (62)$$

where B is given by equation (60) and u is the controller to be designed.

Considering the following uncontrolled sum and error system,

$$\begin{aligned} \dot{E}_1^E &= -10E_1^E + 10E_2^E, \\ \dot{E}_2^E &= 28E_1^E - E_2^E - E_1^E E_3^e - X_3^e E_1^E + X_1^E E_3^e, \\ \dot{E}_3^e &= -\frac{8}{3}E_3^e + E_1^E E_2^E - X_1^E E_2^E - X_2^E E_1^E, \end{aligned} \quad (63)$$

if $E_2^E = 0$, then the following system

$$\begin{aligned} \dot{E}_1^E &= -10E_1^E, \\ \dot{E}_3^e &= -\frac{8}{3}E_3^e - X_2^E E_1^E, \end{aligned} \quad (64)$$

is globally asymptotically stable.

Thus, $(G(X, Y, E), B)$ can be stabilized, and according to Theorem 3, the controller is designed as

$$u = KE = k(t)B^T E = k(t)\begin{pmatrix} 0 & 1 & 0 \end{pmatrix}E = k(t)E_2^E, \quad (65)$$

$$\begin{aligned} \dot{E}_1^E &= -10E_1^E + 10E_2^E, \\ \dot{E}_2^E &= 28E_1^E - E_2^E - E_1^E E_3^e - X_3^e E_1^E + X_1^E E_3^e + k(t)E_2^E, \\ \dot{E}_3^e &= -\frac{8}{3}E_3^e + E_1^E E_2^E - X_1^E E_2^E - X_2^E E_1^E, \end{aligned} \quad (66)$$

and $\dot{k}(t) = -\|E\|^2$.

To demonstrate the validity and correctness of the derived theoretical results, numerical simulation is conducted by setting the following initial conditions: $x_1(0) = 1.2$, $x_2(0) = -2.3$, $x_3(0) = 3.2$, $y_1(0) = 5.8$, $y_2(0) = -6.2$, $y_3(0) = 7.1$, and $k(0) = -1$. Figure 1 shows that the sum and error system is asymptotically stable; Figure 2 shows that the states of the master

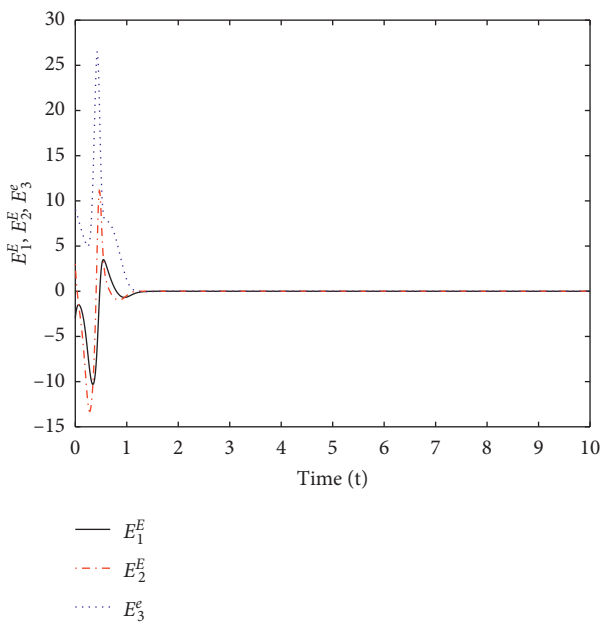

FIGURE 1: The sum and error system is asymptotically stable.

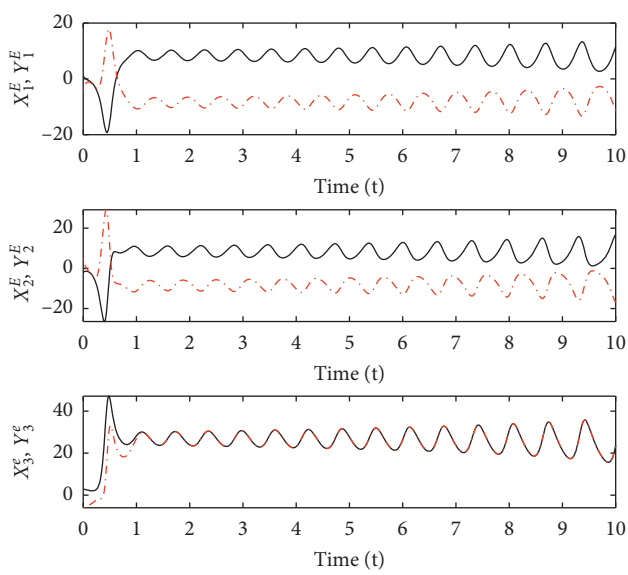

FIGURE 2: X_1^E, X_2^E, X_3^e and Y_1^E, Y_2^E, Y_3^e, respectively.

system (49) and the controlled slave system (53), respectively. Figure 3 shows that the feedback gain $k(t)$ tends to a constant.

Example 2. The Chen–Lee system [25]:

$$\dot{x} = f(x) = \begin{pmatrix} f_1(x) \\ f_2(x) \\ f_3(x) \end{pmatrix} = \begin{pmatrix} -x_2x_3 + 5x_1 \\ x_1x_3 - 10x_2 \\ \frac{1}{3}x_1x_2 - 3.8x_3 \end{pmatrix}, \tag{67}$$

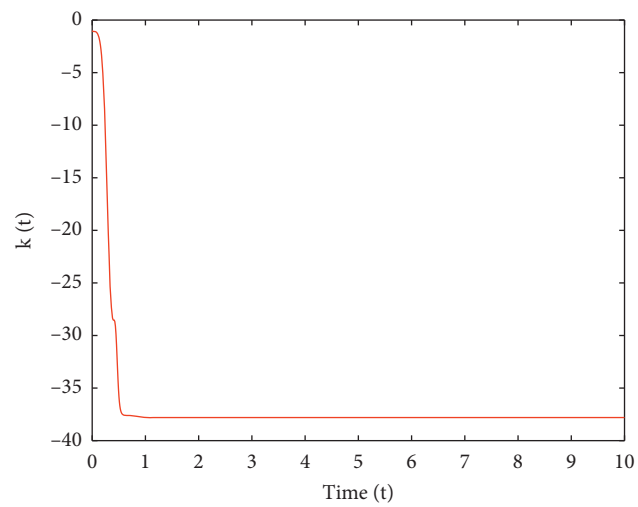

FIGURE 3: $k(t)$ tends to a constant.

where $x \in R^3$ is the state and $f(x) \in R^3$ is a continuous vector function.

According to the algebraic equation (23), it results in

$$\begin{cases} \alpha_2\alpha_3 = \alpha_1, \\ \alpha_1\alpha_3 = \alpha_2, \\ \alpha_1\alpha_3 = \alpha_2. \end{cases} \tag{68}$$

There are three solutions for equation (68), i.e.,

$$\beta_1^{(2)} = \begin{pmatrix} \alpha_{i_1} \\ \alpha_{i_2} \\ \alpha_{i_3} \end{pmatrix} = \begin{pmatrix} \alpha_2 \\ \alpha_3 \\ \alpha_1 \end{pmatrix} = \begin{pmatrix} -1 \\ -1 \\ 1 \end{pmatrix}, \tag{69}$$

$$\beta_2^{(2)} = \begin{pmatrix} \alpha_{i_1} \\ \alpha_{i_3} \\ \alpha_{i_2} \end{pmatrix} = \begin{pmatrix} \alpha_1 \\ \alpha_3 \\ \alpha_2 \end{pmatrix} = \begin{pmatrix} -1 \\ -1 \\ 1 \end{pmatrix}, \tag{70}$$

$$\beta_3^{(2)} = \begin{pmatrix} \alpha_{i_1} \\ \alpha_{i_2} \\ \alpha_{i_3} \end{pmatrix} = \begin{pmatrix} \alpha_1 \\ \alpha_2 \\ \alpha_3 \end{pmatrix} = \begin{pmatrix} -1 \\ -1 \\ 1 \end{pmatrix}. \tag{71}$$

For the solution given in equation (69), $\alpha_1 = 1$ and $\alpha_2 = \alpha_3 = -1$.

By Algorithm 1, it results in

$$T = \begin{pmatrix} \delta_3^{i_1} \\ \delta_3^{i_2} \\ \delta_3^{i_3} \end{pmatrix} = \begin{pmatrix} \delta_3^2 \\ \delta_3^3 \\ \delta_3^1 \end{pmatrix} = \begin{pmatrix} 0 & 1 & 0 \\ 0 & 0 & 1 \\ 1 & 0 & 0 \end{pmatrix}. \tag{72}$$

Thus, let $X^E = (X_1^E, X_2^E)^T = (x_2, x_3)^T$, $X^e = x_1$; then, the Chen–Lee system (67) is rewritten as follows:

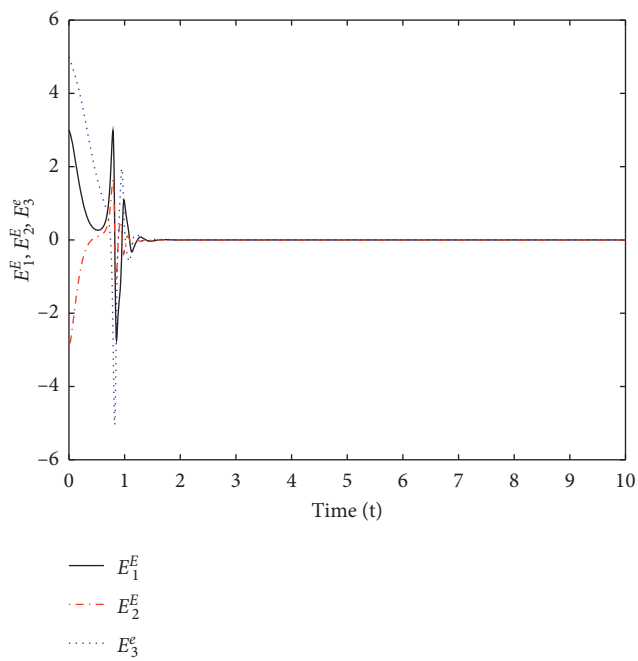

FIGURE 4: The sum and error system is asymptotically stable.

$$\dot{X}^E = F^E\left(X^E, X^e\right),$$
$$\dot{X}^e = F^e\left(X^E, X^e\right), \tag{73}$$

$$F^E\left(X^E, X^e\right) = M\left(X^e\right)X^E, \tag{74}$$

$$M\left(X^e\right) = \begin{pmatrix} -10 & X^e \\ \frac{1}{3}X^e & -3.8 \end{pmatrix}, \tag{75}$$

$$F^e\left(X^E, X^e\right) = 5X^e - X_1^E X_2^E, \tag{76}$$

and $F^e\left(X^E, X^e\right) = F^e\left(-X^E, X^e\right)$.

Next, the slave Chen–Lee system is given as

$$\dot{Y}^E = F^E\left(Y^E, Y^e\right) + B^E u,$$
$$\dot{Y}^e = F^e\left(Y^E, Y^e\right) + B^e u, \tag{77}$$

$$F^E\left(Y^E, Y^e\right) = M\left(Y^e\right)Y^E, \tag{78}$$

$$M\left(Y^e\right) = \begin{pmatrix} -10 & Y^e \\ \frac{1}{3}Y^e & -3.8 \end{pmatrix}, \tag{79}$$

$$F^e\left(Y^E, Y^e\right) = 5Y^e - Y_1^E Y_2^E, \tag{80}$$

$$B^E = \begin{pmatrix} 0 & 0 \\ 1 & 0 \end{pmatrix},$$
$$B^e = \begin{pmatrix} 0 & 1 \end{pmatrix}, \tag{81}$$

and $F^e\left(Y^E, Y^e\right) = F^e\left(-Y^E, Y^e\right)$; the controller u is designed as follows:

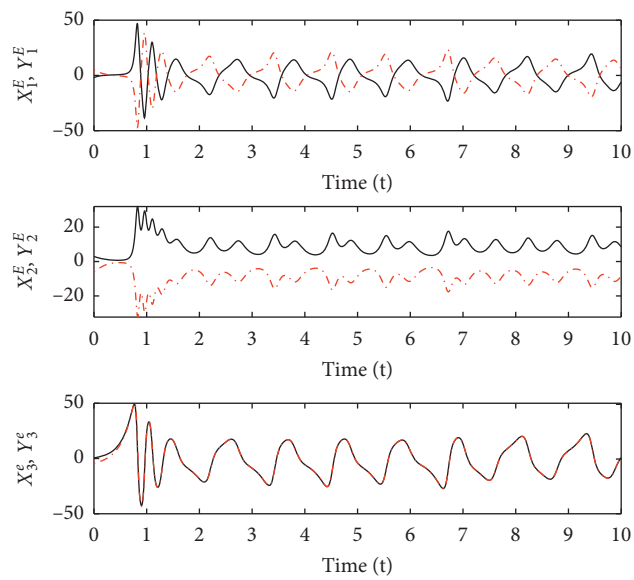

FIGURE 5: X_1^E, X_2^E, X_3^e and Y_1^E, Y_2^E, Y_3^e, respectively.

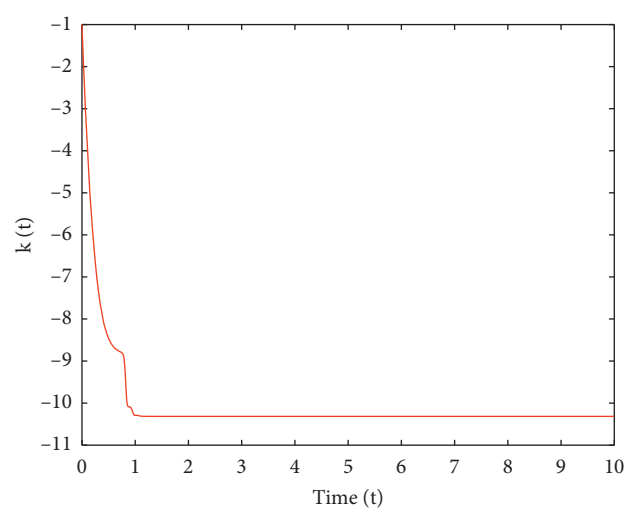

FIGURE 6: $k(t)$ tends to a constant.

$$u = KE = k(t)B^T E = k(t)\begin{pmatrix} 0 & 1 & 0 \\ 0 & 0 & 1 \end{pmatrix}E = \begin{pmatrix} k(t)E_2^E \\ k(t)E_3^e \end{pmatrix}, \tag{82}$$

and $\dot{k}(t) = -\|E\|^2$.

Similarly, for this example, numerical simulation is conducted by setting following initial conditions: $x_1(0) = 1.2$, $x_2(0) = -3.1$, $x_3(0) = 1.2$, $y_1(0) = 4.8$, $y_2(0) = -3.2$, $y_3(0) = 7.6$, and $k(0) = -1$. Figure 4 shows that the sum and error system is asymptotically stable; Figure 5 shows the states X_1^E, X_2^E, X_3^e and Y_1^E, Y_2^E, Y_3^e, respectively. Figure 6 shows that the feedback gain $k(t)$ tends to a constant.

For solutions given in equations (70) and (71), similar results can be obtained by the same procedure:

6. Conclusions

In this paper, we investigated a new synchronization phenomenon that is the simultaneity of synchronization and antisynchronization for a class of chaotic systems. We developed a systematic method that can be used for proving the existence of the simultaneity of synchronization and antisynchronization, deriving all solutions for this type of synchronization phenomenon and then designing the corresponding physical controllers. To verify the validity and effectiveness of the theoretical results, two illustrative examples based on numerical simulations were provided.

In the future, microcontroller-based applications and predefined-time chaos synchronization problem need to be developed based on the results of this study.

Data Availability

No data were used to support this study. In our paper, we only use MATLAB for simulation. Therefore, we can only provide simulation programming, which can be obtained from the corresponding author upon request.

Conflicts of Interest

The authors declare that there are no conflicts of interest regarding the publication of this paper.

Acknowledgments

This work is supported by the Shandong Province Key Research and Development Program (Grant No. 2019GGX101056), the Natural Science Foundation of Shandong Province (Grant No. ZR2018MF016).

References

[1] L. M. Pecora and T. L. Carroll, "Synchronization in chaotic systems," *Physical Review Letters*, vol. 64, no. 8, pp. 821–824, 1990.

[2] E. Ott, C. Grebogi, and J. A. Yorke, "Controlling chaos," *Physical Review Letters*, vol. 64, no. 11, pp. 1196–1199, 1990.

[3] R. Guo, "A simple adaptive controller for chaos and hyperchaos synchronization," *Physics Letters A*, vol. 372, no. 34, pp. 5593–5597, 2008.

[4] A. Göksu, U. E. Kocamaz, and Y. Uyaroğlu, "Synchronization and control of chaos in supply chain management," *Computers & Industrial Engineering*, vol. 86, pp. 107–115, 2015.

[5] X. Yi, R. Guo, and Y. Qi, "Stabilization of chaotic systems with both uncertainty and disturbance by the UDE-based control method," *IEEE Access*, vol. 8, no. 1, pp. 62471–62477, 2020.

[6] G. Wang, "Stabilization and synchronization of genesio-tesi system via single variable feedback controller," *Physics Letters A*, vol. 374, no. 28, pp. 2831–2834, 2010.

[7] J. Sieber, E. O. Chenko, and M. Wolfrum, "Controlling unstable chaos: stabilizing chimera states by feedback," *Physical Review Letter*, vol. 112, no. 5, 2014.

[8] D. Meng and Y. Li, "Adaptive synchronization of 4-dimensional energy resource unknown time-varying delay systems," *IEEE Access*, vol. 5, pp. 21258–21263, 2017.

[9] T. Wang, D. Wang, and K. Wu, "Chaotic adaptive synchronization control and application in chaotic secure communication for industrial internet of things," *IEEE Access*, vol. 6, pp. 8584–8590, 2018.

[10] Z. Wang, Y. Sun, and B. Liang, "Synchronization control for bilateral teleoperation system with position error constraints: a fixed-time approach," *ISA Transactions*, vol. 93, pp. 125–136, 2019.

[11] L. Liu, R. Guo, J. Ji, Z. H. Miao, and J. Zhou, "Practical consensus tracking control of multiple nonholonomic wheeled mobile robots in polar coordinates," *International Journal of Robust Nonlinear Control*, vol. 30, no. 10, pp. 3831–3847, 2020.

[12] W. Wang, X. Jia, Z. Wang et al., "Fixed-time synchronization of fractional order memristive mam neural networks by sliding mode control," *Neurocomputing*, vol. 401, no. 8, pp. 364–376, 2020.

[13] M. Luo and M. Pourgholi, "Robust fixed-time synchronization of fractional order chaotic using free chattering nonsingular adaptive fractional sliding mode controller design," *Chaos, Solitons & Fractals*, vol. 113, no. 8, pp. 135–147, 2018.

[14] A. M. Alimi, C. Aouiti, and E. A. Assali, "Finite-time and fixed-time synchronization of a class of inertial neural networks with multi-proportional delays and its application to secure communication," *Neurocomputing*, vol. 332, no. 3, pp. 29–43, 2019.

[15] H. Jiang, Y. Liu, L. Zhang, and J. Yu, "Anti-phase synchronization and symmetry-breaking bifurcation of impulsively coupled oscillators," *Communications in Nonlinear Science and Numerical Simulation*, vol. 39, no. 10, pp. 199–208, 2016.

[16] L. Ren and R. Guo, "Synchronization and antisynchronization for a class of chaotic systems by a simple adaptive controller," *Mathematical Problems in Engineering*, vol. 2015, Article ID 434651, 7 pages, 2015.

[17] R. Guo, "Projective synchronization of a class of chaotic systems by dynamic feedback control method," *Nonlinear Dynamics*, vol. 90, no. 1, pp. 53–64, 2017.

[18] G.-D. Lin, Y.-T. Gao, L. Wang, D. X. Meng, and X. Yu, "Elastic-inelastic-interaction coexistence and double wronskian solutions for the whitham-broer-kaup shallow-water-wave model," *Communications in Nonlinear Science and Numerical Simulation*, vol. 16, no. 8, pp. 3090–3096, 2011.

[19] I. Aviram and A. Rabinovitch, "Bifurcation analysis of bacteria and bacteriophage coexistence in the presence of bacterial debris," *Communications in Nonlinear Science and Numerical Simulation*, vol. 17, no. 1, pp. 242–254, 2012.

[20] W. Jiang and B. Niu, "On the coexistence of periodic or quasi-periodic oscillations near a hopf-pitchfork bifurcation in NFDE," *Communications in Nonlinear Science and Numerical Simulation*, vol. 18, no. 3, pp. 464–477, 2013.

[21] J. Kengne, Z. Njitacke Tabekoueng, and H. B. Fotsin, "Coexistence of multiple attractors and crisis route to chaos in autonomous third order duffing-holmes type chaotic oscillators," *Communications in Nonlinear Science and Numerical Simulation*, vol. 36, no. 7, pp. 29–44, 2016.

[22] A. Naimzada and M. Pireddu, "An evolutive discrete exchange economy model with heterogeneous preferences," *Chaos, Solitons & Fractals*, vol. 111, no. 12, pp. 35–43, 2018.

[23] Q. Zhang, J. Lü, and S. Chen, "Coexistence of anti-phase and complete synchronization in the generalized lorenz system," *Communications in Nonlinear Science and Numerical Simulation*, vol. 15, no. 10, pp. 3067–3072, 2010.

[24] E. N. Lorenz, "Deterministic nonperiodic flow," *Journal of Atmospheric Science*, vol. 20, no. 2, pp. 130–141, 1963.

[25] J.-H. Chen, "Controlling chaos and chaotification in the chen-lee system by multiple time delays," *Chaos, Solitons & Fractals*, vol. 36, no. 4, pp. 843–852, 2008.

Hindawi
Mathematical Problems in Engineering
Volume 2020, Article ID 6080636, 9 pages
https://doi.org/10.1155/2020/6080636

Research Article

Fixed-Time Flocking and Collision Avoidance Problem of a Cucker–Smale Model

Fen Nie and Xiaojun Duan

College of Liberal Arts and Sciences, National University of Defense Technology, Changsha 410073, China

Correspondence should be addressed to Xiaojun Duan; xj_duan@163.com

Received 1 March 2020; Revised 22 June 2020; Accepted 29 June 2020; Published 21 July 2020

Guest Editor: Cuimei Jiang

Multiagent systems are used in artificial intelligence, control theory, and social sciences. In this article, we studied a Cucker–Smale model with a continuous non-Lipschitz protocol. The methodology presented in the current paper is based on the explicit construction of a Lyapunov functional. By using the fixed-time control technology, we show that the flocking can occur in fixed-time and collision avoiding when a singular communication function with a weighted sum of sign functions of the relative velocities among agents, and we can obtain the estimation of the converging time which is independent of the initial states of agents. Theoretical results are supported by numerical simulations.

1. Introduction

In recent years, multiagent systems have various applications in widely fields such as biology, robotics, and control theory as well as sociology and economics [1–6]. Each agent typically has only a local, limited impact on other agents via the connections with its neighbor individuals in the given system, and the coherent behavior of the agents caused the emerging phenomenon in terms of flocking, in which the agents reach final agreement on controlled variables of interest. Multiagent dynamical systems are typically fragment for modelling of birds and fishes in nature world, and more and more scientists realized the importance of these models. Among others, the celebrated Cucker–Smale model [7, 8] provides a framework to explain the self-organizing behavior in various complex systems, and the Cucker–Smale model is given by the following ODE system:

$$\begin{cases} \dfrac{\mathrm{d}x_i}{\mathrm{d}t} = v_i, \quad t > 0, i = 1, 2, \ldots, N, \\ \dfrac{\mathrm{d}v_i}{\mathrm{d}t} = \displaystyle\sum_{j=1}^{N} a_{ij}\left(\left\|x_j - x_i\right\|\right)\left(v_j - v_i\right). \end{cases} \tag{1}$$

Subjecting to the initial configuration,

$$\left(x_i(0), v_i(0)\right) = \left(x_{i0}, v_{i0}\right). \tag{2}$$

Here, N is the number of particles, $x_i = (x_i^1, x_i^2, \ldots, x_i^d) \in \mathbb{R}^d$ and $v_i = (v_i^1, v_i^2, \ldots, v_i^d) \in \mathbb{R}^d$ denote the position and velocity of the ith particle at the time t, and a_{ij} quantify the way the birds influence each other:

$$a_{ij}^{CS}\left(\left\|x_j - x_i\right\|\right) = \frac{\psi\left(\left\|x_j - x_i\right\|\right)}{N}. \tag{3}$$

$\psi(r)$ called influence function quantifies the pairwise influence of the agent j on the alignment of the agent i, as a function of the distance: that is,

$$\psi_{ij}\left(\left\|x_j - x_i\right\|\right) = \frac{1}{\left(1 + \left\|x_j - x_i\right\|^2\right)^{\beta}}. \tag{4}$$

In [7], it is shown that the unconditional flocking occurs when $\beta < (1/2)$, while the conditional flocking occurs under some restricted conditions on the initial positions and velocities when $\beta \geq (1/2)$. In [9], the authors introduced the Cucker–Smale model with a singular communication weight influence function:

$$\psi(s) = s^{-\alpha}. \tag{5}$$

The authors extended the conclusions of unconditional flocking to $\beta \leq (1/2)$ by the energy method. In [10], the authors introduced a nonsymmetric influence function and took into account relative distance between agents instead of the distance between agents:

$$a_{ij}^{MT}\left(\|x_k - x_i\|\right) = \frac{\psi\left(\|x_k - x_i\|\right)}{\sum_{1\leq k\leq N}\psi\left(\|x_k - x_i\|\right)}. \tag{6}$$

Based on the notion of active sets, a sufficient condition for flocking was derived. The Cucker–Smale model was extensively studied, see, for example, time delay [11–15], pattern formation [16, 17], and hierarchical structure [14, 18–21]. However, the flocking phenomenon described in the most previous works is an asymptotic behavior without considered to collision avoidance behavior. In fact, the issue of collision avoiding plays a significant role in our real life, there are terrible consequences if collision avoidance is not considered. Meanwhile, under some occasional perturbations, individuals in bird flocks or fish schools can return back to ordered group motion after adjusting their states in a short time. In [22, 23], the authors introduced a modified Cucker–Smale mode by adding a term which prevents collisions. In [24], the authors used singular value influence function (5), through the Lyapunov method, when the initial value lies in the set of the admissible initial configurations can avoid collision. In [25], the authors improve the result of [24], when $\alpha > 1$, as long as the initial value satisfies with $i \neq j$ and $x_{i0} \neq x_{j0}$, and there will be no collision in the process of flocking; when $\alpha \geq 2$, the authors consider the singular communication weight of the form:

$$\psi_\delta(s) = (s - \delta)^{-\alpha}. \tag{7}$$

Expand the set of singular points of ψ from 0 to $[0, \delta]$, if the initial data satisfy with condition that the difference between any two agents is greater than the control parameter δ, there will also be no collision in the process of flocking, and the minimum distance between agents is greater than the control parameter δ. In [26], the authors introduced a Cucker–Smale model with a continuous non-Lipschitz protocol, and then the flocking can occur in finite time when the communication rate function is locally Lipschitz continuous and has a lower bound. In [27], the authors introduced a Cucker–Smale model with a continuous non-Lipschitz protocol, by constructing a Lyapunov functional to obtain the finite-time flocking, which is the convergence time depending on the initial values. Although finite-time flocking has favourable properties, the estimation of convergence time depends on initial states of networked agents, and this restricts the applications in practice if the knowledge of initial conditions is unavailable in advance. There are lots of works in the field of fix-time consensus [28–30], and we know little about considering the fixed-time flocking and collision avoidance of the Cucker–Smale model.

The main purpose of this article is to investigate the fixed-time flocking and collision avoidance of a Cucker–Smale model. The remaining of this paper is organized as follows. In Section 2, a Cucker–Smale model with continuous non-Lipschitz protocol is presented and some useful preliminaries are also given in this section. The existence of a global smooth solution is obtained in Section 3, Section 4 states the definition of fixed-time flocking and proved the fixed-time flocking and collision avoidance results, and some numerical results are given in Section 5. Section 6 concludes this paper.

2. Problem Statement and Preliminaries

Consider a model consisting of N autonomous agents. $x_i = (x_i^1, x_i^2, \ldots, x_i^d) \in \mathbb{R}^d$ and $v_i = (v_i^1, v_i^2, \ldots, v_i^d) \in \mathbb{R}^d$ denote the position and velocity of the i th particle at the time t, respectively, and the modified Cucker–Smale model in this paper can be described by the following equations:

$$\begin{cases} \dfrac{\mathrm{d}x_i}{\mathrm{d}t} = v_i, \quad t > 0, i = 1, 2, \ldots, N, \\[2ex] \dfrac{\mathrm{d}v_i}{\mathrm{d}t} = \dfrac{k_1}{N}\displaystyle\sum_{j=1}^{N}\psi\left(r_{ij} - \delta\right)\left(v_j - v_i\right) + \dfrac{k_2}{N}\displaystyle\sum_{j=1}^{N}\dfrac{1}{r_{ij} + R}\mathrm{sig}\left(v_j - v_i\right)^p + \dfrac{k_3}{N}\displaystyle\sum_{j=1}^{N}\dfrac{1}{r_{ij} + R}\mathrm{sig}\left(v_j - v_i\right)^q. \end{cases} \tag{8}$$

Subjecting to initial configuration,

$$\left(x_i(0), v_i(0)\right) = \left(x_{i0}, v_{i0}\right), \tag{9}$$

where $0 < p < 1 < q$ are two control parameters, k_1, k_2, and k_3 measure the interaction strength, and ψ was defined in (7); that is,

$$\psi\left(r_{ij} - \delta\right) = \left(r_{ij} - \delta\right)^{-\alpha}, \tag{10}$$

where $r_{ij} \doteq |x_i - x_j|$ is the distance of any two agents:

$$\begin{aligned} sig\left(v_j - v_i\right)^p = \Big\{&\mathrm{sgn}\left(v_j^1 - v_i^1\right)\left|v_j^1 - v_i^1\right|^p, \\ &\ldots, \mathrm{sgn}\left(v_j^d - v_i^d\right)\left|v_j^d - v_i^d\right|^p\Big\}, \end{aligned} \tag{11}$$

where $\mathrm{sgn}(\cdot)$ is the signum function:

$$\mathrm{sgn}(s) = \begin{cases} 1, & s > 0, \\ 0, & s = 0, \\ -1, & s < 0. \end{cases} \tag{12}$$

$\delta > 0, R > 0$ are two control parameters to make particles mutually exclude and attract with each other.

We have the following lemmas, which play an important role in the proof of the main results.

Lemma 1 (see [31]). *Consider the following equation:*

$$\dot{x} = f(t, x), x(0) = x_0, \tag{13}$$

where $x \in \mathbb{R}^n$ and $f: \mathbb{R}_+ \times \mathbb{R}^n \longrightarrow \mathbb{R}^n$ is a nonlinear continuous function. Assume the origin is an equilibrium point of (13). If there exists a continuous radially unbounded function $H: \mathbb{R}^n \longrightarrow \mathbb{R}_+ \cup \{0\}$ such that

(i) $H(z) = 0 \Leftrightarrow z = 0$,

(ii) for some positive numbers $\vartheta, \kappa > 0, 0 < a < 1 < b$, any solution $z(t)$ satisfies the inequality:

$$\dot{H}(z(t)) \leq -\vartheta H^a(z(t)) - \kappa H^b(z(t)). \tag{14}$$

Then, the origin is globally fixed-time stable and $H(t) \equiv 0$ if

$$t \geq \frac{1}{\vartheta(1-a)} + \frac{1}{\kappa(b-1)}. \tag{15}$$

Lemma 2 (see [32]). *Let $y \in \mathbb{R}^n$ and $0 < r < s$. Then, the following norm equivalence property holds:*

$$\left(\sum_{i=1}^{n} |y_i|^s\right)^{(1/s)} \leq \left(\sum_{i=1}^{n} |y_i|^r\right)^{(1/r)}, \tag{16}$$

$$\left(\frac{1}{n}\sum_{i=1}^{n} |y_i|^s\right)^{(1/s)} \geq \left(\frac{1}{n}\sum_{i=1}^{n} |y_i|^r\right)^{(1/r)}. \tag{17}$$

3. A Global Existence Theory

Throughout the paper, we use $x \doteq (x_1, x_2, \ldots, x_N)$, where $x_i = (x_i^1, x_i^2, \ldots, x_i^d) \in \mathbb{R}^d$ denote the position of the particles while $v = \dot{x}$ is the velocity. For vectors $x_i, v_i \in \mathbb{R}^d$, their Euclidean norms and the inner products are defined as follows:

$$\begin{aligned} \|x_i\| &\doteq \left(\sum_{k=1}^{d} \left(x_i^k\right)^2\right)^{1/2}, \\ \|v_i\| &\doteq \left(\sum_{k=1}^{d} \left(v_i^k\right)^2\right)^{1/2}, \end{aligned} \tag{18}$$

where x_i^k and v_i^k are the kth components of x_i and v_i. Respectively, we consider macroscopic variables:

$$\begin{aligned} x_c &= \frac{1}{N}\sum_{j=1}^{N} x_i, \\ v_c &= \frac{1}{N}\sum_{j=1}^{N} v_i. \end{aligned} \tag{19}$$

By the symmetry of the indices, we have

$$\begin{aligned} \sum_{i=1}^{N} \frac{\mathrm{d}v_i}{\mathrm{d}t} &= \frac{k_1}{N}\sum_{i=1}^{N}\sum_{j=1}^{N} \psi\left(r_{ij} - \delta\right)\left(v_j - v_i\right) \\ &+ \frac{k_2}{N}\sum_{i=1}^{N}\sum_{j=1}^{N} \frac{1}{r_{ij} + R}\mathrm{sig}\left(v_j - v_i\right)^p \\ &+ \frac{k_3}{N}\sum_{i=1}^{N}\sum_{j=1}^{N} \frac{1}{r_{ij} + R}\mathrm{sig}\left(v_j - v_i\right)^q = 0. \end{aligned} \tag{20}$$

Hence, we have explicit dynamics for the macroscopic variables:

$$\begin{aligned} \frac{\mathrm{d}x_c}{\mathrm{d}t} &= v_c, \\ \frac{\mathrm{d}v_c}{\mathrm{d}t} &= 0, \end{aligned} \tag{21}$$

which yields that

$$\begin{aligned} v_c(t) &= v(0), \\ x_c(t) &= x_c(0) + t v_c(0), \quad t \geq 0. \end{aligned} \tag{22}$$

We consider the fluctuations $(\widehat{x}_i, \widehat{v}_i)$:

$$\begin{aligned} \widehat{x}_i &\doteq x_i - x_c, \\ \widehat{v}_i &\doteq v_i - v_c. \end{aligned} \tag{23}$$

Then, systems (8)-(9) can be written as

$$\begin{cases} \dfrac{\mathrm{d}\widehat{x}_i}{\mathrm{d}t} = \widehat{v}_i, \quad t > 0, i = 1, 2, \ldots, N, \\ \dfrac{\mathrm{d}\widehat{v}_i}{\mathrm{d}t} = \dfrac{k_1}{N}\displaystyle\sum_{j=1}^{N} \psi\left(r_{ij} - \delta\right)\left(\widehat{v}_j - \widehat{v}_i\right) + \dfrac{k_2}{N}\displaystyle\sum_{j=1}^{N} \dfrac{1}{r_{ij} + R}\mathrm{sig}\left(\widehat{v}_j - \widehat{v}_i\right)^p + \dfrac{k_3}{N}\displaystyle\sum_{j=1}^{N} \dfrac{1}{r_{ij} + R}\mathrm{sig}\left(\widehat{v}_j - \widehat{v}_i\right)^q. \end{cases} \tag{24}$$

With the initial value,

$$(\widehat{x}_i(0), \widehat{v}_i(0)) = (\widehat{x}_{i0}, \widehat{v}_{i0}). \tag{25}$$

Through simple calculation, we can get

$$\widehat{x}_c = \frac{1}{N}\sum_{i=1}^{N}\widehat{x}_i = 0, \qquad \widehat{v}_c = \frac{1}{N}\sum_{i=1}^{N}\widehat{v}_i = 0. \tag{26}$$

For convenience, we take the hat out of the variables and use (x_i, v_i) instead of $(\widehat{x}_i, \widehat{v}_i)$. It is easy to see that

$$\sum_{i=1}^{N} x_i = 0, \qquad \sum_{i=1}^{N} v_i = 0, \quad t \in [0, T). \tag{27}$$

The main goal of this section is to consider the existence of a global smooth solution of systems (8)-(9). For this purpose, we introduce the maximal life span $T(x_0)$ for the initial data x_0 as follows:

$$T_0 = \sup\{s \in \mathbb{R}_+, \exists solution\,(x(t), v(t)) \text{for systems in a time interval}\,[0, s)\}. \tag{28}$$

Let

$$\mathscr{L}^{\alpha-2}(t) \doteq \frac{1}{N^2}\sum_{i,j=1}^{N}\left(\left|x_i(t) - x_j(t)\right| - \delta\right)^{-(\alpha-2)}. \tag{29}$$

Now, we are in the position to present the main result of this section.

Theorem 1. *Assume that $\alpha \geq 2$ and the initial datum satisfies*

$$\left|x_i(0) - x_j(0)\right| > \delta \text{ for any } 1 \leq i \neq j \leq N. \tag{30}$$

Then, there exists a global smooth solution (x_i, v_i) to systems (8)-(9). Moreover, for $t \geq 0$, when $\alpha = 2$, we have

$$\left|\frac{1}{N^2}\sum_{i,j=1}^{N}\log\left(\left|x_i(t) - x_j(t)\right| - \delta\right)\right| \leq \left|\frac{1}{N^2}\sum_{i,j=1}^{N}\log\left(\left|x_i(0) - x_j(0)\right| - \delta\right)\right| + \frac{T_0}{2} + \frac{1}{2N}\sum_{i=1}^{N}\left|v_i(0)\right|^2, \tag{31}$$

when $\alpha > 2$, we have

$$\mathscr{L}^{\alpha-2}(t) \leq \mathscr{L}^{\alpha-2}(0)e^{Ct} + Ce^{Ct}\frac{1}{N}\sum_{i=1}^{N}\left|v_i(0)\right|^2, \tag{32}$$

where C is a constant depending only on α.

Proof. Throughout the proof, we will denote for simplicity $T_0 \doteq T(x_0)$. Clearly, if the distances between agents are bigger than δ for any finite time, then the solution can be prolonged indefinitely and $T_0 = \infty$. Moreover, if (31) or (32) holds, then $\inf_{t\geq 0}\min_{i,j=1,\ldots,N}|x_i(t) - x_i(t)| > \delta$ and $T_0 = \infty$. Therefore, in order to finish the proof it suffices to show (19) or (20), first we provide the energy dissipation of system (8), by $(8)_2$ and a symmetry argument, and we have

$$\frac{\mathrm{d}}{\mathrm{d}t}\left(\frac{1}{N}\sum_{i=1}^{N}\left|v_i(t)\right|^2\right) = \frac{2}{N}\sum_{i=1}^{N}\langle v_i(t), \frac{\mathrm{d}}{\mathrm{d}t}v_i(t)\rangle = A_1 + A_2 + A_3, \tag{33}$$

where

$$\begin{aligned} A_1 &= \frac{2k_1}{N}\sum_{i=1}^{N}\langle v_i(t), \sum_{j=1}^{N}\psi\left(r_{ij} - \delta\right)\left(v_j(t) - v_i(t)\right)\rangle, \\ A_2 &= \frac{2k_2}{N}\sum_{i=1}^{N}\langle v_i(t), \sum_{j=1}^{N}\frac{1}{r_{ij} + R}sig\left(v_j(t) - v_i(t)\right)^p\rangle, \\ A_3 &= \frac{2k_3}{N}\sum_{i=1}^{N}\langle v_i(t), \sum_{j=1}^{N}\frac{1}{r_{ij} + R}sig\left(v_j(t) - v_i(t)\right)^q\rangle. \end{aligned} \tag{34}$$

By the result of Theorem 1 in [27], we have

$$A_1 \leq -\frac{k_1}{N^2}\sum_{i,j=1}^{N}\frac{\left|v_j - v_i\right|^2}{\left(\left|x_j - x_i\right| - \delta\right)^{\alpha}}, \tag{35}$$

$$A_2 \leq -\frac{k_2}{N^2}\sum_{i,j=1}^{N}\frac{1}{r_{ij} + R}\left|v_j - v_i\right|^{p+1}, \tag{36}$$

$$A_3 \leq -\frac{k_3}{N^2}\sum_{i,j=1}^{N}\frac{1}{r_{ij} + R}\left|v_j - v_i\right|^{q+1}. \tag{37}$$

Thus, substituting (35)–(37) into (33), integrating the differential inequality (33) from 0 to t yields that

$$\begin{aligned} &\frac{1}{N}\sum_{i=1}^{N}\left|v_i(t)\right|^2 + \int_0^t\frac{k_1}{N^2}\sum_{i,j=1}^{N}\frac{\left|v_j - v_i\right|^2}{\left(\left|x_j - x_i\right| - \delta\right)^{\alpha}}x \\ &+ \int_0^t\frac{k_2}{N^2}\sum_{i,j=1}^{N}\frac{1}{r_{ij} + R}\left|v_j - v_i\right|^{p+1}ds \\ &+ \int_0^t\frac{k_3}{N^2}\sum_{i,j=1}^{N}\frac{1}{r_{ij} + R}\left|v_j - v_i\right|^{q+1}ds = \frac{1}{N}\sum_{i=1}^{N}\left|v_i(0)\right|^2, \quad \text{for } t \in [0, T_0). \end{aligned} \tag{38}$$

And this yields

$$\int_0^t\frac{k_1}{N^2}\sum_{i,j=1}^{N}\frac{\left|v_j - v_i\right|^2}{\left(\left|x_j - x_i\right| - \delta\right)^{\alpha}}\mathrm{d}s = \frac{1}{N}\sum_{i=1}^{N}\left|v_i(0)\right|^2, \quad \text{for } t \in [0, T_0). \tag{39}$$

By the same processes of the proof of Theorem 1 in [27], we have that (31) and (32) are established and there is no collision between agents for all time and $T_0 = \infty$.

4. Fixed-Time Flocking

In this section, we shall show that systems (8)-(9) with continuous non-Lipschitz protocol have a fixed-time flocking. First, we first introduce the definition of the fixed-time flocking.

Definition 1. Systems (8)-(9) are said to reach a fixed-time flocking if and only if the system satisfies the following two conditions:

(i) Velocity alignment: the velocity fluctuations go to zero in the fixed-time T, and the time function T is called the convergence time independent of the initial values:

$$\left\|v_i - v_j\right\| = 0, \quad \forall t \geq T, \quad \text{for } i, j = 1, 2, \ldots, N. \tag{40}$$

(ii) Forming a group: the position fluctuations are uniformly bounded in time t:

$$\sup_{0 \leq t \leq \infty} \left\|x_i - x_j\right\|^2 < \infty, \quad \text{for } i, j = 1, 2, \ldots, N. \tag{41}$$

Theorem 2. *Assume that $\alpha \geq 2, 0 < p < 1 < q$, and the initial datum satisfies (30). Then, systems (8)-(9) can reach a fixed-time flocking. Moreover, the convergence time is independent of the initial states of agents which is estimated by*

$$T \leq T^* \doteq \frac{2}{\vartheta(1-p)} + \frac{2}{\kappa(q-1)}, \tag{42}$$

where
$\vartheta = (k_2 (2N)^{(p+1)/2} / N(M+R)), \kappa = (k_3/(M+R)) 2^{(q+1)/2} d^{(1-q)/2}$ *and* $M = \max_{i \neq j}\{|x_j - x_i|\}$.

Proof. Let $x(t) = (x_1(t), x_2(t), \ldots, x_N(t)) \in \mathbb{R}^{dN}$ and $v(t) = (v_1(t), v_2(t), \ldots, v_N(t)) \in \mathbb{R}^{dN}$. Take the candidate Lyapunov function:

$$V(t) \doteq \sum_{i=1}^{N} \left\|v_i\right\|^2, \tag{43}$$

let

$$X(t) \doteq \sum_{i=1}^{N} \left\|x_i\right\|^2. \tag{44}$$

By using (27), we have

$$\sum_{1 \leq i, j \leq N} \left\|v_j - v_i\right\|^2 = 2N \sum_{i=1}^{N} \left\|v_i\right\|^2 = 2NV, \tag{45}$$

$$\sum_{1 \leq i, j \leq N} \left\|x_j - x_i\right\|^2 = 2N \sum_{i=1}^{N} \left\|x_i\right\|^2 = 2NX. \tag{46}$$

It is easy to see that the difference of all individuals' velocities will tend to zero in fixed-time if the function $V(t)$ tends to 0 in fixed-time, and the diameter of a group is bounded if the function $X(t)$ is bound:

$$\begin{aligned}
\frac{\mathrm{d}}{\mathrm{d}t} V(t) &= 2 \sum_{i=1}^{N} \langle v_i(t), \frac{\mathrm{d}}{\mathrm{d}t} v_i(t) \rangle = NA_1 \\
&\quad + \frac{2k_2}{N} \sum_{i,j=1}^{N} \langle v_i(t), \frac{1}{r_{ij} + R} \operatorname{sig}\left(v_j - v_i\right)^p \rangle \\
&\quad + \frac{2k_3}{N} \sum_{i,j=1}^{N} \langle v_i(t), \frac{1}{r_{ij} + R} \operatorname{sig}\left(v_j - v_i\right)^q \rangle \\
&\leq NA_1 - \frac{k_2}{N} \sum_{i,j=1}^{N} \frac{1}{r_{ij} + R} \sum_{k=1}^{d} \left|v_{jk} - v_{ik}\right|^{p+1} \\
&\quad - \frac{k_3}{N} \sum_{i,j=1}^{N} \frac{1}{r_{ij} + R} \sum_{k=1}^{d} \left|v_{jk} - v_{ik}\right|^{q+1}.
\end{aligned} \tag{47}$$

Note that $0 < p < 1 < q$; then, employing Lemma 2, one can easily get that

$$\begin{aligned}
&\left(\sum_{k=1}^{d} \left|v_{jk} - v_{ik}\right|^{p+1}\right)^{1/(p+1)} \geq \left(\sum_{k=1}^{d} \left|v_{jk} - v_{ik}\right|^{2}\right)^{1/2} = \left\|v_j(t) - v_i(t)\right\|, \\
&\left(\sum_{k=1}^{d} \left|v_{jk} - v_{ik}\right|^{q+1}\right)^{1/(q+1)} \geq d^{1/(q+1)} \left(\frac{1}{d} \sum_{k=1}^{d} \left|v_{jk} - v_{ik}\right|^{2}\right)^{1/2} \\
&\qquad = d^{\frac{1-q}{2(1+q)}} \left\|v_j(t) - v_i(t)\right\|.
\end{aligned} \tag{48}$$

Which means

$$\sum_{k=1}^{d} \left|v_{jk} - v_{ik}\right|^{p+1} \geq \left\|v_j(t) - v_i(t)\right\|^{p+1}, \tag{49}$$

$$\sum_{k=1}^{d} \left|v_{jk} - v_{ik}\right|^{q+1} \geq d^{(1-q)/2} \left\|v_j(t) - v_i(t)\right\|^{q+1}. \tag{50}$$

Therefore, combining (47)–(50) gives that

$$\begin{aligned}
\frac{\mathrm{d}}{\mathrm{d}t} V(t) &\leq NA_1 - \frac{k_2}{N} \sum_{i,j=1}^{N} \frac{1}{r_{ij} + R} \left\|v_j(t) - v_i(t)\right\|^{p+1} \\
&\quad - \frac{k_3}{N} d^{(1-q)/2} \sum_{i,j=1}^{N} \frac{1}{r_{ij} + R} \left\|v_j(t) - v_i(t)\right\|^{q+1}.
\end{aligned} \tag{51}$$

It follows from (31) and (32) that there exists a positive constant M, such that $|x_i - x_j| < M$. Noting that $A_1 \leq 0$, then we have from (51) that

$$\begin{aligned}\frac{\mathrm{d}}{\mathrm{d}t}V(t) \le & -\frac{k_2}{N(M+R)}\sum_{i,j=1}^{N}\left\|v_j(t)-v_i(t)\right\|^{p+1} \\ & -\frac{k_3}{N(M+R)}d^{(1-q)/2}\sum_{i,j=1}^{N}\left\|v_j(t)-v_i(t)\right\|^{q+1} \\ = & -\frac{k_2}{N(M+R)}\sum_{i,j=1}^{N}\left(\left\|v_j(t)-v_i(t)\right\|^2\right)^{(p+1)/2} \\ & -\frac{k_3}{N(M+R)}d^{(1-q)/2}\sum_{i,j=1}^{N}\left(\left\|v_j(t)-v_i(t)\right\|^2\right)^{(q+1)/2}.\end{aligned} \tag{52}$$

Choosing $s = 1$ and $r = ((p+1)/2)$ and applying (16) to the processing inequality show that

$$\sum_{i,j=1}^{N}\left(\left\|v_j(t)-v_i(t)\right\|^2\right)^{(p+1)/2} \ge \left(\sum_{i,j=1}^{N}\left\|v_j(t)-v_i(t)\right\|^2\right)^{(p+1)/2}. \tag{53}$$

Choosing $s = ((q+1)/2)$ and $r = 1$ and applying (17), we get that

$$\sum_{i,j=1}^{N}\left(\left\|v_j(t)-v_i(t)\right\|^2\right)^{(q+1)/2} \ge N^{((1-q)/2)}\left(\sum_{i,j=1}^{N}\left\|v_j(t)-v_i(t)\right\|^2\right)^{(q+1)/2}. \tag{54}$$

It follows from (45) that

$$\begin{aligned}\frac{d}{dt}V(t) \le & -\frac{k_2(2N)^{(p+1)/2}}{N(M+R)}V(t)^{(p+1)/2} \\ & -\frac{k_3}{(M+R)}2^{(q+1)/2}d^{(1-q)/2}V(t)^{(q+1)/2}.\end{aligned} \tag{55}$$

It is easy to see that $V(t)$ is a continuous and positive definite function. So, by Lemma 1, when $a = (p+1)/2$ and $b = (q+1)/2$, we have

$$V(t) \equiv 0, t \ge T, \tag{56}$$

and the convergence time independent of the initial values is estimated by

$$\begin{aligned}T \le T^* \doteq & \frac{1}{\vartheta(1-((p+1)/2))}+\frac{1}{\kappa(((q+1)/2)-1)} \\ = & \frac{2}{\vartheta(1-p)}+\frac{2}{\kappa(q-1)},\end{aligned} \tag{57}$$

where $\vartheta = (k_2(2N)^{(p+1)/2}/N(M+R))$ and $\kappa = ((k_3/(M+R))2^{(q+1)/2}d^{(1-q)/2})$, which implies that condition (i) of the definition of fixed-time flocking holds.

Now, we prove condition (ii) of the definition of fixed-time flocking that the function $X(t)$ is bounded.

It follows from (55) that $V(t)$ is a nonincreasing function with respect to t. That is, when $t > 0, V(0) \ge V(t) \ge 0$. By the triangle inequality and Cauchy–Schwarz inequality, we have

$$\frac{\mathrm{d}X(t)}{\mathrm{d}t} = 2\sum_{i=1}^{N}\langle x_i, v_i\rangle \le 2\sum_{i=1}^{N}\|x_i\|\|v_i\| \le 2X^{1/2}V^{1/2}. \tag{58}$$

Integrating differential inequality (58) from 0 to t yields that

$$X^{1/2}(t) \le X^{1/2}(0) + \int_0^t V^{1/2}(t)\mathrm{d}t. \tag{59}$$

If $t < T$, then it deduces from (59) that

$$X^{1/2}(t) \le X^{1/2}(0) + \int_0^T V^{1/2}(t)\mathrm{d}t \le X^{1/2}(0) + V^{1/2}(0)T < \infty. \tag{60}$$

If $t > T$, then it deduces from (55) and (59) that

$$\begin{aligned}X^{1/2}(t) \le & X^{1/2}(0) + \int_0^T V^{1/2}(t)\mathrm{d}t + \int_T^t V^{1/2}(t)\mathrm{d}t \le X^{1/2}(0) \\ & + \int_0^T V^{1/2}(t)\mathrm{d}t \le X^{1/2}(0) + V^{1/2}(0)T < \infty.\end{aligned} \tag{61}$$

Thus, combining the processing inequality with (46) implies that

$$\sup_{0\le t\le\infty}\left\|x_i - x_j\right\|^2 < \infty, \quad \text{for } i, j = 1, 2, \ldots, N. \tag{62}$$

This completes the proof. □

Remark 1. Compared to [27], the convergence time is estimated by

$$T \le T^* \doteq \frac{2N(M+R)}{k_2(1-\beta)(2N)^{(1+\beta)/2}}\left(\sum_{i=1}^{N}\|v_{i0}\|^2\right)^{(1-\beta)/2}, \tag{63}$$

which is formulated by the initial states of the all agents. We added the term

$$\frac{k_3}{N}\sum_{j=1}^{N}\frac{1}{r_{ij}+R}sig\left(v_j - v_i\right)^q, \tag{64}$$

to the control protocol, the advantage of Theorem 2 is that the convergence time is independent of the initial states of agents which is estimated by

$$T \le T^* \doteq \frac{2N(M+R)}{k_2(2N)^{(p+1)/2}(1-p)} + \frac{2(M+R)}{k_3 d^{(1-q)/2}2^{(q+1)/2}(q-1)}. \tag{65}$$

5. Simulations

Example 1. Choose $N = 30, 0 < p = 0.2 < 1 < q = 2, d = 2, k_1 = 1, k_2 = k_3 = 2, \delta = 0.8, \alpha = 2$, and $R = 2$, using the Euler algorithm, step length $h = 0.01$, for the random initial position generated on $[0, 20]$ and random velocity on $[0, 2]$, and the initial minimum distance between agents is satisfying (30); then, the following simulation results (Figures 1–3) are obtained. In Figure 1, the x, y direction velocity of the all agents is presented, and the velocity of all

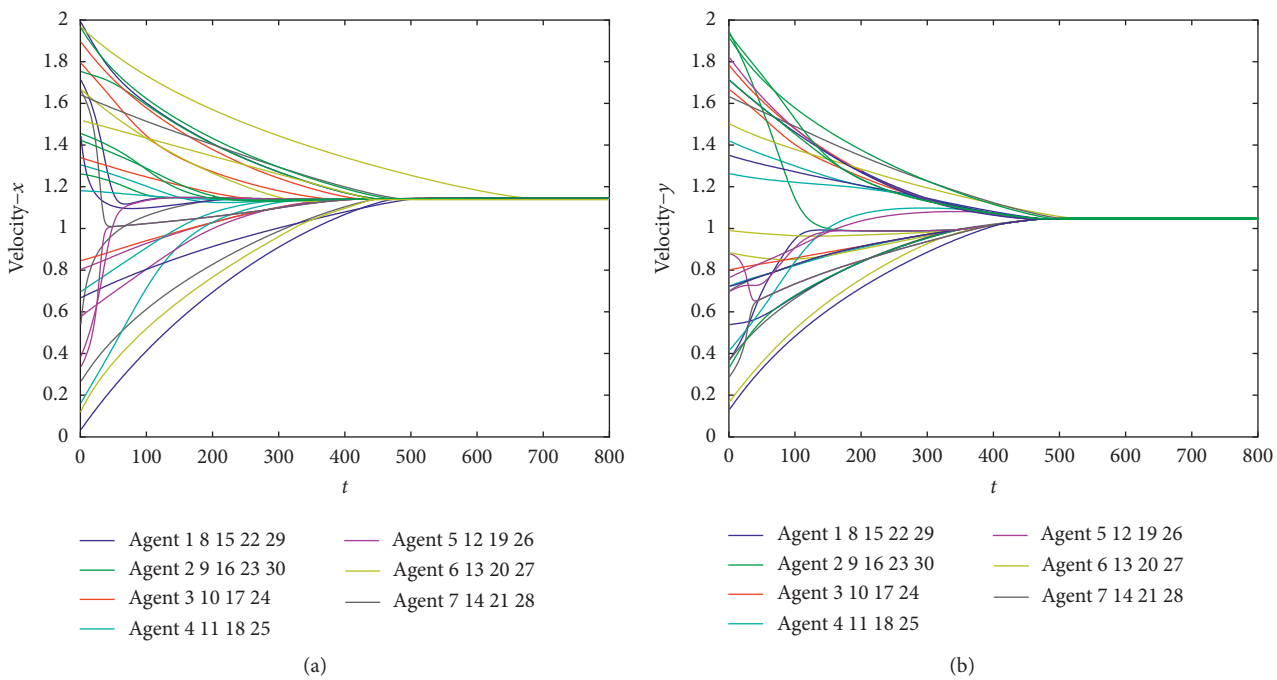

Figure 1: The velocity of agents with $k_2 = k_3 = 2$.

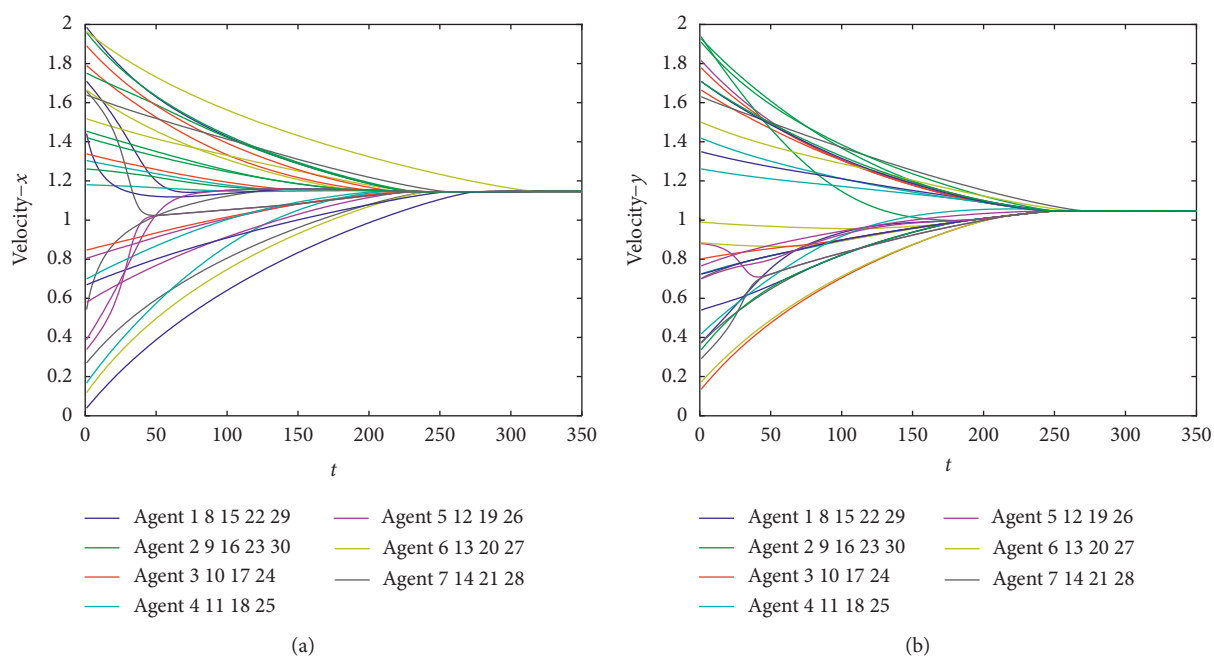

Figure 2: The velocity of agents with $k_2 = k_3 = 4$.

agents converges to the same value after about $t = 7$. In order to shorten the convergence time of the system, according to formula (42), under the condition that the parameter N, p, q was determined and increasing the parameter value of k_2, k_3 was used to shorten the convergence time of the system. In Figure 2, take $k_2 = k_3 = 4$, other parameters are the same as those in Figure 1 and the velocity of all agents converges to the same value about $t = 3$, which is half shorter than that of Figure 1. Moreover, Figure 3, shows that the minimum distance between all agents is stable after $t = 0.5$ and the maximum distance between all agents is stable after $t = 6$. Meanwhile, Figure 3 explains that the minimum distance among all agents is about $0.842 > \delta$.

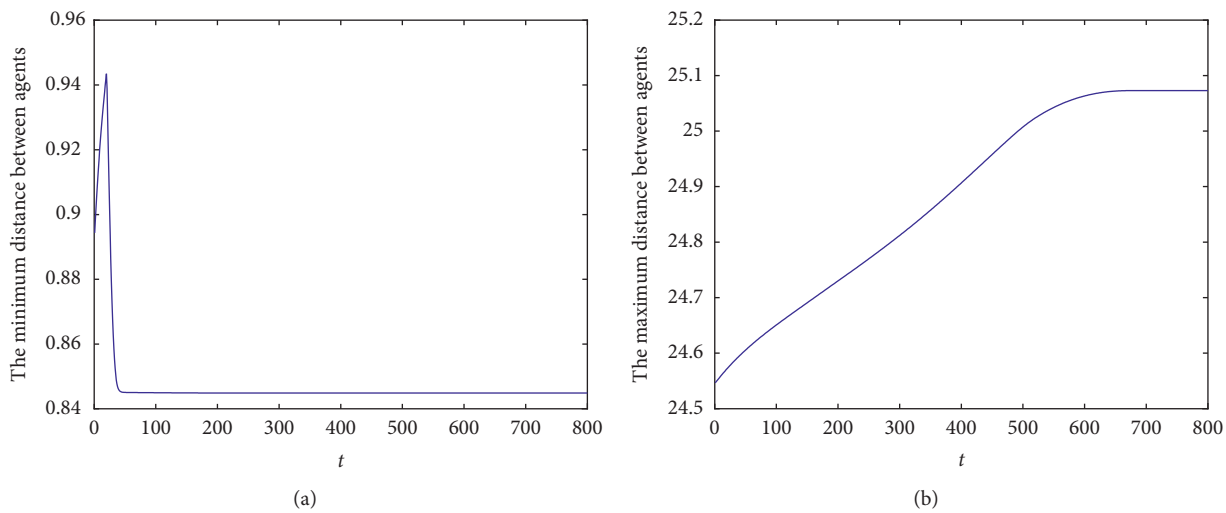

Figure 3: The minimum and the maximum distance between agents.

6. Conclusion

In this paper, we have investigated the flocking problem of a modified Cucker–Smale model with a continuous non-Lipschitz protocol. By using a Lyapunov functional, we show that the flocking can occur and collision avoidance when a singular communication function with a weighted sum of sign functions of the relative velocities among agents. The main results demonstrate that the flocking converging time is independent of the initial states of agents.

Data Availability

The data used to support the findings of this study are included within the article.

Conflicts of Interest

The authors declare that there are no conflicts of interest regarding the publication of this paper.

Acknowledgments

This work was supported by the National Natural Science Foundation of China (grant no. 11771450).

References

[1] A. B. T. Barbaro, K. Taylor, P. F. Trethewey, L. Youseff, and B. Birnir, "Discrete and continuous models of the dynamics of pelagic fish: application to the capelin," *Mathematics and Computers in Simulation*, vol. 79, no. 12, pp. 3397–3414, 2009.

[2] B. Birnir, "An ode model of the motion of pelagic fish," *Journal of Statistical Physics*, vol. 128, no. 1-2, pp. 535–568, 2007.

[3] J. A. Cañizo, J. A. Carrillo, and J. Rosado, "A well-posedness theory in measures for some kinetic models of collective motion," *Mathematical Models and Methods in Applied Sciences*, vol. 21, no. 3, pp. 515–539, 2011.

[4] T. Li, N. Pintus, and G. Viglialoro, "Properties of solutions to porous medium problems with different sources and boundary conditions," *Zeitschrift Für Angewandte Mathematik Und Physik*, vol. 70, no. 3, pp. 1–18, 2019.

[5] T. Li and G. Viglialoro, "Boundedness for a nonlocal reaction chemotaxis model even in the attraction-dominated regime," 2020, http://arxiv.org/abs/2004.10991.

[6] C. M. Topaz, A. L. Bertozzi, and M. A. Lewis, "A nonlocal continuum model for biological aggregation," *Bulletin of Mathematical Biology*, vol. 68, no. 7, pp. 1601–1623, 2006.

[7] F. Cucker and S. Smale, "Emergent behavior in flocks," *IEEE Transactions on Automatic Control*, vol. 52, no. 5, pp. 852–862, 2007.

[8] F. Cucker and S. Smale, "On the mathematics of emergence," *Japanese Journal of Mathematics*, vol. 2, no. 1, pp. 197–227, 2007.

[9] S. Yeal Ha and J. Guo Liu, "A simple proof of the Cucker-Smale flocking dynamics and mean-field limit," *Communications in Mathematical Sciences*, vol. 7, no. 2, pp. 297–325, 2009.

[10] S. Motsch and E. Tadmor, "A new model for self-organized dynamics and its flocking behavior," *Journal of Statistical Physics*, vol. 144, no. 5, pp. 923–947, 2011.

[11] P. Young and H. Jan, "Cucker-smale model with normalized communication weights and time delay," *Kinetic and Related Models*, vol. 10, no. 4, pp. 1011–1033, 2017.

[12] R. Erban, J. Haškovec, and Y. Sun, "A cucker-smale model with noise and delay," *SIAM Journal on Applied Mathematics*, vol. 76, no. 4, pp. 1535–1557, 2016.

[13] Y. Liu and J. Wu, "Flocking and asymptotic velocity of the Cucker-Smale model with processing delay," *Journal of Mathematical Analysis and Applications*, vol. 415, no. 1, pp. 53–61, 2014.

[14] C. Pignotti and I. Reche Vallejo, "Flocking estimates for the cucker-smale model with time lag and hierarchical leadership," *Journal of Mathematical Analysis and Applications*, vol. 464, no. 2, pp. 1313–1332, 2018.

[15] X. Wang, L. Wang, and J. Wu, "Impacts of time delay on flocking dynamics of a two-agent flock model," *Communications in Nonlinear Science and Numerical Simulation*, vol. 70, pp. 80–88, 2019.

[16] X. Li, Y. Liu, and J. Wu, "Flocking and pattern motion in a modified cucker-smale model," *Bulletin of the Korean Mathematical Society*, vol. 53, no. 5, pp. 1327–1339, 2016.

[17] H. Liu, X. Wang, Y. Liu, and X. Li, "On non-collision flocking and line-shaped spatial configuration for a modified singular cucker-smale model," *Communications in Nonlinear Science and Numerical Simulation*, vol. 75, pp. 280–301, 2019.

[18] F. Dalmao and E. Mordecki, "Cucker-smale flocking under hierarchical leadership and random interactions," *SIAM Journal on Applied Mathematics*, vol. 71, no. 4, pp. 1307–1316, 2011.

[19] F. Dalmao and E. Mordecki, "Hierarchical cucker-smale model subject to random failure," *IEEE Transactions on Automatic Control*, vol. 57, no. 7, pp. 1789–1793, 2012.

[20] J. G. Dong, "Flocking under hierarchical leadership with a free-will leader," *International Journal of Robust & Nonlinear Control*, vol. 30, no. 11, pp. 1891–1898, 2012.

[21] J. Shen, "Cucker-smale flocking under hierarchical leadership," *SIAM Journal on Applied Mathematics*, vol. 68, no. 3, pp. 694–719, 2007.

[22] F. Cucker and J.-G. Dong, "Avoiding collisions in flocks," *IEEE Transactions on Automatic Control*, vol. 55, no. 5, pp. 1238–1243, 2010.

[23] J. Park, H. J. Kim, and S.-Y. Ha, "Cucker-smale flocking with inter-particle bonding forces," *IEEE Transactions on Automatic Control*, vol. 55, no. 11, pp. 2617–2623, 2010.

[24] S. M. Ahn, H. Choi, Y. Seung, and H. Lee, "On collision-avoiding initial configurations to cucker-smale type flocking models," *Communications in Mathematical Sciences*, vol. 10, no. 2, pp. 625–643, 2012.

[25] J. A. Carrillo, Y.-P. Choi, J. Peszek, and P. Jan, "Sharp conditions to avoid collisions in singular cucker-smale interactions," *Nonlinear Analysis: Real World Applications*, vol. 37, pp. 317–328, 2017.

[26] Y. Han, D. Zhao, and Y. Sun, "Finite-time flocking problem of a cucker-smale-type self-propelled particle model," *Complexity*, vol. 21, no. S1, pp. 354–361, 2015.

[27] H. Liu, X. Wang, X. Li, and Y. Liu, "Finite-time flocking and collision avoidance for second-order multi-agent systems," *International Journal of Systems Science*, vol. 51, no. 1, pp. 102–115, 2020.

[28] B. Ning, Q. L. Han, and Z. Zuo, "Distributed optimization for multiagent systems: an edge-based fixed-time consensus approach," *IEEE Transactions on Cybernetics*, vol. 49, no. 1, pp. 1–11, 2019.

[29] B. Zhang and Y. Jia, "Fixed-time consensus protocols for multi-agent systems with linear and nonlinear state measurements," *Nonlinear Dynamics*, vol. 82, no. 4, pp. 1683–1690, 2015.

[30] Z. Zuo, "Nonsingular fixed-time consensus tracking for second-order multi-agent networks," *Automatica*, vol. 54, pp. 305–309, 2015.

[31] A. Polyakov, "Nonlinear feedback design for fixed-time stabilization of linear control systems," *IEEE Transactions on Automatic Control*, vol. 57, no. 8, pp. 2106–2110, 2012.

[32] H. H. Godfrey, J. E. Littlewood, and P. George, *Inequalities*, Cambridge University Press, Cambridge, UK, 1952.

Hindawi
Mathematical Problems in Engineering
Volume 2020, Article ID 7623481, 10 pages
https://doi.org/10.1155/2020/7623481

Research Article

Transient Antiseepage Analysis of the Relief Well in Beijiang Dike

Wenbing Xu,[1] Chuan Xu,[2] Qinghe Yao,[1] Trevor Hocksun Kwan,[1] and Sheng Wang[1]

[1]*Department of Applied Mechanics and Engineering, Sun Yat-Sen University, Guangzhou, Guangdong, China*
[2]*Taishan Nuclear Power Joint Venture Co., Ltd., Guangzhou, Guangdong, China*

Correspondence should be addressed to Qinghe Yao; yaoqhe@mail.sysu.edu.cn

Received 23 April 2020; Accepted 20 May 2020; Published 20 July 2020

Guest Editor: Rongwei Guo

In this paper, the seepage finite element method (FEM) is used to simulate the transient seepage of Beijiang Dike, and antiseepage solutions are designed and discussed. By comparing the measured data of a piezometer with the steady-state calculation model, the calculated results are compatible very well with the measured data. Aiming to improve the ability to respond in extreme weather conditions, we calculate the transient seepage field after the water level suddenly rises in a short time and then select the relief well as the antiseepage measure and optimize it. The results show that when the water level is 15.78 m, the slope reaches 0.5, and the embankment is damaged. With the increase of penetration depth, the effect of drainage and decompression in the depth of 3/5 and 4/5 is relatively small due to geological strips. Due to different geological conditions, the same relief wells are placed in different positions with a wide gap in effect, the antiseepage effect is the best when the horizontal distance is 95 m, and the effect is the best when the depth is 16.5 m. The research results can be used to guide the seepage prevention and control design of Beijiang Dike.

1. Introduction

Embankment engineering is the foundation of the flood control engineering system and an important barrier against flood [1]. For a long time, China's embankment project lacks sufficient attention and research; there are still many problems such as unstable quality of levee body, poor impervious capability, and lack of effective monitoring measures. Among all safety problems, seepage failures are the most critical and common problem in levee engineering [2, 3]. In 1998, an extreme flood occurred in the Yangtze River, and the seepage danger in the middle and lower reaches of the Yangtze River reached 65,100, accounting for 88% of the total risk. Among the seven large crevasses, 5 of them were due to the penetration deformation and the osmotic failure, which eventually led to the collapse of the embankment [4]. Since then, researchers have paid more attention to the safety of dike engineering, and seepage analysis of dike engineering has become one of the current research hotspots [5–8].

Seepage analysis is a study of fluid mechanics, geotechnical mechanics, and other interdisciplinary fields. In 1856, French scholar Henry Darcy used a vertical circular pipe to conduct sand seepage experiment, which was the first seepage analysis method. Then, he proposed Darcy's law [9]. In 1889, people first deduced the seepage differential equation. After that, the analytical method of seepage analysis has been applied by a large number of researchers, and a series of fruitful results have been achieved, which promotes the development of seepage-related research rapidly. However, the analytical method is difficult in practical application because it has the defects of large amount of calculation and general adaptability in dealing with more complex problems, so it is relatively difficult to apply in practical engineering. In 1922, Pavlovski developed an electrical simulation method for seepage analysis due to the difficulty of seepage in nonuniform permeable medium and complex boundary. In 1931, Richards established Richards equation for unsaturated seepage analysis by further derivation of mass conservation law and generalized Darcy law [10]. Then, Fredlund and Lam [11] put forward the saturated-unsaturated seepage control equation in the following research, which brought a qualitative leap to the engineering construction.

The seepage analysis method of dike engineering mainly includes model experiment, numerical simulation, and data

analysis [12–14]. Model experiments often require a large amount of workforce and material resources; therefore, they are expensive. Due to the limitation of experimental conditions, it is difficult to conduct comprehensive research of various special working conditions. Data analysis requires an on-site survey and collection of a large number of monitoring data, which often requires high economic costs. The numerical simulation has lower cost and higher precision and can simulate a variety of working conditions, and the appropriate conditions can be obtained to obtain higher precision results. Therefore, relevant research is currently conducted using numerical simulation.

Many scholars use the finite element analysis (FEA) method to simulate seepage in dike engineering. Moran [15] first applied the finite element method to analyze the steady flow of incompressible fluid in saturated porous media and put forward the view that the finite element method is applicable to all field problems calculated by the variational formula. However, he did not optimize the antiseepage scheme. Zhang [16] conducted typical conditions for the present situation of an embankment project in the middle and lower reaches of the Yangtze River. The seepage field of dike foundation was simulated and calculated by a finite element numerical simulation method. The effects of the thickness of the strong permeable layer hidden in the ground and exposed to the surface, the width of the dyke, and the degree of cutting of the channel on the levee were also studied. However, there is lack of analysis of the critical conditions when the dam is damaged. Vermeer et al. [17,18] use a first-order reliability method of adaptive response surface coupled with numerical simulation and reliability analysis to analyze transient seepage. Considering the influence of transient seepage in an embankment on stability, analysis of stable phreatic line is the key to the stability control. Although a new seepage analysis method is adopted, the analysis of seepage slope and other factors is lacking. Wu et al. [19] used the finite element program COMSOL to solve the influence of rainfall seepage, deformation, and stability of soil slope. Through the finite element analysis software GeoStudio, Qiu et al. [20] carried out numerical analysis of seepage stability of the stable flow of embankment engineering combined with engineering examples, focusing on the comparison and evaluation of seepage characteristics before and after pile foundation construction. Although the above two people used different software to make a detailed analysis of the seepage of the slopes and embankments, there was lack of antiseepage schemes.

In the simulation study of the antiseepage effect of the relief well, Zhang[21] analyzed the effectiveness of various antiseepage measures of Beijiang Dike through the analysis of measured data and the simulation calculation of steady seepage field. He believed that the seepage control and decompression project was sufficient for the dike section. He also evaluated the seepage control safety of the dike, which provided a reference for the construction of the dike. Based on steady-state seepage, Li [22] calculated the penetration depth, diameter of the well casing, well spacing, the elevation of water outlet, and permeability of the filter layer in the two-dimensional seepage finite element method. Based on the geological data of the Beijiang Dike, the model of the Shijiao segment section of the Beijiang Dike is established. On this basis, the transient seepage field of the relief well is optimized and the seepage flow is reduced under extreme conditions in the actual dike project. Protecting the safety of dikes is of great significance.

Located in the lower reaches of the Beijiang River, Beijiang Dike is an important barrier for the defence of the Xijiang and Beijiang floods in Guangzhou and is also a national first-class dike. The total population of the dike area is more than 5 million, and the cultivated land is 44.66 million square meters. It is one of the seven significant embankments in China. However, there are few safety analyses for it, especially in extreme weather. Therefore, this paper will adopt seepage finite element software to simulate the seepage field of Beijiang embankment instantaneously and verify it by comparing with the measured value of the pressure pipe.

As mentioned in the literature above, most of the current simulation analysis of relief wells is based on steady seepage field, which lacks the support for analysis of transient behaviour. Few studies have been carried out to calculate the change of seepage control effect of relief wells in the case of short-term water level surges. For the study of transient seepage fields, the dangerous water level at which the dike is about to be destroyed can be calculated. At the same time, the choice of the best relief wells also provides an excellent reference value for the difficult-to-test wells in practical engineering. Based on the transient seepage field, the influence of various design schemes of relief wells on the phreatic line and seepage flow rate is studied, and the optimal seepage control scheme of relief wells under the transient seepage field is obtained.

2. Governing Equation

According to Darcy's law, the seepage equation of porous media can be expressed as follows [23]:

$$Q = KAj = -KA\frac{\partial h}{\partial l}, V = Kj, \tag{1}$$

where Q is seepage quantity; K is hydraulic conductivity; A is seepage cross-sectional area; j is gradient; h is hydraulic head; l is head loss; and V is the average flow velocity of the seepage model.

The differential formula of Darcy's law is as follows:

$$V = -\frac{K}{\mu}\left(\frac{\partial p}{\partial z} + \rho g\right), \tag{2}$$

where μ is viscosity; K is permeability; P is pressure; ρ is density; and G is acceleration of gravity.

According to the law of conservation of mass, it is generally believed that the mass of the fluid does not increase or decrease when it moves in the seepage field. It is assumed that there is fluid inflow in all directions of the unit body. The inflow rate is assumed to be V_x, V_y, and V_y, respectively, and the side lengths are expressed by dx, dy, and dz, respectively, as shown in Figure 1.

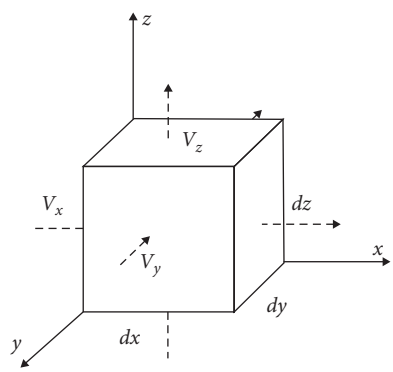

Figure 1: Velocity vector diagram and flow diagram of seepage unit.

The total seepage quantity in the cell can be calculated by superposition of the seepage quantity in x, y, and z directions:

$$-\left(\frac{\partial \rho\, V_x}{\partial x}+\frac{\partial \rho\, V_y}{\partial y}+\frac{\partial \rho\, V_z}{\partial z}\right)\mathrm{d}x\,\mathrm{d}y\,\mathrm{d}z=-\rho\left(\frac{\partial V_x}{\partial x}+\frac{\partial V_y}{\partial y}+\frac{\partial V_z}{\partial z}\right)\mathrm{d}x\,\mathrm{d}y\,\mathrm{d}z. \tag{3}$$

The change rate of a point with mass M in the cell can be expressed as follows:

$$\frac{\partial M}{\partial \mathrm{t}}=\frac{\partial(n\rho\,\mathrm{d}x\,\mathrm{d}y\,\mathrm{d}z)}{\partial \mathrm{t}}=\frac{\partial(n\rho V)}{\partial \mathrm{t}}, \tag{4}$$

where n is the porosity of soil; ρ is the density of water; and V is the volume of unit.

According to the law of conservation of mass, formula (3) is simplified, and the following formula can be obtained:

$$-\left(\frac{\partial V_x}{\partial x}+\frac{\partial V_y}{\partial y}+\frac{\partial V_z}{\partial z}\right)=\rho g(\propto+n\beta)\frac{\partial H}{\partial t}. \tag{5}$$

Equation (5) is the compressible seepage continuity equation of saturated soil. Since the compression modulus of soil and water is 0, formula (5) can be changed into

$$\frac{\partial V_x}{\partial x}+\frac{\partial V_y}{\partial y}+\frac{\partial V_z}{\partial z}=0. \tag{6}$$

Equation (6) is the continuity equation when the incompressible fluid moves in the rigid structure medium.

Richard extended Darcy's law to unsaturated seepage in 1931 and obtained the fundamental differential equation of unsaturated seepage：

$$\frac{\partial}{\partial x}\left(k_x\frac{\partial h}{\partial x}\right)+\frac{\partial}{\partial y}\left(k_y\frac{\partial h}{\partial y}\right)+\frac{\partial}{\partial z}\left(k_z\frac{\partial h}{\partial z}\right)+q=\frac{\partial w}{\partial t}, \tag{7}$$

where k_x, k_y, k_z is hydraulic conductivity along three directions, q is boundary flow of the element body, w is unit volume water content, and t is time.

When the hydraulic conductivity in the x, y, and z directions remains unchanged, and the unit is not subject to external rainfall and evaporation, there is no external inflow and outflow. We know

$$k_x\frac{\partial^2 h}{\partial x^2}+k_y\frac{\partial^2 h}{\partial y^2}+k_z\frac{\partial^2 h}{\partial z^2}=0\,. \tag{8}$$

If the permeability coefficient is isotropic and equal, equation (8) will become the Laplace operator:

$$\frac{\partial^2 h}{\partial x^2}+\frac{\partial^2 h}{\partial y^2}+\frac{\partial^2 h}{\partial z^2}=0. \tag{9}$$

Combining the continuity equation with Darcy' law results in Poisson's equation:

$$k_x\frac{\partial^2 h}{\partial x^2}+k_y\frac{\partial^2 h}{\partial y^2}=q. \tag{10}$$

Although equations (8) and (10) are for stable seepage differential equation, it can still be used when the fluid is incompressible and in unstable flow.

When the fluid is in turbulence, according to formula (5),

$$\frac{\partial}{\partial \mathrm{x}}\left(k_x\frac{\partial h}{\partial x}\right)+\frac{\partial}{\partial \mathrm{y}}\left(k_y\frac{\partial h}{\partial y}\right)+\frac{\partial}{\partial \mathrm{z}}\left(k_z\frac{\partial h}{\partial z}\right)=-\rho g(\propto+n\beta)\frac{\partial h}{\partial t}=S_s\frac{\partial h}{\partial t}, \tag{11}$$

where S_s is the unit storage capacity ($1/L$).

When the permeability coefficient is assumed to be isotropic, formula (11) can be changed to

$$\frac{\partial^2 h}{\partial x^2}+\frac{\partial^2 h}{\partial y^2}+\frac{\partial^2 h}{\partial z^2}=\frac{S_s}{k}\frac{\partial h}{\partial t}. \tag{12}$$

The gradient of homogeneous soil on permeable foundation can be calculated by the following formula.

Along the exudate,

$$J = \frac{1}{\sqrt{1+m^2}}\left(\frac{h}{y}\right)^{0.5}, \tag{13}$$

where m is the slope rate; h is the height of fluid escape point; and y is the fluid flow distance.

3. Numerical Modelling

3.1. Physical Conditions. This paper takes the Beijiang Dike as the research object and analyses the seepage field of the dike and the optimization of the antiseepage scheme of the relief well. The Beijiang Dike in Guangdong Province is located on the left bank of the lower reaches of the Beijiang River, with a total length of 63.346 km. It is a flood control barrier for Guangzhou and the Pearl River Delta. It belongs to the first-class levee of the China and is one of the seven levees guaranteed by the whole country. More than 90% of piping effect of Beijiang Dike is caused by seepage of embankment foundation. Flood hazards are mainly concentrated in the area of the pile number 7 + 000 – 10 + 980. In case of large floods, there are many dangers such as piping and sand bursting in pits, lowlands, ditches, and wells behind dikes. Some of them are very serious and need to be vigorously rescued to survive the floods. Therefore, seepage analysis is needed to solve related problems.

The seepage finite element analysis (FEA) method is used to model and analyze the 8 + 230 section of the Shijiao segment of Beijiang Dike. The height of the dike section is 17.85 m, the total length of the section is 181 m, the width of the top of the dike is 8.0 m, the ratio of the upstream batter is 1 : 3, the ratio of the downstream slope above the original road surface is 1 : 3, and the ratio of the downstream slope below the original road surface is 1 : 38. The Shijiao segment is built on a robust permeable layer about 15~25 m thick. The cross section of the embankment is approximately trapezoidal, and the materials of the embankment body include silt, clay, silty clay, and artificial fill.

The upper layer of dike foundation is clay, and the lower is a strong permeable layer, which mainly includes fine sand layer, medium-coarse sand layer, and gravel layer. Assuming that the permeability of soil in the same region is uniform, it is an isotropic medium [24–26], the geological parameters are shown in Table 1, and the model schematic diagram is shown in Figure 2.

3.2. Verification of Grid Independence. For numerical simulation, it is necessary to determine the independence between the number of meshes used in the calculation and the results obtained, that is, to verify the grid independence. The outer river level is 11.38 meters, and the global element size of the grid is set to 0.7 m, 1 m, and 1.3 m. The measured value of the water head is provided by the Beijiang Dike administration department.

From Table 2, it is not difficult to find that three different grid values almost coincide with each other. It can be concluded that the grids with 1 m element size are grid-independent, so we can choose the grids with 1 m element size for numerical simulation.

3.3. Validation of Effectiveness. The validation of the model is mainly based on the comparison between the numerical simulation of the water head of the phreatic line and the actually measured water head of the piezometric pipe under four working conditions. It is known that three pressure measuring pipes are located at horizontal distances of 48 m, 134 m, and 181 m under the conditions of water level of 8.7 m, 9.54 m, 10.56 m, and 11.38 m in the outer river. The measured values of water head are shown in Table 3.

The boundary conditions of numerical simulation are as follows: the upstream water level is in the outer river, and the downstream water level is in the measured value of a B3 piezometer. The simulation results are shown in Figure 2.

After obtaining the specific numerical simulation data, we compare the numerical simulation data with the actual value of the pressure tube and show it in the form of a graph. Figure 3 shows the numerical simulation head value under the condition of 8.7 m, 9.54 m, 10.56 m, and 11.38 m of the outer river and the actual measured head value of the piezometer tube.

Through the analysis and comparison of Figure 4, we can see that the theoretical value of pressure measurement management simulated by the model is very close to the actual measurement value. The maximum error value is not more than 0.32 m. Meanwhile, the minimum error is 0 and the average error value is 0.104 m. Generally speaking, the simulation value is larger than the measured value, and the simulation results are more conservative and safe. The comprehensive results show that the established numerical simulation model is very close to the actual situation.

4. Numerical Results and Discussion

In this section, the transient state of Shijiao segment is simulated numerically. Then, the antiseepage measures and optimization of the use of the relief well are proposed for the dike. Through numerical simulation, we can analyze various embankment conditions including steady state, transient state, and antiseepage measures with relief wells, including phreatic line, seepage quantity, and gradient. The boundary conditions of the outer river level (upstream water level) are set in Table 4.

4.1. Transient Seepage Analysis. The most probable cause of embankment failure in practical engineering is the seepage damage. Under the seepage action of the dike body and foundation, soil particles are lost and local damage is deformed (such as piping or flowing soil) due to its mechanical or chemical action. The seepage of water will increase the phreatic of soil and decrease the suction of the matrix in the unsaturated area, thus increasing the possibility of slope instability. Especially, when the water level changes, the sudden rise and fall of the water level in the dam body will make the seepage stress in the soil body larger, which is easier to destroy the slope soil body. Therefore, the transient

Table 1: Model hydraulic conductivity table.

Material	Dam body	Fine sand layer	Medium-coarse sand layer	Gravel layer
Hydraulic conductivity K (cm/s)	1.94×10^{-4}	5.7×10^{-2}	2.2×10^{-1}	1.3×10^{-1}

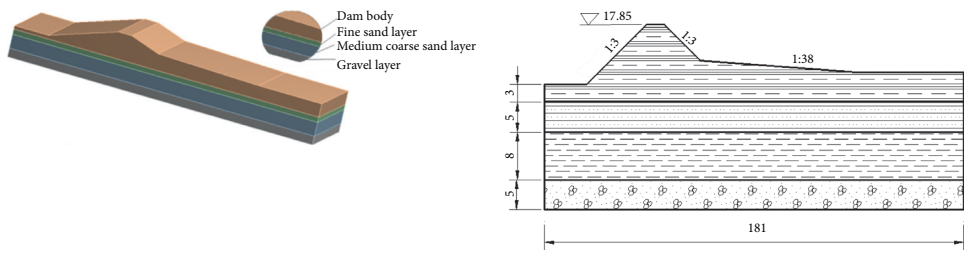

(a) (b)

Figure 2: Schematic diagram of the embankment (unit: m). (a) Three-dimensional dike. (b) Typical section diagram of Shijiao segment.

Table 2: Grid independence validation (unit: m).

Pressure tube head	0.7 m grid	1 m grid	1.3 m grid	Measured value
B0	11.38	11.38	11.38	11.38
B1	10.86	10.82	10.88	10.71
B2	10.24	10.2	10.18	10.17
B3	9.76	9.74	9.75	9.76

Table 3: Measured water level of the 8 + 232 piezometric pipe (unit: m).

Manometer number	8.7 outer river level	9.54 outer river level	11.38 outer river level	10.56 outer river level
B1	8.69	9.02	10.71	9.92
B2	8.53	8.99	10.17	9.76
B3	8.36	9.02	9.76	9.32

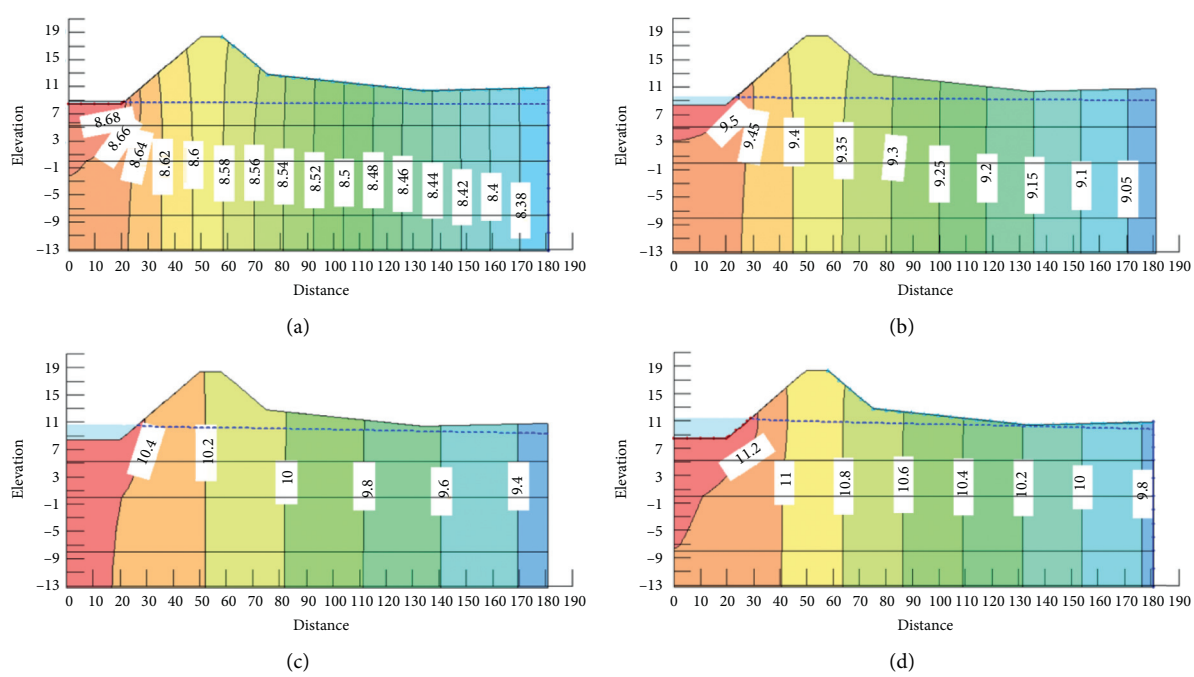

(a) (b) (c) (d)

Figure 3: Numerical simulation results where the outer river water level is (a) 8.7 m, (b) 9.54 m, (c) 10.56 m, and (d) 11.38 m.

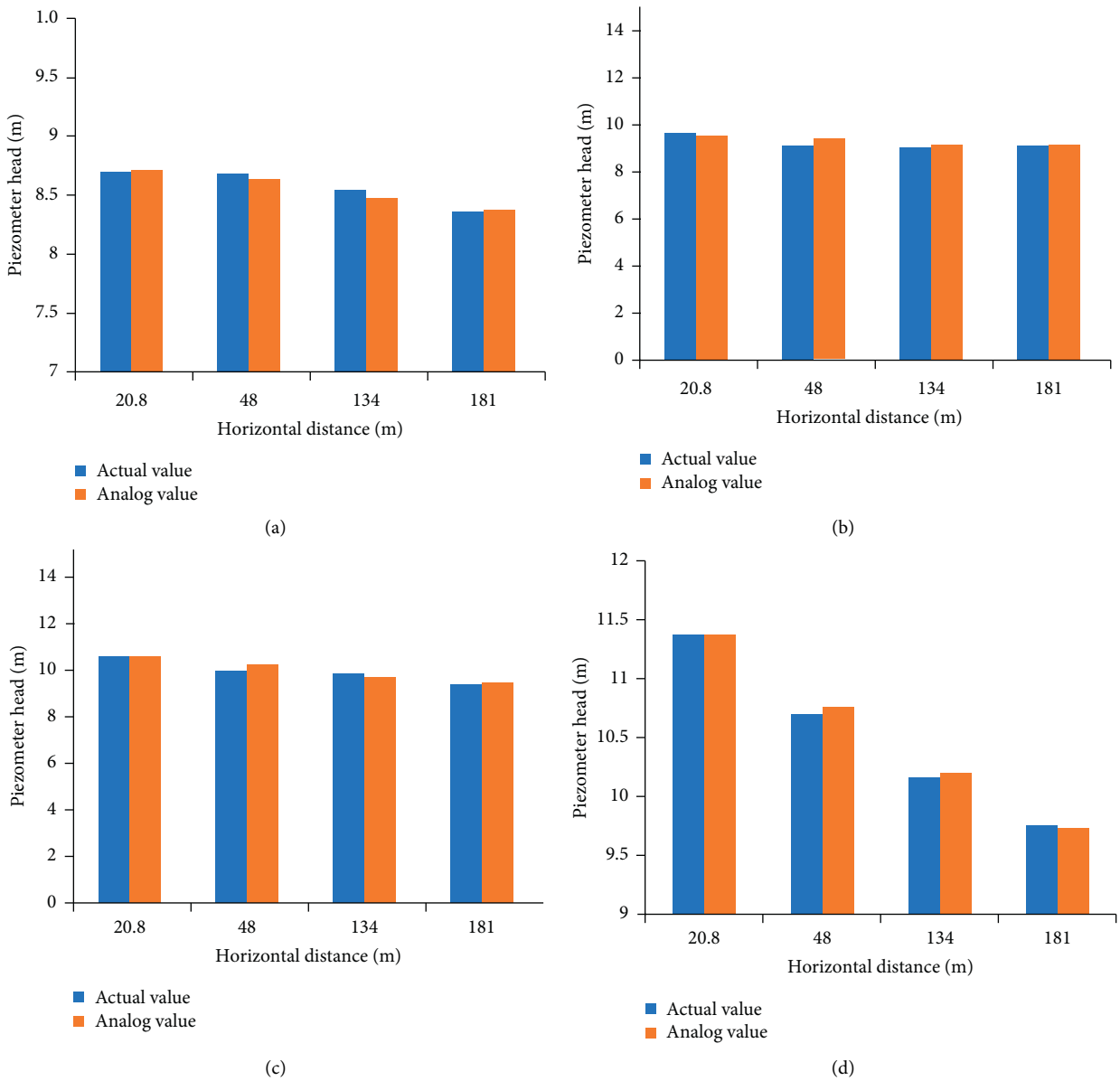

Figure 4: Comparison between calculated head value and measured head value where the outer river water level is (a) 8.7 m, (b) 9.54 m, (c) 10.56 m, and (d) 11.38 m.

Table 4: Boundary conditions of the transient upstream water level.

Time (hour)	Outer river level (meter)
0	9.5
6	10
12	10.5
18	11.5
24	12.5
30	13.5
36	14
42	14.5
48	15
60	16
72	17

analysis of the embankment can better predict the water level when the embankment is damaged, which has a strong guiding significance for the safe operation of the embankment. In Figure 5, elevation and distance units are meters.

From Figure 5, it can be concluded that as the water level increases, the change of phreatic line becomes larger and larger, equipotential line value of dam section increases, and the lowest equipotential line value reaches 11 at the highest water level. When the outer river level is about 15 meters, the phreatic line crosses the foot of the backwater slope above the original road surface. With the increase of rainfall, piping and flowing soil will easily occur here.

From Figure 6(a) seepage quantity variation chart, it can be seen that the transient seepage quantity is larger than the

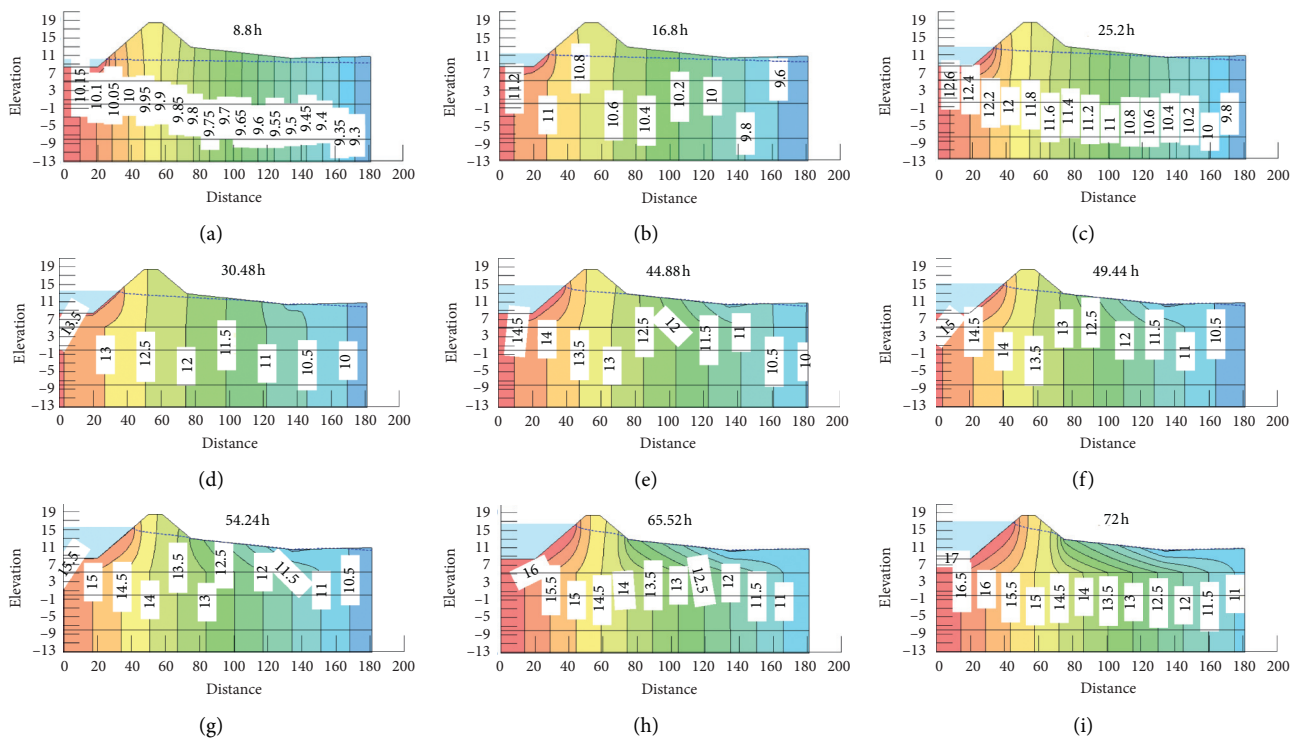

Figure 5: Transient numerical simulation of phreatic line variation.

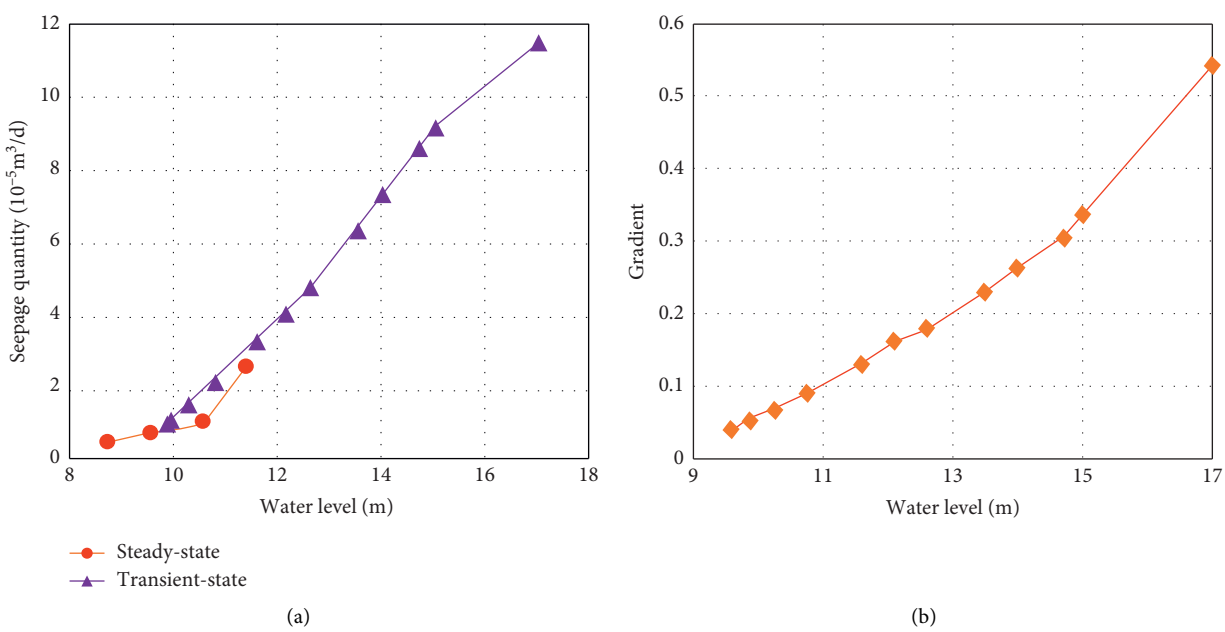

Figure 6: (a) Changes in transient and steady-state seepage quantity. (b) Changes in transient gradient.

steady seepage flow under the same water level, and the maximum seepage quantity reaches 9.43×10^{-5} m^3/d. Higher safety measures should be taken when the same water level falls in the rain. With the increase of the water level, the seepage of the dam body increases gradually, and the gradient of dam body increases in a curve. When the water level is 15.78 m, the gradient reaches 0.5 [27] and the embankment is damaged. In order to increase the safety of the embankment, we add the antiseepage measures of relief wells to the embankment.

4.2. Seepage Analysis of Relief Wells. As one of the primary seepage control means, relief wells are widely used in dike

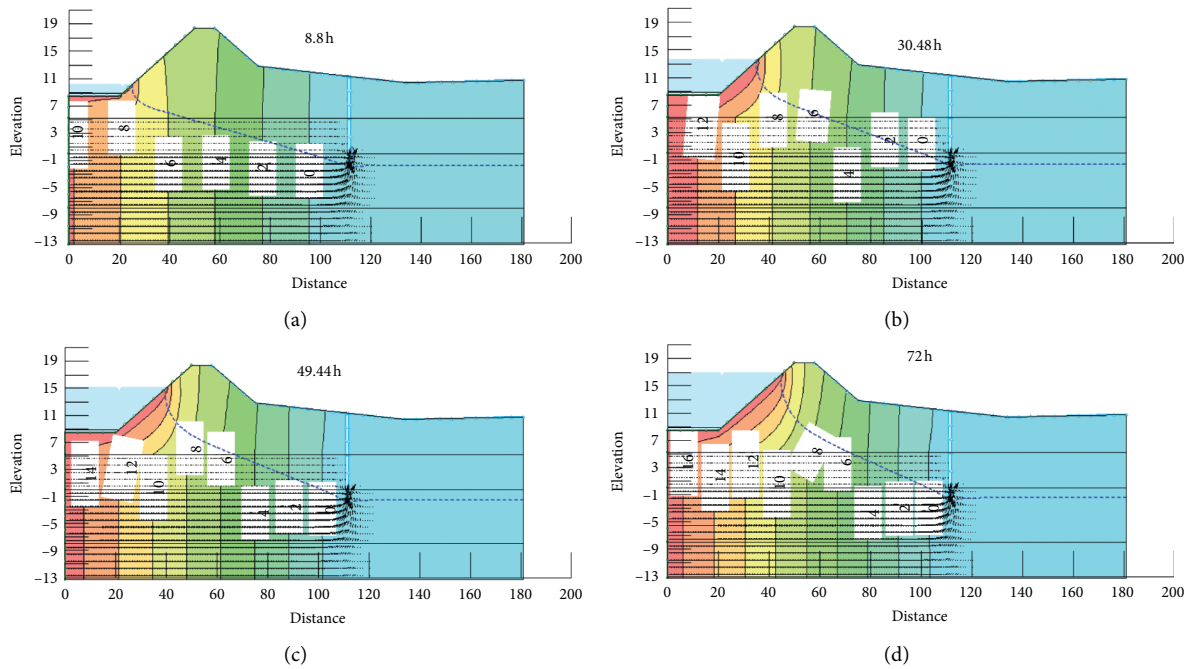

Figure 7: Variation diagram of the phreatic line in numerical simulation of relief wells.

engineering. Relief wells are often used in dikes and dams. If the design and construction are unreasonable or the operation and management are not good, the output of water will be small, the effect of decompression will be poor, and the safety of dikes will be endangered. Therefore, it is of considerable significance to study the location and penetration depth of relief wells.

We analyzed the relief well depths of 10 m, 11 m, 12.5 m, and 16.5 m and analyzed the relief wells with a penetration depth of 12.5 m at horizontal distances of 84 m, 94 m, and 114 m.

The higher the water level of the outer river, the higher the height of the phreatic line and the greater the risk of breaking dikes. As shown in Figure 7, the relief well goes deep into the strong permeable layer. It can be seen that the height of the phreatic line of the relief well decreases obviously after the relief well has passed (the lowering elevation is between 8 m and 12 m) as shown in Figure 8, and a large amount of water is discharged from the relief well to prevent piping, flowing soil, swamping, and other phenomena. The equipotential line value on the left side of the relief well has almost changed to 0, which shows that the relief well plays a significant role.

As shown in Figure 9(a), the effect of drainage and decompression of relief wells is greatly affected by penetration depth, which gradually increases with the increase of penetration depth. When penetration depth increases from 9 m to 11 m, the effect of drainage and decompression is relatively small. As shown in Figure 9(a), the seepage quantity of the four relief wells increases with the increase of the water level. It can be seen that the depth of the relief wells

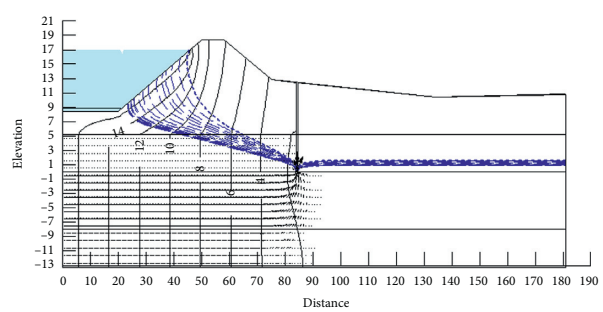

Figure 8: Variation diagram of phreatic line in numerical simulation of relief wells.

is 16.5 m, which has the best seepage control effect on the embankment. The optimal seepage quantity is 4.51×10^{-10} m^3/d, which is remarkable when the seepage quantity is 10^{-5} m^3/d compared with that without the relief wells. It can be seen that if comprehensive factors such as economy and technology are not considered, the deeper the penetration depth of relief wells in different permeability coefficients, the better.

In Figure 9(b), we place the relief wells with a depth of 12.5 m at horizontal distances of 84 m, 95 m, and 114 m. The seepage quantity varies from one well to another, with a difference of nearly 10 times. It can be seen that due to the different geological conditions, the same relief wells in different locations have a vast difference in effect. It can be seen from the figure that the seepage control effect is the best when the horizontal distance is 95 m, and the minimum seepage quantity is 2.37×10^{-10} m^3/d.

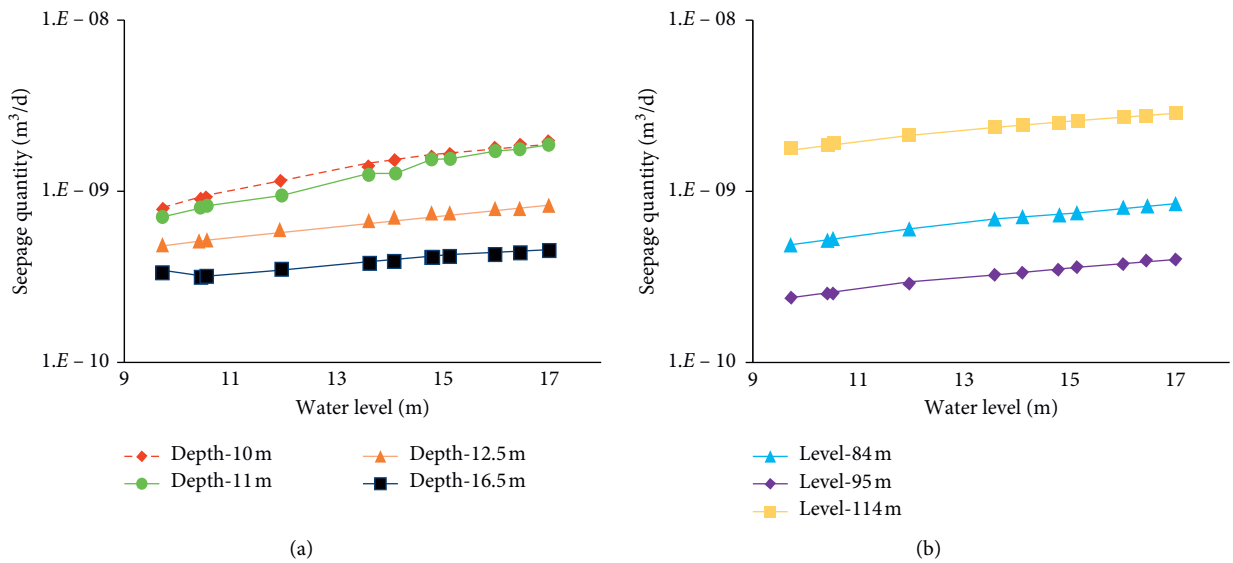

Figure 9: Seepage quantity of added relief wells. (a) Seepage quantity of relief wells with different depths. (b) Seepage quantity of relief wells with different positions.

5. Conclusions

The geological variation of embankment foundation is great, the terrain is complex, and a lot of data are difficult to observe. This paper calculates the transient seepage field of the embankment by numerical simulation and chooses appropriate antiseepage measures of relief wells. Finally, different antiseepage schemes are analyzed.

(1) The average error value of model validation is 0.104 m, which is close to the actual situation. We can accurately and effectively simulate the seepage field and get the gradient, the phreatic line, and the seepage velocity. When the water level is 15.78 m, the gradient reaches 0.5 and the embankment is damaged. Accurate numerical simulation can provide sufficient support for the safety evaluation of embankment seepage.

(2) As a seepage control measure, the effect of relief wells is significantly different from that of non-pressure-relief wells. The minimum seepage quantity after relief wells is $8.4 \times 10^{-10}\,m^3/d$ and without a relief well is $1.65 \times 10^{-5}\,m^3/d$. The lowering of the water head of the phreatic line is up to 12 m, and the lowering of seepage quantity is beneficial to prevent piping, flowing soil, swamping, and other phenomena in the embankment, which plays an indispensable role in the safety of the embankment.

(3) At the same water level, the transient seepage quantity is larger than the steady seepage quantity. Therefore, the safety hazards of dikes are greater when rapid rainfall occurs, and safer antiseepage measures should be taken.

Data Availability

The raw/processed data required to reproduce these findings cannot be shared at this time as the data also form part of an ongoing study.

Conflicts of Interest

The authors declare that they have no conflicts of interest.

Authors' Contributions

Wenbing Xu, Chuan Xu, and Qinghe Yao contributed equally to this work.

Acknowledgments

This work was partly supported by the National Key R&D Program for HPC under grant no. 2016YFB0200603 and the National Key R&D Program for International Cooperation, grant no. 2018YFE9103900. The Guangdong MEPP Fund (no. GDOE[2019] A01), the project of the Guangzhou Science and Technology Program, grant no. 201704030089, and the NSFC project (grant no. 11972384) also supported this research.

References

[1] X. F. Guo, D. Dias, and Q. J. Pan, "Probabilistic stability analysis of an embankment dam considering soil spatial variability," *Computers and Geotechnics*, vol. 113, pp. 093–103, 2019.

[2] A. Kacimov and Y. Obnosov, "Analytical solutions for seepage near material boundaries in dam cores: the davison-kalinin problems revisited," *Applied Mathematical Modelling*, vol. 36, no. 3, pp. 1286–1301, 2012.

[3] T. Jiang, J. Zhang, W. Wan, S. Cui, and D. Deng, "3D transient numerical flow simulation of groundwater bypass seepage at the dam site of Dongzhuang hydro-junction," *Engineering Geology*, vol. 231, pp. 176–189, 2017.

[4] W. J. Hu, *Test and Numerical Simulation Study on Seepage Control Effect of Embankment Foundation Engineering with Weak Permeable Layer*, Tianjin University, Tianjin, China, 2017.

[5] G. Gottardi, C. G. Gragnano, I. Rocchi, and M. Bittelli, "Assessing river embankment stability under transient seepage conditions," *Procedia Engineering*, vol. 158, pp. 350–355, 2016.

[6] P. Khanh and L. Hyobum, "Influence of hydraulic characteristics on stability of unsaturated slope under transient seepage conditions," *Landslides*, vol. 15, no. 9, pp. 1787–1799, 2018.

[7] S. Li, J. Wang, L. Li, S. Shi, and Z. Zhou, "The theoretical and numerical analysis of water inrush through filling structures," *Mathematics and Computers in Simulation*, vol. 162, pp. 115–134, 2019.

[8] L. Yao, S. Feng, X. Mao, Z. Huo, S. Kang, and D. A. Barry, "Coupled effects of canal lining and multi-layered soil structure on canal seepage and soil water dynamics," *Journal of Hydrology*, vol. 430-431, pp. 91–102, 2012.

[9] S. P. Neuman, "Theoretical derivation of darcy's law," *Acta Mechanica*, vol. 25, no. 3-4, pp. 153–170, 1977.

[10] L. A. Richards, "Capillary conduction of liquids through porous mediums," *Physics*, vol. 1, no. 5, pp. 318–333, 1931.

[11] L. Lam, D. G. Fredlund, and S. L. Barbour, "Transient seepage model for saturated-unsaturated soil systems: a geotechnical engineering approach," *Canadian Geotechnical Journal*, vol. 24, no. 4, pp. 565–580, 1987.

[12] Y. Qing, H. Z. Li, J. H. Jing et al., "Experimental studies on seepage failure of the top stratum at a weak spot in double-layer dike foundations," *Advanced Materials Research*, vol. 368–373, pp. 2387–2393, 2012.

[13] F. Armin, S. Farzin, and M. Behnam, "Optimum size for clay core of alavian earth dam by numerical simulation," *Iranica Journal of Energy & Environment*, vol. 5, no. 3, pp. 240–246, 2014.

[14] F. R. Salazar, M. Á. Toledo, and E. Oñate, "Data-based models for the prediction of dam behaviour: a review and some methodological considerations," *Archives of Computational Methods in Engineering*, vol. 24, no. 1, pp. 1–21, 2017.

[15] M. C. Morán, *Analysis of Seepage and Dam Slope Stability of Dam Body of Fosi Reservoir*, Taiyuan University of Technology, Taiyuan, China, 2014.

[16] J. F. Zhang, G. S. Zhu, and G. L. Cao, "Numerical simulation study on the diffusion deformation expansion process and the control function of suspended cutoff wall," *Journal of Yangtze River Scientific Research Institute*, vol. 21, no. 6, pp. 47–50, 2004.

[17] A. Mocllmann, P. A. Vermeer, and M. Huber, "A probabilistic finite element analysis of embankment stability under transient seepage conditions," *Georisk: Assessment and Management of Risk for Engineered Systems and Geohazards*, vol. 5, no. 2, pp. 110–119, 2011.

[18] M. Huber, A. Moellmann, and P. A. Vermeer, "PC-River-reliability analysis of embankment stability," *Georisk: Assessment and Management of Risk for Engineered Systems and Geohazards*, vol. 5, no. 2, pp. 132–142, 2011.

[19] L. Z. Wu, L. M. Zhang, Y. Zhou et al., "Analysis of multi-phase coupled seepage and stability in anisotropic slopes under rainfall condition," *Environmental Earth Sciences*, vol. 76, no. 14, p. 469, 2017.

[20] K. H. Qiu, D. W. Lu, and B. Huang, "Numerical analysis of seepage stability of embankment engineering," *Yangtze River*, vol. 42, no. s2, pp. 155-156, 2011.

[21] T. Zhang, "Analysis on the effect of anti-seepage engineering of shijiao segment in beijiang dike," *Chinese Journal of Rock Mechanics and Engineering*, vol. 28, no. 11, pp. 2235–2241, 2009.

[22] J. J. Li, "Numerical analysis of influencing factors of the operation effect of the relief well," *Journal of Yangtze River Scientific Research Institute*, vol. 33, no. 5, pp. 151–154, 2016.

[23] S. Whitaker, "Flow in porous media I: a theoretical derivation of darcy's law," *Transport in Porous Media*, vol. 1, no. 1, pp. 3–25, 1986.

[24] Z. Y. Ai, Y. F. Chen, and X. B. Jiang, "Behavior of laterally and vertically loaded piles in multi-layered transversely isotropic soils," *Applied Mathematical Modelling*, vol. 51, pp. 561–573, 2017.

[25] Y. C. Cheng and Z. Y. Ai, "Consolidation analysis of transversely isotropic layered saturated soils in the Cartesian coordinate system by extended precise integration method," *Applied Mathematical Modelling*, vol. 40, no. 4, pp. 2692–2704, 2016.

[26] R. T. Yan, X. Y. Zhao, M. B. Yu et al., "Isotropic compression characteristics of clayey soil saturated bysalty solution," *Rock & Soil Mechanics*, vol. 39, no. 1, pp. 129–138, 2018.

[27] J. Q. Zhao, "Stability analysis of embankment seepage in aihe treatment project based on hydraulics method," *Shaanxi Water Resources*, vol. 2, pp. 134-135, 2017.

Hindawi
Mathematical Problems in Engineering
Volume 2020, Article ID 4806387, 7 pages
https://doi.org/10.1155/2020/4806387

Research Article

Least Squares Differential Quadrature Method for the Generalized Bagley–Torvik Fractional Differential Equation

Constantin Bota, Bogdan Căruntu, Mădălina Sofia Pașca, Dumitru Țucu, and Marioara Lăpădat

Department of Mathematics, Politehnica University Timisoara, Victoriei Square 2, Timisoara 300 006, Romania

Correspondence should be addressed to Bogdan Căruntu; bogdan.caruntu@upt.ro

Received 21 April 2020; Revised 12 June 2020; Accepted 17 June 2020; Published 16 July 2020

Guest Editor: Yi Qi

In this paper, the least squares differential quadrature method for computing approximate analytical solutions for the generalized Bagley–Torvik fractional differential equation is presented. This new method is introduced as a straightforward and accurate method, fact proved by the examples included, containing a comparison with previous results obtained by using other methods.

1. Introduction

Even though the fractional calculus is a relatively old concept, dating back from the time of the mathematicians L'Hospital and Leibniz in the 17th century, it has seen a significant development in the last decades only. The fractional differential equations have numerous applications in biology, physics, chemistry, and engineering, which is why many scientists are concerned about finding more effective ways to solve them. Unfortunately, finding analytical solutions for fractional differential equations is often difficult or even impossible, which is why in recent years various numerical and approximate methods have been developed. One of the fractional differential equations with wide applicability in engineering is the Bagley–Torvik equation. This equation was introduced by Bagley and Torvik in [1] in 1984 to "model a motion of a rigid plate immersed in a Newtonian fluid" and in [2] for modeling the damping properties of the polymers. In engineering (construction, biotechnology, and chemistry), condensing polymers are widely used, and in their study, the Bagley–Torvik equation is the one employed [3, 4].

Bagley–Torvik-type fractional differential equations have been studied both numerically and analytically in numerous articles. Among the methods used to solve this equation, we mention the following: numerical methods [5], Adomian decomposition method [6], discrete spline methods [7], Haar wavelet method [8, 9], homotopy perturbation method [10], sinc collocation method [11, 12], cubic spline method [13], quadratic spline solution [14], B-spline collocation method [15, 16], Chebyshev collocation method [17], hybrid functions approximation [18], harmonic wavelets [19], predictor-corrector method of Adams type [20], spectral methods [21], fractional natural decomposition method [22], and finite element method [23].

The motivation of this paper is to introduce a new method for obtaining analytical approximate solutions for fractional differential equations. This method is obtained as a combination of the differential quadrature method (DQM) ([24]) and the least squares method (LSM), and we named it the least squares differential quadrature method (LSDQM). We applied this new method to find solutions of the following generalized Bagley–Torvik fractional differential equation [25]:

$$A \cdot y''(x) + B(x) \cdot D_x^{\alpha} y(x) = f\left(x,\ y(x),\ D_x^{\beta} y(x),\ y'(x)\right), \tag{1}$$

where $y(x)\colon [a,b] \longrightarrow \mathbb{R}$, $\alpha \in (1,2)$, $\beta \in (0,1)$, together with the conditions:

$$y(a) = \mu_0, \quad \nu_1 \cdot y'(a) + \nu_2 \cdot y(b) = \mu_1, \tag{2}$$

where μ_0, μ_1, ν_0, and ν_1 are constants (for $\nu_1 = 0$, we obtain boundary conditions, while for $\nu_2 = 0$, we obtain initial conditions). $A \in \mathbb{R}$, $B(x)$ and $f(x)$ are given such that problems (1) and (2) satisfy the existence and uniqueness conditions for a continuous solution [25].

D_x^γ denotes Caputo's fractional derivative:

$$D_x^\gamma y(x) = \frac{1}{\Gamma(n-\gamma)} \cdot \int_0^x (x-\zeta)^{-(\gamma-n+1)} \cdot y^{(n)}(\zeta) d\zeta, \quad n-1 < \gamma \le n,\ n \in \mathbb{N}^*. \tag{3}$$

In the next section, we will present the least squares differential quadrature method (LSDQM), and in the third section, some numerical examples are presented followed by the conclusions.

2. The Least Squares Differential Quadrature Method

First, we will consider a numerical mesh of the interval $I = [a, b]$ by means of a partition Δ_M consisting of $M + 1$ points: $a = x_0 < x_1 < x_2 < \cdots < x_{M-1} < x_M = bp = 0.007$. In order to find an approximate solution of the generalized Bagley–Torvik problems (1) and (2), we will compute the values of a certain functional (the functional (12) introduced in the following) at the point x_i.

To equation (1), we attach the following operator:

$$\mathscr{D}^\alpha(y(x)) = A \cdot y''(x) + B(x) \cdot D_x^\alpha y(x) - f\left(x,\ y(x),\ D_x^\beta y(x),\ y\prime(x)\right). \tag{4}$$

We denote by $\tilde{y}(x)$ an approximate solution of equation (1). By replacing in $\mathscr{D}^\alpha$ the exact solution $y(x)$ with this approximate solution, we obtain the following reminder:

$$\mathscr{R}(x, \tilde{y}(x)) = \mathscr{D}^\alpha(\tilde{y}(x)). \tag{5}$$

Definition 1. We call an ϵ-approximate solution of problems (1) and (2) related to the partition Δ_M an approximate polynomial solution, which satisfies the following relations:

$$\left|\mathscr{R}(x_i, \tilde{y}(x_i))\right| < \varepsilon, \quad i = \overline{0, M}, \tag{6}$$

$$\tilde{y}(a) = \mu_0, \quad \nu_1 \cdot \tilde{y}'(a) + \nu_2 \cdot \tilde{y}(b) = \mu_1. \tag{7}$$

Definition 2. We consider the sequence of polynomials:

$$P_N(x) = \sum_{k=0}^{N} c_k x^k, \quad c_k \in \mathbb{R},\ k = \overline{0, N}. \tag{8}$$

We call the sequence of polynomials $P_N(x)$ convergent to the solution of problems (1) and (2) if

$$\lim_{N \longrightarrow \infty} \mathscr{D}^\alpha(P_N(x)) = 0. \tag{9}$$

Taking into account the above definitions, we will compute ϵ-approximate polynomial solutions for a Bagley–Torvik problem of the types (1) and (2) by taking the steps described in the following algorithm:

(i) *Step 1.* we will compute an approximate solution of the type

$$T_N(x) = \sum_{k=0}^{N} \tilde{c}_k x^k, \tag{10}$$

where the sequence of polynomials must also satisfy the boundary conditions:

$$T_N(a) = \mu_0, \quad \nu_1 \cdot T_N'(a) + \nu_2 \cdot T_N(b) = \mu_1, \tag{11}$$

and the constants $\tilde{c}_k$ are calculated in the following steps.

(ii) *Step 2.* From the boundary conditions, we obtain $\tilde{c}_0$ and $\tilde{c}_1$ as functions of $\tilde{c}_2, \tilde{c}_3, \ldots, \tilde{c}_N$. Thus, the expression of $T_N(x)$ from now on will be a function of x and $\tilde{c}_2, \tilde{c}_3, \ldots, \tilde{c}_N$ only.

(iii) *Step 3.* We attach to problems (1) and (2) the functional $\mathscr{F}(\tilde{c}_2, \tilde{c}_3, \ldots, \tilde{c}_N)$:

$$\mathscr{F} = \sum_{i=0}^{M} \mathscr{R}^2(x_i, T_N(x_i)) == \sum_{i=0}^{M} \left(A \cdot T_N''(x_i) + B(x) \cdot D_x^\alpha T_N(x_i) - f\left(x,\ T_N(x_i),\ D_x^\beta y(x),\ T_N'(x_i)\right)\right)^2. \tag{12}$$

(iv) *Step 4.* By minimizing the functional (12), we obtain the values of the coefficients $\tilde{c}_2^0, \tilde{c}_3^0, \ldots, \tilde{c}_N^0$ which give the minimum of (12).

(v) *Step 5.* After computing $\tilde{c}_2^0, \tilde{c}_3^0, \ldots, \tilde{c}_N^0$, we return to the boundary conditions and obtain the final value of $\tilde{c}_0$ and $\tilde{c}_1$.

(vi) *Step 6.* Finally, we replace the values $\tilde{c}_0^0, \tilde{c}_1^0, \tilde{c}_2^0, \tilde{c}_3^0, \ldots, \tilde{c}_N^0$, calculate in the expression of $T_N(x)$, and denote by $T_N^0(x) = \sum_{k=0}^{N} \tilde{c}_k^0 x^k$ the analytical approximate polynomial solution by LSDQM of problems (1) and (2).

The following convergence theorem is satisfied:

Theorem 1. *The sequence of polynomials $T_N(x)$ satisfies the following relation:*

$$\lim_{N\longrightarrow\infty} \mathscr{R}^2\left(x_i, T_N\left(x_i\right)\right) = 0, \quad i = \overline{0, M}. \tag{13}$$

Proof. Let $y(x)$ be an exact solution of problems (1) and (2), which means from hypothesis that there exists a sequence of polynomials $P_N(x) = \sum_{k=0}^{N} c_k x^k$, $c_k \in \mathbb{R}$, $k = \overline{0, N}$ converging to $y(x)$ (according to the Weierstrass theorem on Polynomial Approximation, see [24]), i.e., $\lim_{N\longrightarrow\infty} P_N(x) = y(x)$, $\forall x \in I$. Taking into account Definition 2, this means that $P_N(x)$ satisfies

$$\lim_{N\longrightarrow\infty} \mathscr{D}^{\alpha}\left(P_N(x)\right) = 0. \tag{14}$$

Denoting by $c_2^0, c_3^0, \ldots, c_N^0$ the values of the coefficients c_k which give the minimum of the functional (12), it follows that $\mathscr{F}(c_2^0, c_3^0, \ldots, c_N^0) \leq \mathscr{F}(c_2, c_3, \ldots, c_N)$. If $T_N^0(x) = \sum_{k=0}^{N} \tilde{c}_k^0 x^k$ is the approximate solution by LSDQM (with $\tilde{c}_0^0$ and $\tilde{c}_1^0$ computed by using the initial conditions), we obtain

$$\sum_{i=0}^{M} \mathscr{R}^2\left(x_i, T_N^0\left(x_i\right)\right) \leq \sum_{i=0}^{M} \mathscr{R}^2\left(x_i, P_N\left(x_i\right)\right). \tag{15}$$

Hence, $\lim_{N\longrightarrow\infty}(\sum_{i=0}^{M} \mathscr{R}^2(x_i, \quad T_N^0(x_i))) \leq \leq \lim_{N\longrightarrow\infty}(\sum_{i=0}^{M} \mathscr{R}^2(x_i, P_N(x_i)))$.

We conclude that $\lim_{N\longrightarrow\infty} \mathscr{R}^2(x_i, T_N^0(x_i)) = 0$. □

2.1. Error Estimation. We can rewrite equation (1) as

$$A \cdot y''(x) + B(x) \cdot D_x^{\alpha} y(x) - f_1\left(y(x), D_x^{\beta} y(x), y(x)\right) = f_2(x). \tag{16}$$

We denote with $\mathscr{L}$ the following operator:

$$\mathscr{L}(y(x)) = A \cdot y''(x) + B(x) \cdot D_x^{\alpha} y(x) - f_1\left(y(x), D_x^{\beta} y(x), y\prime(x)\right). \tag{17}$$

Thus, equation (1) becomes

$$\mathscr{L}(y(x)) = f_2(x). \tag{18}$$

Using (for simplicity) the notation: $\mathscr{R}(x) = \mathscr{R}(x, \tilde{y}(x)) = \mathscr{D}^{\alpha}(\tilde{y}(x))$, in (4), we obtain

$$\mathscr{R}(x) = \mathscr{L}(\tilde{y}(x)) - f_2(x), \tag{19}$$

with $\tilde{y}$ as an approximate solution for problems (1) and (2), which means as $\tilde{y}$ satisfies

$$\mathscr{L}(\tilde{y}(x)) = A \cdot y''(x) + B(x) \cdot D_x^{\alpha} y(x) - f_1\left(y(x), D_x^{\beta} y(x), y\prime(x)\right) = f_2(x) + \mathscr{R}(x), \tag{20}$$

together with the conditions:

$$\tilde{y}(a) = \mu_0, \quad \nu_1 \cdot \tilde{y}'(a) + \nu_2 \cdot \tilde{y}(b) = \mu_1. \tag{21}$$

We define the error function in the following way: $\tilde{e}(x) = y(x) - \tilde{y}(x)$, where $y(x)$ is the exact solution for problems (1) and (2) and we obtain (using (18) and (19)) the differential equation for the error function:

$$\mathscr{L}(\tilde{e}(x)) = \mathscr{L}(y(x)) - \mathscr{L}(\tilde{y}(x)) = -\mathscr{R}(x), \tag{22}$$

with the conditions:

$$\tilde{e}(a) = 0, \quad \nu_1 \cdot \tilde{e}'(a) + \nu_2 \cdot \tilde{e}(b) = 0. \tag{23}$$

The problem for the error function becomes

$$\mathscr{L}(\tilde{e}(x)) = -\mathscr{R}(x). \tag{24}$$

Solving (24) together with (23) in the same manner as described above for problems (1) and (2), we obtain the approximation $\tilde{e}(x)$. We will be able to determine the absolute maximum error:

$$E = \max[|\tilde{e}(x)|, \quad 0 \leq x \leq 1]. \tag{25}$$

In this manner, we can estimate the error without knowing the exact solution of the initial problems (1) and (2).

Remark 1. We remark that the above theorem proves the convergence of LSDQM since as the degree of the polynomial increases the remainder corresponding to the approximation tends to zero. This fact is illustrated in the second example.

3. Numerical Examples

In this section, we will present some examples of problems including generalized Bagley–Torvik fractional differential equations together with boundary or initial conditions and problems solved using the least squares differential quadrature method (LSDQM).

3.1. Example 1. We consider the generalized Bagley–Torvik equation [26, 27]:

$$y''(x) + x^{(1/2)} \cdot D^{\alpha} y(x) + By(x) = -x^{(1/3)} \cdot y(x) - x^{(1/4)} \cdot D^{\beta} y(x) - x^{(1/5)} y(x) + f_2(x), \tag{26}$$

together with the initial conditions: $y(0) = 2$, $y\prime(0) = 0$, where $f_2(x) = 1 - (x^{(1/2)}/\Gamma(3-\alpha)) \cdot x^{2-\alpha} - x^{(1/3)} \cdot x - (x^{(1/4)}/\Gamma(3-\beta)) \cdot x^{2-\beta} + x^{(1/5)} \cdot (2 - (1/2) \cdot x^2)$, $\alpha = 1.234$, and $\beta = 0.333$. The exact solution of this problem is $y(x) = 2 - (1/2) \cdot x^2$.

Approximate solutions for this problem with absolute errors larger than 10^{-4} were proposed by El-Mesiry et al. in [26] and with absolute errors larger than 10^{-5} by Li and Zhao in [27].

We applied LSDQM to find an approximate analytical solution on the $[0, 1]$ interval for (26).

In Step 1, we choose an approximate solution $\tilde{y}(x)$ of the following type:

$$\tilde{y}(x) = \tilde{c}_0 + \tilde{c}_1 x + \tilde{c}_2 x^2. \tag{27}$$

In Step 2, by using the initial conditions, we find $\tilde{c}_0 = 2$ and $\tilde{c}_1 = 0$, and the approximate solution becomes

$$\tilde{y}(x) = 2 + \tilde{c}_2 x^2. \tag{28}$$

In Step 3, the corresponding reminder (5) is

$$\begin{aligned}\mathscr{R}(\tilde{y}) = \tilde{c}_2\left(2x^{(4/3)} + x^{(11/5)} + \frac{1000x^{(633/500)}}{383\Gamma(383/500)} + \frac{2000000x^{(1917/1000)}}{1111889\Gamma(667/1000)} + 2\right) + x^{(4/3)} \\ + \frac{x^{(11/5)}}{2} + \frac{x^{(633/500)}}{\Gamma(883/500)} + \frac{x^{(1917/1000)}}{\Gamma(2667/1000)} + 1.\end{aligned} \tag{29}$$

We consider the simplest possible partition Δ_1: $0 = x_0 < x_1 = 1$, and we attach to the equation the functional $\mathscr{F}(\tilde{c}_2) = \sum_{i=0}^{1} \mathscr{R}^2(x_i, T_1(x_i))$ (too long to be included here).

In Step 4, in order to find the minimum of this functional, we can compute the stationary points by equating to zero its first derivative (the computations are performed using the software Wolfram Mathematica). We obtain $\tilde{c}_2 = 1/2$, and it is easy to show (by means of the second derivative) that this stationary point is indeed the minimum.

In the case of this problem, Step 5 is not needed since we already have the final values of $\tilde{c}_0$ and $\tilde{c}_1$.

Finally, in Step 6, we replace $\tilde{c}_0 = 2$, $\tilde{c}_1 = 0$, and $\tilde{c}_2 = 1/2$ in the initial expression of $\tilde{y}(x)$, thus obtaining the exact solution of the equation: $\tilde{y}(x) = 2 - (1/2) \cdot x^2$.

We remark that, in the case of this example, we could choose any partition Δ_M since the particular form of the remainder (5) assures the fact that the stationary point is always $\tilde{c}_2 = 1/2$ no matter how large M is.

3.2. Example 2. We consider the fractional Bagley–Torvik boundary value problem [21]:

$$y''(x) + D^{\alpha} y(x) + y(x) = f_2(x), \tag{30}$$

$$\begin{aligned} f_2(x) = &-\frac{4c^3 x_1^{3/2} F_2\left(1; (5/4), (7/4); -(1/4)c^2x^2\right)}{3\sqrt{\pi}} \\ &- c^2 \sin(cx) + \sin(cx),\end{aligned} \tag{31}$$

$$\begin{aligned} y(0) &= 0, \\ y(1) &= \sin(c),\end{aligned} \tag{32}$$

where $[a, b] = [0, 1]$, $\alpha = 1.5$, and F is the generalized hypergeometric function.

The exact solution of this problem is $y(x) = \sin(c \cdot x)$.

We remark the fact that if the exact solutions of the problem is a polynomial function (as in the case of the first example), then, naturally, in applying the first step of our method, we have chosen an approximate polynomial solution (10) of the same degree as the exact solution. Since, in this example, the exact solution is not a polynomial, we computed approximate polynomial solutions of several degrees, and for each degree, we calculated the maximal value of the absolute error on the whole interval $[0, 1]$ for $c = 1$. The results presented in Table 1 together with a comparison with previous results from [21] clearly illustrate the convergence of the method.

The approximate polynomial solutions computed by LSDQM using an equidistant partition Δ_{100} are

$$\tilde{y}_4(x) = 0.0196467x^4 - 0.181975x^3 + 0.00382023x^2 + 0.999979x, \tag{33}$$

$$\tilde{y}_5(x) = 0.00720937x^5 + 0.00159936x^4 - 0.167467x^3 + 0.000129252x^2 + 1.x, \tag{34}$$

$$\tilde{y}_6(x) = -0.000658967x^6 + 0.00918884x^5 - 0.000526231x^4 - 0.166518x^3 - 0.0000146541x^2 + 1.x, \tag{35}$$

$$\begin{aligned}\tilde{y}_7(x) = &-0.000172399x^7 - 0.0000548963x^6 + 0.00838255x^5 - 0.0000217806x^4 \\ &- 0.166662x^3 - 3.209289 \cdot 10^{-7}x^2 + 1.x,\end{aligned} \tag{36}$$

$$\begin{aligned}\tilde{y}_8(x) = &0.0000117989x^8 - 0.000219638x^7 + 0.0000202955x^6 + 0.00832241x^5 \\ &+ 3.233537 \cdot 10^{-6}x^4 - 0.166667x^3 + 2.3498896 \cdot 10^{-8}x^2 + 1.x,\end{aligned} \tag{37}$$

Table 1: Maximal absolute errors for approximate polynomial solutions of various degrees obtained using LSDQM for example 2.

Degree	Maximal error [21]	Maximal error LSDQM
4	$3.4 \cdot 10^{-4}$	$6.3979 \cdot 10^{-5}$
5	—	$1.3366 \cdot 10^{-6}$
6	—	$8.2879 \cdot 10^{-8}$
7	—	$1.3333 \cdot 10^{-9}$
8	$4.3 \cdot 10^{-7}$	$7.3808 \cdot 10^{-11}$
9	—	$1.0573 \cdot 10^{-12}$
10	—	$6.5171 \cdot 10^{-14}$

$$\begin{aligned}\widetilde{y}_9(x) = {} & 2.40043968 \cdot 10^{-6} x^9 + 9.888419 \cdot 10^{-7} x^8 - 0.000199677 x^7 \\ & + 9.028126 \cdot 10^{-7} x^6 + 0.00833296 x^5 + 8.6069828 \cdot 10^{-8} x^4 - 0.166667 x^3 \end{aligned} \tag{38}$$

$$+ 3.73299399 \cdot 10^{-10} x^2 + 1.x, \tag{39}$$

$$\begin{aligned}\widetilde{y}_{10}(x) = {} & -1.3736474 \cdot 10^{-7} x^{10} + 3.0878011 \cdot 10^{-6} x^9 - 4.5494814 \cdot 10^{-7} x^8 - 0.000198028 x^7 \\ & - 2.0494998 \cdot 10^{-7} x^6 + 0.0083334 x^5 - 1.31793399 \cdot 10^{-8} x^4 - 0.166667 x^3 - 4.5065671 \cdot 10^{-11} x^2 + 1.x. \end{aligned} \tag{40}$$

3.3. Example 3. Choosing in (1) $A = 0$, $B(x) = 0$, $f(x, y(x), D_x^\beta y(x), y\prime(x)) = D_x^\beta y(x) + y^2(x) - 1$, $[a, b] = [0, 1]$, $\mu_0 = \mu_1 = \nu_0 = \nu_1 = 0$, and $\alpha \in (0, 1]$, we obtain the problem [5, 28]:

$$D_x^\beta y(x) + y^2(x) - 1 = 0, \tag{41}$$

$$y(0) = 0. \tag{42}$$

This equation is actually a Riccati-type equation, and for $\alpha = 1$, the exact solution of the problem is $y(x) = (e^{2x} - 1/e^{2x} + 1)$.

Following the LSDQM steps presented in the previous section, we computed approximate polynomial solutions $\widetilde{y}(x)$ of the 9th degree for problems (41) and (42) choosing in turn $\beta = 1$, $\beta = 0.9$, $\beta = 0.8$, and $\beta = 0.7$. The solutions are computed on the $[0, 1]$ interval using again an equidistant partition Δ_{100}. The results are presented in Figure 1.

For example, the approximate polynomial solutions corresponding to $\beta = 1$ is

$$\begin{aligned}\widetilde{y}(x) = {} & -0.0106498 \cdot x^9 + 0.0567197 \cdot x^8 - 0.103159 \cdot x^7 + 0.0253074 \cdot x^6 + \\ & + 0.125356 \cdot x^5 + 0.00150329 \cdot x^4 - 0.333491 \cdot x^3 + 7.88553637 \cdot 10^{-6} \cdot x^2 + 1 \cdot x. \end{aligned} \tag{43}$$

The maximal absolute error corresponding to this approximation is $4.11 \cdot 10^{-9}$.

We remark that the results presented in Figure 1 are in good agreement with previously obtained results [5].

3.4. Example 4. While LSDQM, as most methods of this type, works best on small intervals, it can also be successfully employed in the case of large intervals. In order to illustrate this feature, we consider the Bagley–Torvik problem [6]:

$$y''(x) + D_x^\alpha y(x) + y(x) = 0, \tag{44}$$

$$\begin{aligned} y(0) &= 1, \\ y\prime(0) &= 0, \end{aligned} \tag{45}$$

where $\alpha \in (1, 2)$.

The exact solution of this problem is not known.

An approximate solution obtained by using the Adomian decomposition method was proposed in [6] by V. Daftardar-Gejji and H. Jafari.

For $\alpha = 1.5$, using an equidistant partition Δ_{10} on the interval $I = [0, 20]$, we obtain the approximate analytical solution, presented in Figure 2:

$$\widetilde{y} = -4.24381 \cdot 10^{-9} \cdot x^9 + 3.757992 \cdot 10^{-7} \cdot x^8 - 0.0000130166 \cdot x^7 + 0.00021244, \tag{46}$$

$$x^6 - 0.00133775 \cdot x^5 - 0.00503943 \cdot x^4 + 0.108157 \cdot x^3 - 0.404114 \cdot x^2 + 1. \tag{47}$$

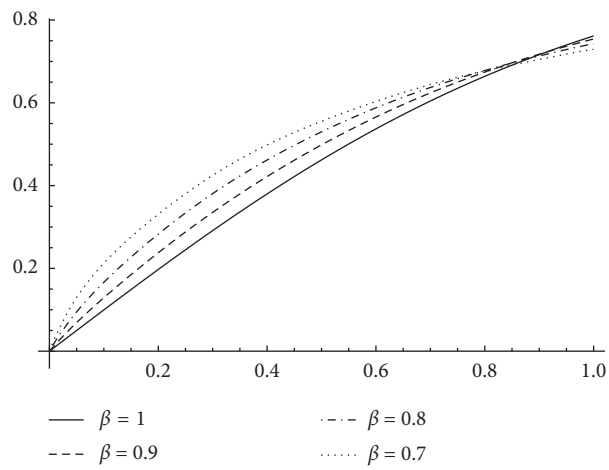

Figure 1: Approximate solutions for problems (41) and (42) corresponding to several values of β.

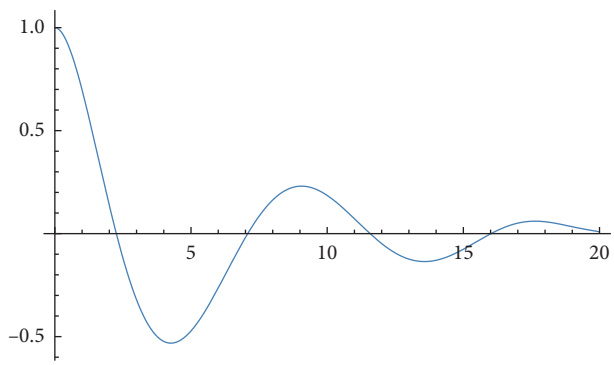

Figure 2: Approximate solution for the problems (44) and (45) corresponding to $\alpha = 1.5$.

We remark that our result is in very good agreement with the one in [6].

4. Conclusions

In this paper, the application of the least squares differential quadrature method (LSDQM) to the Bagley–Torvik fractional differential equation is presented.

Due to the fact that the method is relative straightforward, the approximations may be obtained in a quick and simple manner. The numerical examples included clearly illustrate the accuracy of the method by means of comparisons with solutions previously computed by other methods. If the exact solution of the problem is itself a polynomial, then usually LSDQM is able to find the exact solution, as in the case of the first example. If not, in most of the cases, the solutions provided by LSDQM are not only more precise, but being of the simplest form (i.e., polynomial solutions), they are much easier to use in subsequent computation than many of the solutions provided by other methods.

Data Availability

All the necessary data are included in the paper.

Conflicts of Interest

The authors declare that there are no conflicts of interest.

References

[1] P. J. Torvik and R. L. Bagley, "On the appearance of the fractional derivative in the behavior of real materials," *Journal of Applied Mechanics*, vol. 51, no. 2, pp. 294–298, 1984.

[2] R. L. Bagley and P. J. Torvik, "Fractional calculus-a different approach to the analysis of viscoelastically damped structures," *AIAA Journal*, vol. 21, no. 5, pp. 741–748, 1983.

[3] T. Aleroev, S. Erokhin, and E. Kekharsaeva, "Modeling of deformation-strength characteristics of polymer concrete using fractional calculus," *IOP Conf. Series: Materials Science and Engineering*, vol. 365, Article ID 032004, 2018.

[4] B. H. E. Ibrahim, Q. Dong, and Z. Fan, "Existence for boundary value problems of two-term Caputo fractional differential equations," *The Journal of Nonlinear Sciences and Applications*, vol. 10, no. 2, pp. 511–520, 2017.

[5] H. Jafari, H. Tajadodi, H. Nazari, and C. M. Khalique, "Numerical solution of non-linear Riccati differential equations with fractional order," *International Journal of Nonlinear Sciences and Numerical Simulation*, vol. 11, pp. 179–182, 2010.

[6] V. Daftardar-Gejji and H. Jafari, "Adomian decomposition: a tool for solving a system of fractional differential equations,"

Journal of Mathematical Analysis and Applications, vol. 301, no. 2, pp. 508–518, 2005.

[7] W. K. Zahra and M. Van Daele, "Discrete spline methods for solving two point fractional bagley-torvik equation," *Applied Mathematics and Computation*, vol. 296, pp. 42–56, 2017.

[8] M. U. Rehman and R. A. Khan, "A numerical method for solving boundary value problems for fractional differential equations," *Applied Mathematical Modeling*, vol. 36, no. 3, pp. 894–907, 2012.

[9] S. Micula and C. Cattani, "On a numerical method based on wavelets for fredholm-hammerstein integral equations of the second kind," *Mathematical Methods in the Applied Sciences*, vol. 41, no. 18, pp. 9103–9115, 2018.

[10] Y.-G. Wang, H.-F. Song, and D. Li, "Solving two-point boundary value problems using combined homotopy perturbation method and green's function method," *Applied Mathematics and Computation*, vol. 212, no. 2, pp. 366–376, 2009.

[11] S. Alkan, K. Yildirim, and A. Secer, "An efficient algorithm for solving fractional differential equations with boundary conditions," *Open Physics*, vol. 14, no. 1, pp. 6–14, 2016.

[12] S. Yüzbasi, "Numerical solution of the Bagley-Torvik equation by the bessel collocation method," *Mathematical Methods in the Applied Science*, vol. 36, pp. 300–312, 2013.

[13] W. K. Zahra and S. M. Elkholy, "Cubic spline solution of fractional Bagley Torvik equation," *Electronic Journal of Mathematical Analysis and Applications*, vol. 1, no. 2, pp. 230–241, 2013.

[14] W. K. Zahra and S. M. Elkholy, "Quadratic spline solution for boundary value problem of fractional order," *Numerical Algorithms*, vol. 59, no. 3, pp. 373–391, 2012.

[15] K. Thula and P. Roul, "A high-order B-spline collocation method for solving nonlinear singular boundary value problems arising in engineering and applied science," *Mediterranean Journal of Mathematics*, vol. 15, 2018.

[16] H. Allouche, A. Tazdayte, and K. Tigma, "Highly accurate method for solving singular boundary-value problems via padé approximation and two-step quartic *B*-spline collocation," *Mediterranean Journal of Mathematics*, vol. 19, 2019.

[17] H. Jafari, A. Babaei, and S. Banihashemi, "A novel approach for solving an inverse reaction-diffusion-convection problem," *Journal of Optimization Theory and Applications*, vol. 183, no. 2, pp. 688–704, 2019.

[18] S. Mashayekhi and M. Razzaghi, "Numerical solution of the fractional bagley-torvik equation by using hybrid functions approximation," *Mathematical Methods in the Applied Sciences*, vol. 39, no. 3, pp. 353–365, 2016.

[19] C. Cattani, "A review on harmonic wavelets and their fractional extension," *Journal of Advanced Engineering and Computation*, vol. 2, no. 4, pp. 224–238, 2018.

[20] K. Diethelm and J. Ford, "Numerical solution of the bagley-torvik equation," *BIT Numerical Mathematics*, vol. 42, no. 3, pp. 490–507, 2002.

[21] E. H. Doha, A. H. Bhrawy, and S. S. Ezz-Eldien, "Efficient chebyshev spectral methods for solving multi-term fractional orders differential equations," *Applied Mathematical Modelling*, vol. 35, no. 12, pp. 5662–5672, 2011.

[22] M. S. Rawashdeh and H. Al-Jammal, "Numerical solutions for systems of nonlinear fractional ordinary differential equations using the FNDM," *Mediterranean Journal of Mathematics*, vol. 13, no. 6, pp. 4661–4677, 2016.

[23] M. Badr, A. Yazdani, and H. Jafari, "Stability of a finite volume element method for the time-fractional advection-diffusion equation," *Numerical Methods for Partial Differential Equations*, vol. 34, no. 5, pp. 1459–1471, 2018.

[24] C. Shu, *Differential Quadrature and its Application in Engineering*, Springer, New York, NY, USA,, 2000.

[25] S. Stanek, "Two-point boundary value problems for the generalized bagley-torvik fractional differential equation," *Central European Journal of Mathematics*, vol. 11, no. 3, pp. 574–593, 2013.

[26] A. E. M. El-Mesiry, A. M. A. El-Sayed, and H. A. A. El-Saka, "Numerical methods for multi-term fractional (arbitrary) orders differential equations," *Applied Mathematics and Computation*, vol. 160, no. 3, pp. 683–699, 2005.

[27] Y. Li and W. Zhao, "Haar wavelet operational matrix of fractional order integration and its applications in solving the fractional order differential equations," *Applied Mathematics and Computation*, vol. 216, no. 8, pp. 2276–2285, 2010.

[28] B. Căruntu, C. Bota, M. S. Paşca, and M. Lăpădat, "Approximate solutions for Riccati differential equation of fractional order using the Least Squares differential quadrature method," *Scientific Bulletin of the "Politehnica" University of Timisoara*, vol. 64, no. 78, pp. 18–28, 2019.

Hindawi
Mathematical Problems in Engineering
Volume 2020, Article ID 6507593, 13 pages
https://doi.org/10.1155/2020/6507593

Research Article

Sensorless Control of Brushless Doubly Fed Induction Generator with Nonlinear Loads for Stand-Alone Power Generation Systems

Wantai Liu,[1] **Weicai Xie**,[2] **Yunong Lv**,[1] **and Zhan Zhou**[1]

[1]*Hunan Electrical College of Technology, Xiangtan 411101, China*
[2]*Hunan Institute of Engineering, Xiangtan 411101, China*

Correspondence should be addressed to Wantai Liu; 50488727@qq.com

Received 5 February 2020; Revised 20 May 2020; Accepted 1 June 2020; Published 11 July 2020

Guest Editor: Yi Qi

This paper presents a sensorless control scheme for the stand-alone brushless doubly fed induction generator (BDFIG) feeding nonlinear loads. The fundamental and harmonic components of the distorted power winding (PW) voltage caused by the nonlinear loads are extracted and controlled separately. A rotor speed observer is employed to estimate the speed based on the PW voltage and control winding (CW) current without the need of any other machine parameters except for the number of pole pairs. Since the d- and q-axis references of the CW current from the PW voltage control loop contain both dc and ac components, which cannot be tracked easily by conventional PI controllers, a CW predictive current controller is designed to regulate the CW current. Finally, the performance of the proposed control scheme is verified by comprehensive experiments on a 35-kVA prototype BDFIG.

1. Introduction

The brushless doubly fed induction generator (BDFIG) contains two stator windings with different pole pairs, one of which is called power winding (PW) and the other one called control winding (CW) [1]. A specially designed rotor allows an indirect coupling between the two stator windings [2]. A stand-alone BDFIG can generate voltage with constant amplitude and frequency by employing a fractionally rated power converter while the rotor speed and load are changing, which are suitable for variable speed constant frequency (VSCF) power generation systems [3]. As shown in Figure 1, the stand-alone BDFIG control system includes both the CW side converter (CSC) supplying the CW with frequency-variable exciting current and the load side converter (LSC) connected between the dc bus and the loads for regulating the dc bus voltage and achieving bidirectional energy flow. Generally, the electrical loads include both linear loads (such as air conditioners and lighting equipment) and nonlinear loads (typically the front rectifier of converters driving fans, pumps, winders, and so on).

However, a nonlinear load would result in a distorted PW three-phase current, which could produce harmonic voltage drops across the three-phase impedances of the PW, resulting in a distorted PW voltage. In order to make the BDFIG power generation system to generate a voltage, which has constant amplitude and frequency with as few harmonics as possible under the nonlinear load condition, it is necessary to propose an effective and enhanced control strategy. In addition, the control of the CSC needs the information of the rotor position and speed. However, the conventional control strategies obtain the rotor position and speed by employing the corresponding sensors, which would increase the cost and decrease the reliability of the system. So, it is necessary to eliminate the rotor position and speed sensors.

The vector control schemes of BDFIGs for grid-connected wind power generation have been developed under balanced operation [4], unbalanced operation [5, 6], and

low-voltage ride through [7]. However, all control schemes proposed in [4–7] employ the rotor position/speed sensor to acquire the rotor position/speed. Some other papers, such as [8, 9], have discussed the rotor speed observers for the grid-connected brushless doubly fed reluctance generator (BDFRG) similar to the grid-connected BDFIG. It is noted that these rotor speed observers proposed in [8, 9] both need specific parameters of the PW inductance and resistance to estimate the flux. However, in the stand-alone BDFIG system, nonlinear loads are frequently connected to the system, leading to distorted PW voltage and current. Therefore, it is difficult to accurately estimate the PW flux, and consequently the observed rotor speed is inaccurate. Moreover, the dependence on the machine parameters can also reduce the robustness of the observer.

Generally, a grid-connected wind power generation system needs to control the active and reactive power, whereas in a stand-alone power generation system, the amplitude and frequency of the output voltage should be stabilized when the rotor speed or load varies. Therefore, the control scheme of a stand-alone BDFIG is different from that of a grid-connected BDFIG. For the stand-alone BDFIG, a control scheme based on the CW current orientation has been designed without considering nonlinear load conditions [10]. Besides, a direct voltage control scheme has been developed under linear load conditions [11]. The transient control of reactive current for the LSC in the stand-alone BDFIG power generation system has been proposed in [12] to improve the quality of the output voltage. Some studies have investigated the control scheme of the stand-alone doubly fed induction generator (DFIG) under nonlinear load conditions [13–15]; there are few related studies on BDFIG. A harmonic voltage and current elimination method for stand-alone BDFIG with nonlinear loads has been proposed in [16]. However, this method is achieved by using a speed sensor.

This paper presents an enhanced sensorless control scheme of the stand-alone BDFIG under nonlinear load conditions. The fundamental and harmonic components of the PW voltage are extracted and then regulated separately. A new rotor speed observer is designed to observe the rotor position and speed based on the PW voltage and CW current. Since the d- and q-axis references of the CW current from the PW voltage control loop contain both dc and ac components, the predictive control method is introduced to regulate the CW current. Comprehensive experimental results on a 35-kVA prototype BDFIG are presented to validate the effectiveness of the proposed control scheme.

The following sections of this paper is organized as follows: firstly, the operational principle and dynamic model of BDFIG are introduced in Section 2; the system analysis and modeling under nonlinear loads is presented in Section 3; the control scheme is proposed in Section 4; experimental results are illustrated in Section 5; and finally the conclusions are drawn in Section 6.

2. Operational Principle and Dynamic Model of BDFIG

2.1. Basic Operational Principle of BDFIG. The BDFIG rotor mechanical angular frequency can be determined by the PW and CW angular frequencies as follows:

$$\omega_{\mathrm{r}} = \frac{\left(\omega_{\mathrm{p}} + \omega_{\mathrm{c}}\right)}{\left(p_{\mathrm{p}} + p_{\mathrm{c}}\right)}, \tag{1}$$

where p_{p} and p_{c} are the numbers of pole pairs of PW and CW, ω is the angular frequency, and the subscripts p, c, and r indicate the PW, CW, and rotor, respectively.

In order to keep ω_{p} constant, ω_{c} should be changed with the variation of the rotor speed according to the following expression derived from (1):

$$\omega_{\mathrm{c}} = \omega_{\mathrm{r}}\left(p_{\mathrm{p}} + p_{\mathrm{c}}\right) - \omega_{\mathrm{p}}. \tag{2}$$

2.2. Dynamic Vector Model of BDFIG. The unified reference frame vector model proposed in [17] is employed in this paper. In the fundamental reference frame ($\mathrm{d}q^{+1}$) rotating at the speed of ω_{p}, this model can be expressed as

$$\begin{cases} \mathrm{u}_{\mathrm{pdq}}^{+1} = R_{\mathrm{p}}\mathbf{i}_{\mathrm{pdq}}^{+1} + s\boldsymbol{\psi}_{\mathrm{pdq}}^{+1} + j\omega_{\mathrm{p}}\boldsymbol{\psi}_{\mathrm{pdq}}^{+1}, \\ \boldsymbol{\psi}_{\mathrm{pdq}}^{+1} = L_{\mathrm{p}}\mathbf{i}_{\mathrm{pdq}}^{+1} + L_{\mathrm{pr}}i_{\mathrm{rdq}}^{+1}, \\ \mathbf{u}_{\mathrm{cdq}}^{+1} = R_{\mathrm{c}}\mathbf{i}_{\mathrm{cdq}}^{+1} + s\boldsymbol{\psi}_{\mathrm{cdq}}^{+1} + j\left[\omega_{\mathrm{p}} - \left(p_{\mathrm{p}} + p_{\mathrm{c}}\right)\omega_{\mathrm{r}}\right]\boldsymbol{\psi}_{\mathrm{cdq}}^{+1}, \\ \boldsymbol{\psi}_{\mathrm{cdq}}^{+1} = L_{\mathrm{c}}\mathbf{i}_{\mathrm{cdq}}^{+1} + L_{\mathrm{cr}}\mathbf{i}_{\mathrm{rdq}}^{+1}, \\ \mathbf{u}_{\mathrm{rdq}}^{+1} = R_{r}\mathbf{i}_{\mathrm{rdq}}^{+1} + s\boldsymbol{\psi}_{\mathrm{rdq}}^{+1} + j\left(\omega_{\mathrm{p}} - p_{\mathrm{p}}\omega_{\mathrm{r}}\right)\boldsymbol{\psi}_{\mathrm{rdq}}^{+1}, \\ \boldsymbol{\psi}_{\mathrm{rdq}}^{+1} = L_{\mathrm{r}}\mathbf{i}_{\mathrm{rdq}}^{+1} + L_{\mathrm{pr}}\mathbf{i}_{\mathrm{pdq}}^{+1} + L_{\mathrm{cr}}\mathbf{i}_{\mathrm{cdq}}^{+1}, \end{cases} \tag{3}$$

where $\mathbf{u}_{\mathrm{dq}}$, $\mathbf{i}_{\mathrm{dq}}$, and $\boldsymbol{\psi}_{\mathrm{dq}}$ represent the voltage, current, and flux vectors, R_{p}, R_{c}, and R_{r} the resistances of PW, CW, and rotor, L_{p}, L_{c}, and L_{r} the self-inductances of PW, CW, and rotor, L_{cr} and L_{cr} the coupling inductances between the stator and rotor windings, respectively, s the differential operator $d/\mathrm{d}t$, and superscripts +1 the fundamental reference frame.

3. System Analysis and Modelling

3.1. System Analysis. Nonlinear loads make the PW current distorted, which in turn causes abundant harmonic current in the CW due to the indirect coupling between the two stator windings through the rotor. And then, the PW harmonic current results in harmonic-voltage drop on the three-phase internal impedances of the PW.

Therefore, under nonlinear load conditions, the PW terminal voltage of the stand-alone BDFIG would contain significant harmonic components and consequently degrade the performance of other linear loads connected to the system. Among these harmonic components, the fifth and seventh harmonic components are the most significant ones. Figure 2 presents the impact of the nonlinear loads on the stand-alone BDFIG system.

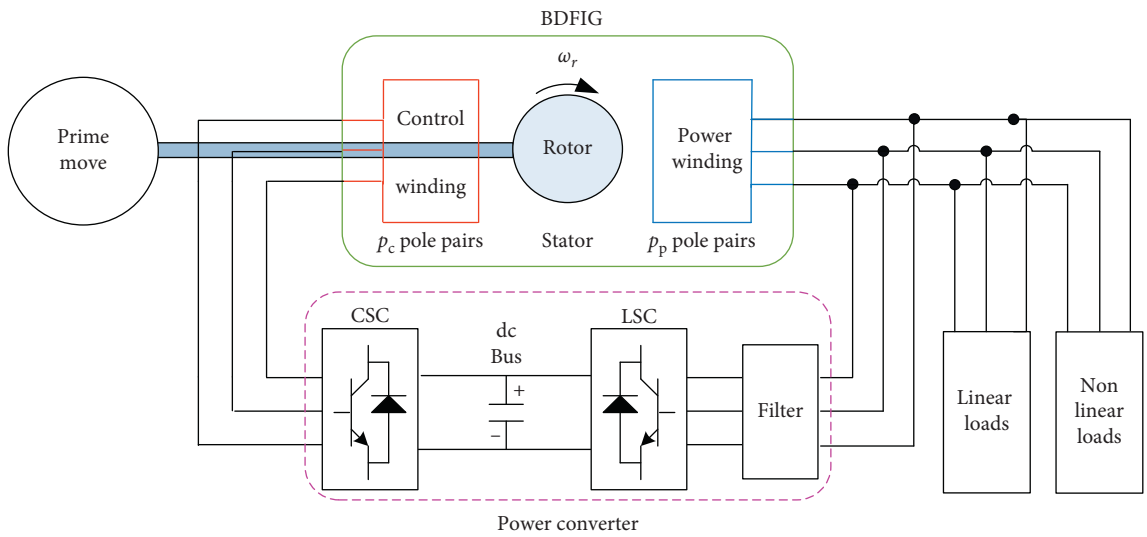

Figure 1: Configuration of the BDFIG-based stand-alone power generation system.

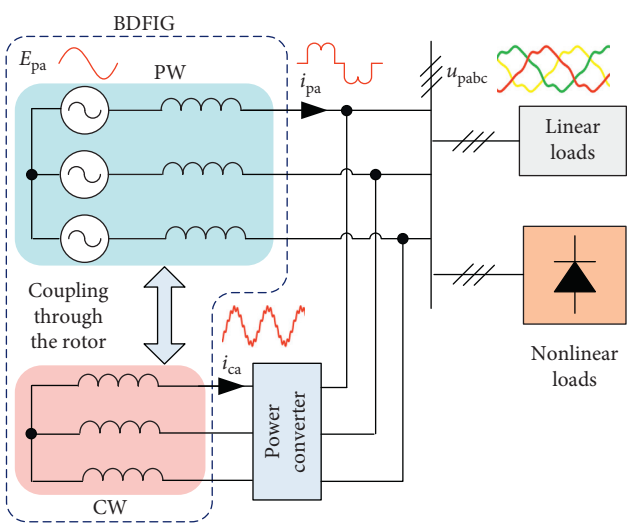

Figure 2: Impact of the nonlinear loads on the stand-alone BDFIG.

3.2. Mathematical Modelling. In order to derive the dynamic vector model of the stand-alone BDFIG under nonlinear loads, the other two reference frames need to be defined as shown in Figure 3. The negative fifth harmonic reference frame (dq^{-5}) rotates at the angular speed of -5ω_p, and the positive seventh harmonic reference frame (dq^{+7}) at the angular speed of 7ω_p.

The relationship among the expressions of an arbitrary vector $\mathbf{F}_{dq}$ in different reference frames can be presented as

$$\mathbf{F}_{dq}^{+1} = \mathbf{F}_{dq}^{-5} e^{-j6\omega_p t}, \tag{4}$$

$$\mathbf{F}_{dq}^{+1} = \mathbf{F}_{dq}^{+7} e^{j6\omega_p t}, \tag{5}$$

where the superscripts +1, −5, and +7 represent the fundamental, the negative fifth harmonic, and the positive seventh harmonic reference frames, respectively.

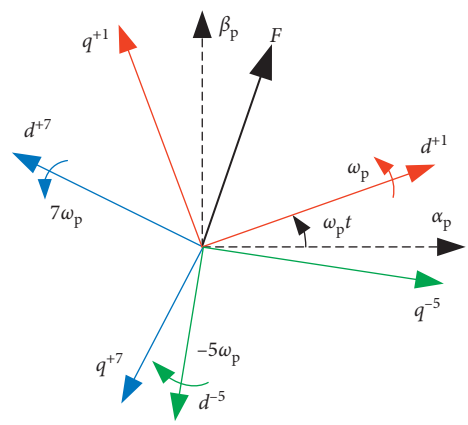

Figure 3: The fundamental and harmonic reference frames in the dynamic vector model of the stand-alone BDFIG under nonlinear loads.

Under nonlinear loads, the general electrical vector $\mathbf{F}_{dq}^{+1}$ of a BDFIG in the reference frame dq^{+1} can be expressed as

$$\mathbf{F}_{dq}^{+1} = \mathbf{F}_{dq1}^{+1} + \mathbf{F}_{dq5}^{+1} + \mathbf{F}_{dq7}^{+1}, \tag{6}$$

where the subscripts 1, 5, and 7 indicate the fundamental, the fifth harmonic, and the seventh harmonic components, respectively.

Substituting (4) and (5) into (6), the following can be obtained:

$$\mathbf{F}_{dq}^{+1} = \mathbf{F}_{dq1}^{+1} + \mathbf{F}_{dq5}^{-5} e^{-j6\omega_p t} + \mathbf{F}_{dq7}^{+7} e^{j6\omega_p t}. \tag{7}$$

From (7), the voltage, current, and flux vectors of the PW in the fundamental reference frame can be expressed as

$$\mathbf{u}_{pdq}^{+1} = \mathbf{u}_{pdq1}^{+1} + \mathbf{u}_{pdq5}^{-5} e^{-j6\omega_p t} + \mathbf{u}_{pdq7}^{+7} e^{j6\omega_p t}, \tag{8}$$

$$\mathbf{i}_{pdq}^{+1} = \mathbf{i}_{pdq1}^{+1} + \mathbf{i}_{pdq5}^{-5} e^{-j6\omega_p t} + \mathbf{i}_{pdq7}^{+7} e^{j6\omega_p t}, \tag{9}$$

$$\boldsymbol{\psi}_{\mathrm{pdq}}^{+1} = \boldsymbol{\psi}_{\mathrm{pdq1}}^{+1} + \boldsymbol{\psi}_{\mathrm{pdq5}}^{-5} e^{-j6\omega_{\mathrm{p}}t} + \boldsymbol{\psi}_{\mathrm{pdq7}}^{+7} e^{j6\omega_{\mathrm{p}}t}, \tag{10}$$

By substituting (8)–(10) into the first part of (3), the PW fundamental- and harmonic-voltage equations in the corresponding reference frames can be derived as

$$\mathbf{u}_{\mathrm{pdq1}}^{+1} = R_{\mathrm{p}}\mathbf{i}_{\mathrm{pdq1}}^{+1} + s\boldsymbol{\psi}_{\mathrm{pdq1}}^{+1} + j\omega_{\mathrm{p}}\boldsymbol{\psi}_{\mathrm{pdq1}}^{+1}, \tag{11}$$

$$\mathbf{u}_{\mathrm{pdq5}}^{-5} = R_{\mathrm{p}}\mathbf{i}_{\mathrm{pdq5}}^{-5} + s\boldsymbol{\psi}_{\mathrm{pdq5}}^{-5} + j\left(-5\omega_{\mathrm{p}}\right)\boldsymbol{\psi}_{\mathrm{pdq5}}^{-5}, \tag{12}$$

$$\mathbf{u}_{\mathrm{pdq7}}^{+7} = R_{\mathrm{p}}\mathbf{i}_{\mathrm{pdq7}}^{+7} + s\boldsymbol{\psi}_{\mathrm{pdq7}}^{+7} + j7\omega_{\mathrm{p}}\boldsymbol{\psi}_{\mathrm{pdq7}}^{+7}, \tag{13}$$

Similarly, the PW fundamental- and harmonic-flux equations can be obtained by

$$\boldsymbol{\psi}_{\mathrm{pdq1}}^{+1} = L_{\mathrm{p}}\mathbf{i}_{\mathrm{pdq1}}^{+1} + L_{\mathrm{pr}}\mathbf{i}_{\mathrm{rdq1}}^{+1}, \tag{14}$$

$$\boldsymbol{\psi}_{\mathrm{pdq5}}^{-5} = L_{\mathrm{p}}\mathbf{i}_{\mathrm{pdq5}}^{-5} + L_{\mathrm{pr}}\mathbf{i}_{\mathrm{rdq5}}^{-5}, \tag{15}$$

$$\boldsymbol{\psi}_{\mathrm{pdq7}}^{+7} = L_{\mathrm{p}}\mathbf{i}_{\mathrm{pdq7}}^{+7} + L_{\mathrm{pr}}\mathbf{i}_{\mathrm{rdq7}}^{+7}. \tag{16}$$

A similar method can also be employed to derive the fundamental- and harmonic-voltage and flux equations of the CW and rotor. And then, by ignoring those harmonics with the order more than seventh, the dynamic vector model of the BDFIG under nonlinear loads can be decomposed into three sets of equations as follows:

$$\begin{cases} \mathbf{u}_{\mathrm{pdq1}}^{+1} = R_{\mathrm{p}}\mathbf{i}_{\mathrm{pdq1}}^{+1} + s\boldsymbol{\psi}_{\mathrm{pdq1}}^{+1} + j\omega_{\mathrm{p}}\boldsymbol{\psi}_{\mathrm{pdq1}}^{+1}, \\ \boldsymbol{\psi}_{\mathrm{pdq1}}^{+1} = L_{\mathrm{p}}\mathbf{i}_{\mathrm{pdq1}}^{+1} + L_{\mathrm{pr}}\mathbf{i}_{\mathrm{rdq1}}^{+1}, \\ \mathbf{u}_{\mathrm{cdq1}}^{+1} = R_{\mathrm{c}}\mathbf{i}_{\mathrm{cdq1}}^{+1} + s\boldsymbol{\psi}_{\mathrm{cdq1}}^{+1} + j\left[\omega_{\mathrm{p}} - \left(p_p + p_c\right)\omega_{\mathrm{r}}\right]\boldsymbol{\psi}_{\mathrm{cdq1}}^{+1}, \\ \boldsymbol{\psi}_{\mathrm{cdq1}}^{+1} = L_{\mathrm{c}}\mathbf{i}_{\mathrm{cdq1}}^{+1} + L_{\mathrm{cr}}\mathbf{i}_{\mathrm{rdq1}}^{+1}, \\ \mathbf{u}_{\mathrm{rdq1}}^{+1} = R_{\mathrm{r}}\mathbf{i}_{\mathrm{rdq1}}^{+1} + s\boldsymbol{\psi}_{\mathrm{rdq1}}^{+1} + j\left(\omega_{\mathrm{p}} - p_{\mathrm{p}}\omega_{\mathrm{r}}\right)\boldsymbol{\psi}_{\mathrm{rdq1}}^{+1}, \\ \boldsymbol{\psi}_{\mathrm{rdq1}}^{+1} = L_{\mathrm{r}}\mathbf{i}_{\mathrm{rdq1}}^{+1} + L_{\mathrm{pr}}\mathbf{i}_{\mathrm{pdq1}}^{+1} + L_{\mathrm{cr}}\mathbf{i}_{\mathrm{cdq1}}^{+1}, \end{cases} \tag{17}$$

$$\begin{cases} \mathbf{u}_{\mathrm{pdq5}}^{-5} = R_{\mathrm{p}}\mathbf{i}_{\mathrm{pdq5}}^{-5} + s\boldsymbol{\psi}_{\mathrm{pdq5}}^{-5} + j\left(-5\omega_{\mathrm{p}}\right)\boldsymbol{\psi}_{\mathrm{pdq5}}^{-5}, \\ \boldsymbol{\psi}_{\mathrm{pdq5}}^{-5} = L_{\mathrm{p}}\mathbf{i}_{\mathrm{pdq5}}^{-5} + L_{\mathrm{pr}}\mathbf{i}_{\mathrm{rdq5}}^{-5}, \\ \mathbf{u}_{\mathrm{cdq5}}^{-5} = R_{\mathrm{c}}\mathbf{i}_{\mathrm{cdq5}}^{-5} + s\boldsymbol{\psi}_{\mathrm{cdq5}}^{-5} + j\left[-5\omega_{\mathrm{p}} - \left(p_{\mathrm{p}} + p_{\mathrm{c}}\right)\omega_{\mathrm{r}}\right]\boldsymbol{\psi}_{\mathrm{cdq5}}^{-5}, \\ \boldsymbol{\psi}_{\mathrm{cdq5}}^{-5} = L_{\mathrm{c}}\mathbf{i}_{\mathrm{cdq5}}^{-5} + L_{\mathrm{cr}}\mathbf{i}_{\mathrm{rdq5}}^{-5}, \\ \mathbf{u}_{\mathrm{rdq5}}^{-5} = R_{\mathrm{r}}\mathbf{i}_{\mathrm{rdq5}}^{-5} + s\boldsymbol{\psi}_{\mathrm{rdq5}}^{-5} + j\left(-5\omega_{\mathrm{p}} - p_{\mathrm{p}}\omega_{\mathrm{r}}\right)\boldsymbol{\psi}_{\mathrm{rdq5}}^{-5}, \\ \boldsymbol{\psi}_{\mathrm{rdq5}}^{-5} = L_{\mathrm{r}}\mathbf{i}_{\mathrm{rdq5}}^{-5} + L_{\mathrm{pr}}\mathbf{i}_{\mathrm{pdq5}}^{-5} + L_{\mathrm{cr}}\mathbf{i}_{\mathrm{cdq5}}^{-5}, \end{cases} \tag{18}$$

$$\begin{cases} \mathbf{u}_{\mathrm{pdq7}}^{+7} = R_{\mathrm{p}}\mathbf{i}_{\mathrm{pdq7}}^{+7} + s\boldsymbol{\psi}_{\mathrm{pdq7}}^{+7} + j7\omega_{\mathrm{p}}\boldsymbol{\psi}_{\mathrm{pdq7}}^{+7}, \\ \boldsymbol{\psi}_{\mathrm{pdq7}}^{+7} = L_{\mathrm{p}}\mathbf{i}_{\mathrm{pdq7}}^{+7} + L_{\mathrm{pr}}\mathbf{i}_{\mathrm{rdq7}}^{+7}, \\ \mathbf{u}_{\mathrm{cdq7}}^{+7} = R_{\mathrm{c}}\mathbf{i}_{\mathrm{cdq7}}^{+7} + s\boldsymbol{\psi}_{\mathrm{cdq7}}^{+7} + j\left[7\omega_{\mathrm{p}} - \left(p_{\mathrm{p}} + p_{\mathrm{c}}\right)\omega_{\mathrm{r}}\right]\boldsymbol{\psi}_{\mathrm{cdq7}}^{+7}, \\ \boldsymbol{\psi}_{\mathrm{cdq7}}^{+7} = L_{\mathrm{c}}\mathbf{i}_{\mathrm{cdq7}}^{+7} + L_{\mathrm{cr}}\mathbf{i}_{\mathrm{rdq7}}^{+7}, \\ \mathbf{u}_{\mathrm{rdq7}}^{+7} = R_{\mathrm{r}}\mathbf{i}_{\mathrm{rdq7}}^{+7} + s\boldsymbol{\psi}_{\mathrm{rdq7}}^{+7} + j\left(7\omega_{\mathrm{p}} - p_{\mathrm{p}}\omega_{\mathrm{r}}\right)\boldsymbol{\psi}_{\mathrm{rdq7}}^{+7}, \\ \boldsymbol{\psi}_{\mathrm{rdq7}}^{+7} = L_{\mathrm{r}}\mathbf{i}_{\mathrm{rdq7}}^{+7} + L_{\mathrm{pr}}\mathbf{i}_{\mathrm{pdq7}}^{+7} + L_{\mathrm{cr}}\mathbf{i}_{\mathrm{cdq7}}^{+7}, \end{cases} \tag{19}$$

where (17)–(19) are the fundamental, fifth harmonic, and seventh harmonic equations, respectively.

4. Design of Control Scheme

The overall control scheme for the enhanced sensorless control of the stand-alone BDFIG with nonlinear loads is shown in Figure 4. The PW fundamental-voltage controller, based on the PW fundamental-voltage vector orientation, is employed to regulate the amplitude and frequency of the PW fundamental voltage. The PW harmonic-voltage controller can eliminate the fifth and seventh harmonic components of the PW voltage. Then, it summarizes the outputs of both PW fundamental- and harmonic-voltage controllers in order to get the references of the CW d- and q-component currents. By theoretical analysis, it is known that the references of CW d- and q-component currents contain both dc and ac parts, which cannot be tracked easily by conventional PI controllers. Therefore, a predictive current controller is employed to regulate the CW current. In addition, the multiple second-order generalized integrator-based PLL (MSOGI-PLL) [18] is used to extract the α- and β-components of the fundamental, fifth, and seventh harmonics of the PW voltage. The improved rotor speed observer can estimate the rotor position and speed of the BDFIG based on the PW voltage and CW current.

4.1. Control of PW Fundamental Voltage. The PW fundamental-voltage controller is based on the PW fundamental voltage vector orientation and can be derived from (17). By splitting the first part of (17) into d- and q-components, the PW fundamental voltage in the reference frame dq^{+1}, u_{pd1}^{+1} and u_{pq1}^{+1}, can be obtained by

$$\mathbf{u}_{\mathrm{pd1}}^{+1} = R_{\mathrm{p}}\mathbf{i}_{\mathrm{pd1}}^{+1} + s\boldsymbol{\psi}_{\mathrm{pd1}}^{+1} - \omega_{\mathrm{p}}\boldsymbol{\psi}_{\mathrm{pq1}}^{+1}, \tag{20}$$

$$\mathbf{u}_{\mathrm{pq1}}^{+1} = R_{\mathrm{p}}\mathbf{i}_{\mathrm{pq1}}^{+1} + s\boldsymbol{\psi}_{\mathrm{pq1}}^{+1} + \omega_{\mathrm{p}}\boldsymbol{\psi}_{\mathrm{pd1}}^{+1}. \tag{21}$$

Generally, the sampling period of the power converters for BDFIG is smaller than 1 ms, which results in the PW flux

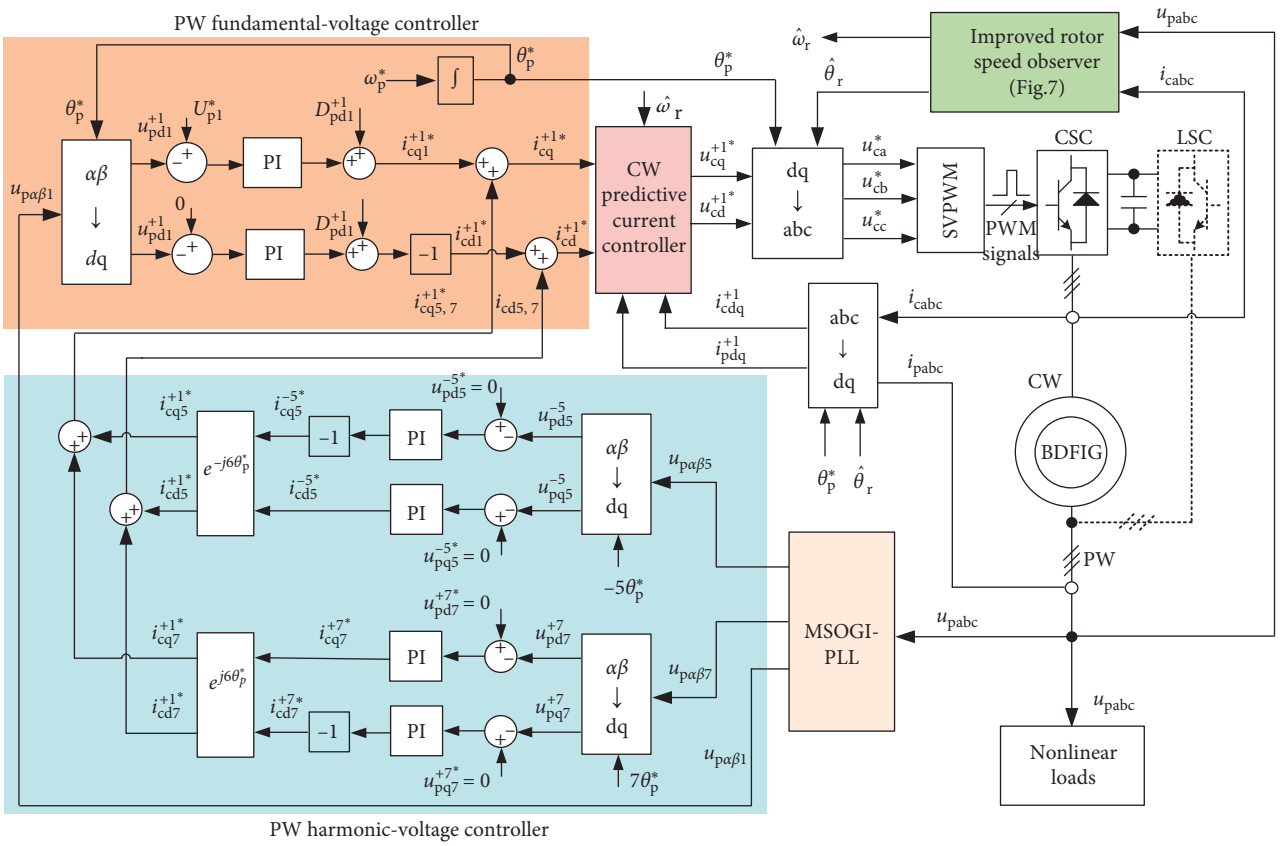

Figure 4: The overall control scheme for the enhanced sensorless control of the stand-alone BDFIG with nonlinear loads.

being regarded as a constant during one sampling period. Hence, the differential terms of the flux linkages in (20) and (21) are approximately equal to 0, and equations (20) and (21) can be simplified as

$$\mathbf{u}_{\mathrm{pd1}}^{+1} = R_{\mathrm{p}}\mathbf{i}_{\mathrm{pd1}}^{+1} - \omega_{\mathrm{p}}\boldsymbol{\psi}_{\mathrm{pq1}}^{+1}, \tag{22}$$

$$\mathbf{u}_{\mathrm{pq1}}^{+1} = R_{\mathrm{p}}\mathbf{i}_{\mathrm{pq1}}^{+1} + \omega_{\mathrm{p}}\boldsymbol{\psi}_{\mathrm{pd1}}^{+1}. \tag{23}$$

Besides, the PW resistance R_{p} is usually very small, resulting in the first term on the right side of (22) and (23) being much smaller than the second term. Hence, the first term on the right side of (22) and (23) can be neglected. Consequently, equations (22) and (23) can be simplified as

$$\mathbf{u}_{\mathrm{pd1}}^{+1} \approx -\omega_{\mathrm{p}}\boldsymbol{\psi}_{\mathrm{pq1}}^{+1}, \tag{24}$$

$$\mathbf{u}_{\mathrm{pq1}}^{+1} \approx \omega_{\mathrm{p}}\boldsymbol{\psi}_{\mathrm{pd1}}^{+1}. \tag{25}$$

Converting the second part of (17) into the form of d- and q-components, the following can be obtained:

$$\boldsymbol{\psi}_{\mathrm{pd1}}^{+1} = L_{\mathrm{p}}\mathbf{i}_{\mathrm{pd1}}^{+1} + L_{\mathrm{pr}}\mathbf{i}_{\mathrm{rd1}}^{+1}, \tag{26}$$

$$\boldsymbol{\psi}_{\mathrm{pq1}}^{+1} = L_{\mathrm{p}}\mathbf{i}_{\mathrm{pq1}}^{+1} + L_{\mathrm{pr}}\mathbf{i}_{\mathrm{rq1}}^{+1}. \tag{27}$$

From the fifth and sixth parts of (17), with the rotor voltage equivalent to zero, the d- and q-components of the rotor current can be derived as

$$\mathbf{i}_{\mathrm{rd1}}^{+1} = -\alpha_1^{+1}\mathbf{i}_{\mathrm{cd1}}^{+1} + \alpha_2^{+1}\mathbf{i}_{\mathrm{cq1}}^{+1} + \alpha_3^{+1}\mathbf{i}_{\mathrm{pd1}}^{+1} + \alpha_4^{+1}\mathbf{i}_{\mathrm{pq1}}^{+1}, \tag{28}$$

$$\mathbf{i}_{rq1}^{+1} = -\beta_1^{+1}\mathbf{i}_{\mathrm{cq1}}^{+1} + \beta_2^{+1}\mathbf{i}_{\mathrm{cd1}}^{+1} + \beta_3^{+1}\mathbf{i}_{\mathrm{pq1}}^{+1} + \beta_4^{+1}\mathbf{i}_{\mathrm{pd1}}^{+1}. \tag{29}$$

The detailed expressions for $\alpha_1^{+1} \sim \alpha_4^{+1}$, and $\beta_1^{+1} \sim \beta_4^{+1}$ can be seen in Appendix.

Substituting (28) into (26) and substituting (29) into (27), the PW fundamental flux can be derived as

$$\boldsymbol{\psi}_{\mathrm{pd1}}^{+1} = -L_{\mathrm{pr}}\alpha_1^{+1}\mathbf{i}_{\mathrm{cd1}}^{+1} + L_{\mathrm{pr}}\alpha_2^{+1}\mathbf{i}_{\mathrm{cq1}}^{+1} + \left(L_{\mathrm{p}} + L_{\mathrm{pr}}\alpha_3^{+1}\right)\mathbf{i}_{\mathrm{pd1}}^{+1} + L_{\mathrm{pr}}\alpha_4^{+1}\mathbf{i}_{\mathrm{pq1}}^{+1}, \tag{30}$$

$$\begin{aligned}\boldsymbol{\psi}_{\mathrm{pq1}}^{+1} = {} & -L_{\mathrm{pr}}\beta_1^{+1}\mathbf{i}_{\mathrm{cq1}}^{+1} + L_{\mathrm{pr}}\beta_2^{+1}\mathbf{i}_{\mathrm{cd1}}^{+1} + \left(L_{\mathrm{p}} + L_{\mathrm{pr}}\beta_3^{+1}\right)\mathbf{i}_{\mathrm{pq1}}^{+1} \\ & + L_{\mathrm{pr}}\beta_4^{+1}\mathbf{i}_{\mathrm{pd1}}^{+1}.\end{aligned} \tag{31}$$

By substituting (30) into (24) and substituting (31) into (25), the relationship between the PW voltage and the CW current can be obtained by

$$-\mathbf{i}_{\mathrm{cd1}}^{+1} = \left[\frac{1}{\left(\omega_{\mathrm{p}}L_{\mathrm{pr}}\alpha_1^{+1}\right)}\right]\mathbf{u}_{\mathrm{pq1}}^{+1} + D_{\mathrm{pd1}}^{+1}, \tag{32}$$

$$\mathbf{i}_{\mathrm{cq1}}^{+1} = \left[\frac{1}{\left(\omega_{\mathrm{p}}L_{\mathrm{pr}}\beta_1^{+1}\right)}\right]\mathbf{u}_{\mathrm{pd1}}^{+1} + D_{\mathrm{pq1}}^{+1}. \tag{33}$$

The detailed expressions for D_{pd1}^{+1} and D_{pq1}^{+1} can be found in Appendix. $1/(\omega_{\mathrm{p}}L_{\mathrm{pr}}\alpha_1^{+1})$ is the transfer function from $\mathbf{u}_{\mathrm{pq1}}^{+1}$

to $-\mathbf{i}_{\mathrm{cd1}}^{+1}$, and $1/(\omega_{\mathrm{p}}L_{\mathrm{pr}}\beta_1^{+1})$ the transfer function from $\mathbf{u}_{\mathrm{pd1}}^{+1}$ to $\mathbf{i}_{\mathrm{cq1}}^{+1}$. It is noted that $1/(\omega_{\mathrm{p}}L_{\mathrm{pr}}\alpha_1^{+1})$ is equal to $1/(\omega_{\mathrm{p}}L_{\mathrm{pr}}\beta_1^{+1})$ according to (A.1). From (32) and (33), $\mathbf{u}_{\mathrm{pd1}}^{+1}$ and $\mathbf{u}_{\mathrm{pq1}}^{+1}$ can be controlled by $\mathbf{i}_{\mathrm{cq1}}^{+1}$ and $\mathbf{i}_{\mathrm{cd1}}^{+1}$, respectively. D_{pd1}^{+1} and D_{pq1}^{+1} are the disturbance terms, including the cross-coupling disturbance between d- and q-components of the CW current and the coupling disturbance between the PW and CW, and can be used as the feedforward compensation to improve the dynamic ability of the control loop.

Since the PW fundamental-voltage controller is based on the PW fundamental voltage vector orientation, the d-axis of the reference frame dq^{+1} is forced to align with the PW fundamental-voltage vector, and the references of the d- and q-components of the PW fundamental voltage, $\mathbf{u}_{\mathrm{pd1}}^{+1*}$ and $\mathbf{u}_{\mathrm{pq1}}^{+1*}$, should be set to

$$\begin{aligned}\mathbf{u}_{\mathrm{pd1}}^{+1*} &= U_{\mathrm{p1}}^{*},\\ \mathbf{u}_{\mathrm{pq1}}^{+1*} &= 0,\end{aligned} \tag{34}$$

where U_{p1}^{*} is the reference of the PW fundamental voltage amplitude. According to (32)–(34), the PW fundamental-voltage controller can be obtained as shown in Figure 4.

4.2. Control of PW Harmonic Voltage. From (18), by using the derivation method similar to that in the control of PW fundamental voltage, the relationship between the PW voltage and the CW current in the fifth harmonic reference frame (dq^{-5}) can be derived as

$$\mathbf{i}_{\mathrm{cd5}}^{-5} = \left[\frac{1}{\left(5\omega_{\mathrm{p}}L_{\mathrm{pr}}\alpha_1^{-5}\right)}\right]\mathbf{u}_{\mathrm{pq5}}^{-5} + D_{\mathrm{pd5}}^{-5}, \tag{35}$$

$$-\mathbf{i}_{\mathrm{cq5}}^{-5} = \left[\frac{1}{\left(5\omega_{\mathrm{p}}L_{\mathrm{pr}}\beta_1^{-5}\right)}\right]\mathbf{u}_{\mathrm{pd5}}^{-5} + D_{\mathrm{pq5}}^{-5}. \tag{36}$$

The detailed expressions for α_1^{-5}–α_4^{-5}, β_1^{-5}–β_4^{-5}, D_{pd5}^{-5}, and D_{pq5}^{-5} have been given in Appendix. In (35) and (36), $1/(5\omega_{\mathrm{p}}L_{\mathrm{pr}}\alpha_1^{-5})$ is the transfer function from u_{pq5}^{-5} to i_{cd5}^{-5}, $1/(5\omega_{\mathrm{p}}L_{\mathrm{pr}}\beta_1^{-5})$ the transfer function from u_{pd5}^{-5} to $-i_{\mathrm{cq5}}^{-5}$, and D_{pd5}^{-5} and D_{pq5}^{-5} the disturbance terms. Therefore, the d- and q-components of the PW fifth harmonic voltage, u_{pd5}^{-5} and u_{pq5}^{-5}, can be controlled by i_{cq5}^{-5} and i_{cd5}^{-5}, respectively.

Similarly, the relationship between the PW voltage and the CW current in the seventh harmonic reference frame (dq^{+7}) can be obtained from (19) as follows:

$$-i_{\mathrm{cd7}}^{+7} = \left[\frac{1}{\left(7\omega_{\mathrm{p}}L_{\mathrm{pr}}\alpha_1^{+7}\right)}\right]u_{\mathrm{pq7}}^{+7} + D_{\mathrm{pd7}}^{+7}, \tag{37}$$

$$i_{\mathrm{cq7}}^{+7} = \left[\frac{1}{\left(7\omega_{\mathrm{p}}L_{\mathrm{pr}}\beta_1^{+7}\right)}\right]u_{\mathrm{pd7}}^{+7} + D_{\mathrm{pq7}}^{+7}. \tag{38}$$

The detailed expressions for α_1^{+7}–α_4^{+7}, β_1^{+7}–β_4^{+7}, D_{pd7}^{+7}, and D_{pd7}^{+7} have been given in Appendix. Similarly, the d- and q-components of the PW seventh harmonic voltage, u_{pd7}^{+7} and u_{pq7}^{+7}, can be controlled by i_{cq7}^{+7} and i_{cd7}^{+7}, respectively.

In order to eliminate the fifth and seventh harmonic components in the PW voltage, these references of the d- and q-components of the PW harmonic voltage, u_{pd5}^{-5*}, u_{pq5}^{-5*}, u_{pd7}^{+7*}, and u_{pq7}^{+7*}, should be set to

$$u_{\mathrm{pd5}}^{-5*} = u_{\mathrm{pq5}}^{-5*} = u_{\mathrm{pd7}}^{+7*} = u_{\mathrm{pq7}}^{+7*} = 0. \tag{39}$$

According to (35)–(38), the PW harmonic-voltage controller can be designed as shown in Figure 4. Since the harmonic component of the PW voltage is much smaller than the fundamental one, the dynamic performance requirements of the harmonic-voltage controller can be lower than that of the fundamental-voltage controller. Therefore, the disturbance terms D_{pd5}^{-5}, D_{pq5}^{-5}, u_{pd7}^{+7}, and u_{pq7}^{+7} are not used as the feedforward compensation of the control loop due to their dependence on the machine parameters. Although the dynamic performance would be compromised, the stability could be guaranteed. Besides, it is noteworthy that the CW current references obtained by the PW harmonic-voltage controller should be transformed to the fundamental reference frame (dq^{+1}) according to (4) and (5), so as that the CW current controller can be designed in the reference frame dq^{+1}.

4.3. Design of CW Predictive Current Controller. Since the CW current references contain both the dc and ac components, the conventional PI controller is not suitable in this case. An improved predictive current control strategy for unbalanced stand-alone doubly fed induction generator (DFIG) has been proposed to track the ac references of the rotor current in [19]. However, such method has not been used in the BDFIG. In this paper, a CW predictive current controller is designed. The proposed current controller is derived in the reference frame dq^{+1}.

From the fifth and sixth parts of (3), according to [10], the d- and q-components of the rotor current in the reference frame dq^{+1} can be simplified as

$$i_{\mathrm{rd}}^{+1} = -\frac{L_{\mathrm{pr}}i_{\mathrm{pd}}^{+1} + L_{\mathrm{cr}}i_{\mathrm{cd}}^{+1}}{L_{\mathrm{r}}} - \frac{R_{\mathrm{r}}\left(L_{\mathrm{pr}}i_{\mathrm{pq}}^{+1} + L_{\mathrm{cr}}i_{\mathrm{cq}}^{+1}\right)}{L_{\mathrm{r}}^2\left(\omega_{\mathrm{c}} - p_{\mathrm{c}}\omega_{\mathrm{r}}\right)}, \tag{40}$$

$$i_{\mathrm{rq}}^{+1} = -\frac{\left(L_{\mathrm{pr}}i_{\mathrm{pq}}^{+1} + L_{\mathrm{cr}}i_{\mathrm{cq}}^{+1}\right)}{L_{\mathrm{r}}}. \tag{41}$$

By substituting (40) and (41) into the third part of (3), the d- and q-components of the CW voltage in the reference frame dq^{+1}, u_{cd}^{+1} and u_{cq}^{+1}, can be obtained by

$$u_{\mathrm{cd}}^{+1} = R_{\mathrm{c}}i_{\mathrm{cd}}^{+1} + \sigma_{\mathrm{c}}L_{\mathrm{c}}si_{\mathrm{cd}}^{+1} + D_{\mathrm{cd}}^{+1}, \tag{42}$$

$$u_{\mathrm{cq}}^{+1} = \left(R_{\mathrm{c}} + \frac{R_{\mathrm{r}}L_{\mathrm{cr}}^2\omega_{\mathrm{c}}}{L_{\mathrm{r}}^2\left(\omega_{\mathrm{c}} - p_{\mathrm{c}}\omega_{\mathrm{r}}\right)}\right)i_{\mathrm{cq}}^{+1} + \sigma_{\mathrm{c}}L_{\mathrm{c}}si_{\mathrm{cq}}^{+1} + D_{\mathrm{cq}}^{+1}, \tag{43}$$

where $\sigma_{\mathrm{c}} = 1 - L_{\mathrm{cr}}^2/(L_{\mathrm{c}}L_{\mathrm{r}})$ is the leakage constant of the CW and D_{cd}^{+1} and D_{cq}^{+1} are the disturbance terms indicating the cross coupling between d- and q-components of the CW current and the indirect coupling between the PW and CW. The detailed expressions for D_{cd}^{+1} and D_{cq}^{+1} can be seen in Appendix. The CW frequency ω_{c} is obtained by using (2).

Discretizing (42) and (43), the CW voltage at the kth sampling period can be expressed as

$$u_{\mathrm{cd}}^{+1}(k)=\left[\frac{R_{\mathrm{c}}i_{\mathrm{cd}}^{+1}(k)+\sigma_{\mathrm{c}}L_{\mathrm{c}}\Delta i_{\mathrm{cd}}^{+1}(k)}{T_{\mathrm{s}}}\right]+D_{\mathrm{cd}}^{+1}(k), \tag{44}$$

$$\begin{aligned}u_{\mathrm{cq}}^{+1}(k)=&\left(R_{\mathrm{c}}+\frac{R_{\mathrm{r}}L_{\mathrm{cr}}^{2}\omega_{\mathrm{c}}}{L_{\mathrm{r}}^{2}(\omega_{\mathrm{c}}-p_{\mathrm{c}}\omega_{\mathrm{r}})}\right)i_{\mathrm{cq}}^{+1}(k)\\&+\frac{\sigma_{\mathrm{c}}L_{\mathrm{c}}\Delta i_{\mathrm{cq}}^{+1}(k)}{T_{\mathrm{s}}}+D_{\mathrm{cq}}^{+1}(k),\end{aligned} \tag{45}$$

where $\Delta i_{\mathrm{cd}}^{+1}$ and $\Delta i_{\mathrm{cq}}^{+1}$ are the differences of the CW d- and q-component currents between two adjacent sampling periods and T_{s} is the sampling interval. $\Delta i_{\mathrm{cd}}^{+1}(k)$ and $\Delta i_{\mathrm{cq}}^{+1}(k)$ are defined as

$$\begin{aligned}\Delta i_{\mathrm{cd}}^{+1}(k)&=i_{\mathrm{cd}}^{+1}(k+1)-i_{\mathrm{cd}}^{+1}(k),\\\Delta i_{\mathrm{cq}}^{+1}(k)&=i_{\mathrm{cq}}^{+1}(k+1)-i_{\mathrm{cq}}^{+1}(k).\end{aligned} \tag{46}$$

It is difficult to predict accurately the actual CW currents $i_{\mathrm{cd}}^{+1}(k+1)$ and $i_{\mathrm{cq}}^{+1}(k+1)$. However, the target of the CW predictive current controller is to minimize the CW current errors at the (k+1)th sampling period; therefore, the reference CW currents $i_{\mathrm{cd}}^{+1*}(k+1)$ and $i_{\mathrm{cq}}^{+1*}(k+1)$ at the (k+1)th sampling period could be used to replace the actual ones in (46). The reference CW currents at the (k+1)th sampling period can be obtained by the linear extrapolation method as follows:

$$\begin{aligned}i_{\mathrm{cd}}^{+1*}(k+1)&=2i_{\mathrm{cd}}^{+1*}(k)-i_{\mathrm{cd}}^{+1*}(k-1),\\i_{\mathrm{cq}}^{+1*}(k+1)&=2i_{\mathrm{cq}}^{+1*}(k)-i_{\mathrm{cq}}^{+1*}(k-1).\end{aligned} \tag{47}$$

Hence, the differences of the CW currents between the (k+1)th and the kth sampling periods can be expressed as

$$\begin{aligned}\Delta i_{\mathrm{cd}}^{+1}(k)&=2i_{\mathrm{cd}}^{+1*}(k)-i_{\mathrm{cd}}^{+1*}(k-1)-i_{\mathrm{cd}}^{+1}(k),\\\Delta i_{\mathrm{cq}}^{+1}(k)&=2i_{\mathrm{cq}}^{+1*}(k)-i_{\mathrm{cq}}^{+1*}(k-1)-i_{\mathrm{cq}}^{+1}(k).\end{aligned} \tag{48}$$

By substituting (48) to (44) and (45), the d- and q-component references of the CW voltage, $u_{\mathrm{cd}}^{+1*}(k)$ and $u_{\mathrm{cq}}^{+1*}(k)$, can be obtained. The three-phase CW voltage references can be calculated according to the coordinate transformation method proposed in [17], which requires the estimated rotor position $\widehat{\theta}_{\mathrm{r}}$ and the reference of the PW voltage phase θ_{p}^{*}.

4.4. Extraction of PW Harmonic Voltage. According to the analysis in Section 3, under nonlinear load conditions, the PW voltage contains significant harmonic components, especially the fifth and the seventh harmonics. In order to suppress these harmonics in the PW voltage, these harmonics need to be extracted accurately and then input to the PW harmonic-voltage controller. In the previous studies for control of the stand-alone DFIG under nonlinear load conditions [13, 14], a band-pass filter is employed to extract the harmonic components, but the dynamic response is highly degraded because the frequencies of the fundamental, fifth, and seventh harmonics are relatively close.

In this paper, a MSOGI [18] and a stationary-frame phase-locked loop (PLL) [20] are employed to estimate these harmonic components. Hence, the scheme for the PW harmonic voltage extraction is called the MSOGI-PLL, as shown in Figure 5. The MSOGI consists of three dual second-order generalized integrators (DSOGIs), which are used to extract the fundamental, fifth harmonic, and seventh harmonic components of the PW voltage, respectively. The stationary-frame PLL is employed to estimate the fundamental frequency and phase angle based on the α- and β-components of the fundamental PW voltage. The resonance frequencies of the three DSOGIs are 1, 5, and 7 times the fundamental frequency, respectively. The variable k is the damping factor of the first DSOGI, and the damping factors of the second and the third DSOGIs are set to $k/5$ and $k/7$, respectively, in order to guarantee the same bandwidth for all the DSOGIs.

4.5. Rotor Speed Observer. This paper employs an improved rotor speed observer to estimate the rotor speed [21]. By making integration of (1), it can get the relationship among the rotor position θ_r, the PW voltage vector angle θ_p, and the CW current vector angle θ_c, as expressed by

$$(p_{\mathrm{p}}+p_{\mathrm{c}})\theta_{\mathrm{r}}=\theta_{\mathrm{p}}+\theta_{\mathrm{c}}. \tag{49}$$

From (49), the difference $\Delta\theta_{\mathrm{r}}$ between the actual and estimated rotor position in the vicinity of the equilibrium point can be derived as

$$\begin{aligned}(p_{\mathrm{p}}+p_{\mathrm{c}})\Delta\theta_{\mathrm{r}}&=(p_{\mathrm{p}}+p_{\mathrm{c}})(\theta_{\mathrm{r}}-\widehat{\theta}_{\mathrm{r}})=(\theta_{\mathrm{p}}+\theta_{\mathrm{c}})-(p_{\mathrm{p}}+p_{\mathrm{c}})\widehat{\theta}_{\mathrm{r}}\\&\approx\sin\left[(\theta_{\mathrm{p}}+\theta_{\mathrm{c}})-(p_{\mathrm{p}}+p_{\mathrm{c}})\widehat{\theta}_{\mathrm{r}}\right].\end{aligned} \tag{50}$$

According to (50), a stationary-frame PLL can be employed to obtain the estimated rotor position $\widehat{\theta}_{\mathrm{r}}$ and rotor speed $\widehat{\omega}_{\mathrm{r}}$. The basic rotor speed observer is proposed, as shown in Figure 6, which is based on the three-phase PW voltage and the three-phase CW current.

According to the analysis in Section 3, a nonlinear load can result in distorted PW voltage and CW current, which would cause inaccurate rotor position and speed estimation by using the basic rotor speed observer. In order to overcome this problem, the PW voltage and CW current need to be prefiltered before their input to the basic rotor speed observer. Fortunately, as it can be seen from Figure 5, the α- and β-components of the PW fundamental voltage, $u_{\mathrm{p}\alpha1}$ and $u_{\mathrm{p}\beta1}$, have been extracted by the MSOGI-PLL. In addition, the two low-pass filters are employed to adaptively filter the CW current, in order to obtain the α- and β-components, $i_{\mathrm{c}\alpha1}$ and $i_{\mathrm{c}\beta1}$, of the CW fundamental current. The resonance frequency of the two SOGIs is derived from (2). Finally, the quantities $u_{\mathrm{p}\alpha1}$, $u_{\mathrm{p}\beta1}$, $i_{\mathrm{c}\alpha1}$, and $i_{\mathrm{c}\beta1}$ are input to the basic rotor speed observer to obtain the accurate rotor position and speed. The improved rotor speed observer is presented in Figure 7.

5. Experimental Results

5.1. Experimental Setup. The experimental setup is shown in Figure 8. The experiments are performed on a 35-kVA prototype BDFIG, whose detailed parameters are listed in Table 1. A

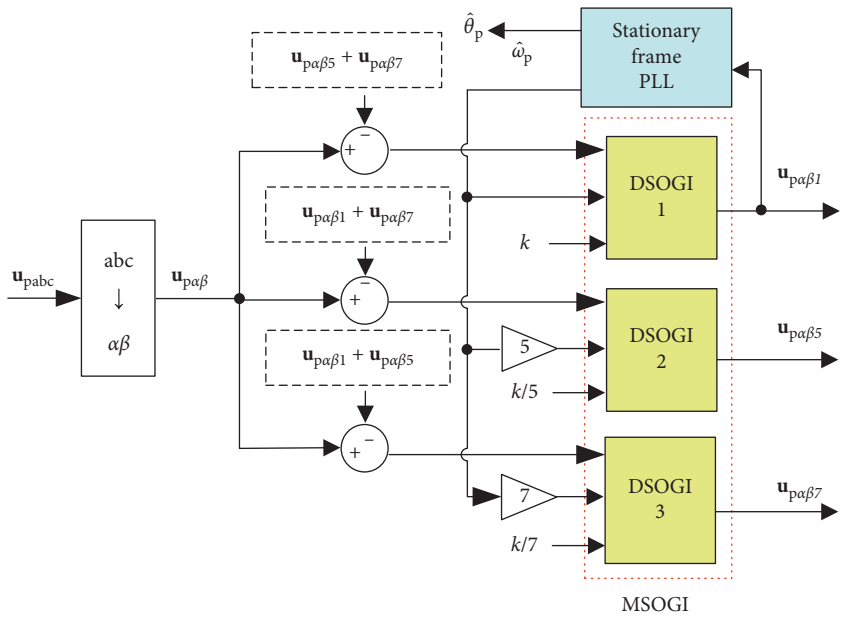

Figure 5: The MSOGI-PLL for the extraction of PW harmonic voltage.

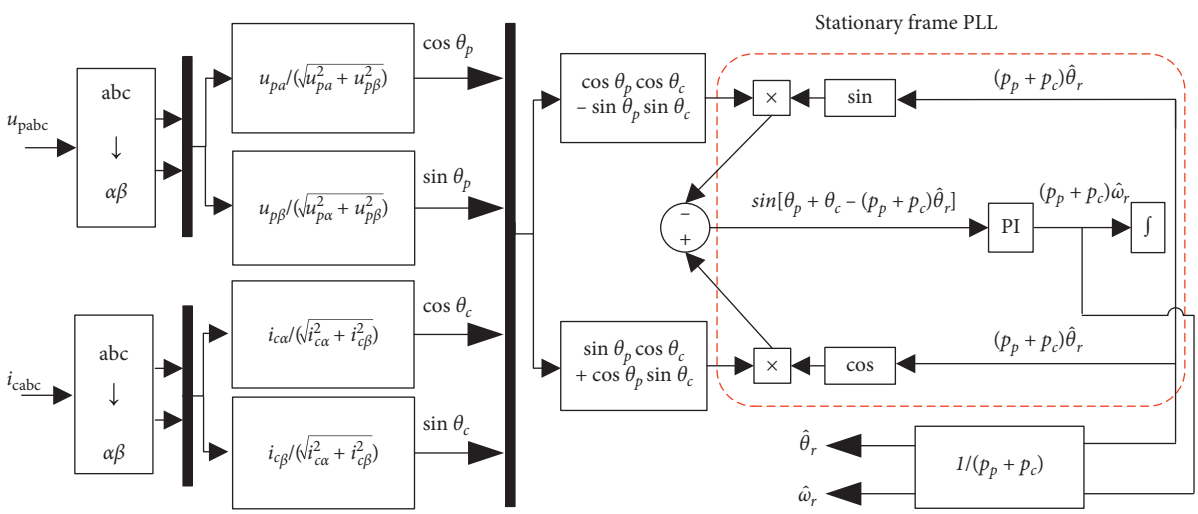

Figure 6: Structure of the basic rotor speed observer.

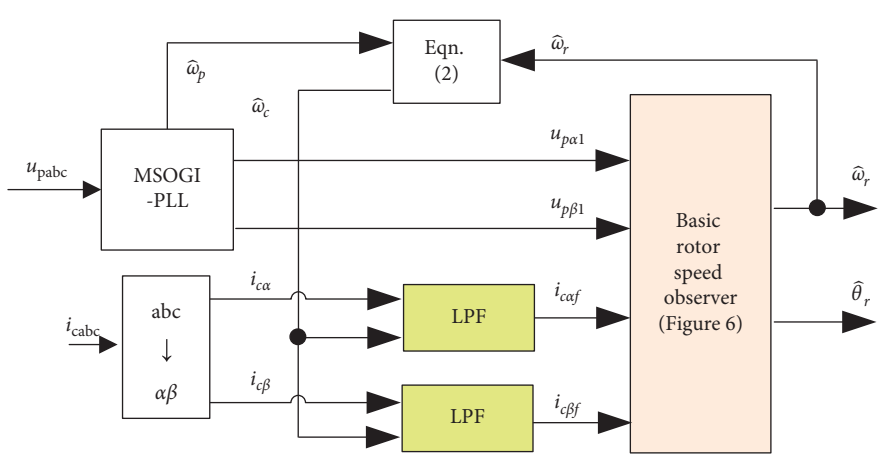

Figure 7: The improved rotor speed observer for the stand-alone BDFIG under nonlinear load conditions.

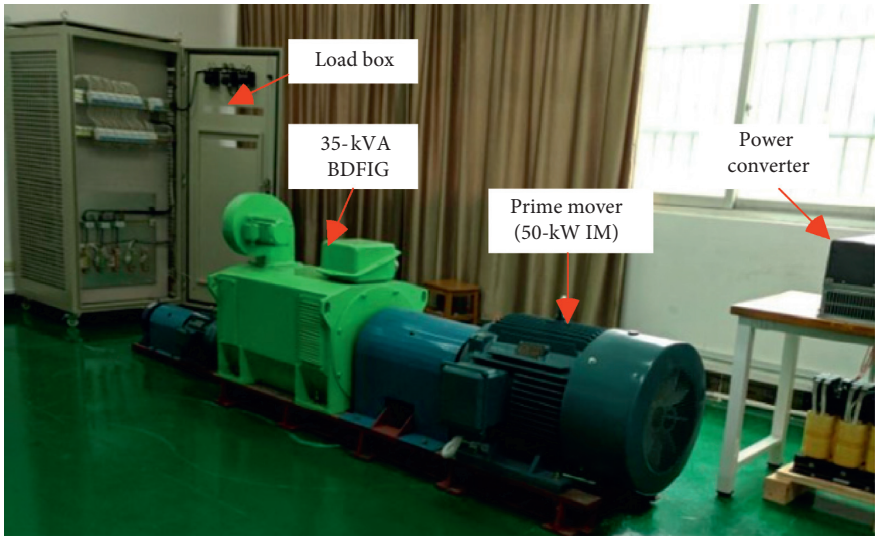

Figure 8: Photograph of the experimental setup.

50-kW three-phase induction motor is used as a prime mover. The reference RMS and frequency of the PW line voltage are set to 380 V and 50 Hz, respectively. The nonlinear load is a three-phase diode rectifier supplying a resistive load of 25 Ω.

5.2. Performance Test of the Rotor Speed Observer. The performance test of the rotor speed observer is carried out without the activation of the PW harmonic-voltage controller, which is regarded as the most demanding operation condition for the observer due to the severely distorted PW voltage and CW current. The test results are shown in Figure 9.

At the beginning, the stand-alone BDFIG runs under no-load condition at the rotor speed of 600 rpm. At 0.44 s, the connection of the nonlinear load leads to significant distortion of the PW voltage and CW current. Due to a sudden connected nonlinear load at 0.44 s, the amplitude of PW voltage drops from 537 to 98 V, which results in the amplitude of CW current being increased from 30 to 96 A under the control of the system. And, a severe transient drop of the rotor speed occurs due to a sudden increased load on the prime mover. Between 2.4 and 10 s, the rotor speed rises from 600 to 930 rpm and then drops to 890 rpm. During the whole process, the basic and improved rotor speed observers give a similar response speed. Therefore, in the improved observer, the prefiltering of the PW voltage and the CW current does not result in the dynamic performance degradation. Besides, the rotor speed estimated by the basic observer is always with a fluctuation of about 24 rpm peak-to-peak value, whereas the fluctuation of the improved observer is significantly reduced to about 4 rpm. Hence, the improved observer can provide satisfactory performance for the stand-alone BDFIG with nonlinear loads.

5.3. Experimental Results under Constant Rotor Speed. Figure 10 presents the experimental results with and without the activation of the PW harmonic-voltage controller at the rotor speed of 600 rpm. It can be seen that, without the activation of the PW harmonic-voltage controller, the amplitude of the fifth harmonic voltage reaches about 30 V and that of the seventh harmonic voltage to 25 V. After the activation of the PW harmonic-voltage controller, some harmonics are injected into the CW current to compensate the distortion of the PW voltage, and consequently the amplitudes of the fifth and seventh harmonic voltages are reduced to nearly zero within 50 ms. With the activation of the PW harmonic-voltage controller, the total harmonic distortion (THD) of the PW voltage is significantly reduced from 8.1% to 2.6%. And, it can be noted that, without the activation of the PW harmonic-voltage controller, the amplitudes of the seventh and nineteenth harmonic voltages are almost the same. Actually, the nineteenth harmonic component in PW voltage is mainly caused by the PWM modulation of LSC. Since this paper focuses on eliminating the harmonics produced by nonlinear loads rather than those caused by the modulation of power converters, the compensation for the nineteenth harmonic component of PW voltage is not considered in the design of the control scheme. Besides, after the activation of the PW harmonic-voltage

Table 1: Main parameters of the prototype BDFIG.

Parameter	Value
Capacity	35 kVA
Speed range	600–1200 rpm
PW and CW pole pairs	1, 3
PW-rated voltage and current	380 V, 53 A
CW voltage and current range	0–350 V, 0–50 A
PW, CW, and rotor resistances	0.5102 Ω, 0.3350 Ω, 0.4129 Ω
PW, CW, and rotor self-inductances	0.4865 H, 0.0312 H, 0.2034 H
Mutual inductance between PW and rotor	0.4128 H
Mutual inductance between CW and rotor	0.0314 H

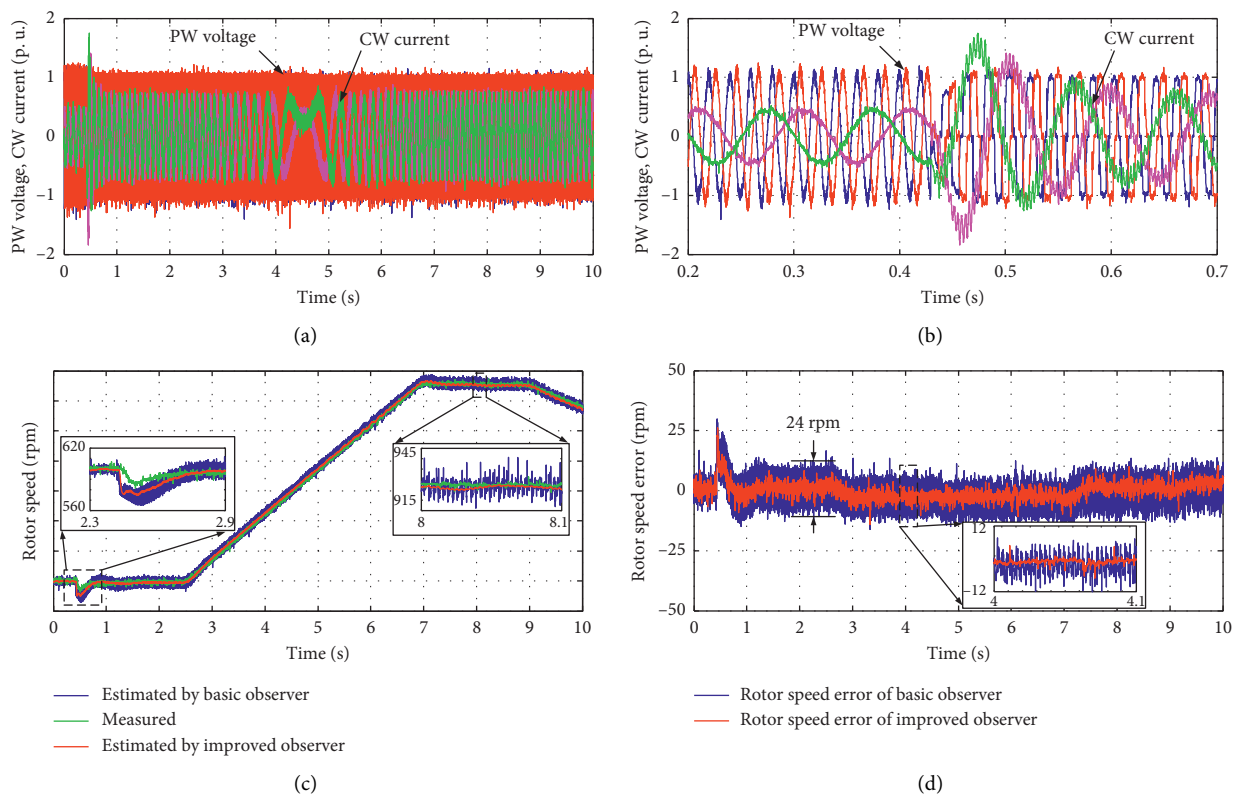

Figure 9: Test results of the rotor speed observer without the PW harmonic-voltage controller being activated. (a) PW voltage (1 p.u. = 500 V) and CW current (1 p.u. = 60 A). (b) Detailed view of (a). (c) Rotor speeds observed by the basic and improved observers. (d) Rotor speed errors of the basic and improved observers.

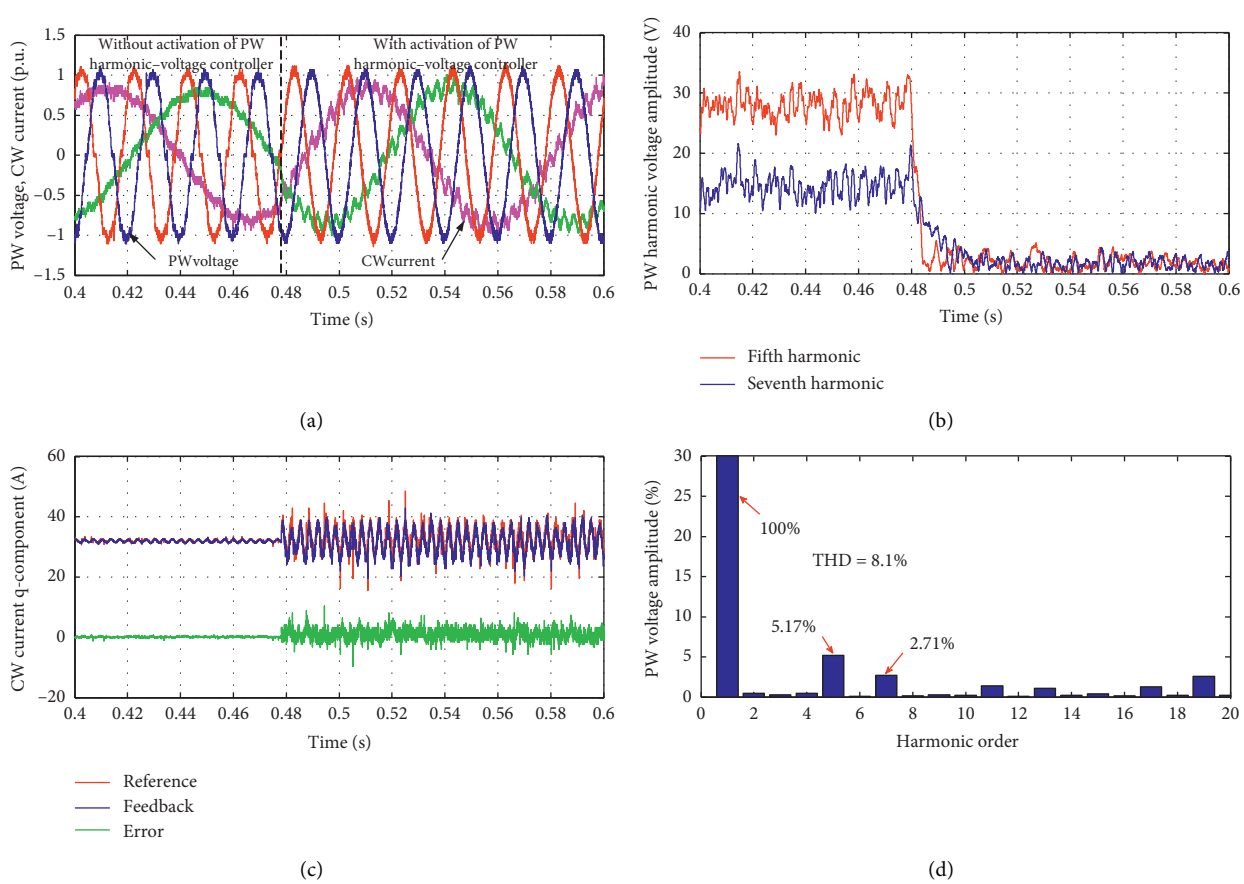

Figure 10: Continued.

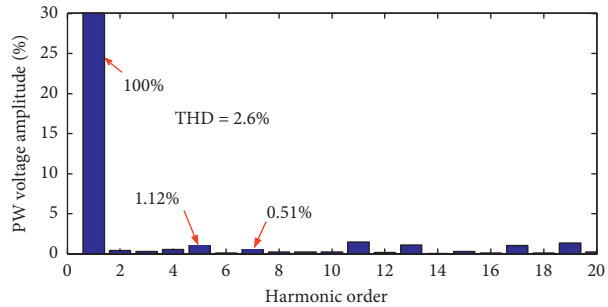

(e)

Figure 10: Experimental results with and without the activation of the PW harmonic-voltage controller at the rotor speed of 600 rpm. (a) PW line voltage (1 p u= 500 V) and CW phase current (1 p u = 60 A). (b) Amplitude of PW harmonic voltage. (c) Reference, feedback, and error of the q-component of the CW current. (d) Harmonic spectrum of PW voltage before activation of the PW harmonic-voltage controller. (e) Harmonic spectrum of PW voltage after activation of the PW harmonic-voltage controller.

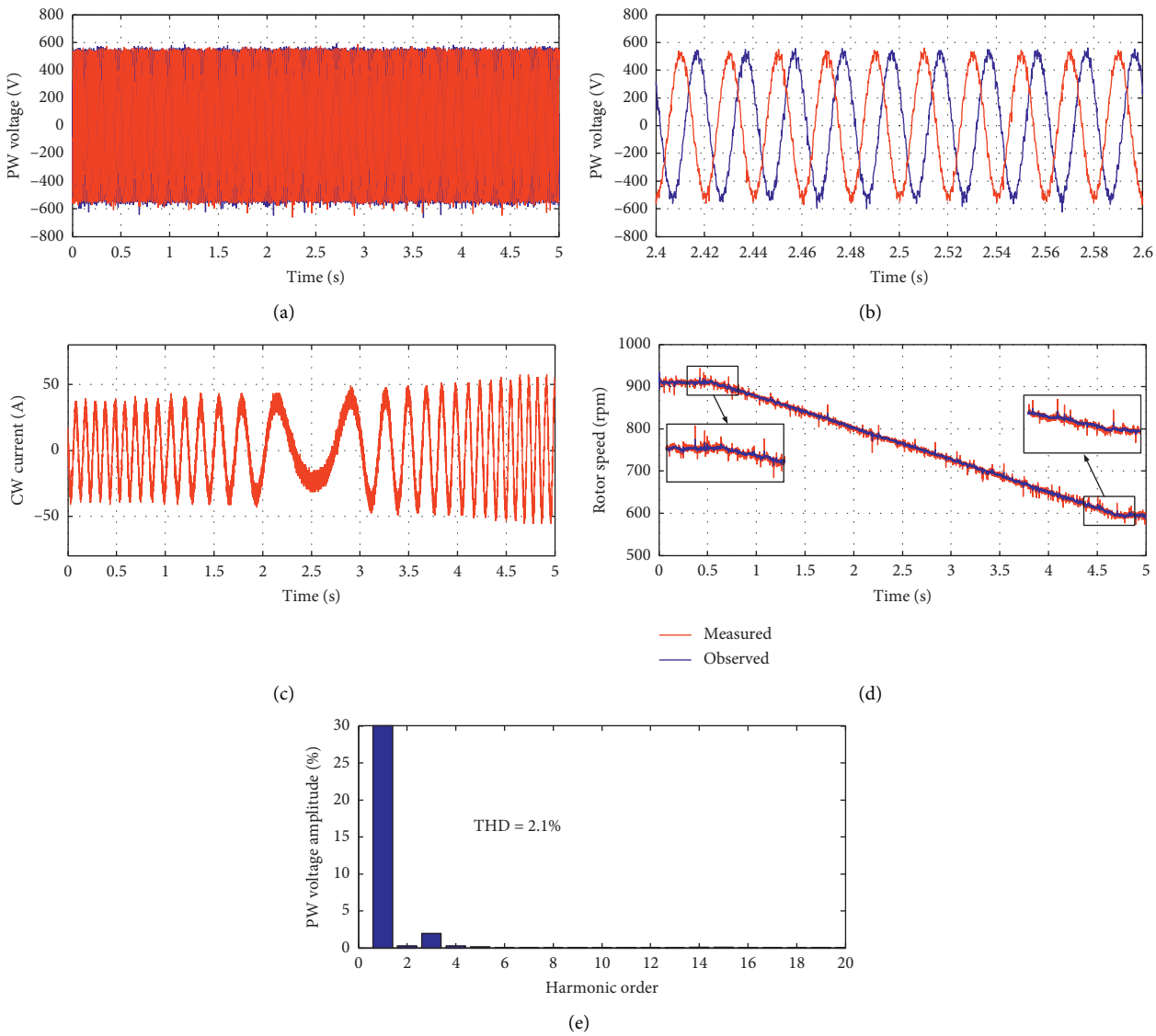

Figure 11: Experimental results with the activation of the PW harmonic-voltage controller during the rotor speed dropping from 900 rpm (supersynchronous speed) to 600 rpm (subsynchronous speed). (a) PW line voltage. (b) Enlarged view of the PW line voltage between 2.4 s and 2.6 s (c) CW phase current. (d) Measured and observed rotor speed. (e) Harmonic spectrum of the PW voltage at the rotor speed of 900 rpm.

controller, the reference of the q-component of the CW current is composed of ac and dc parts and can be well tracked by the proposed CW predictive current controller. Due to the limited number of analog output channels in the control system, the quantities about the CW current d-component are not acquired and shown.

5.4. Experimental Results under Variable Rotor Speed. In order to validate the dynamic performance of the control system under the variable rotor speed, the experiments have been carried out in the typical rotor speed range (from the supersynchronous speed 900 rpm to the subsynchronous speed 600 rpm). The experimental results are presented in Figure 11. Through the whole process, the amplitude and frequency of the PW voltage are almost constant. The rotor speed can be estimated very well by using the improved rotor speed observer. The THD of the PW voltage at the rotor speed of 900 rpm is about 2.1% and that at 600 rpm has been presented in Figure 10(e).

6. Conclusion

This paper presents an enhanced sensorless control scheme for the stand-alone BDFIG with nonlinear loads. The PW fundamental-voltage controller, based on the PW fundamental-voltage vector orientation, is used to control the amplitude and frequency of the PW fundamental voltage. The PW harmonic-voltage controller is employed to eliminate the harmonics of the PW voltage, especially the fifth and seventh ones. A rotor speed observer is proposed to estimate the rotor position and speed from the PW voltage and CW current. The predictive control method is introduced to this system to regulate the CW current. Comprehensive experiments demonstrate that the proposed scheme can significantly improve the performance of the stand-alone BDFIG under nonlinear loads.

Appendix

$$\alpha_1^n = \beta_1^n = \frac{L_r L_{cr}\left(n\omega_p - p_p\omega_r\right)^2 + L_{cr}\left(L_r s^2 + R_r s\right)}{\left(L_r s + R_r\right)^2 + L_r^2\left(n\omega_p - p_p\omega_r\right)^2}, \tag{A.1}$$

$$\alpha_2^n = \beta_2^n = -\frac{R_r L_{cr}\left(n\omega_p - p_p\omega_r\right)}{\left(L_r s + R_r\right)^2 + L_r^2\left(n\omega_p - p_p\omega_r\right)^2}, \tag{A.2}$$

$$\alpha_3^n = \beta_3^n = -\frac{L_r L_{pr}\left(n\omega_p - p_p\omega_r\right)^2 + L_{pr}\left(L_r s^2 + R_r s\right)}{\left(L_r s + R_r\right)^2 + L_r^2\left(n\omega_p - p_p\omega_r\right)^2}, \tag{A.3}$$

$$\alpha_4^n = \beta_4^n = -\frac{R_r L_{pr}\left(n\omega_p - p_p\omega_r\right)}{\left(L_r s + R_r\right)^2 + L_r^2\left(n\omega_p - p_p\omega_r\right)^2}, \tag{A.4}$$

$$D_{pd1}^{+1} = -\frac{\left[L_{pr}\alpha_2^{+1} i_{cq1}^{+1} + \left(L_p + L_{pr}\alpha_3^{+1}\right) i_{pd1}^{+1} + L_{pr}\alpha_4^{+1} i_{pq1}^{+1}\right]}{\left(L_{pr}\alpha_1^{+1}\right)}, \tag{A.5}$$

$$D_{pq1}^{+1} = \frac{\left[L_{pr}\beta_2^{+1} i_{cd1}^{+1} + \left(L_p + L_{pr}\beta_3^{+1}\right) i_{pq1}^{+1} + L_{pr}\beta_4^{+1} i_{pd1}^{+1}\right]}{\left(L_{pr}\beta_1^{+1}\right)}, \tag{A.6}$$

$$D_{pd5}^{-5} = \frac{\left[L_{pr}\alpha_2^{-5} i_{cq5}^{-5} + \left(L_p + L_{pr}\alpha_3^{-5}\right) i_{pd5}^{-5} + L_{pr}\alpha_4^{-5} i_{pq5}^{-5}\right]}{\left(L_{pr}\alpha_1^{-5}\right)}, \tag{A.7}$$

$$D_{pq5}^{-5} = \frac{-\left[L_{pr}\beta_2^{-5} i_{cd5}^{-5} + \left(L_p + L_{pr}\beta_3^{-5}\right) i_{pq5}^{-5} + L_{pr}\beta_4^{-5} i_{pd5}^{-5}\right]}{\left(L_{pr}\beta_1^{-5}\right)}, \tag{A.8}$$

$$D_{pd7}^{+7} = \frac{-\left[L_{pr}\alpha_2^{+7} i_{cq7}^{+7} + \left(L_p + L_{pr}\alpha_3^{+7}\right) i_{pd7}^{+7} + L_{pr}\alpha_4^{+7} i_{pq7}^{+7}\right]}{\left(L_{pr}\alpha_1^{+7}\right)}, \tag{A.9}$$

$$D_{pq7}^{+7} = \frac{\left[L_{pr}\beta_2^{+7} i_{cd7}^{+7} + \left(L_p + L_{pr}\beta_3^{+7}\right) i_{pq7}^{+7} + L_{pr}\beta_4^{+7} i_{pd7}^{+7}\right]}{\left(L_{pr}\beta_1^{+7}\right)}, \tag{A.10}$$

$$D_{cd}^{+1} = -\omega_c \frac{L_{pr} L_{cr} i_{pq}^{+1}}{L_r}, \tag{A.11}$$

$$D_{cq}^{+1} = -\omega_c \sigma_c L_c i_{cd}^{+1} + \frac{L_{pr} L_{cr} \omega_c}{L_r} i_{pd}^{+1} + \frac{R_r L_{pr} L_{cr} \omega_c}{L_r^2\left(\omega_c - p_c\omega_r\right)} i_{pq}^{+1}. \tag{A.12}$$

In (A.1)–(A.4), the parameter n corresponds to +1, −5, or +7 for fundamental, fifth, and seventh components.

Data Availability

The data used to support the findings of this study are included within the article.

Conflicts of Interest

The authors declare that they have no conflicts of interest.

References

[1] R. A. McMahon, P. C. Roberts, X. Wang, and P. J. Tavner, "Performance of BDFM as generator and motor," *IEE Proceedings - Electric Power Applications*, vol. 153, no. 2, pp. 289–299, 2006.

[2] F. Xiong and X. Wang, "Design of a low-harmonic-content wound rotor for the brushless doubly fed generator," *IEEE Transactions on Energy Conversion*, vol. 29, no. 1, pp. 158–168, 2014.

[3] Y. Liu, W. Ai, B. Chen, and K. Chen, "Control design of the brushless doubly-fed machines for stand-alone VSCF ship

shaft generator systems," *Journal of Power Electronics*, vol. 16, no. 1, pp. 259–267, 2016.

[4] S. Shao, E. Abdi, F. Barati, and R. A. McMahon, "Stator-flux-oriented vector control for brushless doubly-fed induction generator," *IEEE Trans. Ind. Electron.*vol. 56, no. 10, pp. 4220–4228, 2009.

[5] S. Shao, T. Long, E. Abdi, and R. A. McMahon, "Dynamic control of the brushless doubly fed induction generator under unbalanced operation," *IEEE Transactions on Industrial Electronics*, vol. 60, no. 6, pp. 2465–2476, 2013.

[6] J. Chen, W. Zhang, B. Chen, and Y. Ma, "Improved vector control of brushless doubly fed induction generator under unbalanced grid conditions for offshore wind power generation," *IEEE Transactions on Energy Conversion*, vol. 31, no. 1, pp. 293–302, 2016.

[7] S. Tohidi, H. Oraee, M. R. Zolghadri, S. Shao, and P. Tavner, "Analysis and enhancement of low-voltage ride-through capability of brushless doubly fed induction generator," *IEEE Transactions on Industrial Electronics*, vol. 60, no. 3, pp. 1146–1155, 2013.

[8] S. Ademi and M. Jovanović, "A novel sensorless speed controller design for doubly-fed reluctance wind turbine generators," *Energy Conversion and Management*, vol. 120, pp. 229–237, 2016.

[9] S. Ademi, M. G. Jovanovic, H. Chaal, and W. Cao, "A new sensorless speed control scheme for doubly fed reluctance generators," *IEEE Transactions on Energy Conversion*, vol. 31, no. 3, pp. 993–1001, 2016.

[10] Y. Liu, B. Chen, G. Luo, W. Ai, and K. Chen, "Control design and experimental verification of the brushless doubly-fed machine for stand-alone power generation applications," *IET Electric Power Applications*, vol. 10, no. 1, pp. 25–35, 2016.

[11] X. Wei, M. Cheng, W. Wang, P. Han, and R. Luo, "Direct voltage control of dual-stator brushless doubly fed induction generator for stand-alone wind energy conversion systems," *IEEE Trans. Magn.,* vol. 52, no. 7, 2016.

[12] X. Wang, H. Lin, and Z. Wang, "Transient control of the reactive current for the line-side converter of the brushless doubly-fed induction generator in stand-alone operation," *IEEE Transactions on Power Electronics*, vol. 32, no. 10, pp. 8193–8203, 2017.

[13] V.-T. Phan and H.-H. Lee, "Control strategy for harmonic elimination in stand-alone DFIG applications with nonlinear loads," *IEEE Transactions on Power Electronics*, vol. 26, no. 9, pp. 2662–2675, 2011.

[14] V.-T. Phan and H.-H. Lee, "Performance enhancement of stand-alone DFIG systems with control of rotor and load side converters using resonant controllers," *IEEE Transactions on Industry Applications*, vol. 48, no. 1, pp. 199–210, 2012.

[15] V.-T. Phan, D.-T. Nguyen, Q.-N. Trinh, C.-L. Nguyen, and T. Logenthiran, "Harmonics rejection in stand-alone doubly-fed induction generators with nonlinear loads," *IEEE Transactions on Energy Conversion*, vol. 31, no. 2, pp. 815–817, 2016.

[16] Y. Liu, W. Xu, F. Xiong, and F. Blaabjerg, "Harmonic voltage and current elimination of stand-alone brushless doubly-fed induction generator with nonlinear loads for ship shaft power generation applications," in *Proceedings of the 2018 IEEE Energy Conversion Congress and Exposition (ECCE)*, pp. 7349–7355, Portland, OR, USA, September 2018.

[17] J. Poza, E. Oyarbide, D. Roye, and M. Rodriguez, "Unified reference frame dq model of the brushless doubly fed machine," *IEE Proceedings - Electric Power Applications*, vol. 153, no. 5, pp. 726–734, 2006.

[18] P. Rodriguez, A. Luna, I. Candela, R. Mujal, R. Teodorescu, and F. Blaabjerg, "Multiresonant frequency-locked loop for grid synchronization of power converters under distorted grid conditions," *IEEE Transactions on Industrial Electronics*, vol. 58, no. 1, pp. 127–138, 2011.

[19] V.-T. Phan and H.-H. Lee, "Improved predictive current control for unbalanced stand-alone doubly-fed induction generator-based wind power systems," *IET Electric Power Applications*, vol. 5, no. 3, pp. 275–287, 2011.

[20] S.-K. Chung, "Phase-locked loop for grid-connected three-phase power conversion systems," *IEE Proceedings - Electric Power Applications*, vol. 147, no. 3, pp. 213–219, 2000.

[21] Y. Liu, W. Xu, T. Long, and F. Blaabjerg, "An improved rotor speed observer for standalone brushless doubly-fed induction generator under unbalanced and nonlinear loads," *IEEE Transactions on Power Electronics*, vol. 35, no. 1, pp. 775–788, 2020.

Hindawi
Mathematical Problems in Engineering
Volume 2020, Article ID 3920535, 8 pages
https://doi.org/10.1155/2020/3920535

Research Article

Nonlinear Global Stabilization Control for the Underactuated WAcrobot System

Shuli Gong,[1] **Ancai Zhang**,[2,3] **Zhi Liu**,[2,3] **Zhenxing Li**,[2,3] **Chengdong Yang**,[3,4] **and Xinghui Zhang**[2,3]

[1]*School of Mathematics and Statistics, Linyi University, Linyi, Shandong 276000, China*
[2]*School of Automation and Electrical Engineering, Linyi University, Linyi, Shandong 276000, China*
[3]*Key Laboratory of Complex Systems and Intelligent Computing in Universities of Shandong, Linyi, Shandong 276000, China*
[4]*School of Information Science and Engineering, Linyi University, Linyi, Shandong 276000, China*

Correspondence should be addressed to Ancai Zhang; zhangancai123@hotmail.com

Received 20 April 2020; Accepted 9 June 2020; Published 3 July 2020

Guest Editor: Ping Zhao

A WAcrobot is an underactuated nonlinear system that has three degrees of freedom (DOF) and two inputs. This paper discusses the global stabilization control problem for this 3-DOF underactuated system. A new control strategy is developed to solve this problem. The strategy first changes the 3-DOF WAcrobot system to be a 2-DOF reduced-order model in finite time. This transforms the stabilizing control of the WAcrobot system into that of the reduced-order model. After that, nonsingular control laws that globally stabilize the reduced-order model at the origin are designed. It guarantees the stabilizing control objective of the WAcrobot to be achieved. Finally, a simulation experimental example demonstrates the validity of the presented theoretical results. Simulation results show the advantage of our strategy over others.

1. Introduction

In our daily life, many natural systems essentially have nonlinear characteristics. It is meaningful to discuss the control problem for the nonlinear systems [1–5]. An underactuated mechanical system is a typical example of nonlinear systems, which has fewer control inputs than the number of systems' degrees of freedom (DOF). Compared with the fully actuated system, the underactuated system has the characteristics of light weight, low energy consumption, and flexible movement because of the reduction of actuators. Such systems can be widely used in health care, space exploration, transportation, military, and other fields [6–9]. However, the reduction of inputs makes the system possess nonlinear constraints. And the constraints are usually second-order nonholonomic [10]. This means that the states of the system are in uncontrollable manifolds of the configuration space. The control design of an underactuated mechanical system is challenging in the nonlinear control area. Many researchers have devoted their efforts to the study on underactuated systems in the past few years [11–15].

Since the 1990s, the control problems for the simplest underactuated system (that is, the 2-DOF underactuated system) have been attracting much attention. In order to explore the nonlinear control strategy, many experimental models of 2-DOF underactuated systems have been presented in the laboratory. The models include Acrobot [16], Pendubot [17], TORA [18], and Pendulum-cart [19]. The stabilization control issue is a commonly addressed problem for these 2-DOF underactuated mechanical systems. And many stabilizing control methods have been developed, e.g., a partial feedback linearization method [20], an energy-based method [21], a nonsmooth Lyapunov function method [22], an equivalent-input disturbance method [23], and a trajectory tracking strategy [24].

With the deepening of the research work, the control problems presented by an n-DOF ($n \geq 3$) underactuated system need to be further explored since multi-DOF systems are more consistent with the reality of natural systems.

However, this problem is not easy to solve because the nonlinear dynamics and constraint equations of underactuated systems become more complicated with the increase of the DOF. To solve the control problems for multi-DOF underactuated systems, it is necessary to study the simplest case, i.e., $n = 3$. Recently, some 3-DOF underactuated system models have been presented. Their dynamic analysis and control design have been intensively discussed [25–28]. Among them, a WAcrobot model (see Figure 1) is a typical example. This mechanical system has a wheel and a double inverted pendulum. The wheel rolls in a horizontal plane driven by an actuator. And the double pendulum freely rotates in a vertical plane driven by an actuator at the second joint. The first joint of the pendulum is passive. Note that the WAcrobot is a 3-DOF underactuated system, and it is the combination of a wheel and an Acrobot.

The WAcrobot has a good application prospect in the mobile robotic area. It is a perfect test bed for illustrating a nonlinear control algorithm for multi-DOF underactuated systems. So, it is meaningful to study the problems presented by this mechanical system. In [29], the swing-up and stabilization control of the WAcrobot were discussed. The authors used noncollocated feedback linearization and linear quadratic regulator technique to achieve the system's control objective. In addition to this paper, there are no related research results about this system. Since the WAcrobot possesses common inherent nonlinear features of multi-DOF underactuated systems, it is necessary to explore more control methods for it. This inspires our study in this paper.

The global stabilization control problem for the WAcrobot is addressed in this paper. By using the inherent dynamic coupling relationship, we first change the WAcrobot into a 2-DOF reduced-order system in finite time. And then, the global stabilization of the reduced-order model is discussed. Stabilizing control laws are developed, and the condition that avoids the singularity in the control law is also presented. Finally, numerical experiments demonstrate the validity of the theoretical analysis results. Simulation results show the advantage of our strategy over the results in [29]. Moreover, the presented strategy gives a good guidance for the solution of motion control of other multi-DOF underactuated mechanical systems.

2. Dynamic Motion Equations of the WAcrobot System

For the physical model of a WAcrobot system shown in Figure 1, $\theta_1(t)$, m_1, J_1, and L_1 are the rotational angle, the mass, the moment of inertia, and the radius of the wheel, respectively. For $i = 2, 3$, $\theta_1(t)$, m_i, J_i, and L_i are the rotational angle, the mass, the moment of inertia, and the length of the ith pendulum, respectively, and L_{ci} is the distance from the ith joint to the center of mass (COM) of the ith pendulum. Moreover, $\tau_1(t)$ and $\tau_2(t)$ are the input torques applied on the wheel and the 2nd pendulum, respectively, and g is the gravity acceleration constant ($\approx 9.81\ \mathrm{m/s^2}$).

We take the plane in which the center of the circle is located on as the zero potential energy reference plane. A

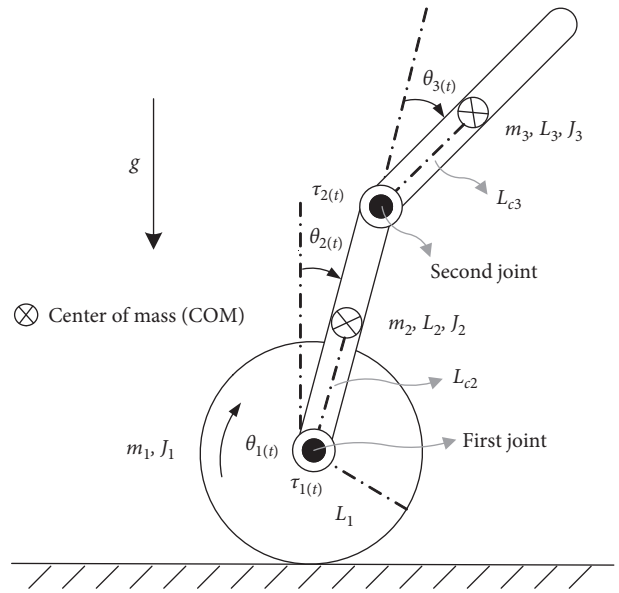

Figure 1: Physical model of the WAcrobot system.

simple calculation gives the potential energy of the WAcrobot as

$$\begin{cases} P(\boldsymbol{\theta}) = \beta_1 \cos\theta_2 + \beta_2 \cos(\theta_2 + \theta_3), \\ \beta_1 = (m_2 L_{c2} + m_3 L_2) g, \\ \beta_2 = m_3 L_3 g, \end{cases} \tag{1}$$

where $\theta = [\theta_1, \theta_2, \theta_3]^\top$. In addition, the kinetic energy of the system is

$$K(\boldsymbol{\theta}, \dot{\theta}) = \frac{1}{2}\dot{\theta}^\top M(\boldsymbol{\theta})\dot{\theta}, \tag{2}$$

where

$$M(\boldsymbol{\theta}) = \begin{bmatrix} M_{11} & M_{12}(\boldsymbol{\theta}) & M_{13}(\boldsymbol{\theta}) \\ M_{21}(\boldsymbol{\theta}) & M_{22}(\boldsymbol{\theta}) & M_{23}(\boldsymbol{\theta}) \\ M_{31}(\boldsymbol{\theta}) & M_{32}(\boldsymbol{\theta}) & M_{33} \end{bmatrix},$$

$$\begin{cases} M_{11} = \alpha_1,\ M_{22}(\boldsymbol{\theta}) = \alpha_2 + \alpha_4 + 2\alpha_6 \cos\theta_3, \\ M_{33} = \alpha_4, \\ M_{12}(\boldsymbol{\theta}) = M_{21}(\boldsymbol{\theta}) = \alpha_3 \cos\theta_2 + \alpha_5 \cos(\theta_2 + \theta_3), \\ M_{13}(\boldsymbol{\theta}) = M_{31}(\boldsymbol{\theta}) = \alpha_5 \cos(\theta_2 + \theta_3), \\ M_{23}(\boldsymbol{\theta}) = M_{32}(\boldsymbol{\theta}) = \alpha_4 + \alpha_6 \cos\theta_2, \\ \alpha_1 = (m_1 + m_2 + m_3) L_1^2 + J_1, \\ \alpha_2 = m_2 L_{c2}^2 + J_2 + m_3 L_2^2, \\ \alpha_3 = (m_2 L_{c2} + m_3 L_2) L_1, \\ \alpha_4 = m_3 L_{c3}^2 + J_3, \\ \alpha_5 = m_3 L_1 L_{c3}, \\ \alpha_6 = m_3 L_2 L_{c3}. \end{cases} \tag{3}$$

The Lagrangian function of the WAcrobot system is taken to be $L(\theta, \dot{\theta}) = K(\theta, \dot{\theta}) - P(\theta)$. We get the Euler–Lagrange motion equations of the system as

$$\begin{cases} \dfrac{\mathrm{d}}{\mathrm{d}t}\left[\dfrac{\partial L(\boldsymbol{\theta},\dot{\theta})}{\partial \dot{\theta}_1}\right] - \dfrac{\partial L(\boldsymbol{\theta},\dot{\theta})}{\partial \theta_1} = \tau_1, \\ \dfrac{\mathrm{d}}{\mathrm{d}t}\left[\dfrac{\partial L(\boldsymbol{\theta},\dot{\theta})}{\partial \dot{\theta}_2}\right] - \dfrac{\partial L(\boldsymbol{\theta},\dot{\theta})}{\partial \theta_2} = 0, \\ \dfrac{\mathrm{d}}{\mathrm{d}t}\left[\dfrac{\partial L(\boldsymbol{\theta},\dot{\theta})}{\partial \dot{\theta}_3}\right] - \dfrac{\partial L(\boldsymbol{\theta},\dot{\theta})}{\partial \theta_3} = \tau_2. \end{cases} \tag{4}$$

These dynamic equations can be rewritten in the following form:

$$M(\boldsymbol{\theta})\ddot{\theta} + \mathbf{H}(\boldsymbol{\theta},\dot{\theta}) + \mathbf{G}(\boldsymbol{\theta}) = \boldsymbol{\tau}, \tag{5}$$

where

$$\mathbf{H}(\boldsymbol{\theta},\dot{\theta}) = \begin{bmatrix} H_1(\boldsymbol{\theta},\dot{\theta}) \\ H_2(\boldsymbol{\theta},\dot{\theta}) \\ H_3(\boldsymbol{\theta},\dot{\theta}) \end{bmatrix},$$

$$\mathbf{G}(\boldsymbol{\theta}) = \begin{bmatrix} 0 \\ G_2(\boldsymbol{\theta}) \\ G_3(\boldsymbol{\theta}) \end{bmatrix},$$

$$\boldsymbol{\tau} = \begin{bmatrix} \tau_1 \\ 0 \\ \tau_2 \end{bmatrix},$$

$$\begin{cases} H_1(\boldsymbol{\theta},\dot{\theta}) = -\alpha_3\dot{\theta}_2^2\sin\theta_2 - \alpha_5\left(\dot{\theta}_2+\dot{\theta}_3\right)^2\sin(\theta_2+\theta_3), \\ H_2(\boldsymbol{\theta},\dot{\theta}) = -\alpha_6\left(2\dot{\theta}_2+\dot{\theta}_3\right)\dot{\theta}_3\sin\theta_3, \\ H_3(\boldsymbol{\theta},\dot{\theta}) = \alpha_6\dot{\theta}_2^2\sin\theta_3, \\ G_2(\boldsymbol{\theta}) = -\beta_1\sin\theta_2 - \beta_2\sin(\theta_2+\theta_3), \\ G_3(\boldsymbol{\theta}) = -\beta_2\sin(\theta_2+\theta_3). \end{cases} \tag{6}$$

Denote $\Xi(\theta,\dot{\theta}) = K(\theta,\dot{\theta}) + P(\theta)$ to be the total energy of the WAcrobot. From (5), we easily obtain

$$\dot{\Xi}(\boldsymbol{\theta},\dot{\theta}) = \dot{\theta}^{\top}\boldsymbol{\tau} = \dot{\theta}_1\tau_1 + \dot{\theta}_3\tau_2. \tag{7}$$

Let $x_1 = \theta_1$, $x_2 = \dot{\theta}_1$, $x_3 = \theta_2$, $x_4 = \dot{\theta}_2$, $z_1 = \theta_3$, $z_2 = \dot{\theta}_3$, $\mathbf{x} = [x_1, x_2, x_3, x_4]^{\top}$, and $\mathbf{z} = [z_1, z_2]^{\top}$. Then, it is not difficult to obtain the state space form of (5) as

$$\begin{cases} \dot{x}_1 = x_2, \\ \dot{x}_2 = \Upsilon_1(\mathbf{x},\mathbf{z}) + \Phi_1(\mathbf{x},\mathbf{z})\tau_1 + \Psi_1(\mathbf{x},\mathbf{z})\tau_2, \\ \dot{x}_3 = x_4, \\ \dot{x}_4 = \Upsilon_2(\mathbf{x},\mathbf{z}) + \Phi_2(\mathbf{x},\mathbf{z})\tau_1 + \Psi_2(\mathbf{x},\mathbf{z})\tau_2, \\ \dot{z}_1 = z_2, \\ \dot{z}_2 = \Upsilon_3(\mathbf{x},\mathbf{z}) + \Phi_3(\mathbf{x},\mathbf{z})\tau_1 + \Psi_3(\mathbf{x},\mathbf{z})\tau_2, \end{cases} \tag{8}$$

where

$$\begin{bmatrix} \Upsilon_1(\mathbf{x},\mathbf{z}) \\ \Upsilon_2(\mathbf{x},\mathbf{z}) \\ \Upsilon_3(\mathbf{x},\mathbf{z}) \end{bmatrix} = M^{-1}(\boldsymbol{\theta})\begin{bmatrix} -H_1(\boldsymbol{\theta},\dot{\theta}) \\ -H_2(\boldsymbol{\theta},\dot{\theta}) - G_2(\boldsymbol{\theta}) \\ -H_3(\boldsymbol{\theta},\dot{\theta}) - G_3(\boldsymbol{\theta}) \end{bmatrix},$$
$$\begin{bmatrix} \Phi_1(\mathbf{x},\mathbf{z}) & \Psi_1(\mathbf{x},\mathbf{z}) \\ \Phi_2(\mathbf{x},\mathbf{z}) & \Psi_2(\mathbf{x},\mathbf{z}) \\ \Phi_3(\mathbf{x},\mathbf{z}) & \Psi_3(\mathbf{x},\mathbf{z}) \end{bmatrix} = M^{-1}(\boldsymbol{\theta})\begin{bmatrix} 1 & 0 \\ 0 & 0 \\ 0 & 1 \end{bmatrix}. \tag{9}$$

It follows from (9) that both $\Psi_3(\mathbf{x},\mathbf{z})$ and $\Phi_1(\mathbf{x},\mathbf{z})\Psi_3(\mathbf{x},\mathbf{z}) - \Phi_3(\mathbf{x},\mathbf{z})\Psi_1(\mathbf{x},\mathbf{z})$ are order principal determinants of $M^{-1}(\theta)$. Since $M^{-1}(\theta)$ is a positive definite matrix, we get

$$\begin{cases} \Psi_3(\mathbf{x},\mathbf{z}) > 0, \\ \Phi_1(\mathbf{x},\mathbf{z})\Psi_3(\mathbf{x},\mathbf{z}) - \Phi_3(\mathbf{x},\mathbf{z})\Psi_1(\mathbf{x},\mathbf{z}) > 0. \end{cases} \tag{10}$$

3. Reduced-Order Model of the WAcrobot System

The control objective discussed in this paper is to design controllers τ_1 and τ_2 to globally stabilize WAcrobot system (8) at $[\mathbf{x},\mathbf{z}]^{\top} = \mathbf{0}$. Note that the nonlinear dynamics of (8) is very complicated. In order to simplify the structure of system (8), we design

$$\tau_2 = \frac{W(z_1,z_2) - \Upsilon_3(\mathbf{x},\mathbf{z}) - \Phi_3(\mathbf{x},\mathbf{z})\tau_1}{\Psi_3(\mathbf{x},\mathbf{z})}, \tag{11}$$

where

$$W(z_1,z_2) = -r_2\left(z_2^{5/3} + r_1^{5/3}z_1\right)^{1/5}, \tag{12}$$

and r_1 and r_2 are positive constants. This is a relationship between control torques τ_1 and τ_2. Substituting (11) into (8) yields

$$\begin{cases} \dot{x}_1 = x_2, \\ \dot{x}_2 = \Upsilon_1(\mathbf{x},\mathbf{z}) + \dfrac{\Psi_1(\mathbf{x},\mathbf{z})\left[W(z_1,z_2) - \Upsilon_3(\mathbf{x},\mathbf{z})\right]}{\Psi_3(\mathbf{x},\mathbf{z})} \\ \quad + \left[\Phi_1(\mathbf{x},\mathbf{z}) - \dfrac{\Psi_1(\mathbf{x},\mathbf{z})\Phi_3(\mathbf{x},\mathbf{z})}{\Psi_3(\mathbf{x},\mathbf{z})}\right]\tau_1, \\ \dot{x}_3 = x_4, \\ \dot{x}_4 = \Upsilon_2(\mathbf{x},\mathbf{z}) + \dfrac{\Psi_2(\mathbf{x},\mathbf{z})\left[W(z_1,z_2) - \Upsilon_3(\mathbf{x},\mathbf{z})\right]}{\Psi_3(\mathbf{x},\mathbf{z})} \\ \quad + \left[\Phi_2(\mathbf{x},\mathbf{z}) - \dfrac{\Psi_2(\mathbf{x},\mathbf{z})\Phi_3(\mathbf{x},\mathbf{z})}{\Psi_3(\mathbf{x},\mathbf{z})}\right]\tau_1, \end{cases} \tag{13a}$$

$$\begin{cases} \dot{z}_1 = z_2, \\ \dot{z}_2 = W(z_1,z_2) = -r_2\left(z_2^{5/3} + r_1^{5/3}z_1\right)^{1/5}. \end{cases} \tag{13b}$$

It is clear that (13a) and (13b) are a nonlinear cascade system, and the state variable $\mathbf{z}$ is separated from others. According to the results in [30], the finite-time stabilization of subsystem (13b) at $\mathbf{z} = \mathbf{0}$ is achieved. As a result, system (13a) and (13b) becomes the following form in finite time

$$\begin{cases} \dot{x}_1 = x_2, \\ \dot{x}_2 = f_1(\mathbf{x}) + g_1(\mathbf{x})\tau_1, \\ \dot{x}_3 = x_4, \\ \dot{x}_4 = f_2(\mathbf{x}) + g_2(\mathbf{x})\tau_1, \end{cases} \tag{14}$$

where

$$\begin{aligned} f_1(\mathbf{x}) &= \frac{\Upsilon_1(\mathbf{x},\mathbf{0})\Psi_3(\mathbf{x},\mathbf{0}) - \Upsilon_3(\mathbf{x},\mathbf{0})\Psi_1(\mathbf{x},\mathbf{0})}{\Psi_3(\mathbf{x},\mathbf{0})}, \\ f_2(\mathbf{x}) &= \frac{\Upsilon_2(\mathbf{x},\mathbf{0})\Psi_3(\mathbf{x},\mathbf{0}) - \Upsilon_3(\mathbf{x},\mathbf{0})\Psi_2(\mathbf{x},\mathbf{0})}{\Psi_3(\mathbf{x},\mathbf{0})}, \\ g_1(\mathbf{x}) &= \frac{\Phi_1(\mathbf{x},\mathbf{0})\Psi_3(\mathbf{x},\mathbf{0}) - \Phi_3(\mathbf{x},\mathbf{0})\Psi_1(\mathbf{x},\mathbf{0})}{\Psi_3(\mathbf{x},\mathbf{0})}, \\ g_2(\mathbf{x}) &= \frac{\Phi_2(\mathbf{x},\mathbf{0})\Psi_3(\mathbf{x},\mathbf{0}) - \Phi_3(\mathbf{x},\mathbf{0})\Psi_2(\mathbf{x},\mathbf{0})}{\Psi_3(\mathbf{x},\mathbf{0})}. \end{aligned} \tag{15}$$

From (10), it is easy to obtain $g_1(\mathbf{x}) > 0$ for $\mathbf{x} \in \mathbb{R}^4$.

In fact, nonlinear system (14) is the zero dynamics of cascade system (13a) and (13b). In other words, (14) is a reduced-order system of the WAcrobot. The physical model of (12) is shown in Figure 2. In order to achieve the control objective of the WAcrobot, it is necessary to design a controller τ_1 such that system (14) is stabilized at $\mathbf{x} = \mathbf{0}$.

4. Design of the Stabilizing Controller for the Reduced-Order Model

This section discusses the design of a stabilizing controller τ_1 for reduced-order system (14) under the condition $\mathbf{z} = \mathbf{0}$.

Let $E(x) = \Xi(\theta, \dot{\theta})|_{\mathbf{z}=\mathbf{0}}$. From (1), (2), and (7), it is easy to get $E(0) = \beta_1 + \beta_2$ and $\dot{E}(x) = x_2\tau_1$. A Lyapunov function for system (14) is constructed to be

$$V(\mathbf{x}) = \frac{\mu_1}{2}\widehat{E}^2(\mathbf{x}) + \frac{\mu_2}{2}x_1^2 + \frac{\mu_3}{2}x_2^2, \tag{16}$$

where $\widehat{E}(\mathbf{x}) = E(x) - E(0)$ and $\mu_i > 0\,(i = 1, 2, 3)$ are constants. The derivative of $V(\mathbf{x})$ is

$$\begin{aligned} \frac{\mathrm{d}V(\mathbf{x})}{\mathrm{d}t} &= \mu_1\widehat{E}(\mathbf{x})\dot{E}(x) + \mu_2 x_1\dot{x}_1 + \mu_3 x_2\dot{x}_2 \\ &= \mu_1\widehat{E}(\mathbf{x})x_2\tau_1 + \mu_2 x_1 x_2 + \mu_3 x_2\left[f_1(\mathbf{x}) + g_1(\mathbf{x})\tau_1\right] \\ &= \left\{\left[\mu_1\widehat{E}(\mathbf{x}) + \mu_3 g_1(\mathbf{x})\right]\tau_1 + \mu_2 x_1 + \mu_3 f_1(\mathbf{x})\right\}x_2. \end{aligned} \tag{17}$$

We design the control law τ_1 to be

$$\tau_1 = \frac{-\gamma z_2 - \mu_2 x_1 - \mu_3 f_1(\mathbf{x})}{\mu_1\widehat{E}(\mathbf{x}) + \mu_3 g_1(\mathbf{x})}, \tag{18}$$

where $\gamma > 0$ is a constant. Combining (17) and (18) gives

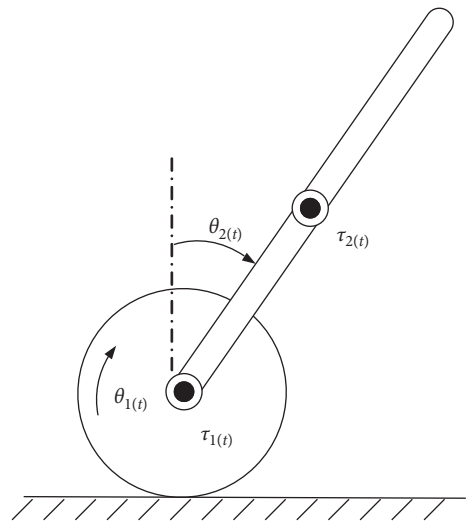

Figure 2: Physical model of (14).

$$\frac{\mathrm{d}V(\mathbf{x})}{\mathrm{d}t} = -\gamma x_2^2 \le 0. \tag{19}$$

From Figure 2, it is easy to deduce that system (14) has the same dynamic properties as the Pendubot. As a result, following the same analytical procedure given in Section 4 of [22] yields that $E(x) \longrightarrow E(0)$, $x_1 \longrightarrow 0$, and $x_2 \longrightarrow 0$ based on (16) and (19). This means that the control law (18) drives system (14) to converge the set

$$\begin{aligned} \Omega &= \{\mathbf{x} \mid x_1 = 0, x_2 = 0, E(x) = E(0)\} \\ &= \{\mathbf{x} \mid x_1 = 0, x_2 = 0, \omega(x_3, x_4) = 0\}, \end{aligned} \tag{20}$$

where

$$\omega(x_3, x_4) = M_{22}(0)x_4^2 - 2(\beta_1 + \beta_2)[1 - \cos x_3]. \tag{21}$$

Since $x_4 = \dot{x}_3$, we have that $\omega(x_3, x_4) = 0$ which describes a homoclinic orbit around $x_3 = x_4 = 0$. Thus, the state variable $\mathbf{x}$ in Ω can enter any arbitrarily small neighbourhood area of $\mathbf{x} = 0$. In this area, system (14) approximates the following linear system:

$$\dot{x} = A\mathbf{x} + B\tau_1, \tag{22}$$

where

$$\begin{aligned} A &= \begin{bmatrix} 0 & 1 & 0 & 0 \\ 0 & 0 & A_1 & 0 \\ 0 & 0 & 0 & 1 \\ 0 & 0 & A_2 & 0 \end{bmatrix}, \\ B &= \begin{bmatrix} 0 \\ B_1 \\ 0 \\ B_2 \end{bmatrix}, \end{aligned} \tag{23}$$

where

$$A_1 = \left.\frac{\partial f_1(\mathbf{x})}{\partial x_3}\right|_{\mathbf{x}=\mathbf{0}} = \frac{a_1c_3 - a_3c_1}{c_3},$$
$$A_2 = \left.\frac{\partial f_2(\mathbf{x})}{\partial x_3}\right|_{\mathbf{x}=\mathbf{0}} = \frac{a_2c_3 - a_3c_2}{c_3},$$
$$B_1 = g_1(\mathbf{x})\big|_{\mathbf{x}=\mathbf{0}} = \frac{b_1c_3 - b_3c_1}{c_3},$$
$$B_2 = g_2(\mathbf{x})\big|_{\mathbf{x}=\mathbf{0}} = \frac{b_2c_3 - b_3c_2}{c_3}, \tag{24}$$
$$U = \begin{bmatrix} a_1 & b_1 & c_1 \\ a_2 & b_2 & c_2 \\ a_3 & b_3 & c_3 \end{bmatrix} = M^{-1}(\mathbf{0}) \begin{bmatrix} 0 & 1 & 0 \\ \beta_1 + \beta_2 & 0 & 0 \\ \beta_2 & 0 & 1 \end{bmatrix}.$$

Let $\Lambda = [B, AB, A^2B, A^3B]$. It is easy to obtain

$$\det[\Lambda] = B_2^2[A_2B_1 - A_1B_2]^2 = \frac{(b_2c_3 - b_3c_2)^2 \det^2[\Lambda]}{c_3^4}. \tag{25}$$

Since $M^{-1}(\mathbf{0})$ is a positive definite matrix, it follows from (24) that $c_3 > 0, \det[U] \neq 0$, and $b_2c_3 - b_3c_2 \neq 0$. From (25), we have $\det[\Lambda] > 0$. As a result, linear time-invariant system (22) is controllable. So, the following Riccati matrix equation has a positive definite solution P:

$$A^\top P + PA - PBR^{-1}B^\top P = -Q, \tag{26}$$

where $R > 0$ and $Q \in \mathbb{R}^{4\times 4}$ is a positive definite matrix. From the quadratic optimal control theory, the control law

$$\tau_1 = -R^{-1}B^\top P, \tag{27}$$

stabilizes linear system (22) at $\mathbf{x} = \mathbf{0}$ quickly.

From the above statements, we get that the use of the control law τ_1 in (18) and (27) in sequence guarantees the global stabilization of reduced-order system (14) at $\mathbf{x} = \mathbf{0}$.

Remark 1. Note that the control law τ_1 in (18) is singular when $\mu_1\widehat{E}(\mathbf{x}) + \mu_3 g_1(\mathbf{x}) = 0$. This case occurs only when $E(x) < E(0)$ (i.e., $\widehat{E}(\mathbf{x}) < 0$) because $\mu_1 > 0$, $\mu_3 > 0$, and $g_1(\mathbf{x}) > 0$. When $E(x) < E(0)$, it follows from (1) and (2) that

$$0 > \widehat{E}(\mathbf{x}) \geq (\beta_1 + \beta_2)\cos x_2 - E(0) \geq -2E(0). \tag{28}$$

So, we have

$$\mu_1\widehat{E}(\mathbf{x}) + \mu_3 g_1(\mathbf{x}) \geq \mu_3 g_1(\mathbf{x}) - 2\mu_1 E(0). \tag{29}$$

From (29), it is easy to obtain that the singularity of τ_1 in (18) does not occur if

$$\mu_3 g_1(\mathbf{x}) - 2\mu_1 E(0) > 0. \tag{30}$$

We select the control parameters such that

$$\mu_3 > \frac{2\mu_1 E(0)}{\rho},$$
$$\rho = \min\{g_1(\mathbf{x})\}. \tag{31}$$

This condition guarantees (30) to hold. In other words, the control law in (18) is not singular under condition (31).

Remark 2. There are eight control parameters in this paper, i.e., r_1 and r_2 in (12); μ_1, μ_2, and μ_3 in (16); γ in (19); and R and Q in (26). In order to make the control design process clear, a selected guideline for these parameters is given as follows:

(1) An optimal set of r_1 and r_2 is selected for (12) that makes the stabilization time of (13b) to be smallest

(2) For fixed γ, a set of μ_1, μ_2, and μ_3 is chosen to make reduced-order system (14) enter an arbitrarily small neighbourhood area of $\mathbf{x} = 0$

(3) A set of R and Q is selected for the control law τ_1 that stabilizes system (22) at the origin

5. Numerical Example

A numerical example is presented in this section in order to verify the validity of our presented theoretical results. In the simulation experiment, the physical parameters of the WAcrobot were chosen to be [29]

$$\begin{cases} m_1 = 1.22\,\text{kg}, \\ m_2 = 0.28\,\text{kg}, \\ m_3 = 0.72\,\text{kg}, \\ L_1 = 0.05\,\text{m}, \\ L_2 = 0.15\,\text{m}, \\ L_3 = 0.45\,\text{m}, \\ L_{c2} = 0.075\,\text{m}, \\ L_{c3} = 0.225\,\text{m}, \\ J_1 = 0.00153\,\text{kg}\cdot\text{m}^2, \\ J_2 = 0.000598\,\text{kg}\cdot\text{m}^2, \\ J_3 = 0.013138\,\text{kg}\cdot\text{m}^2. \end{cases} \tag{32}$$

The initial condition was selected to be

$$\left[\theta_1, \theta_2, \theta_3, \dot{\theta}_1, \dot{\theta}_2, \dot{\theta}_3\right]^\top = [0, \pi, 0, 0, 0, 0.1]^\top. \tag{33}$$

The physical meaning of (33) is that the double inverted pendulum of the WAcrobot begins to move from the straight-down position with a small velocity, while the wheel is stationary at the origin. The control parameters in (12) were selected to be $r_1 = 1$ and $r_2 = 5$. The simulation results of subsystem (13b) are shown in Figure 3. Note that θ_3 and $\dot{\theta}_3$ converge to zero in 0.25 seconds. It means that WAcrobot system (8) changes to reduced-order system (14) quickly. This demonstrates the validity of the presented theoretical results in Section 3.

To show the validity of the stabilizing controller for reduced-order model (14), the parameters in (16) and (18) were chosen as

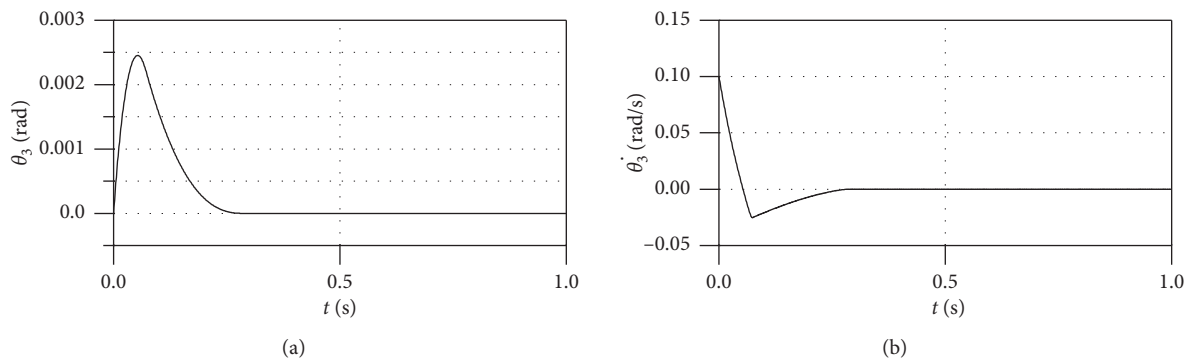

Figure 3: Time response of θ_3 and $\dot{\theta}_3$ with $r_1 = 1$ and $r_2 = 5$ in (13b).

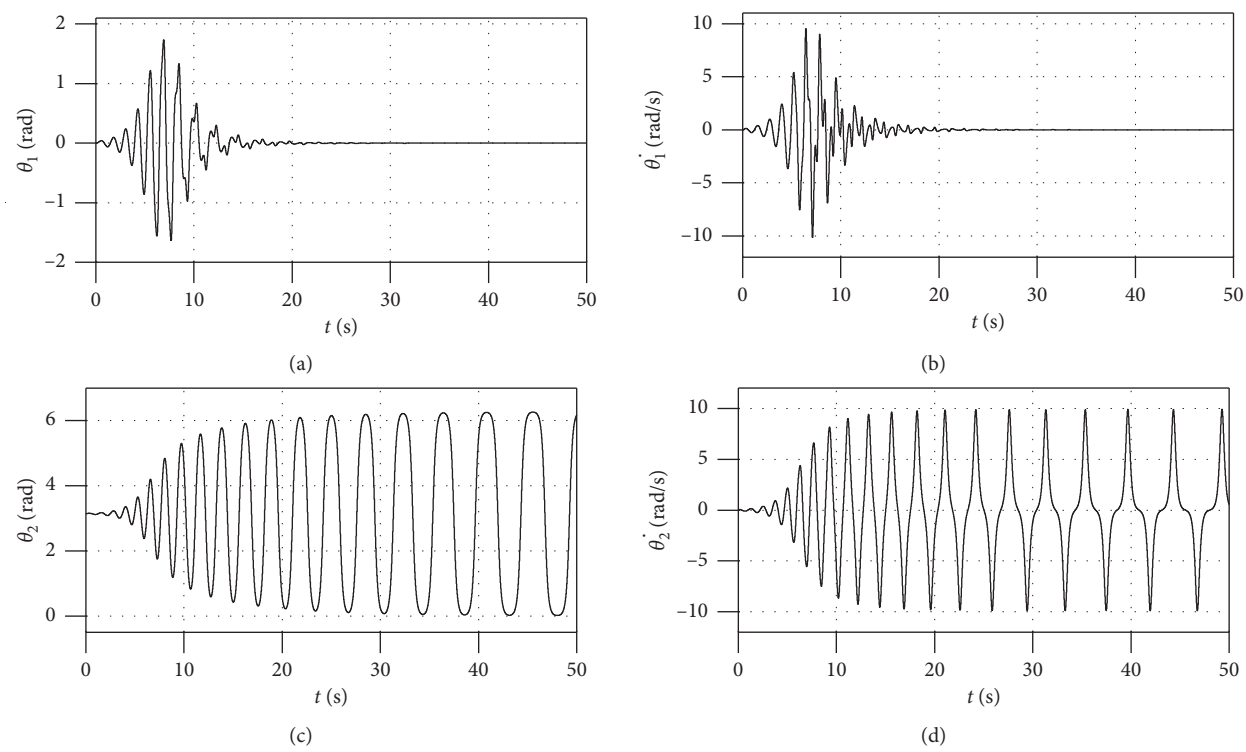

Figure 4: Time response of θ_1, $\dot{\theta}_1$, θ_2, and $\dot{\theta}_2$ by controllers (11) and (18).

$$\begin{cases} \mu_1 = 350, \\ \mu_2 = 200, \\ \mu_3 = 15, \\ \gamma = 50, \\ R = 0.5, \\ Q = 0.01 I_4, \end{cases} \tag{34}$$

where I_4 is a 4×4 identity matrix. A simple calculation gives $\rho = 141.25$ and $2\mu_1 E(0)/\rho = 14.147$. Thus, condition (31) is satisfied. Figure 4 shows the simulation results for $\mathbf{x}(t)$ by controllers (11) and (18). It is clear that θ_1 and $\dot{\theta}_1$ are stabilized at zero while θ_2 and $\dot{\theta}_2$ are in a homoclinic orbit. This shows the validity of the theoretical results in Section 4.

When $\mathbf{x}(t)$ enters the small neighbourhood area of $\mathbf{x}(\mathbf{t}) = 0$ at $t = 30$ s, the controller τ_1 switches to (27) from (18). The simulation results of controllers and $\mathbf{x}(t)$ are shown in Figures 5 and 6, respectively. Note that the switch of τ_1 from (18) to (27) causes small sudden changes in θ_1 and $\dot{\theta}_1$ at $t = 30$ s. Moreover, it is clear that the WAcrobot can be quickly stabilized at the origin in 40 seconds, and the maximal value of inputs is less than 1.1 Nm. Compared with the results in [29], the value of inputs in this paper is more smaller, and the motion process of the WAcrobot system is more smooth and natural. This provides guarantee for the safe and stable operation of the control system. All these

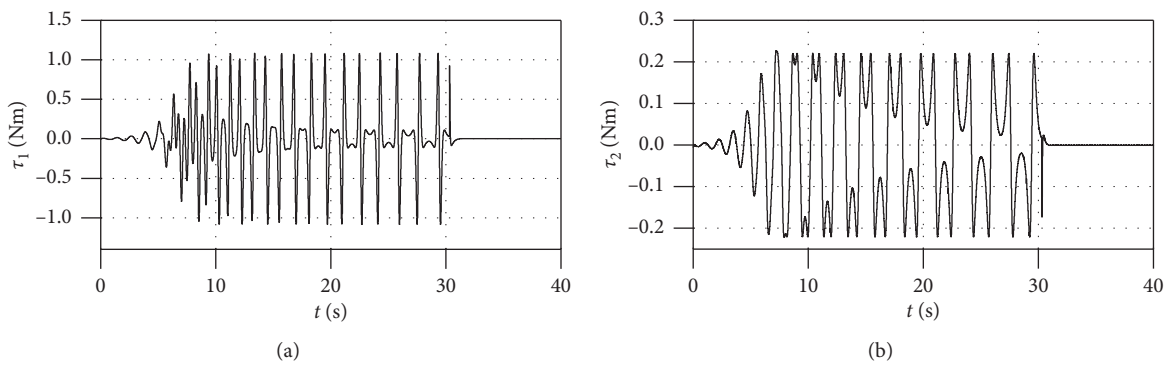

Figure 5: Time response of τ_1 and τ_2.

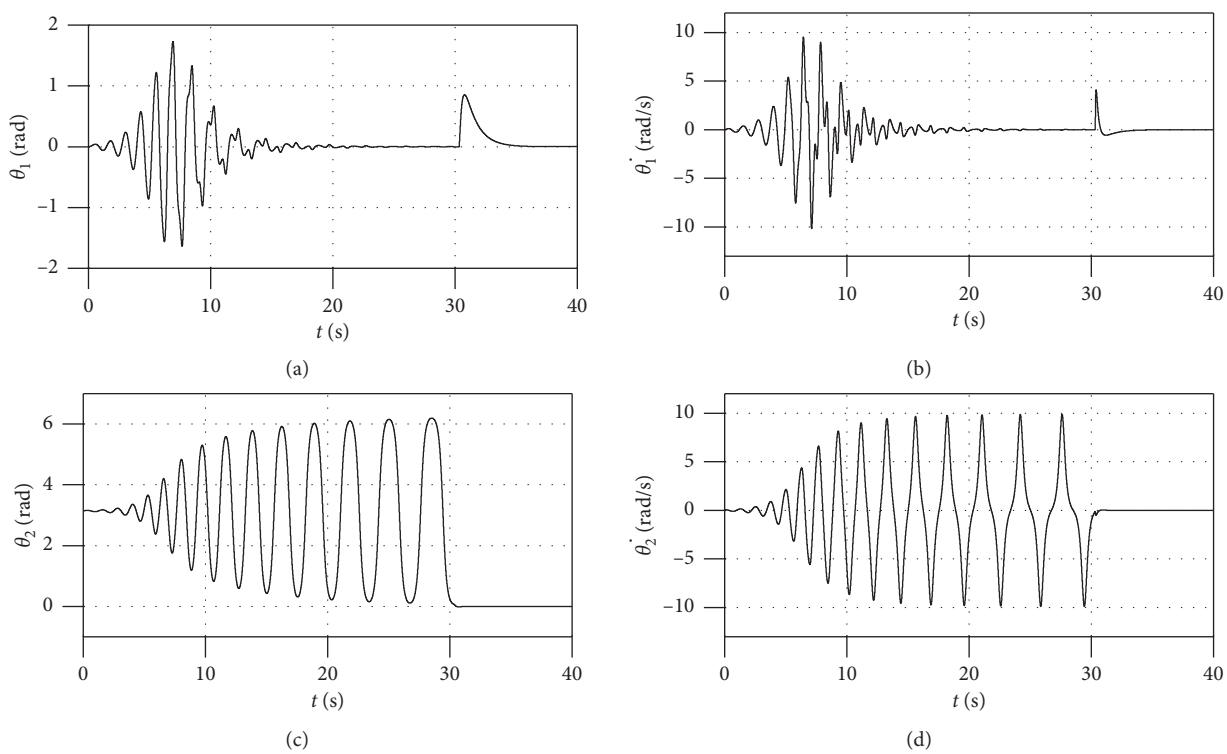

Figure 6: Time response of θ_1, $\dot{\theta}_1$, θ_2, and $\dot{\theta}_2$ by controllers (11), (18), and (27).

demonstrate the advantages of our presented control strategy.

6. Conclusion

This paper addressed the global stabilization of a 3-DOF underactuated WAcrobot system. A novel stabilizing control strategy was developed. First, the 3-DOF WAcrobot was changed to be a 2-DOF reduced-order model in finite time. This makes the stabilizing control of the WAcrobot be easy to handle. And then, the stabilizing control laws were designed that globally stabilize the reduced-order system at the origin. And the condition that avoids the singularity in the stabilizing control law was also presented. Finally, the numerical simulation example showed the validity of the proposed theoretical results. In the future, we will extend the new strategy to the stabilization of other multi-DOF underactuated systems [31] and will also further explore other stabilizing control methods for the WAcrobot system.

Data Availability

The data used to support the findings of this study are available from the corresponding author upon request.

Conflicts of Interest

The authors declare that they have no conflicts of interest.

Acknowledgments

This work was supported in part by the Natural Science Foundation Program of Shandong Province under Grant no.

ZR2019YQ28, the Development Plan of Youth Innovation Team of University in Shandong Province under Grant no. 2019KJN007, and the National Natural Science Foundation of China under Grant nos. 61773193, 61703194, 61803194, and 61903171.

References

[1] P. Zhao, D.-H. Zhai, Y. Sun, and Y. Li, "Adaptive finite-time control of a class of Markovian jump nonlinear systems with parametric and dynamic uncertainties," *Nonlinear Analysis: Hybrid Systems*, vol. 29, pp. 234–246, 2018.

[2] C. Jiang, F. Zhang, and T. Li, "Synchronization and anti-synchronization of *N*-coupled fractional-order complex chaotic systems with ring connection," *Mathematical Methods in the Applied Sciences*, vol. 41, no. 7, pp. 2625–2638, 2018.

[3] X. Yi, R. Guo, and Y. Qi, "Stabilization of chaotic systems with both uncertainty and disturbance by the UDE-based control method," *IEEE Access*, vol. 8, pp. 62471–62477, 2020.

[4] H. Chen and N. Sun, "Nonlinear control of underactuated systems subject to both actuated and unactuated state constraints with experimental verification," *IEEE Transactions on Industrial Electronics*, vol. 67, no. 9, pp. 7702–7714, 2019.

[5] N. Sun, D. Liang, Y. Wu, Y. Chen, Y. Qin, and Y. Fang, "Adaptive control for pneumatic artificial muscle systems with parametric uncertainties and unidirectional input constraints," *IEEE Transactions on Industrial Informatics*, vol. 16, no. 2, pp. 969–979, 2020.

[6] N. Sun, Y. Fu, T. Yang, J. Zhang, Y. Fang, and X. Xin, "Nonlinear motion control of complicated dual rotary crane systems without velocity feedback: design, analysis, and hardware experiments," *IEEE Transactions on Automation Science and Engineering*, vol. 17, no. 2, pp. 1017–1029, 2020.

[7] Y. Liu and H. Yu, "A survey of underactuated mechanical systems," *IET Control Theory & Applications*, vol. 7, no. 7, pp. 921–935, 2013.

[8] W. Chen, C. Xiong, W. Chen, and S. Yue, "Mechanical adaptability analysis of underactuated mechanisms," *Robotics and Computer-Integrated Manufacturing*, vol. 49, pp. 436–447, 2018.

[9] M. Abdeetedal and M. R. Kermani, "Grasp and stress analysis of an underactuated finger for proprioceptive tactile sensing," *IEEE/ASME Transactions on Mechatronics*, vol. 23, no. 4, pp. 1619–1629, 2018.

[10] G. Oriolo and Y. Nakamura, "Control of mechanical systems with second-order nonholonomic constraints: underactuated manipulators," in *Proceedings of the 30th IEEE Conference on Decision and Control*, pp. 2398–2403, Brighton, UK, December 1991.

[11] Y. Wang, X. Lai, P. Zhang, and M. Wu, "Adaptive robust control for planar *n*-link underactuated manipulator based on radial basis function neural network and online iterative correction method," *Journal of the Franklin Institute*, vol. 355, no. 17, pp. 8373–8391, 2018.

[12] X. Xin, "Linear strong structural controllability and observability of an n-link underactuated revolute planar robot with active intermediate joint or joints," *Automatica*, vol. 94, pp. 436–442, 2018.

[13] N. Sun, Y. Wu, H. Chen, and Y. Fang, "Antiswing cargo transportation of underactuated tower crane systems by a nonlinear controller embedded with an integral term," *IEEE Transactions on Automation Science and Engineering*, vol. 16, no. 3, pp. 1387–1398, 2019.

[14] A. Zhang, J. She, J. Qiu, C. Yang, and F. Alsaadi, "Design of motion trajectory and tracking control for underactuated cart-pendulum system," *International Journal of Robust Nonlinear Control*, vol. 29, no. 9, pp. 2458–2470, 2019.

[15] S. Roy and S. Baldi, "Towards structure-independent stabilization for uncertain underactuated Euler-Lagrange systems," *Automatica*, vol. 113, Article ID 108775, 2020.

[16] X. Lai, Z. Cai, J.-H. She, and Y. Ohyama, "Fuzzy control strategy for acrobots combining model-free and model-based control," *IEE Proceedings—Control Theory and Applications*, vol. 146, no. 6, pp. 505–510, 1999.

[17] X. Xin, S. Tanaka, J. She, and T. Yamasaki, "New analytical results of energy-based swing-up control for the Pendubot," *International Journal of Non-linear Mechanics*, vol. 52, pp. 110–118, 2013.

[18] M. Jankovic, D. Fontaine, and P. V. Kokotovic, "TORA example: cascade- and passivity-based control designs," *IEEE Transactions on Control Systems Technology*, vol. 4, no. 3, pp. 292–297, 1996.

[19] D. Gutirrez, H. Rłos, J. A. Rosales, and R. Galvn-Guerra, "Finite and fixed-time state estimation: pendulum-cart system," *IFAC-PapersOnLine*, vol. 50, no. 1, pp. 7139–7144, 2017.

[20] M. Spong, "The swing up control problem for the acrobot," *IEEE Control Systems Magazine*, vol. 15, no. 1, pp. 44–55, 1995.

[21] X. Xin and M. Kaneda, "Analysis of the energy-based swing-up control of the Acrobot," *International Journal of Robust and Nonlinear Control*, vol. 17, no. 16, pp. 1503–1524, 2007.

[22] X. Lai, J. She, S. Yang, and M. Wu, "Comprehensive unified control strategy for underactuated two-link manipulators," *IEEE Transactions on Systems Man and Cybernetics Part B*, vol. 39, no. 2, pp. 389–398, 2009.

[23] J. She, A. Zhang, X. Lai, and M. Wu, "Global stabilization of 2-DOF underactuated mechanical systemsłan equivalent-input-disturbance approach," *Nonlinear Dynamics*, vol. 69, no. 1-2, pp. 495–509, 2012.

[24] A. Zhang, X. Lai, M. Wu, and J. She, "Stabilization of underactuated two-link gymnast robot by using trajectory tracking strategy," *Applied Mathematics and Computation*, vol. 253, pp. 193–204, 2015.

[25] X. Xin and M. Kaneda, "Swing-up control for a 3-DOF gymnastic robot with passive first joint: design and analysis," *IEEE Transactions on Robotics*, vol. 23, no. 6, pp. 1277–1285, 2007.

[26] A. Zhang, X. Lai, M. Wu, and J. She, "Global stabilization of underactuated spring-coupled three-link horizontal manipulator using position measurements only," *Applied Mathematical Modelling*, vol. 39, no. 7, pp. 1917–1928, 2015.

[27] Q. Yang and R. Yang, "Nonsingular terminal sliding mode based passive fault-tolerant control of a 3-DOF helicopter system," *IFAC-PapersOnLine*, vol. 51, no. 24, pp. 1368–1372, 2018.

[28] L. Scalera, A. Gasparetto, and D. Zanotto, "Design and experimental validation of a 3-DOF underactuated pendulum-like robot," *IEEE/ASME Transactions on Mechatronics*, vol. 25, no. 1, pp. 217–228, 2020.

[29] M. M. Dalvand, B. Shirinzadeh, and S. Nahavandi, "Swing-up and stability control of wheeled Acrobot (WAcrobot)," *Automatika*, vol. 55, no. 1, pp. 32–40, 2014.

[30] G. He and Z. Geng, "Finite-time stabilization of a comb-drive electrostatic microactuator," *IEEE/ASME Transactions on Mechatronics*, vol. 17, no. 1, pp. 107–115, 2012.

[31] D. Liu, X. Lai, Y. Wang, X. Wan, and M. Wu, "Position control for planar four-link underactuated manipulator with a passive third joint," *ISA Transactions*, vol. 87, pp. 46–54, 2019.

Hindawi
Mathematical Problems in Engineering
Volume 2020, Article ID 6761383, 10 pages
https://doi.org/10.1155/2020/6761383

Research Article

Pressure Control of High-Pressure Oil Pipe

Wenrui Qu,[1] **Lei Liu**,[1] **and Qun Zhao**[2]

[1]*School of Mathematics and Statistics, Qilu University of Technology (Shandong Academy of Sciences), University Road 3501, Changqing District, Jinan, Shandong Province, China*
[2]*Department of Transportation Studies, Texas Southern University, 3100 Cleburne Street, Houston, Texas 77004, USA*

Correspondence should be addressed to Qun Zhao; qun.zhao@tsu.edu

Received 23 April 2020; Accepted 30 May 2020; Published 29 June 2020

Guest Editor: Ping Zhao

In this paper, to realize the pressure stability control of high-pressure oil pipe, the dynamic differential equation of fuel oil inlet and outlet is established based on the theory of mass conservation. According to the change of the pressure in the high-pressure tubing, an optimization model is established to achieve precise control of the working time of each part of the high-pressure oil pipe.

1. Introduction

Fuel entering and ejecting high-pressure fuel pipe is the basis of many fuel engines. When the high-pressure fuel system is working, fuel enters the high-pressure fuel pipe from the oil inlet valve and then ejects from the fuel injector at the other end. The intermittent working process of fuel entering and ejecting will lead to the change of the pressure in the high-pressure oil pipe, which will cause the deviation of the quantity of fuel ejected, thus affect the working efficiency of the engine, and even cause the direct economic loss due to the fault [1, 2]; therefore, it is of great significance to reasonably control the pressure of the high-pressure oil pipe so as to stabilize the pressure in the pipe.

In this paper, a dynamic differential equation of fuel oil inlet and outlet is established based on the theory of mass conservation and a Matlab visual simulation tool is developed. To be more specific, three questions are answered: (1) How to determine the oil supply time of the one-way oil inlet valve? (2) How to determine cam angular velocity? (3) How to adjust the oil supply strategy if adding another injection nozzle?

The following example is used to illustrate the model development and problem-solving process. Figure 1 is the structure of a high-pressure oil pipe. As shown in the picture, the length of the inner cavity of the high-pressure oil pipe is 500 mm, the inner diameter is 10 mm, and the diameter of the small hole A at the oil supply inlet is 1.4 mm.

The oil supply time is controlled by the one-way valve switch, which closes for 10 ms after each opening. The injector works 10 times per second, and the injection time is 2.4 ms each time. When the injector is working, the injection rate from nozzle B to the outside is shown in Figure 2. The pressure provided by the high-pressure oil pump at inlet A is 160 MPa, and the initial pressure in the high-pressure oil pipe is 100 MPa.

2. Literature Review

To solve the pressure control problem of high-pressure oil pipe, He et al. [3] used differential equations and improved continuous differential equation theory to develop a cam angular velocity determination model, a one-way valve control model based on piecewise function fitting and continuous differential equations. In their study, the pressure change in the pipe during the working process of the system was ignored. Lu et al. [4] established a difference equation model to replace the differential equation description, avoided the derivative function in the equation, and solved it in an iterative method, but the accuracy of their model was not as high as that of the differential equation model. Zhang et al. [5] conducted a detailed analysis and

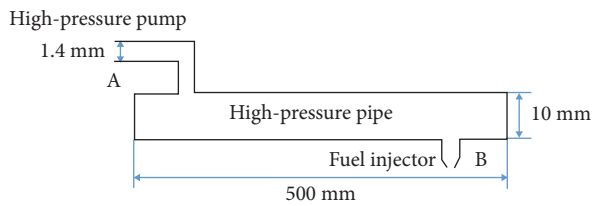

Figure 1: Schematic diagram of the high-pressure oil pipe.

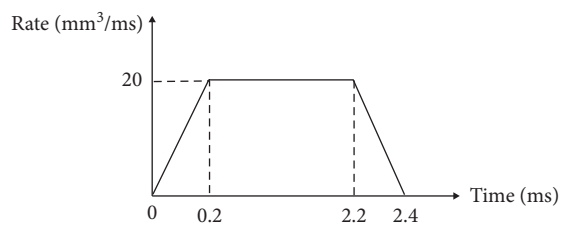

Figure 2: Schematic diagram of injection rate.

discussion on how to improve the working efficiency of the system by establishing the simulation mathematical model. However, they did not consider the dynamic process of quality change in the injection process. Wang et al. [6] established the optimization model and solution method of cam speed. However, in their results, the pressure in the tube fluctuated greatly. Zhu [7] used the iterative method to solve the problem. The method is universal, which can not only solve the stable state, but also solve the pressure rise in the high-pressure oil pipe. However, it requires to be able to calculate the state data of each end point of the system, and the iterative algorithm is sometimes not conducive to the solution of the computer. Cai et al. [8] analyzed the control scheme of oil injection strategy from a macro perspective, combined with the data results of two different high-pressure tubing models. The proposed pressure control scheme of high-pressure tubing can meet the requirements of different parameters and performance of different high-pressure tubing and can make the pressure in the high-pressure tubing stable, but considering many factors, it is cumbersome.

In this paper, an algorithm based on the differential equation, optimization model, and simulation model was developed. This algorithm can minimize pressure fluctuations and make the solution more accurate.

3. Symbols and Assumptions

In order to facilitate the study of the problem and simplify the process of solution, some symbols are uniformly defined and assumptions are made which are consistent with the actual situation.

3.1. Symbols. The symbols and their explanation are provided in Table 1.

3.2. Assumptions

(1) The pressure in the high-pressure oil pipe is uniform, regardless of the viscous resistance of the oil

(2) The influence of the change of fuel temperature on the model during the operation of the high-pressure oil pipe is not considered

(3) There will be no fuel leakage in the whole working system

(4) The one-way valve and oil nozzle both work properly

(5) The working condition of the oil nozzle has nothing to do with its position

(6) The opening and closing of the valve are completed instantaneously

4. Model 1: Dynamic Differential Equation Model

4.1. Problem 1: How to Determine the Oil Supply Time of the One-Way Oil Inlet Valve? The pressure of oil pipe in unit time is determined by the quantity of oil in Q_A and the quantity of oil out Q_B. According to the given conditions, the functions of the quantity of oil in and out at time t, the density ρ of oil, and the internal pressure P_2 are obtained. Based on the given relationship between the injection rate and time at the fuel injector B, the quantity of oil injected Q_B can be calculated. Finally, the dynamic pressure equation in the high-pressure oil pipe is established and solved according to the quantity of oil in and out. In this paper, the work of high-pressure oil pipe is divided into adjustment state and stable state. In the adjustment state, the internal air pressure reaches 150 MPa by adjusting the opening time of the one-way valve, and then it enters the stable state; i.e., the amount of oil flowing in and out within a working cycle satisfies the dynamic equation of the high-pressure oil pipe.

4.2. Model Preparation. According to the speed of the oil supply end and the oil outlet end about time t, the differential dynamic equilibrium equation is established to solve problem 1.

To unify the dimension in the calculation and derivation process, the following conversion formulas are used to convert the unit:

Unit conversion: $1\,\text{s} = 1 \times 10^3\,\text{ms}$, $1\,\text{m} = 1 \times 10^3\,\text{mm}$, $1\,\text{MPa} = 1 \times 10^6\,\text{Pa}$

Circle area formula: $s = \pi r^2 = \pi (d/2)^2$

Column volume formula: $V = \pi r^2 h$

4.3. Model Establishment. When the pressure in the pipe is stable at 100 MPa, the dynamic differential equation model was developed following the three steps:

Step 1. Calculate the quantity of oil Q_A flowing into oil supply end A.

According to the flow formula, the oil supply quantity is calculated:

$$Q_A = CA\sqrt{\frac{2\Delta P}{\rho}} = CA\sqrt{\frac{2}{\rho}(P1 - P2)}, \tag{1}$$

Table 1: Symbols and explanation.

Symbol	Explanation	Unit
Q_A	The oil supply quantity at the oil supply end A in t time	m^3/s
Q_B	Output of fuel injection end in one injection time	m^3/s
ρ	Density of fuel	mg/mm^3
A	The area of the small circular hole area	m^2
E	Modulus of elasticity	
P_1	Supply end pressure	Pa
P_2	Total volume of high-pressure oil pipe	Pa
$P(t)$	Pressure variation function in tube	Pa
V	Internal pressure of high-pressure oil pipe	m^3
T	One working cycle of high-pressure oil pump	s

where flow coefficient $C = 0.85$ and the area of the hole $A = \pi r^2 = \pi (d/2)^2 = 3.14 \times ((1.4 \times 10^{-3})/2)^2 = 1.5386 \times 10^{-6}\,\mathrm{m}^2$

According to the data that indicates the relationship between the elastic modulus E and pressure, by using the polyfit function in Matlab to fit a 3th-degree polynomial, the function of elastic modulus on pressure can be obtained:

$$E(P) = aP^3 + bP^2 + cP + d. \tag{2}$$

Then, based on the fact that the pressure change of fuel is proportional to the density change and the ratio coefficient is E/ρ, the function between density and the change of pressure can be derived; that is,

$$\Delta P = \frac{E}{\rho}\Delta\rho\,\mathrm{m}^3/\mathrm{s}. \tag{3}$$

The simplified expression is

$$\Delta P = \int_{P_1}^{P} \frac{\mathrm{d}P}{E} = \ln\frac{\rho_1}{\rho_0}\,\mathrm{m}^3/\mathrm{s}. \tag{4}$$

To sum up, within the time period T, the quantity of oil supply can be expressed as

$$Q_A = \begin{cases} CA\sqrt{\dfrac{2}{\rho}(P_1 - P_2)}, & 0 \le t < T, \\ 0, & T \le t \le T + 0.01. \end{cases} \tag{5}$$

Step 2. Calculate the oil output Q_B at the oil injection end B.

According to the graph of oil injection rate and time, as shown in Figure 2, the resolution function corresponding to each segment is calculated separately to obtain the flow velocity function at the injection end:

$$V_B = \begin{cases} q_1 = 0.1t, & 0 \le t < 0.0002, \\ q_2 = 2 \times 10^{-5}, & 0.0002 \le t < 0.0022, \\ q_3 = 2 \times 10^{-5} - 1 \times 10^{-4}(t - 2.2), & 0.0022 \le t < 0.0024, \\ 0, & 0.0024 \le t < 0.1. \end{cases} \tag{6}$$

According to the integration of time t, the outflow volume in one injection process is

$$Q_B = \int (q_1 + q_2 + q_3)\mathrm{d}t. \tag{7}$$

Step 3. Establish the dynamic pressure equation in the high-pressure oil pipe.

Based on the quantity of oil in and out, the dynamic pressure equation in the high-pressure oil pipe can be expressed as

$$P = \int \frac{E}{V}(Q_A - Q_B), \tag{8}$$

where $V = \pi r^2 h = 3.14 \times ((1 \times 10^{-2})/2)^2 \times 0.5 = 3.925 \times 10^{-5}\,\mathrm{m}^3$.

By fitting the search function, the change of P is ensured to be as small as possible so that the pressure in the high-pressure tubing is maintained at about 100 MPa.

When the pressure in the pipe increases to 150 MPa, the working state of high-pressure oil pipe can be divided into adjustment state and stable state. In the adjustment state, the opening time of one-way valve is adjusted by time T_1 (2 s, 5 s, 10 s); after T_1 period, the pressure in the oil pipe reaches 150 MPa. Set the opening time of the valve at the oil supply end as T_0; we can get $Q_{A1} \cdot T_0 + Q_0 = Q_1 - Q_B \cdot T_1$.

Then, formula (5) is improved to

$$Q_{A1} = \begin{cases} CA\sqrt{\dfrac{2}{\rho}(P_1 - P_2)}, & 0 \le t < T_0, \\ 0, & T_0 \le t \le T_1. \end{cases} \tag{9}$$

Finally, the high-pressure oil pipe enters the next working state. In the stable state, the working principle of the tubing is similar to the previous analysis. Based on the quantity of oil in and out, the dynamic pressure equation in the high-pressure pipe is established as follows:

$$P = \int \frac{E}{V}(Q_{A2} - Q_B), \tag{10}$$

$$Q_{A2} = \begin{cases} CA\sqrt{\frac{2}{\rho}(P_1 - P_2)}, & T_1 \le t < T, \\ 0, & T \le t \le T + 0.01. \end{cases} \tag{11}$$

By fitting the search function, the change is kept as small as possible so that the pressure in the high-pressure tubing is maintained at about 150 MPa:

$$\begin{aligned} T &= 2\,\text{s}: P(t) = 100 + 0.025t, \\ \rho(t) &= 0.85 + 4.34 \times 10^{-4}t, \\ T &= 5\,\text{s}: P(t) = 100 + 0.01t, \\ \rho(t) &= 0.85 + 1.74 \times 10^{-4}t, \\ T &= 10\,\text{s}: P(t) = 100 + 0.005t, \\ \rho(t) &= 0.85 + 8.68 \times 10^{-5}t. \end{aligned} \tag{12}$$

The equation is established by converting the pressure difference into the mass difference:

$$\Delta m = m_A - m_B, \tag{13}$$

where

$$m_A = \rho \int_0^T CA\sqrt{\frac{2(160 - P(t))}{\rho_{160}}}\mathrm{d}t. \tag{14}$$

It can be seen that the opening time of the oil pipe is reduced when the pressure in the pipe increases from 100 MPa to 150 MPa.

4.4. Problem Solving

Step 1. The elastic modulus E is fitted by the third-order function (2) of the *polyfit* function in Matlab, and the fitting error is analyzed.

The functional relationship between the elastic modulus and the pressure is obtained:

$$\begin{aligned} E(P) = {} & 1.00037752 \times 10^{-4}P^3 - 1.082481397 \times 10^{-3}P^2 \\ & + 5.474444341310P + 1.531868405848778 \times 10^3. \end{aligned} \tag{15}$$

Figure 3 shows a comparison between the fitting curve and the given data.

It can be seen from the fitting comparison chart that the fitting curve has a high degree of agreement with the original data set, and the cubic fitting effect is good, which can accurately describe the functional relationship between elastic modulus E and pressure P.

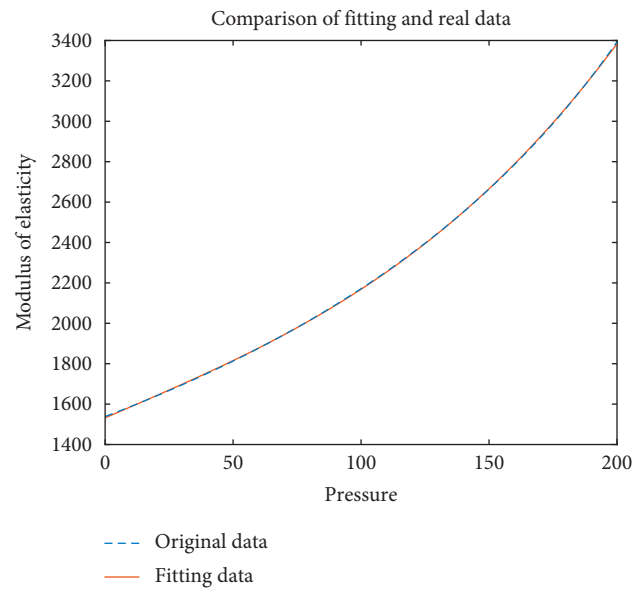

Figure 3: Comparison between the fitting curve and original data.

Step 2. Calculation of oil output Q_B.

The flow rate function integrates the time t to obtain the outflow of the primary injection process 2.4×10^{-3} s:

$$\begin{aligned} Q_B &= \int (q_1 + q_2 + q_3)\mathrm{d}t, \\ &= \int_0^{0.0002} 0.1t\,\mathrm{d}t + \int_{0.0002}^{0.0022} 2 \times 10^{-5}\,\mathrm{d}t \\ &\quad + \int_{0.0022}^{0.0024} 2 \times 10^{-5} - 1 \times 10^{-4}(t - 2.2)\,\mathrm{d}t, \\ &= 4.4 \times 10^{-8}\,\mathrm{m}^3/\mathrm{s}. \end{aligned} \tag{16}$$

Step 3. Bring in dynamic pressure equation (10), and the following results are obtained:

$$\begin{aligned} P = 1 \times 10^8 &= \int \frac{E}{V}(Q_A - Q_B)\mathrm{d}t \\ &= \int \frac{E(1 \times 10^8)}{3.925 \times 10^{-5}}\left(Q_A - 4.4 \times 10^{-8}\right)\mathrm{d}t. \end{aligned} \tag{17}$$

With Matlab, it could be found that $T = 3.06$ ms, which means when the opening time of one-way valve is 3.06 ms, the pressure in the high-pressure oil pipe could be stable at 100 MPa.

Step 4. When the pressure in the high-pressure oil pipe is stable at 150 MPa, if working process of the high-pressure oil pump is divided into the adjustment stage and the balance stage, then the working rules of the oil pump under the three adjustment stages are as follows:

The adjustment process is as follows:

$$T_2 = \begin{cases} 0.898\,\text{ms/time} & t \in [0, 2] \\ 0.761\,\text{ms/time} & t \in (2, \infty) \end{cases}$$

The adjustment process is as follows: $T_5 = \begin{cases} 0.752\,\text{ms/time} & t \in [0,5] \\ 0.761\,\text{ms/time} & t \in (5,\infty) \end{cases}$

The adjustment process is as follows: $T_{10} = \begin{cases} 0.532\,\text{ms/time} & t \in [0,10] \\ 0.761\,\text{ms/time} & t \in (10,\infty) \end{cases}$

To sum up, see Table 2 for the adjustment scheme of three times. It can be seen that when the adjustment process is 2 s, the opening time of high-pressure oil pump is 0.898 ms each time within 0–2 s, and when it reaches a stable state after 2 s, the single opening time of oil pump is 0.761 ms.

5. Model 2: Dynamic Pressure Model of Liquid Mass

5.1. Problem 2: How to Determine Cam Angular Velocity? When the pressure and other factors change, the constant is the quality of the liquid in the fuel supply end and the quality of the liquid out of the fuel injection end. In a working cycle of the high-pressure oil pipe system, in order to maintain the stability of the pressure in the pipe, the quality of the fuel in and out is equal.

For problem 2, the fuel supply end compresses the low-pressure fuel oil by the rotation of the cam. Firstly, according to the relationship between the cam edge curve and the angle, combined with the working data of the plunger system, the movement range of the plunger is 0 to 10.626 mm. The rotation angle of the plunger from the compression to the low point, after the compression to the high point, then back to the low point is θ, and the amount of oil pressed is Q_A. This process is recorded as one working cycle T. Next, according to the movement curve of the needle valve and the geometry of the injector nozzle [9], the relation curve between the injection rate and the time is obtained, and the mass of the fuel injected in unit time m_B is calculated. Then a working cycle $T = (m_A'/m_B) \times 1\,\text{s}$ at the oil supply end is calculated, and finally, the cam angular velocity $\omega = \theta/T$ is obtained.

5.2. Model Preparation. In the whole working system of high-pressure oil pipe, the pressure in the pipe can be kept stable only when the mass of injected fuel is always equal. The following gives the concept of conservation of mass and its application formula.

Conservation of mass: in any isolated system, the total mass remains unchanged no matter what changes or processes occur. In other words, any changes, including chemical reaction and nuclear reaction, can not eliminate substances but changes the original form or structure of substances, so this law is also known as the law of material immortality [10].

Liquid mass, density, volume relationship: $m = \rho v$.

5.3. Problem Solving

Step 1. Calculate the mass m_A' of the injection flow Q_A in a working cycle T; the schematic diagram of the high-pressure oil pump is as shown in Figure 4.

Table 2: Adjustment plan.

Status time	2 s	5 s	10 s
Adjustment status (ms/time)	0.898	0.752	0.532
Stable status (ms/time)	0.761	0.761	0.761

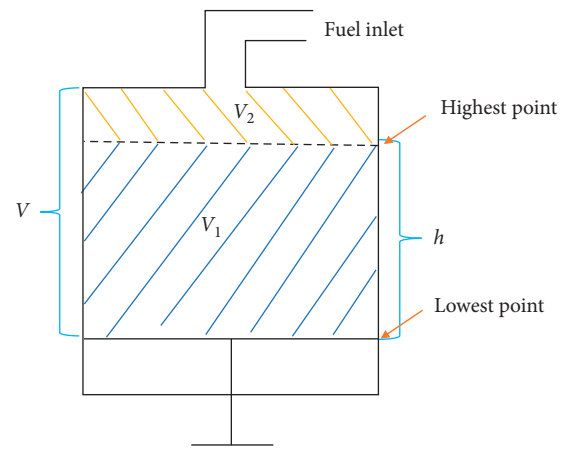

Figure 4: Schematic diagram of the high-pressure oil pump.

Fit the relationship between the cam edge curve and the angle, and the result is shown in Figure 5.

The maximum compression value of cam is $h = 5.313 - (-5.313) = 10.626$ mm; that is, the compression range is $0 \sim 10.626$ mm. The plunger is compressed from the low point to the high point and returns to the original position, which is recorded as a cycle T, and the effective volume of ramrod compression is $V_1 = sh = \pi \times ((5 \times 10^{-3})/2)^2 \times 1.0826 \times 10^{-2}\,\text{m}^3$. The residual volume of the plunger rod is $V_2 = 2 \times 10^{-8}\,\text{m}^3$, so the total volume of the plunger bar is $V = (V_1 + V_2)m^3$.

When the plunger is at a low point, the fuel pressure is 0.5 MPa; according to the density formula $\Delta P = (E/\rho)\,\Delta\rho\,\text{m}^3/\text{s}$, the density is calculated as ρ_0. When the plunger is at the highest point, because the pressure in the plunger cavity is greater than the pressure in the high-pressure oil pipe, the check valve connecting the plunger cavity and the high-pressure oil pipe is opened, so the pressure in the pipe can be regarded as 100 MPa. According to the density formula, the corresponding fuel density is ρ_1. The quality of fuel that is pressed into the high-pressure fuel line in one cycle is $m_A' = \rho_0 V - \rho_1 V_2$.

Step 2. Calculate the mass m_B of the ejected flow Q_B in one second.

The schematic diagram of the injector nozzle is shown in Figure 6.

In the initial stage, that is, when the needle valve is closed, the height h_1 from the bottom to the top of the cone meets the following requirements: $(((2.5/2) \times 10^{-3})/\ h_1) = \tan 9^\circ$, reduced to $h_1 = ((1.25 \times 10^{-3})/\tan 9^\circ) = 7.892 \times 10^{-3}$ m. In the process of needle valve rising, the flow rate of fuel increases gradually. When the lower end of the needle valve reaches the height h_2, that is to say, the area of the circular ring formed by the bottom of the needle valve and

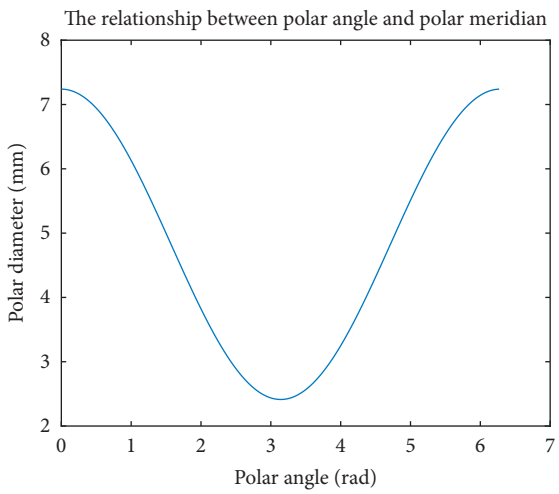

Figure 5: Fitting curve of polar diameter and polar angle.

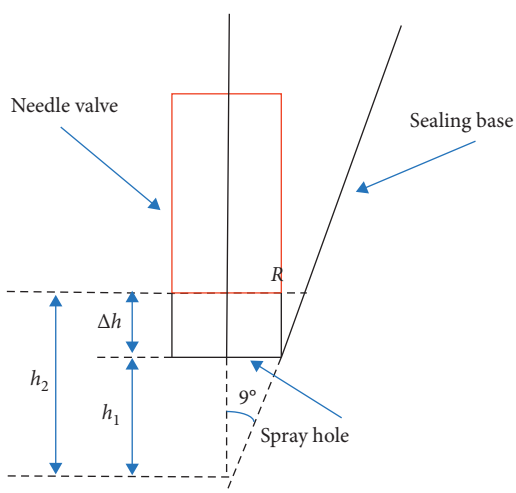

Figure 6: Structure of the fuel injection nozzle.

the inner surface of cone S is equal to the area of a small hole, the flow rate reaches the maximum. At this time, the outer radius R of a circular ring meets the requirements: $\pi R^2 - \pi(1.25 \times 10^{-3})^2 = \pi(0.7 \times 10^{-3})^2$. The result is $R = 1.433 \times 10^{-3}$ m. In a right triangle, $h_2 = (R/\tan 9^\circ) = 9.045 \times 10^{-3}$ m, and the rising height of the needle valve is as follows:

$$\Delta h = h_2 - h_1 \begin{cases} = 0, & \text{the flow rate is 0,} \\ \in (0, 1.153], & \text{flow rate increases,} \\ > 1.153, & \text{velocity unchanged,} \\ \in [1.153, 0), & \text{velocity decreases.} \end{cases} \tag{18}$$

Performing three times fitting for the given needle method motion, the fitting curve is shown in Figure 7.

According to the rising height node of needle valve, the time node of flow rate change can be obtained, and then the functional relationship between flow rate and ring area can be obtained:

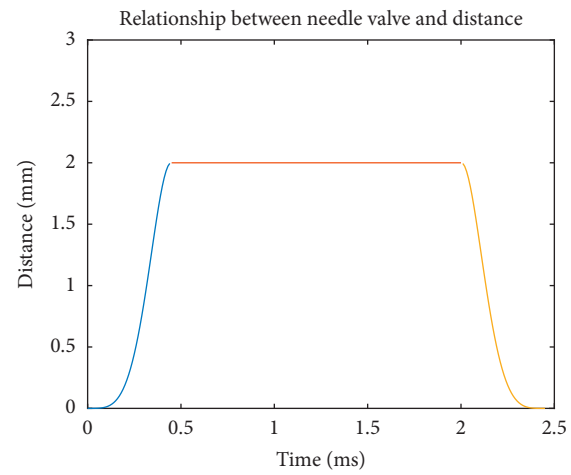

Figure 7: Curve of moving distance and time of needle valve.

$$Q = CS\sqrt{\frac{2\Delta P}{\rho}}. \tag{19}$$

To sum up, the quality of oil ejected in unit time is $m_B = Q \times T \times \rho_{100} = 0.85Q$.

Step 3. Balance stage.

To make the pressure in the high-pressure oil pipe at 100 MPa, that is, $m_A = m_B$; then,

$$T = \frac{m_A'}{m_A} \times 1\,\text{s} = \frac{m_A'}{m_B} \times 1\,\text{s}. \tag{20}$$

The angular velocity of the cam is $\omega = \theta/T$, where $\theta = 6.27$ rad.

The speed curve of the injection end is shown in Figure 8.

The results obtained by taking the known data into formula (20) are as follows:

$$\begin{aligned} m_A' &= 151.2711\,\text{mg}, \\ m_B &= 329.493\,\text{mg}, \\ T &= \frac{m_A'}{m_B} \times 1\,\text{s} = 1.02\,\text{s}, \\ \omega &= \frac{\theta}{T} = 27.243\,\text{rad/s}. \end{aligned} \tag{21}$$

6. Model 3: Dynamic Model of Double Nozzles

6.1. Problem 3: How to Adjust the Oil Supply Strategy If Another Injection Nozzle Is Added? If adding another injection nozzle with the same working rule based on the model developed in Problem 2, without considering the influence of its position distribution. Then installing another pressure relief valve to control the pressure in the high-pressure oil pipe. According to the previous analysis, the pressure relief valve is opened and the fuel returns when the pressure in the high-pressure oil pipe is greater than 100 MPa. In the whole

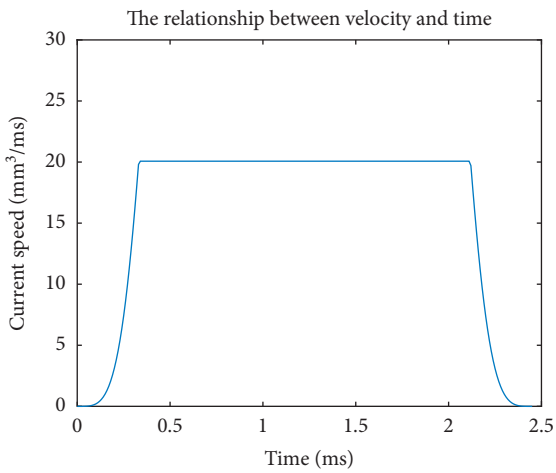

Figure 8: Curve of velocity versus time.

process of pressure regulation, the minimum pressure fluctuation of a system is the optimal objective, and a single objective programming model is established based on the constraint equation of fuel quality [11]. The changed oil pipe is shown in Figure 9.

6.2. Model Preparation. In the calculation of high-pressure oil pump, a function is used to fit the change of oil supply pressure.

Fitting is to connect a series of points on a plane with a smooth curve. Generally, the fitting curve can be expressed by function, and a commonly used fitting method is the least square curve fitting method. In Matlab, polyfit can also be used to fit polynomials.

6.3. Problem Solving. Adding an injector with the same working rule, that is, there are two injectors in the system, which are recorded as q_1 and q_2, respectively, regardless of the impact of their location distribution. Two scenarios are considered when solving this problem.

Scenario 1. The starting working time of two fuel injection nozzles is the same.

Adding an injector with the same working rule based on problem 2, in this case, it can be considered that the oil output in the same time is 2 times that in question 2, and the time to achieve stable oil pressure in the pipe is 1/2 of the original.

In unit time, the quality of the oil out of the injector end is $m_B' = 2m_B$, and the amount of oil in a working cycle T of the injector end A in a cycle remains unchanged to m_A'. With equation (18),

$$T' = \frac{m_A'}{2m_B} \times 1\,\mathrm{s} = \frac{T}{2}. \tag{22}$$

And the angular velocity of the cam is

$$\omega' = \frac{\theta}{T'} = 2\varpi = 54.486\,\mathrm{rad/s}. \tag{23}$$

Scenario 2. The starting working time of two fuel injection nozzles is inconsistent.

If nozzle q_1 starts to work from 0 and nozzle q_2 starts to work from t, then in t time, the oil delivery quality of the system is

$$m_2 = \begin{cases} \displaystyle\int_0^T CA\sqrt{\frac{2(P_1 - P_2)}{\rho_1}}\,\mathrm{d}t, & T < t, \\ \displaystyle\int_0^T CA\sqrt{\frac{2(P_1 - P_2)}{\rho_1}}\,\mathrm{d}t + \int_t^T CA\sqrt{\frac{2(P_1 - P_2')}{\rho_1}}\,\mathrm{d}t, & T < t. \end{cases} \tag{24}$$

In the whole process of pressure regulation, the minimum pressure fluctuation of a system is the optimal objective, and the objective function is $\min \int_0^T |P(t)| - 100\mathrm{d}t$.

The constraints are

$$\text{s.t} \quad \begin{cases} \displaystyle CA\sqrt{\frac{2(P_1 - P_2)}{\rho_1}} + \frac{\mathrm{d}m}{\mathrm{d}t} = 0, \\ \displaystyle T = \frac{2\pi t}{\omega}. \end{cases} \tag{25}$$

A single objective programming model is established, the optimal angular velocity of the cam is 245.63 rad/s in a system cycle, and the initial working time difference of the two nozzles is 1/2 cycle.

When adding a pressure reducing valve, if taking time as an independent variable, the fuel oil pressure input and nozzle injection could be calculated. By multiplying the difference by the elastic modulus E, the derived formula is

$$P = \int \frac{E}{V}(Q_A - Q_B)\mathrm{d}t. \tag{26}$$

It is simulated circularly and the image is drawn. The simulation results are shown in Figure 10.

It can be seen from Figure 10 that when the single valve is not working, the air pressure in the high-pressure oil pipe will fluctuate up and down, which is not stable. When the single pressure reducing valve is opened, the simulation results are as shown in Figure 11.

After opening, the pressure in the pipe tends to be stable, and the pressure reducing valve plays an important role in stabilizing the air pressure in the tubing when the working time is about 20 ms.

7. Model Validation

Inspection idea: during the working process of high-pressure oil pipe, when the pressure inside the oil pipe fluctuates within a certain range, it can be regarded as stable, which can increase the service life of the whole oil supply system. In this paper, the real-time monitoring of the pressure in the tube during the working process of the oil tube is carried out, and the change curve of the pressure in the tube with time t is drawn, as shown in Figure 12.

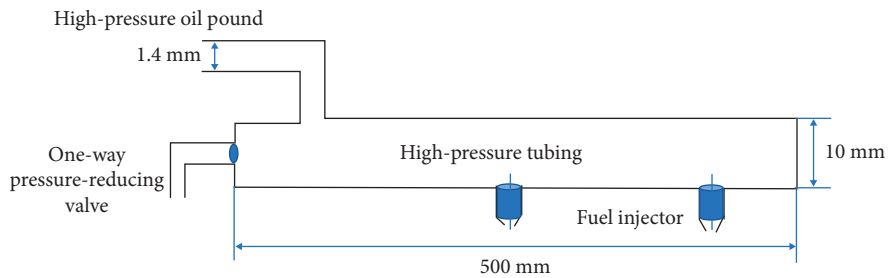

Figure 9: Schematic diagram of high-pressure oil pipe.

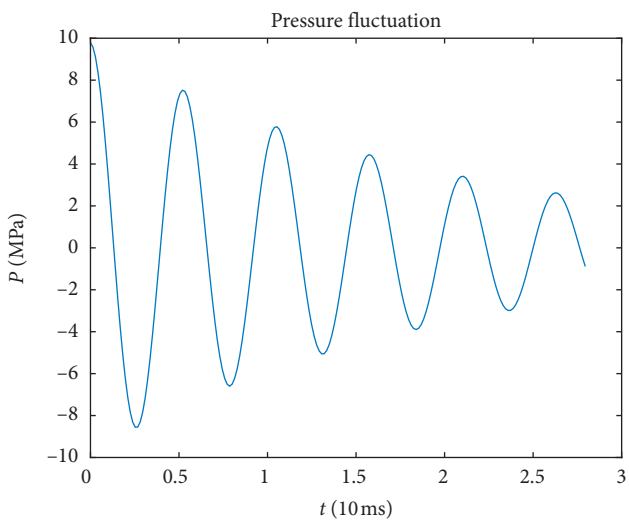

Figure 10: Simulation results of internal pressure.

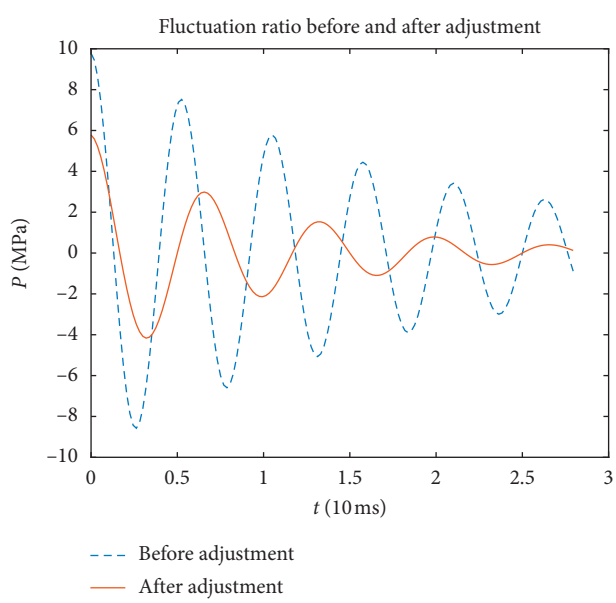

Figure 11: Air pressure simulation diagram after adding single pressure reducing valve.

It can be seen that, during the working process of high-pressure oil pipe, the air pressure in the pipe always changes periodically between 96 MPa and 104 MPa, and the pipe can

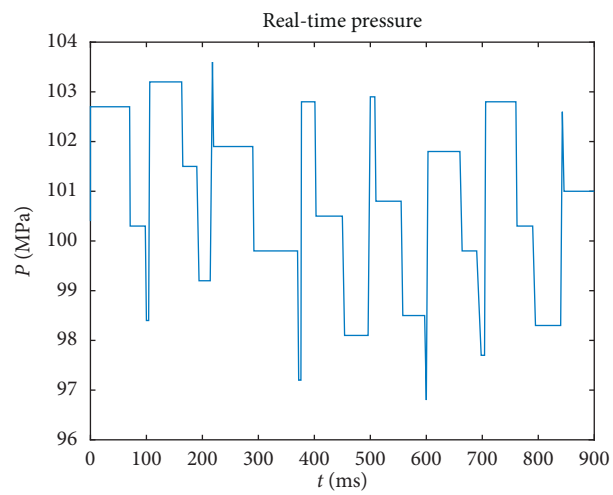

Figure 12: Real-time pressure.

be regarded as a stable state, which shows that the model has precise control on all parts of the oil pipe, thus making the whole oil supply system more stable.

8. Model Evaluation

8.1. Advantages

(1) In the dynamic differential equilibrium equation model of question 1, the time is subdivided, the relation between the oil supply rate and the pressure difference and time is fully considered, and the oil supply end is precisely controlled by the flow rate of the oil injection end; in the adjustment state, the linear function is used to fit the pressure change in the high-pressure oil pipe, which simplifies the solution.

(2) In the process of solving the second problem, based on the conservation of mass, a dynamic equation model with mass as the link is established, and a constant quantitative equation is established in many variable quantities to eliminate the interference of temperature and other factors on the solution process.

(3) In the process of solving problem 3, this paper adopts the method of function fitting to eliminate the influence of the irregular change of oil supply of high-

pressure oil pump on the solution of the problem and improve the efficiency of the solution.

(4) Finally, for the model testing, the simulation model is established to test the working system of high-pressure oil pipes one by one [12]. It is a powerful simulation tool, which enables users to simulate the operation of a real dynamic system with the minimum cost in the graphic mode, and can establish the dynamic system model and carry out simulation model in an intuitive way, and use the visual modeling, which can quickly and accurately build the block diagram model of the dynamic system, and improve the accuracy and reliability of the model.

8.2. Disadvantages

(1) In the process of solving problem one, because of the particularity of solving a differential equation, the analytical solution is difficult to solve. In this paper, the numerical solution is used for approximate substitution, resulting in errors.

(2) In this paper, the change of system temperature caused by friction and other factors is not considered in the model.

8.3. Conclusion. To sum up, the purpose of this paper is to study the pressure control problem of the high-pressure oil pipe of the fuel engine, with the known parameters to calculate the pressure density and other indexes by using the numerical solution of differential equation flexibly. The fluid density and pressure model of high-pressure oil pipe are established, and the pressure stability of high-pressure oil pipe is maintained by using visual simulation tools. At the same time, the control scheme of fuel injection nozzle and pressure relief valve is studied to precisely control the working time of each part of high-pressure oil pipe, so as to improve the service life of engine.

9. Future Work

In reality, there will be differences in the pressure in the high-pressure oil pipe, which is related to the elastic deformation in the pipe, the transmission mode of fuel in the pipe, and other factors. The function of the pressure in the pipe can be constructed to refine the change of the pressure in the pipe, to quantify the injection rate at the injection end more accurately, as to precisely regulate the oil supply end.

In the solution model of problem 2, the fuel supply end drives the plunger to pressurize the low fuel oil through the cam rotation. In this process, due to the influence of friction, the volume and pressure of fuel oil will be affected. Therefore, the temperature influence factor can be added in the process of solving the fuel supply quality to eliminate the influence of temperature change.

In question 3, the position of the fuel injector will affect the injection rate [13]. Theoretically, the closer the position of the fuel injector is to the fuel supply end, the greater the injection rate is. The position of the two fuel injectors relative to the fuel supply end can be considered to comprehensively adjust the oil supply time, which is more practical.

In the working system of high-pressure oil pipe, the model in this paper realizes the mutual correlation and precise regulation of various components. In the era of the rapid development of big data, the model can be applied to the sensing process of the robot, self-regulation of medical instruments and correction equipment, etc. [14], which has a wide application prospect and research value.

Data Availability

The cam edge curve, needle valve motion curve, and elastic modulus pressure data used to support the findings of this study are available from the corresponding author upon request.

Conflicts of Interest

The authors declare that they have no conflicts of interest.

References

[1] H. Jiangfeng, W. Xiang, and Y. Changcheng, "Modal analysis of high-pressure oil pipe of engine based on finite element method," *Journal of Hubei Institute of Automotive Industry*, vol. 4, 2018.

[2] H. Shuangjie, *Research on High-Pressure Common Rail Injection System of Diesel Engine*, Hangzhou University of Electronic Science and technology, Hangzhou, China, 2018.

[3] Y. He, Z. Jiaming, G. Zhengshuai et al., "Study on pressure control of high-pressure tubing based on continuous differential equation," *Journal of Qilu University of Technology*, vol. 33, no. 6, pp. 74–80, 2019.

[4] Y. Lu, W. Shen, and X. Qian, "Pressure control of high-pressure tubing based on difference equation," *Science and Technology Innovation and Application*, vol. 7, pp. 25–27, 2020.

[5] A. Zhang, W. Zhao, X. Zhang, Y. Wang, and Z. Su, "Research on pressure control theory of high-pressure tubing based on simulation model," *Electronic Testing*, vol. 1, pp. 63–65, 2020.

[6] Y. Wang, W. Liu, and S. Yao, "Optimization model and application of high-pressure tubing pressure control," *Science and Technology Innovation and Application*, vol. 36, pp. 20–22, 2019.

[7] D. Zhu, "Iterative teaching in mathematical modeling," *Chinese Journal of Multimedia and Network Teaching*, vol. 5, pp. 239–241, 2020.

[8] J. Cai, Y. Lin, Li Shu, S. Xu, and J. Zeng, "Modeling and numerical analysis of a class of high-pressure tubing control problems," *Contemporary Chemical Research*, vol. 9, pp. 36–39, 2020.

[9] Y. Wang, *Design and Numerical Calculation of Fuel Injection System for Medium and High-Speed Diesel Engines*, Harbin Engineering University, Harbin, China, 2004.

[10] Y. Song, *Simulation of Pressure Dynamic Characteristics of High-Pressure Common Rail System of Diesel Engine*, Zhejiang University, Hangzhou, China, 2005.

[11] H. Xiao, *Dictionary of Decision Science*, People's Publishing House, Beijing, China, 1995.

[12] S. Liu, T. Dong, R. Meng et al., "Study on simulation design of diesel engine injection process," *Journal of Internal Combustion Engine*, no. 2, pp. 56–65, 1990.

[13] P. Linop, B. Maione, and A. Brizzo, "Nonlinear modeling and control of a Common rail injection system for diesel engines," *Applied Mathematical Modelling*, vol. 31, no. 9, pp. 1770–1784, 2007.

[14] Q. Wang, B. Hu, C. Xiao, and Y. Su, "Development and application of ultra-high-pressure strengthening technology for high-pressure oil pipe of diesel engine," *Mechanical Engineer*, vol. 5, 2013.

Hindawi
Mathematical Problems in Engineering
Volume 2020, Article ID 2468134, 12 pages
https://doi.org/10.1155/2020/2468134

Research Article

Multistability and Formation of Spiral Waves in a Fractional-Order Memristor-Based Hyperchaotic Lü System with No Equilibrium Points

Bo Yan,[1] **Shaobo He**,[2] **and Shaojie Wang**[3]

[1]*College of Computer and Electrical Engineering, Hunan University of Arts and Science, Changde 415000, China*
[2]*School of Physics and Electronics, Central South University, Changsha 410083, China*
[3]*College of Electrical and Information Engineering, Shaoyang University, Shaoyang 422000, China*

Correspondence should be addressed to Shaobo He; heshaobo_123@163.com

Received 19 April 2020; Accepted 21 May 2020; Published 29 June 2020

Guest Editor: Rongwei Guo

Multistablity analysis and formation of spiral wave in the fractional-order nonlinear systems is a recent hot topic. In this paper, dynamics, coexisting attractors, complexity, and synchronization of the fractional-order memristor-based hyperchaotic Lü system are investigated numerically by means of bifurcation diagram, Lyapunov exponents (LEs), chaos diagram, and sample entropy (SampEn) algorithm. The results show that the system has rich dynamics and high complexity. Meanwhile, coexisting attractors in the system are observed and hidden dynamics are illustrated by changing the initial conditions. Finally, the network based on the system is built, and the emergence of spiral waves is investigated and chimera states are observed.

1. Introduction

A new two-terminal circuit element called memristor characterized by a relationship between the charge and the flux was postulated as the fourth basic circuit element by Chua [1] in 1971. Memristor is short for memory resistor, and its memristance depends on how much electric charge flows through it in a particular direction [2]. Until 2008, researchers at HP Labs firstly published a paper in *Nature* and reported the realization of the memristor [3]. Since then, applications of the memristor have attracted lots of attention of scholars and a big progress in the fields such as secure communications [4, 5], neural network [6, 7], chaos [8, 9], and simulation of neural network behaviour [10, 11] and the memristor oscillators' behaviour [12, 13] has been made.

Memristor is a nonlinear electronic element. When the memristor is introduced, the chaotic oscillation of the circuit could be more complex due to its nonlinearity. So the research of memristor-based chaotic systems and its dynamic characteristics has become a new hot spot. In recent years, relevant research results have been obtained [9, 14–16]. Fractional calculus is a topic which is more than 300 years old [17]. Lots of physical phenomena show that the fractional-order model can describe the characteristics of the actual system more accurately than the classical integer-order model [18]. Based on this consideration, the application of fractional-order system has attracted more and more researchers' attention [19, 20]. When the fractional calculus is introduced into the memristor-based chaotic circuit, a more accurate model for the real situation is obtained. Nowadays, many research studies on chaotic dynamics of the fractional-order memristor-based chaotic system have been conducted [21–25]. Among these studies, Rajagopal et al. [24] analyzed the dynamic properties of the fractional-order memristor system with no equilibrium points through Lyapunov exponents and phase diagrams for the first time. Prakash et al. [25] found rich chaotic behaviours of a novel fractional-order memristor-based chaotic jerk system with no equilibrium points by bifurcation diagram, attractors, and instantaneous phase plots. As

a result, the analysis of chaotic dynamical behaviours of the fractional-order memristor-based chaotic systems without equilibrium points is an interesting topic.

Recently, Qiao et al. [26] designed a novel improved memristor-based hyperchaotic Lü circuit without any equilibrium points by adding a linear feedback term, a constant term, and a memristor to the classical Lü chaotic system [27]. The coexisting hidden dynamical behaviours of this system are analyzed. However, the fractional-order chaotic dynamics of the system have not been investigated. Moreover, collective behaviours in the coupled nonlinear network have aroused much research interests, and these networks usually consist of nonlinear chaotic systems [28, 29], neural models [30, 31], and neural models with memristors [32, 33]. In fact, these networks can present different kinds of dynamical behaviours such as synchronization and chimera states. However, there are few reports on the formation of spiral waves in the network of fractional-order memristor-based hyperchaotic systems with no equilibrium points. Thus, the dynamics in the network of the new fractional-order memristor-based Lü system need further investigations.

The rest of this paper is organized as follows. Section 2 presents the details of the solution algorithm and mathematical model of the fractional-order memristor-based hyperchaotic Lü system. Section 3 investigates dynamics properties and complexity of the system by using bifurcation, Lyapunov exponents, and SampEn algorithm. The multiple coexisting hidden attractors are also illustrated with different initial conditions. Section 4 investigates the synchronization of the system by the ring network structure of the neuron network. Section 5 gives the conclusion.

2. The Fractional-Order Memristor-Based Hyperchaotic Lü System

2.1. The Mathematical Model. The most commonly used memristor-based dynamical system [16] is described as

$$\begin{cases} i = (\alpha + \beta\varphi^2)u, \\ \dot{\varphi} = u, \end{cases} \tag{1}$$

where u and i are the input voltage variable and the input current variable of the memristor, respectively, φ is the internal magnetic flux, α and β are two positive constants, and $\alpha + \beta\varphi^2$ is a memductance function describing the flux-dependent rate of change of charge. Qiao et al. [26] designed the memristor-based hyperchaotic Lü system, and its equations are given by

$$\begin{cases} \dot{x} = a(y - x) + g(\alpha + \beta w^2)y, \\ \dot{y} = by - xz - dx + e, \\ \dot{z} = xy - cz, \\ \dot{w} = y. \end{cases} \tag{2}$$

Here, by introducing the fractional calculus to this system, a novel fractional-order memristor-based hyperchaotic Lü system is constructed, and the mathematical model is given by

$$\begin{cases} D_{t_0}^q x = a(y - x) + g(\alpha + \beta w^2)y, \\ D_{t_0}^q y = by - xz - dx + e, \\ D_{t_0}^q z = xy - cz, \\ D_{t_0}^q w = y, \end{cases} \tag{3}$$

where $D_{t_0}^q$ is the q-order Caputo differential operator [34], x, y, z, and w are state variables, a, b, c, d, and e are the control parameters of classical Lü system [27], and g is the gain of the memristor. The Caputo fractional-order definition is given in Definition 1.

Definition 1 (see [34]). The Caputo fractional-order derivative definition is given by

$$D_{t_0}^q \mathbf{x}(t) = \begin{cases} \dfrac{1}{\Gamma(1-q)} \displaystyle\int_{t_0}^{t} \frac{\dot{x}(\tau)}{(t-\tau)} \mathrm{d}\tau, & 0 < q < 1, \\ \dot{\mathbf{x}}(t), & q = 1, \end{cases} \tag{4}$$

where $q \in R^+$ and $\Gamma(\cdot)$ is the Gamma function.

In order to analyze the dynamic and complexity characteristics of this fractional-order memristor-based hyperchaotic Lü system, we fix the system parameters as $a = 36$, $b = 20$, $c = 3$, $d = 5$, $e = 0.1$, $\alpha = 4$, and $\beta = 0.18$ and select the gain parameter g as the only adjustable parameter of the system.

It can be obtained by (3):

$$\begin{aligned} \nabla^q V &= \frac{\partial D_{t_0}^q x}{\partial x} + \frac{\partial D_{t_0}^q y}{\partial y} + \frac{\partial D_{t_0}^q y}{\partial z} + \frac{\partial D_{t_0}^q w}{\partial w} \\ &= -a + b - c = -19 < 0, \end{aligned} \tag{5}$$

where $\nabla^q V < 0$ means that this fractional-order memristor-based hyperchaotic Lü system is dissipative. It also indicates that the improvement of Lü system and the introduction of memristor and fractional calculus do not change the dissipation proprieties of the original classical Lü system.

Let $D_{t_0}^q x = D_{t_0}^q y = D_{t_0}^q z = D_{t_0}^q w = 0$; obviously, (3) has no real solutions and the fractional-order memristor-based hyperchaotic Lü system has no equilibrium. As shown in Ref [26], the integer-order hyperchaotic Lü system has hidden attractors. According to the definition of the hidden attractors [35], the generated attractors and limit cycles of system (3) are all hidden because this fractional-order system investigated in this paper also has no equilibrium points.

2.2. The Numerical Analysis Methods. The predictor-corrector method is an effective method for solving fractional-order equations. According to Kai et al. [36], it is also called the Adams–Bashforth–Moulton algorithm. Suppose that the fractional-order nonlinear system is defined as

$$\begin{cases} D_{t_0}^q \mathbf{x}(t) = f(\mathbf{x}, \mathbf{x}(t)), & 0 \le t \le T, \\ \mathbf{x}^{(k)}(0) = \mathbf{x}_0^{(k)}, & k = 0, 1, 2, \ldots, \lceil q \rceil - 1, \end{cases} \tag{6}$$

where $\mathbf{x}(t) = [x(t), y(t), z(t), w(t)]$, $\mathbf{x}^{(k)} = \mathbf{x}_0^{(k)}$ is the initial condition of the system, $0 < q \leq 1$, $\lceil \cdot \rceil$ is the ceil function, and $D_{t_0}^q \mathbf{x}(t)$ is the Caputo derivative. Formula (6) is equivalent to the Volterra integral equation [33, 37]:

$$\mathbf{x}(t) = \sum_{k=0}^{\lceil q \rceil - 1} \mathbf{x}_0^{(k)} \frac{t^k}{k!} + \frac{1}{\Gamma(\alpha)} \int_0^T (t-\tau)^{q-1} f(\tau, \mathbf{x}(\tau)) \mathrm{d}\tau. \quad (7)$$

Let $h = T/N$, $t_j = jh$ ($j = 0, 1, \ldots, N \in Z^+$), and T be the upper limit for solving this integral equation. Then, the correction formula of formula (7) is

$$\begin{aligned} \mathbf{x}_h(t_{n+1}) = &\sum_{k=0}^{\lceil q \rceil - 1} \mathbf{x}_0^{(k)} \frac{t_{n+1}^k}{k!} + \frac{h^q}{\Gamma(q+2)} f\left(t_{n+1}, \mathbf{x}_h^p(t_{n+1})\right) \\ &+ \frac{h^q}{\Gamma(q+2)} \sum_{j=0}^{n} a_{j,n+1} f\left(t_j, \mathbf{x}_h(t_j)\right), \end{aligned} \quad (8)$$

in which

$$\begin{aligned} \mathbf{x}_h^p(t_{n+1}) &= \sum_{k=0}^{\lceil q \rceil - 1} \mathbf{x}_0^{(k)} \frac{t_{n+1}^k}{k!} + \frac{1}{\Gamma(q)} \sum_{j=0}^{n} b_{j,n+1} f\left(t_j, \mathbf{x}_h(t_j)\right), \\ b_{j,n+1} &= \frac{h^q}{q} \left[(n-j+1)^q - (n-j)^q \right], \quad 0 \leq j \leq n, \\ a_{j,n+1} &= \begin{cases} n^{q+1} - (n-q)(n+1)^q, & j = 0, \\ (n-j+2)^{q+1} + (n-j)^{q+1} - 2(n-j+1)^{q+1}, & 1 \leq j \leq n. \end{cases} \end{aligned} \quad (9)$$

The utilized source Matlab code of the predictor-corrector method can be downloaded online (http://www.sourcecodeonline.com/details/predictorcorrector_pece_method_for_fractional_differential_equations.html); the function name is "FDE12.m." In [38], the method about how to use "FDE12.m" to solve fraction-order system is described in detail. The LEs (Lyapunov exponents) [39] of system (6) can be calculated as follows. Firstly, suppose $\Lambda_k(t)$ is the eigenvalue of $f(x, x(t))$, $k = 1, 2, \ldots, d$, where d is the dimension of the system. The orbit $\mathbf{x}(t)$ can be given in terms of the tangent linear extension:

$$D_{t_0}^q v = (\nabla f)_{x(t)}^T \cdot v, \quad (10)$$

where $\mathbf{v}$ is a vector evolving in the tangent bundle of the manifold and the superscript "T" denotes the transpose. Then, the LEs can be defined as the limit eigenvalues of the symmetric operator:

$$\Lambda_k(t) = \frac{1}{t} \sqrt{A(t) \cdot A^T(t)}, \quad (11)$$

where $A(t)$ is the exponential of $f(x, x(t))$ computed along the trajectory $\mathbf{x}(t)$. Thus, we can obtain $|\Lambda_1(t)| \leq |\Lambda_2(t)| \leq \cdots \leq |\Lambda_d(t)|$. Finally, The LEs of the trajectory $\mathbf{x}(t)$ obtained by system (6) can be determined by

$$\lambda_k = \lim_{t \longrightarrow \infty} \sup \frac{1}{t} \ln \left| \Lambda_k(t) \right|. \quad (12)$$

3. Numerical Analysis

3.1. Bifurcations and Lyapunov Exponents. Dynamics of the system with the variation of g and q are analyzed by means of bifurcation diagram, LEs, and phase diagrams. Three cases are presented.

Case 1. Fix $q = 0.998$: let the gain parameter g vary from 0 to 20 with step size of 0.04 and the initial condition be $[x_0; y_0; z_0; w_0] = [1; 0; 1; 0]$. Bifurcation diagram and LEs are illustrated in Figure 1. It is shown in Figure 1 that the system is periodic for $g \in [0.3, 2.1]$ and [3.5, 7.8], is chaotic for $g \in [0, 0.3]$, [2.1, 3.5], and [14.5, 15.2], is hyperchaotic for $g \in [7.8, 14.5]$, and is convergent for $g \in [15.2, 20]$. In this case, chaotic and periodic states are alternate in the interval $g \in [0, 7.8]$. It shows the rich dynamics in the system.

Case 2. Fix $g = 10$: vary the derivative order q from 0.94 to 1 with step size of 1.2×10^{-4}. Set the initial condition as $[x_0; y_0; z_0; w_0] = [1; 0; 1; 0]$. Dynamical analysis results are shown in Figure 2. It is shown in Figure 2 that the system is hyperchaotic when $q > 0.972$. Meanwhile, when $q \in [0.965, 0.972]$, the system vibrates between chaotic and hyperchaotic states. For the rest values of q, the system is convergent.

Case 3: Vary parameter g from 1 to 16 with step size of 0.04 and increase derivative order q from 0.94 to 1 with step size 1.2×10^{-4}. Thus, the parameter space is divided as a 400×500 grid. As with above cases, the initial condition is given by $[x_0; y_0; z_0; w_0] = [1; 0; 1; 0]$. Maximum Lyapunov exponent-based contour plot in the parameter plane g-q is shown in Figure 3. Chaotic region is observed in a triangular area located in the top left of the q-g parameter plane. When the derivative order q takes different values, the system has relative larger maximum Lyapunov exponents with smaller g. Meanwhile, the maximum Lyapunov exponents of the system decrease with the increase of derivative order q. Finally, it can be found out that the minimum order for chaos is $q = 0.927$.

Phase portraits of the system with the initial condition $[x_0; y_0; z_0; w_0] = [1; 0; 1; 0]$ and different g and q are plotted in Figure 4. Four sets of parameters are given, and they are $q = 0.995$ and $g = 0.3$ for Figure 4(a), $q = 0.995$ and $g = 1$ for Figure 4(b), $q = 0.995$ and $g = 3$ for Figure 4(c), and $q = 0.995$ and $g = 14$ for Figure 4(d). Different states including periodic circle, chaotic attractor, and hyperchaotic attractor are observed in the system. According to the above analyses, the conclusion can be drawn that the fractional-order memristor-based hyperchaotic Lü system has rich dynamical behaviours.

3.2. SampEn Complexity Analysis. Sample entropy (SampEn) [40, 41] is a measure of the probability size of a new model generated by a time series when its dimension changes. The greater the complexity of the time series is, the greater the probability for a new model that the time series will produce and the greater the entropy holds. The SampEn algorithm can be briefly described as follows:

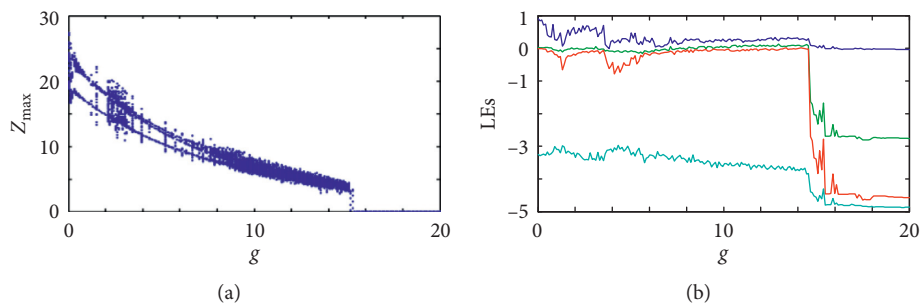

Figure 1: Dynamical behaviours with derivative order $q = 0.998$ and varying memristor gain g. (a) Bifurcation diagram. (b) LEs.

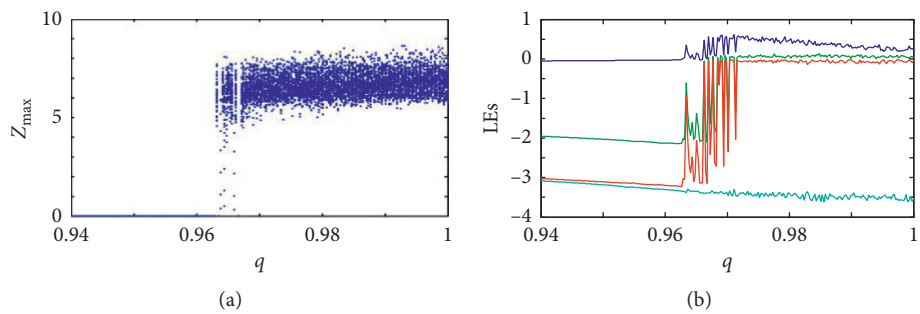

Figure 2: Dynamical behaviours with memristor gain $g = 10$ and varying derivative order q. (a) Bifurcation diagram. (b) LEs.

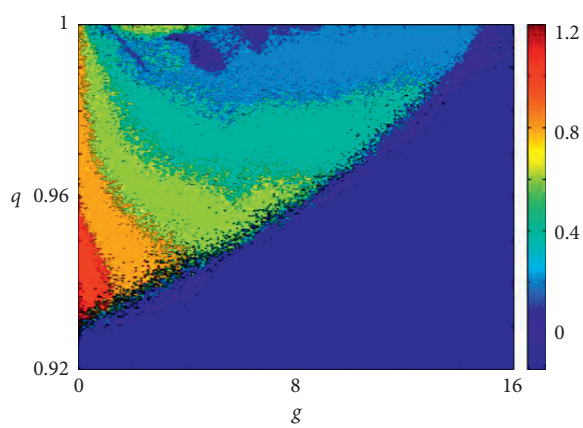

Figure 3: Maximum Lyapunov exponent contour plot in the g-q parameter plane.

Step 1. Given a time series $\{x(i), i = 0, 1, 2, \ldots, N-1\}$, if m represents embedding dimension, then the m-dimensional vectors can be expressed as

$$X(i) = [x(i), x(i+1), \ldots, x(i+m-1)], \quad i = 1, 2, \ldots, N-m. \tag{13}$$

Step 2. Define the Euclidean distance between $X(i)$ and $X(j)$ as the maximum absolute difference between their corresponding scalar elements, i.e.,

$$d[X(i), X(j)] = \underset{k=0 \longrightarrow m-1}{Max} \{|X(i+k) - X(j+k)|\}. \tag{14}$$

Step 3. Define the criterion of similarity r as a positive real number. Count the number of $d[X(i), X(j)] < r$ and its ratio to total distance $N-m$ denoted as $B_r^m(i)$, $i = 0, 1, 2, \ldots, N-m$, $j = 0, 1, 2, \ldots, N-m$, and $i \neq j$. Then, the average value of $B^m(i)$ can be calculated as

$$B^m(r) = \frac{1}{N-m+1} \sum_{i=0}^{N-m} B_i^m(r). \tag{15}$$

Step 4. Similarly, change m to $m+1$ and repeat Steps 1 to 3; $B^{(m+1)}(r)$ also can be obtained as

$$B^{m+1}(r) = \frac{1}{N-m+1} \sum_{i=0}^{N-m} B_i^{m+1}(r). \tag{16}$$

Finally, theoretically, the SampEn is defined as

$$\text{SampEn}(m, r) = -\ln \frac{B^{m+1}(r)}{B^m(r)}. \tag{17}$$

The value of SampEn is related to the values of m and r. Usually, m ranges from 2 to 5, and r takes 0.1 to 0.25 times of the standard deviation (SD) of the original time series. This article takes $m = 2$ and $r = 0.2$SD.

SampEn complexity of the fractional-order memristor-based hyperchaotic Lü system with parameter g and q is analyzed, and the results are shown in Figure 5. Time series z is used for complexity measure and length of the time series is 10000 with the first 3000 points of data removed. The parameters used for Figure 5(a) are the same as that used for Figure 1. And the parameters used for Figure 5(b) are the same as that used for Figure 2. From Figure 5, we can see that higher complexity is found when the system is chaotic or

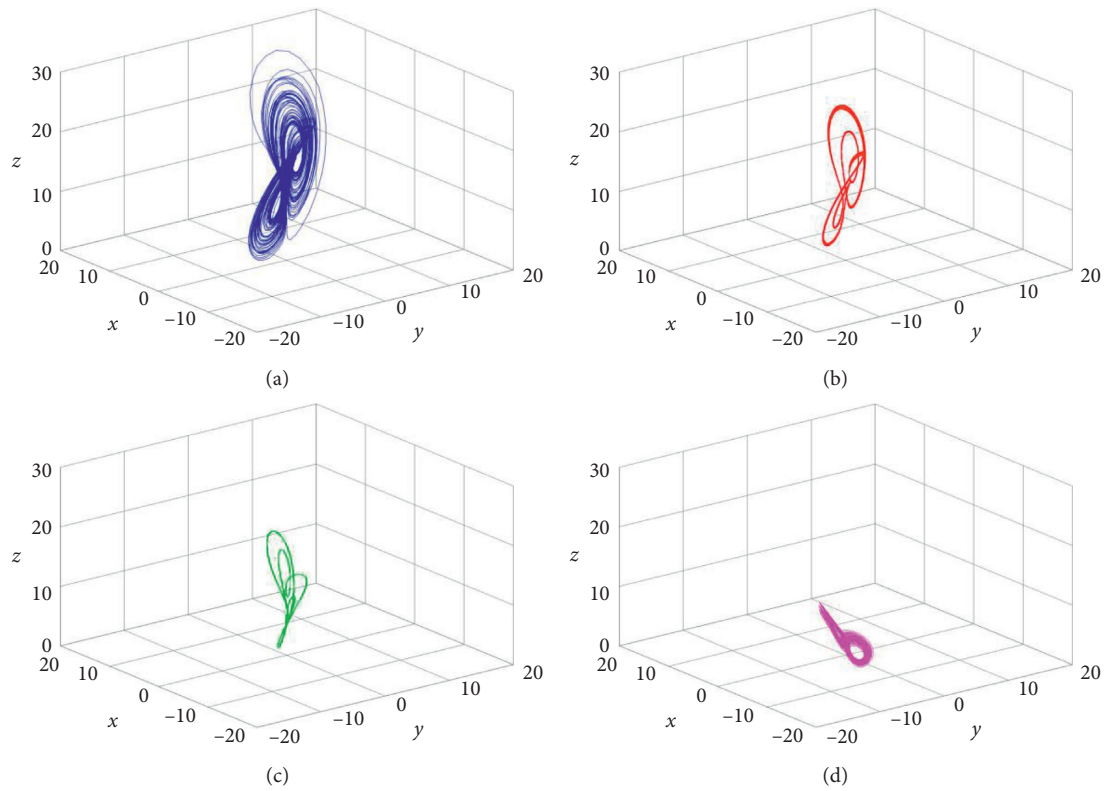

Figure 4: Phase diagrams with derivative order $q = 0.995$ and different memristor gain g: (a) $g = 0.3$; (b) $g = 1$; (c) $g = 3$; (d) $g = 14$.

hyperchaotic. This result agrees well with the analysis results by the corresponding maximum Lyapunov exponents. Comparing Figure 5(a) with Figure 1(b), it can be seen that the difference of the SampEn complexity is more obvious in Figure 5(a) than the difference of corresponding maximum Lyapunov exponents in Figure 1(b), which indicates that SampEn complexity is more convenient in distinguishing chaotic with nonchaotic states of the system.

Let parameter g vary from 0 to 16 with step size of 0.004, derivative order q vary from 0.94 to 1 with step size 1.2×10^{-4}, and the initial condition be $[x_0; y_0; z_0; w_0] = [1; 0; 1; 0]$. SampEn complexity in the parameter plane g-q is calculated and shown in Figure 6. Obviously, the higher complexity region in Figure 6 matches well with the larger maximum Lyapunov exponents area in Figure 3. However, unlike the maximum Lyapunov exponent plane, the SampEn complexity plane does not change gradually but is divided into three regions: chaos, periodic cycle, and convergence. The upper right corner in Figure 6 is periodic region. So, the SampEn complexity analysis results are more intuitive and obvious.

3.3. Coexisting Hidden Dynamics. Coexisting attractors can be observed in this system. Fix $q = 0.998$ and $g = 5$; four phase diagrams are shown in different forms in Figure 7 because of the different initial conditions. When $x_0 = y_0 = z_0 = w_0 = 0$ and $x_0 = y_0 = z_0 = w_0 = 1$, the system is periodic but has different number of cycles. When $x_0 = y_0 = z_0 = w_0 = 3$ and $x_0 = y_0 = z_0 = w_0 = 5$, the system is chaotic, but Figure 7(d) shows the weak chaotic state. When g varies from 4.8 to 5, the bifurcation diagrams for the corresponding 4 different initial conditions are shown in Figure 8. The blue points are for $x_0 = y_0 = z_0 = w_0 = 0$, red points are for $x_0 = y_0 = z_0 = w_0 = 1$, blue points are for $x_0 = y_0 = z_0 = w_0 = 3$, and magenta points are for $x_0 = y_0 = z_0 = w_0 = 5$. It can be seem from Figure 8 that the system trajectory shows the multiple stable phenomena of coexistence for different periodic limit cycles, chaos, and weak chaos due to the different initial conditions.

In order to further study the effect of initial conditions on the dynamics of the system, the SampEn complexity chaos diagram for different parameters is illustrated in Figure 9. Comparing Figure 9(a) with Figure 9(b), it can be seen that the effect of initial conditions on system dynamics is multidimensional. Each initial component will play a role in the dynamics of the system. Comparing Figure 9(c) with Figure 9(d), we can find that when the derivative order q is different, the effect of initial value on system dynamics is also different. By comparing the four figures in Figure 9, it can be found that the SampEn complexity diagrams are different with different initial conditions and SampEn algorithm is an effective method for the analysis of the hidden dynamics in the system.

Compared with the basin attraction plots, the SampEn-based chaos diagrams illustrate the dynamics and complexity of the system with different initial conditions. If the complexity is different, the state of the system is different. Thus, it can show the multistability of the system in the initial plane through a complexity of view. Since complexity

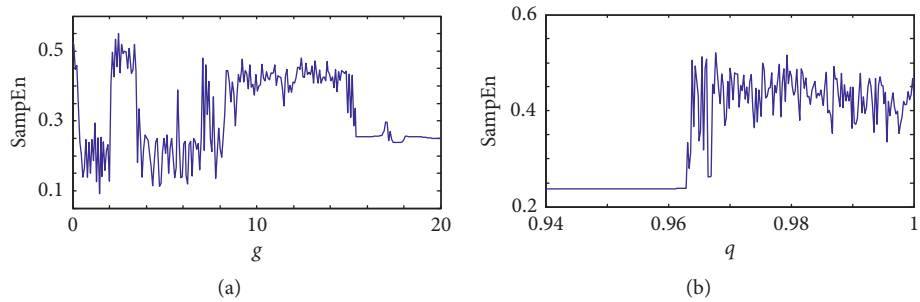

Figure 5: SampEn complexity analysis results with derivative order q parameter g with initial condition $[x_0; y_0; z_0; w_0] = [1; 0; 1; 0]$. (a) $q = 0.998$ and varying gain g. (b) $g = 10$ and varying derivative order q.

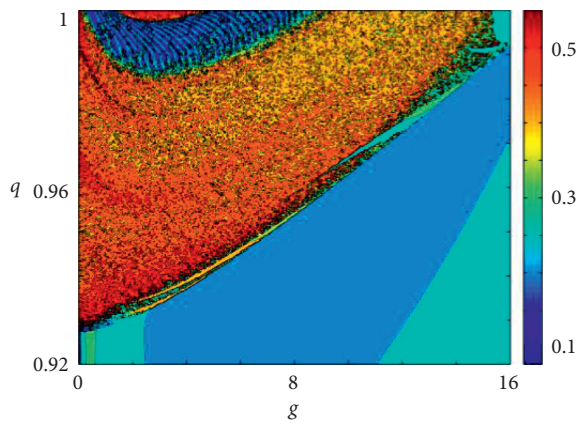

Figure 6: SampEn complexity contour plots in the g-q parameter plane.

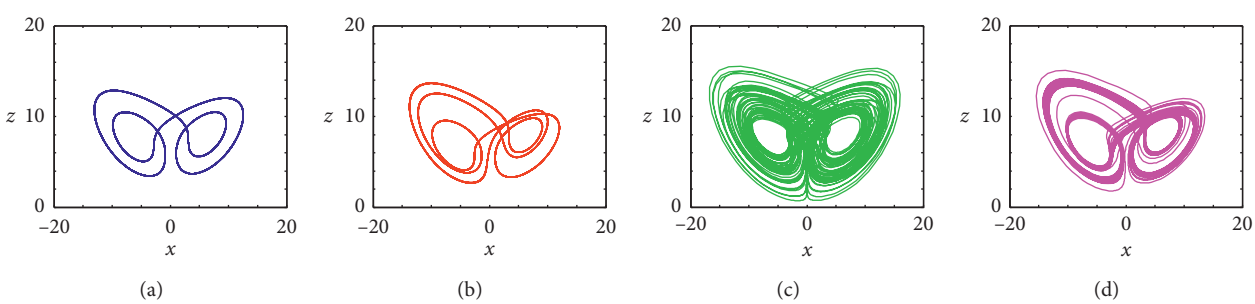

Figure 7: Coexisting attractors with $q = 0.998$, $g = 5$, and different initial conditions. (a) $x_0 = y_0 = z_0 = w_0 = 0$. (b) $x_0 = y_0 = z_0 = w_0 = 1$. (c) $x_0 = y_0 = z_0 = w_0 = 3$. (d) $x_0 = y_0 = z_0 = w_0 = 5$.

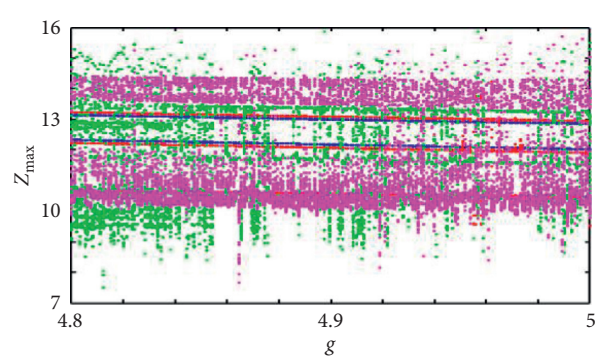

Figure 8: Bifurcation diagram in the range $g \in [4.85]$ with $q = 0.998$ and different initial conditions.

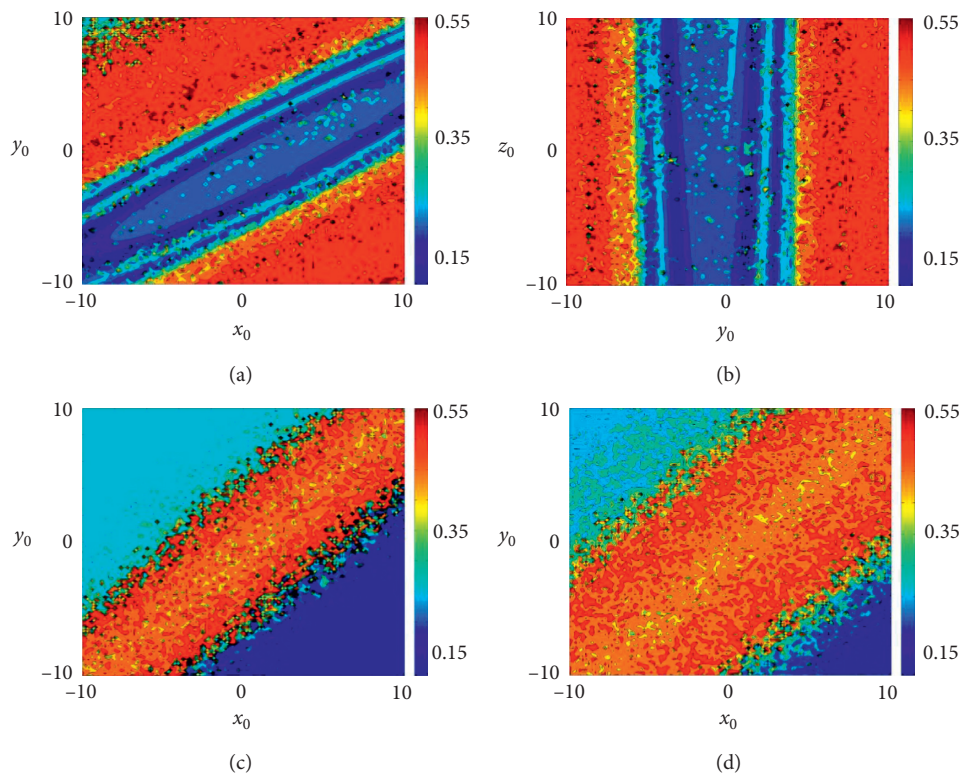

Figure 9: SampEn complexity-based chaos diagram. (a) $q = 0.998$, $g = 5$, $w_0 = z_0 = 1$, $x_0 - y_0$ plane. (b) $q = 0.998$, $g = 5$, $x_0 = w_0 = 1$, $y_0 - z_0$ plane. (c) $q = 0.94$, $g = 0.1$, $w_0 = z_0 = 1$, $x_0 - y_0$ plane. (d) $q = 0.97$, $g = 0.1$, $w_0 = z_0 = 1$, $x_0 - y_0$ plane.

measure just needs a segment of time series, it is very convenient to detect the coexisting attractors in the multistability systems. However, it can only detect the coexisting states with different complexity. Usually, it means that there exists coexisting chaotic attractors and periodic circles.

4. Wave Formations of the Fractional-Order Ring Network

4.1. The Structure of the Ring Network. To further capture the complex dynamics of the system, we construct a ring network of nonlinear systems which are coupled locally to the nearby 3 nodes with a coupling strength of D. The ring network structure of the neuron network is depicted in Figure 10 and can be numerically defined as

$$\begin{cases} D_{t_0}^q x_i = a(y_i - x_i) + g(\alpha + \beta w_i^2) y_i + \left(\frac{D}{3}\right) \sum (x_{3\in\text{Nodes}} - x_i), \\ D_{t_0}^q y_i = b y_i - x_i z_i - d z_i + e + \left(\frac{D}{3}\right) \sum (y_{3\in\text{Nodes}} - y_i), \\ D_{t_0}^q z_i = x_i y_i - c z_i + \left(\frac{D}{3}\right) \sum (z_{3\in\text{Nodes}} - z_i), \\ D_{t_0}^q w_i = y_i + \left(\frac{D}{3}\right) \sum (w_{3\in\text{Nodes}} - w_i), \end{cases} \tag{18}$$

```
Input: i, N
Output: Nodes
if i = 1
   Nodes = [2, 3, N − 1];
elseif i = 2
   Nodes = [1, N, 4];
elseif i = N − 1
   Nodes = [1, N, N − 3];
elseif i = N
   Nodes = [2, N − 1, N − 2];
elseif i%2 = 1
   Nodes = [i + 1, i − 2, i + 2];
else
   Nodes = [i − 1, i − 2, i + 2];
end if
```

Algorithm 1: The algorithm to find the nodes near node i.

where $i = 1$ to N. N is the number of nodes. The set *nodes* contain the three nodes near the target node. As shown in Figure 10, the nearby nodes of node 1 are node 2, node 3, and node 49, while the nearby nodes of node 36 are node 34, node 35, and node 38. To find the nodes, Algorithm 1 is used.

In order to derive the dynamics of the neuronal ring network, we also fix the system parameters as $a = 36$, $b = 20$, $c = 3$, $d = 5$, $e = 0.1$, $\alpha = 4$, and $\beta = 0.18$ and vary the gain parameter g. In Figure 10, the built network has 50 nodes, and thus $N = 50$.

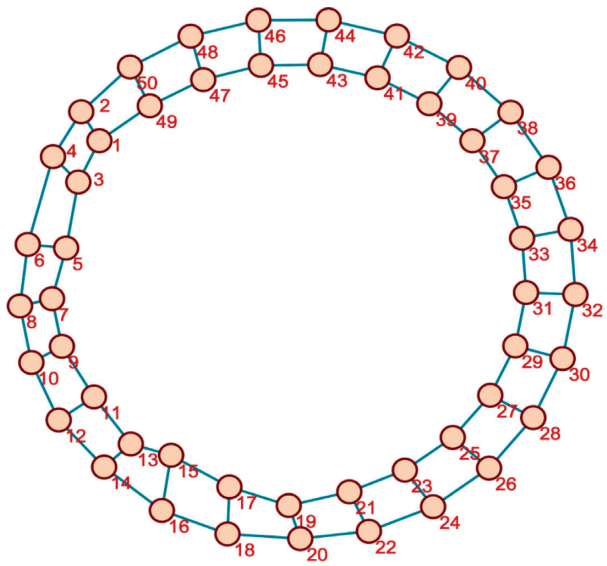

Figure 10: Model of the ring network structure of the network (by Pajek 64 5.08).

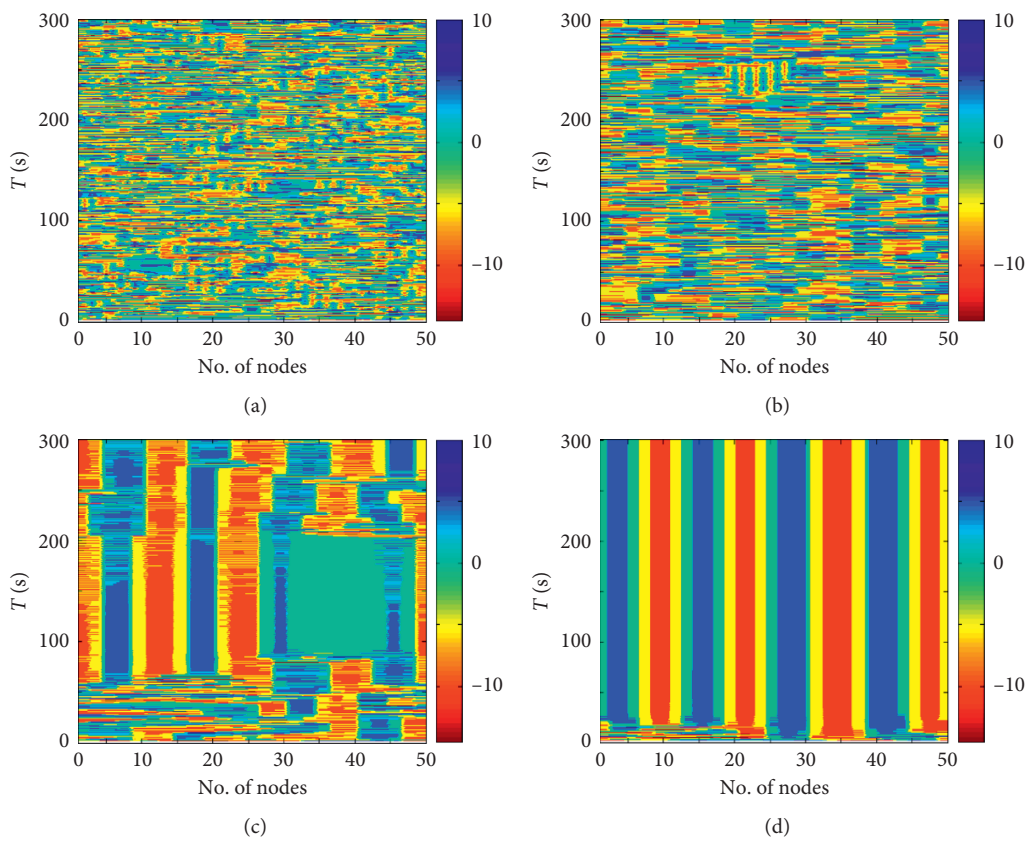

Figure 11: Spatiotemporal patterns of the ring network for different coupling strengths of Case 1. (a) $D = 2$. (b) $D = 4$. (c) $D = 6$. (d) $D = 8$.

4.2. Numerical Simulation of the Fractional-Order Network. Spatiotemporal patterns of the model with the variation of g and q are analyzed for different coupling strengths. Three cases are presented.

Case 1. Fix $q = 0.998$, $g = 3$, and various coupling strengths. The spatiotemporal patterns are shown in Figure 11. In these figures, the level of excitability of the network is illustrated by colours. We can see that when the coupling strength $D = 2$ and 4, only unsynchronized nodes are shown in Figures 11(a) and 11(b). When the coupling strength D increases to 6, some synchronized neurons are found in Figure 11(c), but there are still

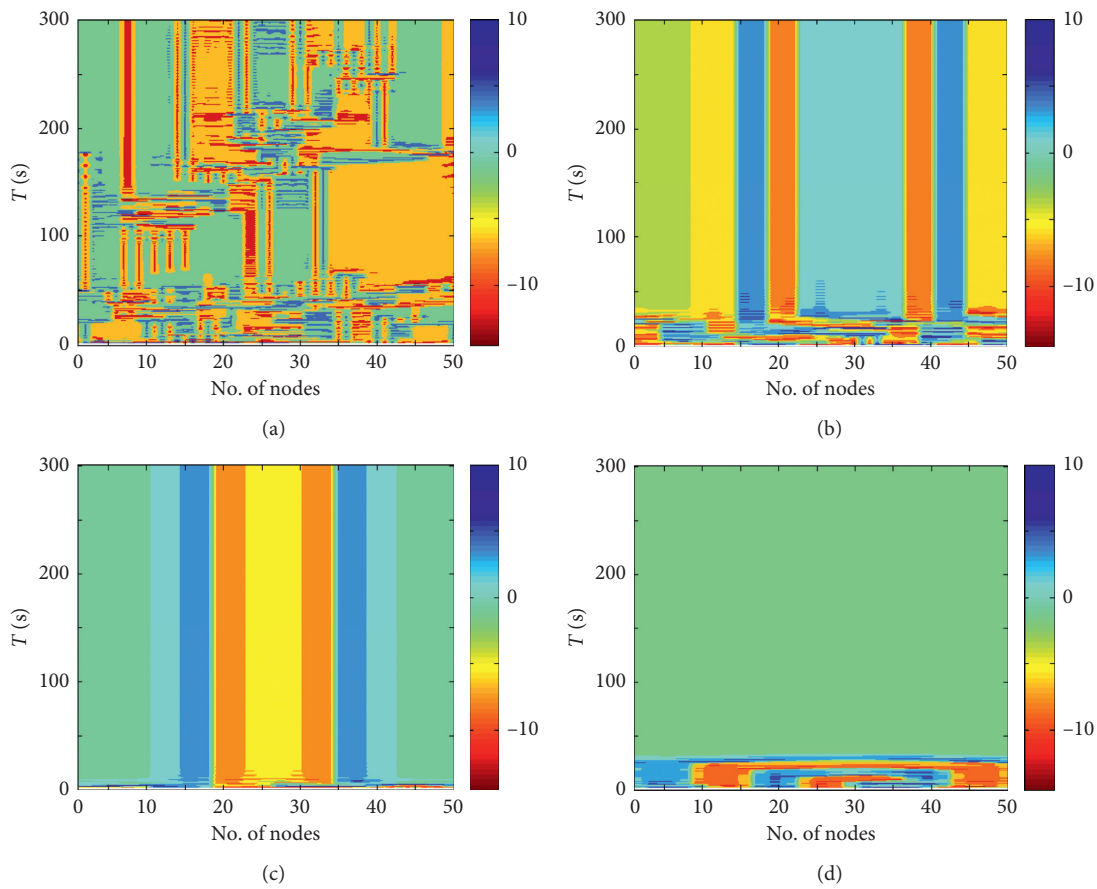

Figure 12: Spatiotemporal patterns of the ring network for different coupling strengths of Case 2. (a) $D = 2$. (b) $D = 4$. (c) $D = 6$. (d) $D = 8$.

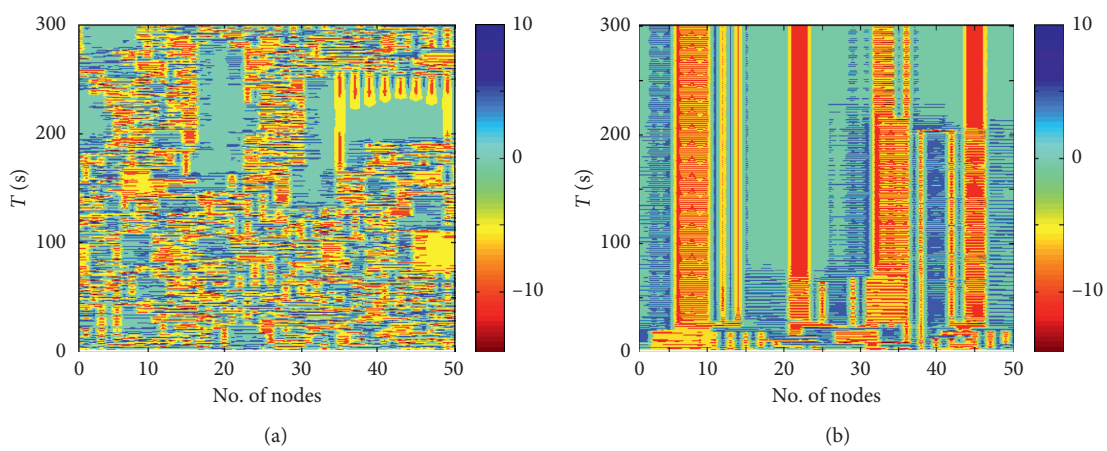

Figure 13: Continued.

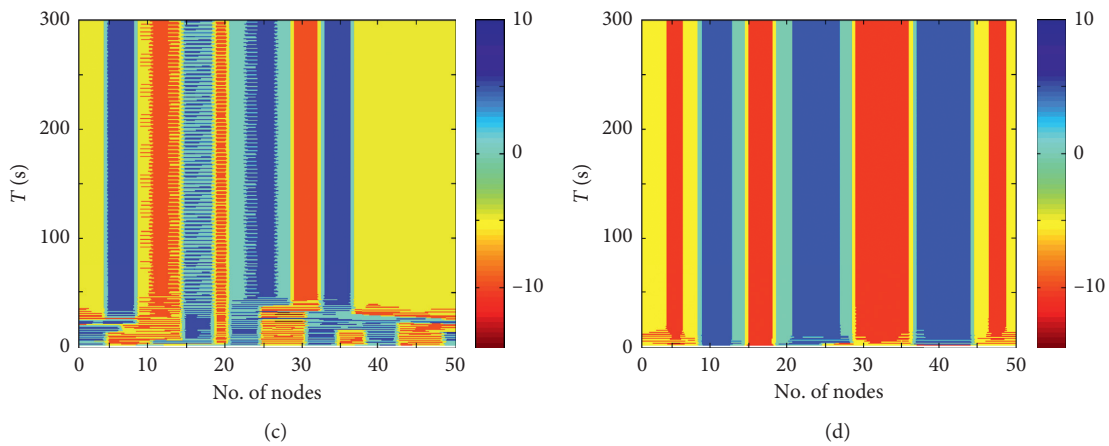

Figure 13: Spatiotemporal patterns of the neuronal ring network for different coupling strengths of Case 3. (a) $D = 1$. (b) $D = 2$. (c) $D = 4$. (d) $D = 6$.

many unsynchronized nodes. By further increasing the coupling strength to $D = 8$, the systems in the network are synchronized locally.

Case 2. Fix $q = 0.998$, $g = 8$, and various coupling strengths. It can be seen from Figure 12 that the spatiotemporal behaviours for $D = 2$ show clear indication of coherent and incoherent nodes. But when the coupling strength is $D = 4$ and 6, some of the systems have synchronization with their nearby nodes. However, by further increasing the coupling strength to $D = 8$, all of the systems are synchronized.

Case 3. Fix $q = 0.97$, $g = 3$, and various coupling strengths. Figure 13 shows that the systems are not synchronized for the coupling strength $D = 1$. With the coupling strength increasing gradually, the number of synchronized systems increases. When the coupling strength $D = 6$, all nodes are in a local synchronization state between different nodes.

As shown in Figures 11–13, the behaviours of the network are different with different coupling strengths. When the coupling strength is small, the network does not show synchronization. For instance, it is shown in Figures 11(a) and 11(b) that the network is not synchronized. When the coupling strength is large, the network can be synchronized. For example, Figure 12(d) shows that there exists synchronization. The chimera state means coexistence of synchronization and asynchronization in the network. According to Figures 11–13, there are different kinds of chimera state in the network. The network with different fractional-order derivative order has different dynamics. As for the coupling strength for chimera states in the network, it should be proper. According to the analysis results, when the coupling strength $D \in [2, 4]$, the chimera states are observed. Moreover, the derivative order also affects the dynamics of the network. In Case 1, we fix $q = 0.998$ and in Case 3 we let $q = 0.97$, and it is shown in Figures 11 and 13 that the dynamics of the network are different. It is easier for the network with $q = 0.97$ to synchronize or to show chimera states.

5. Conclusions

In this paper, a fractional-order memristor-based hyperchaotic system with no equilibrium points has been numerically analyzed by employing the predictor-corrector method. It shows that the system has rich dynamical behaviours, and different states including periodic circle, chaotic attractor, and hyperchaotic attractor are plotted in the system. The minimum derivative order of generating chaos is found, and it is $q = 0.927$. Meanwhile, through numerical simulation, the coexisting hidden attractors are observed with different initial conditions. Moreover, the SampEn complexity verifies the hidden dynamic characteristics of the system and it shows that this complexity analysis algorithm can be employed to detect the multiple coexisting attractors. Finally, by constructing the ring network structure of the system, it can be found that with increase of the coupling strength, the state of the network is different. The network can have the global synchronization state with large coupling strength, while in most cases, the network shows chimera states with proper coupling strength.

Data Availability

All data, models, and code generated or used during the study appear in the submitted article.

Conflicts of Interest

The authors declare that there are no conflicts of interest regarding the publication of this paper.

Acknowledgments

This study was supported by the National Natural Science Foundation for Theoretical Physics of China (grant nos. 61901530 and 11747150), the Hunan Provincial Department of Education General Project Fund (no. B08004056), the China Postdoctoral Science Foundation (grant no.

2019M652791), and the Postdoctoral Creative Talent Support Programme (grant no. BX20180386).

References

[1] L. Chua, "Memristor-the missing circuit element," *IEEE Transactions on Circuit Theory*, vol. 18, no. 5, pp. 507–519, 1971.

[2] O. Kavehei, A. Iqbal, Y. S. Kim et al., "The fourth element: characteristics, modelling and electromagnetic theory of the memristor," *Proceedings of the Royal Society A: Mathematical, Physical and Engineering Sciences*, vol. 466, no. 2120, pp. 2175–2202, 2010.

[3] D. B. Strukov, G. S. Snider, D. R. Stewart, and R. S. Williams, "The missing memristor found," *Nature*, vol. 453, no. 7191, pp. 80–83, 2008.

[4] T.-C. Lin, F.-Y. Huang, Z. Du, and Y.-C. Lin, "Synchronization of fuzzy modeling chaotic time delay memristor-based Chua's circuits with application to secure communication," *International Journal of Fuzzy Systems*, vol. 17, no. 2, pp. 206–214, 2015.

[5] C. S. Pappu, T. L. Carroll, and B. C. Flores, "Simultaneous radar-communication systems using controlled chaos-based frequency modulated waveforms," *IEEE Access*, vol. 8, pp. 48361–48375, 2020.

[6] M. S. Tarkov, "Mapping weight matrix of a neural network's layer onto memristor crossbar," *Optical Memory and Neural Networks*, vol. 24, no. 2, pp. 109–115, 2015.

[7] B. Bao, H. Qian, Q. Xu et al., "Coexisting behaviors of asymmetric attractors in hyperbolic-type memristor based hopfield neural network," *Frontiers in Computational Neuroscience*, vol. 11, p. 81, 2017.

[8] J. Ruan, K. H. Sun, J. Mou, S. He, and L. Zhang, "Fractional-order simplest memristor-based chaotic circuit with new derivative," *The European Physical Journal Plus*, vol. 133, no. 1, p. 3, 2018.

[9] F. Yuan, G. Wang, and X. Wang, "Extreme multistability in a memristor-based multi-scroll hyper-chaotic system," *Chaos: An Interdisciplinary Journal of Nonlinear Science*, vol. 26, no. 7, pp. 507–519, 2016.

[10] X. Hu, S. Duan, G. Chen, and L. Chen, "Modeling affections with memristor-based associative memory neural networks," *Neurocomputing*, vol. 223, pp. 129–137, 2017.

[11] N. Shao, S. B. Zhang, and S. Y. Shao, "A phenomenological memristor model for synaptic memory and learning behaviors," *Chinese Physics B*, vol. 26, no. 11, p. 536, 2017.

[12] F. Corinto, M. A. Ascoli, and M. Gilli, "Nonlinear dynamics of memristor oscillators," *IEEE Transactions on Circuits and Systems I: Regular Papers*, vol. 58, no. 6, pp. 1323–1336, 2011.

[13] V. V. Rakitin and S. G. Rusakov, "Operating principles of reactance-less memristor-based oscillators," *Journal of Communications Technology and Electronics*, vol. 62, no. 6, pp. 621–625, 2017.

[14] S. Vaidyanathan, V. T. Pham, C. K. Volos, and L. T. Phuoc, "A memristor-based hyperchaotic system with hidden attractors: dynamics, synchronization and circuital emulating," *Journal of Engineering Science and Technology Review*, vol. 8, no. 2, pp. 205–214, 2015.

[15] B. Xu, G. Wang, H. H.-C. Iu, S. Yu, and F. Yuan, "A memristor-meminductor-based chaotic system with abundant dynamical behaviors," *Nonlinear Dynamics*, vol. 96, no. 1, pp. 765–788, 2019.

[16] B. C. Bao, H. Bao, N. Wang, M. Chen, and Q. Xu, "Hidden extreme multistability in memristive hyperchaotic system," *Chaos, Solitons & Fractals*, vol. 94, pp. 102–111, 2017.

[17] K. B. Oldham and J. Spanier, "The fractional calculus," *Mathematical Gazette*, vol. 56, no. 247, pp. 396–400, 1974.

[18] R. Hilfer, *Applications of Fractional Calculus in Physics*, World Scientific, Singapore, 2000.

[19] S. He, S. Banerjee, and K. Sun, "Can derivative determine the dynamics of fractional-order chaotic system?" *Chaos, Solitons and Fractals*, vol. 115, pp. 14–22, 2018.

[20] H. Wang, S. He, and K. Sun, "Complex dynamics of the fractional-order Rössler system and its tracking synchronization control," *Complexity*, vol. 2018, Article ID 4019749, 13 pages, 2018.

[21] L. Teng, H. H. C. Lu, X. Wang, and X. Wang, "Chaotic behaviour in fractional-order memristor-based simplest chaotic circuit using fourth degree polynomial," *Nonlinear Dynamics*, vol. 77, no. 1-2, pp. 231–241, 2014.

[22] W. Hu, D. Ding, Y. Zhang, N. Wang, and D. Liang, "Hopf bifurcation and chaos in a fractional order delayed memristor-based chaotic circuit system," *Optik*, vol. 130, no. 2, pp. 189–200, 2017.

[23] N. Yang, C. Xu, C. Wu, R. Jia, and C. Liu, "Modeling and analysis of a fractional-order generalized memristor-based chaotic system and circuit implementation," *International Journal of Bifurcation and Chaos*, vol. 27, no. 13, Article ID 1750199, 2017.

[24] K. Rajagopal, L. Guessas, A. Karthikeyan et al., "Fractional-order memristor no equilibrium chaotic system with its adaptive sliding mode synchronization and genetically optimized fractional order PID synchronization," *Complexity*, vol. 2017, Article ID 1892618, 19 pages, 2017.

[25] P. Prakash, J. P. Singh, and B. K. Roy, "Fractional-order memristor-based chaotic Jerk system with no equilibrium point and its fractional-order backstepping control," *IFAC-PapersOnLine*, vol. 51, no. 1, pp. 1–6, 2018.

[26] X. H. Qiao, Y. Xu, Y. X. Sun, and H.-G. Wu, "Hidden dynamical characteristics in memristor-based hyperchaotic Lü system," *Journal of University of Electronic Science and Technology of China*, vol. 47, no. 3, pp. 84–91, 2018.

[27] J. Lü and G. Chen, "A new chaotic attractor coined," *International Journal of Bifurcation and Chaos*, vol. 12, no. 3, pp. 659–661, 2002.

[28] S. He, K. Sun, and H. Wang, "Synchronisation of fractional-order time delayed chaotic systems with ring connection," *The European Physical Journal Special Topics*, vol. 225, no. 1, pp. 97–106, 2016.

[29] X. Chen, J. H. Park, J. Cao, and J. Qiu, "Sliding mode synchronization of multiple chaotic systems with uncertainties and disturbances," *Applied Mathematics and Computation*, vol. 308, pp. 161–173, 2017.

[30] X. Mao and Z. Wang, "Stability, bifurcation, and synchronization of delay-coupled ring neural networks," *Nonlinear Dynamics*, vol. 84, no. 2, pp. 1063–1078, 2016.

[31] X. Mao, J. Sun, and S. Li, "Dynamics of delay-coupled Fitz-Hugh-Nagumo neural rings," *Chaos*, vol. 28, Article ID 013104, 2018.

[32] Y. Zhang, X. Wang, and E. G. Friedman, "Memristor-based circuit design for multilayer neural networks," *IEEE Transactions on Circuits and Systems I: Regular Papers*, vol. 65, no. 2, pp. 677–686, 2018.

[33] C. Li, D. Belkin, Y. Li et al., "Efficient and self-adaptive in-situ learning in multilayer memristor neural networks," *Nature Communications*, vol. 9, no. 1, p. 2385, 2018.

[34] A. Carpinteri and F. Mainardi, *Fractals and Fractional Calculus in Continuum Mechanics*, Springer, Berlin, Germany, 1997.

[35] G. A. Leonov, N. V. Kuznetsov, and V. I. Vagaitsev, "Localization of hidden Chua's attractors," *Physics Letters A*, vol. 375, no. 23, pp. 2230–2233, 2011.

[36] D. Kai, N. J. Ford, and A. D. Freed, "A predictor-corrector approach for the numerical solution of fractional differential equations," *Nonlinear Dynamics*, vol. 29, no. 4, pp. 3–22, 2002.

[37] H. Sun, A. Abdelwahab, and B. Onaral, "Linear approximation of transfer function with a pole of fractional power," *IEEE Transactions on Automatic Control*, vol. 29, no. 5, pp. 441–444, 1984.

[38] M.-F. Danca and N. Kuznetsov, "Matlab code for Lyapunov exponents of fractional-order systems," *International Journal of Bifurcation and Chaos*, vol. 28, no. 5, Article ID 1850067, 2018.

[39] M.-F. Danca, M. Fečkan, N. V. Kuznetsov, and G. Chen, "Fractional-order PWC systems without zero Lyapunov exponents," *Nonlinear Dynamics*, vol. 92, no. 3, pp. 1061–1078, 2018.

[40] P. Ramanand, V. Nampoori, and R. Sreenivasan, "Complexity quantification of dense array EEG using sample entropy analysis," *Journal of Integrative Neuroscience*, vol. 3, no. 3, pp. 343–358, 2004.

[41] Y. Jia, H. Gu, and Q. Luo, "Sample entropy reveals an age-related reduction in the complexity of dynamic brain," *Scientific Reports*, vol. 7, no. 1, p. 7990, 2017.

Hindawi
Mathematical Problems in Engineering
Volume 2020, Article ID 4298230, 9 pages
https://doi.org/10.1155/2020/4298230

Research Article

Mixed H_2/H_∞ Control for Itô-type Stochastic Time-Delay Systems with Applications to Clothing Hanging Device

Yan Qi,[1] Min Zhang,[2] and Zhiguo Yan[2]

[1]*School of Fine Arts and Design, University of Jinan, Jinan 250022, China*
[2]*School of Electrical Engineering and Automation, Qilu University of Technology (Shandong Academy of Sciences), Jinan 250353, China*

Correspondence should be addressed to Zhiguo Yan; yanzg500@sina.com

Received 16 April 2020; Accepted 20 May 2020; Published 20 June 2020

Guest Editor: Yi Qi

This paper deals with the problem of mixed H_2/H_∞ control for Itô-type stochastic time-delay systems. First, the H_2/H_∞ control problem for stochastic time-delay systems is presented, which considers the mean square stability, H_2 control performance index, and the ability of disturbance attenuation of the closed-loop systems. Second, by choosing an appropriate Lyapunov–Krasoviskii functional and using matrix inequality technique, some sufficient conditions for the existence of state feedback H_2/H_∞ controller for stochastic time-delay systems are obtained in the form of linear matrix inequalities. Third, two convex optimization problems with linear matrix inequality constraints are formulated to design the optimal mixed H_2/H_∞ controller which minimizes the guaranteed cost of the closed-loop systems with known and unknown initial functions, and the corresponding algorithm is given to optimize H_2/H_∞ performance index. Finally, a numerical example is employed to show the effectiveness and feasibility of the proposed method.

1. Introduction

Over the past decades, there has been a rapid increase of interest in the study of stochastic systems due to the importance of stochastic models in science and engineering, such as finance systems [1] and power systems [2]. And a lot of excellent results have been obtained. For example, Zhu et al. [3] investigated the tracking control issue of stochastic systems subject to time-varying full state constraints and input saturation. In [4], the stability of a class of discrete-time stochastic nonlinear systems with external disturbances was considered. The finite-time tracking control of a class of stochastic quantized nonlinear systems was studied in [5]. Furthermore, since stochasticity and time delay are the main sources resulting in the complexities of systems in reality, considerable interests have been focused on a general model of stochastic time-delay systems. For example, the problem of guaranteed cost robust stable control was considered via state feedback for a class of uncertain stochastic systems with time-varying delay in [6]. In [7], the mean square exponential stability of neutral-type linear stochastic time-delay systems with three different delays by using the Lyapunov–Krasovskii functionals was studied. In [8], the finite-time dissipative control for stochastic interval systems with time delay and Markovian switching was investigated. Some other nice results can be referred to [9–17] and the references therein.

At present, H_∞ control has been receiving increased attention because it can suppress external interference, and many efforts have been devoted to extending the results for H_∞ control over the last few decades. For instance, Ma and Liu [18] investigated the finite-time H_∞ control problem for singular Markovian jump system with actuator fault through the sliding mode control approach. In [19], the problem of nonfragile observer-based H_∞ control for stochastic time-delay systems was considered. The problems of robust stabilization and robust H_∞ control with maximal decay rate were investigated for discrete-time stochastic systems with time-varying norm-bounded parameter uncertainties in [20]. Some other nice results can be referred to [21–26]. On the contrary, H_∞ control is an effective way to attenuate the disturbance, while H_2 control can guarantee quadratic

performance cost. By combining H_2 control and H_∞ control theory, the mixed H_2/H_∞ control theory is obtained. Owing to the fact that the mixed H_2/H_∞ control can minimize a desired control performance and eliminate the effect of disturbance, it is more attractive than the sole H_∞ control in engineering practice. For example, Gao et al. [12] investigated the problem of H_2/H_∞ control for nonlinear stochastic systems with time-delay and state-dependent noise. H_2/H_∞ control problem of stochastic systems with random jumps was solved in [27]. Sathananthan et al. [28] studied guaranteed cost H_∞ control of linear stochastic Markovian switching systems. Although the problem of H_2/H_∞ control has been investigated, there are few literature studies on Itô-type stochastic time-delay systems.

Motivated by the abovementioned discussions, in this work, we aim to investigate the mixed H_2/H_∞ control for Itô-type stochastic time-delay systems. It is difficult to design state feedback H_2/H_∞ controller because of the complicated structure of the system. The main contributions of this paper are as follows. (i) The definition of H_2/H_∞ control for Itô-type stochastic time-delay systems is presented, which considers stability, H_2 control performance index, and H_∞ control performance index. (ii) The new sufficient conditions for the existence of state feedback H_2/H_∞ controller are provided in the form of linear matrix inequalities. (iii) An algorithm is given to optimize H_2/H_∞ performance index.

The organization of this paper is as follows. Section 2 is devoted to the problem statement, preliminaries, and lemmas. Section 3 provides the sufficient conditions for the existence of state feedback H_2/H_∞ controller for Itô-type stochastic time-delay systems. Section 4 gives an algorithm to solve the theorems. Section 5 presents a numerical example to demonstrate the effectiveness of the proposed method. Section 6 is our conclusions.

Notations: A' denotes the transpose of matrix A; $\mathrm{tr}(A)$ indicates the trace of matrix A; $A > 0$ ($A \geq 0$) indicates that A is a positive definite (positive semidefinite) matrix; $I_{n\times n}$ represents a n-dimensional identity matrix; $\mathscr{R}^n$ shows n-dimensional Euclidean space; E represents the mathematical expectation of random process; and the asterisk "*" in the matrix indicates symmetry term.

2. Preliminaries

Consider the following Itô-type stochastic time-delay system described by

$$\begin{cases} dx(t) = [A_{11}x(t) + A_{12}x(t-\tau) + B_{11}u(t) + B_{12}v(t)]dt + [A_{21}x(t) + A_{22}x(t-\tau) + B_{21}u(t)]dw(t), \\ z(t) = C_1x(t) + D_1u(t), \\ x(t) = \phi(t), \forall t \in [-\tau, 0], \end{cases} \tag{1}$$

where $x(t)$ is the state of the system, $u(t)$ is the control input, $z(t)$ is the control output, $\phi(t)$ is the initial state function, and $w(t)$ is a one-dimensional standard Wiener process defined on probability space $(\Omega, \mathscr{F}, \mathscr{F}_t, \mathrm{P})$. $\mathscr{F}_t$ stands for the smallest σ-algebra generated by $w(s)$, $0 \leq s \leq t$, i.e., $\mathscr{F}_t = \sigma\{w(s) \mid 0 \leq s \leq t\}$. $\tau > 0$ is the time delay. A_{11}, A_{12}, A_{21}, A_{22}, B_{11}, B_{12}, C_1, and D_1 are constant matrices with appropriate dimensions.

Next, a new definition of the mean square stability for system (1) is given.

Definition 1. System (1) ($u(t) \equiv 0$ and $v(t) \equiv 0$) is said to be mean square stable, if

$$\lim_{t\longrightarrow\infty} E\|x(t)\|^2 = 0. \tag{2}$$

Then, some lemmas for obtaining the main results are introduced.

Lemma 1 (see [29]). *Let $V(t,x) \in C^{1,2}(R_+, R^n)$ be a scalar function, and $V(t,x) > 0$, for the following stochastic system:*

$$dx(t) = a(x)dt + b(x)dw(t). \tag{3}$$

The Itô formula of $V(t,x)$ is given as follows:

$$dV(t,x) = LV(t,x)dt + \frac{\partial V'(t,x)}{\partial x} b(x)dw(t), \tag{4}$$

where

$$LV(t,x) = \frac{\partial V(t,x)}{\partial t} + \frac{\partial V'(t,x)}{\partial x} a(x) + \frac{1}{2} b'(x) \frac{\partial^2 V(t,x)}{\partial x^2} b(x). \tag{5}$$

Lemma 2 (see [30]). *For given $x \in R^n$, $y \in R^m$, $N \in R^{n\times m}$, and $\rho > 0$, then we have*

$$2x'Ny \leq \rho x'x + \frac{1}{\rho} y'N'Ny. \tag{6}$$

Lemma 3 (see [6]). *For some real matrices $N, M' = M$ and $R = R' > 0$, the following three conditions are equivalent:*

$$\begin{gathered} M + NR^{-1}N' < 0, \\ \begin{bmatrix} M & N \\ N' & -R \end{bmatrix} < 0, \\ \begin{bmatrix} M & -N \\ -N' & -R \end{bmatrix} < 0. \end{gathered} \tag{7}$$

3. Mixed H_2/H_∞ Control for Stochastic Time-Delay Systems

In this section, a state feedback H_2/H_∞ controller will be designed.

We consider a state feedback controller for system (1) is

$$u(t) = Kx(t), \tag{8}$$

where K is the state feedback gain to be determined.

The closed-loop system can be obtained by substituting (2) into (1):

$$\begin{cases} dx(t) = [A_{11}x(t) + A_{12}x(t-\tau) + B_{11}Kx(t) + B_{12}v(t)]dt + [A_{21}x(t) + A_{22}x(t-\tau) + B_{21}Kx(t)]dw(t), \\ z(t) = C_1x(t) + D_1Kx(t), \\ x(t) = \phi(t), \quad \forall t \in [-\tau, 0]. \end{cases} \tag{9}$$

Associated with system (1), the cost function is provided as follows:

$$J_s(x(t), u(t)) = E\int_0^\infty (x'(t)Tx(t) + u'(t)Ru(t))\mathrm{d}t, \tag{10}$$

where $T = T' > 0$ and $R = R' > 0$ are the given positive scalars or given weighting matrices.

By substituting (2) into (4), we can obtain

$$J_s(x(t)) = E\int_0^\infty (x'(t)Tx(t) + x'(t)K'RKx(t))\mathrm{d}t. \tag{11}$$

Based on the above analysis, the problem of H_2/H_∞ control for stochastic time-delay systems is provided as follows.

Definition 2. For a given scalar $\gamma > 0$, if there exist a positive scalar J_s^* and a state feedback controller (2) such that

(i) The closed-loop system (3) is asymptotically stable in mean square sense.

(ii) H_2 cost function (5) satisfies $J_s(x(t)) \le J_s^*$ under the condition of $v(t) = 0$.

(iii) For any nonzero disturbance $v(t)$, the control output $z(t)$ satisfies the following inequality with zero initial condition:

$$E\int_0^\infty \|z(t)\|^2\mathrm{d}s < \gamma^2 E\int_0^\infty \|v(t)^2\|\mathrm{d}s, \tag{12}$$

then (2) is said to be a state feedback H_2/H_∞ controller for system (1).

The sufficient conditions for the existence of the state feedback H_2/H_∞ controller (2) are given below. For this reason, an important lemma is first given.

Lemma 4. *For a given scalar $\gamma > 0$ and two symmetric positive definite matrices T and R, if there are two symmetric positive definite matrices P and Q such that*

$$\begin{bmatrix} \Gamma_{11} & PA_{12} + (A_{21} + B_{21}K)'PA_{22} & PB_{12} \\ * & -Q + A_{22}'PA_{22} & 0 \\ * & * & -\gamma^2 I \end{bmatrix} < 0, \tag{13}$$

hold, where $\Gamma_{11} = Q + (A_{21} + B_{21}K)'P(A_{21} + B_{21}K) + 2(A_{11} + B_{11}K)'P + (C_1 + D_1K)'(C_1 + D_1K) + T + K'RK$, then (2) is a mixed H_2/H_∞ controller of system (3), and the corresponding guaranteed cost for system (3) is $J_s^* = E[x'(0)Px(0) + \int_{-\tau}^0 x'(s)Qx(s)ds]$.

Proof. The following proof is divided into three parts. First, it is proved that the closed-loop system (3) is mean square stable.

According to Lemma 3, condition (7) implies

$$\begin{bmatrix} \Gamma_{11} + \frac{1}{\gamma^2}PB_{12}B_{12}'P & PA_{12} + (A_{21} + B_{21}K)'PA_{22} \\ * & -Q + A_{22}'PA_{22} \end{bmatrix} < 0. \tag{14}$$

Due to $T > 0$, $R > 0$, and $\gamma > 0$, we can obtain $(C_1 + D_1K)'(C_1 + D_1K) > 0$, $(1/\gamma^2)PB_{12}B_{12}'P > 0$, and $K'RK > 0$; then, (8) implies

$$\begin{bmatrix} \Sigma_{11} & PA_{12} + (A_{21} + B_{21}K)'PA_{22} \\ * & -Q + A_{22}'PA_{22} \end{bmatrix} < 0, \tag{15}$$

where $\Sigma_{11} = Q + (A_{21} + B_{21}K)'P(A_{21} + B_{21}K) + 2(A_{11} + B_{11}K)'P$.

Let a quadratic function $V(x(t), t) = x'(t)Px(t) + \int_{-\tau}^0 x'(t+s)Qx(t+s)\mathrm{d}s$ and the differential generation operator of system (3) be $L_1V(x(t))$ with $v = 0$; then,

$$\begin{aligned}
&L_1V(x(t),t)\\
&= x'(t)Qx(t) - x'(t-\tau)Qx(t-\tau) + 2\left[x'(t)(A_{11}+B_{11}K)' + x'(t-\tau)A_{12}'\right]Px(t)\\
&\quad + \left[x'(t)(A_{21}+B_{21}K)' + x'(t-\tau)A_{22}'\right]P\left[(A_{21}+B_{21}K)x(t) + A_{22}x(t-\tau)\right]\\
&= x'(t)Qx(t) - x'(t-\tau)Qx(t-\tau) + 2\left[x'(t)(A_{11}+B_{11}K)' + x'(t-\tau)A_{12}'\right]Px(t)\\
&\quad + x'(t-\tau)A_{22}'PA_{22}x(t-\tau) + x'(t)(A_{21}+B_{21}K)'P(A_{21}+B_{21}K)x(t)\\
&\quad + 2x'(t-\tau)A_{22}'P(A_{21}+B_{21}K)x(t),
\end{aligned} \tag{16}$$

that is,

$$L_1V = \begin{bmatrix} x(t) \\ x(t-\tau) \end{bmatrix}' \begin{bmatrix} \Omega_{11} & PA_{12} + (A_{21}+B_{21}K)'PA_{22} \\ * & -Q + A_{22}'PA_{22} \end{bmatrix} \begin{bmatrix} x(t) \\ x(t-\tau) \end{bmatrix}, \tag{17}$$

where $\Omega_{11} = Q + (A_{11}+B_{11}K)'P + P(A_{11}+B_{11}K) + (A_{21}+B_{21}K)'P(A_{21}+B_{21}K)$.

In the light of (9), we can derive that $L_1V(x(t),t) < 0$, that is, the closed-loop system (3) is asymptotically stable in mean square sense.

Secondly, we prove that the control output $z(t)$ satisfies H_∞ index for any nonzero disturbance $v(t)$ under zero initial condition.

According to (7), $T > 0$, and $K'RK > 0$, we can obtain

$$\begin{bmatrix} \Psi_{11} & PA_{12} + (A_{21}+B_{21}K)'PA_{22} & PB_{12} \\ * & -Q + A_{22}'PA_{22} & 0 \\ * & * & -\gamma^2 I \end{bmatrix} < 0, \tag{18}$$

where $\Psi_{11} = Q + (A_{21}+B_{21}K)'P(A_{21}+B_{21}K) + 2(A_{11}+B_{11}K)'P + (C_1+D_1K)'(C_1+D_1K)$.

Notice that

$$\begin{aligned}
&E\int_0^\infty \left(z'z - \gamma^2 v'v\right)\mathrm{d}t = E\int_0^\infty\\
&\quad \left\{\left[x'(t)(C_1+D_1K)'(C_1+D_1K)x(t) - \gamma^2 v'v\right]\right.\\
&\quad \left.\mathrm{d}t + L_2V - L_2V\right\}\\
&\le E\int_0^\infty \left\{\left[x'(t)(C_1+D_1K)'(C_1+D_1K)x(t) - \gamma^2 v'v\right]\right.\\
&\quad \left.\mathrm{d}t + L_2V\right\},
\end{aligned} \tag{19}$$

where $L_2V(x(t))$ is the infinitesimal operator of system (3) for any nonzero disturbance $v(t)$, and

$$\begin{aligned}
&L_2V(x(t),t)\\
&= x'(t)Qx(t) - x'(t-\tau)Qx(t-\tau) + 2\\
&\left[(A_{11}+B_{11}K)x(t) + A_{12}x(t-\tau) + B_{12}v(t)\right]'Px(t)\\
&\quad + \left[(A_{21}+B_{21}K)x(t) + A_{22}x(t-\tau)\right]'P\left[(A_{21}+B_{21}K)x(t) + A_{22}x(t-\tau)\right]\\
&= x'(t)Qx(t) - x'(t-\tau)Qx(t-\tau)\\
&\quad + 2x'(t)(A_{11}+B_{11}K)'Px(t) + x'(t)(A_{21}+B_{21}K)'\\
&P(A_{21}+B_{21})x(t) + 2x'(t-\tau)A_{12}'Px(t) + 2v'(t)B_{12}'Px(t)\\
&\quad + 2x'(t)(A_{21}+B_{21}K)'PA_{22}x(t-\tau) + x'(t-\tau)A_{22}'PA_{22}x(t-\tau).
\end{aligned} \tag{20}$$

Then, we can see that

$$E\int_0^\infty \left(z'z - \gamma^2 v'v\right)\mathrm{d}t \le E\int_0^\infty \begin{bmatrix} x(t) \\ x(t-\tau) \\ v(t) \end{bmatrix}' \begin{bmatrix} \Psi_{11} & \Psi_{12} & PB_{12} \\ * & -Q + A_{22}'PA_{22} & 0 \\ * & * & -\gamma^2 I \end{bmatrix} \begin{bmatrix} x(t) \\ x(t-\tau) \\ v(t) \end{bmatrix} \mathrm{d}t, \tag{21}$$

where $\Psi_{12} = PA_{12} + (A_{21} + B_{21}K)'PA_{22}$.

Based on (12), we can see $E\int_0^\infty (z'z - \gamma^2 v'v)\mathrm{d}t \le 0$, that is, (12) implies that $E\int_0^\infty \|z(t)\|^2\mathrm{d}t < \gamma^2 E\int_0^\infty \|v(t)\|^2\mathrm{d}t$. Therefore, system (3) satisfies H_∞ index.

Thirdly, we prove that system (3) satisfies H_2 index under the condition of $v(t) = 0$.

Based on (13) and (14), $(C_1 + D_1K)'(C_1 + D_1K) > 0$, and $(1/\gamma^2)PB_{12}B_{12}'P > 0$, we obtain that

$$\begin{bmatrix} \Theta_{11} & PA_{12} + (A_{21} + B_{21}K)'PA_{22} \\ * & -Q + A_{22}'PA_{22} \end{bmatrix} < 0, \tag{22}$$

holds, where $\Theta_{11} = \Omega_{11} + T + K'RK$.

Due to

$$\begin{aligned} &E\int_0^\infty (x'(t)Tx(t) + u'(t)Ru(t))\mathrm{d}t \\ &= E\int_0^\infty [(x'(t)(T + K'RK)x(t) + L_1V - L_1V]\mathrm{d}t \\ &= E\int_0^\infty [x'(t)(T + K'RK)x(t) + L_1V]\mathrm{d}t - E\int_0^\infty \mathrm{d}V \\ &\quad = E\int_0^\infty [x'(t)(T + K'RK)x(t) + L_1V] \\ &\quad \mathrm{d}t - EV(x(\infty), \infty) + EV(x(0), 0) \\ &\quad = E\int_0^\infty \begin{bmatrix} x(t) \\ x(t-\tau) \end{bmatrix}' \begin{bmatrix} \Theta_{11} & \Psi_{12} \\ * & \Theta_{14} \end{bmatrix} \begin{bmatrix} x(t) \\ x(t-\tau) \end{bmatrix} \\ &\quad \mathrm{d}t + EV(x(0), 0), \end{aligned} \tag{23}$$

where $\Theta_{14} = -Q + A_{22}'PA_{22}$.

In view of (22), we obtain

$$\begin{bmatrix} \Theta_{11} & \Psi_{12} \\ * & \Theta_{14} \end{bmatrix} < 0. \tag{24}$$

According to (23) and (24), we can see

$$\begin{aligned} J_s &= E\int_0^\infty (x'(t)Tx(t) + u'(t)Ru(t))\mathrm{d}t \\ &< EV(x(0), 0) \\ &= E\left[x'(0)Px(0) + \int_{-\tau}^0 x'(s)Qx(s)\mathrm{d}s\right] \\ &= J_s^*. \end{aligned} \tag{25}$$

The proof is completed here. □

In order to solve the complex problem to seek the solution caused by the nonlinear terms in Lemma 4, we give the following Lemma 5.

Lemma 5. *For a given scalar $\gamma > 0$ and two symmetric positive definite matrices $\widetilde{T}$ and $\widetilde{R}$, if there are two symmetric positive definite matrices $\widetilde{P}$ and $\widetilde{Q}$ and a matrix M such that*

$$\begin{bmatrix} \Xi_{11} & \Xi_{12} & A_{12}\widetilde{Q} & 0 & \widetilde{P} & 2\widetilde{P}A_{21}' & 2M'B_{21}' & B_{12} \\ * & \Xi_{22} & 0 & 0 & 0 & 0 & 0 & 0 \\ * & * & -\widetilde{Q} & \sqrt{3}\,\widetilde{Q}A_{22}' & 0 & 0 & 0 & 0 \\ * & * & * & -\widetilde{P} & 0 & 0 & 0 & 0 \\ * & * & * & * & -\widetilde{Q} & 0 & 0 & 0 \\ * & * & * & * & * & -\widetilde{P} & 0 & 0 \\ * & * & * & * & * & * & -\widetilde{P} & 0 \\ * & * & * & * & * & * & * & -\gamma^2 I \end{bmatrix} < 0 \tag{26}$$

hold, where $\Xi_{11} = \widetilde{P}A_{11}' + A_{11}\widetilde{P} + M'B_{11}' + B_{11}M$, $\Xi_{12} = [\sqrt{3}\,\widetilde{P}C_1', \widetilde{P}, \sqrt{3}\,M'D_1', M']$, and $\Xi_{22} = diag\left\{-I, -\widetilde{T}, -I, -\widetilde{R}\right\}$; then, (8) is a mixed H_2/H_∞ controller of system (9), and the corresponding guaranteed cost for system (9) is $J_s^* = E[x'(0)\,\widetilde{P}^{-1}x(0) + \int_{-\tau}^0 x'(s)\widetilde{Q}^{-1}x(s)ds]$. In this case, $K = M\widetilde{P}^{-1}$.

Proof. According to Lemma 2 and (13), if the following inequality

$$\begin{bmatrix} \Upsilon_{11} & PA_{12} & PB_{12} \\ * & -Q + 3A_{22}'PA_{22} & 0 \\ * & * & -\gamma^2 I \end{bmatrix} < 0 \tag{27}$$

hold, where $\Upsilon_{11} = Q + 4A_{21}'PA_{21} + 4K'B_{21}'PB_{21}K + 2A_{11}'P + 2K'B_{11}'P + 3C_1'C_1 + 3K'D_1'D_1K + T + K'RK$, then (13) holds.

Using $\mathrm{diag}\{P^{-1}, Q^{-1}, I\}$ to premultiply and postmultiply inequality (27), we have

$$\begin{bmatrix} \widetilde{\Upsilon}_{11} & A_{12}Q^{-1} & B_{12} \\ * & -Q^{-1} + 3Q^{-1}A_{22}'PA_{22}Q^{-1} & 0 \\ * & * & -\gamma^2 I \end{bmatrix} < 0, \tag{28}$$

hold, where $\widetilde{\Upsilon}_{11} = P^{-1}QP^{-1} + 4P^{-1}A_{21}'PA_{21}P^{-1} + 4P^{-1}K'B_{21}'PB_{21}KP^{-1} + 2P^{-1}A_{11}' + 2P^{-1}K'B_{11}' + 3P^{-1}C_1'C_1P^{-1} + 3P^{-1}K'D_1'D_1KP^{-1} + P^{-1}TP^{-1} + P^{-1}K'RKP^{-1}$. Let $\widetilde{P} = P^{-1}$, $M = K\widetilde{P}$, $\widetilde{Q} = Q^{-1}$, $\widetilde{R} = R^{-1}$, and $\widetilde{T} = T^{-1}$; by Lemma 3, we obtain (26) from (28).

Summarizing the process, the proof is completed. □

Next, in order to get the least upper bound for cost function among all the possible solutions to inequality (26), the convex optimization problem is provided as follows.

Theorem 1. *For system (9), if the following optimization problem*

$$\min_{\gamma>0,\alpha>0,W>0,\widetilde{P}>0,\widetilde{Q}>0,M} [\alpha + tr(W)] \tag{29}$$

subject to (26) and

$$\begin{bmatrix} -\alpha & x'(0) \\ x(0) & -\widetilde{P} \end{bmatrix} < 0, \tag{30}$$

$$\begin{bmatrix} -W & N' \\ N & -\widetilde{Q} \end{bmatrix} < 0, \tag{31}$$

has a solution α, W, $\widetilde{P}$, $\widetilde{Q}$, and M, then controller $u(t) = M\widetilde{P}^{-1}x(t)$ is an optimal state feedback H_2/H_∞ controller which ensures the minimization of guaranteed cost $J_s^* = E[x'(0)\widetilde{P}^{-1}x(0) + \int_{-\tau}^{0} x'(s)\widetilde{Q}^{-1}x(s)ds]$ for system (9), where $\int_{-\tau}^{0} x(s)x'(s)ds = NN'$.

Proof. From Lemma 5, the controller $u(t) = M\widetilde{P}^{-1}x(t)$ is a guaranteed cost control law of system (9). (30) is equivalent to $x'(0)\widetilde{P}^{-1}x(0) < \alpha$; (31) is equivalent to $N'\widetilde{Q}^{-1}N < W$.

Therefore, we can obtain

$$\begin{aligned} \int_{-\tau}^{0} x'(s)\widetilde{Q}x(s)\mathrm{d}s &= \int_{-\tau}^{0} \mathrm{tr}\left(x'(s)\widetilde{Q}^{-1}x(s)\right)\mathrm{d}s \\ &= \mathrm{tr}\left(NN'\widetilde{Q}^{-1}\right) = \mathrm{tr}\left(N'\widetilde{Q}^{-1}N\right) < \mathrm{tr}(W). \end{aligned} \tag{32}$$

Thus, we can obtain $J_s^* < \alpha + \mathrm{tr}(W)$.

Therefore, the minimization of $\alpha + \mathrm{tr}(W)$ implies the minimization of guaranteed cost for system (9).

The proof is completed here. □

Remark 1. It is an ideal case that the initial function is known. However, in general, the initial function of system (1) is not known, but the guaranteed cost depends on it. In order to avoid the dependence, we assume that the initial function is a white noise process with zero expectation function and unit covariance function.

When the initial function is not known, we have

$$\begin{aligned} J_s^* &= E\left[x'(0)\widetilde{P}^{-1}x(0) + \int_{-\tau}^{0} x'(s)\widetilde{Q}^{-1}x(s)\mathrm{d}s\right] \\ &= E\left[\mathrm{tr}\left(x(0)x'(0)\widetilde{P}^{-1}\right)\right] + \int_{-\tau}^{0} E\left[\mathrm{tr}\left(x(s)x'(s)\widetilde{Q}^{-1}\right)\right]\mathrm{d}s \\ &= \mathrm{tr}\left(E\left(x(0)x'(0)\widetilde{P}^{-1}\right)\right) + \int_{-\tau}^{0} \mathrm{tr}\left(E\left(x(s)x'(s)\widetilde{Q}^{-1}\right)\right)\mathrm{d}s \\ &= \mathrm{tr}\left(\widetilde{P}^{-1}\right) + \tau \times \mathrm{tr}\left(\widetilde{Q}^{-1}\right). \end{aligned} \tag{33}$$

Therefore, we have the following optimization problem:

$$\min_{\gamma>0,W_1>0,W_2>0,\widetilde{P}>0,\widetilde{Q}>0,M} \left[\mathrm{tr}(W_1) + \tau \times \mathrm{tr}(W_2)\right], \tag{34}$$

which subjects to (26) and

$$\begin{bmatrix} W_1 & I \\ I & \widetilde{P} \end{bmatrix} > 0, \tag{35}$$

$$\begin{bmatrix} W_2 & I \\ I & \widetilde{Q} \end{bmatrix} > 0. \tag{36}$$

Theorem 2. *If there exist solution to (26), (34)–(36) then controller $u(t) = M\widetilde{P}^{-1}x(t)$ is an optimal state feedback H_2/H_∞ controller which ensures the minimization of guaranteed cost (18) for system (1).*

Proof. From Lemma 5, the controller $u(t) = M\widetilde{P}^{-1}x(t)$ is a H_2/H_∞ controller of system (9). We can see (34) is equivalent to $0 < \widetilde{P}^{-1} < W_1$ and (35) is equivalent to $0 < \widetilde{Q}^{-1} < W_2$ from Lemma 3. Therefore, the minimization of $tr(W_1) + \tau \times tr(W_2)$ implies the minimization of the guaranteed cost for system (1).

The proof is complete. □

4. Numerical Algorithms

In this section, an algorithm is presented in order to find the minimum value of $\alpha + \mathrm{tr}(W)$ in Theorem 1. The similar algorithm can also be applied to Theorem 2.

By analyzing (26), (30), (31) in Theorem 1, we find that if (26), (30), (31) have no feasible solutions when γ takes the initial value, then (26), (30), (31) will have no feasible

solutions for all $\gamma > 0$. Next, we search for γ from the initial value that makes (26), (30), (31) have feasible solutions to optimize $\alpha + \mathrm{tr}(W)$ by using linear search algorithm. The specific algorithm is as follows.

5. Numerical Examples

The coefficient matrices of system (1) are given as follows:

$$\begin{aligned}
A_{11} &= \begin{bmatrix} -30 & 10 \\ -10 & -20 \end{bmatrix}, \\
A_{12} &= \begin{bmatrix} 0.1 & 0.2 \\ 0 & 0.1 \end{bmatrix}, \\
A_{21} &= \begin{bmatrix} -2.7 & 0.8 \\ 0.9 & -1.6 \end{bmatrix}, \\
A_{22} &= \begin{bmatrix} -0.2 & -0.5 \\ -0.3 & -1.4 \end{bmatrix}, \\
B_{11} &= \begin{bmatrix} -4 \\ 3 \end{bmatrix}, \\
B_{12} &= \begin{bmatrix} 0.1 & -0.1 \\ 0.5 & 0.7 \end{bmatrix}, \\
B_{21} &= \begin{bmatrix} -1 \\ 2 \end{bmatrix}, \\
C_1 &= \begin{bmatrix} 2 & 1 \\ 2 & 3 \end{bmatrix}, \\
D_1 &= \begin{bmatrix} -1 \\ 3 \end{bmatrix}, \\
N &= \begin{bmatrix} 2 \\ 1 \end{bmatrix}, \\
T &= \begin{bmatrix} 4 & -3 \\ -3 & 4 \end{bmatrix}, \\
R &= 1, \\
\tau &= 1.
\end{aligned} \tag{37}$$

First case: when the initial function is known and $x(0) = [\,1 \;\; 2\,]'$, $t \in [-1, 0]$. In order to find the minimum value of $\alpha + \mathrm{tr}(W)$, we obtain the relationship between $\alpha + \mathrm{tr}(W)$ and γ by Algorithm 1, which is shown in Figure 1.

As can be seen from Figure 1, $\alpha + \mathrm{tr}(W)$ decreases with the increase of γ, and $\min[\alpha + \mathrm{tr}(W)] = 38.4173$ when $\gamma = 0.4$, and $\min[\alpha + \mathrm{tr}(W)] = 29.7250$ when $\gamma = 1.98$.

Take $\gamma = 0.8$, according to Theorem 1, we obtain that

$$\begin{aligned}
\widetilde{P} &= \begin{bmatrix} 0.8484 & 0.0215 \\ 0.0215 & 0.5896 \end{bmatrix}, \\
\widetilde{Q} &= \begin{bmatrix} 18.8352 & -4.2480 \\ -4.2480 & 1.0503 \end{bmatrix}, \\
M &= [\,0.0629 \;\; -0.0472\,], \\
W &= 23.0449, \\
\alpha &= 7.7981.
\end{aligned} \tag{38}$$

Therefore, the optimal state feedback H_2/H_∞ controller is $u(t) = [0.0762 - 0.0828]x(t)$, and the guaranteed cost of closed-loop system is $J_s^* = 30.8430$.

Take external disturbance $v(t) = \sin(t)$, then we can obtain the curves of x_1 and x_2 and $E\|x(t)\|^2$ in Figure 2. From Figure 2, we can see that $E\|x(0)\|^2 = 5$ and $\lim_{t\to\infty} E\|x(t)\|^2 = 0$, that is, closed-loop system (9) is mean square stable.

Second case: when the initial function is a white noise process with zero expectation function and unit covariance function, in order to find the minimum value of $\mathrm{tr}(W_1) + \tau \times \mathrm{tr}(W_2)$, we obtain the relationship between $\mathrm{tr}(W_1) + \tau \times \mathrm{tr}(W_2)$ and γ by Algorithm 1, which is shown in Figure 3.

As can be seen from Figure 3, $\mathrm{tr}(W_1) + \tau \times \mathrm{tr}(W_2)$ decreases with the increase of γ, and $\min[\mathrm{tr}(W_1) + \tau \times \mathrm{tr}(W_2)] = 19.5450$ when $\gamma = 0.4$, $\min[\mathrm{tr}(W_1) + \tau \times \mathrm{tr}(W_2)] = 13.6648$ when $\gamma = 1.98$.

Take $\gamma = 0.8$, according to Theorem 2, we obtain that

$$\begin{aligned}
\widetilde{P} &= \begin{bmatrix} 0.8520 & 0.0217 \\ 0.0217 & 0.5889 \end{bmatrix}, \\
\widetilde{Q} &= \begin{bmatrix} 20.5511 & -4.6765 \\ -4.6765 & 1.1567 \end{bmatrix}, \\
M &= [\,0.0629 \;\; -0.0472\,], \\
\mathrm{tr}(W_1) &= 2.8746, \\
\mathrm{tr}(W_2) &= 11.4205.
\end{aligned} \tag{39}$$

Step 1: Given the values of τ.
Step 2: Using linear search algorithm, if a series of $\gamma_i\,(i = 1, \cdots, n)$ can be found to make inequalities (26), (30), (31) have feasible solutions, then turn to *Step 3*; otherwise, turn to *Step 7*.
Step 3: Let $i = 1$, then we take γ_i.
Step 4: Solve the following minimization problem:
$\min_{s.t.\,(20),(24),(25)} \alpha + \mathrm{tr}\,(W)$.
Step 5: Let $i = i + 1$, if $i + 1 > n$, then turn to *Step 6*; otherwise, let $\gamma_i = \gamma_{i+1}$, and turn to *Step 4*.
Step 6: There are solutions to this problem, printing data, and then stop.
Step 7: There is no solution to this problem and stop.

Algorithm 1: Linear search algorithm.

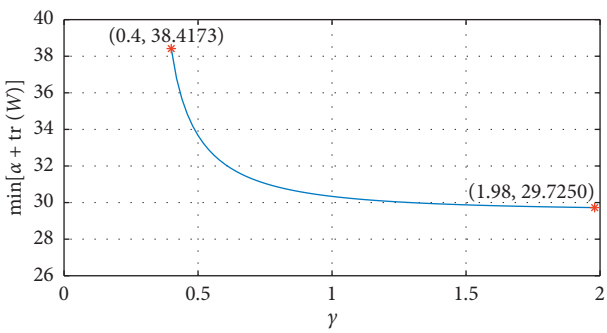

Figure 1: When $\gamma \in [0, 2]$, the minimum upper bound of $\alpha + \mathrm{tr}\,(W)$.

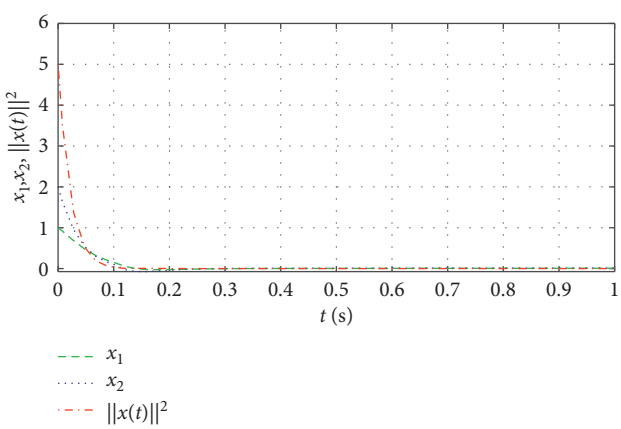

Figure 2: When $t \in [0, 1]$, the response for $E\|x(t)\|^2$.

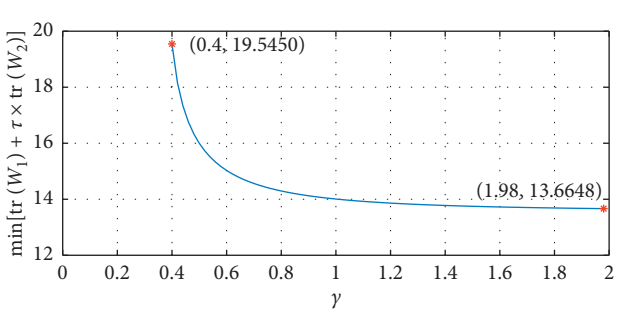

Figure 3: When $\gamma \in [0, 2]$, the minimum upper bound of $\mathrm{tr}\,(W_1) + \tau \times \mathrm{tr}\,(W_2)$.

Therefore, the optimal state feedback H_2/H_∞ controller is $u(t) = [0.0759 - 0.0829]x(t)$, and the guaranteed cost of closed-loop system is $J_s^* = 14.2951$.

6. Conclusion

In this paper, the mixed H_2/H_∞ control problem for Itô-type stochastic time-delay systems is presented, and the description of H_2/H_∞ control problem for stochastic time-delay systems is given. On the basis of matrix transformation and convex optimization method, state feedback H_2/H_∞ controller is obtained to make the system satisfy H_∞ performance index and H_2 performance index. Moreover, an algorithm is given to solve state feedback controller and optimize H_2/H_∞ performance index. Finally, a numerical example is used to show the feasibility of the results. In the future work, we will investigate mixed H_2/H_∞ control for the more complex systems, such as, stochastic Markov jump systems with time delay.

Data Availability

The data used to support the findings of this study are available from the corresponding upon request.

Conflicts of Interest

The authors declare that there are no conflicts of interest regarding the publication of this paper.

Acknowledgments

This work was supported by the National Natural Science Foundation of China (Grant nos. 61877062 and 61977043), China Postdoctoral Science Foundation (Grant no. 2017M610425), and Open Foundation of Key Laboratory of Pulp and Paper Science and Technology of Ministry of Education of China (Grant no. KF201419).

References

[1] C.-F. Wu, B.-S. Chen, and W. Zhang, "Multiobjective investment policy for a nonlinear stochastic financial system: a fuzzy approach," *IEEE Transactions on Fuzzy Systems*, vol. 25, no. 2, pp. 460–474, 2017.

[2] R. Yu and S. Gao, "Applications of probabilistic production simulation in power system," *Power System Protection and Control*, vol. 40, no. 11, pp. 149–155, 2012.

[3] Q. Zhu, Y. Liu, and G. Wen, "Adaptive neural network control for time-varying state constrained nonlinear stochastic systems with input saturation," *Information Sciences*, vol. 527, pp. 191–209, 2020.

[4] W. Xie and Q. Zhu, "Stability of discrete-time stochastic nonlinear systems with event-triggered state-feedback control," *Physica A: Statistical Mechanics and Its Applications*, vol. 547, p. 123823, 2020.

[5] F. Wang, L. Zhang, S. Zhou, and Y. Huang, "Neural network-based finite-time control of quantized stochastic nonlinear systems," *Neurocomputing*, vol. 362, pp. 195–202, 2019.

[6] P. Cui, C. Zhang, and M. Wang, "Guaranteed cost control of stochastic uncertain systems with time-varying Delays," in *Proceedings of the 6th World Congress on Intelligent Control and Automation*, Dalian, China, June 2006.

[7] Z.-Y. Li, S. Shang, and J. Lam, "On stability of neutral-type linear stochastic time-delay systems with three different delays," *Applied Mathematics and Computation*, vol. 360, pp. 147–166, 2019.

[8] G. Chen, Y. Gao, and S. Zhu, "Finite-time dissipative control for stochastic interval systems with time-delay and Markovian switching," *Applied Mathematics and Computation*, vol. 310, pp. 169–181, 2017.

[9] H. Wang, B. Chen, and C. Lin, "Adaptive neural control for strict-feedback stochastic nonlinear systems with time-delay," *Neurocomputing*, vol. 77, no. 1, pp. 267–274, 2012.

[10] R. Nie, Q. Ai, S. He, Z. Yan, X. Luan, and F. Liu, "Robust finite-time control and estimation for uncertain time-delayed switched systems by observer—based sliding mode technique," *Optimal Control Applications and Methods*, Wiley, Hoboken, NJ, USA, 2020.

[11] Z. Yan, Y. Song, and J. H. Park, "Finite-time stability and stabilization for stochastic markov jump systems with mode-dependent time delays," *ISA Transactions*, vol. 68, pp. 141–149, 2017.

[12] M. Gao, L. Sheng, and W. Zhang, "Stochastic H2/H∞ control of nonlinear systems with time-delay and state-dependent noise," *Applied Mathematics and Computation*, vol. 266, pp. 429–440, 2015.

[13] S. Luo and F. Deng, "A note on delay-dependent stability of Itô-type stochastic time-delay systems," *Automatica*, vol. 105, pp. 443–447, 2019.

[14] S. He, H. Fang, M. Zhang, F. Liu, and Z. Ding, "Adaptive optimal control for a class of nonlinear systems: the online policy iteration approach," *IEEE Transactions on Neural Networks and Learning Systems*, vol. 31, no. 2, pp. 549–558, 2020.

[15] P. Cheng, J. Wang, S. He, X. Luan, and F. Liu, "Observer-based asynchronous fault detection for conic-type nonlinear jumping systems and its application to separately excited DC motor," *IEEE Transactions on Circuits and Systems I: Regular Papers*, vol. 67, no. 3, pp. 951–962, 2020.

[16] H. Min, S. Xu, B. Zhang, and Q. Ma, "Globally adaptive control for stochastic nonlinear time-delay systems with perturbations and its application," *Automatica*, vol. 102, pp. 105–110, 2019.

[17] B. Zhou and W. Luo, "Improved Razumikhin and Krasovskii stability criteria for time-varying stochastic time-delay systems," *Automatica*, vol. 89, pp. 382–391, 2018.

[18] Y. Ma and Y. Liu, "Finite-time H_∞ sliding mode control for uncertain singular stochastic system with actuator faults and bounded transition probabilities," *Nonlinear Analysis: Hybrid Systems*, vol. 33, pp. 52–75, 2019.

[19] J. Zhou, J. Park, and Q. Ma, "Non-fragile observer-based H_∞ control for stochastic time-delay systems," *Applied Mathematics and Computation*, vol. 291, pp. 69–83, 2016.

[20] J. Feng and S. Xu, "Robust H_∞ control with maximal decay rate for linear discrete-time stochastic systems," *Journal of Mathematical Analysis and Applications*, vol. 353, no. 1, pp. 460–469, 2009.

[21] Y. Ren, W. Wang, W. Zhou, and M. Shen, "Stochastic incremental H∞ control for discrete-time switched systems with disturbance dependent noise," *Information Sciences*, vol. 513, pp. 519–535, 2020.

[22] Z. Yan, M. Zhang, Y. Song, and S. Zhong, "Finite-time H_∞ control for Itô-type nonlinear time-delay stochastic systems," *IEEE Access*.

[23] S. He, H. Fang, M. Zhang, F. Liu, X. Luan, and Z. Ding, "Online policy iterative-based H∞ optimization algorithm for a class of nonlinear systems," *Information Sciences*, vol. 495, pp. 1–13, 2019.

[24] H. Liu, X. Li, X. Liu, and H. Wang, "Backstepping-based decentralized bounded-H∞ adaptive neural control for a class of large-scale stochastic nonlinear systems," *Journal of the Franklin Institute*, vol. 356, no. 15, pp. 8049–8079, 2019.

[25] D. Zhang, J. Cheng, D. Zhang, and K. Shi, "Nonfragile H_∞ control for periodic stochastic systems with probabilistic measurement," *ISA Transactions*, vol. 86, pp. 39–47, 2019.

[26] X. Xing, Y. Liu, and B. Niu, "H_∞ control for a class of stochastic switched nonlinear systems: an average dwell time method," *Nonlinear Analysis: Hybrid Systems*, vol. 19, pp. 198–208, 2016.

[27] Q. Zhang and Q. Sun, "A maximum principle approach to stochastic H_2/H_∞ control with random jumps," *Acta Mathematica Scientia*, vol. 35, no. 2, pp. 348–358, 2015.

[28] S. Sathananthan, M. J. Knap, and L. H. Keel, "Guaranteed cost H_∞ control of linear stochastic markovian switching systems," *IFAC Proceedings Volumes*, vol. 44, no. 1, pp. 5459–5464, 2011.

[29] F. B. Hanson, "Applied stochastic processes and control for jump-diffusions: modelling," *Analysis and Computation*, SIAM, Philadelphia, PA, USA, 2007.

[30] Z. Yan, G. Zhang, and J. Wang, "Non-fragile robust finite-time H_∞ control for nonlinear stochastic itô systems using neural network," *International Journal of Control, Automation and Systems*, vol. 10, no. 5, pp. 873–882, 2012.

Hindawi
Mathematical Problems in Engineering
Volume 2020, Article ID 2539196, 9 pages
https://doi.org/10.1155/2020/2539196

Research Article

Convergence Analysis of a Trust-Region Multidimensional Filter Method for Nonlinear Complementarity Problems

C. W. Wu,[1] **J. P. Cao**,[2] **and L. F. Wang**[2]

[1]*Department of Math, Xi'an High-Tech Institute, Xi'an 710025, Shaanxi Province, China*
[2]*Xi'an High-Tech Institute, Xi'an 710025, Shaanxi Province, China*

Correspondence should be addressed to C. W. Wu; wucongweihome@hotmail.com

Received 15 March 2020; Revised 16 May 2020; Accepted 20 May 2020; Published 19 June 2020

Guest Editor: Cuimei Jiang

For solving nonlinear complementarity problems, a new algorithm is proposed by using multidimensional filter techniques and a trust-region method. The algorithm is shown to be globally convergent under the reasonable assumptions and does not depend on any extra restoration procedure. In particular, it shows that the subproblem is a convex quadratic programming problem, which is easier to be solved. The results of numerical experiments show its efficiency.

1. Introduction

Let $F(x)\colon \mathfrak{R}^n \longmapsto \mathfrak{R}^n$ be a continuous differentiable function. The nonlinear complementarity problem (NCP) is to find a vector $x \in \mathfrak{R}^n$ such that

$$\begin{aligned} x &\geq 0, \\ F(x) &\geq 0, \\ x^T F(x) &= 0. \end{aligned} \tag{1}$$

For convenience, denote $\mathcal{J} = \{1, 2, \ldots, n\}$. Throughout this paper, $\|\cdot\|$ denotes the Euclidean norm.

The traditional approach for NCP involves reformulating the problem as an optimization problem [1–12] or a nonlinear differentiable function [13–18]. In this paper, a new method for solving this optimization problem is based on the class of trust-region methods and also filter methods introduced by Fletcher and Leyffer in 1997 and subsequently published as [19]. This technique has important reference value for many nonlinear system problems [20–22]. The idea of filter methods is that trial points are accepted as long as they could reduce the value of objective function or improve the feasibility, which is different from the conventional approach of combining these two measures by a penalty function. Filter approaches play an important role to balance the objective function and constraints and have advantages over penalty function methods. Numerical experiments have shown the impressing efficiency of filter methods [19, 23]. The global convergence proof of filter-SQP algorithm is given by Fletcher et al. [24], and relevant superlinear local convergence is achieved by Ulbrich [25].

Because of good numerical results, filter techniques are extensively studied to handle the nonlinear complementarity problem [7–9, 26, 27]. Most of the contributions to NCP of filter algorithms rely on an external "restoration procedure" [19, 27–29] whose purpose is to reduce constraint infeasibilities, since the filter idea introduced by Fletcher and Leyffer [19] is based on constrained optimization problems, and the constrained optimization problems transformed by NCP may be infeasible. Gould et al. [30, 31] proposed a multidimensional filter algorithm for nonlinear unconstrained optimization problems instead of a two-dimensional filter [19] for constrained optimization problems. This motivates us to consider the possibility of reformulating NCP as an unconstrained optimization problem and solving the optimization by a multidimensional filter method. In spite of the fact, we suggest a reformulation of NCP as an optimization problem with nonnegativity constraints because Fischer [2] points out that stationary points with

negative components can be avoided in contrast to the reformulation as unconstrained minimization problem. Unfortunately, the multidimensional filter method is proposed on unconstrained optimization [30, 31].

There are two main motivations of this paper. One is to find an effective method to overcome the influence of "restoration procedure" on the efficiency of the algorithm. The other is to find a technology to solve the constrained optimization problem with nonnegative constraints by using a multidimensional filter method, just like solving the unconstrained optimization problem, so as to solve the NCP problem. Our proposal is to reformulate NCP as an optimization problem with nonnegative constraints and solve the optimization by a multidimensional filter method. The gradient-projection method [32] shows that the first-order optimality condition of the nonnegativity constrained optimization problem is equivalent to the fact that the projected gradient is zero, which is similar to the optimality condition of the unconstrained optimization problem. The characteristics of NCP make sure that the trust-region subproblem of the equivalent reformulation is a convex quadratic programming problem because the matrix B in the subproblem is a positive semidefinite symmetric matrix. Even we find that the twice continuously differentiability of $F(x)$ implies that B is uniformly bounded. It is very important for the global convergent analysis of our algorithm. Especially, the new algorithm does not depend on any extra restoration procedure because it always remains the compatibility of the trust-region subproblem.

This paper is organized as follows: the algorithm and preliminaries are introduced in Section 2 and the global convergence analysis for the proposed method is given in Section 3. Some numerical results are reported in Section 4. The final section gives some conclusions.

2. The Algorithm and Preliminaries

In this section, we will describe the specific strategies and motivations for solving problem (1) and finally present a multidimensional filter algorithm for the nonlinear complementarity problem.

2.1. Equivalent Model and Gradient-Projection Method. We consider using the Fischer–Burmeister function [33] to reformulate NCP as the following optimization problem and solve the optimization by a multidimensional filter method:

$$\min_{x\geq 0} \quad f_\mu(x) := \frac{1}{2}\Phi_\mu(x)^T\Phi_\mu(x), \tag{2}$$

where $\mu \geq 0$ is a smooth parameter, and $\Phi_\mu(x) = \left(\sqrt{x_1^2 + F_1^2(x) + \mu^2} - x_1 - F_1(x), \ldots, \sqrt{x_n^2 + F_n^2(x) + \mu^2} - x_n - F_n(x)\right)^T$. For $\mu = 0$, we get the following equivalence relation [34]: x^*solves (1) $\Longleftrightarrow x^*$ solves (2). Nonnegative constraints in optimization problem (2) can help to avoid stationary points with negative components [2], but it brings some troubles to the multidimensional filter method [30, 31]. Therefore, we use a gradient-projection method [32] and define the "projected" gradient of $f_\mu(x)$ into the feasible set of problem (2) as follows:

$$\overline{g}_{\mu,i}(x) = \begin{cases} g_{\mu,i}(x), & x_i \geq g_{\mu,i}(x), \\ x_i, & x_i < g_{\mu,i}(x), \end{cases} \tag{3}$$

where $g_{\mu,i}(x)$ is the i-th component of the $g_\mu(x)$, $g_\mu(x) := \nabla_x f_\mu(x)$ and $i \in \mathcal{I}$.

The advantage of this strategy is obvious: x_μ^* is a KKT point of problem (2) if and only if $\overline{g}_\mu(x_\mu^*) = 0$. So, we can use a multidimensional filter method to solve problem (2) when μ approaches to zero just as we can solve unconstrained optimization problem.

2.2. Trust-Region Subproblem. To solve problem (2), we compute a trial step d_k by finding an approximation to the solution of the trust-region subproblem:

$$\begin{aligned} \min \quad & Q_k(d) = f_{\mu_k}(x_k) + \nabla_x f_{\mu_k}(x_k)^T d + \frac{1}{2} d^T B_k d, \\ \text{s.t.} \quad & x_k + d \geq 0, \quad \|d\|_\infty \leq \Delta_k, \end{aligned} \tag{4}$$

where x_k is the current iteration point, Δ_k is the trust-region radius, and $B_k = \nabla_x \Phi_{\mu_k}(x_k) \nabla_x \Phi_{\mu_k}(x_k)^T$, and $\nabla_x \Phi_\mu(x) := (b_{ij})_{nn}$, $b_{ij} = (\partial \Phi_{\mu,j}(x)/\partial x_i)$. The positive parameters μ_k tend to zero during the iterate of algorithm. A trial point x_k^+ is then computed by the trial step d_k; denote $x_k^+ = x_k + d_k$.

Subproblem (4) obviously has a solution $d = 0$ at least. Therefore, our new algorithm does not depend on any extra restoration procedure [19, 27–29] because it always remains the compatibility of the trust-region subproblem. Especially, we note that the characteristics of NCP make sure that the trust-region subproblem of the equivalent reformulation is a convex quadratic programming problem, which is comparatively easy to solve.

2.3. The Multidimensional Filter Mechanism. Whether the new trial point x_k^+ can be considered as a successful point requires the following multidimensional filter mechanism [30, 32] to assist in judgment. This mechanism helps the components of function $\overline{g}_\mu(x)$ to approach to zero evenly and provides an effective rule to judge whether x_k^+ is accepted. In practical computation, a iterate point x_k is said to dominate another point x_l if and only if $|\overline{g}_{\mu_{k-1},i}(x_k)| \leq |\overline{g}_{\mu_{l-1},i}(x_l)|$, $\forall i \in \mathcal{I}$. Besides, a filter set $\mathcal{F}$ is a set of points such that no pair dominates any other.

Acceptability rule: a new trial point x_k^+ is acceptable for the filter $\mathcal{F}_k$ if and only if

$$\forall x_l \in \mathcal{F}_k, \exists j \in \mathcal{I}, \left|\overline{g}_{\mu_k,j}(x_k^+)\right| \leq \left|\overline{g}_{\mu_{l-1},j}(x_l)\right| - \gamma_g \left\|\overline{g}_{\mu_{l-1}}(x_l)\right\|, \tag{5}$$

where $\gamma_g \in (0, (1/\sqrt{n}))$. If an iterate x_k is acceptable for the filter $\mathcal{F}_k$, we add it to the filter and remove from it every $x_l \in \mathcal{F}_k$ such that $|\overline{g}_{\mu_k,i}(x_k^+)| \leq |\overline{g}_{\mu_{l-1},i}(x)_l|$ for all $i \in \mathcal{I}$, i.e.,

$$\mathscr{F}_{k+1} = \mathscr{F}_k \cup \{x_k^+\} \backslash \mathscr{D}_k, \tag{6}$$

where

$$\mathscr{D}_k = \left\{ x_l \in \mathscr{F}_k \left| \overline{g}_{\mu_k,i}(x_k^+) \le \overline{g}_{\mu_{l-1},i}(x_l) \right|, \forall i \in \mathscr{I} \right\}. \tag{7}$$

2.4. A Multidimensional Filter Algorithm for NCPs. In this part, we will present a multidimensional filter algorithm for nonlinear complementarity problem (1).

Algorithm 1. A multidimensional filter algorithm for NCPs.

Step 0: initialization. An initial point and an initial trust-region radius Δ_0 are given. Let an initial point x_0, an initial trust-region radius $\Delta_0 > 0$, and an initial filter set $\mathscr{F}_0 = (10^5, \ldots, 10^5)^T$ be given, as well as constants ε, $\gamma_g \in (0, (1/\sqrt{n}))$, $0 < \gamma_1 < \gamma_2 < 1 < \gamma_3$, $0 < \eta_1 < \eta_2 < 1$, $0 < \Delta_0 \le \Delta_{max}$. Compute $f_{\mu_0}(x_0)$, $g_{\mu_0}(x_0)$, $\overline{g}_{\mu_0}(x_0)$, B_0, set $k := 0$.

Step 1: test for optimality. If $\|\overline{g}_{\mu_k}(x_k)\| + \mu_k < \varepsilon$, stop.

Step 2: determine a trial step. Compute a solution d_k of subproblem (4).

Step 3: if $d_k = 0$, set $x_{k+1} = x_k, \mu_{k+1} = \theta\mu_k, B_{k+1} = B_k$, $k := k+1$, and go to Step 1; otherwise, set $x_k^+ = x_k + d_k$, and compute $f_{\mu_k}(x_k^+)$, $\overline{g}_{\mu_k}(x_k^+)$.

Step 4: test for optimality. If $\|\overline{g}_{\mu_k}(x_k^+)\| + \mu_k < \varepsilon$, stop; otherwise, compute

$$\rho_k = \frac{f_{\mu_k}(x_k) - f_{\mu_k}(x_k^+)}{Q_k(0) - Q_k(d_k)}. \tag{8}$$

Step 5: tests to accept the trial step.

(i) If $\rho_k \ge \eta_1$, set $x_{k+1} = x_k^+$, $\mathscr{F}_{k+1} = \mathscr{F}_k \cup \{x_k^+\} \backslash \mathscr{D}_k$;
(ii) Besides, if $\rho_k < \eta_1$ and x_k^+ is acceptable for the filter $\mathscr{F}_k$, set $x_{k+1} = x_k^+$, $\mathscr{F}_{k+1} = \mathscr{F}_k \cup \{x_k^+\} \backslash \mathscr{D}_k$,
(iii) Otherwise, set $x_{k+1} = x_k$, $\mathscr{F}_{k+1} = \mathscr{F}_k$.

Step 6: update the trust-region radius and the smooth parameter.

$$\Delta_{k+1} = \begin{cases} [\gamma_1\Delta_k, \gamma_2\Delta_k], & \text{if } \rho_k < \eta_1, \\ (\gamma_2\Delta_k, \Delta_k], & \text{if } \rho_k \in [\eta_1, \eta_2), \\ \min\{\Delta_{\max}, \gamma_3\Delta_k\}, & \text{if } \rho_k \ge \eta_2. \end{cases} \tag{9}$$

$$\mu_{k+1} = \begin{cases} \theta\mu_k, & \text{if } \mu_k > 0.1\left\|\overline{g}_{\mu_k}(x_{k+1})\right\|, \\ \mu_k, & \text{otherwise.} \end{cases} \tag{10}$$

Step 7: compute $f_{\mu_{k+1}}(x_{k+1})$, $g_{\mu_{k+1}}(x_{k+1})$, $\overline{g}_{\mu_{k+1}}(x_{k+1})$, B_{k+1}, set $k := k+1$, and go to Step 1.

Note that, there is an advantage to choosing a large $\Delta_{k+1} = \gamma_3\Delta_k$ when $\rho_k \ge \eta_2$, but it may be unwise to choose it to be too large; hence, we give a upper bound $\Delta_{\max}$ and set $\Delta_{k+1} = \min\{\Delta_{\max}, \gamma_3\Delta_k\}$ when $\rho_k \ge \eta_2$. Specifically, $B_{k+1} = \nabla_x\Phi_{\mu_{k+1}}(x_{k+1})\nabla_x\Phi_{\mu_{k+1}}(x_{k+1})^T$ can be computed easily instead of updating B_{k+1} with higher numerical expenditure (e.g., BFGS). By the way, from (8), we are surprised to find that the smooth parameter μ_k does not tend to zero before $\|\overline{g}_{\mu_k}(x_k)\|$ during our algorithm. In other words, $f_{\mu_k}(x)$ is twice continuously differentiable form beginning to end; this is a critical condition to our algorithm.

3. Analysis for Global Convergence

Global convergence properties of Algorithm 1 will be proved under the following assumptions.

A1. $F(x)$: $\mathfrak{R}^n \longrightarrow \mathfrak{R}^n$ is a twice continuously differentiable function.

A2. The iterates x_k remain in a closed, bounded convex domain Ω of $\mathfrak{R}^n$.

Note that, for subproblem (4), A1 and A2 together imply that B_k is uniformly bounded on Ω. In other words, there exist constants $\kappa_{\text{umb}} > 0$ such that $|B_k| \le \kappa_{\text{umb}}$, $\forall k$.

3.1. Well Definedness. Let d_k denote the solution of (4), then we have some technical lemmas which are very important for the global convergence of Algorithm 1.

Lemma 1. *If $d_k = 0$, we have $\overline{g}_{\mu_k}(x_k) = 0$.*

Proof. We first change the constraint $\|d\|_\infty \le \Delta_k$ to another form $d + \Delta_k e \ge 0$ and $d - \Delta_k e \le 0$, then we have the Lagrange function of (4):

$$\begin{aligned} L(d, \lambda, \overline{\mu}, \widehat{\mu}) = Q_k(d) - \lambda^T(x_k + d) - \overline{\mu}^T(d + \Delta_k e) \\ + \widehat{\mu}^T(d - \Delta_k e), \end{aligned} \tag{11}$$

where $\lambda, \overline{\mu}, \widehat{\mu} \in R^n$ are Lagrange multipliers, $e = (1, 1, \ldots, 1)^T \in \mathfrak{R}^n$. Since d_k is the solution of (4), we then obtain that

$$\begin{cases} \nabla_d L(d_k, \lambda, \overline{\mu}, \widehat{\mu}) = 0, \quad \lambda, \overline{\mu}, \widehat{\mu} \ge 0, \\ x_k + d_k \ge 0, \\ d_k + \Delta_k e \ge 0, \\ d_k - \Delta_k e \le 0, \\ \lambda^T(x_k + d_k) = \overline{\mu}^T(d_k + \Delta_k e) = \widehat{\mu}^T(d_k - \Delta_k e) = 0. \end{cases} \tag{12}$$

Observe that $d_k = 0$ and $\Delta_k > 0$ ensure that

$$\begin{cases} g_{\mu_k}(x_k) = \lambda + \overline{\mu} - \widehat{\mu}, \\ \lambda, x_k \ge 0, \\ \lambda^T x_k = 0, \\ \overline{\mu} = \widehat{\mu} = 0. \end{cases} \tag{13}$$

Thus, $x_k^T g_{\mu_k}(x_k) = 0$, i.e., $\overline{g}_{\mu_k}(x_k) = 0$. □

Lemma 2 (see [32]). *iere exists a constant $\kappa_{mdc} \in (0, 1)$ such that*

$$Q_k(0) - Q_k(d_k) \geq \kappa_{\mathrm{mdc}} \left\| \overline{g}_{\mu_k}(x_k) \right\| \min\left\{ \frac{\left\| \overline{g}_{\mu_k}(x_k) \right\|}{1 + [B_k]}, \Delta_k \right\}. \tag{14}$$

Lemma 3 (see [35]). *Suppose that A1 and A2 hold. If* $\overline{g}_{\mu_k}(x_k) \neq 0$ *and*

$$\Delta_k \leq \min\left\{ \frac{\kappa_{\mathrm{mdc}}(1-\eta_2)}{\kappa_{\mathrm{ubh}}}, \frac{1}{1+\kappa_{\mathrm{umb}}} \right\} \cdot \left\| \overline{g}_{\mu_k}(x_k) \right\|, \tag{15}$$

we have $\rho_k \geq \eta_2$, *and* $\Delta_{k+1} \geq \Delta_k$.

Consequently, we may now obtain that the trust-region radius cannot become arbitrarily small if the iterates stay away from first-order critical points.

Lemma 4. *Suppose that A1 and A2 hold. Suppose furthermore that there exists a constant* $\kappa_{lpg} > 0$ *such that* $\|\overline{g}_{\mu_k}(x_k)\| \geq \kappa_{lpg}$ *for all k. Then, there is a constant* $\kappa_{lbd} > 0$ *such that* $\Delta_k \geq \kappa_{lbd}$ *for all k.*

Proof. Assume that iteration k_0 is the first such that

$$\Delta_{k_0} \leq \gamma_1 \kappa_{\mathrm{lpg}} \cdot \min\left\{ \frac{\kappa_{\mathrm{mdc}}(1-\eta_2)}{\kappa_{\mathrm{ubh}}}, \frac{1}{1+\kappa_{\mathrm{umb}}} \right\}. \tag{16}$$

Then, we have from our assumption $\|\overline{g}_{\mu_k}(x_k)\| \geq \kappa_{\mathrm{lpg}}$ and (9) that $\gamma_1 \Delta_{k-1} \leq \Delta_k$, $\forall k$, and hence, $\Delta_{k_0-1} \leq \min\{(\kappa_{\mathrm{mdc}}(1-\eta_2)/\kappa_{\mathrm{ubh}}), (1/1+\kappa_{\mathrm{umb}})\} \cdot \|\overline{g}_{\mu_{k_0-1}}(x_{k_0-1})\|$. It implies that (15) holds and thus $\Delta_{k_0-1} \leq \Delta_{k_0}$. But this contradicts the fact that iteration k_0 is the first such that (16) holds, and our initial assumption is therefore impossible. □

3.2. Convergence to Stationary Points. For convenience of discussion, we shall denote $\mathcal{T} = \{k \mid d_k = 0\}$ as the set of zero-solution of (4) iterations, denote $\mathcal{S} = \{k \mid x_{k+1} \neq x_k\}$ as the set of successful iterations, denote $\mathcal{U} = \{k \mid \rho_k < \eta_1,\ x_k^+ \text{ is not accepted by } \mathcal{F}_k\}$ as the set of unsuccessful iterations, and denote $\mathcal{P} = \{k \mid \rho_k < \eta_1,\ x_k^+ \text{ is accepted by } \mathcal{F}_k\}$ as the set of iterations which is not accepted by trust-region rule but filter rule (5). Now, we consider the first-order global convergent conclusion of our algorithm in the following three cases: $|\mathcal{T}| = +\infty$, $|\mathcal{U}| = +\infty$, and $|\mathcal{S}| = +\infty$.

Theorem 1. *Suppose that A1 and A2 hold and that* $|\mathcal{T}| = +\infty$, *then* $\lim_{k\in\mathcal{T}} (\|\overline{g}_{\mu_k}(x_k)\| + \mu_k) = 0$.

Proof. Note that, if $|\mathcal{T}| = +\infty$, Lemma 1 implies that $\overline{g}_{\mu_k}(x_k) = 0$. Moreover, by the mechanism of updating μ_k (10), we have $\mu_{k+1} = \theta\mu_k$. Then, we get the first-order global convergence of our Algorithm 1 $\lim_{k\in\mathcal{T}} (\|\overline{g}_{\mu_k}(x_k)\| + \mu_k) = 0$, i.e., Algorithm 1 can be terminated with finite steps. □

Theorem 2. *Suppose that A1 and A2 hold and that* $|\mathcal{U}| = +\infty$, *then* $\lim_{k\in\mathcal{U}} (\|\overline{g}_{\mu_k}(x_k)\| + \mu_k) = 0$.

Proof. Assume, to arrive at a contradiction, that there exist $\varepsilon > 0$ and k_0 such that

$$\left\| \overline{g}_{\mu_k}(x_k) \right\| + \mu_k \geq \varepsilon, \quad \forall k > k_0. \tag{17}$$

Since $|\mathcal{U}| = +\infty$, there exists a positive integer $k_1 > k_0$ such that

$$x_k = x_{k_1}, \quad \forall k \geq k_1. \tag{18}$$

By the mechanism of updating μ_k (10), we can consider two cases. □

Case 1. $\lim_{k\longrightarrow\infty}\mu_k \neq 0$, i.e., there exists a positive integer $k_2 \geq k_1$ such that $\mu_k = \mu_{k_2}$ for all $k \geq k_2$. By Algorithm 1, we obtain that

$$\begin{aligned} &\Delta_k \leq \gamma_2^{k-k_2} \Delta_{k_2}, \\ &\mu_k \leq 0.1 \left\| \overline{g}_{\mu_k}(x_{k+1}) \right\|, \end{aligned} \tag{19}$$

for all $k \geq k_2$. Hence, we can deduce from (18) and (19) that $\|\overline{g}_{\mu_k}(x_k)\| \geq \kappa_{\mathrm{lpg}}$ for all $k \geq k_2$, where $\kappa_{\mathrm{lpg}} = 10\mu_{k_2}$. Note that $\gamma_2 \in (0,1)$ in Algorithm 1, so we have $\lim_{k\longrightarrow\infty}\Delta_k = 0$. Applying Lemma 4, there is a constant $\kappa_{\mathrm{lbd}} > 0$ such that $\Delta_k \geq \kappa_{\mathrm{lbd}}$ for all k, which contradicts the fact $\lim_{k\longrightarrow\infty}\Delta_k = 0$, as stated in (19). Therefore, Case 1 cannot hold.

Case 2. $\lim_{k\longrightarrow\infty}\mu_k = 0$. We deduce from (17) that there is a integer $k_3 \geq k_1$ such that $\|\overline{g}_{\mu_k}(x_k)\| \geq 0.5\varepsilon \geq 10\mu_k$ for all $k \geq k_3$, i.e., $\mu_k \leq 0.1\|\overline{g}_{\mu_k}(x_k)\| = 0.1\|\overline{g}_{\mu_k}(x_{k+1})\|$, for all $k \geq k_3$. By the mechanism of updating μ_k, then we have $\mu_k = \mu_{k_3}$ for all $k \geq k_3$, which contradicts $\lim_{k\longrightarrow\infty}\mu_k = 0$. Thus, Case 2 cannot hold. Our initial assumption must then be false.

Theorem 3. *Suppose that A1 and A2 hold and that* $|\mathcal{S}| = +\infty$, *then* $\lim_{k\in\mathcal{S}} (\|\overline{g}_{\mu_k}(x_k)\| + \mu_k) = 0$.

Proof. Assume, to arrive at a contradiction, that there exist $\varepsilon > 0$ and k_0 such that

$$\left\| \overline{g}_{\mu_k}(x_k) \right\| + \mu_k \geq \varepsilon, \quad \forall k > k_0. \tag{20}$$

By the mechanism of updating μ_k (10), we can consider two cases. □

Case 3. $\lim_{k\longrightarrow\infty}\mu_k \neq 0$, i.e., there exists a positive integer $k_1 > k_0$ such that $\mu_k = \mu_{k_1}$ for all $k \geq k_1$. Observe first that (10) implies that $\mu_k \leq 0.1\|\overline{g}_{\mu_k}(x_{k+1})\| = 0.1\|\overline{g}_{\mu_{k+1}}(x_{k+1})\|$, $\forall k \geq k_1$. Let $\kappa_{\mathrm{lpg}} = 10\mu_{k_1}$, then

$$\left\| \overline{g}_{\mu_k}(x_k) \right\| \geq \kappa_{\mathrm{lpg}}, \quad \forall k > k_1. \tag{21}$$

(i) $|\mathcal{P}| < +\infty$ (i.e. $|\mathcal{S}\backslash\mathcal{P}| = +\infty$). That means there exists a positive integer $k_2 \geq k_1$ such that either $k \in \mathcal{S}\backslash\mathcal{P}$ or $k \in \overline{\mathcal{S}}$ for all $k \geq k_2$. Besides, we can deduce from $|\mathcal{S}| = +\infty$ that $\rho_k \geq \eta_1$ for all $k \in \mathcal{S}\backslash\mathcal{P}$. Then, by (9), we have that for all $k > k_2$,

$$\begin{aligned}
&f_{\mu_{k_2}}(x_{k_2}) - f_{\mu_k}(x_k) \\
&= \sum_{j=k_2, j\in\mathcal{S}\setminus\mathcal{P}}^{k-1} \left(f_{\mu_j}(x_j) - f_{\mu_{j+1}}(x_{j+1})\right) + \sum_{j=k_2, j\in\overline{\mathcal{S}}}^{k-1} \left(f_{\mu_j}(x_j) - f_{\mu_{j+1}}(x_{j+1})\right) \\
&= \sum_{j=k_2, j\in\mathcal{S}\setminus\mathcal{P}}^{k-1} \left(f_{\mu_j}(x_j) - f_{\mu_{j+1}}(x_{j+1})\right) \geq \sum_{j=k_2, j\in\mathcal{S}/\mathcal{P}}^{k-1} \eta_1\left(Q_j(0) - Q_j(d_j)\right) \\
&\geq \eta_1\kappa_{\mathrm{mdc}}\kappa_{\mathrm{lpg}} \cdot \sum_{j=k_2, j\in\mathcal{S}/\mathcal{P}}^{k-1} \min\left\{\frac{\kappa_{\mathrm{lpg}}}{1+\kappa_{\mathrm{umb}}}, \Delta_j\right\}.
\end{aligned} \tag{22}$$

Hence, we deduce from the boundedness of $\{f_{\mu_k}(x_k)\}$ that $\lim_{k>k_2}\Delta_k = 0$. But it derives a contradiction from (21) and Lemma 3.

(ii) $|\mathcal{P}| = +\infty$. Assumptions A1 and A2 show that $\{\|\overline{g}_{\mu_k}(x_{k+1})\|\}$ is a bounded subsequence. Then, there exists an infinite subsequence $\{k_i\}_{k_i>k_1} \subseteq \mathcal{P}$ such that

$$\lim_{i\longrightarrow\infty}\left\|\overline{g}_{\mu_{k_i}}(x_{k_i+1})\right\| = \|\overline{g}_\infty\| \geq \kappa_{\mathrm{lpg}}. \tag{23}$$

By definition of $k_i \in \mathcal{P}$, x_{k_i+1} is acceptable for the current filter $\mathcal{F}_{k_i}$. This implies, by (21) and filter mechanism (5), that, for each $x_k \in \mathcal{F}_{k_i}$, there exists an index $j(k) \in \mathcal{J}$ such that

$$\begin{aligned}
\left|\overline{g}_{\mu_{k_i},j(k)}(x_{k_i+1})\right| &\leq \left|\overline{g}_{\mu_{k-1},j(k)}(x_k)\right| - \gamma_g\left\|\overline{g}_{\mu_{k-1}}(x_k)\right\| \\
&= \left|\overline{g}_{\mu_{k-1},j(k)}(x_k)\right| - \gamma_g\left\|\overline{g}_{\mu_k}(x_k)\right\| \\
&\leq \left|\overline{g}_{\mu_{k-1},j(k)}(x_k)\right| - \gamma_g\kappa_{\mathrm{lpg}}.
\end{aligned} \tag{24}$$

If $x_{k_{i-1}+1} \notin \mathcal{F}_{k_i}$, we obtain from (6) and (7) that there exists $x_{k_s} \in \mathcal{F}_{k_i}$ such that $|\overline{g}_{\mu_{k_s-1},j}(x_{k_s})| \leq |\overline{g}_{\mu_{k_{i-1}},j}(x_{k_{i-1}+1})|$, $\forall j \in \mathcal{J}$. Thus, (24) ensures that there exists an index $j(k_s) \in \mathcal{J}$ such that

$$\left|\overline{g}_{\mu_{k_i},j(k_s)}(x_{k_i+1})\right| - \left|\overline{g}_{\mu_{k_{i-1}},j(k_s)}(x_{k_{i-1}+1})\right| \leq -\gamma_g\kappa_{\mathrm{lpg}}. \tag{25}$$

If $x_{k_{i-1}+1} \in \mathcal{F}_{k_i}$, (23) implies that there exists an index $j(k_{i-1}+1) \in \mathcal{J}$ such that

$$\left|\overline{g}_{\mu_{k_i},j(k_{i-1}+1)}(x_{k_i+1})\right| - \left|\overline{g}_{\mu_{k_{i-1}},j(k_{i-1}+1)}(x_{k_{i-1}+1})\right| \leq -\gamma_g\kappa_{\mathrm{lpg}}. \tag{26}$$

Since the finite possibility of $j(k_{i-1}+1)$, let $j(k_{i-1}+1) = j_0$. Then, the left-hand side of inequality (25) and (26) tends to zero when i tends to infinity because of (23), which is impossible. In a word, Case 3 does not happen.

Case 4. $\lim_{k\longrightarrow\infty}\mu_k = 0$. The infiniteness of $|\mathcal{S}|$ and (10) implies that there exists a infinite index $\mathcal{K} \subseteq \mathcal{S}$ such that $\lim_{k\in\mathcal{K}}\|\overline{g}_{\mu_k}(x_{k+1})\| = \lim_{k\in\mathcal{K}}\|\overline{g}_{\mu_k}(x_k^+)\| = 0$. We then obtain that $\lim_{k\in\mathcal{K}}(\|\overline{g}_{\mu_k}(x_k^+)\| + \mu_k) = 0$, which contradicts (20), and therefore, Case 4 cannot hold, yielding the desired result.

4. Numerical Experiments

Now, we give some numerical results for the following 10 complementarity test problems in Table 1. The values for the constants used in our tests are $\mu_0 = 10^{-5}$, $\gamma_g = 10^{-3}$, $\gamma_1 = 0.25$, $\gamma_3 = 2$, $\eta_1 = 0.25$, $\eta_2 = 0.95$, $\Delta_0 = 2$, $\theta = 0.1$, $\Delta_{\max} = 10^3$, $\varepsilon = 10^{-5}$, $\mathcal{F}_0 = (10^5, \ldots, 10^5)^T$. The iteration is terminated once $\|f_{\mu_k}(x_k)\| \leq 10^{-5}$.

In addition, we use the nonlinear equations to carry out large-scale data experiments. Let $p(x) = 0$ be a (large-scale) differentiable system of nonlinear equations and let $x^* \in R^n$ be defined by $x^* = (1, 0, 1, 0, \ldots)^T$. For all $i \in \mathcal{J}$, set

$$F_i(x) = \begin{cases} p_i(x) - p_i(x^*), & \text{if } i \text{ odd or}, i > r, \\ p_i(x) - p_i(x^*) + 1, & \text{otherwise}, \end{cases} \tag{27}$$

where $r \geq 0$ is a given integer. In this way, x^* is a solution of the nonlinear complementarity (but not necessarily its unique solution). As done in [36], we used the collection of 6 large-scale problems (Examples 5–10) form Lukšan [37]. Some numerical results for these test problems are presented in Table 1.

Example 1. (Kojima–Shindo nonlinear complementarity test problem)

(i) Degenerate example [7, 10, 11, 27, 38, 39]:

$$F(x) = \begin{pmatrix} 3x_1^2 + 2x_1x_2 + 2x_2^2 + x_3 + 3x_4 - 6 \\ 2x_1^2 + x_1 + x_2^2 + 10x_3 + 2x_4 - 2 \\ 3x_1^2 + x_1x_2 + 2x_2^2 + 2x_3 + 9x_4 - 9 \\ x_1^2 + 3x_2^2 + 2x_3 + 3x_4 - 3 \end{pmatrix}. \tag{28}$$

(ii) Nondegenerate example [10, 38]:

Table 1: Numerical result of test problems.

Example	Start point x_0	n	iter	Resf
1.1	$(0,0,0,0)^T$	4	7	$4.43e-12$
1.2	$(0,0,0,0)^T$	4	9	$7.98e-15$
2	$(3,2,1,2,3)^T$	5	2	$1.43e-13$
3.1	$(2,\ldots,2)^T$	10^3	8	$1.66e-11$
3.2	$(2,\ldots,2)^T$	10^3	5	$1.05e-14$
4.1	$(0.5,\ldots,0.5)^T$	10^3	5	$6.60e-14$
4.2	$(0,\ldots,0)^T$	500	5	$5.78e-10$
4.3	$(0,\ldots,0)^T$	80	9	$1.92e-08$
4.4	$(1,\ldots,1)^T$	10^3	3	$8.00e-16$
5	—	100	16	$1.65e-08$
5	—	10^3	72	$1.63e-10$
6	$(1,0,1,0,\ldots)^T$	100	5	$4.03e-15$
6	$(1,0,1,0,\ldots)^T$	10^3	6	$6.23e-14$
7	$(0,\ldots,0)^T$	100	14	$1.49e-11$
7	$(0,\ldots,0)^T$	10^3	25	$1.94e-10$
8	$(-1.2,1,-1.2,1,\ldots)^T$	100	1	$3.97e-24$
8	$(-1.2,1,-1.2,1,\ldots)^T$	10^3	3	$9.25e-15$
9	—	100	15	$3.61e-12$
9	—	10^3	15	$3.04e-11$
10	$(-1,\ldots,-1)^T$	100	7	$5.53e-10$
10	$(-1,\ldots,-1)^T$	10^3	7	$4.35e-19$

$$F(x)=\begin{pmatrix} 3x_1^2+2x_1x_2+2x_2^2+x_3+3x_4-6 \\ 2x_1^2+x_1+x_2^2+3x_3+2x_4-2 \\ 3x_1^2+x_1x_2+2x_2^2+2x_3+3x_4-1 \\ x_1^2+3x_2^2+2x_3+3x_4-3 \end{pmatrix}. \tag{29}$$

Example 1 (i) has a degenerate solution $((\sqrt{6}/2),0,0,(1/2))^T$ and a nondegenerate solution $(1,0,3,0)^T$. Example 1 (ii) has only one solution $((\sqrt{6}/2),0,0,(1/2))^T$ which is nondegenerate.

Example 2 (Kanzow nonlinear complementarity test problem [10, 40]). We choose $F=(F_1,\ldots,F_n)^T\colon \mathfrak{R}^n \longmapsto \mathfrak{R}^n$ with

$$F_i(x)=2(x_i-i+2)\cdot \exp\left\{\sum_{i=1}^{5}(x_i-i+2)^2\right\},\quad 1\le i\le 5. \tag{30}$$

Example 2 has only one solution $(0,0,1,2,3)^T$.

Example 3 (see [41]). *We choose* $F=(F_1,\ldots,F_n)^T\colon \mathfrak{R}^n \longmapsto \mathfrak{R}^n$ *with*

$$F_i(x)=-x_{i-1}+2x_i-x_{i+1}+\frac{1}{3}x_i^3-b_i,\quad 1\le i\le n, \tag{31}$$

where n is a positive integer and $x_0=x_{n+1}=0$. We choose the constant $b=((-1)^1,\ldots,(-1)^i,\ldots,(-1)^n)^T$ and $b=((-1)^1\sqrt{1},\ldots,(-1)^i\sqrt{i},\ldots,(-1)^n\sqrt{n})^T$, respectively.

Example 4. We consider the following four linear complementarity problem [7, 11, 27, 39, 42–44]: $F(x)=M_ix+q$, $i=1,2,3,4$, where $q=(-1,\ldots,-1)^T$, and M_1,M_2,M_3,M_4 are given as follows, respectively:

$$\begin{pmatrix} 4 & -2 & & \\ 1 & 4 & \ddots & \\ & \ddots & \ddots & -2 \\ & & 1 & 4 \end{pmatrix},$$
$$\begin{pmatrix} 4 & -1 & & \\ -1 & 4 & \ddots & \\ & \ddots & \ddots & -1 \\ & & -1 & 4 \end{pmatrix},$$
$$\begin{pmatrix} (1/n) & & & \\ & (2/n) & & \\ & & \ddots & \\ & & & (n/n) \end{pmatrix}, \tag{32}$$
$$\begin{pmatrix} 1 & 2 & 2 & \ldots & 2 \\ & 1 & 2 & \ldots & 2 \\ & & 1 & \ldots & 2 \\ & & & \ddots & \vdots \\ & & & & 1 \end{pmatrix}.$$

Example 5. Countercurrent reader problem [37]:

$$p_k(x)=\begin{cases} \alpha-(1-\alpha)x_{k+2}-x_k(1+4x_{k+1}), & \text{if } k=1, \\ -(2-\alpha)x_{k+2}-x_k(1+4x_{k-1}), & \text{if } k=2, \\ \alpha x_{k-2}-(1-\alpha)x_{k+2}-x_k(1+4x_{k+1}), & \text{if } k\in(2,n-1) \text{ and } \operatorname{mod}(k,2)=1, \\ \alpha x_{k-2}-(2-\alpha)x_{k+2}-x_k(1+4x_{k-1}), & \text{if } k\in(2,n-1) \text{ and } \operatorname{mod}(k,2)=1, \\ \alpha x_{k-2}-x_k(1+4x_{k+1}), & \text{if } k=n-1, \\ \alpha x_{k-2}-(2-\alpha)x_k(1+4x_{k-1}), & \text{if } k=n, \end{cases} \tag{33}$$

where $\alpha = (1/2)$. We choose the following initial point $\overline{x}$:

$$\overline{x}_k = \begin{cases} 0.1, & \text{if } \operatorname{mod}(k,8) = 1, \\ 0.2, & \text{if } \operatorname{mod}(k,8) = 2 \text{ and } \operatorname{mod}(k,8) = 0, \\ 0.3, & \text{if } \operatorname{mod}(k,8) = 3 \text{ and } \operatorname{mod}(k,8) = 7, \\ 0.4, & \text{if } \operatorname{mod}(k,8) = 4 \text{ and } \operatorname{mod}(k,8) = 6, \\ 0.5, & \text{if } \operatorname{mod}(k,8) = 5. \end{cases} \tag{34}$$

Example 6. Extended Powell badly scaled function [37]:

$$p_k(x) = \begin{cases} 10000 x_k x_{k+1}, & \text{if } \operatorname{mod}(k,2) = 1, \\ e^{-x_{k-1}} + e^{-x_k} - 1.0001, & \text{if } \operatorname{mod}(k,2) = 0. \end{cases} \tag{35}$$

Example 7. Trigonometric exponential system [37]:

$$p_k(x) = \begin{cases} 3x_k^3 + 2x_{k+1} - 5 + \sin(x_k - x_{k+1})\sin(x_k + x_{k+1}), & \text{if } k = 1, \\ 3x_k^3 + 2x_{k+1} - 5 + \sin(x_k - x_{k+1})\sin(x_k + x_{k+1}), & \\ +4x_k - x_{k-1}e^{x_{k-1} - x_k}, & \text{if } k \in (1, n), \\ 4x_k - x_{k-1}e^{x_{k-1} - x_k}, & \text{if } k = n. \end{cases} \tag{36}$$

Example 8. Extended Rosenbrock function [37]:

$$p_k(x) = \begin{cases} 10(x_{k+1} - x_k^2), & \text{if } \operatorname{mod}(k,2) = 1, \\ 1 - x_{k-1}, & \text{if } \operatorname{mod}(k,2) = 0. \end{cases} \tag{37}$$

Example 9. Extended Cragg and Levy Function [37].

$$p_k = \begin{cases} (e^{x_k} - x_{k+1})^2, & \text{if } \operatorname{mod}(k,4) = 1, \\ 10(x_k - x_{k+1})^3, & \text{if } \operatorname{mod}(k,4) = 2, \\ \tan^2(x_k - x_{k+1}), & \text{if } \operatorname{mod}(k,4) = 3, \\ x_k - 1, & \text{if } \operatorname{mod}(k,4) = 0. \end{cases} \tag{38}$$

We choose the following initial point $\overline{x}$ as $\overline{x}_k = \begin{cases} 1, & \text{if } \operatorname{mod}(k,4) = 1, \\ 2, & \text{otherwise.} \end{cases}$

Example 10. Broyden tridiagonal problem [37]:

$$p_k(x) = \begin{cases} (3 - 2x_k)x_k - 2x_{k+1} + 1, & \text{if } k = 1, \\ (3 - 2x_k)x_k - x_{k-1} - 2x_{k+1} + 1, & \text{if } k \in (1, n), \\ (3 - 2x_k)x_k - x_{k-1} + 1, & \text{if } k = n. \end{cases} \tag{39}$$

The computational results are listed in Table 1, in which iter denotes the number of iterations, and Resf stands for the computing accuracy, i.e., Resf $= f_{\mu_k}(x_k)$. The numerical results show that Algorithm 1 is robust and efficient. The number of iterations and computing accuracy for most problems are satisfactory.

5. Conclusions

In this work, we have proposed multidimensional filter techniques for solving nonlinear complementarity problem (1) and have shown this algorithm to be globally convergent under a weaker assumption because assumptions A1 and A2 imply that the matrix sequence $\{B_k\}$ in subproblem (4) is uniformly bounded. Moreover, we are surprised to find that $B_{k+1} = \nabla_x \Phi_{\mu_k}(x_k) \nabla_x \Phi_{\mu_k}(x_k)^T$ can be computed easily instead of updating B_{k+1} by utilizing some methods (e.g., BFGS). The new algorithm differs from other traditional filter methods [7, 27, 39] for nonlinear complementarity problems; subproblem (4) is consistent throughout, so we do not need any extra restoration procedure which means higher numerical expenditure. Besides, we used the gradient-projection technique which makes sure that the optimality condition of constrained optimization problem (2) is equivalent to the fact that the projected gradient is zero, so the multidimensional filter techniques based on unconstrained optimization problem is suitable for problem (2). Finally, in this context, we provide a reasonable and effective way to balance the projected gradient $\overline{g}_{\mu_k}(x_k)$ and the smooth parameter μ_k and then ensure that $\liminf_{k \longrightarrow +\infty} \|\overline{g}_{\mu_k}(x_k)\| + \mu_k = 0$. The results of numerical experiments show its efficiency.

Data Availability

The data used to support the findings of this study are available from the corresponding author upon request.

Conflicts of Interest

The authors declare that there are no conflicts of interest in this work.

Acknowledgments

The authors thank the anonymous reviewers for the careful reading of the manuscript and their valuable comments. This work was supported by the National Defence Pre-Research Foundation of China.

References

[1] A. Fischer, "Solution of monotone complementarity problems with locally Lipschitzian functions," *Mathematical Programming*, vol. 76, no. 3, pp. 513–532, 1997.

[2] A. Fischer, "New constrained optimization reformulation of complementarity problems," *Journal of Optimization Theory and Applications*, vol. 97, no. 1, pp. 105–117, 1998.

[3] C. Geiger and C. Kanzow, "On the resolution of monotone complementarity problems," *Computational Optimization and Applications*, vol. 5, no. 2, pp. 155–173, 1996.

[4] M. V. Solodov, "Stationary points of bound constrained minimization reformulations of complementarity problems," *Journal of Optimization Theory and Applications*, vol. 94, no. 2, pp. 449–467, 1997.

[5] N. Yamashita, "Properties of restricted NCP functions for nonlinear complementarity problems," *Journal of Optimization Theory and Applications*, vol. 98, no. 3, pp. 701–717, 1998.

[6] O. L. Mangasarian and M. V. Solodov, "Nonlinear complementarity as unconstrained and constrained minimization," *Mathematical Programming*, vol. 62, no. 1-3, pp. 277–297, 1993.

[7] H. Wang and D. Pu, "A kind of nonmonotone filter method for nonlinear complementarity problem," *Journal of Applied Mathematics and Computing*, vol. 36, no. 1-2, pp. 27–40, 2011.

[8] M. Huang and D. Pu, "A trust-region SQP method without a penalty or a filter for nonlinear programming," *Journal of Computational and Applied Mathematics*, vol. 281, pp. 107–119, 2015.

[9] K. Su, X. Lu, and W. Liu, "An improved filter method for nonlinear complementarity problem," *Mathematical Problems in Engineering*, vol. 2013, Article ID 450829, 7 pages, 2013.

[10] X. Fan, T. Xu, and F. Gao, "Solving nonlinear complementarity problem by a smoothing homotopy method," *Taiwanese Journal of Mathematics*, vol. 19, no. 1, pp. 51–63, 2015.

[11] B. Fan, C. Ma, A. Wu, and C. Wu, "A Levenberg-Marquardt method for nonlinear complementarity problems based on nonmonotone trust region and line search techniques," *Mediterranean Journal of Mathematics*, vol. 15, pp. 118–136, 2018.

[12] J. Liu and S. Li, "Unconstrained optimization reformulation for stochastic nonlinear complementarity problems," *Applicable Analysis*, pp. 1–22, 2019.

[13] H. Zheng and L. Liu, "The sign-based methods for solving a class of nonlinear complementarity problems," *Journal of Optimization Theory and Applications*, vol. 180, no. 2, pp. 480–499, 2019.

[14] H. Zheng, "Improved convergence theorems of modulus-based matrix splitting iteration method for nonlinear complementarity problems of H-matrices," *Calcolo*, vol. 54, no. 4, pp. 1481–1490, 2017.

[15] S.-L. Xie, H.-R. Xu, and J.-P. Zeng, "Two-step modulus-based matrix splitting iteration method for a class of nonlinear complementarity problems," *Linear Algebra and Its Applications*, vol. 494, pp. 1–10, 2016.

[16] H. Zheng and L. Liu, "A two-step modulus-based matrix splitting iteration method for solving nonlinear complementarity problems of H_+-matrices," *Computational and Applied Mathematics*, vol. 37, no. 4, pp. 5410–5423, 2018.

[17] C. Ma and N. Huang, "Modified modulus-based matrix splitting algorithms for a class of weakly nondifferentiable nonlinear complementarity problems," *Applied Numerical Mathematics*, vol. 108, pp. 116–124, 2016.

[18] R. Li and J.-F. Yin, "Accelerated modulus-based matrix splitting iteration methods for a restricted class of nonlinear complementarity problems," *Numerical Algorithms*, vol. 75, no. 2, pp. 339–358, 2017.

[19] R. Fletcher and S. Leyffer, "Nonlinear programming without a penalty function," *Mathematical Programming*, vol. 91, no. 2, pp. 239–269, 2002.

[20] C. Jiang, A. Zada, M. T. Senel, and T. Li, "Synchronization of bidirectional N-coupled fractional-order chaotic systems with ring connection based on antisymmetric structure," *Advances in Difference Equations*, vol. 2019, no. 1, pp. 456–471, 2019.

[21] A. Yang, L. Li, Z. Wang, and R. Guo, "Tracking control of a class of chaotic systems," *Symmetry*, vol. 11, no. 4, pp. 568–579, 2019.

[22] R. Xu and F. Zhang, "ε-Nash mean-field games for general linear-quadratic systems with applications," *Automatica*, vol. 114, pp. 108835–108840, 2020.

[23] A. Wächter and L. T. Biegler, "On the implementation of an interior-point filter linesearch algorithm for large scale nonlinear programming," *Mathematical Programming*, vol. 106, no. 1, pp. 25–57, 2006.

[24] R. Fletcher, S. Leyffer, and P. L. Toint, "On the global convergence of a filter—SQP algorithm," *SIAM Journal on Optimization*, vol. 13, no. 1, pp. 44–59, 2002.

[25] S. Ulbrich, "On the superlinear local convergence of a filter-SQP methods," *Mathematical Programming*, vol. 100, pp. 217–245, 2004.

[26] J. Long and S. Zeng, "A projection-filter method for solving nonlinear complementarity problems," *Applied Mathematics and Computation*, vol. 216, no. 1, pp. 300–307, 2010.

[27] P.-y. Nie, "A filter method for solving nonlinear complementarity problems," *Applied Mathematics and Computation*, vol. 167, no. 1, pp. 677–694, 2005.

[28] R. Fletcher, N. I. M. Gould, S. Leyffer, P. L. Toint, and A. Wächter, "Global convergence of a trust-region SQP-filter algorithm for general nonlinear programming," *SIAM Journal on Optimization*, vol. 13, no. 3, pp. 635–659, 2002.

[29] P. S. Ferreira, E. W. Karas, M. Sachine, and F. N. C. Sobral, "Global convergence of a derivative-free inexact restoration filter algorithm for nonlinear programming," *Optimization*, vol. 66, no. 2, pp. 271–292, 2017.

[30] N. I. M. Gould, C. Sainvitu, and P. L. Toint, "A filter-trust-region method for unconstrained optimization," *SIAM Journal on Optimization*, vol. 16, no. 2, pp. 341–357, 2005.

[31] N. I. M. Gould, S. Leyffer, and P. L. Toint, "A multidimensional filter algorithm for nonlinear equations and nonlinear least-squares," *SIAM Journal on Optimization*, vol. 15, no. 1, pp. 17–38, 2004.

[32] C. Sainvitu and P. L. Toint, "A filter-trust-region method for simple-bound constrained optimization," *Optimization Methods and Software*, vol. 22, no. 5, pp. 835–848, 2007.

[33] C. Kanzow and H. Pieper, "Jacobian smoothing methods for nonlinear complementarity problems," *SIAM Journal on Optimization*, vol. 9, no. 2, pp. 342–373, 1999.

[34] J. Zhu and B. Hao, "A new smoothing method for solving nonlinear complementarity problems," *Open Mathematics*, vol. 17, no. 1, pp. 104–119, 2019.

[35] A. R. Conn, N. I. M. Gould, and P. L. Toint, *Trust Region Method*, MPS and SIAM, Philadelphia, PA, USA, 2000.

[36] F. Facchinei and C. Kanzow, "A nonsmooth inexact Newton method for the solution of large-scale nonlinear complementarity problems," *Mathematical Programming*, vol. 76, no. 3, pp. 493–512, 1997.

[37] L. Lukšan, "Inexact trust region method for large sparse systems of nonlinear equations," *Journal of Optimization Theory and Applications*, vol. 81, pp. 569–590, 1994.

[38] J. D. Ding and H. Y. Yin, "A new homotopy method for nonlinear complementarity problems," *Numerical Mathematics Theory Methods and Applications*, vol. 16, pp. 155–163, 2007.

[39] K. Su and H.-p. Cai, "A modified SQP-filter method for nonlinear complementarity problem," *Applied Mathematical Modelling*, vol. 33, no. 6, pp. 2890–2896, 2009.
[40] T. Ni and P. Wang, "A smoothing-type algorithm for solving nonlinear complementarity problems with a non-monotone line search," *Applied Mathematics and Computation*, vol. 216, no. 7, pp. 2207–2214, 2010.
[41] C. Huang and S. Wang, "A power penalty approach to a nonlinear complementarity problem," *Operations Research Letters*, vol. 38, no. 1, pp. 72–76, 2010.
[42] H. Yu and D. Pu, "Smoothing Levenberg-Marquardt method for general nonlinear complementarity problems under local error bound," *Applied Mathematical Modelling*, vol. 35, no. 3, pp. 1337–1348, 2011.
[43] J.-l. Zhang and X. Zhang, "A smoothing Levenberg-Marquardt method for NCP," *Applied Mathematics and Computation*, vol. 178, no. 2, pp. 212–228, 2006.
[44] H. Zheng, W. Li, and S. Vong, "An iteration method for nonlinear complementarity problems," *Journal of Computational and Applied Mathematics*, vol. 372, Article ID 112681, 2020.

Hindawi
Mathematical Problems in Engineering
Volume 2020, Article ID 8572959, 16 pages
https://doi.org/10.1155/2020/8572959

Research Article

Maximum Principle for Near-Optimality of Mean-Field FBSDEs

Ruijing Li[1] and Chaozhu Hu[2]

[1]*School of Statistics and Mathematics, Guangdong University of Finance and Economics, Guangzhou 510320, Guangdong, China*
[2]*School of Science, Hubei University of Technology, Wuhan 430068, Hubei, China*

Correspondence should be addressed to Chaozhu Hu; huchaozhu@126.com

Received 13 April 2020; Revised 16 May 2020; Accepted 18 May 2020; Published 8 June 2020

Guest Editor: Rongwei Guo

The present paper concerns with a near-optimal control problem for systems governed by mean-field forward-backward stochastic differential equations (FBSDEs) with mixed initial-terminal conditions. Utilizing Ekeland's variational principle as well as the reduction method, the necessary and sufficient near-optimality conditions are established in the form of Pontryagin's type. The results are obtained under restriction on the convexity of the control domain. As an application, a linear-quadratic stochastic control problem is solved explicitly.

1. Introduction

Near-optimal control problems have attracted more attentions in recent years due to its distinct advantages, such as existence under minimal assumptions, availability in most practical cases, and convenience for implementation both analytically and numerically. The study of this theory can be traced back to Ekeland [1] and later greatly developed by Zhou [2–4] for deterministic and stochastic cases. Since then, many works have been devoted to the near-optimality of various stochastic control systems. Without being exhaustive, let us refer to [5–13] and the references therein.

In 2015, Zhang et al. [14] investigated the near-optimality necessary conditions for classical linear FBSDEs, where the control domain was with nonconvexity. Via convergence technique as well as reduction method, they established the near-optimal maximum principle. Soon afterwards, under the same assumptions, Zhang [15] presented the near-optimal sufficient conditions for such classical linear FBSDEs. Especially, in 2018, by defining viscosity solution with perturbation factor to dispense the illusory differentiability condition of value function, Zhang and Zhou [16] established the necessary near-optimality conditions for stochastic recursive systems by virtue of dynamic programming principle. Another noteworthy thing is that, for recent years, some authors started research studies on near-optimal control problems for delay systems. For example, Zhang [17] first studied near-optimal control problems for linear stochastic delay systems. By anticipated backward stochastic differential equations method as well as maximum principle, necessary condition and sufficient verification theorem were provided. Then, also under restriction on convexity control domain, Wang and Wu [18] investigated near-optimal control problem for nonlinear stochastic delay systems. By Ekeland's variational principle and corresponding moment estimations, they presented the sufficient as well as necessary near-optimality conditions. For more details, refer to [19, 20] and the references therein.

However, to the best of our knowledge, few papers can be found in the literature on the near-optimality of mean-field backward stochastic differential equations (BSDEs). This new kind of mean-field BSDEs was first introduced by Buckdahn et al. [21], which were derived as a limit of some highly dimensional system of FBSDEs, corresponding to a large number of particles. It has been shown in Buckdahn et al. [22] that, such a mean-field BSDE described the viscosity solution of the associated nonlocal partial differential equations. Henceforth, many authors take into account of this system of McKean-Vlasov type (Lasry and Lions [23]) adapted for different frameworks, for example, Xu and Wu

[24] presented a maximum principle for optimal control problems governed by backward stochastic partial differential equations of mean-field type, and for other related works, refer to [25–28].

As we can see that all the above literature studies are about mean-field problems involving expectations as mean-field terms. In fact, there is another line dealing with mean-field problems, which involve large-population as mean-field terms to describe the impact of the population's collective behaviors on all agents (Huang et al. [29]) such as the work of Huang [30] and Xu and Shi [31] as well as the work of Xu and Zhang [32] all concerned with general mean-field linear-quadratic-Gaussian (LQG) games of stochastic large-population systems; through the consistency condition, they derived the decentralized strategies and further verified the asymptotic near-optimality property (namely, ε-Nash equilibrium) of decentralized strategies for the LQ games. On the contrary, a relevant work of Hafayed and Abbas [8] dealing with near-optimal control problems has established necessary and sufficient conditions for mean-field singular stochastic systems in the case of controlled diffusion coefficient. Particularly, in the concluding section, it is pointed out that the establishment of necessary and sufficient near-optimal conditions for mean-field FBSDEs also remains an open problem. Motivated by this fact with the addition of above described mean-field theory application background in economics and finance, this paper is to discuss near-optimal control problems for mean-field FBSDEs, where the controlled state systems are with mixed initial-terminal conditions.

The main contribution of this paper lies in the initial introduction of three first-order adjoint equations to eliminate the corresponding variational processes during dual analysis; another is rooted in the usage of reduction method to guarantee the well-posedness of the first-order adjoint equations with mixed initial-terminal conditions. Via classical convex variational technique and Ekeland's variational principle, a necessary condition of Pontryagin's type is derived. Then, under some additional assumptions, we prove that the near-maximum condition on the Hamiltonian function is a sufficient condition for near-optimality. It is remarkable that our results extend those of [5] essentially to the framework of mean-field theory.

The rest of this paper is organized as follows. In Section 2, we state some preliminaries and basic definitions. In Sections 3 and 4, we establish the main theorems and provide its detailed proof. In Section 5, an example of a linear-quadratic control problem is worked out to illustrate the theoretical applications. Finally, some concluding remarks are given in Section 6.

2. Preliminaries

Let $(\Omega, \mathcal{F}, \{\mathcal{F}_t\}_{t\geq 0}, P)$ be a filtered probability space satisfying the usual condition, on which a one-dimensional standard Brownian motion $(W_t)_{t\geq 0}$ is defined, $\mathcal{F} = \{\mathcal{F}_s, 0 \leq s \leq T\}$ be the natural filtration generated by $(W_t)_{t\geq 0}$ and augmented by all P-null sets, i.e.,

$$\mathcal{F}_s = \sigma\{W_r, r \leq s\} \vee \mathcal{N}_p, \quad s \in [0, T], \tag{1}$$

where $\mathcal{N}_p$ is the set of all P-null subsets. We now introduce some spaces of random variables and stochastic processes.

$L^2_{\mathcal{F}}(\Omega; R) = \{\mathcal{F}$ − measurable random variable X: $E|X|^2 < \infty\}$

$\mathcal{S}^2_{\mathcal{F}}(0, T; R) = \{\mathcal{F}$ − adapted and continuous process ψ: $E[\sup_{t\in[0,T]} |\psi_t|^2] < \infty\}$

$\mathcal{H}^2_{\mathcal{F}}(0, T; R) = \{\mathcal{F}$ − adapted process ψ: $E[\int_0^T |\psi_t|^2 dt] < \infty\}$

$M^2[0, T] := \mathcal{S}^2_{\mathcal{F}}(0, T; R) \times \mathcal{S}^2_{\mathcal{F}}(0, T; R) \times \mathcal{H}^2_{\mathcal{F}}(0, T; R)$

Clearly, $M^2[0, T]$ is a Banach space. Any process in $M^2[0, T]$ is defined by $\Theta := (x, y, z)$ with the norm

$$\|\Theta\|_{M^2[0,T]} := \left\{E\left[\sup_{t\in[0,T]} |x_t|^2 + \sup_{t\in[0,T]} |y_t|^2 + \int_0^T |z_t|^2 dt\right]\right\}^{1/2}. \tag{2}$$

We study the near-optimal control problem of the following controlled mean-field FBSDEs having mixed initial-terminal conditions:

$$\begin{cases} dx_t = b(t, x_t, Ex_t, u_t)dt + \sigma(t, x_t, Ex_t, u_t)dW_t, \\ -dy_t = f(t, x_t, y_t, z_t, Ex_t, Ey_t, Ez_t, u_t)dt - z_t dW_t, \\ x_0 = \gamma(x_T, y_0), \\ y_T = h(x_T, y_0), \end{cases} \tag{3}$$

where b, σ: $[0, T] \times R^2 \times U \longrightarrow R$; f: $[0, T] \times R^6 \times U \longrightarrow R$; h, γ: $R \times R \longrightarrow R$; and U is a given convex closed set of R. The cost functional to be minimized over the space $\mathcal{U} = L^2_{\mathcal{F}}(0, T; U)$ of admissible controls takes the form

$$J(u) = E\left\{\int_0^T l(t, x_t, y_t, z_t, Ex_t, Ey_t, Ez_t, u_t)dt + \varphi(x_T, y_0)\right\}, \tag{4}$$

with l: $[0, T] \times R^6 \times U \longrightarrow R$; φ: $R \times R \longrightarrow R$.

Definition 1 (see [4]). Both a family of admissible pairs $\{(x^\varepsilon, y^\varepsilon, z^\varepsilon, u^\varepsilon)\}$ parameterized by $\varepsilon > 0$ and any element $(x^\varepsilon, y^\varepsilon, z^\varepsilon, u^\varepsilon)$ in the family are called near-optimal if

$$\left|J(u^\varepsilon) - \inf_{u\in\mathcal{U}} J(u)\right| \leq r(\varepsilon), \tag{5}$$

holds for sufficiently small ε, where r is a function of ε satisfying $r(\varepsilon) \longrightarrow 0$ as $\varepsilon \longrightarrow 0$. The estimate $r(\varepsilon)$ is called an error bound. If $r(\varepsilon) = C\varepsilon^\delta$ for some $\delta > 0$ independent of the constant C, then u^ε is called near-optimal with order ε^δ. Particularly, when $r(\varepsilon) = \varepsilon$, u^ε is called ε-optimal. The near-optimal control problem under consideration in this paper is as follows.

Problem $\mathcal{A}$. Find $u^\varepsilon \in \mathcal{U}$ such that

$$J(u^\varepsilon) = \inf_{v\in\mathcal{U}} J(v) + \varepsilon. \tag{6}$$

Some notations and assumptions are presented before giving the well-posedness of system (3). We denote the norm by $|\cdot|$ of an Euclidean space.

(A_1) The functions b, σ, f, and l are $\mathscr{F}$-progressively measurable in u, continuously differentiable in $x, y, z, \tilde{x}, \tilde{y}$, and $\tilde{z}$, and the derivatives of b, σ, f, and l with respect to $x, y, z, \tilde{x}, \tilde{y}$, and $\tilde{z}$ are bounded. Moreover, for some constant $C > 0$,

$$\begin{aligned}&(1+|x|+|\tilde{x}|)^{-1}|b(t,x,\tilde{x},u)|+(1+|x|+|\tilde{x}|)^{-1}|\sigma(t,x,\tilde{x},u)|\\&\quad+(1+|x|+|y|+|z|+|\tilde{x}|+|\tilde{y}|+|\tilde{z}|)^{-1}|f(t,x,y,z,\tilde{x},\tilde{y},\tilde{z},u)|\\&\quad+(1+|x|+|y|+|z|+|\tilde{x}|+|\tilde{y}|+|\tilde{z}|)^{-1}|l(t,x,y,z,\tilde{x},\tilde{y},\tilde{z},u)|\le C.\end{aligned} \tag{7}$$

(A_2) h, γ, and φ are continuously differentiable in x and y, and the derivatives of h, γ, and φ with respect to x and y are bounded. Moreover, for some constant $C > 0$, $\rho = h, \gamma, \varphi$

$$(1+|x|+|y|)^{-1}|\rho(x,y)|\le C. \tag{8}$$

(A_3) There is a constant $C > 0$ and $\beta \in [0,1]$ such that

$$\begin{aligned}&\left|b_x(t,x,\tilde{x},u)-b_x\left(t,x\prime,\tilde{x}',u\right)\right|+\left|b_{\tilde{x}}(t,x,\tilde{x},u)-b_{\tilde{x}}\left(t,x\prime,\tilde{x}',u\right)\right|\\&\quad+\left|\sigma_x(t,x,\tilde{x},u)-\sigma_x\left(t,x\prime,\tilde{x}',u\right)\right|+\left|\sigma_{\tilde{x}}(t,x,\tilde{x},u)-\sigma_{\tilde{x}}\left(t,x\prime,\tilde{x}',u\right)\right|\\&\quad\le C\left(|x-x\prime|^{\beta}+\left|\tilde{x}-\tilde{x}'\right|^{\beta}\right),\\&\left|f_i(t,x,y,z,\tilde{x},\tilde{y},\tilde{z},u)-f_i\left(t,x\prime,y\prime,z\prime,\tilde{x}',\tilde{y}',\tilde{z}',u\right)\right|\\&\quad+\left|l_i(t,x,y,z,\tilde{x},\tilde{y},\tilde{z},u)-l_i\left(t,x\prime,y\prime,z\prime,\tilde{x}',\tilde{y}',\tilde{z}',u\right)\right|\\&\quad\le C\left(|x-x\prime|^{\beta}+|y-y\prime|^{\beta}+|z-z\prime|^{\beta}+\left|\tilde{x}-\tilde{x}'\right|^{\beta}+\left|\tilde{y}-\tilde{y}'\right|^{\beta}+\left|\tilde{z}-\tilde{z}'\right|^{\beta}\right).\end{aligned} \tag{9}$$

Furthermore,

$$\begin{aligned}&\left|\rho_x(x,y)-\rho_x(x\prime,y\prime)\right|+\left|\rho_y(x,y)-\rho_y(x\prime,y\prime)\right|\\&\quad\le C\left(|x-x\prime|^{\beta}+|y-y\prime|^{\beta}\right),\end{aligned} \tag{10}$$

where $i = x, y, z, \tilde{x}, \tilde{y}, \tilde{z}$ and $\rho = h, \gamma, \varphi$.

Remark 1. Under assumptions $(A_1)-(A_3)$ via Theorem 2 in [33], the mean-field stochastic system (3) admits a unique adapted solution $(x, y, z) \in M^2[0,T]$.

In fact, due to the mixed initial-terminal conditions in the state equation, even if we have the well-posedness of the state equation via the Lyapunov operator introduced in [34], the well-posedness of the first-order adjoint equation seems to be not guaranteed. To overcome this difficulty, we introduce a reduction method inspired by the study of optimality variational principle for controlled FBSDEs with mixed initial-terminal conditions [35]. First, we pose the following problem.

Problem $\mathscr{B}$. Find $(x_0^\varepsilon, y_0^\varepsilon, u^\varepsilon) \in \mathscr{R} := R \times R \times \mathscr{U}$ such that

$$J\left(x_0^\varepsilon, y_0^\varepsilon, u^\varepsilon\right) = \inf_{(x_0,y_0,u)\in\mathscr{U}} J\left(x_0, y_0, u\right) + \varepsilon, \tag{11}$$

where (x_0, y_0, u) is subject to the forward control system:

$$\begin{cases}\mathrm{d}x_t = b(t,x_t,Ex_t,u_t)\mathrm{d}t+\sigma(t,x_t,Ex_t,u_t)\mathrm{d}W_t,\\ -\mathrm{d}y_t = f(t,x_t,y_t,z_t,Ex_t,Ey_t,Ez_t,u_t)\mathrm{d}t - z_t\mathrm{d}W_t,\\ x(0) = x_0,\\ y(0) = y_0,\end{cases} \tag{12}$$

with the mixed initial-terminal state constraints:

$$\begin{aligned}x_0 &= \gamma(x_T, y_0),\\ y_T &= h(x_T, y_0).\end{aligned} \tag{13}$$

It is remarkable that, for Problem $\mathscr{A}$, the mean-field system (3) has a unique solution (x, y, z) under $(A_1)-(A_3)$, which implies that $y(0)$ is unique and completely determinate. While, for Problem $\mathscr{B}$, $y(0)$ is arbitrary and viewed as a control variable. It just needs to satisfy the near-optimal state constraints at time T. So, Problem $\mathscr{A}$ is embedded into Problem $\mathscr{B}$. Hence, if the triple $(x_0^\varepsilon, y_0^\varepsilon, u^\varepsilon)$ is the near-optimal control of $\mathscr{B}$, then u^ε is near-optimal for Problem $\mathscr{A}$. In the following section, we will adopt the classical convex variational technique to solve Problem $\mathscr{B}$.

3. Necessary Condition of Near-Optimality

This section is devoted to the study of the main theorem. For simplicity, we denote

$$\begin{cases} b_j := b_j(t, x_t, Ex_t, u_t), \\ \sigma_j := \sigma_j(t, x_t, Ex_t, u_t), \\ f_j := f_j(t, \Gamma_t, u_t), \\ l_j := l_j(t, \Gamma_t, u_t), \\ \rho_{x_T} = \rho_{x_T}(x_T, y_0), \\ \rho_{y_0} = \rho_{y_0}(x_T, y_0), \\ j \in \{x, y, z, \tilde{x}, \tilde{y}, \tilde{z}\}, \\ \Gamma_t = (x_t, y_t, z_t, Ex_t, Ey_t, Ez_t), \\ \rho = h, \gamma, \varphi. \end{cases} \tag{14}$$

For any $u \in \mathcal{U}$ and the corresponding state processes (x, y, z), we define the first-order adjoint equation as

$$\begin{cases} d\xi_t = \left\{ f_y \xi_t + l_y + E\left[f_{\tilde{y}} \xi_t + l_{\tilde{y}} \right] \right\} dt \\ \quad + \left\{ f_z \xi_t + l_z + E\left[f_{\tilde{z}} \xi_t + l_{\tilde{z}} \right] \right\} dW_t, \\ -d\eta_t = \{ -f_x \xi_t + b_x \eta_t + \sigma_x \zeta_t - l_x \} dt \\ \quad + \left\{ E\left[-f_{\tilde{x}} \xi_t + b_{\tilde{x}} \eta_t + \sigma_{\tilde{x}} \zeta_t - l_{\tilde{x}} \right] \right\} dt - \zeta_t dW_t, \\ \xi_0 = -\theta_0 \varphi_{y_0} - \eta_0 \gamma_{y_0} + \xi_T h_{y_0}, \\ \eta_T = -\xi_T h_{x_T} + \eta_0 \gamma_{x_T} + \theta_0 \varphi_{x_T}. \end{cases} \tag{15}$$

Remark 2. Under assumptions $(A_1) - (A_3)$, the adjoint equation (15) admits a unique adapted solution $(\xi, \eta, \zeta) \in M^2[0, T]$. The well-posedness of the corresponding adjoint system will be provided in the derivation process of Theorem 1.

Define a metric on $\mathcal{U}$ by

$$d(u, u\prime) = \left[E \int_0^T |u - u\prime|^2 dt \right]^{1/2}, \quad \forall u, u\prime \in \mathcal{U}. \tag{16}$$

Since U is closed, it can be shown that $(\mathcal{U}, d)$ is a complete metric space. Next, we will present some continuity of the state processes and adjoint processes with respect to the metric d.

Lemma 1. *For any $0 < \alpha < 1$ and $0 < p \le 2$, there is a constant $C = C(\alpha, p) > 0$ such that, for any $u, \overline{u} \in \mathcal{U}$ along with the corresponding trajectories (x, y, z) and $(\overline{x}, \overline{y}, \overline{z})$, it follows that*

$$\begin{gathered} E\left(\sup_{t \in [0,T]} |x_t - \overline{x}_t|^p \right) \le C\, d(u, \overline{u})^{\alpha p/2}, \\ \sup_{t \in [0,T]} E|y_t - \overline{y}_t|^p + E \int_0^T |z_t - \overline{z}_t|^p dt \le C\, d(u, \overline{u})^{\alpha p/2}. \end{gathered} \tag{17}$$

Proof. Applying the classical methods as Lemma 4 in [5] for dealing with mean-field FBSDEs, together with Burkholder–Davis–Gundy inequality and Gronwall's inequality, we can logically obtain the estimates. □

Lemma 2. *Let $(A_1) - (A_3)$ hold, for any $0 < \alpha < 1$ and $1 < p < 2$ satisfying $(1 + \alpha\beta)p < 2$, and there is a constant $C = C(\alpha, \beta, p) > 0$ such that, for any $u, \overline{u} \in \mathcal{U}$, along with the corresponding trajectories (x, y, z) and $(\overline{x}, \overline{y}, \overline{z})$ and the solutions (ξ, η, ζ) and $(\overline{\xi}, \overline{\eta}, \overline{\zeta})$ of the corresponding adjoint equation (15), it holds that*

$$\begin{gathered} E \int_0^T \left| \xi_t - \overline{\xi}_t \right|^p dt \le C\, d(u, \overline{u})^{\alpha\beta p/2}, \\ E \int_0^T \left(\left| \eta_t - \overline{\eta}_t \right|^p + \left| \zeta_t - \overline{\zeta}_t \right|^p \right) dt \le C\, d(u, \overline{u})^{\alpha\beta p/2}. \end{gathered} \tag{18}$$

Proof. Applying the classical methods as Lemma 5 in [5] for dealing with mean-field FBSDEs, we can naturally obtain the estimates. □

Theorem 1. *Let $(A_1) - (A_3)$ hold, for any $\varepsilon > 0$, u^ε is an ε-optimal control of problem $\mathcal{B}$. Then, for any $\kappa \in [0, (1/3))$, there exist three parameters θ_0^ε, $\overline{\theta}_0^\varepsilon$, and $\overline{\theta}_T^\varepsilon$ with $|\theta_0^\varepsilon|^2 + E|\overline{\theta}_0^\varepsilon|^2 + E|\overline{\theta}_T^\varepsilon|^2 = 1$, and $\theta_0^\varepsilon \ge 0$ holds that*

$$\begin{aligned} -C\varepsilon^\kappa \theta_0^\varepsilon \le E \int_0^T & \left(\eta_t^\varepsilon \left[b(t, x_t^\varepsilon, Ex_t^\varepsilon, u_t) - b(t, x_t^\varepsilon, Ex_t^\varepsilon, u_t^\varepsilon) \right] + \zeta_t^\varepsilon \left[\sigma(t, x_t^\varepsilon, Ex_t^\varepsilon, u_t) - \sigma(t, x_t^\varepsilon, Ex_t^\varepsilon, u_t^\varepsilon) \right] \right. \\ & \left. - \xi_t^\varepsilon \left[f(t, \Gamma_t^\varepsilon, u_t) - f(t, \Gamma_t^\varepsilon, u_t^\varepsilon) \right] - \left[l(t, \Gamma_t^\varepsilon, u_t) - l(t, \Gamma_t^\varepsilon, u_t^\varepsilon) \right] \right) dt, \quad \forall u \in U, \end{aligned} \tag{19}$$

where $(\xi^\varepsilon, \eta^\varepsilon, \zeta^\varepsilon) \in M^2[0, T]$ is the solution of the first-order adjoint equation (15) corresponding to u^ε.

Proof. Under the assumption (A_2), it is easy to check that $J(x_0, y_0, u)$ is lower semicontinuous on $\mathcal{R} := R \times R \times \mathcal{U}$, which is a complete metric space under the following metric:

$$d_{\mathcal{R}}(\Theta, \tilde{\Theta}) = \left[|x_0 - \tilde{x}_0|^2 + |y_0 - \tilde{y}_0|^2 + d(u, \tilde{u})^2 \right]^{1/2}, \quad \forall \Theta = (x_0, y_0, u),\ \tilde{\Theta} = (\tilde{x}_0, \tilde{y}_0, \tilde{u}) \in \mathcal{R}. \tag{20}$$

By Ekeland's variational principle [1], there exists an admissible control $(\tilde{x}_0^\varepsilon, \tilde{y}_0^\varepsilon, \tilde{u}^\varepsilon) \in \mathscr{R}$ such that

$$\begin{cases} d_{\mathscr{R}}\left((x_0^\varepsilon, y_0^\varepsilon, u^\varepsilon), (\tilde{x}_0^\varepsilon, \tilde{y}_0^\varepsilon, \tilde{u}^\varepsilon)\right) \le \varepsilon^{2/3}, \\ \tilde{J}^\varepsilon\left((\tilde{x}_0^\varepsilon, \tilde{y}_0^\varepsilon, \tilde{u}^\varepsilon)\right) \le \tilde{J}^\varepsilon(x_0, y_0, u), \quad \forall (x_0, y_0, u) \in \mathscr{R}, \end{cases} \tag{21}$$

where

$$\tilde{J}^\varepsilon(x_0, y_0, u) = J(x_0, y_0, u) + \varepsilon^{1/3} d_{\mathscr{R}}\left((x_0, y_0, u), (\tilde{x}_0^\varepsilon, \tilde{y}_0^\varepsilon, \tilde{u}^\varepsilon)\right). \tag{22}$$

It means that $(\tilde{x}_0^\varepsilon, \tilde{y}_0^\varepsilon, \tilde{u}^\varepsilon)$ is optimal for system (12) with the new cost functional $\tilde{J}^\varepsilon(x_0, y_0, u)$. On the contrary, due to the mixed initial-terminal endpoint constraints in problem $\mathscr{B}$, we need to introduce the penalty functional to transform the original problem with endpoint constraints to the penalized optimal control problem with no endpoint constraints.

Let $(\tilde{x}_0^\varepsilon, \tilde{y}_0^\varepsilon, \tilde{u}^\varepsilon)$ be an optimal control of problem $\mathscr{B}$, with the corresponding optimal state process $(\tilde{x}^\varepsilon, \tilde{y}^\varepsilon, \tilde{z}^\varepsilon)$. Without loss of generality, we assume that $\tilde{J}^\varepsilon(\tilde{x}_0^\varepsilon, \tilde{y}_0^\varepsilon, \tilde{u}^\varepsilon) = 0$. For any $\delta > 0$ and $(x_0, y_0, u) \in \mathscr{R}$, we define the penalty functional:

$$\begin{aligned} &J^{\delta,\varepsilon}(x_0, y_0, u) \\ &= \left\{\left[\tilde{J}^\varepsilon(x_0, y_0, u) + \delta\right]^2 + E\left[\left|x_0 - \gamma(x_T, y_0)\right|^2 + \left|y_T - h(x_T, y_0)\right|^2\right]\right\}^{1/2}. \end{aligned} \tag{23}$$

Obviously,

$$\begin{aligned} &J^{\delta,\varepsilon}(x_0, y_0, u) > 0, \\ &J^{\delta,\varepsilon}(\tilde{x}_0^\varepsilon, \tilde{y}_0^\varepsilon, \tilde{u}^\varepsilon) = \delta \le \inf_{(x_0, y_0, u) \in \mathscr{R}} J^{\delta,\varepsilon}(x_0, y_0, u) + \delta. \end{aligned} \tag{24}$$

By Ekeland's variational principle, there exists a 3-tuple $(x_0^{\delta,\varepsilon}, y_0^{\delta,\varepsilon}, u^{\delta,\varepsilon}) \in \mathscr{R}$ such that

$$\begin{cases} J^{\delta,\varepsilon}\left(x_0^{\delta,\varepsilon}, y_0^{\delta,\varepsilon}, u^{\delta,\varepsilon}\right) \le J^{\delta,\varepsilon}(\tilde{x}_0^\varepsilon, \tilde{y}_0^\varepsilon, \tilde{u}^\varepsilon) = \delta, \\ \left|x_0^{\delta,\varepsilon} - \tilde{x}_0^\varepsilon\right|^2 + \left|y_0^{\delta,\varepsilon} - \tilde{y}_0^\varepsilon\right|^2 + d\left|u^{\delta,\varepsilon}, \tilde{u}^\varepsilon\right|^2 \le \delta, \\ -\sqrt{\delta}\left[\left|x_0^{\delta,\varepsilon} - x_0\right|^2 + \left|y_0^{\delta,\varepsilon} - y_0\right|^2 + d\left(u^{\delta,\varepsilon}, u\right)^2\right]^{1/2} \le J^{\delta,\varepsilon}(x_0, y_0, u) - J^{\delta,\varepsilon}\left(x_0^{\delta,\varepsilon}, y_0^{\delta,\varepsilon}, u^{\delta,\varepsilon}\right), \quad \forall (x_0, y_0, u) \in \mathscr{R}. \end{cases} \tag{25}$$

Therefore, $(x_0^{\delta,\varepsilon}, y_0^{\delta,\varepsilon}, u^{\delta,\varepsilon})$ is optimal for system (13) with the new cost functional:

$$J^{\delta,\varepsilon}(x_0, y_0, u) + \sqrt{\delta}\left[\left|x_0^{\delta,\varepsilon} - x_0\right|^2 + \left|y_0^{\delta,\varepsilon} - y_0\right|^2 + d\left(u^{\delta,\varepsilon}, u\right)^2\right]^{1/2}. \tag{26}$$

So far, we have transformed the original problem with endpoint constraints to the penalized optimal control problem with no endpoint constraints, and the optimal 3-tuple $(x_0^{\delta,\varepsilon}, y_0^{\delta,\varepsilon}, u^{\delta,\varepsilon})$ approaches $(\tilde{x}_0^\varepsilon, \tilde{y}_0^\varepsilon, \tilde{u}^\varepsilon)$ as $\delta \longrightarrow 0$. In the following, a convex perturbation is employed to obtain a maximum principle for $(x_0^{\delta,\varepsilon}, y_0^{\delta,\varepsilon}, u^{\delta,\varepsilon})$. To this end, let $\Theta = (x_0, y_0, u) \in \mathscr{R}$ such that $\Theta^{\delta,\varepsilon} + \Theta = (x_0^{\delta,\varepsilon} + x_0, y_0^{\delta,\varepsilon} + y_0, u^{\delta,\varepsilon} + u) \in \mathscr{R}$; then, for any $\varepsilon > 0$,

$$\Theta_t^{\varepsilon,\delta,\varepsilon} = \Theta_t^{\delta,\varepsilon} + \varepsilon\Theta_t \in \mathscr{R}, \quad t \in [0, T]. \tag{27}$$

Let $(x^{\varepsilon,\delta,\varepsilon}, y^{\varepsilon,\delta,\varepsilon}, z^{\varepsilon,\delta,\varepsilon})$ be the state processes corresponding to $(x_0^{\varepsilon,\delta,\varepsilon}, y_0^{\varepsilon,\delta,\varepsilon}, u^{\varepsilon,\delta,\varepsilon})$, and the processes $(x_1^{\varepsilon,\delta,\varepsilon}, y_1^{\varepsilon,\delta,\varepsilon}, z_1^{\varepsilon,\delta,\varepsilon})$ be the solution of the following variational equations:

$$\begin{cases} \mathrm{d}x_{1,t}^{\varepsilon,\delta,\varepsilon} = \left\{b_x^{\delta,\varepsilon} x_{1,t}^{\varepsilon,\delta,\varepsilon} + b_{\tilde{x}}^{\delta,\varepsilon} E\left[x_{1,t}^{\varepsilon,\delta,\varepsilon}\right] + \Delta b^{\delta,\varepsilon} I_{S_{\varepsilon,t}}\right\}\mathrm{d}t + \left\{\sigma_x^{\delta,\varepsilon} x_{1,t}^{\varepsilon,\delta,\varepsilon} + \sigma_{\tilde{x}}^{\delta,\varepsilon} E\left[x_{1,t}^{\varepsilon,\delta,\varepsilon}\right] + \Delta\sigma^{\delta,\varepsilon} I_{S_{\varepsilon,t}}\right\}\mathrm{d}W_t, \\ -\mathrm{d}y_{1,t}^{\varepsilon,\delta,\varepsilon} = \left\{f_x^{\delta,\varepsilon} x_{1,t}^{\varepsilon,\delta,\varepsilon} + f_y^{\delta,\varepsilon} y_{1,t}^{\varepsilon,\delta,\varepsilon} + f_z^{\delta,\varepsilon} z_{1,t}^{\varepsilon,\delta,\varepsilon} + f_{\tilde{x}}^{\delta,\varepsilon} E\left[x_{1,t}^{\varepsilon,\delta,\varepsilon}\right] + f_{\tilde{y}}^{\delta,\varepsilon} E\left[y_{1,t}^{\varepsilon,\delta,\varepsilon}\right] + f_{\tilde{z}}^{\delta,\varepsilon} E\left[z_{1,t}^{\varepsilon,\delta,\varepsilon}\right] + \Delta f^{\delta,\varepsilon} I_{S_{\varepsilon,t}}\right\}\mathrm{d}t - z_{1,t}^{\varepsilon,\delta,\varepsilon}\mathrm{d}W_t, \\ x_{1,0}^{\varepsilon,\delta,\varepsilon} = \sqrt{\varepsilon}\, x_0, \\ y_{1,0}^{\varepsilon,\delta,\varepsilon} = \sqrt{\varepsilon}\, y_0, \end{cases} \tag{28}$$

where for simplicity of notations, we still use $\rho_j^{\delta,\varepsilon}$ corresponding to $(x^{\delta,\varepsilon}, y^{\delta,\varepsilon}, z^{\delta,\varepsilon}, u^{\delta,\varepsilon})$, $\rho = b, \sigma, f$. Then, we have the following estimates, whose proofs are similar to those given in [27]

$$\begin{cases} E\left(\sup\limits_{t\in[0,T]}\left|x_{1,t}^{\varepsilon,\delta,\varepsilon}\right|^2\right)+E\left(\sup\limits_{t\in[0,T]}\left|x_t^{\varepsilon,\delta,\varepsilon}-x_t^{\delta,\varepsilon}\right|^2\right)\le C\varepsilon, \\ E\left(\sup\limits_{t\in[0,T]}\left|x_t^{\varepsilon,\delta,\varepsilon}-x_t^{\delta,\varepsilon}-x_{1,t}^{\varepsilon,\delta,\varepsilon}\right|^2\right)\le C\varepsilon^2, \\ E\left(\sup\limits_{t\in[0,T]}\left|y_{1,t}^{\varepsilon,\delta,\varepsilon}\right|^2\right)+E\left(\sup\limits_{t\in[0,T]}\left|y_t^{\varepsilon,\delta,\varepsilon}-y_t^{\delta,\varepsilon}\right|^2\right)\le C\varepsilon, \\ E\left(\sup\limits_{t\in[0,T]}\left|y_t^{\varepsilon,\delta,\varepsilon}-y_t^{\delta,\varepsilon}-y_{1,t}^{\varepsilon,\delta,\varepsilon}\right|^2\right)\le C\varepsilon^2, \\ E\int_0^T\left|z_{1,t}^{\varepsilon,\delta,\varepsilon}\right|^2\mathrm{d}t+E\int_0^T\left|z_t^{\varepsilon,\delta,\varepsilon}-z_t^{\delta,\varepsilon}\right|^2\mathrm{d}t\le C\varepsilon, \\ E\int_0^T\left|z_t^{\varepsilon,\delta,\varepsilon}-z_t^{\delta,\varepsilon}-z_{1,t}^{\varepsilon,\delta,\varepsilon}\right|^2\mathrm{d}t\le C\varepsilon^2. \end{cases} \tag{29}$$

Noting that $d(u_t^{\varepsilon,\delta,\varepsilon},u_t^{\delta,\varepsilon})\le C\varepsilon$, from the last relation in (25), we derive

$$\begin{aligned} -\varepsilon\sqrt{\delta}\sqrt{|x_0|^2+|y_0|^2+C} &\le J^{\delta,\varepsilon}\left(x_0^{\varepsilon,\delta,\varepsilon},y_0^{\varepsilon,\delta,\varepsilon},u^{\varepsilon,\delta,\varepsilon}\right)-J^{\delta,\varepsilon}\left(x_0^{\delta,\varepsilon},y_0^{\delta,\varepsilon},u^{\delta,\varepsilon}\right) \\ &= \frac{J^{\delta,\varepsilon}\left(x_0^{\varepsilon,\delta,\varepsilon},y_0^{\varepsilon,\delta,\varepsilon},u^{\varepsilon,\delta,\varepsilon}\right)^2-J^{\delta,\varepsilon}\left(x_0^{\delta,\varepsilon},y_0^{\delta,\varepsilon},u^{\delta,\varepsilon}\right)^2}{J^{\delta,\varepsilon}\left(x_0^{\varepsilon,\delta,\varepsilon},y_0^{\varepsilon,\delta,\varepsilon},u^{\varepsilon,\delta,\varepsilon}\right)+J^{\delta,\varepsilon}\left(x_0^{\delta,\varepsilon},y_0^{\delta,\varepsilon},u^{\delta,\varepsilon}\right)} \\ &= \frac{\left[\tilde{J}^{\varepsilon}\left(x_0^{\varepsilon,\delta,\varepsilon},y_0^{\varepsilon,\delta,\varepsilon},u^{\varepsilon,\delta,\varepsilon}\right)+\delta\right]^2-\left[\tilde{J}^{\varepsilon}\left(x_0^{\delta,\varepsilon},y_0^{\delta,\varepsilon},u^{\delta,\varepsilon}\right)+\delta\right]^2}{J^{\delta,\varepsilon}\left(x_0^{\varepsilon,\delta,\varepsilon},y_0^{\varepsilon,\delta,\varepsilon},u^{\varepsilon,\delta,\varepsilon}\right)+J^{\delta,\varepsilon}\left(x_0^{\delta,\varepsilon},y_0^{\delta,\varepsilon},u^{\delta,\varepsilon}\right)} \\ &\quad+\frac{E\left[\left|x_0^{\varepsilon,\delta,\varepsilon}-\gamma\left(x_T^{\varepsilon,\delta,\varepsilon},y_0^{\varepsilon,\delta,\varepsilon}\right)\right|^2-\left|x_0^{\delta,\varepsilon}-\gamma\left(x_T^{\delta,\varepsilon},y_0^{\delta,\varepsilon}\right)\right|^2\right]}{J^{\delta,\varepsilon}\left(x_0^{\varepsilon,\delta,\varepsilon},y_0^{\varepsilon,\delta,\varepsilon},u^{\varepsilon,\delta,\varepsilon}\right)+J^{\delta,\varepsilon}\left(x_0^{\delta,\varepsilon},y_0^{\delta,\varepsilon},u^{\delta,\varepsilon}\right)} \\ &\quad+\frac{E\left[\left|y_T^{\varepsilon,\delta,\varepsilon}-h\left(x_T^{\varepsilon,\delta,\varepsilon},y_0^{\varepsilon,\delta,\varepsilon}\right)\right|^2-\left|y_T^{\delta,\varepsilon}-h\left(x_T^{\delta,\varepsilon},y_0^{\delta,\varepsilon}\right)\right|^2\right]}{J^{\delta,\varepsilon}\left(x_0^{\varepsilon,\delta,\varepsilon},y_0^{\varepsilon,\delta,\varepsilon},u^{\varepsilon,\delta,\varepsilon}\right)+J^{\delta,\varepsilon}\left(x_0^{\delta,\varepsilon},y_0^{\delta,\varepsilon},u^{\delta,\varepsilon}\right)} \\ &= \theta_0^{\varepsilon,\delta,\varepsilon}\left[\tilde{J}^{\varepsilon}\left(x_0^{\varepsilon,\delta,\varepsilon},y_0^{\varepsilon,\delta,\varepsilon},u^{\varepsilon,\delta,\varepsilon}\right)-\tilde{J}^{\varepsilon}\left(x_0^{\delta,\varepsilon},y_0^{\delta,\varepsilon},u^{\delta,\varepsilon}\right)\right] \\ &\quad+E\left\{\overline{\theta}_0^{\varepsilon,\delta,\varepsilon}\left(x_0^{\varepsilon,\delta,\varepsilon}-\gamma\left(x_T^{\varepsilon,\delta,\varepsilon},y_0^{\varepsilon,\delta,\varepsilon}\right)-\left[x_0^{\delta,\varepsilon}-\gamma\left(x_T^{\delta,\varepsilon},y_0^{\delta,\varepsilon}\right)\right]\right)\right\} \\ &\quad+E\left\{\overline{\theta}_T^{\varepsilon,\delta,\varepsilon}\left(y_T^{\varepsilon,\delta,\varepsilon}-h\left(x_T^{\varepsilon,\delta,\varepsilon},y_0^{\varepsilon,\delta,\varepsilon}\right)-\left[y_T^{\delta,\varepsilon}-h\left(x_T^{\delta,\varepsilon},y_0^{\delta,\varepsilon}\right)\right]\right)\right\} \\ &= \left(\theta_0^{\delta,\varepsilon}+o(1)\right)\left[\tilde{J}^{\varepsilon}\left(x_0^{\varepsilon,\delta,\varepsilon},y_0^{\varepsilon,\delta,\varepsilon},u^{\varepsilon,\delta,\varepsilon}\right)-\tilde{J}^{\varepsilon}\left(x_0^{\delta,\varepsilon},y_0^{\delta,\varepsilon},u^{\delta,\varepsilon}\right)\right] \\ &\quad+E\left[\left(\overline{\theta}_0^{\delta,\varepsilon}+o(1)\right)\left(x_0^{\varepsilon,\delta,\varepsilon}-\gamma\left(x_T^{\varepsilon,\delta,\varepsilon},y_0^{\varepsilon,\delta,\varepsilon}\right)-\left[x_0^{\delta,\varepsilon}-\gamma\left(x_T^{\delta,\varepsilon},y_0^{\delta,\varepsilon}\right)\right]\right)\right] \\ &\quad+E\left[\left(\overline{\theta}_T^{\delta,\varepsilon}+o(1)\right)\left(y_T^{\varepsilon,\delta,\varepsilon}-h\left(x_T^{\varepsilon,\delta,\varepsilon},y_0^{\varepsilon,\delta,\varepsilon}\right)-\left[y_T^{\delta,\varepsilon}-h\left(x_T^{\delta,\varepsilon},y_0^{\delta,\varepsilon}\right)\right]\right)\right], \end{aligned} \tag{30}$$

with

$$\begin{cases} \theta_0^{\varepsilon,\delta,\varepsilon} = \dfrac{2\displaystyle\int_0^1 \left[\lambda \widetilde{J}^{\varepsilon}\left(x_0^{\varepsilon,\delta,\varepsilon}, y_0^{\varepsilon,\delta,\varepsilon}, u^{\varepsilon,\delta,\varepsilon}\right) + (1-\lambda)\widetilde{J}^{\varepsilon}\left(x_0^{\delta,\varepsilon}, y_0^{\delta,\varepsilon}, u^{\delta,\varepsilon}\right) + \delta\right] \mathrm{d}\lambda}{J^{\delta,\varepsilon}\left(x_0^{\varepsilon,\delta,\varepsilon}, y_0^{\varepsilon,\delta,\varepsilon}, u^{\varepsilon,\delta,\varepsilon}\right) + J^{\delta,\varepsilon}\left(x_0^{\delta,\varepsilon}, y_0^{\delta,\varepsilon}, u^{\delta,\varepsilon}\right)}, \\ \overline{\theta}_0^{\varepsilon,\delta,\varepsilon} = \dfrac{x_0^{\varepsilon,\delta,\varepsilon} - \gamma\left(x_T^{\varepsilon,\delta,\varepsilon}, y_0^{\varepsilon,\delta,\varepsilon}\right) + x_0^{\delta,\varepsilon} - \gamma\left(x_T^{\delta,\varepsilon}, y_0^{\delta,\varepsilon}\right)}{J^{\delta,\varepsilon}\left(x_0^{\varepsilon,\delta,\varepsilon}, y_0^{\varepsilon,\delta,\varepsilon}, u^{\varepsilon,\delta,\varepsilon}\right) + J^{\delta,\varepsilon}\left(x_0^{\delta,\varepsilon}, y_0^{\delta,\varepsilon}, u^{\delta,\varepsilon}\right)}, \\ \theta_T^{\varepsilon,\delta,\varepsilon} = \dfrac{y_T^{\varepsilon,\delta,\varepsilon} - h\left(x_T^{\varepsilon,\delta,\varepsilon}, y_0^{\varepsilon,\delta,\varepsilon}\right) + y_T^{\delta,\varepsilon} - h\left(x_T^{\delta,\varepsilon}, y_0^{\delta,\varepsilon}\right)}{J^{\delta,\varepsilon}\left(x_0^{\varepsilon,\delta,\varepsilon}, y_0^{\varepsilon,\delta,\varepsilon}, u^{\varepsilon,\delta,\varepsilon}\right) + J^{\delta,\varepsilon}\left(x_0^{\delta,\varepsilon}, y_0^{\delta,\varepsilon}, u^{\delta,\varepsilon}\right)}, \end{cases} \tag{31}$$

and

$$\begin{cases} \theta_0^{\delta,\varepsilon} = \dfrac{\widetilde{J}^{\varepsilon}\left(x_0^{\delta,\varepsilon}, y_0^{\delta,\varepsilon}, u^{\delta,\varepsilon}\right) + \delta}{J^{\delta,\varepsilon}\left(x_0^{\delta,\varepsilon}, y_0^{\delta,\varepsilon}, u^{\delta,\varepsilon}\right)}, \\ \overline{\theta}_0^{\delta,\varepsilon} = \dfrac{x_0^{\delta,\varepsilon} - \gamma\left(x_T^{\delta,\varepsilon}, y_0^{\delta,\varepsilon}\right)}{J^{\delta,\varepsilon}\left(x_0^{\delta,\varepsilon}, y_0^{\delta,\varepsilon}, u^{\delta,\varepsilon}\right)}, \\ \theta_T^{\delta,\varepsilon} = \dfrac{y_T^{\delta,\varepsilon} - h\left(x_T^{\delta,\varepsilon}, y_0^{\delta,\varepsilon}\right)}{J^{\delta,\varepsilon}\left(x_0^{\delta,\varepsilon}, y_0^{\delta,\varepsilon}, u^{\delta,\varepsilon}\right)}. \end{cases} \tag{32}$$

It is necessary to point out that $\theta_0^{\delta,\varepsilon} \geq 0$, and $|\theta_0^{\delta,\varepsilon}|^2 + E|\overline{\theta}_0^{\delta,\varepsilon}|^2 + E|\theta_T^{\delta,\varepsilon}|^2 = 1$. Thus, there exists a subsequence still denoted by $(\theta_0^{\delta,\varepsilon}, \overline{\theta}_0^{\delta,\varepsilon}, \theta_T^{\delta,\varepsilon})$ convergent, i.e.,

$$\lim_{\delta \longrightarrow 0}\left(\theta_0^{\delta,\varepsilon}, \overline{\theta}_0^{\delta,\varepsilon}, \theta_T^{\delta,\varepsilon}\right) = \left(\theta_0^{\varepsilon}, \overline{\theta}_0^{\varepsilon}, \theta_T^{\varepsilon}\right). \tag{33}$$

We claim that $\theta_0^{\varepsilon} \neq 0$. The detailed illustration of this point refers to [35]. Here, $(\theta_0^{\varepsilon}, \overline{\theta}_0^{\varepsilon}, \theta_T^{\varepsilon})$ is called the Lagrange multiplier of the corresponding optimal 3-tuple $(\widetilde{x}_0^{\varepsilon}, \widetilde{y}_0^{\varepsilon}, \widetilde{u}^{\varepsilon})$. On the contrary,

$$\begin{aligned} &\theta_0^{\varepsilon,\delta,\varepsilon}\left[\widetilde{J}^{\varepsilon}\left(x_0^{\varepsilon,\delta,\varepsilon}, y_0^{\varepsilon,\delta,\varepsilon}, u^{\varepsilon,\delta,\varepsilon}\right) - \widetilde{J}^{\varepsilon}\left(x_0^{\delta,\varepsilon}, y_0^{\delta,\varepsilon}, u^{\delta,\varepsilon}\right)\right] \\ &\quad = \theta_0^{\varepsilon,\delta,\varepsilon}\left[J\left(x_0^{\varepsilon,\delta,\varepsilon}, y_0^{\varepsilon,\delta,\varepsilon}, u^{\varepsilon,\delta,\varepsilon}\right) + \varepsilon^{1/3} d_{\mathscr{R}}\left(\left(x_0^{\varepsilon,\delta,\varepsilon}, y_0^{\varepsilon,\delta,\varepsilon}, u^{\varepsilon,\delta,\varepsilon}\right), \left(\widetilde{x}_0^{\varepsilon}, \widetilde{y}_0^{\varepsilon}, \widetilde{u}^{\varepsilon}\right)\right) - J\left(x_0^{\delta,\varepsilon}, y_0^{\delta,\varepsilon}, u^{\delta,\varepsilon}\right)\right. \\ &\qquad \left. - \varepsilon^{1/3} d_{\mathscr{R}}\left(\left(x_0^{\delta,\varepsilon}, y_0^{\delta,\varepsilon}, u^{\delta,\varepsilon}\right), \left(\widetilde{x}_0^{\varepsilon}, \widetilde{y}_0^{\varepsilon}, \widetilde{u}^{\varepsilon}\right)\right)\right] \\ &\quad = \theta_0^{\varepsilon,\delta,\varepsilon}\left[J\left(x_0^{\varepsilon,\delta,\varepsilon}, y_0^{\varepsilon,\delta,\varepsilon}, u^{\varepsilon,\delta,\varepsilon}\right) - J\left(x_0^{\delta,\varepsilon}, y_0^{\delta,\varepsilon}, u^{\delta,\varepsilon}\right)\right] \\ &\qquad + \varepsilon^{1/3}\theta_0^{\varepsilon,\delta,\varepsilon}\left[d_{\mathscr{R}}\left(\left(x_0^{\varepsilon,\delta,\varepsilon}, y_0^{\varepsilon,\delta,\varepsilon}, u^{\varepsilon,\delta,\varepsilon}\right), \left(\widetilde{x}_0^{\varepsilon}, \widetilde{y}_0^{\varepsilon}, \widetilde{u}^{\varepsilon}\right)\right) - d_{\mathscr{R}}\left(\left(x_0^{\delta,\varepsilon}, y_0^{\delta,\varepsilon}, u^{\delta,\varepsilon}\right), \left(\widetilde{x}_0^{\varepsilon}, \widetilde{y}_0^{\varepsilon}, \widetilde{u}^{\varepsilon}\right)\right)\right] \\ &\quad \leq \theta_0^{\varepsilon,\delta,\varepsilon}\left[J\left(x_0^{\varepsilon,\delta,\varepsilon}, y_0^{\varepsilon,\delta,\varepsilon}, u^{\varepsilon,\delta,\varepsilon}\right) - J\left(x_0^{\delta,\varepsilon}, y_0^{\delta,\varepsilon}, u^{\delta,\varepsilon}\right)\right] + \varepsilon^{1/3}\theta_0^{\varepsilon,\delta,\varepsilon} d_{\mathscr{R}}\left(\left(x_0^{\varepsilon,\delta,\varepsilon}, y_0^{\varepsilon,\delta,\varepsilon}, u^{\varepsilon,\delta,\varepsilon}\right), \left(x_0^{\delta,\varepsilon}, y_0^{\delta,\varepsilon}, u^{\delta,\varepsilon}\right)\right) \\ &\quad \leq \theta_0^{\varepsilon,\delta,\varepsilon}\left[J\left(x_0^{\varepsilon,\delta,\varepsilon}, y_0^{\varepsilon,\delta,\varepsilon}, u^{\varepsilon,\delta,\varepsilon}\right) - J\left(x_0^{\delta,\varepsilon}, y_0^{\delta,\varepsilon}, u^{\delta,\varepsilon}\right)\right] + \varepsilon\varepsilon^{1/3}\theta_0^{\varepsilon,\delta,\varepsilon}\sqrt{|x_0|^2 + |y_0|^2 + C}. \end{aligned} \tag{34}$$

From (A_3) and (29), we can deduce

$$
\begin{aligned}
&J\left(x_0^{\varepsilon,\delta,\varepsilon}, y_0^{\varepsilon,\delta,\varepsilon}, u^{\varepsilon,\delta,\varepsilon}\right) - J\left(x_0^{\delta,\varepsilon}, y_0^{\delta,\varepsilon}, u^{\delta,\varepsilon}\right) \\
&= E\int_0^T \left\{l\left(t, \Gamma_t^{\varepsilon,\delta,\varepsilon}, u_t^{\varepsilon,\delta,\varepsilon}\right) - l\left(t, \Gamma_t^{\delta,\varepsilon}, u_t^{\delta,\varepsilon}\right)\right\}\mathrm{d}t + E\left\{\varphi\left(x_T^{\varepsilon,\delta,\varepsilon}, y_0^{\varepsilon,\delta,\varepsilon}\right) - \varphi\left(x_T^{\delta,\varepsilon}, y_0^{\delta,\varepsilon}\right)\right\} \\
&= E\int_0^T \left\{l\left(t, \Gamma_t^{\delta,\varepsilon}, u_t^{\varepsilon,\delta,\varepsilon}\right) - l\left(t, \Gamma_t^{\delta,\varepsilon}, u_t^{\delta,\varepsilon}\right)\right\}\mathrm{d}t \\
&\quad + E\int_0^T\int_0^1 \left\{l_x^{\varepsilon,\delta,\varepsilon}\left(x_t^{\varepsilon,\delta,\varepsilon} - x_t^{\delta,\varepsilon}\right) + l_y^{\varepsilon,\delta,\varepsilon}\left(y_t^{\varepsilon,\delta,\varepsilon} - y_t^{\delta,\varepsilon}\right) + l_z^{\varepsilon,\delta,\varepsilon}\left(z_t^{\varepsilon,\delta,\varepsilon} - z_t^{\delta,\varepsilon}\right)\right\}\mathrm{d}\lambda\mathrm{d}t \\
&\quad + E\int_0^T\int_0^1 \left\{l_{\tilde{x}}^{\varepsilon,\delta,\varepsilon}\left(Ex_t^{\varepsilon,\delta,\varepsilon} - Ex_t^{\delta,\varepsilon}\right) + l_{\tilde{y}}^{\varepsilon,\delta,\varepsilon}\left(Ey_t^{\varepsilon,\delta,\varepsilon} - Ey_t^{\delta,\varepsilon}\right) + l_{\tilde{z}}^{\varepsilon,\delta,\varepsilon}\left(Ez_t^{\varepsilon,\delta,\varepsilon} - Ez_t^{\delta,\varepsilon}\right)\right\}\mathrm{d}\lambda\mathrm{d}t \\
&\quad + E\left[\varphi\left(x_T^{\varepsilon,\delta,\varepsilon}, y_0^{\varepsilon,\delta,\varepsilon}\right) - \varphi\left(x_T^{\delta,\varepsilon}, y_0^{\varepsilon,\delta,\varepsilon}\right) + \varphi\left(x_T^{\delta,\varepsilon}, y_0^{\varepsilon,\delta,\varepsilon}\right) - \varphi\left(x_T^{\delta,\varepsilon}, y_0^{\delta,\varepsilon}\right)\right] \\
&= E\int_0^T \left\{l\left(t, \Gamma_t^{\delta,\varepsilon}, u_t^{\varepsilon,\delta,\varepsilon}\right) - l\left(t, \Gamma_t^{\delta,\varepsilon}, u_t^{\delta,\varepsilon}\right) + l_x^{\delta,\varepsilon}x_{1,t}^{\varepsilon,\delta,\varepsilon} + l_{\tilde{x}}^{\delta,\varepsilon}E\left[x_{1,t}^{\varepsilon,\delta,\varepsilon}\right] + l_y^{\delta,\varepsilon}y_{1,t}^{\varepsilon,\delta,\varepsilon} + l_{\tilde{y}}^{\delta,\varepsilon}E\left[y_{1,t}^{\varepsilon,\delta,\varepsilon}\right] + l_z^{\delta,\varepsilon}z_{1,t}^{\varepsilon,\delta,\varepsilon} + l_{\tilde{z}}^{\delta,\varepsilon}E\left[z_{1,t}^{\varepsilon,\delta,\varepsilon}\right]\right\}\mathrm{d}t \\
&\quad + E\int_0^T\int_0^1 \left\{\left(l_x^{\varepsilon,\delta,\varepsilon} - l_x^{\delta,\varepsilon}\right)x_{1,t}^{\varepsilon,\delta,\varepsilon} + \left(l_y^{\varepsilon,\delta,\varepsilon} - l_y^{\delta,\varepsilon}\right)y_{1,t}^{\varepsilon,\delta,\varepsilon} + \left(l_z^{\varepsilon,\delta,\varepsilon} - l_z^{\delta,\varepsilon}\right)z_{1,t}^{\varepsilon,\delta,\varepsilon} + \left(l_{\tilde{x}}^{\varepsilon,\delta,\varepsilon} - l_{\tilde{x}}^{\delta,\varepsilon}\right)E\left[x_{1,t}^{\varepsilon,\delta,\varepsilon}\right] + \left(l_{\tilde{y}}^{\varepsilon,\delta,\varepsilon} - l_{\tilde{y}}^{\delta,\varepsilon}\right)E\left[y_{1,t}^{\varepsilon,\delta,\varepsilon}\right]\right. \\
&\quad \left. + \left(l_{\tilde{z}}^{\varepsilon,\delta,\varepsilon} - l_{\tilde{z}}^{\delta,\varepsilon}\right)E\left[z_{1,t}^{\varepsilon,\delta,\varepsilon}\right]\right\}\mathrm{d}\lambda\mathrm{d}t \\
&\quad + E\int_0^1 \varphi_{x_T}\left(x_T^{\delta,\varepsilon} + \lambda\left(x_T^{\varepsilon,\delta,\varepsilon} - x_T^{\delta,\varepsilon}\right), y_0^{\varepsilon,\delta,\varepsilon}\right)\left(x_T^{\varepsilon,\delta,\varepsilon} - x_T^{\delta,\varepsilon}\right)\mathrm{d}\lambda \\
&\quad + E\int_0^1 \varphi_{y_0}\left(x_T^{\delta,\varepsilon}, y_0^{\delta,\varepsilon} + \lambda\left(y_0^{\varepsilon,\delta,\varepsilon} - y_0^{\delta,\varepsilon}\right)\right)\left(y_0^{\varepsilon,\delta,\varepsilon} - y_0^{\delta,\varepsilon}\right)\mathrm{d}\lambda \\
&= E\int_0^T \left\{l\left(t, \Gamma_t^{\delta,\varepsilon}, u_t^{\varepsilon,\delta,\varepsilon}\right) - l\left(t, \Gamma_t^{\delta,\varepsilon}, u_t^{\delta,\varepsilon}\right) + l_x^{\delta,\varepsilon}x_{1,t}^{\varepsilon,\delta,\varepsilon} + l_{\tilde{x}}^{\delta,\varepsilon}E\left[x_{1,t}^{\varepsilon,\delta,\varepsilon}\right] + l_y^{\delta,\varepsilon}y_{1,t}^{\varepsilon,\delta,\varepsilon} + l_{\tilde{y}}^{\delta,\varepsilon}E\left[y_{1,t}^{\varepsilon,\delta,\varepsilon}\right] + l_z^{\delta,\varepsilon}z_{1,t}^{\varepsilon,\delta,\varepsilon} + l_{\tilde{z}}^{\delta,\varepsilon}E\left[z_{1,t}^{\varepsilon,\delta,\varepsilon}\right]\right\}\mathrm{d}t \\
&\quad + E\left\{\varphi_{x_T}\left(x_T^{\delta,\varepsilon}, y_0^{\delta,\varepsilon}\right)x_{1,T}^{\varepsilon,\delta,\varepsilon} + \varphi_{y_0}\left(x_T^{\delta,\varepsilon}, y_0^{\delta,\varepsilon}\right)y_{1,0}^{\varepsilon,\delta,\varepsilon}\right\} \\
&\quad + E\int_0^1 \left\{\left[\varphi_{x_T}\left(x_T^{\delta,\varepsilon} + \lambda\left(x_T^{\varepsilon,\delta,\varepsilon} - x_T^{\delta,\varepsilon}\right), y_0^{\delta,\varepsilon}\right) - \varphi_{x_T}\left(x_T^{\delta,\varepsilon}, y_0^{\delta,\varepsilon}\right)\right]x_{1,T}^{\varepsilon,\delta,\varepsilon}\right\}\mathrm{d}\lambda \\
&\quad + E\int_0^1 \left\{\left[\varphi_{y_0}\left(x_T^{\delta,\varepsilon}, y_0^{\delta,\varepsilon} + \lambda\left(y_0^{\varepsilon,\delta,\varepsilon} - y_0^{\delta,\varepsilon}\right)\right) - \varphi_{y_0}\left(x_T^{\delta,\varepsilon}, y_0^{\delta,\varepsilon}\right)\right]y_{1,0}^{\varepsilon,\delta,\varepsilon}\right\}\mathrm{d}\lambda + o(\varepsilon) \\
&= E\int_0^T \left\{l\left(t, \Gamma_t^{\delta,\varepsilon}, u_t^{\varepsilon,\delta,\varepsilon}\right) - l\left(t, \Gamma_t^{\delta,\varepsilon}, u_t^{\delta,\varepsilon}\right) + l_x^{\delta,\varepsilon}x_{1,t}^{\varepsilon,\delta,\varepsilon} + l_{\tilde{x}}^{\delta,\varepsilon}E\left[x_{1,t}^{\varepsilon,\delta,\varepsilon}\right] + l_y^{\delta,\varepsilon}y_{1,t}^{\varepsilon,\delta,\varepsilon} + l_{\tilde{y}}^{\delta,\varepsilon}E\left[y_{1,t}^{\varepsilon,\delta,\varepsilon}\right] + l_z^{\delta,\varepsilon}z_{1,t}^{\varepsilon,\delta,\varepsilon} + l_{\tilde{z}}^{\delta,\varepsilon}E\left[z_{1,t}^{\varepsilon,\delta,\varepsilon}\right]\right\}\mathrm{d}t \\
&\quad + E\left\{\varphi_{x_T}\left(x_T^{\delta,\varepsilon}, y_0^{\delta,\varepsilon}\right)x_{1,T}^{\varepsilon,\delta,\varepsilon} + \varphi_{y_0}\left(x_T^{\delta,\varepsilon}, y_0^{\delta,\varepsilon}\right)y_{1,0}^{\varepsilon,\delta,\varepsilon}\right\} + o(\varepsilon),
\end{aligned}
\tag{35}
$$

where $l_j^{\varepsilon,\delta,\varepsilon} = l_j(t, \Gamma_t^{\delta,\varepsilon} + \varepsilon(\Gamma_t^{\varepsilon,\delta,\varepsilon} - \Gamma_t^{\delta,\varepsilon}), u_t^{\varepsilon,\delta,\varepsilon})$, $j = x, y, z, \tilde{x}, \tilde{y}, \tilde{z}$. Similarly,

$$
\begin{aligned}
&E\left\{\overline{\theta}_0^{\varepsilon,\delta,\varepsilon}\left(x_0^{\varepsilon,\delta,\varepsilon} - \gamma\left(x_T^{\varepsilon,\delta,\varepsilon}, y_0^{\varepsilon,\delta,\varepsilon}\right) - \left[x_0^{\delta,\varepsilon} - \gamma\left(x_T^{\delta,\varepsilon}, y_0^{\delta,\varepsilon}\right)\right]\right)\right\} \\
&\quad = E\left\{\overline{\theta}_0^{\varepsilon,\delta,\varepsilon}\left(x_{1,0}^{\varepsilon,\delta,\varepsilon} - \gamma_{x_T}\left(x_T^{\delta,\varepsilon}, y_0^{\delta,\varepsilon}\right)x_{1,T}^{\varepsilon,\delta,\varepsilon} - \gamma_{y_0}\left(x_T^{\delta,\varepsilon}, y_0^{\delta,\varepsilon}\right)y_{1,0}^{\varepsilon,\delta,\varepsilon}\right)\right\} + o(\varepsilon), \\
&\quad E\left\{\overline{\theta}_T^{\varepsilon,\delta,\varepsilon}\left(y_T^{\varepsilon,\delta,\varepsilon} - h\left(x_T^{\varepsilon,\delta,\varepsilon}, y_0^{\varepsilon,\delta,\varepsilon}\right) - \left[y_T^{\delta,\varepsilon} - h\left(x_T^{\delta,\varepsilon}, y_0^{\delta,\varepsilon}\right)\right]\right)\right\} \\
&\quad = E\left\{\overline{\theta}_T^{\varepsilon,\delta,\varepsilon}\left(y_{1,T}^{\varepsilon,\delta,\varepsilon} - h_{x_T}\left(x_T^{\delta,\varepsilon}, y_0^{\delta,\varepsilon}\right)x_{1,T}^{\varepsilon,\delta,\varepsilon} - h_{y_0}\left(x_T^{\delta,\varepsilon}, y_0^{\delta,\varepsilon}\right)y_{1,0}^{\varepsilon,\delta,\varepsilon}\right)\right\} + o(\varepsilon).
\end{aligned}
\tag{36}
$$

Then, taking notice of (30), we can further obtain

$$
\begin{aligned}
&-\varepsilon\sqrt{|x_0|^2+|y_0|^2+C}\left(\sqrt{\delta}+\varepsilon^{1/3}\theta_0^{\varepsilon,\delta,\varepsilon}\right)\\
&\quad\le\theta_0^{\varepsilon,\delta,\varepsilon}E\int_0^T\left\{l\left(t,\Gamma_t^{\delta,\varepsilon},u_t^{\varepsilon,\delta,\varepsilon}\right)-l\left(t,\Gamma_t^{\delta,\varepsilon},u_t^{\delta,\varepsilon}\right)+l_x^{\delta,\varepsilon}x_{1,t}^{\varepsilon,\delta,\varepsilon}+l_{\tilde{x}}^{\delta,\varepsilon}E\left[x_{1,t}^{\varepsilon,\delta,\varepsilon}\right]+l_y^{\delta,\varepsilon}y_{1,t}^{\varepsilon,\delta,\varepsilon}+l_{\tilde{y}}^{\delta,\varepsilon}E\left[y_{1,t}^{\varepsilon,\delta,\varepsilon}\right]+l_z^{\delta,\varepsilon}z_{1,t}^{\varepsilon,\delta,\varepsilon}+l_{\tilde{z}}^{\delta,\varepsilon}E\left[z_{1,t}^{\varepsilon,\delta,\varepsilon}\right]\right\}\mathrm{d}t\\
&\quad+\theta_0^{\varepsilon,\delta,\varepsilon}E\left\{\varphi_{x_T}\left(x_T^{\delta,\varepsilon},y_0^{\delta,\varepsilon}\right)x_{1,T}^{\varepsilon,\delta,\varepsilon}+\varphi_{y_0}\left(x_T^{\delta,\varepsilon},y_0^{\delta,\varepsilon}\right)y_{1,0}^{\varepsilon,\delta,\varepsilon}\right\}\\
&\quad+E\left\{\overline{\theta}_0^{\varepsilon,\delta,\varepsilon}\left(x_{1,0}^{\varepsilon,\delta,\varepsilon}-\gamma_{x_T}\left(x_T^{\delta,\varepsilon},y_0^{\delta,\varepsilon}\right)x_{1,T}^{\varepsilon,\delta,\varepsilon}-\gamma_{y_0}\left(x_T^{\delta,\varepsilon},y_0^{\delta,\varepsilon}\right)y_{1,0}^{\varepsilon,\delta,\varepsilon}\right)\right\}\\
&\quad+E\left\{\overline{\theta}_T^{\varepsilon,\delta,\varepsilon}\left(y_{1,T}^{\varepsilon,\delta,\varepsilon}-h_{x_T}\left(x_T^{\delta,\varepsilon},y_0^{\delta,\varepsilon}\right)x_{1,T}^{\varepsilon,\delta,\varepsilon}-h_{y_0}\left(x_T^{\delta,\varepsilon},y_0^{\delta,\varepsilon}\right)y_{1,0}^{\varepsilon,\delta,\varepsilon}\right)\right\}+o(\varepsilon).
\end{aligned}
\tag{37}
$$

Let us introduce the following first-order BSDEs:

$$
\begin{cases}
d\tilde{\xi}_t^{\varepsilon,\delta,\varepsilon}=\left\{f_y^{\delta,\varepsilon}\tilde{\xi}_t^{\varepsilon,\delta,\varepsilon}+l_y^{\delta,\varepsilon}+E\left[f_{\tilde{y}}^{\delta,\varepsilon}\tilde{\xi}_t^{\varepsilon,\delta,\varepsilon}+l_{\tilde{y}}^{\delta,\varepsilon}\right]\right\}dt+\left\{f_z^{\delta,\varepsilon}\tilde{\xi}_t^{\varepsilon,\delta,\varepsilon}+l_z^{\delta,\varepsilon}+E\left[f_{\tilde{z}}^{\delta,\varepsilon}\tilde{\xi}_t^{\varepsilon,\delta,\varepsilon}+l_{\tilde{z}}^{\delta,\varepsilon}\right]\right\}dW_t,\\
-d\tilde{\eta}_t^{\varepsilon,\delta,\varepsilon}=\left\{-f_x^{\delta,\varepsilon}\tilde{\xi}_t^{\varepsilon,\delta,\varepsilon}+b_x^{\delta,\varepsilon}\tilde{\eta}_t^{\varepsilon,\delta,\varepsilon}+\sigma_x^{\delta,\varepsilon}\tilde{\zeta}_t^{\varepsilon,\delta,\varepsilon}-l_x^{\delta,\varepsilon}+E\left[-f_{\tilde{x}}^{\delta,\varepsilon}\tilde{\xi}_t^{\varepsilon,\delta,\varepsilon}+b_{\tilde{x}}^{\delta,\varepsilon}\tilde{\eta}_t^{\varepsilon,\delta,\varepsilon}+\sigma_{\tilde{x}}^{\delta,\varepsilon}\tilde{\zeta}_t^{\varepsilon,\delta,\varepsilon}-l_{\tilde{x}}^{\delta,\varepsilon}\right]\right\}dt-\tilde{\zeta}_t^{\varepsilon,\delta,\varepsilon}dW_t,\\
\tilde{\xi}_T^{\varepsilon,\delta,\varepsilon}=\overline{\theta}_T^{\varepsilon,\delta,\varepsilon},\\
\tilde{\eta}_T^{\varepsilon,\delta,\varepsilon}=-\overline{\theta}_T^{\varepsilon,\delta,\varepsilon}h_{x_T}^{\delta,\varepsilon}-\overline{\theta}_0^{\varepsilon,\delta,\varepsilon}\gamma_{x_T}^{\delta,\varepsilon}+\theta_0^{\varepsilon,\delta,\varepsilon}\varphi_{x_T}^{\delta,\varepsilon},
\end{cases}
\tag{38}
$$

where $\rho_{x_T}^{\delta,\varepsilon}=\rho_{x_T}(x_T^{\delta,\varepsilon},y_0^{\delta,\varepsilon})$, $\rho=h,\gamma,\varphi$. Applying Itô's formula to $\tilde{\xi}_t^{\varepsilon,\delta,\varepsilon}y_{1,t}^{\varepsilon,\delta,\varepsilon}+\tilde{\eta}_t^{\varepsilon,\delta,\varepsilon}x_{1,t}^{\varepsilon,\delta,\varepsilon}$ fulfills

$$
\begin{aligned}
&E\left\{\overline{\theta}_T^{\varepsilon,\delta,\varepsilon}y_{1,T}^{\varepsilon,\delta,\varepsilon}-\left(\overline{\theta}_T^{\varepsilon,\delta,\varepsilon}h_{x_T}^{\delta,\varepsilon}+\overline{\theta}_0^{\varepsilon,\delta,\varepsilon}\gamma_{x_T}^{\delta,\varepsilon}-\theta_0^{\varepsilon,\delta,\varepsilon}\varphi_{x_T}^{\delta,\varepsilon}\right)x_{1,T}^{\varepsilon,\delta,\varepsilon}\right\}-\sqrt{\varepsilon}E\left\{\tilde{\xi}_0^{\varepsilon,\delta,\varepsilon}y_0+\tilde{\eta}_0^{\varepsilon,\delta,\varepsilon}x_0\right\}\\
&\quad=E\int_0^T\left\{\left(l_x^{\delta,\varepsilon}+El_{\tilde{x}}^{\delta,\varepsilon}\right)x_{1,t}^{\varepsilon,\delta,\varepsilon}+\left(l_y^{\delta,\varepsilon}+El_{\tilde{y}}^{\delta,\varepsilon}\right)y_{1,t}^{\varepsilon,\delta,\varepsilon}+\left(l_z^{\delta,\varepsilon}+El_{\tilde{z}}^{\delta,\varepsilon}\right)z_{1,t}^{\varepsilon,\delta,\varepsilon}+\tilde{\eta}_t^{\varepsilon,\delta,\varepsilon}\Delta b^{\delta,\varepsilon}+\tilde{\zeta}_t^{\varepsilon,\delta,\varepsilon}\Delta\sigma^{\delta,\varepsilon}-\tilde{\xi}_t^{\varepsilon,\delta,\varepsilon}\Delta f^{\delta,\varepsilon}\right\}I_{S_{\varepsilon,t}}\mathrm{d}t.
\end{aligned}
\tag{39}
$$

Combining (37) and (39), yields

$$
\begin{aligned}
&-\varepsilon\sqrt{|x_0|^2+|y_0|^2+C}\left(\sqrt{\delta}+\varepsilon^{1/3}\theta_0^{\varepsilon,\delta,\varepsilon}\right)\\
&\quad\le\sqrt{\varepsilon}E\left\{\left(\overline{\theta}_0^{\varepsilon,\delta,\varepsilon}+\tilde{\eta}_0^{\varepsilon,\delta,\varepsilon}\right)x_0+\left(\theta_0^{\varepsilon,\delta,\varepsilon}\varphi_{y_0}^{\delta,\varepsilon}-\overline{\theta}_0^{\varepsilon,\delta,\varepsilon}\gamma_{y_0}^{\delta,\varepsilon}-\overline{\theta}_T^{\varepsilon,\delta,\varepsilon}h_{y_0}^{\delta,\varepsilon}+\tilde{\xi}_0^{\varepsilon,\delta,\varepsilon}\right)y_0\right\}\\
&\quad+E\int_0^T\left(\tilde{\eta}_t^{\varepsilon,\delta,\varepsilon}\Delta b^{\delta,\varepsilon}+\tilde{\zeta}_t^{\varepsilon,\delta,\varepsilon}\Delta\sigma^{\delta,\varepsilon}-\tilde{\xi}_t^{\varepsilon,\delta,\varepsilon}\Delta f^{\delta,\varepsilon}-\Delta l^{\delta,\varepsilon}\right)I_{S_{\varepsilon,t}}\mathrm{d}t+o(\varepsilon).
\end{aligned}
\tag{40}
$$

To derive the first-order adjoint equation with mixed initial-terminal conditions, divide $\sqrt{\varepsilon}$ in (40) and then send $\varepsilon\longrightarrow 0$, $\delta\longrightarrow 0$, and we see that

$$
E\left\{\left(\overline{\theta}_0^{\varepsilon}+\tilde{\eta}_0^{\varepsilon}\right)x_0+\left(\theta_0^{\varepsilon}\varphi_{y_0}^{\varepsilon}-\overline{\theta}_0^{\varepsilon}\gamma_{y_0}^{\varepsilon}-\overline{\theta}_T^{\varepsilon}h_{y_0}^{\varepsilon}+\tilde{\xi}_0^{\varepsilon}\right)y_0\right\}\ge 0,\quad\forall(x_0,y_0)\in R\times R,
\tag{41}
$$

which implies

$$\begin{aligned}\widetilde{\eta}_0^\varepsilon &= -\overline{\theta}_0^\varepsilon,\\ \widetilde{\xi}_0^\varepsilon &= -\theta_0^\varepsilon\varphi_{y_0}^\varepsilon - \widetilde{\eta}_0^\varepsilon\gamma_{y_0}^\varepsilon + \widetilde{\xi}_T^\varepsilon h_{y_0}^\varepsilon.\end{aligned} \tag{42}$$

Meanwhile, by taking $(x_0, y_0) = (0,0)$ in (40), dividing this inequality by ε, and then sending $\varepsilon \longrightarrow 0$, $\delta \longrightarrow 0$, the variational inequality follows:

$$\begin{aligned}-C\varepsilon^{1/3}\theta_0^\varepsilon \le E\int_0^T &\big(\widetilde{\eta}_t^\varepsilon\left[b\left(t,\widetilde{x}_t^\varepsilon,E\widetilde{x}_t^\varepsilon,u_t\right)-b\left(t,\widetilde{x}_t^\varepsilon,E\widetilde{x}_t^\varepsilon,\widetilde{u}_t^\varepsilon\right)\right]+\widetilde{\zeta}_t^\varepsilon\left[\sigma\left(t,\widetilde{x}_t^\varepsilon,E\widetilde{x}_t^\varepsilon,u_t\right)-\sigma\left(t,\widetilde{x}_t^\varepsilon,E\widetilde{x}_t^\varepsilon,\widetilde{u}_t^\varepsilon\right)\right]\\ &-\widetilde{\xi}_t^\varepsilon\left[f\left(t,\widetilde{\Gamma}_t^\varepsilon,u_t\right)-f\left(t,\widetilde{\Gamma}_t^\varepsilon,\widetilde{u}_t^\varepsilon\right)\right]-\left[l\left(t,\widetilde{\Gamma}_t^\varepsilon,u_t\right)-l\left(t,\widetilde{\Gamma}_t^\varepsilon,\widetilde{u}_t^\varepsilon\right)\right]\mathrm{d}t,\end{aligned} \tag{43}$$

where $\widetilde{\Gamma}_t^\varepsilon = (\widetilde{x}_t^\varepsilon, \widetilde{y}_t^\varepsilon, \widetilde{z}_t^\varepsilon, E\widetilde{x}_t^\varepsilon, E\widetilde{y}_t^\varepsilon, E\widetilde{z}_t^\varepsilon)$. On the contrary, from (38) and (42), we can present the adjoint equation with mixed initial-terminal conditions as follows:

$$\begin{cases}\mathrm{d}\widetilde{\xi}_t^\varepsilon = \left\{f_y^\varepsilon\widetilde{\xi}_t^\varepsilon + l_y^\varepsilon + E\left[f_{\underset{\sim}{y}}^\varepsilon\widetilde{\xi}_t^\varepsilon + l_{\underset{\sim}{y}}^\varepsilon\right]\right\}\mathrm{d}t + \left\{f_z^\varepsilon\widetilde{\xi}_t^\varepsilon + l_z^\varepsilon + E\left[f_{\underset{\sim}{z}}^\varepsilon\widetilde{\xi}_t^\varepsilon + l_{\underset{\sim}{z}}^\varepsilon\right]\right\}\mathrm{d}W_t,\\ -\mathrm{d}\widetilde{\eta}_t^\varepsilon = \left\{-f_x^\varepsilon\widetilde{\xi}_t^\varepsilon + b_x^\varepsilon\widetilde{\eta}_t^\varepsilon + \sigma_x^\varepsilon\widetilde{\zeta}_t^\varepsilon - l_x^\varepsilon + E\left[-f_{\underset{\sim}{x}}^\varepsilon\widetilde{\xi}_t^\varepsilon + b_{\underset{\sim}{x}}^\varepsilon\widetilde{\eta}_t^\varepsilon + \sigma_{\underset{\sim}{x}}^\varepsilon\widetilde{\zeta}_t^\varepsilon - l_{\underset{\sim}{x}}^\varepsilon\right]\right\}\mathrm{d}t - \widetilde{\zeta}_t^\varepsilon\mathrm{d}W_t,\\ \widetilde{\xi}_0^\varepsilon = -\theta_0^\varepsilon\varphi_{y_0}^\varepsilon - \widetilde{\eta}_0^\varepsilon\gamma_{y_0}^\varepsilon + \widetilde{\xi}_T^\varepsilon h_{y_0}^\varepsilon,\\ \widetilde{\eta}_T^\varepsilon = -\widetilde{\xi}_T^\varepsilon h_{x_T}^\varepsilon + \widetilde{\eta}_0^\varepsilon\gamma_{x_T}^\varepsilon + \theta_0^\varepsilon\varphi_{x_T}^\varepsilon,\end{cases} \tag{44}$$

whose well-posedness can be deduced directly virus the above derivative process (Remark 2). Now, consider (43) again but with $(\widetilde{x}^\varepsilon, \widetilde{y}^\varepsilon, \widetilde{z}^\varepsilon, \widetilde{u}^\varepsilon)$, etc., replaced by $(x^\varepsilon, y^\varepsilon, z^\varepsilon, u^\varepsilon)$, etc. We are about to derive an estimate for the term similar to the right side of (43) with respect to $(x^\varepsilon, y^\varepsilon, z^\varepsilon, u^\varepsilon)$, etc. To this end, we first estimate the following difference:

$$\begin{aligned}&E\int_0^T\{\widetilde{\eta}_t^\varepsilon\left[b\left(t,\widetilde{x}_t^\varepsilon,E\widetilde{x}_t^\varepsilon,u_t\right)-b\left(t,\widetilde{x}_t^\varepsilon,E\widetilde{x}_t^\varepsilon,\widetilde{u}_t^\varepsilon\right)\right]-\eta_t^\varepsilon\left[b\left(t,x_t^\varepsilon,Ex_t^\varepsilon,u_t\right)-b\left(t,x_t^\varepsilon,Ex_t^\varepsilon,u_t^\varepsilon\right)\right]\}\mathrm{d}t\\ &\quad= E\int_0^T\left(\widetilde{\eta}_t^\varepsilon-\eta_t^\varepsilon\right)\left[b\left(t,\widetilde{x}_t^\varepsilon,E\widetilde{x}_t^\varepsilon,u_t\right)-b\left(t,\widetilde{x}_t^\varepsilon,E\widetilde{x}_t^\varepsilon,\widetilde{u}_t^\varepsilon\right)\right]\mathrm{d}t\\ &\qquad+E\int_0^T\eta_t^\varepsilon\left[b\left(t,\widetilde{x}_t^\varepsilon,E\widetilde{x}_t^\varepsilon,u_t\right)-b\left(t,x_t^\varepsilon,Ex_t^\varepsilon,u_t\right)\right]\mathrm{d}t-E\int_0^T\eta_t^\varepsilon\left[b\left(t,\widetilde{x}_t^\varepsilon,E\widetilde{x}_t^\varepsilon,\widetilde{u}_t^\varepsilon\right)-b\left(t,x_t^\varepsilon,Ex_t^\varepsilon,u_t^\varepsilon\right)\right]\mathrm{d}t\\ &\quad= \Xi_1+\Xi_2+\Xi_3.\end{aligned} \tag{45}$$

Due to Lemma 2, for any $\kappa \in [0, (1/3))$, by using the similar arguments as developed in [7] the proof of Theorem 1, we can also prove that

$$\begin{aligned}\Xi_1 &= E\int_0^T\left(\widetilde{\eta}_t^\varepsilon-\eta_t^\varepsilon\right)\left[b\left(t,\widetilde{x}_t^\varepsilon,E\widetilde{x}_t^\varepsilon,u_t\right)-b\left(t,\widetilde{x}_t^\varepsilon,E\widetilde{x}_t^\varepsilon,\widetilde{u}_t^\varepsilon\right)\right]\mathrm{d}t \le C\varepsilon^\kappa,\\ \Xi_2 &= E\int_0^T\eta_t^\varepsilon\left[b\left(t,\widetilde{x}_t^\varepsilon,E\widetilde{x}_t^\varepsilon,u_t\right)-b\left(t,x_t^\varepsilon,Ex_t^\varepsilon,u_t\right)\right]\mathrm{d}t \le C\varepsilon^\kappa,\\ \Xi_3 &= E\int_0^T\eta_t^\varepsilon\left[b\left(t,\widetilde{x}_t^\varepsilon,E\widetilde{x}_t^\varepsilon,\widetilde{u}_t^\varepsilon\right)-b\left(t,x_t^\varepsilon,Ex_t^\varepsilon,u_t^\varepsilon\right)\right]\mathrm{d}t \le C\varepsilon^\kappa,\end{aligned} \tag{46}$$

i.e.,

$$E\int_0^T\{\widetilde{\eta}_t^\varepsilon[b(t,\widetilde{x}_t^\varepsilon,E\widetilde{x}_t^\varepsilon,u_t)-b(t,\widetilde{x}_t^\varepsilon,E\widetilde{x}_t^\varepsilon,\widetilde{u}_t^\varepsilon)]-\eta_t^\varepsilon[b(t,x_t^\varepsilon,Ex_t^\varepsilon,u_t)-b(t,x_t^\varepsilon,Ex_t^\varepsilon,u_t^\varepsilon)]\}\mathrm{d}t\le C\varepsilon^\kappa. \tag{47}$$

Similarly, via Lemma 2, we also have

$$\begin{aligned}E\int_0^T&\{\widetilde{\zeta}_t^\varepsilon[\sigma(t,\widetilde{x}_t^\varepsilon,E\widetilde{x}_t^\varepsilon,u_t)-\sigma(t,\widetilde{x}_t^\varepsilon,E\widetilde{x}_t^\varepsilon,\widetilde{u}_t^\varepsilon)]-\zeta_t^\varepsilon[\sigma(t,x_t^\varepsilon,Ex_t^\varepsilon,u_t)-\sigma(t,x_t^\varepsilon,Ex_t^\varepsilon,u_t^\varepsilon)]\\&-\widetilde{\xi}_t^\varepsilon\left[f\left(t,\widetilde{\Gamma}_t^\varepsilon,u_t\right)-f\left(t,\widetilde{\Gamma}_t^\varepsilon,\widetilde{u}_t^\varepsilon\right)\right]+\xi_t^\varepsilon[f(t,\Gamma_t^\varepsilon,u_t)-f(t,\Gamma_t^\varepsilon,u_t^\varepsilon)]\\&-\left[l\left(t,\widetilde{\Gamma}_t^\varepsilon,u_t\right)-l\left(t,\widetilde{\Gamma}_t^\varepsilon,\widetilde{u}_t^\varepsilon\right)\right]+\left[l(t,\Gamma_t^\varepsilon,u_t)-l(t,\Gamma_t^\varepsilon,u_t^\varepsilon)\right]\Big\}\mathrm{d}t\le C\varepsilon^\kappa.\end{aligned} \tag{48}$$

Therefore, the desired result (20) follows immediately by combining (43)–(48).

Since (x_0, y_0, u) is arbitrary, we draw the desired conclusion and summarize it as follows. □

Theorem 2. *Suppose $(A_1)-(A_3)$ hold. For any $\varepsilon>0$, u^ε is an ε-optimal control of problem $\mathscr{A}$. Then, for any $\kappa\in[0,(1/3))$, there exist three nonnegative parameters θ_0^ε, $\overline{\theta}_0^\varepsilon$, and $\overline{\theta}_T^\varepsilon$ with $|\theta_0^\varepsilon|^2+E|\overline{\theta}_0^\varepsilon|^2+E|\overline{\theta}_T^\varepsilon|^2=1$ and $\theta_0^\varepsilon\ge 0$ such that, for any $x_0\in R$, $y_0\in R$, and $u\in\mathscr{U}$, the necessary condition (20) holds a.e. a.s., where $(\xi^\varepsilon,\eta^\varepsilon,\zeta^\varepsilon)$ is the solution of (15) corresponding to u^ε.*

Define the Hamiltonian $H(t,x,y,z,u,\xi,\eta,\zeta)$ by

$$\begin{aligned}H(t,x,y,z,u,\xi,\eta,\zeta)&=-\xi f(t,\Gamma,u)+\eta b(t,x,Ex,u)\\&\quad+\zeta\sigma(t,x,Ex,u)-l(t,\Gamma,u),\end{aligned} \tag{49}$$

then we have the following form of necessity conditions.

Corollary 1. *Under the assumptions of Theorem 2, it holds that*

$$\begin{aligned}&E\int_0^T H(t,x_t^\varepsilon,y_t^\varepsilon,z_t^\varepsilon,u_t^\varepsilon,\xi_t^\varepsilon,\eta_t^\varepsilon,\zeta_t^\varepsilon)\mathrm{d}t\\&\quad\ge\sup_{u\in\mathscr{U}}E\int_0^T H(t,x_t^\varepsilon,y_t^\varepsilon,z_t^\varepsilon,u_t,\xi_t^\varepsilon,\eta_t^\varepsilon,\zeta_t^\varepsilon)\mathrm{d}t-C\theta_0^\varepsilon\varepsilon^\kappa.\end{aligned} \tag{50}$$

Proof. According to the definition of the control $u^{\varepsilon,\delta,\varepsilon}$, the point $u\in U$ can be replaced by any admissible control $u\in\mathscr{U}$, and the subsequent arguments still go through. Therefore, the conclusion in Theorem 2 holds for any $u\in\mathscr{U}$, which is an easy variant of our corollary. □

Remark 3. If the coefficients of system (3) do not depend on the expected values of the states, Theorem 2 reduces to the near-maximum condition for the classical system under convex control domain.

Remark 4. For exact optimality, the integral form and the pointwise form of the maximum condition is equivalent; however, it is not the case for near-optimality. We can only deduce the near maximum condition in an integral form.

Remark 5. If $\varepsilon=0$, we can obtain a stochastic maximum principle for controlled mean-field FBSDEs with the control domain of convexity assumption.

4. Sufficient Condition of Near-Optimality

In this section, we will prove that the near-maximum condition of the Hamiltonian H in the integral form is sufficient for near-optimality under some additional assumptions.

(A_4) Let b, σ, f, and l be differentiable in u, and there exists a constant $C>0$ such that

$$\begin{cases}|b(t,x,\widetilde{x},u_1)-b(t,x,\widetilde{x},u_2)|+|b_u(t,x,\widetilde{x},u_1)-b_u(t,x,\widetilde{x},u_2)|+|\sigma(t,x,\widetilde{x},u_1)-\sigma(t,x,\widetilde{x},u_2)|+|\sigma_u(t,x,\widetilde{x},u_1)-\sigma_u(t,x,\widetilde{x},u_2)|\le C|u_1-u_2|,\\|f(t,\Gamma,u_1)-f(t,\Gamma,u_2)|+|f_u(t,\Gamma,u_1)-f_u(t,\Gamma,u_2)|+|l(t,\Gamma,u_1)-l(t,\Gamma,u_2)|+|l_u(t,\Gamma,u_1)-l_u(t,\Gamma,u_2)|\le C|u_1-u_2|.\end{cases} \tag{51}$$

Theorem 3. *Let $(A_1)-(A_4)$ hold, and assume that the Hamiltonian $H(t,\cdot,\cdot,\cdot,\cdot,\xi_t^\varepsilon,\eta_t^\varepsilon,\zeta_t^\varepsilon)$ is concave for a.e. $t\in[0,T]$, P-a.s., h is concave, and φ and γ are convex. Let $\Lambda_t^\varepsilon=(\xi^\varepsilon,\eta^\varepsilon,\zeta^\varepsilon)$ be the solution of the adjoint equation (15) associated with $(x^\varepsilon,y^\varepsilon,z^\varepsilon,u^\varepsilon)$. If, for any $u\in\mathscr{U}$ and some $\varepsilon>0$,*

$$\sup_{u\in\mathcal{U}} E\int_0^T H(t,x_t^\varepsilon,y_t^\varepsilon,z_t^\varepsilon,u_t,\Lambda_t^\varepsilon)\mathrm{d}t \le E\int_0^T H(t,x_t^\varepsilon,y_t^\varepsilon,z_t^\varepsilon,u_t^\varepsilon,\Lambda_t^\varepsilon)\mathrm{d}t+\varepsilon, \tag{52}$$

holds, then we have

$$J(u^\varepsilon)\le \inf_{u\in\mathcal{U}} J(u)+C\varepsilon^{1/2}, \tag{53}$$

where $C>0$ is a constant independent of ε.

Proof. Fix $\varepsilon>0$, for any $u,v\in\mathcal{U}$, and define a new metric $\overline{d}$ on $\mathcal{U}$ as follows:

$$\overline{d}(u,v)=E\int_0^T \nu_t^\varepsilon|u_t-v_t|\mathrm{d}t, \tag{54}$$

with $\nu_t^\varepsilon=1+|\xi_t^\varepsilon|+|\eta_t^\varepsilon|+|\zeta_t^\varepsilon|$. Obviously, $\overline{d}$ is a complete metric on $\mathcal{U}$ as a weighted L^1 norm. Define a functional $\overline{J}$ on $\mathcal{U}$ by

$$\overline{J}(u)=E\int_0^T H(t,x_t^\varepsilon,y_t^\varepsilon,z_t^\varepsilon,u_t,\Lambda_t^\varepsilon)\mathrm{d}t. \tag{55}$$

A simple calculation shows that

$$|\overline{J}(u)-\overline{J}(v)|\le CE\int_0^T \nu_t^\varepsilon|u_t-v_t|\mathrm{d}t. \tag{56}$$

Therefore, $\overline{J}$ is continuous on $\mathcal{U}$ with respect to $\overline{d}$. Then, by using (52) and Ekeland's variational principle, there exists a $\widehat{u}^\varepsilon\in\mathcal{U}$ such that

$$\overline{d}(\widehat{u}^\varepsilon,u^\varepsilon)\le\varepsilon^{1/2}, \tag{57}$$

and

$$E\int_0^T \widetilde{H}(t,x_t^\varepsilon,y_t^\varepsilon,z_t^\varepsilon,\widehat{u}_t^\varepsilon)\mathrm{d}t=\max_{u\in\mathcal{U}} E\int_0^T \widetilde{H}(t,x_t^\varepsilon,y_t^\varepsilon,z_t^\varepsilon,u_t)\mathrm{d}t, \tag{58}$$

where

$$\widetilde{H}(t,x,y,z,u)=H(t,x,y,z,u,\Lambda)-\varepsilon^{1/2}\nu_t^\varepsilon|u-\widehat{u}^\varepsilon|. \tag{59}$$

The integral-form maximum condition (58) implies a pointwise maximum condition, that is, for a.e. $t\in[0,T]$ and P-a.s.,

$$\widetilde{H}(t,x_t^\varepsilon,y_t^\varepsilon,z_t^\varepsilon,\widehat{u}_t^\varepsilon)=\max_{u\in\mathcal{U}}\widetilde{H}(t,x_t^\varepsilon,y_t^\varepsilon,z_t^\varepsilon,u_t). \tag{60}$$

Then, by Lemma 2.3 of Yong and Zhou [36], we have $0\in\partial_u\widetilde{H}(t,x_t^\varepsilon,y_t^\varepsilon,z_t^\varepsilon,\widehat{u}_t^\varepsilon)$. By using (59) and the fact that the generalized gradient of the sum of two functions is contained in the sum of the generalized gradients of the two functions, we deduce

$$\partial_u\widetilde{H}(t,x_t^\varepsilon,y_t^\varepsilon,z_t^\varepsilon,\widehat{u}_t^\varepsilon)=\partial_u H(t,x_t^\varepsilon,y_t^\varepsilon,z_t^\varepsilon,\widehat{u}_t^\varepsilon,\Lambda_t^\varepsilon)+\left[-\varepsilon^{1/2}\nu_t^\varepsilon,\varepsilon^{1/2}\nu_t^\varepsilon\right]. \tag{61}$$

Furthermore, since H is differentiable in u, there exists a $\vartheta_t^\varepsilon\in[-\varepsilon^{1/2}\nu_t^\varepsilon,\varepsilon^{1/2}\nu_t^\varepsilon]$, such that

$$H_u(t,x_t^\varepsilon,y_t^\varepsilon,z_t^\varepsilon,\widehat{u}_t^\varepsilon,\Lambda_t^\varepsilon)=-\vartheta_t^\varepsilon. \tag{62}$$

Consequently, by (A_4), we can prove that

$$\begin{aligned}&|H_u(t,x_t^\varepsilon,y_t^\varepsilon,z_t^\varepsilon,u_t^\varepsilon,\Lambda_t^\varepsilon)|\\&\le|H_u(t,x_t^\varepsilon,y_t^\varepsilon,z_t^\varepsilon,u_t^\varepsilon,\Lambda_t^\varepsilon)-H_u(t,x_t^\varepsilon,y_t^\varepsilon,z_t^\varepsilon,\widehat{u}_t^\varepsilon,\Lambda_t^\varepsilon)|\\&\quad+|H_u(t,x_t^\varepsilon,y_t^\varepsilon,z_t^\varepsilon,\widehat{u}_t^\varepsilon,\Lambda_t^\varepsilon)|\\&\le C\nu_t^\varepsilon|u_t^\varepsilon-\widehat{u}_t^\varepsilon|+\varepsilon^{1/2}\nu_t^\varepsilon.\end{aligned} \tag{63}$$

By the concavity of $H(t,\cdot,\cdot,\cdot,\cdot,\Lambda_t^\varepsilon)$, we have

$$\begin{aligned}&H(t,x_t,y_t,z_t,u_t,\Lambda_t^\varepsilon)-H(t,x_t^\varepsilon,y_t^\varepsilon,z_t^\varepsilon,u_t^\varepsilon,\Lambda_t^\varepsilon)\\&\le H_{\widetilde{x}}^\varepsilon(Ex_t-Ex_t^\varepsilon)+H_{\widetilde{y}}^\varepsilon(Ey_t-Ey_t^\varepsilon)+H_{\widetilde{z}}^\varepsilon(Ez_t-Ez_t^\varepsilon)\\&\quad+H_x^\varepsilon(x_t-x_t^\varepsilon)+H_y^\varepsilon(y_t-y_t^\varepsilon)+H_z^\varepsilon(z_t-z_t^\varepsilon)+H_u^\varepsilon(u_t-u_t^\varepsilon),\end{aligned} \tag{64}$$

for any (x,y,z,u), where $H_j^\varepsilon=H_j(t,x_t^\varepsilon,y_t^\varepsilon,z_t^\varepsilon,u_t^\varepsilon,\Lambda_t^\varepsilon)$, $j=x,y,z,\widetilde{x},\widetilde{y},\widetilde{z}$.

Taking integrations, from (57) and (63), follows

$$\begin{aligned}&E\int_0^T[H(t,x_t,y_t,z_t,u_t,\Lambda_t^\varepsilon)-H(t,x_t^\varepsilon,y_t^\varepsilon,z_t^\varepsilon,u_t^\varepsilon,\Lambda_t^\varepsilon)]\mathrm{d}t\\&\le E\int_0^T H_{\widetilde{x}}^\varepsilon(Ex_t-Ex_t^\varepsilon)\mathrm{d}t+E\int_0^T H_{\widetilde{y}}^\varepsilon(Ey_t-Ey_t^\varepsilon)\mathrm{d}t\\&\quad+E\int_0^T H_{\widetilde{z}}^\varepsilon(Ez_t-Ez_t^\varepsilon)\mathrm{d}t+E\int_0^T H_x^\varepsilon(x_t-x_t^\varepsilon)\mathrm{d}t\\&\quad+E\int_0^T H_y^\varepsilon(y_t-y_t^\varepsilon)\mathrm{d}t+E\int_0^T H_z^\varepsilon(z_t-z_t^\varepsilon)\mathrm{d}t+C\varepsilon^{1/2}.\end{aligned} \tag{65}$$

Applying Itô's formula to $\xi_t^\varepsilon(y_t-y_t^\varepsilon)+\eta_t^\varepsilon(x_t-x_t^\varepsilon)$, we obtain

$$\begin{aligned}
&E[\xi_T^\varepsilon(h(x_T,y_0)-h(x_T^\varepsilon,y_0^\varepsilon))]+E\left[\left(-\xi_T^\varepsilon h_{x_T}^\varepsilon+\eta_0^\varepsilon\gamma_{x_T}^\varepsilon+\theta_0^\varepsilon\varphi_{x_T}^\varepsilon\right)(x_T-x_T^\varepsilon)\right]\\
&\quad-E\left[\left(-\theta_0^\varepsilon\varphi_{y_0}^\varepsilon-\eta_0^\varepsilon\gamma_{y_0}^\varepsilon+\xi_T^\varepsilon h_{y_0}^\varepsilon\right)(y_0-y_0^\varepsilon)\right]-E[\eta_0^\varepsilon(\gamma(x_T,y_0)-\gamma(x_T^\varepsilon,y_0^\varepsilon))]\\
&\quad=E\int_0^T[H(t,x_t,y_t,z_t,u_t,\Lambda_t^\varepsilon)-H(t,x_t^\varepsilon,y_t^\varepsilon,z_t^\varepsilon,u_t^\varepsilon,\Lambda_t^\varepsilon)+l(t,\Gamma_t,u_t)-l(t,\Gamma_t^\varepsilon,u_t^\varepsilon)]\mathrm{d}t\\
&\quad-E\int_0^T\left[EH_{\tilde{x}}^\varepsilon\right](x_t-x_t^\varepsilon)\mathrm{d}t-E\int_0^T\left[EH_{\tilde{y}}^\varepsilon\right](y_t-y_t^\varepsilon)\mathrm{d}t\\
&\quad-E\int_0^T\left[EH_{\tilde{z}}^\varepsilon\right](z_t-z_t^\varepsilon)\mathrm{d}t-E\int_0^T H_x^\varepsilon(x_t-x_t^\varepsilon)\mathrm{d}t\\
&\quad-E\int_0^T H_y^\varepsilon(y_t-y_t^\varepsilon)\mathrm{d}t-E\int_0^T H_z^\varepsilon(z_t-z_t^\varepsilon)\mathrm{d}t.
\end{aligned}\tag{66}$$

Since h is concave, we have

$$\begin{aligned}
&E\left\{\xi_T^\varepsilon(h(x_T,y_0)-h(x_T^\varepsilon,y_0^\varepsilon))-\xi_T^\varepsilon h_{x_T}^\varepsilon(x_T-x_T^\varepsilon)\right.\\
&\quad\left.-\xi_T^\varepsilon h_{y_0}^\varepsilon(y_0-y_0^\varepsilon)\right\}\geq 0.
\end{aligned}\tag{67}$$

Similarly, by the convexity of φ and γ yielding

$$E\left\{\varphi_{x_T}^\varepsilon(x_T-x_T^\varepsilon)+\varphi_{y_0}^\varepsilon(y_0-y_0^\varepsilon)\right\}\leq E[\varphi(x_T,y_0)-\varphi(x_T^\varepsilon,y_0^\varepsilon)],\tag{68}$$

$$E\left\{\gamma_{x_T}^\varepsilon(x_T-x_T^\varepsilon)+\gamma_{y_0}^\varepsilon(y_0-y_0^\varepsilon)\right\}\leq E[\gamma(x_T,y_0)-\gamma(x_T^\varepsilon,y_0^\varepsilon)].\tag{69}$$

Combining (65) and (67)–(69), we can finally get the following result:

$$J(u^\varepsilon)\leq J(u)+C\varepsilon^{1/2}.\tag{70}$$

Since u is arbitrary, we can draw the conclusion. □

Corollary 2. *Under the assumptions of Theorem 3, a sufficient condition for an admissible control u^ε to be ε-optimal is*

$$\begin{aligned}
&\sup_{u\in\mathscr{U}}E\int_0^T H(t,x_t^\varepsilon,y_t^\varepsilon,z_t^\varepsilon,u,\Lambda_t^\varepsilon)\mathrm{d}t\\
&\quad\leq E\int_0^T H(t,x_t^\varepsilon,y_t^\varepsilon,z_t^\varepsilon,u_t^\varepsilon,\Lambda_t^\varepsilon)\mathrm{d}t+\left(\frac{\varepsilon}{C}\right)^2.
\end{aligned}\tag{71}$$

5. A Linear-Quadratic Problem

Consider the near-optimal control problem.

Problem $\mathscr{P}^\varepsilon$. Minimize $J^\varepsilon(u)=E[\int_0^1((\sqrt{2}/2)u_t^2+(\sqrt{2}\,\varepsilon/2)u_t^2)\mathrm{d}t+(\sqrt{2}/2)x_1^2+(\sqrt{2}/2)y_0^2]$, subject to

$$\begin{cases}
\mathrm{d}x_t=\{x_t+Ex_t+u_t\}\mathrm{d}t+\{x_t+Ex_t+u_t\}\mathrm{d}W_t,\\
-\mathrm{d}y_t=\{x_t+y_t+z_t+Ex_t+Ey_t+Ez_t+u_t\}\mathrm{d}t-z_t\mathrm{d}W_t,\\
x_0=x_1-\dfrac{1}{2}y_0,\\
y_1=\dfrac{1}{2}x_1+\dfrac{1}{2}y_0,
\end{cases}\tag{72}$$

where $\varepsilon>0$ is a small parameter, and the control domain is limited as $\mathscr{U}=[-1,1]$.

In view of the practical point, it is difficult to find a near-optimal control for $\mathscr{P}^\varepsilon$ directly. So, we adopt the approach, in which $\mathscr{P}^\varepsilon$ is firstly approximated by a simpler one (Problem $\mathscr{P}$), and then an optimal control u^* for $\mathscr{P}$ is obtained. Finally, it is proved that u^* is near-optimal for $\mathscr{P}^\varepsilon$. This method has been applied to the hierarchical controls of stochastic manufacturing systems [37].

Problem $\mathscr{P}$. Minimize $J(u)=E[\int_0^1(\sqrt{2}/2)u_t^2\mathrm{d}t+(\sqrt{2}/2)x_1^2+(\sqrt{2}/2)y_0^2]$, subject to

$$\begin{cases}
\mathrm{d}x_t=\{x_t+Ex_t+u_t\}\mathrm{d}t+\{x_t+Ex_t+u_t\}\mathrm{d}W_t,\\
-\mathrm{d}y_t=\{x_t+y_t+z_t+Ex_t+Ey_t+Ez_t+u_t\}\mathrm{d}t-z_t\mathrm{d}W_t,\\
x_0=x_1-\dfrac{1}{2}y_0,\\
y_1=\dfrac{1}{2}x_1+\dfrac{1}{2}y_0.
\end{cases}\tag{73}$$

Let u be an optimal admissible control of $\mathscr{P}$, and the corresponding optimal trajectory is denoted by (x,y,z). Set $\theta_0=(\sqrt{2}/2)$, for a given admissible triple (x,y,z,u), the corresponding first-order adjoint equation is presented as

$$\begin{cases} d\xi_t = \{\xi_t + E\xi_t\}dt + \{\xi_t + E\xi_t\}dW_t, \\ -d\eta_t = \{-\xi_t + \eta_t + \zeta_t + E[-\xi_t + \eta_t + \zeta_t]\}dt - \zeta_t dW_t, \\ \xi_0 = -y_0 + \frac{1}{2}\eta_0 + \frac{1}{2}\xi_1, \\ \eta_1 = -\frac{1}{2}\xi_1 + \eta_0 + x_1. \end{cases} \tag{74}$$

From Remark 5 and Theorem 2, the candidate optimal control u should satisfy

$$\frac{\sqrt{2}}{2}v_t^2 - (\eta_t + \zeta_t - \xi_t)v_t \le \frac{\sqrt{2}}{2}u_t^2 - (\eta_t + \zeta_t - \xi_t)u_t, \quad \forall v \in \mathcal{U}. \tag{75}$$

Then, we have

$$u_t = \begin{cases} \mu_t, & \mu_t \in [-1, 1], \\ 1, & \mu_t \in (-\infty, -1], \\ -1, & \mu_t \in [1, +\infty), \end{cases} \tag{76}$$

with $\mu_t = (\sqrt{2}/2)(\eta_t + \zeta_t - \xi_t)$.

We claim that the control u defined by (76) is optimal for Problem $\mathcal{P}$, which will be illustrated in the following proposition. Now, we are about to show that the same optimal control is near-optimal for $\mathcal{P}^\varepsilon$ when ε is sufficiently small. Denote by (x^*, y^*, z^*, u^*) the optimal state and optimal control under (76) and (ξ^*, η^*, ζ^*) the corresponding solution of (74). Then, the Hamiltonian function for $\mathcal{P}$ is

$$\begin{aligned} H(t, x_t, y_t, z_t, u_t, \Lambda_t) = &-\frac{\sqrt{2}}{2}u_t^2 - (\xi_t - \eta_t - \zeta_t)u_t \\ &+ (\eta_t + \zeta_t)(x_t + Ex_t) \\ &- \xi_t(x_t + y_t + z_t + Ex_t + Ey_t + Ez_t). \end{aligned} \tag{77}$$

Since u^* is optimal, it necessarily maximizes the Hamiltonian function a.s., namely,

$$u_t^* + \frac{\sqrt{2}}{2}(\xi_t^* - \eta_t^* - \zeta_t^*) = 0, \quad P - \text{a.s. a.e.} \tag{78}$$

However, the Hamiltonian function for $\mathcal{P}^\varepsilon$ is

$$\begin{aligned} H_\varepsilon(t, x_t, y_t, z_t, u_t, \Lambda_t) = &-\frac{\sqrt{2}}{2}(1+\varepsilon)u_t^2 - (\xi_t - \eta_t - \zeta_t)u_t \\ &+ (\eta_t + \zeta_t)(x_t + Ex_t) \\ &- \xi_t(x_t + y_t + z_t + Ex_t + Ey_t + Ez_t). \end{aligned} \tag{79}$$

Obviously, it is concave. Moreover, it is maximized at u^ε, which satisfies

$$u_t^\varepsilon = \frac{u_t^*}{1+\varepsilon}. \tag{80}$$

Hence,

$$\begin{aligned} &\sup_{u\in\mathcal{U}} E\int_0^1 H_\varepsilon(t, x_t^*, y_t^*, z_t^*, u_t, \Lambda_t^*)dt - E\int_0^1 H_\varepsilon(t, x_t^*, y_t^*, z_t^*, u_t^*, \Lambda_t^*)dt \\ &\le E\int_0^1 \sup_{u\in\mathcal{U}} H_\varepsilon(t, x_t^*, y_t^*, z_t^*, u_t, \Lambda_t^*)dt - E\int_0^1 H_\varepsilon(t, x_t^*, y_t^*, z_t^*, u_t^*, \Lambda_t^*)dt \\ &= E\int_0^1 \{H_\varepsilon(t, x_t^*, y_t^*, z_t^*, u_t^\varepsilon, \Lambda_t^*) - H_\varepsilon(t, x_t^*, y_t^*, z_t^*, u_t^*, \Lambda_t^*)\}dt \\ &= E\int_0^1 \frac{\varepsilon^2}{2(1+\varepsilon)}(u_t^*)^2 dt \\ &\le C\varepsilon. \end{aligned} \tag{81}$$

According to Theorem 3, u^* is near-optimal for $\mathcal{P}^\varepsilon$ with an error order of ε when ε is sufficiently small.

Proposition 1. *The control u^* defined by (76) together with the corresponding trajectory (x^*, y^*, z^*) is an optimal solution for Problem $\mathcal{P}$.*

Proof. Suppose (x, y, z) is the trajectory of system (73) controlled by $u \in \mathcal{U}$. By the convexity of a function, we have

$$\begin{aligned} \frac{\sqrt{2}}{2}x_1^2 - \frac{\sqrt{2}}{2}(x_1^*)^2 &\ge \sqrt{2}x_1^*(x_1 - x_1^*), \\ \frac{\sqrt{2}}{2}y_0^2 - \frac{\sqrt{2}}{2}(y_0^*)^2 &\ge \sqrt{2}y_0^*(y_0 - y_0^*). \end{aligned} \tag{82}$$

Applying Itô's formula to $\xi_t^*(y_t - y_t^*) + \eta_t^*(x_t - x_t^*)$, we obtain

$$E[x_1^*(x_1 - x_1^*) + y_0^*(y_0 - y_0^*)] = E\int_0^1 (\xi_t^* - \eta_t^* - \zeta_t^*)(u_t - u_t^*)dt. \tag{83}$$

Then,

$$\begin{aligned} J(u) - J(u^*) &\geq E\left\{\int_0^1 \left[\frac{\sqrt{2}}{2}u_t^2 - \frac{\sqrt{2}}{2}(u_t^*)^2\right]\mathrm{d}t + \sqrt{2}\,x_1^*(x_1 - x_1^*) + \sqrt{2}\,y_0^*(y_0 - y_0^*)\right\} \\ &= E\int_0^1 \left[\frac{\sqrt{2}}{2}u_t^2 - \frac{\sqrt{2}}{2}(u_t^*)^2 + \sqrt{2}(\xi_t^* - \eta_t^* - \zeta_t^*)(u_t - u_t^*)\right]\mathrm{d}t. \end{aligned} \tag{84}$$

From (76), we have

$$\begin{aligned} \frac{\sqrt{2}}{2}u_t^2 + \sqrt{2}(\xi_t^* - \eta_t^* - \zeta_t^*)u_t &\geq \frac{\sqrt{2}}{2}(u_t^*)^2 \\ &+ \sqrt{2}(\xi_t^* - \eta_t^* - \zeta_t^*)u_t^*, \quad \forall u \in \mathscr{U}. \end{aligned} \tag{85}$$

The inequality above implies that

$$J(u) - J(u^*) \geq 0, \quad \forall u \in \mathscr{U}. \tag{86}$$

Therefore, u^* is the optimal control for $\mathscr{P}$, and (x^*, y^*, z^*) is the optimal trajectory. □

6. Conclusion

This paper discussed near-optimal control problems for mean-field FBSDEs with mixed initial-terminal conditions. Firstly, we initially introduce three first-order adjoint equations to operate dual analysis with corresponding variational processes. Secondly, the reduction method is adopted to guarantee the well-posedness of the first-order adjoint equations also with mixed initial-terminal conditions. Furthermore, by introducing the penalty functional, the original problem with endpoint constraints is transformed as penalized optimal control problem with no endpoint constraints. Via convex variational technique as well as Ekeland's variational principle, the necessary condition of Pontryagin's type is established. Finally, to illustrate the application of our theoretical results, a linear-quadratic problem is worked out. In our future work, we will develop the research on near-optimality to solve both theoretical and practical problems.

Data Availability

No data were used to support this study.

Conflicts of Interest

The authors declare that they have no conflicts of interest regarding the publication of this paper.

Acknowledgments

This research was supported by the National Natural Science Foundation of China (Grant no. 11901112), and National Natural Science Foundation of China (Grant no. 11701161), and High level introduction of talent research start-up fund of Hubei University of Technology (Grant no. BSQD14067).

References

[1] I. Ekeland, "Non convex minimization problems," *Bulletin of the American Mathematical Society*, vol. 1, no. 3, pp. 443–475, 1979.

[2] X. Y. Zhou, "Deterministic near-optimal control, part 1: necessary and sufficient conditions for near-optimality," *Journal of Optimization Theory and Applications*, vol. 85, no. 2, pp. 473–488, 1995.

[3] X. Y. Zhou, "Deterministic near-optimal controls. Part II: dynamic programming and viscosity solution approach," *Mathematics of Operations Research*, vol. 21, no. 3, pp. 655–674, 1996.

[4] X. Y. Zhou, "Stochastic near-optimal controls: necessary and sufficient conditions for near-optimality," *SIAM Journal on Control and Optimization*, vol. 36, no. 3, pp. 929–947, 1998.

[5] K. Bahlali, N. Khelfallah, and B. Mezerdi, "Necessary and sufficient conditions for near-optimality in stochastic control of FBSDEs," *Systems & Control Letters*, vol. 58, no. 12, pp. 857–864, 2009.

[6] R. Guo, "Projective synchronization of a class of chaotic systems by dynamic feedback control method," *Nonlinear Dynamics*, vol. 90, no. 1, pp. 53–64, 2017.

[7] M. Hafayed, A. Abba, and S. Boukaf, "On Zhou's maximum principle for near-optimal control of mean-field forward-backward stochastic systems with jumps and its applications," *International Journal of Modelling, Identification and Control*, vol. 25, no. 1, pp. 1–16, 2016.

[8] M. Hafayed and S. Abbas, "On near-optimal mean-field stochastic singular controls: necessary and sufficient conditions for near-optimality," *Journal of Optimization Theory and Applications*, vol. 160, no. 3, pp. 778–808, 2014.

[9] J. Huang, X. Li, and G. Wang, "Near-optimal control problems for linear forward-backward stochastic systems," *Automatica*, vol. 46, no. 2, pp. 397–404, 2010.

[10] E. Hui, J. Huang, X. Li, and G. Wang, "Near-optimal control for stochastic recursive problems," *Systems & Control Letters*, vol. 60, no. 3, pp. 161–168, 2011.

[11] M. Tang, "Stochastic maximum principle of near-optimal control of fully coupled forward-backward stochastic differential equation," *Abstract and Applied Analysis*, vol. 2014, Article ID 361259, 12 pages, 2014.

[12] S. Yang, "The necessary and sufficient conditions for stochastic differential systems with multi-time state cost functional," *Systems & Control Letters*, vol. 114, pp. 11–18, 2018.

[13] X. Yi, R. Guo, and Y. Qi, "Stabilization of chaotic systems with both uncertainty and disturbance by the UDE-based control method," *IEEE Access*, vol. 8, no. 1, pp. 62471–62477, 2020.

[14] L. Zhang, J. Huang, and X. Li, "Necessary condition for near optimal control of linear forward-backward stochastic differential equations," *International Journal of Control*, vol. 88, no. 8, pp. 1594–1608, 2015.

[15] L. Zhang, "Sufficient condition for near-optimal control of general controlled linear forward-backward stochastic differential equations," *International Journal of Dynamics and Control*, vol. 5, no. 2, pp. 306–313, 2017.

[16] L. Zhang and Q. Zhou, "Near-optimal control of stochastic recursive systems via viscosity solution," *Journal of Optimization Theory and Applications*, vol. 178, no. 2, pp. 363–382, 2018.

[17] F. Zhang, "Maximum principle for near-optimality of stochastic delay control problem," *Advances in Difference Equations*, vol. 2017, no. 1, p. 98, 2017.

[18] Y. Wang and Z. Wu, "Necessary and sufficient conditions for near-optimality of stochastic delay systems," *International Journal of Control*, vol. 91, no. 8, pp. 1–24, 2017.

[19] G. Ren and B. Liu, "Near-optimal control for a singularly perturbed linear stochastic singular system with Markovian jumping parameters," *European Journal of Control*, vol. 50, pp. 88–95, 2019.

[20] Y. Zhang, S. Li, and L. Liao, "Near-optimal control of nonlinear dynamical systems: a brief survey," *Annual Reviews in Control*, vol. 47, pp. 71–80, 2019.

[21] R. Buckdahn, B. Djehiche, J. Li, and S. Peng, "Mean-field backward stochastic differential equations: a limit approach," *The Annals of Probability*, vol. 37, no. 4, pp. 1524–1565, 2009.

[22] R. Buckdahn, J. Li, and S. Peng, "Mean-field backward stochastic differential equations and related partial differential equations," *Stochastic Processes and Their Applications*, vol. 119, no. 10, pp. 3133–3154, 2009.

[23] J.-M. Lasry and P.-L. Lions, "Mean field games," *Japanese Journal of Mathematics*, vol. 2, no. 1, pp. 229–260, 2007.

[24] R. M. Xu and T. T. Wu, "Mean-field backward stochastic evolution equations in Hilbert spaces and optimal control for BSPDEs," *Mathematical Problems in Engineering*, vol. 2014, Article ID 718948, 18 pages, 2014.

[25] D. Andersson and B. Djehiche, "A maximum principle for SDEs of mean-field type," *Applied Mathematics & Optimization*, vol. 63, no. 3, pp. 341–356, 2011.

[26] R. Buckdahn, B. Djehiche, and J. Li, "A general stochastic maximum principle for SDEs of mean-field type," *Applied Mathematics & Optimization*, vol. 64, no. 2, pp. 197–216, 2011.

[27] J. Li, "Stochastic maximum principle in the mean-field controls," *Automatica*, vol. 48, no. 2, pp. 366–373, 2012.

[28] Y. Shen and T. K. Siu, "The maximum principle for a jump-diffusion mean-field model and its application to the mean-variance problem," *Nonlinear Analysis: Theory, Methods & Applications*, vol. 86, pp. 58–73, 2013.

[29] J. Huang, S. Wang, and Z. Wu, "Backward mean-field linear-quadratic-Gaussian (LQG) games: full and partial information," *IEEE Transactions on Automatic Control*, vol. 61, no. 12, pp. 3784–3796, 2016.

[30] M. Huang, "Large-population LQG games involving a major player: the Nash certainty equivalence principle," *SIAM Journal on Control and Optimization*, vol. 48, no. 5, pp. 3318–3353, 2010.

[31] R. Xu and J. Shi, "ε-Nash mean-field games for linear-quadratic systems with random jumps and applications," *International Journal of Control*, pp. 1–11, 2019.

[32] R. M. Xu and F. Zhang, "ε-Nash mean-field games for general linear-quadratic systems with applications," *Automatica*, vol. 114, Article ID 108835, 2020.

[33] A. Bensoussan, S. C. P. Yam, and Z. Zhang, "Well-posedness of mean-field type forward-backward stochastic differential equations," *Stochastic Processes and Their Applications*, vol. 125, no. 9, pp. 3327–3354, 2015.

[34] J. M. Yong, "Forward-backward stochastic differential equations with mixed initial-terminal conditions," *Transactions of the American Mathematical Society*, vol. 362, no. 2, pp. 1047–1096, 2010.

[35] J. Yong, "Optimality variational principle for controlled forward-backward stochastic differential equations with mixed initial-terminal conditions," *SIAM Journal on Control and Optimization*, vol. 48, no. 6, pp. 4119–4156, 2010.

[36] J. M. Yong and X. Y. Zhou, *Stochastic Controls, Hamiltonian Systems and HJB Equations*, Springer-Verlag, Berlin, Germany, 1999.

[37] X. Y. Zhou and S. P. Sethi, "A sufficient condition for near-optimal stochastic controls and its application to manufacturing systems," *Applied Mathematics & Optimization*, vol. 29, no. 1, pp. 67–92, 1994.

Hindawi
Mathematical Problems in Engineering
Volume 2020, Article ID 5369859, 8 pages
https://doi.org/10.1155/2020/5369859

Research Article

$L(p,q)$-Label Coloring Problem with Application to Channel Allocation

Zhenbin Liu [1,2,3] **and Yuqiang Wu** [1,2]

[1] *School of Mathematical Sciences, Qufu Normal University, Qufu, China*
[2] *College of Engineering, Qufu Normal University, Qufu, China*
[3] *Science and Information College, Qingdao Agricultural University, Qingdao 266109, China*

Correspondence should be addressed to Zhenbin Liu; lzbzj@163.com

Received 3 April 2020; Accepted 4 May 2020; Published 3 June 2020

Guest Editor: Cuimei Jiang

In this paper, the $L(p,q)$-coloring problem of the graph is studied with application to channel allocation of the wireless network. First, by introducing two new logical operators, some necessary and sufficient conditions for solving the $L(p,q)$-coloring problem are given. Moreover, it is noted that all solutions of the obtained logical equations are corresponding to each coloring scheme. Second, by using the semitensor product, the necessary and sufficient conditions are converted to an algebraic form. Based on this, all coloring schemes can be obtained through searching all column indices of the zero columns. Finally, the obtained result is applied to analyze channel allocation of the wireless network. Furthermore, an illustration example is given to show the effectiveness of the obtained results in this paper.

1. Introduction

It is well known that the coloring problem is a basic and classical problem in graph theory. Graph coloring is originated from famous conjecture called four-colour conjecture [1] and widely used in many real-life areas [2–4], such as scheduling and timetabling in engineering, air traffic flow management, and channel allocation of mobiles. There are various forms of graph coloring, such as set coloring, list coloring, T-coloring, and $L(n_1, n_2, \cdots, n_s)$-coloring (n_i denotes a nonnegative integer, $i = 1, 2, \cdots, s$). The labeling problems of graphs arise in many networking and telecommunication contexts. The channel allocation problem is first formulated as a graph coloring problem by Hale [5]. Furthermore, Griggs and Yeh formulated this problem as a graph labeling problem [6]. $L(p,q)$-label coloring is one kind of graph labeling, which has major application in channel allocation [5, 7–10]. Thus, it is still more interesting to introduce a new method to study the coloring problem.

Recently, Cheng et al. and Li et al. provided a new mathematical method, which is called the semitensor product with matrices [11–13] to study logical systems [14–23], probability logical networks [24, 25], game theory [26, 27], coloring problem [1, 10, 28], and some other related fields [29–31]. Wang et al. first studied the graph problem by using the semitensor product [1]. In [1], the maximum (weight) stable set and vertex coloring problems of graphs were investigated with application to the group consensus of multiagent systems, and an algorithm was established to find all the internally stable sets for any graph. In [28], Zhong et al. investigated the minimum stable set and core of the graph and established an algorithm to find all the externally stable sets.

This paper studies the $L(p,q)$-coloring problem of the graph with application to channel allocation of the wireless network. Some necessary and sufficient conditions for solving the $L(p,q)$-coloring problem are first made by introducing two new logical operators. Moreover, it is noted that all solutions of the obtained logical equations are corresponding to each coloring scheme. Then, by using the semitensor product, the necessary and sufficient conditions are converted to an algebraic form. Based on this, all coloring

schemes can be obtained through searching all column indices of the zero columns. Finally, the obtained results are applied to analyze channel allocation of the wireless network. Furthermore, an illustration example is given to show the effectiveness of the obtained results in this paper.

The rest of this paper is organized as follows. Section 2 gives some necessary preliminaries on the semitensor product of matrices and $L(p,q)$-labeling. The main results are shown in Section 3. In Section 4, we apply the obtained results to the channel allocation of the wireless network, which is followed by the conclusion in Section 5.

2. Preliminaries

In this section, we give some necessary preliminaries on the semitensor product, the pseudo-Boolean function, and graph theory, which will be used in the sequel.

First, we give some notations to be used in this paper.

$\mathscr{D}_k = \{0, 1, \cdots, k-1\}$, especially, $\mathscr{D}: = \mathscr{D}_2 = \{0, 1\}$.

δ_n^i: the i-th column of the identity matrix I_n.

Denote by $\mathrm{Col}_b(B)$ the b-th column of matrix B and by $\mathrm{Col}(B)$ the set of all columns of matrix B.

$\mathbb{R}^{n\times r}$: the set of $n \times r$ real matrices, where $\mathbb{R}$ denotes the set of real numbers.

$\Delta_n: = \left\{\delta_n^i \mid i = 1, 2, \cdots, n\right\}$, and for simplicity, let $\Delta: = \Delta_2$. Identify $k - i \sim \delta_k^i$, $i = 1, 2, \cdots, k$, which implies $\mathscr{D}_k \sim \Delta_k$, where $p \sim q$ means they are equivalent.

A matrix $L \in \mathbb{R}^{n\times r}$ is called a logical matrix if columns of L are of the form of δ_n^i. Denote by $\mathscr{L}_{n\times r}$ the set of $n \times r$ logical matrices.

If $L \in \mathscr{L}_{n\times r}$, it can be expressed as $L = [\delta_n^{i_1}\ \delta_n^{i_2} \cdots \delta_n^{i_r}]$. For the sake of compactness, it is briefly denoted by $L = \delta_n[i_1\, i_2 \cdots i_r]$.

Next, we give some definitions and results about the semitensor product.

Definition 1 (see [11]). The semitensor product of two matrices $A \in \mathbb{R}^{m\times n}$ and $B \in \mathbb{R}^{p\times q}$ is

$$A \propto B = \left(A \otimes I_{\alpha/n}\right)\left(B \otimes I_{\alpha/p}\right), \tag{1}$$

where $\alpha = lcm(n, p)$ is the least common multiple of n and p and $\otimes$ is the Kronecker product.

Throughout this paper, the default matrix product is the semitensor product. The semitensor product is a generalization of the conventional matrix product. Thus, we can simply call it "product" and omit the symbol "$<imes$" without confusion.

Definition 2 (see [11]). A swap matrix $W_{[m,n]}$ is an $mn \times mn$ matrix defined as follows: its rows and columns are labeled by double index (i, j), the columns are arranged by the ordered multiindex $Id(i, j; m, n)$, and the rows are arranged by the ordered multiindex $Id(j, i; n, m)$. Then, the element at the position $[(I, J), (i, j)]$ is

$$w_{(I,J)(i,j)} = \delta_{i,j}^{I,J} = \begin{cases} 1, & I = i \text{ and } J = j; \\ 0, & \text{otherwise.} \end{cases} \tag{2}$$

Remark 1. When $m = n$, $W_{[m,n]}$ is briefly rewritten as $W_{[n]}$. Furthermore, from Definition 2, $W_{[m,n]}$ can be written as the following form for all m, n:

$$\begin{aligned} W_{[m,n]} = \delta_{mn}[&1m+1\cdots\ (i-1)m+1\cdots\ (n-1)m+1 \\ &2\ \ m+2\cdots\ (i-1)m+2\cdots\ (n-1)m+2 \\ &\vdots \\ &m\ m+m\cdots(i-1)m+m\cdots(n-1)m+m] \\ \text{or } W_{[m,n]} = \left[\delta_n^1 \propto \delta_m^1 \cdots \delta_n^n \propto \delta_m^1 \ \vdots\ \delta_n^1 \propto \delta_m^2 \cdots \delta_n^n \propto \delta_m^2 \ \vdots\ \cdots \ \vdots\ \delta_n^1 \propto \delta_m^m \cdots \delta_n^n \propto \delta_m^m\right]. \end{aligned} \tag{3}$$

Now, we list some basic properties of the semitensor product [11]:

(1) Let $X \in \mathbb{R}^m$ and $Y \in \mathbb{R}^n$ be column vectors. Then,

$$W_{[m,n]}XY = YX. \tag{4}$$

(2) Let $X \in \mathbb{R}^t$ be a column vector. Then,

$$XA = \left(I_t \otimes A\right)X. \tag{5}$$

(3) Let $X = \delta_t^i \in \mathbb{R}^t$ be a logical vector. Then,

$$X^2 = M_{r,t}X, \tag{6}$$

where

$$\begin{aligned} M_{r,t} &= \delta_{t^2}\left[1\,t+2\cdots(i-1)t+i\cdots t^2\right] \\ &= \left[\delta_t^1 \propto \delta_t^1\ \delta_t^2 \propto \delta_t^2\ \cdots\ \delta_t^t \propto \delta_t^t\right] \in \mathscr{L}_{t^2\times t}. \end{aligned} \tag{7}$$

(4) Let $X = \delta_t^i \in \mathbb{R}^t$ be a logical vector and $A \in \mathbb{R}^{m\times nt}$. Then,

$$AX = A_i, \tag{8}$$

where $A_i \in \mathbb{R}^{m\times n}$ is the i-th block of $A = [A_1\, A_2 \cdots A_t]$. Especially, when $n = 1$,

$$AX = \mathrm{Col}_i(A). \tag{9}$$

Lemma 1 (see [11]). *Any logical function $y = f(x_1, x_2, \cdots, x_n)$ with logical variables $x_i \in \mathcal{D}_k$, $i = 1, \cdots, n$, can be expressed in a multilinear form as*

$$y = f(x_1, x_2, \cdots, x_n) = M_f x_1 x_2 \cdots x_n, \tag{10}$$

where $y \in \Delta_k$ and $M_f \in \mathcal{L}_{k\times k^n}$ is unique, called the structural matrix of f.

Remark 2. The first row of the structural matrix M_f corresponds to the truth value of the logical function $f(x_1, x_2, \cdots, x_s)$.

Now, we list the structural matrices for some basic k-valued logical operators [11], which will be used later.

Negation (): $x = k - 1 - x$, which has a structural matrix as $M_{n,k} = \delta_k[k\,k-1 \cdots 2\,1]$.

Conjunction ($\wedge$): $x\wedge y = \min\{x, y\}$, which has a structural matrix as

$$M_{c,k} = \delta_k[1\,2\,3\cdots k \vdots 2\,2\,3\cdots k \vdots 3\,3\,3\cdots k \vdots \cdots \vdots k\,k\,k\cdots k]. \tag{11}$$

Disjunction ($\vee$): $x\vee y = \max\{x, y\}$, which has a structural matrix as

$$M_{d,k} = \delta_k[1\,1\,1\cdots 1 \vdots 1\,2\,2\cdots 2 \vdots 1\,2\,3\cdots 3 \vdots \cdots \vdots 1\,2\,3\cdots k]. \tag{12}$$

Exclusive or ($\overline{\vee}$): $x\overline{\vee} y = \begin{cases} 1, & x = y \\ 0, & x \neq y \end{cases}$, which has a structural matrix as

$$M_{\overline{\vee},k} = \delta_k[1\,k\,k\cdots k \vdots k\,1\,k\cdots k \vdots k\,k\,1\cdots k \vdots \cdots \vdots k\,k\,k\cdots 1]. \tag{13}$$

Dummy operator (σ_d): $\sigma_d x^2 = x$, which has a structural matrix as

$$E_{d,k} = \delta_k[1\,2\,3\cdots k \vdots \cdots \vdots 1\,2\,3\cdots k]. \tag{14}$$

The following concepts and properties will be used in the next section.

Definition 3 (see [12]). An n-ary pseudo-Boolean function $f(x_1, x_2, \cdots, x_n)$ is a mapping from $\mathcal{D}^n$ to $\mathbb{R}$, where $\mathcal{D}^n := \underbrace{\mathcal{D}\times\mathcal{D}\times\cdots\times\mathcal{D}}_{n}$.

A graph G consists of a vertex (node) set $V = \{v_1, v_2, \cdots, v_n\}$ and an edge set $E \subset V\times V$ denoted by $\mathcal{G} = \{V, E\}$.

Lemma 2 (see [32]). *Given a simple graph $\mathcal{G} = (V, E)$, an $L(p,q)$-labeling f of $\mathcal{G}$ is an integer assignment $f: V \longrightarrow \{1, 2, \cdots, k\}$ such that*

$$|f(u) - f(v)| \geq \begin{cases} p, & d(u,v) = 1, \\ q, & d(u,v) = 2, \end{cases} \tag{15}$$

where $u, v \in V$, $d(u,v)$ denotes the distance between u and v, and p, q are two given positive integers.

3. Main Results

In this section, we investigate the $L(p,q)$-label coloring problem by the semitensor product method and present the main results of this paper.

Consider a graph $\mathcal{G}$ with n nodes $V = \{v_1, v_2, \cdots, v_n\}$. Assume that the adjacency matrix, $A = [a_{ij}]$, of $\mathcal{G}$ is given as

$$a_{ij} = \begin{cases} 1, & v_j \in \mathcal{N}_i \\ 0, & v_j \notin \mathcal{N}_i, \end{cases} \tag{16}$$

where $\mathcal{N}_i$ denotes a neighbor set of node i.

It is noted that $a_{ij} = a_{ji}$ for an undirected graph and $a_{ii} = 0$ in our study since the graph G is a simple graph. Furthermore, let $B = [b_{ij}]$, where $b_{ii} = 0$ and $b_{ij} = a_{i1}\times_b b_{1j} +_b a_{i2}\times_b b_{2j} +_b \cdots +_b a_{in}\times_b b_{nj}$, "$\times_b$" and "$+_b$" are, respectively, Boolean addition and Boolean multiplication. It is easy to obtain that $d(v_i, v_j) = 1$ when $a_{ij} = 1$ and $d(v_i, v_j) = 2$ when $b_{ij} = 1$.

Let $S = \{0, 1, 2, \cdots, k-1\}$. For all $v_i \in V$, assign it an integer $y_i \in S$, i.e., $f(v_i) = y_i$. We need two logical operators as

$$\begin{aligned} \oslash_{k+}(x) &= \begin{cases} x+1, & x = 0, 1, 2, \cdots, k-2; \\ k-1, & x = k-1; \end{cases} \\ \oslash_{k-}(x) &= \begin{cases} x-1, & x = 1, 2, \cdots, k-2, k-1; \\ 0, & x = 0. \end{cases} \end{aligned} \tag{17}$$

Moreover, the structural matrices are

$$\begin{aligned} M_{\oslash_{k+}} &= \delta_k[1\,1\,2\cdots k-1], \\ M_{\oslash_{k-}} &= \delta_k[2\,3\cdots k\,k]. \end{aligned} \tag{18}$$

Then, we have the following result to determine whether the $L(p,q)$-label problem is solved.

Theorem 1. *Consider an undirected graph $\mathcal{G}$ with n nodes $V = \{v_1, v_2, \cdots, v_n\}$. Its $L(p,q)$-label problem is solved if and only if the logical equations*

$$\left\{ \sum_{i=1}^{n} \sum_{j>i} \left[a_{ij} \bigvee_{s=0}^{p-1} \left\{ \left[y_i \overline{\vee} \oslash_{k+}^{s}(y_j) \right] \vee \left[y_i \overline{\vee} \oslash_{k-}^{s}(y_j) \right] \right\} \right] = 0. \sum_{i=1}^{n} \sum_{j>i} \left[b_{ij} \bigvee_{s=0}^{q-1} \left\{ \left[y_i \overline{\vee} \oslash_{k+}^{s}(y_j) \right] \vee \left[y_i \overline{\vee} \oslash_{k-}^{s}(y_j) \right] \right\} \right] = 0, \right. \tag{19}$$

are solved. That is,

$$\sum_{i=1}^{n}\sum_{j>i}\left\{a_{ij}\bigvee_{s=0}^{p-1}\left\{\left[y_i\overline{\vee}\oslash_{k+}^{s}\left(y_j\right)\right]\vee\left[y_i\overline{\vee}\oslash_{k-}^{s}\left(y_j\right)\right]\right\}+b_{ij}\bigvee_{s=0}^{q-1}\left\{\left[y_i\overline{\vee}\oslash_{k+}^{s}\left(y_j\right)\right]\vee\left[y_i\overline{\vee}\oslash_{k-}^{s}\left(y_j\right)\right]\right\}\right\}=0, \tag{20}$$

is solved.

Proof. Necessity: assume that $L(p,q)$ coloring of $\mathcal{G}$ is solvable, and $A=[a_{ij}]$ is the adjacent matrix of the graph $\mathcal{G}$. For all v_i and $v_j\in V(v_i\neq v_j)$, when $d(v_i,v_j)=1$, $|f(v_i)-f(v_j)|\geq p$. It is easy to see that $d(v_i,v_j)=1\Leftrightarrow a_{ij}=1$ and $|f(v_i)-f(v_j)|\geq p\Leftrightarrow f(v_i)\neq f(v_j)\pm s$, $s=0,1,2,\cdots,p-1$. That is, $y_i\geq y_j+p$ when $y_i\geq y_j$ or $y_i\leq y_j-p$ when $y_i\leq y_j$.

Since $y_i\in\{0,1,\cdots,k-1\}$, we introduce the logical operators $\oslash_{k+}$ and $\oslash_{k-}$, and then we have $y_i\geq y_j+p$ is equivalent to $\vee_{s=0}^{p-1}[y_i\overline{\vee}\oslash_{k+}^{s}(y_j)]=0$, and $y_i\leq y_j-p$ is equivalent to $\vee_{s=0}^{p-1}[y_i\overline{\vee}\oslash_{k-}^{s}(y_j)]=0$. That is, $|f(v_i)-f(v_j)|\geq p$ is equivalent to

$$\vee_{s=0}^{p-1}\left\{\left[y_i\overline{\vee}\oslash_{k+}^{s}\left(y_j\right)\right]\vee\left[y_i\overline{\vee}\oslash_{k-}^{s}\left(y_j\right)\right]\right\}=0. \tag{21}$$

Then, we have $a_{ij}\vee_{s=0}^{p-1}\left\{[y_i\overline{\vee}\oslash_{k}^{s}(y_j)]\vee[y_i\overline{\vee}\oslash_{k}^{s}(y_j)]\right\}=0$ for all i,j. Since $a_{ij}=a_{ji}$ for the undirected graph and $|y_i-y_j|=|y_j-y_i|$, we obtain that

$$\sum_{i=1}^{n}\sum_{j>i}\left[a_{ij}\bigvee_{s=0}^{p-1}\left\{\left[y_i\overline{\vee}\oslash_{k+}^{s}\left(y_j\right)\right]\vee\left[y_i\overline{\vee}\oslash_{k-}^{s}\left(y_j\right)\right]\right\}\right]=0. \tag{22}$$

Set $B=[b_{ij}]$, where $b_{ij}=a_{i1}\times_b a_{1j}+_b a_{i2}\times_b a_{2j}+_b\cdots+_b a_{in}\times_b a_{nj}\,(i\neq j)$ and $b_{ii}=0$, $i,j=1,2,\cdots,n$. Obviously, $d(v_i,v_j)=2\Leftrightarrow b_{ij}=1$. Similarly, when $d(v_i,v_j)=2$, we have

$$\sum_{i=1}^{n}\sum_{j>i}\left[b_{ij}\bigvee_{s=0}^{q-1}\left\{\left[y_i\overline{\vee}\oslash_{k+}^{s}\left(y_j\right)\right]\vee\left[y_i\overline{\vee}\oslash_{k-}^{s}\left(y_j\right)\right]\right\}\right]=0. \tag{23}$$

Therefore, from (22) and (23), we obtain that (19) is satisfied, and the necessity is proved.

Sufficiency: suppose that (19) is satisfied. Then, for all i, j, we have

$$a_{ij}\cdot\left(\bigvee_{s=0}^{p-1}\left\{\left[y_i\overline{\vee}\oslash_{k+}^{s}\left(y_j\right)\right]\vee\left[y_i\overline{\vee}\oslash_{k-}^{s}\left(y_j\right)\right]\right\}\right)=0, b_{ij}\cdot\left(\bigvee_{s=0}^{q-1}\left\{\left[y_i\overline{\vee}\oslash_{k+}^{s}\left(y_j\right)\right]\vee\left[y_i\overline{\vee}\oslash_{k-}^{s}\left(y_j\right)\right]\right\}\right)=0. \tag{24}$$

From (24), if $a_{ij}=1$, $\vee_{s=0}^{p-1}\left\{[y_i\overline{\vee}\oslash_{k+}^{s}(y_j)]\vee[y_i\overline{\vee}\oslash_{k-}^{s}(y_j)]\right\}=0$. Then, $y_i\overline{\vee}\oslash_{k+}^{s}(y_j)=0$ or $y_i\overline{\vee}\oslash_{k-}^{s}(y_j)=0$, i.e., $y_i\neq y_j\pm s$, $s=0,1,\cdots,p-1$. Therefore, $|y_i-y_j|\geq p$. Similarly, if $b_{ij}=1$, $|y_i-y_j|\geq q$ by (24).

Since $a_{ij}=1\Leftrightarrow d(v_i,v_j)=1$ and $b_{ij}=1\Leftrightarrow d(v_i,v_j)=2$, we have the $L(p,q)$ coloring of the graph $\mathcal{G}$ is solvable, and the proof is complete. □

It is note that, for a directed graph $\mathcal{G}$, we have the following corollary.

Corollary 1. *Consider a directed graph $\mathcal{G}$ with n nodes $V=\{v_1,v_2,\cdots,v_n\}$. Its $L(p,q)$-label problem is solved if and only if*

$$\sum_{i=1}^{n}\sum_{j\neq i}\left\{a_{ij}\bigvee_{s=0}^{p-1}\left\{\left[y_i\overline{\vee}\oslash_{k+}^{s}\left(y_j\right)\right]\vee\left[y_i\overline{\vee}\oslash_{k-}^{s}\left(y_j\right)\right]\right\}+b_{ij}\bigvee_{s=0}^{q-1}\left\{\left[y_i\overline{\vee}\oslash_{k+}^{s}\left(y_j\right)\right]\vee\left[y_i\overline{\vee}\oslash_{k-}^{s}\left(y_j\right)\right]\right\}\right\}=0, \tag{25}$$

is solved.

Let $x=\delta_k^{k-y}$, $y\in S=\{0,1,2,\cdots,k-1\}$. Then, $y=[k-1,k-2,\cdots,1,0]x$. Using the semitensor product and the vector form of logical variables, we have the following results.

Theorem 2. *Logical equations (19) are solved if and only if there exists at least an integer $v\,(1\leq v\leq k^n)$ such that the v-th column of matrix M is 0, where*

$$\begin{cases} M = \sum_{i=1}^{n} \sum_{j>i} \left[a_{ij} M_{ij,p} + b_{ij} M_{ij,q}\right], \\ M_{ij,s} = M_s M_{ij}, \quad i, j = 1, 2, \cdots, n, i \neq j,\ s = p, q, \\ M_s = J_k M_{d,k}^{s-1} Q_0 \left[(I_{k^2} \otimes Q_1) M_{r,k^2}\right] \cdots \left[(I_{k^2} \otimes Q_s) M_{r,k^2}\right], \\ M_{ij} = E_{d,k}^{n-2} W_{[k^j, k^{n-j}]} W_{[k^i, k^{j-1-i}]}\ (i < j), \\ Q_l = M_{d,k} M_{\overline{\nabla},k} \left[I_k \otimes M_{\oslash_{k+}}^{l}\right] \left[I_{k^2} \otimes \left(M_{\overline{\nabla},k} \left[I_k \otimes M_{\oslash_{k-}}^{l}\right]\right)\right] M_{r,k^2}, l = 0, 1, \cdots, s-1, \end{cases} \tag{26}$$

$J_k = [k-1\ k-2 \cdots 10]$, *and the product is* " $\propto$ "

Proof. Using the semitensor product and the vector form of logical variables, there exists one matrix $M \in R^{1 \times k^n}$ such that the left-hand side of equation (13) is $M x_1 x_2 \cdots x_n$, where $x_i = \delta_k^{k-y_i} \in \Delta_k$, $i = 1, 2, \cdots, n$. Equation (13) is solved if and only if there exists at least an integer $i\,(1 \le i \le k^n)$ such that the ith column of matrix M is 0. Now, we only need to study matrix M.

Since the logical form of $[y_i \overline{\nabla} \oslash_{k+}^{s}(y_j)] \vee [y_i \overline{\nabla} \oslash_{k-}^{s}(y_j)]$ is

$$\begin{aligned} M_{d,k}\left[M_{\overline{\nabla},k} x_i M_{\oslash_{k+}}^{s} x_j\right]\left[M_{\overline{\nabla},k} x_i M_{\oslash_{k-}}^{s} x_j\right] &= M_{d,k}\left\{M_{\overline{\nabla},k}\left[I_k \otimes M_{\oslash_{k+}}^{s}\right] x_i x_j\right\}\left\{M_{\overline{\nabla},k}\left[I_k \otimes M_{\oslash_{k-}}^{s}\right] x_i x_j\right\} \\ &= M_{d,k} M_{\overline{\nabla},k}\left[I_k \otimes M_{\oslash_{k+}}^{s}\right]\left[I_{k^2} \otimes \left(M_{\overline{\nabla},k}\left[I_k \otimes M_{\oslash_{k-}}^{s}\right]\right)\right]\left(x_i x_j\right)^2 \\ &= M_{d,k} M_{\overline{\nabla},k}\left[I_k \otimes M_{\oslash_{k+}}^{s}\right]\left[I_{k^2} \otimes \left(M_{\overline{\nabla},k}\left[I_k \otimes M_{\oslash_{k-}}^{s}\right]\right)\right] M_{r,k} x_i x_j \\ &\triangleq Q_s x_i x_j, \end{aligned} \tag{27}$$

we have

$$\begin{aligned} \bigvee_{s=0}^{p-1}\left\{\left[y_i \overline{\nabla} \oslash_{k+}^{s}\left(y_j\right)\right] \vee \left[y_i \overline{\nabla} \oslash_{k-}^{s}\left(y_j\right)\right]\right\} &= J_k M_{d,k}^{p-1}\left(Q_0 x_i x_j\right)\left(Q_1 x_i x_j\right) \cdots \left(Q_{p-1} x_i x_j\right) \\ &= J_k M_{d,k}^{p-1} Q_0 \left[(I_{k^2} \otimes Q_1) M_{r,k^2} x_i x_j\right] \\ &= J_k M_{d,k}^{p-1} Q_0 \left[(I_{k^2} \otimes Q_1) M_{r,k^2}\right] \cdots \left[\left(I_{k^2} \otimes Q_{p-1}\right) M_{r,k^2}\right] x_i x_j \\ &\triangleq M_p x_i x_j\ (i < j), \end{aligned} \tag{28}$$

where

$$\begin{aligned} M_p &= J_k M_{d,k}^{p-1} Q_0 \left[(I_{k^2} \otimes Q_1) M_{r,k^2}\right] \cdots \left[\left(I_{k^2} \otimes Q_{p-1}\right) M_{r,k^2}\right], \\ Q_s &= M_{d,k} M_{\overline{\nabla},k}\left[I_k \otimes M_{\oslash_{k+}}^{s}\right]\left[I_{k^2} \otimes \left(M_{\overline{\nabla},k}\left[I_k \otimes M_{\oslash_{k-}}^{s}\right]\right)\right] M_{r,k^2}, \quad s = 0, 1, \cdots, p-1. \end{aligned} \tag{29}$$

Furthermore,

$$\begin{aligned} x_i x_j &= E_{d,k}^{n-2} x_{j+1} \cdots x_n x_{i+1} \cdots x_{j-1} x_1 \cdots x_{i-1} x_i x_j \\ &= E_{d,k}^{n-j} W_{[k^j, k^{n-j}]} x_{i+1} \cdots x_{j-1} x_1 \cdots x_{i-1} x_i x_j \cdots x_n \\ &= E_{d,k}^{n-j} W_{[k^j, k^{n-j}]} W_{[k^i, k^{j-1-i}]} x_1 \cdots x_{i-1} x_i x_{i+1} \cdots x_{j-1} x_j \cdots x_n \\ &\triangleq M_{ij} x_1 x_2 \cdots x_n\ (i < j), \\ &\bigvee_{s=0}^{p-1}\left\{\left[y_i \overline{\nabla} \oslash_{k+}^{s}\left(y_j\right)\right] \vee \left[y_i \overline{\nabla} \oslash_{k-}^{s}\left(y_j\right)\right]\right\} = M_p M_{ij} x = M_{ij,p} x, \end{aligned} \tag{30}$$

where $x = x_1 x_2 \cdots x_n$, $M_{ij,p} = M_p M_{ij}\,(i, j, = 1, 2, \cdots, n)$,

$$M_{ij} = E_{d,k}^{n-j} W_{k^2,k^{n-j}} E_{d,k}^{j-1-i} W_{k,k^{j-1-i}} E_{d,k}^{i-1}\,(i < j), \tag{31}$$

and the product is " $\propto$ ".

Therefore,

$$\sum_{i=1}^{n}\sum_{j>i}\left\{a_{ij}\bigvee_{s=0}^{p-1}\left\{\left[y_i\overline{\vee}\varnothing_{k+}^{s}\left(y_j\right)\right]\vee\left[y_i\overline{\vee}\varnothing_{k-}^{s}\left(y_j\right)\right]\right\}+b_{ij}\bigvee_{s=0}^{q-1}\left\{\left[y_i\overline{\vee}\varnothing_{k+}^{s}\left(y_j\right)\right]\vee\left[y_i\overline{\vee}\varnothing_{k-}^{s}\left(y_j\right)\right]\right\}\right\}, = \sum_{i=1}^{n}\sum_{j>i}\left(a_{ij}M_{ij,p}+b_{ij}M_{ij,q}\right)x. \tag{32}$$

Thus, logical equations (19) are solved if and only if there exists $x = \delta_{k^n}^{v}$ such that

$$\sum_{i=1}^{n}\sum_{j>i}\left(a_{ij}M_{ij,p}+b_{ij}M_{ij,q}\right)x = Mx = 0, \tag{33}$$

that is, the v-th column of M is zero. Then, the proof is complete. □

Based on Theorem 2, we give the following algorithm to find all for the $L(p, q)$ coloring solutions of the given graph.

$$\begin{cases} S_{1,k}^{n} &= \delta_k\left[\underbrace{1\cdots1}_{k^{n-1}}\underbrace{2\cdots2}_{k^{n-1}}\cdots\underbrace{k\cdots k}_{k^{n-1}}\right], \\ S_{2,k}^{n} &= \delta_k\left[\underbrace{1\cdots1}_{k^{n-2}}\underbrace{2\cdots2}_{k^{n-2}}\cdots\underbrace{k\cdots k}_{k^{n-2}}\underbrace{1\cdots1}_{k^{n-2}}\underbrace{2\cdots2}_{k^{n-2}}\cdots\underbrace{k\cdots k}_{k^{n-2}}\right], \\ &\vdots \\ S_{n,k}^{n} &= \delta_k\left[\underbrace{\underbrace{12\cdots k}_{k}\cdots\underbrace{12\cdots k}_{k}}_{k^{n-1}}\right]. \end{cases} \tag{34}$$

Using formula (24), compute $x_i = S_{i,k}^{n}\delta_{k^n}^{s_t}$ and $y_i = [k-1\ \cdots\ 1\ 0]\,x_i$, $i = 1, 2, \cdots, n$. Set

$$S(s_t) = \{f \mid f(v_i) = y_i, \quad i = 1, 2, \cdots, n\}. \tag{35}$$

Then, all $L(p, q)$-label coloring plans of $\mathcal{G}$ are $\{S(s_t) \mid t = 1, 2, \cdots, m\}$. □

4. Illustrative Example

In this section, we give an example to illustrate the effectiveness of the results/algorithms obtained in this paper.

In order to avoid interference with each other, different channels need to be assigned to different base stations in the wireless network. Moreover, the main object of the channel allocation problem is to search an allocation scheme which has the channel as least as possible. Some mathematical models can be used to study the channel allocation problem of the wireless network, including T-coloring, list coloring, set coloring, and $L(p_1, p_2, \cdots, p_n)$-coloring. The most commonly used model is $L(2, 1)$-coloring. Denote by $\mathcal{G}(V, E)$ the topological graph of the wireless network, where V is a node set denoting base stations or their users and E denotes an edge set. Now, we will use the $L(2, 1)$-coloring model to analyze the channel allocation of the wireless network.

Example 1. Construct the telecommunication base stations among four cities denoted by $A \sim D$, respectively. Denote a city by one vertex of the graph. If the base station constructed in city X can cover city Y, then there is an edge between X and Y. Now, the covering graph of base stations $\mathcal{G} = \{\mathcal{V}, \mathcal{E}\}$ is established as shown in Figure 1. Our target is to search all schemes for channel allocation of the wireless network. In the wireless network, the channel interval is greater than or equal to 2 for two adjacent base stations and greater than or equal to 1 for two base stations with distance 2.

From Figure 1, we have its adjacency matrix as the following:

$$A = \begin{bmatrix} 0 & 1 & 1 & 1 \\ 1 & 0 & 0 & 1 \\ 1 & 0 & 0 & 1 \\ 1 & 1 & 1 & 0 \end{bmatrix}. \tag{36}$$

According to A, we have by the above definition

$$B = \begin{bmatrix} 0 & 1 & 1 & 1 \\ 1 & 0 & 1 & 1 \\ 1 & 1 & 0 & 1 \\ 1 & 1 & 1 & 0 \end{bmatrix}. \tag{37}$$

Using Algorithm 1, we can compute the matrix M defined in (26) by the semitensor product. Then, by Matlab, $k = 5$ different channels which are denoted by 0, 1, 2, 3, and 4 are needed to satisfy the requirement in the channel allocation of the wireless network. Moreover, all detailed schemes are corresponding to

$$\mathrm{Col}_i(M) = 0, i = 97, 117, 221, 241, 385, 405, 509, 529. \tag{38}$$

The corresponding channel schemes are shown in Table 1.

For example, for $i = 97$, $y_1 = 4, y_2 = 1, y_3 = 0, y_4 = 3$. That is, channels 4, 1, 0, and 3 are, respectively, assigned to stations A, B, C, and D which satisfies the requirement in the channel allocation of the wireless network. Moreover, from the table, there are at least 4 channels to satisfy the graph.

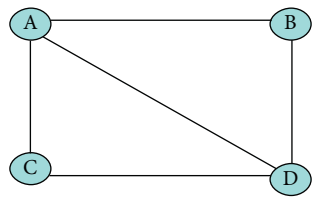

Figure 1: A topological graph of the wireless network.

(1) Compute matrix M by (20).
(2) If there is no common k such that $Col_k(M) = 0$, then $\mathcal{G}$ has no $L(p,q)$-label coloring solution, and stop the calculation. Otherwise, find out the number s such that $Col_s(M) = 0$ and denote these by $s_1, s_2, \ldots, s_m$.
(3) For each index $s_1, s_2, \ldots, s_m$, let $\propto_{i=1}^{n} x_i = \delta_{k^n}^{s_i}$, $t = 1, 2, \ldots, m$. Let [11]

Algorithm 1: Given a graph $\mathcal{G}$ with nodes $\mathcal{V} = \{v_1, v_2, \ldots, v_n\}$, establish a logical function $f(v_i) = y_i \in \{0, 1, \ldots, k-1\}$ and let $x_i = \delta_k^{k-y_i}$, $i = 1, 2, \ldots, n$. To determine all $L(p,q)$-label coloring plans of $\mathcal{G}$, we can do by the following steps:

Table 1: Corresponding channel schemes.

i	(y_1, y_2, y_3, y_4)	(A, B, C, D)
97	(4, 1, 0, 3)	(4, 1, 0, 3)
117	(4, 0, 1, 3)	(4, 0, 1, 3)
221	(3, 1, 0, 4)	(3, 1, 0, 4)
241	(3, 0, 1, 4)	(3, 0, 1, 4)
385	(1, 4, 3, 0)	(1, 4, 3, 0)
405	(1, 3, 4, 0)	(1, 3, 4, 0)
509	(0, 4, 3, 1)	(0, 4, 3, 1)
529	(0, 3, 4, 1)	(0, 3, 4, 1)

5. Conclusion

The $L(p,q)$-coloring problem of the graph is studied with application to channel allocation of the wireless network in this paper. The necessary and sufficient conditions for solving the $L(p,q)$-coloring problem are given by introducing two new logical operators. Moreover, it is noted that all solutions of the obtained logical equations are corresponding to each coloring scheme. By using the semitensor product, the necessary and sufficient conditions are converted to an algebraic form. Based on this, all coloring schemes can be obtained through searching all column indices of the zero columns. Furthermore, an illustration example on channel allocation of the wireless network is given to show the effectiveness of the obtained results in this paper. In future, we plan to study other coloring problems by using the semitensor product method, i.e., T-coloring, list coloring, and set coloring.

Data Availability

The data used to support the findings of this study are included within the article.

Conflicts of Interest

The authors declare that they have no conflicts of interest.

Acknowledgments

This work was supported by the National Natural Science Foundation of China (G61673243, G69674001, and G61403223), the Postdoctoral Science Foundation Funded Project of China (2017M612234), and the Research Fund for High-Level Personnel of Qingdao Agricultural University (631426).

References

[1] Y. Wang, C. Zhang, and Z. Liu, "A matrix approach to graph maximum stable set and coloring problems with application to multi-agent systems," *Automatica*, vol. 48, no. 7, pp. 1227–1236, 2012.
[2] R. J. Lipton and R. E. Tarjan, "A separator theorem for planar graphs," *SIAM Journal on Applied Mathematics*, vol. 36, no. 2, pp. 177–189, 1979.
[3] G. Serpen and A. Parvin, "On the performance of hopfield network for graph search problem," *Neurocomputing*, vol. 14, no. 4, pp. 365–381, 1997.
[4] R. Tarjan, "Depth-first search and linear graph algorithms," *SIAM Journal on Computing*, vol. 1, no. 2, pp. 146–160, 1972.
[5] W. K. Hale, "Frequency assignment: theory and applications," *Proceedings of the IEEE*, vol. 45, 1980.
[6] J. R. Griggs and R. K. Yeh, "Labelling graphs with a condition at distance 2," *SIAM Journal on Discrete Mathematics*, vol. 5, no. 4, pp. 586–595, 1992.
[7] S. Amanathulla, S. Sahoo, and M. Pal, "$L(3,1,1)$-labeling numbers of square of paths, complete graphs and complete bipartite graphs," *Journal of Intelligent and Fuzzy Systems*, vol. 36, 2019.
[8] S. Ghosh, P. Sarkar, and A. Pal, "Exact algorithm for $L(2, 1)$ labeling of cartesian product between complete bipartite graph and cycle," *Harmony Search and Nature Inspired Optimization Algorithms*, vol. 741, pp. 325–334, 2018.
[9] S. Paul, M. Pal, and A. Pal, "$L(2,1)$-labeling of interval graphs," *Journal of Applied Mathematics and Computing*, vol. 49, no. 1-2, pp. 419–432, 2015.
[10] M. Xu and L. Sun, "The $L(2,1)$-labeling problem via the semitensor product method," in *Proceedings of the 37th Chinese Control Conference*, pp. 823–828, Wuhan, China, 2018.

[11] D. Cheng, H. Qi, and Z. Li, *Analysis and Control of Boolean Networks: A Semi-tensor Product Approach*, Springer, London, UK, 2011.

[12] H. Li, G. Zhao, P. Guo, and Z. Liu, *Analysis and Control of Finite-Value Systems*, CRC Press, Boca Raton, FL, USA, 2018.

[13] H. Li, G. Zhao, M. Meng, and J. Feng, "A survey on applications of semi-tensor product method in engineering," *Science China-Information Sciences*, vol. 61, no. 1, pp. 1–17, 2018.

[14] Y. Guo, P. Wang, W. Gui, and C. Yang, "Set stability and set stabilization of boolean control networks based on invariant subsets," *Automatica*, vol. 61, pp. 106–112, 2015.

[15] H. Li and Y. Wang, "Further results on feedback stabilization control design of boolean control networks," *Automatica*, vol. 83, pp. 303–308, 2015.

[16] H. Li and Y. Wang, "Lyapunov-based stability and construction of lyapunov functions for boolean networks," *SIAM Journal on Control and Optimization*, vol. 55, no. 6, pp. 3437–3457, 2017.

[17] H. Li, Y. Wang, and Z. Liu, "A semi-tensor product approach to pseudo-boolean functions with application to boolean control networks," *Asian Journal of Control*, vol. 16, no. 4, pp. 1073–1081, 2014.

[18] H. Li, L. Xie, and Y. Wang, "On robust control invariance of boolean control networks," *Automatica*, vol. 68, pp. 392–396, 2016.

[19] H. Li, L. Xie, and Y. Wang, "Output regulation of boolean control networks," *IEEE Transactions on Automatic Control*, vol. 62, no. 6, pp. 2993–2998, 2017.

[20] L. Lin, S. Zhu, Y. Liu, Z. Wang, and F. E. Alsaadi, "Output regulation of boolean control networks with nonuniform sampled-data control," *IEEE Access*, vol. 7, pp. 50691–50696, 2019.

[21] M. Meng, J. Lam, X. Li, and J.-E. Li, "l_1-gain analysis and model reduction problem for Boolean control networks," *Information Sciences*, vol. 348, pp. 68–83, 2016.

[22] M. Meng, G. Xiao, C. Zhai, and G. Li, "Controllability of markovian jump boolean control networks," *Automatica*, vol. 10, pp. 70–76, 2019.

[23] J. Zhong, J. Lu, T. Huang, W. Daniel, and C. Ho, "Controllability and synchronization analysis of identical-hierarchy mixed-valued logical control networks," *IEEE Transactions on Cybernetics*, vol. 47, no. 11, pp. 3482–3493, 2016.

[24] Y. Liu, L. Wang, J. Lu, and J. Cao, "Sampled-data stabilization of probabilistic boolean control networks," *Systems & Control Letters*, vol. 124, pp. 106–111, 2019.

[25] Z. Liu, Y. Wang, and H. Li, "Controllability of context-sensitive probabilistic mix-valued logical control networks with constraints," *Asian Journal of Control*, vol. 17, no. 1, pp. 246–254, 2015.

[26] S. Fu, Y. Wang, and G. Zhao, "A matrix approach to the analysis and control of networked evolutionary games with bankruptcy mechanism," *Asian Journal of Control*, vol. 19, no. 2, pp. 717–727, 2017.

[27] Y. Wang and D. Cheng, "Stability and stabilization of a class of finite evolutionary games," *Journal of the Franklin Institute*, vol. 354, no. 3, pp. 1603–1617, 2017.

[28] J. Zhong, J. Lu, C. Huang, L. Li, and J. Cao, "Finding graph minimum stable set and core via semi-tensor product approach," *Neurocomputing*, vol. 174, pp. 588–596, 2016.

[29] Z. Liu, Y. Wang, and D. Cheng, "Nonsingularity of feedback shift registers," *Automatica*, vol. 55, no. 5, pp. 247–253, 2015.

[30] B. Wang, M. Feng, and J.-E. Meng, "Matrix approach to detectability of discrete event systems," *Journal of the Franklin Institute*, vol. 356, no. 12, pp. 6460–6477, 2019.

[31] J. Zhao, Z. Chen, and Z. Liu, "A novel matrix approach for the stability and stabilization analysis of colored petri nets," *Science China-Information Sciences*, vol. 62, no. 9, p. 192202, 2019.

[32] F. Tao and G. Gu, "$L(2,1)$-labeling problem on distance graphs," *Journal of Southeast University*, vol. 20, no. 1, pp. 122–125, 2004.

Hindawi
Mathematical Problems in Engineering
Volume 2020, Article ID 1768507, 11 pages
https://doi.org/10.1155/2020/1768507

Research Article

A Necessary Condition for Optimal Control of Forward-Backward Stochastic Control System with Lévy Process in Nonconvex Control Domain Case

Hong Huang,[1] **Xiangrong Wang**,[2] **and Ying Li**[3,4]

[1]*School of Data and Computer Science, Shandong Women's University, Jinan 250300, China*
[2]*Institute of Financial Engineering, Shandong University of Science and Technology, Qingdao 266590, China*
[3]*Office of Academic Research, Shandong Women's University, Jinan 250300, China*
[4]*College of Computer Science and Engineering, Shandong University of Science and Technology, Qingdao 266590, China*

Correspondence should be addressed to Ying Li; cherry_jn@126.com

Received 10 April 2020; Accepted 18 May 2020; Published 3 June 2020

Guest Editor: Yi Qi

This paper analyzes one kind of optimal control problem which is described by forward-backward stochastic differential equations with Lévy process (FBSDEL). We derive a necessary condition for the existence of the optimal control by means of spike variational technique, while the control domain is not necessarily convex. Simultaneously, we also get the maximum principle for this control system when there are some initial and terminal state constraints. Finally, a financial example is discussed to illustrate the application of our result.

1. Introduction

Stochastic optimal control is an important matter that cannot be neglected in modern control theory in long days. As is known to all, Pontryagin's [1] maximum principle is one of the main ways to settle the stochastic optimal control problem. By introducing the Hamiltonian function, a necessary condition for the optimal control of stochastic control systems was given by him, which was called the maximum condition. From that time, plenty of works on this issue have been done. Peng [2] was the first one to prove the general maximum principle of the forward-backward stochastic control system with diffusion coefficient containing the control variable by the technique of the second-order Taylor expansion and the second-order duality. He [3] was also the first one to demonstrate the maximum principle of forward-backward stochastic control systems from the view of backward stochastic differential equations (BSDE). In Peng's paper [3], the control domain was convex (in local form); Xu [4] extended this conclusion to the case of the nonconvex control domain (in global form), but the control variables were not included in the diffusion coefficient. And these results were extended to the fully coupled case in the form of local and global by Shi and Wu [5, 6] in 1998 and in 2006, respectively. On the basis of these works, Situ [7] was the first to obtain the maximum principle of the forward stochastic control system with global form of random jumps in 1991. Shi and Wu [8] and Shi [9] acquired the maximum principle for a kind of forward-backward stochastic control system with Poisson jumps in the form of local and global, respectively. The fully coupled forward-backward stochastic control system was extended by Liu et al. [10] at the base of Shi and Wu [8], and in the meanwhile, they also obtained the maximum principle with the control system be constrained about initial-terminal state constraints. Considering that in real life, the decision makers could only get partial information but not complete information in most cases; many scholars have paid attention to the partial observable stochastic optimal control problem and have achieved many results (see, for example, [11–13]). Traditionally, when using a stochastic partial differential equation called the Zakai equation to transform a full-information optimal control problem to the partially observable case, scholars will encounter a difficult problem: an infinite-dimensional optimal control problem. Wang and Wu [14] proposed a backward separation approach and replaced the original state and observation equation with the Zakai equation,

and lots of complicated stochastic calculi in infinite-dimensional spaces were avoided in this way. Based on this approach, Xiao [15] studied a partially observed optimal control of forward-backward stochastic systems with random jumps and obtained the maximum principle and sufficient conditions of an optimal control under some certain convexity assumptions. Wang et al. [16] proved the maximum principles for forward-backward stochastic control systems with correlated state and observation noises. More recent conclusions of the partially observed stochastic control problem can be seen from the studies conducted by Wang et al. [17], Zhang et al. [18], and Xiong et al. [19].

In these years, through the study of mathematical economics and mathematical finance, many scholars turn their attention to the stochastic control system driven by Lévy process. In 2000, Nualart and Schoutens [20] built a pair of pairwise strongly orthonormal martingales which was called the Teugels martingale. Meanwhile, under some exponential moment conditions, they also obtained a martingale representation in that paper. Under these two important conclusions, for BSDE driven by the Teugels martingale, they [21] proved the existence and uniqueness theorem of its solution in the next year. From then on, a number of important results were proved: Meng and Tang [22] obtained the maximum principle of the forward stochastic control system driven by Lévy process. A necessary and sufficient condition for the existence of the optimal control of backward stochastic control systems driven by Lévy process was deduced by Tang and Zhang [23] through convex variation methods and duality techniques. For the forward-backward stochastic control system driven by Lévy process, there are also a lot of achievements: based on the existence and uniqueness theorem of FBSDEL [24], Zhang et al. [25] obtained a necessary condition of the optimal control and verification theorem, but in their control system, the backward state variables y_t and z_t did not enter the forward part. Wang and Huang [26] extended this result to the fully coupled control system and obtained the continuity result depending on parameters about FBSDEL and the local form maximum principle. Subsequently, Huang et al. [27] studied this control system with terminal state constraints and obtained the corresponding necessary maximum principle using Ekeland's variational. For more recent conclusions about the stochastic control problem driven by Lévy process, please refer to [28–30].

In this paper, we will study the optimal control problem for forward-backward stochastic control systems driven by Lévy process, which could be considered as a nonconvex control domain case that is extended from the result of [25]. With the technique of spike variation and Ekeland's variational principle, the maximum principle of this type of control system and the control system with initial and final state constraints are obtained.

The structure of this paper is as follows. Section 2 describes some of the preparations used in this paper. The maximum principle and the one with initial and terminal state constraints as the major results of this paper will be shown in Sections 3 and 4. As an application of the maximum principle, Section 5 gives an optimal consumption problem in the financial market. Section 6 is the summary of this article.

2. Preliminary Statement

Let $(\Omega, \mathscr{F}_t, P)$ be a complete probability space which satisfied the usual conditions, and the information structure is given by $\mathscr{F}_t$ which is generated by two processes: a standard Brownian motion $\{B_t\}_{0\le t\le T}$ valued in R^d and an independent 1-dimensional Lévy process $\{L_t\}_{0\le t\le T}$ of the form $L_t = b_t + l_t$; here, l_t is a pure jump process. And assume that Lévy measure ν satisfies the following two conditions; thereby, Lévy process $\{L_t\}_{0\le t\le T}$ has moments in all orders.

(i) $\int_R (1\wedge x^2)\nu(\mathrm{d}x) < \infty$.

(ii) $\int_{(-\varepsilon,\varepsilon)^c} e^{\lambda|x|}\nu(\mathrm{d}x) < \infty$, $\forall \varepsilon > 0$ and some $\lambda > 0$.

Denote $L_t^1 = L_t$, $\triangle L_t = L_t - L_{t-}$, and $L_t^i = \sum_{0<s\le t}(\triangle L_s)^i$ for $i \ge 2$. And let $Y_t^i = L_t^i - E[L_t^i]$ $(i \ge 1)$ be the compensated power jump process of order i; then, Teugels martingale is defined by $H_t^i = \sum_{j=1}^i c_{ij} Y_t^j$; the coefficients c_{ij} correspond to orthonormalization of the polynomials $1, x, x^2, \cdots$ with respect to the measure $\mu(\mathrm{d}x) = v(\mathrm{d}x) + \sigma^2\delta_0(\mathrm{d}x)$.

Then, $\{H_t^i\}_{i=1}^\infty$ are pairwise strongly orthogonal martingales, and their predictable quadratic variation processes are $\langle H_t^i, H_t^j\rangle = \delta_{ij}t$, δ_{ij} is an indicator function here. And $[H^i, H^j]_t - \langle H_t^i, H_t^j\rangle$ is an $\mathscr{F}_t$–martingale; for more details of the Teugels martingale, see Nualart and Schoutens [20].

In the following of this section, we shall assume some notations: for a Hilbert space $\mathscr{H}$,

$l^2(\mathscr{H}) := \left\{\phi \mid \mathscr{H} - \text{valued}, \sum_{i=1}^\infty \|\phi^i\|^2 < \infty\right\}$.

$L^2(\Omega, \mathscr{H}) := \{\xi \mid$
$\mathscr{H}$ valued, $\mathscr{F}_T -$ measurable, $E|\xi|^2 < \infty\}$.

$l^2(0, T; \mathscr{H}) := \{\phi_t^i \mid l^2(\mathscr{H})-$
valued, $\mathscr{F}_t -$ measurable, $\sum_{i=1}^\infty E\int_0^T \|\phi_t^i\|^2 \mathrm{d}t < \infty\}$.

$M^2(0, T; \mathscr{H}) := \{\phi(\cdot) \mid$
$\mathscr{H} -$ valued, $\mathscr{F}_t -$ measurable, $E\int_0^T |\phi_t|^2 \mathrm{d}t < \infty\}$.

For the following FBSDEL,

$$\begin{cases} \mathrm{d}x_t = b(t, x_t, y_t, z_t, r_t)\mathrm{d}t + \sigma(t, x_t, y_t, z_t, r_t)\mathrm{d}B_t + \sum_{i=1}^\infty g^i(t, x_{t-}, y_{t-}, z_t, r_t)\mathrm{d}H_t^i, \\ -\mathrm{d}y_t = f(t, x_t, y_t, z_t, r_t)\mathrm{d}t - z_t\mathrm{d}B_t - \sum_{i=1}^\infty r_t^i \mathrm{d}H_t^i, \\ x_0 = a, y_T = \Phi(x_T), \end{cases} \tag{1}$$

where (x_t, y_t, z_t, r_t) take the value in $\Omega \times [0,T] \times R^n \times R^m \times R^{m\times d} \times l^2(R^m)$ and mappings b, σ, g, and f take the value in R^n, $R^{n\times d}$, $l^2(R^n)$, and R^m, respectively. Convenient for writing, set column vector $\alpha = (x, y, z)^T$ and $A(t,\alpha,r) = (-M^\tau f(t,\alpha,r), Mb(t,\alpha,r), M\sigma(t,\alpha,r))^T$, where M is a $m \times n$ full rank matrix.

Assumption 1

(i) All mappings in equation (1) are uniformly Lipschitz continuous in their own arguments, respectively.

(ii) For all $(\omega, t) \in \Omega \times [0,T]$, $l(\omega, t, 0, 0, 0, 0) \in M^2(0,T; R^{n+m+m\times d}) \times l^2(0,T; R^m)$ for $l = b, f, \sigma$, respectively, and $g(\omega, t, 0, 0, 0, 0) \in l^2(R^n)$.

(iii) $\langle \Phi(\overline{x}) - \Phi(x), M(\overline{x} - x)\rangle \geq \beta |M\widehat{x}|^2$.

(iv) $\langle A(t,\overline{\alpha},\overline{r}) - A(t,\alpha,r), \overline{\alpha} - \alpha\rangle + \sum_{i=1}^{\infty}\langle M\widehat{g^i}, \widehat{r^i}\rangle \leq -\mu_1 |M\widehat{x}|^2 - \mu_2(|M^\tau\widehat{y}|^2 + |M^\tau\widehat{z}|^2 + \sum_{i=1}^{\infty}\|M^\tau\widehat{r^i}\|^2)$, where $\overline{\alpha} = (\overline{x}, \overline{y}, \overline{z}), \widehat{x} = \overline{x} - x, \widehat{y} = \overline{y} - y, \widehat{z} = \overline{z} - z$, $\widehat{r^i} = \overline{r}^i - r^i, \widehat{g^i} = g^i(t,\overline{\alpha},\overline{r}) - g^i(t,\alpha,r)$. μ_1, μ_2, and β are nonnegative constants which satisfied $\mu_1 + \mu_2 > 0$, $\mu_2 + \beta > 0$, and $\mu_1 > 0, \beta > 0$(resp. $\mu_2 > 0$) when $m > n$ (resp. $n > m$).

Then, the following existence and uniqueness of the solution conclusion holds.

Lemma 1. *There exists a unique solution in $M^2(0,T;\mathscr{H})$ satisfying FBSDEL (1) under Assumption 1.*

The detailed certification process of this conclusion can be seen in [24].

3. Stochastic Maximum Principle

In this section, for any given admissible control $u(\cdot)$, we consider the following stochastic control system:

$$\begin{cases} \mathrm{d}x_t = b(t, x_t, u_t)\mathrm{d}t + \sigma(t, x_t)\mathrm{d}B_t + \sum_{i=1}^{\infty} g^i(t, x_{t-})\mathrm{d}H_t^i, \\ -\mathrm{d}y_t = f(t, x_t, y_t, z_t, r_{t,}, u_t)\mathrm{d}t - z_t\mathrm{d}B_t - \sum_{i=1}^{\infty} r_t^i \mathrm{d}H_t^i, \\ x_0 = a,\ y_T = \Phi(x_T),\ t \in [0,T], \end{cases} \tag{2}$$

where $a \in R^n$ is given. An admissible control $u(\cdot) \in M^2(0,T;R^p)$ is an $\mathscr{F}_t$-predictable process which takes values in a nonempty subset U of R^p; U_{ad} is the set of all admissible controls.

And the performance criterion is

$$J(u) = E\gamma(y_0), \tag{3}$$

where $\gamma: R^m \longrightarrow R$ is a given Frechet differential function.

Our optimal control problem amounts to determining an admissible control $u^* \in U_{\mathrm{ad}}$ such that

$$J(u^*(\cdot)) = \inf_{u(\cdot)\in U_{\mathrm{ad}}} J(u(\cdot)). \tag{4}$$

In order to get the necessary conditions for the optimal control, we assume u_t^* is the optimal control, and the corresponding solution of (2) is recorded as $(x_t^*, y_t^*, z_t^*, r_t^*)$ and introduce the "spike variational control" as follows:

$$u_t^\varepsilon = \begin{cases} v_t, & \tau \leq t \leq \tau + \varepsilon, \\ u_t^*, & \text{otherwise}, \end{cases} \tag{5}$$

and $(x_t^\varepsilon, y_t^\varepsilon, z_t^\varepsilon, r_t^\varepsilon)$ are the state trajectories of u_t^ε; here, v_t is an arbitrary admissible control and ε is a sufficiently small constant.

We also need the following assumption and variational equation (6).

Assumption 2

(i) b, f, g, σ, Φ, and γ are continuously differentiable with respect to (x, y, z, r, u), and the derivatives are all bounded.

(ii) There exists a constant $C > 0$, and it holds that $|\gamma_y| \leq C(1 + |y|)$.

$$\begin{cases} \mathrm{d}X_t = [b_x(t)X_t + b(t, u_t^\varepsilon) - b(t, u_t^*)]\mathrm{d}t + \sigma_x(t)X_t\mathrm{d}B_t + \sum_{i=1}^{\infty} g_x^i(t)X_t\mathrm{d}H_t^i, \\ -\mathrm{d}Y_t = [f_x(t)X_t + f_y(t)Y_t + f_z(t)Z_t + f_r(t)R_t + f(t, u_t^\varepsilon) - f(t, u_t^*)]\mathrm{d}t, \\ -Z_t\mathrm{d}B_t - \sum_{i=1}^{\infty} R_t^i\mathrm{d}H_t^i, \\ X_0 = 0, \\ Y_T = \Phi_x(t)X_T. \end{cases} \tag{6}$$

Here, $b_x(t) = b_x(t, x_t^*, u_t^*)$, $\sigma_x(t) = \sigma_x(t, x_t^*)$, $g_x^i(t) = g_x^i(t, x_t^*)$, $b(t, u_t^\varepsilon) = b(t, x_t^\varepsilon, u_t^\varepsilon)$, $b(t, u_t^*) = b(t, x_t^*, u_t^*)$, $f_w(t) = f_w(t, x_t^*, y_t^*, z_t^*, r_t^*, u_t^*)$, $(w = x, y, z \cdot r)$, $f(t, u_t^\varepsilon) = f(x_t^\varepsilon, y_t^\varepsilon, z_t^\varepsilon, r_t^\varepsilon, u_t^\varepsilon)$, and $f(t, u_t^*) = f(x_t^*, y_t^*, z_t^*, r_t^*, u_t^*)$.

Lemma 2. *Suppose Assumptions 1 and 2 hold; for the first-order variation X, Y, Z, R, we have the following estimations:*

$$\sup_{0\le t\le T} E|X_t|^2 \le C\varepsilon^2, \tag{7}$$

$$\sup_{0\le t\le T} E|X_t|^4 \le C\varepsilon^4, \tag{8}$$

$$\sup_{0\le t\le T} E|Y_t|^2 \le C\varepsilon^2, \tag{9}$$

$$\sup_{0\le t\le T} E|Y_t|^4 \le C\varepsilon^4, \tag{10}$$

$$\sup_{0\le t\le T} E\int_0^T |Z_t|^2 \mathrm{d}s \le C\varepsilon^2, \tag{11}$$

$$\sup_{0\le t\le T} E\left(\int_0^T |Z_t|^2 \mathrm{d}s\right)^2 \le C\varepsilon^4, \tag{12}$$

$$\sup_{0\le t\le T} E\int_0^T \|R_t\|^2 \mathrm{d}s \le C\varepsilon^2, \tag{13}$$

$$\sup_{0\le t\le T} E\left(\int_0^T \|R_t\|^2 \mathrm{d}s\right)^2 \le C\varepsilon^4. \tag{14}$$

Proof. We first prove inequations (7) and (8). For the forward part of the first-order variation equation, we have

$$\begin{aligned} E|X_t|^2 &= E\left\{\int_0^t [b_x(s)X_s + b(s, u_s^\varepsilon) - b(s, u_s^*)]\mathrm{d}s + \sigma_x(s)X_s \mathrm{d}B_s + \sum_{i=1}^\infty g_x^i(s)X_s \mathrm{d}H_s^i\right\}^2 \\ &\le 4\left\{E\left(\int_0^t b_x(s)X_s \mathrm{d}s\right)^2 + E\left(\int_0^t [b(s, u_s^\varepsilon) - b(s, u_s^*)]\mathrm{d}s\right)^2 + E\int_0^t [\sigma_x(s)X_s]^2 \mathrm{d}s + E\int_0^t \left[\sum_{i=1}^\infty g_x^i(s)X_s\right]^2 \mathrm{d}s\right\} \\ &\le 12C^2 TE\int_0^t X_s^2 \mathrm{d}s + 4E\left(\int_0^t [b(s, u_s^\varepsilon) - b(s, u_s^*)]\mathrm{d}s\right)^2. \end{aligned} \tag{15}$$

Applying Gronwall's inequation, we have

$$E|X_t|^2 \le C\varepsilon^2, \quad \text{for all } t \in [0, T]. \tag{16}$$

Similarly, (8) holds.

We next estimate Y_t, Z_t, and R_t; the backward part of the first-order variation equation can be rewritten as

$$\begin{aligned} Y_t + \int_t^T Z_s \mathrm{d}B_s + \int_t^T \sum_{i=1}^\infty R_s^i \mathrm{d}H_s^i = \Phi_x(t)X_T + \int_t^T [&f_x(t)X_t \\ &+ f_y(t)Y_t + f_z(t)Z_t \\ &+ f_r(t)R_t \\ &+ f(t, u_t^\varepsilon) - f(t, u_t^*)]\mathrm{d}t. \end{aligned} \tag{17}$$

Squaring both sides of (17) and using the fact of

$$\begin{aligned} EY_t \int_t^T Z_s \mathrm{d}B_s &= 0, \\ EY_t \int_t^T \sum_{i=1}^\infty R_s^i \mathrm{d}H_s^i &= 0, \\ E\int_t^T Z_s \mathrm{d}B_s \int_t^T \sum_{i=1}^\infty R_s^i dH_s^i &= 0, \end{aligned} \tag{18}$$

we get

$$\begin{aligned} &E|Y_t|^2 + E\int_t^T Z_s^2 \mathrm{d}s + E\int_t^T \left(\sum_{i=1}^\infty R_s^i\right)^2 \mathrm{d}H_s^i \\ &= E\left\{\Phi_x(t)X_T + \int_t^T \left[f_x(t)X_t + f_y(t)Y_t + f_z(t)Z_t + f_r(t)R_t + f(t, u_t^\varepsilon) - f(t, u_t^*)\right]\mathrm{d}t\right\}^2 \\ &\le 6C^2 EX_T^2 + 6C^2 TE\int_t^T X_s^2 \mathrm{d}s + 6C^2 TE\int_t^T Y_s^2 \mathrm{d}s + 6C^2(T-t)E\int_t^T Z_s^2 \mathrm{d}s \\ &\quad + 6C^2(T-t)E\int_t^T \left(\sum_{i=1}^\infty R_s^i\right)^2 \mathrm{d}s + 6E\left(\int_t^T (f(s, u_s^\varepsilon) - f(s, u_s^*))\mathrm{d}s\right)^2. \end{aligned} \tag{19}$$

When $t \in [T-\delta, T]$ with $\delta = 1/12C^2$, we have

$$\begin{aligned} &E|Y_t|^2 + \frac{1}{2}E\int_t^T Z_s^2 \mathrm{d}s + \frac{1}{2}E\int_t^T \left(\sum_{i=1}^{\infty} R_s^i\right)^2 \mathrm{d}H_s^i \\ &\le 6C^2 E X_T^2 + 6C^2 T E\int_t^T X_s^2 \mathrm{d}s + 6C^2 T E \\ &\cdot \int_t^T Y_s^2 \mathrm{d}s + 6E\left(\int_t^T \left(f(s,u_s^\varepsilon) - f(s,u_s^*)\right)\mathrm{d}s\right)^2. \end{aligned} \tag{20}$$

Applying Gronwall's inequation, we have

$$\begin{aligned} &\sup_{0\le t\le T} E|Y_t|^2 \le C\varepsilon^2, \quad t \in [T-\delta, T]; \\ &\sup_{0\le t\le T} E\int_0^T |Z_t|^2 \mathrm{d}s \le C\varepsilon^2, \quad t \in [T-\delta, T]; \\ &\sup_{0\le t\le T} E\int_0^T \|R_t\|^2 \mathrm{d}s \le C\varepsilon^2, \quad t \in [T-\delta, T]. \end{aligned} \tag{21}$$

Consider the BSDE of the first-order variation equation in the interval $[t, T-\delta]$:

$$\begin{aligned} &Y_t + \int_t^{T-\delta} Z_s \mathrm{d}B_s + \int_t^{T-\delta}\sum_{i=1}^{\infty} R_s^i \mathrm{d}H_s^i = Y_{T-\delta} \\ &\quad + \int_t^{T-\delta}\left[f_x(t)X_t + f_y(t)Y_t + f_z(t)Z_t \right. \\ &\quad \left. + f_r(t)R_t + f(t,u_t^\varepsilon) - f(t,u_t^*)\right]\mathrm{d}t. \end{aligned} \tag{22}$$

Thus,

$$\begin{aligned} &E|Y_t|^2 + E\int_t^{T-\delta} Z_s^2 \mathrm{d}s + E\int_t^{T-\delta}\left(\sum_{i=1}^{\infty} R_s^i\right)^2 \mathrm{d}H_s^i, \\ &= E\left\{Y_{T-\delta} + \int_t^{T-\delta}\left[f_x(t)X_t + f_y(t)Y_t + f_z(t)Z_t + f_r(t)R_t \right.\right. \\ &\quad \left.\left. + f(t,u_t^\varepsilon) - f(t,u_t^*)\right]\mathrm{d}t\right\}^2 \\ &\le 6C^2 E X_T^2 + 6C^2 T E\int_t^{T-\delta} X_s^2 \mathrm{d}s + 6C^2 T E\int_t^{T-\delta} Y_s^2 \mathrm{d}s \\ &\quad + 6C^2(T-t)E\int_t^{T-\delta} Z_s^2 \mathrm{d}s + 6C^2(T-t)E \\ &\quad \cdot \int_t^{T-\delta}\left(\sum_{i=1}^{\infty} R_s^i\right)^2 \mathrm{d}s + 6E\left(\int_t^{T-\delta}\left(f(s,u_s^\varepsilon) - f(s,u_s^*)\right)\mathrm{d}s\right)^2. \end{aligned} \tag{23}$$

So, when $t \in [T-2\delta, T]$ with $\delta = 1/12C^2$, we have

$$\begin{aligned} &\sup_{0\le t\le T} E|Y_t|^2 \le C\varepsilon^2, \quad t \in [T-2\delta, T], \\ &\sup_{0\le t\le T} E\int_0^T |Z_t|^2 \mathrm{d}s \le C\varepsilon^2, \quad t \in [T-2\delta, T], \\ &\sup_{0\le t\le T} E\int_0^T \|R_t\|^2 \mathrm{d}s \le C\varepsilon^2, \quad t \in [T-2\delta, T]. \end{aligned} \tag{24}$$

After a finite number of iterations, (9), (11), and (13) are obtained. And (10), (12), and (14) can be proved by using a similar method and the following inequalities: $E(\int_t^T Z_s \mathrm{d}B_s)^4 \ge \beta_1 E(\int_t^T Z_s^2 \mathrm{d}s)^2, \beta_1 > 0$; $E(\int_t^T \sum_{i=1}^{\infty} R_s^i \mathrm{d}H_s^i)^4 \ge \beta_2 E(\int_t^T (\sum_{i=1}^{\infty} R_s^i)^2 \mathrm{d}s)^2, \beta_2 > 0$. □

Lemma 3. *Under hypothesis, Assumptions 1 and 2, it holds the following four estimations:*

$$\sup_{0\le t\le T} E|x_t^\varepsilon - x_t^* - X_t|^2 \le C_\varepsilon \varepsilon^2, \quad C_\varepsilon \longrightarrow 0, \text{when } \varepsilon \longrightarrow 0, \tag{25}$$

$$\sup_{0\le t\le T} E|y_t^\varepsilon - y_t^* - Y_t|^2 \le C_\varepsilon \varepsilon^2, \quad C_\varepsilon \longrightarrow 0, \text{when } \varepsilon \longrightarrow 0, \tag{26}$$

$$E\int_0^T |z_t^\varepsilon - z_t^* - Z_t|^2 \mathrm{d}s \le C_\varepsilon \varepsilon^2, \quad C_\varepsilon \longrightarrow 0, \text{when } \varepsilon \longrightarrow 0, \tag{27}$$

$$E\int_t^T \|r_t^\varepsilon - r_t^* - R_t\|^2 \mathrm{d}s \le C_\varepsilon \varepsilon^2, \quad C_\varepsilon \longrightarrow 0, \text{when } \varepsilon \longrightarrow 0. \tag{28}$$

Proof. To prove (25), we observe that

$$\begin{aligned} &\int_0^t b(s, x_s^* + X_s, u_s^\varepsilon)\mathrm{d}s + \int_0^t \sigma(s, x_s^* + X_s)\mathrm{d}B_s \\ &\quad + \int_0^t \sum_{i=1}^{\infty} g^i(s, x_{s-}^* + X_{s-})\mathrm{d}H_s^i \\ &= \int_0^t \left[b(s, x_s^*, u_s^\varepsilon) + \int_0^1 b_x(s, x_s^* + \lambda X_s, u_s^\varepsilon)\mathrm{d}\lambda X_s\right]\mathrm{d}s \\ &\quad + \int_0^t \left[\sigma(s, x_s^*) + \int_0^1 \sigma_x(s, x_s^* + \lambda X_s)\mathrm{d}\lambda X_s\right]\mathrm{d}B_s \\ &\quad + \int_0^t \left[\sum_{i=1}^{\infty} g^i(s, x_s^*) + \int_0^1 \sum_{i=1}^{\infty} g_x^i(s, x_s^* + \lambda X_s) d\lambda X_s\right]\mathrm{d}H_s^i \\ &= \int_0^t b(s, x_s^*, u_s^*)\mathrm{d}s + \int_0^t \sigma(s, x_s^*)\mathrm{d}B_s + \int_0^t \sum_{i=1}^{\infty} g^i(s, x_s^*)\mathrm{d}H_s^i \\ &\quad + \int_0^t b_x(s, x_s^*, u_s^*)X_s \mathrm{d}s + \int_0^t \sigma_x(s, x_s^*)X_s \mathrm{d}B_s \\ &\quad + \int_0^t \sum_{i=1}^{\infty} g_x^i(s, x_{s-}^*)\mathrm{d}H_s^i \\ &\quad + \int_0^t \left[b(s, x_s^*, u_s^\varepsilon) - b(s, x_s^*, u_s^*)\right]\mathrm{d}s + \int_0^t A^\varepsilon \mathrm{d}s \\ &\quad + \int_0^t B^\varepsilon \mathrm{d}B_s + \int_0^t C^\varepsilon \mathrm{d}H_s^i \\ &= x_t^* - x_0 + X_t + \int_0^t A^\varepsilon \mathrm{d}s + \int_0^t B^\varepsilon \mathrm{d}B_s + \int_0^t C^\varepsilon \mathrm{d}H_s^i, \end{aligned} \tag{29}$$

where

$$A^{\varepsilon} = \int_0^1 [b_x(s, x_s^* + \lambda X_s, u_s^{\varepsilon}) - b_x(s, x_s^*, u_s^*)]\mathrm{d}\lambda X_s,$$
$$B^{\varepsilon} = \int_0^1 [\sigma_x(s, x_s^* + \lambda X_s) - \sigma_x(s, x_s^*)]\mathrm{d}\lambda X_s, \tag{30}$$
$$C^{\varepsilon} = \int_0^1 \left[\sum_{i=1}^{\infty}\left(g_x^i(s, x_s^* + \lambda X_s) - g_x^i(s, x_s^*)\right)\right]\mathrm{d}\lambda X_s.$$

It follows easily from Lemma 2 that

$$\sup_{0\le t\le T} E\left[\left(\int_0^t A^{\varepsilon}\mathrm{d}s\right)^2 + \left(\int_0^t B^{\varepsilon}\mathrm{d}B_s\right)^2 + \left(\int_0^t C^{\varepsilon}\mathrm{d}H_s^i\right)^2\right] = o(\varepsilon^2). \tag{31}$$

Since

$$x_t^{\varepsilon} - x_0 = \int_0^t b(s, x_s^{\varepsilon}, u_s^{\varepsilon})\mathrm{d}s + \int_0^t \sigma(s, x_s^{\varepsilon})\mathrm{d}B_s + \int_0^t \sum_{i=1}^{\infty} g^i(s, x_{s-}^{\varepsilon})\mathrm{d}H_s^i, \tag{32}$$

then

$$\begin{aligned} x_t^{\varepsilon} - x_t^* - X_t &= \int_0^t [b(s, x_s^{\varepsilon}, u_s^{\varepsilon}) - b(s, x_s^* + X_s, u_s^{\varepsilon})]\mathrm{d}s \\ &\quad + \int_0^t [\sigma(s, x_s^{\varepsilon}) - \sigma(s, x_s^* + X_s)]\mathrm{d}B_s \\ &\quad + \int_0^t \sum_{i=1}^{\infty}\left(g^i(s, x_{s-}^{\varepsilon}) - g^i(s, x_{s-}^* + X_{s-})\right)\mathrm{d}H_s^i \\ &\quad + \int_0^t A^{\varepsilon}\mathrm{d}s + \int_0^t B^{\varepsilon}\mathrm{d}B_s + \int_0^t C^{\varepsilon}\mathrm{d}H_s^i \\ &= \int_0^t D^{\varepsilon}(x_s^{\varepsilon} - x_s^* - X_s)\mathrm{d}s + \int_0^t E^{\varepsilon}(x_s^{\varepsilon} - x_s^* - X_s)\mathrm{d}B_s \\ &\quad + \int_0^t F^{\varepsilon}(x_s^{\varepsilon} - x_s^* - X_s)\mathrm{d}H_s^i, \end{aligned} \tag{33}$$

with $D^{\varepsilon} = \int_0^1 b_x(s, x_s^* + X_s + \lambda(x_s^{\varepsilon} - x_s^* - X_s), u_s^{\varepsilon})\mathrm{d}\lambda$, $E^{\varepsilon} = \int_0^1 \sigma_x(s, x_s^* + X_s + \lambda(x_s^{\varepsilon} - x_s^* - X_s))\mathrm{d}\lambda$, and $F^{\varepsilon} = \int_0^1 \sum_{i=1}^{\infty} g_x^i(s, x_s^* + X_s + \lambda(x_s^{\varepsilon} - x_s^* - X_s))\mathrm{d}\lambda$.

By Gronwall's inequation, we have

$$\sup_{0\le t\le T} E\left|x_t^{\varepsilon} - x_t^* - X_t\right|^2 \le C_{\varepsilon}\varepsilon^2, \quad C_{\varepsilon} \longrightarrow 0, \text{when } \varepsilon \longrightarrow 0. \tag{34}$$

Next, we prove (26), (27),, (28); it can be easily checked that

$$\begin{aligned} &-\int_t^T f(s, x_s^* + X_s, y_s^* + Y_s, z_s^* + Z_s, r_s^* + R_s, u_s^{\varepsilon})\mathrm{d}s \\ &\quad + \int_t^T (s, z_s^* + Z_s)\mathrm{d}B_s + \int_t^T \sum_{i=1}^{\infty} g^i(s, x_{s-}^* + X_{s-})\mathrm{d}H_s^i \\ &\quad = \Phi(x_T^*) - y_t^* + \Phi_x(x_T^*)X_T - Y_t - \int_t^T G^{\varepsilon}\mathrm{d}s. \end{aligned} \tag{35}$$

Here,

$$\begin{aligned} G^{\varepsilon} = &\int_0^1 (f_x(s, x_s^* + \lambda X_s, y_s^* + \lambda Y_s, z_s^* \\ &+ \lambda Z_s, r_s^* + \lambda R_s, u_s^{\varepsilon}) - f_x(s))\mathrm{d}\lambda X_s \\ &+ \int_0^1 \left(f_y(s, x_s^* + \lambda X_s, y_s^* + \lambda Y_s, z_s^* \right. \\ &\left. + \lambda Z_s, r_s^* + \lambda R_s, u_s^{\varepsilon}) - f_y(s)\right)\mathrm{d}\lambda Y_s \\ &+ \int_0^1 (f_z(s, x_s^* + \lambda X_s, y_s^* + \lambda Y_s, z_s^* \\ &+ \lambda Z_s, r_s^* + \lambda R_s, u_s^{\varepsilon}) - f_z(s))\mathrm{d}\lambda Z_s \\ &+ \int_0^1 (f_r(s, x_s^* + \lambda X_s, y_s^* + \lambda Y_s, z_s^* \\ &+ \lambda Z_s, r_s^* + \lambda R_s, u_s^{\varepsilon}) - f_r(s))\mathrm{d}\lambda R_s. \end{aligned} \tag{36}$$

Since

$$\begin{aligned} y_t^{\varepsilon} = &\Phi(x_T^{\varepsilon}) + \int_t^T f(s, x_s^{\varepsilon}, y_s^{\varepsilon}, z_s^{\varepsilon}, r_s^{\varepsilon}, u_s^{\varepsilon})\mathrm{d}s - \int_t^T z_s\mathrm{d}B_s \\ &- \int_t^T \sum_{i=1}^{\infty} r_s^{i,\varepsilon}\mathrm{d}H_s^i, \end{aligned} \tag{37}$$

then

$$\begin{aligned} y_t^{\varepsilon} - y_t^* - Y_t = &\Phi(x_T^{\varepsilon}) - \Phi(x_T^*) - \Phi_x(x_T^*)X_T + \int_t^T [f(s, x_s^{\varepsilon}, y_s^{\varepsilon}, z_s^{\varepsilon}, r_s^{\varepsilon}, u_s^{\varepsilon}) - f(s, x_s^* + X_s, y_s^* + Y_s, z_s^* + Z_s, r_s^* + R_s, u_s^{\varepsilon}]\mathrm{d}s \\ &- \int_t^T (z_s^{\varepsilon} - z_s^* - Z_s)\mathrm{d}B_s - \int_t^T \sum_{i=1}^{\infty}\left(r_s^{i,\varepsilon} - r_s^{i,*} - R_s\right)\mathrm{d}H_s^i + \int_t^T G^{\varepsilon}\mathrm{d}s. \end{aligned} \tag{38}$$

Squaring both sides of the equation above, we get

$$E\left|y_t^\varepsilon - y_t^* - Y_t\right|^2 + E\int_t^T \left(z_s^\varepsilon - z_s^* - Z_s\right)^2 \mathrm{d}s - E\int_t^T \sum_{i=1}^{\infty}\left(r_s^{i,\varepsilon} - r_s^{i,*} - R_s\right)^2 \mathrm{d}s$$
$$= E\left\{\left[f\left(s, x_s^\varepsilon, y_s^\varepsilon, z_s^\varepsilon, r_s^\varepsilon, u_s^\varepsilon\right) - f\left(s, x_s^* + X_s, y_s^* + Y_s, z_s^* + Z_s, r_s^* + R_s, u_s^\varepsilon\right)\right]\mathrm{d}s + \Phi\left(x_T^\varepsilon\right) - \Phi\left(x_T^*\right) - \Phi_x\left(x_T^*\right)X_T + \int_t^T G^\varepsilon \mathrm{d}s\right\}^2. \tag{39}$$

From Lemma 2 and equation (25), we have

$$\begin{aligned} \sup_{0\le t\le T} E\left(\int_t^T G^\varepsilon \mathrm{d}s\right)^2 &= o\left(\varepsilon^2\right), \\ E\left[\Phi\left(x_T^\varepsilon\right) - \Phi\left(x_T^*\right) - \Phi_x\left(x_T^*\right)X_T\right]^2 &= o\left(\varepsilon^2\right). \end{aligned} \tag{40}$$

Then, we can get (26), (27), and (28) by applying the iterative method to the above relations. □

Lemma 4 (variational inequality). *Under the conditions that Assumptions 1 and 2 are established, we can get the following variational inequality:*

$$E\gamma_y\left(y_0^*\right)Y_0 \ge o(\varepsilon). \tag{41}$$

Proof. From the four estimations in Lemma 3, we have the following estimation:

$$E\left[\gamma\left(y_0^\varepsilon\right) - \gamma\left(y_0^* + Y_0\right)\right] = o(\varepsilon). \tag{42}$$

Therefore,

$$0 \le E\left[\gamma\left(y_0^* + Y_0\right) - \gamma\left(y_0^*\right)\right] + o(\varepsilon) = E\gamma_y\left(y_0^*\right)Y_0 + o(\varepsilon). \tag{43}$$

We introduce the following Hamiltonian function $H: [0,T]\times R^n \times R^m \times R^{m\times d} \times l^2(R^m) \times U \times R^n \times R^m \times R^{n\times d} \times l^2(R^n)$ as

$$\begin{aligned} H(t,x,y,z,r,u,p,q,w,k) &= \langle p, b(t,x,u)\rangle + \langle w, \sigma(t,x)\rangle \\ &\quad + \langle k, g(t,x)\rangle - \langle q, f(t,x,y,z,r,u)\rangle, \end{aligned} \tag{44}$$

and the following adjoint equation

$$\begin{cases} \mathrm{d}q_t = H_y\left(u_t^*\right)\mathrm{d}t + H_z\left(u_t^*\right)\mathrm{d}B_t + \sum_{i=1}^{\infty} H_r^i\left(u_t^*\right)\mathrm{d}H_t^i, \\ -\mathrm{d}p_t = H_x\left(u_t^*\right)\mathrm{d}t - w_t\mathrm{d}B_t - \sum_{i=1}^{\infty} k_{t-}^i \mathrm{d}H_t^i, \\ q_0 = \gamma_y\left(y_0^*\right), p_T = -\Phi_x\left(x_T^*\right)q_T, \quad t\in[0,T], \end{cases} \tag{45}$$

where

$$\begin{aligned} H_x\left(u_t^*\right) &= H_x\left(t, x_t^*, y_t^*, z_t^*, r_t^*, u_t^*, p_t, q_t, w_t, k_t\right), \\ H_y\left(u_t^*\right) &= H_y\left(t, x_t^*, y_t^*, z_t^*, r_t^*, u_t^*, p_t, q_t, w_t, k_t\right), \\ H_z\left(u_t^*\right) &= H_z\left(t, x_t^*, y_t^*, z_t^*, r_t^*, u_t^*, p_t, q_t, w_t, k_t\right), \\ H_r\left(u_t^*\right) &= H_r\left(t, x_t^*, y_t^*, z_t^*, r_t^*, u_t^*, p_t, q_t, w_t, k_t\right). \end{aligned} \tag{46}$$

It is easily check that adjoint equation (45) has a unique solution quartet $(p_t, q_t, w_t, k_t) \in M^2(0,T; R^{n+m+m\times d}) \times l^2(0,T;R^m)$.

Then, we get the main result of this section. □

Theorem 1. *Let hypothesis, Assumptions 1 and2, hold; u_t^* is an optimal control, and the corresponding optimal state trajectories are $(x_t^*, y_t^*, z_t^*, r_t^*)$; let (p_t, q_t, w_t, k_t) be the solution of adjoint equation (45); and then, for each admissible control $u_t \in U_{ad}[0,T]$, we have*

$$\begin{aligned} &H\left(t, x_t^*, y_t^*, z_t^*, r_t^*, u_t, p_t, q_t, w_t, k_t\right) \\ &\quad \ge H\left(t, x_t^*, y_t^*, z_t^*, r_t^*, u_t^*, p_t, q_t, w_t, k_t\right) \text{a.s.a.e.}. \end{aligned} \tag{47}$$

Proof. Applying Itô's formula to $\langle p, X\rangle$ and $\langle q, Y\rangle$, it follows from (6), (45), and the variational inequality that

$$\begin{aligned} &E\int_0^T \left[H\left(t, x_t, y_t, z_t, r_t, u_t^\varepsilon, p_t, q_t, w_t, k_t\right)\right. \\ &\quad \left. - H\left(t, x_t, y_t, z_t, r_t, u_t^*, p_t, q_t, w_t, k_t\right)\right]\mathrm{d}t = E\gamma_y\left(y_0^*\right)Y_0 \ge o(\varepsilon). \end{aligned} \tag{48}$$

By the definition of u_t^ε, we know that, for any $u \in U_{\mathrm{ad}}[0,T]$, the following inequation holds:

$$\begin{aligned} &E\left[H\left(t, x_t, y_t, z_t, r_t, u_t^\varepsilon, p_t, q_t, w_t, k_t\right)\right. \\ &\quad \left. - H\left(t, x_t, y_t, z_t, r_t, u_t^*, p_t, q_t, w_t, k_t\right)\right] \ge 0. \end{aligned} \tag{49}$$

Then, (47) can be easily checked. □

4. Stochastic Control Problem with State Constraints

In this part, we are going to discuss stochastic control problems with state constraints in control system (2). Specifically, the initial state constraints and final state constraints are as follows:

$$\begin{aligned} EG_1\left(x_T\right) &= 0, \\ EG_0\left(y_0\right) &= 0, \end{aligned} \tag{50}$$

where $G_1 : R^n \longrightarrow R^{n_1}(n_1 < n)$, $G_0 : R^m \longrightarrow R^{m_1}(m_1 < m)$. Our optimal control problem is to find $u^* \in U_{\text{ad}}$ such that

$$J(u^*(\cdot)) = \inf_{u(\cdot)\in U_{\text{ad}}} J(u(\cdot)), \tag{51}$$

subject to the state constraints (50). In the following, we will apply Ekeland's variational principle to solve this optimal control problem. Firstly, we need the following assumptions.

Assumption 3. Control domain U is assumed to be closed, the mappings in state constraints G_1, G_0 are continuously differentiable, and G_{1x}, G_{0y} are bounded.

For $\forall u_1(\cdot), u_2(\cdot) \in U_{\text{ad}}$, let

$$d(u_1(\cdot), u_2(\cdot)) = \left|\left\{E\left|u_1(\cdot) - u_2(\cdot)\right|^2 > 0; t \in [0,T]\right\}\right|. \tag{52}$$

Same as Section 3, we also assume u_t^* be the optimal control, and the corresponding optimal state trajectories are $(x_t^*, y_t^*, z_t^*, r_t^*)$. In order to solve the constraint problem, we need the following penalty cost functional, for any $\rho > 0$:

$$J_\rho(u) = \left\{\left|E[G_1(x_T)]\right|^2 + \left|E[G_0(y_0)]\right|^2 + \left|J(u) - J(u^*) + \rho\right|^2\right\}^{1/2}. \tag{53}$$

It can be checked that $J_\rho(u) : U_{\text{ad}} \longrightarrow R^1$ is continuous, and for any $u(\cdot) \in U_{ad}$,

$$\begin{gathered} J_\rho(u) \geq 0, J_\rho(u^*) = \rho, \\ J_\rho(u^*) \leq \inf_{u(\cdot)\in U_{\text{ad}}} J_\rho(u) + \rho. \end{gathered} \tag{54}$$

It can be obtained by Ekeland's variational principle that there exists $u_t^\rho \in U_{\text{ad}}$ such that

$$\begin{cases} \text{(i) } J_\rho(u^\rho) \leq J_\rho(u^*) = \rho, \\ \text{(ii) } d(u^\rho, u^*) \leq \sqrt{\rho}, \\ \text{(iii) } J_\rho(v) \geq J_\rho(u^\rho) - \sqrt{\rho}\, d(u^\rho, v), \quad \text{for } \forall v(\cdot) \in U_{\text{ad}}. \end{cases} \tag{55}$$

For fixed ρ and admissible control u_t^ρ, we define the spike variation as follows:

$$u_t^{\rho,\varepsilon} = \begin{cases} v_t, & \tau \leq t \leq \tau + \varepsilon; \\ u_t^\rho, & \text{otherwise}, \end{cases} \tag{56}$$

for any $\varepsilon > 0$, and it is easy to check from (iii) of (55) that

$$J_\rho(u^{\rho,\varepsilon}) - J_\rho(u^\rho) + \sqrt{\rho} d(u^{\rho,\varepsilon}, u^\rho) \geq 0. \tag{57}$$

Let $(x_t^\rho, y_t^\rho, z_t^\rho, r_t^\rho)$ be the trajectories corresponding to u_t^ρ and $(x_t^{\rho,\varepsilon}, y_t^{\rho,\varepsilon}, z_t^{\rho,\varepsilon}, r_t^{\rho,\varepsilon})$ be the trajectories corresponding to $u_t^{\rho,\varepsilon}$. The variational equation we used in this section is the same as the one in Section 3, with $u_t^* = u_t^\rho$ and $(x_t^*, y_t^*, z_t^*, r_t^*) = (x_t^\rho, y_t^\rho, z_t^\rho, r_t^\rho)$. And we also assume that the solution of this variational equation is $(X_t^\rho, Y_t^\rho, Z_t^\rho, R_t^\rho)$. Similar to the approach in Lemmas 2 and 3, it can be shown that

$$\begin{aligned} &\sup_{0\leq t\leq T} E\left|x_t^{\rho,\varepsilon} - x_t^\rho - X_t^\rho\right|^2 \leq C_\varepsilon \varepsilon^2, \quad C_\varepsilon \longrightarrow 0, \text{when } \varepsilon \longrightarrow 0, \\ &\sup_{0\leq t\leq T} E\left|y_t^{\rho,\varepsilon} - y_t^\rho - Y_t^\rho\right|^2 \leq C_\varepsilon \varepsilon^2, \quad C_\varepsilon \longrightarrow 0, \text{when } \varepsilon \longrightarrow 0, \\ &E\int_0^T \left|z_t^{\rho,\varepsilon} - z_t^\rho - Z_t^\rho\right|^2 \mathrm{d}s \leq C_\varepsilon \varepsilon^2, \quad C_\varepsilon \longrightarrow 0, \text{when } \varepsilon \longrightarrow 0, \\ &E\int_0^T \left\|r_t^{\rho,\varepsilon} - r_t^\rho - R_t^\rho\right\|^2 \mathrm{d}s \leq C_\varepsilon \varepsilon^2, \quad C_\varepsilon \longrightarrow 0, \text{when } \varepsilon \longrightarrow 0. \end{aligned} \tag{58}$$

Then, by (57), the following variational inequality holds:

$$\begin{aligned} &J_\rho(u^{\rho,\varepsilon}) - J_\rho(u^\rho) + \sqrt{\rho} d(u^{\rho,\varepsilon}, u^\rho) \\ &= \frac{J_\rho^2(u^{\rho,\varepsilon}) - J_\rho^2(u^\rho)}{J_\rho(u^{\rho,\varepsilon}) + J_\rho(u^\rho)} + \varepsilon\sqrt{\rho} \\ &= \langle h_1^{\rho,\varepsilon}, E[G_{1x}(x_T^\rho)]X_T^\rho\rangle + \langle h_0^{\rho,\varepsilon}, E\left[G_{0y}(y_0^\rho)\right]Y_0^\rho\rangle \\ &\quad + h^{\rho,\varepsilon} E\left[\gamma_y(y_0^\rho)Y_0^\rho\right] + \varepsilon\sqrt{\rho} + o(\varepsilon), \end{aligned} \tag{59}$$

where

$$\begin{aligned} h_1^{\rho,\varepsilon} &= \frac{2E[G_1(x_T^\rho)]}{J_\rho(u^{\rho,\varepsilon}) + J_\rho(u^\rho)}, \\ h_0^{\rho,\varepsilon} &= \frac{2E[G_0(y_0^\rho)]}{J_\rho(u^{\rho,\varepsilon}) + J_\rho(u^\rho)}, \\ h^{\rho,\varepsilon} &= \frac{2E[\gamma(y_0^\rho) - \gamma(y_0) + \rho]}{J_\rho(u^{\rho,\varepsilon}) + J_\rho(u^\rho)}. \end{aligned} \tag{60}$$

Now, let $(p_t^{\rho,\varepsilon}, q_t^{\rho,\varepsilon}, w_t^{\rho,\varepsilon}, k_t^{\rho,\varepsilon})$ be the solution of

$$\begin{cases} -\mathrm{d}p_t^{\rho,\varepsilon} = \left[\left(b_x^\rho(t)\right)^\tau p_t^{\rho,\varepsilon} - \left(f_x^\rho(t)\right)^\tau q_t^{\rho,\varepsilon} + \left(\sigma_x^\rho(t)\right)^\tau w_t^{\rho,\varepsilon} + \sum_{i=1}^\infty \left(g_x^\rho(t)\right)^\tau k_t^{\rho,\varepsilon})^i\right]\mathrm{d}t, \\ -w_t^{\rho,\varepsilon}\mathrm{d}B_t - \sum_{i=1}^\infty \left(k_t^{\rho,\varepsilon}\right)^i \mathrm{d}H_t^i, \\ \mathrm{d}q_t^{\rho,\varepsilon} = \left(f_y^\rho(t)\right)^\tau q_t^{\rho,\varepsilon} dt + \left(f_z^\rho(t)\right)^\tau q_t^{\rho,\varepsilon} dB_t + \sum_{i=1}^\infty \left(f_r^{\rho,i}(t)\right)^\tau) q_t^{\rho,\varepsilon}\mathrm{d}H_t^i, \\ q_0 = -G_{0,y}(y_0^\rho)h_0^{\rho,\varepsilon} + \gamma_y(y_0^\rho)h^{\rho,\varepsilon}, p_T = G_{1x}(x_T^\rho)h_1^{\rho,\varepsilon} - \Phi_x(x_T^\rho)q_T^{\rho,\varepsilon}, \quad t \in [0,T]. \end{cases} \tag{61}$$

Here, $b_x^\rho(t) = b_x(t, x_t^\rho, u_t^\rho)$, $\sigma_x^\rho(t) = \sigma_x(t, x_t^\rho)$, $f_y^\rho(t) = f_y(t, x_t^\rho, y_t^\rho, z_t^\rho, r_t^\rho, u_t^\rho)$, etc. Applying It$\hat{o}$'s formula to $\langle X_t^\rho, q_t^{\rho,\varepsilon}\rangle + \langle Y_t^\rho, p_t^{\rho,\varepsilon}\rangle$, variational inequality (59) can be rewritten as

$$\begin{aligned} &H(t, x_t^\rho, y_t^\rho, z_t^\rho, r_t^\rho, u_t^{\rho,\varepsilon}, p_t^{\rho,\varepsilon}, q_t^{\rho,\varepsilon}, w_t^{\rho,\varepsilon}, k_t^{\rho,\varepsilon}) \\ &\quad - H(t, x_t^\rho, y_t^\rho, z_t^\rho, r_t^\rho, u_t^\rho, p_t^{\rho,\varepsilon}, q_t^{\rho,\varepsilon}, w_t^{\rho,\varepsilon}, k_t^{\rho,\varepsilon}) \\ &\quad + \varepsilon\sqrt{\rho} + o(\varepsilon) \geq 0, \quad \forall v_t \in U, \text{a.e., a.s.,} \end{aligned} \tag{62}$$

where the Hamiltonian function H is defined as (44). Since

$$\lim_{\varepsilon \longrightarrow 0}\left(\left|h_0^{\rho,\varepsilon}\right|^2 + \left|h_1^{\rho,\varepsilon}\right|^2 + \left|h^{\rho,\varepsilon}\right|^2\right) = 1, \tag{63}$$

there exists a convergent subsequence, still denoted by $(h_0^{\rho,\varepsilon}, h_1^{\rho,\varepsilon}, h^{\rho,\varepsilon})$ such that $(h_0^{\rho,\varepsilon}, h_1^{\rho,\varepsilon}, h^{\rho,\varepsilon}) \longrightarrow (h_0^\rho, h_1^\rho, h^\rho)$ when $\varepsilon \longrightarrow 0$ with $|h_0^\rho|^2 + |h_1^\rho|^2 + |h^\rho|^2 = 1$.

Let $(p_t^\rho, q_t^\rho, w_t^\rho, k_t^\rho)$ be the solution of

$$\begin{cases} -\mathrm{d}p_t^\rho = \left[(b_x^\rho(t))^\tau p_t^\rho - (f_x^\rho(t))^\tau q_t^\rho + (\sigma_x^\rho(t))^\tau w_t^\rho + \sum_{i=1}^{\infty}(g_x^\rho(t))^\tau k_t^{\rho})^i\right]\mathrm{d}t, \\ -w_t^\rho \mathrm{d}B_t - \sum_{i=1}^{\infty}(k_t^\rho)^i \mathrm{d}H_t^i, \\ \mathrm{d}q_t^\rho = \left((f_y^\rho(t))^\tau q_t^\rho \mathrm{d}t + (f_z^\rho(t))^\tau q_t^\rho \mathrm{d}B_t + \sum_{i=1}^{\infty}\left(f_r^{\rho,i}(t)\right)^\tau\right) q_t^\rho \mathrm{d}H_t^i, \\ q_0 = -G_{0,y}(y_0^\rho)h_0^\rho + \gamma_y(y_0^\rho)h^\rho,\ p_T = G_{1x}(x_T^\rho)h_1^\rho - \Phi_x(x_T^\rho)q_T^\rho, \quad t \in [0, T]. \end{cases} \tag{64}$$

From the continuous dependence of the solutions of FBSDEs with Lévy process on the parameters, we can prove that the following convergence holds: $(p_t^{\rho,\varepsilon}, q_t^{\rho,\varepsilon}, w_t^{\rho,\varepsilon}, k_t^{\rho,\varepsilon}) \longrightarrow (p_t^\rho, q_t^\rho, w_t^\rho, k_t^\rho)$; then, in equation (62), it implies that

$$\begin{aligned} &H(t, x_t^\rho, y_t^\rho, z_t^\rho, r_t^\rho, v_t, p_t^\rho, q_t^\rho, w_t^\rho, k_t^\rho) \\ &\quad - H(t, x_t^\rho, y_t^\rho, z_t^\rho, r_t^\rho, u_t^\rho, p_t^\rho, q_t^\rho, w_t^\rho, k_t^\rho) \\ &\quad + \sqrt{\rho} \geq 0, \quad \forall v_t \in U, \text{a.e., a.s..} \end{aligned} \tag{65}$$

Similarly, there exists a convergent subsequence $(h_0^\rho, h_1^\rho, h^\rho)$ such that $(h_0^\rho, h_1^\rho, h^\rho) \longrightarrow (h_0, h_1, h)$ when $\rho \longrightarrow 0$ with $|h_0|^2 + |h_1|^2 + |h|^2 = 1$. Since $u_t^\rho \longrightarrow u_t^*$, as $\rho \longrightarrow 0$, we have $(x_t^\rho, y_t^\rho, z_t^\rho, r_t^\rho) \longrightarrow (x_t^*, y_t^*, z_t^*, r_t^*)$ and $(X_t^\rho, Y_t^\rho, Z_t^\rho, R_t^\rho) \longrightarrow (X_t, Y_t, Z_t, R_t)$, which is the solution of the variational equation as same as (6).

The following adjoint equation is introduced:

$$\begin{cases} -\mathrm{d}p_t = \left[(b_x(t))^\tau p_t - (f_x(t))^\tau q_t + (\sigma_x(t))^\tau w_t + \sum_{i=1}^{\infty}(g_x(t))^\tau k_t)^i\right]\mathrm{d}t, \\ -w_t \mathrm{d}B_t - \sum_{i=1}^{\infty}(k_t)^i \mathrm{d}H_t^i, \\ \mathrm{d}q_t = \left((f_y(t))^\tau q_t \mathrm{d}t + (f_z(t))^\tau q_t \mathrm{d}B_t + \sum_{i=1}^{\infty}\left(f_r^{\rho,i}(t)\right)^\tau\right) q_t \mathrm{d}H_t^i, \\ q_0 = -G_{0,y}(y_0)h_0 + \gamma_y(y_0)h,\ p_T = G_{1x}(x_T)h_1 - \Phi_x(x_T)q_T, \quad t \in [0, T]. \end{cases} \tag{66}$$

Similarly, it can be proved that $(p_t^\rho, q_t^\rho, w_t^\rho, k_t^\rho) \longrightarrow (p_t, q_t, w_t, k_t)$; then, inequation (65) implies

$$\begin{aligned} &H(t, x_t^*, y_t^*, z_t^*, r_t^*, v_t, p_t, q_t, w_t, k_t) \\ &\quad - H(t, x_t^*, y_t^*, z_t^*, r_t^*, u_t^*, p_t, q_t, w_t, k_t) \geq 0, \forall v_t \in U, \text{a.e., a.s..} \end{aligned} \tag{67}$$

Then, we get the following theorem:

Theorem 2. *Let Assumptions 1–3 hold; u_t^* is an optimal control, and the corresponding optimal state trajectories are $(x_t^*, y_t^*, z_t^*, r_t^*)$, and (p_t, q_t, w_t, k_t) is the solution of adjoint equation (66); then, there exists nonzero constant $(h_1, h_0, h) \in (R^{n_1} \times R^{m_1} \times R)$ with $|h_0|^2 + |h_1|^2 + |h|^2 = 1$ such that, for any admissible control $v_t \in U_{ad}[0, T]$, the maximum condition (67) holds.*

This conclusion can be drawn from the above analysis directly.

5. A Financial Example

In this section, we will study the problem of optimal consumption rate selection in the financial market, which will naturally inspire our research to the forward-backward stochastic optimal control problem in Section 3.

Assume the investor's asset process x_t $(t \geq 0)$ in the financial market is described by the following stochastic differential equation with the Teugels martingale:

$$\begin{cases} \mathrm{d}x_t = [\mu_t x_t - C_t]\mathrm{d}t + \sigma_t x_t \mathrm{d}B_t + \sum_{i=1}^{\infty} g_t^i x_t \mathrm{d}H_t^i, \\ x_0 = W > 0,\ t \in [0, T], \end{cases} \tag{68}$$

where μ_t and $\sigma_t \neq 0$ are the expected return and volatility of the value process x_t at time t, respectively, and C_t is the consumption rate process. Assume μ_t, σ_t, g_t, and C_t are all uniformly bounded $\mathscr{F}_t$–measurable random processes. The purpose of investors is to select the optimal consumption strategy C_t^* at time $t \geq 0$, minimizing the following recursive utility:

$$J(C(\cdot)) = E[y_0], \tag{69}$$

where y_t is the following backward stochastic process:

$$\begin{cases} -dy_t = \left[Le^{-rt}\dfrac{C_t^{1-R}}{1-R} - ry_t\right]\mathrm{d}t - z_t \mathrm{d}B_t - \sum_{i=1}^{\infty} r_t^i \mathrm{d}H_t^i, \\ y_T = -x_T > 0, \quad t \in [0, T], \end{cases} \tag{70}$$

with constant $L > 0$, the discount factor $r > 0$, and the Arrow–Pratt measure of risk aversion $R \in (0, 1)$.

If the consumption process C_t is regarded as a control variable, then combining (68) with (70), we encounter the following control system:

$$\begin{cases} \mathrm{d}x_t = [\mu_t x_t - C_t]\mathrm{d}t + \sigma_t x_t \mathrm{d}B_t + \sum_{i=1}^{\infty} g_t^i x_t \mathrm{d}H_t^i, \\ -\mathrm{d}y_t = \left[Le^{-rt}\dfrac{C_t^{1-R}}{1-R} - ry_t\right]\mathrm{d}t - z_t \mathrm{d}B_t - \sum_{i=1}^{\infty} r_t^i \mathrm{d}H_t^i, \\ x_0 = W > 0, y_T = -x_T > 0, \quad t \in [0, T], \end{cases} \tag{71}$$

which is obviously a special case of stochastic control system (2) with $b(t, x, u) = \mu_t x_t - C_t$, $\sigma(t, x) = \sigma_t x_t$, $g(t, x) = g_t^i x_t$, $\Phi_x(x_T) = -X_T$ and $f(t, x, y, z, r, u) = Le^{-rt}(C_t^{1-R}/(1-R)) - ry_t$.

We can check that both Assumptions 1 and 2 are satisfied. Then, we can use our maximum principle (Theorem 1) to solve the above optimization problem. Let C_t^* be an optimal consumption rate and x_t^*, y_t^* be the corresponding wealth process and recursive utility process. In this case, the Hamiltonian function H reduces to

$$\begin{aligned} H(t, x_t^*, y_t^*, C_t, p_t^*, q_t^*, w_t^*, k_t^*) &= \langle p_t^*, \mu_t x_t^* - C_t\rangle \\ &+ \langle w_t^*, \sigma_t x_t^*\rangle + \langle k_t^*, g_t^i x_t^*\rangle - \langle q_t^*, Le^{-rt}\frac{C_t^{1-R}}{1-R} - ry_t^*\rangle, \end{aligned} \tag{72}$$

and $(p_t^*, q_t^*, w_t^*, k_t^*)$ is the solution of the following adjoint equation:

$$\begin{cases} \mathrm{d}q_t = rq_t \mathrm{d}t \\ -\mathrm{d}p_t = \left[\mu_t p_t + \sigma_t w_t + \sum_{i=1}^{\infty} (k_t^i)^\tau g_t^i\right]\mathrm{d}t - w_t \mathrm{d}B_t - \sum_{i=1}^{\infty} k_t^i \mathrm{d}H_t^i, \\ q_0 = 1, p_T = q_T, \quad t \in [0, T]. \end{cases} \tag{73}$$

According to the maximum principle (47), we have

$$p_t^* = -Le^{-rt}(C_t^*)^{-R} q_t^*, \tag{74}$$

and the optimal consumption rate

$$C_t^* = \left(-\frac{e^{rt}}{L}\frac{p_t^*}{q_t^*}\right)^{-1/R}. \tag{75}$$

By solving FBSDE (73), we get $q_t^* = e^{rt}$, $p_t^* = e^{rt}e^{\mu(T-t)}$, and $w_t^* = k_t^* = 0$. Then, we get the optimal consumption rate of the investor which is

$$C_t^* = \left(-\frac{e^{rT}}{L}e^{\mu(T-t)}\right)^{-1/R}, \quad t \in [0, T]. \tag{76}$$

6. Conclusions

In this paper, a nonconvex control domain case of the forward-backward stochastic control driven by Lévy process is considered, and we obtain the global stochastic maximum principle for this stochastic control problem. And then, the problem of stochastic control with initial and final state constraints on the state variables is discussed, and a necessary condition about existence of the optimal control is also acquired. A financial example of optimal consumption is discussed to illustrate the application of the stochastic maximum principle.

Data Availability

No data were used to support this study.

Conflicts of Interest

The authors declare that they have no conflicts of interest.

Acknowledgments

This work was supported by the NNSF (11701335), Shandong NSF (ZR2019BG015), NSSF (17BGL058), Shandong Provincial Higher Education Science and Technology Plan Project (J18KA236), and Shandong Women's College High-level Research Project Cultivation Foundation (2018GSPGJ07).

References

[1] L. S. Pontryakin, V. G. Boltyanskti, R. V. Gamkrelidze, and E. F. Mischenko, *The Mathematical Theory of Optimal Control Processes*, John Wiley, New York, NY, USA, 1962.

[2] S. Peng, "A general stochastic maximum principle for optimal control problems," *SIAM Journal on Control and Optimization*, vol. 28, no. 4, pp. 966–979, 1990.

[3] S. G. Peng, "Backward stochastic differrntial equations and application to optimal control," *Applied Mathematics & Optimization*, vol. 27, no. 4, pp. 125–144, 1993.

[4] W. S. Xu, "Stochastic maximum principle for optimal control problem of forward and backward system," *Journal of Australian Mathematical Sciences*, vol. 37, pp. 249–259, 1998B.

[5] Z. Wu, "Maximum principle for optimal control problem of fully coupled forward-backward stochastic control system," *System Science and Mathematical Sciences*, vol. 11, no. 3, pp. 249–259, 1998.

[6] J. T. Shi and Z. Wu, "The maximum principle for fully coupled forward-backward stochastic control system," *Acta Automatica Sinica*, vol. 32, no. 2, pp. 161–169, 2006.

[7] R. Situ, "A maximum principle for optimal controls of stochastic systems with random jumps," in *Proceedings of the National Conference on Control Theory and its Applications*, Qingdao, China, 1991.

[8] J. Shi and Z. Wu, "Maximum principle for forward-backward stochastic control system with random jumps and applications to finance," *Journal of Systems Science and Complexity*, vol. 23, no. 2, pp. 219–231, 2010.

[9] J. T. Shi, "Global maximum principle for forward-backward stochastic control system with Poisson jumps," *Asian Journal of Control*, vol. 16, no. 1, pp. 1–11, 2014.

[10] M. Liu, X. Wang, and H. Huang, "Maximum principle for forward-backward control system driven by Itô-Lévy processes under initial-terminal constraints," *Mathematical Problems in Engineering*, vol. 2017, pp. 1–13, 2017.

[11] S. Tang, "The maximum principle for partially observed optimal control of stochastic differential equations," *SIAM Journal on Control and Optimization*, vol. 36, no. 5, pp. 1596–1617, 1998.

[12] Q. Meng, "A maximum principle for optimal control problem of fully coupled forward-backward stochastic systems with partial information," *Science in China Series A: Mathematics*, vol. 52, no. 7, pp. 1579–1588, 2009.

[13] B. Øksendal and A. Sulem, "Maximum principles for optimal control of forward backward stichastic differential equations with jumps," *SIAM J Control Optim\enleadertwodots*, vol. 48, pp. 2845–2976, 2009.

[14] G. Wang and Z. Wu, "Kalman-Bucy filtering equations of forward and backward stochastic systems and applications to recursive optimal control problems," *Journal of Mathematical Analysis and Applications*, vol. 342, no. 2, pp. 1280–1296, 2008.

[15] H. Xiao, "The maximum principle for partially observed optimal control of forward-backward stochastic systems with random jumps," *Journal of Systems Science and Complexity*, vol. 24, no. 6, pp. 1083–1099, 2011.

[16] G. Wang, Z. Wu, and J. Xiong, "Maximum principles for forward-backward stochastic control systems with correlated state and observation noises," *SIAM Journal on Control and Optimization*, vol. 51, no. 1, pp. 491–524, 2013.

[17] G. Wang, C. Zhang, and W. Zhang, "Stochastic maximum principle for mean-field type optimal control under partial information," *IEEE Transactions on Automatic Control*, vol. 59, no. 2, pp. 522–528, 2014.

[18] S. Q. Zhang, J. Xiong, and X. D. Liu, "Stochastic maximum principle for partially observed forward backward stochastic differential equations with jumps and regime switching," *Science China Information Sciences*, vol. 61, no. 7, pp. 1–13, 2018.

[19] J. Xiong, S. Q. Zhang, S. Zhang, and Y. Zhuang, "A partially observed non-zero sum differential game of forward-backward stochastic differential equations and its application in finance," *Mathematical Control & Related Fields*, vol. 9, no. 2, pp. 257–276, 2019.

[20] D. Nualart and W. Schoutens, "Chaotic and predictable representations for Lévy processes," *Stochastic Processes and Their Applications*, vol. 90, no. 1, pp. 109–122, 2000.

[21] D. Nualart and W. Schoutens, "Backward stochastic differential equations and Feynman-Kac formula for Levy processes, with applications in finance," *Bernoulli*, vol. 7, no. 5, pp. 761–776, 2001.

[22] Q. Meng and M. Tang, "Necessary and sufficient conditions for optimal control of stochastic systems associated with Lévy processes," *Science in China Series F: Information Sciences*, vol. 52, no. 11, pp. 1982–1992, 2009.

[23] M. Tang and Q. Zhang, "Optimal variational principle for backward stochastic control systems associated with Lévy processes," *Science China Mathematics*, vol. 55, no. 4, pp. 745–761, 2012.

[24] F. Baghery, N. Khelfallah, B. Mezerdi, and I. Turpin, "Fully coupled forward backward stochastic differential equations driven by Lévy processes and application to differential games," *De Gruyter*, vol. 22, no. 3, pp. 151–161, 2014.

[25] F. Zhang, M. N. Tang, and Q. X. Meng, "Sochastic maximum principle for forward-backward stochastic control systems associated with Lévy processes," *Chinese Annals of Mathematics*, vol. 35A, no. 1, pp. 83–100, 2014.

[26] X. R. Wang and H. Huang, "Maximum principle for forward-backward stochastic control system driven by Lévy process," *Mathematical Problems in Engineering*, vol. 2015, Article ID 702802, 12 pages, 2015.

[27] H. Huang, X. Wang, and M. Liu, "A maximum principle for fully coupled forward-backward stochastic control system driven by Lévy process with terminal state constraints," *Journal of Systems Science and Complexity*, vol. 31, no. 4, pp. 859–874, 2018.

[28] P. Muthukumar and R. Deepa, "Infinite horizon optimal control of forward backward stochastic system driven by Teugels martingales with Lévy process," *Stochastic and Dynamics*, vol. 3, no. 17, pp. 1–17, 2017.

[29] J. B. Wu and Z. M. Liu, "Optimal control of mean-field backward doubly stochastic systems driven by Ito-Lévy processes," *International Journal of Control*, vol. 93, no. 4, pp. 953–970, 2018.

[30] W. Wang, J. Wu, and Z. Liu, "The optimal control of fully-coupled forward-backward doubly stochastic systems driven by Itô-Lévy processes," *Journal of Systems Science and Complexity*, vol. 32, no. 4, pp. 997–1018, 2019.

Hindawi
Mathematical Problems in Engineering
Volume 2020, Article ID 1693971, 9 pages
https://doi.org/10.1155/2020/1693971

Research Article

Fuzzy Second-Order Sliding Mode Control Design for a Two-Cell DC-DC Converter

Hanene Medhaffar and Nabil Derbel

Control and Energy Management Laboratory (CEMLab), Sfax Engineering School, University of Sfax, Sfax, Tunisia

Correspondence should be addressed to Hanene Medhaffar; hanene.medhaffar@isgis.usf.tn

Received 7 February 2020; Accepted 8 May 2020; Published 29 May 2020

Guest Editor: Cuimei Jiang

This paper presents a fuzzy second-order sliding mode controller for a two-cell DC-DC converter. For this aim, a second-order sliding mode controller and a type-2 fuzzy system are combined to achieve an adequate control. For this reason, backgrounds on the type-2 fuzzy sets and on the second-order sliding mode control applied to discrete systems have been presented briefly. A proposed control algorithm is then presented combining these two robust approaches. The asymptotic stability of the overall controlled system has been ensured using the Lyapunov theory. The efficiency and the robustness of the proposed controller have been tested by simulations.

1. Introduction

DC-DC converters are power electronic circuits used in a large variety of applications in electrical industry and power systems. These circuits are highly nonlinear and uncertain systems due to their switching properties, varying load, and inaccurate passive elements [1, 2].

Multicell converters have been widely used in real applications due to their ability to support high voltages. Indeed, structures of these converters consist of a series connection of switching devices with passive storage elements, which generate intermediate voltage levels allowing for the reduction of the voltage in all switches by dividing it between intermediate levels [3]. Moreover, multicell converters can be associated very easily due to their modular structure [4].

Nevertheless, it has been shown that multicell DC-DC converters may exhibit chaotic behavior under traditional controllers [5]. Several control techniques have been proposed for controlling chaos [6] or in chaos synchronization problems [7, 8]. Therefore, the control method influences the dynamical behavior of the power converter. Many conventional control approaches, dealing with this subject, can be found in the literature like PID [9] or sliding mode control.

The concept of the sliding mode control has drawn the attention of researchers in the last three decades. It is noted that the sliding mode control is a powerful robust control strategy treating the model uncertainties and external disturbances. The design and the implementation of the discrete-time sliding mode control have later been considered [10–12] and are still in progress because large classes of continuous systems are controlled by digital signal processors and microprocessors. The application of this control law is confronted to a serious problem: the chattering phenomenon. High-order sliding mode control has been suggested in order to cancel this phenomenon [13, 14]. Thus, this method consists of reducing to zero, not only the sliding function but also its high-order derivatives. Oscillations generated by the discontinuous control are transferred to the higher derivatives of the sliding function in order to reduce oscillation amplitudes while system's robustness remains intact [15]. However, this control strategy requires the knowledge of a dynamic model of the system or a disturbance estimation scheme. Fuzzy logic control has been proposed in an attempt to control nonlinear systems whose parameters are inaccurate, presenting neglected dynamics as well as time-varying systems. However, fuzzy control seems to be deficient in formal analysis and robustness aspects. To overcome this disadvantage, great efforts have been done in the integration of the combination of fuzzy techniques and sliding mode control to improve system control performances [16, 17]. In recent

years, there has been an increasing interest in the type-2 fuzzy-based control [18–20] since type-2 fuzzy systems have better effects on performances of the controlled system than type-1 fuzzy systems where it is difficult to determine parameters associated with the rule base and membership functions [21–23]. Moreover, type-2 fuzzy systems give more degrees of freedom for a better representation of uncertainties compared to type-1 fuzzy sets [24].

The main objective of this work is to design a discrete-time second-order sliding mode control strategy enhanced by a stable adaptive type-2 fuzzy inference system to cope with modeling inaccuracies and external disturbances that can arise. Numerical simulations are performed on the two-cell converter for the illustration and the verification of the proposed controller.

2. Two-Cell DC-DC Converter

The two-cell DC-DC converter is presented in Figure 1 where the binary command signals U_1 and U_2 are the outputs of a digital pulse width modulator (DPWM). The aim of this control is to achieve a constant voltage $V_c = (E/2)$ and a constant output current $i_L = i_R = I_r$. The two-cell DC-DC converter is based on a buck chopper altered to allow higher input supply E using two switching cells separated by a flying capacitor C [25].

The control signals are the evolution of the duty cycles d_1 and d_2 which correspond to two switches S_1 and S_2.

It should be noted that if the floating capacitor voltage V_c is equal to half of the input voltage, the total stress is shared equally between both switches that make this structure suitable for high-voltage applications [26].

As we have two switches S_1 and S_2, we can easily define four different operating topologies (see Table 1).

Clearly, a linear system is obtained for each topology. Consequently, a closed-form solution can be obtained for each topology to which a solution of the state space is [5]

$$\begin{bmatrix} \dfrac{\mathrm{d}i_L}{\mathrm{d}t} \\ \dfrac{\mathrm{d}V_c}{\mathrm{d}t} \end{bmatrix} = \begin{bmatrix} -\dfrac{R}{L} & (d_1 - d_2)\dfrac{1}{L} \\ (d_2 - d_1)\dfrac{1}{C} & 0 \end{bmatrix} \begin{bmatrix} i_L \\ V_c \end{bmatrix} + \begin{bmatrix} \dfrac{E}{L}(1 - d_1) \\ 0 \end{bmatrix}. \tag{1}$$

The control variables are the duty cycles of the switches S_i, $i = 1, 2$. This system can be discretized using the Euler approximation as

$$\begin{bmatrix} i_L(k+1) \\ V_c(k+1) \end{bmatrix} = \begin{bmatrix} 1 - \dfrac{RT}{L} & (d_1(k) - d_2(k))\dfrac{T}{L} \\ (d_2(k) - d_1(k))\dfrac{T}{C} & 1 \end{bmatrix} \begin{bmatrix} i_L(k) \\ V_c(k) \end{bmatrix} + \begin{bmatrix} \dfrac{ET}{L}(1 - d_1(k)) \\ 0 \end{bmatrix}. \tag{2}$$

For the sake of reducing the number of parameters of the system, the following dimensionless and simplified model can be considered [27]:

$$\begin{bmatrix} i_L'(k+1) \\ V_c'(k+1) \end{bmatrix} = \begin{bmatrix} (1 - \delta_L) i_L'(k) + \delta_L \\ V_c'(k) \end{bmatrix} + \begin{bmatrix} \delta_L (V_c'(k) - 1) & -\delta_L V_c'(k) \\ -\delta_c i_L'(k) & \delta_c i_L'(k) \end{bmatrix} \begin{bmatrix} d_1(k) \\ d_2(k) \end{bmatrix}, \tag{3}$$

where T is the switching period and

$$i_L' = \frac{R}{E} i_L, \qquad V_c' = \frac{V_c}{E}. \tag{4}$$

Constants δ_L and δ_c are expressed by

$$\delta_L = \frac{RT}{L}, \qquad \delta_c = \frac{T}{RC}. \tag{5}$$

Let us define the following new state variables:

$$x(k) = \begin{bmatrix} x_1(k) \\ x_2(k) \end{bmatrix} = \begin{bmatrix} i_L'(k) \\ V_c'(k) \end{bmatrix}. \tag{6}$$

Therefore, we obtain the following model:

$$\begin{aligned} x(k+1) &= \begin{bmatrix} f_1(x(k)) \\ f_2(x(k)) \end{bmatrix} + \begin{bmatrix} g_{11}(k) & g_{12}(k) \\ g_{21}(k) & g_{22}(k) \end{bmatrix} \begin{bmatrix} d_1(k) \\ d_2(k) \end{bmatrix} \\ &= f[x(k)] + g[x(k)]u(k), \end{aligned} \tag{7}$$

where $f(k) = f[x(k)]$ and $g(k) = g[x(k)]$ should be identified by fuzzy systems.

Moreover, the applied duty cycles are not $d_1(k)$ and $d_2(k)$ but sat $(d_1(k))$ and sat $(d_2(k))$ where the saturation function is given by

$$\mathrm{sat}(x) = \frac{1}{2}(1 + |x| - |x - 1|). \tag{8}$$

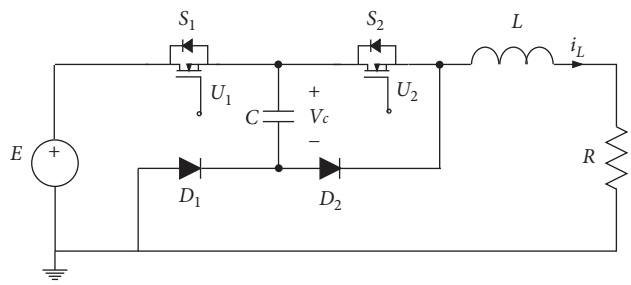

Figure 1: A two-cell DC-DC buck converter.

Table 1: Different topologies of the two-cell DC-DC converter.

Topologies	State of S_1	State of S_2
Topology 1	Off	On
Topology 2	On	On
Topology 3	On	Off
Topology 4	Off	Off

3. Second-Order Discrete Sliding Mode Controller

The high-order sliding mode control concept has been introduced in the 1980s with the aim of resolving the chattering phenomenon. Indeed, the proposed strategy transfers the discontinuity on the higher derivatives of the control law. In order to obtain a discrete second-order sliding mode controller, the following second-order sliding function vector ($\sigma = [\sigma_1, \sigma_2]^T$) is considered:

$$\sigma(k+1) = s(k+1) + \beta s(k), \tag{9}$$

where $\beta = \mathrm{diag}(\beta_1, \beta_2)$ with $0 < \beta_i < 1$, $i = 1, 2$ and $s(k)$ is defined by

$$s(k) = \begin{bmatrix} s_1(k) \\ s_2(k) \end{bmatrix} = \begin{bmatrix} e_1(k) + \lambda_1 e_1(k-1) \\ e_2(k) + \lambda_2 e_2(k-1) \end{bmatrix}, \tag{10}$$

where $e_1(k) = x_1(k) - I'_{rd}$ and $e_2(k) = x_2(k) - V'_{cd}$. I'_{rd} and V'_{cd} are the desired output current and voltage, respectively.

$s(k)$ can be rewritten as follows:

$$s(k) = e(k) + \lambda e(k-1), \tag{11}$$

where $e(k) = [e_1(k), e_2(k)]^T$ and $\lambda = \mathrm{diag}(\lambda_1, \lambda_2)$.

The equivalent control should satisfy the following criteria to ensure ideal sliding motion [28]:

$$\sigma(k+1) = \sigma(k) = 0. \tag{12}$$

Thus, using equations (7), (11), and (12), the equivalent control vector can be calculated as follows:

$$u_{\mathrm{eq}}(k) = [g(k)]^{-1}[x_d - f(k) - \lambda e(k) - \beta s(k)], \tag{13}$$

where $x_d = [I'_{rd}, V'_{cd}]^T$.

The robustness is ensured by the addition of a discontinuous term (sign of the second-order sliding function vector). By analogy to the continuous-time case, the following control at the instant k is then [29]

$$u(k) = [g(k)]^{-1}[x_d - f(k) - \lambda e(k) - \beta s(k) + u_{\mathrm{dis}}(k)], \tag{14}$$

where $u_{\mathrm{dis}}(k) = u_{\mathrm{dis}}(k-1) - \rho\,\mathrm{sign}(\sigma(k))$.

In [28], the authors propose another version of $u_{\mathrm{dis}}(k)$ as follows:

$$u_{\mathrm{dis}}(k) = -\rho\,\mathrm{sign}[\sigma(k-1)], \tag{15}$$

where $\rho = \mathrm{diag}(\rho_1, \rho_2) > 0$. In the following, this switching function will be applied. To obtain the sliding mode control law, we will use fuzzy systems to approximate unknown system functions $f(k)$ and $g(k)$. Moreover, an adaptive adjusting law will be designed.

4. Type-2 Fuzzy System

The type-2 fuzzy system is an extension of the type-1 fuzzy system where uncertainties are represented by the addition of extra dimensions, which provide more degrees of freedom for a greater representation of uncertainties compared to type-1. In addition, using type-2 fuzzy set to represent fuzzy inputs and outputs will result in the reduction of the fuzzy logic rule base when compared to use of type-1 fuzzy sets. Indeed, type-2 fuzzy sets help to cover the same range as type-1 fuzzy sets with smaller number of labels and the rule reduction will be greater when the number of the fuzzy logic inputs increases [30]. In order to approximate unknown system functions $f(k)$ and $g(k)$, the proposed type-2 fuzzy system is characterized by fuzzy IF-THEN rules. Similar to the type-1 fuzzy system, the type-2 fuzzy system includes a fuzzifier, a rule base, a fuzzy inference engine, and an output processor. In the type-2 fuzzy system, the output processor includes a type-reducer and a defuzzifier [31].

While designing type-2 fuzzy systems for the estimation of unknown system functions, type-2 Gaussian membership functions with uncertain standard deviations are used in the fuzzification process of inputs $x_1(k)$ and $x_2(k)$. This choice is motivated by the fact that they are easier to represent and optimize, are always continuous, and are faster to compute for small rule basis [24]. Mathematical expressions for membership functions are expressed as

$$\mu(x_i(k)) = \exp\left(-\frac{(x_i(k) - m_i)^2}{2\sigma_i^2}\right), \quad i = 1, 2, \tag{16}$$

where m_i and σ_i are centers and widths of membership functions.

In general, both m_i and σ_i may be uncertain in the intervals $[m_{1i}, m_{2i}]$ and $[\sigma_{1i}, \sigma_{2i}]$, respectively. The present work assumes that centers do not have any uncertainty and it considers only membership functions with uncertain standard deviation.

Each input variable ($x_1(k)$ or $x_2(k)$) is quantified into fuzzy sets. In this paper, the singleton fuzzification strategy is considered.

The adopted form for rules is the zero-order Sugeno model where parameters of consequent parts are taken as singletons and they will be tuned, later, by adaptive laws.

The knowledge base for the fuzzy logic system comprises a collection of fuzzy IF-THEN rules of the form:

$$R_{(j)}\text{: If } \left[\left(x_1(k) \text{ is } A_{1j}\right) \text{ and } \left(x_2(k) \text{ is } A_{2j}\right)\right] \text{ then } \left[\left(y(x(k)) = b_j\right)\right], \tag{17}$$

where $j = 1, \ldots, H$. H is the rule number of the fuzzy logic system.

The inference engine combines fired rules and gives a mapping from input type-2 fuzzy sets to output fuzzy sets. Each membership function of the antecedent part is represented by a lower and an upper membership function $\underline{\mu}_{A_{ij}}(x_i(k))$ and $\overline{\mu}_{A_{ij}}(x_i(k))$ [22]:

$$\mu_{A_{ij}}(x_i(k)) = \left[\underline{\mu}_{A_{ij}}(x_i(k)), \overline{\mu}_{A_{ij}}(x_i(k))\right]. \tag{18}$$

The firing strengths can be calculated adopting the product inference as

$$\begin{aligned} \underline{h}_j &= \underline{\mu}_{A_{1j}}(x_1(k)) \times \underline{\mu}_{A_{2j}}(x_2(k)), \\ \overline{h}_j &= \overline{\mu}_{A_{1j}}(x_1(k)) \times \overline{\mu}_{A_{2j}}(x_2(k)). \end{aligned} \tag{19}$$

For computing the output of the fuzzy system, we use the type-reduction approach and then defuzzification operations. The type-reduction approach combines the firing interval of rules and the corresponding rule consequents. There are several methods for it's design and the most commonly used is the center-of-sets type-reducer [32].

In our design, we bypass the type reduction and compute the defuzzified output directly by adopting the method of Nie and Tan [33].

Thus, the output of the fuzzy system is computed as

$$y(x(k)) = \frac{\sum_{j=1}^{H} b_j\left(\underline{h}_j + \overline{h}_j\right)}{\sum_{j=1}^{H}\left(\underline{h}_j + \overline{h}_j\right)}. \tag{20}$$

By introducing the concept of fuzzy basis function vector ξ, equation (20) can be rewritten as

$$y(x(k)) = \theta^T \xi(k), \tag{21}$$

where $\theta = [b_1, \ldots, b_H]^T$, $\xi(k) = [\xi_1(k), \ldots, \xi_H(k)]$, and

$$\xi_j(k) = \frac{\left(\underline{h}_j + \overline{h}_j\right)}{\sum_{i=1}^{H}\left(\underline{h}_i + \overline{h}_i\right)}. \tag{22}$$

5. Fuzzy Second-Order Sliding Mode Control

In order to derive the sliding mode control, fuzzy functions $\widehat{f}_i(x(k)/\theta_{f_i})$ and $\widehat{g}_{ij}(x(k)/\theta_{g_{ij}})$ are used to approximate $f_i(x(k))$ and $g_{ij}(x(k))$, respectively, where $i, j = 1, 2$. They are expressed by

$$\begin{aligned} \widehat{f}_i\left(x(k)/\theta_{f_i}\right) &= \theta_{f_i}^T \xi_{f_i}(x(k)), \\ \widehat{g}_{ij}\left(x(k)/\theta_{g_{ij}}\right) &= \theta_{g_{ij}}^T \xi_{g_{ij}}(x(k)), \end{aligned} \tag{23}$$

where $\xi_{f_i}(x(k))$ and $\xi_{g_{ij}}(x(k))$ are vectors of fuzzy basis which are supposed to be fixed, while parameters θ_{f_i} and $\theta_{g_{ij}}$ are variables which will be designed by adaptive laws.

Then, we can select the control law as

$$\begin{aligned} u(k) = {} & \left[\widehat{g}\left(x(k)/\theta_g\right)\right]^{-1}\left[x_d - \widehat{f}\left(x(k)/\theta_f\right) - \lambda e(k)\right. \\ & \left. - \beta s(k) + u_{\text{dis}}(k)\right]. \end{aligned} \tag{24}$$

Let $\theta_{f_i}^*$ and $\theta_{g_{ij}}^*$ be optimal parameter vectors of fuzzy logic systems. Minimum approximation errors can be defined as follows:

$$\begin{aligned} w_{f_i}(k) &= f_i(x(k)) - \widehat{f}_i\left(x(k)/\theta_{f_i}^*\right), \\ w_{g_{ij}}(k) &= g_{ij}(x(k)) - \widehat{g}_{ij}\left(x(k)/\theta_{g_{ij}}^*\right). \end{aligned} \tag{25}$$

Therefore, $\sigma(k)$ can be rewritten as

$$\begin{aligned} \sigma(k) &= s(k+1) + \beta s(k) \\ &= e(k+1) + \lambda e(k) + \beta s(k) \\ &= x(k+1) - x_d + \lambda e(k) + \beta s(k) \\ &= f(k) + g(k)u(k) - \widehat{g}\left(x(k)/\theta_g\right)u(k) - \widehat{f}\left(x(k)/\theta_f\right) - \lambda e(k) - \beta s(k) + u_{\text{dis}}(k) + \lambda e(k) + \beta s(k) \\ &= f(k) - \widehat{f}\left(x(k)/\theta_f\right) + \left(g(k) - \widehat{g}\left(x(k)/\theta_g\right)\right)u(k) + u_{\text{dis}}(k) \\ &= \widehat{f}\left(x(k)/\theta_f^*\right) - \widehat{f}\left(x(k)/\theta_f\right) + w_f(k) + \left(\widehat{g}\left(x(k)/\theta_g^*\right) - \widehat{g}\left(x(k)/\theta_g\right) + w_g(k)\right)u(k) + u_{\text{dis}}(k). \end{aligned} \tag{26}$$

Then, $\sigma_i(k)$ can be expressed by

$$\begin{aligned}\sigma_i(k) &= \hat{f}_i\left(x(k)/\theta_{f_i}^*\right) - \hat{f}_i\left(x(k)/\theta_{f_i}\right) + w_{f_i}(k) \\ &\quad + \sum_{j=1}^{2}\left[\hat{g}_{ij}\left(x(k)/\theta_{g_{ij}}^*\right) - \hat{g}_{ij}\left(x(k)/\theta_{g_{ij}}\right) + w_{g_{ij}}(k)\right]u_j(k) + u_{i,\mathrm{dis}}(k) \\ &= \Phi_{f_i}^T(k)\xi_{f_i}(x(k)) + w_{f_i}(k) + \sum_{j=1}^{2}\left[\Phi_{g_{ij}}^T(k)\xi_{g_{ij}}(x(k)) + w_{g_{ij}}(k)\right]u_j(k) + u_{i,\mathrm{dis}}(k) \\ &= \Phi_{f_i}^T(k)\xi_{f_i}(x(k)) + \sum_{j=1}^{2}\left[\Phi_{g_{ij}}^T(k)\xi_{g_{ij}}(x(k))\right]u_j(k) + W_i(k) + u_{i,\mathrm{dis}}(k),\end{aligned} \tag{27}$$

where $\Phi_{f_i}(k)$ and $\Phi_{g_{ij}}$ represent the fuzzy parameter errors such that

$$\begin{aligned}\Phi_{f_i}(k) &= \theta_{f_i}^* - \theta_{f_i}(k), \\ \Phi_{g_{ij}}(k) &= \theta_{g_{ij}}^* - \theta_{g_{ij}}(k).\end{aligned} \tag{28}$$

$W_i(k)$ is the minimum approximation error that can be defined as follows:

$$W_i(k) = w_{f_i}(k) + \sum_{j=1}^{2} w_{g_{ij}}(k)u_j(k). \tag{29}$$

Theorem 1. *The following adaptive laws for adjusting parameter vectors θ_f and θ_g:*

$$\Delta\theta_{f_i}(k+1) = \rho_f\sigma_i(k)\xi_{f_i}(x(k+1)), \tag{30}$$

$$\Delta\theta_{g_{ij}}(k+1) = \rho_g\sigma_i(k)\xi_{g_{ij}}(x(k+1))u_j(k+1), \tag{31}$$

asymptotically stabilize system (7) controlled by (24), where ρ_f and ρ_g are positive constants which determine the rate of adaptation.

Proof. The Lyapunov function candidate is chosen as

$$V(k) = \sum_{i=1}^{2} V_i(k), \tag{32}$$

where

$$\begin{aligned}V_i(k) &= \frac{1}{2}\sigma_i^2(k) + \frac{1}{2\rho_f}\left(\Phi_{f_i}(k+1)^T\Phi_{f_i}(k+1)\right) \\ &\quad + \frac{1}{2\rho_g}\sum_{j=1}^{2}\left(\Phi_{g_{ij}}(k+1)^T\Phi_{g_{ij}}(k+1)\right).\end{aligned} \tag{33}$$

Then, $\Delta V_i(k) = V_i(k+1) - V_i(k)$ can be calculated using a Taylor series expansion:

$$\begin{aligned}V_i(k+1) &= V_i(k) + \frac{\partial V_i(k)}{\partial\sigma_i(k)}\Delta\sigma_i(k) + \frac{\partial V_i(k)}{\partial\Phi_{f_i}(k+1)}\Delta\Phi_{f_i}(k+1) \\ &\quad + \frac{\partial V_i(k)}{\partial\Phi_{g_{ij}}(k+1)}\Delta\Phi_{g_{ij}}(k+1) + \underbrace{O\left(\Delta\sigma_i(k), \Delta\Phi_{f_i}(k+1), \Delta\Phi_{g_{ij}}(k+1)\right)^2}_{O_k}.\end{aligned} \tag{34}$$

$\Delta V_i(k)$ can be obtained by substituting the values of the partial derivatives into equation (34):

$$\Delta V_i(k) = \sigma_i(k)\Delta\sigma_i(k) + \frac{1}{\rho_f}\Phi_{f_i}(k+1)^T\Delta\Phi_{f_i}(k+1) + \frac{1}{\rho_g}\sum_{j=1}^{2}\Phi_{g_{ij}}(k+1)^T\Delta\Phi_{g_{ij}}(k+1) + O_k. \tag{35}$$

Equation (35) can be simplified after substituting $\Delta\sigma_i(k) \equiv \sigma_i(k+1) - \sigma_i(k)$ and equation (27) at $k+1$ time steps:

$$\begin{aligned}
\Delta V_i(k) &= \sigma_i(k)\left[\sigma_i(k+1) - \sigma_i(k)\right] + \frac{1}{\rho_f}\Phi_{f_i}(k+1)^T \Delta\Phi_{f_i}(k+1) \\
&\quad + \frac{1}{\rho_g}\sum_{j=1}^{2}\Phi_{g_{ij}}(k+1)^T \Delta\Phi_{g_{ij}}(k+1) + O_k \\
&= \sigma_i(k)\left[\Phi_{f_i}^T(k+1)\xi_{f_i}(x(k+1)) + \sum_{j=1}^{2}\left(\Phi_{g_{ij}}^T(k+1)\xi_{g_{ij}}(x(k+1))\right)u_j(k+1) + W_i(k+1) + u_{i,\mathrm{dis}}(k+1)\right] \\
&\quad - \sigma_i^2(k) + \frac{1}{\rho_f}\Phi_{f_i}(k+1)^T \Delta\Phi_{f_i}(k+1) + \frac{1}{\rho_g}\sum_{j=1}^{2}\Phi_{g_{ij}}(k+1)^T \Delta\Phi_{g_{ij}}(k+1) + O_k \\
&= -\sigma_i^2(k) + \frac{1}{\rho_f}\Phi_{f_i}(k+1)^T \underbrace{\left[\rho_f \xi_{f_i}(x(k+1))\sigma_i(k) + \Delta\Phi_{f_i}(k+1)\right]}_{=0} + \sigma_i(k)W_i(k+1) \\
&\quad + \sigma_i(k)u_{i,\mathrm{dis}}(k+1) + \frac{1}{\rho_g}\sum_{j=1}^{2}\Phi_{g_{ij}}(k+1)^T \underbrace{\left[\rho_g \xi_{g_{ij}}(x(k+1))\sigma_i(k)u_j(k+1) + \Delta\Phi_{g_{ij}}(k+1)\right]}_{=0} + O_k \\
&= -\sigma_i^2(k) + \sigma_i(k)W_i(k+1) - \rho_i\left|\sigma_i(k)\right| + O_k,
\end{aligned} \tag{36}$$

where

$$\begin{aligned}
\Delta\Phi_{f_i}(k+1) &= -\Delta\theta_{f_i}(k+1), \\
\Delta\Phi_{g_{ij}}(k+1) &= -\Delta\theta_{g_{ij}}(k+1).
\end{aligned} \tag{37}$$

It is obvious that the term $W_i(k+1)$ should be very small in the adaptive fuzzy system [34], verifying

$$\left|W_i(k+1)\right| \le \varepsilon_i \ll \rho_i, \tag{38}$$

where ε_i is a positive small parameter.

Then, adaptive laws (30) and (31) yield

$$\begin{aligned}
\Delta V_i(k) &\le -\sigma_i^2(k) + \varepsilon_i\left|\sigma_i(k)\right| - \rho_i\left|\sigma_i(k)\right| + O_k \\
&\le -\sigma_i^2(k) - (\rho_i - \varepsilon_i)\left|\sigma_i(k)\right| + O_k \le 0.
\end{aligned} \tag{39}$$

Consequently, $\Delta V(k) \le 0$ which guarantees the stability of the system. □

6. Simulation Results

In order to illustrate and validate the proposed control scheme, numerical simulation was carried out. The parameter values used for the power stage circuit are as follows: $R = 25\,\Omega$, $L = 10\,\mathrm{mH}$, $C = 16\,\mu\mathrm{F}$, $E = 90\,\mathrm{V}$, and $f_s = 25\,\mathrm{kHz}$. The aim is to achieve a constant voltage $V'_{cd} = 0.5$ and a constant output current $I'_{rd} = 0.6$. To approximate unknown system functions $f(k)$ and $g(k)$, $x_1(k)$ or $x_2(k)$ is quantified into five fuzzy sets: NL—negative large, NS—negative small, ZO—zero, PS—positive small, and PL—positive large, as shown in Figure 2.

In Figure 3, we represent the time evolution of the current and the voltage in the two-cell DC-DC converter. We can notice that the voltage requires about 7 switching periods to drive the two-cell converter to the desired value V_{cd}.

Figure 4 illustrates the evolution of the duty cycles $d_1(k)$ and $d_2(k)$ which converge promptly to a constant value.

It is obvious that the control objective is achieved: the proposed control scheme offers a fast tracking and a smooth control action. Moreover, this result is obtained without using the details of the plant dynamics in the development of the control law.

In order to illustrate the robustness of the proposed controller, we have considered a variation of the resistance R which becomes 1.25 times its initial value after 20 periods. Figure 5 presents the evolution of the current and the voltage after applying this perturbation. It is obvious that this disturbance is rejected effectively by the controller, and the state variables reach their desired values, rapidly.

Figure 6 illustrates a comparison between a proposed control and a PI controller proposed in [5]. The PI controller is given by

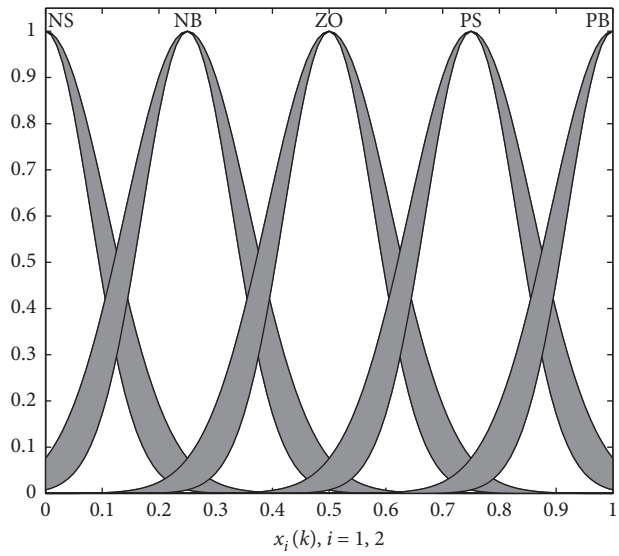

Figure 2: $x_1(k)$ and $x_2(k)$ membership functions.

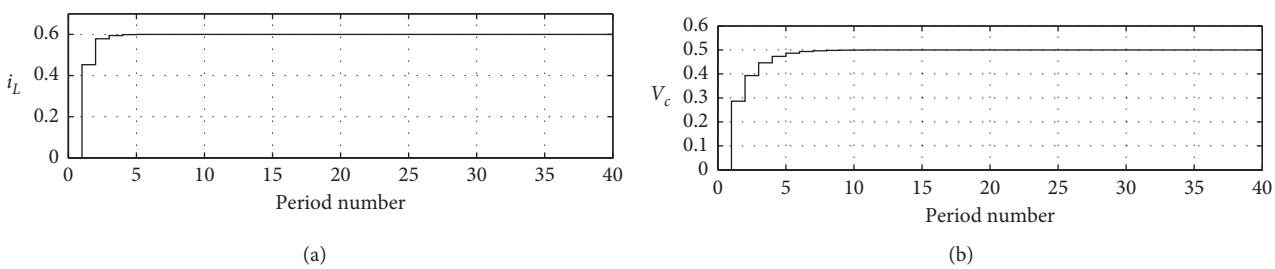

(a) (b)

Figure 3: Time evolution of the current and the voltage.

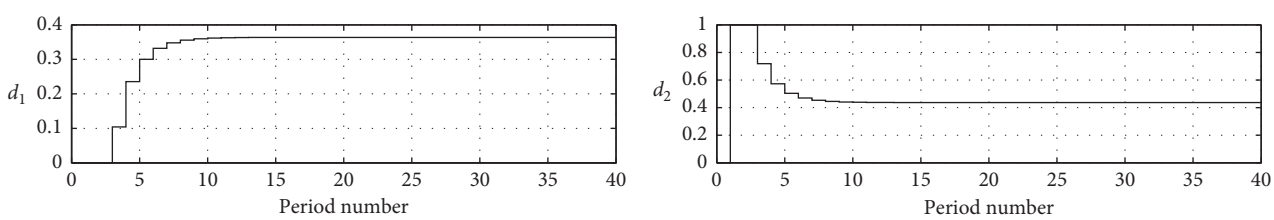

(a) (b)

Figure 4: Time evolution of the duty cycles.

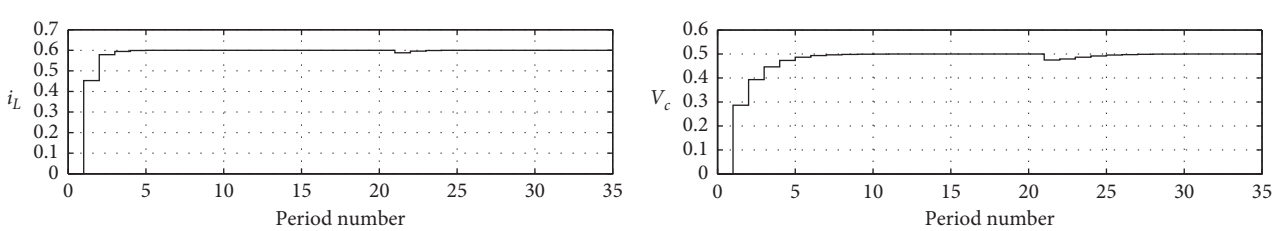

(a) (b)

Figure 5: Time evolution of the current and the voltage.

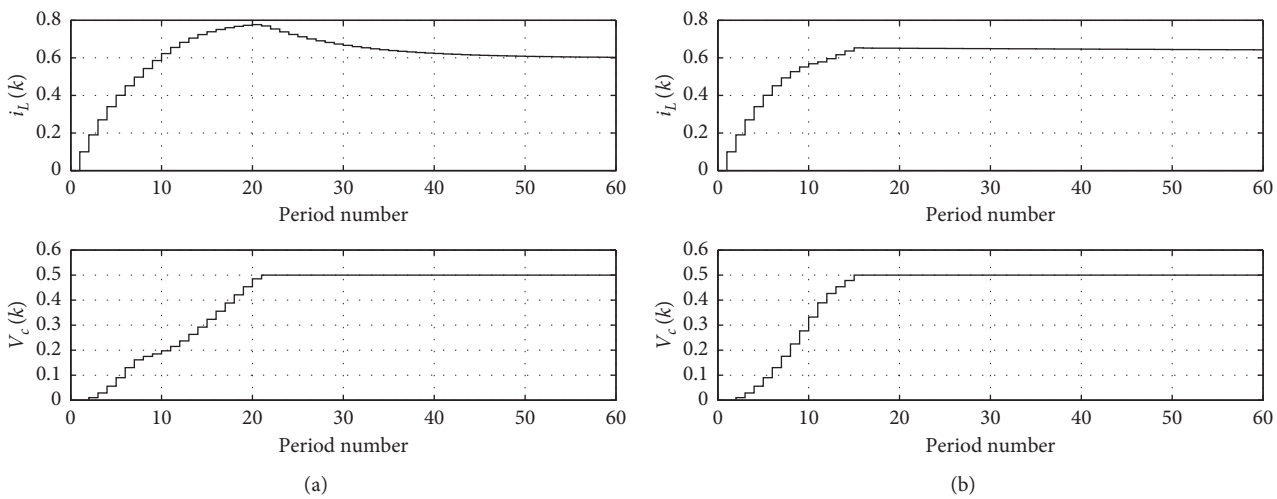

Figure 6: Simulation results of a PI controller: (a) for $k_i = 8$; (b) for $k_i = 0.4$.

$$\begin{aligned} d_1(k) &= k_i\left[i_L'(k) - I_{rd}'\right] + k_v\left[V_c'(k) - V_{cd}'\right] + u(k), \\ d_2(k) &= k_i\left[i_L'(k) - I_{rd}'\right] - k_v\left[V_c'(k) - V_{cd}'\right] + u(k), \end{aligned} \tag{40}$$

where

$$u(k) = u(k-1) + \frac{k_i}{T_i}\left[i_L'(k) - I_{rd}'\right]. \tag{41}$$

In [5], the authors calculate optimal parameters of a PI controller giving the faster response. The controller requires about 40 switching periods to drive the two-cell converter to the desired values and the current presents an important overshoot.

Figure 6 presents the behavior of the two-cell converter under the action of a PI controller with $k_v = (50/6)$ while k_i is fixed first at $k_i = 8$ and then at $k_i = 0.4$. Obviously, desired values were reached without static errors with $k_i = 8$ but it presents an overshoot on the current response. When k_i is decreased, the overshoot is reduced but it makes a very slowly acting system. Thus, it is clear that the proposed controller achieves better performances than a PI controller. It is to be noted that for small values of the gain k_i, there is no static error on both current and voltage, but the systems become too slow. For example, in Figure 6(b), this error goes to zero after more than 400 switching periods.

7. Conclusion

In this paper, we have proposed a discrete type-2 fuzzy second-order sliding mode controller for two-cell DC-DC converter which inherits the advantages of both sliding mode control and fuzzy systems. The second-order sliding mode control has been proposed as a robust method to control nonlinear and uncertain systems. Moreover, an online fuzzy adaptation scheme has been suggested to approximate unknown nonlinear functions. Simulation results on a DC-DC converter show the applicability and the effectiveness of the proposed controller.

Data Availability

The data used in this study are available within the article.

Conflicts of Interest

The authors declare that they have no conflicts of interest.

References

[1] Y. Lee, C. Chiu, and C. Shen, "Adaptive fuzzy terminal sliding mode control of DC-DC buck converters via PSoC," in *Proceedings of the 2010 IEEE International Conference on Control Applications, Part of 2010 IEEE Multi-Conference on Systems and Control Yokohama*, Yokohama, Japan, September 2010.

[2] T. Geyer, G. Papafotiou, and M. Morari, "On the optimal control of switch-mode DC-DC converters," *Hybrid Systems: Computation and Control*, vol. 2993, pp. 342–356, 2004.

[3] K. Koubaa, *Analysis and Control of the Chaotic Behavior in a Multi-Cell DC/DC Buck Converter*, Nova Science Publishers, New York, NY, USA, 2018.

[4] B. Robert and A. EL Aroudi, "Discrete time model of a multi-cell DC/DC converter: non linear approach," *Mathematics and Computers in Simulation*, vol. 71, no. 4–6, pp. 310–319, 2006.

[5] M. Feki, A. El Aroudi, and B. G. M. Robert, "Multi-cell DC-DC converters: modelling, analysis and control," in *Proceedings of the International Multi-Conference on Systems, Signals and Devices*, Sousse, Tunisia, March 2011.

[6] A. Yang, L. Li, Z. Wang, and R. Guo, "Tracking control of a class of chaotic systems," *Symmetry*, vol. 11, no. 4, p. 568, 2019.

[7] C. Jiang, A. Zada, M. Tamer Senel, and T. Li, "Synchronization of bidirectional N-coupled fractional-order chaotic systems with ring connection based on antisymmetric structure," *Advances in Difference Equations*, vol. 2019, no. 1, pp. 1–16, 2019.

[8] C. Jiang, F. Zhang, and T. Li, "Synchronization and anti-synchronization of N-coupled fractional-order complex chaotic systems with ring connection," *Mathematical Methods in the Applied Sciences*, vol. 41, no. 7, pp. 2625–2638, 2018.

[9] M. He and J. Xu, "Nonlinear PID in digital controlled buck converters," in *Proceedings of the APEC 07—Twenty-Second Annual IEEE Applied Power Electronics Conference and Exposition*, pp. 1461–1465, Anaheim, CA, USA, March 2007.

[10] K. Furuta, "Sliding mode control of a discrete system," *Systems & Control Letters*, vol. 14, no. 2, pp. 145–152, 1990.

[11] W. Gao, Y. Wang, and A. Homaifa, "Discrete-time variable structure control systems," *IEEE Transactions on Industrial Electronics*, vol. 42, no. 2, pp. 117–122, 1995.

[12] H. Sira-Ramirez, "Non-linear discrete variable structure systems in quasi-sliding mode," *International Journal of Control*, vol. 54, no. 5, pp. 1171–1187, 1991.

[13] R. Fellag, M. Hamerlain, and S. Laghrouche, "Discrete first and second order sliding mode controllers for a pneumatic artificial muscles robot manipulator," in *Proceedings of the 2015 4th International Conference on Electrical Engineering (ICEE)*, pp. 1–6, IEEE, Boumerdes, Algeria, December 2015.

[14] D. Khadija, L. Majda, and N. Ahmed Said, "Discrete second order sliding mode control for nonlinear multivariable systems," in *Proceedings of the 2012 16th IEEE Mediterranean Electrotechnical Conference*, pp. 387–390, IEEE, Yasmine Hammamet, Tunisia, March 2012.

[15] M. Mihoub, A. S. Nouri, and R. B. Abdennour, "Real-time application of discrete second order sliding mode control to a chemical reactor," *Control Engineering Practice*, vol. 17, no. 9, pp. 1089–1095, 2009.

[16] H. Medhaffar, M. Feki, and N. Derbel, "Stabilizing periodic orbits of chua's system using adaptive fuzzy sliding mode controller," *International Journal of Intelligent Computing and Cybernetics*, vol. 12, no. 1, pp. 102–126, 2019.

[17] R. Sakthivel, V. Nithya, P. Selvaraj, and O. M. Kwon, "Fuzzy sliding mode control design of Markovian jump systems with time-varying delay," *Journal of the Franklin Institute*, vol. 355, no. 14, pp. 6353–6370, 2018.

[18] N. N. Karnik, J. M. Mendel, and Q. Liang, "Type-2 fuzzy logic systems," *IEEE Transactions on Fuzzy Systems*, vol. 7, no. 6, pp. 643–658, 1999.

[19] J. M. Mendel, "Type-2 fuzzy sets as well as computing with words," *IEEE Computational Intelligence Magazine*, vol. 14, no. 1, pp. 82–95, 2019.

[20] N. N. Karnik and J. M. Mendel, "Centroid of a type-2 fuzzy set," *Information Sciences*, vol. 132, no. 1–4, pp. 195–220, 2001.

[21] H. Wu and J. M. Mendel, "Uncertainty bounds and their use in the design of interval type-2 fuzzy logic systems," *IEEE Transactions on Fuzzy Systems*, vol. 10, no. 5, pp. 622–639, 2002.

[22] J. M. Mendel, "Advances in type-2 fuzzy sets and systems," *Information Sciences*, vol. 177, no. 1, pp. 84–110, 2007.

[23] H. A. Hagras, "A hierarchical type-2 fuzzy logic control architecture for autonomous mobile robots," *IEEE Transactions on Fuzzy Systems*, vol. 12, no. 4, pp. 524–539, 2004.

[24] I. Atacak, "Design of a hybrid type-2 fuzzy logic/proportional integral controller for single-phase three-wire inverter system," *Scientific Research and Essays*, vol. 6, no. 23, pp. 5049–5064, 2011.

[25] K. Kaoubaâ, J. Pelaez-Restrepo, M. Feki, B. G. M. Robert, and A. E. Aroudi, "Improved static and dynamic performances of a two-cell DC-DC buck converter using a digital dynamic time-delayed control," *International Journal of Circuit Theory and Applications*, vol. 40, no. 4, pp. 395–407, 2012.

[26] K. Koubaa and M. Feki, "Quasi-periodicity, chaos and coexistence in the time delay controlled two-cell DC-DC buck converter," *International Journal of Bifurcation and Chaos*, vol. 24, no. 10, Article ID 1450124, 2014.

[27] R. Hamza, M. Feki, N. Derbel, B. G. M. Robert, and A. El Aroudi, "Controller design and analysis for a two-cell DC-DC converter in the presence of saturation," *International Journal of Bifurcation and Chaos*, vol. 21, no. 1, pp. 341–361, 2011.

[28] M. R. Amini, M. Shahbakhti, and S. Pan, "Adaptive discrete second-order sliding mode control with application to nonlinear automotive systems," *Journal of Dynamic Systems, Measurement, and Control*, vol. 140, no. 12, Article ID 121010, 2018.

[29] Y. Kali, M. Saad, K. Benjelloun, and A. Fatemi, "Discrete-time second order sliding mode with time delay control for uncertain robot manipulators," *Robotics and Autonomous Systems*, vol. 94, pp. 53–60, 2017.

[30] J. M. Mendel, *Uncertain Rule-Based Fuzzy Logic Systems: Introduction and New Directions*, Prentice-Hall, Upper Saddle River, NJ, USA, 2001.

[31] O. Castillo and P. Melin, *Type-2 Fuzzy Logic: Theory and Applications*, Springer-Verlag, Berlin, Germany, 2008.

[32] D. Wu and J. M. Mendel, "Designing practical interval type-2 fuzzy logic systems made simple," in *Proceedings of the 2014 IEEE International Conference on Fuzzy Systems (FUZZ-IEEE)*, Beijing, China, July 2014.

[33] M. Nie and W. W. Tan, "Towards an efficient type-reduction method for interval type-2 fuzzy logic systems," in *Proceedings of the 2008 IEEE International Conference on Fuzzy Systems (IEEE World Congress on Computational Intelligence)*, pp. 1425–1432, Hong Kong, China, June 2008.

[34] L. X. Wang, *Adaptive Fuzzy Systems and Control*, Prentice-Hall, Englewood Cliffs, NJ, USA, 1994.

Hindawi
Mathematical Problems in Engineering
Volume 2020, Article ID 7962542, 9 pages
https://doi.org/10.1155/2020/7962542

Research Article

Tempered Mittag–Leffler Stability of Tempered Fractional Dynamical Systems

Jingwei Deng, Weiyuan Ma, Kaiying Deng, and Yingxing Li

School of Mathematics and Computer Science, Northwest Minzu University, Lanzhou 730030, China

Correspondence should be addressed to Weiyuan Ma; mwy2004@126.com

Received 11 February 2020; Revised 1 May 2020; Accepted 14 May 2020; Published 29 May 2020

Guest Editor: Cuimei Jiang

Due to finite lifespan of the particles or boundedness of the physical space, tempered fractional calculus seems to be a more reasonable physical choice. Stability is a central issue for the tempered fractional system. This paper focuses on the tempered Mittag–Leffler stability for tempered fractional systems, being much different from the ones for pure fractional case. Some new lemmas for tempered fractional Caputo or Riemann–Liouville derivatives are established. Besides, tempered fractional comparison principle and extended Lyapunov direct method are used to construct stability for tempered fractional system. Finally, two examples are presented to illustrate the effectiveness of theoretical results.

1. Introduction

Fractional derivatives were first proposed by Leibnitz soon after the more familiar classic integer order derivatives. In recent decades, the study of fractional differential systems has attracted wide attention. Compared with the classical calculus, fractional calculus can better characterize memory and hereditary properties of processes and materials. They are now used to model the dynamical evolution in the fields of physics, chemistry, biology, and so on. Fractional calculus can be most easily understood in terms of probability. The relationships among random walks, Brownian motion, and diffusion processes were given in [1]. It is more reasonable to replace classic derivatives by fractional analogues in the diffusion equation [2].

Fractional calculus involves the operation of convolution with a power law function. Multiplying by an exponential factor results in tempered fractional derivatives and integrals [3], this exponential tempering has many merits both in mathematical and practical. A truncated Lévy flight was investigated to capture the natural cutoff in real physical systems [4]. Without a sharp cutoff, the tempered Lévy flight was studied as a smoother alternative [5]. Cartea and del-Castillo-Negrete [6] explored the tempered fractional diffusion equation by the tempered Lévy flight. In finance, the tempered stable process models describe price fluctuations with semiheavy tails [7–10]. Tempered fractional time derivatives can be also found in geophysics [11–13], Brownian motion [14], and so on.

As in classical calculus, stability analysis is still one of the most important tasks in fractional differential system [15–20]. It is a basic feature in fractional physical and biological systems, such as Duffing oscillator [21], neural networks [22–24], and predator-prey models [25]. At present, Lyapunov method has been applied to analyze Mittag–Leffler stability of different fractional systems [26–30]. Li et al. [26, 27] obtained a series of conclusions on the Mittag–Leffler stable for nonlinear fractional equations. In [28], Mittag–Leffler stability of multiple equilibrium points of fractional recurrent neural networks was considered. In [29], a convex and positive definite function was used to analyze Mittag–Leffler stable for fractional system. In [30], the authors presented the Lyapunov stability analysis for fractional nonlinear systems with impulses.

As far as we know, no paper has discussed stability analysis for tempered fractional system. Motivated by this, we think it is very necessary and meaningful to study Mittag–Leffler stability of tempered fractional dynamical systems both in theoretical research and practical application. Because tempered fractional operators combine with nonlocal, weak singularity, and exponential factors [31–33], it has many differences to fractional case in stability analysis. In this paper, tempered Mittag–Leffler

stability is first proposed. It is a more appropriate concept for tempered fractional system. Tempered comparison principle and some inequalities are given for tempered fractional calculus or systems. Then, sufficient conditions for tempered Mittag–Leffler stability are provided and verified by the Lyapunov method. Finally, the theoretical results are applied to some examples.

This paper is organized as follows. In Section 2, some necessary definitions and lemmas are prepared. Section 3 mainly discusses the sufficient criterions ensuring Mittag–Leffler stability of the tempered fractional systems. In Section 4, two examples are presented to show the effectiveness of theoretical results. We conclude the paper with some discussions in Section 5.

2. Preliminaries

Tempered fractional calculus plays an important role in different fields [34, 35]. In practical application, many different tempered fractional derivatives are proposed, such as Caputo, Riemmann–Liouville, and Riesz. Some definitions and lemmas are stated below, which will be used later.

Definition 1 (see [13]). The tempered fractional integral of order $\alpha > 0$ and tempered parameter $\lambda \geq 0$ is defined as

$$ {}_aI_t^{\alpha,\lambda} x(t) = \frac{1}{\Gamma(\alpha)} \int_a^t e^{-\lambda(t-s)} (t-s)^{\alpha-1} x(s) \mathrm{d}s, \tag{1} $$

where Γ presents the Euler gamma function.

Definition 2 (see [3]). The tempered fractional Caputo derivative of tempered parameter $\lambda \geq 0$ is defined as

$$ {}_a^C D_t^{\alpha,\lambda} x(t) := e^{-\lambda t} {}_a^C D_t^{\alpha} \left(e^{\lambda t} u(t)\right) = \frac{e^{-\lambda t}}{\Gamma(n-\alpha)} \int_a^t \frac{1}{(t-s)^{\alpha-n+1}} \cdot \frac{\mathrm{d}^n \left(e^{\lambda s} x(s)\right)}{\mathrm{d}s^n} \mathrm{d}s, \tag{2} $$

where $n-1 \leq \alpha < n, n \in \mathbb{N}$, and ${}_a^C D_t^{\alpha}$ is the Caputo fractional derivative.

Definition 3 (see [9]). The tempered fractional Riemann–Liouville derivative of tempered parameter $\lambda \geq 0$ is defined as

$$ {}_aD_t^{\alpha,\lambda} u(t) := e^{-\lambda t} {}_aD_t^{\alpha} \left(e^{\lambda t} u(t)\right) = \frac{e^{-\lambda t}}{\Gamma(n-\alpha)} \frac{\mathrm{d}^n}{\mathrm{d}t^n} \int_a^t \frac{e^{\lambda s} u(s)}{(t-s)^{\alpha-n+1}} \mathrm{d}s, \tag{3} $$

where $n-1 \leq \alpha < n, n \in \mathbb{N}$, and ${}_aD_t^{\alpha}$ is the Riemann–Liouville fractional derivative operator.

In order to study the stability of tempered fractional systems, several lemmas are needed.

Lemma 1 (see [36]). *Let $0 < \alpha < 1, \lambda \geq 0$ and $t \geq a$, then*

$$ {}_a^C D_t^{\alpha,\lambda} (x(t)) = {}_aD_t^{\alpha,\lambda} (x(t)) - \frac{e^{-\lambda t} (t-a)^{-\alpha}}{\Gamma(1-\alpha)} \left[e^{\lambda t} x(t)_{t=a}\right]. \tag{4} $$

Lemma 2 (see [36]). *Let $0 < \alpha < 1, \lambda \geq 0$, then*

(i) ${}_aI_t^{\alpha,\lambda} [{}_a^C D_t^{\alpha,\lambda} x(t)] = x(t) - e^{-\lambda(t-a)} x(a)$, ${}_a^C D_t^{\alpha,\lambda} [{}_aI_t^{\alpha,\lambda} x(t)] = x(t)$

(ii) ${}_aI_t^{\alpha,\lambda} [{}_aD_t^{\alpha,\lambda} x(t)] = x(t) - (e^{-\lambda t} (t-a)^{\alpha-1}/\Gamma(\alpha)) [{}_aD_t^{\alpha,\lambda} (e^{\lambda t} u(t))|_{t=a}]$ and ${}_aD_t^{\alpha,\lambda} [{}_aI_t^{\alpha,\lambda} x(t)] = x(t)$

Lemma 3 (see [36]). The Laplace transform of tempered fractional integral and *Caputo derivative (2) are given as*

(i) $\mathscr{L}\left\{{}_0I_t^{\alpha,\lambda} (x(t))\right\} = (\lambda + s)^{-\alpha} X(s)$

(ii) $\mathscr{L}\left\{{}_0^C D_t^{\alpha,\lambda} x(t)\right\} = (s+\lambda)^{\alpha} X(s) - \sum_{k=0}^{n-1} (s+\lambda)^{\alpha-k-1} [(\mathrm{d}^k/\mathrm{d}t^k)(e^{\lambda t} x(t))]|_{t=0}$, where $X(s) = \mathscr{L}\{x(t)\}$ denotes the Laplace transform of $x(t)$

3. Main Results

In this section, tempered fractional comparison principles, some inequalities, and tempered Mittag–Leffler stability are derived.

3.1. Tempered Fractional Comparison Principles. In this section, we establish tempered fractional comparison principles.

Lemma 4. Assume that ${}_0^C D_t^{\alpha,\lambda} x(t) \geq {}_0^C D_t^{\alpha,\lambda} y(t)$, $x(0) = y(0)$, $\alpha \in (0,1)$ *and* $\lambda \geq 0$, *then* $x(t) \geq y(t)$.

Proof. Following from ${}_0^C D_t^{\alpha,\lambda} x(t) \geq {}_0^C D_t^{\alpha,\lambda} y(t)$, there exists a function $m(t) \geq 0$ such that

$$ {}_0^C D_t^{\alpha,\lambda} x(t) = m(t) + {}_0^C D_t^{\alpha,\lambda} y(t). \tag{5} $$

By Lemma 3, equation (5) yields

$$ (s+\lambda)^{\alpha} X(s) - (s+\lambda)^{\alpha-1} x(0) = M(s) + (s+\lambda)^{\alpha} Y(s) - (s+\lambda)^{\alpha-1} y(0). \tag{6} $$

According to $x(0) = y(0)$, we have

$$ (s+\lambda)^{\alpha} X(s) = M(s) + (s+\lambda)^{\alpha} Y(s), \tag{7} $$

Thus,

$$ X(s) = Y(s) + (s+\lambda)^{-\alpha} M(s). \tag{8} $$

Taking the inverse Laplace transform on (8), solution of system (5) can be written as

$$ \begin{aligned} x(t) &= y(t) + {}_0I_t^{\alpha,\lambda} m(t) \\ &= y(t) + \frac{1}{\Gamma(\alpha)} \int_0^t e^{-\lambda(t-\tau)} (t-\tau)^{\alpha-1} m(\tau) \mathrm{d}\tau. \end{aligned} \tag{9} $$

According to $m(t) \geq 0$, therefore we obtain $x(t) \geq y(t)$. □

Lemma 5. *Assume that* ${}_0D_t^{\alpha,\lambda}x(t) \geq {}_0D_t^{\alpha,\lambda}y(t)$, $x(0) = y(0)$, *and* $\alpha \in (0,1)$, *then* $x(t) \geq y(t)$.

Proof. From Lemma 1 and ${}_0D_t^{\alpha,\lambda}x(t) \geq {}_0D_t^{\alpha,\lambda}y(t)$, we derive

$$ {}_0^CD_t^{\alpha,\lambda}(x(t)) + \frac{e^{-\lambda t}t^{-\alpha}}{\Gamma(1-\alpha)}x(0) \geq {}_0^CD_t^{\alpha,\lambda}(y(t)) + \frac{e^{-\lambda t}t^{-\alpha}}{\Gamma(1-\alpha)}y(0). \tag{10} $$

That is ${}_0^CD_t^{\alpha,\lambda}(x(t)) \geq {}_0^CD_t^{\alpha,\lambda}(y(t))$. From Lemma 4, we obtain $x(t) \geq y(t)$. □

3.2. Some Inequalities. In this section, we construct some inequalities for tempered fractional derivatives or systems.

From Lemma 1, we could easily obtain the following lemma.

Lemma 6. *The relationship between* ${}_0^CD_t^{\alpha,\lambda}x(t)$ *and* ${}_0D_t^{\alpha,\lambda}x(t)$ *is as follows:*

$$ \begin{cases} {}_0^CD_t^{\alpha,\lambda}x(t) \leq {}_0D_t^{\alpha,\lambda}x(t), & \text{if } x(0) \geq 0, \\ {}_0^CD_t^{\alpha,\lambda}x(t) \geq {}_0D_t^{\alpha,\lambda}x(t), & \text{if } x(0) \leq 0, \end{cases} \tag{11} $$

where $\alpha \in (0,1)$.

Lemma 7. *If* $x(t) \in C^1([0,+\infty),\mathbb{R})$ is a continuously differentiable function, the following inequality holds:

$$ {}_0^CD_t^{\alpha,\lambda}\left|x(t^+)\right| \leq \operatorname{sgn}(x(t)){}_0^CD_t^{\alpha,\lambda}x(t), \quad 0<\alpha<1,\ \lambda \geq 0, \tag{12} $$

where $x(t^+) = lim_{\tau \longrightarrow t^+}x(t)$.

Proof. We take $y(t) = e^{\lambda t}x(t)$ into Theorem 2 in [22]

$$ {}_0^CD_t^{\alpha}\left|y(t^+)\right| \leq \operatorname{sgn}(y(t)){}_0^CD_t^{\alpha}y(t), \quad 0<\alpha<1, \tag{13} $$

for the Caputo fractional derivative. That is,

$$ {}_0^CD_t^{\alpha}\left(e^{\lambda t}\left|x(t^+)\right|\right) \leq \operatorname{sgn}(x(t)){}_0^CD_t^{\alpha}\left(e^{\lambda t}x(t)\right). \tag{14} $$

Multiplying both sides of equation (14) by $e^{-\lambda t}$, it gives

$$ e^{-\lambda t}\,{}_0^CD_t^{\alpha}\left(e^{\lambda t}\left|x(t^+)\right|\right) \leq \operatorname{sgn}(x(t))e^{-\lambda t}\,{}_0^CD_t^{\alpha}\left(e^{\lambda t}x(t)\right). \tag{15} $$

Using Definition 2, we obtain (12).

Consider the following tempered fractional system

$$ {}_{t_0}D_t^{\alpha,\lambda}x(t) = f(t,x(t)), \quad 0<t<T, \tag{16} $$

subjects to the proper initial conditions, where $\alpha \in (0,1)$, $\lambda \geq 0$, D denotes either ${}_a^CD_t^{\alpha,\lambda}$ or ${}_aD_t^{\alpha,\lambda}$, $f: [t_0,+\infty] \times \mathscr{D} \longrightarrow \mathbb{R}^n$ is piecewise continuous in t and locally Lipschitz in x, and $\mathscr{D} \subset \mathbb{R}^n$ is a domain contain the origin. □

Theorem 1. *For the real-valued continuous function* $f(t,x)$ *in (16), we have*

$$ \left\|{}_0I_t^{\alpha,\lambda}f(t,x)\right\| \leq {}_0I_t^{\alpha,\lambda}\|f(t,x)\|, \tag{17} $$

where $\alpha > 0, \lambda \geq 0$, *and* $\|\cdot\|$ denotes an arbitrary norm.

Proof. It follows from (1) that

$$ \begin{aligned} \left\|{}_0I_t^{\alpha,\lambda}f(t,x(t))\right\| &= \left\|\frac{1}{\Gamma(\alpha)}\int_0^t e^{-\lambda(t-s)}(t-s)^{\alpha-1}f(s,x(s))\mathrm{d}s\right\| \\ &\leq \frac{1}{\Gamma(\alpha)}\int_0^t e^{-\lambda(t-s)}(t-s)^{\alpha-1}\|f(s,x(s))\|\mathrm{d}s \\ &= {}_0I_t^{\alpha,\lambda}\|f(t,x(t))\|. \end{aligned} \tag{18} $$

□

Theorem 2. *If* $x = 0$ *is an equilibrium point of system (16) with* ${}_{t_0}D_t^{\alpha,\lambda} = {}_0^CD_t^{\alpha,\lambda}$ *and* $f(t,x)$ *is Lipschitz on* x *with Lipschitz constant* l *and piecewise continuous with respect to* t*; then, we have*

$$ \|x(t)\| \leq \|x(0)\|e^{-\lambda t}E_\alpha(lt^\alpha). \tag{19} $$

Proof. By applying the tempered fractional integral operator ${}_0I_t^{\alpha,\lambda}$ to system (16), it follows from Lemma 2 and Lipschitz condition in $f(t,x)$ that

$$ \begin{aligned} \left|\left\|x(t)\right\| - e^{-\lambda t}\left\|x(0)\right\|\right| &\leq \left\|x(t) - e^{-\lambda t}x(0)\right\| \\ &= \left\|{}_0I_t^{\alpha,\lambda}\left[{}_0^CD_t^{\alpha,\lambda}x(t)\right]\right\| = \left\|{}_0I_t^{\alpha,\lambda}f(t,x(t))\right\| \\ &\leq {}_0I_t^{\alpha,\lambda}\|f(t,x(t))\| \leq l\,{}_0I_t^{\alpha,\lambda}\|x(t)\|. \end{aligned} \tag{20} $$

There exists a function $M(t) \geq 0$ such that

$$ \|x(t)\| - e^{-\lambda t}\|x(0)\| = l\,{}_0I_t^{\alpha,\lambda}\|x(t)\| - M(t). \tag{21} $$

Combining with Lemma 3 and Laplace transform to (21), we obtain

$$ \|x(s)\| = \frac{(s+\lambda)^{\alpha-1}\|x(0)\| - (s+\lambda)^\alpha M(s)}{(s+\lambda)^\alpha - l}, \tag{22} $$

where $\|x(s)\| = \mathscr{L}\{\|x(t)\|\}$. Taking the inverse Laplace transform to (22) gives

$$ \|x(t)\| = \|x(0)\|e^{-\lambda t}E_\alpha(lt^\alpha) - M(t) * \left[e^{-\lambda t}t^{-1}E_{\alpha,0}(lt^\alpha)\right], \tag{23} $$

where $*$ denotes the convolution operator. Obviously, $e^{-\lambda t}t^{-1}E_{\alpha,0}(lt^\alpha) \geq 0$, then inequality $\|x(t)\| \leq \|x(0)\|e^{-\lambda t}E_\alpha(lt^\alpha)$ is obtained. □

3.3. Tempered Mittag–Leffler Stability. In this section, some sufficient conditions are established for the tempered Mittag–Leffler stability of system (16).

Definition 4. If and only if $f(t,\bar{x}) = {}_{t_0}D_t^{\alpha,\lambda}\bar{x}$, then $\bar{x} \in \mathbb{R}^n$ is an equilibrium point of tempered fractional system (16).

Definition 5. Assume $\overline{x} = 0$ is an equilibrium point of system (16), the solution of (16) is said to be tempered Mittag–Leffler stable if

$$\|x(t)\| \le \left[m(x(t_0))e^{-\lambda t}E_\alpha\left(-l(t-t_0)^\alpha\right)\right]^b, \tag{24}$$

where $\alpha > 0, \lambda \ge 0, l > 0, b > 0$, and $m(0) = 0, m(x) \ge 0$ satisfies locally Lipschitz condition.

Remark 1. Tempered Mittag–Leffler stability is a generalization of Mittag–Leffler stability. When $\lambda = 0$, tempered Mittag–Leffler stability can be reduced to Mittag–Leffler stability [26, 27].

Remark 2. Both Mittag–Leffler stability and tempered Mittag–Leffler stability imply asymptotic stability, that is, $\|x(t)\| \longrightarrow 0$ as $t \longrightarrow \infty$.

Theorem 3. *Assume $x = 0$ be an equilibrium point for (16) and domain $\mathscr{D} \subset \mathbb{R}^n$ contains the origin. Let $V(t, x(t)) : [0, +\infty) \times \mathscr{D} \longrightarrow \mathbb{R}$ be a continuously differentiable function and locally Lipschitz with respect to x, such that*

$$\alpha_1\|x(t)\|^a \le V(t, x(t)) \le \alpha_2\|x(t)\|^{ab}, \tag{25}$$

$${}_0^C D_t^{\beta,\lambda} V(t, x(t)) \le -\alpha_3\|x(t)\|^{ab}, \tag{26}$$

where $t \ge 0$, $x \in \mathscr{D}$, $\beta \in (0, 1)$, and $\alpha_1, \alpha_2, \alpha_3, a$, and b are given positive constants, then $x = 0$ is tempered Mittag–Leffler stable. If the assumptions hold globally on $\mathbb{R}^n$, then $x = 0$ is globally tempered Mittag–Leffler stable.

Proof. It follows from equations (25) and (26) that

$${}_0^C D_t^{\beta,\lambda} V(t, x(t)) \le -\frac{\alpha_3}{\alpha_2} V(t, x(t)). \tag{27}$$

There exists a function $M(t) \ge 0$ such that

$${}_0^C D_t^{\beta,\lambda} V(t, x(t)) + M(t) = -\frac{\alpha_3}{\alpha_2} V(t, x(t)). \tag{28}$$

Taking the Laplace transform to (28) gives

$$(s+\lambda)^\beta V(s) - (s+\lambda)^{\beta-1}V(0) + M(s) = -\frac{\alpha_3}{\alpha_2}V(s), \tag{29}$$

where nonnegative constant $V(0) = V(0, x(0))$ and $V(s) = \mathscr{L}\{V(t, x(t))\}$. We rewrite this in the form

$$V(s) = \frac{V(0)(s+\lambda)^{\beta-1} - M(s)}{(s+\lambda)^\beta + (\alpha_3/\alpha_2)}. \tag{30}$$

Applying the inverse Laplace transform to (30), unique solution of (28) is

$$V(t) = V(0)e^{-\lambda t}E_\beta\left(-\frac{\alpha_3}{\alpha_2}t^\beta\right) - M(t) * \left[e^{-\lambda t}t^{\beta-1}E_{\beta,\beta}\left(-\frac{\alpha_3}{\alpha_2}t^\beta\right)\right]. \tag{31}$$

Because $t^{\beta-1}$ and $E_{\beta,\beta}(-(\alpha_3/\alpha_2)t^\beta)$ are nonnegative functions, we obtain

$$V(t) \le V(0)e^{-\lambda t}E_\beta\left(-\frac{\alpha_3}{\alpha_2}t^\beta\right). \tag{32}$$

Substituting (32) into (25) satisfies

$$\|x(t)\| \le \left[\frac{V(0)}{\alpha_1}e^{-\lambda t}E_\beta\left(-\frac{\alpha_3}{\alpha_2}t^\beta\right)\right]^{1/a}, \tag{33}$$

and $x(0) = 0$ if and only if $(V(0)/\alpha_1)e^{-\lambda t} = 0$.

Because $V(t, x)$ is local Lipschitz condition with respect to x and $x(0) = 0$ if and only if $V(0, x(0)) = 0$, then $(V(0, x(0))/\alpha_1)e^{-\lambda t}$ satisfies local Lipschitz condition about $x(0)$. So, system (16) is tempered Mittag–Leffler stable. □

Theorem 4. *Assume all conditions in Theorem 3 are satisfied except replacing ${}_0^C D_t^{\beta,\lambda}$ by ${}_0 D_t^{\beta,\lambda}$, then we have*

$$\|x(t)\| \le \left[\frac{V(0)}{\alpha_1}e^{-\lambda t}E_\beta\left(-\frac{\alpha_3}{\alpha_2}t^\beta\right)\right]^{1/a}. \tag{34}$$

Proof. It follows from Lemma 6 and $V(t, x) \ge 0$ that

$${}_0^C D_t^{\beta,\lambda} V(t, x) \le {}_0 D_t^{\beta,\lambda} V(t, x) \le -\alpha_3\|x(t)\|^{ab}. \tag{35}$$

A similar proof method in Theorem 3 shows result (35). □

Theorem 5. *For the tempered fractional system (10), where ${}_0 D_t^{\alpha,\lambda} = {}_0 D_t^{\alpha,\lambda}$, $f(t, x)$ is Lipschitz on x with constant $l > 0$, and $f(t, 0) = 0$, if there exists a Lyapunov candidate $V(t, x)$ yielding*

$$\alpha_1\|x(t)\|^a \le V(t, x(t)) \le \alpha_2\|x(t)\|, \tag{36}$$

$$\dot{V}(t, x(t)) \le -\alpha_3\|x(t)\|, \tag{37}$$

where $\alpha_3 > \lambda\alpha_2$, $\alpha_1, \alpha_2, \alpha_3, a$ are given positive constants and $\dot{V}(t, x(t)) = (dV(t, x)/dt)$, then

$$\|x(t)\| \le \left[\frac{V(0)}{\alpha_1}e^{-\lambda t}E_{1-\alpha}\left(-\frac{\alpha_3 - \lambda\alpha_2}{\alpha_2}t^{1-\alpha}\right)\right]^{1/a}. \tag{38}$$

Proof. From (1) and (2), we find that tempered fractional derivative on $V(t, x)$ can be represented in the form

$$\begin{aligned}
{}_0^C D_t^{1-\alpha,\lambda} V(t, x) &= \frac{e^{-\lambda t}}{\Gamma(\alpha)}\int_0^t \frac{1}{(t-s)^{1-\alpha}}\frac{\mathrm{d}\left(e^{\lambda s}V(s, x(s))\right)}{\mathrm{d}s}\mathrm{d}s \\
&= \frac{e^{-\lambda t}}{\Gamma(\alpha)}\int_0^t \frac{1}{(t-s)^{1-\alpha}}\Big(\lambda e^{\lambda s}V(s, x(s)) \\
&\quad + e^{\lambda s}\dot{V}(s, x(s))\Big)\mathrm{d}s \\
&= \lambda\frac{e^{-\lambda t}}{\Gamma(\alpha)}\int_0^t \frac{e^{\lambda s}V(s, x(s))}{(t-s)^{1-\alpha}}\mathrm{d}s + \frac{e^{-\lambda t}}{\Gamma(\alpha)}\int_0^t \\
&\quad \frac{e^{\lambda s}\dot{V}(s, x(s))}{(t-s)^{1-\alpha}}\mathrm{d}s \\
&= \lambda\, {}_0 I_t^{\alpha,\lambda} V(t, x(t)) + {}_0 I_t^{\alpha,\lambda}\dot{V}(t, x(t)).
\end{aligned} \tag{39}$$

Using (36) and (37) and Lipschitz condition on $f(t,x)$, we obtain

$$\begin{aligned} {}_0^C D_t^{1-\alpha,\lambda} V(t,x) &\le \lambda\alpha_2\, {}_0I_t^{\alpha,\lambda}\|x(t)\| - \alpha_3\, {}_0I_t^{\alpha,\lambda}\|x(t) \\ &= -(\alpha_3 - \lambda\alpha_2)\, {}_0I_t^{\alpha,\lambda}\|x(t)\|\| \\ &\le -(\alpha_3 - \lambda\alpha_2) l^{-1}\, {}_0I_t^{\alpha,\lambda}\|f(t,x(t))\|. \end{aligned} \tag{40}$$

We can use Lemmas 7 and 2 to write

$$\begin{aligned} {}_0^C D_t^{1-\alpha,\lambda} V(t,x) &\le -(\alpha_3 - \lambda\alpha_2) l^{-1}\left\| {}_0I_t^{\alpha,\lambda} f(t,x(t))\right\| \\ &= -(\alpha_3 - \lambda\alpha_2) l^{-1}\|x(t)\|, \end{aligned} \tag{41}$$

where ${}_0D_t^{\alpha-1}(e^{\lambda t}u(t))|_{t=0} = 0$. By the same proof in Theorem 3, conclusion (38) holds. □

4. Applications

In this section, we will give three examples to demonstrate theoretical analysis. The Adams–Bashforth–Moulton method [37] is employed for solving tempered fractional differential equations in the simulations.

Example 1. Consider the tempered fractional Riemann–Liouville system:

$${}_0D_t^{\alpha,\lambda} x(t) = -|x(t)|, \quad 0 < \alpha < 1,\ \lambda \ge 0, \tag{42}$$

where $x(0) > 0$. The Lyapunov function candidate is chosen as $V(t,x) = |x|$. From Lemma 1, we obtain

$${}_0^C D_t^{\alpha,\lambda} V = {}_0^C D_t^{\alpha,\lambda}|x| \le {}_0D_t^{\alpha,\lambda}|x| = -|V|. \tag{43}$$

By Theorem 3, we have

$$|x(t)| \le |x(0)| e^{-\lambda t} E_\alpha(-t^\alpha). \tag{44}$$

Then, $x = 0$ is tempered Mittag–Leffler stable. To verify the result, we choose parameters as $\alpha = 0.95$ and $x(0) = 4$ and the tempered parameters as $\lambda = 2, 4, 6, 8$, respectively. The time evolution of the system states (42) is shown in Figure 1. It is presented that the solution of system (42) converges to the equilibrium point $x = 0$. The larger the tempered parameter λ is, the faster the convergence speed becomes.

Example 2. Consider the tempered fractional Caputo Hopfield neural networks:

$${}_0^C D_t^{\alpha,\lambda} x_i(t) = -a_i x_i(t) + \sum_{j=1}^n b_{ij} f_j(x_j(t)) + I_i, \tag{45}$$

where $0 < \alpha < 1, \lambda \ge 0, i = 1, 2, \ldots, n$ and n is number of units. $x_i(t)$ is the ith state, f_j is the jth activation function, b_{ij} is constant connection weight of the jth neuron on the ith neuron, $a_i > 0$ denotes the resting rate when the ith neuron disconnected, and I_i is the external inputs. Under the conditions

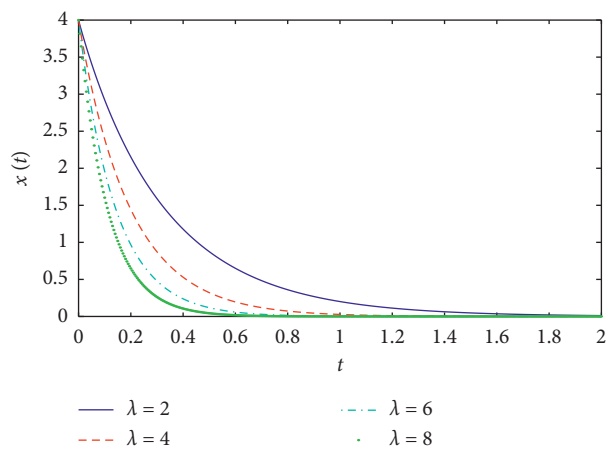

Figure 1: Time evolution of system states $x(t)$ with different tempered parameters λ in Example 1.

$$|f_j(x)| \le l_j|x|, \quad l_j > 0,\ j = 1, 2, \ldots, n, \tag{46}$$

$$c_i = a_i - \sum_{j=1}^n |b_{ji}| l_i > 0, \quad i = 1, 2, \ldots, n, \tag{47}$$

system (45) is globally tempered Mittag–Leffler stable.

Let $x(t) = (x_1, x_2, \ldots, x_n)^T$ be any solution of system (45). We choose Lyapunov function as follows:

$$V(t, x(t)) = \|x(t)\| = \sum_{i=1}^n |x_i(t)|. \tag{48}$$

By inequalities (46) and (47) and Lemma 7, tempered fractional Caputo derivative on $V(t, x(t))$ can be written as

$$\begin{aligned} {}_0^C D_t^{\alpha,\lambda} V(t,x(t)) &= \sum_{i=1}^n {}_0^C D_t^{\alpha,\lambda}|x_i(t)| \le \sum_{i=1}^n \operatorname{sgn}(x_i(t))\, {}_0^C D_t^{\alpha,\lambda} x_i(t) \\ &\le -a_i \sum_{i=1}^n |x_i(t)| + \sum_{i=1}^n \sum_{j=1}^n l_j |b_{ij}| |x_j(t)| \\ &= \sum_{i=1}^n \left[-a_i + \sum_{j=1}^n l_i |b_{ji}|\right] |x_i(t)| \\ &\le -c\|x(t)\|, \end{aligned} \tag{49}$$

where $c = \min\{c_1.c_2, \ldots, c_n\}$. From (49) and Theorem 3, system (45) is globally tempered Mittag–Leffler stable.

To illustrate the effectiveness of Example 2, in system (45), we let $x = (x_1, x_2, x_3)^T, \alpha = 0.98$, $x_1(0) = 5, x_2(0) = -3, x_3(0) = 3, f_j(x_j) = \tanh(x_j)$, and $c_j = 6$ for $j = 1, 2, 3$ and

$$A = (a_{ij})_{3\times 3} = \begin{bmatrix} 2 & -1.2 & 0 \\ 1.8 & 1.71 & 1.15 \\ -4.75 & 0 & 1.1 \end{bmatrix}. \tag{50}$$

It is obvious that condition (47) is satisfied. Let tempered parameters $\lambda = 0, 2, 4, 6$, respectively. As shown in Figure 2,

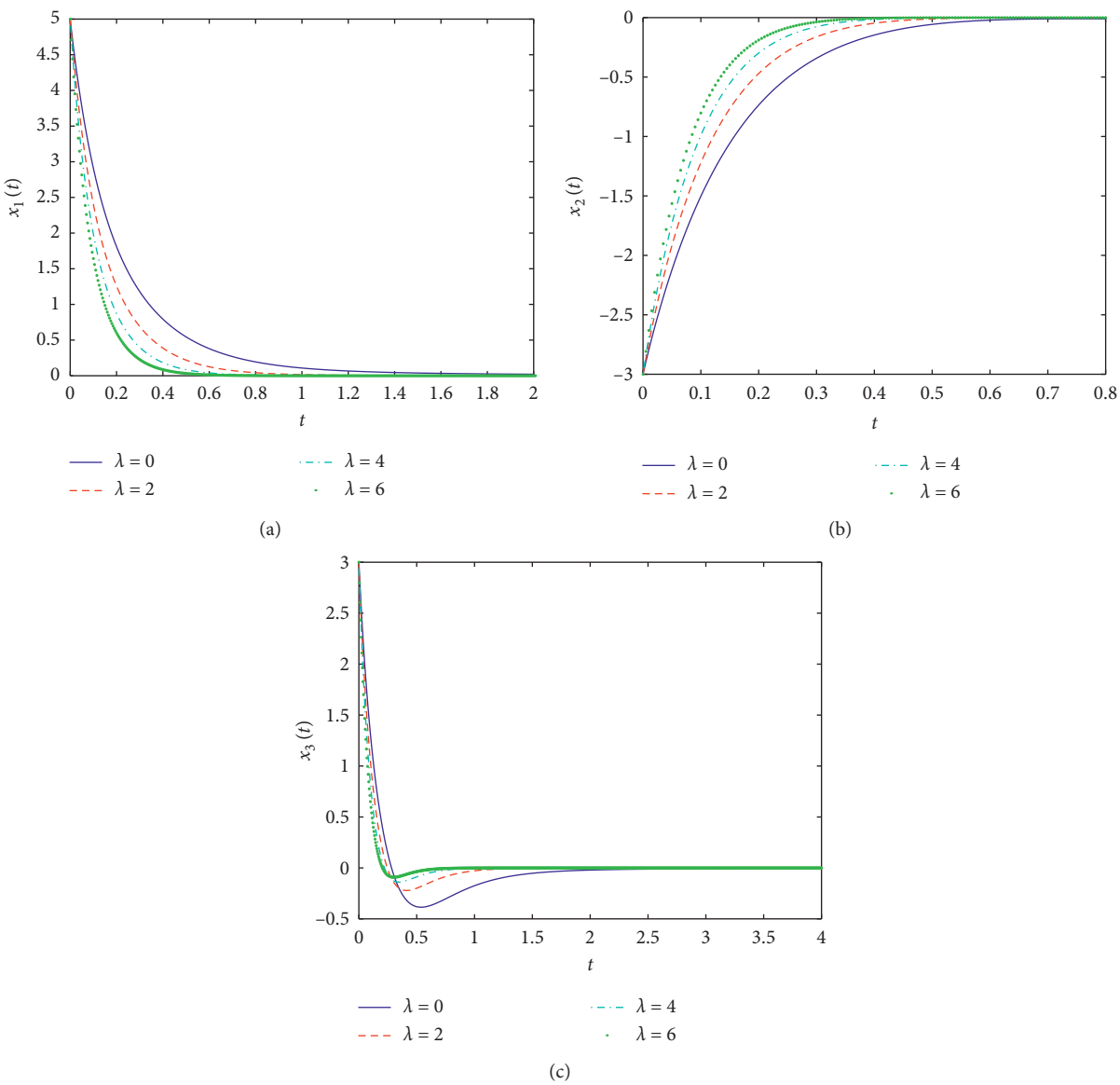

Figure 2: Time evolution of system states $x(t)$ with different tempered parameters λ in Example 2.

the equilibrium point $x = 0$ is tempered Mittag–Leffler stable and the solution of system (45) converges to $x = 0$.

Example 3. Consider the following tempered fractional system:

$$\begin{aligned} {}_0^C D_t^{\alpha,\lambda} x_1 &= -2x_1 + \frac{\sin(x_3)}{1+t^2} x_1, \\ {}_0^C D_t^{\alpha,\lambda} x_2 &= -2x_2 + \cos(x_1) x_2, \\ {}_0^C D_t^{\alpha,\lambda} x_3 &= x_3, \end{aligned} \tag{51}$$

where $0 < \alpha < 1, \lambda \geq 0$ and $x(t) = (x_1(t), x_2(t), x_3(t)) \in \mathbb{R}^3$.

Let the Lyapunov function $V(t,x) = |x_1| + |x_2|$. By Lemma 7, we obtain

$$\begin{aligned} {}_0^C D_t^{\alpha,\lambda} V(t,x) &\leq \operatorname{sgn}(x_1(t)) {}_0^C D_t^{\alpha,\lambda} x_1(t) + \operatorname{sgn}(x_2(t)) {}_0^C D_t^{\alpha,\lambda} x_2(t) \\ &= \operatorname{sgn}(x_1(t)) \left(-2x_1(t) + \frac{\sin(x_3(t))}{1+t^2} x_1(t) \right) \\ &\quad + \operatorname{sgn}(x_2(t)) (-2x_2(t) + \cos(x_1(t)) x_2(t)) \\ &\leq -2|x_1(t)| + \frac{\sin(x_3(t))}{1+t^2} |x_1(t)| - 2|x_2(t)| \\ &\quad + \cos(x_1(t)) |x_2(t)| \\ &\leq -(|x_1(t)| + |x_2(t)|). \end{aligned} \tag{52}$$

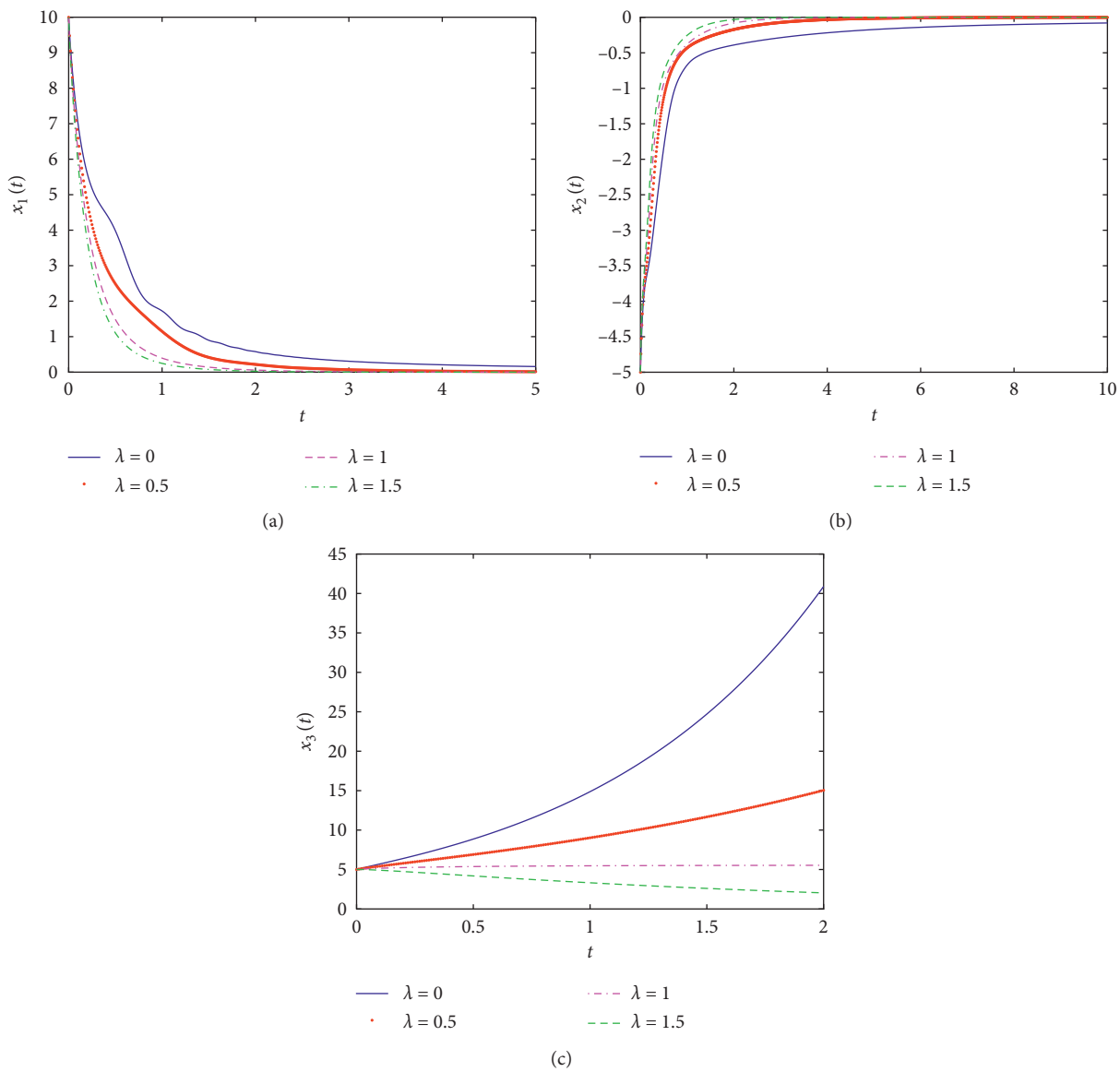

Figure 3: Time evolution of system states $x(t)$ with different tempered parameters λ in Example 3.

Then, the conditions of Theorem 3 are satisfied. Hence, $x = 0$ is globally tempered Mittag–Leffler stable with respect to (x_1, x_2). Take $\alpha = 0.9, x_1(0) = 10, x_2(0) = -5$, and $x_3(0) = 5$. The numerical simulation is shown as Figure 3 with different tempered parameters $\lambda = 0, 0.5, 1, 1.5$. It is obvious $x_1(t)$ and $x_2(t)$ converge to 0. When tempered parameter of the system increase, the part solution of system converges faster.

5. Conclusions

In this paper, we present some stability results for the tempered fractional systems. Based on the Laplace transform, we obtain the comparison principle for the tempered fractional systems. Some theorems about tempered Mittag–Leffler stability are derived, which enrich the knowledge of the system theory and the tempered fractional calculus and are helpful in characterizing the tempered fractional system models. Furthermore, we will study stability of tempered fractional systems with time-varying delays in future work.

Data Availability

The authors affirm that all data necessary for confirming the conclusions of the article are present in the article.

Conflicts of Interest

The authors declare that there are no conflicts of interest regarding the publication of this paper.

Acknowledgments

This work was supported by the introduction of talent, the Northwest University for Nationalities, special Funds for Talents (nos. xbmuyjrc201916, xbmuyjrc201632), the

Humanities and Social Sciences Planning Projects of the Ministry of Education of P. R. China under Grant (no. 19YJAZH010), and Fundamental Research Funds for the Central Universities (no. 31920180119).

References

[1] A. Einstein, "Über die von der molekularkinetischen theorie der wärme geforderte bewegung von in ruhenden flüssigkeiten suspendierten teilchen," *Annalen der Physik*, vol. 322, no. 8, pp. 549–560, 1905.

[2] J. Klafter and I. M. Sokolov, "Anomalous diffusion spreads its wings," *Physics World*, vol. 18, no. 8, pp. 29–32, 2005.

[3] F. Sabzikar, M. M. Meerschaert, and J. Chen, "Tempered fractional calculus," *Journal of Computational Physics*, vol. 293, pp. 14–28, 2015.

[4] R. N. Mantegna and H. E. Stanley, "Stochastic process with ultraslow convergence to a Gaussian: the truncated lévy flight," *Physical Review Letters*, vol. 73, no. 22, pp. 2946–2949, 1994.

[5] I. Koponen, "Analytic approach to the problem of convergence of truncated Lévy flights towards the Gaussian stochastic process," *Physical Review E*, vol. 52, no. 1, pp. 1197–1199, 1995.

[6] Á. Cartea and D. del-Castillo-Negrete, "Fluid limit of the continuous-time random walk with general Lévy jump distribution functions," *Physical Review E*, vol. 76, no. 4, Article ID 041105, 2007.

[7] P. Carr, H. Geman, D. B. Madan, and M. Yor, "The fine structure of asset returns: an empirical investigation," *The Journal of Business*, vol. 75, no. 2, pp. 305–332, 2002.

[8] P. Carr, H. Geman, D. B. Madan, and M. Yor, "Stochastic volatility for Lévy processes," *Mathematical Finance*, vol. 13, no. 3, pp. 345–382, 2003.

[9] Á. Cartea and D. del-Castillo-Negrete, "Fractional diffusion models of option prices in markets with jumps," *Physica A: Statistical Mechanics and its Applications*, vol. 374, no. 2, pp. 749–763, 2007.

[10] O. E. Barndorff-Nielsen, "Processes of normal inverse Gaussian type," *Finance and Stochastics*, vol. 2, no. 1, pp. 41–68, 1997.

[11] M. M. Meerschaert, Y. Zhang, and B. Baeumer, "Tempered anomalous diffusions in heterogeneous systems," *Geophysical Research Letters*, vol. 35, no. 17, 2008.

[12] Y. Zhang and M. M. Meerschaert, "Gaussian setting time for solute transport in fluvial systems," *Water Resources Research*, vol. 47, no. 8, 2011.

[13] M. M. Meerschaert, F. Sabzikar, M. S. Phanikumar, and A. Zeleke, "Tempered fractional time series model for turbulence in geophysical flows," *Journal of Statistical Mechanics: Theory and Experiment*, vol. 2014, no. 9, p. 9023, 2014.

[14] M. M. Meerschaert and F. Sabzikar, "Tempered fractional Brownian motion," *Statistics & Probability Letters*, vol. 83, no. 10, pp. 2269–2275, 2013.

[15] C. Li and F. Zhang, "A survey on the stability of fractional differential equations," *The European Physical Journal Special Topics*, vol. 193, no. 1, pp. 27–47, 2011.

[16] C. Jiang, F. Zhang, and T. Li, "Synchronization and anti-synchronization of N-coupled fractional-order complex chaotic systems with ring connection," *Mathematical Methods in the Applied Sciences*, vol. 41, no. 7, pp. 2625–2638, 2018.

[17] C. Jiang, A. Zada, M. Tamer Senel, and T. Li, "Synchronization of bidirectional N-coupled fractional-order chaotic systems with ringconnection based on antisymmetric structure," *Advances in Difference Equations*, vol. 2019, no. 1, p. 456, 2019.

[18] S. Huang and Q. Tian, "Marcinkiewicz estimates for solution to fractional elliptic Laplacian equation," *Computers & Mathematics with Applications*, vol. 78, no. 5, pp. 1732–1738, 2019.

[19] M. Hong, W. Sun, S. Liu, and T. Xuan, "Coherence analysis and Laplacian energy of recursive trees with controlled initial states," *Frontiers of Information Technology & Electronic Engineering*, 2019.

[20] W. Sun, M. Sun, J. Guan, and Q. Jia, "Robustness of coherence in noisy scale-free networks and applications to identification of influential spreaders," *IEEE Transactions on Circuits and Systems II: Express Briefs*, 2020.

[21] X. Gao and J. Yu, "Chaos in the fractional order periodically forced complex Duffing's oscillators," *Chaos, Solitons and Fractals*, vol. 24, no. 4, pp. 1097–1104, 2005.

[22] S. Zhang, Y. Yu, and H. Wang, "Mittag-Leffler stability of fractional-order Hopfield neural networks," *Nonlinear Analysis: Hybrid Systems*, vol. 16, pp. 104–121, 2015.

[23] S. Yang, J. Yu, C. Hu, and H. Jiang, "Quasi-projective synchronization of fractional-order complex-valued recurrent neural networks," *Neural Networks*, vol. 104, pp. 104–113, 2018.

[24] W. Ma, C. Li, Y. Wu, and Y. Wu, "Synchronization of fractional fuzzy cellular neural networks with interactions," *Chaos: An Interdisciplinary Journal of Nonlinear Science*, vol. 27, no. 10, Article ID 103106, 2017.

[25] E. Ahmed, A. M. A. El-Sayed, and H. A. A. El-Saka, "Equilibrium points, stability and numerical solutions of fractional-order predator-prey and rabies models," *Journal of Mathematical Analysis and Applications*, vol. 325, no. 1, pp. 542–553, 2007.

[26] Y. Li, Y. Chen, and I. Podlubny, "Mittag-Leffler stability of fractional order nonlinear dynamic systems," *Automatica*, vol. 45, no. 8, pp. 1965–1969, 2009.

[27] Y. Li, Y. Chen, and I. Podlubny, "Stability of fractional-order nonlinear dynamic systems: Lyapunov direct method and tempered Mittag-Leffler stability," *Computers & Mathematics with Applications*, vol. 59, no. 5, pp. 1810–1821, 2010.

[28] P. Liu, Z. Zeng, and J. Wang, "Multiple Mittag-Leffler stability of fractional-order recurrent neural networks," *IEEE Transactions on Systems, Man, and Cybernetics: Systems*, vol. 47, no. 8, pp. 2279–2288, 2017.

[29] W. Chen, H. Dai, Y. Song, and Z. Zhang, "Convex Lyapunov functions for stability analysis of fractional order systems," *IET Control Theory & Applications*, vol. 11, no. 7, pp. 1070–1074, 2017.

[30] X. Yang, C. Li, T. Huang, and Q. Song, "Mittag-Leffler stability analysis of nonlinear fractional-order systems with impulses," *Applied Mathematics and Computation*, vol. 293, pp. 416–422, 2017.

[31] W. Deng, B. Li, W. Tian, and P. Zhang, "Boundary problems for the fractional and tempered fractional operators," *Multiscale Modeling & Simulation*, vol. 16, no. 1, pp. 125–149, 2018.

[32] W. Deng and Z. Zhang, "Variational formulation and efficient implementation for solving the tempered fractional problems," *Numerical Methods for Partial Differential Equations*, vol. 34, no. 4, pp. 1224–1257, 2018.

[33] W. Ma, C. Li, and J. Deng, "Synchronization in tempered fractional complex networks via auxiliary system approach," *Complexity*, vol. 2019, Article ID 6071412, 12 pages, 2019.

[34] A. Fernandez and C. Ustaoğlu, "On some analytic properties of tempered fractional calculus," *Journal of Computational and Applied Mathematics*, vol. 366, Article ID 112400, 2020.
[35] Y. Yan, W. Deng, and D. Nie, "A finite-difference approximation for the one-and two-dimensional tempered fractional Laplacian," *Communications on Applied Mathematics and Computation*, vol. 2, no. 1, pp. 129–145, 2020.
[36] C. Li, W. Deng, and L. Zhao, "Well-posedness and numerical algorithm for the tempered fractional ordinary differential equations," *American Institute of Mathematical Science*, vol. 24, no. 4, pp. 1989–2015, 2019.
[37] J. Deng, L. Zhao, and Y. Wu, "Fast predictor-corrector approach for the tempered fractional differential equations," *Numerical Algorithms*, vol. 74, no. 3, pp. 717–754, 2017.

Hindawi
Mathematical Problems in Engineering
Volume 2020, Article ID 3869089, 7 pages
https://doi.org/10.1155/2020/3869089

Research Article

An Optimal Control Problem Governed by Nonlinear First Order Dynamic Equation on Time Scales

Jian-Ping Sun,[1,2] **Qiu-Yan Ren**,[1,3] **and Ya-Hong Zhao**[2]

[1]*College of Electrical and Information Engineering, Lanzhou University of Technology, Lanzhou 730050, China*
[2]*Department of Applied Mathematics, Lanzhou University of Technology, Lanzhou 730050, China*
[3]*College of Technology and Engineering, Lanzhou University of Technology, Lanzhou 730050, China*

Correspondence should be addressed to Jian-Ping Sun; jpsun@lut.cn

Received 20 March 2020; Revised 10 May 2020; Accepted 11 May 2020; Published 26 May 2020

Guest Editor: Rongwei Guo

In this paper, we are concerned with a class of optimal control problem governed by nonlinear first order dynamic equation on time scales. By imposing some suitable conditions on the related functions, for any given control policy, we first obtain the existence of a unique solution for the nonlinear controlled system. Then, we study the existence of an optimal solution for the optimal control problem.

1. Introduction

The theory of time scales was introduced by Hilger in [1] in order to unify discrete and continuous analysis. Some foundational definitions and results from the calculus on time scales will be defined in Section 2. For more details, one can see [2–4].

In recent years, the calculus of variations and optimal control problems on time scales have attracted the attention of some researchers. For example, [5–8] discussed the calculus of variations on time scales and [9–12] studied some maximum principles on time scales, while [13–16] investigated the existence of optimal solutions or the necessary conditions of optimality for some optimal control problems on time scales.

In 2017, Guo [17] studied the projective synchronization problem of a class of chaotic systems in arbitrary dimensions. Firstly, a necessary and sufficient condition for the existence of the projective synchronization problem was presented. Secondly, an algorithm was proposed to obtain all the solutions of the projective synchronization problem. Thirdly, a simple and physically implementable controller was designed to ensure the realization of the projective synchronization. Finally, some numerical examples were provided to verify the effectiveness and the validity of the proposed results.

In 2020, Xu and Zhang [18] investigated general mean-field linear-quadratic (LQ) games of stochastic large-population system, where the individual diffusion coefficient could depend on both the state and the control of the agent, and the control weight in the cost functional could be indefinite. The asymptotic suboptimality property of the decentralized strategies for the LQ games was derived through the consistency condition. A pricing problem was also studied, for which the decentralized suboptimal price was obtained.

Throughout this paper, we always assume that $\mathbb{T}$ is a time scale, $T > 0$ is fixed, $0, T \in \mathbb{T}$ and $\sigma^2(T) = \sigma(T)$. For each interval $\mathbf{I}$ of $\mathbb{R}$, we denote by $\mathbf{I}_{\mathbb{T}} = \mathbf{I} \cap \mathbb{T}$.

Suppose that there is a flock of sheep in a pasture. We consider the changes in the number of sheep during a time interval $[0, \sigma(T)]_{\mathbb{T}}$. It is well known that the supply of herbage, which influences growth rate and reproductive ability of sheep, is one of the main ways to control the number of sheep. Now, we define some related functions as follows:

$x(t)$ is the number of sheep at time t

$r(t)$ is the number of births per unit of time at time t

$p(t)$ is the number of sales per sheep per unit of time at time t

$u(t)$ is the amount of herbage supplied at time t

$q(t)$ is the number of sheep converted by per unit of herbage supplied per unit of time at time t

Let U_{ad} be the admissible control set. Then, for any given control policy $u \in U_{\text{ad}}$, it is easy to know that the changes in the number of sheep can be described by the following linear dynamic equation:

$$x^{\Delta}(t) + p(t)x(\sigma(t)) = r(t) + q(t)u(t), \quad t \in [0,T]_{\mathbb{T}}. \tag{1}$$

At the same time, in order to keep steady development, we may assume that the number of sheep at the beginning is equal to that at the end, that is,

$$x(0) = x(\sigma(T)). \tag{2}$$

Suppose that x_u is the solution of the controlled systems (1) and (2) corresponding to the control policy u and x_d is the desired value. Recently, the authors [19] considered the optimal control problem (P_0). Find a $u_0 \in U_{\text{ad}}$ such that

$$J(u_0) \le J(u), \quad \text{for all } u \in U_{\text{ad}}, \tag{3}$$

where

$$J(u) = \int_0^T \left[x_u(\sigma(t)) - x_d(t)\right]^2 \Delta t + \int_0^T u^2(t)\Delta t, \quad u \in U_{\text{ad}}, \tag{4}$$

is the quadratic cost functional.

Motivated greatly by the abovementioned works, in this paper, we suppose that the controlled system is governed by the following more general nonlinear periodic boundary value problem:

$$\begin{cases} x^{\Delta}(t) + p(t)x(\sigma(t)) = f(t, x(t), x(\sigma(t))) + g(u(t)), \quad t \in [0,T]_{\mathbb{T}}, \\ x(0) = x(\sigma(T)). \end{cases} \tag{5}$$

First, by imposing some suitable conditions on p, f, and g, for any given control policy $u \in U_{\text{ad}}$, we obtain the existence of a unique solution x_u for the nonlinear controlled system (5). Then, we study the optimal control problem (P). Find a $u_0 \in U_{\text{ad}}$ such that

$$J(u_0) \le J(u), \quad \text{for all } u \in U_{\text{ad}}, \tag{6}$$

where

$$J(u) = \int_0^T \left[x_u(\sigma(t)) - x_d(t)\right]^2 \Delta t + \int_0^T h(u(t))\Delta t, \quad u \in U_{\text{ad}}, \tag{7}$$

where x_d is the desired value and $h: \mathbb{R} \longrightarrow [0,\infty)$ is continuous.

2. Preliminaries

In this section, we will provide some foundational definitions and results from the calculus on time scales.

Definition 1. We define the forward jump operator $\sigma: \mathbb{T} \longrightarrow \mathbb{T}$ by

$$\sigma(t) := \inf\{s \in \mathbb{T}: s > t\}, \quad \text{for all } t \in \mathbb{T}, \tag{8}$$

while the backward jump operator $\rho: \mathbb{T} \longrightarrow \mathbb{T}$ is defined by

$$\rho(t) := \sup\{s \in \mathbb{T}: s < t\}, \quad \text{for all } t \in \mathbb{T}. \tag{9}$$

In this definition, we put $\inf\varnothing = \sup\mathbb{T}$ and $\sup\varnothing = \inf\mathbb{T}$, where $\varnothing$ denotes the empty set. If $\sigma(t) > t$, we say that t is right-scattered, while if $\rho(t) < t$, we say that t is left-scattered. Also, if $t < \sup\mathbb{T}$ and $\sigma(t) = t$, then t is called right-dense, and if $t > \inf\mathbb{T}$ and $\rho(t) = t$, then t is called left-dense. If $\mathbb{T}$ has a left-scattered maximum m, then we define $\mathbb{T}^k = \mathbb{T} - \{m\}$, otherwise $\mathbb{T}^k = \mathbb{T}$. Finally, the graininess function $\mu: \mathbb{T} \longrightarrow [0,\infty)$ is defined by

$$\mu(t) := \sigma(t) - t, \quad \text{for all } t \in \mathbb{T}. \tag{10}$$

Definition 2. Assume $f: \mathbb{T} \longrightarrow \mathbb{R}$ is a function and let $t \in \mathbb{T}^k$. Then, we define $f^{\Delta}(t)$ to be the number (provided it exists) with the property that given any $\varepsilon > 0$, there is a neighborhood U of t (i.e., $U = (t-\delta, t+\delta)_{\mathbb{T}}$ for some $\delta > 0$) such that

$$\left|f(\sigma(t)) - f(s) - f^{\Delta}(t)(\sigma(t) - s)\right| \le \varepsilon|\sigma(t) - s|, \quad \text{for all } s \in U. \tag{11}$$

We call $f^{\Delta}(t)$ the delta derivative of f at t.

Moreover, we say that f is delta differentiable (or in short, differentiable) on $\mathbb{T}^k$ provided $f^{\Delta}(t)$ exists for all $t \in \mathbb{T}^k$. The function $f^{\Delta}: \mathbb{T}^k \longrightarrow \mathbb{R}$ is then called the (delta) derivative of f on $\mathbb{T}^k$. A function $F: \mathbb{T} \longrightarrow \mathbb{R}$ is called an antiderivative of $f: \mathbb{T} \longrightarrow \mathbb{R}$ provided

$$F^{\Delta}(t) = f(t) \text{ holds for all } t \in \mathbb{T}^k. \tag{12}$$

If $F: \mathbb{T} \longrightarrow \mathbb{R}$ is an antiderivative of $f: \mathbb{T} \longrightarrow \mathbb{R}$, then we define the Cauchy integral by

$$\int_a^b f(t)\Delta t = F(b) - F(a), \quad \text{for all } a, b \in \mathbb{T}. \tag{13}$$

Definition 3. A function $f: \mathbb{T} \longrightarrow \mathbb{R}$ is called rd-continuous provided it is continuous at right-dense points in $\mathbb{T}$ and its left-sided limits exist (finite) at left-dense points in $\mathbb{T}$.

Definition 4. We say that a function $p: \mathbb{T} \longrightarrow \mathbb{R}$ is regressive provided

$$1 + \mu(t)p(t) \ne 0, \quad \text{for all } t \in \mathbb{T}^k, \tag{14}$$

holds. The set of all regressive and rd-continuous functions will be denoted by $\mathscr{R}$. We define the set of positively

regressive functions $\mathscr{R}^+$ as the set consisting of those $p \in \mathscr{R}$ satisfying

$$1 + \mu(t)p(t) > 0, \quad \text{for all } t \in \mathbb{T}. \tag{15}$$

Lemma 1. *Let $p \in \mathscr{R}$, $t_0 \in \mathbb{T}$, and $e_p(\cdot, t_0)$ be the exponential function on $\mathbb{T}$. Then,*

(i) $e_p(t,t) \equiv 1$ for all $t \in \mathbb{T}$

(ii) $e_p^{\Delta}(t,t_0) = p(t)e_p(t,t_0)$ for all $t \in \mathbb{T}^k$

Moreover, if $p \in \mathscr{R}^+$, then

$$e_p(t,t_0) > 0, \quad \text{for all } t \in \mathbb{T}. \tag{16}$$

Lemma 2. *Let f be a continuous function on $[a,b]_{\mathbb{T}}$ that is differentiable on $[a,b)_{\mathbb{T}}$. Then, f is increasing, decreasing, nondecreasing, and nonincreasing on $[a,b]_{\mathbb{T}}$ if $f^{\Delta}(t) > 0$, $f^{\Delta}(t) < 0$, $f^{\Delta}(t) \geq 0$, and $f^{\Delta}(t) \leq 0$ for all $t \in [a,b)_{\mathbb{T}}$, respectively.*

Lemma 3. *Let $\{f_n\}_{n=1}^{\infty}$ be a sequence of Δ integrable functions on $[a,b]_{\mathbb{T}}$ and suppose that $f_n \longrightarrow f$ uniformly on $[a,b)_{\mathbb{T}}$ for a function f defined on $[a,b]_{\mathbb{T}}$. Then, f is Δ integrable from a to b and*

$$\int_a^b f(t)\Delta t = \lim_{n\longrightarrow\infty} \int_a^b f_n(t)\Delta t. \tag{17}$$

In the remainder of this paper, we always assume that Banach space

$$C([a,b]_{\mathbb{T}}, \mathbb{R}) = \{y \mid y\colon [a,b]_{\mathbb{T}} \longrightarrow \mathbb{R} \text{ is continuous}\}, \tag{18}$$

is equipped with the norm $\|y\| = \max_{t\in[a,b]_{\mathbb{T}}}|y(t)|$, $p\colon [0,T]_{\mathbb{T}} \longrightarrow (0,\infty)$ is rd-continuous, and denote

$$M = \frac{1}{e_p(\sigma(T),0) - 1}. \tag{19}$$

Then, it is easy to see that $M > 0$.

Lemma 4 (see [20]). *For any $y \in C([0,T]_{\mathbb{T}}, \mathbb{R})$, the following first order linear periodic boundary value problem*

$$\begin{cases} x^{\Delta}(t) + p(t)x(\sigma(t)) = y(t), & t \in [0,T]_{\mathbb{T}}, \\ x(0) = x(\sigma(T)), \end{cases} \tag{20}$$

has a unique solution

$$x(t) = \frac{1}{e_p(t,0)}\left[\int_0^t e_p(s,0)y(s)\Delta s + M\int_0^{\sigma(T)} e_p(s,0)y(s)\Delta s\right], \quad t \in [0,\sigma(T)]_{\mathbb{T}}. \tag{21}$$

3. Main Results

First, we list the following two conditions which we shall use in the sequel.

(A_1) $f\colon [0,T]_{\mathbb{T}} \times \mathbb{R}^2 \longrightarrow \mathbb{R}$ is continuous and there exists $0 < L < (M/2(1+M)^2\sigma(T))$ such that

$$|f(t,\omega_1,\nu_1) - f(t,\omega_2,\nu_2)| \leq L(|\omega_1 - \omega_2| + |\nu_1 - \nu_2|), \quad t \in [0,T]_{\mathbb{T}}, \omega_1, \omega_2, \nu_1, \nu_2 \in \mathbb{R}. \tag{22}$$

(A_2) $g\colon \mathbb{R} \longrightarrow \mathbb{R}$ and there exists $K > 0$ such that

$$|g(\omega) - g(\nu)| \leq K|\omega - \nu|, \quad \omega, \nu \in \mathbb{R}. \tag{23}$$

From now on, we always suppose that the control space is $C([0,T]_{\mathbb{T}}, \mathbb{R})$ and the admissible control set U_{ad} is a compact subset of $C([0,T]_{\mathbb{T}}, \mathbb{R})$.

Lemma 5. *Assume that conditions (A_1) and (A_2) are satisfied. Then, for any given control policy $u \in U_{ad}$, the nonlinear controlled system (5) has a unique solution x_u and*

$$x_u(t) = \frac{1}{e_p(t,0)}\left\{\int_0^t e_p(s,0)[f(s,x_u(s),x_u(\sigma(s))) + g(u(s))]\Delta s + M\int_0^{\sigma(T)} e_p(s,0)[f(s,x_u(s),x_u(\sigma(s))) + g(u(s))]\Delta s\right\}, \quad t \in [0,\sigma(T)]_{\mathbb{T}}. \tag{24}$$

Proof. For any fixed $u \in U_{\text{ad}}$, we define an operator $\Phi_u\colon C([0,\sigma(T)]_{\mathbb{T}}, \mathbb{R}) \longrightarrow C([0,\sigma(T)]_{\mathbb{T}}, \mathbb{R})$ as follows:

$$(\Phi_u x)(t) = \frac{1}{e_p(t,0)}\left\{\int_0^t e_p(s,0)[f(s,x(s),x(\sigma(s))) + g(u(s))]\Delta s + M\int_0^{\sigma(T)} e_p(s,0)[f(s,x(s),x(\sigma(s))) + g(u(s))]\Delta s\right\}, \quad t \in [0,\sigma(T)]_{\mathbb{T}}. \tag{25}$$

Obviously, x is a solution of the nonlinear controlled system (5) if and only if x is a fixed point of Φ_u in $C([0,\sigma(T)]_{\mathbb{T}},\mathbb{R})$.

Let $x, y \in C([0,\sigma(T)]_{\mathbb{T}},\mathbb{R})$. Then, in view of Lemmas 1 and 2 and (A_1), we have

$$\begin{aligned}
\left|(\Phi_u x)(t)-(\Phi_u y)(t)\right| &= \frac{1}{e_p(t,0)}\left|\int_0^t e_p(s,0)[f(s,x(s),x(\sigma(s)))-f(s,y(s),y(\sigma(s)))]\Delta s\right. \\
&\quad \left. +M\int_0^{\sigma(T)} e_p(s,0)[f(s,x(s),x(\sigma(s)))-f(s,y(s),y(\sigma(s)))]\Delta s\right| \\
&\le \frac{1}{e_p(t,0)}\left\{\int_0^t e_p(s,0)|f(s,x(s),x(\sigma(s)))-f(s,y(s),y(\sigma(s)))|\Delta s\right. \\
&\quad \left. +M\int_0^{\sigma(T)} e_p(s,0)|f(s,x(s),x(\sigma(s)))-f(s,y(s),y(\sigma(s)))|\Delta s\right\} \\
&\le (1+M)\int_0^{\sigma(T)} e_p(s,0)|f(s,x(s),x(\sigma(s)))-f(s,y(s),y(\sigma(s)))|\Delta s \\
&\le L(1+M)\int_0^{\sigma(T)} e_p(s,0)[|x(s)-y(s)|+|x(\sigma(s))-y(\sigma(s))|]\Delta s \\
&\le 2L(1+M)\|x-y\|\int_0^{\sigma(T)} e_p(s,0)\Delta s \\
&\le \frac{2L(1+M)^2\sigma(T)}{M}\|x-y\|, \quad t\in[0,\sigma(T)]_{\mathbb{T}},
\end{aligned} \tag{26}$$

so

$$\left\|\Phi_u x-\Phi_u y\right\| \le \frac{2L(1+M)^2\sigma(T)}{M}\|x-y\|, \tag{27}$$

which together with $0<L<(M/2(1+M)^2\sigma(T))$ implies that $\Phi_u\colon C([0,\sigma(T)]_{\mathbb{T}},\mathbb{R}) \longrightarrow C([0,\sigma(T)]_{\mathbb{T}},\mathbb{R})$ is a contraction mapping.

Therefore, it follows from Banach contraction principle that Φ_u has a unique fixed point $x_u \in C([0,\sigma(T)]_{\mathbb{T}},\mathbb{R})$. This indicates that the nonlinear controlled system (5) has a unique solution x_u and

$$\begin{aligned}
x_u(t) = \frac{1}{e_p(t,0)}\left\{\int_0^t e_p(s,0)\left[f\left(s,x_u(s),x_u(\sigma(s))\right)+g(u(s))\right]\Delta s\right. \\
\left. +M\int_0^{\sigma(T)} e_p(s,0)\left[f\left(s,x_u(s),x_u(\sigma(s))\right)+g(u(s))\right]\Delta s\right\}, \quad t\in[0,\sigma(T)]_{\mathbb{T}}.
\end{aligned} \tag{28}$$

Theorem 1. *Assume that conditions (A_1) and (A_2) are satisfied and $h\colon \mathbb{R} \longrightarrow [0,\infty)$ is continuous. Then, the optimal control problem (P) has an optimal solution $u_0 \in U_{ad}$.*

Proof. First, it follows from Lemma 5 that, for any given control policy $u \in U_{\mathrm{ad}}$, the nonlinear controlled system (5) has a unique solution x_u and

$$\begin{aligned}
x_u(t) = \frac{1}{e_p(t,0)}\left\{\int_0^t e_p(s,0)\left[f\left(s,x_u(s),x_u(\sigma(s))\right)+g(u(s))\right]\Delta s\right. \\
\left. +M\int_0^{\sigma(T)} e_p(s,0)\left[f\left(s,x_u(s),x_u(\sigma(s))\right)+g(u(s))\right]\Delta s\right\}, \quad t\in[0,\sigma(T)]_{\mathbb{T}}.
\end{aligned} \tag{29}$$

Next, in view of $J(u)=\int_0^T [x_u(\sigma(t))-x_d(t)]^2\Delta t+\int_0^T h(u(t))\Delta t$, $u\in U_{\mathrm{ad}}$, it is obvious that $\inf_{u\in U_{\mathrm{ad}}} J(u)$ exists. Thus, by the definition of infimum, we know that there exists a sequence $\{u_n\}_{n=1}^{\infty}\subset U_{\mathrm{ad}}$ such that

$$\lim_{n\longrightarrow\infty} J(u_n)=\inf_{u\in U_{\mathrm{ad}}} J(u). \tag{30}$$

On the one hand, since U_{ad} is a compact subset of $C([0,T]_{\mathbb{T}},\mathbb{R})$ and $\{u_n\}_{n=1}^{\infty}\subset U_{\mathrm{ad}}$, $\{u_n\}_{n=1}^{\infty}$ has a convergent subsequence in U_{ad}. Without loss of generality, we may assume that $\{u_n\}_{n=1}^{\infty}$ converges in U_{ad}, that is, there exists $u_0\in U_{\mathrm{ad}}$ such that

$$\lim_{n\longrightarrow\infty} u_n=u_0. \tag{31}$$

On the other hand, in view of Lemmas 1 and 2, (A_1) and (A_2), for any $n=1,2,\ldots$, we have

$$\begin{aligned}
\left|x_{u_n}(t)-x_{u_0}(t)\right| &= \frac{1}{e_p(t,0)}\Bigg|\int_0^t e_p(s,0)\left[f\left(s,x_{u_n}(s),x_{u_n}(\sigma(s))\right)-f\left(s,x_{u_0}(s),x_{u_0}(\sigma(s))\right)+g(u_n(s))-g(u_0(s))\right]\Delta s\\
&\quad +M\int_0^{\sigma(T)} e_p(s,0)\left[f\left(s,x_{u_n}(s),x_{u_n}(\sigma(s))\right)-f\left(s,x_{u_0}(s),x_{u_0}(\sigma(s))\right)+g(u_n(s))-g(u_0(s))\right]\Delta s\Bigg|\\
&\le \int_0^t e_p(s,0)\left|f\left(s,x_{u_n}(s),x_{u_n}(\sigma(s))\right)-f\left(s,x_{u_0}(s),x_{u_0}(\sigma(s))\right)+g(u_n(s))-g(u_0(s))\right|\Delta s\\
&\quad +M\int_0^{\sigma(T)} e_p(s,0)\left|f\left(s,x_{u_n}(s),x_{u_n}(\sigma(s))\right)-f\left(s,x_{u_0}(s),x_{u_0}(\sigma(s))\right)+g(u_n(s))-g(u_0(s))\right|\Delta s\\
&\le (1+M)\int_0^{\sigma(T)} e_p(s,0)\left|f\left(s,x_{u_n}(s),x_{u_n}(\sigma(s))\right)-f\left(s,x_{u_0}(s),x_{u_0}(\sigma(s))\right)+g(u_n(s))-g(u_0(s))\right|\Delta s\\
&\le (1+M)\int_0^{\sigma(T)} e_p(s,0)\left[\left|f\left(s,x_{u_n}(s),x_{u_n}(\sigma(s))\right)-f\left(s,x_{u_0}(s),x_{u_0}(\sigma(s))\right)\right|+\left|g(u_n(s))-g(u_0(s))\right|\right]\Delta s\\
&\le (1+M)\int_0^{\sigma(T)} e_p(s,0)\left\{L\left[\left|x_{u_n}(s)-x_{u_0}(s)\right|+\left|x_{u_n}(\sigma(s))-x_{u_0}(\sigma(s))\right|\right]+K\left|u_n(s)-u_0(s)\right|\right\}\Delta s\\
&\le (1+M)\left(2L\left\|x_{u_n}-x_{u_0}\right\|+K\left\|u_n-u_0\right\|\right)\int_0^{\sigma(T)} e_p(s,0)\Delta s\\
&\le \frac{2L(1+M)^2\sigma(T)}{M}\left\|x_{u_n}-x_{u_0}\right\|+\frac{K(1+M)^2\sigma(T)}{M}\left\|u_n-u_0\right\|,\quad t\in[0,\sigma(T)]_{\mathbb{T}},
\end{aligned} \tag{32}$$

so, for any $n=1,2,\ldots$, we obtain

$$\left\|x_{u_n}-x_{u_0}\right\|\le\frac{K(1+M)^2\sigma(T)}{M-2L(1+M)^2\sigma(T)}\left\|u_n-u_0\right\|, \tag{33}$$

which together with (31) implies that

$$\lim_{n\longrightarrow\infty} x_{u_n}=x_{u_0}. \tag{34}$$

Thus, in view of Lemma 3, (31), and (34), we obtain

$$\begin{aligned}
\lim_{n\longrightarrow\infty} J(u_n) &= \lim_{n\longrightarrow\infty}\left(\int_0^T\left[x_{u_n}(\sigma(t))-x_d(t)\right]^2\Delta t+\int_0^T h(u_n(t))\Delta t\right)\\
&= \int_0^T \lim_{n\longrightarrow\infty}\left[x_{u_n}(\sigma(t))-x_d(t)\right]^2\Delta t+\int_0^T \lim_{n\longrightarrow\infty} h(u_n(t))\Delta t\\
&= \int_0^T\left[x_{u_0}(\sigma(t))-x_d(t)\right]^2\Delta t+\int_0^T h(u_0(t))\Delta t\\
&= J(u_0),
\end{aligned} \tag{35}$$

which together with (30) indicates that

$$J(u_0) = \inf_{u \in U_{\mathrm{ad}}} J(u). \tag{36}$$

Therefore, $J(u_0) \le J(u)$ for all $u \in U_{\mathrm{ad}}$. This shows that u_0 is an optimal solution of the optimal control problem (P). □

Example 1. Let $\mathbb{T} = [0,1] \cup [2,3]$. We suppose that the controlled system is governed by the following nonlinear periodic boundary value problem

$$\begin{cases} x^{\Delta}(t) + x(\sigma(t)) = Dt^2\left[x(t)\arctan x(t) - \frac{1}{2}\ln\left(1 + x^2(t)\right) + \frac{\pi}{4}\sin^2 x(\sigma(t))\right] + u(t), \quad t \in [0,3]_{\mathbb{T}}, \\ x(0) = x(3), \end{cases} \tag{37}$$

where

$$D = \frac{2(2e^2 - 1)}{9\pi[28e^4 - 4e^2 + 1]}. \tag{38}$$

In view of $\mathbb{T} = [0,1] \cup [2,3]$, $T = 3$ and $p(t) \equiv 1$ for $t \in [0,3]_{\mathbb{T}}$, it is not difficult to obtain that

$$M = \frac{1}{2e^2 - 1}. \tag{39}$$

Since $f(t,\omega,v) = Dt^2[\omega\arctan\omega - (1/2)\ln(1+\omega^2) + (\pi/4)\sin^2 v]$ for $(t,\omega,v) \in [0,3]_{\mathbb{T}} \times \mathbb{R}^2$ and $g(\omega) = \omega$ for $\omega \in \mathbb{R}$, it is obvious that $f\colon [0,3]_{\mathbb{T}} \times \mathbb{R}^2 \longrightarrow \mathbb{R}$ is continuous and (A_2) is satisfied. Moreover, if we choose $L = (9\pi D/2)$, then $0 < L < (M/2(1+M)^2\sigma(T))$ and it follows from Lagrange mean value theorem that

$$\begin{aligned} &\left|f(t,\omega_1,v_1) - f(t,\omega_2,v_2)\right| \\ &\quad = Dt^2\left|\omega_1\arctan\omega_1 - \frac{1}{2}\ln\left(1+\omega_1^2\right) + \frac{\pi}{4}\sin^2 v_1 - \omega_2\arctan\omega_2 + \frac{1}{2}\ln\left(1+\omega_2^2\right) - \frac{\pi}{4}\sin^2 v_2\right| \\ &\quad \le 9D\left[\left|\omega_1\arctan\omega_1 - \frac{1}{2}\ln\left(1+\omega_1^2\right) - \omega_2\arctan\omega_2 + \frac{1}{2}\ln\left(1+\omega_2^2\right)\right| + \frac{\pi}{4}\left|\sin^2 v_1 - \sin^2 v_2\right|\right] \\ &\quad \le \frac{9\pi D}{2}\left(\left|\omega_1 - \omega_2\right| + \left|v_1 - v_2\right|\right) \\ &\quad = L\left(\left|\omega_1 - \omega_2\right| + \left|v_1 - v_2\right|\right), \quad t \in [0,3]_{\mathbb{T}}, \omega_1, \omega_2, v_1, v_2 \in \mathbb{R}. \end{aligned} \tag{40}$$

This shows that (A_1) is fulfilled.

For any given constant $N > 0$, let $U_{\mathrm{ad}} = \{u \in C([0,3]_{\mathbb{T}}, \mathbb{R}) \mid u(0) = 0 \text{ and } |u(t_1) - u(t_2)| \le N|t_1 - t_2| \text{ for all } t_1, t_2 \in [0,3]_{\mathbb{T}}\}$. Then, it is easy to verify that U_{ad} is a compact subset of $C([0,3]_{\mathbb{T}}, \mathbb{R})$.

By Lemma 5, we know that, for any given control policy $u \in U_{\mathrm{ad}}$, the nonlinear controlled system (37) has a unique solution x_u.

Now, we consider the optimal control problem (P^*). Find a $u_0 \in U_{\mathrm{ad}}$ such that

$$J(u_0) \le J(u), \quad \text{for all } u \in U_{\mathrm{ad}}, \tag{41}$$

where

$$J(u) = \int_0^3 \left[x_u(\sigma(t)) - x_d(t)\right]^2 \Delta t + \int_0^3 u^2(t)\Delta t, \quad u \in U_{\mathrm{ad}}, \tag{42}$$

where x_d is the desired value.

Since $h(\omega) = \omega^2$ for $\omega \in \mathbb{R}$, $h\colon \mathbb{R} \longrightarrow [0,\infty)$ is continuous, thus, all the conditions of Theorem 1 are satisfied. Therefore, it follows from Theorem 1 that the optimal control problem (P^*) has an optimal solution $u_0 \in U_{\mathrm{ad}}$.

4. Conclusions

In this paper, we consider a class of optimal control problem governed by nonlinear first order dynamic equation on time scales. First, by imposing some suitable conditions on the related functions and applying Banach contraction principle, for any given control policy, we obtain the existence of a unique solution for the nonlinear controlled system. Next, we prove that the optimal control problem has an optimal solution in the admissible control set. Finally, an example is also given to illustrate the main result of this paper.

Data Availability

No data were used to support this study.

Conflicts of Interest

The authors declare that there are no conflicts of interest regarding the publication of this paper.

Acknowledgments

This work was supported by the National Natural Science Foundation of China (Grant no. 11661049).

References

[1] S. Hilger, "Analysis on measure chains—a unified approach to continuous and discrete calculus," *Results in Mathematics*, vol. 18, no. 1-2, pp. 18–56, 1990.

[2] V. Lakshmikantham, S. Sivasundaram, and B. Kaymakcalan, *Dynamic Systems on Measure Chains*, Kluwer Academic Publishers, Boston, MA, USA, 1996.

[3] M. Bohner and A. Peterson, *Dynamic Equations on Time Scales: An Introduction with Applications*, Birkhäuser, Boston, MA, USA, 2001.

[4] M. Bohner and A. Peterson, *Advances in Dynamic Equations on Time Scales*, Birkhäuser, Boston, MA, USA, 2003.

[5] Z. Bartosiewicz, N. Martins, and D. F. M. Torres, "The second Euler-Lagrange equation of variational calculus on time scales," *European Journal of Control*, vol. 17, no. 1, pp. 9–18, 2011.

[6] R. A. C. Ferreira, A. B. Malinowska, and D. F. M. Torres, "Optimality conditions for the calculus of variations with higher-order delta derivatives," *Applied Mathematics Letters*, vol. 24, no. 1, pp. 87–92, 2011.

[7] R. Hilscher and V. Zeidan, "First order conditions for generalized variational problems over time scales," *Computers and Mathematics with Applications*, vol. 62, no. 9, pp. 3490–3503, 2011.

[8] A. B. Malinowska, N. Martins, and D. F. M. Torres, "Transversality conditions for infinite horizon variational problems on time scales," *Optimization Letters*, vol. 5, no. 1, pp. 41–53, 2011.

[9] P. Stehlik and B. Thompson, "Maximum principles for second order dynamic equations on time scales," *Journal of Mathematical Analysis and Applications*, vol. 331, no. 2, pp. 913–926, 2007.

[10] R. Hilscher and V. Zeidan, "Weak maximum principle and accessory problem for control problems on time scales," *Nonlinear Analysis: Theory, Methods & Applications*, vol. 70, no. 9, pp. 3209–3226, 2009.

[11] S. Zhou and H. Li, "Maximum principles for dynamic equations on time scales and their applications," *Journal of Applied Mathematics*, vol. 2014, Article ID 434582, 6 pages, 2014.

[12] M. Bohner, K. Kenzhebaev, O. Lavrova, and O. Stanzhytskyi, "Pontryagin's maximum principle for dynamic systems on time scales," *Journal of Difference Equations and Applications*, vol. 23, no. 7, pp. 1161–1189, 2017.

[13] Y. Gong and X. Xiang, "A class of optimal control problems of systems governed by the first order linear dynamic equations on time scales," *Journal of Industrial & Management Optimization*, vol. 5, no. 1, pp. 1–10, 2009.

[14] G. Liu, X. Xiang, and Y. Peng, "Nonlinear integro-differential equations and optimal control problems on time scales," *Computers & Mathematics with Applications*, vol. 61, no. 2, pp. 155–169, 2011.

[15] D. A. Carlson, "The existence of optimal controls for problems defined on time scales," *Journal of Optimization Theory and Applications*, vol. 166, no. 2, pp. 351–376, 2015.

[16] O. E. Lavrova, "Conditions for the existence of optimal control for some classes of differential equations on time scales," *Journal of Mathematical Sciences*, vol. 222, no. 3, pp. 276–295, 2017.

[17] R. Guo, "Projective synchronization of a class of chaotic systems by dynamic feedback control method," *Nonlinear Dynamics*, vol. 90, no. 1, pp. 53–64, 2017.

[18] R. Xu and F. Zhang, "ϵ-nash mean-field games for general linear-quadratic systems with applications," *Automatica*, vol. 114, Article ID 108835, 2020.

[19] Q.-Y. Ren, J.-P. Sun, and Y.-H. Zhao, "The existence of optimal solutions for an optimal control problem defined on time scales," *Dynamic Systems and Applications*, 2014, In press.

[20] J.-P. Sun and W.-T. Li, "Existence of solutions to nonlinear first-order PBVPs on time scales," *Nonlinear Analysis: Theory, Methods & Applications*, vol. 67, no. 3, pp. 883–888, 2007.

Hindawi
Mathematical Problems in Engineering
Volume 2020, Article ID 1672595, 11 pages
https://doi.org/10.1155/2020/1672595

Research Article

Global Robust Stabilization Control for Nonlinear Time-Delay Systems with Dead-Zone Input and Complex Dynamics

Lingrong Xue,[1] Zhen-Guo Liu,[2] Junjun Chen,[2] and Fujing Xu[2]

[1]*School of Information Management, Shanxi University of Finance and Economics, Taiyuan 030006, China*
[2]*Department of Automation, Shanxi University, Taiyuan 030006, China*

Correspondence should be addressed to Zhen-Guo Liu; lzg819@163.com

Received 28 February 2020; Revised 23 April 2020; Accepted 24 April 2020; Published 26 May 2020

Guest Editor: Rongwei Guo

This article investigates the robust stabilization problem for nonlinear time-delay systems with dead-zone input and complex dynamics. By flexibly using the inequality technique, the backstepping control method, and skillfully introducing a new Lyapunov–Krasovskii functional, we obtain a stable controller without using unmeasurable signals in the dynamic subsystem. The control system is guaranteed to be stable finally. Two simulation examples are given to verify the control strategy.

1. Introduction

Many practical models in engineering are nonlinear systems such as the flexible-joint robot [1], the wheeled inverted pendulum [2], and the autonomous underwater vehicle [3]. In the past few years, scholars have focused on studying nonlinear systems, such as [4–11]. For numerous nonlinear systems, the time-delay phenomenon which may lead to system instability often exists and is inevitable [12]. Nonlinear systems sometimes involve complex dynamics, in which the information of the states is not available. For more results on nonlinear systems with complex dynamics, we refer the reader to [13]. Besides the time delay, nonlinear conditions, and complex dynamics, specific control inputs such as the dead-zone input [14, 15] can also have a significant impact on the system. Considering the above facts, the nonlinear time-delay systems with dead-zone input and complex dynamics are investigated in this paper.

In recent years, some complicated linear systems have been studied. For example, Xu and Zhang [16] considered the stochastic large population system and presented a novel strategy for linear-quadratic games. However, different from linear systems, control problems of nonlinear systems are often difficult since they have more complicated dynamics. Specially, Guo [17] studied nonlinear chaotic systems and raised a physically implementable controller to solve the projective synchronization problem. In engineering practice, lots of nonlinear systems can be approximated by using linear systems at the origin; thus, the theory of linear systems can be applied. However, some systems may not be linearized at the origin or can be linearized but have uncontrollable Jacobian linearization [18, 19]. So, it is necessary to study nonlinear control design methods for those systems. Besides, time-delay problems cannot be ignored for the system control design, since ignoring it may make the system unstable. Many scholars have studied the associated control design for systems with time delay (for example, see the adaptive control problem [20], the stabilization problem [21], and the tracking problem [22]).

In recent years, the control design for systems with complex dynamics has been one of the interesting topics. Particularly, with the choice of a state observer, the adaptive control problem of systems containing complex dynamics was solved in [23]. By utilizing a new Lyapunov function, the adaptive tracking problem was studied in [24] for systems with input saturation and complex dynamics. On the other hand, time delay may bring negative effects to the stability of systems. Therefore, scholars have studied control problems for nonlinear systems with time delay. For systems involving time delay and complex dynamics, in [25], by the neural network method and the Lyapunov–Krasovskii functional, the tracking control design was studied. In [26], a modified

strategy of adding a power integrator was applied for stochastic delayed nonlinear systems with complex dynamics. Subsequently, this technique was further applied to systems with uncertainty in [27].

In practice, dead zone may exist in the actuator or the control input of the system. There have been some related reports mainly discussing the neural method and the fuzzy method. Specially, the neural control method [28] and the adaptive fuzzy control method [29] were applied to solve adaptive control problems of nonlinear systems. Recently, the Lyapunov–Krasovskii functional control approach has been used to study the nonlinear tracking control of systems containing dead-zone input and implies that the approach is important for systems with time delay, see [30]. However, this method is not extended to solve the robust stabilization problem for systems involving time delay, dead-zone input, and complex dynamics. Also, few studies in the literature considered the robust control problem for the system.

The difficulty and the contribution of this paper are as follows:

(i) Considering that the system of this paper involves complicated dynamics, time delay, external disturbances, and input dead zone, the robust stabilization control problem of this paper is more challenging. The existing methods are difficult to solve the problem of this paper. Particularly, the homogeneous domination approach [5] has not proposed a strategy to solve the input dead-zone problem, and the tuning functions-based robust control method [7] has not give a solution to the complicated dynamics. The neural control method [28] and the fuzzy method [29] are difficult to give appropriate bounds for the nonlinear time-delay terms. The continuous control methods in [31, 32] did not provide a strategy to deal with the external disturbances. This article will consider more complicated nonlinear systems and present a control strategy to solve the control problem.

(ii) A new robust stabilization strategy is raised. By recursively selecting a Lyapunov–Krasovskii functional and by presenting a modified backstepping control technique, a stable controller without utilizing the unmeasurable states is successfully constructed.

2. Problem Formulation and Preliminaries

Consider the nonlinear system as follows:

$$\begin{cases} \dot{\eta} = A\eta + \phi_0(x_1, x_1(t-\tau)), \\ \dot{x}_i = d_i(t)x_{i+1} + \phi_i(\eta, \eta(t-\tau), \overline{x}_i, \overline{x}_i(t-\tau)), \quad i = 1, \ldots, n-1, \\ \dot{x}_n = d_n(t)u(v) + \phi_n(\eta, \eta(t-\tau), x, x(t-\tau)), \end{cases} \tag{1}$$

where $\eta = [\eta_1, \ldots, \eta_m]^\top \in R^m$ is the unmeasurable dynamics and $x = [x_1, \ldots, x_n]^\top \in \mathscr{R}^n$ is the state vector which is measurable. $\overline{x}_i = [x_1, \ldots, x_i]^\top$. $\eta(t-\tau) = [\eta_1(t-\tau), \ldots, \eta_m(t-\tau)]^\top$ and $\overline{x}_i(t-\tau) = [x_1(t-\tau), \ldots, x_i(t-\tau)]^\top$. τ is the constant time delay. $A \in R^{m\times m}$ is the Hurwitz matrix that satisfies $A^\top P + PA \le -Q$, where P and Q are positive definite symmetric matrices. The control coefficients $d_j(t) \in \mathscr{R}$, $j = 1, \ldots, n$ satisfy $d \le d_j(t) \le \overline{d}$ with $d \ge 0$ and $\overline{d} \ge 0$. $\phi_k \in \mathscr{R}$, $k = 0, 1, \ldots, n$, are continuous functions. The dead-zone input $u(v)$ is

$$u(v) = \begin{cases} m_r(t)(v - b_r(t)), & v \ge b_r(t), \\ 0, & -b_l(t) < v < b_r(t), \\ m_l(t)(v + b_l(t)), & v \le -b_l(t), \end{cases} \tag{2}$$

where $m_r(t) > 0, m_l(t) > 0, b_r(t) > 0$, and $b_l(t) > 0$ the are time-varying functions.

To facilitate the problem simply, let $\varpi = (q/p) \ge 0$, where q and p are the even integer and the odd integer, respectively. Therefore, define the constants $\varepsilon_1 = 1$ and $\varepsilon_j = \varepsilon_{j-1} + \varpi$, $j = 2, \ldots, n$. Next, we need the following assumptions.

Assumption 1. The nonlinear terms satisfy the following:

$$\begin{aligned} &\left|\phi_0(x_1, x_1(t-\tau))\right| \le C_0\left(\left|x_1\right| + \left|x_1(t-\tau)\right|\right), \\ &\left|\phi_i(\eta, \eta(t-\tau), \overline{x}_i, \overline{x}_i(t-\tau))\right| \le C\left(\|\eta\|^{\varepsilon_{i+1}} + \|\eta(t-\tau)\|^{\varepsilon_{i+1}} + \sum_{j=1}^{i}\left|x_j\right|^{\varepsilon_{i+1}/\varepsilon_j} + \sum_{j=1}^{i}\left|x_j(t-\tau)\right|^{\varepsilon_{i+1}/\varepsilon_j}\right) + M_0(t), \quad i = 1, \ldots, n, \end{aligned} \tag{3}$$

where $C_0 > 0$ and $C > 0$ are constants and $M_0(t)$ is a bounded disturbance.

Assumption 2. There are constants $\underline{m}_r > 0, \underline{m}_l > 0, \overline{b}_r > 0$, and $\overline{b}_l > 0$ satisfying

$$\underline{m}_r \le m_r(t), \quad \underline{m}_l \le m_l(t), \quad b_r(t) \le \overline{b}_r, \text{ and } \quad b_l(t) \le \overline{b}_l. \tag{4}$$

Next, Lemma 1 is provided for control design.

Lemma 1 (see [30]). *For given $m > 0$ and $n > 0$ and functions $a(x, y) > 0$ and $c(x, y) > 0$, there holds*

$$\left|a(x,y)x^m y^n\right| \le c(x,y)|x|^{m+n} + \frac{n}{m+n} \cdot \left(\frac{m}{(m+n)c(x,y)}\right)^{m/n} |a(x,y)|^{m+n/n}|y|^{m+n}. \tag{5}$$

3. Main Results

Theorem 1. *For system (1), suppose that Assumptions 1-2 hold. Then, under the following transformation*

$$\begin{aligned} \zeta_1 &= x_1, \\ \zeta_i &= x_i - \alpha_{i-1}, \\ \alpha_i &= -g_i \zeta_i^{\varepsilon_{i+1}/\varepsilon_i}, \quad i = 2, \ldots, n, \end{aligned} \tag{6}$$

there exists a robust controller:

$$v = \begin{cases} \dfrac{\alpha_n}{\underline{m}_r} + \overline{b}_r, & \alpha_n > 0, \\ 0, & \alpha_n = 0, \\ \dfrac{\alpha_n}{\underline{m}_l} - \overline{b}_l, & \alpha_n < 0. \end{cases} \tag{7}$$

where $\alpha_n = -g_n \zeta_n^{\varepsilon_{n+1}/\varepsilon_n}$. The controller ensures that the considered system is globally stable.

Proof. We divide the proof into several parts.

3.1. Part I: Robust Control Design. We construct the controller by using the modified backstepping technique.

Step 1: defining $\sigma = \varepsilon_n$ and choosing $U_0 = 1/\sigma(\eta^\top P\eta)^\sigma$, we have

$$\begin{aligned} \dot{U}_0 &= (\eta^\top P\eta)^{\sigma-1}\left(\eta^\top P(A\eta + \phi_0) + (A\eta + \phi_0)^\top P\eta\right) \\ &= (\eta^\top P\eta)^{\sigma-1}(\eta^\top (PA + A^\top P)\eta + 2\eta^\top P\phi_0). \end{aligned} \tag{8}$$

Noting that $\lambda_p\|\eta\|^2 \le \eta^\top P\eta \le \lambda_P\|\eta\|^2$ and $\eta^\top(PA + A^\top P)\eta \le -\lambda_q\|\eta\|^2$, where λ_p is the minimal eigenvalue of P and λ_P is the maximal eigenvalues of P. λ_q is the minimal eigenvalue of Q. Then, introduce $\zeta_1 = x_1$ and define $\lambda = \min\{\lambda_p, \lambda_q\}$. From Assumption 1 and Lemma 1, we get

$$\dot{U}_0 \le -\lambda^\sigma\|\eta\|^{2\sigma} + 2(\eta^\top P\eta)^{\sigma-1}\eta^\top P\phi_0 = -\lambda^\sigma\|\eta\|^{2\sigma} + \Delta, \tag{9}$$

$$\begin{aligned} \Delta &= 2(\eta^\top P\eta)^{\sigma-1}\eta^\top P\phi_0 \le 2\lambda_P^{\sigma-1}\|\eta\|^{2\sigma-2}\cdot\|\eta\|\cdot\|P\|\cdot|\phi_0| \\ &\le 2\lambda_P^{\sigma-1}\|P\|\|\eta\|^{2\sigma-1}C_0\left(|\zeta_1| + |\zeta_1(t-\tau)|\right) \\ &\le \frac{1}{n+2}\lambda^\sigma\|\eta\|^{2\sigma} + \gamma_{01}(C_0,\lambda_P)\zeta_1^{\frac{2\sigma}{\varepsilon_1}} + \gamma_{02}(C_0,\lambda_P)e^{-\mu\tau}\zeta_1^{\frac{2\sigma}{\varepsilon_1}}(t-\tau), \end{aligned} \tag{10}$$

where $\gamma_{01}(C_0, \lambda_P)$ and $\gamma_{02}(C_0, \lambda_P)$ are the positive constants depended on C_0 and λ_P. Substituting (10) into (9), it yields

$$\begin{aligned} \dot{U}_0 \le& -\frac{n+1}{n+2}\lambda^\sigma\|\eta\|^{2\sigma} + \gamma_{01}(C_0,\lambda_P)\zeta_1^{2\sigma/\varepsilon_1} \\ &+ \gamma_{02}(C_0,\lambda_P)e^{-\mu\tau}\zeta_1^{2\sigma/\varepsilon_1}(t-\tau). \end{aligned} \tag{11}$$

By Lemma 1 and Assumption 1, there are constants $\gamma_{11} > 0$ and $M_1 > 0$ such that

$$\begin{aligned} \left|x_1^{2\sigma-\varepsilon_2/\varepsilon_1}\phi_1\right| &\le C|x_1|^{2\sigma-\varepsilon_2/\varepsilon_1}\Big(\|\eta\|^{\varepsilon_2} + \|\eta(t-\tau)\|^{\varepsilon_2} + |x_1|^{\varepsilon_2/\varepsilon_1} \\ &\quad + |x_1(t-\tau)|^{\varepsilon_2/\varepsilon_1}\Big) + |M_0||x_1|^{2\sigma-\varepsilon_2/\varepsilon_1} \\ &\le \gamma_{11}\zeta_1^{2\sigma/\varepsilon_1} + \frac{1}{n+2}\lambda^\sigma\|\eta\|^{2\sigma} \\ &\quad + \frac{1}{2(n+2)}e^{-\mu\tau}\lambda^\sigma\|\eta(t-\tau)\|^{2\sigma} \\ &\quad + e^{-\mu\tau}\zeta_1^{2\sigma/\varepsilon_1}(t-\tau) + \frac{M_0^{2\sigma/\varepsilon_2}}{M_1}. \end{aligned} \tag{12}$$

Introduce the transformation $\zeta_2 = x_2 - \alpha_1$, and choose $V_1 = U_0 + U_1 + W_1 + T_1$, where $U_1 = n/2(n+2)\lambda^\sigma \int_{t-\tau}^{t} e^{\mu(s-t)}\|\eta(s)\|^{2\sigma}\mathrm{d}s.$, $W_1 = (\varepsilon_1/2\sigma - \varpi)\zeta_1^{2\sigma-\varpi/\varepsilon_1}$, and $T_1 = (n+\gamma_{02})\int_{t-\tau}^{t} e^{\mu(s-t)}\zeta_1^{2\sigma/\varepsilon_1}(s)\mathrm{d}s$. $\mu > 0$ is a constant. Then, it follows from (11) and (12) that

$$\begin{aligned}\dot{V}_1 &= \dot{U}_0 + \zeta_1^{2\sigma-\varepsilon_2/\varepsilon_1}\left(d_1x_2+\phi_1\right) + \left(n+\gamma_{02}\right)\zeta_1^{2\sigma/\varepsilon_1} - \left(n+\gamma_{02}\right)e^{-\mu\tau}\zeta_1^{2\sigma/\varepsilon_1}(t-\tau) + \frac{n}{2(n+2)}\lambda^\sigma\|\eta\|^{2\sigma} \\ &\quad - \frac{n}{2(n+2)}e^{-\mu\tau}\lambda^\sigma\|\eta(t-\tau)\|^{2\sigma} - \mu\left(U_1+T_1\right) \\ &\le -\frac{n}{2(n+2)}\lambda^\sigma\|\eta\|^{2\sigma} + d_1\zeta_2\zeta_1^{2\sigma-\varepsilon_2/\varepsilon_1} + d_1\alpha_1\zeta_1^{2\sigma-\varepsilon_2/\varepsilon_1} + \left(n+\gamma_{01}+\gamma_{02}+\gamma_{11}\right)\zeta_1^{2\sigma/\varepsilon_1} \\ &\quad + \frac{M_0^{2\sigma/\varepsilon_2}}{M_1} - (n-1)e^{-\mu\tau}\zeta_1^{2\sigma/\varepsilon_1}(t-\tau) - \frac{n-1}{2(n+2)}e^{-\mu\tau}\lambda^\sigma\|\eta(t-\tau)\|^{2\sigma} - \mu\left(U_1+T_1\right).\end{aligned} \tag{13}$$

Selecting the virtual control $\alpha_1 = -1/d\,(2n+\gamma_{01}+\gamma_{02}+\gamma_{11})\zeta_1^{(\varepsilon_2/\varepsilon_1)} \overset{\text{def}}{=} -g_1\zeta_1^{\varepsilon_2/\varepsilon_1}$, and substituting it into (13), it yields that

$$\begin{aligned}\dot{V}_1 &\le -\frac{n}{2(n+2)}\lambda^\sigma\|\eta\|^{2\sigma} - n\zeta_1^{2\sigma/\varepsilon_1} + d_1\zeta_2\zeta_1^{2\sigma-\varepsilon_2/\varepsilon_1} + \frac{M_0^{2\sigma/\varepsilon_2}}{M_1} \\ &\quad - \mu\left(U_1+T_1\right) - (n-1)e^{-\mu\tau}\zeta_1^{2\sigma/\varepsilon_1}(t-\tau) \\ &\quad - \frac{n-1}{2(n+2)}e^{-\mu\tau}\lambda^\sigma\|\eta(t-\tau)\|^{2\sigma}.\end{aligned} \tag{14}$$

Step k ($k = 2,\ldots,n-1$): for step $k-1$, suppose that there exist transformations (6) and a Lyapunov–Krasovskii functional V_{k-1} such that there exist the following inequality:

$$\begin{aligned}\dot{V}_{k-1} &\le -\frac{n-k+2}{2(n+2)}\lambda^\sigma\|\eta\|^{2\sigma} - (n-k+2)\sum_{j=1}^{k-1}\zeta_j^{2\sigma/\varepsilon_j} + d_{k-1}\zeta_k\zeta_{k-1}^{2\sigma-\varepsilon_k/\varepsilon_{k-1}} \\ &\quad + \sum_{j=1}^{k-1}\frac{M_0^{2\sigma/\varepsilon_{j+1}}}{M_j} - \mu\left(U_1+\sum_{j=1}^{k-1}T_j\right) - (n-k+1)e^{-\mu\tau}\sum_{j=1}^{k-1}\zeta_j^{2\sigma/\varepsilon_j} \\ &\quad \cdot (t-\tau) - \frac{n-k+1}{2(n+2)}e^{-\mu\tau}\lambda^\sigma\|\eta(t-\tau)\|^{2\sigma}.\end{aligned} \tag{15}$$

Next, we prove it still holds for $i = k$. Choosing

$$\begin{aligned}V_k &= V_{k-1} + W_k + T_k, \\ W_k &= \frac{\varepsilon_k}{2\sigma-\varpi}\zeta_k^{2\sigma-\varpi/\varepsilon_k}, \\ T_k &= (n-i+1)\int_{t-\tau}^{t} e^{\mu(s-t)}\zeta_k^{2\sigma/\varepsilon_k}(s)\mathrm{d}s.\end{aligned} \tag{16}$$

introducing $\zeta_{k+1} = x_{k+1} - \alpha_k$, and taking the derivative of V_k, it can be deduced that

$$\begin{aligned}\dot{V}_k &\le -\frac{n-k+2}{2(n+2)}\lambda^\sigma\|\eta\|^{2\sigma} - (n-k+2)\sum_{j=1}^{k-1}\zeta_j^{2\sigma/\varepsilon_j} \\ &\quad + d_{k-1}\zeta_k\zeta_{k-1}^{2\sigma-\varepsilon_k/\varepsilon_{k-1}} + \sum_{j=1}^{k-1}\frac{M_0^{2\sigma/\varepsilon_{j+1}}}{M_j} - \mu\left(U_1+\sum_{j=1}^{k}T_j\right) \\ &\quad - (n-k+1)e^{-\mu\tau}\sum_{j=1}^{k}\zeta_j^{2\sigma/\varepsilon_j}(t-\tau) \\ &\quad - \frac{n-k+1}{2(n+2)}e^{-\mu\tau}\lambda^\sigma\|\eta(t-\tau)\|^{2\sigma} + (n-k+1)\zeta_k^{2\sigma/\varepsilon_k} \\ &\quad + \zeta_k^{2\sigma-\varepsilon_{k+1}/\varepsilon_k}\left(\phi_k - \sum_{j=1}^{k-1}\frac{\partial\alpha_{k-1}}{\partial x_j}\left(d_jx_{j+1}+\phi_j\right)\right) \\ &\quad + d_k\zeta_{k+1}\zeta_k^{2\sigma-\varepsilon_{k+1}/\varepsilon_k} + d_k\alpha_k\zeta_k^{2\sigma-\varepsilon_{k+1}/\varepsilon_k}.\end{aligned} \tag{17}$$

On the basis of $d_{k-1} \le \overline{d}$ and Lemma 1, there is a constant $\gamma_{11} > 0$ such that

$$d_{k-1}\zeta_k\zeta_{k-1}^{2\sigma-\varepsilon_k/\varepsilon_{k-1}} \le \frac{1}{3}\zeta_{k-1}^{2\sigma/\varepsilon_{k-1}} + \gamma_{k1}\zeta_k^{2\sigma/\varepsilon_k}. \tag{18}$$

Similarly to the proof of (12), one obtains

$$\begin{aligned}\left|\zeta_k^{2\sigma-\varepsilon_{k+1}/\varepsilon_k}\phi_k\right| &\le C\left|\zeta_k\right|^{2\sigma-\varepsilon_{k+1}/\varepsilon_k}\Bigg(\|\eta\|^{\varepsilon_{k+1}}+\|\eta(t-\tau)\|^{\varepsilon_{k+1}}\\ &\quad+\sum_{j=1}^{k}\left|\zeta_j-g_{j-1}\zeta_{j-1}^{\varepsilon_j/\varepsilon_{j-1}}\right|^{\varepsilon_{k+1}/\varepsilon_j}\\ &\quad+\sum_{j=1}^{k}\left|\zeta_j(t-\tau)-g_{j-1}\zeta_{j-1}^{\varepsilon_j/\varepsilon_{j-1}}(t-\tau)\right|^{\varepsilon_{k+1}/\varepsilon_j}\Bigg)\\ &\quad+\left|M_0\right|\left|\zeta_k\right|^{2\sigma-\varepsilon_{k+1}/\varepsilon_k}\\ &\le \gamma_{k2}\zeta_k^{2\sigma/\varepsilon_k}+\frac{1}{4(n+2)}\lambda^{\sigma}\|\eta\|^{2\sigma}\\ &\quad+\frac{1}{4(n+2)}e^{-\mu\tau}\lambda^{\sigma}\|\eta(t-\tau)\|^{2\sigma}\\ &\quad+\frac{1}{2}e^{-\mu\tau}\sum_{j=1}^{k}\zeta_j^{2\sigma/\varepsilon_j}(t-\tau)+\frac{M_0^{2\sigma/\varepsilon_{k+1}}}{M_{k1}}+\frac{1}{3}\sum_{j=1}^{k-1}\zeta_j^{2\sigma/\varepsilon_j},\end{aligned} \tag{19}$$

where $\gamma_{k2}>0$ and $M_{k1}>0$ are constants. From Assumption 1, we have

$$\begin{aligned}\left|d_jx_{j+1}+\phi_j\right| &\le d\left(\left|\zeta_{j+1}\right|+g_j\left|\zeta_j\right|^{\epsilon_{j+1}/\epsilon_j}\right)+C\Bigg(\|\eta\|^{\epsilon_{j+1}}+\|\eta(t-\tau)\|^{\epsilon_{j+1}}+\sum_{i=1}^{j}\left|\zeta_i-g_{i-1}\zeta_{i-1}^{\epsilon_i/\epsilon_{i-1}}\right|^{\epsilon_{j+1}/\epsilon_i}+\sum_{i=1}^{j}\left|\zeta_i(t-\tau)-g_{i-1}\zeta_{i-1}^{\epsilon_i/\epsilon_{i-1}}(t-\tau)\right|^{\epsilon_{j+1}/\epsilon_i}\Bigg)\\ &\quad+\left|M_0\right|.\end{aligned} \tag{20}$$

Utilizing (20) and Lemma 1 and noting that $|(\partial\alpha_{k-1}/\partial x_j)| = g_jg_{j+1}\cdots g_{k-1}(\varepsilon_k/\varepsilon_j)|\zeta_j|^{\varpi/\varepsilon_j}|\zeta_{j+1}|^{\varpi/\varepsilon_{j+1}}\cdots|\zeta_{k-1}|^{\varpi/\varepsilon_{k-1}}$, it follows that

$$\begin{aligned}\left|\frac{\partial\alpha_{k-1}}{\partial x_j}\right|\left|d_jx_{j+1}+\phi_j\right| &\le \Bigg(d\left(\left|\zeta_{j+1}\right|+g_j\left|\zeta_j\right|^{\varepsilon_{j+1}/\varepsilon_j}\right)+C\Bigg(\|\eta\|^{\varepsilon_{j+1}}+\|\eta(t-\tau)\|^{\varepsilon_{j+1}}+\sum_{i=1}^{j}\left|\zeta_i-g_{i-1}\zeta_{i-1}^{\varepsilon_i/\varepsilon_{i-1}}\right|^{\varepsilon_{j+1}/\varepsilon_i}\\ &\quad+\sum_{i=1}^{j}\left|\zeta_i(t-\tau)-g_{i-1}\zeta_{i-1}^{\varepsilon_i/\varepsilon_{i-1}}(t-\tau)\right|^{\varepsilon_{j+1}/\varepsilon_i}\Bigg)+\left|M_0\right|\Bigg)g_jg_{j+1}\cdots g_{k-1}\frac{\varepsilon_k}{\varepsilon_j}\left|\zeta_j\right|^{\varpi/\varepsilon_j}\left|\zeta_{j+1}\right|^{\varpi/\varepsilon_{j+1}}\cdots\left|\zeta_{k-1}\right|^{\varpi/\varepsilon_{k-1}}\\ &\le C_{j1}\sum_{i=1}^{j}\left|\zeta_i\right|^{\varepsilon_{j+1}/\varepsilon_i}+C_{j2}\sum_{i=1}^{j}\left|\zeta_i(t-\tau)\right|^{\varepsilon_{j+1}/\varepsilon_i}+C_{j3}\|\eta\|^{\varepsilon_{k+1}}+C_{j4}\|\eta(t-\tau)\|^{\varepsilon_{k+1}}\\ &\quad+\left|M_0\right|g_jg_{j+1}\cdots g_{k-1}\frac{\varepsilon_k}{\varepsilon_j}\left|\zeta_j\right|^{\varpi/\varepsilon_j}\left|\zeta_{j+1}\right|^{\varpi/\varepsilon_{j+1}}\cdots\left|\zeta_{k-1}\right|^{\varpi/\varepsilon_{k-1}},\end{aligned} \tag{21}$$

where $C_{jk} > 0, k = 1, \ldots, 4$ are constants. It can be deduced from (21) and Lemma 1 that

$$\left| -\zeta_k^{2\sigma-\varepsilon_{k+1}/\varepsilon_k} \sum_{j=1}^{k-1} \frac{\partial \alpha_{k-1}}{\partial x_j}\left(d_j x_{j+1} + \phi_j\right) \right| \le \gamma_{k3}\zeta_k^{2\sigma/\varepsilon_k} + \frac{1}{4(n+2)}\lambda^\sigma \|\eta\|^{2\sigma} + \frac{1}{4(n+2)} e^{-\mu\tau}\lambda^\sigma \|\eta(t-\tau)\|^{2\sigma} + \frac{1}{2} e^{-\mu\tau} \sum_{j=1}^{k} \zeta_j^{2\sigma/\varepsilon_j}(t-\tau) + \frac{M_0^{2\sigma/\varepsilon_{k+1}}}{M_{k2}} + \frac{1}{3}\sum_{j=1}^{k-1} \zeta_j^{2\sigma/\varepsilon_j}, \tag{22}$$

where $\gamma_{k3} > 0$ and $M_{k2} > 0$ are constants. Choosing M_k such that $1/M_k = (1/M_{k1}) + (1/M_{k2})$ and using (19) and (22), it yields that

$$\zeta_k^{2\sigma-\varepsilon_{k+1}/\varepsilon_k}\left(\phi_k - \sum_{j=1}^{k-1} \frac{\partial \alpha_{k-1}}{\partial x_j}\left(d_j x_{j+1} + \phi_j\right)\right) \le \left(\gamma_{k2} + \gamma_{k3}\right)\zeta_k^{2\sigma/\varepsilon_k} + \frac{1}{2(n+2)}\lambda^\sigma \|\eta\|^{2\sigma} + \frac{1}{2(n+2)} e^{-\mu\tau}\lambda^\sigma |\eta(t-\tau)|^{2\sigma} + e^{-\mu\tau} \sum_{j=1}^{k} \zeta_j^{2\sigma/\varepsilon_j}(t-\tau) + \frac{M_0^{2\sigma/\varepsilon_{k+1}}}{M_k} + \frac{2}{3}\sum_{j=1}^{k-1} \zeta_j^{2\sigma/\varepsilon_j}. \tag{23}$$

Now, we construct the virtual control $\alpha_k = -1/d(2n - 2k + 2 + \gamma_{k1} + \gamma_{k2} + \gamma_{k3})\zeta_k^{(\varepsilon_{k+1}/\varepsilon_k)} \overset{\text{def}}{=} -g_k\zeta_k^{\varepsilon_{k+1}/\varepsilon_k}$. With the help of (17), (18), and (23), it is deduced that

$$\dot{V}_k \le -\frac{n-k+1}{2(n+2)}\lambda^\sigma \|\eta\|^{2\sigma} - (n-k+1)\sum_{j=1}^{k} \zeta_j^{2\sigma/\varepsilon_j} + d_k\zeta_{k+1}\zeta_k^{2\sigma-\varepsilon_{k+1}/\varepsilon_k} - \mu\left(U_1 + \sum_{j=1}^{k} T_j\right) - (n-k)e^{-\mu\tau}\sum_{j=1}^{k} \zeta_j^{2\sigma/\varepsilon_j}(t-\tau) - \frac{n-k}{2(n+2)} e^{-\mu\tau}\lambda^\sigma \|\eta(t-\tau)\|^{2\sigma} + \sum_{j=1}^{k} \frac{M_0^{2\sigma/\varepsilon_{j+1}}}{M_j}. \tag{24}$$

This completes the control design for step $k = 2, \ldots, n-1$.

Step n: in this step, we choose $V_n = V_{n-1} + W_n + T_n, W_n = (\varepsilon_n/2\sigma - \varpi)\zeta_n^{2\sigma-\varpi/\varepsilon_n}$ and $T_n = \int_{t-\tau}^{t} e^{\mu(s-t)}\zeta_n^{2\sigma/\varepsilon_n}(s)\mathrm{d}s$, and using (24), some simple computations lead to

$$\dot{V}_n \le -\frac{2}{2(n+2)}\lambda^\sigma \|\eta\|^{2\sigma} - 2\sum_{j=1}^{n-1} \zeta_j^{2\sigma/\varepsilon_j} + d_{n-1}\zeta_n\zeta_{n-1}^{2\sigma-\varepsilon_n/\varepsilon_{n-1}} + \sum_{j=1}^{n-1} \frac{M_0^{2\sigma/\varepsilon_{j+1}}}{M_j} - \mu\left(U_1 + \sum_{j=1}^{n} T_j\right) - e^{-\mu\tau}\sum_{j=1}^{n} \zeta_j^{2\sigma/\varepsilon_j}(t-\tau) - \frac{1}{2(n+2)} e^{-\mu\tau}\lambda^\sigma \|\eta(t-\tau)\|^{2\sigma} + \zeta_n^{2\sigma/\varepsilon_n} + \zeta_n^{2\sigma-\varepsilon_{n+1}/\varepsilon_n}\left(\phi_n - \sum_{j=1}^{n-1} \frac{\partial \alpha_{n-1}}{\partial x_j}\left(d_j x_{j+1} + \phi_j\right)\right) + d_n u(v)\zeta_n^{2\sigma-\varepsilon_{n+1}/\varepsilon_n}. \tag{25}$$

Similar to (18) and (23), by Lemma 1, we obtain that

$$d_{n-1}\zeta_n\zeta_{n-1}^{2\sigma-\varepsilon_n/\varepsilon_{n-1}} \le \frac{1}{3}\zeta_{n-1}^{2\sigma/\varepsilon_{n-1}} + \gamma_{n1}\zeta_n^{2\sigma/\varepsilon_n}, \tag{26}$$

$$\zeta_n^{2\sigma-\varepsilon_{n+1}/\varepsilon_n}\left(\phi_n - \sum_{j=1}^{n-1}\frac{\partial\alpha_{n-1}}{\partial x_j}\left(d_j x_{j+1} + \phi_j\right)\right) \le (\gamma_{n2}+\gamma_{n3})\zeta_n^{2\sigma/\varepsilon_n} + \frac{1}{2(n+2)}\lambda^\sigma\|\eta\|^{2\sigma} + \frac{1}{2(n+2)}e^{-\mu\tau}\lambda^\sigma\|\eta(t-\tau)\|^{2\sigma} + e^{-\mu\tau}\sum_{j=1}^{n}\zeta_j^{2\sigma/\varepsilon_j}(t-\tau) + \frac{M_0^{2\sigma/\varepsilon_{n+1}}}{M_n} + \frac{2}{3}\sum_{j=1}^{n-1}\zeta_j^{2\sigma/\varepsilon_j}, \tag{27}$$

where the constants $\gamma_{n1}\ge 0, \gamma_{n2}\ge 0, \gamma_{n3}\ge 0$, and $M_n \ge 0$. Now, we choose the virtual control $\alpha_n = -1/d(2+\gamma_{n1}+\gamma_{n2}+\gamma_{n3})\zeta_n^{(\varepsilon_{n+1}/\varepsilon_n)} \overset{\text{def}}{=} -g_n\zeta_n^{\varepsilon_{n+1}/\varepsilon_n}$, which, and (25)–(27), give that

$$\dot{V}_n \le -\frac{1}{2(n+2)}\lambda^\sigma\|\eta\|^{2\sigma} - \sum_{j=1}^{n}\zeta_j^{2\sigma/\varepsilon_j} - \mu\left(U_1 + \sum_{j=1}^{n}T_j\right) + \sum_{j=1}^{n}\frac{M_0^{2\sigma/\varepsilon_{j+1}}}{M_j} + d_n(u(v)-\alpha_n)\zeta_n^{2\sigma-\varepsilon_{n+1}/\varepsilon_n}. \tag{28}$$

Finally, we choose the control input v as (7), Then, by using (2), it follows that

$$u(v)-\alpha_n = \begin{cases} m_r\left(\dfrac{\alpha_n}{\underline{m}_r} + \bar{b}_r - b_r\right) - \alpha_n, & \alpha_n > 0, \\ 0, & \alpha_n = 0, \\ m_l\left(\dfrac{\alpha_n}{\underline{m}_l} + \bar{b}_l - b_l\right) - \alpha_n, & \alpha_n < 0, \end{cases} \tag{29}$$

which further renders that $d_n(u(v)-\alpha_n)\zeta_n^{2\sigma-\varepsilon_{n+1}/\varepsilon_n} \le 0$. Then, using (28), we get

$$\dot{V}_n \le -\frac{1}{2(n+2)}\lambda^\sigma\|\eta\|^{2\sigma} - \sum_{j=1}^{n}\zeta_j^{2\sigma/\varepsilon_j} - \mu\left(U_1 + \sum_{j=1}^{n}T_j\right) + \sum_{j=1}^{n}\frac{M_0^{2\sigma/\varepsilon_{j+1}}}{M_j}. \tag{30}$$

3.2. Part II: Stability Analysis. Since $U_0 = 1/\sigma(\eta^\top P\eta)^\sigma$ and $\lambda_p\|\eta\|^2 \le \eta^\top P\eta \le \lambda_P\|\eta\|^2$, we have $\|\eta\|^{2\sigma} \ge (\sigma/\lambda_P^\sigma)U_0$, which leads to

$$-\frac{1}{2(n+2)}\lambda^\sigma\|\eta\|^{2\sigma} \le -\frac{\sigma}{2(n+2)\lambda_P^\sigma}\lambda^\sigma U_0. \tag{31}$$

Defining $\Delta_j = (2\sigma-\varpi/2\sigma)(\delta_j\varpi/2\sigma)^{\varpi/2\sigma-\varpi}(\varepsilon_j/2\sigma-\varpi)^{2\sigma/2\sigma-\varpi}$ and $\Delta m = \min_{1\le j\le n}(1/\Delta_j)$, it follows from Lemma 1 that $W_j = (\varepsilon_j/2\sigma-\varpi)\zeta_j^{2\sigma-\varpi/\varepsilon_j} \le (1/\delta_j) + \Delta_j\zeta_j^{2\sigma/\varepsilon_j}$, which renders that

$$-\sum_{j=1}^{n}\zeta_j^{2\sigma/\varepsilon_j} \le -\Delta m\sum_{j=1}^{n}W_j + \sum_{j=1}^{n}\frac{1}{\delta_j\Delta_j}. \tag{32}$$

Substituting (31) and (32) into (28), it yields that

$$\dot{V}_n \le -\frac{\sigma}{2(n+2)\lambda_P^\sigma}\lambda^\sigma U_0 - \Delta m\sum_{j=1}^{n}W_j + \sum_{j=1}^{n}\frac{1}{\delta_j\Delta_j} - \mu\left(U_1 + \sum_{j=1}^{n}T_j\right) + \sum_{j=1}^{n}\frac{M_0^{2\sigma/\varepsilon_{j+1}}}{M_j} \le -\rho_1 V_n + \rho_2, \tag{33}$$

where $\rho_1 = \min\{(\sigma/2(n+2)\lambda_P^\sigma)\lambda^\sigma, \Delta m, \mu\}$ and $\rho_2 = \sum_{j=1}^{n}(1/\delta_j\Delta_j) + \sum_{j=1}^{n}(M_0^{2\sigma/\varepsilon_{j+1}}/M_j)$. By the definition of U_0, U_1, W_i, and $T_i, i = 1,\ldots,n$, it follows that

$$\begin{aligned} U_0 + U_1 &= \frac{1}{\sigma}(\eta^\top P\eta)^\sigma + \frac{n}{2(n+2)}\lambda^\sigma\int_{t-\tau}^{t}e^{\mu(s-t)}\|\eta(s)\|^{2\sigma}ds \\ &\le \frac{\lambda_P^\sigma}{\sigma}\|\eta\|^{2\sigma} + \frac{n\tau\lambda^\sigma}{2(n+2)}\sup_{-\tau\le k\le 0}e^{\mu k}\|\eta(k+t)\|^{2\sigma} \\ &\le \left(\frac{\lambda_P^\sigma}{\sigma} + \frac{n\tau\lambda^\sigma}{2(n+2)}\right)\sup_{-\tau\le k\le 0}\|\eta(k+t)\|^{2\sigma}, \\ \sum_{i=1}^{n}W_i &= \sum_{i=1}^{n}\frac{\varepsilon_i}{2\sigma-\varpi}\zeta_i^{2\sigma-\varpi/\varepsilon_i} \le \frac{\varepsilon_n}{2\sigma-\varpi}\sum_{i=1}^{n}\sup_{-\tau\le k\le 0}\zeta_i^{2\sigma-\varpi/\varepsilon_i}(k+t), \\ \sum_{i=1}^{n}T_i &= \gamma_{02}\int_{t-\tau}^{t}e^{\mu(s-t)}\zeta_1^{2\sigma/\varepsilon_1}(s)ds + \sum_{i=1}^{n}(n-i+1) \\ &\quad\cdot\int_{t-\tau}^{t}e^{\mu(s-t)}\zeta_i^{2\sigma/\varepsilon_i}(s)ds \le (n+\gamma_{02})\tau\sum_{i=1}^{n}\sup_{-\tau\le k\le 0}\zeta_i^{2\sigma/\varepsilon_i}(k+t). \end{aligned} \tag{34}$$

which lead to

$$V_n = U_0 + U_1 + \sum_{i=1}^{n}W_i + \sum_{i=1}^{n}T_i \le \varphi_1\left(\sup_{-\tau\le k\le 0}\Xi(k+t)\right), \tag{35}$$

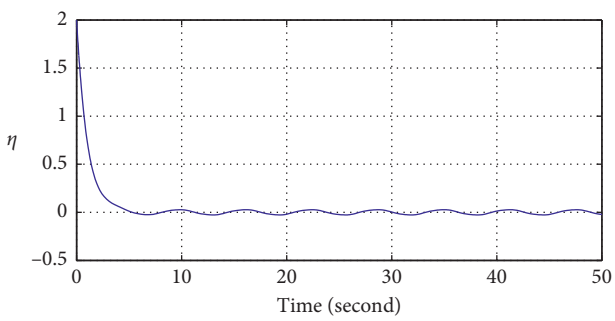

Figure 1: : The trajectory of η.

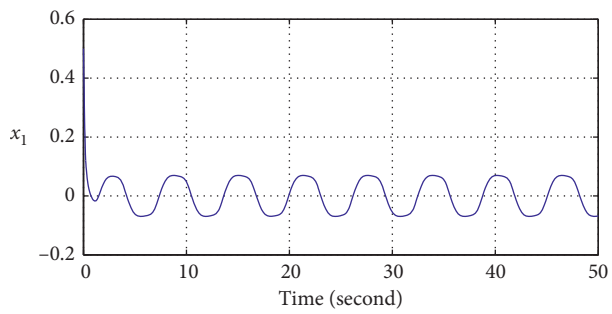

Figure 2: : The trajectory of x_1.

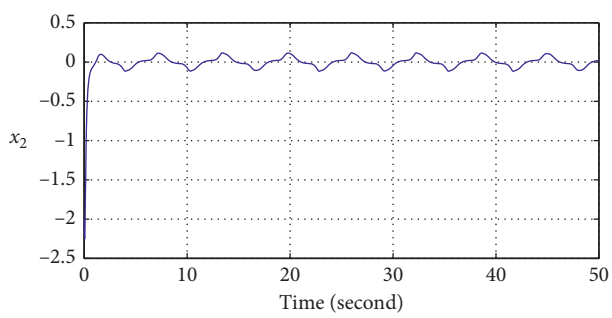

Figure 3: : The trajectory of x_2.

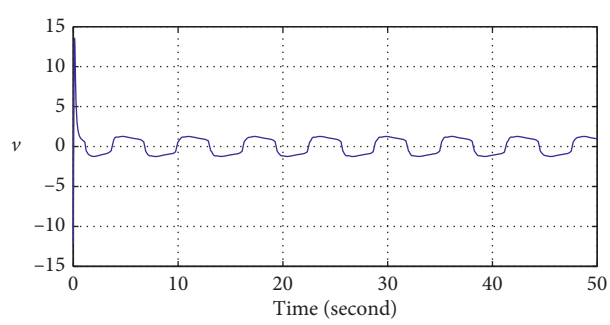

Figure 4: : The trajectory of v.

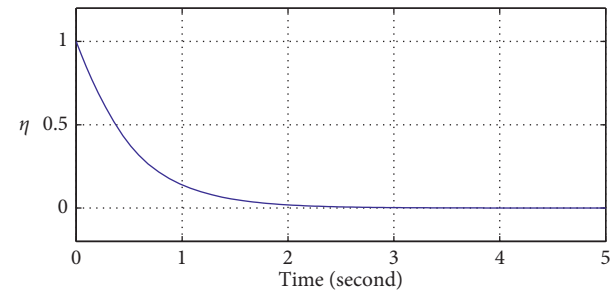

Figure 5: : The trajectory of η.

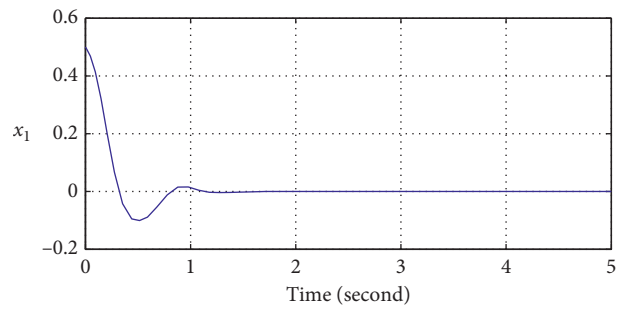

Figure 6: : The trajectory of x_1.

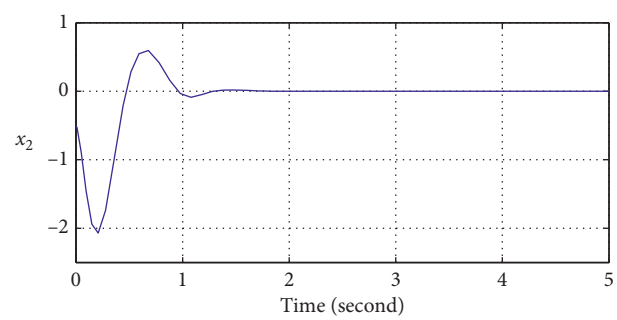

Figure 7: The trajectory of x_2.

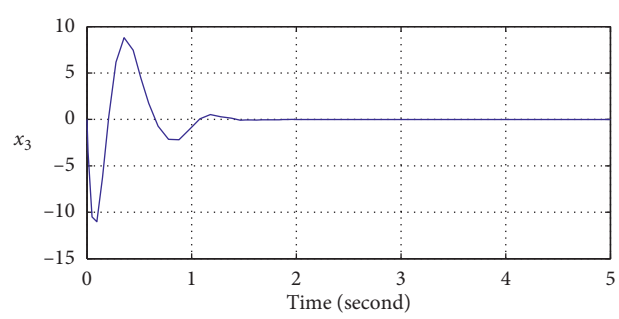

Figure 8: The trajectory of x_3.

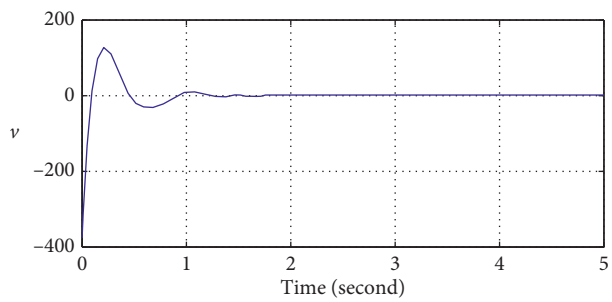

Figure 9: The trajectory of v.

where the function $\varphi_1 \in K_\infty$ and $\Xi(t) = [\eta(t)^\top, \zeta(t)^\top]^\top$. On the other hand, there exists a function $\varphi_2 \in K_\infty$ such that

$$V_n = U_0 + U_1 + \sum_{i=1}^{n} W_i + \sum_{i=1}^{n} T_i \geq \frac{\lambda_p^\sigma}{\sigma}\|\eta\|^{2\sigma} + \sum_{i=1}^{n} \frac{\varepsilon_i}{2\sigma - \varpi}\zeta_i^{2\sigma-\varpi/\varepsilon_i} \geq \varphi_2(\Xi(t)). \tag{36}$$

In view of (28), (35), and (36), and using Lemma 3.2.4 in [33], we obtain

$$\dot{V}_n \leq \left(V_n(0) - \frac{\rho_2}{\rho_1}\right)e^{-\rho_1 t} + \frac{\rho_2}{\rho_1}, \tag{37}$$

which indicates that η and ζ are bounded. From $\zeta_1 = x_1, \zeta_i = x_i - \alpha_{i-1}, \alpha_1 = -g_1\zeta_1^{\varepsilon_2/\varepsilon_1}$, and $\alpha_i = -g_i\zeta_i^{\varepsilon_{i+1}/\varepsilon_i}, i = 2, \ldots, n$, the states of $\eta, x_1, \ldots, x_n$ are bounded, which indicates the system composed of (1) and (7) is globally stable.

4. Simulation Example

Example 1. Consider the following nonlinear time-delay system:

$$\begin{cases} \dot{\eta} = -\eta + 0.5x_1, \\ \dot{x}_1 = x_2 + x_1^{5/3}(t - 0.2), \\ \dot{x}_2 = u(v) + x_2^{7/5} + 0.3\sin(t), \end{cases} \tag{38}$$

where η is the unmeasurable state, x_1 and x_2 are the measurable states, $u(v)$ is the dead-zone input given in (2) with $b_r = 0.4 + 0.1\sin(t), b_l = 0.4 - 0.1\sin(t)$, and v is the input of the system. We see that Assumptions 1-2 are satisfied for system (32) with $\varpi = 2/3, \varepsilon_1 = 1, \varepsilon_2 = 5/3, \varepsilon_3 = 7/3$, and $\overline{b}_r = \overline{b}_l = 0.5$, and $\underline{m}_r = \underline{m}_l = m_r = m_l = 1$. Applying the above control method, we choose $\alpha_2 = -15(x_2 + 9x_1^{5/3})^{7/5}$. Then, the actual controller is constructed as

$$v = \begin{cases} \alpha_2 + \overline{b}_r, & \alpha_2 > 0, \\ 0, & \alpha_2 = 0, \\ \alpha_2 - \overline{b}_l, & \alpha_2 < 0. \end{cases} \tag{39}$$

In the simulation, choose $\eta(0) = 2, x_1(0) = 0.5$, and $x_2(0) = -2$. Figures 1–4 give the trajectories of η, x_1, and x_2 and the control input v. All signals in systems (38) and (39) are bounded. Hence, the validity of the presented control method is verified.

Example 2. Consider the following system:

$$\begin{cases} \dot{\eta} = -2\eta + \dfrac{1}{1+\eta^2}\eta x_1, \\ \dot{x}_1 = x_2 + x_1^{1/3}x_1^{2/3}(t - 0.5), \\ \dot{x}_2 = x_3 - 5\sin(x_1) - x_2 + \sin(x_1(t - 0.5)), \\ \dot{x}_3 = u(v) + 10x_2 - 5x_3, \end{cases} \tag{40}$$

where η is the unmeasurable state, x_1, x_2, x_3 are the system states, v is the control input, and $u(v)$ is the dead-zone input defined in (2) with $b_r = 0.5 + \sin(t)$ and $b_l = 0.5 - \sin(t)$. It can be deduced that $|(x_1\eta/1 + \eta^2)| \leq |x_1|$, $|x_1^{1/3}x_1^{2/3}(t - 0.5) \leq |x_1| + 2/3|x_1(t - 0.5)|$, $|-5\sin(x_1) - x_2 + \sin(x_1 \quad (t - 0.5))| \leq 5|x_1| + |x_2| + |x_1(t - 0.5)|$, and $|10x_2 - 5x_3| \leq 10|x_2| + 5|x_3|$. In this example, $\varpi = 0, \varepsilon_1 = \varepsilon_2 = \varepsilon_3 = \varepsilon_4 = 1$, and $\overline{b}_r = \overline{b}_l = 1.5$, and $\underline{m}_r = \underline{m}_l == 1$. Thus, all conditions of Assumptions 1-2 are satisfied. Using the control design method in Section 3, we can design the actual controller as follows:

$$v = \begin{cases} \alpha_3 + \overline{b}_r, & \alpha_3 > 0, \\ 0, & \alpha_3 = 0, \\ \alpha_3 - \overline{b}_l, & \alpha_3 < 0. \end{cases} \tag{41}$$

where $\alpha_3 = -15(x_3 + 10(x_2 + 6x_1))$.

In the simulation, the initial conditions are selected as $\eta(0) = 1, x_1(0) = 0.5, x_2(0) = -0.5$, and $x_3(0) = 0$. Figures 5–9 show the trajectories of η, x_1, x_2, x_3, and the control input v. It can be seen that all signals in systems (34) and (35) are bounded. Hence, the presented control method is effective.

5. Conclusions

The robust stabilization for nonlinear systems with dead-zone input and time delay has been studied. Because the system involves the dead-zone input, time-delay, disturbance, and unmeasurable states, the stabilization control in this work is more challenging. A robust stable controller has been designed via the Lyapunov–Krasovskii functional and the backstepping technique. Another interesting problem is as follows: When the considered system includes uncertainty parameters, and only the system output is measurable, how can we design the adaptive controller via the output feedback control method?

Data Availability

The data used to support the findings are included within this article.

Conflicts of Interest

The authors declare no conflicts of interest in preparing this article.

Acknowledgments

This work was supported by the National Natural Science Foundation of China (Grant no. 61903239), Youth Science and Technology Research Foundation of the ShanXi Science and Technology Department of China (Grant no. 201801D221167), and Scientific and Technological Innovation Programs of Higher Education Institutions in Shanxi (STIP) (Grant no. 2019L0492).

References

[1] W. Sun, S. F. Su, J. Xia, and V. T. Nguyen, "Adaptive fuzzy tracking control of flexible-joint robots with full-state constraints," *IEEE Transactions on Systems, Man, and Cybernetics: Systems*, vol. 49, no. 11, pp. 2201–2209, 2018.

[2] W. Sun, S. Su, J. Xia, and Y. Wu, "Adaptive tracking control of wheeled inverted pendulums with periodic disturbances," *IEEE Transactions on Cybernetics*, vol. 50, no. 5, pp. 1867–1876, 2018.

[3] Z. Zhang and Y. Wu, "Adaptive fuzzy tracking control of autonomous underwater vehicles with output constraints," *IEEE Transactions on Fuzzy Systems*, 2020.

[4] C. Qian, "A homogeneous domination approach for global output feedback stabilization of a class of nonlinear systems," in *Proceedings of the American Control Conference*, pp. 4708–4715, IEEE, Portland, OR, USA, June 2005.

[5] J. Polendo and C. Qian, "A generalized homogeneous domination approach for global stabilization of inherently nonlinear systems via output feedback," *International Journal of Robust and Nonlinear Control*, vol. 17, no. 7, pp. 605–629, 2007.

[6] C. C. Chen, "A unified approach to finite-time stabilization of high-order nonlinear systems with and without an output constraint," *International Journal of Robust and Nonlinear Control*, vol. 29, no. 2, pp. 393–407, 2019.

[7] Z. Zhang, J. Lu, and S. Xu, "Tuning functions-based robust adaptive tracking control of a class of nonlinear systems with time delays," *International Journal of Robust and Nonlinear Control*, vol. 22, no. 14, pp. 1631–1646, 2012.

[8] Z.-Y. Sun, C.-H. Zhang, and Z. Wang, "Adaptive disturbance attenuation for generalized high-order uncertain nonlinear systems," *Automatica*, vol. 80, pp. 102–109, 2017.

[9] N. Duan, H. Min, and X. Qin, "Adaptive stabilization of stochastic nonlinear systems disturbed by unknown time delay and covariance noise," *Mathematical Problems in Engineering*, vol. 2017, Article ID 8084529, 9 pages, 2017.

[10] Q. Meng, T. Zhao, C. Qian, Z.-y. Sun, and P. Ge, "Integrated stability control of AFS and DYC for electric vehicle based on non-smooth control," *International Journal of Systems Science*, vol. 49, no. 7, pp. 1518–1528, 2018.

[11] Q. Meng, C. Qian, and R. Liu, "Dual-rate sampled-data stabilization for active suspension system of electric vehicle," *International Journal of Robust and Nonlinear Control*, vol. 28, no. 5, pp. 1610–1623, 2018.

[12] J. K. Hale and S. M. V. Lunel, *Introduction to Functional Differential Equations*, Springer Science & Business Media, Berlin, Germany, 2013.

[13] M. Krstić, P. V. Kokotovic, and I. Kanellakopoulos, *Nonlinear and Adaptive Control Design*, John Wiley & Sons, Inc., Hoboken, NJ, USA, 1995.

[14] X. Zhao, P. Shi, X. Zheng, and L. Zhang, "Adaptive tracking control for switched stochastic nonlinear systems with unknown actuator dead-zone," *Automatica*, vol. 60, pp. 193–200, 2015.

[15] F. Gao, Y. Wu, and Y. Liu, "Finite-time stabilization for a class of switched stochastic nonlinear systems with dead-zone input nonlinearities," *International Journal of Robust and Nonlinear Control*, vol. 28, no. 9, pp. 3239–3257, 2018.

[16] R. Xu and F. Zhang, "ϵ-Nash mean-field games for general linear-quadratic systems with applications," *Automatica*, vol. 114, p. 108835, 2020.

[17] R. Guo, "Projective synchronization of a class of chaotic systems by dynamic feedback control method," *Nonlinear Dynamics*, vol. 90, no. 1, pp. 53–64, 2017.

[18] C. Qian and W. Lin, "A continuous feedback approach to global strong stabilization of nonlinear systems," *IEEE Transactions on Automatic Control*, vol. 46, no. 7, pp. 1061–1079, 2001.

[19] W. Zha, C. Qian, and S. Yan, "Controller design for a class of nontriangular nonlinear systems with input dependent growth rate," *International Journal of Robust and Nonlinear Control*, vol. 29, no. 5, pp. 1325–1338, 2019.

[20] Z.-G. Liu and Y.-Q. Wu, "Universal strategies to explicit adaptive control of nonlinear time-delay systems with different structures," *Automatica*, vol. 89, pp. 151–159, 2018.

[21] F. Gao, Y. Wu, and F. Yuan, "Global output feedback stabilisation of high-order nonlinear systems with multiple time-varying delays," *International Journal of Systems Science*, vol. 47, no. 10, pp. 2382–2392, 2016.

[22] L. Xue, Z. Liu, Z. Sun, and W. Sun, "New results on robust tracking control for a class of high-order nonlinear time-delay systems," *International Journal of Systems Science*, vol. 50, no. 10, pp. 2002–2014, 2019.

[23] M. Cui, "Adaptive output feedback stabilization of random nonlinear systems with unmodeled dynamics driven by colored noise," *Mathematical Problems in Engineering*, vol. 2019, Article ID 8581374, 10 pages, 2019.

[24] Z. Song, P. Li, Z. Wang, X. Huang, and W. Liu, "Adaptive tracking control for switched uncertain nonlinear systems with input saturation and unmodeled dynamics," *IEEE Transactions on Circuits and Systems II: Express Briefs*, 2020.

[25] H. Wang, Y. Zou, P. X. Liu, X. Zhao, J. Bao, and Y. Zhou, "Neural-network-based tracking control for a class of time-delay nonlinear systems with unmodeled dynamics," *Neurocomputing*, 2019.

[26] L. Xue, W. Zhang, and Y. Lin, "Global output tracking control for high-order stochastic nonlinear systems with SISS inverse dynamics and time-varying delays," *Journal of the Franklin Institute*, vol. 353, no. 13, pp. 3249–3270, 2016.

[27] L. Xue, W. Zhang, and X. Xie, "Global practical tracking for stochastic time-delay nonlinear systems with SISS-like inverse dynamics," *Science China Information Sciences*, vol. 60, no. 12, Article ID 122201, 2017.

[28] Z. Wang, J. Yuan, Y. Pan, and D. Che, "Adaptive neural control for high order Markovian jump nonlinear systems with unmodeled dynamics and dead zone inputs," *Neurocomputing*, vol. 247, pp. 62–72, 2017.

[29] S. Yin, P. Shi, and H. Yang, "Adaptive fuzzy control of strict-feedback nonlinear time-delay systems with unmodeled dynamics," *IEEE Transactions on Cybernetics*, vol. 46, no. 8, pp. 1926–1938, 2015.

[30] Z. Liu, L. Xue, W. Sun, and Z. Sun, "Robust output feedback tracking control for a class of high-order time-delay nonlinear systems with input dead-zone and disturbances," *Nonlinear Dynamics*, vol. 97, no. 2, pp. 921–935, 2019.

[31] Z. Sun, Y. Shao, C. Chen, and Q. Meng, "Global output-feedback stabilization for stochastic nonlinear systems: a double-domination approach," *International Journal of Robust and Nonlinear Control*, vol. 28, no. 15, pp. 4635–4646, 2018.

[32] Z.-Y. Sun, Y. Shao, and C.-C. Chen, "Fast finite-time stability and its application in adaptive control of high-order nonlinear system," *Automatica*, vol. 106, pp. 339–348, 2019.

[33] P. A. Ioannou and J. Sun, *Robust Adaptive Control*, Courier Corporation, Chelmsford, MA, USA, 1996.

Hindawi
Mathematical Problems in Engineering
Volume 2020, Article ID 9216019, 9 pages
https://doi.org/10.1155/2020/9216019

Research Article

Parameter Identification and Control Algorithm of Electrohydraulic Servo System for Robotic Excavator Based on Improved Hammerstein Model

Shen Jinxing,[1] Cui Hongxin,[2,3] Feng Ke,[1] Zhang Hong,[1] and Li Huanliang[1]

[1]*College of Field Engineering, Army Engineering University of PLA, Nanjing 210007, China*
[2]*Institute of Systems Engineering, Academy of People's Armed Police, Beijing 100012, China*
[3]*Institute of System Engineering, Military Academy of Sciences, Beijing 100101, China*

Correspondence should be addressed to Cui Hongxin; chx503207@163.com

Received 26 February 2020; Accepted 11 May 2020; Published 23 May 2020

Guest Editor: Cuimei Jiang

In view of the nonlinearity and time-varying characteristics of the electrohydraulic servo system of the robotic excavator, a nonlinear adaptive identification and control algorithm based on improved Hammerstein model is proposed. The Hammerstein algorithm model can approximate the nonlinear system with enough precision, but for the time-varying systems is not satisfactory. In order to compensate for the influence of time-varying factors, the fuzzy control module is designed to adaptively update the forgetting factor. The experimental results show that the improved Hammerstein model error is about 40.11% less than the classical Hammerstein model error. This proves that the improved Hammerstein model is feasible and effective to describe the electrohydraulic servo system of the robotic excavator.

1. Introduction

In order to continuously improve the operation efficiency and operation quality of excavator, and to expand the application areas of the excavator, autonomous operation has become an important research direction [1, 2]. A key problem of the excavator's autonomous operation is how to establish the scientific effective model of the electrohydraulic servo system and improve the trajectory tracking accuracy of the robotic excavator [3, 4]. Due to the existence of dead zone, saturation, nonlinear friction, and the nonsymmetry of hydraulic cylinder, the electrohydraulic servo system has strong nonlinear and time-varying characteristics [5–8]. Traditionally, the mechanism modeling method [9] and the linear identification algorithm [10] are used to establish the mathematical model of the nonlinear system. In the modeling process, the mechanism modeling method makes some assumptions and simplifies the system, resulting in a certain error between the established model and the actual system. The linear model identification algorithm establishes the model of the approximation system according to the input and output data, but the model cannot describe the nonlinear characteristics such as friction and dead zone.

Many researchers have done a lot of works in this field. Tri et al. [11] proposed and designed an adaptive control algorithm based on a modified backstepping algorithm with the iterative learning scheme for the trajectory control of an electrohydraulic actuator; experimental results showed that the proposed controller can provide excellent tracking response. Yung et al. [12] designed a controller based on a proportional feedback, a disturbance compensator, and a relay controller for a hydraulic cylinder in mobile hydraulics applications; the controller shows its robustness to different lowering velocities by comparing with a PI controller. Guo et al. [13] carried out a study on the nonlinear cascade trajectory tracking control for an electrohydraulic system using the sliding mode control and the backstepping technique, and the stability of the controller was proved based on Lyapunov theory. Both the simulation and experimental results proved the excellent tracking

performance of proposed approaches. Boaventura et al. [14] conducted an investigation on impedance control for a hydraulic robot actuator, many relevant aspects regarding the control algorithm were presented, and the experiment showed that tracking capabilities of the system were improved. Yao et al. [15] carried out a study on high-accuracy tracking control for hydraulic actuators, an improved LuGre friction model was derived, and then, an adaptive backstepping controller was proposed. Experimental results showed the controller can not only achieve the excellent asymptotic tracking performance but also ensure the robustness. Besides, the hybrid synchronization problem of chaotic systems was also investigated [16–19]. From all the research studies above, we can find that many valuable results have been obtained in the research field of hydraulic servo system. However, existing studies focused on the nonlinear characteristics, and little research on the time-varying characteristics has been done.

According to the strong nonlinear and time-varying characteristics of the electrohydraulic servo system, an adaptive identification algorithm based on the Hammerstein model is proposed. Hammerstein model [20, 21] consists of static nonlinear module and dynamic linear module. Its linear module is described by discrete autoregressive model, and nonlinear module is described by piecewise polynomial basis function. The Hammerstein model can effectively describe the nonlinear system, and the output error is significantly smaller than the linear identification algorithm. However, when the algorithm is used for nonlinear systems with time-varying parameters, the identification results are not satisfactory. Therefore, on the basis of the Hammerstein nonlinear identification algorithm, the limited memory method is introduced, fuzzy control module is designed, and the forgetting factor is adaptively adjusted by the fuzzy algorithm. The identified model can be updated in real time to better approximate the actual system.

The rest of the paper is organized as follows. In Section 2, the mathematical model of the electrohydraulic servo system is established by using the mechanism modeling method, and the nonlinearity and time-varying characteristics of the system are analyzed. In Section 3, the Hammerstein model structure is presented, and the identification algorithm of the electrohydraulic servo system based on the Hammerstein algorithm is developed. In Section 4, the forgetting factor is introduced, and the fuzzy control model is established to tune the forgetting factor in real time. In Section 5, the experimental setup and experimental procedure are explained, and the experimental results are discussed. In Section 6, conclusions are presented in the final section.

2. Model Analysis of Electrohydraulic Servo System

The electrohydraulic servo system of the robotic excavator is mainly composed of pilot electrohydraulic proportional valve, valve-controlled asymmetric hydraulic cylinder, sensor, and control system, etc. The system model can be represented by the dynamic equation of electrohydraulic proportional valve, flow equation of spool valve, the flow continuity equation of hydraulic cylinder, the hydraulic cylinder, and the load force balance equation.

The electrohydraulic proportional valve is a conversion unit between the electric signal and the hydraulic output, and the corresponding pressure output is related to the input signal, which is used to move the spool of the multiway directional valve. This can be expressed by the first-order linear differential equations:

$$\tau_v \dot{x}_v + x_v = K_1 u, \tag{1}$$

where x_v is the main spool displacement, τ_v is the time constant, K_1 is the gain of the electrohydraulic proportional valve, and u is the system input.

The movement of the robotic excavator's working device can be simplified as the valve control asymmetric hydraulic cylinder system. The pressure fluid and load can be seen as a mass-spring-damped oscillation system. The system schematic diagram is shown in Figure 1. A_1 and A_2 are the effective areas of the cylinder chambers; p_1 and p_2 are the pressures in cylinder chambers; q_1 and q_2 are inlet flow and return flow; p_s and p_0 are system pressure and return pressure; y is the cylinder piston displacement; m is the equivalent mass of the piston and workload; B_p is the viscous damping coefficient; K is the load elasticity coefficient; F_L is the disturbance force.

Take the forward movement of the hydraulic cylinder as an example to establish the mathematic model of the valve-controlled cylinder system. The load pressure equation of the hydraulic cylinder in steady state is as follows:

$$p_L = \frac{F}{A_1} = p_1 - n p_2, \tag{2}$$

where p_L is the load pressure; $n = A_2/A_1$ is the effective area ratio.

The flow of the directional valve is related to the pressure of inlet and outlet and the speed of the piston. The flow calculation formula of the directional valve is as follows:

$$\begin{cases} q_1 = C_d \omega x_v \sqrt{\dfrac{2}{\rho}\left(P_S - P_1\right)} = A_1 \dfrac{\mathrm{d}y}{\mathrm{d}t}, \\ q_2 = C_d \omega x_v \sqrt{\dfrac{2}{\rho} P_2} = A_2 \dfrac{\mathrm{d}y}{\mathrm{d}t}, \end{cases} \tag{3}$$

where C_d is the flow coefficient, ω is the area gradient of the valve, and ρ is the liquid density.

According to equations (2) and (3), the load flow equation of the spool valve can be obtained:

$$q_L = q_1 = C_d \omega x_v \sqrt{\frac{2\left(P_S - P_L\right)}{\rho\left(1 + n^3\right)}}. \tag{4}$$

Its linearized expression is as follows:

$$q_L = K_q x_v - K_c p_L, \tag{5}$$

where K_q is the flow gain and K_c is the pressure-flow gain.

Ignoring the influence of the pipeline on the hydraulic system, and assuming that the pressure in the working

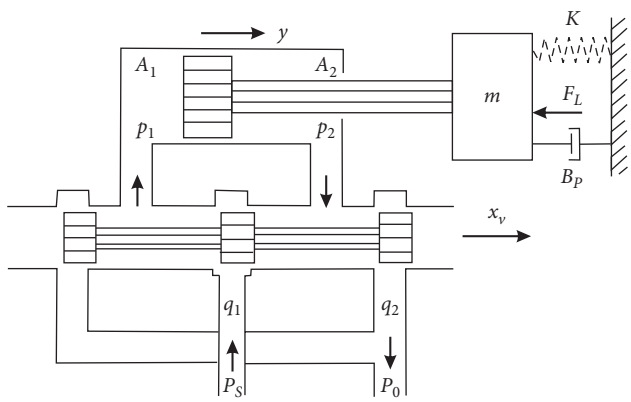

Figure 1: Schematic diagram of servo hydraulic cylinder system.

chamber of the hydraulic cylinder is equal everywhere, the flow continuity equation of the hydraulic cylinder is as follows [22]:

$$\begin{cases} q_1 = C_{ip}(p_1 - p_2) + C_{ep}p_1 + \dfrac{V_1}{\beta_e}\dfrac{\mathrm{d}p_1}{\mathrm{d}t} + \dfrac{\mathrm{d}V_1}{\mathrm{d}t}, \\ q_2 = C_{ip}(p_1 - p_2) - C_{ep}p_2 - \dfrac{V_2}{\beta_e}\dfrac{\mathrm{d}p_2}{\mathrm{d}t} - \dfrac{\mathrm{d}V_2}{\mathrm{d}t}, \end{cases} \tag{6}$$

where $V_1 = V_{01} + A_1 y$ and $V_2 = V_{02} - A_2 y$; V_{01} and V_{02} are the initial volumes of the hydraulic cylinder; C_{ip} and C_{ep} are internal leakage and external leakage coefficients; β_e is liquid bulk elastic modulus.

At this point, the calculation formula of load pressure is as follows:

$$q_L = q_1 = A_1\frac{\mathrm{d}y}{\mathrm{d}t} + C_{ip}(P_1 - P_2) + C_{ep}P_1\frac{V_1}{\beta_e}\frac{\mathrm{d}p_1}{\mathrm{d}t}. \tag{7}$$

From equation (3) and equation (6), the load pressure equation can be obtained:

$$q_L = C_{iL}P_L + C_{es}P_s + \frac{V_t}{4\beta_e}\frac{\mathrm{d}p_L}{\mathrm{d}t} + A_1\frac{\mathrm{d}y}{\mathrm{d}t}, \tag{8}$$

where V_t is the equivalent volume, $V_t = 4V_1/1 + n^3$, and $V_1 = LA_1/2$, L is the total stroke of the hydraulic cylinder piston; $C_{iL} = ((n^2 + 1)C_{ip} + C_{ep})/1 + n^3$ is equivalent leakage coefficient; $C_{es} = (n^3(C_{ep} + C_{ip}) - n^2C_{ip})/1 + n^3$ is additional leakage coefficient.

The load force of the hydraulic cylinder includes inertial force, viscous damping force, elastic force, and random load force. According to Newton's second law, the force equilibrium equation can be obtained:

$$A_1P_1 - A_2P_2 = A_1P_L = m\frac{\mathrm{d}^2y}{\mathrm{d}t} + B_p\frac{\mathrm{d}y}{\mathrm{d}t} + Ky + F_L. \tag{9}$$

The piston displacement of the hydraulic cylinder under the action of the system input u and the external load force F_L can be obtained based on the above equations:

$$Y = \frac{(K_1K_q/\tau_v s + 1)U - C_{es}P_sA_1 - (K_C + C_{iL} + (V_t/4\beta_e)s)F_L}{(K_C + C_{iL} + (V_t/4\beta_e)s)(ms^2 + B_ps + K) + A_1^2 s}. \tag{10}$$

It can be seen from the transfer function of the electrohydraulic servo system that some parameters are difficult to be calculated. Due to the nonlinear factors such as dead zone, saturation, and friction, the system has strong nonlinear and time-varying characteristics; at the same time, the linear terms are cross-coupled with the nonlinear terms. If the parameters of the electrohydraulic servo system are identified directly, several state variables need to be measured, in addition to increasing the test cost; the measurement noise is also introduced to produce larger identification error. Therefore, it is necessary to design an identification algorithm which can accurately describe the nonlinear and time-varying characteristics of the system.

3. Nonlinear Identification Algorithm Based on Hammerstein

The Hammerstein algorithm model describes the nonlinear system by the combination of static nonlinear module and dynamic linear module, and its system structure diagram is shown in Figure 2, where $u(k)$, $x(k)$, $v(k)$, and $y(k)$ are identification input, intermediate state, noise sequence, and system output, respectively. $N(\cdot)$ and $L(z)$ are nonlinear module and linear module. The linear and nonlinear characteristics are distinguished by the intermediate state $x(k)$, which can be used to decouple the linear and nonlinear models. The Hammerstein algorithm only requires the input and output data, which can effectively reduce the measurement noise and improve the identification precision [23].

Due to the asymmetric characteristics of friction in the electrohydraulic servo system, the nonlinear part of the Hammerstein algorithm is represented by piecewise polynomial function [24], and the input and output relationship of the nonlinear part is as follows:

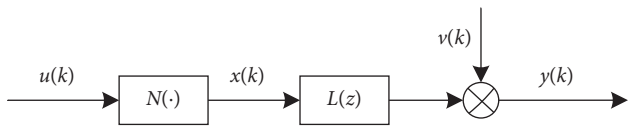

Figure 2: Hammerstein system identification structure.

$$x(k) = \begin{cases} f(u(k)) = \sum_{k=1}^{r} f_k u^k(k), & u(k) \geq 0, \\ g(u(k)) = \sum_{k=1}^{r} g_k u^k(k), & u(k) < 0, \end{cases} \tag{11}$$

where f_k and g_k are nonlinear coefficients and r is the order of the polynomial.

The linear part of the Hammerstein model is represented by a discrete autoregressive model, namely:

$$A\left(z^{-1}\right)y(k) = z^{-n_k}B\left(z^{-1}\right)x(k) + v(k), \tag{12}$$

where $A(z^{-1}) = 1 + a_1 z^{-1} + a_2 z^{-2} + \cdots + a_{n_a} z^{-n_a}$; $B(z^{-1}) = b_0 + b_1 z^{-1} + b_2 z^{-2} + \cdots + b_{n_b} z^{-n_b}$; n_k is system delay; $a_i\,(i = 1, 2, \cdots, n_a)$ and $b_j\,(j = 0, 1, \cdots, n_b)$ are linear coefficients.

Take the case of $u(k) > 0$. Substituting equation (11) into equation (12), the least square format based on the Hammerstein model can be simplified as follows:

$$y(k) = \phi^T(k)\theta + v(k). \tag{13}$$

The autoregressive variable $\phi(k)$ and the estimated parameter vector θ are as follows:

$$\begin{aligned} \phi(k) &= (-y(k-1), \ldots, -y(k-n_a), u(k-n_k), \\ &\quad \ldots, u(k-n_k-n_b), \ldots, u^r(k-n_k), \ldots, u^r(k-n_k-n_b)); \\ \theta &= \left(a_1, \ldots, a_{n_a}, C_{10}, \ldots, C_{1n_b}, C_{20}, \ldots, C_{(r-1)n_b}, C_{r0}, \ldots, C_{rn_b}\right)^T; \end{aligned} \tag{14}$$

where $C_{ij} = f_i b_j$.

The estimated value of θ can be obtained by the least square method:

$$\widehat{\theta} = \left(\Phi^T\Phi\right)^{-1}\Phi^T Y, \tag{15}$$

where $Y = [y(1), y(2), \ldots, y(N)]^T$ and $\Phi = [\phi^T(1), \phi^T(2), \ldots, \phi^T(N)]$.

Using the normalization method, and let $f_1 = 1$. The following equation can be obtained:

$$\begin{bmatrix} C_{10} & C_{11} & \cdots & C_{1n_b} \\ C_{20} & C_{21} & \cdots & C_{2n_b} \\ \vdots & \vdots & & \vdots \\ C_{r0} & C_{r1} & \cdots & C_{rn_b} \end{bmatrix} = \begin{bmatrix} b_0 & b_1 & \cdots & b_{n_b} \\ f_2 b_0 & f_2 b_1 & \cdots & f_2 b_{n_b} \\ \vdots & \vdots & & \vdots \\ f_r b_0 & f_r b_1 & \cdots & f_r b_{n_b} \end{bmatrix}. \tag{16}$$

After matrix transformation, the expression of f_k is as follows:

$$f_k = \frac{\sum_{j=0}^{n_b} C_{1j} C_{kj}}{\sum_{j=0}^{n_b} C_{1j}^2}, \quad (j = 0, 1, \ldots, n_b; k = 0, 1, \ldots, r). \tag{17}$$

According to equation (16), the intermediate variable $x(k)$ can be calculated in the iterative process.

4. Adaptive Dynamic Identification Based on Fuzzy Algorithm

Due to the time-varying characteristics of the electrohydraulic servo system, the problem of model mismatch may occur over the long run, which requires the system model has to be frequently updated. At the same time, it is necessary to consider the phenomenon of "data saturation" in the update process, that is, the impact of new data on parameter estimation becomes weaker and weaker over time. When the system is highly variable, the Hammerstein model will not be able to quickly track the changes in the system, causing the identification to fail. Therefore, the "forgetting factor" is introduced to solve the problem of data saturation.

According to the limited memory recursive least square algorithm [25], the following equation can be obtained:

$$\widehat{\theta}(k) = \widehat{\theta}(k-1) + K(k)\left[y(k) - \phi^T(k)\widehat{\theta}(k-1)\right], \tag{18}$$

$$P(k) = \frac{1}{\lambda}\left[1 - K(k)\phi^T(k)\right]P(k-1), \tag{19}$$

$$K(k) = \frac{P(k-1)\phi(k)}{\lambda + \phi^T(k)P(k-1)\phi(k)}, \tag{20}$$

where $P(k) = (\Phi^T\Phi)^{-1}$.

The forgetting factor λ is the weight of the old data in the identification process. The bigger the forgetting factor λ, the smaller the influence of the new data on the identification results. The smaller the forgetting factor λ, the greater the impact of the new data on the identification results. Therefore, in order to solve the problem of model mismatch, when the system changes slowly, it can adopt the larger forgetting factor λ to reduce the influence of the sensor's interference error on the model; when the system changes rapidly, it should adopt the smaller forgetting factor λ to make the model match the system more quickly.

In order to adapt to this change and obtain the optimal forgetting factor in real time, a fuzzy controller [26, 27] is designed to update the forgetting factor. The input of the controller is the displacement error e and the error variation Δe. Let the fuzzy universes of the error e and error variation Δe be $[-3, +3]$, and their lingual variables are {NB, NM, NS, ZO, PS, PM, PB} = $\{-3, -2, -1, 0, 1, 2, 3\}$. The output of the controller is forgetting factor and its lingual variables are {VS, MS, S, B, MB, VB} $=\{0.75, 0.80, 0.85, 0.90, 0.95, 1.0\}$.

The linear function can adjust the factors to reduce the error rapidly. The curve function is relatively smooth and is conducive to the stability of control. The membership function of fuzzy controller is designed based on the advantages of above two functions. When the error is large, the speed of adjustment is mainly considered and the trigonometric membership function is adopted; when the error is small, the stationarity is considered mainly and the curve membership function is adopted. The curve membership function is shown in Figure 3, and the corresponding fuzzy control rules are shown in Table 1.

The methods of defuzzification include weighted average method, maximum membership function method, and gravity method. According to the advantages and disadvantages of these methods, the gravity method is chosen for defuzzification, its calculation formula is as follows:

$$\lambda^* = \frac{\sum(\mu(x)^* p)}{\sum \mu(x)}, \tag{21}$$

where λ^* is the updated value of forgetting factor λ.

The overall control structure and data flow of the electrohydraulic servo system of the robotic excavator are shown in Figure 4. In the figure, y_r is the desired displacement and y is the actual displacement.

In summary, the steps of adaptive identification and control for robotic excavator based on Hammerstein are as follows:

Step 1: according to the mechanism characteristics of the electrohydraulic servo system of the robotic excavator, set the values of n_a, n_b, and n_k

Step 2: set the values of $\widehat{\theta}(0)$, $P(0)$, and forgetting factor λ

Step 3: offline identification; calculate the nonlinear module coefficients of the Hammerstein model

Step 4: collect the experimental data of the electrohydraulic servo system of the robotic excavator

Step 5: update the forgetting factor by fuzzy control algorithm

Step 6: update the linear module coefficients of the Hammerstein model

Step 7: calculate the next output $u(k+1)$ of the controller

Step 8: return to Step 4 and continue the loop

5. Experimental Analysis

The experimental prototype of the robotic excavator is developed from the existing backhoe mountain excavator, which is composed of backhoe mountain excavator, sensor control system, and the 3D laser radar. The working device of the robotic excavator is composed of boom, arm, telescopic arm, and bucket in series, as shown in Figure 5. Each joint is driven by servo hydraulic cylinder, and the displacement of the piston rod is measured by using the cable type of absolute encoder, as shown in Figure 6.

The structure of electrohydraulic proportional position control system of the robotic excavator's working device is the same, which is mainly composed of the electrohydraulic pilot proportional pressure reducing valve, LUDV multiway valve, hydraulic cylinder, and the cable type absolute encoder used to measure the displacement of the hydraulic cylinder piston rod, as shown in Figure 6.

The DSP controller is connected with main control computer and encoder through CAN bus. The main control computer gives the target position of the piston rod of the hydraulic cylinder, and the controller collects the displacement of the piston rod as the feedback, takes the difference between the target position and the feedback as the input of the controller, and then sends the control amount to the driver. The driver generates the PWM signal PWM and changes the voltage of the electrohydraulic pilot proportional reducing valve by adjusting the duty ratio of the PWM signal value. Therefore, the input pressure of LUDV multiway valve can be controlled to control the flow of the hydraulic cylinder, and then the movement of the working device can be driven by the piston rod of the hydraulic cylinder.

In order to study the nonlinear dynamic characteristics of the electrohydraulic servo system of the robotic excavator, take the boom control system for example, and the combination of low amplitude sinusoidal signal is used as excitation signal (as shown in Figure 7(a)). The stable low-speed output signal of the boom is shown in Figure 7(b).

It can be seen from Figure 7(b) that when the excitation signal is near 0, the output remains almost constant due to dead zone characteristics; when the input is sinusoidal symmetric signal, the output shows a downward trend, which is that the response characteristic of the positive and negative direction is asymmetrical.

In order to verify the effectiveness of the adaptive Hammerstein nonlinear identification algorithm, the system model of the electrohydraulic servo system of the robotic excavator is identified by the classical Hammerstein nonlinear identification algorithm (CHNLIA) and adaptive Hammerstein nonlinear identification algorithm (AHNLIA), respectively, which is combined with the control algorithm to form the controller, and the control performance of two algorithms is compared by experiments.

Based on the hydraulic control theory, the linear module orders of the Hammerstein model structure are set to $n_a = 3$, $n_b = 1$, and $n_k = 1$; the polynomial order of the nonlinear module is set to $r = 3$. The basic universe of error e is $[-4, 4]$, and the basic universe of error variation Δe is $[-2, 2]$. Let $f_1 = 1.0$, based on the adaptive Hammerstein nonlinear identification algorithm, and the model parameters of the boom control system of the robotic excavator are obtained, as shown in Table 2.

For the same test data, the model parameters of the boom control system of the robotic excavator are identified by the classical Hammerstein nonlinear identification algorithm again. The identified system model is compared with the actual system, and servo tracking experiment is carried out. The experimental results of the two algorithms are shown in Figure 8.

It can be seen from Figure 8 that the adaptive Hammerstein nonlinear identification algorithm (AHNLIA) has

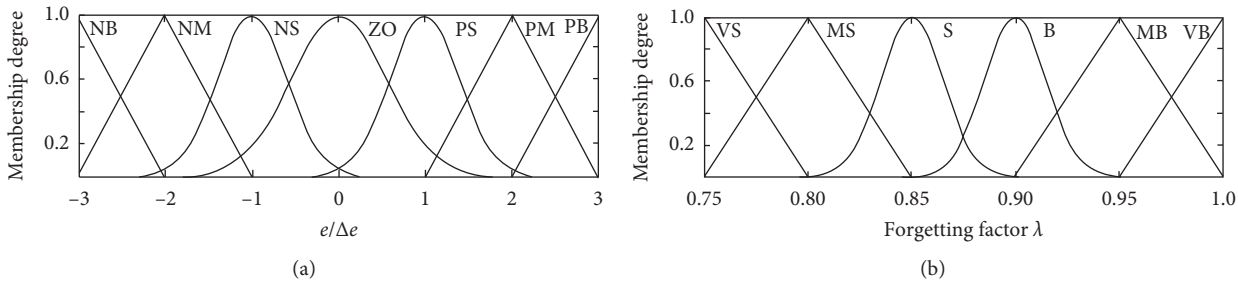

Figure 3: Input and output curves of the membership function.

Table 1: Fuzzy control rules.

$\Delta e/e$	NB	NM	NS	ZO	PS	PM	PB
NB	VS	VS	MS	S	B	MB	MB
NM	VS	MS	S	B	MB	VB	B
NS	MS	S	B	MB	MB	VB	S
ZO	S	S	VB	VB	VB	S	MS
PS	S	B	MB	VB	B	S	MS
PM	S	MB	MB	MB	S	MS	VS
PB	MB	MB	VB	S	S	VS	VS

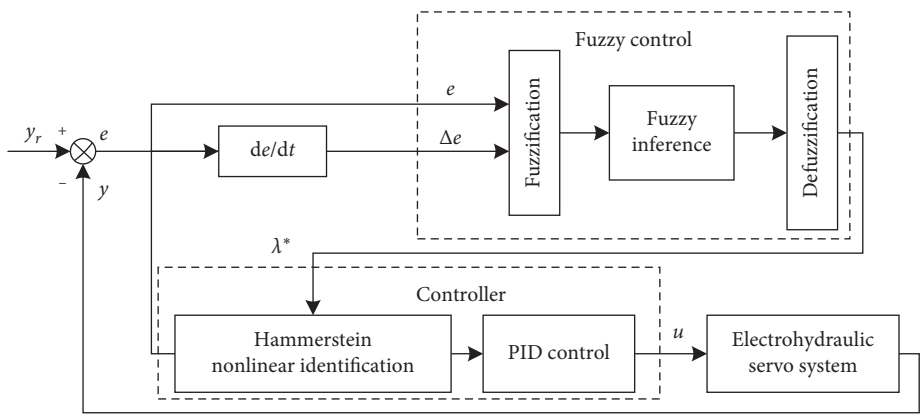

Figure 4: Structure diagram of controller.

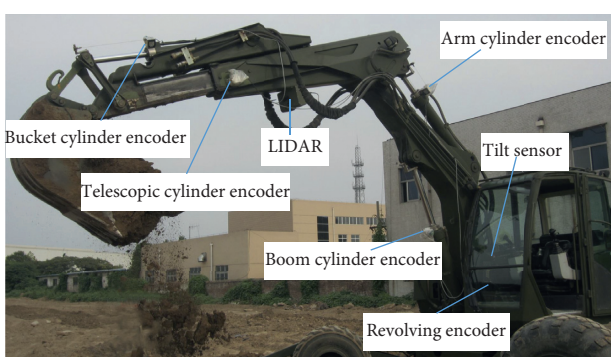

Figure 5: Experimental prototype of the robotic excavator.

better approximation accuracy than the classical Hammerstein nonlinear identification algorithm (CHNLIA). The calculated standard deviation of the CHNLIA is $\sigma_1 = 5.8921$, and the error of the identified model is obvious when the hydraulic cylinder changes its motion direction. The calculated standard deviation of the AHNLIA is $\sigma_2 = 3.5287$, the

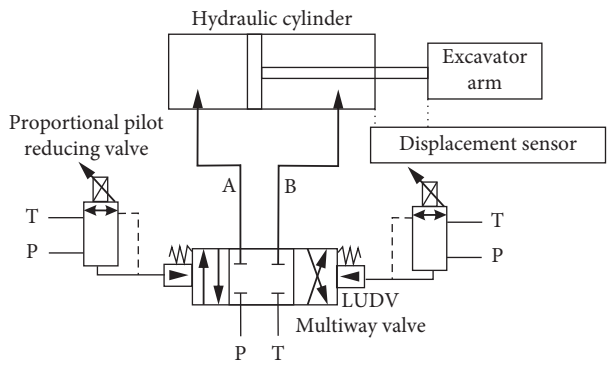

Figure 6: Electrohydraulic servo control system of the robotic excavator.

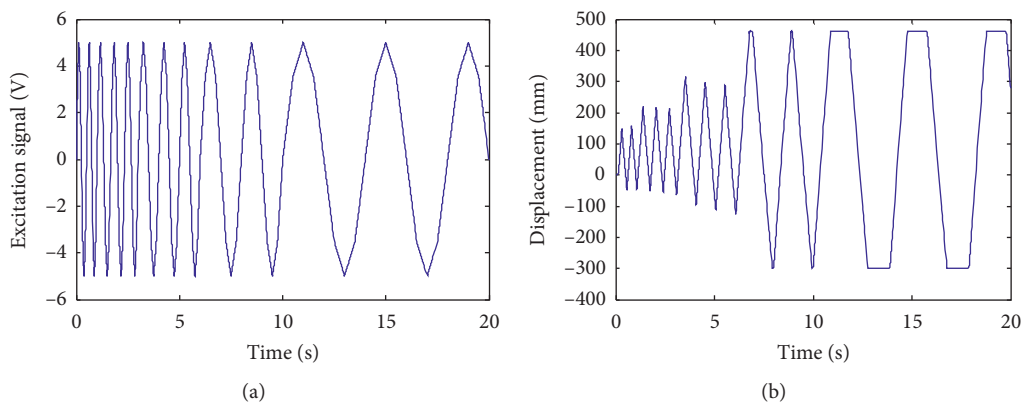

Figure 7: Input and output signal of the identification experiment. (a) Open-loop input and (b) output signal.

Table 2: Model parameters of the electrohydraulic servo system.

Name	Estimated value	Name	Estimated value
a_1	−0.9923	b_1	0.8375
a_2	0.0236	f_1	1.0
a_3	0.0042	f_2	0.0924
b_0	0.7237	f_3	−0.0133

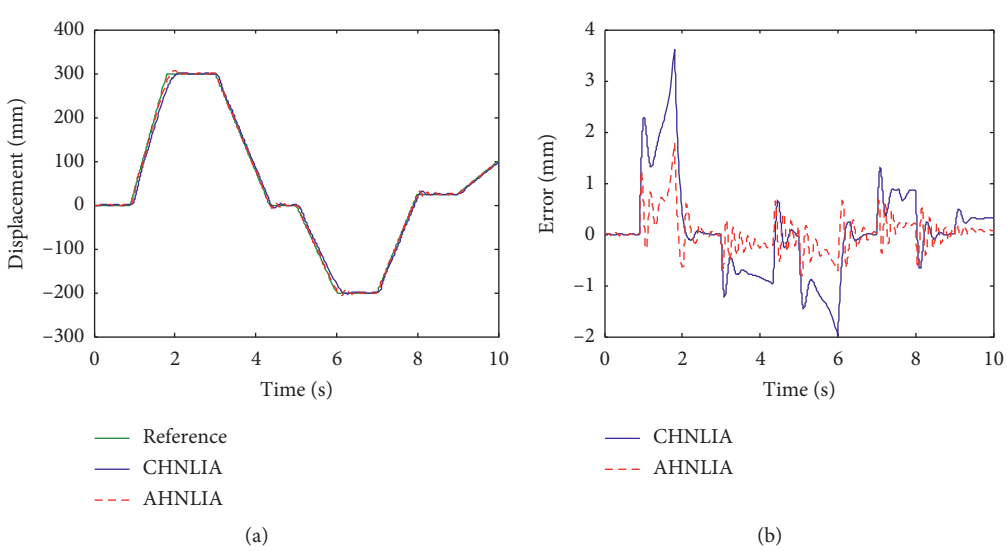

Figure 8: Comparison curves of output and output error. (a) Output comparison curve and (b) error comparison curve.

error of the algorithm fluctuates within a small range, and the hydraulic cylinder always stays near the designated position. It can be seen that the identification error of the AHNLIA is about 40.11% lower than that of the CHNLIA, and it can describe the dynamic characteristics of the electrohydraulic servo system of the robotic excavator more accurately.

6. Conclusion

On the basis of establishing the nonlinear model of the electrohydraulic servo system of the robotic excavator, the complex dynamic characteristics of the system are analyzed. Due to the nonlinear and time-varying characteristics of the electrohydraulic servo system, it is difficult to establish a precise mathematical model. The Hammerstein model with dynamic linear module and static nonlinear module is applied to describe the system; a forgetting factor is introduced to adjust the model, and the fuzzy control module is designed to adaptively update the forgetting factor. The identification results provide a reference model for the adaptive control of the robotic excavator, and the model predictive control can be used to track the predetermined trajectory accurately.

Experimental results show that the tracking accuracy of the adaptive Hammerstein nonlinear identification algorithm is improved significantly compared with the classical Hammerstein identification algorithm, which can describe the dynamic characteristics of the electrohydraulic servo system of the robotic excavator more accurately. The method provides a reference for the identification and control of other nonlinear time-varying systems in the industrial field.

Data Availability

The data used to support the findings of this study are available from the corresponding author upon request.

Conflicts of Interest

The authors declare that they have no conflicts of interest.

Acknowledgments

This work was supported by the military doctoral candidate funded project of the PLA, China (Grant no. 2015JY138).

References

[1] D. Wang, L. Zheng, H. Yu, W. Zhou, and L. Shao, "Robotic excavator motion control using a nonlinear proportional-integral controller and cross-coupled pre-compensation," *Automation in Construction*, vol. 64, pp. 1–6, 2016.

[2] K. Skonieczny, D. Wettergreen, and W. R. Whittaker, "Advantages of continuous excavation in lightweight planetary robotic operations," *The International Journal of Robotics Research*, vol. 35, no. 9, pp. 1121–1139, 2016.

[3] J. Park, D. Cho, S. Kim, Y. B. Kim, P. Y. Kim, and H. J. Kim, "Utilizing online learning based on echo-state networks for the control of a hydraulic excavator," *Mechatronics*, vol. 24, no. 8, pp. 986–1000, 2014.

[4] S. Jianpeng, Q. Long, Z. Xiaogang et al., "Electro-hydraulic velocity and position control based on independent metering valve control in mobile construction equipment," *Automation in Construction*, vol. 94, pp. 73–84, 2018.

[5] Y. Zhu, W. L. Jiang, X. D. Kong et al., "Study on nonlinear dynamics characteristics of electro hydraulic servo system," *Nonlinear Dynamics*, vol. 80, no. 1-2, pp. 723–737, 2015.

[6] Q. Guo, T. Yu, and D. Jiang, "Robust H∞ positional control of 2-DOF robotic arm driven by electro-hydraulic servo system," *Isa Transactions*, vol. 59, pp. 55–64, 2015.

[7] W.-h. Ding, H. Deng, Y.-m. Xia, and X.-g. Duan, "Tracking control of electro-hydraulic servo multi-closed-chain mechanisms with the use of an approximate nonlinear internal model," *Control Engineering Practice*, vol. 58, pp. 225–241, 2017.

[8] Y. He, J. Wang, and R. Hao, "Adaptive robust dead-zone compensation control of electro-hydraulic servo systems with load disturbance rejection," *Journal of Systems Science and Complexity*, vol. 28, no. 2, pp. 341–359, 2015.

[9] A. Kovari, "Effect of leakage in electrohydraulic servo systems based on complex nonlinear mathematical model and experimental results," *Acta Polytechnica Hungarica*, vol. 12, no. 3, pp. 2015–2129, 2015.

[10] X. Wang and S. Wang, "New approach of friction identification for electro-hydraulic servo system based on evolutionary algorithm and statistical logics with experiments," *Journal of Mechanical Science and Technology*, vol. 30, no. 5, pp. 2311–2317, 2016.

[11] N. M. Tri, D. N. C. Nam, H. G. Park, and K. K. Ahn, "Trajectory control of an electro hydraulic actuator using an iterative backstepping control scheme," *Mechatronics*, vol. 29, pp. 96–102, 2015.

[12] I. Yung, C. Vázquez, and L. B. Freidovich, "Robust position control design for a cylinder in mobile hydraulics applications," *Control Engineering Practice*, vol. 69, pp. 36–49, 2017.

[13] K. Guo, J. Wei, J. Fang, R. Feng, and X. Wang, "Position tracking control of electro-hydraulic single-rod actuator based on an extended disturbance observer," *Mechatronics*, vol. 27, pp. 47–56, 2015.

[14] T. Boaventura, J. Buchli, C. Semini, and D. G. Caldwell, "Model-based hydraulic impedance control for dynamic robots," *IEEE Transactions on Robotics*, vol. 31, no. 6, pp. 1324–1336, 2015.

[15] J. Yao, W. Deng, and Z. Jiao, "Adaptive control of hydraulic actuators with LuGre model-based friction compensation," *IEEE Transactions on Industrial Electronics*, vol. 62, no. 10, pp. 6469–6477, 2015.

[16] A. Yang, L. Li, Z. Wang, and R. Guo, "Tracking control of a class of chaotic systems," *Symmetry*, vol. 11, no. 4, p. 568, 2019.

[17] G. Rongwei, "Projective synchronization of a class of chaotic systems by dynamic feedback control method," *Nonlinear Dynamics*, vol. 90, no. 1, pp. 53–64, 2017.

[18] Z. Wang and R. Guo, "Hybrid synchronization problem of a class of chaotic systems by an universal control method," *Symmetry*, vol. 10, no. 11, p. 552, 2018.

[19] R. Ling, G. Rongwei, and E. V. Uchechukwu, "Coexistence of synchronization and anti-synchronization in chaotic systems," *Archives of Control Sciences*, vol. 26, no. 1, pp. 69–79, 2016.

[20] J. Chen and X. Wang, "Identification of Hammerstein systems with continuous nonlinearity," *Information Processing Letters*, vol. 115, no. 11, pp. 822–827, 2015.

[21] N. I. Chaudhary and M. A. Z. Raja, "Identification of Hammerstein nonlinear ARMAX systems using nonlinear

adaptive algorithms," *Nonlinear Dynamics*, vol. 79, no. 2, pp. 1385–1397, 2015.

[22] K. Baghestan, S. M. Rezaei, H. A. Talebi, and M. Zareinejad, "An energy-saving nonlinear position control strategy for electro-hydraulic servo systems," *Isa Transactions*, vol. 59, pp. 268–279, 2015.

[23] A. Gotmare, R. Patidar, and N. V. George, "Nonlinear system identification using a cuckoo search optimized adaptive Hammerstein model," *Expert Systems with Applications*, vol. 42, no. 5, pp. 2538–2546, 2015.

[24] N. Zhang, J. Cao, L. A. James, and T. E. Johansen, "Streamline tracing methods based on piecewise polynomial pressure approximations," *Water Resources Research*, vol. 54, no. 9, pp. 7029–7045, 2018.

[25] R. Xu, Q. Chen, G. Yang et al., "Identification of a certain mechanism's recoiling mass by limited memory least square method," *Journal of Vibroengineering*, vol. 16, no. 1, pp. 513–521, 2014.

[26] Y. Li and S. Tong, "Adaptive fuzzy output-feedback stabilization control for a class of switched nonstrict-feedback nonlinear systems," *IEEE Transactions on Cybernetics*, vol. 47, no. 4, pp. 1007–1016, 2017.

[27] J. Wu and J. Li, "Adaptive fuzzy control for perturbed strict-feedback nonlinear systems with predefined tracking accuracy," *Nonlinear Dynamics*, vol. 83, no. 3, pp. 1185–1197, 2016.

Hindawi
Mathematical Problems in Engineering
Volume 2020, Article ID 2045654, 8 pages
https://doi.org/10.1155/2020/2045654

Research Article

Matrix Expression of Shapley Value in Graphical Cooperative Games

Yuanhua Wang,[1] **Fuad E. Alsaadi**,[2] **Zheng Liu**,[1] **Xiaomeng Wu**,[1] **and Xiyu Liu**[1]

[1]*Business School, Shandong Normal University, Ji'nan 250014, China*
[2]*Department of Electrical and Computer Engineering, Faculty of Engineering, King Abdulaziz University, Jeddah 21589, Saudi Arabia*

Correspondence should be addressed to Yuanhua Wang; wyh_1005@163.com

Received 11 March 2020; Accepted 31 March 2020; Published 22 May 2020

Guest Editor: Rongwei Guo

This paper studies a class of cooperative games, called graphical cooperative games, where the internal topology of the coalition depends on a prescribed communication graph among players. First, using the semitensor product of matrices, the value function of graphical cooperative games can be expressed as a pseudo-Boolean function. Then, a simple matrix formula is provided to calculate the Shapley value of graphical cooperative games. Finally, some practical examples are presented to illustrate the application of graphical cooperative games in communication-based coalitions and establish the significance of the Shapley value in different communication networks.

1. Introduction

Game theory provides a formal mathematical formation to describe the complex interactions among rational players [1]. In general, game theory can be divided into two branches: noncooperative games and cooperative games. In noncooperative game theory, the fundamental unit of study is the individual player, and the theory studies the strategic choices in the interactions among competing players. By contrast, the fundamental unit in cooperative game theory is the set of players or coalition, and the theory studies the behaviour of rational players when they cooperate. The fundamental problem in cooperative game theory is how to allocate the profit or value of a coalition to its individual players in such a way that players are encouraged to cooperate. A fair allocation that has been widely used is the Shapley value [2].

In recent years, there has been an increasing amount of research on using graph theory to cooperative games, where the players are interconnected and communicate with others in a network graph. For modelling the communication graph, cooperative games in the graph form, called graphical cooperative games or graphical coalitional games, are introduced by Myerson in [3]. These are games where the internal structure of the coalition is described by a network. In the network, nodes represent players and two players are interpreted to have an edge between them if and only if they can communicate with each other. In such games, unlike the value of a coalition depending solely on the members of that coalition in canonical cooperative games, the value function will be dependent of how the players are interconnected within the coalition. In [4–6], the formation and stability of coalitions given an underlying communication graph are studied, and its applications to communication networks have been investigated. In [7], the graphical coalitional games are studied with applications to economic and social networks, and the authors have analyzed the stability of networks when players can choose to form and maintain the links between them. This game model is also used to study biologic networks [8] and so on.

It is pointed out in [3] that the Shapley value is the only possible function that provides a fair allocation in graphical coalitional games. However, its computational complexity becomes an obstacle both in practical applications and

theoretical deductions [9]; a remark is also presented in [6] to state that "the Shaple value is computationally expensive, but for fairly large structures one time computation is still affordable. For such a graph that even one time computation is not affordable, approximations can be used for its computation." In our recent work [10], a simple matrix formula is obtained to calculate the Shapley value and the basic mathematical method is the semitensor product of matrices (STP), which is a generalization of the traditional matrix product [11]. This method has been successfully applied in the analysis and control problems of logical networks [12–25], and then it has been used in finite game theory [26–30], evolutionary games [31–38], finite automata [39, 40], graph theory [41], etc. Unlike the canonical cooperative games being considered in [10], this paper studies a new class of cooperative games, called graphical cooperative games. Wang et al. [10] have provided the matrix formulas to calculate the symmetric and weighted Shapley values for canonical cooperative n-person games. However, this paper proposes a simple formula to calculate the Shapley value of graphical cooperative games, and it is more computationally complex than the formulas in [10].

The paper is organized as follows. A brief review for the STP method and graphical cooperative games is presented in Section 2. In Section 3, the matrix formula of the Shapley value in graphical cooperative games is presented. Section 4 discusses the practical applications of graphical cooperative games to some communication networks. Section 5 is a brief conclusion.

Before ending this section, we present some notations used in this paper. $\mathscr{D} := \{0,1\}$. $\Delta_n := \left\{\delta_n^i \mid i = 1,\cdots,n\right\}$, where δ_n^i is the ith column of the identity matrix I_n. $\mathbb{R}^n$ is the n dimensional Euclidean space. $\mathscr{M}_{m\times n}$ denotes the set of $m\times n$ real matrices. $\mathrm{Col}(M)$ ($\mathrm{Row}(M)$) is the set of columns (rows) of M and $\mathrm{Col}_i(M)$ ($\mathrm{Row}_i(M)$) is the ith column (row) of M. $\mathbf{1}_\ell = \underbrace{(1,1,\ldots,1)}_{\ell}{}^T$. A matrix $L \in \mathscr{M}_{m\times n}$ is called a logical matrix if the columns of L are of the form of δ_m^k, that is, $\mathrm{Col}(L) \subset \Delta_m$. Denote by $\mathscr{L}_{m\times n}$ the set of $m\times n$ logical matrixes.

2. Preliminaries

2.1. Semitensor Product of Matrices. The basic technique used in this paper is the STP of matrices. We can refer to [11] for details.

Definition 1. Let $M \in \mathscr{M}_{m\times n}$, $N \in \mathscr{M}_{p\times q}$, and $t = \mathrm{lcm}\{n,p\}$ be the least common multiple of n and p. The STP of M and N is defined as

$$M \ltimes N := \left(M \otimes I_{t/n}\right)\left(N \otimes I_{t/p}\right) \in \mathscr{M}_{mt/n\times qt/p}, \tag{1}$$

where $\otimes$ is the Kronecker product. As a generalization of the conventional matrix product, the STP of matrices keeps the useful properties of the conventional matrix product available. For convenience, the symbol " $\ltimes$ " may be omitted without confusion.

Next, we present some properties of the STP used in this paper.

Proposition 1. *Let $X \in \mathbb{R}^m$ be a column and M be a matrix. Then,*

$$X \ltimes M = \left(I_m \otimes M\right)X. \tag{2}$$

The STP has pseudocommutative properties, and the swap matrix is defined as follows.

Definition 2 The matrix $W_{[m,n]} \in \mathscr{M}_{mn\times mn}$, defined by

$$\begin{aligned} W_{[m,n]} = \delta_{mn}[&1, m+1, \cdots, (n-1)m+1; 2, m \\ &+ 2, \ldots, (n-1)m+2;\ \ldots; m, 2m, \ldots, nm], \end{aligned} \tag{3}$$

is called the (m,n)th dimensional swap matrix.

Proposition 2. *Let $X \in \mathbb{R}^m$ and $Y \in \mathbb{R}^n$ be two columns. Then,*

$$W_{[m,n]} \ltimes X \ltimes Y = Y \ltimes X. \tag{4}$$

If x is a logical variable, then $x \in \mathscr{D}$. To use vector expression of logical values, we identify $1 \sim \delta_2^1 \in \Delta$ and $0 \sim \delta_2^2 \in \Delta$. Now, a pseudological (or logical) function can be expressed as an algebraic form.

Theorem 1. *Let $f : \mathscr{D}^n \longrightarrow \mathbb{R}$ (or $f : \mathscr{D}^n \longrightarrow \mathscr{D}$) be a pseudological (or logical) function. Then, there exists a unique vector (or matrix) $M_f \in \mathbb{R}^{1\times 2^n}$ (or $M_f \in \mathscr{L}_{2\times 2^n}$), such that*

$$f\left(x_1, x_2, \ldots, x_n\right) = M_f \ltimes_{i=1}^{n} x_i, \tag{5}$$

where M_f is called the structure vector (or matrix) of f, which can be calculated as

$$Col_j\left(M_f\right) = f\left(\delta_{k^n}^j\right), \quad j = 1, 2, \cdots, k^n. \tag{6}$$

2.2. Graphical Cooperative Games. In essence, a canonical cooperative game involves a set of players, denoted by $N = \{1, 2, \ldots, n\}$, who seek to form cooperative groups in order to strengthen their positions in the game. Any subset of N is called a coalition, and N is called the grand coalition. The second fundamental concept of the canonical cooperative game is the characteristic function or value function, denoted by v: $2^N \longrightarrow \mathbb{R}$ with $v(\varnothing) = 0$, which quantifies the worth of a coalition in a game. Therefore, a canonical cooperative game can be denoted by a pair (N, v) [4]. In general, we can identify a cooperative game (N, v) with its value function v, since for every v a different game may be defined.

Next, we give the definition of graphical cooperative games.

Definition 3 (see [6]). A graphical cooperative game is denoted by $\Gamma = (G, v)$, where

(1) $G = (V, E)$ is an undirected graph with $V = \{1, 2, \ldots, n\}$ a finite nonempty set of players and $E \subseteq V \times V$ a set of edges. The elements of V are also called nodes or vertices. The number of elements in V is called the order or size of G and is denoted as

$|G| = n$. In this paper, we only consider that G is a simple graph, that is, G does not contain self-loops and multiple edges. Let $S = (V', E')$ be a graph such that $V' \subseteq V$ and $E' \subseteq E$; then, S is called a subgraph of G. If E' contains all the edges $e = \{i, j\} \in E$ with $i, j \in V'$, then S is called an induced subgraph of G and denoted as $S \subseteq G$.

(2) v: $2^G \longrightarrow \mathbb{R}$ is called the value function or characteristic function with $v(\varnothing) = 0$, where 2^G is the collection of all the induced subgraphs of G. It should be noted that v is required to satisfy four axioms of value [6].

For every induced subgraph $S \subseteq G$, that is, $S \in 2^G$, the value function $v(S)$ can be expressed as a pseudological function v: $\mathscr{D}^n \longrightarrow \mathbb{R}$ by using the logical variables; then, we have

$$v(S) = v\left(x_1^S, x_2^S, \cdots, x_n^S\right), \quad S \in 2^G, \tag{7}$$

where $x_i^S \in \mathscr{D}$ is a logical variable and

$$x_i^S = \begin{cases} 1, & i \in S, \\ 0, & i \notin S. \end{cases} \tag{8}$$

Define a lexicographic order as

$$T \prec S \longleftrightarrow d(T) > d(S), \tag{9}$$

where $d(R) = \sum_{i=1}^{n} 2^{n-i} x_i^R$ is a decimal number corresponding to each induced subgraph $R \in 2^G$, and its binary number is $b(R) = x_1^R x_2^R \cdots x_n^R$. That is, we can describe $b(R_1) = 1\,1 \cdots 1\,1$, $b(R_2) = 1\,1 \cdots 1\,0$, $b(R_3) = 1\,1 \cdots 0\,1$, $\cdots$, $b(R_{2^n}) = 0\,0 \cdots 0\,0$.

Using Theorem 1, for every pseudological function v, we can find its structure vector $C_v \in \mathbb{R}^{2^n}$, such that equation (7) can be expressed into its matrix form as

$$v(S) = C_v x^S, \tag{10}$$

where $x^S = \propto_{i=1}^{n} x_i^S \in \Delta_{2^n}$ and $C_v := [v(b(R_1)), v(b(R_2)), \ldots, v(b(R_{2^n}))]$. Because of $v(\varnothing) = 0$, the last element of C_v is 0, that is, $v(b(R_{2^n})) = 0$.

3. Matrix Formula of the Shapley Value in Graphical Cooperative Games

In this section, we give a matrix formula to calculate the Shapley value in graphical cooperative games in order to reduce the computational complexity. First, we define the Shapley value of player i in graphical cooperative games.

Definition 4 (see [6]). Consider a graphical cooperative game $\Gamma = (G, v)$; the Shapley value of player i is defined as

$$\varphi_v^G(i) = \frac{1}{|G|} \sum_{S \subseteq G \backslash \{i\}} \frac{(v(S \cup \{i\}) - v(S))}{\binom{|G|-1}{|S|}}, \quad i = 1, 2, \cdots, n, \tag{11}$$

where $S \subseteq G \backslash \{i\}$ means S is an induced subgraph of $G \backslash \{i\}$, and $S \cup \{i\}$ is an induced subgraph of G that contains all the players in S and player i.

Since $|G| = n$, then we have

$$\binom{|G|-1}{|S|} = C_{n-1}^{|S|} = \frac{(n-1)!}{|S|!\,(n-1-|S|)!}. \tag{12}$$

Plugging it into (11) yields

$$\begin{aligned} \varphi_v^G(i) &= \sum_{S \subseteq G \backslash \{i\}} \frac{|S|!\,(n-1-|S|)!}{n(n-1)!} [v(S \cup \{i\}) - v(S)] \\ &= \sum_{S \subseteq G \backslash \{i\}} \frac{|S|!\,(n-1-|S|)!}{n!} [v(S \cup \{i\}) - v(S)]. \end{aligned} \tag{13}$$

According to (10), we have the matrix expression as

$$\begin{aligned} v(S \cup \{i\}) - v(S) &= C_v \left(x_1^S \cdots x_{i-1}^S \begin{bmatrix} 1 \\ 0 \end{bmatrix} x_{i+1}^S \cdots x_n^S - x_1^S \cdots x_{i-1}^S \begin{bmatrix} 0 \\ 1 \end{bmatrix} x_{i+1}^S \cdots x_n^S \right) \\ &= C_v \left(W_{[2,2^{i-1}]} \begin{bmatrix} 1 \\ 0 \end{bmatrix} x_1^S \cdots x_{i-1}^S x_{i+1}^S \cdots x_n^S - W_{[2,2^{i-1}]} \begin{bmatrix} 0 \\ 1 \end{bmatrix} x_1^S \cdots x_{i-1}^S x_{i+1}^S \cdots x_n^S \right) \\ &= C_v \left(W_{[2,2^{i-1}]} \begin{bmatrix} 1 \\ -1 \end{bmatrix} x_1^S \cdots x_{i-1}^S x_{i+1}^S \cdots x_n^S \right), \end{aligned} \tag{14}$$

where $\ltimes_{j\neq i}^{n\,j=1} x_j^S \in \Delta_{2^{n-1}}$, and in vector form,

$$x_j^S = \begin{cases} \delta_2^1, & j \in S, \\ \delta_2^2, & j \notin S. \end{cases} \tag{15}$$

It follows that

$$x_1^S \cdots x_{i-1}^S x_{i+1}^S \cdots x_n^S = \delta_{2^{n-1}}^j, \quad j = 1, 2, \cdots, 2^{n-1}. \tag{16}$$

According to Definition 2, we have

$$W_{[2,2^{i-1}]} \begin{bmatrix} 1 \\ -1 \end{bmatrix} = \operatorname{diag}\left(\underbrace{\begin{bmatrix} 1 \\ -1 \end{bmatrix}, \cdots, \begin{bmatrix} 1 \\ -1 \end{bmatrix}}_{2^{i-1}} \right) \in \mathscr{M}_{2^i \times 2^{i-1}}. \tag{17}$$

Then, we obtain that

$$W_{[2,2^{i-1}]} \begin{bmatrix} 1 \\ -1 \end{bmatrix} \delta_{2^{n-1}}^j = \left(W_{[2,2^{i-1}]} \begin{bmatrix} 1 \\ -1 \end{bmatrix} \otimes I_{2^{n-i}} \right) \delta_{2^{n-1}}^j = \operatorname{Col}_j(T_i), \tag{18}$$

where

$$\begin{aligned} T_i &= \left(W_{[2,2^{i-1}]} \begin{bmatrix} 1 \\ -1 \end{bmatrix} \right) \otimes I_{2^{n-i}} \\ &= \operatorname{diag}\left(\underbrace{\begin{bmatrix} I_{2^{n-i}} \\ -I_{2^{n-i}} \end{bmatrix}, \cdots, \begin{bmatrix} I_{2^{n-i}} \\ -I_{2^{n-i}} \end{bmatrix}}_{2^{i-1}} \right) \in \mathscr{M}_{2^n \times 2^{n-1}}. \end{aligned} \tag{19}$$

Similar to the construction in [10], we construct a vector ℓ_j as follows:

$$\begin{cases} \ell_1 = \begin{bmatrix} 1 \\ 0 \end{bmatrix}, \\ \ell_{k+1} = \begin{bmatrix} \ell_k + \mathbf{1}_{2^k} \\ \ell_k \end{bmatrix} \in \mathbb{R}^{2^{k+1}}, \quad k = 1, 2, 3, \cdots. \end{cases} \tag{20}$$

Let $|S| = |\delta_{2^{n-1}}^\alpha| = \ell_{n-1}^\alpha$, $\alpha = 1, 2, \cdots, 2^{n-1}$, where ℓ_{n-1}^α denotes the αth element of ℓ_{n-1}. Use ℓ_{n-1} to construct a new column vector $\eta_{n-1} = [\eta_{n-1}^1, \eta_{n-1}^2, \cdots, \eta_{n-1}^{2^{n-1}}]^T$, where

$$\eta_{n-1}^\alpha = (\ell_{n-1}^\alpha)!\,(n - 1 - \ell_{n-1}^\alpha)!, \quad \alpha = 1, 2, \cdots, 2^{n-1}. \tag{21}$$

Set $\xi = \eta_{n-1}$, and we divide ξ into k equal blocks as follows:

$$\xi = \left[\xi_k^1, \xi_k^2, \cdots, \xi_k^k\right]^T, \quad k = 1, 2, 2^2, \cdots, 2^{n-1}. \tag{22}$$

That is, when $k = 2$, then ξ can be divided into two equal blocks $\xi = \begin{bmatrix} \xi_2^1 \\ \xi_2^2 \end{bmatrix}, \ldots,$ and when $k = 2^{n-1}$, then $\xi = [\xi_{2^{n-1}}^1, \xi_{2^{n-1}}^2, \cdots, \xi_{2^{n-1}}^{2^{n-1}}]^T$.

Based on the abovementioned derivation, the Shapley value (13) can be written as

$$\begin{aligned} \varphi_v^G(i) &= \frac{1}{n!} \sum_{j=1}^{2^{n-1}} C_v \eta_{n-1}^j W_{[2,2^{i-1}]} \begin{bmatrix} 1 \\ -1 \end{bmatrix} \delta_{2^{n-1}}^j \\ &= \frac{1}{n!} C_v \cdot \sum_{j=1}^{2^{n-1}} \eta_{n-1}^j \operatorname{Col}_j(T_i) \\ &= \frac{1}{n!} C_v \cdot \begin{bmatrix} \xi_{2^{i-1}}^1 \\ -\xi_{2^{i-1}}^1 \\ \xi_{2^{i-1}}^2 \\ -\xi_{2^{i-1}}^2 \\ \vdots, \\ \xi_{2^{i-1}}^{2^{i-1}} \\ -\xi_{2^{i-1}}^{2^{i-1}} \end{bmatrix}, \quad i = 1, 2, \cdots, n. \end{aligned} \tag{23}$$

Then, we have the following result for calculating the Shapley value in graphical cooperative games.

Theorem 2. *Consider a graphical cooperative game $\Gamma = (G, v)$, its Shapley value can be calculated by the following matrix formula:*

$$\varphi_v^G = \left[\varphi_v^G(1)\,\varphi_v^G(2)\cdots\varphi_v^G(n)\right] = \frac{1}{n!}\,C_v\cdot\Xi, \tag{24}$$

where

$$\Xi = \begin{bmatrix} & & & \xi_{2^{n-1}}^1 \\ & & & -\xi_{2^{n-1}}^1 \\ & \xi_2^1 & & \xi_{2^{n-1}}^2 \\ \xi_1^1 & -\xi_2^1 & \cdots & -\xi_{2^{n-1}}^2 \\ -\xi_1^1 & \xi_2^2 & & \vdots \\ & -\xi_2^2 & & \xi_{2^{n-1}}^{2^{n-1}} \\ & & & -\xi_{2^{n-1}}^{2^{n-1}} \end{bmatrix} \in \mathscr{M}_{2^n\times n}. \tag{25}$$

Remark 1. In the conversional formula of the Shapley value (13), the computational complexity is $\mathcal{O}(n!^2)$. Using the STP method, a simple matrix form of the Shapley value is provided in Theorem 2. Observing (24), in order to calculate the Shapley value, we just need to discuss the computational complexity of matrix Ξ. Obviously, the dimension of Ξ is $2^n\times n$ and with the help of MATLAB, the matrix Ξ can be easily obtained by using the recursive algorithm, which is the major advantage of Theorem 2.

4. Practical Examples of Graphical Cooperative Games

In this section, we consider some practical examples of graphical cooperative games, which are presented in [6]. These examples show the applications of graphical cooperative games to communication network of sensor nodes. Nodes communicate with each other through links.

Example 1. Assume that the value of a communication network is the number of nodes pairs which can communicate with each other; then, the value function for a connected graph of size n is

$$v_n = \begin{cases} C_n^2, & n>1, \\ 0, & n=1. \end{cases} \tag{26}$$

Three different communication networks between six nodes are shown in Figure 1.

Using (10), the value function of graph G_a shown in Figure 1(a) can be expressed as

$$v_{G_a}(S) = C_v^{G_a}\propto_{i=1}^{6} x_i^S, \tag{27}$$

where $C_v^{G_a}\in\mathbb{R}^{2^6}$ is a row vector; using (26), it is easy to calculate that

$$\begin{aligned} C_v^{G_a} = [&6\,4\,4\,3\,4\,3\,3\,3\,4\,2\,2\,1\,2\,1\,1\,1\,3\,1\,1\,0\,1\,0\,0\,0\,3\,1\,1\,0\,1\,0\,0\,0 \\ &4\,2\,2\,1\,2\,1\,1\,1\,3\,1\,1\,0\,1\,0\,0\,0\,3\,1\,1\,0\,1\,0\,0\,0\,3\,1\,1\,0\,1\,0\,0\,0]. \end{aligned} \tag{28}$$

Then, we construct a column vector $\ell_5\in\mathbb{R}^{2^5}$ as

$$\ell_5 = [5\,4\,4\,3\,4\,3\,3\,2\,4\,3\,3\,2\,3\,2\,2\,1\,4\,3\,3\,2\,3\,2\,2\,1\,3\,2\,2\,1\,2\,1\,1\,0]^T. \tag{29}$$

According to (21), a new column vector ξ can be calculated as

$$\begin{aligned} \xi = [&120\,24\,24\,12\,24\,12\,12\,12\,24\,12\,12\,12\,12\,12\,12\,24 \\ &24\,12\,12\,12\,12\,12\,12\,24\,12\,12\,12\,24\,12\,24\,24\,120]^T. \end{aligned} \tag{30}$$

Now, we divide ξ into k equal blocks, where $k = 1, 2, 2^2, 2^3, 2^4, 2^5$.

Using Theorem 2, we have

$$\Xi = \begin{bmatrix} 120 & 120 & 120 & 120 & 120 & 120 \\ 24 & 24 & 24 & 24 & 24 & -120 \\ 24 & 24 & 24 & 24 & -120 & 24 \\ 12 & 12 & 12 & 12 & -24 & -24 \\ 24 & 24 & 24 & -120 & 24 & 24 \\ 12 & 12 & 12 & -24 & 12 & -24 \\ 12 & 12 & 12 & -24 & -24 & 12 \\ 12 & 12 & 12 & -12 & -12 & -12 \\ \vdots & \vdots & \vdots & \vdots & \vdots & \vdots \\ -12 & -12 & -12 & 12 & 12 & 12 \\ -12 & -12 & -12 & 24 & 24 & -12 \\ -12 & -12 & -12 & 24 & -12 & 24 \\ -24 & -24 & -24 & 120 & -24 & -24 \\ -12 & -12 & -12 & -12 & 24 & 24 \\ -24 & -24 & -24 & -24 & 120 & -24 \\ -24 & -24 & -24 & -24 & -24 & 120 \\ -120 & -120 & -120 & -120 & -120 & -120 \end{bmatrix} \in \mathscr{M}_{2^6\times 6}. \tag{31}$$

According to (24), we can easily obtain its Shapley value by using MATLAB software, which is presented as

$$\varphi_v^{G_a} = \frac{1}{6!}C_v^{G_a}\cdot\Xi = [0.833\ \ 1.333\ \ 0.833\ \ 1\ 1\ 1]. \tag{32}$$

Similarly, the Shapley value of each node in Figures 1(b) and 1(c) can also be given by

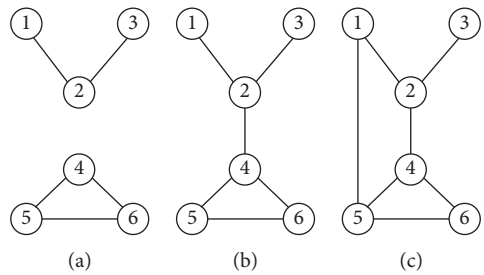

Figure 1: Communication network graphs.

$$\varphi_v^{G_b} = \frac{1}{6!} C_v^{G_b} \cdot \Xi = [1.667 \;\; 4.167 \;\; 1.667 \;\; 3.833 \;\; 1.833 \;\; 1.833],$$

$$\varphi_v^{G_c} = \frac{1}{6!} C_v^{G_c} \cdot \Xi = [\,2.35 \;\; 3.683 \;\; 1.75 \;\; 2.65 \;\; 2.517 \;\; 2.05], \tag{33}$$

where

$$\begin{aligned} C_v^{G_b} &= [15 \;\; 10 \;\; 10 \;\; 6 \;\; 4 \;\; 3 \;\; 3 \;\; 3 \;\; 10 \;\; 6 \;\; 6 \;\; 3 \;\; 2 \;\; 1 \;\; 1 \;\; 1 \;\; 3 \;\; 1 \;\; 1 \;\; 0 \;\; 1 \;\; 0 \;\; 0 \;\; 0 \\ &\quad 3 \;\; 1 \;\; 1 \;\; 0 \;\; 1 \;\; 0 \;\; 0 \;\; 0 \;\; 10 \;\; 6 \;\; 6 \;\; 3 \;\; 2 \;\; 1 \;\; 1 \;\; 1 \;\; 6 \;\; 3 \;\; 3 \;\; 1 \;\; 1 \;\; 0 \;\; 0 \;\; 0 \\ &\quad 3 \;\; 1 \;\; 1 \;\; 0 \;\; 1 \;\; 0 \;\; 0 \;\; 0 \;\; 3 \;\; 1 \;\; 1 \;\; 0 \;\; 1 \;\; 0 \;\; 0 \;\; 0], \\ C_v^{G_c} &= [15 \;\; 10 \;\; 10 \;\; 6 \;\; 10 \;\; 6 \;\; 3 \;\; 3 \;\; 10 \;\; 6 \;\; 6 \;\; 3 \;\; 6 \;\; 3 \;\; 1 \;\; 1 \;\; 6 \;\; 3 \;\; 1 \;\; 0 \;\; 3 \;\; 1 \;\; 0 \;\; 0 \\ &\quad 6 \;\; 3 \;\; 1 \;\; 0 \;\; 3 \;\; 1 \;\; 0 \;\; 0 \;\; 10 \;\; 6 \;\; 6 \;\; 3 \;\; 2 \;\; 1 \;\; 1 \;\; 1 \;\; 6 \;\; 3 \;\; 3 \;\; 1 \;\; 1 \;\; 0 \;\; 0 \;\; 0 \\ &\quad 3 \;\; 1 \;\; 1 \;\; 0 \;\; 1 \;\; 0 \;\; 0 \;\; 0 \;\; 3 \;\; 1 \;\; 1 \;\; 0 \;\; 1 \;\; 0 \;\; 0 \;\; 0]. \end{aligned} \tag{34}$$

It is shown that, in three network graphs, the only difference is the structure vector of value function, which is dependent of its corresponding communication graph. Therefore, for a communication network with the same number of nodes, the matrix Ξ is the same. Besides, it is to be noted that our computational results coincide with the values presented in [6].

Based on the above calculated Shapley values, it can be seen that the more a node is involved in the communication network, the more is its Shapley value. For example, in Figure 1(a), node 2 is more vital than any of the nodes 4, 5, and 6, since node 2 exclusively supports the communication between nodes 1 and 3. Comparing Figures 1(b) and 1(c), the addition of new link between nodes 1 and 5 in Figure 1(c) can support the communication between nodes 1 and 5, which is exclusively supported by the link between nodes 2 and 4 in Figure 1(b); hence, it assigns more Shapley values to nodes 2 and 4 in Figure 1(b).

The following example presented in [6] shows that, for some communication networks with special structure topologies, the Shapley value can be simple to calculate regardless of the number of players.

Example 2. Consider a network with n nodes, the structure topology between them is a star graph with node 1 as the star point. In [6], a simple formula to compute the Shapley value of each node is given and this formula holds for any number n of nodes. Using our matrix formula (24) in Theorem 2, it is also easy to calculate the Shapley value, and it is shown that, for the star graph between n nodes, the computational complexity between the formula in [6] and our matrix formula (24) is the same. Moreover, it is obvious that, in a star graph for the structure vector C_v of value function in (10), the last $\mathbb{R}^{2^{n-1}}$ elements of C_v are all 0, since $x_1^S = 0$. For example, when $n = 6$, the network graph is described in Figure 2, and its structure vector can be calculated that

$$C_v = [15, 10, 10, 6, 10, 6, 6, 3, 10, 6, 6, 3, 6, 3, 3, 1, 10, 6, 6, 3, 6, 3, 3, 1, 6, 3, 3, 1, 3, 1, 1, 0, 0, \cdots, 0] \in \mathbb{R}^{2^6}. \tag{35}$$

Using (24), where Ξ is the same as in example 1, we have its Shapley value as

$$\begin{cases} \varphi_v^G(1) = 5.833, \\ \varphi_v^G(i) = 1.833, \quad i = 2, \cdots, 6. \end{cases} \tag{36}$$

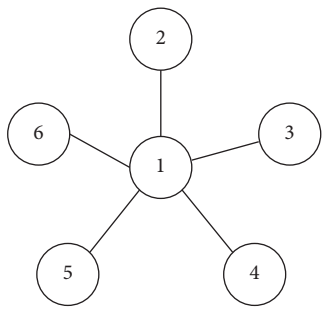

Figure 2: Star graph with six nodes.

It is established that node 1 is the most vital node in this communication graph.

From these two simple examples, it is worth noting the advantage of our result in Theorem 2. Regardless of the structure topology for communication networks, we only need to calculate the matrix Ξ, which is easily obtained by using recursive algorithm with the help of MATLAB. However, it is pointed in [6] that the Shapey value is computationally expensive and for a fairly large graph even one time computation is not affordable.

5. Conclusion

This paper considers a new class of cooperative games, called graphical cooperate games. Using the STP method, the value function is presented as a pseudo-Boolean function, and a corresponding formula is obtained to calculate the Shapley value for graphical cooperate games. Then, the worth of each player in a coalition based on its connectivity in communication network can be explored. Some examples are given to demonstrate the theoretical results. In our future work, we will study more useful properties of graphical cooperative games based on the Shapley value.

With the rapid development of science, the game-theoretic approach will be a promising new method for studying more control problems in the future, such as synchronization [42–49], and consensus problems [50–53].

Data Availability

No data were used to support this study.

Conflicts of Interest

The authors declare that they have no conflicts of interest.

Acknowledgments

This work was supported by the National Natural Science Foundation (NNSF) of China under Grants 61903236, 61876101, 61773371, and 71701115.

References

[1] J. Von Neumann and O. Morgenstern, *Theory of Games and Economic Behavior*, Princeton University Press, Princeton, NJ, USA, 1944.

[2] L. S. Shapley, "17. A value for n-person games," *Contributions to the Theory of Games (AM-28), Volume II*, vol. 2, no. 28, pp. 307–318, 1953.

[3] R. B. Myerson, "Graphs and cooperation in games," *Mathematics of Operations Research*, vol. 2, no. 3, pp. 225–229, 1977.

[4] W. Saad, Z. Han, M. Debbah et al., "Coalitional game theory for communication networks: a tutorial," *IEEE Signal Processing Magazine*, vol. 26, no. 5, pp. 77–97, 2009.

[5] W. Saad, Z. Han, T. Başar et al., "Coalition formation games for collaborative spectrum sensing," *IEEE Transactions on Vehicular Technology*, vol. 60, no. 1, pp. 276–297, 2011.

[6] M. Aurangzeb and F. L. Lewis, "Internal structure of coalitions in competitive and altruistic graphical coalitional games," *Automatica*, vol. 50, no. 2, pp. 335–348, 2014.

[7] M. O. Jackson and A. Watts, "The evolution of social and economic networks," *Journal of Economic Theory*, vol. 106, no. 2, pp. 265–295, 2002.

[8] S. Moretti, V. Fragnelli, F. Patrone et al., "Using coalitional games on biological networks to measure centrality and power of genes," *Bioinformatics*, vol. 26, no. 21, pp. 2721–2730, 2010.

[9] J. R. Marden and A. Wierman, "Distributed welfare games," *Operations Research*, vol. 61, no. 1, pp. 155–168, 2013.

[10] Y. Wang, D. Cheng, and X. Liu, "Matrix expression of Shapley values and its application to distributed resource allocation," *Science China Information Sciences*, vol. 62, no. 2, pp. 22201: 1–11, 2019.

[11] D. Cheng, H. Qi, and Z. Li, *Analysis and Control of Boolean Networks - A Semi-tensor Product Approach*, Springer, London, UK, 2011.

[12] H. Li, X. Xu, and X. Ding, "Finite-time stability analysis of stochastic switched Boolean networks with impulsive effect," *Applied Mathematics and Computation*, vol. 347, pp. 557–565, 2019.

[13] J. Zhong, Y. Liu, K. I. Kou, L. Sun, and J. Cao, "On the ensemble controllability of Boolean control networks using STP method," *Applied Mathematics and Computation*, vol. 358, pp. 51–62, 2019.

[14] Y. Liu, Y. Zheng, H. Li, F. E. Alsaadi, and B. Ahmad, "Control design for output tracking of delayed Boolean control networks," *Journal of Computational and Applied Mathematics*, vol. 327, pp. 188–195, 2018.

[15] Q. Zhu, Y. Liu, J. Lu et al., "Further results on the controllability of Boolean control networks," *IEEE Transactions on Automatic Control*, vol. 64, no. 1, pp. 440–442, 2019.

[16] J. Lu, J. Zhong, C. Huang et al., "On pinning controllability of Boolean control networks," *IEEE Transactions on Automatic Control*, vol. 61, no. 6, pp. 1658–1663, 2016.

[17] H. Li, L. Xie, and Y. Wang, "Output regulation of Boolean control networks," *IEEE Transactions on Automatic Control*, vol. 62, no. 6, pp. 2993–2998, 2017.

[18] J. Lu, H. Li, Y. Liu et al., "Survey on semi-tensor product method with its applications in logical networks and other finite-valued systems," *IET Control Theory & Applications*, vol. 11, no. 13, pp. 2040–2047, 2017.

[19] Y. Li, H. Li, and W. Sun, "Event-triggered control for robust set stabilization of logical control networks," *Automatica*, vol. 95, pp. 556–560, 2018.

[20] X. Xu, Y. Liu, H. Li et al., "Robust set stabilization of Boolean control networks with impulsive effects," *Nonlinear Analysis: Modelling and Control*, vol. 23, no. 4, pp. 553–567, 2018.

[21] G. Zhao and S. Fu, "Matrix approach to trajectory control of higher-order k-valued logical control networks," *IET Control Theory & Applications*, vol. 11, no. 13, pp. 2110–2115, 2017.

[22] Y. Li, H. Li, and X. Ding, "Set stability of switched delayed logical networks with application to finite-field consensus," *Automatica*, vol. 113, 2020.

[23] Y. Zheng, H. Li, X. Ding, and Y. Liu, "Stabilization and set stabilization of delayed Boolean control networks based on trajectory stabilization," *Journal of the Franklin Institute*, vol. 354, no. 17, pp. 7812–7827, 2017.

[24] Y. Wang, X. Zhang, and Y. Hao, "Robust controllability and observability of boolean control networks under different disturbances," *Mathematical Problems in Engineering*, vol. 2019, Article ID 1813594, 2019.

[25] H. Li and Y. Wang, "Lyapunov-based stability and construction of Lyapunov functions for Boolean networks," *SIAM Journal on Control and Optimization*, vol. 55, no. 6, pp. 3437–3457, 2017.

[26] D. Cheng and T. Xu, "Application of STP to cooperative games," in *Proceedings of the 10th IEEE ICCA*, pp. 1680–1685, Zhejiang, China, 2013.

[27] D. Cheng, "On finite potential games," *Automatica*, vol. 50, no. 7, pp. 1793–1801, 2014.

[28] Y. Wang, T. Liu, and D. Cheng, "From weighted potential game to weighted harmonic game," *IET Control Theory & Applications*, vol. 11, no. 13, pp. 2161–2169, 2017.

[29] H. Li, X. Ding, Q. Yang et al., "Algebraic formulation and Nash equilibrium of competitive diffusion games," *Dynamic Games and Applications*, vol. 8, no. 2, pp. 423–433, 2018.

[30] Y. Hao, S. Pan, Y. Qiao et al., "Cooperative control via congestion game approach," *IEEE Transactions on Automatic Control*, vol. 63, no. 12, pp. 4361–4366, 2018.

[31] H. Li, X. Ding, A. Alsaedi et al., "Stochastic set stabilization of n-person random evolutionary Boolean games and its applications," *IET Control Theory & Applications*, vol. 11, no. 13, pp. 2152–2160, 2017.

[32] G. Zhao, H. Li, W. Sun, and F. E. Alsaadi, "Modelling and strategy consensus for a class of networked evolutionary games," *International Journal of Systems Science*, vol. 49, no. 12, pp. 2548–2557, 2018.

[33] P. Guo, H. Zhang, F. E. Alsaadi et al., "Semi-tensor product method to a class of event-triggered control for finite evolutionary networked games," *IET Control Theory & Applications*, vol. 11, no. 13, pp. 2140–2145, 2017.

[34] X. Ding, H. Li, Q. Yang, Y. Zhou, A. Alsaedi, and F. E. Alsaadi, "Stochastic stability and stabilization of n -person random evolutionary Boolean games," *Applied Mathematics and Computation*, vol. 306, pp. 1–12, 2017.

[35] S. Fu, H. Li, G. Zhao et al., "Modelling and strategy optimisation for a kind of networked evolutionary games with memories under the bankruptcy mechanism," *International Journal of Control*, vol. 91, no. 5, pp. 1104–1117, 2018.

[36] G. Zhao, Y. Wang, and H. Li, "A matrix approach to the modeling and analysis of networked evolutionary games with finite memories," *IEEE/CAA Journal of Automatica Sinica*, vol. 5, no. 4, pp. 818–826, 2018.

[37] T. Liu, J. Wang, X. Zhang et al., "Game theoretic control of multiagent systems," *SIAM Journal on Control and Optimization*, vol. 57, no. 3, pp. 1691–1709, 2019.

[38] J. Wang, X. Gao, and Y. Xu, "Intermittent control for demand-side management of a class of networked smart grids," *IET Control Theory & Applications*, vol. 13, no. 8, pp. 1166–1172, 2019.

[39] Y. Yan, Z. Chen, and Z. Liu, "Semi-tensor product approach to controllability and stabilizability of finite automata," *Journal of Systems Engineering and Electronics*, vol. 26, no. 1, pp. 134–141, 2015.

[40] W. Dou, H. Li, and F. E. Alsaadi, "Semitensor product approach to controllability, reachability, and stabilizability of probabilistic finite automata," *Mathematical Problems in Engineering*, vol. 2019, Article ID 8021750, 2019.

[41] J. Zhong, J. Lu, C. Huang, L. Li, and J. Cao, "Finding graph minimum stable set and core via semi-tensor product approach," *Neurocomputing*, vol. 174, pp. 588–596, 2016.

[42] E. Alzahrani, H. Akca, X. Li et al., "New synchronization schemes for delayed chaotic neural networks with impulses," *Neural Computing and Applications*, vol. 28, no. 9, pp. 2823–2837, 2017.

[43] R. Guo, "Projective synchronization of a class of chaotic systems by dynamic feedback control method," *Nonlinear Dynamics*, vol. 90, no. 1, pp. 53–64, 2017.

[44] X. Li, R. Rakkiyappan, and N. Sakthivel, "Non-fragile synchronization control for Markovian jumping complex dynamical networks with probabilistic time-varying coupling delays," *Asian Journal of Control*, vol. 17, no. 5, pp. 1678–1695, 2015.

[45] X. Xu, Y. Liu, H. Li et al., "Synchronization of switched Boolean networks with impulsive effects," *International Journal of Biomathematics*, vol. 11, no. 6, 2018.

[46] Z. Wang and R. Guo, "Hybrid synchronization problem of a class of chaotic systems by an universal control method," *Symmetry*, vol. 10, no. 11, p. 552, 2018.

[47] X. Li, P. duan, J. Cao et al., "Exponential synchronization of neural networks via feedback control in complex environment," *Complexity*, vol. 1, pp. 1–13, 2018.

[48] Y. Li, P. Duan, and H. Li, "Synchronization of switched logical control networks via event-triggered control," *Journal of The Franklin Institute*, vol. 355, no. 12, pp. 5203–5216, 2018.

[49] X. Zhang, X. Lv, and X. Li, "Sampled-data-based lag synchronization of chaotic delayed neural networks with impulsive control," *Nonlinear Dynamics*, vol. 90, no. 3, pp. 2199–2207, 2017.

[50] X. Tan, J. Cao, X. Li et al., "Leader-following mean square consensus of stochastic multi-agent systems with input delay via event-triggered control," *IET Control Theory & Applications*, vol. 12, no. 2, pp. 299–309, 2018.

[51] Y. Li, H. Li, X. Ding, and G. Zhao, "Leader-follower consensus of multiagent systems with time delays over finite fields," *IEEE Transactions on Cybernetics*, vol. 49, no. 8, pp. 3203–3208, 2019.

[52] X. Tan, J. Cao, X. Li et al., "Consensus of leader-following multiagent systems: a distributed event-triggered impulsive control strategy," *IEEE Transactions on Cybernetics*, vol. 49, no. 3, pp. 792–801, 2019.

[53] Y. Li, H. Li, X. Xu et al., "A semi-tensor product approach to minimal-agent consensus control of networked evolutionary games," *IET Control Theory & Applications*, vol. 12, no. 16, pp. 2269–2275, 2018.

Hindawi
Mathematical Problems in Engineering
Volume 2020, Article ID 6037841, 6 pages
https://doi.org/10.1155/2020/6037841

Research Article

Effect of Nonlinear Baseline Length Constraint on Global Navigation Satellite System Compass: A Theoretical Analysis

Yanlong Chen,[1] **Jincheng Fan**,[2] **Guobin Chang**,[3] **and Siyu Zhang**[3]

[1]*State Key Laboratory for Geomechanics and Deep Underground Engineering, China University of Mining and Technology, Xuzhou 221116, China*
[2]*School of Mechanics and Civil Engineering, China University of Mining and Technology, Xuzhou 221116, China*
[3]*School of Environmental Science and Spatial Informatics, China University of Mining and Technology, Xuzhou 221116, China*

Correspondence should be addressed to Guobin Chang; guobinchang@cumt.edu.cn

Received 13 April 2020; Accepted 20 April 2020; Published 22 May 2020

Guest Editor: Rongwei Guo

GNSS (global navigation satellite system) compass is a low-cost, high-precision, and temporally stable north-finding technique. While the nonlinear baseline length constraint is widely known to be important in ambiguity resolution of GNSS compass, its direct effect on yaw angle estimation is theoretically analyzed in this work. Four different methods are considered with different ways in which the length constraint is made use of as follows: one without considering the constraints, one with simple scaling, one with indirect statistical scaling, and one with direct statistical scaling. It is found that simple scaling does not have any effect on yaw estimation; indirect and direct statistical scalings are equivalent to each other with both being able to increase the precision. The analysis and the conclusion developed in this work can go in parallel for the case of the tilt angle estimation.

1. Introduction

Control of a vehicle often relies on measuring necessary parameters of the vehicle [1, 2]. The vehicle's attitude, especially the heading or yaw angle as one of the attitude components, is a vital one of these parameters in many control applications [3]. GNSS compass is a cost-effective method to provide heading information in real time. It is one of the high-precision short-baseline applications [4–6]. By high precision, it is meant that carrier-phase measurements are used in addition to code pseudo ranges. GNSS compass is also a special case of GNSS attitude determination (AD), which can further be viewed as a special case of GNSS antenna array applications [7–9]. In compass, only the yaw or heading of the complete three attitude elements is of interest. GNSS compass (also GNSS AD) is of low cost and is temporally stable and hence finds wide applications. Each piece of carrier-phase measurement can be viewed as high-precision version of pseudo range only when its integer ambiguity has been correctly fixed [10–13]. From this regard, ambiguity resolution (AR) is inevitable in GNSS compass as in other high-precision applications [4, 14–16]. Though single-epoch AR is the most challengeable [17], we should do AR sequentially to fully explore the temporally constant property of the ambiguities [18], as long as cycle slips are absent or repaired in real time [19]. In this work, we are concerned with yaw angle estimation with carrier-phase measurements whose ambiguities have already been fixed at previous epochs. It is widely known that the length constraints of the baselines connecting antennas fixed on the vehicle's body should be given full consideration in the AR of GNSS compass or AD. The nonlinear length constraint enhances the GNSS compass AR model in terms of not only precision but also reliability [20]. However, in AD with vector measurements, the lengths of the vector measurements do not have an effect in general [3, 21]. The AD with vector measurement can be pointwise or sequential, namely, Wahba's problem [22–26] or the attitude filtering problem [27–32]. This is the reason why the vector measurements can be normalized for the sake of better numerical stability.

Does the nonlinear baseline length constraint have an effect on GNSS compass, as long as the ambiguity-fixed measurements are used? Or, how can the constraint have an

effect? If there is an effect, will this effect be positive, namely, with precision increased? In this work, these questions are studied in theory thoroughly and clear answers are given. Four different methods are analyzed with different ways in which the length constraint is considered. The first is called No-Constraint in which the length constraint is completely ignored. The second is called Simple-Scaling in which the baseline vector estimate is simply scaled to be with the known length. The third is called Indirect-Statistical-Scaling in which the baseline vector estimate is scaled statistically by taking the covariance of the estimate into consideration. The fourth is called Direct-Statistical-Scaling in which the baseline vector is estimated by solving a constrained least-squares problem. After briefly introducing the measurement model in Section 2, the four methods are analyzed in Section 3. The effects of the length constraints on the compassing, together with the relationships among them, are the focus of the analysis. This work is concluded in Section 4. Some derivations and proofs are presented as appendices.

2. GNSS Compass Measurement Model

It is shown in Figure 1 that a pair of antennas is rigidly mounted to a vehicle whose yaw or heading is to be determined. The baseline vector linking the antenna-pair is denoted as $\boldsymbol{x}$. Without loss of generality, the baseline vector is in the vehicle body's right-front plane. Then, the baseline vector defines the yaw angle and the tilt angle. We further assume that the baseline vector points to the front. Then, the tilt angle is exactly the pitch angle. The coordinate vector in the local ENU reference frame of the baseline is also denoted as $\boldsymbol{x}$, and let $\boldsymbol{x} = [a\ b\ c]^{\mathrm{T}}$. This will not introduce any confusion, since only the coordinates in the reference frame are involved in this work. So, in the following by the baseline vector, we mean its coordinate vector in the reference frame. The yaw can be computed from the coordinates as follows:

$$\varphi = \arctan\left(\frac{a}{b}\right). \tag{1}$$

For nondedicated receivers [33], double difference carrier-phase measurements can be used to simplify the measurement model by eliminating both satellite and receiver clock errors [17, 34, 35]. Considering only the measurements with corresponding ambiguities fixed, the measurement model is as follows:

$$\mathbf{y} = \mathbf{B}\mathbf{x} + \varepsilon, \tag{2}$$

with $\mathbf{y}$, $\mathbf{B}$, and $\mathbf{Q} = \mathrm{cov}[\varepsilon]$ known. Note that the elements of the measurement vector $\boldsymbol{y}$ may not necessarily be the original double difference carrier phases, but rather some linear combinations of them. The corresponding combined ambiguities, e.g., the wide-lane ones, are relatively easy to be fixed; we assume they have already been fixed at certain previous epochs. Further assume the vehicle's body is rigid and hence we have the following length constraint:

$$\mathbf{x}^{\mathrm{T}}\mathbf{x} = l^2, \tag{3}$$

with l known and time invariant. Note that this is the nonlinear and so-called hard constraint [36, 37]. The models

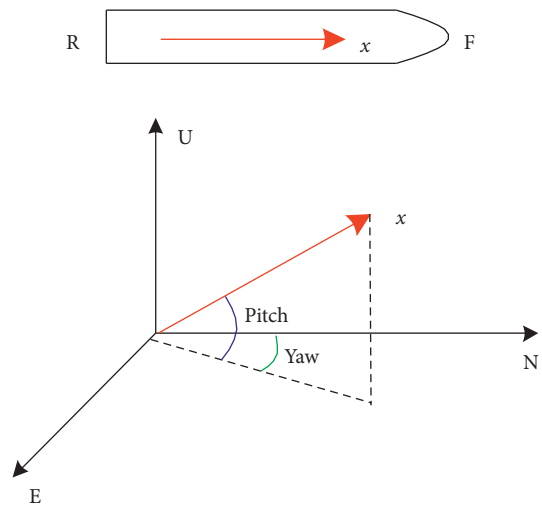

Figure 1: The baseline vector (red line) in the vehicle's body frame (top) and in the local reference frame (bottom). $(\mathbf{x})$ = baseline vector, R = rear, F = from, E = east, N = north, and U = upward.

(1)-(3) represent all the available information relevant to the compassing. Different GNSS compass methods are results of different ways in which the information is used. An important issue concerning these methods is whether the constraint in [3] is used and how it is used.

3. Effect of Baseline Length Constraint in Different Methods

In the following, the four different methods are presented, the effect of the baseline length constraint on the final solution of yaw angle is analyzed, and potential relations among different methods are revealed.

3.1. No-Constraint Method. The first method is called No-Constraint which ignores the constraint completely. It first estimates the baseline vector with least-squares:

$$\begin{aligned}\hat{\mathbf{x}}_1 &= \left[\hat{a}_1\ \ \hat{b}_1\ \ \hat{c}_1\right]^{\mathrm{T}},\\ &= \left(\mathbf{B}^{\mathrm{T}}\mathbf{Q}^{-1}\mathbf{B}\right)^{-1}\mathbf{B}^{\mathrm{T}}\mathbf{Q}^{-1}\mathbf{y},\end{aligned} \tag{4}$$

with the covariance of this estimate being $\mathbf{P}_1 = (\mathbf{B}^{\mathrm{T}}\mathbf{Q}^{-1}\mathbf{B})^{-1}$. Then, the yaw angle with this estimate is calculated according to [1]. For easy reference, the formula is displayed as follows:

$$\hat{\varphi}_1 = \arctan\left(\frac{\mathbf{e}_1^{\mathrm{T}}\hat{\mathbf{x}}_1}{\mathbf{e}_2^{\mathrm{T}}\hat{\mathbf{x}}_1}\right). \tag{5}$$

with $\mathbf{e}_1 = [1\ 0\ 0]^{\mathrm{T}}$ and $\mathbf{e}_2 = [0\ 1\ 0]^{\mathrm{T}}$. The variance of this estimate can be worked according to the error propagation law:

$$\sigma_1^2 = \mathbf{g}^{\mathrm{T}}\mathbf{P}_1\mathbf{g}. \tag{6}$$

with $\mathbf{g}^{\mathrm{T}} = ((\hat{b}_1\mathbf{e}_1^{\mathrm{T}} - \hat{a}_1\mathbf{e}_2^{\mathrm{T}})/(\hat{a}_1^2 + \hat{b}_1^2))$. A derivation of [6] can be found in Appendix A. It is needless to say that the length constraints play no role in this method.

3.2. Simple-Scaling Method. The second method is carried out in steps as follows. First, it estimates the baseline vector as in [4]. Second, it scales the baseline vector as

$$\hat{\mathbf{x}}_2 = \frac{l\hat{\mathbf{x}}_1}{\sqrt{\hat{\mathbf{x}}_1^{\mathrm{T}}\hat{\mathbf{x}}_1}} = k\hat{\mathbf{x}}_1. \tag{7}$$

This step is exactly the reason why it is called simple-scaling. Third, it calculates the yaw angle according to [1]: $\hat{\varphi}_2 = \arctan(\mathbf{e}_1^{\mathrm{T}}\hat{\mathbf{x}}_2/\mathbf{e}_2^{\mathrm{T}}\hat{\mathbf{x}}_2) = \arctan(k\mathbf{e}_1^{\mathrm{T}}\hat{\mathbf{x}}_1/k\mathbf{e}_2^{\mathrm{T}}\hat{\mathbf{x}}_1) = \hat{\varphi}_1$. So, as long as the yaw is to be estimated, the first and the second methods are the same, and it is readily known that their variances are also the same. The baseline length constraint does not have any effect on GNSS compass in this method, either. This may be reminiscent of the case of AD with vector measurements, namely, Wahba's problem, in which the specific length of the vector may be irrelevant to the AD.

As a final note, as long as the baseline vector, rather than the yaw, is of interest, the precision of the solution after simple scaling can be increased or decreased, or remain unchanged, depending on the length of the vector before scaling. For more information on this topic, the interested readers are referred to Appendix B.

3.3. Indirect-Statistical-Scaling Method. The third method is also a stepwise one as the second method. The difference from the second method lies in the second step. In this step, a constrained least-squares estimation is done with the estimate from [4] being treated as pseudo measurement with covariance $\mathbf{P}_1$. The nonlinear constraint equation in [3] is linearized, say around the estimate in [4], as follows. Let $d = l^2 + \hat{\mathbf{x}}_1^{\mathrm{T}}\hat{\mathbf{x}}_1$ and $\mathrm{c} = 2\hat{\mathbf{x}}_1$; then, we have the linearized constraint as follows:

$$d = \mathbf{c}^{\mathrm{T}}\mathbf{x}. \tag{8}$$

The resulting baseline vector estimate is defined as follows:

$$\hat{\mathbf{x}}_3 = \arg\min_x \eta_3 = \arg\min_x \left[(\mathbf{x} - \hat{\mathbf{x}}_1)^{\mathrm{T}}\mathbf{P}_1^{-1}(\mathbf{x} - \hat{\mathbf{x}}_1) + 2\lambda\left(d - \mathbf{c}^{\mathrm{T}}\mathbf{x}\right)\right], \tag{9}$$

where λ denotes the Lagrange multiplier and η is called the Lagrangian. It turns out that the estimate defined in [9] is as follows:

$$\hat{\mathbf{x}}_3 = \mathbf{H}\hat{\mathbf{X}}_1 + d\mathbf{h}. \tag{10}$$

with $\mathbf{h} = (1/\mathbf{c}^{\mathrm{T}}\mathbf{P}_1\mathbf{c})\mathbf{P}_1\mathbf{c}$ and $\mathbf{H} = (\mathbf{I}_3 - \mathbf{h}\mathbf{c}^{\mathrm{T}})$. A derivation of [10] can be found in Appendix C. The covariance is readily known as $\mathbf{P}_3 = \mathbf{H}\mathbf{P}_1\mathbf{H}^{\mathrm{T}}$. We call [10] an Indirect-Statistical-Scaling for brevity. It is indirect because we first estimate the baseline vector without considering the constraint and then modify the estimate by considering the constraint. It is statistical because the statistical information, namely, the covariance $\mathbf{P}_1$, is used in this scaling. The yaw is calculated using this estimate according to [1] and denoted as $\hat{\varphi}_3$.

It is clear that $\hat{\varphi}_3 \neq \hat{\varphi}_1$ in general. The question is can one of the two be always more accurate than the other? The answer is positive as proved in the following. Similar to [6], we know that $\sigma_3^2 = \mathbf{g}^{\mathrm{T}}\mathbf{P}_3\mathbf{g}$. The following can be readily proved:

$$\Delta = \mathbf{P}_1 - \mathbf{P}_3 = \left(\mathbf{c}^{\mathrm{T}}\mathbf{P}_1\mathbf{c}\right)\mathbf{h}\mathbf{h}^{\mathrm{T}}. \tag{11}$$

A derivation can be found in Appendix D. It is readily known that Δ is of rank one; furthermore, besides the zero double eigenvalue, the only nonzero eigenvalue is $(\mathbf{c}^{\mathrm{T}}\mathbf{P}_1\mathbf{c})\mathbf{h}^{\mathrm{T}}\mathbf{h} \geq 0$, because $\mathbf{c}^{\mathrm{T}}\mathbf{P}_1\mathbf{c} \geq 0$ and $\mathbf{h}^{\mathrm{T}}\mathbf{h} \geq 0$. So the matrix Δ is positive semidefinite. So $\sigma_1^2 - \sigma_3^2 = \mathbf{g}^{\mathrm{T}}\mathbf{P}_1\mathbf{g} - \mathbf{g}^{\mathrm{T}}\mathbf{P}_3\mathbf{g} = \mathbf{g}^{\mathrm{T}}(\mathbf{P}_1 - \mathbf{P}_3)\mathbf{g} = \mathbf{g}^{\mathrm{T}}\Delta\mathbf{g} \geq 0$. It means that the precision of $\hat{\varphi}_3$ cannot be lower than $\hat{\varphi}_1$. Only when either of the following two conditions are fulfilled, the two are of equal precision: (1) $\Delta = 0$; (2) $\mathbf{g}$ is one of the eigenvectors of Δ. In practice, the probability of either of the two conditions holding is zero. To summarize, with the indirect statistical scaling in the third method, the baseline length constraint has a positive effect in GNSS compassing, namely, that the precision can be improved by considering the length constraint.

3.4. Direct-Statistical-Scaling Method. The fourth method is a two-step one. It first estimates the baseline vector with constrained least-squares to consider the constraint in [3]. Then, it calculates the yaw using this estimate according to [1]. In the first step, the constrained least-squares solution to the baseline vector is defined as follows:

$$\hat{\mathbf{x}}_4 = \arg\min_x \eta_4 = \arg\min_x \left[(\mathbf{y} - \mathbf{B}\mathbf{x})^{\mathrm{T}}\mathbf{Q}^{-1}(\mathbf{y} - \mathbf{B}\mathbf{x}) + 2\lambda\left(d - \mathbf{c}^{\mathrm{T}}\mathbf{x}\right)\right]. \tag{12}$$

It can be proved, as in Appendix E, that the baseline vector estimate defined in [12] is the same as the one in [10], and hence, the yaw, denoted as $\hat{\varphi}_4$, is the same as $\hat{\varphi}_3$. Their variances are also the same. So, the baseline length constraint has a positive effect on the GNSS compass in this method, namely, that by considering the length constraint, the precision of the yaw estimate can be improved.

3.5. Summary. The above analysis is summarized in Table 1. In a nutshell, (1) with the Simple-Scaling, the baseline length constraint does not have any effect on the GNSS compass; (2) the Indirect-Statistical-Scaling and the Direct-Statistical-Scaling can equivalently produce a positive effect of the baseline length constraint on the GNSS compass.

Table 1: A summary of the five GNSS compass methods.

Method	Description	Effect
No-Constraint	[4] + [1]	None
Simple-Scaling	[4] + [7]+ [1]	None
Indirect-Statistical-Scaling	[4] + [10]+ [1]	Positive
Direct-Statistical-Scaling	[12] + [1]	Positive

4. Conclusion

As long as the antennas are mounted rigidly to the vehicle's rigid body, the baseline length remains unchanged, independent of the vehicle's dynamics. This is a hard and

nonlinear constraint. In a GNSS compass, the yaw angle or heading of the vehicle can be determined with carrier-phase measurements whose ambiguities have been fixed at previous epochs. The question is answered in this work that whether the baseline length constraint has an effect on the yaw angle determined. In a nutshell, the answer is as follows: it depends on the specific method of considering the constraints. If we simply scale the estimated baseline vector to make its length be the true one, namely, to make the constraint fulfilled, the constraint does not have any effect on the yaw angle estimation. However, if the constraint is used through a statistical scaling, it can have a positive effect, namely, that the precision of the yaw estimation can be improved. The statistical scaling can be done indirectly or directly. In the indirect statistical scaling, the constraint is used after the baseline vector is estimated, whereas in the direct statistical scaling, the constraint is used in the baseline vector estimation. They are called statistical because the statistical information, namely, the covariance, is used in both of them. The two statistical scaling methods are equivalent to each other, namely, producing the same yaw estimate with the same variance of this estimation.

As a final note, the analysis and the conclusion developed in this work go in parallel for the case of tilt angle. Depending on the configuration of the baseline vector, this tilt angle can be pitch or roll angle.

Appendix

A. Derivation of [6]

According to the train rule of the derivative, the Jacobian (derivative) of $\widehat{\varphi}_1$ with respect to $\widehat{\mathbf{x}}_1$ is as follows:

$$\begin{aligned}\frac{\partial\widehat{\varphi}_1}{\partial\widehat{\mathbf{x}}_1^{\mathrm{T}}} &= \frac{\partial \arctan\left(\mathbf{e}_1^{\mathrm{T}}\widehat{\mathbf{x}}_1/\mathbf{e}_2^{\mathrm{T}}\widehat{\mathbf{x}}_1\right)}{\partial\widehat{\mathbf{x}}_1^{\mathrm{T}}},\\ &= \frac{\partial \arctan\left(\mathbf{e}_1^{\mathrm{T}}\widehat{\mathbf{x}}_1/\mathbf{e}_2^{\mathrm{T}}\widehat{\mathbf{x}}_1\right)}{\partial\left(\mathbf{e}_1^{\mathrm{T}}\widehat{\mathbf{x}}_1/\mathbf{e}_2^{\mathrm{T}}\widehat{\mathbf{x}}_1\right)}\left[\frac{\partial\left(\mathbf{e}_1^{\mathrm{T}}\widehat{\mathbf{x}}_1/\mathbf{e}_2^{\mathrm{T}}\widehat{\mathbf{x}}_1\right)}{\partial\left(\mathbf{e}_1^{\mathrm{T}}\widehat{\mathbf{x}}_1\right)}\frac{\partial\left(\mathbf{e}_1^{\mathrm{T}}\widehat{\mathbf{x}}_1\right)}{\partial\widehat{\mathbf{x}}_1^{\mathrm{T}}}\right.\\ &\quad\left.+\frac{\partial\left(\mathbf{e}_1^{\mathrm{T}}\widehat{\mathbf{x}}_1/\mathbf{e}_2^{\mathrm{T}}\widehat{\mathbf{x}}_1\right)}{\partial\left(\mathbf{e}_2^{\mathrm{T}}\widehat{\mathbf{x}}_1\right)}\frac{\partial\left(\mathbf{e}_2^{\mathrm{T}}\widehat{\mathbf{x}}_1\right)}{\partial\widehat{\mathbf{x}}_1^{\mathrm{T}}}\right],\\ &= \frac{1}{1+\left(\mathbf{e}_1^{\mathrm{T}}\widehat{\mathbf{x}}_1/\mathbf{e}_2^{\mathrm{T}}\widehat{\mathbf{x}}_1\right)^2}\left[\frac{1}{\mathbf{e}_2^{\mathrm{T}}\widehat{\mathbf{x}}_1}\mathbf{e}_1^{\mathrm{T}}+\frac{-\mathbf{e}_1^{\mathrm{T}}\widehat{\mathbf{x}}_1}{\left(\mathbf{e}_2^{\mathrm{T}}\widehat{\mathbf{x}}_1\right)^2}\mathbf{e}_2^{\mathrm{T}}\right].\end{aligned} \tag{A.1}$$

Substituting $\begin{cases}\widehat{a}_1 = \mathbf{e}_1^{\mathrm{T}}\widehat{\mathbf{x}}_1\\ \widehat{b}_1 = \mathbf{e}_2^{\mathrm{T}}\widehat{\mathbf{x}}_1\end{cases}$ into the above, we have

$$\frac{\partial\widehat{\varphi}_1}{\partial\widehat{\mathbf{x}}_1^{\mathrm{T}}} = \frac{1}{1+\left(\widehat{a}_1/\widehat{b}_1\right)^2}\left[\frac{1}{\widehat{b}_1}\mathbf{e}_1^{\mathrm{T}}+\frac{-\widehat{a}_1}{\left(\widehat{b}_1\right)^2}\mathbf{e}_2^{\mathrm{T}}\right] = \frac{\widehat{b}_1\mathbf{e}_1^{\mathrm{T}}-\widehat{a}_1\mathbf{e}_2^{\mathrm{T}}}{\widehat{a}_1^2+\widehat{b}_1^2}. \tag{A.2}$$

which is exactly $\mathbf{g}^{\mathrm{T}}$ used in [6]. Note that [6] is obtained simply through error or covariance propagation.

B. Effect of Simple-Scaling on the Precision of Baseline Vector Estimation

According to the simple scaling formula, namely, $\widehat{\mathbf{x}}_2 = k\widehat{\mathbf{x}}_1$ with $k = l/\sqrt{\widehat{\mathbf{x}}_1^{\mathrm{T}}\widehat{\mathbf{x}}_1}$, we have the following covariances for $\widehat{\mathbf{x}}_2$:

$$\mathbf{P}_2 = k^2\mathbf{P}_1. \tag{B.1}$$

So, readily we have the following:

$$\begin{cases}\mathbf{P}_2 > \mathbf{P}_1, & \text{when } k > 1,\\ \mathbf{P}_2 = \mathbf{P}_1, & \text{when } k = 1,\\ \mathbf{P}_2 < \mathbf{P}_1, & \text{when } k < 1.\end{cases} \tag{B.2}$$

When we say $\mathbf{P}_2 > \mathbf{P}_1$, we say that $\mathbf{P}_2 - \mathbf{P}_1$ is positive definite and the "smaller than" case goes similarly. From [16], we know that the simple scaling does not necessarily increase the precision of the baseline vector estimation. To be more specific, when the length of the unscaled baseline vector estimate is overly estimated, the simple scaling can even decrease the precision.

C. Derivation of [10]

In order for the Lagrangian to be minimum, its first-order derivative with respect to $\boldsymbol{x}$ should be zero [38–40], namely,

$$\frac{\partial\eta_3}{\partial\mathrm{x}} = 0 \Leftrightarrow \mathbf{P}_1^{-1}\mathbf{x} = \mathbf{P}_1^{-1}\widehat{\mathbf{x}}_1 + \lambda\mathbf{c}. \tag{C.1}$$

The above is equivalent to the following:

$$\mathbf{x} = \widehat{\mathbf{x}}_1 + \lambda\mathbf{P}_1\mathbf{c}. \tag{C.2}$$

Substitute this expression into the length constraint; we can compute the Lagrange multiplier, as follows:

$$\lambda = \frac{d-\mathbf{c}^{\mathrm{T}}\widehat{\mathbf{x}}_1}{\mathbf{c}^{\mathrm{T}}\mathbf{P}_1\mathbf{c}}. \tag{C.3}$$

Substituting (C.3) into (C.2), we have the following estimate:

$$\widehat{\mathbf{x}} = \widehat{\mathbf{x}}_1 + \mathbf{P}_1\mathbf{c}\frac{d-\mathbf{c}^{\mathrm{T}}\widehat{\mathbf{x}}_1}{\mathbf{c}^{\mathrm{T}}\mathbf{P}_1\mathbf{c}} = \left(\mathbf{I}_3 - \frac{1}{\mathbf{c}^{\mathrm{T}}\mathbf{P}_1\mathbf{c}}\mathbf{P}_1\mathbf{c}\mathbf{c}^{\mathrm{T}}\right)\widehat{\mathbf{x}}_1 + d\frac{1}{\mathbf{c}^{\mathrm{T}}\mathbf{P}_1\mathbf{c}}\mathbf{P}_1\mathbf{c}. \tag{C.4}$$

The rightmost expression is exactly that in [10].

D. Derivation of [11]

First, the expression of $\mathbf{P}_3$ is expanded as follows:

$$\begin{aligned}\mathbf{P}_3 &= \mathbf{H}\mathbf{P}_1\mathbf{H}^{\mathrm{T}},\\ &= \mathbf{P}_1 - \frac{2}{\mathbf{c}^{\mathrm{T}}\mathbf{P}_1\mathbf{c}}\mathbf{P}_1\mathbf{c}\mathbf{c}^{\mathrm{T}}\mathbf{P}_1 + \frac{1}{\left(\mathbf{c}^{\mathrm{T}}\mathbf{P}_1\mathbf{c}\right)^2}\mathbf{P}_1\mathbf{c}\mathbf{c}^{\mathrm{T}}\mathbf{P}_1\mathbf{c}\mathbf{c}^{\mathrm{T}}\mathbf{P}_1,\\ &= \mathbf{P}_1 - \frac{2}{\mathbf{c}^{\mathrm{T}}\mathbf{P}_1\mathbf{c}}\mathbf{P}_1\mathbf{c}\mathbf{c}^{\mathrm{T}}\mathbf{P}_1 + \frac{1}{\mathbf{c}^{\mathrm{T}}\mathbf{P}_1\mathbf{c}}\mathbf{P}_1\mathbf{c}\mathbf{c}^{\mathrm{T}}\mathbf{P}_1,\\ &= \mathbf{P}_1 - \frac{1}{\mathbf{c}^{\mathrm{T}}\mathbf{P}_1\mathbf{c}}\mathbf{P}_1\mathbf{c}\mathbf{c}^{\mathrm{T}}\mathbf{P}_1.\end{aligned} \tag{D.1}$$

So, readily we have

$$\begin{aligned}\Delta &= \mathbf{P}_1 - \mathbf{P}_3,\\ &= \frac{1}{\mathbf{c}^{\mathrm{T}}\mathbf{P}_1\mathbf{c}}\mathbf{P}_1\mathbf{c}\mathbf{c}^{\mathrm{T}}\mathbf{P}_1,\\ &= \left(\mathbf{c}^{\mathrm{T}}\mathbf{P}_1\mathbf{c}\right)\mathbf{h}\mathbf{h}^{\mathrm{T}}.\end{aligned} \tag{D.2}$$

Furthermore, we have

$$\left(\mathbf{c}^{\mathrm{T}}\mathbf{P}_1\mathbf{c}\right)\mathbf{h}\mathbf{h}^{\mathrm{T}} = \frac{1}{\mathbf{c}^{\mathrm{T}}\mathbf{P}_1\mathbf{c}}\mathbf{P}_1\mathbf{c}\mathbf{c}^{\mathrm{T}}\mathbf{P}_1. \tag{D.3}$$

With (D.2) and (D.3), we finally have [11].

E. Equivalence between [12] and [10]

Instead of directly working out the solution of [12], we will equivalently prove that the minimizer of η_3 can also minimize η_4. We first rearrange η_3 and η_4 as follows:

$$\begin{aligned}\eta_3 &= \mathbf{x}^{\mathrm{T}}\mathbf{P}_1^{-1}\mathbf{x} - 2\mathbf{x}^{\mathrm{T}}\mathbf{P}_1^{-1}\hat{\mathbf{x}}_1 + \hat{\mathbf{x}}_1^{\mathrm{T}}\mathbf{P}_1^{-1}\hat{\mathbf{x}}_1 + 2\lambda\left(d - \mathbf{c}^{\mathrm{T}}\mathbf{x}\right),\\ &\propto \mathbf{x}^{\mathrm{T}}\mathbf{P}_1^{-1}\mathbf{x} - 2\mathbf{x}^{\mathrm{T}}\mathbf{P}_1^{-1}\hat{\mathbf{x}}_1 + 2\lambda\left(d - \mathbf{c}^{\mathrm{T}}\mathbf{x}\right),\\ &= \mathbf{x}^{\mathrm{T}}\mathbf{B}^{\mathrm{T}}\mathbf{Q}^{-1}\mathbf{B}\mathbf{x} - 2\mathbf{x}^{\mathrm{T}}\mathbf{B}^{\mathrm{T}}\mathbf{Q}^{-1}\mathbf{B}\left(\mathbf{B}^{\mathrm{T}}\mathbf{Q}^{-1}\mathbf{B}\right)^{-1}\mathbf{B}^{\mathrm{T}}\mathbf{Q}^{-1}\mathbf{y}\\ &\quad + 2\lambda\left(d - \mathbf{c}^{\mathrm{T}}\mathbf{x}\right),\\ &= \mathbf{x}^{\mathrm{T}}\mathbf{B}^{\mathrm{T}}\mathbf{Q}^{-1}\mathbf{B}\mathbf{x} - 2\mathbf{x}^{\mathrm{T}}\mathbf{B}^{\mathrm{T}}\mathbf{Q}^{-1}\mathbf{y} + 2\lambda\left(d - \mathbf{c}^{\mathrm{T}}\mathbf{x}\right),\\ &= \xi,\end{aligned} \tag{E.1}$$

$$\begin{aligned}\eta_4 &= \mathbf{x}^{\mathrm{T}}\mathbf{B}^{\mathrm{T}}\mathbf{Q}^{-1}\mathbf{B}\mathbf{x} - 2\mathbf{x}^{\mathrm{T}}\mathbf{B}^{\mathrm{T}}\mathbf{Q}^{-1}\mathbf{y} + \mathbf{y}^{\mathrm{T}}\mathbf{Q}^{-1}\mathbf{y} + 2\lambda\left(d - \mathbf{c}^{\mathrm{T}}\mathbf{x}\right),\\ &\propto \mathbf{x}^{\mathrm{T}}\mathbf{B}^{\mathrm{T}}\mathbf{Q}^{-1}\mathbf{B}\mathbf{x} - 2\mathbf{x}^{\mathrm{T}}\mathbf{B}^{\mathrm{T}}\mathbf{Q}^{-1}\mathbf{y} + 2\lambda\left(d - \mathbf{c}^{\mathrm{T}}\mathbf{x}\right),\\ &= \xi.\end{aligned} \tag{E.2}$$

In both of the above, uninteresting additive terms independent of $\mathbf{x}$ and λ are omitted. So, the two Lagrangians are the same, after omitting different uninteresting additive constants which do not depend on the unknowns including the Lagrangian multipliers. So, the minimizer of one of the two will also minimize the other. This means that the two solutions are the same to each other.

Data Availability

No data were used to support this study.

Conflicts of Interest

The authors declare that there are no conflicts of interest regarding the publication of this paper.

Acknowledgments

This work was funded by the National Natural Science Foundation of China (41774005) and China Postdoctoral Science Foundation (2019M652010 and 2019T120477).

References

[1] X. Yi, R. Guo, and Y. Qi, "Stabilization of chaotic systems with both uncertainty and disturbance by the UDE-based control method," *IEEE Access*, vol. 8, pp. 62471–62477, 2020.

[2] R. Guo, "Projective synchronization of a class of chaotic systems by dynamic feedback control method," *Nonlinear Dynamics*, vol. 90, no. 1, pp. 53–64, 2017.

[3] F. L. Markley and J. L. Crassidis, *Fundamentals of Spacecraft Attitude Determination and Control*, Springer, New York, NY, USA, 2014.

[4] P. Xu et al., "High-rate multi-GNSS attitude determination: experiments, comparisons with inertial measurement units and applications of GNSS rotational seismology to the 2011 Tohoku Mw9. 0 earthquake," *Measurement Science and Technology*, vol. 30, Article ID 024003, 2019.

[5] L. Baroni and H. K. Kuga, "Analysis of attitude determination methods using GPS carrier phase measurements," *Mathematical Problems in Engineering*, vol. 2012, Article ID 596396, 102 pages, 2012.

[6] P. Xu et al., "A large scale of apparent sudden movements in Japan detected by high-rate GPS after the 2011 Tohoku Mw9. 0 earthquake: physical signals or unidentified artifacts?" *Earth, Planets and Space*, vol. 71, pp. 1–16, 2019.

[7] P. J. G. Teunissen, "A-PPP: array-aided precise point positioning with global navigation satellite systems," *IEEE Transactions on Signal Processing*, vol. 60, no. 6, pp. 2870–2881, 2012.

[8] C. E. Cohen, *ttitude determination using gps, A*, Stanford University, Palo Alto, PhD, 1992.

[9] G. Lu, *Development of a GPS Multi-Antenna System for Attitude determination*, University of Calgary, Calgary, Canada, PhD, 1995.

[10] P. J. G. Teunissen, "The least-squares ambiguity decorrelation adjustment: a method for fast GPS integer ambiguity estimation," *Journal of Geodesy*, vol. 70, no. 1-2, pp. 65–82, 1995.

[11] P. Xu, "Voronoi cells, probabilistic bounds, and hypothesis testing in mixed integer linear models," *IEEE Transactions on Information Theory*, vol. 52, pp. 3122–3138, 2006.

[12] P. Xu, C. Shi, and J. Liu, "Integer estimation methods for GPS ambiguity resolution: an applications oriented review and improvement," *Survey Review*, vol. 44, no. 324, pp. 59–71, 2012.

[13] P. Xu, "Random simulation and GPS decorrelation," *Journal of Geodesy*, vol. 75, no. 7-8, pp. 408–423, 2001.

[14] P. J. G. Teunissen, "The affine constrained GNSS attitude model and its multivariate integer least-squares solution," *Journal of Geodesy*, vol. 86, no. 7, pp. 547–563, 2012.

[15] P. J. G. Teunissen, "Integer least-squares theory for the GNSS compass," *Journal of Geodesy*, vol. 84, no. 7, pp. 433–447, 2010.

[16] P. J. G. Teunissen, G. Giorgi, and P. J. Buist, "Testing of a new single-frequency GNSS carrier phase attitude determination method: land, ship and aircraft experiments," *GPS Solutions*, vol. 15, no. 1, pp. 15–28, 2010.

[17] W. Chen, H. Qin, Y. Zhang, and T. Jin, "Accuracy assessment of single and double difference models for the single epoch GPS compass," *Advances in Space Research*, vol. 49, no. 4, pp. 725–738, 2012.

[18] S. Zhang, G. Chang, C. Chen, G. Chen, and L. Zhang, "Parameterization-switching GNSS attitude determination considering the success rate of ambiguity resolution," *Measurement Science and Technology*, Measurement Science and Technology, vol. 31, no. 6, 2020.

[19] G. Chang, T. Xu, Y. Yao, and Q. Wang, "Adaptive Kalman filter based on variance component estimation for the prediction of ionospheric delay in aiding the cycle slip repair of GNSS triple-frequency signals," *Journal of Geodesy*, vol. 92, no. 11, pp. 1241–1253, 2018.

[20] J. Guo, "Quality assessment of the affine-constrained GNSS attitude model," *GPS Solutions*, vol. 23, p. 24, 2019.

[21] J. L. Crassidis, F. L. Markley, and Y. Cheng, "Survey of nonlinear attitude estimation methods," *Journal of Guidance, Control, and Dynamics*, vol. 30, no. 1, pp. 12–28, 2007.

[22] G. Chang, T. Xu, and Q. Wang, "Error analysis of davenport's q method," *Automatica*, vol. 75, pp. 217–220, 2017.

[23] G. Chang, "Total least-squares formulation of Wahba's problem," *Electronics Letters*, vol. 51, no. 17, pp. 1334-1335, 2015.

[24] M. D. Shuster and S. D. Oh, "Three-axis attitude determination from vector observations," *Journal of Guidance and Control*, vol. 4, no. 1, pp. 70–77, 1981.

[25] J. Wu, Z. Zhou, B. Gao, R. Li, Y. Cheng, and H. Fourati, "Fast linear quaternion attitude estimator using vector observations," *IEEE Transactions on Automation Science and Engineering*, vol. 15, no. 1, pp. 307–319, 2018.

[26] B. Chen, "Analytical and iterative solutions to GNSS attitude determination problem in measurement domain," *Mathematical Problems in Engineering*, vol. 2019, pp. 7908675–10, 2019.

[27] F. Qin, L. Chang, S. Jiang, and F. Zha, "A sequential multiplicative extended Kalman filter for attitude estimation using vector observations," *Sensors*, vol. 18, no. 5, p. 1414, 2018.

[28] L. Chang, B. Hu, and K. Li, "Iterated multiplicative extended kalman filter for attitude estimation using vector observations," *IEEE Transactions on Aerospace and Electronic Systems*, vol. 52, no. 4, pp. 2053–2060, 2016.

[29] S. Zhang, G. Chang, C. Chen, L. Zhang, and T. Zhu, "Attitude determination using gyros and vector measurements aided with adaptive kinematics modeling," *Measurement*, vol. 157, p. 107679, 2020.

[30] E. J. Leffert, "Kalman filtering for spacecraft attitude estimation," *Journal of Guidance Control and Dynamics*, vol. 5, pp. 417–429, 1982.

[31] L. Wang, "Attitude determination method by fusing single antenna GPS and low cost MEMS sensors using intelligent Kalman filter algorithm," *Mathematical Problems in Engineering*, vol. 2017, Article ID 4517673, 14 pages, 2017.

[32] L. Wang, "Compounded calibration based on FNN and attitude estimation method using intelligent filtering for low cost MEMS sensor application," *Mathematical Problems in Engineering*, vol. 2019, Article ID 4514873, 13 pages, 2019.

[33] M. E. Cannon and H. Sun, "Experimental assessment of a non-dedicated GPS receiver system for airborne attitude determination," *ISPRS Journal of Photogrammetry and Remote Sensing*, vol. 51, no. 2, pp. 99–108, 1996.

[34] G. Chang, T. Xu, Q. Wang, S. Li, and K. Deng, "GNSS attitude determination method through vectorisation approach," *IET Radar, Sonar & Navigation*, vol. 11, no. 10, pp. 1477–1482, 2017.

[35] G. Chang, T. Xu, and Q. Wang, "Baseline configuration for GNSS attitude determination with an analytical least-squares solution," *Measurement Science and Technology*, vol. 27, no. 12, Article ID 125105, 2016.

[36] Y. Yang, X. Zhang, and J. Xu, "Adaptively constrained kalman filtering for navigation applications," *Survey Review*, vol. 43, no. 322, pp. 370–381, 2011.

[37] Y. Yang, W. Gao, and X. Zhang, "Robust Kalman filtering with constraints: a case study for integrated navigation," *Journal of Geodesy*, vol. 84, no. 6, pp. 373–381, 2010.

[38] P. Xu, J. Liu, and C. Shi, "Total least squares adjustment in partial errors-in-variables models: algorithm and statistical analysis," *Journal of Geodesy*, vol. 86, no. 8, pp. 661–675, 2012.

[39] X. Fang, "On the total least median of squares adjustment for the pattern recognition in point clouds," *Measurement*, vol. 160, Article ID 107794, 2020.

[40] B. Wang, "A universally efficient algorithm and precision assessment for seamless 3D similarity transformation," *Measurement Science and Technology*, 2020.

Hindawi
Mathematical Problems in Engineering
Volume 2020, Article ID 3240210, 14 pages
https://doi.org/10.1155/2020/3240210

Research Article

Neural Dynamics Variations Observer Designed for Robot Manipulator Control Using a Novel Saturated Control Technique

Francisco G. Rossomando,[1] **Emanuel Serrano**,[2] **Carlos M. Soria**,[1] **and Gustavo Scaglia**[2]

[1]*CONICET, Instituto de Automática, Universidad Nacional de San Juan, San Juan CP5400, Argentina*
[2]*CONICET, Instituto de Ingeniería Química, Universidad Nacional de San Juan, San Juan CP5400, Argentina*

Correspondence should be addressed to Francisco G. Rossomando; frosoma@inaut.unsj.edu.ar and Gustavo Scaglia; gscaglia@unsj.edu.ar

Received 11 February 2020; Revised 16 April 2020; Accepted 27 April 2020; Published 21 May 2020

Guest Editor: Rongwei Guo

This work presents a novel controller for the dynamics of robots using a dynamic variations observer. The proposed controller uses a saturated control law based on $\sin(\mathrm{tg}^{-1}(.))$ function instead of $\tanh(.)$. Besides, this function is an alternative to the use of $\tanh(.)$ in saturation control, since it reaches its maximum value more gradually than the hyperbolic tangent function. Using this characteristic, the transition between states is smoother, with similar accuracy to $\tanh(.)$. The controller is designed using a saturated SMC (sliding mode controller) and a dynamic variations observer based on GRNN (general regression neural network). The originality of this work is the use of a combination of adaptive GRNN with a sliding mode controller (SMC) including a new saturation function. Finally, experiments based on trajectory tracking demonstrate the robustness and simplicity of this method.

1. Introduction

Several years ago, the work of many researchers resulted in the development of various controllers for robots and mechatronic systems [1–6]. These algorithms were the first in the literature whose stability was proved using different theories [7–9] or using finite-time stability [10–13].

Moreover, some of these algorithms were implemented on different robot arms [14–16] and subsequent authors proposed different variants of adaptive control for robot manipulators [17–20]. Only a few of those algorithms solve the particular problems present in industrial robots; in this research work, our main objective is to reduce the lack of fidelity present in robot's arms that could vitiate any real benefits from a model-based controller. Because of this specific situation, some authors use some type of estimators to identify such infidelities between models (plant controller) or disturbances to improve controller efficiency. In this case, Mohammadi et al. [21] designed a general systematic disturbance observer for robot manipulators, where the proposed estimator doesn't have restrictions on the number of DOF, configuration, and joints. The disturbance observer has been designed based on the Linear Matrix Inequality (LMI) theory. This method presents different types of convergence depending on the disturbance characteristics, and this technique was designed to minimize large and fast disturbances while the controller drives the output to the desired reference. For efficient operation, the disturbances must be bounded. Also, as stated by Feemster et al. [22], it is necessary that the external disturbance has to be bounded and its period known.

Na et al. [23] proposed an unknown system dynamic estimator (USDE) based on simple algebraic calculations. This estimator can be modified by an unknown disturbance estimator (UDE) for external disturbances. Both estimators can adjust their parameters to approximate the unknown dynamics and disturbances, respectively. This work proposes these estimators in the design of composite controllers for

trajectory tracking, but the estimations do not consider the accelerations of the joints.

Xie et al. [24] proposed a kinematic controller based on global asymptotic stability, which is combined with the speed-based adaptive dynamic compensation controller design. This work uses the $\sin(\mathrm{tg}^{-1}(.))$ function only in its kinematic controller.

Bussola et al. [25] used a redundant SCARA architecture to execute different tasks and compared the performance with a classical SCARA in different situational tasks. This control proposes to use nonlinear control in both cases.

In another work, Freire et al. [26] proposed an adaptive PID control to control a manipulator robot in trajectory tracking. To adjust the PID gains, an ANN to retropropagate the trajectory error is applied. Similarly, Sharma et al. [27] used a recurrent neural network to implement an adaptive PID controller.

Al-Khedher and Alshamasin [28] used artificial neural networks (ANN) for the control of a SCARA robot, and its performance is compared with a classical PD controller. An alternative type of solution has been proposed for robot manipulators control problems in Rossomando and Soria [29]; their work is based on the design of an SMC adaptive controller in discrete time on a discretized model.

Jha and Biswal [30] utilized an ANN model to solve the inverse kinematics problem of a SCARA manipulator; the ANN is based on a multilayer perceptron using a gradient descendent rule to find the weights tuning law.

Yi and Zhai [31] showed a novel control technique for chattering-free in trajectory tracking for the robot's manipulators when external disturbances and different uncertainties are acting on its dynamics. To reduce these undesirable perturbations, a second-order fast nonsingular terminal sliding mode (SOFNTSM) control is designed. This proposal guarantees robustness and ensures convergence. Also, using a simulation technique demonstrates the effectiveness of the control method. More recently, Rosas et al. [32] developed an active compensation of disturbances (ADRC) where the effectiveness of this proposal is applied on a SCARA robot arm.

This paper addresses the role of the disturbance observers in nonlinear electromechanical systems, in a particular case of a robot manipulator. Prior information in dynamic information is manifested in terms of nonlinear matrices (inertia, friction, and Coriolis), and this information is applied to design the control action. However, there are differences between the real and known dynamics that can affect the robot performance in trajectory tracking. To overcome this problem, a neural GRNN estimator is implemented. This observation technique can obtain good estimations of the dynamical differences to reduce the control error. Also, the main contribution of this proposal is the implementation of the $\sin(\mathrm{tg}^{-1}(.))$ function as saturation function in the control law, which is smoother than $\tanh(.)$ or $\mathrm{sat}(.)$ functions. Due to this characteristic, the transition between states can improve the effectiveness of the controller, and similar error levels can be obtained. Also, this bounded function can prevent neural parameters from drifting due to control errors from values outside the saturation's maximum value. These problems sometimes are occasioned by communication errors between the robot's control unit and the PC. Being this last consideration the main novelty of this work. To probe the theoretical results, some experiments on the SCARA Bosch SR-800 arm system were performed. The convergence of the presented control technique and the demonstration of the closed loop system stability is another contribution of this work.

This research work is organized as follows: the section "Model Description" presents a brief description of a robot manipulator model SCARA type. The section "Controller Design" shows the design of the controller based on inverse nonlinear sliding mode control. An overview of GRNN and a function approximation of the different dynamics is presented in the section "GRNN Function Approximation and Adaptive Tuning Laws." Also, in this section, the adaptive tuning laws for the GRNN are obtained. Finally, realistic simulation results and conclusions are given in the sections "Results and Discussion" and "Conclusions," respectively.

2. Model Description

Consider the robot manipulator SCARA type model (Figure 1) described in studies by Rossomando et al. [29] and Freire et al. [26],

$$\mathbf{M}(\mathbf{q})\ddot{\mathbf{q}} + \mathbf{C}(\mathbf{q},\dot{\mathbf{q}})\dot{\mathbf{q}} + \mathbf{f}(\dot{\mathbf{q}}) = \mathbf{u}, \tag{1}$$

where $\mathbf{q} = [q_1, q_2]^T$ are the generalized coordinates of position of the robot arm and $\mathbf{u}$ are the normalized command signals arranged as components of the control signal torque vector $\mathbf{u} = [u_1, u_2]^T$. Moreover, $\mathbf{M}(\mathbf{q})$ is the inertia matrix, $\mathbf{C}(\mathbf{q},\dot{\mathbf{q}})$ is the Coriolis matrix and $\mathbf{f}(\dot{\mathbf{q}})$ is defined as the friction term.

Recalling the terms $\mathbf{C}(\mathbf{q},\dot{\mathbf{q}})\dot{\mathbf{q}} + \mathbf{f}(\dot{\mathbf{q}}) = \mathbf{N}(\mathbf{q},\dot{\mathbf{q}})$ and replacing in the following equation:

$$\mathbf{M}(\mathbf{q})\ddot{\mathbf{q}} + \mathbf{N}(\mathbf{q},\dot{\mathbf{q}}) = \mathbf{u}. \tag{2}$$

Different robotic arms own intrinsic dynamic properties; these properties will be taken into account for the implementation of the control law. The structural properties of the robot arm are as follows [33]:

(1) $\mathbf{M}(\mathbf{q})$ is a symmetric and positive definite matrix

(2) $\dot{\mathbf{M}}(\mathbf{q}) - \mathbf{C}(\mathbf{q},\dot{\mathbf{q}}) \in \mathbb{R}^{n\times n}$ is a skew-symmetric matrix

The known manipulator dynamics is represented by

$$\widehat{\mathbf{M}}(\mathbf{q})\ddot{\mathbf{q}} + \widehat{\mathbf{N}}(\mathbf{q},\dot{\mathbf{q}}) = \mathbf{u}, \tag{3}$$

where equation (3) will be used in the controller design, and the estimated matrices are defined as follows:

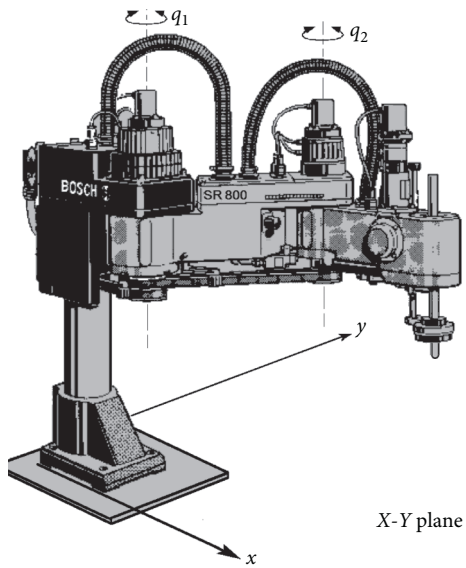

Figure 1: Representation of the 2-DOF robot arm.

$$\widehat{\mathbf{M}}(\mathbf{q}) = \begin{pmatrix} 1.7277 + 0.1908\cos(q_2) & 0.0918 + 0.0954\cos(q_2) \\ 0.0918 + 0.0954\cos(q_2) & 0.0918 \end{pmatrix},$$
$$\widehat{\mathbf{C}}(\mathbf{q}, \dot{\mathbf{q}}) = \begin{pmatrix} 31.8192 - 0.0954\sin(q_2)\dot{q}_2 & -0.0954\sin(q_2)(\dot{q}_2 + \dot{q}_1) \\ 0.3418\sin(q_2)\dot{q}_1 & 12.5783 \end{pmatrix}, \tag{4}$$
$$\widehat{\mathbf{f}}(\dot{\mathbf{q}}) = \begin{pmatrix} 1.0256\,\mathrm{sign}(\dot{q}_1) \\ 1.7842\,\mathrm{sign}(\dot{q}_2) \end{pmatrix}.$$

3. Controller Design

3.1. Neuro Adaptive SMC Controller. In this section, the trajectory tracking control scheme is described. The control scheme is based on the generalized coordinates. First, the equation of motion is represented in terms of joint coordinates. Then, the trajectory tracking control scheme with adaptive neural SMC control is proposed. To start this analysis, the control error signal is defined as

$$\mathbf{e} = \mathbf{q} - \mathbf{q}_{\mathrm{ref}}. \tag{5}$$

Now, in order to apply the control law, a sliding surface is used for the control error signal:

$$\mathbf{r} = \mathrm{diag}\left[\left(\frac{\mathrm{d}}{\mathrm{d}t} + \alpha_1\right), \left(\frac{\mathrm{d}}{\mathrm{d}t} + \alpha_2\right)\right]\mathbf{e} = \dot{\mathbf{e}} + \boldsymbol{\alpha}\mathbf{e}, \tag{6}$$

where $\boldsymbol{\alpha}$ is a diagonal matrix with positive constants $(\alpha_i > 0)$ and each α_i is defined as a design parameter. Deriving equation (6), it leads to

$$\dot{\mathbf{r}} = \ddot{\mathbf{e}} + \boldsymbol{\alpha}\dot{e}. \tag{7}$$

Using equation (7) and replacing equation (5),

$$\ddot{\mathbf{q}} - \ddot{\mathbf{q}}_{\mathrm{ref}} = \dot{\mathbf{r}} - \boldsymbol{\alpha}\dot{e}. \tag{8}$$

From equation (6) and rearranging equation (8),

$$\ddot{\mathbf{q}} = \dot{\mathbf{r}} - \boldsymbol{\alpha}(\mathbf{r} - \boldsymbol{\alpha}\mathbf{e}) + \ddot{\mathbf{q}}_{\mathrm{ref}} = \dot{\mathbf{r}} - \boldsymbol{\alpha}\mathbf{r} + \boldsymbol{\alpha}^2\mathbf{e} + \ddot{\mathbf{q}}_{\mathrm{ref}}. \tag{9}$$

Replacing equation (9) in equation (2),

$$\dot{\mathbf{r}} - \boldsymbol{\alpha}\mathbf{r} + \boldsymbol{\alpha}^2\mathbf{e} + \ddot{\mathbf{q}}_{\mathrm{ref}} = \mathbf{M}^{-1}\mathbf{u} - \mathbf{M}^{-1}\mathbf{N}(\mathbf{q}, \dot{\mathbf{q}}). \tag{10}$$

Obtaining $\dot{\mathbf{r}}$ from equation (10),

$$\dot{\mathbf{r}} = -\mathbf{M}^{-1}\mathbf{N}(\mathbf{q}, \dot{\mathbf{q}}) + \mathbf{M}^{-1}\mathbf{u} + \boldsymbol{\alpha}\mathbf{r} - \boldsymbol{\alpha}^2\mathbf{e} - \ddot{\mathbf{q}}_{\mathrm{ref}}. \tag{11}$$

3.2. Saturation Definition. In this subsection, an approximation of $\sin(\mathrm{tg}^{-1}(.))$ function is proposed. The main objective of this work is to propose an alternative of the $\tanh(.)$ function as a smooth saturation function. Figure 2 shows $\sin(\mathrm{tg}^{-1}(.))$, $\mathrm{sat}(.)$, and $\tanh(.)$ functions, as the $\sin(\mathrm{tg}^{-1}(.))$ function reaches its max value more gradually than the hyperbolic tangent function $\tanh(.)$, and since it presents a smoother transition, this characteristic can be used to take advantage of control applications. In [24], a $\sin(\mathrm{tg}^{-1}(.))$ function was used in a kinematics controller for mobile robot applications, being the tracking accuracy of the robot improved. Now, expressing the $\sin(\mathrm{tg}^{-1}(.))$ function as

$$\sin\left(\mathrm{tg}^{-1}(b_2 r_i)\right) = \frac{b_2 r_i}{\sqrt{1 + (b_2 r_i)^2}}. \tag{12}$$

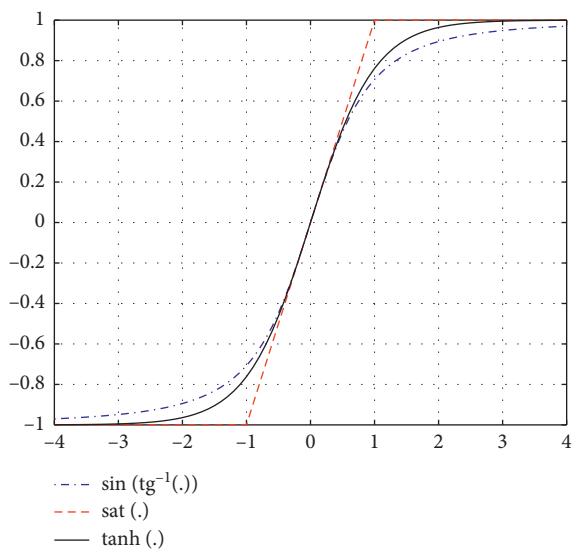

FIGURE 2: sat(.), tanh(.), and sin(tg^{-1}(.)) functions.

Equation (12) changes from trigonometric to an algebraic function. An algebraic function is simpler to implement in microcontrollers and industrial computers.

Assumption 1. It is assumed that the quantity $\sqrt{1+(b_2 r_i)^2}$ is nonnegative along the evolution of the system.

The control law is expressed as

$$\mathbf{u} = \widehat{\mathbf{M}}\left(\widehat{\mathbf{M}}^{-1}\widehat{\mathbf{N}}(\mathbf{q},\dot{\mathbf{q}}) + \ddot{\mathbf{q}}_{\text{ref}} - b_1 \sin\left(\text{tg}^{-1}(b_2\mathbf{r})\right) - \boldsymbol{\xi}_\varepsilon \text{sign}(\mathbf{r})\right), \tag{13}$$

where $\xi_\varepsilon \in \Re^{2\times 2}$, and it is expressed as $\xi_\varepsilon = \text{diag}(\xi_{\varepsilon 1}, \xi_{\varepsilon 2})$. The proposed control structure is shown in Figure 3. Now, closing the control loop and replacing equation (13) in equation (11), we lead to

$$\dot{\mathbf{r}} = -b_1 \sin\left(\text{tg}^{-1}(b_2\mathbf{r})\right) + \boldsymbol{\alpha}\mathbf{r} - \boldsymbol{\alpha}^2\mathbf{e} - \boldsymbol{\xi}_\varepsilon \text{sign}(\mathbf{r}) + \boldsymbol{\delta}(t). \tag{14}$$

From equation (14), $\boldsymbol{\delta}(t)$ denotes the error due to the dynamic difference, and it is expressed as

$$\begin{aligned}\boldsymbol{\delta}(t) &= -\mathbf{M}^{-1}\mathbf{N}(\mathbf{q},\dot{\mathbf{q}}) + \mathbf{M}^{-1}(\mathbf{q})\mathbf{u} - \left(-\widehat{\mathbf{M}}^{-1}\widehat{\mathbf{N}}(\mathbf{q},\dot{q}) + \widehat{\mathbf{M}}^{-1}(\mathbf{q})\mathbf{u}\right)\\ &= \left(-\mathbf{M}^{-1}\mathbf{N}(\mathbf{q},\dot{\mathbf{q}}) + \widehat{\mathbf{M}}^{-1}\widehat{\mathbf{N}}(\mathbf{q},\dot{\mathbf{q}})\right) + \left(\mathbf{M}^{-1}(\mathbf{q}) - \widehat{\mathbf{M}}^{-1}(\mathbf{q})\right)\mathbf{u},\end{aligned} \tag{15}$$

where $\boldsymbol{\delta}$ is considered bounded by

$$\boldsymbol{\delta}(t) \le \boldsymbol{\delta}_0, \tag{16}$$

where $\boldsymbol{\delta}_0$ is a positive constant value.

3.3. GRNN Function Approximation and Adaptive Tuning Laws. In this subsection, a general regression neural network (GRNN) identification technique is presented, where the GRNN is a single-pass neural network which uses a Gaussian activation function in the hidden layer, and it can be used to approximate any continuous function [34].

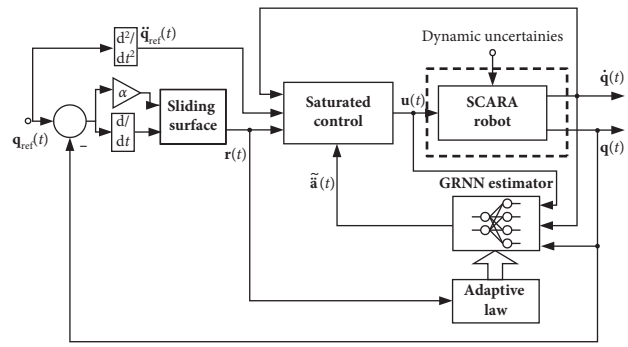

FIGURE 3: Control structure of the robot arm using a neural observer.

The variable $\boldsymbol{\delta}(\mathrm{t})$ represents the unknown parameters due to mass variation of the payload and can be represented as

$$\boldsymbol{\delta}(\mathbf{t}) - \left(\boldsymbol{\varphi}_{MN}^{*T}\boldsymbol{\Psi}(\overline{\mathbf{q}}) + \boldsymbol{\varphi}_M^{*T}\boldsymbol{\chi}(\mathbf{q})\mathbf{u}\right) \le \varepsilon < \infty, \tag{17}$$

or

$$\boldsymbol{\delta}(t) = \boldsymbol{\varphi}_{MN}^{*T}\boldsymbol{\Psi}(\overline{\mathbf{q}}) + \boldsymbol{\varphi}_M^{*T}\boldsymbol{\chi}(\mathbf{q})\mathbf{u} + \boldsymbol{\varepsilon}, \tag{18}$$

where $\overline{\mathbf{q}}$ is the regressor vector and is defined as $\overline{\mathbf{q}} = [\mathbf{q}, \dot{\mathbf{q}}]$. The neuron number is defined as m, and the vector $\Psi(.) \in \Re^{m\times 1}$ is a functions vector where each element is defined as $\Psi_i = \exp(\overline{\mathbf{q}} - \mathbf{z}/2\rho)/\sum_{j=1}^{m}\exp(\overline{\mathbf{q}} - \mathbf{z}_j/2\rho_j)$ and $\mathbf{z} \in \Re^{\dim(\overline{q})\times 1}$ and $\rho \in \Re^{m\times 1}$ define the centers and the spread of each exponential function, respectively. In the same way, the matrix $\boldsymbol{\chi}(.) \in \Re^{m\times n}$ is defined as $\chi_i = \exp(\mathbf{q} - \mathbf{z}/2\rho)/\sum_{j=1}^{m}\exp(\mathbf{q} - \mathbf{z}_j/2\rho_j)$ and $\mathbf{z} \in \Re^{\dim(\mathbf{q})\times 1}$ and $\rho \in \Re^{m\times 1}$ define the centers and the spread of each exponential function, respectively. Besides, $\boldsymbol{\varphi}_{MN}^* \in \mathbf{R}^{n\times m}$ and $\boldsymbol{\varphi}_M^* \in \Re^{n\times m}\mathrm{I}$ are the optimal parameter matrix; each element of $\boldsymbol{\varphi}_{MN}^*$ and $\boldsymbol{\varphi}_M^*$ is constant and unknown. The vector ε is the approximation error and $|\varepsilon_i| \le \xi_{\varepsilon i}$ for $i = 1, 2$. Being $n = 2$ the model output number, the estimation function is chosen as follows:

$$\widehat{\boldsymbol{\delta}}(t) = \widehat{\boldsymbol{\varphi}}_{MN}^T\boldsymbol{\Psi}(\overline{\mathbf{q}}) + \widehat{\boldsymbol{\varphi}}_M^T\boldsymbol{\chi}(\mathbf{q})\mathbf{u}. \tag{19}$$

The GRNN structure has the capacity of approximating any real continuous vector function; in [34, 35], there are different references about this identification technique. Using the estimated output of GRNN equation (19) and taking the difference between equation (18) and equation (19), we obtain

$$\boldsymbol{\delta}(t) - \widehat{\boldsymbol{\delta}}(t) = \widetilde{\boldsymbol{\delta}}(t). \tag{20}$$

The approximation error $\widetilde{\boldsymbol{\delta}}(t)$ can be approximated by

$$\widetilde{\boldsymbol{\delta}}(t) = \left(\boldsymbol{\varphi}_{MN}^{*T}\boldsymbol{\Psi}(\overline{\mathbf{q}}) + \boldsymbol{\varphi}_M^{*T}\boldsymbol{\chi}(\mathbf{q})\mathbf{u} + \boldsymbol{\varepsilon}\right) - \left(\widehat{\boldsymbol{\varphi}}_{MN}^T\boldsymbol{\Psi}(\overline{\mathbf{q}}) + \widehat{\boldsymbol{\varphi}}_M^T\boldsymbol{\chi}(\mathbf{q})\mathbf{u}\right). \tag{21}$$

Taking into account that $\boldsymbol{\varphi}_{MN}^{*T} = \widetilde{\boldsymbol{\varphi}}_{MN}^T + \widehat{\boldsymbol{\varphi}}_{MN}^T$ and $\boldsymbol{\varphi}_M^{*T} = \widetilde{\boldsymbol{\varphi}}_M^T + \widehat{\boldsymbol{\varphi}}_M^T$ and replacing them in equation (21),

$$\widetilde{\boldsymbol{\delta}}(t) = \left(\widetilde{\boldsymbol{\varphi}}_{MN}^T\boldsymbol{\Psi}(\overline{\mathbf{q}}) + \widetilde{\boldsymbol{\varphi}}_M^T\boldsymbol{\chi}(\mathbf{q})\mathbf{u} + \boldsymbol{\varepsilon}\right). \tag{22}$$

Replacing the proposed control law (13) in the robot dynamics (11) and also the neural approximation (22), it leads to

$$\begin{aligned}\dot{\mathbf{r}} &= -b_1 \sin\left(\mathrm{tg}^{-1}\left(b_2\mathbf{r}\right)\right) + \tilde{\boldsymbol{\delta}}(t) + \boldsymbol{\alpha}\mathbf{r} - \boldsymbol{\alpha}^2\mathbf{e} - \xi_\varepsilon \mathrm{sign}(\mathbf{r}) = \cdots \\ &= -b_1 \sin\left(tg^{-1}\left(b_2\mathbf{r}\right)\right) + \left(\tilde{\boldsymbol{\varphi}}_{MN}^T \boldsymbol{\Psi}(\overline{\mathbf{q}}) + \tilde{\boldsymbol{\varphi}}_M^T \boldsymbol{\chi}(\mathbf{q})\mathbf{u} + \boldsymbol{\varepsilon}\right) + \boldsymbol{\alpha}\mathbf{r} \\ &\quad - \boldsymbol{\alpha}^2\mathbf{e} - \xi_{\boldsymbol{\varepsilon}}\mathbf{sign}(\mathbf{r}).\end{aligned} \tag{23}$$

Theorem: the closed-loop system (23) using the proposed control law (13) using the neural approx. (22) has asymptotic stability.

3.3.1. Demonstration. The first step is defining a definite positive Lyapunov's function candidate (LFC) to demonstrate the convergence of the proposed control method.

Defining the LFC as

$$\begin{aligned}\mathscr{L} = \sum_i^2 \Bigg(&\frac{1}{b_2}\sqrt{1+(b_2 r_i)^2} + \frac{1}{2}e_i^2 + \frac{1}{2b_3}\left(\tilde{\boldsymbol{\varphi}}_{MNi}^T \tilde{\boldsymbol{\varphi}}_{MNi}\right) \\ &+ \frac{1}{2b_4}\left(\tilde{\boldsymbol{\varphi}}_{Mi}^T \tilde{\boldsymbol{\varphi}}_{Mi}\right)\Bigg).\end{aligned} \tag{24}$$

Deriving equation (24),

$$\begin{aligned}\dot{\mathscr{L}} = \sum_i^2 \Bigg(&\frac{b_2 r_i}{\sqrt{1+(b_2 r_i)^2}}\dot{r}_i + e_i\dot{e}_i + \frac{1}{b_3}\left(\tilde{\boldsymbol{\varphi}}_{MNi}^T \dot{\tilde{\boldsymbol{\varphi}}}_{MNi}\right) \\ &+ \frac{1}{b_3}\left(\tilde{\boldsymbol{\varphi}}_{Mi}^T \dot{\tilde{\boldsymbol{\varphi}}}_{Mi}\right)\Bigg).\end{aligned} \tag{25}$$

Replacing equation (30) in equation (32),

$$\begin{aligned}\dot{\mathscr{L}} = \sum_i^2 \Bigg(&-\mathrm{b}_1\left(\frac{b_2 r_i}{\sqrt{1+(b_2 r_i)^2}}\right)^2 + \frac{b_2 r_i}{\sqrt{1+(b_2 r_i)^2}}\left(\tilde{\boldsymbol{\varphi}}_{MNi}^T \boldsymbol{\Psi}(\overline{\mathbf{q}}) + \tilde{\boldsymbol{\varphi}}_{Mi}^T \boldsymbol{\chi}(\mathbf{q})\mathbf{u} + \varepsilon_i\right) \\ &+ \cdots + \frac{b_2 r_i}{\sqrt{1+(b_2 r_i)^2}}\left(\alpha_i r_i - \alpha_i^2 e_i\right) - \left(\frac{b_2 r_i}{\sqrt{1+(b_2 r_i)^2}}\right)\xi_{\boldsymbol{\varepsilon}}\mathrm{sign}(r_i) + e_i(r_i - \alpha_i e_i) + \cdots + \frac{1}{b_3}\left(\tilde{\boldsymbol{\varphi}}_{MNi}^T \dot{\tilde{\boldsymbol{\varphi}}}_{MNi}\right) + \frac{1}{b_3}\left(\tilde{\boldsymbol{\varphi}}_{Mi}^T \dot{\tilde{\boldsymbol{\varphi}}}_{Mi}\right)\Bigg).\end{aligned} \tag{26}$$

Rearranging equation (33),

$$\begin{aligned}\dot{\mathscr{L}} \le \sum_i^2 \Bigg(&-\mathrm{b}_1\left(\frac{b_2 r_i}{\sqrt{1+(b_2 r_i)^2}}\right)^2 + \frac{b_2 r_i}{\sqrt{1+(b_2 r_i)^2}}\left(\tilde{\boldsymbol{\varphi}}_{MNi}^T \boldsymbol{\Psi}(\overline{q})\right) + \cdots + \frac{b_2 r_i}{\sqrt{1+(b_2 r_i)^2}}\left(\tilde{\boldsymbol{\varphi}}_{Mi}^T \boldsymbol{\chi}(\mathbf{q})\mathbf{u}\right) \\ &+ \frac{b_2 r_i}{\sqrt{1+(b_2 r_i)^2}}\left(\alpha_i r_i - \alpha_i^2 e_i\right) - \cdots - \left(\frac{b_2 r_i}{\sqrt{1+(b_2 r_i)^2}}\right)\xi_{\varepsilon i}\mathrm{sign}(r_i) + \frac{b_2 r_i}{\sqrt{1+(b_2 r_i)^2}}(\varepsilon_i) + \cdots + e_i(r_i - \alpha_i e_i) \\ &+ \frac{1}{b_3}\left(\tilde{\boldsymbol{\varphi}}_{MNi}^T \dot{\tilde{\boldsymbol{\varphi}}}_{MNi}\right) + \frac{1}{b_3}\left(\tilde{\boldsymbol{\varphi}}_{Mi}^T \dot{\tilde{\boldsymbol{\varphi}}}_{Mi}\right)\Bigg).\end{aligned} \tag{27}$$

Rearranging equation (34),

$$\dot{\mathscr{L}} \leq \sum_{i}^{2} -\left(\mathrm{b}_1 \left(\frac{b_2 r_i}{\sqrt{1+(b_2 r_i)^2}} \right)^2 + \frac{b_2 r_i}{\sqrt{1+(b_2 r_i)^2}} (\varepsilon_i) + \cdots + \frac{b_2 r_i}{\sqrt{1+(b_2 r_i)^2}} \left(\alpha_i r_i - \alpha_i^2 e_i\right) - \xi_{\varepsilon i} \left(\frac{b_2 |r_i|}{\sqrt{1+(b_2 r_i)^2}} \right) + e_i \left(r_i - \alpha_i e_i\right) \right)$$
$$+ \sum_{i}^{2} \left(\tilde{\boldsymbol{\varphi}}_{MNi}^T(t) \left[\frac{b_2 r_i}{\sqrt{1+(b_2 r_i)^2}} \boldsymbol{\Psi}(\overline{q}) + \frac{1}{b_3} \dot{\tilde{\boldsymbol{\varphi}}}_{MNi} \right] \right) + \cdots + \sum_{i}^{2} \left(\tilde{\boldsymbol{\varphi}}_{Mi}^T(t) \left[\frac{b_2 r_i}{\sqrt{1+(b_2 r_i)^2}} \boldsymbol{\chi}(\mathbf{q})\mathbf{u} + \frac{1}{b_4} \dot{\tilde{\boldsymbol{\varphi}}}_{Mi} \right] \right). \tag{28}$$

Taking into account the last terms between brackets in equation (28) and defining $\dot{\tilde{\boldsymbol{\varphi}}}_{MNi}$ as

$$\dot{\tilde{\boldsymbol{\varphi}}}_{MNi} = -\frac{b_3 b_2 r_i}{\sqrt{1+(b_2 r_i)^2}} \boldsymbol{\Psi}(\overline{q}). \tag{29}$$

In the same way, for $\dot{\tilde{\boldsymbol{\varphi}}}_{Mi}$ is obtained in the next equation:

$$\dot{\tilde{\boldsymbol{\varphi}}}_{Mi} = -b_4 \frac{b_2 r_i}{\sqrt{1+(b_2 r_i)^2}} \boldsymbol{\chi}(\mathbf{q})\mathbf{u}. \tag{30}$$

The subindex i in equation (29) and equation (30) denotes the vector weights adjusted by $\mathbf{r}_i$; replacing the same equation in (28) leads to

$$\dot{\mathscr{L}}_i = -b_1 \left(\frac{b_2 r_i}{\sqrt{1+(b_2 r_i)^2}} \right)^2 + \frac{b_2 r_i}{\sqrt{1+(b_2 r_i)^2}} \left(\alpha_i r_i - \alpha_i^2 e_i\right) + e_i \left(r_i - \alpha_i e_i\right) + \Delta_i, \tag{31}$$

where $\Delta_i = (\varepsilon_i b_2 r_i - \xi_{\varepsilon i} |b_2 r_i|)(1/(\sqrt{1+(b_2 r_i)^2})) \leq 0$.

Now, it is necessary to analyze two cases, when $r_i = 0$ and $r_i \neq 0$.

Analyzing the first case $r_i = 0$, all the terms with $b_2 r_i / (\sqrt{1+(b_2 r_i)^2})$ are equal to zero. Thus, $\dot{\mathscr{L}}_i$ can be reduced to

$$\dot{\mathscr{L}}_i = -\alpha_i e_i^2 \leq 0. \tag{32}$$

This expression denotes that the control error is bounded when $r_i = 0$. Analyzing the second case $(r_i \neq 0)$, in this instance, $b_2 r_i / (\sqrt{1+(b_2 r_i)^2}) \neq 0$; rewriting equation (31),

$$\dot{\mathscr{L}}_i = -\left(b_1 - \frac{\alpha_i \sqrt{1+(b_2 r_i)^2}}{b_2} \right) \left(\frac{b_2 r_i}{\sqrt{1+(b_2 r_i)^2}} \right)^2 + \left(-\alpha_i^2 e_i \frac{b_2 r_i}{\sqrt{1+(b_2 r_i)^2}} + e_i r_i \right) - \alpha_i e_i^2 + \Delta_i. \tag{33}$$

Doing the same operation for the second term,

$$\dot{\mathscr{L}}_i = -\left(b_1 - \frac{\alpha_i \sqrt{1+(b_2 r_i)^2}}{b_2} \right) \left(\frac{b_2 r_i}{\sqrt{1+(b_2 r_i)^2}} \right)^2 - \cdots - \left(\alpha_i^2 - \frac{\sqrt{1+(b_2 r_i)^2}}{b_2} \right) e_i \frac{b_2 r_i}{\sqrt{1+(b_2 r_i)^2}} - \alpha_i e_i^2 + \Delta_i. \tag{34}$$

Defining the auxiliary vector $E_i = (e_i \;\; b_2 r_i / (\sqrt{1+(b_2 r_i)^2}))^T$ and rewriting (34) as

$$\dot{\mathscr{L}}_i = -\mathbf{E}_i^T \boldsymbol{\Theta}_i \mathbf{E}_i - \alpha_i e_i^2 + \Delta_i, \tag{35}$$

where $\boldsymbol{\Theta}_i$ is expressed as

$$\boldsymbol{\Theta}_i = \begin{pmatrix} \dfrac{\alpha_i}{2} & \dfrac{\alpha_i^2}{2} - \dfrac{\sqrt{1+(b_2 r_i)^2}}{2b_2} \\ \dfrac{\alpha_i^2}{2} - \dfrac{\sqrt{1+(b_2 r_i)^2}}{2b_2} & b_1 - \dfrac{\alpha_i \sqrt{1+(b_2 r_i)^2}}{b_2} \end{pmatrix}. \tag{36}$$

It is necessary to demonstrate that the matrix $\boldsymbol{\Theta}_i$ is a positive definite to demonstrate the convergence of the presented control technique. Taking into account the Sylvester's criterion, which is a simple way to determine if $\boldsymbol{\Theta}_i$ is a definite positive matrix.

Now computing if the upper left 1-by-1 corner of $\boldsymbol{\Theta}_i$ has a positive determinant. In this case,

$$\frac{\alpha_i}{2} > 0. \tag{37}$$

Consequently, if the upper left 2-by-2 corner of $\boldsymbol{\Theta}_i$ has a positive determinant, where

$$\frac{\alpha_i}{2} \left(\mathrm{b}_1 - \frac{\alpha_i \sqrt{1+(b_2 r_i)^2}}{b_2} \right) - \left(\frac{\alpha_i^2}{2} - \frac{\sqrt{1+(b_2 r_i)^2}}{2b_2} \right)^2 > 0. \tag{38}$$

Expanding the abovementioned equation (38) and rearranging,

$$\left(\frac{\alpha_i}{2}b_1 - \frac{\alpha_i^2\sqrt{1+(b_2r_i)^2}}{2b_2}\right) - \left(\frac{\alpha_i^4}{4} - \frac{\alpha_i^2}{2}\frac{\sqrt{1+(b_2r_i)^2}}{b_2} + \frac{1+(b_2r_i)^2}{4(b_2)^2}\right)$$
$$= \cdots = \frac{\alpha_i}{2}b_1 - \frac{\alpha_i^4}{4} - \frac{1}{4(b_2)^2} - \frac{(r_i)^2}{4} > 0. \tag{39}$$

Then, equation (39) can be expressed as

$$\alpha_i\left(2b_1 - \alpha_i^3\right) > \left(\frac{1}{(b_2)^2} + (r_i)^2\right). \tag{40}$$

From definition of $\mathscr{L}_i$ (equation (24)),

$$\mathscr{L}_i > \frac{1}{b_2}\sqrt{1+(b_2r_i)^2}. \tag{41}$$

Obtaining r_i from the abovementioned equation (41),

$$\frac{\sqrt{(b_2\mathscr{L}_i)^2 - 1}}{b_2} > r_i. \tag{42}$$

Replacing in equation (40),

$$\alpha_i\left(2b_1 - \alpha_i^3\right) > \frac{(b_2\mathscr{L}_i)^2 - 1}{(b_2)^2} + \frac{1}{(b_2)^2}, \tag{43}$$

with condition (i) and condition (ii) and the matrix $\mathbf{\Theta}_i$ which is a definite positive; thus, $\dot{\mathscr{L}}_i$ can be the upper bound by the following expression:

$$\dot{\mathscr{L}}_i \leq -\alpha_i e_i^2, \quad \text{for } \alpha_i\left(2b_1 - \alpha_i^3\right) > (\mathscr{L}_i)^2. \tag{44}$$

From equation (44) $\dot{\mathscr{L}}_i \leq 0$, for all $t \in [0, \infty]$, the sufficient condition for equation (45) can be obtained:

$$\dot{\mathscr{L}}_i \leq -\alpha_i e_i^2, \quad \text{for } \alpha_i\left(2b_1 - \alpha_i^3\right) > (\mathscr{L}_i(0))^2. \tag{45}$$

From the definition of LFC, equation (24), $V_i(0)$ is expressed as

$$\mathscr{L}_i(0) = \frac{1}{b_2}\sqrt{1+(b_2r_i(0))^2} + \frac{1}{2}e_i^2(0) \leq \left(\frac{1}{b_2} + |r_i(0)|\right) + \frac{1}{2}e_i^2(0). \tag{46}$$

Using the abovementioned expression, equation (46) can be rewritten as

$$\dot{\mathscr{L}}_i \leq -\alpha_i e_i^2,$$
$$\text{for } \alpha_i\left(2b_1 - \alpha_i^3\right) > \left(\left(\frac{1}{b_2} + |\dot{e}_i(0)| + \alpha_i|e_i(0)|\right) + \frac{1}{2}e_i^2(0)\right)^2. \tag{47}$$

Based on previous results and considering equations (24), (37), (39), and (47) and Barbalat's lemma [36], these results guarantee the boundedness of the error control signal e_i during the closed loop operation.

4. Results and Discussion

4.1. Experiments. The experiments were performed on the SCARA Bosch SR-800 (Figure 1) arm system. A CPU Intel Dual Core, with 2.6 GHz and 4 GB RAM memory to control the robot arm, is used. Debian Linux has been installed in the CPU and it uses RTAI (Real Time Application Interface). The approach proposed in this paper is applied to the robotic manipulator Bosch SR-800 by controlling the power unit that applies the calculated torques (control actions) to the joints of the robot arm. The first experiment shows different experiments with different neural networks. For performance comparison purposes, in addition to the use of the different saturated controllers to control the robotic manipulator, a nonadaptive SMC controller was also applied to the same robot for reference. In the second set of experiments, different saturated functions were used.

4.2. Adaptive Neural Control Comparison. The first set of experiments was made with different neural networks to compensate for the dynamic variations.

The objective of this approach is to contribute to the use of a new saturation function and prove its efficiency in an adaptive control technique. In the first set of experiments, the basic form of Lissajous "8" is considered as a reference trajectory. The experiment was carried out using three different adaptive techniques using the single saturation function $\sin(\mathrm{tg}^{-1}(.))$, where these controllers were applied on the robot arm to demonstrate their effectiveness. The controllers are based on saturated SMC, the first one uses a nonadaptive SMC, which does not use any on-line adjustment, and the second one, an MLP adaptive controller and the last one, a GRNN adaptive controller based on SMC.

Figure 4 shows the trajectories followed by the robot arm using each one of the control strategies. Figure 5 shows the reference trajectory for each joint (q_1 and q_2) and the followed trajectory. Figure 6 shows the square norm of the control errors generated by each control strategy (the error norm is defined by $\mathbf{e} = \mathrm{sqrt}(e_{q1}^2 + e_{q2}^2)$). The experimental results prove that the highest error was obtained by a nonadaptive SMC controller, which has no on-line calibration. In this case, the effects of the model uncertainties on the error can be observed clearly. The methods that compensate the model uncertainties have a lower error than the previous case. Finally, the lowest error was obtained by the GRNN adaptive SMC strategy, which reduces the trajectory error caused by the model uncertainties. In Figure 7, the control actions of the GRNN adaptive SMC are shown, and the chattering phenomenon can be seen. This phenomenon can be reduced using a low pass filter previous to the electromechanical actuator.

Figure 8 presents the distribution of the errors obtained along with the experiment. In the 1st row, it shows the error distribution using nonadaptive SMC control. The 2nd row presents the error distribution using adaptive GRNN-SMC control. Finally, in the 3rd row, the error distribution using adaptive MLP-SMC control is shown. In Table 1, the performance indicators I*AE* and IT*AE* are presented

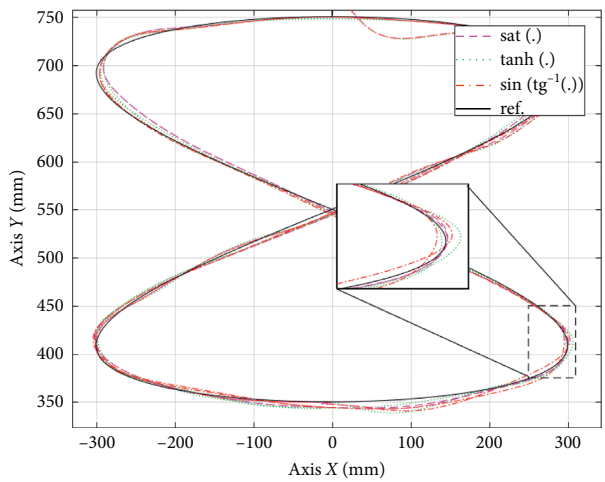

Figure 4: Trajectory followed for the different strategies.

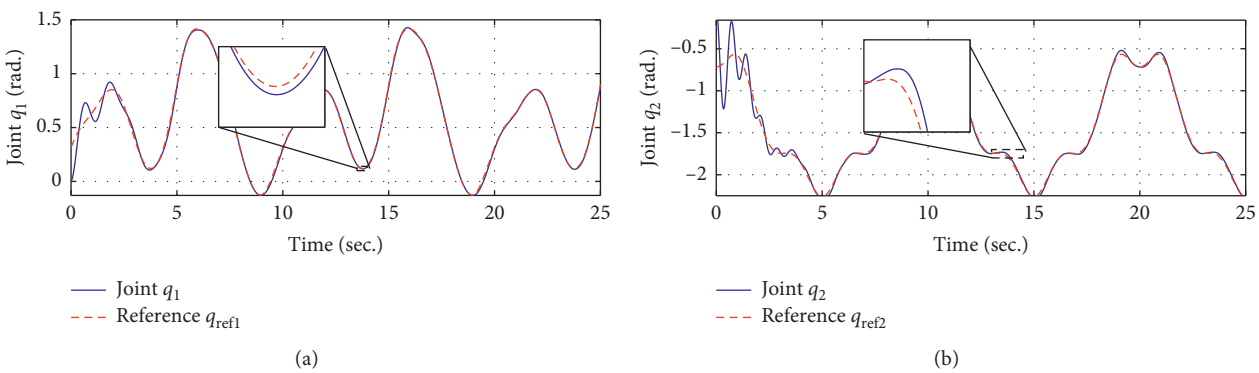

Figure 5: Reference (dashed line) and trajectory followed (solid line).

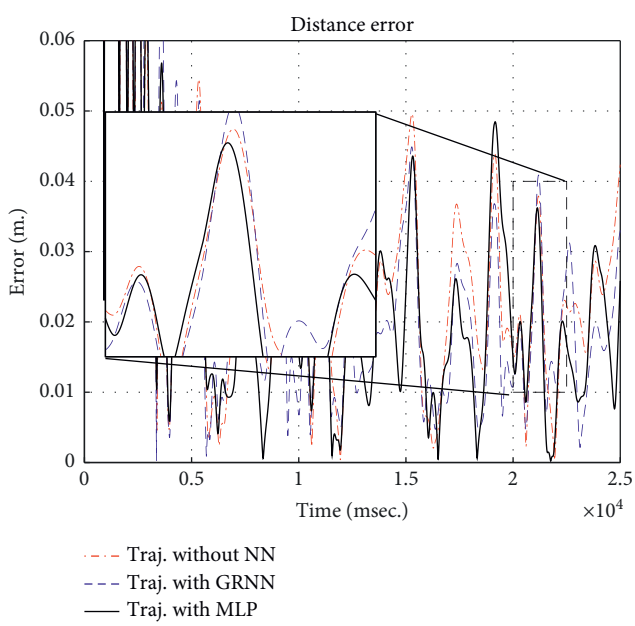

Figure 6: Square norm of the trajectory errors generated by each control strategy.

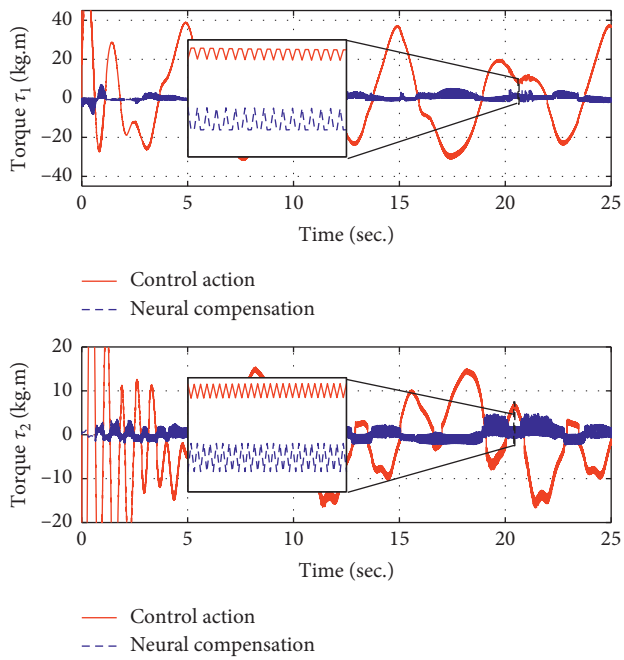

Figure 7: Control actions (adaptive + neural) and neural compensation using adaptive GRNN.

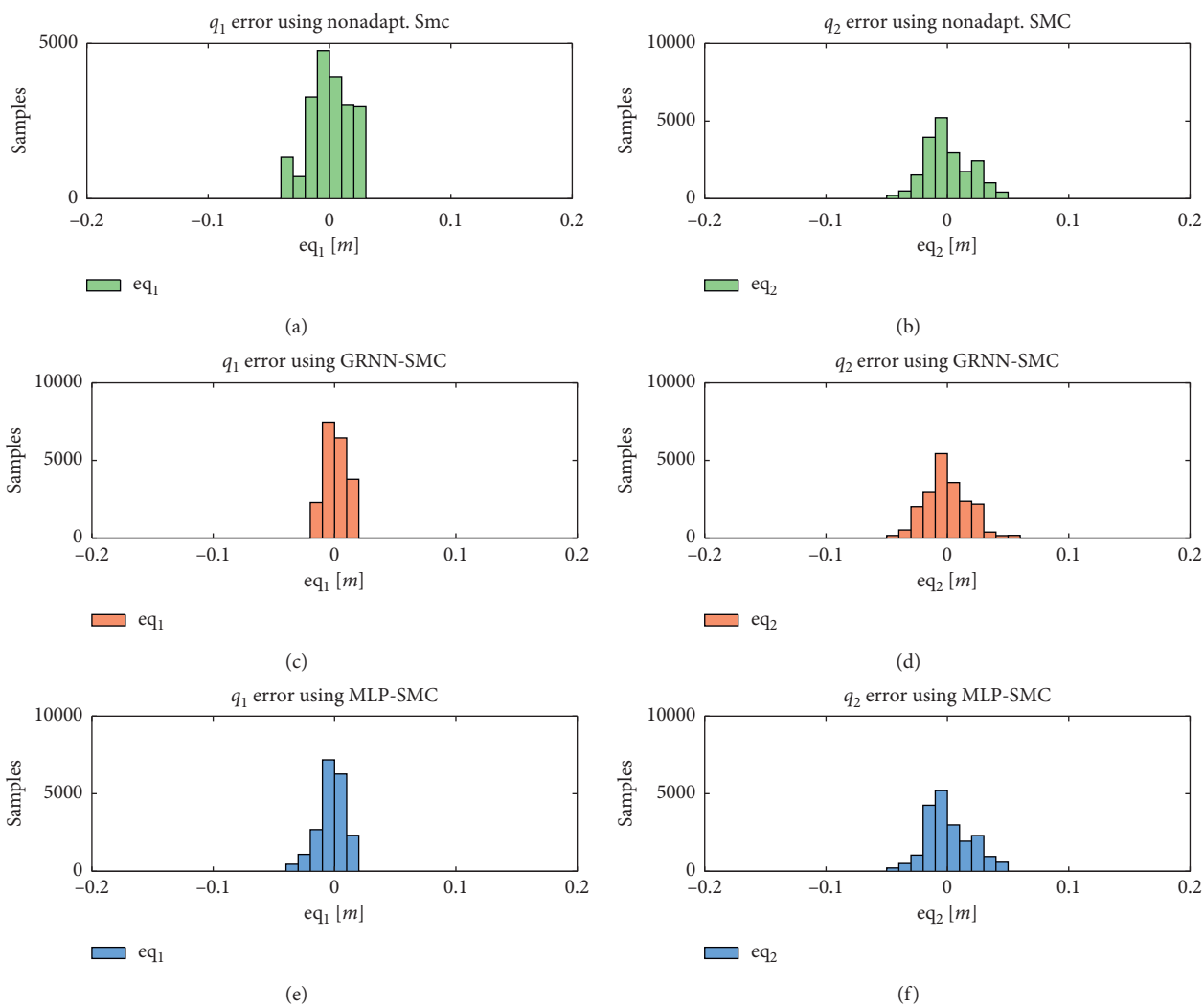

Figure 8: Distribution of the errors obtained along the experiment. (a, b) The error distribution using a nonadaptive SMC controller. (c, d) The error distribution using an adaptive GRNN-SMC controller. (e, f) The error distribution using an adaptive MLP-SMC controller.

Table 1: The performance indexes IAE and ITAE of different controllers using $\sin(\mathrm{tg}^{-1}(.))$.

Controller	IAE	ITAE
Nonadaptive SMC	569.3324	$1.4233e+04$
Adapt. GRNN-SMC	424.7610	$1.0619e+04$
Adapt. MLP-SMC	473.8136	$1.1845e+04$

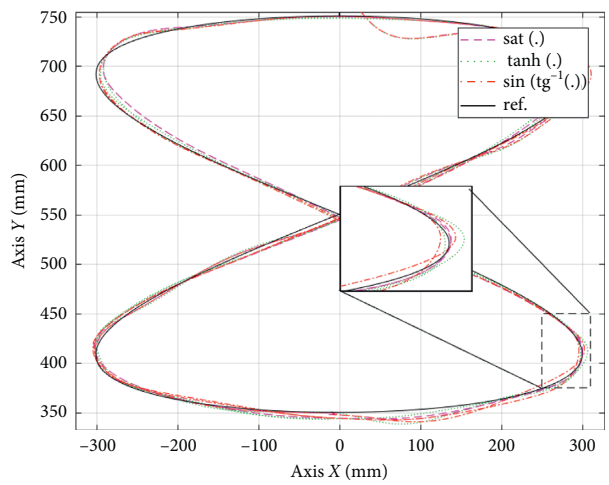

Figure 9: Trajectory followed for the different strategies.

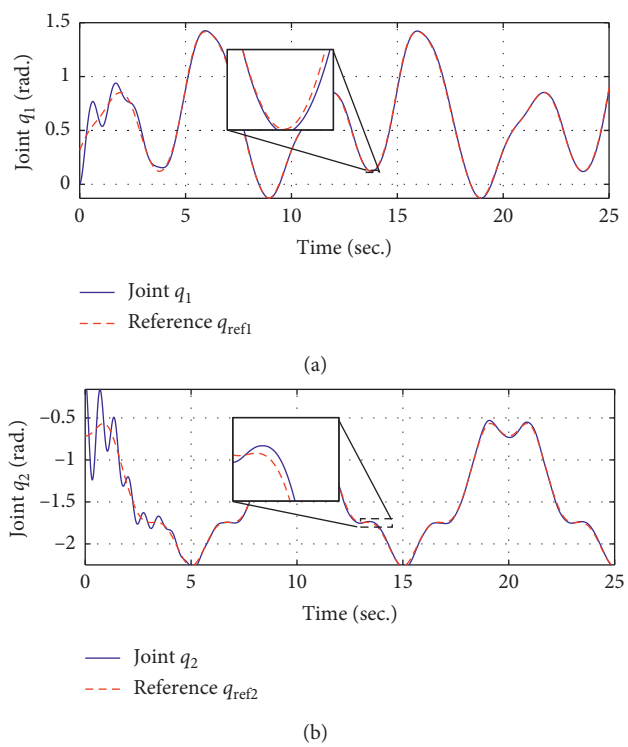

Figure 10: (a) Joint q1. (b) Joint q2. Reference (dashed line) and trajectory followed (solid line).

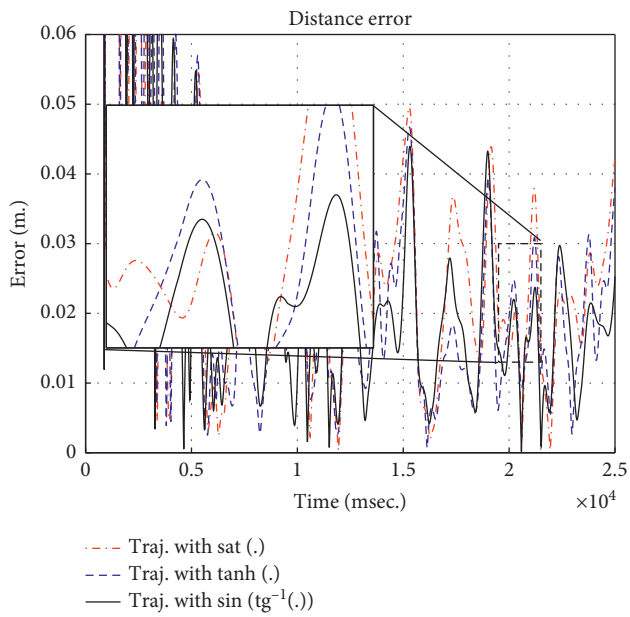

FIGURE 11: Square norm of the trajectory errors generated by each control strategy.

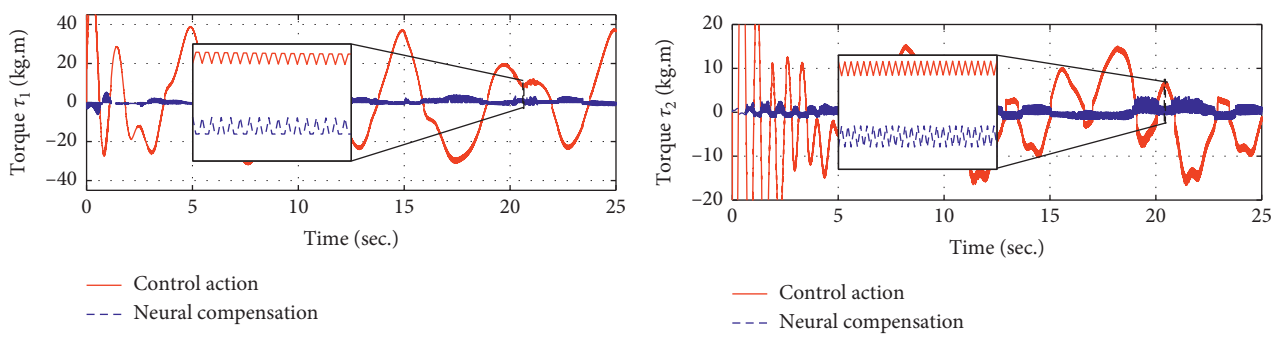

(a) (b)

FIGURE 12: (a) Torque 1. (b) Torque 2. Control actions (adaptive + neural) and neural compensation using adaptive GRNN.

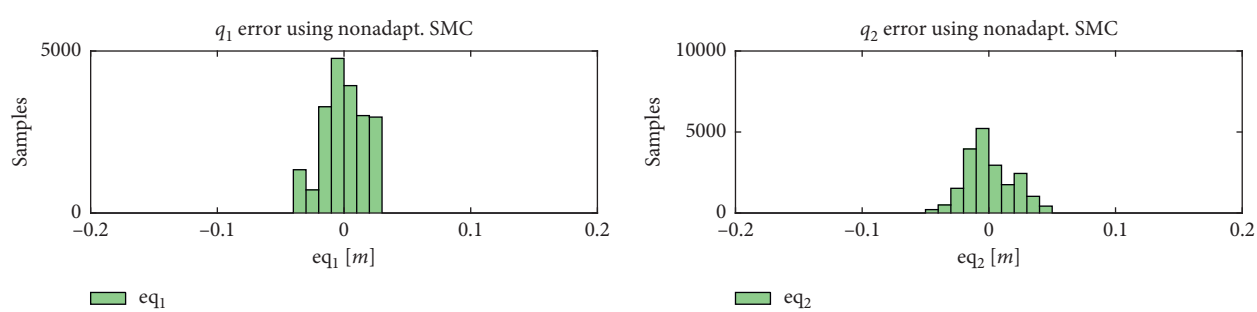

(a) (b)

FIGURE 13: Continued.

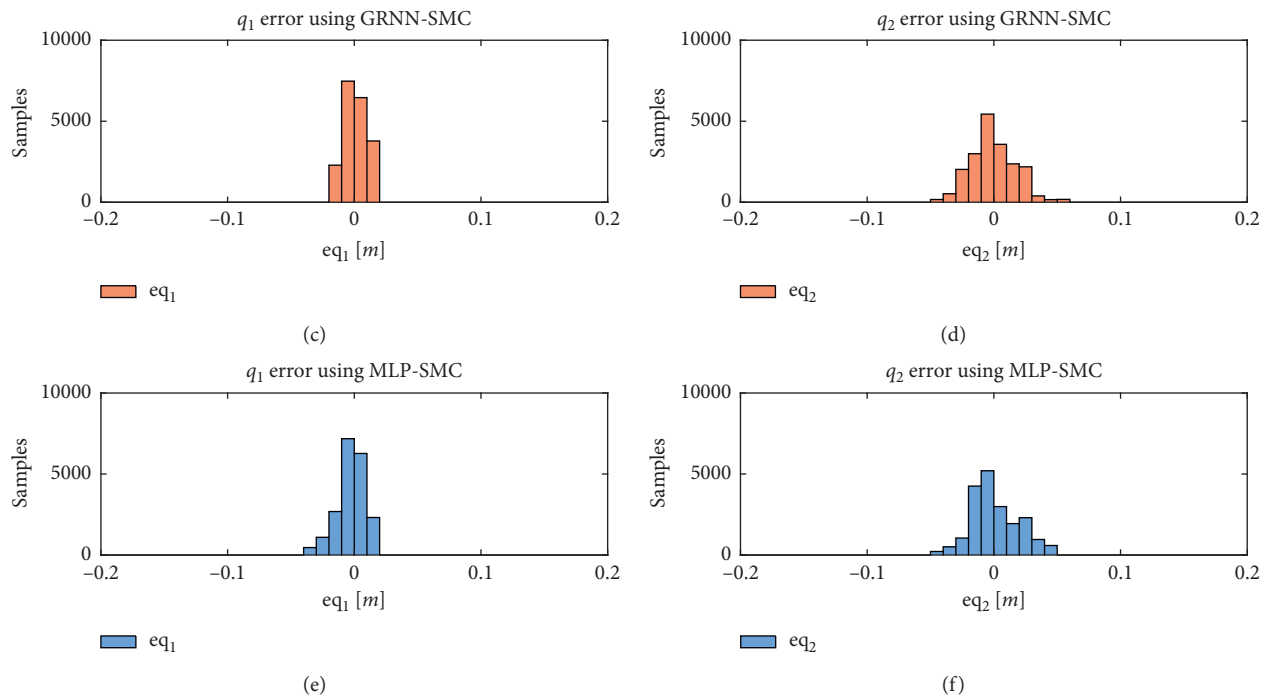

Figure 13: Distribution of the errors obtained along the experiment. (a-b) The error distribution using the sat(.) function. (c-d) The error distribution using the tanh(.) function. (e-f) The error distribution using the $\sin(\mathrm{tg}^{-1}(.))$ function.

Table 2: Performance indexes IAE and the ITAE of different controllers based on adaptive GRNN-SMC using sat(.), tanh(.), and $\sin(\mathrm{tg}^{-1}(.))$.

Controller	IAE	ITAE
sat(.)	482.6992	$1.2067e+04$
tanh(.)	424.7610	$1.0619e+04$
$\sin(\mathrm{tg}^{-1}(.))$	442.6008	$1.1065e+04$

(see equation (48) where T is the total time of the experiments). These indicators are applied on the proposed controllers based on using only $\sin(\mathrm{tg}^{-1}(.))$ function, where the indicators show that the GRNN-SMC controller gets the smallest error as a result:

$$\begin{aligned} \mathrm{IAE} &= \int_0^T \left(\left|e_{q1}\right| + \left|e_{q2}\right|\right) \mathrm{d}t, \\ \mathrm{ITAE} &= \int_0^T t\left(\left|e_{q1}\right| + \left|e_{q2}\right|\right) \mathrm{d}t. \end{aligned} \tag{48}$$

4.3. Dynamical Comparison between Functions. In the second set of the experiment, a dynamical comparison between functions sat(.), tanh(.), and $\sin(\mathrm{tg}^{-1}(.))$ was made. Figure 9 shows the trajectories performed by the robot arm using each one of the control strategies. Figure 10 shows the reference (dashed line) and trajectory followed (solid line), being the maximum error during the initial time. Figure 11 shows the square norm of the control errors generated by each saturation type applied in the control law. In this figure, it is appreciated that two last strategies have got similar errors. In Figure 12, the control actions based on the adaptive GRNN-SMC controller are shown. Both signals are polluted by the chattering effect, but in a percentage of about 10 with respect to the maximum value of the control signal, higher values are dangerous for the electromechanical systems. Figure 13 presents the distribution of the errors obtained along with the experiment. Figures 13(a) and 13(b) show the error distribution using the sat(.) function. Figures 13(c) and 13(d) present the error distribution using the tanh(.) function. Figures 13(e) and 13(f) show the error distribution using the $\sin(\mathrm{tg}^{-1}(.))$ function. Finally, in Table 2, the performance indicators IAE and ITAE are presented. These indicators are applied on alternative controllers based on adaptive GRNN-SMC using different saturation types sat(.), tanh(.), and $\sin(\mathrm{tg}^{-1}(.))$. The denoted indicators show similar results as saturation functions in control. Thus, such functions could be used in different applications when a variable must not exceed a certain maximum value.

Based on these results, the viability of the proposed controller is demonstrated. The good results obtained, despite the nonlinearities and uncertainties of the model, together with the variations in the dynamics of the robot, show the level of robustness of the proposed GRNN-SMC controller. In addition, the stability of the closed loop system was demonstrated analytically and the adjustment laws were obtained using Lyapunov's theory. Another interesting observation is that the selection of the neural net structure of the estimator can improve the accuracy of the proposed control.

In this proposal for intelligent control, it can be considered as a general solution for the control of nonlinear systems. Its uses can be highlighting in robotic systems, in situations where the dynamics are variable or when there are uncertainties associated with the dynamic model.

5. Conclusions

This work presents a saturated control of two techniques using neural networks based on the classical $\mathrm{sat}(.)$,$\tanh(.)$, and $\sin(\mathrm{tg}^{-1}(.))$ functions and also provides the stability proof for a saturated control applied to a robot manipulator.

Comparative experiments of all these control variants have been performed on a standard industrial SCARA manipulator; in all cases, the proposed control gets satisfactory results; in the third case, it has an average error and can be used as an alternative of $\tanh(.)$ or $\mathrm{sat}(.)$ function as saturated control.

The feasibility of applying an uncertainty estimator with a control based on sliding mode control, including its asymptotic stability, was also demonstrated.

The experiments showed that the trajectory followed by the manipulator can be controlled precisely by the use of the proposed method and, at the same time, guarantee the asymptotical convergence.

Data Availability

The MATLAB code and sampled data used to support the findings of this study are available from the corresponding author upon request.

Conflicts of Interest

The authors declare that there are no conflicts of interest regarding the publication of this paper.

Acknowledgments

This work was partially funded by the following Argentine institutions: the National Council of Scientific and Technological Research (CONICET) and Universidad Nacional de San Juan (UNSJ).

References

[1] E. Özgür and Y. Mezouar, "Kinematic modeling and control of a robot arm using unit dual quaternions," *Robotics and Autonomous Systems*, vol. 77, pp. 66–73, 2016.

[2] Y. Pititeeraphab, P. Choitkunnan, N. Thongpance, K. Kullathum, and C. Pintavirooj, "Robot-arm control system using leap motion controller," in *Proceedings of the 2016 International Conference on Biomedical Engineering (BME-HUST) IEEE*, Hanoi, Vietnam, 2016.

[3] Y. Pan, H. Wang, X. Li, and H. Yu, "Adaptive command-filtered backstepping control of robot arms with compliant actuators," *IEEE Transactions on Control Systems Technology*, vol. 26, no. 3, pp. 1149–1156, 2017.

[4] F. Capraro, F. G. Rossomando, C. Soria, and G. Scaglia, "Cascade sliding control for trajectory tracking of a nonholonomic mobile robot with adaptive neural compensator," *Mathematical Problems in Engineering*, vol. 2017, Article ID 8501098, 13 pages, 2017.

[5] A. Rosales, G. Scaglia, V. Mut, and F. D. Sciascio, "Controller designed by means of numeric methods for a benchmark problem: RTAC (rotational translational actuator)," in *Proceedings of the Electronics, Robotics and Automotive Mechanics Conference (CERMA'06)*, pp. 97–104, Cuernavaca, Mexico, 2006.

[6] G. Scaglia, V. Mut, A. Rosales, and O. Quintero, "Tracking control of a mobile robot using linear interpolation,"in *Proceedings of the IMAACA07*, Buenos Aires, Argentina, vol. 1, pp. 11–15, 2007.

[7] G. Scaglia, "Tracking control design in nonlinear multivariable systems: robotic applications," *Mathematical Problems in Engineering*, vol. 2019, Article ID 8643515, 15 pages, 2019.

[8] Q. Han, H. Zhang, and J. Liu, "Nonlinear dynamics of controlled synchronizations of manipulator system," *Mathematical Problems in Engineering*, vol. 2014, Article ID 691464, 9 pages, 2014.

[9] C. W. De Silva, *Intelligent Control: Fuzzy Logic Applications*, CRC Press, Boca Raton, FL, USA, 2018.

[10] R. Guo, "Projective synchronization of a class of chaotic systems by dynamic feedback control method," *Nonlinear Dynamics*, vol. 90, no. 1, pp. 53–64, 2017.

[11] Z. Yan, Y. Song, and J. H. Park, "Quantitative mean square exponential stability and stabilization of stochastic systems with Markovian switching," *Journal of the Franklin Institute*, vol. 355, no. 8, pp. 3438–3454, 2018.

[12] Z. Yan, J. H. Park, and W. Zhang, "A unified framework for asymptotic and transient behavior of linear stochastic systems," *Applied Mathematics and Computation*, vol. 325, pp. 31–40, 2018.

[13] Z. Yan, W. Zhang, and G. Zhang, "Finite-time stability and stabilization of Itô stochastic systems with Markovian switching: mode-dependent parameter approach," *IEEE Transactions on Automatic Control*, vol. 60, no. 9, pp. 2428–2433, 2014.

[14] A. Coronel-Escamilla, F. Torres, J. F. Gómez-Aguilar, R. F. Escobar-Jiménez, and G. V. Guerrero-Ramírez, "On the trajectory tracking control for an SCARA robot manipulator in a fractional model driven by induction motors with PSO tuning," *Multibody System Dynamics*, vol. 43, no. 3, pp. 257–277, 2018.

[15] J. Wu, D. Wang, and L. Wang, "A control strategy of a two degrees-of-freedom heavy duty parallel manipulator," *Journal of Dynamic Systems, Measurement, and Control*, vol. 137, no. 6, Article ID 061007, 2015.

[16] A. Remazeilles, A. Fernandez Iribar, and A. Dominguez Garcia, "Inverse kinematics methods for flexible arm control,"in *Proceedings of the Soft and Stiffness-controllable Robotics Solutions for Minimally Invasive Surgery: The STIFF-LOP Approach*, Pisa, Italy, p. 151, 2018..

[17] H. Wang, "Adaptive control of robot manipulators with uncertain kinematics and dynamics," *IEEE Transactions on Automatic Control*, vol. 62, no. 2, pp. 948–954, 2017.

[18] J. Baek, M. Jin, and S. Han, "A new adaptive sliding-mode control scheme for application to robot manipulators," *IEEE Transactions on Industrial Electronics*, vol. 63, no. 6, pp. 3628–3637, 2016.

[19] S. Fateh and M. M. Fateh, "Adaptive fuzzy control of robot manipulators with asymptotic tracking performance," *Journal of Control, Automation and Electrical Systems*, vol. 31, no. 1, pp. 52–61, 2020.

[20] M. Tong, W. Lin, X. Huo, Z. Jin, and C. Miao, "A model-free fuzzy adaptive trajectory tracking control algorithm based on dynamic surface control," *International Journal of Advanced Robotic Systems*, vol. 17, no. 1, 2020.

[21] A. Mohammadi, M. Tavakoli, H. J. Marquez, and F. Hashemzadeh, "Nonlinear disturbance observer design for robotic manipulators," *Control Engineering Practice*, vol. 21, no. 3, pp. 253–267, 2013.

[22] M. G. Feemster, Y. Fang, and D. M. Dawson, "Disturbance rejection for a magnetic levitation system," *IEEE/ASME Transactions on Mechatronics*, vol. 11, no. 6, pp. 709–717, 2006.

[23] J. Na, B. Jing, Y. Huang, G. Gao, and C. Zhang, "Unknown system dynamics estimator for motion control of nonlinear robotic systems," *IEEE Transactions on Industrial Electronics*, vol. 67, no. 5, pp. 3850–3859, 2019.

[24] D. Xie, S. Wang, and Y. Wang, "Trajectory tracking control of differential drive mobile robot based on improved kinematics controller algorithm," in *Proceedings of the 2018 Chinese Automation Congress (CAC)*, pp. 2675–2680, Xi'an, China, 2018.

[25] R. Bussola, G. Legnani, M. Callegari, G. Palmieri, and M.-C. Palpacelli, "Simulation assessment of the performance of a redundant SCARA," *Robotics*, vol. 8, no. 2, p. 45, 2019.

[26] E. O. Freire, F. G. Rossomando, and C. M. Soria, "Self-tuning of a neuro-adaptive PID controller for a SCARA robot based on neural network," *IEEE Latin America Transactions*, vol. 16, no. 5, pp. 1364–1374, 2018.

[27] R. Sharma, V. Kumar, P. Gaur, and A. P. Mittal, "An adaptive PID like controller using mix locally recurrent neural network for robotic manipulator with variable payload," *ISA Transactions*, vol. 62, pp. 258–267, 2016.

[28] M. A. Al-Khedher and M. S. Alshamasin, "SCARA robot control using neural networks," in *Proceedings of the 2012 4th International Conference on Intelligent and Advanced Systems (ICIAS2012)*, pp. 126–130, Kuala Lumpur, Malaysia, 2012.

[29] F. G. Rossomando and C. M. Soria, "Discrete-time sliding mode neuro-adaptive controller for SCARA robot arm," *Neural Computing and Applications*, vol. 28, no. 12, pp. 3837–3850, 2017.

[30] P. Jha and B. B. Biswal, "A neural network approach for inverse kinematic of a SCARA manipulator," *IAES International Journal of Robotics and Automation*, vol. 3, no. 1, p. 52, 2014.

[31] S. Yi and J. Zhai, "Adaptive second-order fast nonsingular terminal sliding mode control for robotic manipulators," *ISA Transactions*, vol. 90, pp. 41–51, 2019.

[32] A. D. Rosas, V. K. Velazquez, F. L. Olivares, T. A. Camacho, and I. Williams, "Methodology to assess quality of estimated disturbances in active disturbance rejection control structure for mechanical system," *ISA Transactions*, vol. 70, pp. 238–247, 2017.

[33] R. Kelly, V. Santibáñez, and A. Loria, *Control of Robot Manipulators in Joint Space*, Springer Science and Business Media, Leipzig, Alemania, 2016.

[34] S. Samarasinghe, *Neural Networks for Applied Sciences and Engineering: From Fundamentals to Complex Pattern Recognition*, Taylor & Francis Group, Boca Raton, FL, USA, 2016.

[35] Al-MahasnehJ. Ahmad et al., "Applications of general regression neural networks in dynamic systems," *Digital Systems*, vol. 133, 2018.

[36] M. Hou, G. Duan, and M. Guo, "New versions of Barbalat's lemma with applications," *Journal of Control Theory and Applications*, vol. 8, no. 4, pp. 545–547, 2010.

Hindawi
Mathematical Problems in Engineering
Volume 2020, Article ID 8514049, 9 pages
https://doi.org/10.1155/2020/8514049

Research Article

Actuator Fault-Tolerant Control Applied to Three-Tank System

Mondher Amor, Taoufik Ladhari, Salim Hadj Said, and Faouzi M'Sahli

Industrial Systems Study and Renewable Energy Unit, National Engineering School of Monastir, University of Monastir, Ibn El Jazzar Street, Skanes 5019, Monastir, Tunisia

Correspondence should be addressed to Mondher Amor; mondheramor@yahoo.fr

Received 23 March 2020; Accepted 27 April 2020; Published 18 May 2020

Guest Editor: Rongwei Guo

This paper focuses on the application of an active fault-tolerant control (AFTC) to a real nonlinear system using analytic redundancy in case of actuator faults. This approach is composed of the fault detection, isolation, and estimation (FDIE) module and a control compensation module. A high-gain observer (HGO) is used for FDIE; a new control law is then reconstructed by the addition of the estimated actuator fault magnitude to the nominal control law. Experimental results highlight the performance of the proposed approach when it is applied to the hydrographic plant.

1. Introduction

The modern technical process relies on an advanced control system to meet the increased requirement of safety and reliability. The probability of fault occurrence increases with the complexity of the industrial process. For safety-critical systems, such as aircraft, nuclear, chemical, and power production plants, the control system must include automatic supervision of process control to detect and isolate faults as early as possible and to tolerate some component malfunctions [1–4]. In such systems, since the consequence of a minor fault can be catastrophic, the demand for reliability, safety, and fault tolerance is generally high. These types of control systems are often known as the fault-tolerant control (FTC). FTC can be performed by passive methods or by active methods. Passive methods use a robust control technique to ensure that a closed-loop system remains insensitive to certain faults. However, in active methods, a new control system is redesigned by using the desired performance in the faulty-free system.

An AFTC has two subsystems: a module for fault detection, isolation, and estimation (FDIE) and another one for the reconfigurable control (RC). In this paper, the proposed approach is based on the online fault detection, isolation, and estimation of actuator faults using a high-gain observer. Then, a computation of a new control law different from the nominal one is performed in order to compensate for this fault effect and to maintain the three-tank system outputs to their nominal values.

The three-tank plant is a good prototype of many applications in industrial processes, such as water treatment, food industry, chemical and petrochemical plants, and oil and gas systems [1–4]. It is used in water conditioning systems, which provide the user with an abundant supply of luxuriously conditioned water, and in the craft brewing system. This benchmark system represents a rich ground to serve as a test environment for linear and nonlinear control, fault detection and isolation (FDI), and fault-tolerant control (FTC).

The fault detection and isolation is an important research area in system control due to the improvements that it can be reached in terms of safety and reliability of the process. To detect and isolate actuator and component faults around the operating point, authors have proposed in [5] a decoupled linear observer. Many model-based approaches are applied to the hydrographic system for fault detection and estimation [6, 7]. More recently, a bank of observers to detect and isolate actuator and sensor faults around multiple operating points is suggested in [8]. In our previous work [9], we have proposed a high-gain observer to estimate the

actuator fault magnitude, and eventual hardware implementation is achieved.

In the FTC field, despite several methods have been already applied to the three-tank system, few fault accommodation techniques have been considered. Among the model-based approaches that have been applied to the three-tank system, we find fuzzy approaches for fault accommodation [10] and flatness-based active fault-tolerant control [11, 12]. In [13], authors have dealt with FTC for actuator faults; they have proposed an online estimation of an eventual actuator fault and the addition of a new control law for the three-tank system. Other researchers have focused on fault diagnosis and accommodation for sensor and actuator faults, and they have proposed an analytical redundancy method to solve the drawbacks of the hardware redundancy such as cost and space [14]. All these previous works have developed FTC schemes for the linearized three-tank model; this means that their approaches are valid only around the operating point. To overcome previous mis-achievements, this paper focuses on the application of the actuator tolerant-fault control using a nonlinear MIMO model of the three-tank system. The proposed approach is based on the online actuator fault detection using a high-gain observer. The estimates are used in a new control law, which can fastly react to the failure by adding the recovered fault magnitude. The main contribution of this paper compared to previous works is to potentially mitigate the fault-detection delay as well as the fault-compensation time after the fault occurrence.

The remainder of the paper is organized as follows: in Section 2, we represent the three-tank process which is used to illustrate the performance of the proposed AFTC and its dynamical model. The fault detection and estimation module (FDE) and the proposed observer are detailed in Section 3. Section 4 is devoted to the proposed AFTC. Finally, the experimental results and discussion are reported in Section 5 before an illustration of the conclusion remarks.

2. Three-Tank System Presentation

2.1. Plant Description. The hydrographical process described in [15] consists of 3 columns T_1, T_2, and T_3, with the same section S, coupled serially by transfer valves and which can be drained into a reservoir by leakage valves. These leakage valves denoted V_{l1}, V_{l2}, V_{l3}, and V_e have identical effective sections S_n. Two rotary valves V_{t12} and V_{t23} can be used to change the channel section and therefore to change the flow characteristics between the columns. Each leakage valve can be used as a manually adjustable disturbance.

Tanks 1 and 3 are supplied with fluid via 2 pumps of maximum flow $Q_{\max}$. The maximum flow rate of the pump ($6.66 \times 10^{-5}\,\mathrm{m}^3/\mathrm{s}$) is reached when a voltage of 12 V is applied to the pump. Each column is equipped with a pressure sensor giving the liquid level in the tank. The sensors are calibrated to provide output signals ranging from 0 to 5 V corresponding to a change in water level from 0 to 100 cm for each column. The experimental system shown in Figure 1 is equipped with sensors and actuators that communicate via an acquisition card and a computer.

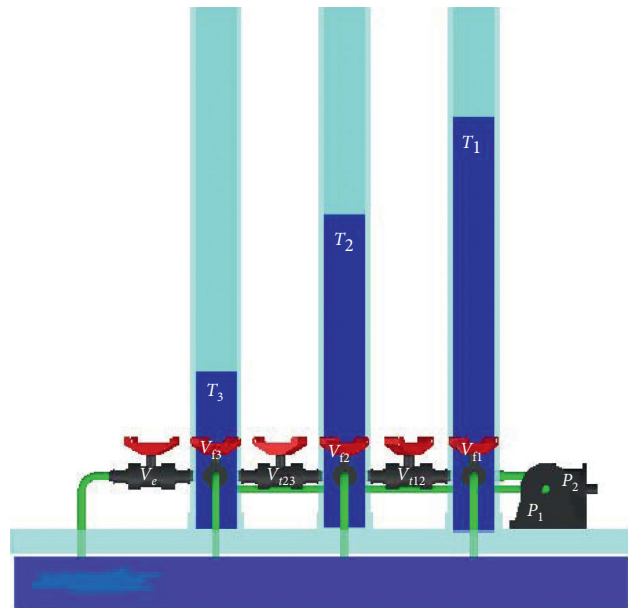

Figure 1: Full structure of the computer design plant.

2.2. Mathematical Model. The state equations are obtained by writing that the variation of the volume of water in tank i ($i = 1$: 3) is equal to the sum of the inflows minus the sum of the outflows. Using the mass equations (flow equilibrium), the system can be easily represented by the following equation:

$$\dot{V}_i = S_i \cdot \frac{\mathrm{d}h_i}{\mathrm{d}t} = \sum Q_{\mathrm{in},i} - \sum Q_{\mathrm{out},i}, \tag{1}$$

where $\sum Q_{\mathrm{in},i}$ and $\sum Q_{\mathrm{out},i}$ represent the total liquid inflows and outflows in tank i, respectively. Then, the mathematical model is specified by the following mass balance equations:

$$\begin{cases} \dot{h}_1(t) = \dfrac{1}{S}\left(Q_1(t) - Q_{12}(t) - Q_{l1}(t)\right), \\ \dot{h}_2(t) = \dfrac{1}{S}\left(Q_{12}(t) - Q_{23}(t) - Q_{l2}(t)\right), \\ \dot{h}_3(t) = \dfrac{1}{S}\left(Q_2(t) + Q_{23}(t) - Q_e(t) - Q_{l3}(t)\right), \end{cases} \tag{2}$$

where t represents the time, h_1, h_2, and h_3 represent the liquid levels in each tank, S represents the cross section of the tanks, Q_1 and Q_2 designate, respectively, the flow rates of pumps P_1 and P_2, Q_{ij} denote the flow rates between tank T_i and T_j, and Q_{li} represents the leakage flow of the corresponding tank when its leak valve is open.

The flows Q_{ij} and Q_e in (2) are given by Torricelli's law as follows:

$$\begin{aligned} Q_{ij}(t) &= a_{zi} S_n \operatorname{sgn}\left(h_i - h_j\right)\sqrt{2g\left|h_i - h_j\right|}, \\ Q_e(t) &= a_{z3} S_n \sqrt{2gh_3}, \end{aligned} \tag{3}$$

where a_{zi} is the outflow coefficient, $\operatorname{sgn}(\cdot)$ is the sign of the argument, and g is the acceleration of gravity. Consequently, the nonlinear 3T model is given as follows:

$$\begin{cases} \dfrac{dh_1}{dt} = -c_1 \operatorname{sign}(h_1 - h_2)\sqrt{|h_1 - h_2|} + \dfrac{Q_1}{S}, \\ \dfrac{dh_2}{dt} = c_1 \operatorname{sign}(h_1 - h_2)\sqrt{|h_1 - h_2|} - c_2 \operatorname{sign}(h_2 - h_3)\sqrt{|h_2 - h_3|}, \\ \dfrac{dh_3}{dt} = c_2 \operatorname{sign}(h_2 - h_3)\sqrt{|h_2 - h_3|} - c_3\sqrt{h_3} + \dfrac{Q_2}{S}, \end{cases} \tag{4}$$

where c_i represents the system parameter given by

$$c_i = \frac{1}{S} a_{zi} S_n \sqrt{2g}; \quad i = 1, \ldots, 3. \tag{5}$$

2.3. Three-Tank System Fault Representation. The three-tank laboratory system is considered as a rich ground to serve as a test environment for the FTC. It is used as a benchmark system that can be affected by various additive and/or multiplicative actuator faults.

An actuator fault can be represented by

$$u_i^f(k) = \alpha_i u_i(k) + u_{i0}, \quad i = 1, 2, \tag{6}$$

where u_i^f and u_i represent the faulty and the normal control action of the ith pump, respectively.

The constant offset is denoted by u_{i0}, and $0 \le \alpha_i \le 1$ denotes a gain degradation of the ith actuator.

In this paper, we have focused only on a partial reduction in actuator efficiency. However, this method fails in the case of complete loss of an actuator, and hardware redundancy is needed.

3. Fault Detection and Estimation (FDE)

3.1. Problem Statement. It is important to be able to carry out the fault detection and estimation before the faults induce a catastrophic effect on the system performance. The observer-based approach is used to generate both residual signals corresponding to the difference between measured and estimated signals and the estimated actuator faults. However, the resultant residual will be equal to zero in case of the unfaulty system. The residual signal is compared to a fixed threshold well chosen to avoid false alarms. To compensate for actuator faults, authors have used in the previous work [9] a high-gain observer whose role is to estimate the actuator fault magnitude which is added to the nominal control law as it is shown in Figure 2.

3.2. Observer Design

3.2.1. Basic Concepts. Consider the MIMO system of the form

$$\begin{cases} \dot{x} = f(u, x) + \overline{\varepsilon}(t), \\ y = \overline{C}x = x^1, \end{cases} \tag{7}$$

with $x = \begin{pmatrix} x^1 \\ x^2 \\ \vdots \\ x^q \end{pmatrix}$; $f(u, x) = \begin{pmatrix} f^1(u, x^1, x^2) \\ f^2(u, x^1, x^2, x^3) \\ \vdots \\ f^{q-1}(u, x) \\ f^q(u, x) \end{pmatrix}$; $\overline{\varepsilon}(t) = \begin{pmatrix} 0 \\ \vdots \\ 0 \\ \varepsilon(t) \end{pmatrix}$, $\varepsilon = \begin{pmatrix} \varepsilon_1 \\ \vdots \\ \varepsilon_{n_q} \end{pmatrix}$; and $\overline{C} = [I_{n_1}, 0_{n_1 \times n_2}, 0_{n_1 \times n_3}, \ldots, 0_{n_1 \times nq}]$, where the state $x \in \mathfrak{R}^n$ and $x^k \in \mathfrak{R}^{n_k}$, $k = 1, \ldots, q$ and $p = n_1 \ge n_2 \ge \cdots \ge n_q$, $\sum_{k=1}^{q} n_k = n$; the input $u(t) \in U$ is a compact subset of $\mathfrak{R}^s$; $f(u, x) \in \mathfrak{R}^n$ with $f^k(u, x) \in \mathfrak{R}^{n_k}$; and $\overline{\varepsilon}(t) \in \mathfrak{R}^n$, where $\varepsilon(t) \in \mathfrak{R}^{n_q}$ with each ε_i, $i = 1, \ldots, n_q$, being an unknown bounded real-valued function which may depend on x, u, uncertain parameters.

3.2.2. Observer Design. Consider the following change of coordinates:

$$\Phi\colon \mathfrak{R}^n \longrightarrow \mathfrak{R}^{n_{1q}},$$

$$x = \begin{pmatrix} x^1 \\ x^2 \\ \vdots \\ x^q \end{pmatrix} \longrightarrow z = \begin{pmatrix} z^1 \\ z^2 \\ \vdots \\ z^q \end{pmatrix};$$

$$\Phi(u, x) = \begin{pmatrix} x^1 \\ f^1(u, x^1, x^2) \\ \dfrac{\partial f^1}{\partial x^2}(u, x^1, x^2) f^2(u, x^1, x^2, x^3) \\ \vdots \\ \left(\displaystyle\prod_{k=1}^{q-2} \frac{\partial f^k}{\partial x^{k+1}}(u, x)\right) f^{q-1}(u, x) \end{pmatrix}, \tag{8}$$

where $z^k \in \mathfrak{R}^{n_1}$, $k = 1, \ldots, q$.

Let us introduce the following notations:

$$\Lambda(u, x) = \operatorname{diag}\left(I_{n_1}, \frac{\partial f^1}{\partial x^2}(u, x), \frac{\partial f^1}{\partial x^2}(u, x) \frac{\partial f^2}{\partial x^3}(u, x), \ldots, \prod_{k=1}^{q-1} \frac{\partial f^k}{\partial x^{k+1}}(u, x) \right). \tag{9}$$

According to Farza et al. [16], the transformation $\Phi(\cdot)$ puts system (6) under the following form:

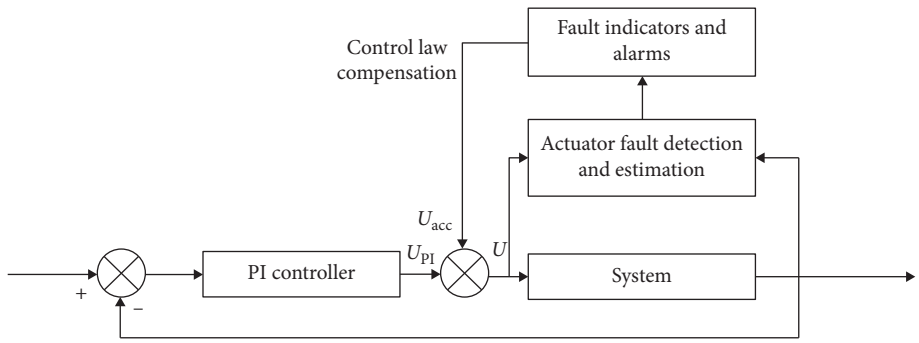

Figure 2: Synoptic scheme of FDE applied to 3TS.

$$\begin{cases} \dot{z} = Az + \varphi(u,z) + \dfrac{\partial \Phi}{\partial x}(u,x)\bar{\varepsilon}(t), \\ y = Cz = z^1, \end{cases} \tag{10}$$

where $\varphi(u,z)$ has a triangular structure:

$$\varphi(u,z) = \begin{pmatrix} \varphi^1(u,z^1) \\ \varphi^2(u,z^1,z^2) \\ \vdots \\ \varphi^k(u,z^1,\ldots,z^k) \\ \vdots \\ \varphi^q(u,z) \end{pmatrix}, \tag{11}$$

with $\varphi^k(u,z) \in \mathfrak{R}^{n_1}$, $k = 1,\ldots,q$, and $C = [I_{n_1}, 0_{n_1},\ldots,0_{n_1}]$ is the $n_1 \times n_{1q}$ matrix with 0_{n_1} denoting the $n_1 \times n_1$ null matrix.

3.2.3. Observer Synthesis. As in many works related to high-gain observer synthesis, the observer design requires the following assumption [15].

A1: each function $f^k(u,x)$, $k = 1,\ldots,q-1$ satisfies the following rank condition.

Rank $((\partial f^k/\partial x^{k+1})(u,x)) = n_{k+1}$, $\forall x \in \mathbb{R}^n$; $\forall u \in U$; moreover, $\exists \alpha, \beta > 0$ such that, for all $k \in \{1,\ldots, q-1\}$, $\forall x \in \mathbb{R}^n$; $\forall u \in U$,

$$\alpha^2 I_{nk+1} \le \left(\frac{\partial f^k}{\partial x^{k+1}}(u,x)\right)^T \frac{\partial f^k}{\partial x^{k+1}}(u,x) \le \beta^2 I_{nk+1}, \tag{12}$$

where I_{nk+1} is the $n_{k+1} \times n_{k+1}$ identity matrix.

A2: the functions $\varphi^i(\cdot)$ for $i \in [1,q]$ are globally Lipschitz with respect to x uniformly in u, i.e., $\exists L > 0$, such that the following inequality holds for $i \in [1,q]$ and x and $\overline{x} \in \mathbb{R}^n$:

$$\left\|\varphi^i(u,x) - \varphi^i(u,\overline{x})\right\| \le L\|x - \overline{x}\|. \tag{13}$$

The candidate observer for system (7) can be specified as

$$\begin{aligned} \dot{\hat{z}} = {} & Az + \varphi(u,\hat{z}) - \theta\Delta_\theta^{-1}S^{-1}k(\hat{z}) - \frac{\partial \varphi}{\partial x}(u,\Phi^c(\hat{z}))\cdot \\ & \cdot\left(\Lambda^+(u,\Phi^c(\hat{z})) - \left(\frac{\partial \Phi}{\partial x}(u,\Phi^c(\hat{z}))\right)^+\right)\theta\Delta_\theta^{-1}S^{-1}k(\tilde{z}^1), \end{aligned} \tag{14}$$

where $\hat{z} = \begin{pmatrix} \hat{z}^1 \\ \hat{z}^2 \\ \vdots \\ \hat{z}^q \end{pmatrix} \in \mathfrak{R}^{n_1 q}$, $\hat{z}^k \in \mathfrak{R}^{n_1}$, $k = 1,\ldots,q$;S and Δ_θ are given by $\Delta_\theta = \operatorname{diag}[I_{n_1}, (1/\theta)I_{n_1},\ldots,(1/\theta^{q-1})I_{n_1}]$, where $\theta > 0$ is a real number.

S is the unique solution of the algebraic Lyapunov equation $S + A^T S + SA - C^T C = 0$, where A and C are, respectively, given by

$$\begin{aligned} A &= \begin{bmatrix} 0 & I_{n_1} & 0 & . & 0 \\ : & . & I_{n_1} & \ddots & . \\ 0 & \ddots & . & . & 0 \\ 0 & \ddots & \ddots & . & I_{n_1} \\ 0 & . & . & 0 & 0 \end{bmatrix}; \\ C &= \left[I_{n_1}, 0_{n_1},\ldots,0_{n_1}\right], \\ \tilde{z} &= \hat{z} - z. \end{aligned} \tag{15}$$

The proof of estimation error convergence is detailed in [16].

3.2.4. Observer Equations in the Original Coordinates. The observer (10) can also be given in the original coordinates x as follows:

$$\dot{\hat{x}} = f(u,\hat{x}) - \theta\Lambda^+(u,\hat{x})\Delta_\theta^{-1}S^{-1}k(\tilde{x}^1) \tag{16}$$

where S, C,Δ_θ, and $\Lambda^+(u,x)$ are given above and $\hat{x} = \begin{pmatrix} \hat{x}^1 \\ \hat{x}^2 \\ \vdots \\ \hat{x}^q \end{pmatrix} \in \mathfrak{R}^n$ with $\hat{x}^k \in \mathfrak{R}^{n_k}$, $k = 1,\ldots,q$;u is the input of the system, and $\tilde{x} = \hat{x} - x$.

4. FTC Strategy

The main objective is to establish a closed-loop regulation to track two reference levels. For this reason, two PI controllers are designed. Each one controls one liquid level. In the safety mode, these controllers can successfully accomplish this task. However, in the case of an actuator fault, nominal performances are affected in the best case, and it can lead to instability in the worst case. To avoid such behaviour, we should use the FTC that allows the accommodation of the control law by the addition of the estimated actuator fault magnitude to the nominal control law. As it is shown in Figure 2, the FTC can be divided into two main tasks: the first one is the FDIE detailed in the third paragraph, and the second one concerns the control law reconfiguration. Once the FDIE is performed, the faulty actuator A_i is identified and isolated, and the residual variable R_i, different to zero can be used as a fault indicator or alarm. To reduce the effect of the actuator fault and to maintain the closed-loop performance, the actuator fault estimated previously is added to the nominal control law.

4.1. Design of the FTC System for Actuator Faults. Consider a nonlinear system given by

$$\begin{cases} \dot{x} = f(x) + g \cdot u, \\ y = c \cdot x, \end{cases} \tag{17}$$

where $x = \begin{pmatrix} x^1 \\ x^2 \\ \vdots \\ x^q \end{pmatrix}$ is the state vector.

In case of actuator faults, system (17) has the following form:

$$\begin{cases} \dot{x} = f(x) + g \cdot u + l \cdot u_f, \\ y = c \cdot x. \end{cases} \tag{18}$$

In this work, compensation to the control law for the faulty system is added, and the new control law is given by

$$u_{\text{FTC}} = u + u_{\text{acc}}, \tag{19}$$

where u is the nominal control law and u_{acc} is the accommodation for the control law; system (18) becomes

$$\begin{cases} \dot{x} = f(x) + g \cdot u + g \cdot u_{\text{acc}} + l \cdot u_f, \\ y = c \cdot x, \end{cases} \tag{20}$$

where additional action must be quickly computed such as the system is recovered as soon as possible; then, the following condition is requested:

$$\begin{gathered} g \cdot u_{\text{acc}} + l \cdot u_f = 0; \\ u_{\text{acc}} = -g^+ \cdot l \cdot u_f, \end{gathered} \tag{21}$$

where g^+ is the pseudo-inverse matrix of g and u_f is the fault actuator estimation.

4.2. Application to the Three-Tank System. The mathematic model of hydrographic system (1) can be written in the following form:

$$\begin{cases} \dot{h} = f(h) + g \cdot Q, \\ y = C \cdot h, \end{cases} \tag{22}$$

where $h = \begin{bmatrix} h_1 \\ h_2 \\ h_3 \end{bmatrix}$, $Q = \begin{bmatrix} Q_1 \\ Q_2 \end{bmatrix}$, $g = \begin{bmatrix} 1/S & 0 \\ 0 & 0 \\ 0 & 1/S \end{bmatrix}$, and $f(h) = \begin{bmatrix} -a_1 \operatorname{sgn}(h_1 - h_2)\sqrt{|h_1 - h_2|} \\ a_1 \operatorname{sgn}(h_1 - h_2)\sqrt{|h_1 - h_2|} - a_2 \operatorname{sgn}(h_2 - h_3)\sqrt{|h_2 - h_3|} \\ a_2 \operatorname{sgn}(h_2 - h_3)\sqrt{|h_2 - h_3|} - a_3\sqrt{h_3} \end{bmatrix}$.

When the system is affected by the actuator fault, the mathematical model is given by

$$\begin{cases} \dot{h} = f(h) + g \cdot Q + l \cdot Q_f, \\ y = C \cdot h, \end{cases} \tag{23}$$

where $l = \begin{bmatrix} 1/S & 0 \\ 0 & 0 \\ 0 & 1/S \end{bmatrix}$ and $Q_f = \begin{bmatrix} Q_{f1} & Q_{f2} \end{bmatrix}^T$.

To estimate the actuator fault denoted by Q_{f1} and Q_{f2}, we use the high-gain observer as follows:

$$\dot{\hat{x}} = f(u, \hat{x}) - K_\theta \Lambda^+(u, \hat{x})\left(\tilde{x}^1\right), \tag{24}$$

where

$$\begin{gathered} x = \begin{bmatrix} x^1 & x^2 \end{bmatrix}^T; \\ x^1 = \begin{bmatrix} h_1 & h_2 & h_3 \end{bmatrix}^T; \\ x^2 = \begin{bmatrix} Q_{f1} & Q_{f2} \end{bmatrix}^T; \\ f(u, \hat{x}) = f(\hat{h}) + g \cdot Q + l \cdot \hat{Q}_f, \\ K_\theta = \begin{bmatrix} 2\theta & 0 & 0 & 0 & 0 \\ 0 & 2\theta & 0 & 0 & 0 \\ 0 & 0 & 2\theta & 0 & 0 \\ 0 & 0 & 0 & \theta^2 & 0 \\ 0 & 0 & 0 & 0 & \theta^2 \end{bmatrix}, \\ \Lambda^+(u, \hat{x}) = \begin{bmatrix} 1 & 0 & 0 \\ 0 & 1 & 0 \\ 0 & 0 & 1 \\ S & 0 & 0 \\ 0 & 0 & S \end{bmatrix}, \\ \tilde{x}^1 = \hat{x}^1 - x^1. \end{gathered} \tag{25}$$

To compensate for the fault actuator as mentioned above, a new control law is applied: $Q_{\text{FTC}} = Q + Q_{\text{acc}}$.

The compensated mathematical model is given by

$$\begin{cases} \dot{h} = f(h) + g \cdot Q + g \cdot Q_{\text{acc}} + l \cdot Q_f, \\ y = C \cdot h. \end{cases} \tag{26}$$

To compensate for the fault actuator, accommodation law must verify $Q_{\text{acc}} = -g^+ \cdot l \cdot Q_f$.

Remark 1. A main feature of the framework is given in [16] that the state observation scheme is based on a nonlinear

class of systems, under which it belongs to the model of the three-tank process. We exploit the solid theoretical basis of the HGO approach to estimate not only the state vector but also the actuator fault. Indeed, the standard state vector (composed of the three liquid levels) is extended to both actuator faults (flow rates) so that the order of the system becomes five instead of three. Thereafter, once the new state vector is reconstructed by the HGO, it is easy to derive the estimation of the flow rates from its two last components.

5. FTC Application

To prove the validity of the FTC strategy proposed in Sections 3 and 4, we apply it to the three-tank system described in the Section 2. The aim is to accomplish a closed-loop regulation of two levels h_1 and h_3 in the presence of actuator faults described by the following scenario. An interface card is used to establish the connection, via the USB port, between the control desk using the Matlab/Simulink environment and the three piezoresistive differential pressure sensors as the input and the motor pump drive board as outputs. Each sensor and its conditioner card deliver a voltage varying between 0 and 5 V corresponding, respectively, to a liquid height of 0 to 100 cm. Using the PWM interface in Simulink library, the interface card associated with the dual-full bridge LM298 applies to the 2 pumps a variable voltage from 0 to +12 V, corresponding to a flow rate ranging from 0 to $Q_{\max}$.

The bench test used in this implantation, shown in Figure 3, is in the laboratory "Study of Industrial Systems and Renewable Energies," "ESIER," at the National Engineers School of Monastir, Tunisia.

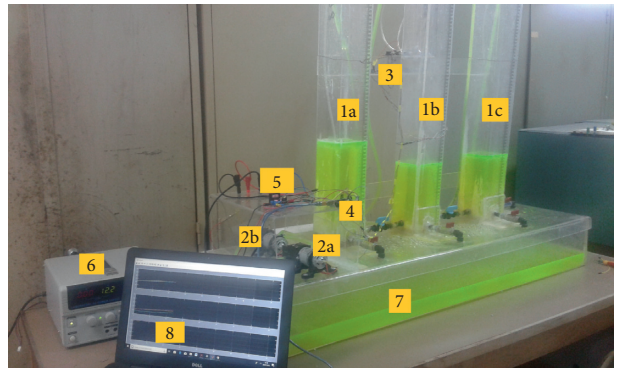

Figure 3: Experimental plant: (1a, 1b, and 1c) 3 cubic tanks; (2a and 2b) 2 DC motor pumps; (3) liquid level sensors; (4) Fio std STM32F10 board; (5) motor driver board; (6) power supply; (7) basin; (8) control desk.

5.1. Fault Scenario

(i) At $t_1 = 300$ s, a constant offset of -4.2 V is added to the applied control law u_1 ($\alpha 1 = 1$, $u_{10} = -4.2$ V)

(ii) At $t_2 = 350$ s, a constant offset of -3.5 V is added to the applied control law u_2 ($\alpha_2 = 1$, $u_{20} = -3.5$ V)

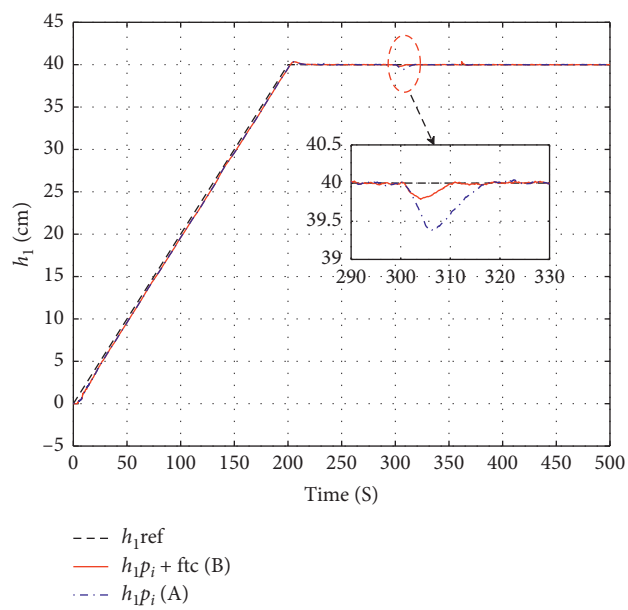

Figure 4: Tracking performance of level 1 in cases A and B.

5.2. Experimental Results. To highlight the proposed AFTC, we compare the tracking performance of the two levels h_1 and h_3 in case A and case B.

In case A, we use a feedback regulation for the two liquid levels based on a PI controller, which means that the process acts without AFTC. In case B, in addition to the PI controller, we use the AFTC module whose role is to add a compensation control law.

As it is shown in Figures 4 and 5, each controlled level decreases, after fault occurrence, to reach a minimum value and then it reaches the desired value after a time delay relative to each case.

The minimum value reached in case A is 39.39 cm for h_1 and 26.41 cm for h_3, while in case B, it reached 39.79 cm and 26.69 cm, respectively, for h_1 and h_3 as it is mentioned in Table 1.

In case A, the PI controller will react to compensate for the fault effect after a time delay of 17.7 s for h_1 and 20.1 s for h_3; However, in case B, the controlled level reached the desired value after 10.6 s and 10.8 s, respectively, for h_1 and h_3.

To evaluate the control performance, we use the mean square error (MSE) criterion defined by

$$\mathrm{MSE} = \frac{1}{n}\sum_{k=1}^{n}\left(y_{\mathrm{ref}}(k) - y(k)\right)^2, \tag{27}$$

where n is the number of measurements, $y_{\mathrm{ref}}(k)$ is the desired output, and $y(k)$ is the system output. The computation of the MSE for outputs y_1 and y_3 in cases A and B is given by Table 1.

As it is shown in Table 1, the MSE of the proposed AFTC approach is smaller than case A when the PI controller acts only to compensate for the actuator fault.

It can be easily seen in Table 1 that the fault detection time t_d in case B is smaller than case A for both liquid levels.

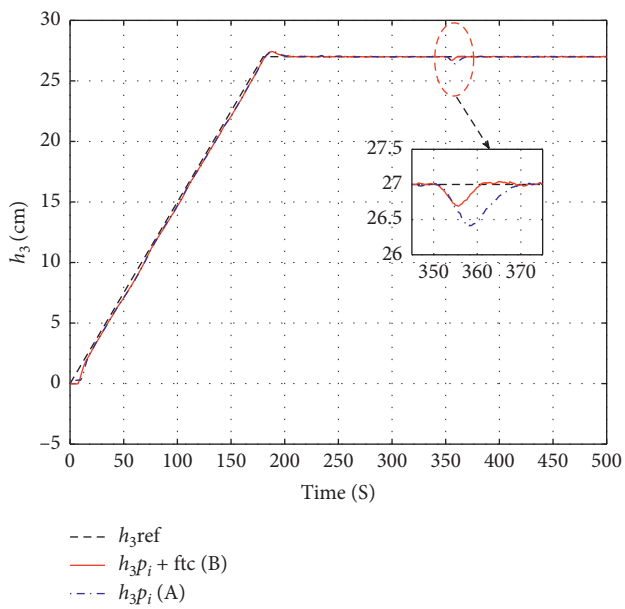

Figure 5: Tracking performance of level 3 in cases A and B.

Table 1: Tracking performance comparison.

	Case A (without AFTC)						Case B (with AFTC)					
h_1	h_{1n} 40 cm	$h_{1\min}$ 39.39 cm	t_f 300 s	t_d 306.5	t_{comp} 317.7 s	MSE 0.0873	h_{1n} 40 cm	$h_{1\min}$ 39.79 cm	t_f 300 s	t_d 303.5	t_{comp} 310.6 s	MSE 0.0824
h_3	h_{3n} 27 cm	$h_{3\min}$ 26.41 cm	t_f 350 s	t_d 358	t_{comp} 370.1 s	MSE 0.0614	h_{3n} 27 cm	$h_{3\min}$ 26.69 cm	t_f 350 s	t_d 355.7	t_{comp} 360.8 s	MSE 0.0549

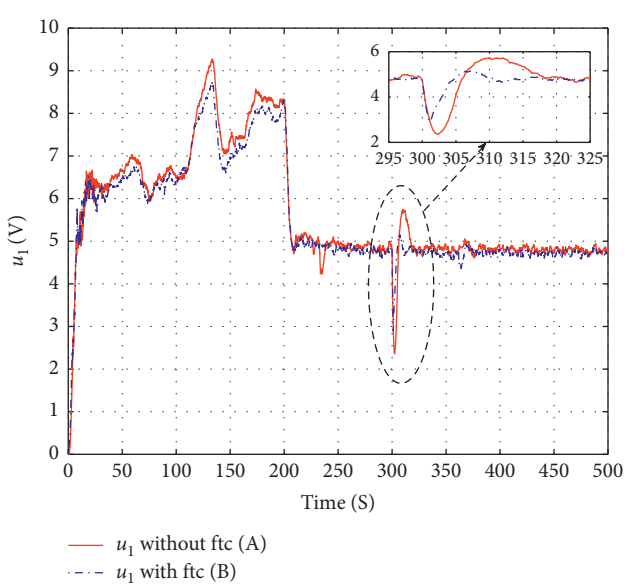

Figure 6: The control law applied to pump 1 in cases A and B.

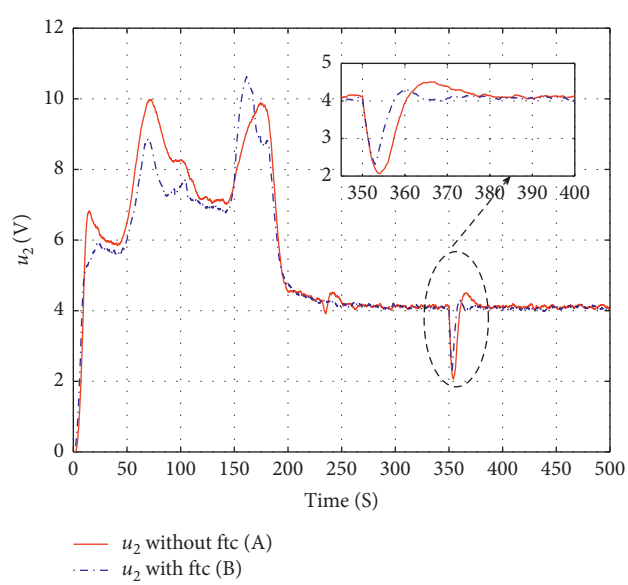

Figure 7: The control law applied to pump 2 in cases A and B.

Compared to the work given in [14], the proposed AFTC has significant merit when comparing the fault detection time t_d which decreases from 16 s to 3.3 s.

In Figures 6 and 7, the control laws applied to motor pumps increase slowly after fault occurrence in case A, but in case B, the control law increases quicker and enables the fast fault compensation with a smaller overshoot.

In Figures 8 and 9, the control law generated by the PI controller in case A increases suddenly after fault occurrence in order to compensate the actuator degradation. But, in case

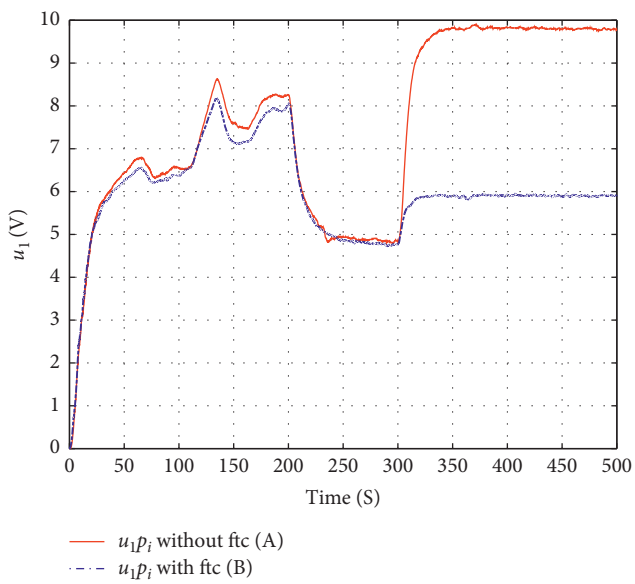

Figure 8: The PI control law applied to pump 1 in cases A and B.

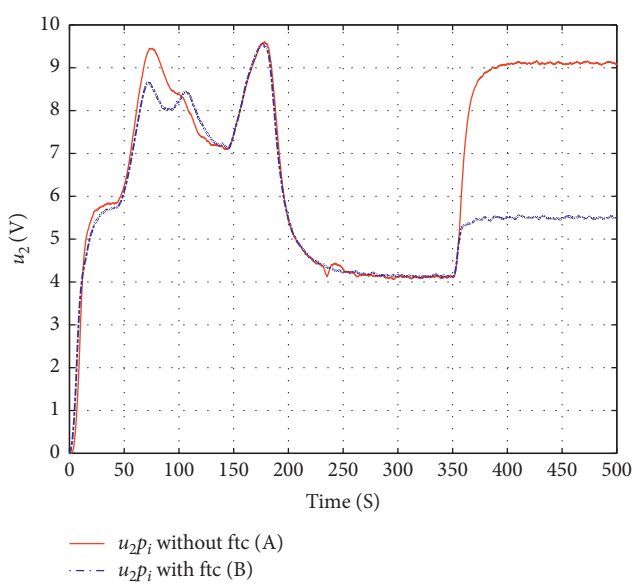

Figure 9: The PI control law applied to pump 2 in cases A and B.

B, the generated PI controller signal is little greater than the nominal control law (fault-free case) because of the estimated actuator fault magnitude injection.

In this experimental task, the operating point is well chosen so that the PI controller can compensate for the fault effect. For this same operating point and fault magnitude, the proposed approach AFTC in case B can compensate easily for the actuator fault. This is another argument that highlights the proposed AFTC.

6. Conclusion

In this paper, a high-gain observer is used to estimate the actuator fault magnitude applied to a three-tank system. In the faulty case, the estimated fault is added to the control law in order to compensate for the fault effect as quickly as possible. Compared to the faulty outputs with a classic PI controller, experimental results show that the compensated output behaviour is closer to the fault-free outputs. This work can be extended using an adaptive observer whose role is to estimate both the unknown output and the unavailable state variable for measurement. Fault sensor reconstruction is also one of our future interests.

Data Availability

The data used to support the findings of this study are available from the corresponding author upon request.

Conflicts of Interest

The authors declare that they have no conflicts of interest.

References

[1] A. Zolghadri, J. Cieslak, D. Efimov et al., "Signal and model-based fault detection for aircraft systems," *IFAC-Papers Online*, vol. 48, no. 21, pp. 1096–1101, 2015.

[2] D. Zhihong, S. Xiaocheng, X. Guoqing, and F. Mingyu, "Fault tolerant control for steam generators in nuclear power plant," *Nuclear Power Engineering*, vol. 31, no. 1, pp. 107–111, 2010.

[3] J. M. Gregor and A. Cinar, "Monitoring, fault diagnosis, fault-tolerant control and optimization: data driven methods," *Computers and Chemical Engineering*, vol. 47, no. 20, pp. 111–120, 2012.

[4] A. Pantea, A. Yazidi, F. Betin et al., "Fault tolerant control of a low speed six-phase induction generator for wind turbines"" *IEEE Transactions on Industry Applications*, vol. 55, no. 1, pp. 426–436, 2019.

[5] D. Koenig, S. Nowakowski, and T. Cecchin, "An original approach for actuator and component fault detection and isolation," in *Proceedings of the 3rd IFAC Symposium on Fault Detection Supervision and Safety for Technical Processes*, pp. 95–105, Hull, UK, 1997.

[6] C. Join, J.-C. Ponsart, D. Sauter, and D. Theilliol, "Nonlinear filter design for fault diagnosis: application to the three-tank system," *IEE Proceedings—Control Theory and Applications*, vol. 152, no. 1, pp. 55–64, 2005.

[7] A. Akhenak, M. Chadli, D. Maquin, and J. Ragot, "State estimation via multiple observer the three-tank system," in *Proceedings of the 5th IFAC Symposium on Fault Detection, Supervision and Safety for Technical Processes*, pp. 1227–1232, Washington DC, USA, 2003.

[8] M. Rodrigues, D. Theilliol, M. Adam-Medina, and D. Sauter, "A fault detection and isolation scheme for industrial systems based on multiple operating models," *Control Engineering Practice*, vol. 16, no. 2, pp. 225–239, 2008.

[9] M. Amor, T. Ladhari, S. Hadj Said, and F. M'Sahli, "Hardware implementation of actuator fault estimation applied to a hydrographic plant," in *Proceedings of the 19th International Conference on Sciences and Techniques of Automatic Control & Computer Engineering (STA)*, pp. 202–207, Sousse, Tunisia, March 2019.

[10] L. F. Mendonc, J. M. C. Sousa, and J. M. G. Sa da Costa, "Fault accommodation of an experimental three tank system using fuzzy predictive control," in *Proceedings of the 2008 IEEE*

International Conference on Fuzzy Systems, Hong Kong, China, June 2008.

[11] M. T. César, L. Loïc, C. Franck, A. G. Efraín, and D. R. David, "Flatness-based fault tolerant control," *DYNA*, vol. 81, no. 188, pp. 131–138, 2014.

[12] R. Seydou, T. Raissi, A. Zolghadri, and D. Efimov, "Actuator fault diagnosis for flat systems: a constraint satisfaction approach," *International Journal of Applied Mathematics and Computer Science*, vol. 23, no. 1, pp. 171–181, 2013.

[13] H. Noura, D. Theilliol, and D. Sauter, "Actuator fault-tolerant control design: demonstration on a three-tank-system," *International Journal of Systems Science*, vol. 31, no. 9, pp. 1143–1155, 2000.

[14] D. Theilliol, H. Noura, and J.-C. Ponsart, "Fault diagnosis and accommodation of a three-tank system based on analytical redundancy," *ISA Transactions*, vol. 41, no. 3, pp. 365–382, 2002.

[15] M. Amor, T. Ladhari, S. Hadj Said, and F. M'Sahli, "On-line continuous-discrete time observer for three-tank system," in *Proceedings of the 15th International Multi-Conference on Systems, Signals & Devices (SSD)*, pp. 566–571, Hammamet, Tunisia, March 2018.

[16] M. Farza, M. M'Saad, and M. Sekher, "A set of observers for a class of nonlinear systems," in *Proceedings of the 16th IFAC World Congress*, Praha, Czech Republic, July 2005.

Hindawi
Mathematical Problems in Engineering
Volume 2020, Article ID 9026804, 15 pages
https://doi.org/10.1155/2020/9026804

Research Article

On the Nonlinear Seismic Responses of Shock Absorber-Equipped Porcelain Electrical Components

Zhubing Zhu,[1,2,3] Lingxin Zhang,[1,2] Yongfeng Cheng,[3] Hulun Guo,[4] and Zhicheng Lu[3]

[1]*Institute of Engineering Mechanics, China Earthquake Administration, Harbin 150080, China*
[2]*Key Laboratory of Earthquake Engineering and Engineering Vibration, China Earthquake Administration, Harbin 150080, China*
[3]*China Electric Power Research Institute, Beijing 100192, China*
[4]*Department of Mechanics, Tianjin University, Tianjin 300072, China*

Correspondence should be addressed to Lingxin Zhang; lingxin_zh@126.com

Received 2 February 2020; Accepted 29 February 2020; Published 15 May 2020

Guest Editor: Ping Zhao

Porcelain electrical equipment is prone to brittle failure due to resonance under seismic effects. To improve its seismic resistance, some researchers have conducted research on shock absorption technology for porcelain electrical equipment. However, extant research fails to provide a detailed and systematic study of the effect of the nonlinear characteristics of these shock absorbers on the performance of equipment under seismic effects. This paper provides a theoretical analysis, verified by shaking table testing, of the performance of a 1000 kV pillar-type porcelain lightning arrester. The Bouc–Wen model is fitted to the force-displacement curve of hysteretic nonlinear metal shock absorbers, and a dynamic model of, and equations for, pillar-type porcelain electrical components are derived, taking into account their nonlinear characteristics. This reveals the influence of the nonlinear characteristics of shock absorbers on the nonlinear seismic response characteristics of these components. Our results indicate that the seismic responses of pillar-type porcelain components can be effectively suppressed by hysteretic nonlinear shock absorbers and that the greater the intensity of the seismic waves, the more obvious the efficiency of shock absorption. However, as the installation radius and yield force of the installed shock absorbers increase, their shock absorption efficiency gradually decreases.

1. Introduction

As voltage classes have improved and the volume and mass of substation electrical equipment have been optimised, the increasing complexity of its structural systems has been paralleled by increases in its "height, size, flexibility, and weight" characteristics, exacerbating its seismic vulnerability and increasing risks of damage during earthquakes [1]. The natural frequency of pillar-type porcelain electrical components, especially ultra-high-voltage electrical equipment, is relatively low, mostly ranging from 1 to 2 Hz [2]. As this falls within the predominant frequency range of seismic waves, such equipment is vulnerable to large seismic forces. In addition, such equipment is made of brittle porcelain material, with poor energy dissipation capability, making it susceptible to severe damage under seismic loading [3–6]. Previous earthquake events have revealed that pillar-type porcelain electrical equipment is prone to brittle failure due to resonance under seismic loading [7–11]. Predominant failure modes include bushing root fracture and equipment dislocation at flange joints due to flange cement failure. An additional mode of earthquake damage reflects tensile stresses affecting interconnecting cables [12–15]. Figure 1 depicts typical seismic loading-induced equipment damage: the upper component is a porcelain insulator and the lower one is a frame. Engineering applications generally use lattice and cylindrical steel frames, or cylindrical concrete frames, with lattice steel frames generally adopted for equipment of voltage classes in excess of 500 kV. In addition, pillar-type porcelain insulators are sometimes directly mounted on a firewall or foundation, without a supporting frame.

Figure 1: Seismic damage to pillar-type porcelain insulators.

Research on shock absorption technology to improve the seismic capacity of pillar-type porcelain insulators has been carried out in China and abroad [16]. China Electric Power Research Institute Co., Ltd. developed a shear-type shock absorber for electrical equipment, which is shown in Figure 2. These are designed to be installed between insulator equipment and their frame, via connecting bolt holes on the flange at the bottom of each equipment. Under normal conditions, these devices act as bolts connecting the insulators with their frames. For equipment that does not need frame in actual engineering, shock absorbers are installed between firewall and foundation. Under seismic loading, each shock absorber's jacket moves up and down relative to its central shaft, and an internal lead alloy element undergoes shear deformation, dissipating seismic energy to achieve shock absorption. Siemens has developed a viscoelastic damper for installation between electrical equipment frames and foundations, as shown in Figure 3. During earthquakes, this damper's piston rod is displaced within it, displacing hydraulic oil for a damping effect. Toshiba has developed a centripetal shock absorber suitable for pillar components, as shown in Figure 4. This device is installed between the electrical equipment and its frame, dissipating earthquake energy via compressive deformation of internal discs. The inner part of the centripetal shock absorber is vertically arranged and combined by discs, which can only be pressed and cannot be pulled. Therefore, the device needs to be installed in two layers; two centripetal shock absorbers in the upper layer and the lower layer at the same position are connected in series via a bolt bar to ensure the shock absorber can consume earthquake energy in tension and compression state.

To date, numerous scholars have undertaken research into the seismic properties of pillar-type porcelain insulators and nonlinear theoretical analysis of related shock absorber-equipped structural systems. Cheng Yongfeng et al. studied the nonlinear responses of shock absorber-equipped pillar-type porcelain insulators under harmonic excitation [17]. Cheng Yongfeng et al. studied the seismic performance of 1000 kV lightning arresters and transformers connected by rigid tubular busbar through shaking table testing [18]. Ye Lieping et al. proposed a nonlinear seismic analysis model for concrete structure, capable of accurately simulating their nonlinear responses to seismic effects [19]. Jean-Bemard

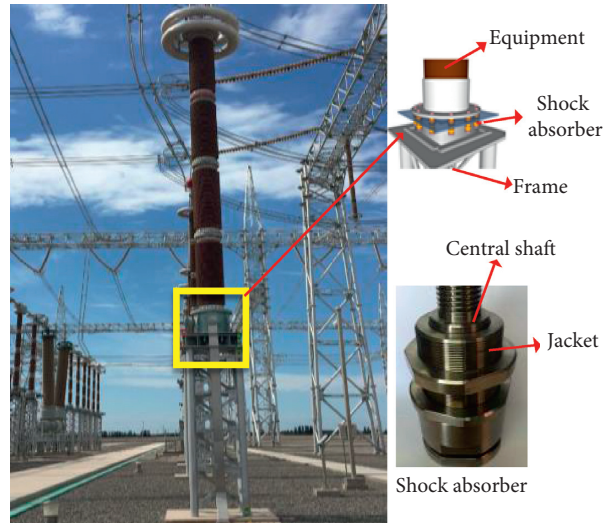

Figure 2: China Electric Power Research Institute's shear-type shock absorber and installation details.

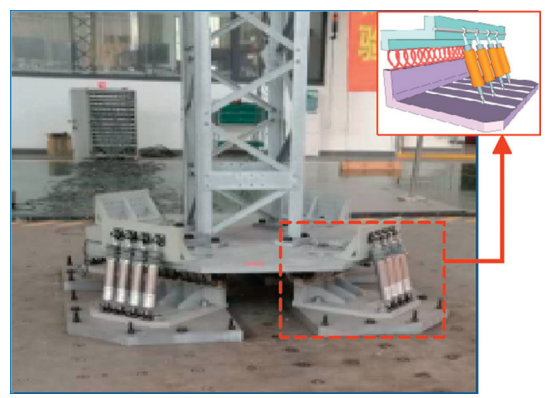

Figure 3: Siemens' viscoelastic damper and installation details.

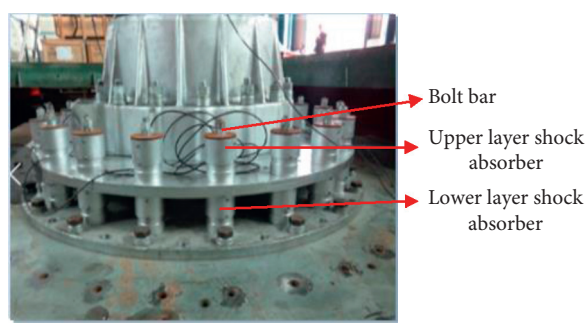

Figure 4: Toshiba's (Japan) centripetal shock absorber and installation details.

Dastous et al. conducted both static and dynamic tests of fixture wiring in order to assess its influence on the seismic performance of electrical equipment. They determined that wiring forms a nonlinear system during earthquakes and that designs retaining a certain degree of relaxation in wiring proved helpful in reducing the nonlinear coupling of interconnected equipment [20–22]. Robyn et al. used

nonlinear frictional contact elements to simulate shock absorbers and performed nonlinear time history analysis on structures equipped with these damping devices. Through comparison of multiple schemes, the accuracy of their analysis was verified, providing a basis for the development of nonlinear shock absorber designs [23].

Under seismic loading of shock absorber-equipped pillar-type porcelain insulator component systems, the shock absorbers are the components with most obvious nonlinear characteristics. These dissipate seismic energy in a nonlinear fashion to reduce the insulators' seismic response. However, while scholars have carried out research on the seismic performance of pillar-type porcelain insulators, as yet this fails to provide a detailed, systematic study of the effects of shock absorbers' nonlinear characteristics on the performance of porcelain insulators under seismic effects. And when pillar-type porcelain electrical components are equipped with shock absorbers with nonlinear characteristics, the structural system as a whole becomes more complex. The application of nonlinear theory to the seismic analysis of these structural systems can thus make a contribution toward raising the level of seismic analysis and of seismic design theory.

2. Dynamic Model and Equations

For this paper, nonlinear dynamic modeling of a 1000 kV pillar-type porcelain lightning arrester with shear-type shock absorbers without frames was conducted, and its dynamic equations were solved, in order to analyze the nonlinear seismic responses of the pillar-type porcelain components. Figure 5 provides a schematic diagram of these lightning arresters. They are composed of four pillar-type porcelain elements connected by flanges. These elements are numbered 1–4 from top to bottom. The main structural parameters of the equipment are shown in Table 1, where the elastic modulus of their porcelain material is 1.1×10^{11} N/m^2 and the weights of the top equalizing ring and other accessories (joints with electrodes and components) are 290 kg and 1801 kg, respectively. According to the shock-absorption design scheme, 20 shear-type shock absorbers are installed at the bottom of the lightning arrester.

2.1. Mechanical and Dynamic Model of the Shock Absorber. The dimensions of the lead alloy in the shock absorber are selected according to the expected seismic intensity, the required damping efficiency, and the number of bolt holes available for installation of these devices. The "restoring force-displacement" test curve of the single shock absorber used in this paper is shown in Figure 6. This figure shows obvious hysteretic nonlinearity. Shock absorber's design parameters are as follows: the yield force is 20 kN, the rigidity before yield is 80 kN/mm, and the equivalent damping ratio is 35%. The commonly used nonlinear models are elastic-plastic mechanical model, viscoelastic mechanical model, and viscous restoring force model. Whether it is an elastic-plastic mechanical model or a viscoelastic mechanical model, there is a sudden change of stiffness at the model's four corners, which is not consistent with the actual situation. Therefore, a smooth curve should be adopted to fit the restoring force-displacement curve of the damping device. The Bouc–Wen model, one of the viscous restoring force models, which has been widely adopted in engineering, can be well fit to this type of nonlinear hysteretic curve and was therefore used to model the shock absorber.

A typical Bouc–Wen model can be described by the following equations:

$$\begin{aligned} F &= k_L \xi + k_N Z, \\ \dot{Z} &= \left[\lambda - (\gamma \operatorname{sign}(\dot{\xi} Z) + \beta)|Z|^n\right]\dot{\xi}, \end{aligned} \tag{1}$$

where F represents the elastic force, ξ represents the displacement, $\dot{\xi}$ represents the displacement velocity, and γ is a parameter related to the yield force of the model.

The parameters of the Bouc–Wen model were determined by comparison of results from the theoretical model and from testing. Figure 7 shows a comparison between the Bouc–Wen model estimates and test results for the shock absorber's force-displacement curve. The Bouc–Wen model uses the following parameters: $k_L = 1 \times 10^6$ N/m, $k_N = 120 \times 10^6$ N/m, $\lambda = 1$, $\gamma = 5000$, $\beta = 1$, and $n = 1$.

In Figure 7, the black lines indicate the test results and the colored line represents estimates derived using the calibrated Bouc–Wen model. The two are in good agreement. In addition, the upper half of the Bouc–Wen model's curve is the result when $\dot{\theta} > 0$, while the lower half is the result when $\dot{\theta} < 0$l; ξ is a function of θ.

We assume that N shock absorbers are uniformly distributed at the bottom of the porcelain pillar, each separated from the next by an angle of $2\pi/N$, as shown in Figure 8(a). A mechanical model of the shock absorber joints is shown in Figure 8(b).

The connection between the shock absorber and the cement part of the flange at the base of the equipment is equivalent to a series spring [17]. The angle of the shock absorbers' surface of action is φ_1, and the spring angle relative to the cement part of the flange at the base of the equipment is φ_2. The angle of the first porcelain pillar is thus $\theta_1 = \varphi_1 + \varphi_2$.

The elastic force experienced by the shock absorber can be written as follows:

$$F_i = k_L \xi_i + k_N Z_i, \tag{2}$$

where $i = 1, 2, 3, ..., N$. This system is also governed by several other equations as follows:

$$\begin{aligned} \dot{Z}_i &= \left[\lambda - \left(\gamma \operatorname{sign}\left(Z_i \dot{\xi}_i\right) + \beta\right)\left|Z_i\right|^n\right]\dot{\xi}_i, \\ \xi_i &= \xi_0 + \varphi_1 R \sin \alpha_i, \end{aligned} \tag{3}$$

where ξ_0 is the static deformation and $\alpha_i = (i-1)\ 2\pi/N$. Denoting the spring stiffness of the flange at the bottom of the first porcelain pillar as k_1, this can be expressed as follows:

$$k_1 \varphi_2 = \sum_{i=1}^{N} F_i R \sin \alpha_i = K\theta_1, \tag{4}$$

where K is the equivalent stiffness. By combining $\theta_1 = \varphi_1 + \varphi_2$ with equation (4), the following equation can be derived:

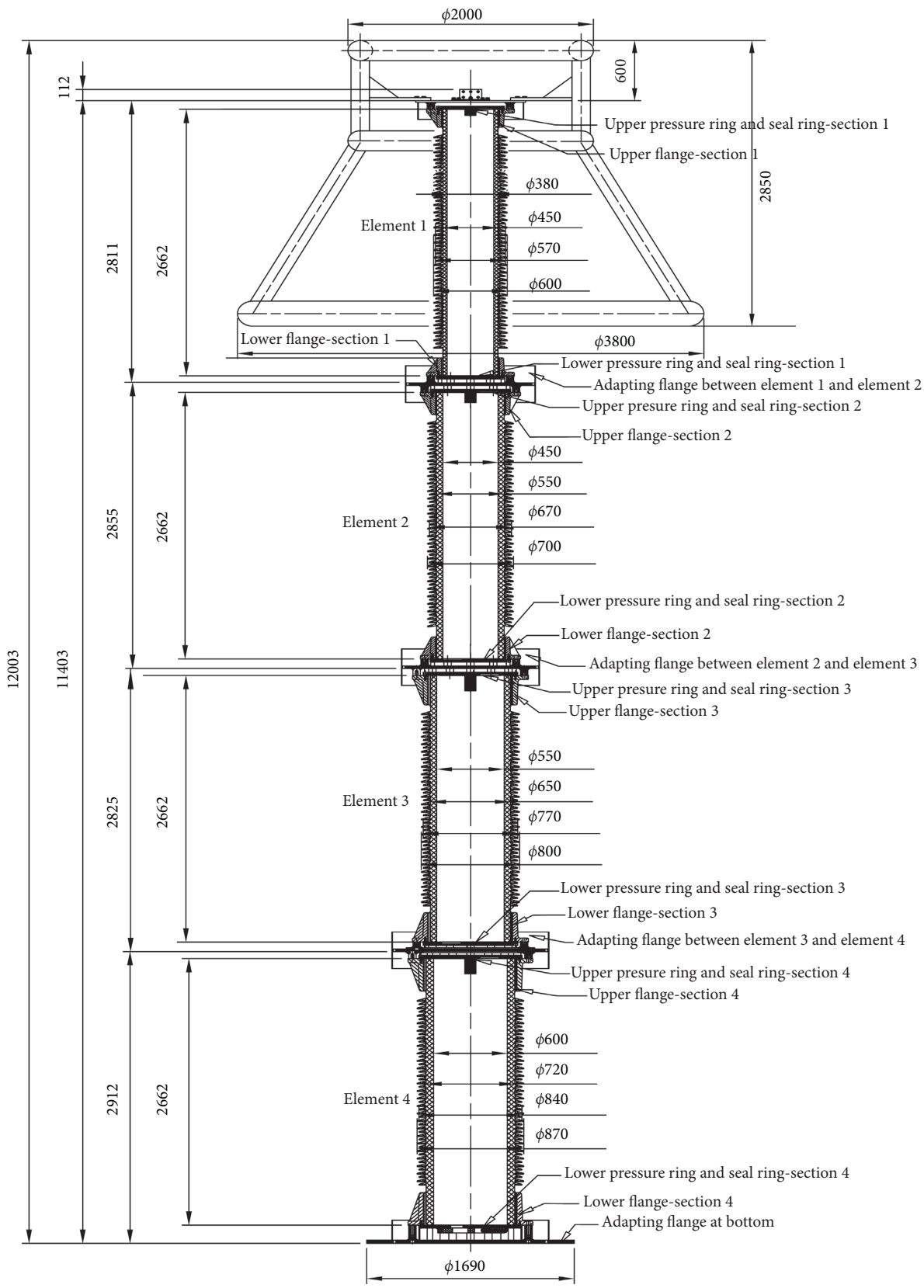

Figure 5: Schematic diagram of lightning arrester.

Table 1: Lightning arrester structural parameters.

Element no.	1	2	3	4
Weight (kg)	940	1212	1349	1571
Length (m)	2.662	2.662	2.662	2.662
Inner diameter (m)	0.38	0.45	0.55	0.60
Outer diameter (m)	0.45	0.55	0.65	0.72

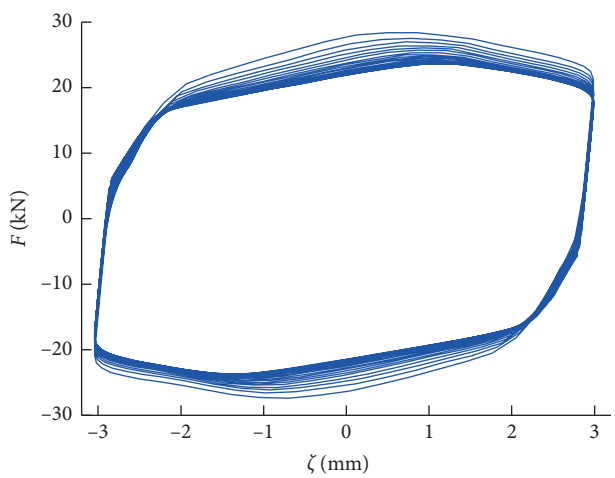

Figure 6: "Restoring force-displacement" curve of shock absorber.

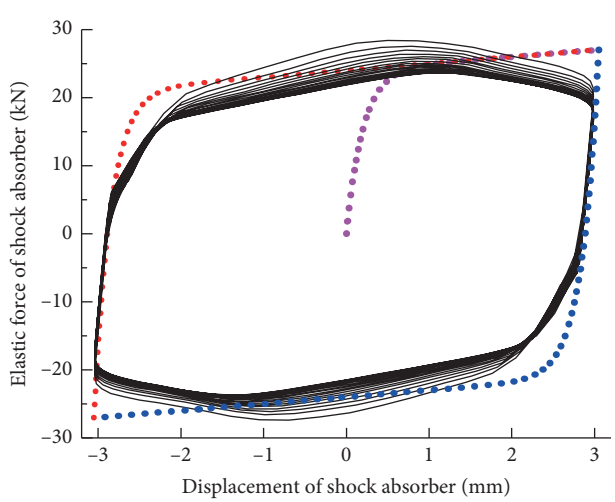

Figure 7: Shock absorber force-displacement curve: Bouc–Wen model estimates and test results.

$$\theta_1 = d_1\varphi_1 + d_2\sum_{i=1}^{N} Z_i \sin\alpha_i, \tag{5}$$

where $d_1 = 1 + (k_L R^2/k_1)\sum_{i=1}^{N}\sin^2\alpha_i$ and $d_2 = k_N R/k_1$.

2.2. Calculation of Flange Joint Bending Stiffness. The pillar-type porcelain components are connected by flanges, with one flange at the upper and lower end of each section. Stiffness is generated at both the cement flanges and porcelain bushings, as shown in Figure 9.

The upper and lower flanges generate total stiffness equivalent to the stiffness of two springs in series. If the stiffness of the flange at the bottom of the upper porcelain pillar is denoted by k_{id}, and the stiffness of the flange at the top of the lower porcelain pillar is denoted by $k_{(i-1)u}$, the equivalent stiffness, k_i, of the two sections of the porcelain pillar can be expressed as follows:

$$k_i = \frac{k_{\mathrm{id}}k_{(i-1)u}}{k_{\mathrm{id}} + k_{(i-1)u}}. \tag{6}$$

The bending stiffness of upper and lower flanges can be calculated according to the equation specified in the *Technical Specification for Seismic Design of Ultra-High-Voltage Porcelain Insulating Electrical Equipment and Installation/Maintenance of Energy Dissipation Devices* (Q/GDW 11132-2013) published by the China Electric Power Research Institute [24]:

$$k_{\mathrm{id}} = \frac{\beta_d d_d h_d^2}{t_d}, \qquad k_{\mathrm{iu}} = \frac{\beta_u d_u h_u^2}{t_u}, \tag{7}$$

where d_u and d_d are the outer diameters of the cement elements between the porcelain bushing and the upper and lower flanges, respectively; h_u and h_d are the heights of the cement between the porcelain bushing and the upper and lower flanges, respectively; t_u and t_d are the clearance distances between the porcelain bushings and the upper and lower flanges, respectively; and β_u and β_d are the bending stiffness coefficients at the connections between the porcelain bushing and the upper and lower flanges, respectively, the value of which is 6.54×10^7 when the outer diameter of the porcelain bushing at the cement element is smaller than 275 mm and is 5.0×10^7 when the outer diameter of the porcelain bushing at the cement element is larger than 275 mm, derived by linear interpolation when the outer diameter of the porcelain bushing at the cement element lies between 275 and 375 mm.

2.3. Dynamic Equation of Shock Absorber and Pillar-Type Porcelain Component System. Taking the 1000 kV pillar-type porcelain lightning arrester as an example, the flange at the bottom of the first pillar-type porcelain component is connected in series with the shock absorber and then consolidated. The elastic potential energy of the shock absorber and the flange joint at the bottom of the first porcelain pillar can now be written as follows:

$$U_A = \frac{1}{2}K\theta_1^2. \tag{8}$$

Differentiating this is equivalent to the following:

$$\delta U_A = K\theta_1\delta\theta_1. \tag{9}$$

If there are N_c porcelain pillar components, there will also be N_c flange joints, and the total elastic potential energy at these flange joints can be calculated as follows:

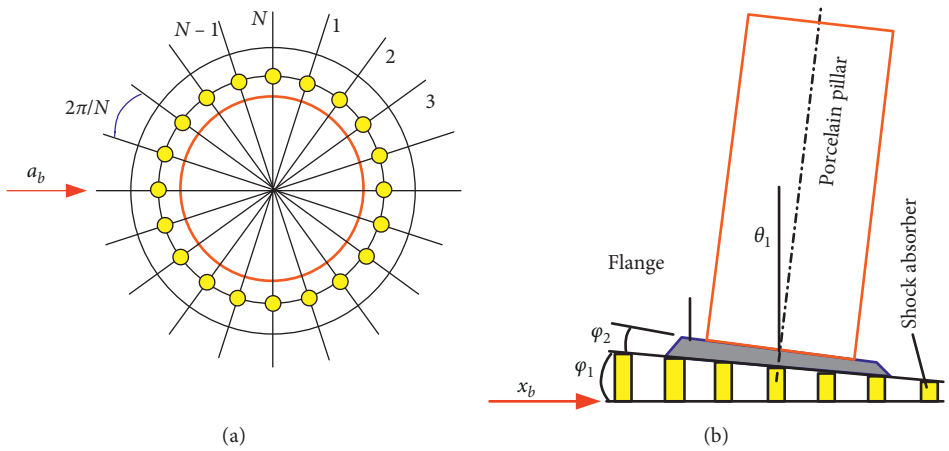

Figure 8: (a) Distribution of shock absorbers at the base of porcelain pillar. (b) Mechanical model of shock absorber joints.

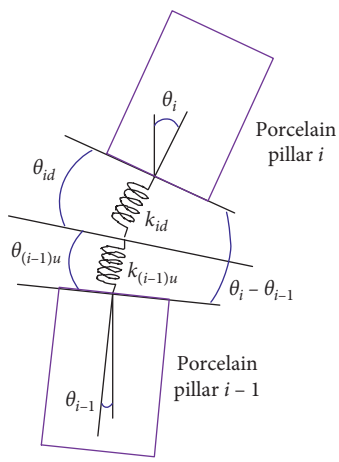

Figure 9: Flange joint.

$$U_k = \frac{1}{2}k_1\theta_1^2 + \sum_{i=2}^{N_c}\left[\frac{1}{2}k_i(\theta_i - \theta_{i-1})^2\right]. \tag{10}$$

The rotation of the porcelain pillars also causes changes in their gravitational potential energy, and their total gravitational potential energy is as follows:

$$U_g = -\frac{1}{2}\sum_{i=1}^{Nc} m_i g\left(\sum_{j=1}^{i} L_j\theta_j^2 - \frac{1}{2}L_i\theta_i^2\right), \tag{11}$$

where L_i and L_j are the lengths of the ith and j^{th} porcelain pillars, respectively.

The total potential energy of the system comprising the porcelain pillars and shock absorbers can be calculated as follows:

$$U = U_k + U_g + U_A. \tag{12}$$

Figure 10 is a schematic diagram of the velocity relationships for the ith porcelain pillar. The dynamic energy of the porcelain pillar includes translational and rotational dynamic energy, described by the following equation:

$$T = \frac{1}{2}\sum_{i=1}^{N_c} m_i v_{c,i}^2 + \frac{1}{2}\sum_{i=1}^{N_c}\frac{1}{12}m_i L_i^2\dot{\theta}_i^2, \tag{13}$$

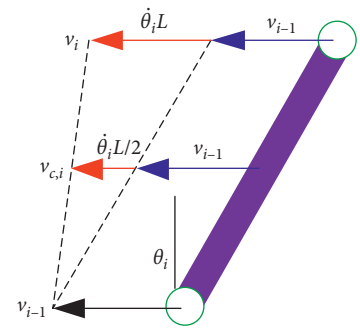

Figure 10: Velocity relationships of the ith porcelain pillar.

where $v_{c,i}$ is the velocity of the centroid of the ith porcelain pillar.

Figure 10 depicts the dynamics of a porcelain pillar, again taking a 1000 kV pillar-type porcelain lightning arrester as an example. The velocity of the flange at the bottom of the first porcelain pillar can be expressed as follows:

$$v_0 = \dot{x}_b, \tag{14}$$

where x_b is seismic effect-induced ground displacement.

The velocity of the centroid of the first porcelain pillar can then be calculated as follows:

$$v_{c,1} = v_0 + \frac{1}{2}L_1\dot{\theta}_1. \tag{15}$$

The velocity of the second porcelain pillar's centroid is then

$$v_{c,2} = v_0 + L_1\dot{\theta}_1 + \frac{1}{2}L_2\dot{\theta}_2. \tag{16}$$

The velocity of the third porcelain pillar's centroid can be written as

$$v_{c,3} = v_0 + L_1\dot{\theta}_1 + L_2\dot{\theta}_2 + \frac{1}{2}L_3\dot{\theta}_3. \tag{17}$$

And the velocity of the fourth porcelain pillar's centroid can be expressed as

$$v_{c,4} = v_0 + L_1\dot{\theta}_1 + L_2\dot{\theta}_2 + L_3\dot{\theta}_3 + \frac{1}{2}L_4\dot{\theta}_4. \tag{18}$$

The system's nonlinear dynamic equation can be derived using Hamilton's principle. Variation in the system's kinetic energy can be expressed as follows:

$$\delta T = -\sum_{i=1}^{N_c}\left[\begin{array}{c} m_i\left(\ddot{x}_b + \sum_{j=1}^{i} L_j\ddot{\theta}_j - \frac{1}{2}L_i\ddot{\theta}_i\right)\delta\left(\sum_{j=1}^{i} L_j\theta_j - \frac{1}{2}L_i\theta_i\right) + \\ \frac{1}{12}m_iL_i^2\ddot{\theta}_i\delta\theta_i \end{array}\right]. \tag{19}$$

The change in its potential energy can be written as

$$\delta U = k_1\theta_1\delta\theta_1 - \sum_{i=1}^{Nc} m_i g\left(\sum_{j=1}^{i} L_j\theta_j\delta\theta_j - \frac{1}{2}L_i\theta_i\delta\theta_i\right) + \sum_{i=2}^{Nc}\left[k_i\left(\theta_i - \theta_{i-1}\right)\right]\delta\left(\theta_i - \theta_{i-1}\right). \tag{20}$$

The dynamic and potential energy of the system can now be substituted into Hamilton's variational equation:

$$\int_{t_1}^{t_2} (\delta T - \delta U)\mathrm{d}t = 0. \tag{21}$$

This yields the following dynamic equation for the system:

$$\begin{aligned}
&\left(\frac{1}{3}m_1 + \sum_{i=2}^{4} m_i\right)L_1^2\ddot{\theta}_1 + \left(\frac{1}{2}m_2 + \sum_{i=3}^{4} m_i\right)L_1L_2\ddot{\theta}_2 + \left(\frac{1}{2}m_3 + m_4\right)L_1L_3\ddot{\theta}_3 \\
&\quad + \frac{1}{2}m_4L_1L_4\ddot{\theta}_4 + k_1\theta_1 - k_2\left(\theta_2 - \theta_1\right) - \left(\frac{1}{2}m_1 + \sum_{i=2}^{4} m_i\right)gL_1\theta_1 \\
&= -\left(\frac{1}{2}m_1 + \sum_{i=2}^{4} m_i\right)L_1\ddot{x}_b, \\
&\quad \cdot \left(\frac{1}{2}m_2 + \sum_{i=3}^{4} m_i\right)L_1L_2\ddot{\theta}_1 + \left(\frac{1}{3}m_2 + \sum_{i=3}^{4} m_i\right)L_2^2\ddot{\theta}_2 + \left(\frac{1}{2}m_3 + m_4\right)L_2L_3\ddot{\theta}_3 \\
&\quad + \frac{1}{2}m_4L_2L_4\ddot{\theta}_4 + k_2\left(\theta_2 - \theta_1\right) - k_3\left(\theta_3 - \theta_2\right) - \left(\frac{1}{2}m_2 + \sum_{i=3}^{4} m_i\right)gL_2\theta_2 \\
&= -\left(\frac{1}{2}m_2 + \sum_{i=3}^{4} m_i\right)L_2\ddot{x}_b, \\
&\quad \cdot \left(\frac{1}{2}m_3 + m_4\right)L_1L_3\ddot{\theta}_1 + \left(\frac{1}{2}m_3 + m_4\right)L_2L_3\ddot{\theta}_2 + \left(\frac{1}{3}m_3 + m_4\right)L_3^2\ddot{\theta}_3 \\
&\quad + \frac{1}{2}m_4L_3L_4\ddot{\theta}_4 + k_3\left(\theta_3 - \theta_2\right) - k_4\left(\theta_4 - \theta_3\right) - \left(\frac{1}{2}m_3 + m_4\right)gL_3\theta_3 \\
&= -\left(\frac{1}{2}m_3 + m_4\right)L_3\ddot{x}_b, \\
&\quad \frac{1}{2}m_4\left(L_1L_4\ddot{\theta}_1 + L_2L_4\ddot{\theta}_2 + L_3L_4\ddot{\theta}_3\right) + \frac{1}{3}m_4L_4^2\ddot{\theta}_4 + k_4\left(\theta_4 - \theta_3\right) \\
&\quad - \frac{1}{2}m_4gL_4\theta_4 = -\frac{1}{2}m_4L_4\ddot{x}_b.
\end{aligned} \tag{22}$$

This equation can be rewritten in the matrix form as

$$\mathbf{M}\ddot{\theta} + \mathbf{K}\boldsymbol{\theta} + \mathbf{N}(\boldsymbol{\theta}) = \mathbf{F}\ddot{x}_b, \tag{23}$$

where

$$M = \begin{bmatrix} M_{11} & M_{12} & M_{13} & M_{14} \\ M_{21} & M_{22} & M_{23} & M_{24} \\ M_{31} & M_{32} & M_{33} & M_{34} \\ M_{41} & M_{42} & M_{43} & M_{44} \end{bmatrix},$$

$$K = \begin{bmatrix} K_{11} & -k_2 & 0 & 0 \\ -k_2 & K_{22} & -k_3 & 0 \\ 0 & -k_3 & K_{33} & -k_4 \\ 0 & 0 & -k_4 & K_{44} \end{bmatrix},$$

$$N(\theta) = \begin{Bmatrix} -k_1\varphi_1 \\ 0 \\ 0 \\ 0 \end{Bmatrix}, \tag{24}$$

$$F = -f \begin{Bmatrix} \left(\frac{1}{2}m_1 + \sum_{i=2}^{4} m_i\right)L_1 \\ \left(\frac{1}{2}m_2 + \sum_{i=3}^{4} m_i\right)L_2 \\ \left(\frac{1}{2}m_3 + m_4\right)L_3 \\ \frac{1}{2}m_4 L_4 \end{Bmatrix}.$$

Several other equations complete the system as follows:

$$\begin{aligned}
\theta &= \{\theta_1 \ \ \theta_2 \ \ \theta_3 \ \ \theta_4\}^T, \\
M_{11} &= \left(\frac{1}{3}m_1 + \sum_{i=2}^{4} m_i\right)L_1^2, \\
M_{12} &= M_{21} = \left(\frac{1}{2}m_2 + \sum_{i=3}^{4} m_i\right)L_1L_2, \\
M_{13} &= M_{31} = \left(\frac{1}{2}m_3 + m_4\right)L_1L_3, \\
M_{14} &= M_{41} = \frac{1}{2}m_4L_1L_4, \\
M_{22} &= \left(\frac{1}{3}m_2 + \sum_{i=3}^{4} m_i\right)L_2^2, \\
M_{23} &= M_{32} = \left(\frac{1}{2}m_3 + m_4\right)L_2L_3, \\
M_{24} &= M_{42} = \frac{1}{2}m_4L_2L_4, \\
M_{33} &= \left(\frac{1}{3}m_3 + m_4\right)L_3^2, \\
M_{34} &= M_{43} = \frac{1}{2}m_4L_3L_4, \\
M_{44} &= \frac{1}{3}m_4L_4^2, \\
K_{11} &= k_1 + k_2 - \left(\frac{1}{2}m_1 + \sum_{i=2}^{4} m_i\right)gL_1, \\
K_{22} &= k_2 + k_3 - \left(\frac{1}{2}m_2 + \sum_{i=3}^{4} m_i\right)gL_2, \\
K_{33} &= k_3 + k_4 - \left(\frac{1}{2}m_3 + m_4\right)gL_3, \\
K_{44} &= k_4 - \frac{1}{2}m_4gL_4.
\end{aligned} \tag{25}$$

Taking the damping of the structure into account, its dynamic equation can be written as follows:

$$\mathbf{M}\ddot{\theta} + \mathbf{C}\dot{\theta} + \mathbf{K}\theta + \mathbf{N}(\theta) = \mathbf{F}\ddot{x}_b, \tag{26}$$

where the damping ratio is $\mathbf{C} = 2\zeta\mathbf{M}\boldsymbol{\Phi}\boldsymbol{\Lambda}\Phi^{-1}$, Φ is the modal matrix, and Λ is a diagonal matrix consisting of the natural frequencies. For equipment without a shock absorber, $\mathbf{N}(\theta)$ in the dynamic equation can be omitted.

3. Seismic Response Analysis

3.1. Ground Motion Input. The seismic wave data adopted were those for artificial wave proposed by the China Electric Power Research Institute. The artificial wave was fitted based on a seismic acceleration response spectrum with a characteristic period of 0.9 s, capable of enveloping the characteristic periods of Category I_0–III soil sites, making them suitable for seismic design and testing and for seismic performance evaluation of HV and UHV electrical equipment [25]. The artificial wave time history and the curve fitted to the artificial wave response spectrum and target spectrum at peak seismic acceleration of 1 g are illustrated in Figure 11.

3.2. Experimental Verification of the Theoretical Model. To ensure that the theoretical model is correct and rational, its results under typical working conditions were compared with results from shaking table testing under the same conditions. During the test, strain gauges were arranged at the root of the porcelain bushing of each lightning arrester element, and the strain converted into a stress response using the elastic modulus. Accelerometers were arranged at the upper flange of each bushing element to provide data-permitting analysis of the dynamics of the equipment. The main operating condition applied during the test was white noise. The frequency of the equipment was tested under this condition and then under 0.3 g seismic test condition and 0.5 g shock absorption test conditions. At the end of the test, the relevant data and signal processing methods in mathematics are used to analyze the test data [26–28].

The natural frequencies of the equipment's seismic model and the shock absorption model were estimated, via solution for the eigenvalues of their dynamic equations, at 2.39 Hz and 2.27 Hz, respectively. These values were similar to the experimental estimates of 2.17 Hz and 2.08 Hz, representing errors of 10.14% and 9.13%, respectively.

Figure 12 provides a comparison of estimates for stress at the bottom of the porcelain pillars derived via theoretical analysis and testing under 0.3 g seismic effects. The results of the theoretical calculation are basically consistent with the experimental results. The maximum stress on the equipment derived from experimental and theoretical analyses was 22.02 MPa and 20.30 MPa, respectively, representing a difference in maximum stress of only 9.04%, confirming the validity of the seismic model without shock absorbers.

Figure 13 provides a comparison of time history for stress at the bottom of the porcelain pillar with shock absorption under a 0.5 g seismic effect. Once again, the results of the theoretical calculation are basically consistent with the experimental results. Estimates of the maximum stress on the equipment under a 0.5 g seismic effect were 11.5 MPa and 10.3 MPa, derived from experimental and theoretical analysis, respectively, representing a difference of only 10.4%, confirming the validity of the model with shock absorption.

3.3. Component Response under Seismic Excitation. To study the influence of ground motion intensity on the shock absorption of a 1000 kV pillar-type porcelain lightning arrester, a comparison of this equipment's seismic responses without and with shock absorption was conducted under conditions of 0.1 g, 0.2 g, 0.3 g, 0.4 g, and 0.5 g ground motion excitation. Figure 14 shows the stress response time history of the equipment for different magnitudes of ground motion excitation. The curve in Figure 15 describes the relationship between the magnitude of seismic wave excitation and shock absorption efficiency. Figure 16 shows the force-displacement relationships of a typical shock absorber under seismic effects of different magnitudes.

The results of this analysis show that as the intensity of seismic excitation increases, the loop in the hysteretic curve formed by the shock absorber increases in size, indicating that it dissipates more energy and has a larger effect, under increased seismic excitation. With seismic excitation of 0.1 g, 0.2 g, 0.3 g, 0.4 g, and 0.5 g, corresponding levels of shock absorption efficiency were 27.56%, 47.21%, 62.23%, 71.59%, and 77.49%, respectively. Absorption efficiency can be written as follows:

$$\eta = \frac{\sigma_1 - \sigma_2}{\sigma_1} \times 100\%, \tag{27}$$

where η is the absorption efficiency and σ_1 and $\sigma_2$are the stress on equipment under seismic conditions before and after installation of shock absorbers.

3.4. Influence of Shock Absorber Parameters on Equipment Seismic Response. Due to requirements concerning the stiffness characteristics of shock absorbers to be connected with electrical components during engineering application, in practice, the stiffness of different types of shock absorbers differs only slightly. Of all the shock absorber parameters, yield force is the main factor affecting their energy dissipation properties. The shock absorber installation radius—the radius of the circle around which the bolt holes for shock absorber installation are arranged—is also a key factor affecting their displacement energy dissipation properties. This study therefore focuses on the influence of shock absorbers' installation radius and yield force on their shock absorption efficiency.

To analyze the influence of the shock absorber installation radius on shock absorption efficiency, this parameter was varied over a 0.4–0.8 m range, and its influence on the shock absorption efficiency of the porcelain pillar system was examined for levels of seismic wave excitation intensity between 0.1 g and 0.5 g. Figure 17 depicts analytically derived relationships between shock absorber installation radius and the shock absorption efficiency of the pillar-type porcelain component. Table 2 shows how shock absorption efficiency varies with installation radius under different magnitudes of seismic excitation.

Figure 17 shows that for a given level of seismic wave excitation, shock absorption efficiency decreases gradually as shock absorber installation radius increases. Under seismic excitation of 0.5 g, shock absorption efficiency decreases from 81.51% to 62.20% as shock absorber installation radius

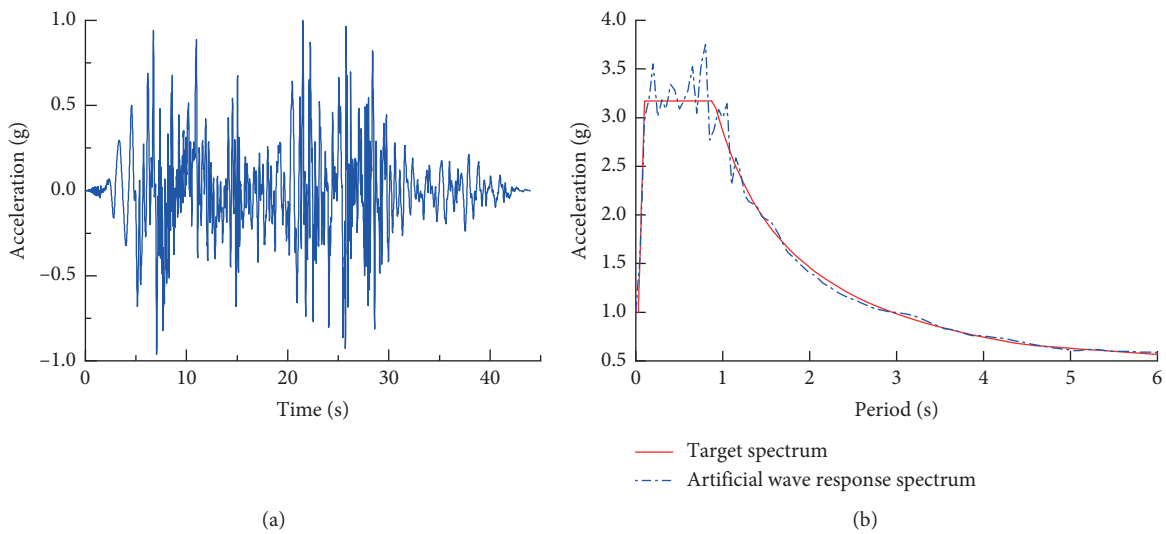

Figure 11: (a) Time history curve of artificial seismic wave. (b) Response-spectrum fitted curve.

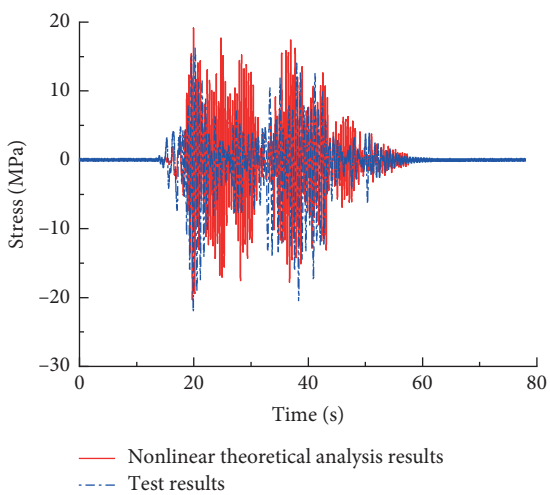

Figure 12: Stress at the bottom of the porcelain pillar under 0.3 g seismic effect.

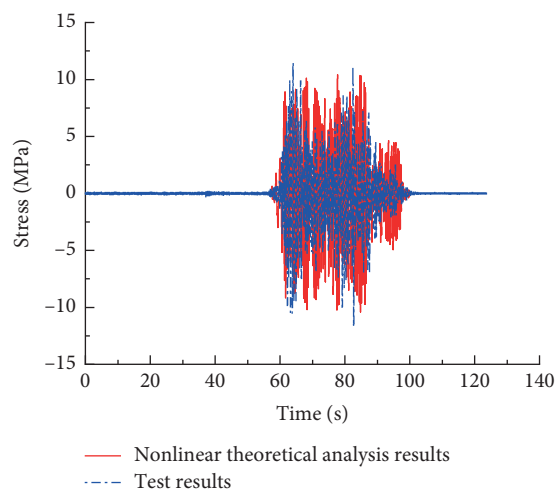

Figure 13: Stress at the bottom of the porcelain pillar under 0.5 g seismic effect with shock absorption.

increases from 0.4 m to 0.8 m. For lower magnitudes of seismic excitation, the porcelain pillar's shock absorption efficiency decreases more rapidly with increases in shock absorber installation radius: with seismic excitation of 0.1 g and a shock absorber installation radius of 0.8 m, shock absorption efficiency falls to the very low level of 3.94%. This represents a roughly 92% decrease in shock absorption efficiency compared with a shock absorber installation radius of 0.4 m. As seismic excitation gradually increases, the influence of shock absorber installation radius on the shock absorption efficiency of the porcelain pillar assembly gradually decreases. With 0.3 g seismic excitation and a 0.8 m installation radius, shock absorption efficiency is 38.74%, 45% lower than when the installation radius is 0.4 m. With 0.5 g seismic excitation and a 0.8 m installation radius, the shock absorption efficiency is 62.2%, only 24% lower than for 0.4 m installation radius. The degree to which shock absorption efficiency declines with installation radius gradually decreases as seismic excitation increases.

The influence of the shock absorber's yield force on shock absorption efficiency was analyzed by estimating the effect of parameter γ on shock absorption efficiency under different intensities of seismic excitation. Figure 18 shows how shock absorption efficiency changes with γ under different intensities of seismic excitation. Table 3 provides shock absorption efficiency values with different values of γ and seismic excitation. In the Bouc–Wen model, γ is closely related to the shock absorber's yield force, and the yield force values corresponding to the relevant values of γ are shown in Table 4.

As can be seen from Figure 18 and Table 3, for a given level of seismic excitation, shock absorption efficiency gradually increases as γ increases. With 0.1 g seismic excitation, shock absorption efficiency is 19.18% for $\gamma = 3{,}000$, rising to 27.56% for $\gamma = 7{,}000$, a 44% increase. With 0.3 g

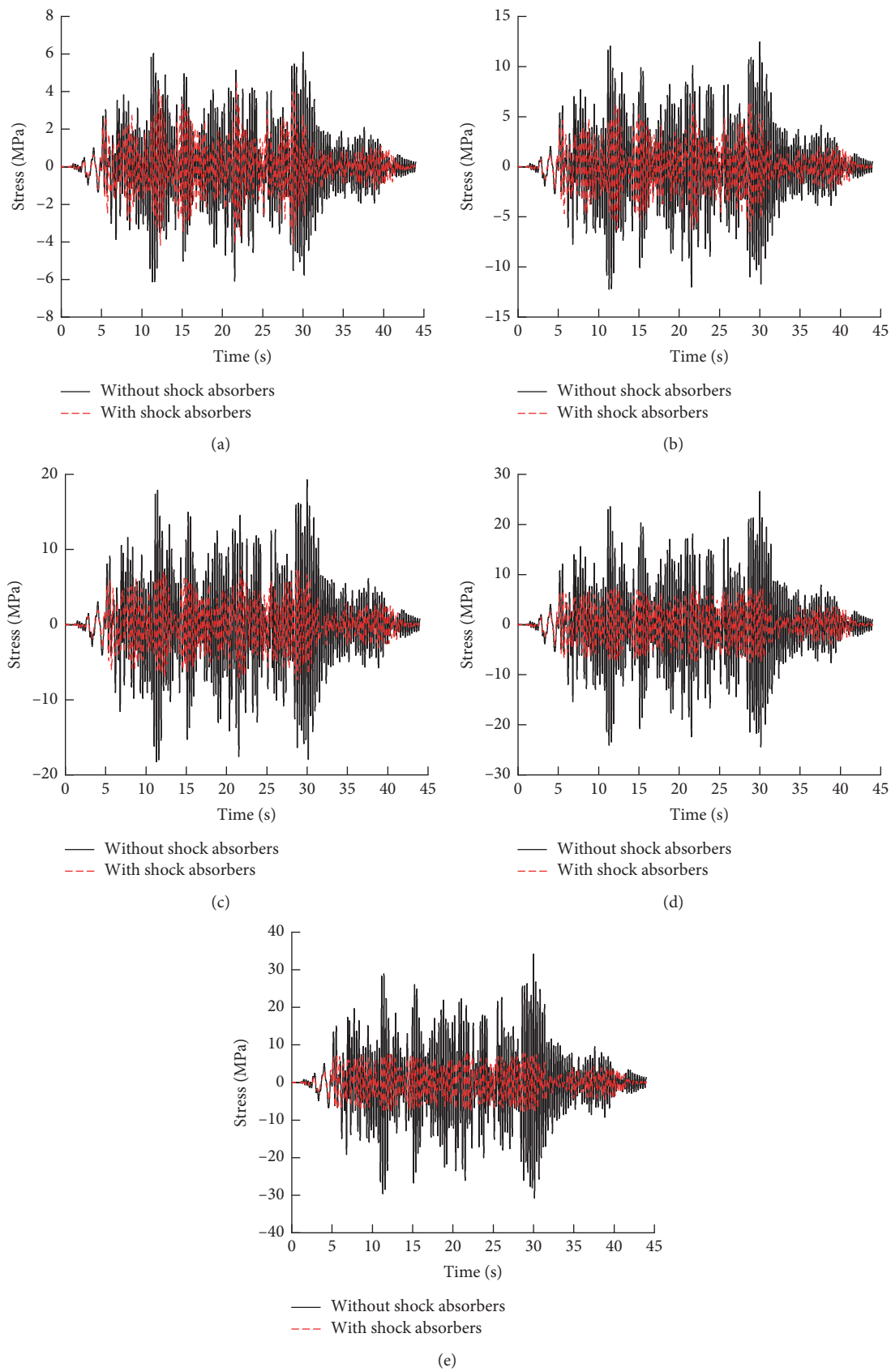

Figure 14: Stress at the bottom of the porcelain pillar under seismic excitation of different magnitudes: (a) 0.1 g, (b) 0.2 g, (c) 0.3 g, (d) 0.4 g, and (e) 0.5 g.

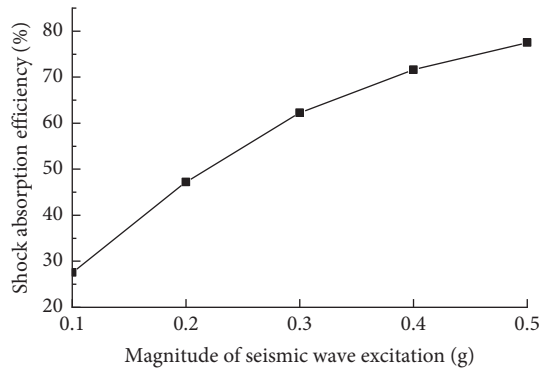

Figure 15: Relationship between seismic wave excitation and shock absorption efficiency.

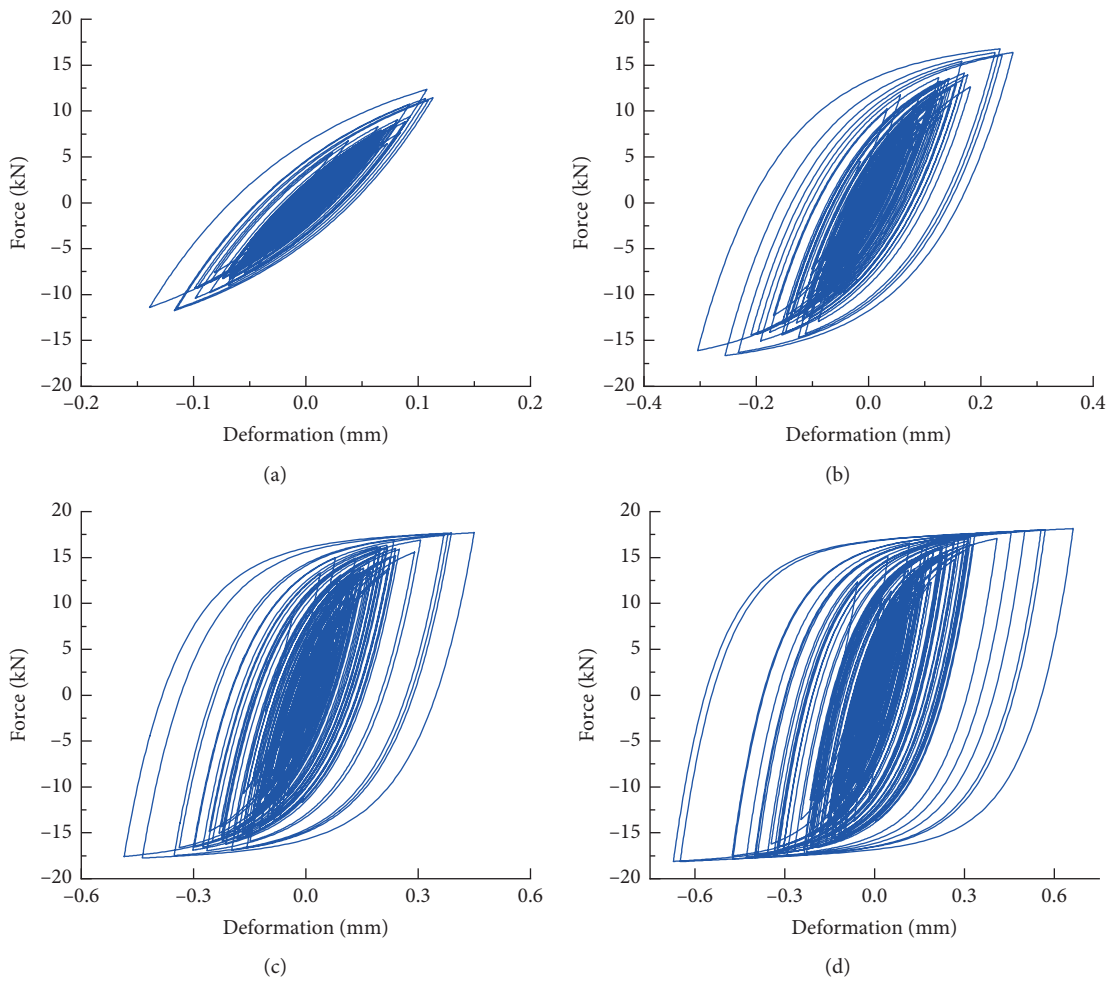

Figure 16: Continued.

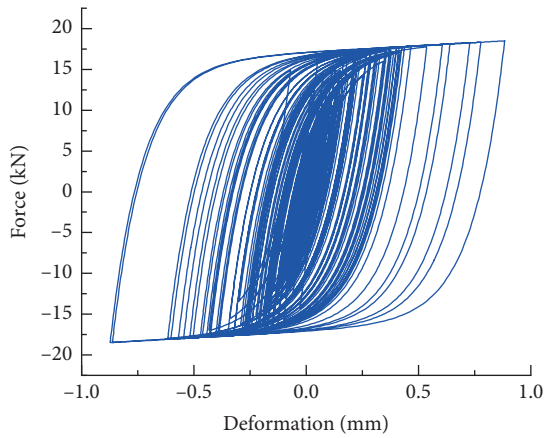

(e)

Figure 16: Force-displacement relationship of typical shock absorbers under seismic effects of different magnitudes: (a) 0.1 g, (b) 0.2 g, (c) 0.3 g, (d) 0.4 g, and (e) 0.5 g.

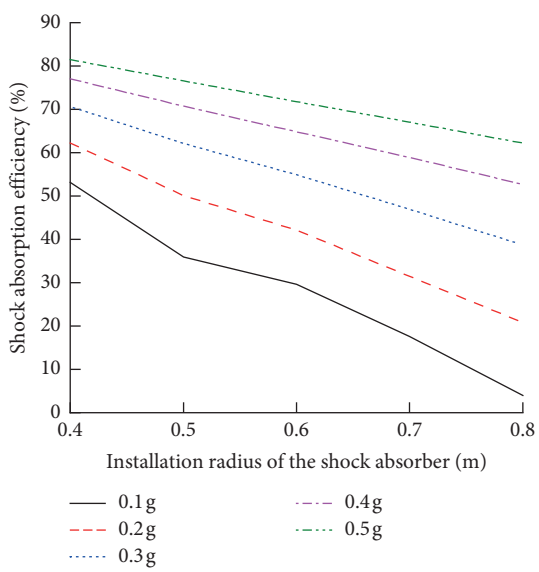

Figure 17: Influence of installation radius on porcelain pillar shock absorption efficiency.

Table 2: Shock absorption efficiency with different installation radii and magnitudes of seismic excitation.

Seismic excitation (g)	Shock absorption efficiency (%)		
	$R = 0.4$	$R = 0.6$	$R = 0.8$
0.1	53.11	29.62	3.94
0.2	62.2	42.14	20.85
0.3	70.67	54.86	38.74
0.4	77.05	64.85	52.67
0.5	81.51	71.80	62.20

seismic excitation, shock absorption efficiency is 35.97% for $\gamma = 3{,}000$, rising to 62.24% for $\gamma = 7{,}000$, a 73% increase. With 0.5 g seismic excitation, shock absorption efficiency is 53.86% for $\gamma = 3{,}000$, rising to 76.9% for $\gamma = 7{,}000$, a 43% increase.

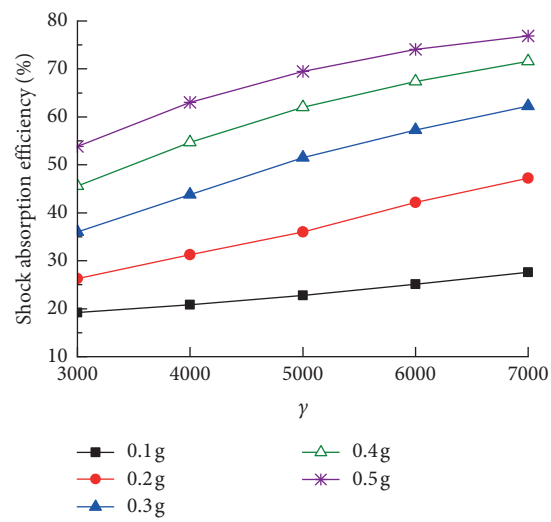

Figure 18: Relationship between shock absorption efficiency and γ.

Table 3: Shock absorption efficiency with different values of γ and magnitudes of seismic excitation.

Seismic excitation (g)	Shock absorption efficiency (%)				
	$\gamma = 3000$	$\gamma = 4000$	$\gamma = 5000$	$\gamma = 6000$	$\gamma = 7000$
0.1	19.18	20.81	22.80	25.07	27.56
0.2	26.29	31.29	36.00	42.12	47.21
0.3	35.97	43.80	51.50	57.25	62.24
0.4	45.60	54.71	62.00	67.42	71.60
0.5	53.86	63.02	69.47	74.07	76.90

Table 4: Yield force of shock absorber for different values of γ.

γ Value	3000	4000	5000	6000	7000
Yield force (kN)	40	30	25	20	18

For a given value of γ, shock absorption efficiency gradually increases with seismic excitation. For $\gamma = 3{,}000$, shock absorption efficiency is 53.86% for 0.5 g seismic

excitation, representing a significant increase of 180% compared to efficiency with 0.1 g seismic excitation. For $\gamma = 5{,}000$, shock absorption efficiency under 0.5 g seismic excitation is 204% higher than that under 0.1 g seismic excitation. For $\gamma = 7{,}000$, shock absorption efficiency under 0.5 g seismic excitation is 179% higher than that under 0.1 g seismic excitation.

These estimates show that for a given level of seismic excitation, the smaller the shock absorber's yield force, the higher the shock absorption efficiency; with the decrease of yield force, the increasing amplitude of shock absorption efficiency increases first and then decreases.

4. Conclusions

This paper applies the Bouc–Wen model to fit restoring force-displacement curves for hysteretic nonlinear metal shock absorbers, avoiding the sharp inflection points introduced by bilinear models. Dynamic models and equations for pillar-type porcelain electrical components were developed, taking their nonlinear characteristics into consideration, allowing examination of the effects of shock absorbers on these components' nonlinear seismic responses. This yielded the following conclusions:

(1) Shaking table test results indicated small differences, not exceeding 11%, between the theoretically and experimentally derived results, illustrating the accuracy of the theoretical model and results derived from this theoretical analysis. This validates the correctness and reasonableness of results from the theoretical model.

(2) Under seismic wave excitation, porcelain pillars' vibration responses can be effectively suppressed using hysteretic nonlinear shock absorbers. The greater the seismic wave intensity, shock absorption devices enter the yield state better and absorb more seismic energy, and thus, the more obvious the efficiency of this shock absorption.

(3) As the installation radius and yield force of the shock absorber increase, its shock absorption efficiency gradually decreases. Thus, during engineering design, reasonable values for the yield force and installation radius of shock absorbers should be selected based on structural characteristics and the required degrees of seismic fortification and the required shock absorption efficiency of the equipment.

(4) For the shock absorption design of electrical equipment in high seismic intensity area, shock absorption efficiency should be more than 50%. During the shock absorption design of 1000 kV arrester equipment, to ensure perfect absorption efficiency under 0.4 g earthquake, the yield force should be between 18 kN~30 kN, and the installation radius of shock absorbers should be about 0.6 m.

Data Availability

The data used to derive the findings of this study are available from the corresponding author upon request.

Conflicts of Interest

The authors declare that there are no conflicts of interest regarding the publication of this paper.

Acknowledgments

This study was funded by the Chinese National Key R&D Program (2018YFC0809400).

References

[1] Y. Yu, G. Li, L. Peng et al., "Investigation and analysis of electric equipment damage in Sichuan power grid caused by Wenchuan earthquake," *Power System Technology*, vol. 32, no. 11, pp. 1–6, 2008.

[2] N. Qiu, Y. Cheng, M. Zhong, Z. Lu, Z. Zhu, and X. Lu, "Progress and prospects in seismic research of 1000 kV UHV AC electrical equipment," *High Voltage Engineering*, vol. 41, no. 5, pp. 1732–1739, 2015.

[3] Y. Cheng, Z. Quanjun, and Z. Lu, "Progress and development trends on seismic measures of electric power equipments in transformer substation," *Power System Technology*, vol. 32, no. 22, pp. 84–89, 2008.

[4] J. Anshel and K. Leon, "IEEE 693 Seismic qualification of composite for substation high-voltage equipment," in *Proceedins of the 13th World Conference on Earthquake Engineering*, Vancouver, Canada, August 2004.

[5] L. Zhenlin, D. Zebing, and L. Zhicheng, "Weibull distribution based seismic vulnerability analysis of porcelain power equipment," *Power System Technology*, vol. 38, no. 4, pp. 1076–1081, 2014.

[6] J. Song, A. Der Kiureghian, and J. L. Sackman, "Seismic interaction in electrical substation equipment connected by non-linear rigid bus conductors," *Earthquake Engineering & Structural Dynamics*, vol. 36, no. 2, pp. 167–190, 2010.

[7] J.-P. Dastous and J.-H. Pierre, "Experimental investigation on the dynamic behavior of flexible conductors between substation equipment during an earthquake," *IEEE Transactions on Power Delivery*, vol. 11, no. 2, pp. 801–807, 1996.

[8] H. Ghalibafian, G. S. Bhuyan, C. Ventura et al., "Seismic behavior of flexible conductors connecting substation equipment-part II: shake table tests," *IEEE Transactions on Power Delivery*, vol. 19, no. 4, pp. 1680–1687, 2004.

[9] A. D. Kiureghian, J. L. Sackman, and K. J. Hong, *Interaction in Interconnected Electrical Substation Equipment Subjected to Earthquake Ground motions*, Pacific Earthquake Engineering Research Center, Richmond, CA, USA, 1999.

[10] A. D. Kiureghian, K. J. Hong, and J. L. Sackman, *Further Studies on Seismic Interaction in Interacted Electrical Substation equipment*, Pacific Earthquake Engineering Research Center, Richmond, CA, USA, 2000.

[11] F. Paolacci, R. Giannini, S. Alessandri, and G. De Felice, "Seismic vulnerability assessment of a high voltage disconnect switch," *Soil Dynamics and Earthquake Engineering*, vol. 67, pp. 198–207, 2014.

[12] R. Karami Mohammadi and A. Pourkashani Tehrani, "An investigation on seismic behavior of three interconnected pieces of substation equipment," *IEEE Transactions on Power Delivery*, vol. 29, no. 4, pp. 1613–1620, 2014.

[13] R. K. Mohammadi, F. Nikfar, and V. Akrami, "Estimation of required slack for conductors connecting substation equipment subjected to earthquake," *IEEE Transactions on Power Delivery*, vol. 27, no. 2, pp. 709–717, 2012.

[14] A. Filiatrault and C. Stearns, "An experimental study on the seismic response of electrical substation equipment interconnected by flexible conductors," in *Proceedings of the Advancing Mitigation Technologies & Disaster Response for Lifeline Systems*, pp. 667–676, Long Beach, CA, USA, August 2003.

[15] K. M. Mosalam and S. Günay, "Seismic performance evaluation of high voltage disconnect switches using real-time hybrid simulation: I. System development and validation," *Earthquake Engineering & Structural Dynamics*, vol. 43, no. 8, pp. 1205–1222, 2014.

[16] Y.-F. Cheng, Z.-B. Dai, L. U. Zhi-Cheng et al., "Study on method of seismic design for electrical equipment with engrgy dissipation devices in China," *High Voltage Apparatus*, vol. 49, no. 9, pp. 69–79, 2013.

[17] Y. Cheng, H. Guo, Z. Zhu, X. Su, and Y. Chen, "Dynamics of a upright Pole coupled with nonlinear hysteretic isolators under harmonic base excitation," *Shock and Vibration*, vol. 2018, Article ID 2497035, 11 pages, 2018.

[18] Y. Cheng, X. Meng, Z. Lu, Z. Liu, N. Qiu, and Y. Ma, "Shaking table test on the seismic performance of ultrahigh voltage interconnected electrical equipment," *China Earthquake Engineering Journal*, vol. 42, no. 2, pp. 292–298, 2019.

[19] L. Ye, X. Lu, Q. Ma, X. Wang, and Z. Miao, "Nonlinear analytical models, methods and examples for concrete structures subject to earthquake loading," *Engineering Mechanics*, vol. 23, no. Sup.2, pp. 131–141, 2006.

[20] J.-B. Dastous and J.-Y. Paquin, "Testing and development of alternative flexible-bus geometries for interconnected substation equipment subjected to earthquakes," *IEEE Transactions on Power Delivery*, vol. 18, no. 3, pp. 772–780, 2003.

[21] J.-B. Dastous, "Guidelines for seismic design of flexible buswork between substation equipmenf," *Earthquake Engineering and Structural Dynamics*, vol. 36, no. 8, pp. 191–208, 2007.

[22] J.-B. Dastous and J.-R. Pierre, "Design methodology for flexible buswork between substation equipment subjected to earthquakes," *IEEE Transactions on Power Delivery*, vol. 22, no. 3, pp. 1490–1497, 2007.

[23] R. M. Mutobe and T. R. Cooper, "Nonlinear analysis of a large bridge with isolation bearings," *Computers & Structures*, vol. 72, no. 1–3, pp. 279–292, 1999.

[24] Q/GDW 11132-2013, *Technical Specification for Seismic Design of Ultra-high Voltage Porcelain Insulating Equipments and Installation/Maintenance to Energy Dissipation Devices*, China Electric Power Press, Beijing, China, 2014.

[25] Z. Liu, Y. Cheng, Z. Lu et al., "Shake table test on UHV standardization lightning arrester installed with shear-type lead dampers," *High Voltage Engineering*, vol. 44, no. 8, pp. 2595–2602, 2018.

[26] D. Zhao, S. X. Ding, H. R. Karimi, and Y. Li, "Robust $H_ \infty$ filtering for two-dimensional uncertain linear discrete time-varying systems: a krein space-based method," *IEEE Transactions on Automatic Control*, vol. 64, no. 12, pp. 5124–5131, 2019.

[27] D. Zhao, Y. Li, C. Ki Ahn, and S. X. Ding, "Optimal state and fault estimation for two-dimensional discrete systems," *Automatica*, vol. 115, p. 108856, 2020.

[28] Z. Dong, H. K. Lam, Y. Li, S. X. Ding, and S. Liu, "A novel approach to state and unknown input estimation for Takagi-Sugeno fuzzy models with applications to fault detection," *IEEE Transactions on Circuits and Systems I: Regular Papers*, pp. 1–11, 2020.

Hindawi
Mathematical Problems in Engineering
Volume 2020, Article ID 1940676, 12 pages
https://doi.org/10.1155/2020/1940676

Research Article

Robust Control for Nonlinear Markov Jump Systems with Partially Unknown Transition Probabilities

Lifan Kang,[1] Yue Wang,[2] and Ting Hou[3]

[1]*College of Mathematics and Systems Science, Shandong University of Science and Technology, Qingdao 266590, China*
[2]*Division of Public Teaching, Jinan Vocational College, Jinan 250103, China*
[3]*School of Mathematics and Statistics, Shandong Normal University, Jinan 250358, China*

Correspondence should be addressed to Ting Hou; ht_math@sina.com

Received 8 February 2020; Revised 4 April 2020; Accepted 8 April 2020; Published 11 May 2020

Guest Editor: Yi Qi

This note focuses on the finite horizon H_2/H_∞ control for stochastic nonlinear jump systems with partially unknown transition probabilities. We derive the nonlinear stochastic bounded real lemma and the nonlinear optimal regular result for the considered system at first. A sufficient condition and a necessary condition for the solution of H_2/H_∞ control are, respectively, offered by four cross-coupled Hamilton–Jacobi equations (HJEs). Besides, numerical examples show the effectiveness of the obtained results.

1. Introduction

Control synthesis is one of the important parts of control theory [1–5]. The H_∞ synthesis aims to seek for a suitable controller to suppress the effect of the exogenous disturbance on the dynamic system below a given level [6–9]. However, it is aware that H_∞ control can guarantee the good robustness of the designed system, but cannot optimize the closed-loop to achieve perfect performance. Because of this, the linear quadratic control (H_2 control) is selected to make up the lack in optimization. Combining the two control methods becomes a natural idea to reach the balance. H_2/H_∞ control not only ensures to repress the influence of the disturbance, but also minimizes the energy cost under the disturbance input [10–12]. So far, H_∞ control and H_2/H_∞ control have been paid continuous attention [13–17]. In particular, for stochastic systems, bounded real lemmas in finite and infinite horizon have been derived for linear models by the coupled Riccati equations method [14, 15], and the coupled Hamilton–Jacobi equations method has been performed for nonlinear models [16, 17]. It can be seen that a local solution to the primal nonlinear H_2/H_∞ control exists if its linearized H_2/H_∞ control problem is solvable. However, most of the existing works on stochastic H_2/H_∞ control are concerned with jump linear systems, while little attention is paid on nonlinear systems with Markov jump.

As we all know, Markov jump systems have been used widely both in theory and in engineering over the past decades [18–24]. The main motivation of research studies is that such models have numerous applications in mechanics, traffic, power, and many other fields in industry and finance. When encountering system failures, sudden environmental changes, and external noise, the structure and parameter factors of dynamics are mutated. The process of state hopping from one mode to another can be marked as Markov jumps. The transition probabilities of a jump process are crucial factors which determine the behavior of a system exactly [25, 26]. Normally, the elements of the transition probability matrix are assumed to be fully known [14, 15]. However, in some practical cases, the transition probabilities may not be fully known, which inspired scholars to study Markov jump systems with partial probability [27–37]. For instance, Zhang and Boukas considered stability and stabilization of Markovian jump systems with partially unknown transition probabilities [27]. In addition, sliding-mode control, H_2, H_∞, and filtering control subject to partially unknown transition probabilities have gained

considerable research interest [29–35]. Nevertheless, to the best of our knowledge, there are no literatures to deal with H_2/H_∞ control for nonlinear jump systems with partially unknown transition probabilities up to now, which is the theoretical significance of this note. More importantly, to get the robust controller, a nonlinear stochastic bounded real lemma is derived.

The remainder of this paper is arranged as follows. The second part provides some useful definitions and lemmas. In the third part, for nonlinear jump systems with partially unknown transition probabilities, a sufficient condition and a necessary condition for the finite horizon H_2/H_∞ control are obtained, respectively. The forth part gives numerical illustrative examples. Conclusions are drawn in the fifth part.

Notations used in this study are as follows. $\mathscr{R}^n$ is the n-dimensional Euclidean space; $A>0\,(A\geq 0)$: A is a positive definite (positive semidefinite) matrix; $E(\cdot)$ is the mathematical expectation; A^T is the transpose of a matrix A; A^{-1} is the inverse of a nonsingular matrix A; $\mathscr{R}^{n\times m}$ is the set of all $n\times m$ real matrices; $\|\cdot\|$ is the Euclidean vector norm; $(\Omega,\mathscr{F},\{\mathscr{F}_t\}_{t\geq 0},\mathscr{P})$ is the completed filtration space with the filtration $\{\mathscr{F}_t\}_{t\geq 0}$ satisfying the usual conditions, i.e., it is right continuous and $\{\mathscr{F}_0\}$ contains all $\mathscr{P}$-null sets; $\mathscr{L}_F^2([0,T],\mathscr{R}^l)$ is the space of all nonanticipative stochastic processes $y(t)\in\mathscr{R}^l$ with respect to an increasing σ-algebra $F_t\,(t\geqslant 0)$, which satisfies $E\int_0^T\|y(t)\|^2\mathrm{d}t<\infty$; $\mathscr{C}^{2,1}(U,[0,T])$: the class of all functions $V(x,t)$ are twice continuously differentiable with respect to $x\in U$ and once continuously differentiable with respect to $t\in[0,T]$, except possibly at the point $x=0$; $I_{n\times n}$ is the identity matrix; $col(x_1,x_2,\ldots,x_n):=[x_1,x_2,\ldots,x_n]'$.

2. Preliminaries

Let us think about the following stochastic nonlinear jump systems described by the Itô-type equation:

$$\begin{cases} \mathrm{d}x(t)=\left[f(x,t,\theta_t)+g(x,t,\theta_t)u(t)+h(x,t,\theta_t)v(t)\right]\mathrm{d}t+\left[l(x,t,\theta_t)+q(x,t,\theta_t)u(t)+s(x,t,\theta_t)v(t)\right]\mathrm{d}\omega(t),\\ \quad x_0\in\mathscr{R}^n,\ \theta_0\in\mathscr{T},\ t\in[0,T],\\ z(t)=col\left[m(x,t,\theta_t),u(t)\right]:=\begin{pmatrix} m(x,t,\theta_t)\\ u(t)\end{pmatrix}, \end{cases} \tag{1}$$

where $x(t)\in\mathscr{R}^n$, $z(t)\in\mathscr{R}^z$, $u(t)\in\mathscr{L}_F^2([0,T],\mathscr{R}^{n_u})$, and $v(t)\in\mathscr{L}_F^2([0,T],\mathscr{R}^{n_v})$ stand for the system state, penalty output, control input, and exogenous disturbance signal, respectively. $\omega(t)$ is an one-dimensional standard wiener process defined on the filtered probability space $(\Omega,\mathscr{F},\mathscr{F}_t,\mathscr{P})$ with $\mathscr{F}_t=\sigma\{\omega(s)\colon 0\leq s\leq t\}$. The stochastic mode jump process θ_t is a continuous-time discrete-state Markov process with values in a finite space $\mathscr{T}=\{1,2,\ldots,N\}$ and is assumed to be independent with $\omega(t)$. The process of transition probabilities are denoted by

$$P\{\theta_{t+\tau}=h\mid\theta_t=r\}=\begin{cases}\pi_{rh}\tau+o(\tau), & r\neq h,\\ 1+\pi_{rr}\tau+o(\tau), & r=h,\end{cases} \tag{2}$$

where $\tau>0$, $\lim_{\tau\longrightarrow 0}(o(\tau)/\tau)=0$, and $\pi_{rh}\geq 0\,(r,h\in\mathscr{T},r\neq h)$ represent the transition rate from mode r at time t to mode h at time $t+\tau$ and $\pi_{rr}=-\sum_{h=1,r\neq h}^N\pi_{rh}$ for all $r\in\mathscr{T}$. So, the transition probabilities matrix is defined by

$$\prod=\begin{pmatrix}\pi_{11} & \pi_{12} & \cdots & \pi_{1N}\\ \pi_{21} & \pi_{22} & \cdots & \pi_{2N}\\ \vdots & \vdots & \ddots & \vdots\\ \pi_{N1} & \pi_{N2} & \cdots & \pi_{NN}\end{pmatrix}. \tag{3}$$

In this paper, we suppose that the transition probabilities are partly unknown. For instance, for $N=4$, the transition rate matrix $\prod$ is given by

$$\prod=\begin{pmatrix}\pi_{11} & ? & \pi_{13} & ?\\ ? & ? & ? & \pi_{24}\\ \pi_{31} & ? & \pi_{33} & ?\\ \pi_{41} & ? & ? & \pi_{44}\end{pmatrix}. \tag{4}$$

In above, we use "?" to sign the unknown element. Furthermore, $\forall r\in\mathscr{T}$, we set $\mathscr{T}=\mathscr{T}_K^r+\mathscr{T}_{UK}^r$, where

$$\begin{aligned}\mathscr{T}_K^r&\triangleq\{h\colon \pi_{rh}\text{ is known}\},\\ \mathscr{T}_{UK}^r&\triangleq\{h\colon \pi_{rh}\text{ is unknown}\}.\end{aligned} \tag{5}$$

In addition, if $\mathscr{T}_K^r\neq\varnothing$, it can be described as $\mathscr{T}_K^r=(\mathscr{K}_1^r,\mathscr{K}_2^r,\ldots,\mathscr{K}_m^r)$, $\forall 1\leq m\leq N$, where $\mathscr{K}_m^r$ is the mth known element and the exponent $\mathscr{K}_m^r$ is the rth row of matrix $\prod$. Then, set $\pi_K^r\triangleq\sum_{j\in\mathscr{T}_K^r}\pi_{rh}$.

Remark 1. When $\mathscr{T}_K^r=0$ and $\mathscr{T}_{UK}^r=\mathscr{T}$, the transition rates in the stochastic process are fully unknown. $\mathscr{T}_K^r=\mathscr{T}$ and $\mathscr{T}_{UK}^r=0$ mean that the transition rates are fully known.

For convenience, we signify $(\cdot)_{\theta_t}:=(\cdot)(x,t,\theta_t)$ throughout the paper, and all coefficients in (1) are thought to be Borel measurable. Meanwhile, assume that $f(0,t,r)\equiv 0$, $g(0,t,r)\equiv 0$ for $\forall(t,r)\in[0,T]\times\mathscr{T}$.

Now, we introduce the following definitions.

Definition 1. Given $\gamma>0$, a feedback control law $u=u_T^*\in\mathscr{L}_{\mathscr{F}}{}^2([0,T],\mathscr{R}^{n_u})$ is called the finite horizon robust H_2/H_∞ control of system (1), if the following conditions are satisfied:

(i) For any nonzero, $v(t) \in \mathscr{L}_{\mathscr{F}}{}^2([0,T],\mathscr{R}^{n_u})$, and the trajectory of the resulted closed-loop by (1) starting from $x_0 = 0$ and $\theta_0 = 0$, we always have

$$E\left\{\int_0^T \|m(x,t,\theta_t)\|^2 + \|u_T^*\|^2 \mathrm{d}t|\theta_0 = r\right\} \le \gamma^2 E\left\{\int_0^T \|v\|^2 \mathrm{d}t|\theta_0 = r\right\}, \quad r \in \mathscr{T}; \tag{6}$$

(ii) When the worst disturbance v_T^* is executed in (1), u_T^* can minimize the quadratic performance $E\left\{\int_0^T [\|m(x,t,\theta_t)\|^2 + \|u\|^2]\mathrm{d}t \mid \theta_0 = r\right\}$, $r \in \mathscr{T}$.

Definition 2 (see [18]). For each $V(x,t,r) \in C^{2,1}(\mathscr{R}^n \times [0,T] \times \mathscr{T}, \mathscr{R})$, we have an operator $\mathscr{L}V$: $\mathscr{R}^n \times [0,T] \times \mathscr{T} \longrightarrow \mathscr{R}$ associated with (1) given by

$$\begin{aligned}\mathscr{L}V(x,t,r) = {} & \frac{\partial V(x,t,r)}{\partial t} + \frac{\partial V'(x,t,r)}{\partial x}[f(x,t,r) + g(x,t,r)u(t) + h(x,t,r)v(t)] + \sum_{h=1}^{N} \pi_{rh} V_h \\ & + \frac{1}{2}[l(x,t,r) + q(x,t,r)u(t) + s(x,t,r)v(t)]^T \times \frac{\partial^2 V(x,t,r)}{\partial x^2}[l(x,t,r) + q(x,t,r)u(t) + s(x,t,r)v(t)].\end{aligned} \tag{7}$$

Definition 3 (see [16]). We set two extreme value functions $\widetilde{V}_T^1(x,s,\theta_t) \in \mathscr{R}^n \times [0,T] \times \mathscr{T} \longmapsto \mathscr{R}^-$ and $\widetilde{V}_T^2(x,s,\theta_t) \in \mathscr{R}^n \times [0,T] \times \mathscr{T} \longmapsto \mathscr{R}^+$ related with (1) as follows:

$$\begin{aligned}\widetilde{V}_T^1(x,s,\theta_t) &= \inf_{\substack{v \in \mathscr{L}_{\mathscr{F}}{}^2([s,T],\mathscr{R}^{n_v}) \\ x(s)=x, u=u_T^*}} J_1^T(u,v), \\ \widetilde{V}_T^2(x,s,\theta_t) &= \inf_{\substack{u \in \mathscr{L}_{\mathscr{F}}{}^2([0,T],\mathscr{R}^{n_u}) \\ x(s)=x, v=v_T^*}} J_2^T(u,v),\end{aligned} \tag{8}$$

in which the performances are as follows:

$$\begin{aligned}J_1^T(u,v;x_0,\theta_0) &:= \gamma^2\|v\|_{[0,T]}^2 - \|z\|_{[0,T]}^2 \\ &= E\left\{\int_0^T \left[\gamma^2\|v\|^2 - \|z\|^2\right]\mathrm{d}t \mid \theta_0 = r\right\}, \quad r \in \mathscr{T}, \\ J_2^T(u,v;x_0,\theta_0) &:= \|z\|_{[0,T]}^2 = E\left\{\int_0^T \|z\|^2 \mathrm{d}t \mid \theta_0 = r\right\}, \quad r \in \mathscr{T}.\end{aligned} \tag{9}$$

Remark 2. The following results are obvious:

$$\begin{aligned}&\widetilde{V}_T^1 \le 0, \widetilde{V}_T^1(x,t,\theta_t) = 0 \quad \text{for} \quad \text{all } x \in \mathscr{R}^n; \\ &\widetilde{V}_T^2 \ge 0, \quad \widetilde{V}_T^2(x,t,\theta_t) = 0 \quad \text{for} \quad \text{all } x \in \mathscr{R}^n.\end{aligned} \tag{10}$$

Remark 3. Let the perturbation operator be denoted by L^T: $\mathscr{L}_{\mathscr{F}}^2([0,T],\mathscr{R}^{n_v}) \longrightarrow \mathscr{L}_{\mathscr{F}}^2([0,T],\mathscr{R}^{n_z})$ with the norm

$$\begin{aligned}\|L^T\| &= \sup_{\substack{v \in \mathscr{L}_{\mathscr{F}}{}^2([0,T],\mathscr{R}^{n_v}) \\ v \ne 0, \theta_0 = r, x_0 = 0}} \frac{\|z(\cdot)\|_{[0,T]}}{\|v(\cdot)\|_{[0,T]}} \\ &= \sup_{\substack{v \in \mathscr{L}_{\mathscr{F}}{}^2([0,T],\mathscr{R}^{n_v}) \\ v \ne 0, \theta_0 = r, x_0 = 0}} \frac{E\left\{\int_0^T \|m(x,t,\theta_t)\|^2 \mathrm{d}t|\theta_0 = r\right\}^{1/2}}{E\left\{\int_0^T \|v\|^2 \mathrm{d}t|\theta_0 = r\right\}^{1/2}}, \quad r \in \mathscr{T}.\end{aligned} \tag{11}$$

It can be checked that (6) is equivalent to $\|L^T\| \le \gamma$.

Next, we state the following lemmas, which will be used later.

Lemma 1. *For a given level $\gamma > 0$, with an initial state $x_0 = 0 \in \mathscr{R}^n$ and $\theta_0 \in \mathscr{T}$, think about the following stochastic perturbed system with Markov jumps:*

$$\begin{cases}\mathrm{d}x(t) = [f(x,t,\theta_t) + h(x,t,\theta_t)v(t)]\mathrm{d}t \\ +[l(x,t,\theta_t) + s(x,t,\theta_t)v(t)]\mathrm{d}w(t), \\ z(t) = m(x,t,\theta_t).\end{cases} \tag{12}$$

If there exists $V(x,t,\theta_t) \in C^{2,1}(\mathscr{R}^n \times [0,T] \times \mathscr{T}, \mathscr{R})$ with system (12) and satisfies the following HJE:

$$\left\{ \begin{aligned} &\Delta_1\left(V_{\theta_t}\right) := \frac{\partial V_{\theta_t}}{\partial t} + \frac{\partial V_{\theta_t}'}{\partial x} f_{\theta_t} - m_{\theta_t}' m_{\theta_t} + \frac{1}{2} l_{\theta_t}' \frac{\partial^2 V_{\theta_t}}{\partial x^2} l_{\theta_t} + \sum_{h \in \mathscr{T}_K^r} \pi_{rh}\left(V_h - T_r\right) - \frac{1}{4}\left(\frac{\partial V_{\theta_t}'}{\partial x} h_{\theta_t} + l_{\theta_t}' \frac{\partial^2 V_{\theta_t}}{\partial x^2} s_{\theta_t}\right) \\ &\left(\gamma^2 I + \frac{1}{2} s_{\theta_t}' \frac{\partial^2 V_{\theta_t}}{\partial x^2} s_{\theta_t}\right)^{-1}\left(h_{\theta_t}' \frac{\partial V_{\theta_t}}{\partial x} + s_{\theta_t}' \frac{\partial^2 V_{\theta_t}}{\partial x^2} l_{\theta_t}\right) = 0, \gamma^2 I + \frac{1}{2} s_{\theta_t}' \frac{\partial^2 V_{\theta_t}}{\partial x^2} s_{\theta_t} > 0, V_h - T_r \geq 0, \quad h \in \mathscr{T}_{UK}^r, r \neq h, V_h - T_r \geq 0, \\ &h \in \mathscr{T}_{UK}^r, r = h, V\left(x, T, \theta_t\right) = 0. \end{aligned} \right. \tag{13}$$

Then, $\|L^T\| \leq \gamma$ holds.

Proof. Noticing that for any symmetric matrix T_r $(r \in \mathscr{T})$, we have $\sum_{h=1}^N \pi_{rh} T_r = 0$. Applying the generalized Itô's formula, one gets

$$\begin{aligned} &\mathscr{L}V\left(x, t, \theta_t\right) \\ &= E\left\{\int_0^T \left[\frac{\partial V_{\theta_t}}{\partial t} + \frac{\partial V_{\theta_t}'}{\partial x}\left(f_{\theta_t} + h_{\theta_t} v\right) + \frac{1}{2}\left(l_{\theta_t} + s_{\theta_t} v\right)' \frac{\partial^2 V_{\theta_t}}{\partial x^2}\left(l_{\theta_t} + s_{\theta_t} v\right) + \sum_{h=1}^N \pi_{\theta_t h} V_h\right] \mathrm{d}t \mid \theta_0 = r\right\} \\ &= E\left\{\int_0^T \left[\frac{\partial V_{\theta_t}}{\partial t} + \frac{\partial V_{\theta_t}'}{\partial x}\left(f_{\theta_t} + h_{\theta_t} v\right) + \frac{1}{2}\left(l_{\theta_t} + s_{\theta_t} v\right)' \frac{\partial^2 V_{\theta_t}}{\partial x^2}\left(l_{\theta_t} + s_{\theta_t} v\right) + \sum_{h=1}^N \pi_{rh} V_h - \sum_{h=1}^N \pi_{rh} T_r\right] \mathrm{d}t \mid \theta_0 = r\right\} \\ &= E\left\{\int_0^T \left[\frac{\partial V_{\theta_t}}{\partial t} + \frac{\partial V_{\theta_t}'}{\partial x}\left(f_{\theta_t} + h_{\theta_t} v\right) + \frac{1}{2}\left(l_{\theta_t} + s_{\theta_t} v\right)' \frac{\partial^2 V_{\theta_t}}{\partial x^2}\left(l_{\theta_t} + s_{\theta_t} v\right) + \sum_{h \in \mathscr{T}_K^r} \pi_{rh}\left(V_h - T_r\right) + \sum_{h \in \mathscr{T}_{UK}^r} \pi_{rh}\left(V_h - T_r\right) \mathrm{d}t\right] \mid \theta_0 = r\right\}. \end{aligned} \tag{14}$$

Then, it can deduced that

$$\begin{aligned} &E\left\{\left[V\left(x_T, T, \theta_T\right) - V\left(x_0, 0, \theta_0\right)\right] \mid \theta_0 = r\right\} \\ &= E\int_0^T \mathscr{L}_T V\left(x, t, \theta_t\right) \\ &= E\left\{\int_0^T \left[\frac{\partial V_{\theta_t}}{\partial t} + \frac{\partial V_{\theta_t}'}{\partial x}\left(f_{\theta_t} + h_{\theta_t} v\right) + \frac{1}{2}\left(l_{\theta_t} + s_{\theta_t} v\right)' \frac{\partial^2 V_{\theta_t}}{\partial x^2}\left(l_{\theta_t} + s_{\theta_t} v\right) + \sum_{h=1}^N \pi_{\theta_t h} V\left(x, t, h\right) + \|z\|^2 - \gamma^2\|v\|^2 - \|z\|^2 + \gamma^2\|v\|^2\right] \mathrm{d}t \mid \theta_0 = r\right\} \\ &= E\left\{\int_0^T \left[\frac{\partial V_{\theta_t}}{\partial t} + \frac{\partial V_{\theta_t}'}{\partial x}\left(f_{\theta_t} + h_{\theta_t} v\right) + \frac{1}{2}\left(l_{\theta_t} + s_{\theta_t} v\right)' \frac{\partial^2 V_{\theta_t}}{\partial x^2}\left(l_{\theta_t} + s_{\theta_t} v\right) + \|z\|^2 - \gamma^2\|v\|^2 - \|z\|^2 + \gamma^2\|v\|^2 + \sum_{h \in \mathscr{T}_K^r} \pi_{rh}\left(V_h - T_r\right)\right. \right. \\ &\quad \left. \left. + \sum_{h \in \mathscr{T}_{UK}^r} \pi_{rh}\left(V_h - T_r\right)\right] \mathrm{d}t \mid \theta_0 = r\right\} \\ &= E\left\{\int_0^T \left(\|z\|^2 - \gamma^2\|v\|^2\right) \mathrm{d}t + \left\|v - v_T^*\right\|_{\left(\gamma, s, V_{\theta_t}\right)}^2 + \Delta_1\left(V_{\theta_t}\right) + \sum_{h \in \mathscr{T}_{UK}^r} \pi_{rh}\left(V_h - T_r\right) \mid \theta_0 = r\right\}, \quad r \in \mathscr{T}, \end{aligned} \tag{15}$$

where

$$\|z\|^2_{(\gamma,s,V_{\theta_t})} = z'\left(\gamma^2 I + \frac{1}{2}s_{\theta_t}'\frac{\partial^2 V_{\theta_t}}{\partial x^2}s_{\theta_t}\right)z,$$

$$\widehat{v}_T^* = -\frac{1}{2}\left(\gamma^2 I + \frac{1}{2}s_{\theta_t}'\frac{\partial^2 V_{\theta_t}}{\partial x^2}s_{\theta_t}\right)^{-1} \cdot \left(h_{\theta_t}'\frac{\partial V_{\theta_t}}{\partial x} + s_{\theta_t}'\frac{\partial^2 V_{\theta_t}}{\partial x^2}l_{\theta_t}\right), \tag{16}$$

$$\pi_{rh} \geq 0\,(\forall r, h \in \mathscr{T}, r \neq h),$$

$$\pi_{rr} = -\sum_{h=1, r\neq h}^{N} \pi_{rh} < 0\,(r \in \mathscr{T}),$$

$$\sum_{h\in\mathscr{T}_{UK}^r} \pi_{rh}(V_h - T_r) \geq 0.$$

Inferring from (14)–(16), it reveals that $\widehat{v}_T^*$ is the corresponding worst disturbance, which yields that

$$\begin{aligned} &E\left\{\int_0^T \|z\|^2 \mathrm{d}t|\theta_0 = r\right\} \\ &= E\left\{\int_0^T \left\{\gamma^2\|v\|^2 - \left\|v - v_T^*\right\|^2_{(\gamma,s,V_{\theta_t})} - \Delta_1\left(V_{\theta_t}\right) - \sum_{h\in\mathscr{T}_{UK}^r} \pi_{rh}(V_h - T_r) + E\left[V(x_T, T, \theta_T) - V(x_0, 0, \theta_0)\right]\right\}\mathrm{d}t \mid \theta_0 = r\right\} \\ &\leq E\left\{\int_0^T \gamma^2\|v\|^2 \mathrm{d}t|\theta_0 = r\right\}. \end{aligned} \tag{17}$$

That is,

$$0 \leq J_1^T(u_T^*, v_T^*; x_0, \theta_0) \leq J_1^T(u_T^*, v; x_0, \theta_0). \tag{18}$$

This lemma is proved. □

Lemma 2. For a given level $\gamma > 0$, with an initial state $x_0 = 0 \in \mathscr{R}^n$, $\theta_0 \in \mathscr{T}$, think about the following nonlinear stochastic controlled system with Markov jumps:

$$\begin{cases} \mathrm{d}x(t) = [f(x,t,\theta_t) + g(x,t,\theta_t)u(t)]\mathrm{d}t \\ +[l(x,t,\theta_t) + q(x,t,\theta_t)u(t)]\mathrm{d}w(t), \\ z(t) = m(x,t,\theta_t). \end{cases} \tag{19}$$

If the following HJE

$$\begin{cases} \Delta_2\left(V_{2\theta_t}\right) := \dfrac{\partial V_{2\theta_t}}{\partial t} + \dfrac{\partial V_{2\theta_t}'}{\partial x} f_{\theta_t} - m_{\theta_t}' m_{\theta_t} + \dfrac{1}{2}l_{\theta_t}'\dfrac{\partial^2 V_{2\theta_t}}{\partial x^2}l_{\theta_t} + \displaystyle\sum_{h\in\mathscr{T}_K^r} \pi_{rh}(V_h - T_r) \\ -\dfrac{1}{4}\left(\dfrac{\partial V_{2\theta_t}'}{\partial x} g_{\theta_t} + l_{\theta_t}'\dfrac{\partial^2 V_{2\theta_t}}{\partial x^2}q_{\theta_t}\right)\left(I + \dfrac{1}{2}q_{\theta_t}'\dfrac{\partial^2 V_{2\theta_t}}{\partial x^2}q_{\theta_t}\right)^{-1}\left(h_{\theta_t}'\dfrac{\partial V_{2\theta_t}}{\partial x} + q_{\theta_t}'\dfrac{\partial^2 V_{2\theta_t}}{\partial x^2}l_{\theta_t}\right) = 0, I \\ +\dfrac{1}{2}q_{\theta_t}'\dfrac{\partial^2 V_{2\theta_t}}{\partial x^2}q_{\theta_t} > 0, V_h - T_r \geq 0, \quad h \in \mathscr{T}_{UK}^r, \quad r \neq h, V_h - T_r \leq 0, \quad h \in \mathscr{T}_{UK}^r, \quad r = h, V_2(x, T, \theta_t) = 0. \end{cases} \tag{20}$$

admits a nonnegative solution $V_2(x,t,\theta_t) \in C^{2,1}(\mathscr{R}^n \times [0,T] \times \mathscr{T}, \mathscr{R})$, *then we have*

$$J_2^T(u_T^*, v_T^*; x_0, \theta_0) \leq J_2^T(u_T, v_T^*; x_0, \theta_0) = V_2(x_0, 0, r), \quad r \in \mathscr{T}, \tag{21}$$

with the optimal control

$$\widehat{u}_T^* = -\frac{1}{2}\left(I + \frac{1}{2}q_{\theta_t}'\frac{\partial^2 V_{2\theta_t}}{\partial x^2}q_{\theta_t}\right)^{-1}\left(g_{\theta_t}'\frac{\partial V_{2\theta_t}}{\partial x} + q_{\theta_t}'\frac{\partial^2 V_{2\theta_t}}{\partial x^2}l_{\theta_t}\right), \tag{22}$$

where

$$J_2^T(u_T, v_T^*; x_0, \theta_0) := \inf_{u \in \mathscr{L}_F^2([0,T], \mathscr{R}^{n_u})} E\left\{\int_0^T \|z\|^2 \mathrm{d}t \mid \theta_0 = r\right\}$$
$$= \inf_{u \in \mathscr{L}_F^2([0,T], \mathscr{R}^{n_u})} E\left\{\int_0^T \left\|m_{\theta_t}\right\|^2 + \|u\|^2 \mathrm{d}t \mid \theta_0 = r\right\}. \tag{23}$$

Proof. Taking integration and expectation in $\mathrm{d}V_2(x,t,\theta_t)$, for any $T > 0$, we get

$$\begin{aligned}
&E\int_0^T \mathrm{d}V_2(x,t,\theta_t) \\
&= E\left\{\int_0^T L_u V_2 \mathrm{d}t + E\int_0^T \left(l_{\theta_t} + q_{\theta_t} u\right)' \frac{\partial V_{2\theta_t}}{\partial x} \mathrm{d}w(t) \mid \theta_0 = r\right\} \\
&= E\left\{\int_0^T \left[\frac{\partial V_{2\theta_t}}{\partial t} + \frac{\partial V_{2\theta_t}'}{\partial x}\left(f_{\theta_t} + g_{\theta_t} u\right)\mathrm{d}t + \frac{1}{2}\left(l_{\theta_t} + q_{\theta_t} u\right)' \frac{\partial^2 V_{2\theta_t}}{\partial x^2}\left(l_{\theta_t} + q_{\theta_t} u\right)\right]\mathrm{d}t + \sum_{h=1}^N \pi_{rh} V(x,t,h) \mid \theta_0 = r\right\} \\
&= E\left\{\int_0^T \left[\frac{\partial V_{2\theta_t}}{\partial t} + \frac{\partial V_{2\theta_t}'}{\partial x}\left(f_{\theta_t} + g_{\theta_t} u\right) + \frac{1}{2}\left(l_{\theta_t} + q_{\theta_t} u\right) \frac{\partial^2 V_{2\theta_t}}{\partial x^2}\left(l_{\theta_t} + q_{\theta_t} u\right)\right]\mathrm{d}t + \sum_{h=1}^N \pi_{rh} V_h - \sum_{h=1}^N \pi_{rh} T_r \mid \theta_0 = r\right\} \\
&= E\left\{\int_0^T \left[\frac{\partial V_{2\theta_t}}{\partial t} + \frac{\partial V_{2\theta_t}'}{\partial t}\left(f_{\theta_t} + g_{\theta_t} u\right)\mathrm{d}t + \frac{1}{2}\left(l_{\theta_t} + q_{\theta_t} u\right)' \frac{\partial^2 V_{2\theta_t}}{\partial x^2}\left(l_{\theta_t} + q_{\theta_t} u\right)\right]\mathrm{d}t + \sum_{h \in \mathscr{T}_K^r} \pi_{rh}\left(V_h - T_r\right)\right. \\
&\quad \left. + \sum_{h \in \mathscr{T}_{UK}^r} \pi_{rh}\left(V_h - T_r\right) \mid \theta_0 = r\right\}, \quad r \in \mathscr{T}.
\end{aligned} \tag{24}$$

By Itô's formula and the completing square technique combined with (24), we obtain

$$\begin{aligned}
&J_2^T(u, v_T^*; x_0, \theta_0) \\
&= E\left\{\int_0^T \|z\|^2 \mathrm{d}t \,\middle|\, \theta_0 = r\right\} \\
&= E\left\{\int_0^T \left(\left\|m_{\theta_t}\right\|^2 + \|u\|^2\right)\mathrm{d}t | \theta_0 = r\right\} \\
&= E\left\{\int_0^T \left(m_{\theta_t}' m_{\theta_t} + u' u\right)\mathrm{d}t + \mathscr{L}V_2(x,t,\theta_t) + V_2(x_0, 0, \theta_0) - EV_2(x,t,\theta_t) | \theta_0 = r\right\} \\
&= E\left\{\int_0^T \left[\frac{\partial V_{2\theta_t}}{\partial t} + l_{\theta_t}' \frac{\partial V_{2\theta_t}'}{\partial x}\left(f_{\theta_t} + g_{\theta_t} u\right) + \frac{1}{2}\left(l_{\theta_t} + q_{\theta_t} u\right)' \frac{\partial^2 V_{2\theta_t}}{\partial x^2}\left(l_{\theta_t} + q_{\theta_t} u\right)\right]\mathrm{d}t + \sum_{h=1}^N \pi_{rh} V(x,t,h) + m_{\theta_t}' m_{\theta_t} + u' u \mathrm{d}t\right. \\
&\quad \left. + V_2(x_0, 0, \theta_0) - EV(x,t,\theta_t) | \theta_0 = r\right\} \\
&= E\left\{\int_0^T \left[\frac{\partial V_{2\theta_t}}{\partial t} + l_{\theta_t}' \frac{\partial V_{2\theta_t}'}{\partial x} f_{\theta_t} + \frac{1}{2} l_{\theta_t}^T \frac{\partial^2 V_{2\theta_t}}{\partial x^2} l_{\theta_t} + m_{\theta_t}' m_{\theta_t} + \sum_{h \in \mathscr{T}_K^r} \pi_{rh}\left(V_h - T_r\right) + \sum_{h \in \mathscr{T}_{UK}^r} \pi_{rh}\left(V_h - T_r\right)\right.\right. \\
&\quad - \frac{1}{4}\left(\frac{\partial^2 V_{2\theta_t}'}{\partial x^2} g_{\theta_t} + l_{\theta_t}' \frac{\partial^2 V_{2\theta_t}}{\partial x^2} q_{\theta_t}\right)\left(I + \frac{1}{2} q_{\theta_t}' \frac{\partial^2 V_{2\theta_t}}{\partial x^2} q_{\theta_t}\right)^{-1} + \left(g_{\theta_t}' \frac{\partial V_{2\theta_t}}{\partial x} + q_{\theta_t}' \frac{\partial^2 V_{2\theta_t}}{\partial x^2} l_{\theta_t}\right) + \left(u - \hat{u}_T^*\right)' \left(I + \frac{1}{2} q_{\theta_t}' \frac{\partial^2 V_{2\theta_t}}{\partial x^2} q_{\theta_t}\right)\left(u - \hat{u}_T^*\right)\Bigg]\mathrm{d}t \\
&\quad \left.\left. + V_2(x_0, 0, \theta_0) - EV(x,t,\theta_t) | \theta_0 = r\right\}\right. \\
&= E\int_0^T \left\|u - \hat{u}_T^*\right\|^2 \mathrm{d}t + \triangle_2\left(V_{2\theta_t}\right) + \sum_{h \in \mathscr{T}_{UK}^r} \pi_{rh}\left(V_h - T_r\right) + V_2(x_0, 0, r) - EV(x,t,\theta_t), \quad r \in \mathscr{T},
\end{aligned} \tag{25}$$

in which the inequality $J_2^T(u_T^*, v_T^*; x_0, \theta_0) \le J_2^T(u_T, v_T^*; x_0, \theta_0) = V_2(x_0, 0, r)$ holds since that $V_2(x, T, \theta_t) = 0$, $\triangle_2(V_{2\theta_t}) = 0$, and $\sum_{h\in\mathcal{T}_{UK}^r} \pi_{rh}(V_h - T_r) \ge 0\,(r = h \text{ or } r \ne h)$. So, from (25), this lemma is obvious with the optimal control (22). □

3. Main Results

In this part, a sufficient condition comes down to Theorem 1 for the solvability of the H_2/H_∞ control with nonlinear jump systems (1).

Theorem 1. *For a given $\gamma > 0$, think about the following four cross-coupled HJEs:*

$$\begin{cases} \triangle_3(V_{1\theta_t}) := \dfrac{\partial V_{1\theta_t}}{\partial t} + \dfrac{\partial V_{1\theta_t}'}{\partial x} f_{\theta_t} - \tilde{m}_{\theta_t}'\tilde{m}_{\theta_t} + \dfrac{1}{2}\tilde{l}_{\theta_t}'\dfrac{\partial^2 V_{\theta_t}}{\partial x^2}\tilde{l}_{\theta_t} + \sum\limits_{h\in\mathcal{T}_K^r} \pi_{rh}(V_h - T_r) - \dfrac{1}{4}\left(\dfrac{\partial V_{1\theta_t}'}{\partial x} h_{\theta_t} + \tilde{l}_{\theta_t}'\dfrac{\partial^2 V_{1\theta_t}}{\partial x^2} s_{\theta_t}\right)\left(\gamma^2 I + \dfrac{1}{2} s_{\theta_t}'\dfrac{\partial^2 V_{\theta_t}}{\partial x^2} s_{\theta_t}\right)^{-1} \\ \left(h_{\theta_t}'\dfrac{\partial V_{\theta_t}}{\partial x} + s_{\theta_t}'\dfrac{\partial^2 V_{\theta_t}}{\partial x^2}\tilde{l}_{\theta_t}\right) = 0, \gamma^2 I + \dfrac{1}{2} s_{\theta_t}'\dfrac{\partial^2 V_{1\theta_t}}{\partial x^2} s_{\theta_t} > 0, V_h - T_r \ge 0, \quad h \in \mathcal{T}_{UK}^r,\ r \ne h, V_h - T_r \le 0, \quad h \in \mathcal{T}_{UK}^r,\ r = h, V_1(x, T, \theta_t) = 0, \end{cases} \tag{26}$$

$$K_1 = -\frac{1}{2}\left(\gamma^2 I + \frac{1}{2} s_{\theta_t}'\frac{\partial^2 V_{1\theta_t}}{\partial x^2} s_{\theta_t}\right)^{-1}\left(h_{\theta_t}'\frac{\partial V_{1\theta_t}}{\partial x} + s_{\theta_t}'\frac{\partial^2 V_{1\theta_t}}{\partial x^2}\tilde{l}_{\theta_t}\right), \tag{27}$$

$$\begin{cases} \triangle_4(V_{2\theta_t}) := \dfrac{\partial V_{2\theta_t}}{\partial t} + \dfrac{\partial V_{2\theta_t}'}{\partial x}\tilde{f}_{\theta_t} - m_{\theta_t}' m_{\theta_t} + \dfrac{1}{2}\tilde{l}_{1\theta_t}'\dfrac{\partial^2 V_{\theta_t}}{\partial x^2}\tilde{l}_{1\theta_t} + \sum\limits_{h\in\mathcal{T}_K^r} \pi_{rh}(V_h - T_r) - \dfrac{1}{4}\left(\dfrac{\partial V_{2\theta_t}'}{\partial x} g_{\theta_t} + \tilde{l}_{1\theta_t}'\dfrac{\partial^2 V_{2\theta_t}}{\partial x^2} s_{\theta_t}\right) \\ \left(I + \dfrac{1}{2} q_{\theta_t}'\dfrac{\partial^2 V_{2\theta_t}}{\partial x^2} q_{\theta_t}\right)^{-1}\left(h_{\theta_t}'\dfrac{\partial V_{2\theta_t}}{\partial x} + q_{\theta_t}'\dfrac{\partial^2 V_{2\theta_t}}{\partial x^2}\tilde{l}_{1\theta_t}\right) = 0, I + \dfrac{1}{2} q_{\theta_t}'\dfrac{\partial^2 V_{2\theta_t}}{\partial x^2} q_{\theta_t} > 0, V_h - T_r \ge 0, \quad h \in \mathcal{T}_{UK}^r,\ r \ne h, V_h - T_r \leqslant 0, \\ h \in \mathcal{T}_{UK}^r,\ r = h, V_1(x, T, \theta_t) = 0, \end{cases} \tag{28}$$

$$K_2 = -\frac{1}{2}\left(I + \frac{1}{2} q_{\theta_t}'\frac{\partial^2 V_{2\theta_t}}{\partial x^2} q_{\theta_t}\right)^{-1}\left(g_{\theta_t}'\frac{\partial V_{2\theta_t}}{\partial x} + q_{\theta_t}'\frac{\partial^2 V_{2\theta_t}}{\partial x^2}\tilde{l}_{1\theta_t}\right). \tag{29}$$

If there exist solutions $(V_{1\theta_t}, V_{2\theta_t})$ with $V_{1\theta_t} \le 0$ and $V_{2\theta_t} \ge 0$ for (26)–(29), then the finite horizon H_2/H_∞ control of nonlinear Markov jumps has a pair of solutions (u_T^*, v_T^*) with $u_T^* = K_2 x$, $v_T^* = K_1 x$, and $J_2^T(u_T^*, v_T^*; x_0, \theta_0) = V_2(x_0, 0, r)$.

Proof. Notice the following transformations in (26)–(29):

$$\begin{aligned} \tilde{f}_{\theta_t} &= f_{\theta_t} + g_{\theta_t} K_2, \\ \tilde{l}_{\theta_t} &= l_{\theta_t} + q_{\theta_t} K_2, \\ \tilde{m}_{\theta_t} &= col(m_{\theta_t}, K_2), \\ \tilde{f}_{1\theta_t} &= f_{\theta_t} + h_{\theta_t} K_1, \\ \tilde{l}_{1\theta_t} &= l_{\theta_t} + s_{\theta_t} K_1. \end{aligned} \tag{30}$$

Substituting $u = K_2 x$ with K_2 defined by (29) into (1), we have

$$\begin{cases} dx(t) = \left[\tilde{f}(x, t, \theta_t) + h(x, t, \theta_t) v(t)\right] dt \\ + \left[\tilde{l}(x, t, \theta_t) + s(x, t, \theta_t) v(t)\right] dw(t), \\ z(t) = (m_{\theta_t}, K_2). \end{cases} \tag{31}$$

Applying Lemma 1 to system (31), we conclude

$$E\left\{\int_0^T \|m_{\theta_t}\|^2 + \|u_T^*\|^2 dt | \theta_0 = r\right\} \le \gamma^2 E\left\{\int_0^T \|v\|^2 dt | \theta_0 = r\right\}, \quad r \in \mathcal{T}, \tag{32}$$

and $v = K_1 x$ is the worst case disturbance. In the meantime, implementing $v = v_T^* = K_1 x$ into (1), one yields that

$$\begin{cases} dx(t) = \left[\tilde{f}_1(x, t, \theta_t) + g(x, t, \theta_t) u(t)\right] dt \\ + \left[\tilde{l}_1(x, t, \theta_t) + q(x, t, \theta_t) u(t)\right] dw(t), \\ x_0 \in \mathcal{R}^n,\ \theta_0 \in \mathcal{T},\ t \in [0, T]. \end{cases} \tag{33}$$

Minimizing $J_2^T(u, v_T^*; x_0, \theta_0)$ under the constraint of (33) is a standard nonlinear quadratic optimal problem. By applying the Lemma 2, $J_2^T(u, v_T^*; x_0, \theta_0)$ achieves its

minimum at $u_T^* = K_2 x$, and $J_2^T(u_T^*, v_T^*; x_0, \theta_0) = V_2(x_0, 0, r)$. By Definition 1, this theorem is proved.

Theorem 2 offers a necessary condition for the H_2/H_∞ control of system (1). □

Theorem 2. *For a given $\gamma > 0$, $\widetilde{V}_{T\theta_t}^1, \widetilde{V}_{T\theta_t}^2 \in \mathscr{C}^{2,1} \in \mathscr{R}^n \times [0,T] \times \mathscr{T}$, think about system (1). If the finite horizon H_2/H_∞ of nonlinear stochastic jump systems has solutions $(u_T^* = K_2 x, v_T^* = K_1 x) \in \mathscr{L}_F^2([0,T], \mathscr{R}^{n_u}) \times ([0,T], \mathscr{R}^{n_u})$ satisfying the following terms:*

$$\begin{cases} \gamma^2 I + \dfrac{1}{2} s_{\theta_t}{}' \dfrac{\partial^2 \widetilde{V}_{T\theta_t}^1}{\partial x^2} s_{\theta_t} > 0, \quad V_T^1(x,t,\theta_t) = 0, \\ I + \dfrac{1}{2} q_{\theta_t}{}' \dfrac{\partial^2 \widetilde{V}_{T\theta_t}^2}{\partial x^2} q_{\theta_t} > 0, \quad V_T^2(x,t,\theta_t) = 0. \end{cases} \tag{34}$$

Sen, $\widetilde{V}_{T\theta_t}^1 \le 0$ and $\widetilde{V}_{T\theta_t}^2 \ge 0$ are the solutions of the four cross-coupled HJEs (26)–(29).

Proof. Substituting $u = u_T^* = K_2 x$ into (1), one reads (31). Hence, (6) holds because (u_T^*, v_T^*) solves the H_2/H_∞ control. By Definition 3, Lemma 1, and Lemma 4.1 of [17], we assert that $\widetilde{V}_{T\theta_t}^1 \le 0$ solves the following HJE:

$$\begin{cases} \mathscr{L}_{u=u_T^*, v=0} \widetilde{V}_T^1 - m_{\vartheta_t}{}' m_{\theta_t} - \|K_2\|^2 - \sum\limits_{h \in \mathscr{T}_K^r} \pi_{rh}(V_h - T_r) \\ \quad - \dfrac{1}{4}\left(\dfrac{\partial \widetilde{V}_{T\theta_t}^1}{\partial x} h_{\theta_t} + \widetilde{l}_{\theta_t}{}' \dfrac{\partial^2 \widetilde{V}_{T\theta_t}^1}{\partial x^2} s_{\theta_t} \right) \left(\gamma^2 I + \dfrac{1}{2} s_{\theta_t}{}' \dfrac{\partial^2 \widetilde{V}_{T\theta_t}^1}{\partial x^2} s_{\theta_t} \right)^{-1} \left(h_{\theta_t}{}' \dfrac{\partial \widetilde{V}_{T\theta_t}^1}{\partial x} + s_{\theta_t}{}' \dfrac{\partial^2 \widetilde{V}_{T\theta_t}^1}{\partial x^2} \widetilde{l}_{\theta_t} \right) = 0, \\ \gamma^2 I + \dfrac{1}{2} s_{\theta_t}{}' \dfrac{\partial^2 \widetilde{V}_{T\theta_t}^1}{\partial x^2} s_{\theta_t} > 0, \\ V_h - T_r \geqslant 0, \quad h \in \mathscr{T}_{UK}^r, \ r \ne h, \\ V_h - T_r \leqslant 0, \quad h \in \mathscr{T}_{UK}^r, \ r = h, \\ \widetilde{V}_T^1(x, T, \theta_t) = 0. \end{cases} \tag{35}$$

Notice the inequality (15), apparently,

$$\begin{aligned} & E\left\{ \int_0^T \left(\gamma^2 \|v\|^2 - \|z\|^2 \right) \mathrm{d}t \,|\, \theta_0 = r \right\} \\ & = V(0,0,\theta_0) - EV(x,t,\theta_t) + E \int_0^T \left\| v - v_T^* \right\|^2_{\left(\gamma, s, \widetilde{V}_{T\theta_t}^1\right)} \mathrm{d}t + \Delta_3\left(V_{1\theta_t}\right) + \sum_{h \in \mathscr{T}_{UK}^r} \pi_{rh}(V_h - T_r). \end{aligned} \tag{36}$$

This, together with (35) and Definition 3, for each $T > 0$

$$\begin{aligned} J_1^T(u_T^*, v; x_0, \theta_0) = {} & \widetilde{V}_T^1(x_0, 0, \theta_0) + E \int_0^T \left\| v - \widetilde{v}_T^* \right\|^2_{\left(\gamma, s, \widetilde{V}_{T\theta_t}^1\right)} \mathrm{d}t \\ & + \sum_{h \in \mathscr{T}_{UK}^r} \pi_{rh}(V_h - T_r). \end{aligned} \tag{37}$$

From (37), we see that $J_1^T(u_T^*, v_T^*; x_0, \theta_0) = \min J_1^T(u_T^*, v; x_0, \theta_0)$, and

$$\widetilde{v}_T^* = -\frac{1}{2}\left(\gamma^2 I + \frac{1}{2} s_{\theta_t}{}' \frac{\partial^2 \widetilde{V}_{T\theta_t}^1}{\partial x^2} s_{\theta_t} \right)^{-1} \left(h_{\theta_t}{}' \frac{\partial \widetilde{V}_{T\theta_t}^1}{\partial x} + s_{\theta_t}{}' \frac{\partial^2 \widetilde{V}_{T\theta_t}^1}{\partial x^2} \widetilde{l}_{\theta_t} \right), \tag{38}$$

is the worst perturbance. So, $v_T^* = \widetilde{v}_T^* = K_1 x$. Then, substituting $v = v_T^* = K_1 x$ into (1), (33) can be obtained. Owing to minimizing $\widetilde{V}_T^2(x, s, \theta_t) = \inf_{u \in \mathscr{L}_{\mathscr{F}}{}^2([0,T], \mathscr{R}^{n_u})} x(s) = x, v = v_T^* J_2^T(u, v)$ under the constraint of (33), we can infer that $u_T^* = K_2 x$ is the optimal solution. Next,

considering the stochastic dynamic programming principle, we can certify that $(\widetilde{V}^2_{T\theta_t}, u^*_T)$ solves the following HJE:

$$-\frac{\partial \widetilde{V}^2_{T\theta_t}}{\partial t} + \max_{u\in\mathscr{L}^2_{\widetilde{F}}([0,T],\mathscr{R}^{n_u})} H\left(x,t,\theta_t,u,-\frac{\partial \widetilde{V}^2_{T\theta_t}}{\partial x},-\frac{\partial^2 \widetilde{V}^2_{T\theta_t}}{\partial x^2}\right) = 0, \tag{39}$$

that is,

$$-\frac{\partial \widetilde{V}^2_{T\theta_t}}{\partial t} + H\left(x,t,\theta_t,u^*_T,-\frac{\partial \widetilde{V}^2_{T\theta_t}}{\partial x},-\frac{\partial^2 \widetilde{V}^2_{T\theta_t}}{\partial x^2}\right) = 0. \tag{40}$$

In this step, the generalized Hamiltonian function is prescribed as follows:

$$\begin{aligned} &H\left(x,t,\theta_t,u,-\frac{\partial \widetilde{V}^2_{T\theta_t}}{\partial x},-\frac{\partial^2 \widetilde{V}^2_{T\theta_t}}{\partial x^2}\right) \\ &\quad := -\|u\|^2 - \left\|m_{\theta_t}\right\|^2 - \frac{\partial \widetilde{V}^{2\prime}_{T\theta_t}}{\partial x}\left(\widetilde{f}_{1\theta_t} + g_{\theta_t}u\right) - \sum_{h=1}^{N}\pi_{rh}V(x,t,h) \\ &\quad - \frac{1}{2}\left(\widetilde{l}_{1\theta_t} + q_{\theta_t}u\right)'\frac{\partial^2 \widetilde{V}^2_{T\theta_t}}{\partial x^2}\left(\widetilde{l}_{1\theta_t} + q_{\theta_t}u\right) = -\Delta_4\left(\widetilde{V}^2_{T\theta_t}\right) + \frac{\partial \widetilde{V}^2_{T\theta_t}}{\partial t} - \left\|u-u^*_T\right\|^2_{\left(1,q,\widetilde{V}^2_{T\theta_t}\right)} - \sum_{h\in\mathscr{T}^r_{UK}}\pi_{rh}\left(V_h - T_r\right), \end{aligned} \tag{41}$$

with

$$\widetilde{u}^*_T = -\frac{1}{2}\left(I + \frac{1}{2}q_{\theta_t}'\frac{\partial^2 \widetilde{V}^2_{T\theta_t}}{\partial x^2}q_{\theta_t}\right)^{-1}\left(g_{\theta_t}'\frac{\partial \widetilde{V}^2_{T\theta_t}}{\partial x} + q_{\theta_t}'\frac{\partial^2 \widetilde{V}^2_{T\theta_t}}{\partial x^2}\widetilde{l}_{1\theta_t}\right). \tag{42}$$

From (41), we get $u^*_T = \widetilde{u}^*_T = K_2x$. Substituting the above u^*_T into (40) and considering Definition 3, it tests that $\widetilde{V}^2_{T\theta_t} \geq 0$ solves the following HJE:

$$\begin{cases} \dfrac{\partial \widetilde{V}^2_{T\theta_t}}{\partial t} + \dfrac{\partial \widetilde{V}^{2\prime}_{T\theta_t}}{\partial x}\widetilde{f}_{1\theta_t} + m_{\theta_t}'m_{\theta_t} + \dfrac{1}{2}\widetilde{l}_{1\theta_t}\dfrac{\partial^2 \widetilde{V}^2_{T\theta_t}}{\partial x^2}\widetilde{l}_{1\theta_t} + \displaystyle\sum_{h\in\mathscr{T}^r_K}\pi_{rh}\left(V_h - T_r\right) \\ \quad -\dfrac{1}{4}\left(\dfrac{\partial \widetilde{V}^{2\prime}_{T\theta_t}}{\partial x}g_{\theta_t} + \widetilde{l}_{1\theta_t}'\dfrac{\partial^2 \widetilde{V}^2_{T\theta_t}}{\partial x^2}q_{\theta_t}\right)\left(I + \dfrac{1}{2}q_{\theta_t}'\dfrac{\partial^2 \widetilde{V}^2_{T\theta_t}}{\partial x^2}q_{\theta_t}\right)^{-1}\left(g_{\theta_t}'\dfrac{\partial \widetilde{V}^2_{T\theta_t}}{\partial x} + q_{\theta_t}'\dfrac{\partial^2 \widetilde{V}^2_{T\theta_t}}{\partial x^2}\widetilde{l}_{1\theta_t}\right) = 0, \\ I + \dfrac{1}{2}q_{\theta_t}'\dfrac{\partial^2 \widetilde{V}^2_{T\theta_t}}{\partial x^2}q_{\theta_t} > 0, \\ V_h - T_r \geq 0, \quad h\in\mathscr{T}^r_{UK},\ r\neq h, \\ V_h - T_r \leq 0, \quad h\in\mathscr{T}^r_{UK},\ r = h, \\ \widetilde{V}^2_T\left(x,T,\theta_t\right) = 0. \end{cases} \tag{43}$$

Combining (35) and (43), the desired result therefore is obtained. □

Remark 4. It should be noted that HJEs (26)–(29) are hard to solve in general. To get the analytic expression of the controller, Takagi–Sugeno fuzzy model is constantly used, which can approximate nonlinear system effectively. The method to solve HJEs (26)–(29) is worth to make further studies.

4. Examples

In this part, we will give two examples to illustrate the usefulness of above results.

Example 1. Think about the following one-dimensional Markov jump systems with three modes:

$$\begin{cases} \mathrm{d}x(t) = \left(-\frac{3}{2}x^3 + xu(t) + \sqrt{2}\,xv(t)\right)\mathrm{d}t + x^2\mathrm{d}w(t), \\ z(t) = col\left(\frac{1}{2}x, u(t)\right), \quad \theta_0 \in \mathcal{T}, \end{cases} \tag{44}$$

$$\begin{cases} \mathrm{d}x(t) = \left(\left(-\frac{1}{2}x^3 - \sqrt{2}\,x^2 - 8x\right) + \sqrt{2}\,u(t) + 4v(t)\right)\mathrm{d}t \\ +\left(x^2 + \sqrt{2}\,x\right)\mathrm{d}w(t), \\ z(t) = col\left(\frac{\sqrt{5}}{2}x, u(t)\right), \quad \theta_0 \in \mathcal{T}, \end{cases} \tag{45}$$

$$\begin{cases} \mathrm{d}x(t) = \left(\left(-\frac{3}{2}x^3 - \sqrt{6}\,x^2 - \frac{25}{2}x\right) + 2u(t) + 2\sqrt{7}\,v(t)\right)\mathrm{d}t \\ +\left(\sqrt{3}\,x^2 + \sqrt{2}\,x\right)\mathrm{d}w(t), \\ z(t) = col\left(\frac{\sqrt{5}}{2}x, u(t)\right), \quad \theta_0 \in \mathcal{T}. \end{cases} \tag{46}$$

We assume that the elements of the transition probabilities matrix $(\prod_1)$ are fully known:

$$\prod_1 = \begin{pmatrix} -\left(\frac{1}{2}\right) & \frac{1}{4} & \frac{1}{4} \\ \frac{1}{2} & -1 & \frac{1}{2} \\ \frac{1}{2} & \frac{1}{2} & -1 \end{pmatrix}. \tag{47}$$

Set $V_{rh}(x) = p_{rh}x^2\,(r = 1, 2, h = 1, 2, 3)$. For given $\gamma = 1$, the corresponding HJEs have solutions with $p_{11} = -1$, $p_{12} = -(1/2)$, $p_{13} = -(1/2)$, $p_{21} = 2$, $p_{22} = (3/2)$, and $p_{23} = (3/2)$. According to Theorem 1, the H_2/H_∞ controller of (44)–(46) can be chosen as $v_T^*(x, t, 1) = \sqrt{2}x^2$, $v_T^*(x, t, 2) = 2x$, $v_T^*(x, t, 3) = \sqrt{7}x\,u_T^*(x, t, 1) = -2x^2$, $u_T^*(x, t, 2) = -(3/\sqrt{2})x$, and $u_T^*(x, t, 3) = -3x$.

Example 2. Think about the following one-dimensional Markov jump systems with three modes:

$$\begin{cases} \mathrm{d}x(t) = \left(-\frac{3}{2}x^3 + \frac{1}{4}u(t) + \frac{1}{2}v(t)\right)\mathrm{d}t + \sqrt{3}\,x^2\mathrm{d}w(t), \\ z(t) = col\left(\frac{1}{2}x, u(t)\right), \quad \theta_0 \in \mathcal{T}, \end{cases} \tag{48}$$

$$\begin{cases} \mathrm{d}x(t) = \left(\left(-\frac{1}{2}x^3 - \sqrt{2}\,x^2 - 8x\right) + \frac{\sqrt{19}}{3}u(t) + \sqrt{\frac{50}{3}}v(t)\right)\mathrm{d}t + \left(x^2 + \sqrt{2}\,x\right)\mathrm{d}w(t), \\ z(t) = col\left(\frac{\sqrt{5}}{2}x, u(t)\right), \quad \theta_0 \in \mathcal{T}, \end{cases} \tag{49}$$

$$\begin{cases} \mathrm{d}x(t) = \left(\left(-\frac{3}{2}x^3 - \sqrt{6}\,x^2 - \frac{25}{2}x\right) + \frac{\sqrt{37}}{3}u(t) + \sqrt{\frac{86}{3}}v(t)\right)\mathrm{d}t + \left(\sqrt{3}\,x^2 + \sqrt{2}\,x\right)\mathrm{d}w(t), \\ z(t) = col\left(\frac{\sqrt{5}}{2}x, u(t)\right), \quad \theta_0 \in \mathcal{T}. \end{cases} \tag{50}$$

The elements of the transition probability matrix $(\prod_2)$ are supposed to be partially unknown:

$$\prod_2 = \begin{pmatrix} -\left(\frac{1}{2}\right) & ? & ? \\ \frac{1}{2} & -1 & ? \\ \frac{1}{2} & ? & -1 \end{pmatrix}, \tag{51}$$

where "?" represents the unaccessible element. Set $V_{rh}(x) = p_{rh}x^2$ $(r = 1, 2, h = 1, 2, 3)$ and $\gamma = 1$. It can be found that $p_{11} = -1$, $p_{12} = -(1/2)$, $p_{13} = -(1/2)$, $p_{21} = 2$, $p_{22} = (3/2)$, and $p_{23} = (3/2)$ solving the corresponding HJEs. According to Theorem 1, the H_2/H_∞ controller of (48)–(50) can be given by $v_T^*(x, t, 1) = (1/2)x$, $v_T^*(x, t, 2) = (5/\sqrt{6})x$, $v_T^*(x, t, 3) = (\sqrt{43/6})x$, $u_T^*(x, t, 1) = -(1/2)x$, $u_T^*(x, t, 2) = -(\sqrt{19}/2)x$, and $u_T^*(x, t, 3) = -(\sqrt{37}/2)x$.

5. Conclusions

This note dealt with the finite horizon H_2/H_∞ control for stochastic nonlinear Markov jump systems with partially unknown transition probabilities. Based on the four cross-

coupled Hamilton–Jacobi equations, a sufficient condition and a necessary condition for the existence of H_2/H_∞ control are respectively drawn, which can be regarded as the generalization of [16] to nonlinear jump models. The validity of the results has been demonstrated by two numerical examples.

Data Availability

No data were used to support this study.

Conflicts of Interest

The authors declare that they have no conflicts of interest.

Acknowledgments

This work was supported by the National Natural Science Foundation of China (61673013), the Natural Science Foundation of Shandong Province (ZR2016JL022), and the Key Research and Development Plan of Shandong Province (2019GGX101052).

References

[1] T. Basar and P. Bernhard, "H_∞-optimal control and related minimax design problems: a dynamic game approach," *IEEE Transactions on Automatic Control*, vol. 41, no. 10, pp. 1397–1399, 1996.

[2] R. Guo, "Projective synchronization of a class of chaotic systems by dynamic feedback control method," *Nonlinear Dynamics*, vol. 90, no. 1, pp. 53–64, 2017.

[3] Z. Wang and R. W. Guo, "Hybrid synchronization problem of a class of chaotic systems by an universal control method," *Symmetry*, vol. 10, no. 11, p. 552, 2018.

[4] H. Cheng, F. Wang, and T. Zhang, "Multi-state dependent impulsive control for Holling I predator-prey model," *Discrete Dynamics in Nature and Society*, vol. 2012, Article ID 181752, 21 pages, 2012.

[5] Y. Li, H. Cheng, and Y. Wang, "A *Lycaon pictus* impulsive state feedback control model with Allee effect and continuous time delay," *Advances in Difference Equations*, vol. 367, 2018.

[6] I. R. Pertersen, V. A. Ugrinovskii, and A. V. Savkin, *Robust Control Design Using H_∞ Methods*, Springer-Verlin, New York, NY, USA, 2000.

[7] J. W. Helton and M. R. James, *Extending H_∞ Control to Nonlinear Systems*, SIAM, Philadelphia, PA, USA, 1999.

[8] V. Dragan, P. Shi, and E. K. Boukas, "Control of singularly perturbed systems with Markovian jump parameters: an H_∞ approach," *Automatica*, vol. 35, no. 8, pp. 1369–1378, 1999.

[9] D. Hinrichsen and A. J. Pritchard, "Stochastic H_∞," *SIAM Journal on Control and Optimization*, vol. 36, no. 5, pp. 1504–1538, 1998.

[10] D. J. N. Limebeer, B. D. O. Anderson, and B. Hendel, "A Nash game approach to mixed H_2/H_∞ control," *IEEE Transactions on Automatic Control*, vol. 39, no. 1, pp. 69–82, 1994.

[11] B. S. Chen, C. S. Tseng, and H. J. Uang, "Mixed H_2/H_∞ fuzzy output feedback control design for nonlinear dynamic systems: an LMI approach," *IEEE Transactions on Fuzzy Systems*, vol. 8, no. 3, pp. 249–265, 2000.

[12] W. Zhang, L. Ma, and T. Zhang, "Discrete-time mean-field stochastic H_2/H_∞ control," *Journal of Systems Science and Complexity*, vol. 30, no. 4, pp. 765–781, 2017.

[13] V. Dragan, M. Toader, and A. M. Stoica, *Mathematical Methods in Robust Control of Discrete-Time Linear Stochastic Systems*, Springer, New York, NY, USA, 2010.

[14] T. Hou, W. Zhang, and H. Ma, "Finite horizon H_2/H_∞ control for discrete-time stochastic systems with Markovian jumps and multiplicative noise," *IEEE Transactions on Automatic Control*, vol. 55, no. 5, pp. 1185–1191, 2010.

[15] T. Hou, W. Zhang, and H. Ma, "Infinite horizon H_2/H_∞ optimal control for discrete-time Markov jump systems with (x, u, v)-dependent noise," *Journal of Global Optimization*, vol. 57, no. 4, pp. 1245–1262, 2013.

[16] W. Zhang and G. Feng, "Nonlinear stochastic H_2/H_∞ control with (x, u, v)-dependent noise: infinite horizon case," *IEEE Transactions on Automatic Control*, vol. 53, no. 5, pp. 1323–1328, 2008.

[17] W. Zhang and B.-S. Chen, "State feedback H_∞ control for a class of nonlinear stochastic systems," *SIAM Journal on Control and Optimization*, vol. 44, no. 6, pp. 1973–1991, 2006.

[18] X. Mao and C. Yuan, *Stochastic Differential Equations with Markovian Switching*, Imperial College Press, London, UK, 2006.

[19] J. Xiong, J. Lam, Z. Shu, and X. Mao, "Stability analysis of continuous-time switched systems with a random switching signal," *IEEE Transactions on Automatic Control*, vol. 59, no. 1, pp. 180–186, 2014.

[20] P. Shi and F. Li, "A survey on Markovian jump systems: modeling and design," *International Journal of Control, Automation and Systems*, vol. 13, no. 1, pp. 1–16, 2015.

[21] Z. Yan, Y. Song, and J. H. Park, "Quantitative mean square exponential stability and stabilization of stochastic systems with Markovian switching," *Journal of the Franklin Institute*, vol. 355, no. 8, pp. 3438–3454, 2018.

[22] Z. Yan, W. Zhang, and G. Zhang, "Finite-time stability and stabilization of Itô stochastic systems with Markovian switching: mode-dependent parameter approach," *IEEE Transactions on Automatic Control*, vol. 60, no. 9, pp. 2428–2433, 2015.

[23] S. Zhou, X. Liu, B. Chen, and H. Liu, "Stability analysis for a class of discrete-time nonhomogeneous Markov jump systems with multiplicative noises," *Complexity*, vol. 2018, Article ID 1586846, 9 pages, 2018.

[24] C. Tan and W. Zhang, "On observability and detectability of continuous-time stochastic Markov jump systems," *Journal of Systems Science and Complexity*, vol. 28, no. 4, pp. 830–847, 2015.

[25] V. P. Jilkov and X. R. Li, "Online Bayesian estimation of transition probabilities for Markovian jump systems," *IEEE Transactions on Signal Processing*, vol. 52, no. 6, pp. 1620–1630, 2004.

[26] L. Zhang and J. Lam, "Necessary and sufficient conditions for analysis and synthesis of Markov jump linear systems with incomplete transition descriptions," *IEEE Transactions on Automatic Control*, vol. 55, no. 7, pp. 1695–1701, 2010.

[27] L. Zhang and E. K. Boukas, "Stability and stabilization of Markovian jump linear systems with partly unknown transition probabilities," *Automatica*, vol. 45, no. 2, pp. 436–468, 2009.

[28] E. Tian, D. Yue, and G. Wei, "Robust control for Markovian jump systems with partially known transition probabilities and nonlinearities," *Journal of the Franklin Institute*, vol. 350, no. 8, pp. 2069–2083, 2013.

[29] L. Zhang and E.-K. Boukas, "Mode-dependent H_∞ filtering for discrete-time Markovian jump linear systems with partly

unknown transition probabilities," *Automatica*, vol. 45, no. 6, pp. 1462–1467, 2009.

[30] J. Xiong and J. Lam, "Robust H_2 control of Markovian jump systems with uncertain switching probabilities," *International Journal of Systems Science*, vol. 40, no. 3, pp. 255–265, 2009.

[31] J. W. Shin and B. Y. Park, ".H_∞ control of Markovian jump systems with incomplete knowledge of transition probabilities," *International Journal of Control Automation and Systems*, vol. 17, no. 4, pp. 2474–2481, 2019.

[32] H. Zhang, J. Wang, and Y. Shi, "Robust sliding-mode control for Markovian jump systems subject to intermittent observations and partially known transition probabilities," *Systems & Control Letters*, vol. 62, no. 12, pp. 1114–1124, 2013.

[33] B.-C. Zheng and G.-H. Yang, "Sliding mode control for Markov jump linear uncertain systems with partly unknown transition rates," *International Journal of Systems Science*, vol. 45, no. 10, pp. 1999–2011, 2014.

[34] S. Xing and F. Deng, "Delay-dependent H_∞ filtering for discrete singular Markov jump systems with Wiener process and partly unknown transition probabilities," *Journal of the Franklin Institute*, vol. 355, no. 13, pp. 6062–6086, 2018.

[35] S. Xing, F. Deng, and T. Hou, "Delay-dependent H_∞ filtering for singular Markov jump systems with Wiener process and generally uncertain transition rates," *International Journal of Systems Science*, vol. 49, no. 8, pp. 1685–1702, 2018.

[36] Z. Yan, J. H. Park, and W. Zhang, "Finite-time guaranteed cost control for Itô Stochastic Markovian jump systems with incomplete transition rates," *International Journal of Robust and Nonlinear Control*, vol. 27, no. 1, pp. 66–83, 2017.

[37] L. Qiu, B. Zhang, G. Xu, J. Pan, and F. Yao, "Mixed H_2/H_∞ control of markovian jump time-delay systems with uncertain transition probabilities," *Information Sciences*, vol. 373, pp. 539–556, 2016.

Hindawi
Mathematical Problems in Engineering
Volume 2020, Article ID 2301085, 9 pages
https://doi.org/10.1155/2020/2301085

Research Article

Delay-Dependent H_∞ Control for T-S Fuzzy Systems with Local Nonlinear Models: An LMI Approach

Zhile Xia

Department of Mathematics, Taizhou University, Zhejiang, Taizhou 318000, China

Correspondence should be addressed to Zhile Xia; zhilexia@163.com

Received 15 March 2020; Revised 9 April 2020; Accepted 21 April 2020; Published 11 May 2020

Guest Editor: Cuimei Jiang

This paper studies the stabilization design scheme with H_∞ performance for a large class of nonlinear discrete-time systems. The system under study is modeled by Takagi-Sugeno (T-S) model with local nonlinearity and state delay. First, the model is changed into an equivalent fuzzy switching model. And then, according to projection theorem and piecewise Lyapunov function (PLF), two new H_∞ control methods are proposed for fuzzy switched systems, which consider the time delay information of the system. Finally, the relationship among all fuzzy subsystems is considered. Because the results are only expressed by a series of linear matrix inequalities (LMIs), the controller can be directly designed by the linear matrix inequalities toolbox of MATLAB.

1. Introduction

As we all know, the T-S fuzzy method is a kind of common and very effective tool for approaching the discrete-time nonlinear complex system [1]. For instance, in [2, 3], it was shown that coupled chaotic systems are a special class of complex systems, which can be processed by the T-S method [4, 5]. In addition, nonlinear neutral differential equations have numerous applications in engineering and natural sciences [6]. By using the T-S method, Pu et al. [7] studied BP neural network and RBF neural network. Bharathi et al. [8] investigated numerical solutions for sophistication single neutrality differential equations with time delay. As shown in [9], asymptotic suboptimality property of the decentralized methods for the linear-quadratic games is proposed. A game-control method based on the fuzzy linearity quadratic adjuster was presented by Ji et al. [10] for emergency collision avoidance. Therefore, it is very important to study the asymptotic stability and controller design of the T-S fuzzy model [11–13]. However, many papers, such as [11–13], depend on a single common positive-definite symmetric matrix P, which needs to satisfy many LMIs. In reality, such a matrix may not exist, especially for systems with high nonlinearity [14]. Therefore, it is conservative to use the common Lyapunov function method to consider the controller design of the T-S model, and its application scope is limited. In order to increase the feasible region of matrix inequalities, a piecewise Lyapunov function (PLF) is proposed in [15, 16], which studied the filter problem for the T-S model with delay. In references [17–19], the fuzzy Lyapunov function (FLF) method was used to study the controller design approaches for the T-S model.

Recently, the T-S fuzzy system with a local nonlinear model (FSwLNM) has received considerable research (see, for instance, [20–30] and references therein). As shown in [20, 21], T-S FSwLNM requires less fuzzy rules, which can reduce the computational complexity. It can also decrease modeling error compared with conventional T-S fuzzy systems. For a class of T-S FSwLNM, Yang and Wang [22] investigated the problem of fault detection, Klug et al. [23] proposed a convex way to study an output feedback controller, and Chang and Hsu [24] investigated the sliding mode control problem with multiple performance indexes for stochastic nonlinear systems. Nguyen et al. [25] proposed a new method to design a limited controller, which has different fuzzy rules from the system. Zhai et al. [26] observed the problems of network-based fault detection and isolation observer design. Huang and Yang [27] investigated the problem of fault estimation. In [28, 29], the fuzzy polynomial system was studied, and the subsequent part of

fuzzy rules was represented by polynomial function. Compared with the general T-S fuzzy system, the fuzzy polynomial system can express the complex nonlinear system more accurately with fewer fuzzy rules.

Based on the above considerations, we will study the delay-dependent controller design method with H_∞ performance index for discrete-time T-S FSwLNM. Adopting PLF and the fuzzy switching model [30], two new design methods of H_∞ controller are derived. These two methods consider the time-delay information of the system, so they are less conservative. By using projection theorem and introducing relaxation matrix variables, there is no product term of Lyapunov matrices and system dynamic matrices in LMIs constraints. Because the derived condition only contains LMIs, the controller gain matrix can be directly designed by the LMIs toolbox of MATLAB.

Notations. This part briefly describes the symbols used in this paper. Symbol $\mathbb{R}^n$ stands for Euclidean space with n dimension. Symbol $\mathbb{R}^{n\times m}$ means the set of real $n\times m$ dimensional matrices. Matrices I and O with appropriate dimensions represent unit matrices and zero matrices. Matrix P is strictly greater than 0, which shows that P is a positive definite symmetric matrix (PDSM). The symbol $\mathrm{diag}\{A_1, A_2, \ldots, A_n\}$ denotes block diagonal matrix. The symbol $\mathrm{sym}\{S\}$ indicates $S+S^T$. Elements of symmetric position of symmetric matrix are represented by *.

2. Preliminaries and Problem Formulation

2.1. Preliminaries. Before giving the main conclusions of this paper, we first present some very important lemmas, which are very important in the process of proving the important conclusions of this paper.

Lemma 1 (see [31]). *Given an $m\times m$-dimensional symmetric real matrix $\mathcal{Z}$ and three matrices $\mathcal{Z}_0$, $\mathcal{X}$, and $\mathcal{Y}$ of proper dimensions, the two sets of inequalities shown as follows are equivalent:*

$$\begin{aligned} &\mathcal{Z}+\mathrm{sym}\left\{\mathcal{X}^T\mathcal{Z}_0\mathcal{Y}\right\}<0,\\ &\mathcal{X}_\perp^T\mathcal{Z}\mathcal{X}_\perp<0,\\ &\mathcal{Y}_\perp^T\mathcal{Z}\mathcal{Y}_\perp<0, \end{aligned} \tag{1}$$

where two matrices $\mathcal{X}_\perp$ and $\mathcal{Y}_\perp$, whose columns are full rank, satisfy the equalities $\mathcal{X}\mathcal{X}_\perp=0$ and $\mathcal{Y}\mathcal{Y}_\perp=0$, respectively.

Lemma 2 (see [32]). *Let ϱ be a given positive integer, $x_h\in\mathbb{R}^n$ be a vector, and $\mathcal{M}\in\mathbb{R}^{n\times n}$ be a semi-PDSM; we have*

$$-\varrho\sum_{h=1}^{\varrho}x_h^T\mathcal{M}x_h\le-\left(\sum_{h=1}^{\varrho}x_h^T\right)\mathcal{M}\left(\sum_{h=1}^{\varrho}x_h\right). \tag{2}$$

Lemma 3 (see [31]). *Given the proper dimension matrices $\mathcal{M}$, $\mathcal{H}$, and $\mathcal{Q}$, the following two sets of inequalities are equivalent:*

$$\begin{aligned} &(1)\begin{bmatrix}\mathcal{Q} & \mathcal{M}\\ * & \mathcal{H}\end{bmatrix}<0,\\ &(2)\ \mathcal{H}<0,\ \mathcal{Q}-\mathcal{M}\mathcal{H}^{-1}\mathcal{M}^T<0. \end{aligned} \tag{3}$$

In this case, we say that the matrix product $\mathcal{Q}-\mathcal{M}\mathcal{H}^{-1}\mathcal{M}^T$ is Schur complement of matrix $\mathcal{H}$.

2.2. Problem Formulation. In order to improve the approximation effect of the fuzzy system and reduce the number of rules, we consider T-S FSwLNM as follows:

Fuzzy rule m: if ϑ_{1t} is υ_{m1t}, …, ϑ_{pt} is υ_{mpt}, then

$$\begin{cases} x_{t+1}=A_mx_t+A_{\tau_0m}x_{t-\tau_0}+G_m\phi_t+G_{\tau_0m}\phi_{t-\tau_0}+B_{1m}\omega_t+B_{2m}u_t,\\ z_t=C_mx_t+C_{\tau_0m}x_{t-\tau_0}+G_{zm}\phi_t+G_{z\tau_0m}\phi_{t-\tau_0}+D_{1m}\omega_t+D_{2m}u_t,\\ x_t=\varsigma_t,\quad -\tau_0\le t<0, \end{cases} \tag{4}$$

where $m\in\{1,2,\ldots,r_0\}$. r_0, υ_{mnt}, and ϑ_{nt} are the rule number, fuzzy sets, and premise variables (usually the state or output of the system), respectively. $x_t\in\mathbb{R}^n$, $z_t\in\mathbb{R}^m$, ς_t, and $u_t\in\mathbb{R}^l$ represent the system state variables, the system output variables to be estimated, the initial conditions, and the controller to be designed, respectively. Positive integer τ_0 represents the constant delay. Disturbance $\omega_t\in l_2[0,\infty)$. $\phi_t\in\mathbb{R}^n$ satisfies

$$\|\phi_t\|_2\le\theta\|x_t\|_2,\quad \theta>0. \tag{5}$$

Similar to [33], we define open subspace Ω_l $(l=1,\ldots,k)$ in state space. The symbol Ω_l^c represents the closed subspace and satisfies

$$\Omega_m^c\cap\Omega_n^c=\partial\Omega_i^{\upsilon_0},\quad m\ne n, m,n=1,\ldots,\kappa, i\in\{1,\ldots,r_0\}, \tag{6}$$

where $\partial\Omega_m^{\upsilon_0}=\{\vartheta\,|\,h_m(\vartheta)=1, 0\le h_m(\vartheta+\delta)<1, |\delta|\ll1,\ |\delta|\ne0\}$. υ_0 is the face indexes set of the polyhedron $\partial\Omega_m=\cup\partial\Omega_m^{\upsilon_0}$. $h_m(\vartheta)=(\omega_m(\vartheta_t)/\sum_{m=1}^{r}\omega_m(\vartheta_t))$, $\omega_m(\vartheta_t)=\prod_{n=1}^{p_0}\mu_{mn}(\vartheta_{nt})$, and $\vartheta_t=[\vartheta_{1t},\vartheta_{2t},\ldots,\vartheta_{pt}]$.

Then, we will rewrite system (4) as an equivalent switched fuzzy model according to the idea of [30], as follows:

Global rule n: if $x_t\in\Omega_n$, then there are the following local rules:

if ϑ_{1t} is υ_{nq1t}, …, ϑ_{pt} is υ_{nqpt}, then

$$\begin{cases} x_{t+1}=A_{nq}x_t+A_{\tau_0nq}x_{t-\tau_0}+G_{nq}\phi_t+G_{\tau_0nq}\phi_{t-\tau_0}+B_{1nq}\omega_t+B_{2nq}u_t,\\ z_t=C_{nq}x_t+C_{\tau_0nq}x_{t-\tau_0}+G_{znq}\phi_t+G_{z\tau_0nq}\phi_{t-\tau_0}+D_{1nq}\omega_t+D_{2nq}u_t,\\ x_t=\varsigma_t,\quad -\tau_0\le t<0, q=1,\ldots,\lambda_n, n=1,\ldots,\kappa, \end{cases} \tag{7}$$

where κ is the number of subspaces divided. Ω_n represents the nth subspace. λ_n is the rule number in the nth subspace.

By using the fuzzy method to deal with system (7), we can achieve

$$\begin{cases} x_{t+1} = \sum_{q=1}^{\lambda_n} h_{nq}\left\{A_{nq}x_t + A_{\tau_0 nq}x_{t-\tau_0} + G_{nq}\phi_t + G_{\tau_0 nq}\phi_{t-\tau_0} + B_{1nq}\omega_t + B_{2nq}u_t\right\}, \\ z_t = \sum_{q=1}^{\lambda_n} h_{nq}\left\{C_{nq}x_t + C_{\tau_0 nq}x_{t-\tau_0} + G_{znq}\phi_t + G_{z\tau_0 nq}\phi_{t-\tau_0} + D_{1nq}\omega_t + D_{2nq}u_t\right\}, \\ x_t = \varsigma_t, \quad -\tau_0 \le t < 0, x(t) \in \Omega_n, \end{cases} \tag{8}$$

where $h_{nq} = h_{nq}(\vartheta_t) = (\prod_{l=1}^{p_0} \upsilon_{nql}(\vartheta_t) / \sum_{q=1}^{\lambda_n} \prod_{l=1}^{p_0} \upsilon_{nql}(\vartheta_t))$.

In each subspace Ω_n, we design independent controllers, that is

Global rule n: if $x_t \in \Omega_n$, then there are the following controllers:

if ϑ_{1t} is υ_{nl1t}, ..., ϑ_{pt} is υ_{nlpt}, then

$$u_t = F_{anl}x_t + F_{a\tau_0 nl}x_{t-\tau_0} + F_{bnl}\phi_t + F_{b\tau_0 nl}\phi_{t-\tau_0}, \quad l = 1, 2, \ldots, \lambda_n. \tag{9}$$

Using fuzzy reasoning technology, fuzzy controller (9) can be written in the following compact form:

$$u_t = \sum_{l=1}^{\lambda_n} h_{nl}\left\{F_{anl}x_t + F_{a\tau_0 nl}x_{t-\tau_0} + F_{bnl}\phi_t + F_{b\tau_0 nl}\phi_{t-\tau_0}\right\}. \tag{10}$$

Combining (8) with (10), we have

$$\begin{cases} x_{t+1} = \widetilde{A}_{nql}x_t + \widetilde{A}_{\tau_0 nql}x_{t-\tau_0} + \widetilde{B}_{1nq}\omega_t + \widetilde{G}_{nql}\phi_t + \widetilde{G}_{\tau_0 nql}\phi_{t-\tau_0}, \\ z_t = \widetilde{C}_{nql}x_t + \widetilde{C}_{\tau_0 nql}x_{t-\tau_0} + \widetilde{D}_{1nq}\omega_t + \widetilde{G}_{znql}\phi_t + \widetilde{G}_{z\tau_0 nql}\phi_{t-\tau_0}, \end{cases} \tag{11}$$

$$\begin{bmatrix} \widetilde{A}_{nql} & \widetilde{A}_{\tau_0 nql} & \widetilde{B}_{1nq} & \widetilde{G}_{nql} & \widetilde{G}_{\tau_0 nql} \\ \widetilde{C}_{nql} & \widetilde{C}_{\tau_0 nql} & \widetilde{D}_{1nq} & \widetilde{G}_{znql} & \widetilde{G}_{z\tau_0 nql} \end{bmatrix} = \sum_{q=1}^{\lambda_n}\sum_{l=1}^{\lambda_n} h_{nq}h_{nl} \begin{bmatrix} \widehat{A}_{nql} & \widehat{A}_{\tau_0 nql} & B_{1nq} & \widehat{G}_{nql} & \widehat{G}_{\tau_0 nql} \\ \widehat{C}_{nql} & \widehat{C}_{\tau_0 nql} & D_{1nq} & \widehat{G}_{znql} & \widehat{G}_{z\tau_0 nql} \end{bmatrix}, \tag{12}$$

with

$$\begin{aligned} \widehat{A}_{nql} &= A_{nq} + B_{2nq}K_{anl}, \\ \widehat{A}_{\tau_0 nql} &= A_{\tau_0 nq} + B_{2nq}K_{a\tau_0 nl}, \\ \widehat{G}_{nql} &= G_{nq} + B_{2nq}K_{bnl}, \\ \widehat{G}_{\tau_0 nql} &= G_{\tau_0 nk} + B_{2nq}K_{b\tau_0 nl}, \\ \widehat{C}_{nql} &= C_{nq} + D_{2nq}K_{anl}, \\ \widehat{C}_{\tau_0 nql} &= C_{\tau_0 nq} + D_{2nq}K_{a\tau_0 nl}, \\ \widehat{G}_{znql} &= G_{znq} + D_{2nq}K_{bnl}, \\ \widehat{G}_{z\tau_0 nql} &= G_{z\tau_0 nq} + D_{2nq}K_{b\tau_0 nl}. \end{aligned} \tag{13}$$

where $x(t) \in \Omega_j$.

Given the upper bound γ of H_∞ index, where $\gamma > 0$, the purpose is to design independent controllers (10) for system (8) in each subspace Ω_j, so that the following two conditions are met:

(1) When the disturbance $\omega_t = 0$, the equilibrium state $x_t = 0$ of system (11) is asymptotically stable.

(2) When the initial condition $\varsigma_t = 0$, the following norm inequalities hold:

$$\|z_t\|_2 < \gamma\|\omega_t\|_2, \quad \forall \omega_t \ne 0. \tag{14}$$

3. Main Results

The set $\Omega = \{(m, n) \mid x_t \in \Omega_m, x_{t+1} \in \Omega_n\}$ indicates that the system state jumps from subspace Ω_m to subspace Ω_n. Of course, the system state may stay in a certain subspace all the time. Next, we can prove the result in Theorem 1.

Theorem 1. *Given a positive real number γ, the H_∞ control problems of controlled system (11) are solved, if there are symmetric positive definite matrices $\begin{bmatrix} P_n & W_{1n} \\ * & W_{2n} \end{bmatrix}$, $\begin{bmatrix} \mathcal{Q}_{11} & \mathcal{Q}_{12} \\ * & \mathcal{Q}_{22} \end{bmatrix}$, R, the nonsingular matrix F_n and matrices $\mathcal{N}_{ns}$ $(s = 1, \ldots, 7)$, K_{anl}, $K_{a\tau_0 nl}$, K_{bnl}, and $K_{b\tau_0 ql}$, $n = 1, 2, \ldots, \kappa$, $l = 1, 2, \ldots, \lambda_n$, such that*

$$\Pi_{mnqq} < 0, \quad q = 1, 2, \ldots, \lambda_n, (n, m) \in \Omega, \tag{15}$$

$$\Pi_{mnql} + \Pi_{mnlq} < 0, \quad 0 < q < l \le \lambda_n, (n, m) \in \Omega, \tag{16}$$

where

$$\Pi_{mnkl} = \begin{bmatrix} \Pi_{11} & \Pi_{12} & \Pi_{13} & \Pi_{14} & \Pi_{15} & \Pi_{16} & \Pi_{17} & \mathcal{N}_{n7} & 0 \\ * & \Phi_1 & \Phi_2 & \Phi_3 & -K_n\mathcal{N}_{n4} & -\mathcal{N}_{n5} & -\mathcal{N}_{n6} & \Phi_4 & \Pi_1^T \\ * & * & \Phi_5 & \Phi_6 & 0 & 0 & 0 & -\mathcal{N}_{n2}^T & \Pi_2^T \\ * & * & * & \Phi_7 & 0 & 0 & 0 & -\mathcal{N}_{n3}^T & 0 \\ * & * & * & * & -\gamma^2 I & 0 & 0 & -\mathcal{N}_{n4}^T & D_{1nq}^T \\ * & * & * & * & * & -I & 0 & -\mathcal{N}_{j5}^T & \Pi_3^T \\ * & * & * & * & * & * & -I & -\mathcal{N}_{n6} & \Pi_4^T \\ * & * & * & * & * & * & * & \Phi_8 & 0 \\ * & * & * & * & * & * & * & * & -I \end{bmatrix},$$

$$\begin{aligned}
\Pi_{11} &= P_m - \mathrm{sym}\{K_n\}, \\
\Pi_{12} &= W_{1m} + \mathcal{N}_{n1} + A_{nq}K_n + B_{2q}K_{anl}, \\
\Pi_{13} &= \mathcal{N}_{n2} - W_{1m} + A_{\tau_0 nq}K_n + B_{2nq}K_{a\tau_0 nl}, \\
\Pi_{14} &= \mathcal{N}_{n3} + W_{1m}, \\
\Pi_{15} &= K_n\mathcal{N}_{n4} + K_n B_{1nq}, \\
\Pi_{16} &= \mathcal{N}_{n5} + G_{nq}K_n + B_{2nq}K_{bnl}, \\
\Pi_{17} &= \mathcal{N}_{n6} + G_{\tau_0 nq}K_n + B_{2nq}K_{b\tau_0 nl}, \\
\Pi_1^T &= C_{nq}K_n + D_{2nq}K_{anl}, \\
\Pi_2^T &= C_{\tau_0 nq}K_n + D_{2nq}K_{a\tau_0 nl}, \\
\Pi_3^T &= G_{znq}K_n + D_{2nq}K_{bnl}, \\
\Pi_4^T &= G_{z\tau_0 nq}K_n + D_{2nq}K_{b\tau_0 nl}, \\
\Phi_1 &= \theta I + R - \mathrm{sym}\{\mathcal{N}_{n1}\} + W_{2m} + \tau_0^2\mathcal{Q}_{11} - \mathcal{Q}_{22} - P_n, \\
\Phi_2 &= \theta I + \mathcal{Q}_{22} - \mathcal{N}_{n2} - W_{2m}, \\
\Phi_3 &= W_{2m} - \mathcal{N}_{n3} - \mathcal{Q}_{12}^T - W_{1n}, \\
\Phi_4 &= \tau^2\mathcal{Q}_{12} - \mathcal{N}_{n1}^T - N_{n7}, \\
\Phi_5 &= W_{2m} - R - \mathcal{Q}_{22}, \\
\Phi_6 &= \mathcal{Q}_{12}^T - W_{2m}, \\
\Phi_7 &= W_{2m} - \mathcal{Q}_{11} - W_{2n}, \\
\Phi_8 &= \tau_0^2\mathcal{Q}_{22} - \mathrm{sym}\{\mathcal{N}_{n7}\}.
\end{aligned} \tag{17}$$

Moreover, the controllers are given by

$$\begin{aligned}
F_{anl} &= K_{anl}K_n^{-1}, \\
F_{a\tau_0 nl} &= K_{a\tau_0 nl}K_n^{-1}, \\
F_{bnl} &= K_{bnl}K_n^{-1}, \\
F_{b\tau_0 nl} &= K_{b\tau_0 nl}K_n^{-1}.
\end{aligned} \tag{18}$$

Proof. Let $\mathcal{U}_n = K_n^{-1}$ and $\mathcal{U} = \mathrm{diag}\{\mathcal{U}_n, \mathcal{U}_n, \mathcal{U}_n, \mathcal{U}_n, I, \mathcal{U}_n, \mathcal{U}_n, \mathcal{U}_n, I\}$. On left side of inequalities (15) and (16), postmultiplying $\mathcal{U}^T$ and premultiplying $\mathcal{U}$, respectively, one has

$$\Omega_{mnqq} < 0, \quad q = 1, 2, \ldots, \lambda_n, \ (n, m) \in \Omega, \tag{19}$$

$$\Omega_{mnql} + \Omega_{mnlq} < 0, \quad 0 < q < l \le \lambda_n, \ (n, m) \in \Omega, \tag{20}$$

where

$$\Omega_{mnql} = \begin{bmatrix} \Omega_{11} & \Omega_{12} & \Omega_{13} & \Omega_{14} & \Omega_{15} & \Omega_{16} & \Omega_{17} & \overline{\mathcal{N}}_{n7} & 0 \\ * & \overline{\Phi}_1 & \overline{\Phi}_2 & \overline{\Phi}_3 & -\mathcal{N}_{n4} & -\overline{\mathcal{N}}_{n5} & -\overline{\mathcal{N}}_{n6} & \overline{\Phi}_4 & \widehat{C}_{nql}^T \\ * & * & \overline{\Phi}_5 & \overline{\Phi}_6 & 0 & 0 & 0 & -\mathcal{N}_{n2}^T & \widehat{C}_{\tau nql}^T \\ * & * & * & \overline{\Phi}_7 & 0 & 0 & 0 & -\overline{\mathcal{N}}_{n3}^T & 0 \\ * & * & * & * & -\gamma^2 I & 0 & 0 & -\overline{\mathcal{N}}_{n4}^T & D_{1nq}^T \\ * & * & * & * & * & -\overline{I} & 0 & -\overline{\mathcal{N}}_{n5}^T & \widehat{G}_{znql}^T \\ * & * & * & * & * & * & -\overline{I} & -\overline{\mathcal{N}}_{n6} & \widehat{G}_{\tau_0 znql}^T \\ * & * & * & * & * & * & * & \overline{\Phi}_8 & 0 \\ * & * & * & * & * & * & * & * & -I \end{bmatrix} \tag{21}$$

and $\overline{X}$ represents $\mathcal{U}_n^T X \mathcal{U}_n$. $\Omega_{11} = \overline{P}_m - \mathrm{sym}\{\mathcal{U}_n\}$, $\Omega_{12} = \overline{W}_{1m} + \overline{\mathcal{N}}_{n1} + \mathcal{U}_n^T \widehat{A}_{nql}$, $\Omega_{13} = \overline{\mathcal{N}}_{n2} - \overline{W}_{1m} + \mathcal{U}_n^T \widehat{A}_{\tau nql}$, $\Omega_{14} = \overline{\mathcal{N}}_{n3} + \overline{W}_{1m}$, $\Omega_{15} = \mathcal{N}_{n4} + B_{1nq}$, $\Omega_{16} = \overline{\mathcal{N}}_{n5} + \mathcal{U}_n^T \widehat{G}_{nkl}$, and $\Omega_{17} = \overline{\mathcal{N}}_{n6} + \mathcal{U}_n^T \widehat{G}_{\tau_0 nql}$.

Based on (19) and (20), we have

$$\begin{aligned} \Omega &= \sum_{k=1}^{\lambda_n} \sum_{l=1}^{\lambda_n} h_{nk} h_{nl} \Omega_{mnkl} = \sum_{q=1}^{\lambda_n} h_{nk}^2 \Omega_{mnqq} \\ &\quad + \sum_{q<l}^{\lambda_n} h_{nq} h_{nl} \left\{ \Omega_{mnql} + \Omega_{mnlq} \right\} \\ &= \Omega_0 + \mathrm{sym}\left\{ \Omega_1^T \Omega_2 \right\} < 0, \end{aligned} \tag{22}$$

where $\Omega_1 = [\mathcal{U}_j, 0, 0, 0, 0, 0, 0, 0, 0,]$, $\Omega_2 = [-I, \widetilde{A}_{nql}, \widetilde{A}_{\tau_0 nql}, 0, \widetilde{B}_{1nq}, \widetilde{G}_{nql}, \widetilde{G}_{\tau_0 nql}, 0, 0]$, and

$$\Omega_0 = \begin{bmatrix} \overline{P}_m & \overline{W}_{1m} + \overline{\mathcal{N}}_{n1} & \overline{\mathcal{N}}_{n2} - \overline{W}_{1m} & \overline{\mathcal{N}}_{n3} + \overline{W}_{1m} & \mathcal{N}_{n4} & \overline{\mathcal{N}}_{n5} & \overline{\mathcal{N}}_{n6} & \overline{\mathcal{N}}_{n7} & 0 \\ * & \overline{\Phi}_1 & \overline{\Phi}_2 & \overline{\Phi}_3 & -\mathcal{N}_{n4} & -\overline{\mathcal{N}}_{n5} & -\overline{\mathcal{N}}_{n6} & \overline{\Phi}_4 & \widetilde{C}_{nql}^T \\ * & * & \overline{\Phi}_5 & \overline{\Phi}_6 & 0 & 0 & 0 & -\mathcal{N}_{n2}^T & \widetilde{C}_{\tau nql}^T \\ * & * & * & \overline{\Phi}_7 & 0 & 0 & 0 & -\overline{\mathcal{N}}_{n3}^T & 0 \\ * & * & * & * & -\gamma^2 I & 0 & 0 & -\overline{\mathcal{N}}_{n4}^T & \widetilde{D}_{1nq}^T \\ * & * & * & * & * & -\overline{I} & 0 & -\overline{\mathcal{N}}_{n5}^T & \widetilde{G}_{znql}^T \\ * & * & * & * & * & * & -\overline{I} & -\overline{\mathcal{N}}_{n6} & \widetilde{G}_{\tau_0 znql}^T \\ * & * & * & * & * & * & * & \overline{\Phi}_8 & 0 \\ * & * & * & * & * & * & * & * & -I \end{bmatrix}. \tag{23}$$

Let $\Omega_{2\perp} = \begin{bmatrix} \widetilde{A}_{nql}, \widetilde{A}_{\tau_0 nql}, 0, \widetilde{B}_{1nq}, \widetilde{G}_{nql}, \widetilde{G}_{\tau_0 nql}, 0, 0 \\ \mathrm{diag}\left\{ \underbrace{I, \ldots, I}_{8\,\text{blocks}} \right\} \end{bmatrix}$, which satisfies $\Omega_2 \Omega_{2\perp} = 0$. Moreover, $[\Omega_2^T, \Omega_{2\perp}]$ is a column full-rank matrix. Then, based on Lemma 1 and inequality (22), we obtain

$$\Omega_{2\perp}^T\Omega_0\Omega_{2\perp} = \begin{bmatrix} \Delta_{11} & \Delta_{12} & \Delta_{13} & \Delta_{14} & \Delta_{15} & \Delta_{16} & \Delta_{17} & \widetilde{C}_{nql}^T \\ * & \Delta_{22} & \Delta_{23} & \Delta_{24} & \Delta_{25} & \Delta_{26} & \Delta_{27} & \widetilde{C}_{\tau nql}^T \\ * & * & \Delta_{33} & \Delta_{34} & \Delta_{35} & \Delta_{36} & \Delta_{37} & 0 \\ * & * & * & \Delta_{44} & \Delta_{45} & \Delta_{46} & \Delta_{47} & \widetilde{D}_{1jq}^T \\ * & * & * & * & \Delta_{55} & \Delta_{56} & \Delta_{57} & \widetilde{G}_{znql}^T \\ * & * & * & * & * & \Delta_{66} & \Delta_{67} & \widetilde{G}_{z\tau_0 nql}^T \\ * & * & * & * & * & * & \Delta_{77} & 0 \\ * & * & * & * & * & * & * & -I \end{bmatrix} < 0, \tag{24}$$

where

$$\begin{aligned}
\Delta_{11} &= \widetilde{A}_{nql}^T\overline{P}_i\widetilde{A}_{nql} + H_e\left\{\left(\overline{W}_{1m} + \overline{\mathcal{N}}_{n1}\right)^T\widetilde{A}_{nql}\right\} + \overline{\Phi}_1, \\
\Delta_{12} &= \widetilde{A}_{nql}^T\overline{P}_m\widetilde{A}_{\tau_0 nql} + \widetilde{A}_{nql}^T\left(\overline{\mathcal{N}}_{n2} - \overline{W}_{1m}\right) \\
&\quad + \left(\overline{W}_{1m} + \overline{\mathcal{N}}_{n1}\right)^T\widetilde{A}_{\tau_0 nql} + \overline{\Phi}_2, \\
\Delta_{13} &= \widetilde{A}_{nql}^T\left(\overline{\mathcal{N}}_{n3} + \overline{W}_{1m}\right) + \overline{\Phi}_3, \\
\Delta_{14} &= \widetilde{A}_{nql}^T\overline{P}_m\widetilde{B}_{1nq} + \left(\overline{W}_{1m} + \overline{\mathcal{N}}_{n1}\right)^T\widetilde{B}_{1nq} + \widetilde{A}_{nql}^T\overline{\mathcal{N}}_{n4} - \overline{\mathcal{N}}_{n4}, \\
\Delta_{15} &= \widetilde{A}_{nql}^T\overline{P}_m\widetilde{G}_{nql} + \left(\overline{\mathcal{N}}_{n1} + \overline{W}_{1n}\right)^T\widetilde{G}_{nql} + \widetilde{A}_{nql}^T\overline{\mathcal{N}}_{n5}, \\
\Delta_{16} &= \widetilde{A}_{nql}^T\overline{P}_m\widetilde{G}_{\tau_0 nql} + \left(\overline{\mathcal{N}}_{n1} + \overline{W}_{1m}\right)^T\widetilde{G}_{\tau_0 nql} + \widetilde{A}_{nql}^T\overline{\mathcal{N}}_{n6} - \overline{\mathcal{N}}_{n6}, \\
\Delta_{17} &= \widetilde{A}_{nql}^T\overline{\mathcal{N}}_{n7} + \overline{\Phi}_4, \\
\Delta_{22} &= \widetilde{A}_{\tau_0 nql}^T\overline{P}_m\widetilde{A}_{\tau_0 nql} + H_e\left\{\left(\overline{\mathcal{N}}_{n2} - \overline{W}_{1m}\right)^T\widetilde{A}_{\tau_0 nql}\right\} + \overline{\Phi}_5, \\
\Delta_{23} &= \widetilde{A}_{\tau nql}^T\left(\overline{\mathcal{N}}_{n3} + \overline{W}_{1m}\right) + \overline{\Phi}_6, \\
\Delta_{24} &= \widetilde{A}_{\tau_0 nql}^T\overline{P}_m\widetilde{B}_{1nq} + \left(\overline{\mathcal{N}}_{n2} - \overline{W}_{1m}\right)^T\widetilde{B}_{1nq} + \widetilde{A}_{\tau_0 nql}^T\overline{\mathcal{N}}_{n4}, \\
\Delta_{25} &= \widetilde{A}_{\tau_0 nql}^T\overline{P}_m\widetilde{G}_{nql} + \left(\overline{\mathcal{N}}_{n2} - \overline{W}_{1m}\right)^T\widetilde{G}_{nql} + \widetilde{A}_{\tau_0 nkl}^T\overline{\mathcal{N}}_{n5}, \\
\Delta_{26} &= \widetilde{A}_{\tau_0 nql}^T\overline{P}_m\widetilde{G}_{\tau_0 nql} + \left(\overline{\mathcal{N}}_{n2} - \overline{W}_{1m}\right)^T\widetilde{G}_{\tau_0 nql} + \widetilde{A}_{\tau_0 nql}^T\overline{\mathcal{N}}_{n6}, \\
\Delta_{27} &= \widetilde{A}_{\tau_0 nql}^T\overline{\mathcal{N}}_{n7} - \overline{\mathcal{N}}_{n2}^T, \\
\Delta_{33} &= \overline{\Phi}_7, \Delta_{34} = \left(\overline{W}_{1m} + \overline{\mathcal{N}}_{n3}\right)^T\widetilde{B}_{1nq}, \\
\Delta_{35} &= \left(\overline{W}_{1m} + \overline{\mathcal{N}}_{n3}\right)^T\widetilde{G}_{nql}, \\
\Delta_{36} &= \left(\overline{W}_{1m} + \overline{\mathcal{N}}_{n3}\right)^T\widetilde{G}_{\tau_0 nql}, \\
\Delta_{37} &= -\overline{\mathcal{N}}_{n3}^T, \\
\Delta_{44} &= \widetilde{B}_{1nq}^T\overline{P}_m\widetilde{B}_{1nq} + H_e\left\{\overline{\mathcal{N}}_{n4}^T\widetilde{B}_{1nq}\right\} - \gamma^2 I, \\
\Delta_{45} &= \widetilde{B}_{1nq}^T\overline{P}_m\widetilde{G}_{nql} + \overline{\mathcal{N}}_{n4}^T\widetilde{G}_{nql} + \widetilde{B}_{1nq}\overline{\mathcal{N}}_{n5}, \\
\Delta_{46} &= \widetilde{B}_{1nq}^T\overline{P}_m\widetilde{G}_{\tau_0 nql} + \overline{\mathcal{N}}_{n4}^T\widetilde{G}_{\tau_0 nql} + \widetilde{B}_{1nq}\overline{\mathcal{N}}_{n6}, \\
\Delta_{47} &= \widetilde{B}_{1nq}^T\overline{\mathcal{N}}_{n7} - \overline{\mathcal{N}}_{n4}^T, \\
\Delta_{55} &= \widetilde{G}_{nql}^T\overline{P}_m\widetilde{G}_{nql} + H_e\left\{\overline{\mathcal{N}}_{n5}^T\widetilde{G}_{nql}\right\} - \overline{I}, \\
\Delta_{57} &= \widetilde{G}_{nql}^T\overline{\mathcal{N}}_{n7} - \overline{\mathcal{N}}_{n5}^T, \\
\Delta_{56} &= \overline{G}_{nql}^T P_m\overline{G}_{\tau_0 nql} + \mathcal{N}_{n5}^T\overline{G}_{\tau_0 nql} + \overline{G}_{nql}^T\mathcal{N}_{n6}, \\
\Delta_{77} &= \overline{\Phi}_8 \\
\Delta_{66} &= \widetilde{G}_{\tau_0 nql}^T\overline{P}_m\widetilde{G}_{\tau_0 nql} + H_e\left\{\overline{\mathcal{N}}_{n6}^T\widetilde{G}_{\tau_0 nql}\right\} - \overline{I}, \\
\Delta_{67} &= \widetilde{G}_{\tau_0 nql}^T\overline{\mathcal{N}}_{n7} - \overline{\mathcal{N}}_{n6}^T.
\end{aligned} \tag{25}$$

Applying the Schur complement described by Lemma 3 to the above inequality, we can obtain

$$\begin{aligned}
\Xi_{mnql} &= \begin{bmatrix} \Delta_{11} & \Delta_{12} & \Delta_{13} & \Delta_{14} & \Delta_{15} & \Delta_{16} & \Psi_{17} \\ * & \Delta_{22} & \Delta_{23} & \Delta_{24} & \Delta_{25} & \Delta_{26} & \Delta_{27} \\ * & * & \Delta_{33} & \Delta_{34} & \Delta_{35} & \Delta_{36} & \Delta_{37} \\ * & * & * & \Delta_{44} & \Delta_{45} & \Delta_{46} & \Delta_{47} \\ * & * & * & * & \Delta_{55} & \Delta_{56} & \Delta_{57} \\ * & * & * & * & * & \Delta_{66} & \Delta_{67} \\ * & * & * & * & * & * & \Delta_{77} \end{bmatrix} \\
&\quad + \begin{bmatrix} \widetilde{C}_{nql}^T \\ \widetilde{C}_{\tau_0 nql}^T \\ 0 \\ \widetilde{D}_{1nq}^T \\ \widetilde{G}_{znql}^T \\ \widetilde{G}_{z\tau_0 nql}^T \\ 0 \end{bmatrix} \begin{bmatrix} \widetilde{C}_{nql}^T \\ \widetilde{C}_{\tau_0 nql}^T \\ 0 \\ \widetilde{D}_{1nq}^T \\ \widetilde{G}_{znql}^T \\ \widetilde{G}_{z\tau_0 nql}^T \\ 0 \end{bmatrix}^T < 0.
\end{aligned} \tag{26}$$

Based on (26), we will prove that Theorem 1 is correct. Construct a discrete-time PLF as follows:

$$\begin{aligned}
\mathcal{V}_t &= \mathcal{V}_{1t} + \mathcal{V}_{2t} + \mathcal{V}_{3t}, \\
\mathcal{V}_{1t} &= \sum_{l=t-\tau_0}^{t-1} x_l^T\overline{R}x_\nu, \\
\mathcal{V}_{2t} &= \tau_0\sum_{\theta=-\tau_0}^{-1}\sum_{l=t+\theta}^{t-1}\begin{bmatrix} x_\nu \\ \pi_l \end{bmatrix}^T\begin{bmatrix} \overline{\mathcal{Q}}_{11} & \overline{\mathcal{Q}}_{12} \\ * & \overline{\mathcal{Q}}_{22} \end{bmatrix}\begin{bmatrix} x_\nu \\ \pi_l \end{bmatrix}, \\
\mathcal{V}_{3t} &= \begin{bmatrix} x_\nu \\ \sum_{\nu=t-\tau_0}^{t-1} x_\nu \end{bmatrix}^T\begin{bmatrix} \overline{P}_n & \overline{W}_{1n} \\ * & \overline{W}_{2n} \end{bmatrix}\begin{bmatrix} x_t \\ \sum_{\nu=t-\tau_0}^{t-1} x_\nu \end{bmatrix},
\end{aligned} \tag{27}$$

where $x_t \in \Omega_n$, $n = 1, 2, \ldots, \kappa$, and $\pi_t = x_{t+1} - x_t$.

Let $\Delta\mathcal{V}_t = \mathcal{V}_{t+1} - \mathcal{V}_t$, we can get

$$\Delta\mathcal{V}_{1t} = x_t^T\overline{R}x_t - x_{t-\tau_0}^T\overline{R}x_{t-\tau_0}, \tag{28}$$

$$\begin{aligned}
\Delta\mathcal{V}_{2t} &= \tau_0^2\begin{bmatrix} x_t \\ \pi_t \end{bmatrix}^T\begin{bmatrix} \overline{\mathcal{Q}}_{11} & \overline{\mathcal{Q}}_{12} \\ * & \overline{\mathcal{Q}}_{22} \end{bmatrix}\begin{bmatrix} x_t \\ \pi_t \end{bmatrix} \\
&\quad - \tau_0\sum_{\nu=t-\tau_0}^{t-1}\begin{bmatrix} x_\nu \\ \pi_\nu \end{bmatrix}^T\begin{bmatrix} \overline{\mathcal{Q}}_{11} & \overline{Q}_{12} \\ * & \overline{\mathcal{Q}}_{22} \end{bmatrix}\begin{bmatrix} x_\nu \\ \pi_\nu \end{bmatrix}.
\end{aligned} \tag{29}$$

Using Lemma 2, we can obtain

$$
\begin{aligned}
&-\tau_0 \sum_{v=t-\tau_0}^{t-1} \begin{bmatrix} x_v \\ \pi_v \end{bmatrix}^T \begin{bmatrix} \overline{\mathcal{Q}}_{11} & \overline{\mathcal{Q}}_{12} \\ * & \overline{\mathcal{Q}}_{22} \end{bmatrix} \begin{bmatrix} x_v \\ \pi_v \end{bmatrix} \\
&\le -\begin{bmatrix} \sum_{v=t-\tau_0}^{t-1} x_v \\ \sum_{v=t-\tau_0}^{t-1} \pi_v \end{bmatrix}^T \begin{bmatrix} \overline{\mathcal{Q}}_{11} & \overline{\mathcal{Q}}_{12} \\ * & \overline{\mathcal{Q}}_{22} \end{bmatrix} \begin{bmatrix} \sum_{l=t-\tau_0}^{t-1} x_v \\ \sum_{v=t-\tau_0}^{t-1} \pi_v \end{bmatrix} \\
&= \begin{bmatrix} \sum_{v=t-\tau_0}^{t-1} x_v \\ x_t - x_{t-\tau_0} \end{bmatrix}^T \begin{bmatrix} -\overline{\mathcal{Q}}_{11} & -\overline{\mathcal{Q}}_{12} \\ * & -\overline{\mathcal{Q}}_{22} \end{bmatrix} \begin{bmatrix} \sum_{v=t-\tau_0}^{t-1} x_v \\ x_t - x_{t-\tau_0} \end{bmatrix} \\
&= \begin{bmatrix} x_t \\ x_{t-\tau_0} \\ \sum_{v=t-\tau_0}^{t-1} x_v \end{bmatrix}^T \begin{bmatrix} -\overline{\mathcal{Q}}_{22} & \overline{\mathcal{Q}}_{22} & -\overline{\mathcal{Q}}_{12}^T \\ * & -\overline{\mathcal{Q}}_{22} & \overline{\mathcal{Q}}_{12}^T \\ * & * & -\overline{\mathcal{Q}}_{11} \end{bmatrix} \begin{bmatrix} x_t \\ x_{t-\tau_0} \\ \sum_{v=t-\tau_0}^{t-1} x_v \end{bmatrix},
\end{aligned}
\tag{30}
$$

$$
\begin{aligned}
\Delta\mathscr{V}_{3t} &= \begin{bmatrix} x_{t+1} \\ \sum_{v=t+1-\tau_0}^{t} x_v \end{bmatrix}^T \begin{bmatrix} \overline{P}_m & \overline{W}_{1m} \\ * & \overline{W}_{2m} \end{bmatrix} \begin{bmatrix} x_{t+1} \\ \sum_{v=t+1-\tau_0}^{t} x_v \end{bmatrix} \\
&\quad - \begin{bmatrix} x_t \\ \sum_{v=t-\tau_0}^{t-1} x_v \end{bmatrix}^T \begin{bmatrix} \overline{P}_n & \overline{W}_{1n} \\ * & \overline{W}_{2n} \end{bmatrix} \begin{bmatrix} x_t \\ \sum_{v=t-\tau_0}^{t-1} x_v \end{bmatrix} \\
&= \zeta_t^T \left\{ \Theta_1 \begin{bmatrix} \overline{P}_m & \overline{W}_{1m} \\ * & \overline{W}_{2m} \end{bmatrix} \Theta_1^T - \Theta_2 \begin{bmatrix} \overline{P}_n & \overline{W}_{1n} \\ * & \overline{W}_{2n} \end{bmatrix} \Theta_2^T \right\} \zeta_t,
\end{aligned}
\tag{31}
$$

$$
\begin{aligned}
\Theta_1 &= \begin{bmatrix} \widetilde{A}_{nql} & \widetilde{A}_{\tau_0 nql} & \widetilde{B}_{1nq} & \widetilde{G}_{nql} & \widetilde{G}_{\tau_0 nql} & 0 & 0 \\ I & -I & I & 0 & 0 & 0 & 0 \end{bmatrix}^T, \\
\Theta_2 &= \begin{bmatrix} I & 0 & 0 & 0 & 0 & 0 & 0 \\ 0 & 0 & I & 0 & 0 & 0 & 0 \end{bmatrix}^T, \\
\zeta_t^T &= \begin{bmatrix} x_t^T & x_{t-\tau_0}^T & \left(\sum_{v=t-\tau_0}^{t-1} x_l^T \right) & \omega_t^T & \phi_t^T & \phi_{t-\tau_0}^T & \pi_t^T \end{bmatrix}
\end{aligned}
\tag{32}
$$

where

Observing system (11) and inequality (5), one has

$$
\begin{aligned}
\mathcal{N} &= 2\xi_t^T \left[\overline{\mathcal{N}}_{n1} \;\; \overline{\mathcal{N}}_{n2} \;\; \overline{\mathcal{N}}_{n3} \;\; \mathcal{U}_n^T \mathcal{N}_{n4} \;\; \overline{\mathcal{N}}_{n5} \;\; \overline{\mathcal{N}}_{n6} \;\; \overline{\mathcal{N}}_{n7} \right]^T \\
&\quad \times \left[\left(\widetilde{A}_{nql} - I \right) x_t + \widetilde{A}_{\tau_0 nql} x_{t-\tau_0} + \widetilde{B}_{1nq} \omega_t \right. \\
&\quad \left. + \widetilde{G}_{nql} \phi_t + \widetilde{G}_{\tau_0 nql} \phi_{t-\tau_0} - \pi_t \right] = 0,
\end{aligned}
\tag{33}
$$

$$
\theta x_t^T \mathcal{U}_n^T \mathcal{U}_n x_t - \phi_t^T \mathcal{U}_n^T \mathcal{U}_n \phi_t \ge 0, \tag{34}
$$

$$
\theta x_{t-\tau_0}^T \mathcal{U}_n^T \mathcal{U}_n x_{t-\tau_0} - \phi_{t-\tau_0}^T \mathcal{U}_n^T \mathcal{U}_n \phi_{t-\tau_0} \ge 0. \tag{35}
$$

Then, from (28)–(35) and considering system (11), one can obtain

$$
\begin{aligned}
&\Delta\mathscr{V}_t + z_t^T z_t - \gamma^2 \omega_t^T \omega_t = \Delta\mathscr{V}_{1t} + \Delta\mathscr{V}_{2t} \\
&\quad + \Delta\mathscr{V}_{3t} + \mathcal{N} + z_t^T z_t - \gamma^2 \omega_t^T \omega_t \\
&\le \Delta\mathscr{V}_{1t} + \Delta\mathscr{V}_{2t} + \Delta\mathscr{V}_{3t} + \mathcal{N} + z_t^T z_t - \gamma^2 \omega_t^T \omega_t \\
&\quad + \theta x_t^T \mathcal{U}_n^T \mathcal{U}_n x_t - \phi_t^T \mathcal{U}_n^T \mathcal{U}_n \phi_t + \theta x_{t-\tau_0}^T \mathcal{U}_n^T \mathcal{U}_n x_{t-\tau_0} \\
&\quad - \phi_{t-\tau_0}^T \mathcal{U}_n^T \mathcal{U}_n \phi_{t-\tau_0} \\
&\le \xi_t^T \Xi_{mnql} \xi_t.
\end{aligned}
\tag{36}
$$

Based on (26), we have

$$
\Delta\mathscr{V}_t + z_t^T z_t - \gamma^2 \omega_t^T \omega_t < 0. \tag{37}
$$

Therefore, when the disturbance is assumed to be zero, the following can be obtained from (28)–(35):

$$
\begin{aligned}
\Delta\mathscr{V}|_{\omega=0} &= \left(\Delta\mathscr{V}_1 + \Delta\mathscr{V}_2 + \Delta\mathscr{V}_3 + \mathcal{N} \right)\big|_{\omega_t=0} \\
&\le \begin{bmatrix} x_t \\ x_{t-\tau_0} \\ \sum_{v=t-\tau_0}^{t-1} x_v \\ \pi_t \end{bmatrix}^T \begin{bmatrix} \Delta_{11} & \Delta_{12} & \Delta_{13} & \Delta_{17} \\ * & \Delta_{22} & \Delta_{23} & \Delta_{27} \\ * & * & \Delta_{33} & \Delta_{37} \\ * & * & * & \Delta_{77} \end{bmatrix} \begin{bmatrix} x_t \\ x_{t-\tau_0} \\ \sum_{v=t-\tau_0}^{t-1} x_v \\ \pi_t \end{bmatrix}.
\end{aligned}
\tag{38}
$$

Using Schur complement, inequality (26) means that $\Delta V|_{\omega=0} < 0$. Therefore, when $\omega(t) = 0$, we can easily obtain the asymptotically stability of system (11). Let

$$
\mathbb{J} = \sum_{l=0}^{\infty} \left[\|z_l\|_2^2 - \gamma^2 \|\omega_l\|_2^2 \right]. \tag{39}
$$

Under the condition that the initial conditions are zero and inequality (37) holds, we can obtain $\mathbb{J} \le \sum_{l=0}^{\infty} [-\Delta\mathscr{V}_l] = -\mathscr{V}_\infty + \mathscr{V}_0 = -\mathscr{V}_\infty < 0$. That is, $\|z\|_2 < \gamma \|\omega\|_2$.

In order to increase the feasible range of the results obtained in Theorem 1, the relationship between the subsystems in each subspace is considered. In addition, the introduced relaxation matrix $M_{nql}\,(q < l < \lambda_n)$ may not be symmetric matrices. Consequently, we can give and prove the following improved results. □

Theorem 2. *Designing fuzzy controller (10) for system (8), the controlled system (11) is asymptotically stable and has H_∞ property upper bound $\gamma\,(\gamma > 0)$, if there exist matrices $\begin{bmatrix} P_n & W_{1n} \\ * & W_{2n} \end{bmatrix} > 0$, $\begin{bmatrix} \mathcal{Q}_{11} & \mathcal{Q}_{12} \\ * & \mathcal{Q}_{22} \end{bmatrix} > 0$, $R > 0$, the nonsingular matrix F_n, matrices $\mathcal{N}_{n\iota}\,(\iota = 1, 2, \ldots, 7)$, K_{anl}, $K_{a\tau_0 nl}$, K_{bnl}, $K_{b\tau_0 nl}$, and $M_{nlq} = M_{nql}^T$, such that the following are feasible:*

$$
\Pi_{mnqq} < M_{nqq}, \quad q = 1, \ldots, \lambda_n, \; (n, m) \in \Omega, \tag{40}
$$

$$
\Pi_{mnql} + \Pi_{mnlq} < M_{nql} + M_{nql}^T, \quad 0 < k < l \le \lambda_n, \; (n, m) \in \Omega, \tag{41}
$$

$$M_n = \begin{bmatrix} M_{n11} & M_{n12} & \cdots & M_{n1\lambda_n} \\ M_{n21} & M_{n22} & \cdots & M_{n2\lambda_n} \\ \vdots & \vdots & \ddots & \vdots \\ M_{n\lambda_n 1} & M_{n\lambda_n 2} & \cdots & N_{n\lambda_n\lambda_n} \end{bmatrix} < 0, \quad n = 1, 2, \ldots, \kappa. \tag{42}$$

The feedback matrices of the controller can be designed as

$$\begin{aligned} F_{anl} &= K_{anl}K_n^{-1}, \\ F_{a\tau_0 nl} &= K_{a\tau_0 nl}K_n^{-1}, \\ F_{bnl} &= K_{bnl}K_n^{-1}, \\ F_{b\tau_0 nl} &= K_{b\tau_0 nl}K_n^{-1}. \end{aligned} \tag{43}$$

Proof. If inequalities (40)–(42) hold, then

$$\Pi_{mnkl} < \sum_{q=1}^{\lambda_n} h_{nq}^2 M_{nqq} + \sum_{q<l}^{\lambda_n} h_{nq}h_{nl}\left(M_{nql} + M_{nql}^T\right) = \mathbf{H}_n^T M_n \mathbf{H}_n < 0, \tag{44}$$

where $\mathbf{H}_n = \left[\, h_{n1}I \;\; h_{n2}I \;\; \cdots \;\; h_{n\lambda_n}I \,\right]^T$.

If inequality (44) has a feasible solution, we can obtain

$$\Delta \mathscr{V}_t + z_t^T z_t - \omega_t^T \omega_t < 0. \tag{45}$$

The next proof process is roughly the same as that of Theorem 2, so it is omitted here. This completes the proof. □

4. Conclusion

By using the fuzzy switched system, PLF, and state movement from one subspace to another, two new H_∞ control schemes with time delay information are derived. The advantages of the proposed method include that the fuzzy posterior contains nonlinear functions, the Lyapunov function is piecewise, and the condition is expressed by linear matrix inequality. In addition, Theorem 2 considers the relationship between fuzzy subsystems. The disadvantage of the proposed method is the introduction of relaxation variables, which increases the computational complexity. However, in order to expand the feasible region of the result and obtain more feasible solutions at the same time, we sometimes need to introduce the relaxation variables. If the conditions have a feasible solution, the controller feedback matrices can be calculated according to the feasible solutions of a set of LMIs. Since fractional-order systems have more dynamic behaviors than integral-order systems [3], we will consider extending the results of this paper to fractional-order T-S fuzzy systems.

Data Availability

The key point of our paper is theoretical derivation. The result simulation can be done with the linear matrix inequality toolbox provided by MATLAB.

Conflicts of Interest

The authors declare that they have no conflicts of interest.

References

[1] T. Takagi and M. Sugeno, "Fuzzy identification of systems and its applications to modeling and control," *IEEE Transactions on Systems, Man, and Cybernetics*, vol. SMC-15, no. 1, pp. 116–132, 1985.

[2] A. Yang, L. Li, Z. Wang, and R. Guo, "Tracking control of a class of chaotic systems," *Symmetry*, vol. 11, no. 4, p. 568, 2019.

[3] C. M. Jiang, A. Zada, M. T. Şenel, and T. X. Li, "Synchronization of bidirectional N-coupled fractional-order chaotic systems with ring connection based on antisymmetric structure," *Advances in Difference Equations*, vol. 2019, no. 1, p. 456, 2019.

[4] A. Khan and S. Kumar, "T-S fuzzy modeling and predictive control and synchronization of chaotic satellite systems," *International Journal of Modelling and Simulation*, vol. 39, no. 3, pp. 203–213, 2019.

[5] X. Wang, J. H. Park, K. She, S. Zhong, and L. Shi, "Stabilization of chaotic systems with T-S fuzzy model and nonuniform sampling: a switched fuzzy control approach," *IEEE Transactions on Fuzzy Systems*, vol. 27, no. 6, pp. 1263–1271, 2019.

[6] T. Li and Y. V. Rogovchenko, "On the asymptotic behavior of solutions to a class of third-order nonlinear neutral differential equations," *Applied Mathematics Letters*, vol. 105, Article ID 106293, 2020.

[7] C. Pu, J. Ren, B. Xue, and A. Yu, "Dynamic self-adaptive learning algorithm research based on T-S RBF fuzzy neutral network," *Journal of Computational Methods in Sciences and Engineering*, vol. 19, no. 1, pp. 209–218, 2019.

[8] D. P. Bharathi, T. Jayakumar, and S. Vinoth, "Numerical solutions of fuzzy multiple hybrid single neutral delay differential equations," *International Journal of Scientific and Technology Research*, vol. 8, no. 9, pp. 520–523, 2019.

[9] R. M. Xu and F. Zhang, "ε-Nash mean-field games for general linear-quadratic systems with applications," *Automatica*, vol. 114, Article ID 108835, 2020.

[10] X. Ji, K. Yang, X. Na, C. Lv, and Y. Liu, "Feedback game-based shared control scheme design for emergency collision avoidance: a fuzzy-linear quadratic regulator approach," *Journal of Dynamic Systems, Measurement and Control*, vol. 141, no. 8, Article ID 0851005, 2019.

[11] J. Tao, R. Lu, H. Su, and Z.-G. Wu, "Filtering of T-S fuzzy systems with nonuniform sampling," *IEEE Transactions on Systems, Man, and Cybernetics: Systems*, vol. 48, no. 12, pp. 2442–2450, 2018.

[12] H. Zhang, S. Lun, and D. Liu, "Fuzzy H_∞ filter design for a class of nonlinear discrete-time systems with multiple time delays," *IEEE Transactions on Fuzzy Systems*, vol. 15, no. 3, pp. 453–469, 2007.

[13] X.-L. Wang and G.-H. Yang, "Fault detection for T-S fuzzy systems with past output measurements," *Fuzzy Sets and Systems*, vol. 365, pp. 98–115, 2019.

[14] G. Feng, M. Chen, D. Sun, and T. Zhang, "Approaches to robust filtering design of discrete time fuzzy dynamic systems," *IEEE Transactions on Fuzzy Systems*, vol. 16, no. 2, pp. 331–340, 2008.

[15] M. Chen, G. Feng, and H. Ma, "A delay-dependent approach to H_∞ filtering for fuzzy time-varying delayed systems," in

Proceedings of the 2007 IEEE International Fuzzy Systems Conference, July 2007.

[16] C. Chen, H. Liu, and X. Guan, ".H_∞ filtering of time-delay T-S fuzzy systems based on piecewise Lyapunov-Krasovskii function," *Signal Processing*, vol. 89, no. 10, pp. 1998–2005, 2009.

[17] Z. Li and S. Xu, "Fuzzy weighting-dependent approach to robust filter design for delayed fuzzy systems," *Signal Processing*, vol. 89, no. 4, pp. 463–471, 2009.

[18] C. Lin, Q.-G. Wang, T. H. Lee, and Y. He, "Fuzzy weighting-dependent approach to H_∞ filter design for time-delay fuzzy systems," *IEEE Transactions on Signal Processing*, vol. 55, no. 6, pp. 2746–2751, 2007.

[19] J. Zhang, Y. Xia, and R. Tao, "New results on H_∞ filtering for fuzzy time-delay systems," *IEEE Transactions on Fuzzy Systems*, vol. 17, no. 1, pp. 128–137, 2009.

[20] J. Dong, Y. Wang, and G. Yang, "Control synthesis of continuous time T-S fuzzy systems with local nonlinear models," *IEEE Transactions on Systems Man, Cybernetics: B, Cybernetics*, vol. 39, no. 5, pp. 1245–1258, 2009.

[21] H. Moodi, M. Farrokhi, T. M. Guerra, and J. Lauber, "On stabilization conditions for T-S systems with nonlinear consequent parts," *International Journal of Fuzzy Systems*, vol. 21, no. 1, pp. 84–94, 2019.

[22] G.-H. Yang and H. Wang, "Fault detection and isolation for a class of uncertain state-feedback fuzzy control systems," *IEEE Transactions on Fuzzy Systems*, vol. 23, no. 1, pp. 139–151, 2015.

[23] M. Klug, E. B. Castelan, V. J. S. Leite, and L. F. P. Silva, "Fuzzy dynamic output feedback control through nonlinear Takagi-Sugeno models," *Fuzzy Sets and Systems*, vol. 263, pp. 92–111, 2015.

[24] W.-J. Chang and F.-L. Hsu, "Sliding mode fuzzy control for Takagi-Sugeno fuzzy systems with bilinear consequent part subject to multiple constraints," *Information Sciences*, vol. 327, pp. 258–271, 2016.

[25] A. Nguyen, P. Coutinho, T. Guerra, and R. Palhares, "Control synthesis for fuzzy systems with local nonlinear models subject to actuator saturation," in *Proceedings of the 2019 IEEE International Conference on Fuzzy Systems*, June 2019.

[26] D. Zhai, A.-Y. Lu, J. Dong, and Q.-L. Zhang, "Event triggered H_-/H_∞ fault detection and isolation for T-S fuzzy systems with local nonlinear models," *Signal Processing*, vol. 138, pp. 244–255, 2017.

[27] S.-J. Huang and G.-H. Yang, "Input-output based fault estimation for T-S fuzzy systems with local nonlinear parts," *IEEE Transactions on Fuzzy Systems*, vol. 25, no. 5, pp. 1320–1328, 2017.

[28] K. Cao, X. Z. Gao, T. Vasilakos, and W. Pedrycz, "Analysis of stability and robust stability of polynomial fuzzy model-based control systems using a sum-of-squares approach," *Soft Computing*, vol. 18, no. 3, pp. 433–442, 2014.

[29] N. Alireza, S. Nguang, S. Akshya, and A. Dhafer, "Stabilisation of discrete-time polynomial fuzzy systems via a polynomial Lyapunov approach," *International Journal of Systems Science*, vol. 49, no. 3, pp. 557–566, 2018.

[30] W.-J. Wang, Y.-J. Chen, and C.-H. Sun, "Relaxed stabilization criteria for discrete-time T-S fuzzy control systems based on a switching fuzzy model and piecewise Lyapunov function," *IEEE Transactions on Systems, Man and Cybernetics, Part B (Cybernetics)*, vol. 37, no. 3, pp. 551–559, 2007.

[31] P. Gahinet and P. Apkarian, "A linear matrix inequality approach to H_∞ control," *International Journal of Robust and Nonlinear Control*, vol. 4, no. 4, pp. 421–448, 1994.

[32] G. Wei, G. Feng, and Z. Wang, "Robust H_∞ control for discrete-time fuzzy systems with infinite-distributed delays," *IEEE Transactions on Fuzzy Systems*, vol. 17, no. 1, pp. 224–232, 2019.

[33] C.-L. Chen, G. Feng, and X.-P. Guan, "Delay-dependent stability analysis and controller synthesis for discrete-time T-S fuzzy systems with time delays," *IEEE Transactions on Fuzzy Systems*, vol. 13, no. 5, pp. 630–643, 2005.

Hindawi
Mathematical Problems in Engineering
Volume 2020, Article ID 4286524, 7 pages
https://doi.org/10.1155/2020/4286524

Research Article

A Time-Varying Gain Design Method for State Feedback Control of Upper Triangular Nonlinear Systems

Yanmin Yin

School of Science, Shandong Jianzhu University, Jinan 250101, China

Correspondence should be addressed to Yanmin Yin; yym@sdjzu.edu.cn

Received 19 March 2020; Accepted 17 April 2020; Published 5 May 2020

Guest Editor: Rongwei Guo

In this paper, a time-varying gain design method is used to investigate the state feedback control problem of upper triangular nonlinear systems. Firstly, the nonlinear term recognizes an incremental rate relying on the unknown constant and the function with respect to time. Then, a time-varying gain design method is utilized to construct a state feedback controller. With the help of a suitable coordinate transformation and a Lyapunov function, one obtains that all the signals of the closed-loop system converge to zero. Finally, two numerical examples are presented to display the effectiveness of the time-varying gain design method.

1. Introduction

Many physical models can be described by nonlinear systems [1–4]. Therefore, the control problem of these physical models can be transformed into the control problem of nonlinear systems [5]. Compared with linear systems, the behavior of nonlinear systems is more diverse [6–10]. The research of control algorithms is generally developed for the specific type of nonlinear systems [11, 12].

In general, many results about nonlinear systems have focused on nonlinear systems with triangular structures, that is, lower triangular nonlinear systems [13, 14] and upper triangular nonlinear systems [15]. The common method for studying lower triangular nonlinear systems is the backstepping design method [16], and the common method for considering upper triangular nonlinear systems is the forwarding design method [17]. Although, based on the iterative design algorithm, these methods can effectively deal with strong nonlinearities, the design procedure is more complicated. In the past few decades, the gain design method is a very effective tool to deal with the control problem of upper triangular nonlinear systems [18].

Based on the coordinate transformation, the time-varying gain design method is an effective strategy for dealing with the uncertain parameter of upper triangular nonlinear systems [19]. By introducing a time-varying function in the controller, it can effectively deal with the nonlinear terms of upper triangular nonlinear systems [20]. Compared with the commonly adaptive control strategy, the time-varying gain design method is more concise, the calculation process is less, and a lot of calculation work is reduced. Furthermore, the time-varying gain design method does not require too many design parameters and avoids complicated calculation process.

This paper uses the time-varying gain design method to study the control problem of upper triangular nonlinear systems. The nonlinear characteristics of the system considering here are more obvious, that is, the unknown constant and the function with respect to time are allowed in the nonlinear terms. Compared with the assumption about the nonlinear terms in [19, 20], the assumption in this paper is more general. Thus, a time-varying gain design method is introduced to achieve the control goals of the concerned system.

2. Preliminaries

In this paper, we consider a class of nonlinear systems in the following form:

$$\begin{cases} \dot{\xi}_1(t) = \xi_2(t) + \psi_1(t, \xi(t), u(t)), \\ \dot{\xi}_2(t) = \xi_3(t) + \psi_2(t, \xi(t), u(t)), \\ \vdots \\ \dot{\xi}_{n-1}(t) = \xi_n(t) + \psi_{n-1}(t, \xi(t), u(t)), \\ \dot{\xi}_n(t) = u(t), \end{cases} \tag{1}$$

where $\xi(t) = [\xi_1(t), \xi_2(t), \ldots, \xi_n(t)]^T \in \mathbb{R}^n$ is the state and $u(t) \in \mathbb{R}$ is the input; the uncertain continuous functions $\psi_i(t, \xi(t), u(t))$: $\mathbb{R}^+ \times \mathbb{R}^n \times \mathbb{R} \longrightarrow \mathbb{R}$, $\quad i = 1, 2, \ldots, n-1$, satisfy the following growth condition.

Assumption 1. For all $(t, \xi(t), u(t)) \in \mathbb{R}^+ \times \mathbb{R}^n \times \mathbb{R}$, the following inequalities hold:

$$\begin{aligned} \left|\psi_i(t, \xi(t), u(t))\right| \le \theta(1+t)^c \Big(&\left|\xi_{i+2}(t)\right| + \left|\xi_{i+3}(t)\right| + \cdots \\ &+ \left|\xi_n(t)\right| + \left|u(t)\right|\Big), \quad i = 1, 2, \ldots, n-1, \end{aligned} \tag{2}$$

where θ is an unknown positive constant and c is a known constant which satisfies $0 \le c < 1$.

Remark 1. Assumption 1 is a reasonable condition. According to Assumption 1, we can know that the nonlinear terms of system (1) can include the unknown constant and the function with respect to time. Therefore, compared with the assumption in [19, 20], Assumption 1 is more general, and the nonlinear characteristics of system (1) are more diverse. The controller designed in this paper is effective for a class of nonlinear systems as long as the nonlinear terms satisfy (2).

The control goal of this paper is to construct a state feedback controller such that all the signals of the closed-loop system converge to zero. As long as the context does not cause confusion, the parameters of the function can be simplified.

3. Main Results

Theorem 1. *When the constant c satisfies $0 < c < 0.5$, all the signals of system (1) can converge to zero by the following controller:*

$$u = -\frac{\beta_1}{(t+1)^{\gamma n}}\xi_1 - \frac{\beta_2}{(t+1)^{\gamma(n-1)}}\xi_2 - \cdots - \frac{\beta_n}{(t+1)^{\gamma}}\xi_n, \tag{3}$$

where β_i, $i = 1, 2, \ldots, n$, are coefficients of the Hurwitz polynomial $\phi(\rho) = \rho^n + \beta_n\rho^{n-1} + \cdots + \beta_2\rho + \beta_1$ and $\gamma = 2c$.

Proof. Let $\gamma = 2c$. One presents the coordinate transformations as follows:

$$\epsilon_i = (t+1)^{\gamma i}\xi_i, \quad i = 1, 2, \ldots, n. \tag{4}$$

Based on (1) and (4), it is obtained that

$$\dot{\epsilon}_i = \frac{1}{(t+1)^{\gamma}}\epsilon_{i+1} + (t+1)^{\gamma i}\psi_i + \frac{\gamma i}{t+1}\epsilon_i, \quad i = 1, 2, \ldots, n, \tag{5}$$

where $\epsilon_{n+1} = u$.

Letting

$$u = -\frac{1}{(t+1)^{\gamma(n+1)}}\left(\beta_1\epsilon_1 + \beta_2\epsilon_2 + \cdots + \beta_n\epsilon_n\right), \tag{6}$$

where β_i, $i = 1, 2, \ldots, n$, are given in (3), the following equation is satisfied:

$$\dot{\epsilon} = \frac{1}{(t+1)^{\gamma}}\Phi\epsilon + \frac{\gamma}{t+1}\Lambda\epsilon + \Psi, \tag{7}$$

where $\epsilon = [\epsilon_1, \epsilon_2, \ldots, \epsilon_n]^T$, $\Lambda = \mathrm{diag}[1, 2, \ldots, n]$, and

$$\begin{aligned} \Phi &= \begin{bmatrix} 0 & 1 & \cdots & 0 \\ \vdots & \vdots & \ddots & 0 \\ 0 & 0 & \cdots & 1 \\ -\beta_1 & -\beta_2 & \cdots & -\beta_n \end{bmatrix}, \\ \Psi &= \begin{bmatrix} (t+1)^{\gamma}\psi_1 \\ \vdots \\ (t+1)^{(n-1)\gamma}\psi_{n-1} \\ 0 \end{bmatrix}. \end{aligned} \tag{8}$$

Because β_i, $i = 1, 2, \ldots, n$, are coefficients of the Hurwitz polynomial $\phi(\rho)$, there is a positive definite matrix Γ satisfying $\Gamma\Phi + \Phi^T\Gamma \le -I$ [21]. Letting $V_\epsilon = \epsilon^T\Gamma\epsilon$, one gets

$$\dot{V}_\epsilon|_{(7)} \le -\frac{1}{(t+1)^{\gamma}}\|\epsilon\|^2 + \frac{2\gamma\|\Lambda\Gamma\|}{t+1}\|\epsilon\|^2 + 2\epsilon^T\Gamma\Psi. \tag{9}$$

By Assumption 1 and (4), one has

$$\begin{aligned} \left|(t+1)^{i\gamma}\psi_i(t, \xi, u)\right| &\le \frac{\theta(1+\delta)}{(t+1)^{1.5\gamma}}\left(\left|\epsilon_1\right| + \left|\epsilon_2\right| + \cdots + \left|\epsilon_n\right|\right) \\ &\le \frac{\sqrt{n}\theta(1+\delta)}{(t+1)^{1.5\gamma}}\|\epsilon\|. \end{aligned} \tag{10}$$

It follows from (10) that

$$2\epsilon^T\Gamma\Psi \le 2\|\epsilon\| \cdot \|\Gamma\| \cdot \|\Psi\| \le \frac{2\|\Gamma\|\sqrt{n(n-1)}\theta(1+\delta)}{(t+1)^{1.5\gamma}}\|\epsilon\|^2. \tag{11}$$

Substituting (11) into (9), one gets

$$\begin{aligned} \dot{V}_\epsilon|_{(7)} \le &-\frac{1}{(t+1)^{\gamma}}\|\epsilon\|^2 + \frac{2\gamma\|\Lambda\Gamma\|}{t+1}\|\epsilon\|^2 \\ &+ \frac{2\|\Gamma\|\sqrt{n(n-1)}\theta(1+\delta)}{(t+1)^{1.5\gamma}}\|\epsilon\|^2. \end{aligned} \tag{12}$$

Since $\gamma = 2c < 1$, there is a finite time T such that

$$-\frac{1}{(t+1)^{\gamma}} + \frac{2\gamma\|\Lambda\Gamma\|}{t+1} + \frac{2\|\Gamma\|\sqrt{n(n-1)}\theta(1+\delta)}{(t+1)^{1.5\gamma}} < 0, \quad t \ge T. \tag{13}$$

Therefore, it is verified from (12) that

$$\dot{V} < -\|\epsilon\|^2, \quad \text{for } t \ge T. \tag{14}$$

Based on (14) and the definition of V, the states ϵ_i, $i = 1, 2, \ldots, n$, converge to zero. By (6), the controller u

converges to zero. From (4), one has that the states ξ_i, $i = 1, 2, \ldots, n$, converge to zero.

Remark 2. From the proof of Theorem 1, we can see that the constant c is a key design parameter. As long as the parameter c satisfies the condition $0 < c < 0.5$, one guarantees that equation (13) holds, and then, one handles the effects of the unknown parameter θ and the function on time in the nonlinear terms. The parameters in controller (3) consist of two parts. One is the parameter γ, which only needs to be satisfied by $\gamma = 2c$. The other part is the Hurwitz polynomial coefficients β_i, $i = 1, 2, \ldots, n$, which are also relatively easy to choose. Therefore, the parameters in controller (3) are better selected, which avoid excessive calculation process.

Theorem 2. *In the case of $c = 0$, the states of system (1) can converge to zero by the following controller:*

$$u = -\frac{\beta_1 \xi_1}{(t+1)^{0.5n}} - \frac{\beta_2 \xi_2}{(t+1)^{0.5(n-1)}} - \cdots - \frac{\beta_n \xi_n}{(t+1)^{0.5}}, \tag{15}$$

where β_i, $i = 1, 2, \ldots, n$, are coefficients of the Hurwitz polynomial $\phi(\rho) = \rho^n + \beta_n \rho^{n-1} + \cdots + \beta_2 \rho + \beta_1$.

Proof. The proof procedure is similar to the proof procedure of Theorem 1. One chooses $\gamma = 0.5$ in (4), and then, controller (15) is designed. In order to avert repetition, the detailed proof is omitted.

Theorem 3. *When the constant c satisfies $0.5 \le c < 1$, all the signals of system (1) can converge to zero by the following controller:*

$$u = -\frac{\beta_1}{(t+1)^n} \xi_1 - \frac{\beta_2}{(t+1)^{n-1}} \xi_2 - \cdots - \frac{\beta_n}{t+1} \xi_n, \tag{16}$$

where β_i, $i = 1, 2, \ldots, n$, are coefficients of the Hurwitz polynomial $\phi(\rho) = \rho^n + \beta_n \rho^{n-1} + \cdots + \beta_2 \rho + \beta_1$.

Proof. One presents the coordinate transformations as follows:

$$\epsilon_i = (t+1)^i \xi_i, \quad i = 1, 2, \ldots, n. \tag{17}$$

Based on (16) and (17), it is obtained that

$$\dot{\epsilon}_i = \frac{1}{t+1} \epsilon_{i+1} + (t+1)^i \psi_i + \frac{i}{t+1} \epsilon_i, \quad i = 1, 2, \ldots, n. \tag{18}$$

Letting

$$u = -\frac{1}{(t+1)^{n+1}} \left(\beta_1 \epsilon_1 + \beta_2 \epsilon_2 + \cdots + \beta_n \epsilon_n \right), \tag{19}$$

where β_i, $i = 1, 2, \ldots, n$, are given in (3), the following equation is satisfied:

$$\dot{\epsilon} = \frac{1}{t+1} \Phi \epsilon + \frac{1}{t+1} \Lambda \epsilon + \Psi, \tag{20}$$

where $\epsilon = [\epsilon_1, \epsilon_2, \ldots, \epsilon_n]^T$, $\Lambda = \mathrm{diag}[1, 2, \ldots, n]$, and

$$\Phi = \begin{bmatrix} 0 & 1 & \cdots & 0 \\ \vdots & \vdots & \ddots & 0 \\ 0 & 0 & \cdots & 1 \\ -\beta_1 & -\beta_2 & \cdots & -\beta_n \end{bmatrix}, \qquad \Psi = \begin{bmatrix} (t+1)\psi_1 \\ \vdots \\ (t+1)^{n-1} \psi_{n-1} \\ 0 \end{bmatrix}. \tag{21}$$

Because β_i, $i = 1, 2, \ldots, n$, are coefficients of the Hurwitz polynomial $\phi(\rho)$, there is a positive definite matrix Γ satisfying $\Gamma(\Phi + \Lambda) + (\Phi + \Lambda)^T \Gamma \le -I$ [21]. Letting $V_\epsilon = \epsilon^T \Gamma \epsilon$, one gets

$$\dot{V}_\epsilon|_{(7)} \le -\frac{1}{t+1} \|\epsilon\|^2 + 2\epsilon^T \Gamma \Psi. \tag{22}$$

By Assumption 1 and (4), one has

$$\begin{aligned} \left| (t+1)^i \psi_i(t, \xi, u) \right| &\le \frac{\theta(1+\delta)}{(t+1)^{2-c}} \left(|\epsilon_1| + |\epsilon_2| + \cdots + |\epsilon_n| \right) \\ &\le \frac{\sqrt{n}\theta(1+\delta)}{(t+1)^{2-c}} \|\epsilon\|. \end{aligned} \tag{23}$$

It follows from (10) that

$$2\epsilon^T \Gamma \Psi \le 2\|\epsilon\| \cdot \|\Gamma\| \cdot \|\Psi\| \le \frac{2\|\Gamma\| \sqrt{n(n-1)} \theta(1+\delta)}{(t+1)^{2-c}} \|\epsilon\|^2. \tag{24}$$

Substituting (11) into (9), one gets

$$\dot{V}_\epsilon|_{(7)} \le -\frac{1}{t+1} \|\epsilon\|^2 + \frac{2\|\Gamma\| \sqrt{n(n-1)} \theta(1+\delta)}{(t+1)^{2-c}} \|\epsilon\|^2. \tag{25}$$

Since $c < 1$, there is a finite time T such that

$$-\frac{1}{t+1} + \frac{2\|\Gamma\| \sqrt{n(n-1)} \theta(1+\delta)}{(t+1)^{2-c}} < 0, \quad t \ge T. \tag{26}$$

Therefore, it is verified from (12) that

$$\dot{V} < -\|\epsilon\|^2, \quad \text{for } t \ge T. \tag{27}$$

Based on (27) and the definition of V, the states ϵ_i, $i = 1, 2, \ldots, n$, converge to zero. By (20), the controller u converges to zero. From (17), one has that the states ξ_i, $i = 1, 2, \ldots, n$, converge to zero.

Remark 3. In this paper, with the help of the Lyapunov function, a new control strategy is proposed for upper triangular nonlinear systems, and state feedback controllers (3), (15), and (16) are designed such that all the signals of the closed-loop system converge to zero. In Theorem 2, when $c = 0$, one can choose $\gamma = 0.5$. Then, controller (15) can ensure the convergence performance of the states. In fact, when $c = 0$, as long as the constant $\gamma < 1$ is selected, the effectiveness of controllers (15) and (16) can be ensured.

4. Simulation Examples

Example 1. One considers the following nonlinear system:

$$\begin{cases} \dot{\xi}_1 = \xi_2 + 0.1(1+t)^{0.2}(\xi_3 + u), \\ \dot{\xi}_2 = \xi_3 + 0.1(1+t)^{0.2}u, \\ \dot{\xi}_n = u. \end{cases} \tag{28}$$

One gets that system (28) satisfies Assumption 1 with $\theta = 0.1$ and $c = 0.2$. Let $\gamma = 0.4$, $\beta_1 = 0.3$, $\beta_2 = 1.2$, and $\beta_3 = 0.7$. Based on Theorem 1, a state feedback controller for system (28) is designed as

$$u = -\frac{3\xi_1}{10(t+1)^{1.2}} - \frac{6\xi_2}{5(t+1)^{0.8}} - \frac{7\xi_3}{10(t+1)^{0.4}}. \tag{29}$$

The initial condition is chosen as $\xi_1(0) = 0.5$, $\xi_2(0) = 0.8$, and $\xi_3(0) = 0.8$. From Figures 1–3, one has that the states ξ_1, ξ_2, and ξ_3 of system (28) converge to zero. The controller u is shown in Figure 4.

Example 2. A practical example about the resonant circuit system is investigated as follows [22]

$$\begin{cases} \dot{i}_{\eta_1} = -\dfrac{v_\tau}{\eta_1} - \dfrac{r_1}{\eta_1} i_{\eta_2} + \dfrac{r_1}{2\eta_1}\sin v_\tau, \\ \dot{v}_\tau = \dfrac{i_{\eta_2}}{\tau} - \dfrac{1}{2\tau}\sin v_\tau, \\ \dot{i}_{\eta_2} = -\dfrac{r_2}{\eta_2} i_{\eta_2} + \dfrac{\mu}{\eta_2}. \end{cases} \tag{30}$$

In system (30), the meaning of the parameters is found in [22]. Following the coordinate transformation in [22], one gets

$$\begin{cases} \dot{\xi}_1 = \xi_2 + 2\xi_3, \\ \dot{\xi}_2 = \xi_3, \\ \dot{\xi}_n = u. \end{cases} \tag{31}$$

One gets that system (30) satisfies Assumption 1 with $\theta = 2$ and $c = 0$. Let $\gamma = 0.5$, $\beta_1 = 0.3$, $\beta_2 = 1.2$, and $\beta_3 = 0.7$. Based on Theorem 2, a state feedback controller for system (30) is designed as

$$u(t) = -\frac{\beta_1\xi_1}{(t+1)^{1.5}} - \frac{\beta_2\xi_2}{(t+1)} - \frac{\beta_3\xi_3}{(t+1)^{0.5}}. \tag{32}$$

The initial condition is chosen as $\xi_1(0) = -0.5$, $\xi_2(0) = -0.3$, and $\xi_3(0) = -0.5$. From Figures 5–7, one has that the states ξ_1, ξ_2, and ξ_3 of system (30) converge to zero. The controller u is shown in Figure 8.

Example 3. One considers the following nonlinear system:

$$\begin{cases} \dot{\xi}_1 = \xi_2 + 0.5(1+t)^{0.9}(\xi_3 + u), \\ \dot{\xi}_2 = \xi_3 + 0.5(1+t)^{0.9}u, \\ \dot{\xi}_n = u. \end{cases} \tag{33}$$

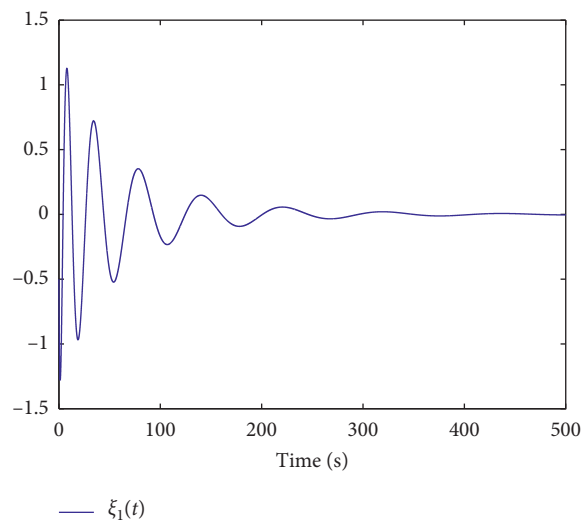

Figure 1: Trajectory of $\xi_1(t)$.

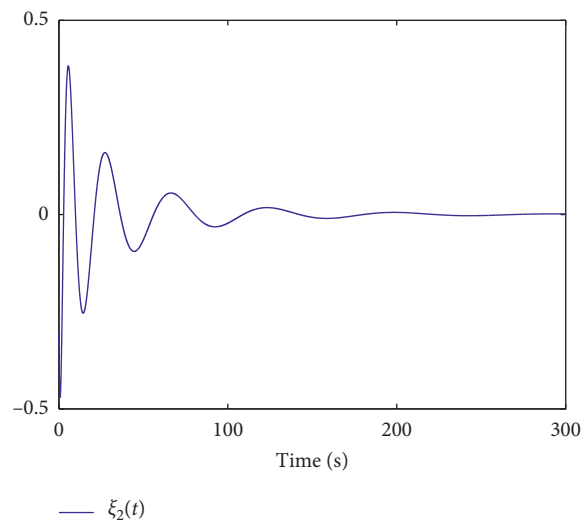

Figure 2: Trajectory of $\xi_2(t)$.

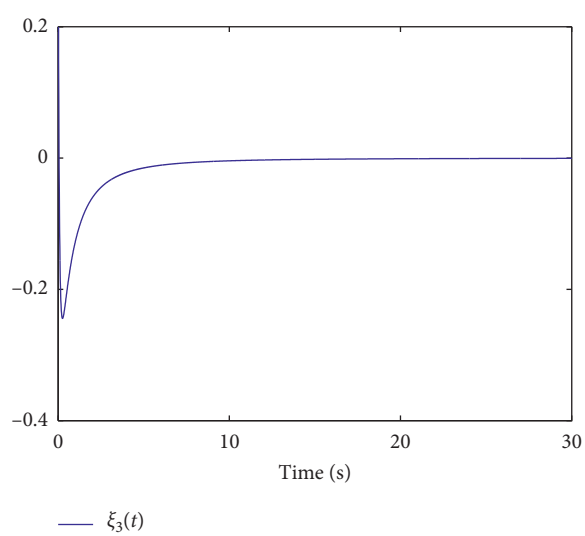

Figure 3: Trajectory of $\xi_3(t)$.

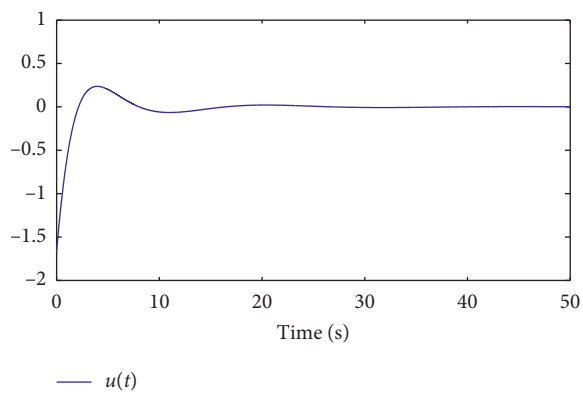

Figure 4: Trajectory of $u(t)$.

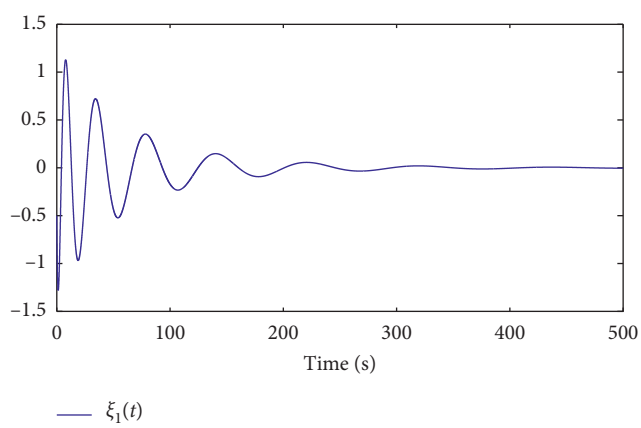

Figure 5: Trajectory of $\xi_1(t)$.

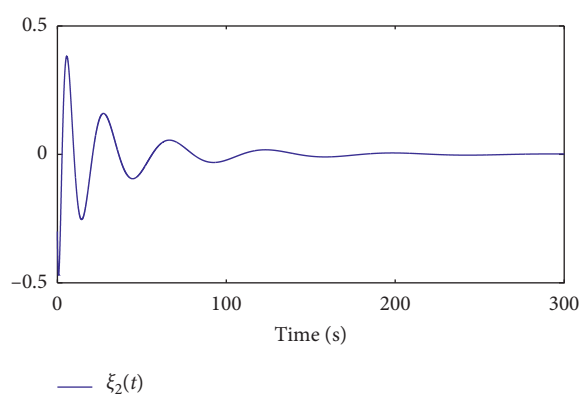

Figure 6: Trajectory of $\xi_2(t)$.

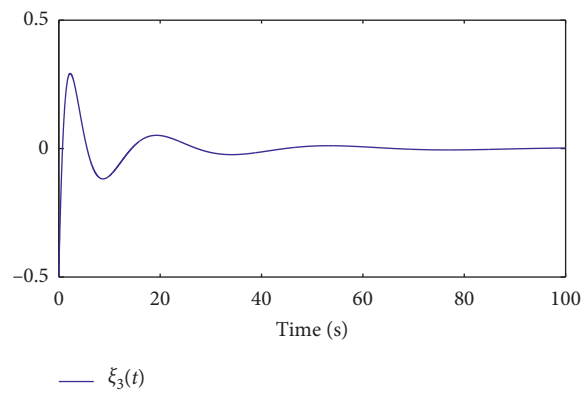

Figure 7: Trajectory of $\xi_3(t)$.

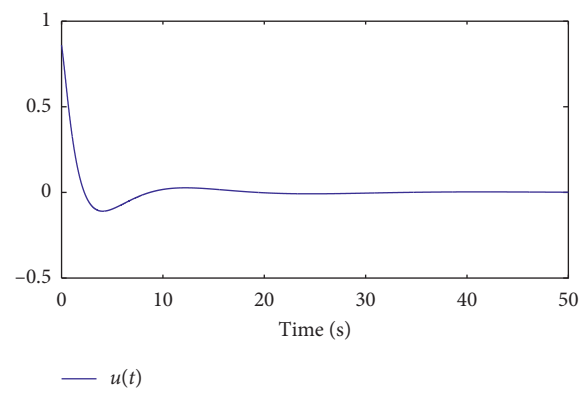

Figure 8: Trajectory of $u(t)$.

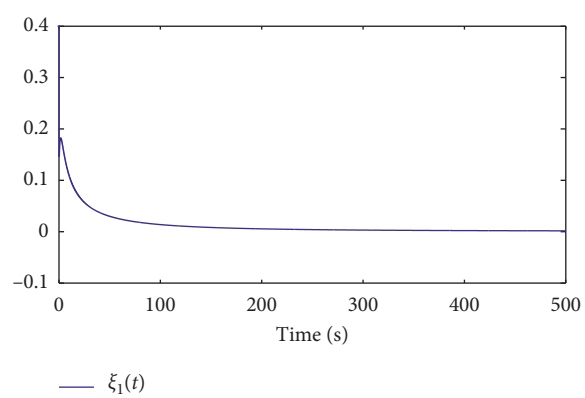

Figure 9: Trajectory of $\xi_1(t)$.

One gets that system (33) satisfies Assumption 1 with $\theta = 0.5$ and $c = 0.9$. Let $\beta_1 = 5$, $\beta_2 = 10$, and $\beta_3 = 5$. Based on Theorem 1, a state feedback controller for system (33) is designed as

$$u = -\frac{5\xi_1}{(t+1)^3} - \frac{10\xi_2}{(t+1)^2} - \frac{5\xi_3}{(t+1)}, \tag{34}$$

The initial condition is chosen as $\xi_1(0) = 0.4$, $\xi_2(0) = 0.4$, and $\xi_3(0) = 0.3$. From Figures 9–11, one has that the states ξ_1, ξ_2, and ξ_3 of system (33) converge to zero. The controller u is shown in Figure 12.

Remark 4. In the two simulation examples, one can see that the parameters in controllers (29), (32), and (34) are relatively easy to select, which do not require a large amount of calculation to deal with the unknown parameter in systems (28), (30), and (33), respectively. In addition, controllers (29), (32), and (34) are effective for a class of nonlinear systems as long as the nonlinear terms satisfy (2). Compared with the example of the results [18, 22], the unknown constant and the function with respect to time are allowed in the nonlinear terms. Compared with the commonly adaptive control strategy, the time-varying gain design method is

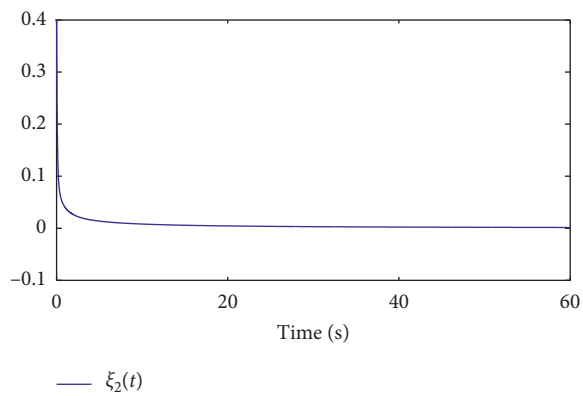

Figure 10: Trajectory of $\xi_2(t)$.

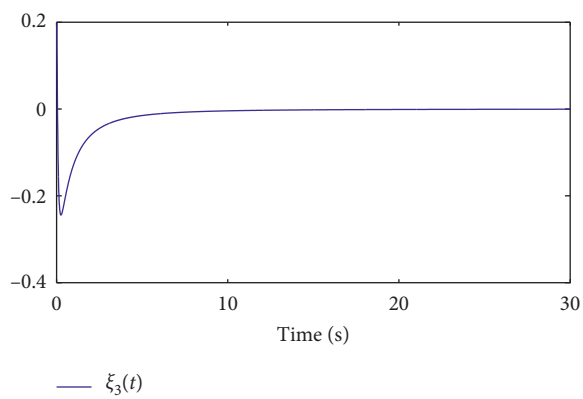

Figure 11: Trajectory of $\xi_3(t)$.

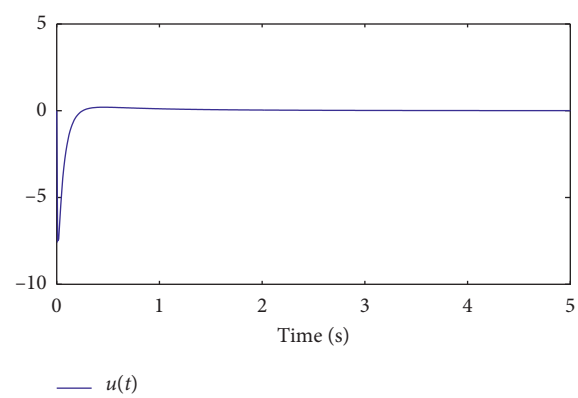

Figure 12: Trajectory of $u(t)$.

more concise, the calculation process is less, and a lot of calculation work is reduced.

5. Conclusion

This paper has investigated the state feedback control problem of upper triangular nonlinear systems. One has assumed that the nonlinear term recognizes an incremental rate relying on the unknown constant and the function with respect to time. A time-varying gain design method has been used to construct a state feedback controller. With the help of a Lyapunov function, one has obtained that all the signals of the closed-loop system have converged to zero. Finally, two numerical examples have been presented to illustrate the effectiveness of the time-varying gain design method.

Data Availability

All figures are made by Matlab.

Conflicts of Interest

The author declares no conflicts of interest.

Acknowledgments

This work was supported by the National Natural Science Foundation of China (nos. 61503214 and 61873334).

References

[1] M. Krstic, I. Kanellakopoulos, and P. V. Kokotovic, *Nonlinear and Adaptive Control Design*, Wiley, New York, NY, USA, 1995.

[2] A. M. Bloch, *Nonholonomic Mechanics and Control*, Springer-Verlag, New York, NY, USA, 2003.

[3] K. Liu, G. Xie, W. Ren, and L. Wang, "Consensus for multi-agent systems with inherent nonlinear dynamics under directed topologies," *Systems & Control Letters*, vol. 62, no. 2, pp. 152–162, 2013.

[4] R. Guo, "Projective synchronization of a class of chaotic systems by dynamic feedback control method," *Nonlinear Dynamics*, vol. 90, no. 1, pp. 53–64, 2017.

[5] H. Li, X. Zhang, and Q. Liu, "Adaptive output feedback control for a class of large-scale output-constrained nonlinear time-delay systems," *IET Control Theory & Applications*, vol. 12, no. 1, pp. 174–181, 2018.

[6] K. Liu and Z. Ji, "Consensus of multi-agent systems with time delay based on periodic sample and event hybrid control," *Neurocomputing*, vol. 270, no. 27, pp. 11–17, 2017.

[7] K. Liu, Z. Ji, and X. Zhang, "Periodic event-triggered consensus of multi-agent systems under directed topology," *Neurocomputing*, vol. 385, no. 14, pp. 33–41, 2020.

[8] R. Xu and F. Zhang, ".ϵ-nash mean-field games for general linear-quadratic systems with applications," *Automatica*, vol. 114, pp. 1–6, 2020.

[9] X. Lu and H. Li, "An improved stability theorem for nonlinear systems on time scales with application to multi-agent systems," *IEEE Transactions on Circuits and Systems II: Express Briefs*, 2020.

[10] X. Yi, R. Guo, and Y. Qi, "Stabilization of chaotic systems with both uncertainty and disturbance by the UDE-based control method," *IEEE Access*, vol. 8, no. 1, pp. 62471–62477, 2020.

[11] C. Qian and J. Li, "Global finite-time stabilization by output feedback for planar systems without observable linearization," *IEEE Transactions on Automatic Control*, vol. 50, no. 6, pp. 885–890, 2005.

[12] H. Li, X. Zhang, and G. Feng, "Event-triggered output feedback control of switched nonlinear systems with input saturation," *IEEE Transactions on Cybernetics*, 2020.

[13] C. Hua, X. Guan, and P. Shi, "Robust backstepping control for a class of time delayed systems," *IEEE Transactions on Automatic Control*, vol. 50, no. 6, pp. 894–899, 2005.

[14] X. Zhang, L. Liu, and G. Feng, "Leader-follower consensus of time-varying nonlinear multi-agent systems," *Automatica*, vol. 52, no. 2, pp. 8–14, 2015.

[15] X. Zhang, L. Baron, Q. Liu, and E.-K. Boukas, "Design of stabilizing controllers with a dynamic gain for feedforward nonlinear time-delay systems," *IEEE Transactions on Automatic Control*, vol. 56, no. 3, pp. 692–697, 2011.

[16] B. Niu and L. Li, "Adaptive backstepping-based neural tracking control for MIMO nonlinear switched systems subject to input delays," *IEEE Transactions on Neural Networks and Learning Systems*, vol. 29, no. 6, pp. 2638–2644, 2018.

[17] X. Ye, J. Huang, and H. Unbehauen, "Decentralized robust stabilization for large-scale feedforward non-linear systems," *International Journal of Control*, vol. 79, no. 12, pp. 1505–1511, 2006.

[18] H. Li, X. Zhang, and L. Chang, "Output feedback regulation of a class of triangular structural nonlinear systems with unknown measurement sensitivity," *International Journal of Systems Science*, vol. 50, no. 13, pp. 2486–2496, 2019.

[19] L. Chang, C. Zhang, X. Zhang, and X. Chen, "Decentralised regulation of nonlinear multi-agent systems with directed network topologies," *International Journal of Control*, vol. 90, no. 11, pp. 2338–2348, 2017.

[20] H. Li, X. Zhang, Z.-M. Wang, and A. Wei, "Global output feedback stabilisation of a class of stochastic systems with unknown growth rate," *International Journal of Control*, 2019.

[21] L. Praly and Z. P. Jiang, "Linear output feedback with dynamic high gain for nonlinear systems," *Systems & Control Letters*, vol. 53, no. 2, pp. 107–116, 2004.

[22] H. Li, X. Zhang, and M. Li, "Design of output feedback controller for stochastic feedforward systems with unknown measurement sensitivity," *ISA Transactions*, vol. 97, pp. 182–188, 2020.

Hindawi
Mathematical Problems in Engineering
Volume 2020, Article ID 8083509, 9 pages
https://doi.org/10.1155/2020/8083509

Research Article

A Novel Hypogenetic Chaotic Jerk System: Modeling, Circuit Implementation, and Its Application

Jiancheng Liu,[1] Karthikeyan Rajagopal,[2] Tengfei Lei,[3] Sezgin Kaçar,[4] Burak Arıcıoğlu,[4] Ünal Çavuşoğlu,[5] Abdullah Hulusi Kökçam,[6] and Anitha Karthikeyan[7]

[1]*Jiangsu Key Laboratory of Meteorological Observation and Information Processing, Nanjing University of Information Science & Technology, Nanjing 210044, China*
[2]*Nonlinear Systems and Applications, Faculty of Electrical and Electronics Engineering, Ton Duc Thang University, Ho Chi Minh City, Vietnam*
[3]*School of Mechanical and Electrical Engineering, Qilu Institute of Technology, Jinan 250200, China*
[4]*Department of Electrical and Electronics Engineering, Faculty of Technology, Sakarya University, Serdivan, Sakarya, Turkey*
[5]*Department of Computer Engineering, Faculty of Computer and Information Sciences, Sakarya University, Serdivan, Sakarya, Turkey*
[6]*Department of Industrial Engineering, Faculty of Engineering, Sakarya University, Serdivan, Sakarya, Turkey*
[7]*Nonlinear Systems and Applications, Faculty of Electrical and Electronics Engineering, Ton Duc Thang University, Ho Chi Minh City, Vietnam*

Correspondence should be addressed to Tengfei Lei; leitengfeicanhe@126.com

Received 23 February 2020; Revised 28 March 2020; Accepted 6 April 2020; Published 4 May 2020

Guest Editor: Ping Zhao

When revising the polarity and amplitude information in the feedback, a unique hypogenetic jerk system was obtained which has two controllers to switch the equilibria between stable and unstable. After providing some basic dynamical analysis, an electronic circuit was implemented, and the phase trajectory in the oscilloscope agrees with the numerical simulation. Further exploration shows that this unique chaotic system has superior performance as a random number generator or in voice encryption application.

1. Introduction

In the literature, chaos has a wide range of application field. In the recent years, chaos or chaotic systems have been frequently employed in the encryption and random number generation (RNG) studies due to noise-like, aperiodic characteristics of the chaotic systems [1]. In the literature, the encryption studies are not only about image encryption [2–5] but also there are encryption studies about text and other multimedia types like audio and video encryption [6]. It shows that chaos has great performance in the encryption system. In fact, RNG studies in the literature can be categorized into true random number generation (TRNG) and pseudo-random number generation (PRNG) regardless of whether they are chaos-based or not [7, 8]. RNG is usually employed in cryptographic studies for key generation process and performance of the encryption which heavily depends on key randomness. This can be achieved with appropriate chaos-based random number generation process. All these constitute our motivation to develop a new chaotic system.

Jerk dynamical systems are realized with a compact electrical circuit structure. Generally, jerk circuits have four connections at the node x, where the derivative of x is determined by the amplitude and polarity of y, and the amplitude and polarity of x influence the derivative of z. We study those chaotic flows with incomplete information transmission from the node x based on the jerk structure and are therefore named hypogenetic chaotic. Jerk system has the simple structure but can also provide applicable chaotic signal [9–13]. When the feedback information from the other variables is not complete, many of the systems can remain chaos [14–16] even in the jerk structure as

hypogenetic flows [14]. Hot research on chaotic systems mainly focuses on chaos control [17–20], Lyapunov exponent calculation and analysis [21, 22], and doubling and growth of attractors [23, 24], and chaotic systems with hidden attractors are also hot research topics because such systems are extremely prone to multistable phenomena, which are a common phenomenon in nature. Considering from equilibrium point, hidden attractors can be mainly of several types, one stable equilibrium[25], a line or plane equilibrium [26, 27], or no equilibrium [28]. Even there are hidden attractors found in some special chaotic systems [29], which have both unstable equilibrium and stable equilibria.

Starting from the classic system, hidden attractor is a very important topic. At the same time, linearization has always been a fundamental state. Is there a class of system whose linear linearization satisfies the characteristics of the chaotic hidden attractor (stable equilibrium system)? The circuit of this kind of system is less disturbed because linearization (sign circuit) is stable and similar to the digital circuit.

Therefore, we propose a class of hypogenetic chaotic system which has the following unique properties: nonlinearity involved includes amplitude information and polarity information, which are of incomplete feedback; there are two knobs which control the stability of equilibria, by which one can turn off the stable states freely.

This paper is organized as follows. In Section 2, we give a model description including basic dynamical analysis, and in Section 3, we show the electronic circuit implementation of the system. Further application discussions including random number generator design and voice encryption application are given in Section 4. In the last section, we give a simple conclusion.

2. Model Description

In this letter, we announce a new jerk system derived by modifying the jerk system proposed in [14] by replacing the nonlinear terms z^2 by $|z|$ and xz by $z\,\mathrm{sgn}(x)$. The proposed system shows a unique property of disorder which has both stable and unstable equilibrium points for different values of parameters.

$$\begin{aligned} \dot{x} &= a_1 y, \\ \dot{y} &= a_2 z, \\ \dot{z} &= a_3 x + a_4|z| + a_5 xy + a_6 z\,\mathrm{sgn}(x) + a_7, \end{aligned} \tag{1}$$

where a_i for $i \in [1, 7]$ are the parameters of the system. Jerk systems have the form $\begin{cases} \dot{x} = y \\ \dot{y} = z \\ \dot{z} = f(x, y, z) \end{cases}$, which can be depicted as $\dddot{x} = f(x, \dot{x}, \ddot{x})$ [30]. When $a_1 = 1$ and $a_2 = 1$, system (1) is Jerk system.

It is simple to verify that the equilibrium point of system (1) is $x = -(a_7/a_3)$, $y = 0$, and $z = 0$, and the characteristic equation of the system is $\lambda^3 + a_6\,\mathrm{sgn}(a_7/a_3)\lambda^2 + (a_2 a_5 a_7/a_3)\lambda - a_1 a_2 a_3 = 0$. According to the Routh–Hurwitz criterion for the real part of the eigenvalues to be positive, the condition is $\delta_1, \delta_0 > 0, \delta_1\delta_2 > \delta_0$, where $\delta_0 = 1, \delta_1 = a_6\,\mathrm{sgn}(a_7/a_3)$, $\delta_2 = (a_2 a_5 a_7/a_3)$, and $\delta_3 = -a_1 a_2 a_3$. For the values of parameters $a_1 = 1, a_2 = 1$, $a_3 = -1, a_4 = -4$, and $a_6 = 1$ and to discuss the effect of parameters on the type of equilibrium points, we vary the parameters a_5, a_7 and investigate the type of equilibrium point with the real part of eigenvalues and the Routh–Hurwitz condition $\delta_1\delta_2 > \delta_0$. Figure 1(a) shows the change in the real part of eigenvalues of system (1) with parameter a_5, and for $a_5 < 1$, the real part of eigenvalues become negative making the equilibrium stable. Similarly, Figure 1(b) is change in the real part of eigenvalues with a_7, and for $a_7 > -0.6$, the equilibrium is stable.

To analyze the stability of the systems using Routh–Hurwitz (RH) criterion, we investigate the two conditions $\delta_1, \delta_0 > 0$ and $\delta_1\delta_2 > \delta_0$. For the parameter values $a_1 = 1$, $a_2 = 1$, $a_3 = -1$, $a_4 = -4$, and $a_6 = 1$, the RH condition modifies to $\delta_0 = 1$, $\delta_1 = -a_5 a_7$, and $\delta_2 = -\mathrm{sign}(a_7)$. We vary the parameters a_5 and a_7 between $[0.7, 2]$ and $[-1.3, -0.6]$, respectively, and the condition $\delta_1\delta_2 > \delta_0$ is plotted as shown in Figure 2 which confirms our claim that the equilibrium is stable when $a_7 > -0.6$ or $a_5 < 1$. Both the eigenvalues and RH investigations confirm that system (1) exhibits both stable (nonhyperbolic) and unstable (hyperbolic) equilibrium points. To the best of our knowledge, this feature has not been investigated in the literature.

To show the 2D phase portraits of the stable and unstable system, we fix $a_7 = -1$ and plot for $a_5 = 0.95$ (stable equilibrium) and $a_5 = 1.6$ (unstable equilibrium) as shown in Figures 3(a) and 3(b), respectively.

The finite-time Lyapunov exponents of system (1) are derived using Wolf's algorithm [1] for both stable and unstable cases and are given in Table 1 with the Kaplan–Yorke dimension (D_{KY}) calculated for a run time of 20,000 s with initial conditions $[-3\ \ 4\ \ -4]$ with other parameters except a_5, a_7 fixed to their respective chaotic values.

To further understand the complete dynamical behavior of the system, we derived the bifurcation plots with parameter a_5 as it governs the equilibrium points of the proposed system. The parameter a_5 is varied between $[0.8, 2]$, and the local maximum of the state variable z is plotted as shown in Figures 4(a) and 4(b) which show the corresponding LEs of the system. It can be seen from Figure 4(a) that, under the change of parameter a_5, the chaos state and periodic state of the system appear alternately, and the way the system changes from the periodic state to chaos is period-doubling bifurcation. By comparing Figures 4(a) and 4(b), the maximum Lyapunov exponent of the system is zero; When the system is chaotic, the largest Lyapunov exponent of the system is positive. When the system is convergent, the largest Lyapunov exponent of the system is negative.

3. Electronic Circuit Implementation of the System

In this section, system (1) is implemented with an electronic circuit. The circuit designed in PSpice medium and its simulation are carried out. The schematic of the designed

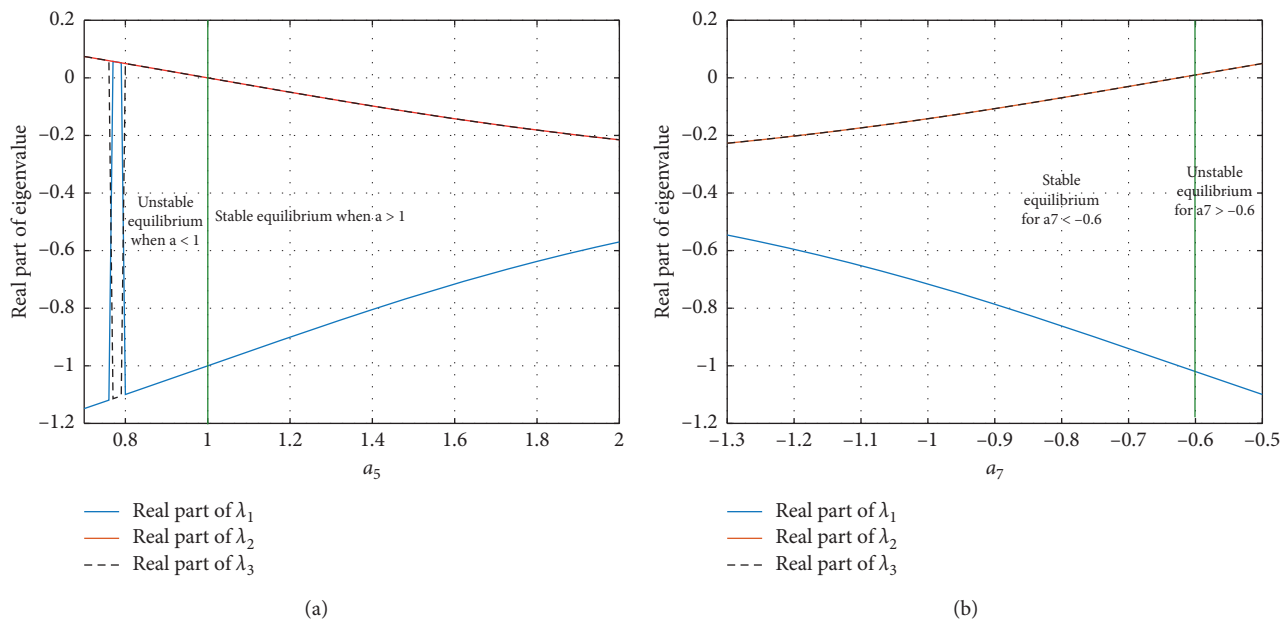

Figure 1: Eigenvalues of the system for various values of (a) a_5 and (b) a_7.

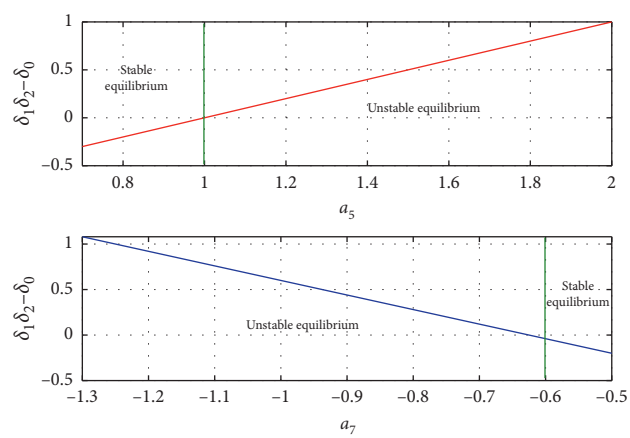

Figure 2: Plots showing the RH condition $\delta_1\delta_2 > \delta_0$ vs. parameters a_5 and a_7.

circuit is given in Figure 5. Here, we applied the traditional method by the multiplier AD633/AD to carry out the function $z\,\mathrm{sgn}(x)$, and the new switch published in [25] was also tried by simulation which shows the same results.

The electronic circuit consists of OpAmps, multiplier ICs, diodes, resistors, and capacitors. The supply voltages of the active elements are +15 V for positive supply inputs and −15 V for negative supply inputs. The value of the resistors used in the circuit is as follows: $R_1 = R_2 = R_3 = 400\,\mathrm{k\Omega}$, $R_4 = R_8 = R_9 = R_{12} = R_{13} = R_{14} = R_{15} = R_{16} = 100\,\mathrm{k\Omega}$, $R_5 = 42\,\mathrm{k\Omega}$, $R_6 = 40\,\mathrm{k\Omega}$, and $R_7 = 6\,\mathrm{M\Omega}$. The values of the capacitor in the circuit are as follows: $C_1 = C_2 = C_3 = 1\,\mathrm{nF}$. The given resistor and capacitor values are for the stable equilibrium case when $a_5 = 0.95$ and $a_7 = -1$. For the unstable equilibrium case (when $a_5 = 1.6$ and $a_7 = -1$), only the value of R_5 resistor will be changed. The value of R_5 resistor is $25\,\mathrm{k\Omega}$.

The real-time electronic circuit application is also realized. The results of the real-time electronic circuit are examined on the oscilloscope. 2D phase portraits of system (1) obtained from the oscilloscope are given in Figures 6(a) and 6(b). The phase portrait of the stable equilibrium case ($a_5 = 0.95$ and $a_7 = -1$) is given in Figure 6(a) while that of the unstable equilibrium case ($a_5 = 1.6$ and $a_7 = -1$) is given in Figure 6(b). Both of them confirm the theoretical prediction in Figure (3).

4. Application Discussion

4.1. Random Number Generator Design and NIST Tests. Random number generator (RNG) is one of the most important applications in which chaotic systems are used. RNGs are used in many different engineering fields, especially communication and cryptography. In this section,

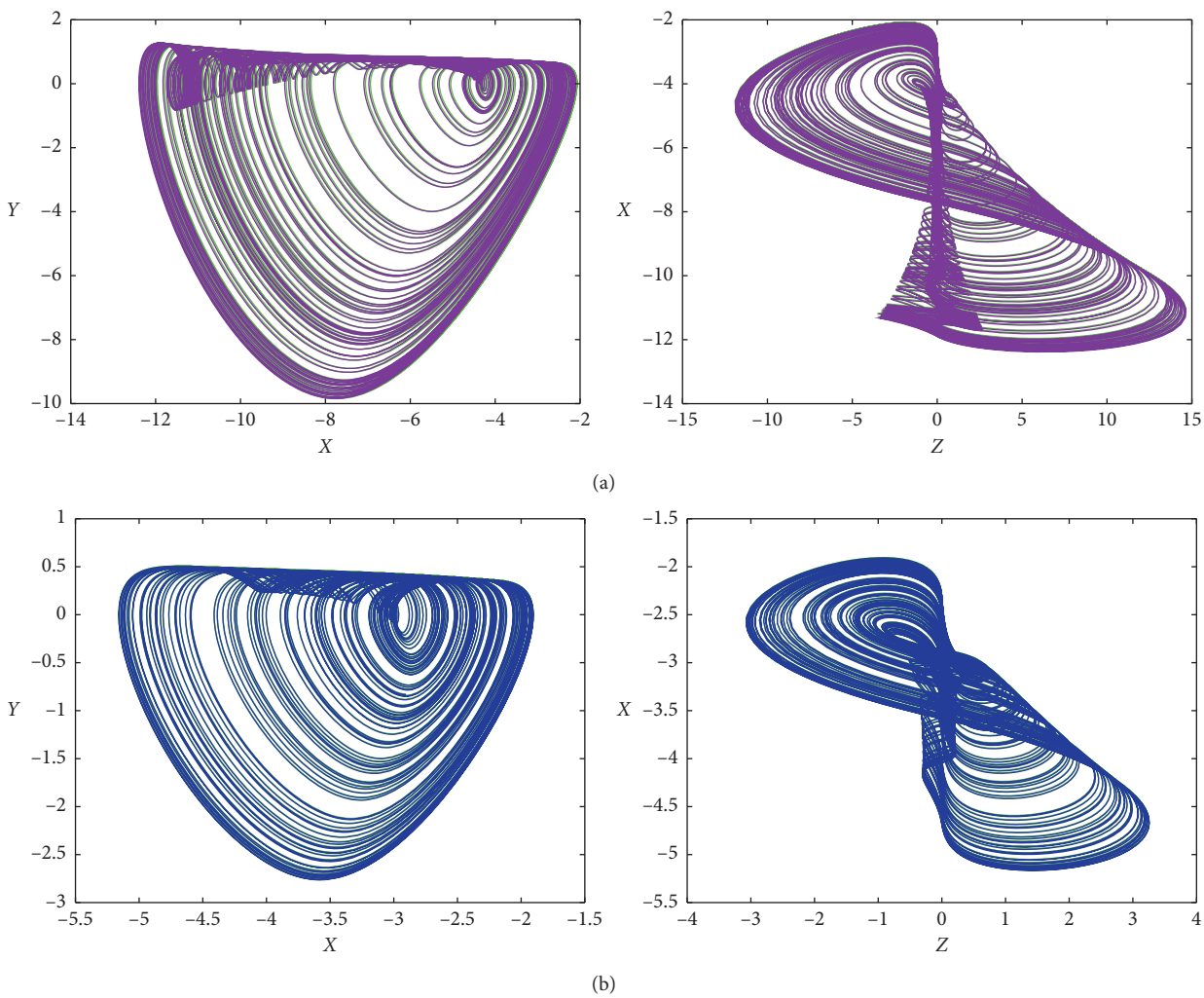

Figure 3: 2D phase portraits of the novel jerk system for $a_1 = 1$, $a_2 = 1$, $a_3 = -1$, $a_4 = -4$, and $a_6 = 1$ and initial conditions $[-3 \;\; 4 \;\; -4]$. Figure 3(a) shows system (1) with a stable equilibrium for $a_5 = 0.95$ and $a_7 = -1$, and Figure 3(b) shows system (1) with a unstable equilibrium for $a_5 = 1.6$ and $a_7 = -1$.

Table 1: Lyapunov exponents and D_{KY} for different parameters.

Parameters	Lyapunov exponents (LEs)	D_{KY}
$a_5 = 0.95, a_7 = -1$	$[0.1196, 0, -1.179]$	2.101
$a_5 = 1.6, a_7 = -1$	$[0.0727, 0, -1.375]$	2.052

a new RNG design has been realized by using the new chaotic jerk system proposed in this study. The flow diagram of the method used in the design of RNG is given in Figure 7.

As shown in the flow diagram, the appropriate initial values, the number of bits taken from the state variables, and the step value for the RK4 algorithm are determined with the help of the new chaotic system. Then, the RK4 algorithm is executed to obtain discrete arrays of state variables and convert them into 32 bit binary arrays. Steps to generate the pseudo-random sequences are as follows.

The system uses the RK4 algorithm and Matlab software to iterate 2,000 times for simulation.

S1: the sequence obtained by the first iteration of the system data = $[x(1), y(1), z(1)]$; the numerical value is kept to the second decimal place.

S2: data = data $*$ 100; data are expressed as a 32 bit binary number: data = $\{b_{31}b_{30}, \ldots, b_2b_1\}_{32}$.

S3: Let data1 = $\{b_7b_6, \ldots, b_2b_1\}_8$, data1 for further test use.

S4: $n = n+1$. Then, it is still stated that the sequence to be generated passes through S2–S4 until $n = 2001$.

Random bit arrays are generated for NIST tests by taking the appropriate number of bits from these arrays. If the generated bit array passes these tests successfully, the RNG design is completed and ready for use in practical applications.

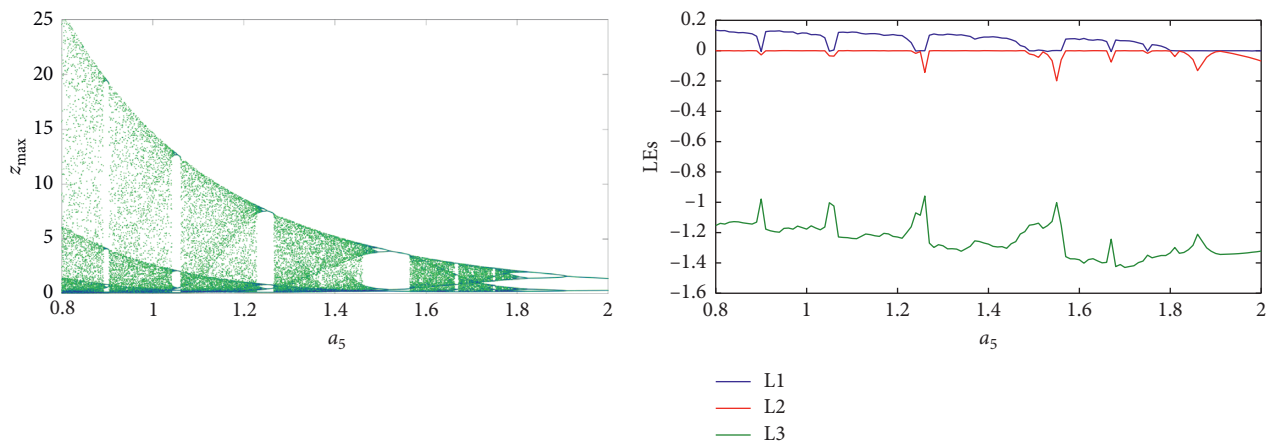

(a) (b)

Figure 4: (a) Bifurcation of the system with a_5; (b) corresponding LEs.

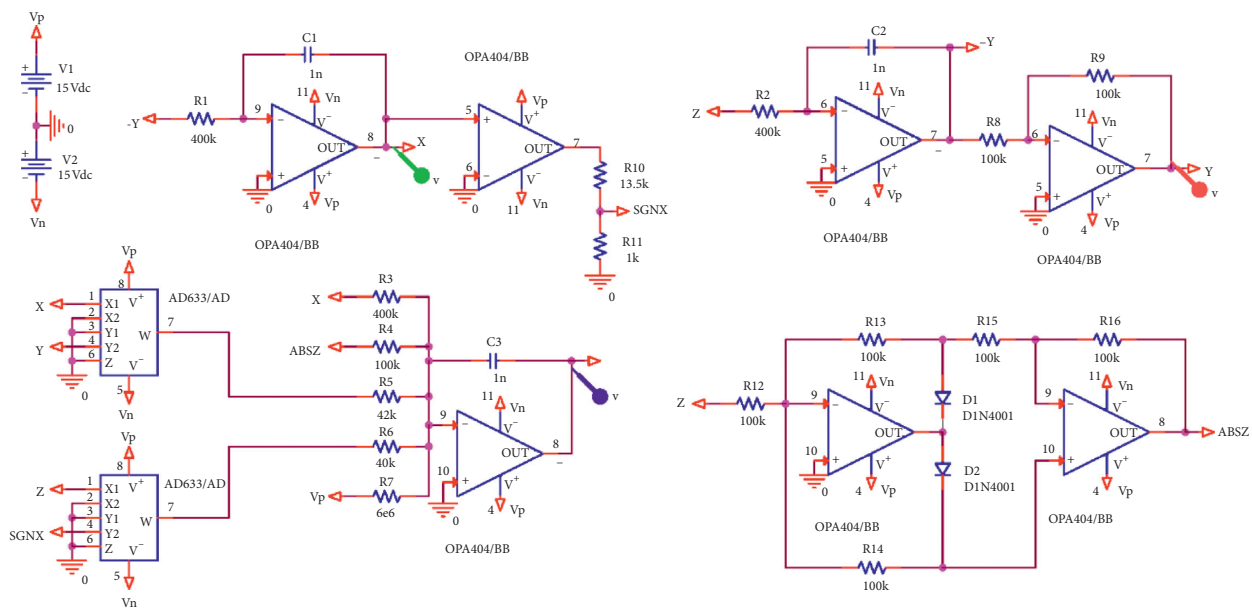

Figure 5: The designed circuit for system (1).

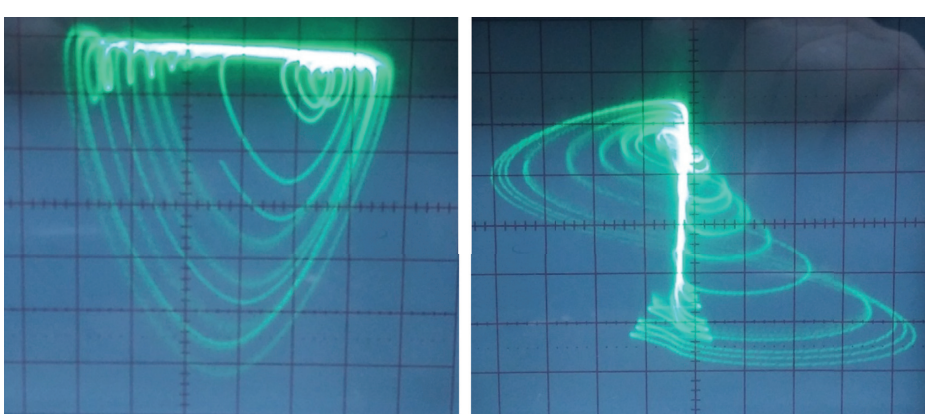

(a)

Figure 6: Continued.

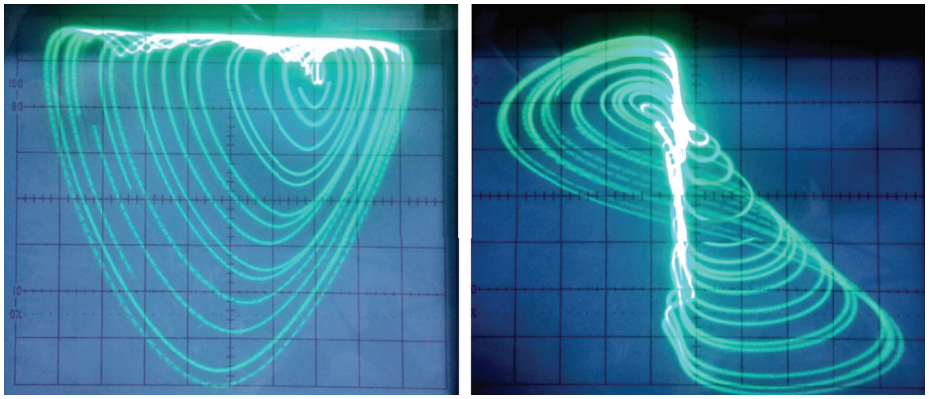

(b)

Figure 6: 2D phase portraits, obtained from the oscilloscope, of the novel system for $a_1 = 1$, $a_2 = 1$, $a_3 = -1$, $a_4 = -4$, and $a_6 = 1$ and initial conditions $[-3 \;\; 4 \;\; -4]$ (a) when $a_5 = 0.95$ and $a_7 = -1$ and (b) when $a_5 = 1.6$ and $a_7 = -1$.

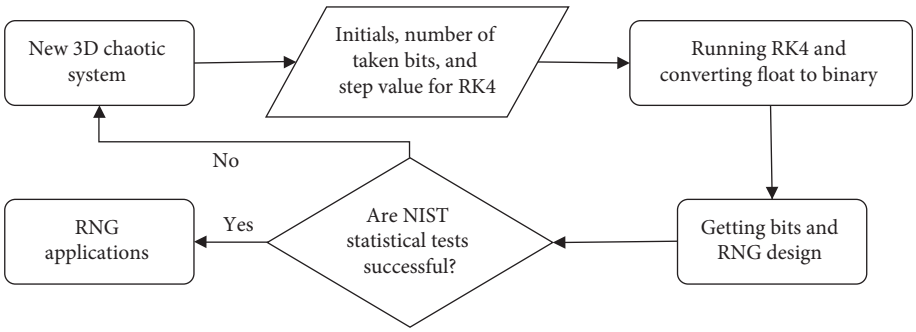

Figure 7: RNG design stages with the proposed 3D chaotic system.

Table 2: 3D chaotic system PRNG NIST-800-22 test results.

Statistical tests	p value $(X \oplus Y \oplus Z)$	p value $(Y \oplus Z)$	p value (Z)	Result
Frequency (monobit) test	0.373465	0.017981	0.485177	Successful
Block-frequency test	0.932102	0.563486	0.720823	Successful
Cumulative-sum test	0.692331	0.029619	0.813864	Successful
Runs test	0.093974	0.417706	0.661739	Successful
Longest-run test	0.651016	0.544020	0.730122	Successful
Binary matrix rank test	0.489777	0.123925	0.328310	Successful
Discrete Fourier transform test	0.393422	0.291282	0.769023	Successful
Nonoverlapping template test	0.058054	0.045477	0.115145	Successful
Overlapping template test	0.245790	0.504454	0.546871	Successful
Maurer's universal statistical test	0.550389	0.259675	0.138921	Successful
Approximate entropy test	0.173084	0.067221	0.503813	Successful
Random excursion test $(x = -4)$	0.617626	0.055541	0.042691	Successful
Random-excursion variant test $(x = -9)$	0.842508	0.227993	0.065864	Successful
Serial test-1	0.651632	0.454848	0.316808	Successful
Serial test-2	0.675012	0.598698	0.073441	Successful
Linear complexity test	0.073771	0.830488	0.259938	Successful

Otherwise, the procedure is repeated by starting over and setting the initial values, the number of bits taken from the state variables, and the step value for RK4. These operations are carried out until the bit array obtained has passed all of the NIST tests. When the process is complete, an RNG is obtained which successfully passed through the NIST tests, which are the most accepted randomness tests in the literature.

The most important randomness test which is accepted internationally is the NIST-800-22 statistical tests. In this test, there are 15 different subtests. An array consisting of at least 1000000 bits must pass all of these tests successfully. That is, the p values obtained at the end of the tests should be equal or greater than 0.001. Table 2 shows the results of the NIST tests of the arrays which are generated by taking 8 bits

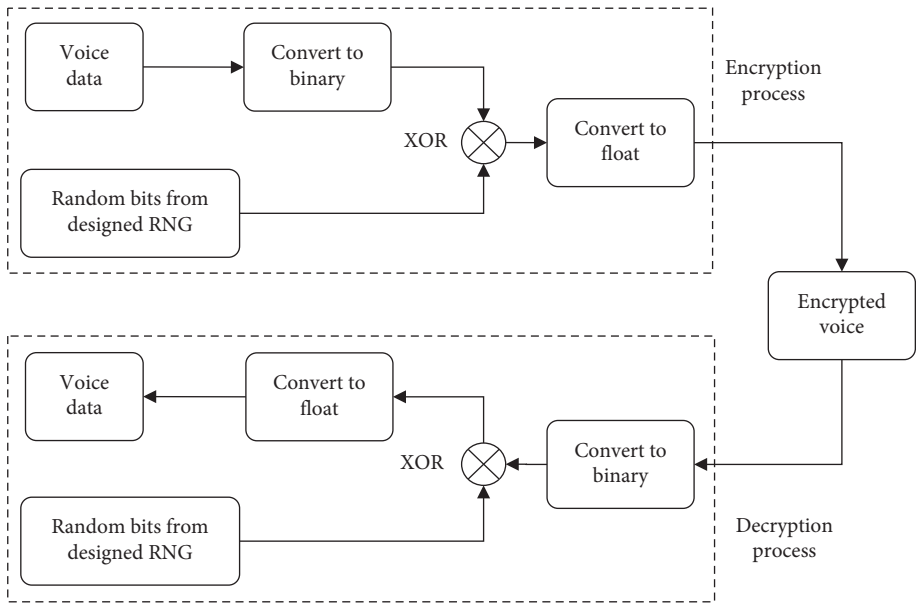

Figure 8: Encryption and decryption process.

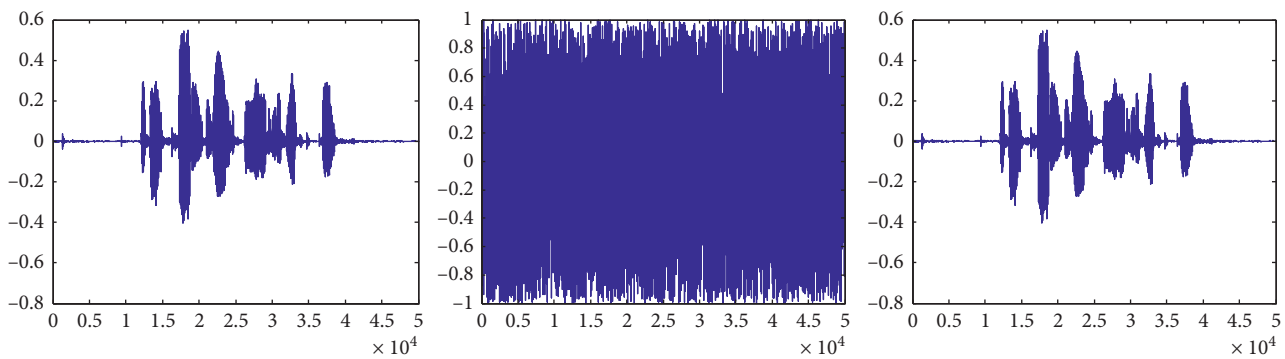

Figure 9: Original, encrypted, and decrypted voice waves, respectively.

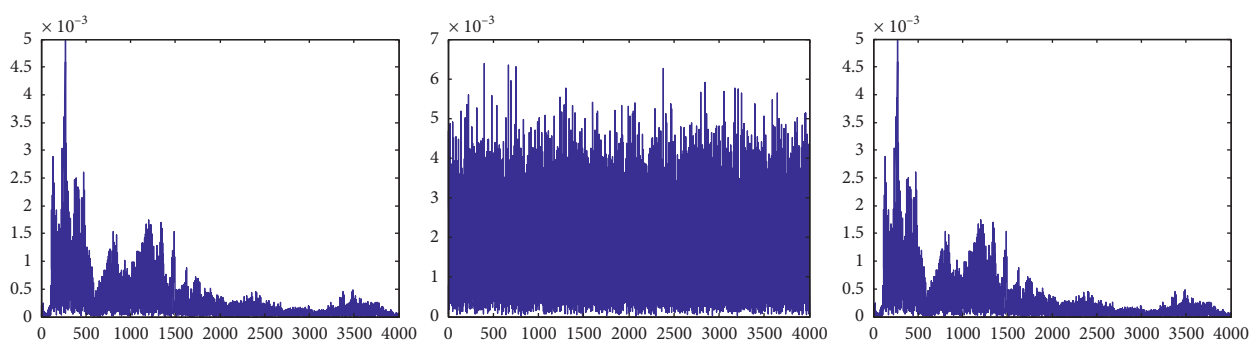

Figure 10: Original, encrypted, and decrypted voice spectrums.

from the state variables of the new chaotic system in each iteration. These arrays have successfully passed all the tests. Thus, it has been shown that the proposed system can be used conveniently in RNG-based engineering applications. The arrays are obtained in three different ways, in which the bit arrays obtained from all state variables are subjected to XOR operation, the Y and Z state variables are subjected to XOR operation, or using the Z state variable alone.

4.2. Voice Encryption Application. In this part of the study, a different application based on the new chaotic system has been realized. In this application, voice encoding and decoding are performed using the RNG designed in the previous section. The block diagram of the application is shown in Figure 8.

As can be seen from Figure 9, these voice data are recorded with noise, and noise is added in the simulation;

the voice data are converted into a binary form and then subjected to XOR operation with a random bit array from the RNG. The encrypted bit array is converted back to the float to get the encrypted voice. In the decoding process, the encrypted voice values are converted into binary form and subjected to XOR operation with bit arrays received from the RNG. The bit array obtained after the XOR operation is converted to a float, and the decoding process is completed.

Figure 9 shows the original, encrypted, and decrypted voice plots, respectively. It is seen that there is no similarity between the encrypted voice and the original voice, and that the original voice can be reacquired at the end of the decoding process. The frequency spectrums of the voice signals are shown in Figure 10. When the spectrums are examined, it is seen that the original and decrypted voice spectrums are the same, and the coded spectrum is completely different from the others and has a homogeneous distribution. This indicates that the encryption and decryption processes are quite good.

5. Conclusion and Discussion

Signum function and absolute value function can remove the amplitude or polarity information in the feedback variable, which sometimes still preserves the basic property in a dynamical system. As a new case, such a hypogenetic jerk system is obtained, which has stable or unstable equilibrium points under different parameters. Moreover, physical experiments prove the chaotic oscillation. Further discussion focuses on random number generator, and voice encryption shows that the new derived chaotic system still exhibits great noise-like randomness.

Data Availability

The data that support the findings of this study are available from the corresponding author upon reasonable request.

Conflicts of Interest

The authors declare that they have no conflicts of interest.

Acknowledgments

This work was supported financially by the National Nature Science Foundation of China (Grant no. 61871230), the Natural Science Foundation of Jiangsu Province (Grant no. BK20181410), and a project funded by the Priority Academic Program Development of Jiangsu Higher Education Institutions.

References

[1] S. Lian, "Efficient image or video encryption based on spatiotemporal chaos system," *Chaos, Solitons & Fractals*, vol. 40, no. 5, pp. 2509–2519, 2009.

[2] G. Chen, Y. Mao, and C. K. Chui, "A symmetric image encryption scheme based on 3D chaotic cat maps," *Chaos, Solitons & Fractals*, vol. 21, no. 3, pp. 749–761, 2004.

[3] Z. H. Guan, F. Huang, and W. Guan, "Chaos-based image encryption algorithm," *Physics Letters A*, vol. 346, no. 1–3, 2005.

[4] X. Wang, L. Teng, and X. Qin, "A novel colour image encryption algorithm based on chaos," *Signal Processing*, vol. 92, no. 4, pp. 1101–1108, 2012.

[5] J. Mou, F. Yang, R. Chu et al., "Image compression and encryption algorithm based on hyper-chaotic map," *Mobile Networks & Applications*, no. 3, pp. 1–13, 2019.

[6] A. Akgul, S. Kacar, B. Aricioglu et al., "Text encryption by using one-dimensional chaos generators and nonlinear equations," in *Proceedings of the International Conference on Electrical & Electronics Engineering*, Mysore, Karnataka, January 2013.

[7] A. P. Johnson, R. S. Chakraborty, and D. Mukhopadyay, "An improved DCM-based tunable true random number generator for xilinx FPGA," *IEEE Transactions on Circuits and Systems II: Express Briefs*, vol. 64, no. 4, pp. 452–456, 2017.

[8] T. T. Kim Hue and T. M. Hoang, "Complexity and properties of a multidimensional cat-hadamard map for pseudo random number generation," *The European Physical Journal Special Topics*, vol. 226, no. 10, pp. 2263–2280, 2017.

[9] S. J. Linz and J. C. Sprott, "Elementary chaotic flow," *Physics Letters A*, vol. 259, no. 3-4, pp. 240–245, 1999.

[10] J. C. Sprott, "A new class of chaotic circuit," *Physics Letters A*, vol. 266, no. 1, pp. 19–23, 2006.

[11] J. C. Sprott, "A new chaotic jerk circuit," *IEEE Transactions on Circuits and Systems II: Express Briefs*, vol. 58, no. 4, pp. 240–243, 2011.

[12] J. C. Sprott, "Simplest dissipative chaotic flow," *Physics Letters A*, vol. 228, no. 4-5, pp. 271–274, 1997.

[13] J. C. Sprott, "Some simple chaotic jerk functions," *American Journal of Physics*, vol. 65, no. 6, pp. 537–543, 1997.

[14] C. Li, J. C. Sprott, and H. Xing, "Hypogenetic chaotic jerk flow," *Physics Letters A*, vol. 380, no. 11-12, 2016.

[15] K. Rajagopal, V. T. Pham, F. R. Tahir et al., "A chaotic jerk system with non-hyperbolic equilibrium: dynamics, effect of time delay and circuit realization," *Pramana*, vol. 90, no. 4, p. 52, 2018.

[16] Q. Lai and S. Chen, "Coexisting attractors generated from a new 4D smooth chaotic system," *International Journal of Control, Automation and Systems*, vol. 14, no. 4, pp. 1124–1131, 2016.

[17] R. Guo, "Projective synchronization of a class of chaotic systems by dynamic feedback control method," *Nonlinear Dynamics*, vol. 90, no. 1, 2017.

[18] Z. Wang and R. Guo, "Hybrid synchronization problem of a class of chaotic systems by an universal control method," *Symmetry*, vol. 10, no. 11, p. 552, 2018.

[19] X. Yi, R. Guo, and Y. Qi, "Stabilization of chaotic systems with both uncertainty and disturbance by the UDE-based control method," *IEEE Access*, vol. 8, 2020.

[20] L. Liu, R. Guo, J. Ji, Z. Miao, and J. Zhou, "Practical consensus tracking control of multiple nonholonomic wheeled mobile robots in polar coordinates," *International Journal of Robust and Nonlinear Control*, pp. 1–17, 2020.

[21] S. Zhou and X. Wang, "Identifying the linear region based on machine learning to calculate the largest lyapunov exponent from chaotic time series," *Chaos: An Interdisciplinary Journal of Nonlinear Science*, vol. 28, no. 12, Article ID 123118, 2018.

[22] S. Zhou, X. Wang, Z. Wang, and C. Zhang, "A novel method based on the pseudo-orbits to calculate the largest lyapunov exponent from chaotic equations," *Chaos*, vol. 29, no. 3, Article ID 033125, 2019.

[23] C. Li, T. Lu, G. Chen, and H. Xing, "Doubling the coexisting attractors," *Chaos*, vol. 29, no. 5, Article ID 051102, 2019.
[24] C. Li, Y. Xu, G. Chen et al., "Conditional symmetry: bond for attractor growing," *Nonlinear Dynamics*, vol. 95, no. 2, 2018.
[25] X. Wang and G. Chen, "A chaotic system with only one stable equilibrium," *Communications in Nonlinear Science and Numerical Simulation*, vol. 17, no. 3, pp. 1264–1272, 2012.
[26] S. Jafari, J. C. Sprott, and M. Molaie, "A simple chaotic flow with a plane of equilibria," *International Journal of Bifurcation and Chaos*, vol. 26, no. 6, Article ID 1650098, 2016.
[27] S. Jafari, A. Ahmadi, A. J. M. Khalaf et al., "A new hidden chaotic attractor with extreme multi-stability," *Aeu International Journal of Electronics & Communications*, vol. 89, pp. 131–135, 2018.
[28] B. Hamdi and S. Hassen, "A new hypersensitive hyperchaotic system with no equilibria," *International Journal of Bifurcation and Chaos*, vol. 27, no. 5, Article ID 1750064, 2017.
[29] X. Y. Hu, C. X. Liu, L. Liu, Y. P. Yao, and G. C. Zheng, "Multi-scroll hidden attractors and multi-wing hidden attractors in a 5-dimensional memristive system," *Chinese Physics B*, vol. 26, no. 11, pp. 124–130, 2017.
[30] K. E. Chlouverakis and J. C. Sprott, "Chaotic hyperjerk systems," *Chaos, Solitons & Fractals*, vol. 28, no. 3, pp. 739–746, 2006.

Hindawi
Mathematical Problems in Engineering
Volume 2020, Article ID 3498796, 8 pages
https://doi.org/10.1155/2020/3498796

Research Article

Copious Closed Forms of Solutions for the Fractional Nonlinear Longitudinal Strain Wave Equation in Microstructured Solids

Haiyong Qin,[1,2] **Mostafa M. A. Khater**,[3,4] **and Raghda A. M. Attia**[3,5]

[1]*School of Mathematics, Qilu Normal University, Jinan 250200, Shandong Province, China*
[2]*School of Control Science and Engineering, Shandong University, Jinan 250061, Shandong, China*
[3]*Department of Mathematics, Faculty of Science, Jiangsu University, Zhenjiang, China*
[4]*Department of Mathematics, Obour Institutes, Cairo, Egypt*
[5]*Department of Basic Science, Higher Technological Institute of 10th Ramadan City, Ramadan City, Egypt*

Correspondence should be addressed to Haiyong Qin; qhymath@hotmail.com

Received 13 February 2020; Accepted 20 March 2020; Published 30 April 2020

Guest Editor: Yi Qi

A computational scheme is employed to investigate various types of the solution of the fractional nonlinear longitudinal strain wave equation. The novelty and advantage of the proposed method are illustrated by applying this model. A new fractional definition is used to convert the fractional formula of these equations into integer-order ordinary differential equations. Soliton, rational functions, the trigonometric function, the hyperbolic function, and many other explicit wave solutions are obtained.

1. Introduction

Fractional nonlinear evolution equation is one of the noticeable branches of science, particularly in recent years. Fractional calculus has a great profound physical background where it is able to formulate many various phenomena in distinct fields such as physics, mechanical engineering, economics, chemistry, signal processing, food supplement, applied mathematics, quasichaotic dynamical systems, hydrodynamics, system identification, statistics, finance, fluid mechanics, solid-state biology, dynamical systems with chaotic dynamical behavior, optical fibers, electric control theory, and economics and diffusion problems. The mathematical modeling of these phenomena will contain a fractional derivative which provides a great explanation of the nonlocal property of these models since it depends on both historical and current states of the problem in contrast with the classical calculus which depends on the current state only. Based on the importance of this kind of calculus, many definitions have been being derived such as conformable fractional derivative, fractional Riemann–Liouville derivatives, Caputo, and Caputo–Fabrizio definition [1–17]. These definitions have been being employed to convert the fractional nonlinear partial differential equations to nonlinear integer-order ordinary differential equation and then the computational and numerical schemes can be applied to get various types of solutions for these models and the examples of these schemes [18–30].

Recently, the mK method is formulated and applied to distinct physical models such as the complex Ginzburg–Landau model, the $(2+1)$-dimensional KD equation and KdV equation, fractional $(N+1)$ sinh-Gordon, biological population, equal width, modified equal width, and Duffing equations [31–40].

This method depends on a new auxiliary equation, which is equal to the Riccati equation [41]. The auxiliary equation of the mK method is given by

$$\mathscr{E}'(\varphi) = \frac{1}{\ln(\mathscr{Q})}\left[\delta \mathscr{Q}^{\mathscr{E}(\varphi)} + \varrho \mathscr{Q}^{-\mathscr{E}(\varphi)} + X\right], \tag{1}$$

where δ, ϱ, χ, and $\mathscr{Q}$ are the arbitrary constants. The Riccati equation is given by

$$\mathscr{R}'(\varphi) = \mathscr{A}_0 + \mathscr{A}_1 \mathscr{R}(\varphi) + \mathscr{A}_2 \mathscr{R}^2(\varphi), \tag{2}$$

where $\mathscr{A}_0, \mathscr{A}_1$, and $\mathscr{A}_2$ are the arbitrary constants. So, equations (1) and (2) are equal when $[\mathscr{E}(\varphi) = \mathscr{R}(\varphi), \chi = A_1, \varrho = A_0, \delta = A_2]$. Using this technique, it leads to the equalling of the mK auxiliary equation with many other analytical methods, but the mK method can obtain more solutions than most of them. This equivalence shows superiority, power, and productivity of the mK method.

In this context, the mK method is employed to construct new formulas of solutions for the fractional nonlinear longitudinal strain wave equation which is given in [42–48]:

$$\mathscr{D}_{tt}^{2\vartheta}\mathscr{M} + \mathscr{M}_{xx} - \gamma\left[\mathscr{L}_1\left(\mathscr{M}^2\right)_{xx} - \mathscr{L}_2\mathscr{M}_{xxxx} + \mathscr{L}_3\mathscr{D}_{tt}^{2\vartheta}\left(\mathscr{M}_{xx}\right)\right] == 0, \tag{3}$$

where $[\gamma, \mathscr{L}_1, \mathscr{L}_2, \mathscr{L}_3]$ are the arbitrary constants.

This model is considered as one of the fundamental models in the microstructure of a material that is used to determine the elasticity, which is caused by the dissipation/energy input in the content. This model contains nonlinear and dissipation terms which are the officials of construct the kink and shock waves. This shows the permanent form in medium points to a possible presence of dispersion or dissipation. The following definition of the $\mathscr{ABR}$ fractional operator [49–52] is applied to equation (3).

Definition 1. It is given in [17] that

$${}^{\mathscr{ABR}}\mathscr{D}_{a+}^{\alpha}\mathscr{F}(t) = \frac{\mathscr{B}(\alpha)}{1-\alpha}\frac{\mathrm{d}}{\mathrm{d}t}\int_a^t \mathscr{F}(x)\mathscr{G}_\alpha\left(\frac{-\alpha(t-\alpha)^\alpha}{1-\alpha}\right)\mathrm{d}x, \tag{4}$$

where $\mathscr{G}_\alpha$ is the Mittag–Leffler function defined by the following formula:

$$\mathscr{G}_\alpha\left(\frac{-\alpha(t-\alpha)^\alpha}{1-\alpha}\right) = \sum_{n=0}^{\infty}\frac{(-\alpha/1-\alpha)^n(t-x)^{\alpha n}}{\Gamma(\alpha n+1)}, \tag{5}$$

and $\mathscr{B}(\alpha)$ is a normalisation function. Thus,

$${}^{\mathscr{ABR}}\mathscr{D}_{a+}^{\alpha}\mathscr{F}(x) = \frac{\mathscr{B}(\alpha)}{1-\alpha}\sum_{n=0}^{\infty}\left(\frac{-\alpha}{1-\alpha}\right)^n {}^{RL}\mathscr{I}_a^{\alpha n}\mathscr{F}(x), \tag{6}$$

leads to

$$\mathscr{M}(x,t) = \mathscr{M}(\varphi),$$
$$\varphi = x + \frac{c(1-\alpha)t^{-\alpha n}}{B(\alpha)\sum_{n=0}^{\infty}(-\alpha/1-\alpha)^n\Gamma(1-\alpha n)}, \tag{7}$$

where c is the arbitrary constant. This wave transformation converts equation (3) to ODE. Integrating the obtained ODEs twice with zero constant of the integration gives

$$\mathscr{M} - \alpha\mathscr{M}^2 + \lambda\mathscr{M}'' = 0, \tag{8}$$

where $[\alpha = \gamma\mathscr{L}_1/c^2 - 1, \lambda = (\gamma(\mathscr{L}_2 - c^2\mathscr{L}_3))/c^2 - 1]$. Calculating the homogeneous balance value in equation (8) yields $n = 2$. Thus, both equations have same general formula of solution and it is given according to the mK method by

$$\begin{aligned}\mathscr{M}(\varphi) &= \sum_{i=1}^{n} a_i\mathscr{Q}^{i\mathscr{E}(\varphi)} + \sum_{i=1}^{n} b_i\mathscr{Q}^{-i\mathscr{E}(\varphi)} + a_0\\ &= a_1\mathscr{Q}^{\mathscr{E}(\varphi)} + a_2\mathscr{Q}^{2\mathscr{E}(\varphi)} + a_0 + b_2\mathscr{Q}^{-2\mathscr{E}(\varphi)} + b_1\mathscr{Q}^{-\mathscr{E}(\varphi)},\end{aligned} \tag{9}$$

where a_0, a_1, a_2, b_1, and b_2 are the arbitrary constants.

The order for the rest of this article is shown as follows: Section 2 applies the mK method to the nonlinear fractional strain wave equation. Section 3 discusses the obtained computational results and explains the comparison between them and that obtained in previous work. Moreover, it shows the comparison between the obtained numerical results. Section 4 gives the conclusion of the whole research.

2. Abundant Wave Solutions of the Fractional Strain Wave Equation

Applying the mK method with its auxiliary equation and the suggested general solutions for the fractional strain wave equation leads to a system of algebraic equations. Using Mathematica 11.2 to find the values of the parameters in this system leads to the following.

2.1. Family I.

$$\left[a_0 \longrightarrow \frac{b_2\left(-\sqrt{(\chi^2-4\delta\varrho)^2} + 8\delta\varrho + \chi^2\right)}{12\varrho^2}, a_1 \longrightarrow 0, a_2 \longrightarrow 0, b_1 \longrightarrow \frac{b_2\chi}{\varrho}, \alpha \longrightarrow -\frac{6\varrho^2}{b_2\sqrt{(4\delta\varrho-\chi^2)^2}},\right.$$
$$\left.\lambda \longrightarrow -\frac{1}{\sqrt{(\chi^2-4\delta\varrho)^2}}, \text{where}\left(\varrho \neq 0, \chi^2 \neq 4\delta\varrho\right)\right]. \tag{10}$$

Consequently, the closed forms of solutions for the fractional strain waves model are given as follows:

When $[\chi^2 - 4\delta\varrho < 0 \,\&\, \delta \neq 0]$,

$$\begin{aligned}
\mathcal{M}_1(x,t) &= \frac{b_2}{12}\left[\frac{48\delta^2}{\left(\chi - \sqrt{4\delta\varrho - \chi^2}\,\tan\left((1/2)\sqrt{4\delta\varrho - \chi^2}\,\left(x - \left((\alpha - 1)ct^{-2\alpha}/B(\alpha)\sum_{n=0}^{\infty}\left(-(\alpha/1 - \alpha)\right)^n\Gamma(1 - \alpha n)\right)\right)\right)\right)^2}\right.\\
&\quad - \frac{24\delta\chi}{\chi\varrho - \varrho\sqrt{4\delta\varrho - \chi^2}\,\tan\left((1/2)\sqrt{4\delta\varrho - \chi^2}\,\left(x - \left((\alpha - 1)ct^{-2\alpha}/B(\alpha)\sum_{n=0}^{\infty}\left(-(\alpha/1 - \alpha)\right)^n\Gamma(1 - \alpha n)\right)\right)\right)}\\
&\quad \left. + \frac{-\sqrt{\left(\chi^2 - 4\delta\varrho\right)^2} + 8\delta\varrho + \chi^2}{\varrho^2}\right],\\
\mathcal{M}_2(x,t) &= \frac{b_2}{12}\left[\frac{48\delta^2}{\left(\chi - \sqrt{4\delta\varrho - \chi^2}\,\cot\left((1/2)\sqrt{4\delta\varrho - \chi^2}\,\left(x - \left((\alpha - 1)ct^{-2\alpha}/B(\alpha)\sum_{n=0}^{\infty}\left(-(\alpha/1 - \alpha)\right)^n\Gamma(1 - \alpha n)\right)\right)\right)\right)^2}\right.\\
&\quad - \frac{24\delta\chi}{\chi\varrho - \varrho\sqrt{4\delta\varrho - \chi^2}\,\cot\left((1/2)\sqrt{4\delta\varrho - \chi^2}\,\left(x - \left((\alpha - 1)ct^{-2\alpha}/B(\alpha)\sum_{n=0}^{\infty}\left(-(\alpha/1 - \alpha)\right)^n\Gamma(1 - \alpha n)\right)\right)\right)}\\
&\quad \left. + \frac{-\sqrt{\left(\chi^2 - 4\delta\varrho\right)^2} + 8\delta\varrho + \chi^2}{\varrho^2}\right].
\end{aligned} \tag{11}$$

When $[\chi^2 - 4\delta\varrho > 0 \,\&\, \delta \neq 0]$,

$$\begin{aligned}
\mathcal{M}_3(x,t) &= \frac{b_2}{12}\left[\frac{48\delta^2}{\left(\chi - \sqrt{4\delta\varrho - \chi^2}\tanh\left((1/2)\sqrt{\chi^2 - 4\delta\varrho}\,\left(x - \left((\alpha - 1)ct^{-2\alpha}/B(\alpha)\sum_{n=0}^{\infty}\left(-(\alpha/1 - \alpha)\right)^n\Gamma(1 - \alpha n)\right)\right)\right) + \chi\right)^2}\right.\\
&\quad - \frac{24\delta\chi}{\chi\varrho - \varrho\sqrt{4\delta\varrho - \chi^2}\tanh\left((1/2)\sqrt{\chi^2 - 4\delta\varrho}\,\left(x - \left((\alpha - 1)ct^{-2\alpha}/B(\alpha)\sum_{n=0}^{\infty}\left(-(\alpha/1 - \alpha)\right)^n\Gamma(1 - \alpha n)\right)\right)\right) + \chi\varrho}\\
&\quad \left. + \frac{-\sqrt{\left(\chi^2 - 4\delta\varrho\right)^2} + 8\delta\varrho + \chi^2}{\varrho^2}\right],\\
\mathcal{M}_4(x,t) &= \frac{b_2}{12}\left[\frac{48\delta^2}{\left(\chi - \sqrt{4\delta\varrho - \chi^2}\coth\left((1/2)\sqrt{\chi^2 - 4\delta\varrho}\,\left(x - \left((\alpha - 1)ct^{-2\alpha}/B(\alpha)\sum_{n=0}^{\infty}\left(-(\alpha/1 - \alpha)\right)^n\Gamma(1 - \alpha n)\right)\right)\right) + \chi\right)^2}\right.\\
&\quad \left. - \frac{24\delta\chi}{\chi\varrho - \varrho\sqrt{4\delta\varrho - \chi^2}\coth\left((1/2)\sqrt{\chi^2 - 4\delta\varrho}\,\left(x - \left((\alpha - 1)ct^{-2\alpha}/B(\alpha)\sum_{n=0}^{\infty}\left(-(\alpha/1 - \alpha)\right)^n\Gamma(1 - \alpha n)\right)\right)\right) + \chi\varrho + \left(-\sqrt{\left(\chi^2 - 4\delta\varrho\right)^2} + 8\delta\varrho + \chi^2/\varrho^2\right)}\right].
\end{aligned} \tag{12}$$

When $[\delta\varrho > 0 \,\&\, \varrho \neq 0 \,\&\, \delta \neq 0 \,\&\, \chi = 0]$,

$$\begin{aligned}
\mathcal{M}_5(x,t) &= \frac{b_2\left(\delta\varrho\left(3\cot^2\left(\sqrt{\delta\varrho}\,\left(x - \left((\alpha - 1)ct^{-2\alpha}/B(\alpha)\sum_{n=0}^{\infty}\left(-(\alpha/1 - \alpha)\right)^n\Gamma(1 - \alpha n)\right)\right)\right) + 2\right) - \sqrt{\delta^2\varrho^2}\right)}{3\varrho^2},\\
\mathcal{M}_6(x,t) &= \frac{b_2\left(\delta\varrho\left(3\tan^2\left(\sqrt{\delta\varrho}\,\left(x - \left((\alpha - 1)ct^{-2\alpha}/B(\alpha)\sum_{n=0}^{\infty}\left(-(\alpha/1 - \alpha)\right)^n\Gamma(1 - \alpha n)\right)\right)\right) + 2\right) - \sqrt{\delta^2\varrho^2}\right)}{3\varrho^2}.
\end{aligned} \tag{13}$$

When $[\delta\varrho < 0 \,\&\, \varrho \neq 0 \,\&\, \delta \neq 0 \,\&\, \chi = 0]$,

$$\begin{aligned}\mathscr{M}_7(x,t) &= -\frac{b_2\left(3\delta\varrho\,\mathrm{csch}^2\left(\sqrt{-\delta\varrho}\left(x-\left((\alpha-1)ct^{-2\alpha}/B(\alpha)\sum_{n=0}^{\infty}\left(-(\alpha/1-\alpha)\right)^n\Gamma(1-\alpha n)\right)\right)\right)+\sqrt{\delta^2\varrho^2}+\delta\varrho\right)}{3\varrho^2},\\ \mathscr{M}_8(x,t) &= -\frac{b_2\left(\delta\varrho\left(3\tanh^2\left(\sqrt{-\delta\varrho}\left(x-\left((\alpha-1)ct^{-2\alpha}/B(\alpha)\sum_{n=0}^{\infty}\left(-(\alpha/1-\alpha)\right)^n\Gamma(1-\alpha n)\right)\right)\right)-2\right)+\sqrt{\delta^2\varrho^2}\right)}{3\varrho^2}.\end{aligned} \tag{14}$$

When $[\chi = 0 \,\&\, \varrho = -\delta]$,

$$\begin{aligned}\mathscr{M}_9(x,t) = \frac{b_2}{3}\Bigg[&\frac{12}{\left(\exp\left(2\varrho\left(x-\left((\alpha-1)ct^{-2\alpha}/B(\alpha)\sum_{n=0}^{\infty}\left(-(\alpha/1-\alpha)\right)^n\Gamma(1-\alpha n)\right)\right)\right)+1\right)^2}\\ &+6\tanh\left(\varrho\left(x-\frac{(\alpha-1)ct^{-2\alpha}}{B(\alpha)\sum_{n=0}^{\infty}\left(-(\alpha/1-\alpha)\right)^n\Gamma(1-\alpha n)}\right)\right)-\frac{\sqrt{\varrho^4}}{\varrho^2}-5\Bigg]a.\end{aligned} \tag{15}$$

When $[\chi = (\varrho/2) = \kappa \,\&\, \delta = 0]$,

$$\begin{aligned}\mathscr{M}_{10}(x,t) = b_2\Bigg[&\frac{1}{\left(\exp\left(\kappa\left(x-\left((\alpha-1)ct^{-2\alpha}/B(\alpha)\sum_{n=0}^{\infty}\left(-(\alpha/1-\alpha)\right)^n\Gamma(1-\alpha n)\right)\right)\right)-2\right)^2}\\ &+\frac{1}{2\exp\left(\kappa\left(x-\left((\alpha-1)ct^{-2\alpha}/B(\alpha)\sum_{n=0}^{\infty}\left(-(\alpha/1-\alpha)\right)^n\Gamma(1-\alpha n)\right)\right)\right)-4}-\frac{\sqrt{\kappa^4}}{48\kappa^2}+\frac{1}{48}\Bigg].\end{aligned} \tag{16}$$

When $[\chi = \delta = 0 \,\&\, \varrho \neq 0]$,

$$\mathscr{M}_{11}(x,t) = \frac{b_2}{\varrho^2\left(x-\left((\alpha-1)ct^{-2\alpha}/B(\alpha)\sum_{n=0}^{\infty}\left(-(\alpha/1-\alpha)\right)^n\Gamma(1-\alpha n)\right)\right)^2}. \tag{17}$$

When $[\chi = 0 \,\&\, \varrho = \delta]$,

$$\mathscr{M}_{12}(x,t) = \frac{1}{3}b_2\left(3\cot^2\left(-\frac{(\alpha-1)c\varrho t^{-2\alpha}}{B(\alpha)\sum_{n=0}^{\infty}\left(-(\alpha/1-\alpha)\right)^n\Gamma(1-\alpha n)}+C+x\varrho\right)-\frac{\sqrt{\varrho^4}}{\varrho^2}+2\right). \tag{18}$$

When $[\delta = 0 \,\&\, \chi \neq 0 \,\&\, \varrho \neq 0]$,

$$\begin{aligned}\mathscr{M}_{13}(x,t) = \frac{b_2}{12}\Bigg[&\frac{\chi^2\left(1-\left(12\varrho/\varrho-\chi\exp\left(\chi\left(x-\left((\alpha-1)ct^{-2\alpha}/B(\alpha)\sum_{n=0}^{\infty}\left(-(\alpha/1-\alpha)\right)^n\Gamma(1-\alpha n)\right)\right)\right)\right)\right)-\sqrt{\chi^4}}{\varrho^2}\\ &+\frac{12}{\left(\exp\left(\chi\left(x-\left((\alpha-1)ct^{-2\alpha}/B(\alpha)\sum_{n=0}^{\infty}\left(-(\alpha/1-\alpha)\right)^n\Gamma(1-\alpha n)\right)\right)\right)-(\varrho/\chi)\right)^2}\Bigg].\end{aligned} \tag{19}$$

2.2. Family II.

$$\begin{aligned}\Bigg[&a_0 \longrightarrow \frac{\sqrt{(\chi^2-4\delta\varrho)^2}-8\delta\varrho-\chi^2}{2\alpha\sqrt{(\chi^2-4\delta\varrho)^2}}, a_1 \longrightarrow -\frac{6\delta\chi}{\alpha\sqrt{(\chi^2-4\delta\varrho)^2}}, a_2 \longrightarrow -\frac{6\delta^2}{\alpha\sqrt{(4\delta\varrho-\chi^2)^2}}, b_1 \longrightarrow 0, b_2 \longrightarrow 0,\\ &\lambda \longrightarrow -\frac{1}{\sqrt{(\chi^2-4\delta\varrho)^2}}, \text{where}\left(\delta \neq 0, \alpha \neq 0, 4\delta\varrho \neq \chi^2\right)\Bigg].\end{aligned} \tag{20}$$

Consequently, the closed forms of solutions for the fractional strain waves model are given as follows:

When $[\chi^2 - 4\delta\varrho < 0 \,\&\, \delta \neq 0]$,

$$\mathscr{M}_{14}(x,t) = \left[3\left(\chi^2 - 4\delta\varrho\right)\tan^2\left(\frac{1}{2}\sqrt{4\delta\varrho - \chi^2}\left(x - \frac{(\alpha-1)ct^{-2\alpha}}{B(\alpha)\sum_{n=0}^{\infty}(-(\alpha/1-\alpha))^n\Gamma(1-\alpha n)}\right)\right) + \sqrt{\left(\chi^2 - 4\delta\varrho\right)^2} - 8\delta\varrho + 2\chi^2\right] \times \left(\frac{1}{2\alpha\sqrt{\left(\chi^2 - 4\delta\varrho\right)^2}}\right),$$

$$\mathscr{M}_{15}(x,t) = \left[3\left(\chi^2 - 4\delta\varrho\right)\cot^2\left(\frac{1}{2}\sqrt{4\delta\varrho - \chi^2}\left(x - \frac{(\alpha-1)ct^{-2\alpha}}{B(\alpha)\sum_{n=0}^{\infty}(-(\alpha/1-\alpha))^n\Gamma(1-\alpha n)}\right)\right) + \sqrt{\left(\chi^2 - 4\delta\varrho\right)^2} - 8\delta\varrho + 2\chi^2\right] \times \left(\frac{1}{2\alpha\sqrt{\left(\chi^2 - 4\delta\varrho\right)^2}}\right). \tag{21}$$

When $[\chi^2 - 4\delta\varrho > 0 \,\&\, \delta \neq 0]$,

$$\mathscr{M}_{16}(x,t) = \left[3\left(\chi^2 - 4\delta\varrho\right)\operatorname{sech}^2\left(\frac{1}{2}\sqrt{\chi^2 - 4\delta\varrho}\left(x - \frac{(\alpha-1)ct^{-2\alpha}}{B(\alpha)\sum_{n=0}^{\infty}(-(\alpha/1-\alpha))^n\Gamma(1-\alpha n)}\right)\right) + \sqrt{\left(\chi^2 - 4\delta\varrho\right)^2} + 4\delta\varrho - \chi^2\right] \times \left(\frac{1}{2\alpha\sqrt{\left(\chi^2 - 4\delta\varrho\right)^2}}\right),$$

$$\mathscr{M}_{17}(x,t) = \left[3\left(4\delta\varrho - \chi^2\right)\coth^2\left(\frac{1}{2}\sqrt{\chi^2 - 4\delta\varrho}\left(x - \frac{(\alpha-1)ct^{-2\alpha}}{B(\alpha)\sum_{n=0}^{\infty}(-(\alpha/1-\alpha))^n\Gamma(1-\alpha n)}\right)\right) + \sqrt{\left(\chi^2 - 4\delta\varrho\right)^2} - 8\delta\varrho + 2\chi^2\right] \times \left(\frac{1}{2\alpha\sqrt{\left(\chi^2 - 4\delta\varrho\right)^2}}\right). \tag{22}$$

When $\delta\varrho > 0 \,\&\varrho \neq 0 \,\&\, \delta \neq 0 \,\&\chi = 0$,

$$\mathscr{M}_{18}(x,t) = \frac{1}{2\alpha\sqrt{\delta^2\varrho^2}}\left[-3\delta\varrho\sec^2\left(\sqrt{\delta\varrho}\left(x - \frac{(\alpha-1)ct^{-2\alpha}}{B(\alpha)\sum_{n=0}^{\infty}(-(\alpha/1-\alpha))^n\Gamma(1-\alpha n)}\right)\right) + \sqrt{\delta^2\varrho^2} + \delta\varrho\right],$$

$$\mathscr{M}_{19}(x,t) = \frac{1}{2\alpha\sqrt{\delta^2\varrho^2}}\left[-3\delta\varrho\csc^2\left(\sqrt{\delta\varrho}\left(x - \frac{(\alpha-1)ct^{-2\alpha}}{B(\alpha)\sum_{n=0}^{\infty}(-(\alpha/1-\alpha))^n\Gamma(1-\alpha n)}\right)\right) + \sqrt{\delta^2\varrho^2} + \delta\varrho\right]. \tag{23}$$

When $[\delta\varrho < 0 \,\&\, \varrho \neq 0 \,\&\, \delta \neq 0 \,\&\, \chi = 0]$,

$$\mathscr{M}_{20}(x,t) = \frac{1}{2\alpha}\left[\frac{\delta\varrho\left(3\tanh^2\left(\sqrt{-\delta\varrho}\,\left(x - \left((\alpha-1)ct^{-2\alpha}/B(\alpha)\sum_{n=0}^{\infty}\left(-(\alpha/1-\alpha)\right)^n\Gamma(1-\alpha n)\right)\right)\right) - 2\right)}{\sqrt{\delta^2\varrho^2}} + 1\right],$$
$$\mathscr{M}_{21}(x,t) = \frac{1}{2\alpha\sqrt{\delta^2\varrho^2}}\left[3\delta\varrho\,\mathrm{csch}^2\left(\sqrt{-\delta\varrho}\left(x - \frac{(\alpha-1)ct^{-2\alpha}}{B(\alpha)\sum_{n=0}^{\infty}\left(-(\alpha/1-\alpha)\right)^n\Gamma(1-\alpha n)}\right)\right) + \sqrt{\delta^2\varrho^2} + \delta\varrho\right]. \tag{24}$$

When $[\chi = 0 \,\&\, \varrho = -\delta]$,

$$\mathscr{M}_{22}(x,t) = \frac{1}{2\alpha\sqrt{\varrho^4}}\left[-3\varrho^2\coth^2\left(\varrho\left(x - \frac{(\alpha-1)ct^{-2\alpha}}{B(\alpha)\sum_{n=0}^{\infty}\left(-(\alpha/1-\alpha)\right)^n\Gamma(1-\alpha n)}\right)\right) + \sqrt{\varrho^4} + 2\varrho^2\right]. \tag{25}$$

When $[\chi = \delta = \kappa \,\&\, \varrho = 0]$,

$$\mathscr{M}_{23}(x,t) = \frac{1}{2\alpha}\left[1 - \frac{\sqrt{\kappa^4}\left(3\mathrm{csch}^2\left((1/2)\kappa\left(x - \left((\alpha-1)ct^{-2\alpha}/B(\alpha)\sum_{n=0}^{\infty}\left(-(\alpha/1-\alpha)\right)^n\Gamma(1-\alpha n)\right)\right)\right) + 1\right)}{\kappa^2}\right]. \tag{26}$$

When $\varrho = 0 \,\&\, \chi \neq 0 \,\&\, \delta \neq 0$,

$$\mathscr{M}_{24}(x,t) = \frac{-1}{2\alpha}\left[\frac{\sqrt{\chi^4}}{\chi^2}\left(\frac{48}{\left(\delta\exp\left(\chi\left(x - \left((\alpha-1)ct^{-2\alpha}/B(\alpha)\sum_{n=0}^{\infty}\left(-(\alpha/1-\alpha)\right)^n\Gamma(1-\alpha n)\right)\right)\right) - 2\right)^2} + \frac{24}{\delta\exp\left(\chi\left(x - \left((\alpha-1)ct^{-2\alpha}/B(\alpha)\sum_{n=0}^{\infty}\left(-(\alpha/1-\alpha)\right)^n\Gamma(1-\alpha n)\right)\right)\right) - 2} + 1\right) - 1\right]. \tag{27}$$

When $[\chi = 0 \,\&\, \varrho = \delta]$,

$$\mathscr{M}_{25}(x,t) = \frac{1}{2\alpha\sqrt{\varrho^4}}\left[-3\varrho^2\sec^2\left(-\frac{(\alpha-1)c\varrho t^{-2\alpha}}{B(\alpha)\sum_{n=0}^{\infty}\left(-(\alpha/1-\alpha)\right)^n\Gamma(1-\alpha n)} + C + x\varrho\right) + \sqrt{\varrho^4} + \varrho^2\right]. \tag{28}$$

3. Results and Discussion

This section is divided into two main parts. The first part shows studying the obtained computational solutions for the fractional suggested model, while the second part presents a comparison between them and other obtained results in previous work.

(1) The solutions obtained in this paper:

(i) In this research paper, the fractional nonlinear longitudinal strain wave equation is investigated by the employment of the mK method and a new fractional definition ($\mathscr{ABR}$). Abundant explicit closed forms of solutions are obtained (twenty five solutions).

(2) The previously obtained solutions in previous work:

(i) In [53], two analytical methods were applied to three different models involving our two investigated models. However, they used two schemes but a very few special solutions were obtained.

(ii) The two analytical schemes in [53] are just a special case of the mK method when $[\mathscr{Q}^{\mathscr{M}(\varphi)} = (G'/G), \varrho = -\mu, \chi = -\lambda, \delta = 1]$.

(iii) Equation (22) is equal to equation (3.9) in [53] when $[e_0 = -12\delta(\mu + d(d-\lambda)), -3(\lambda^2 - 4\mu) = \delta\lambda\varrho]$.

(iv) All other solutions obtained in this paper are considered new solutions when compared with those obtained in [53].

4. Conclusion

In our research paper, we solved the flaws and disadvantages of the (G'/G)-expansion methods that are used in [53] by M. Ali Akbar et al., and as shown in the previous section, it is just a particular case of our applied method in this research paper. Moreover, a new definition of fractional derivative is

used, successfully converting the fractional from our abovementioned models to integer-order ordinary differential equations. Abundance new solutions for both the models were obtained.

Data Availability

The data that support the findings of this study are available from the corresponding author upon reasonable request.

Conflicts of Interest

The authors declare that they have no conflicts of interest.

Acknowledgments

This research was supported by the National Natural Science Foundation of China, Grant nos. 61973193 and 61807010, Shandong Provincial Natural Science Foundation (Grant nos. ZR2017BA009 and ZR2016AB04), a project of Shandong Province Higher Educational Science and Technology Program (Grant no. J17KB121), and Foundation for Young Teachers of Qilu Normal University (Grant nos. 2016L0605, 2015L0603, 2017JX2311, and 2017JX2312).

References

[1] M. M. Al Qurashi, A. Yusuf, A. Yusuf, A. I. Aliyu, and M. Inc, "Optical and other solitons for the fourth-order dispersive nonlinear Schrödinger equation with dual-power law nonlinearity," *Superlattices and Microstructures*, vol. 105, pp. 183–197, 2017.

[2] B. Dumitru and O. P. Agrawal, "Fractional Hamilton formalism within Caputo's derivative," *Czechoslovak Journal of Physics*, vol. 56, no. 10-11, pp. 1087–1092, 2006.

[3] B. Dumitru and S. I. Muslih, "About Lagrangian formulation of classical fields within Riemann–Liouville fractional derivatives," in *Proceedings of the ASME 2005 International Design Engineering Technical Conferences and Computers and Information in Engineering Conference*, American Society of Mechanical Engineers Digital Collection, Long Beach, CA, USA, pp. 1457–1464, September 2005.

[4] A. El-Ajou, M. N. Oqielat, Z. Al-Zhour, S. Kumar, and S. Momani, "Solitary solutions for time-fractional nonlinear dispersive PDEs in the sense of conformable fractional derivative," *Chaos: An Interdisciplinary Journal of Nonlinear Science*, vol. 29, no. 9, Article ID 093102, 2019.

[5] E. F. D. Goufo, S. Kumar, and S. B. Mugisha, "Similarities in a fifth-order evolution equation with and with no singular kernel," *Chaos, Solitons & Fractals*, vol. 130, Article ID 109467, 2020.

[6] N. Heymans and I. Podlubny, "Physical interpretation of initial conditions for fractional differential equations with Riemann-Liouville fractional derivatives," *Rheologica Acta*, vol. 45, no. 5, pp. 765–771, 2006.

[7] R. Hilfer, "Fractional diffusion based on riemann-liouville fractional derivatives," *The Journal of Physical Chemistry B*, vol. 104, no. 16, pp. 3914–3917, 2000.

[8] M. Inc, A. Yusuf, A. I. Aliyu, and D. Baleanu, "Optical soliton solutions for the higher-order dispersive cubic-quintic nonlinear Schrödinger equation," *Superlattices and Microstructures*, vol. 112, pp. 164–179, 2017.

[9] A. Kumar and S. Kumar, "A modified analytical approach for fractional discrete KdV equations arising in particle vibrations," *Proceedings of the National Academy of Sciences, India Section A: Physical Sciences*, vol. 88, no. 1, pp. 95–106, 2018.

[10] S. Kumar, K. Amit, S. Abbas, M. A. Qurashi, and B. Dumitru, "A modified analytical approach with existence and uniqueness for fractional Cauchy reaction–diffusion equations," *Advances in Difference Equations*, vol. 2020, no. 1, p. 28, 2020.

[11] S. Kumar, K. Amit, S. Momani, M. Aldhaifallah, and K. S. Nisar, "Numerical solutions of nonlinear fractional model arising in the appearance of the stripe patterns in two-dimensional systems," *Advances in Difference Equations*, vol. 2019, no. 1, p. 413, 2019.

[12] J. Losada and J. Nieto, "Properties of a new fractional derivative without singular kernel," *Progress in Fractional Differentiation and Applications*, vol. 1, no. 2, pp. 87–92, 2015.

[13] Y. U. R. I. I. Luchko and R. Gorenflo, "An operational method for solving fractional differential equations with the Caputo derivatives," *Acta Mathematica Vietnamica*, vol. 24, no. 2, pp. 207–233, 1999.

[14] V. F. Morales-Delgado, J.-F. Gómez-Aguilar, S. Kumar, and M. A. Taneco-Hernández, "Analytical solutions of the Keller-Segel chemotaxis model involving fractional operators without singular kernel," *The European Physical Journal Plus*, vol. 133, no. 5, p. 200, 2018.

[15] N. A. Shah and I. Khan, "Heat transfer analysis in a second grade fluid over and oscillating vertical plate using fractional caputo–fabrizio derivatives," *The European Physical Journal C*, vol. 76, no. 7, p. 362, 2016.

[16] F. Tchier, A. Yusuf, A. I. Aliyu, and M. Inc, "Soliton solutions and conservation laws for lossy nonlinear transmission line equation," *Superlattices and Microstructures*, vol. 107, pp. 320–336, 2017.

[17] A. Yusuf, M. İnç, and M. Bayram, "Soliton solutions for kudryashov-sinelshchikov equation," *Sigma Journal of Engineering and Natural Sciences*, vol. 37, no. 2, 2019.

[18] O. A. Arqub, A. El-Ajou, and S. Momani, "Constructing and predicting solitary pattern solutions for nonlinear time-fractional dispersive partial differential equations," *Journal of Computational Physics*, vol. 293, pp. 385–399, 2015.

[19] V. Benci and D. F. Fortunato, "Solitary waves of the nonlinear klein-gordon equation coupled with the maxwell equations," *Reviews in Mathematical Physics*, vol. 14, no. 4, pp. 409–420, 2002.

[20] K. A. Gepreel and S. Omran, "Exact solutions for nonlinear partial fractional differential equations," *Chinese Physics B*, vol. 21, no. 11, Article ID 110204, 2012.

[21] R. Guo, "Projective synchronization of a class of chaotic systems by dynamic feedback control method," *Nonlinear Dynamics*, vol. 90, no. 1, pp. 53–64, 2017.

[22] J.-H. He, "Exp–function method for fractional differential equations," *International Journal of Nonlinear Sciences and Numerical Simulation*, vol. 14, no. 6, pp. 363–366, 2013.

[23] J.-H. He and X.-H. Wu, "Construction of solitary solution and compacton-like solution by variational iteration method," *Chaos, Solitons & Fractals*, vol. 29, no. 1, pp. 108–113, 2006.

[24] M. Inc, "The approximate and exact solutions of the space- and time-fractional Burgers equations with initial conditions by variational iteration method," *Journal of Mathematical Analysis and Applications*, vol. 345, no. 1, pp. 476–484, 2008.

[25] M. M. A. Khater, A. R. Seadawy, and D. Lu, "Elliptic and solitary wave solutions for Bogoyavlenskii equations system, couple Boiti-Leon-Pempinelli equations system and Time-

fractional Cahn-Allen equation," *Results in Physics*, vol. 7, pp. 2325–2333, 2017.

[26] M. Kurulay and M. Bayram, "Approximate analytical solution for the fractional modified KdV by differential transform method," *Communications in Nonlinear Science and Numerical Simulation*, vol. 15, no. 7, pp. 1777–1782, 2010.

[27] W. Liu and K. Chen, "The functional variable method for finding exact solutions of some nonlinear time-fractional differential equations," *Pramana*, vol. 81, no. 3, pp. 377–384, 2013.

[28] C. Lu, C. Fu, and H. Yang, "Time-fractional generalized Boussinesq equation for Rossby solitary waves with dissipation effect in stratified fluid and conservation laws as well as exact solutions," *Applied Mathematics and Computation*, vol. 327, pp. 104–116, 2018.

[29] Z. Wang and R. Guo, "Hybrid synchronization problem of a class of chaotic systems by an universal control method," *Symmetry*, vol. 10, no. 11, p. 552, 2018.

[30] A. Yang, L. Li, Z. Wang, and R. Guo, "Tracking control of a class of chaotic systems," *Symmetry*, vol. 11, no. 4, p. 568, 2019.

[31] A. A. Alderremy, R. A. M. Attia, J. F. Alzaidi, D. Lu, and M. Khater, "Analytical and semi-analytical wave solutions for longitudinal wave equation via modified auxiliary equation method and adomian decomposition method," *Thermal Science*, vol. 355, 2019.

[32] A. T. Ali, M. M. A. Khater, R. A. M. Attia, Abdel-Haleem Abdel-Aty, and D. Lu, "Abundant numerical and analytical solutions of the generalized formula of hirota–satsuma coupled KdV system," *Chaos, Solitons & Fractals*, vol. 131, Article ID 109473, 2019.

[33] R. A. M. Attia, D. Lu, and M. M. A. Khater, "Chaos and relativistic energy–momentum of the nonlinear time fractional Duffing equation," *Mathematical and Computational Applications*, vol. 24, no. 1, p. 10, 2019.

[34] M. Khater, R. Attia, and D. Lu, "Modified auxiliary equation method versus three nonlinear fractional biological models in present explicit wave solutions," *Mathematical and Computational Applications*, vol. 24, no. 1, p. 1, 2019.

[35] M. M. A. Khater and R. A. M. Attia, D. Lu, Explicit lump solitary wave of certain interesting $(3+1)$-dimensional waves in physics via some recent traveling wave methods," *Entropy*, vol. 21, no. 4, p. 397, 2019.

[36] M. M. A. Khater, D. Lu, and R. A. M. Attia, "Dispersive long wave of nonlinear fractional Wu–Zhang system via a modified auxiliary equation method," *AIP Advances*, vol. 9, no. 2, Article ID 025003, 2019.

[37] M. M. A. Khater, D. Lu, and R. A. M. Attia, "Lump soliton wave solutions for the $(2+1)$-dimensional Konopelchenko–Dubrovsky equation and KdV equation," *Modern Physics Letters B*, vol. 33, no. 18, Article ID 1950199, 2019.

[38] Li Jing, Y. Qiu, D. Lu, A. M. Raghda, and M. Khater, "Study on the solitary wave solutions of the ionic currents on microtubules equation by using the modified Khater method," *Thermal Science*, vol. 23, no. Suppl. 6, pp. 2053–2062, 2019.

[39] H. Qin, A. M. Raghda, M. Khater, and D. Lu, "Ample soliton waves for the crystal lattice formation of the conformable time-fractional $(N+1)$ Sinh-Gordon equation by the modified Khater method and the Painlevé property," *Journal of Intelligent & Fuzzy Systems*, vol. 38, no. 3, pp. 2745–2752, 2004.

[40] H. Rezazadeh, A. Korkmaz, M. M. A. Khater, M. Eslami, D. Lu, and R. A. M. Attia, "New exact traveling wave solutions of biological population model via the extended rational sinh-cosh method and the modified Khater method," *Modern Physics Letters B*, vol. 33, no. 28, p. 1950338, 2019.

[41] H. Rezazadeh, A. Korkmaz, M. Eslami, J. Vahidi, and R. Asghari, "Traveling wave solution of conformable fractional generalized reaction Duffing model by generalized projective Riccati equation method," *Optical and Quantum Electronics*, vol. 50, no. 3, p. 150, 2018.

[42] Z. Ayati, K. Hosseini, and M. Mirzazadeh, "Application of Kudryashov and functional variable methods to the strain wave equation in microstructured solids," *Nonlinear Engineering*, vol. 6, no. 1, pp. 25–29, 2017.

[43] A. Berezovski, J. Engelbrecht, A. Salupere, K. Tamm, T. Peets, and M. Berezovski, "Dispersive waves in microstructured solids," *International Journal of Solids and Structures*, vol. 50, no. 11-12, pp. 1981–1990, 2013.

[44] A. Berezovski, J. Engelbrecht, and M. Berezovski, "Waves in microstructured solids: a unified viewpoint of modeling," *Acta Mechanica*, vol. 220, no. 1–4, pp. 349–363, 2011.

[45] J. Engelbrecht, A. Berezovski, P. Franco, and M. Braun, "Waves in microstructured materials and dispersion," *Philosophical Magazine*, vol. 85, no. 33–35, pp. 4127–4141, 2005.

[46] J. . Engelbrecht and P. Franco, "Waves in microstructured solids with nonlinearities in microscale," *Proceedings-Estonian Academy of Sciences Physics Mathematics*, vol. 52, pp. 12–20, 2003.

[47] P. Franco, P. Cermelli, A. Porubov et al., "Nonlinear waves in 1–D solids with microstructure," *Materials Chemistry and Physics*, vol. 7, no. 1, pp. 9–16, 2004.

[48] A. V. Porubov, P. Franco, and G. A. Maugin, "Selection of two–dimensional nonlinear strain waves in micro–structured media," *Comptes Rendus Mecanique*, vol. 332, no. 7, pp. 513–518, 2004.

[49] A. Atangana and J. F. Gómez-Aguilar, "Numerical approximation of Riemann-Liouville definition of fractional derivative: from Riemann-Liouville to Atangana-Baleanu," *Numerical Methods for Partial Differential Equations*, vol. 34, no. 5, pp. 1502–1523, 2018.

[50] A. Atangana and I. Koca, "Chaos in a simple nonlinear system with Atangana-Baleanu derivatives with fractional order," *Chaos, Solitons & Fractals*, vol. 89, pp. 447–454, 2016.

[51] M. M. A. Khater and B. Dumitru, "On new analytical and semi–analytical wave solutions of the Quadratic–cubic fractional nonlinear schrödinger equation," *chaos, solitons & fractals*, 2020.

[52] M. M. A. Khater and B. Dumitru, "On the new explicit computational and numerical solutions of the fractional nonlinear space–time Telegraph equation," *Modern physics letter A*, 2019.

[53] H. Naher and F. A. Abdullah, "New generalized and improved (G'/G)-expansion method for nonlinear evolution equations in mathematical physics," *Journal of the Egyptian Mathematical Society*, vol. 22, no. 3, pp. 390–395, 2014.

Hindawi
Mathematical Problems in Engineering
Volume 2020, Article ID 9159158, 6 pages
https://doi.org/10.1155/2020/9159158

Research Article

Automated Classification of Atrial Fibrillation Using Artificial Neural Network for Wearable Devices

Fengying Ma, Jingyao Zhang, Wei Liang, and Jingyu Xue

School of Electrical Engineering and Automation, Qilu University of Technology, Shandong Academy of Sciences, Jinan, China

Correspondence should be addressed to Wei Liang; dzhlw0918@qlu.edu.cn

Received 15 February 2020; Accepted 18 March 2020; Published 25 April 2020

Guest Editor: Ping Zhao

Atrial fibrillation (AF), as one of the most common arrhythmia diseases in clinic, is a malignant threat to human health. However, AF is difficult to monitor in real time due to its intermittent nature. Wearable electrocardiogram (ECG) monitoring equipment has flourished in the context of telemedicine due to its real-time monitoring and simple operation in recent years, providing new ideas and methods for the detection of AF. In this paper, we propose a low computational cost classification model for robust detection of AF episodes in ECG signals, using RR intervals of the ECG signals and feeding them into artificial neural network (ANN) for classification, to compensate the defect of the computational complexity in traditional wearable ECG monitoring devices. In addition, we compared our proposed classifier with other popular classifiers. The model was trained and tested on the AF Termination Challenge Database and MIT-BIH Arrhythmia Database. Experimental results achieve the highest sensitivity of 99.3%, specificity of 97.4%, and accuracy of 98.3%, outperforming most of the others in the recent literature. Accordingly, we observe that ANN using RR intervals as an input feature can be a suitable candidate for automatic classification of AF.

1. Introduction

Atrial fibrillation (AF), a major cardiac arrhythmia abnormality in the clinic, is associated with substantial complications that threaten people's health [1, 2], such as hypertension, diabetes, heart failure, and cardiovascular disease [3–5]. The reason that AF real-time monitoring has gained much attention is not only because AF causes a high mortality rate but also because the duration of AF is relatively short to capture. Hence, we urgently need an automated AF real-time detection mechanism that could analyze massive amounts of electrocardiogram (ECG) signals to lighten the burden on physicians [6].

The diagnosis of AF is based on the recording of subject's ECG signal, medical history, and clinical evaluation [7, 8]. Thus, the development of ECG which has heart rhythm and physiological information is an important basis and makes automatic detection and diagnosis of heart disease better in real time of AF [9–11]. Since AF happens unpredictably and due to the high requirement of timely treatment, more and more wearable devices that can analyze ECG signal are used for the real-time diagnosis of these subjects [12]. However, traditional ECG monitoring equipment has many inadequacies. In addition to complicated operation outside, the problem of insufficient consideration for multiscene applications also exists, which is one of the limitations. There are many difficult problems in real-time diagnosis. Wearable ECG monitoring device as a real-time detection device can meet the requirement of collecting ECG signals and preliminary diagnosis by using the human sensor networks. It can also promote the development of telemedicine. Hence, the classification algorithm for AF detection in real time that can be used in wearable ECG monitoring devices is significant.

The existing wearable ECG monitoring device transmits the individual ECG parameter information to the remote server through wireless transmission and combines with various mobile terminals to achieve the goal of completing the ECG monitoring task [13]. The flowchart of the detection of arrhythmia in the wearable device is shown in Figure 1. Feature extraction is a nonnegligible part in the analysis of arrhythmia diseases. There are two main methods of AF

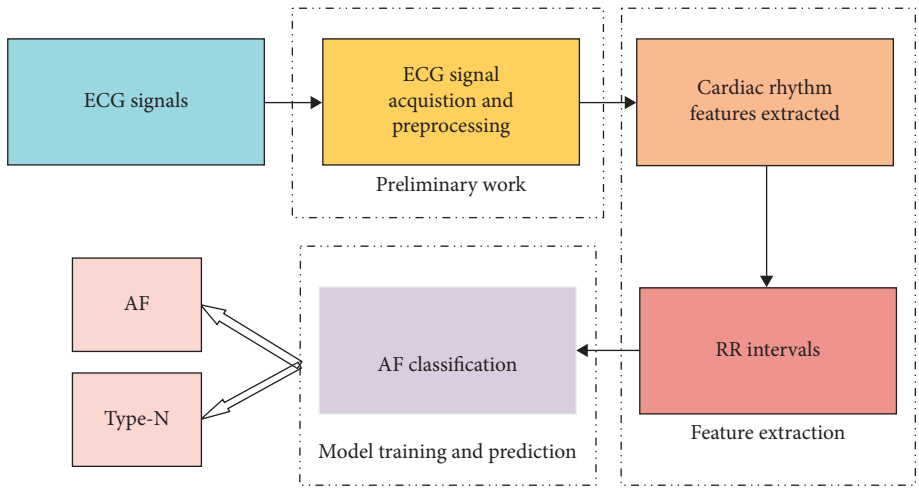

Figure 1: The process of identification and analysis of AF in wearable ECG monitoring equipment.

detection in terms of feature selection. The first method is to diagnose without P waves and f waves [14]. However, this detection method requires signal with high quality, and there are certain difficulties in practical applications. The second method is based on the RR intervals. The distribution of RR intervals during AF differs from the distribution during normal sinus rhythm [15]. The R wave is the most prominent feature of the ECG and easy to locate. In recent years, many scholars have studied the AF detection algorithm based on RR interval features and made great progress [16]. Support vector machine (SVM) and linear discriminant (LD) is a widely used classification method in ECG arrhythmia detection. Lin et al. used the RR interval as a feature input and linear discriminant (LD) to classify ECG heartbeats [17]. Huang et al. proposed the use of random projection with support vector machine (SVM) and RR interval to classify ECG heartbeats [18]. In addition to SVM and LD, various machine learning techniques are also used as classifiers. Swapna et al. applied a series of samples centered on the R peak of the heartbeat, using a convolutional neural network (CNN), recurrent structures such as recurrent neural network (RNN), long short-term memory (LSTM), gated recurrent unit (GRU), and hybrid of CNN and recurrent structures to automatically detect the abnormality [19]. Related to this article, Afdala et al. presented a new feature that is Shannon entropy for RR interval and classifier by ANN for detecting AF [20]. In terms of diagnostic methods, machine learning technology is a new and advanced arrhythmia detection method developed in recent years. As a traditional model, ANN is of great significance for accelerating AF detection [17].

In the research studies, these methods have made some achievements using RR intervals combined with different classifiers in the detection of AF, but they have some defects, such as computational complexity, and their accuracy cannot satisfy the current needs. Hence, a detection method with low calculating complexity, high precision, and stability is required by the wearable ECG monitoring device.

In this paper, our motivation is to build a system with lower computational cost and an excellent classification performance to detect AF in real time. The choice of features and classifiers is the most important part of this system. The feature we selected for this experiment is the sequence of RR intervals of the ECG because the R peak with strong robustness is the most prominent characteristic in ECG. We input the selected feature into ANN using lightweight algorithms for classification, choose the appropriate number of hidden neurons and network parameters, and verify them in AF Termination Challenge Database and MIT-BIH Arrhythmia Database. And we compared the results obtained in the ANN model with other more commonly used models. The results present that the ANN model we proposed is better than other models for the detection of AF. The contributions of this method include the following:

(i) We propose an ANN model with lower computational complexity which has much reliable and higher classification accuracy than some of the models previously proposed for AF detection in wearable ECG monitoring devices.

(ii) We use the rhythm characteristics, the RR intervals, as input dataset to the network instead of using complex traditional data to achieve the requirements of lower computational complexity. And we achieve the desired accuracy only using this feature.

The remainder of this paper is organized as follows. Section 2 covers the ANN model based on RR interval algorithms for AF detection in detail. Section 3 presents the experimental methods on the database and its results. Finally, the research of this study and the planning of future work are described in Section 4.

2. Material and Methods

2.1. Artificial Neural Network (ANN). ANN developed by Hecht-Nielsen [21], as a pattern recognition machine learning method, was used in the detection of AF; it mimics brain mechanisms through a series of interconnected nodes, just as the brain has many neuronal connections [22]. The model in this study is a feed-forward neural network.

Figure 2 shows a block diagram of a three-layer feed-forward neural network including input layers, hidden layers, and output layers.

In this model, the input value x is the RR interval of the ECG we extracted, and the number of input nodes is the same as the number of input parameters. y is the output vector of the hidden layer, and O indicates that the detection result obtained by the output layer is AF or N. The constant $\eta \in (0, 1)$ is the proportionality coefficient, which reflects the learning rate during training. Weight is the most important link of ANN simulation neuron association, where v represents the weight between the input layer and the hidden layer (the adjustment formula of v is shown in equation (1)) and W represents the weight corresponding to the hidden layer and the output signal. The adjustment formula is shown in equation (2). The principle of adjusting the weight is to reduce the error continuously. The offset value b is a factor associated with the stored information. The use of cross-entropy as a performance function facilitates the implementation of this process. So far, there is no defined algorithm for choosing the number of hidden nodes. Most of them can only be obtained through sufficient experience or extensive experiments [23, 24]. We set our ANN classifier by adjusting the parameters of the ANN to optimize the classification outcomes.

$$\Delta v_{ij} = \eta \delta_j^y x_i = \eta \left(\sum_{k=1}^{l} \delta_k^o w_{jk} \right) y_j \left(1 - y_j\right) x_i. \quad (1)$$

$$\Delta w_{jk} = \eta \delta_k^o y_j = \eta \left(d_k - o_k\right) o_k \left(1 - o_k\right) y_j, \quad (2)$$

The activation function used in the hidden layer node is the sigmoid function. Equation (3) is the calculation process of the activation function f, and equation (4) is the calculation method of the output layer. The output of the network is compared with the probability threshold (the default value is 0.5).

$$f(x) = \frac{1}{1 + e^{-x}}, \quad (3)$$

$$y_j = f\left(\sum_{j=0}^{m} w_{jk} y_j \right), \qquad k = 1, 2, \ldots, l. \quad (4)$$

2.2. Data Collection and Processing. The experimental data selected in this paper are from the ECG database in Physionet provided by the Massachusetts Institute of Technology, which is the internationally recognized standard ECG database. The experimental data in this paper were collected from two different datasets. Heartbeat waveform of the AF patient was recorded for 80 minutes in the AF Termination Challenge Database and the normal ECG records were obtained from MIT-BIH Arrhythmia Database. Each record has an annotation file associated with it and normal heartbeats dominate the database. To avoid bias in the experimental results, we choose the same number of RR intervals for AF and N records. We divide the data into training sets, validators, and test sets. The validation set is used to determine whether the model has reached sufficient accuracy for a given training set. Without validation procedures, the model may overfit.

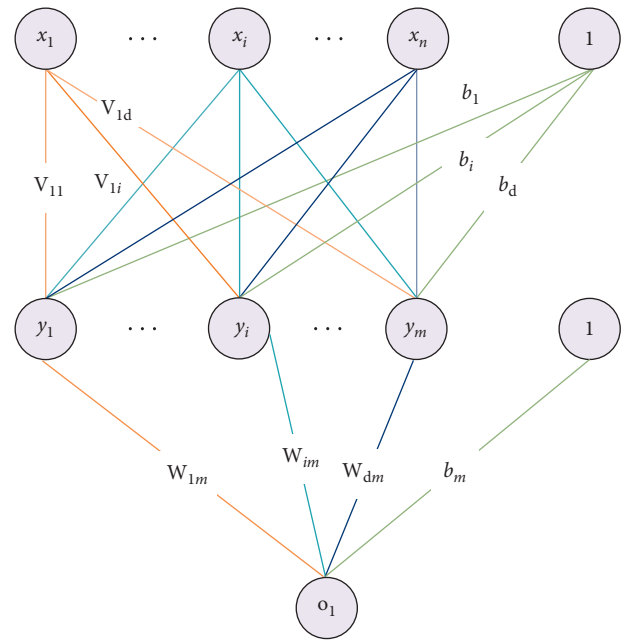

Figure 2: ANN structure diagram for AF detection.

For the deep learning (DL) models, it learn directly from data rather than from previous knowledge, so data processing and analysis are crucial, and functional implementation relies heavily on data. Using the raw ECG signal directly as an input will increase the computational complexity, and it will be affected by the power frequency interference and low-frequency noise, which will also have a great impact on the calculation accuracy. The reason for converting the original ECG record in the database to RR intervals instead of using the raw ECG record directly is that using RR intervals can highlight AF behavior while ensuring reduced computational complexity [12]. Most public ECG datasets have corresponding comments. RR intervals are easy to obtain from R position [17]. We use RR intervals as an input, which is obtained by simple processing of the following equation:

$$RR(n) = R(n+1) - R(n), \quad n = 1, \ldots N - 1, \quad (5)$$

where $RR(n)$ is the change between the nth and $n+1$th R peak and N is the total number of RR intervals.

2.3. The Performance Measures. In order to estimate the performance of the heart rhythm classification, several performance indicators have been used; they are sensitivity, specificity, and accuracy [25]. They are defined as follows:

$$\text{sensitivity} = \frac{\text{TP}}{\text{TP} + \text{FN}} \times 100\%, \quad (6)$$

$$\text{specificity} = \frac{\text{TN}}{\text{TN} + \text{FP}} \times 100\%, \quad (7)$$

$$\text{accuracy} = \frac{\text{TN} + \text{TP}}{\text{TN} + \text{FP} + \text{FN} + \text{TP}} \times 100\%, \quad (8)$$

where TP is true positive, FN is false negative, TN is true negative, and FP is false positive. In general, the best test results are to maximize these four indicators [14].

3. Experiment and Results

3.1. Experiment. This section describes the details in the experiments and results of the network model. Hidden layer neurons in ANN are significant parameters which affect the classification results and greatly affect the performance of the algorithm [25]. In order to find the optimal number of hidden neurons, we put the prepared dataset into the model and tested by sensitivity, specificity, and overall accuracy under the number of hidden layer neurons to achieve better classification results. Through our experiments, we determine the number of hidden layer neurons and set other parameters of the ANN such as learning rate, number of hidden layers, and other parameters as the optimal parameters, as shown in Table 1. Finally, a separate test set was used to verify the classification results of the model. The test set and the training set did not have the same continuous data. The results of this study were analyzed using confusion matrix, error distribution histogram, and ROC curve.

3.2. Results. In this paper, our objective is to use the RR intervals of the ECG signal as the input data to test the classification accuracy in the ANN model. Table 2 shows the accuracy of model output when the input dataset is RR intervals and the number of hidden layer neurons is set as 10, 15, 20, 25, 30, and 35, respectively, under the condition of ANN's optimal parameters. According to these tables, when the input dataset is RR intervals and the number of hidden layer neurons is set to 25, the ANN model could get the highest accuracy rate of 98.3%, sensitivity of 97.4%, and specificity of 99.3%.

Besides, the performance of ANN can be evaluated by a confusion matrix. The confusion matrix is an intuitive analysis table that summarizes the results predicted by the classification model. The calculation outcomes of the confusion matrix in the training set and the test set are shown in Figure 3. The dark part of confounding matrix is the sample number of correct classification, while the light part is the sample number of the wrong classification. In the confusion matrix of training results, we can obtain that the number of TP is 15956, the number of FP is 409, the number of FN is 114, and the number of TN is 15521. The number of TP in test data is 1934, the number of FP is 56, the number of FN is 18, and the number of TN is 1992.

The ROC Curve is often used as an indicator to measure the degree of fitting a model. It calculates a series of true rates and false-positive rates by setting successive variables to different thresholds and then uses the false-positive rate as the ordinate. The ratio is plotted on the abscissa; the larger the area under the curve, the higher the diagnostic accuracy.

Table 1: The parameters of the model.

Parameters	Value
Learning rate initial value	0.01
Number of input layer neurons	10
Number of hidden layer neurons	1
Number of output layer neurons	1

Table 2: Classification accuracy of different number of hidden layer neurons.

The number of hidden layer neurons	Sensitivity (%)	Specificity (%)	Accuracy (%)
10	99.2	96.7	97.9
15	99.2	95.3	97.1
20	99.3	95.6	97.4
25	99.3	97.4	98.3
30	99.1	96.5	97.8
35	99.3	94.1	96.6

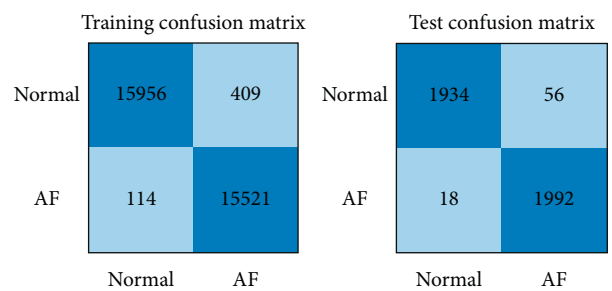

Figure 3: Confusion matrix.

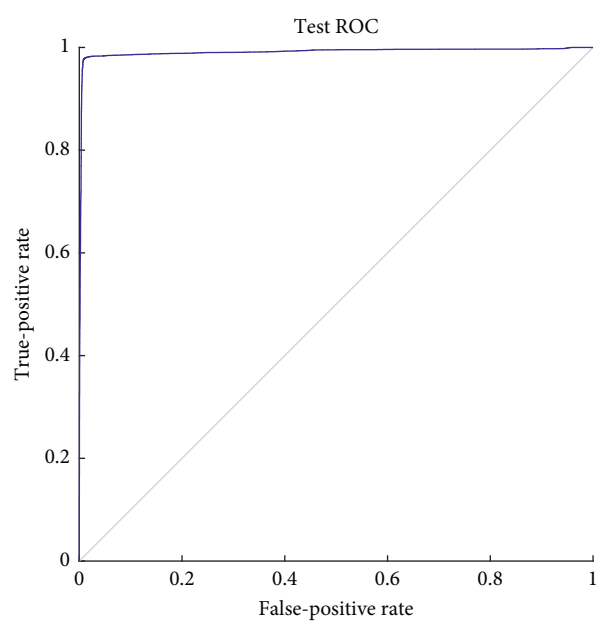

Figure 4: ROC curve.

In other words, the closer the curve is to the ideal value of the upper left corner, the better the model fits. The ROC curve for this experiment is shown in Figure 4. And according to

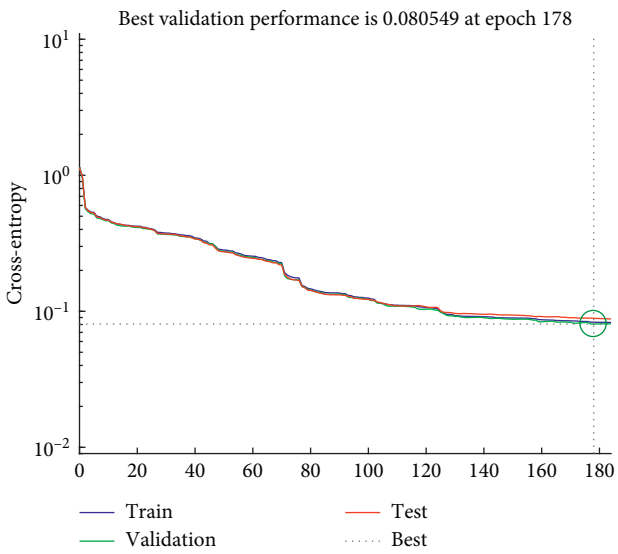

Figure 5: The epochs of stable classification error are 178.

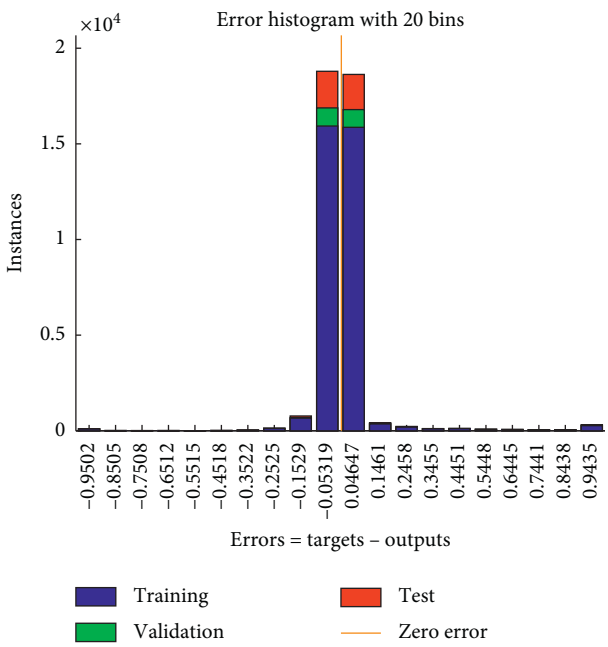

Figure 6: Error histogram.

Figure 5, when the epochs are 178, the classification error tends to be stable.

Figure 6 describes an error distribution histogram, and the horizontal coordinate is the difference value between the target value and the output value. It shows that most of our training data are concentrated in the optimal error that is the zero point, and this indicates a good classification result.

Based on the above discussion, we believe that the accurate results of the AF model based on the RR intervals as the input dataset are better than other methods for the AF classification. Moreover, we can use this model as an appropriate method for detecting AF. Table 3 summarizes the results of other ECG classification methods compared with the ANN model. It illustrates that the accuracy of 97.8% for the proposed RR-based AF classification model is higher than the classification method proposed previously.

Table 3: Selected work on the automated detection of AF beats using ECG signals.

Features	Classifier	Accuracy (%)
RR intervals	LD	72.9
RR intervals	SVM	94.1
RR intervals	CNN	96.58
RR intervals	LSTM	75.66
RR intervals	ANN	98.2

4. Conclusion

This article has conducted in-depth research on the ECG classification algorithm. In view of the characteristics of the ECG, our objective is to use the RR intervals of the ECG signal as the input data to test the classification accuracy in the ANN model. Table 3 shows the accuracy of model output when the input dataset is RR intervals and the number of hidden layer neurons is set as 10, 15, 20, 25, and 30, respectively, under the condition of ANN's optimal parameters. According to this table, when the number of hidden layer neurons is set to 25, the ANN model could get the highest accuracy rate of 98.3%, sensitivity of 99.3%, and specificity of 97.4%.

This computer-aided diagnosis reduces the risk of intervention and helps us make sense of data. This research has some issues that need further consideration and discussion. For instance, all the experiments in this paper are based on simulation software. To improve the practical value of the proposed algorithm, it can be implemented in the actual ECG monitoring system platform. In future work, the selection of network structure and parameters and the construction of features from medical knowledge are worth further research. Monitoring needs to consider more comprehensive features for a higher accuracy rate of classification than before. ANN has great advantages in dealing with fuzzy data and nonlinear data, but it needs to improve in feature extraction. Deep learning and methods for big data can be good alternatives to show great manufacturability in dealing with future work. We plan to increase the number of data for various types of arrhythmia disease classification and consider using other faster and more accurate methods for feature extraction to achieve the classification of different types of arrhythmia diseases.

Data Availability

The data used to support the findings of this study have not been made available because the data also form part of an ongoing study. The original data of the study can be obtained at https://physionet.org/.

Conflicts of Interest

The authors declare that they have no conflicts of interest.

References

[1] S. M. Narayan, M. K. Rodrigo, C. A. Ewski et al., "Ablation of focal impulses and eotational sources: what can Be learned from differing procedural outcomes?" *Current Cardiovascular Risk Reports*, vol. 11, no. 9, p. 27, 2017.

[2] J. Zhao, B. J. Hansen, Y. Wang et al., "Three-dimensional integrated functional, structural, and computational mapping to define the structural fingerprints of heart-specific atrial fibrillation drivers in human heart ex vivo," *Journal of the American Heart Association*, vol. 6, no. 8, Article ID e005922, 2017.

[3] K. H. Humphries, C. R. Kerr, S. J. Connolly et al., "New-onset atrial fibrillation," *Circulation*, vol. 103, no. 19, pp. 2365–2370, 2001.

[4] J.-Y. Le Heuzey, O. Paziaud, O. Piot et al., "Cost of care distribution in atrial fibrillation patients: the COCAF Study," *American Heart Journal*, vol. 147, no. 1, p. 121126, 2004.

[5] S. Stewart, N. Murphy, A. Walker, A. McGuire, and J. McMurray, "Cost of an emerging epidemic: an economic analysis of AF in the UK," *Heart*, vol. 90, no. 3, p. 286292, 2004.

[6] U. R. Acharya, L. O. Shu, Y. Hagiwara et al., "A deep convolutional neural network model to classify heartbeats," *Computers in Biology and Medicine*, vol. 89, pp. 389–396, 2017.

[7] T. Furlan, D. Kosuta, V. Grilj et al., "Treatment of patients with chronic heart failure: does management in heart failure clinic improve adherence to guidelines for the treatment of heart failure," *European Journal of Heart Failure*, vol. 211, no. SI, p. 420, 2019.

[8] T. Thong, J. McNames, M. Aboy, and B. Goldstein, "Prediction of paroxysmal atrial fibrillation by analysis of atrial premature complexes," *IEEE Transactions on Biomedical Engineering*, vol. 51, no. 4, pp. 561–569, 2004.

[9] N. A. Abdul-Kadir, S. N. Mat, and M. A. Othman, "Dynamic ECG features for atrial fibrillation recognition," *Computer Methods and Programs in Biomedicine*, vol. 136, pp. 143–150, 2016.

[10] Z. Xiong, "ECG signal classification for the detection of cardiac arrhythmias using a convolutional recurrent neural network," *Physiological Measurement*, vol. 39, Article ID 0940069, 2018.

[11] R. Guo, "Projective synchronization of a class of chaotic systems by dynamic feedback control method," *Nonlinear Dynamics*, vol. 90, no. 1, p. 5364, 2017.

[12] R. S. Andersen, A. Peimankar, and S. Puthusserypady, "A deep learning approach for real-time detection of atrial fibrillation," *Expert Systems with Applications*, vol. 115, pp. 465–473, 2019.

[13] C. Park, P. Chou, Y. Bai et al., "An ultra-wearable, wireless, low power ECG monitoring system," in *Proceedings of the Biomedical Circuits and Systems Conference IEEE*, pp. 241–244, London, UK, November–December 2006.

[14] R. He, K. Wang, N. Zhao et al., "Automatic detection of AF based on continuous wavelet transform and 2D convolutional neural networks," *Frontiers in Physiology*, vol. 9, no. 1206, 2018.

[15] Z. J. Yao, Z. Y. Zhu, and Y. X. Chen, *AF Detection by Multi-scale Convolutional Neural Networks*, pp. 1159–1164, IEEE, New York, NY, USA, 2017.

[16] C. C. Lin and C. M. Yang, "Heartbeat classification using normalized RR intervals and wavelet features," in *Proceedings of the 2014 International Symposium on Computer*, Consumer and Control, Taichung, Taiwan, June 2014.

[17] G. Swapna, K. P. Soman, and R. Vinayakumar, "Automated detection of cardiac arrhythmia using deep learning techniques," *Procedia Computer Science*, vol. 132, pp. 1192–1201, 2018.

[18] H. Huang, J. Liu, Q. Zhu, R. Wang, and G. Hu, "A new hierarchical method for inter-patient heartbeat classification using random projections and RR intervals," *BioMedical Engineering OnLine*, vol. 13, no. 1, p. 90, 2014.

[19] R. S. Andersen, A. Peimankar, and S. Puthusserypady, "Automatic detection of atrial fibrillation using basic Shannon entropy of RR interval feature," *Journal of Physics*, vol. 795, Article ID 012038, 2017.

[20] R. Hecht-Nielsen, *Theory of the Backpropagation Neural Network. Neural Networks for Perception*, Vol. 6593, Academic Press, Cambridge, MA, USA, 1992.

[21] A. B. Rad, "ECG-based classification of resuscitation cardiac rhythms for retrospective data analysis," *IEEE Transactions on Biomedical Engineering*, vol. 64, no. 10, pp. 2411–2418, 2017.

[22] S. C. Matta, Z. Sankari, and S. Rihana, "Heart rate variability analysis using neural network models for automatic detection of lifestyle activities," *Biomedical Signal Processing and Control*, vol. 42, pp. 145–157, 2018.

[23] J. b. Wang, P. Wang, and S. Wanga, "Automated detection of atrial fibrillation in ECG signals based on wavelet packet transform and correlation function of random process," *Biomedical Signal Processing and Control*, vol. 55, Article ID 101662, 2020.

[24] S. Mondal and P. Choudhary, "Detection of normal and abnormal ECG signal using ANN," *Advances in Intelligent Systems and Computing*, pp. 25–37, 2019.

[25] D. M. W. Powers, "Evaluation: from precision, recall and ffactor to roc, informedness, markedness correlation," *Journal of Machine Learning Technologies*, vol. 2, pp. 37–63, 2011.

Hindawi
Mathematical Problems in Engineering
Volume 2020, Article ID 5393058, 9 pages
https://doi.org/10.1155/2020/5393058

Research Article

Gait Recognition Based on the Feature Extraction of Gabor Filter and Linear Discriminant Analysis and Improved Local Coupled Extreme Learning Machine

Hongli Guo,[1] Bin Li,[1,2,3] Youmei Zhang,[1] Yu Zhang,[1] Wei Li,[1] Fengjuan Qiao,[1] Xuewen Rong,[4] and Shuwang Zhou[2,3]

[1]*School of Mathematics and Statistics, Qilu University of Technology (Shandong Academy of Sciences), Jinan 250353, China*
[2]*Shandong Computer Science Center (National Supercomputer Center in Jinan), Jinan 250041, China*
[3]*Shandong Artificial Intelligence Institute, Jinan 250041, China*
[4]*School of Control Science and Engineering, Shandong University, Jinan 250061, China*

Correspondence should be addressed to Bin Li; ribbenlee@126.com

Received 20 February 2020; Accepted 26 March 2020; Published 25 April 2020

Guest Editor: Yi Qi

A gait energy image contains much gait information, which is one of the most effective means to recognize gait characteristics. The accuracy of gait recognition is greatly affected by covariates, such as the viewing angle, occlusion of clothing, and walking speed. Gait features differ somewhat by angles. Therefore, how to improve the recognition accuracy of a cross-view gait is a challenging task. This study proposes a new gait recognition algorithm structure. A Gabor filter is used to extract gait features from gait energy images, since it can extract features of different directions and scales. We use linear discriminant analysis (LDA) to tackle the problem that the feature dimension restricts the process. Finally, the improved local coupled extreme learning machine based on particle swarm optimization is used for the classification process of the extracted features of the gait. The proposed method and other current mainstream algorithms are compared in terms of the recognition accuracy based on the CASIA-A and CASIA-B datasets, and the simulation results show that the proposed algorithm has good performance and performs well at cross-view gait recognition.

1. Introduction

Identity recognition is a foundation of human social life, and increasing interest in biometrics of recognition algorithms has led to rapid improvements in biometric technologies with better performance. Biometric recognition is identification based on personal physiological or behavioral characteristics [1]. Common biometric recognition technologies include facial, fingerprint, palm print, and iris recognition. Biological patterns and features are usually unique and are impossible to forge or copy [2], so biometric authentication has great advantages over the traditional authentication.

A person's gait, or way of walking, is a complex spatiotemporal biological feature that can be used to distinguish an individual [3], and hence, to realize personal identification [4]. Research [5] shows that the human gait is unique, and it is difficult to fake. We all have the experience of identifying friends and family through gait information. Unlike biometrics, such as the face, fingerprint, and iris, gait sequences can be collected undisturbed at long distances with minimal cooperation [6]. Therefore, gait recognition has the advantages that it requires no contact and is non-invasive. Furthermore, gait is difficult to hide or camouflage [7].

Gait recognition methods can be categorized as model-based [8–10] or appearance-based [11, 12]. Model-based methods construct the gait image to analyze the changes of parameters in the movement process and obtain static or dynamic parameter information of the body, such as height, leg length, swing angle, swing frequency of arms or legs, and

stride length. Lee and Grimson [13] proposed to divide the silhouette of a foreground walking person into seven regions, fit each with an ellipse, and obtain the parameter information as the gait characteristics for classification and recognition. Cunado et al. [14] modeled the leg as two linked pendulums, one being the thigh between the knee and hip and the other the calf between the knee and ankle. They extracted the step length and distance from the hip to the ankle as gait characteristics for identification and classification. Training and test sequences are often selected from gait sequences captured from different angles [15]. The model-based method is difficult as regards model construction, which requires the simulation of gait information. Another problem is the complexity of parameter calculation.

Appearance-based methods focus on the shape of the silhouette or the overall movement of an individual. For example, an appearance-based method analyzes the changes of the contour of a walker over time [16] to obtain spatiotemporal characteristics for gait recognition. Wu et al. [17] proposed a nonnegative matrix factorization (NMF) method to obtain the local structure features of a human body to compensate for the loss of accuracy. A two-dimensional linear discriminant analysis (2DLDA) was proposed to project features into the discriminant space to improve classification. Aggarwal and Vishwakarma [18] proposed a 2D spatiotemporal template to describe gait motion, calculate Zernike moment invariants, and extract features from the spatial distribution of the directional gradient and the new mean method of directional pixels. More and Deore [19] proposed to fuse dynamic and static features for gait recognition, using a cross-wavelet transform to extract dynamic features, and a bipartite graph model to extract static features, followed by normalized feature fusion. In the Bayesian framework, k-means clustering is used for classification and recognition. Appearance-based methods are increasingly popular because they do not require modeling of all or part of the human body, they have low computational complexity, and they are insensitive to the quality of the profile image.

Gait recognition has three steps: target detection, feature extraction, and recognition. Feature extraction plays an important role in the recognition process and directly affects its accuracy. Hence, a suitable feature extraction algorithm is necessary. The Gabor filter is increasingly used in image processing [20]. Biological studies have shown that its expression of frequency and direction is similar to that of the human visual system [21], it can well simulate the sensory field function of single cells in the cerebral cortex, and it is a biomimetic mathematical model. In addition, it can carry out multidirection and multiscale feature extraction. Therefore, we use a Gabor filter with eight directions and five scales to extract features from the gait energy image, and the output of the Gabor filter is the extracted feature of the gait. However, the gait feature dimension increases the computing cost, and high-dimension features contain some redundant information, so it is necessary to reduce the dimension of the data extracted by means of the Gabor filter. For this, we use linear discriminant analysis (LDA), which is a supervised algorithm that can choose the best projection direction of classification performance and enhance the linear separability of data. It is a powerful tool for data dimensionality reduction. An improved local coupled extreme learning machine based on the particle swarm optimization (LC-PSO-ELM) algorithm is used to classify the gait feature and achieve better recognition accuracy. To demonstrate the algorithm's effectiveness, we compare the dimension-reduction method to principal component analysis (PCA), and the proposed method of gait recognition in this paper is compared with the other current mainstream algorithms based on the CASIA-A and CASIA-B benchmark gait databases of the Institute of Automation, Chinese Academy of Sciences. The simulation results show that the proposed method can improve the recognition accuracy of gait and performs well at cross-view gait recognition.

The contributions of this study can be summarized as follows:

(1) An automatic gait recognition structure is proposed

(2) A Gabor filter is used to extract features of the gait energy map, and LDA is used to reduce the feature dimension, thus retaining as much feature information as possible

(3) An improved local coupled extreme learning machine based on the particle swarm optimization (LC-PSO-ELM) algorithm is used to classify the extracted feature of the gait, which can improve the recognition accuracy at cross-view

The rest of this study is arranged as follows: the gait feature extraction method is described in Section 2. Dimension reduction and the recognition method are described in Section 3. Experimental results and discussion are presented in Section 4. Section 5 presents our conclusions.

2. Gait Feature Extraction

Feature extraction is an important step in gait recognition. In this study, a Gabor filter is used to extract gait features from a gait energy image (GEI).

2.1. Gait Energy Image. The GEI is one of the most effective ways to represent gait information [22]. It is the average silhouette of a gait cycle, which is a normalized cumulative energy image in a complete cycle [23]. The random noise of the image sequence in the periodic process is suppressed in the process of averaging the image. The obtained average image is robust and contains rich static and dynamic information. More and more researchers prefer to extract gait features from the GEI [24]. It is defined as

$$GEI(x, y) = \frac{1}{N} \sum_{t=1}^{N} B_t(x, y), \tag{1}$$

where N is the number of frames of the silhouette image in a period and $B_t(x, y)$ is the gait silhouette at the time t. The GEI generation process is shown in Figure 1.

Figure 1: The generation process of gait energy image.

2.2. Gabor Filter. A Gabor function can be used for edge detection in image processing. The two-dimensional Gabor filter can obtain the optimal localization in the spatial and frequency domains, so it can well describe the local structure information of an image corresponding to the spatial scale, spatial location, and direction selectivity. The frequency and direction representation of a Gabor filter are close to those of the human vision system and are often used to represent and describe texture features [25, 26]. We choose the following two-dimensional Gabor kernel form [27]:

$$\psi_{u,v}(z) = \frac{||k_{u,v}||^2}{\sigma^2} e^{-\left(||k_{u,v}||^2||x||^2\right)/2\sigma^2}\left[e^{ik_{u,v^2}} - e^{-\left(\sigma^2/2\right)}\right], \quad (2)$$

where u and v define the direction and scale, respectively, of the Gabor kernel, $z = (x, y)$, $||\cdot||$ represents modulus calculation, $k_{u,v} = k_v e^{i\varphi_u}$, $k_v = k_{\max}/f^v$, and $\varphi_u = \pi u/8$, $k_{\max}$ is the maximum frequency, and f is the distribution coefficient of the kernel function in the frequency domain. In this paper, the Gabor filter is used to extract the features of five scales and eight directions. We set the parameters of formula (2) as $v = \{0, ..., 4\}$, $u = \{0, ..., 7\}$, $\sigma = 2\pi$, $k_{\max} = 0.5\pi$, and $f = \sqrt{2}$. We extract features of gait energy images by a Gabor kernel with 40 directions and scales. The extracted features are represented by a high-dimensional column vector, and high-dimensional gait feature data can be obtained from the output of the Gabor filter.

3. Dimension Reduction and Recognition Methods

The extracted feature of the gait based on the Gabor filter is high-dimensional data, and the character dimension for the classification algorithm is 4400. Therefore, some dimensionality reduction methods should be used to decrease the input complexity of the classification algorithm. In this study, we use LDA for dimension reduction of gait features.

3.1. Linear Discriminant Analysis. LDA is widely used for dimension reduction [28]. This algorithm can produce a reduced sample whose data have the maximum distance between classes and the minimum variance within classes in the new dimension space and the best linear separability. For the n-dimensional feature data, LDA adopts the orthogonal transformation method to obtain m-dimensional new feature data that are unrelated and are beneficial to classification, while minimizing information loss and $m < n$. Considering the classification information of data, the algorithm can make the data easier to identify after dimension reduction. The algorithm selects the axis of the orthogonal transformation in the direction of large data variance. It reduces the correlation of different types of data and causes the transformation result to highlight the differences of feature data [29].

Given the input and output datasets $(x_i, t_i), i = 1, \ldots, L$, where $x_i \in R^n$, $t_i \in R^q$,and L is the number of datasets. Assume that the data matrix is grouped as $C = [C_1, \ldots, C_k]$, where k is the number of classes. Suppose u_{k_i} and $\sum_{k_i}$ are the mean vector and covariance matrix of the class k_i, respectively. Let k_i and k_j be two arbitrary classes in the group of C, the projection of the center of these two classes on a straight line is, respectively, $w^t u_{k_i}$ and $w^t u_{k_j}$, and the covariance of the two types of classes is $w^T \sum_{k_i} w$ and $w^T \sum_{k_j} w$, respectively. The LDA method projects high-dimensional data onto a lower dimensional space by maximizing the interclass variance from different classes and minimizing intraclass variance from the same class simultaneously, thus achieving maximum class discrimination in the dimensionality-reduced space. That is, a matrix $w$is calculated based on the objective function J as follows [30]:

$$J = \frac{||w^T u_{k_i} - w^T u_{k_j}||_2^2}{w^T \sum_{k_i} w + w^T \sum_{k_j} w} = \frac{w^T\left(u_{k_i} - u_{k_j}\right)\left(u_{k_i} - u_{k_j}\right)w}{w^T\left(\sum_{k_i} + w^T \sum_{k_j}\right)w}. \quad (3)$$

The intraclass divergence matrix is defined as follows:

$$S_w = \sum_{k_i} + \sum_{k_j} = \sum_{x \in k_i}\left(x - u_{k_i}\right)\left(x - u_{k_i}\right)^T + \sum_{x \in k_j}\left(x - u_{k_j}\right)\left(x - u_{k_j}\right)^T. \quad (4)$$

The class dispersion matrix is defined as follows:

$$S_b = \left(u_{k_i} - u_{k_j}\right)\left(u_{k_i} - u_{k_j}\right)^T. \quad (5)$$

Therefore, the general form of matrix representation of above objective function (3) can be obtained as follows:

$$J = \frac{\left|w^T S_b w\right|}{\left|w^T S_w w\right|}. \quad (6)$$

3.2. Recognition Method

3.2.1. Extreme Learning Machine. Extreme learning machine (ELM) is a fast learning algorithm that was proposed by Huang in 2006 [31]. Unlike the traditional single-hidden layer neural network, ELM can randomly initialize the input weight and bias and obtain the corresponding output weight. The

calculation is relatively simple, the computational complexity is low, and it has been studied and used by many researchers. In this paper, an improved ELM algorithm based on the local coupled extreme learning machine (LC-ELM) [32] and particle swarm optimization (PSO) is used for gait recognition. We first introduce the basic ELM learning algorithm.

For a single-hidden-layer neural network, suppose there are arbitrary samples (X_i, t_i), $X_i[x_{i1}, x_{i2,...}, x_{ip}]^T \in R^p$, $t_i = [t_{i1}, t_{i2}, ..., t_{iq}] \in R^q$. A neural network with N neurons in a hidden layer can be expressed as follows:

$$O_j = \sum_{i=1}^{N} \beta_i g\left(W_i \cdot X_j + b_i\right), \quad i = 1, ..., N,\ j = 1, 2, ..., M, \tag{7}$$

where $g(x)$ is the activation function, M is the number of the input samples, W_i is the input weight, β_i is the output weight, b_i is the bias of hidden layer neurons, and $W_i \cdot X_j$ is the inner product of W_i and X_j.

The goal of ELM neural network learning is to minimize the output error, which can be expressed as follows:

$$\sum_{j=1}^{M} ||O_j - t_j|| = 0. \tag{8}$$

The above M equations can be written compactly as

$$H\beta = T, \tag{9}$$

where $\beta = [\beta_1, \ldots, \beta_N]^T_{N\times q}$ and $T = [t_1, \ldots, t_N]^T{}_{M\times q}$. H is called the hidden-layer output matrix of the ELM learning algorithm [33].

The training process of ELM learning algorithm is equivalent to finding a least squares solution $\widehat{\beta}$ of the linear system $H\beta = T$, and the above equation can be translated to

$$\widehat{\beta} = H^+ T, \tag{10}$$

where H^+ is the Moore–Penrose generalized inverse of H.

ELM algorithms are implemented by a fully coupled framework between the input layer and hidden layer. This fully coupled structure may incur higher computing costs when ELM has many hidden nodes and higher dimensions of input data.

3.2.2. Improved Extreme Learning Machine. To reduce the amount of computation, Qu [32] proposed LC-ELM, which was to decouple the input layer and the hidden layer based on ELM. Each hidden node is assigned a parameter in an input space [34]. Given a learning sample, the fuzzy membership function is used to measure the distance between the hidden node and the input sample as the activation degree of the hidden node. A fuzzy membership function and similarity relation are used to realize LC-ELM, which can reduce the complexity of the weight search space and improve the generalization performance. LC-ELM can be expressed as follows:

$$f\left(X_j\right) = \sum_{i=1}^{N} \beta_i g\left(W_i \cdot X_j + b_i\right) F\left(S\left(X_j, d_i\right)\right), \quad i = 1, ..., N,\ j = 1, 2, ..., M. \tag{11}$$

In the LC-ELM learning algorithm, the similarity relation $S(X, d_i)$ denotes the distance between the input X and the i-th hidden layer neurons, which is expressed as the address d_i. $F(\cdot)$ is a fuzzy membership function, and there are many choices, such as a Gaussian, sigmoid, or reverse sigmoid function. The underlying radius parameter r is kept in $F(\cdot)$ to adjust the width of the activation area, which is also an optimized parameter, to match the address parameter d_i. Combining the structure of LCFNN with the learning mechanism of ELM, LC-ELM also is a three-step learning algorithm whose network parameters (input weights W, biases b between the input layer and hidden layer, and address d of hidden neurons) are assigned randomly, which is the same as ELM [32].

Compared with ELM, LC-ELM reduces the complexity of the algorithm structure, but its parameters are input randomly, and it may not be optimal, which will affect its performance. We propose a local coupled extreme learning machine based on particle swarm optimization [34] to improve the performance. This algorithm uses a particle swarm optimization strategy to optimize the four parameters (W, b, d, r) in LC-ELM, so as to improve its accuracy and generalization performance.

Therefore, the particles in the searching space of the LC-PSO-ELM are composed of a set by the parameter values of input weights, hidden biases, address, and radius, which can be defined as

$$\theta \in \begin{bmatrix} w_{11}, w_{12}, ..., w_{1L}, w_{21}, w_{22}, ..., w_{2L}, ..., w_{p1}, ..., w_{pL}, ..., b_1, b_2, ..., b_N, \\ d_{11}, d_{12}, ..., d_{1L}, d_{21}, d_{22}, ..., d_{2L}, ..., d_{p1}, d_{p2}, ..., d_{pL}, ..., r_1, r_2, ..., r_L, \end{bmatrix}, \tag{12}$$

where $W = \{W_i | W_i \in R^p,\ i = 1, ..., L\}$, $b \in R^L$, $d = \{d_i | d_i \in R^p, i = 1, 2, .., L\}$, and $r \in R^L$. When the optimal parameters of the local coupled extreme learning machine based on the particle swarm optimization algorithm are established based on formula (12), the weights between the hidden layer and the output layer of the algorithm are determined analytically based on formula (10). The flowchart of the LC-PSO-ELM algorithm is shown in Figure 2.

LC-PSO-ELM improves accuracy and generalization performance, and hence, we use it to recognize and classify gait features after dimension reduction.

4. Experiment and Analysis

To evaluate algorithm performance, we used the CASIA gait database [35] of the Center of Biometrics and Safety Technology, Institute of Automation, Chinese Academy of

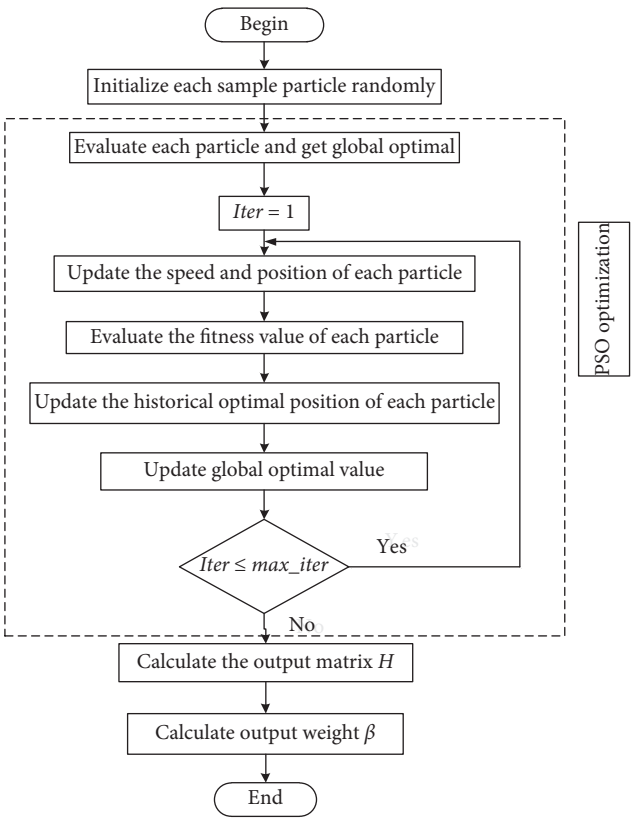

Figure 2: Flow chart of local coupled extreme learning machine based on the particle swarm optimization.

Sciences. We conducted three experiments, identified as A, B, and C, based on the CASIA-A and CASIA-B datasets. Experiment A examined the gait data of 20 subjects from the CASIA-A database. Each tester had 12 gait sequences with angles of 0°, 45°, and 90°. There was no angle discrimination. The gait data from all perspectives were examined together and were divided into training and testing sets at a 7 : 3 ratio. This small volume of experimental data was used to verify the superiority of the proposed algorithm. The experimental results are shown in Table 1.

The normal sequences in CASIA-B were used in experiment B. The database contained 124 gait sequences. The data volume was large, and there were many cross angles (0°, 18°, ..., 162°, 180°). We did not consider cross view in this experiment. The results are shown in Table 2.

The normal sequences in CASIA-B were also used in experiment C, which mainly considered the influence of cross view. The difference between the training and test sets was 18 degrees. The results are shown in Table 3. The average results of six trials with different training and test sets are shown.

4.1. Experimental Details. First, we compare the performance of the ELM and LC-PSO-ELM learning algorithms based on the gait data, as shown in Table 4. We selected the sigmoid function as the activation function for the two algorithms. The wave kernel $S(x, y) = (\theta/||x - y||)\sin(||x - y||/\theta)$ was selected as the similarity function. The population size NP was set at 200, the maximum iteration time was 50, and the other control parameters are listed in Table 5.

Table 1: Performance comparison of ELM and LC-PSO-ELM based on dimensional reduction methods of PCA or LDA on the CASIA-A dataset.

Algorithm	Training accuracy (%)	Testing accuracy (%)
ELM + PCA	99.76	93.10
LC-PSO-ELM + PCA	98.77	**93.52**
ELM + LDA	98.35	97.82
LC-PSO-ELM + LDA	98.67	**98.24**

Table 2: Comparison of gait recognition results on the CASIA-A dataset.

Algorithm	Recognition rate (%)
Liu et al. [4]	97.38
Chai [36]	92.25
Proposed method	**98.24**

Because the performance of ELM and LC-PSO-ELM is greatly influenced by hidden neurons, it is necessary to determine the number of these to ensure better classification performance. The experiment was performed by gradually increasing the number of hidden neurons, and the test results were recorded separately. The number of hidden neurons corresponding to the best classification result was identified as the best number for the algorithm. To show the superiority of the proposed method, we ran simulations with the dimension reduction and classification methods. The curve of the experimental results with the number of neurons in the hidden layer is shown in Figure 3. For each curve, the red curve represents the training accuracy, and the blue curve is the test accuracy.

Figure 3 including four subgraphs of Figures 3(a)–3(d) shows accuracy results of dimension reduction using the ELM algorithm with PCA and LDA, respectively. As is known, PCA is also a common dimensionality reduction method. Different from LDA, PCA is unsupervised. It neglects the classification information and only ensures that the internal information of data is maximized after dimension reduction. In the experiments, the input dimension of data based on the LDA method is 123, and the input dimension of data based on the PCA method is 240 in the classification method, respectively.

Subgraphs of Figures 3(c) and 3(d), respectively, represent the accuracy results of classification using LC-PSO-ELM after dimensionality reduction by the two methods. The accuracy increases with the number of neurons in the hidden layer and then tends to stabilize. The best number of hidden layer neurons differs by an algorithm. Fewer hidden layer neurons are needed for gait recognition from data after dimension reduction by LDA. Comparing Figure 3, the number of hidden layer neurons corresponding to the best classification results in subgraphs of Figures 3(b) and 3(d) is

Table 3: Performance comparison of different gait recognition methods on the CASIA-B dataset.

Algorithm	View											Average
	0°	18°	36°	54°	72°	90°	108°	126°	144°	162°	180°	
[37]	90.52	88.31	84.91	87.93	88.79	87.93	92.24	90.09	87.5	86.64	89.66	88.59
[38]	88.13	87.43	90.21	93.43	94.17	91.54	92.51	93.00	93.38	88.92	90.00	91.12
[39]	90.8	97.9	99.4	96.9	93.6	91.7	95	97.80	98.9	96.8	85.8	95
[40]	96.30	**98.20**	**98.50**	95.40	94.30	**99.90**	**98.60**	97	97.40	99.20	96.10	97.35
Ours	**99.47**	97.16	98.21	**99.08**	**98.28**	98.80	97.31	**98.99**	**99.48**	**99.09**	**99.40**	**98.66**

Table 4: Parameter configuration of ELM and LC-PSO-ELM learning algorithms.

Configurations	ELM	LC-PSO-ELM
Input weight and hidden layer biases	RN in [−1, 1]	NDRN (normally distributed random numbers)
Activation function	Sigmoid	Sigmoid
Hidden node address and window radius	—	NDRN
Similarity	—	Wave kernel
Fuzzy membership function	—	$F(x) = \frac{2}{1+\exp(x/r)}$

Table 5: Control parameters used in the LC-PSO-ELM learning algorithm.

Algorithm	$w_{\max}$	$w_{\min}$	$c_{\max}$	$c_{\min}$	c_1	c_2
LC-PSO-ELM	0.9	0.4	2.5	0.5	2	2

9 and 6, respectively, which means that LDA is more conducive to dimension reduction classification. After using the same method for data dimensionality reduction, LC-PSO-ELM needs fewer hidden neurons to obtain the best classification results. In addition, it is obvious that in subgraphs of Figures 3(c) and 3(d), fewer hidden neurons are needed to obtain the best classification results, about 145 and 6, respectively.

Compared with the traditional ELM algorithm, LC-PSO-ELM can simplify the algorithm structure, optimize the parameters of the neural networks, reduce the influence of random input parameters, and improve classification performance. The subgraph of Figure 3(d) shows the best classification performance being obtained most quickly, and the combination of LDA dimension reduction and LC-PSO-ELM classification can obtain higher recognition accuracy, which has certain advantages.

Therefore, as shown in Table 6 in the experiments of simulations, in pursuit of better generalization performance of different algorithms, the hidden neurons of ELM learning algorithm based on dimensional reduction methods of PCA or LDA are 275 and 10 in CASIA-A dataset, respectively, While the hidden neurons of the LC-PSO-ELM learning algorithm are 140 and 8, respectively. In the CASIA-B dataset with and without considering influence of cross view, the hidden neurons of the LC-PSO-ELM learning algorithm based on LDA are between 8 and 25 for increasing the generalization performance of different cross angles (0°, 18°, ..., 162°, 180°).

4.2. Experimental Results. Performance comparison between the ELM learning algorithm and the LC-PSO-ELM learning algorithm based on different dimensional reduction methods of PCA or LDA on the CASIA-A dataset is illustrated in Table 1. The recognition accuracies of ELM and LC-PSO-ELM based on LDA are 97.82% and 98.24%, while the algorithms based on PCA are 93.10% and 93.52%, respectively, which shows that the LDA for data dimensionality reduction is more conducive to classification.

Compared with ELM, the LC-PSO-ELM algorithm obtains higher recognition accuracy, demonstrating that LC-PSO-ELM has better classification performance with a compact network configuration of fewer hidden neurons.

In Table 2, the proposed method of LC-PSO-ELM based on the LDA dimensional reduction method and two other algorithms of the references of [4, 36] are compared based on the recognition accuracy of testing process on the CASIA-A datasets. The proposed algorithm structure achieves the highest recognition accuracy of 98.24%, which is, respectively, 5.9% and 0.86% greater than the existing algorithms of references of [4, 36], with 92.25% and 97.38%. The proposed algorithm structure has a certain effectiveness and superiority for gait recognition.

To demonstrate the superior performance of the proposed algorithm, Table 3 compares it to state-of-the-art methods based on gait recognition accuracy on the CASIA-B datasets. The algorithm achieves almost all the best classification accuracy results. Among the compared methods, Binsaadoon and El-Alfy [37] used the FLGBP method, with 88.59% average accuracy of gait recognition in 11 views. Zhang et al. [38] used the KPCA-LPP method and achieved 91.12% average gait recognition accuracy. Chao et al. [39] achieved 95% average gait recognition accuracy using the method of regarding the gait as a set. Wolf et al. [40] used the 3DCNN method with average gait recognition accuracy of 97.35%. The proposed algorithm improved the average gait recognition accuracy by 10.07%, 7.54%, 3.66%, and 1.31%, respectively, over the studies of Binsaadoon, Zhang, Chao, and Wolf.

In recent years, Yu et al. [41] proposed a gait recognition framework that is more sensitive to the perspective drawing of a walking gait, which caused the recognition accuracy to differ greatly, with an average

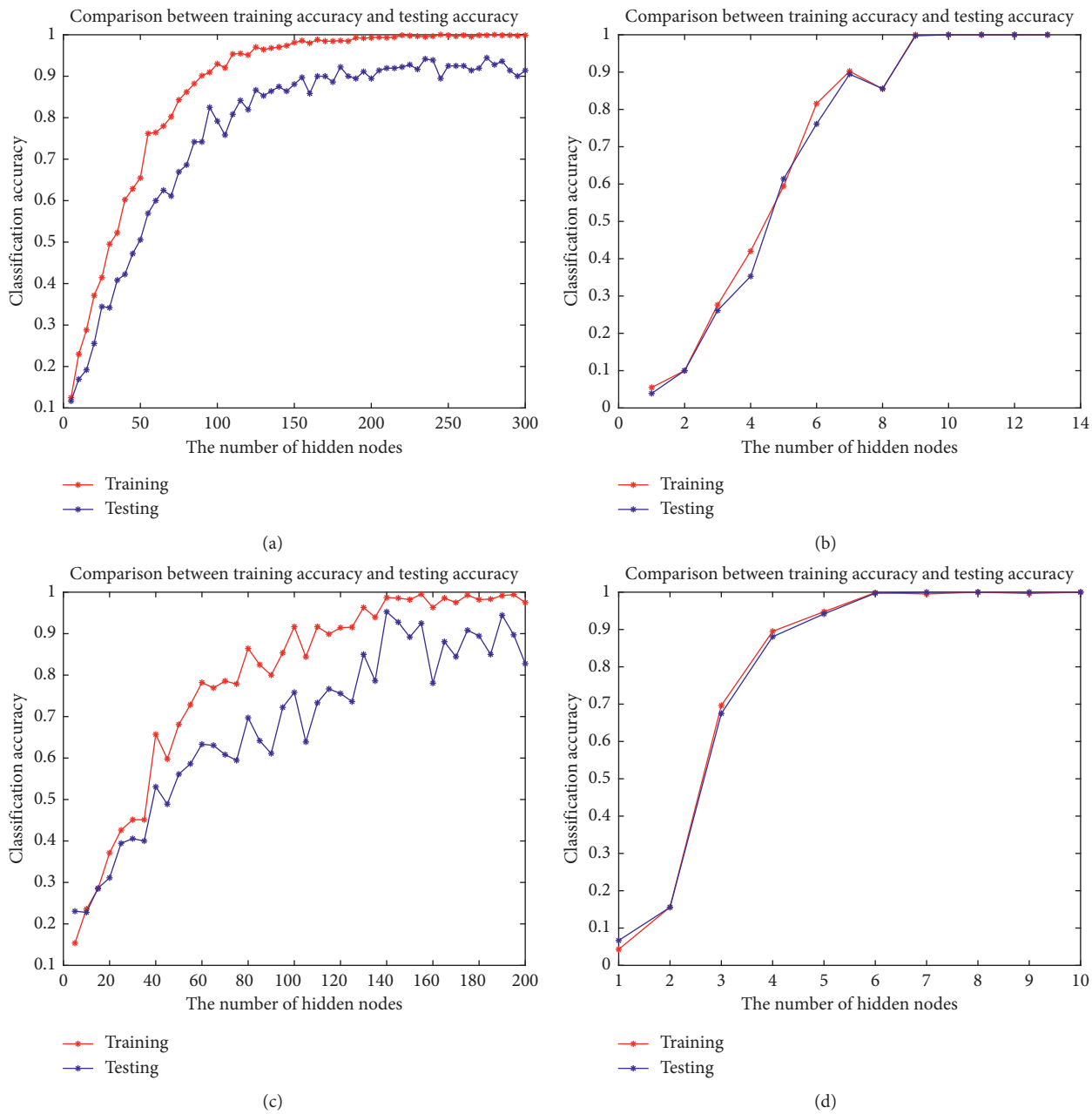

Figure 3: Generalization performance curves for ELM and LC-PSO-ELM algorithms with different dimensional reduction methods. (a) ELM for PCA dimension reduction data. (b) ELM for LDA dimension reduction data. (c) LC-PSO-ELM for PCA dimension reduction data. (d) LC-PSO-ELM for LDA dimension reduction data.

Table 6: Number of hidden neurons of different algorithms on CASIA problem.

Dataset algorithms	CASIA-A	CASIA-B	CASIA-B considering influence of cross view
ELM + PCA	**275**		
LC-PSO-ELM + PCA	**140**		
ELM + LDA	**10**		
LC-PSO-ELM + LDA	**8**	**8–25**	**8–25**

recognition rate of 38.53%. Wang et al. [42] proposed a method based on multiview gait sequence fusion, with an average gait recognition accuracy of 88.75%. Wang et al. [43] used the TS-GAN method and achieved 88.1% average gait recognition accuracy. The results of the CASIA-B dataset with considering influence of cross view are shown in Table 7 based on the proposed method and the above gait recognition approaches.

Table 7: Performance comparison of different gait recognition methods on the CASIA-B dataset with considering influence of cross view.

Algorithm	View										Training testing	Average
	0° 18°	18° 36°	36° 54°	54° 72°	72° 90°	90° 108°	108° 126°	126° 144°	144° 162°	162° 180°		
[41]	31.9	39.9	28.8	23.0	81.5	82.3	37.1	26.6	5.6	28.6	—	38.53
[42]	84.69	87.84	88.66	91.92	91.95	90.04	88.20	88.50	89.56	86.25	—	88.75
[43]	86	95	89	88	88	93	89	**96**	84	73	—	88.1
Ours	**95.18**	**97.81**	**96.44**	**95.23**	**94.60**	**95.79**	**95.82**	95.48	**95.81**	**95.83**	—	**95.80**

Compared with the above methods, the proposed algorithm improved the average gait recognition accuracy by 57.27%, 7.05%, and 7.7%, respectively. The highest recognition accuracy was 99.48%, the lowest was 97.16%, and hence, there is little difference between the highest and lowest accuracy. The proposed algorithm attained almost all of the best classification accuracy figures from different views.

In conclusion, in this paper, a gait recognition method based on LC-PSO-ELM and the LDA dimensional reduction method is proposed and the performance is compared with some gait recognition methods on the CASIA dataset with and without considering influence of cross view. Table 2 shows results under the same view, while Tables 3 and 7 are under different views. The proposed algorithm has good recognition accuracy of gait and can be effectively applied to gait recognition. In particular, Table 7 shows that cross-view gait recognition based on the proposed method also has high accuracy. The proposed algorithm can effectively avoid the impact of different views on gait recognition.

5. Conclusions

As a promising biometric technology, gait recognition has attracted wide attention. We used a Gabor filter to extract multidirectional and multiscale features from gait energy images. Linear discriminant analysis was used to reduce the dimensionality of feature data. The improved extreme learning machine algorithm was used for recognition and classification. We conducted experiments on the CASIA datasets, and the results demonstrate the effectiveness of the proposed method. The algorithm has low complexity and good generalization performance. However, this study does not consider the influence of covariate factors, such as clothes and bags, as well as that of cross view, where the angle difference is more obvious. Hence, subsequent research will focus on recognition and classification under cross view and covariate factors.

Data Availability

The data used to support the findings of this research are included in the article. Further data and codes generated or used during the study can be obtained from the corresponding author upon request.

Conflicts of Interest

The authors declare that there are no conflicts of interest regarding the publication of this paper.

Acknowledgments

This work was supported by the National Natural Science Foundation of China (grant no. 61973185 and 61773226), the Development Plan of the Young Innovation Team in Colleges and Universities of Shandong Province (grant no. 2019KJN011), the Shandong Province Key Research and Development Program (grant no. 2018GGX103054), and the Young Doctor Cooperation Foundation of Qilu University of Technology (Shandong Academy of Sciences) (grant no. 2018BSHZ2008).

References

[1] Q. H. Xiao, "Technology review-biometrics-technology, application, challenge, and computational intelligence solutions," *IEEE Computational Intelligence Magazine*, vol. 2, no. 2, pp. 5–25, 2007.

[2] A. K. Jain, A. Ross, and S. Prabhakar, "An introduction to biometric recognition," *IEEE Transactions on Circuits and Systems for Video Technology*, vol. 14, no. 1, pp. 4–20, 2004.

[3] H. Arshad, M. A. Khan, and M. Sharif, "Multi-level features fusion and selection for human gait recognition: an optimized framework of Bayesian model and binomial distribution," *International Journal of Machine Learning and Cybernetics*, vol. 10, no. 6, pp. 3601–3618, 2019.

[4] Z. Y. Liu, G. Yang, and G. C. Feng, "Gait recognition based on gabor wavelet and local binary pattern," *Zhongshan Daxue Xuebao/Acta Scientiarum Natralium Universitatis Sunyatseni*, vol. 53, no. 4, pp. 1–7, 2014.

[5] S. Tao, X. Zhang, H. Cai, Z. Lv, C. Hu, and H. Xie, "Gait based biometric personal authentication by using MEMS inertial sensors," *Journal of Ambient Intelligence and Humanized Computing*, vol. 9, no. 5, pp. 1705–1712, 2018.

[6] H. El-Alfy, I. Mitsugami, and Y. Yagi, "Gait recognition based on normal distance maps," *IEEE Transactions on Cybernetics*, vol. 48, no. 5, pp. 1526–1539, 2018.

[7] Z. Zhang, M. Hu, and Y. Wang, "A survey of advances in biometric gait recognition," in *Biometric Recognition*, pp. 150–158, Springer, 2011.

[8] L. Wang, H. Ning, T. Tan, and W. Hu, "Fusion of static and dynamic body biometrics for gait recognition," *IEEE Transactions on Circuits and Systems for Video Technology*, vol. 14, no. 2, pp. 149–158, 2003.

[9] R. Tanawongsuwan and A. Bobick, "Gait recognition from time-normalized joint-angle trajectories in the walking plane," in *Proceedings of the 2001 IEEE Computer Society Conference on Computer Vision and Pattern Recognition*, pp. 726–731, Kauai, HI, USA, December 2001.

[10] F. Tafazzoli and R. Safabakhsh, "Model-based human gait recognition using leg and arm movements," *Engineering*

Applications of Artificial Intelligence, vol. 23, no. 8, pp. 1237–1246, 2010.

[11] J. Han and B. Bhanu, "Individual recognition using gait energy image," *IEEE Transactions on Pattern Analysis and Machine Intelligence*, vol. 28, no. 2, pp. 316–322, 2006.

[12] S. Yu, L. Wang, W. Hu, and T. Tan, "Gait analysis for human identification in frequency domain," in *Proceedings of the Third International Conference on Image and Graphics*, pp. 282–285, Hong Kong, China, December 2004.

[13] L. Lee and W. E. L. Grimson, "Gait analysis for recognition and classification," in *Proceedings of the IEEE Conference on Face & Gesture Recognition*, pp. 1–8, Washington, DC, USA, August 2002.

[14] D. Cunado, M. S. Nixon, and J. N. Carter, "Using gait as a biometric, via phase-weighted magnitude spectra," in *Proceedings of International Conference on Audio- and Video-Based Biometric Person Authentication*, pp. 93–102, Crans-Montana, Switzerland, March 1997.

[15] N. V. Boulgouris, D. Hatzinakos, and K. N. Plataniotis, "Gait recognition: a challenging signal processing technology for biometric identification," *IEEE Signal Processing Magazine*, vol. 22, no. 6, pp. 78–90, 2005.

[16] S. A. Niyogi and E. H. Adelson, "Analyzing and recognizing walking figures in XYT,," in *Proceedings of IEEE Conference on Computer Vision and Pattern Recognition*, pp. 469–474, Seattle, WA, USA, June 1994.

[17] C. Wu, Y. Song, and Y. Zhang, "Multi-view gait recognition using NMF and 2DLDA," *Multimedia Tools and Applications*, vol. 78, no. 24, pp. 35789–35811, 2019.

[18] H. Aggarwal and D. K. Vishwakarma, "Covariate conscious approach for gait recognition based upon zernike moment invariants," *IEEE Transactions on Cognitive and Developmental Systems*, vol. 10, no. 2, pp. 397–407, 2018.

[19] S. A. More and P. J. Deore, "Gait recognition by cross wavelet transform and graph model," *IEEE/CAA Journal of Automatica Sinica*, vol. 5, no. 3, pp. 718–726, 2018.

[20] A. O. Lishani, L. Boubchir, E. Khalifa, and A. Bouridane, "Gabor filter bank-based GEI features for human gait recognition," in *Proceedings of 39th International Conference on Telecommunications and Signal*, pp. 648–651, Vienna, Austria, June 2016.

[21] S. Gupta, J. Jaafar, and W. F. W. Ahmad, "Static hand gesture recognition using local gabor filter," *Procedia Engineering*, vol. 41, pp. 827–832, 2012.

[22] J. Liu and N. Zheng, "Gait history image: a novel temporal template for gait recognition," in *Proceedings of 2007 IEEE International Conference on Multimedia*, pp. 663–666, Beijing, China, July 2007.

[23] A. Roy, S. Sural, and J. Mukherjee, "Gait recognition using pose kinematics and pose energy image," *Signal Processing*, vol. 92, no. 3, pp. 780–792, 2012.

[24] L. Chao, L. Y. Jia, and D. C. Shi, "Identity recognition algorithm using improved gabor feature selection of gait energy image," *Journal of Physics: Conference Series*, vol. 787, no. 1, pp. 1–6, 2017.

[25] Z. Zhang, X. Yu, F. You, G. Siedel, W. He, and L. Yang, "A front vehicle detection algorithm for intelligent vehicle based on improved gabor filter and SVM," *Recent Patents on Computer Science*, vol. 8, no. 1, pp. 32–40, 2015.

[26] S. Khan, M. Hussain, H. Aboalsamh, and G. Bebis, "A comparison of different Gabor feature extraction approaches for mass classification in mammography," *Multimedia Tools and Applications*, vol. 76, no. 1, pp. 33–57, 2015.

[27] D. Tao, X. Li, X. Wu, and S. J. Maybank, "General tensor discriminant analysis and gabor features for gait recognition," *IEEE Transactions on Pattern Analysis and Machine Intelligence*, vol. 29, no. 10, pp. 1700–1715, 2007.

[28] Z.-T. Liu, Q. Xie, M. Wu, W.-H. Cao, Y. Mei, and J.-W. Mao, "Speech emotion recognition based on an improved brain emotion learning model," *Neurocomputing*, vol. 309, pp. 145–156, 2018.

[29] S. Ji and J. Ye, "Generalized Linear Discriminant Analysis: a unified framework and efficient model selection," *IEEE Transactions on Neural Networks*, vol. 19, no. 10, pp. 1768–1782, 2008.

[30] X. Huang and N. V. Boulgouris, "Gait recognition with shifted energy image and structural feature extraction," *IEEE Transactions on Image Processing*, vol. 21, no. 4, pp. 2256–2268, 2012.

[31] G. B. Huang, Q. Y. Zhu, and C. K. Siew, "Extreme learning machine: theory and applications," *Neurocomputing*, vol. 70, no. 1–3, pp. 489–501, 2006.

[32] Y. Qu, "Local coupled extreme learning machine," *Neural Computing and Applications*, vol. 27, no. 1, pp. 27–33, 2016.

[33] B. Li, Y. B. Li, and X. W. Rong, "The extreme learning machine learning algorithm with tunable activation function," *Neural Computing and Applications*, vol. 22, no. 3-4, pp. 531–539, 2012.

[34] H. Guo, B. Li, W. Li, F. Qiao, X. Rong, and Y. Li, "Local coupled extreme learning machine based on particle swarm optimization," *Algorithms*, vol. 11, no. 11, p. 174, 2018.

[35] Data Sources [Online]: http://www.cbsr.ia.ac.cn/china/Gait%20Databases%20CH.asp.

[36] B. C. Chai, "Gait recognition method based on mobile pendulum," *Journal of Zhejiang Wanli University*, vol. 23, pp. 91–95, 2010.

[37] A. G. Binsaadoon and E.-S. M. El-Alfy, "Improved method for gait representation and recognition," in *Proceedings of World Symposium on Computer Applications & Research,*, pp. 59–64, Cairo, Egypt, March 2016.

[38] W. H. Zhang, M. Zhang, and W. Fan, "Multi-view gait recognition method based on dynamic and static feature fusion," in *Proceedings of International Conference on Sensor Networks and Signal Processing*, pp. 287–291, Xi'an, China, October 2018.

[39] H. Chao, Y. He, J. Zhang, and J. Feng, "GaitSet: regarding gait as a set for cross-view gait recognition," *Proceedings of the Thirty-Third AAAI Conference on Artificial Intelligence*, vol. 33, pp. 8126–8133, 2019.

[40] T. Wolf, M. Babaee, and G. Rigoll, "Multi-view gait recognition using 3D convolutional neural networks," in *Proceedings of 2016 IEEE International Conference on Image Processing*, pp. 4165–4169, Phoenix, AZ, USA, September 2016.

[41] S. Yu, D. Tan, and T. Tan, "A framework for evaluating the effect of view angle, clothing and carrying condition on gait recognition," in *Proceedings of 18th International Conference on Pattern Recognition*, pp. 4165–4169, Hong Kong, China, August 2006.

[42] Y. Wang, S. Yu, Y. Wang, and T. Tan, "Gait recognition based on fusion of multi-view gait sequences," in *Advances in Biometrics*, pp. 605–611, Springer, 2005.

[43] Y. Wang, C. Song, Y. Huang, Z. Wang, and L. Wang, "Learning view invariant gait features with two-stream GAN," *Neurocomputing*, vol. 339, pp. 245–254, 2019.

Hindawi
Mathematical Problems in Engineering
Volume 2020, Article ID 7617010, 11 pages
https://doi.org/10.1155/2020/7617010

Research Article

Development of a Novel Soft Sensor with Long Short-Term Memory Network and Normalized Mutual Information Feature Selection

Dongfeng Li,[1] Zhirui Li,[2] and Kai Sun [3]

[1]*Shandong Experimental High School, Jinan 250001, China*
[2]*School of Microelectronics, Shandong University, Jinan 250001, China*
[3]*School of Electrical Engineering and Automation, Qilu University of Technology (Shandong Academy of Sciences), Jinan 250353, China*

Correspondence should be addressed to Kai Sun; sunkai79@qlu.edu.cn

Received 1 February 2020; Accepted 21 February 2020; Published 25 April 2020

Guest Editor: Ping Zhao

In this paper, a novel soft sensor is developed by combining long short-term memory (LSTM) network with normalized mutual information feature selection (NMIFS). In the proposed algorithm, LSTM is designed to handle time series with high nonlinearity and dynamics of industrial processes. NMIFS is conducted to perform the input variable selection for LSTM to simplify the excessive complexity of the model. The developed soft sensor combines the excellent dynamic modelling of LSTM and precise variable selection of NMIFS. Simulations on two actual production datasets are used to demonstrate the performance of the proposed algorithm. The developed soft sensor could precisely predict the objective variables and has better performance than other methods.

1. Introduction

Due to technological constraints, sensor characteristics, environmental factors, etc., many variables cannot be measured or the measurement frequency is very low in actual industrial processes. Soft measurement provides an excellent solution to construct mathematical models from easily measured variables to hard ones [1–3]. Neural networks (NNs) are advanced methods that can precisely model complex and nonlinear system and therefore have been widely used in soft sensors [4–6]. Heidari et al. [7] developed a new multi-layer perceptron (MLP) network to estimate nanofluid relative viscosity, which are more accurate than other NN structures. Sheela and Deepa [8] designed a synthesized model by combining self-organizing maps (SOMs) with MLP and then applied it to forecast the wind speed of a renewable energy process. He et al. [9] developed an auto-associative hierarchical NN for a soft sensor of chemical processes, and its application to a purified terephthalic acid solvent process demonstrated the effectiveness of the algorithm. Zabadaj et al. [10] proposed an effective soft sensor for the supervisory control of biotransformation production, and the efficiency of the approach was demonstrated. Rehrla et al. [11] developed a soft sensor method for estimating the active pharmaceutical ingredient concentration from the system data and the soft sensor model was tested in the three different continuous production lines. A novel approach of supervised latent factor analysis was proposed based on system data regression modelling, which can effectively predict heterogeneous variances, and soft sensors are established for quality estimate in the two case studies [12].

However, industrial systems are intrinsic complex and have high temporal correlations between dataset samples. That is, process data are time series with strong nonlinearities and dynamics, which increases the difficulty of modelling with conventional NNs. Recently, a powerful type of NN named long short-term memory (LSTM) was

designed to handle sequence dependence [13–15]. An LSTM network is more significant in learning long-term temporal dependencies since its memory cells can maintain its state over a long time and standardize the information moving into and out of the cell. Therefore, LSTM networks have been effectively used in many different fields, such as precipitation nowcasting [16], traffic forecasting [17], human action recognition [18], etc. Due to its advantages, LSTM has also been applied in soft sensor development in industrial processes. Yuan et al. developed a supervised LSTM network for a soft sensor and demonstrated the superiority of the proposed soft sensor by two actual industrial datasets [19]. Sun proposed a new LSTM network by combining unsupervised feature selection and supervised dynamic modelling methods for a soft sensor and validated the network by a practical CO_2 absorption column [20].

The rapid evolution of distributed control systems (DCSs) presents us a lot of data, but also another trouble in nonlinear soft sensing: excessive input variables. If the NN was trained with excessive input variables, the amount of calculations will increase and more computing power is required. In the meantime, the prediction accuracy of the NN is worsened due to extraneous variables creating additional noise in the dataset. Hence, many researchers have focused on the efficiency of variable selection approaches for soft sensors [21–23]. In recent years, mutual information (MI)-based variable selection approaches have been widely studied due to their efficacy and ease of realization [24]. Hanchuan et al. [25] proposed a minimal redundancy maximal correlation criterion to reduce redundancy and apply primitive methods of relevance and redundancy to select significant input variables. Estevez et al. [26] proposed an enhanced version of MIFS and minimal redundancy maximal correlation that imported the normalized MI as an evaluation of redundancy. The developed NMIFS algorithm showed better performance by compensating for the MI partial to multiple features and limiting its setpoint range [0, 1].

This paper develops a new soft sensor algorithm by combining LSTM with NMIFS, in which the NMIFS is used to compress input variables of LSTM. The primary contributions of the paper are summarized as follows:

(1) A novel feature selection approach for LSTM with NMIFS is designed. The developed method can effectively reduce the excessive complexity caused by redundant candidate variables and then improve the modelling performance of LSTM.

(2) The developed soft sensor algorithm is implemented in two practical industrial processes.

(3) Comparative simulation results demonstrate that the developed soft sensor model has better performance and flexibility in performing feedback control.

This paper is arranged as follows: Section 2 presents background theories of the NMIFS and LSTM, and Section 3 describes the development of the presented approach. Section 4 presents the simulation results and an analysis of the developed soft sensor with datasets of actual processes. Some conclusions are given in Section 5.

2. Theoretical Overview

2.1. Input Variable Selection Techniques. The existence of redundant input variables in the training of the NN often complicates the model, deteriorates the accuracy, and even brings about overfitting. The goal of the input variable feature selection (IVFS) is to exactly select n variables from the initial candidate variable set C as the input variable set S in the modelling, where C includes multifarious input variables of the algorithm. During variable selection, variables that have less influence on target variable will be deleted from S.

The IVFS algorithm can be applied in a variety of means: (1) sequential forward selection, selecting an input from C to join S every time until the prediction accuracy of the model is no longer improved; (2) sequential backward selection, where S initially includes all input variables and input variables are deleted one at a time until the model performance is no longer improved; or (3) global optimization, which finds the optimal solution among all the variable selection approaches.

It can be demonstrated that if there are m candidate variables in C, the selection of the m input variables results in $(2^m - 1)$ subsets in total. S is hard to be found with large number of candidate variables. Based on this consideration, a statistical indicator to calculate the extent of dependence between input and output variables is selected, and then the input variable before modelling with NNs is selected. This method of separating variable selection procedures from model calibration procedures can produce a more efficient IVFS algorithm, and the resulting S has wider applicability to different NN algorithms. It is worth noting that the effectiveness of the IVFS approach is based on the statistical standard applied.

MI is considered as an excellent evaluation standard because it is a random measure and does not make assumptions about the structure of the dependencies between variables. MI is also found to be impervious to data transformations and noise.

2.2. Normalized Mutual Information. Suppose that there are two random variables X and Y, where X is the input variable and the output variable Y depends on X. The definition of MI of $I(X;Y)$ for a continuous variable can be shown as follows [27]:

$$I(X;Y) = \iint p(X,Y)\log\frac{p(X,Y)}{p(X)p(Y)}\,\mathrm{d}X\mathrm{d}Y, \tag{1}$$

where $p(X,Y)$ is the joint probability density function (PDF) of two variables and $p(X)$ and $p(Y)$ are the marginal PDFs of X and Y. Figure 1 shows the entropy of X and Y and its relationship to their MI, in which $H(X)$ and $H(Y)$ are entropies, and $H(X\mid Y)$ and $H(Y\mid X)$ are conditional entropies, respectively.

Generally speaking, MI has three basic attributes:

(1) Symmetry: $I(X;Y) = I(Y;X)$. The quantity of information abstracted from Y about X is equal to that

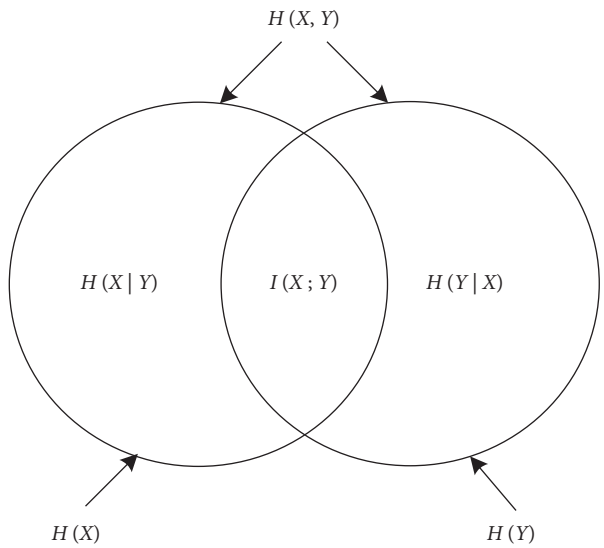

Figure 1: Structure diagram of entropy and MI.

from X about Y. The only difference is the angle of the observer.

(2) Positive: $I(X;Y) \geq 0$. Extracting information about one event from another, the worst case is zero information ($I(X;Y) = 0$). Being aware of one event does not strengthen the uncertainty of another.

(3) Extremum: $I(X;Y) \leq H(X)$, $I(Y;X) \leq H(Y)$. The quantity of information abstracted from one case about another is at maximum same as the entropy of the other case, rather than exceeding the amount of information contained by the other event itself.

The MI $I(X;Y)$ provides dependencies for X and Y measurements and provides reference information for variable selection algorithms, which makes the computation of MI a crucial procedure in MI-based input variable selection approaches [28, 29]. However, the mathematical expression form of the PDF in equation (1) is unconscious in practical problems. A variety of approximate prediction algorithms of MI have been extensively researched to analyze PDFs. For example, kernel density estimation (KDE) is an advanced technique that superposes a basis function on each point of the feature data, usually a Gaussian function. The PDF approximation can then be obtained by adopting an envelope of all the basic functions superimposed on each point. Although these kinds of algorithms bring superior approximation results, the computation load is very high, especially in large-scale problems. Histogram methods provide another competitive method, with admissible precision and significantly more computational performance than KDE methods.

When MI is applied to practical cases, the calculation results fluctuate greatly, and it is difficult to directly compare the similarity between several variables and the target variables used as indicators [30]. This paper introduces a method to normalize MI. There are several methods of doing so. The general idea is to use entropy as the denominator to regulate the value of MI to between 0 and 1. One common implementation is the following formula:

$$N(X,Y) = 2\frac{I(X,Y)}{H(X)+H(Y)}. \tag{2}$$

Then, NMI can be used to evaluate the resemblance between candidate and target input variables.

2.3. Long Short-Term Memory. The LSTM network is applied to predicting target variables with relatively long intervals and postponements in the time series. The structure of neurons in LSTM is shown in Figure 2. It includes a cell state and three gate settings: the cell state is used to record neuron status, the input and output gates are used to receive and output parameters, respectively, and the forget gate is used to dominate the degree of forgetting of the previous unit state [31, 32].

The detailed structure and operation mechanism of LSTM are shown in Figure 3. The forgotten part of the memory unit is decided by the input x_t in the forgetting gate together with the state memory unit S_{t-1} and the intermediate output h_{t-1}. The retention vector in the memory unit is determined by the changed x_t in the input gate through the sigmoid and tanh functions. The intermediate output h_t is determined by the updated S_t and output o_t. The calculation formula is as follows:

$$\begin{aligned} f_t &= \sigma\left(W_{fx}x_t + W_{fh}h_{t-1} + b_f\right), \\ i_t &= \sigma\left(W_{ix}x_t + W_{ih}h_{t-1} + b_i\right), \\ g_t &= \varnothing\left(W_{gx}x_t + W_{gh}h_{t-1} + b_g\right), \\ o_t &= \sigma\left(W_{ox}x_t + W_{oh}h_{t-1} + b_o\right), \\ S_t &= g_t \odot i_t + S_{t-1} \odot f_t, \\ h_t &= \varnothing\left(S_t\right) \odot o_t, \end{aligned} \tag{3}$$

where f_t, i_t, g_t, o_t, h_t, and S_t are the states of the forgetting gate, input gate, input node, output gate, intermediate output, and status unit, respectively; W_{fx}, W_{fh}, W_{ix}, W_{ih}, W_{gx}, W_{gh}, W_{ox}, and W_{oh} are the matrix weight multiplied by input x_t of the corresponding gate and the intermediate output h_{t-1}, respectively; b_f, b_i, b_g, and b_o are the biases of the corresponding gates; $\odot$ indicates that the elements in the vector are multiplied by bits; and σ and $\varnothing$ represent the transformation of the sigmoid and tanh function, respectively.

3. Development of NMIFS-LSTM

The evaluation function plays a pivotal role in the MI feature selection, which directly affects the final performance of the algorithm. The method of selecting the variable with the most MI of output variable Y and input variable X_i is the most direct solution. The evaluation function is shown in

$$R = I\left(X_i;Y\right). \tag{4}$$

The MIFS [33] method introduces penalty terms based on the measure of relevance, which incorporates correlation and redundancy between variables. The evaluation function is shown in

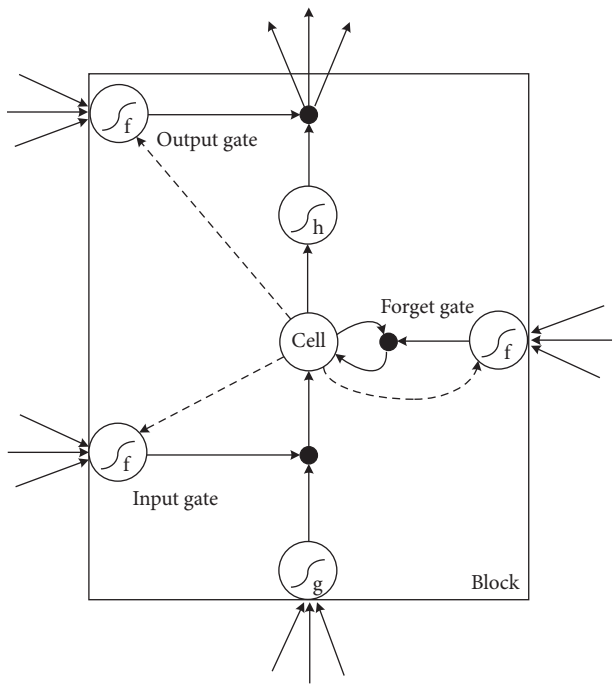

Figure 2: LSTM neuron structure.

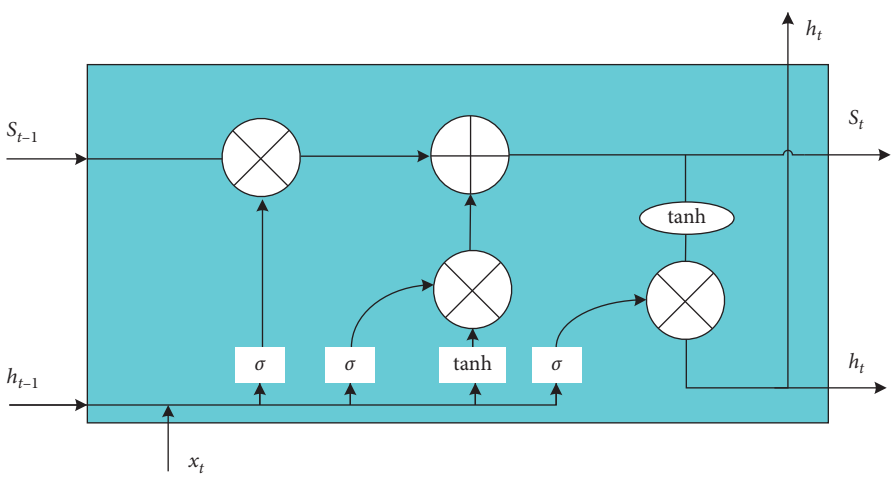

Figure 3: LSTM internal unit structure.

$$R = I(X_i; Y) - \beta \sum_{x_{s \in S}} I(X_i; X_s), \tag{5}$$

where S is the selected feature subset, X_s is the selected feature, and parameter β controls the degree of penalty for redundant items.

In order to reduce the dependence on parameter β, Kwak and Chong-Ho Choi [34] proposed the method of MIFS-U, and the evaluation function expression is exhibited as

$$R = I(X_i; Y) - \beta \sum_{x_{s \in S}} \frac{I(X_s; Y)}{H(X_s)} I(X_i; X_s). \tag{6}$$

Hanchuan et al. [25] enhanced MIFS and developed the minimal redundancy maximal relevance algorithm, which establishes a relationship between sample size and parameter β. The mean value of MI is used as the redundancy evaluation index to avoid the selection of parameter β. The evaluation function can be shown as

$$R = I(X_i; Y) - \frac{1}{|S|} \beta \sum_{x_{s \in S}} I(X_i; X_s). \tag{7}$$

The standardized MI between variables was defined by Estevez et al. [26], and the NMIFS algorithm was proposed. Its evaluation function can be expressed as

$$R = I(X_i; Y) - \frac{1}{|S|} \beta \sum_{x_{s \in S}} NI(X_i; X_s), \tag{8}$$

where the standardized MI is performed as equation (9). The regularized MI compensates for the bias of MI to

```
Input: dataset imprent MT shadow
Output: predicted value
Begin algorithm
  Initialize
  LSTM is trained to determine network hyperparameters and network structure;
  Set F = n; S = empty set (n = number of input variables);
  Computation of NMI with LSTM;
    For i = 1:j (j is frequency of the stop criterion)
      ∀f_i ∈ F compute I (L; f_i);
      Find a first variable f_i that maximizes I(Lf_i) and obtain RMSE;
      Set F ⟵ F/{f_i}, set S ⟵ {{f_i}}, set i = 1;
        Choose the next variable f_i = argmax, f_i ∈F−S(min f_s ∈S(I(f_i, f_s; L))) and obtain new RMSE;
      set F ⟵ F/{f_i}; set S ⟵ S ∪ {f_i}, j = j + 1;
      if new RMSE > RMSE
        Break
      Else
        RMSE = newRMSE, return and select the next variable;
      End if
        Repeat until |S| = j;
    End for
  Retrain with selected subset
  Calculate predicted value
End algorithm
```

Algorithm 1: Pseudocode of NMIFS-LSTM.

multivalued variables, and the regularized MI value is strictly restricted to the interval of [0, 1].

$$NI(X_i; X_s) = \frac{I(X_i; X_s)}{\min\{H(X_i), H(X_s)\}}. \tag{9}$$

In this paper, a novel variable selection method of NMIFS-LSTM is developed. This method combines NMIFS and LSTM, and after that, the root mean square error (RMSE) of the LSTM network is used as the evaluation standard. The proposed algorithm aims to eliminate redundant variables and improve model accuracy. The pseudocode of NMIFS-LSTM can be shown in Algorithm 1.

The operating mechanism of the NMIFS-LSTM algorithm is mainly divided into two parts. In the algorithm, we build a model for prediction by LSTM with NMI for variable selection. The LSTM NN is trained to determine network hyperparameters and structure. Parameter F is set to "initial set of n variables" and parameter S set to "empty set." The calculation method is NMI with the LSTM of RMSE and the first variable is chosen. We continue to choose next variables every step until the model gets worse or meets the stop criterion. Finally, the selected subset is modeled and the predicted value is obtained. The flowchart of the developed NMIFS-LSTM-based soft sensor model is shown in Figure 4.

4. Simulation Results and Discussion

In this paper, all algorithms use a common dataset with the same variable selection method after several trials in the same simulation environment setting. All established models were simulated in the same experimental environment. The program for algorithm simulation was coded in MATLAB 2019 and run under a Windows 8.1 operating system. The simulation results are recorded with the following standards:

(1) Model size (MS) means the number of candidate variables selected in the ultimate algorithm

(2) PMSE means the mean square error (MSE) is a measure that reflects the difference between the actual and value predicted value and can be calculated as follows:

$$\text{PMSE} = \frac{1}{n_t}\sum_{i=1}^{n_t}(y_i - \hat{y}_i)^2, \tag{10}$$

where y_i and $\hat{y}_i$ are the actual value and predicted value in the algorithm model of the output variable, respectively, and n_t represents the number of datasets in the testing samples

(3) Coefficient of determination (R^2) denotes the square of sample correlation coefficients between the real value and prediction value

4.1. Application to a Debutanizer. To verify the efficacy of the developed soft sensor model, it was applied to a real debutanizer column. The flow diagram of actual debutanizer column unit is given in Figure 5. In the refining industry, the main function of the process is to separate butane from natural gas. At first, the entering liquid is heated into hot steam and then sent into the main tower (T102). The hot vapour condenses into liquid and is separated into a set of fractions with different boiling points. Butane and propane

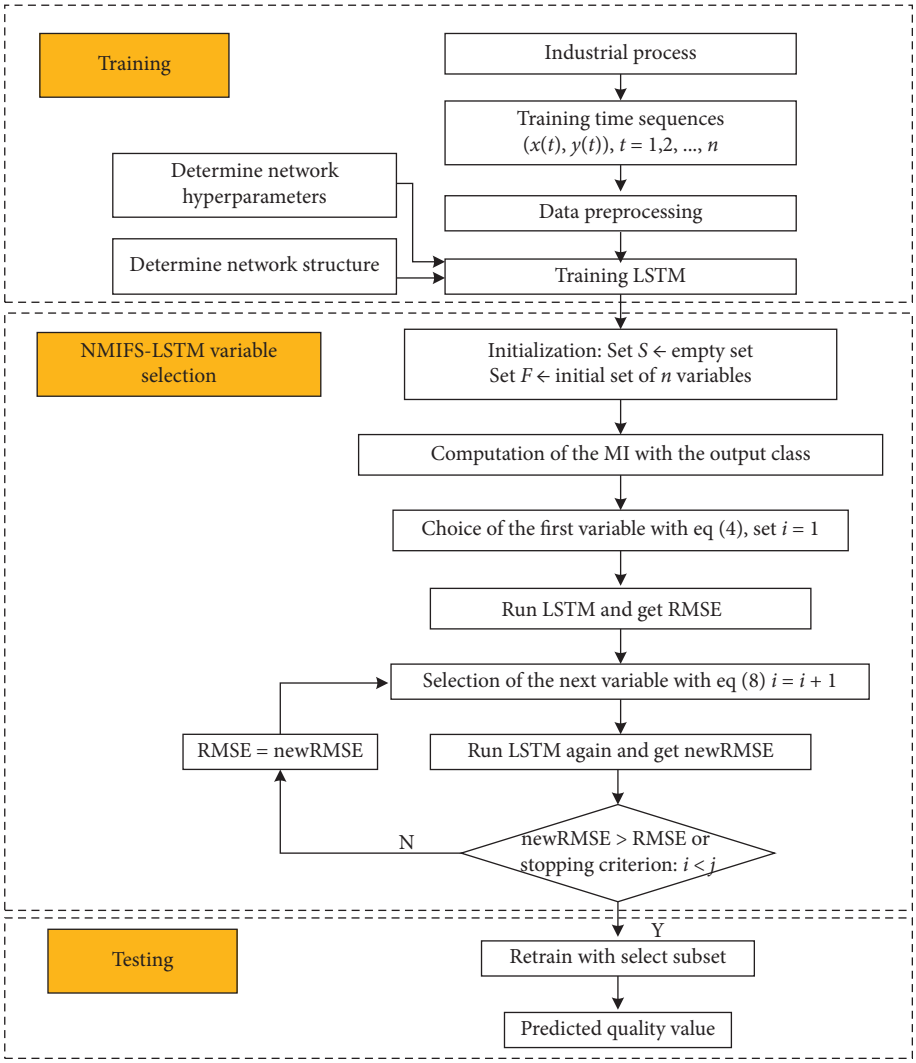

Figure 4: Flowchart of the proposed NMIFS-LSTM-based soft sensor model.

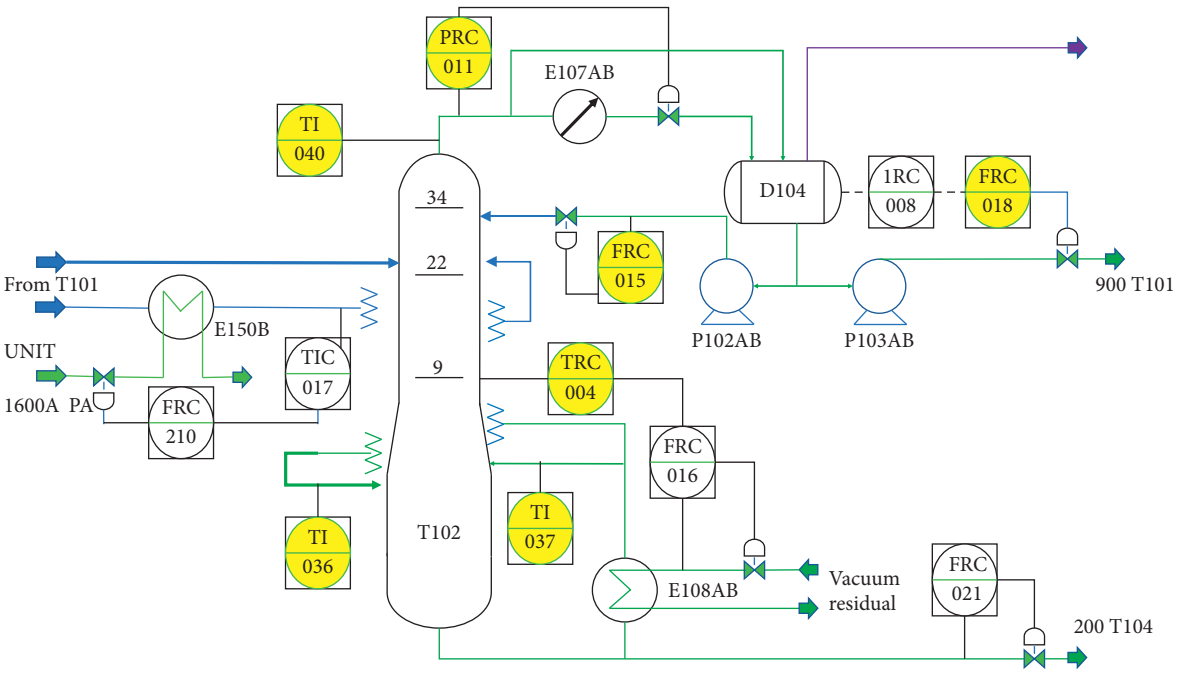

Figure 5: Brief diagram of debutanizer column.

Table 1: Candidate input variables of debutanizer column.

Input Variable	ID	Description
x_1	TI-040	Top temperature
x_2	PRC-011	Top pressure
x_3	FRC-015	Reflux flow
x_4	FRC-018	Flow to next system
x_5	TRC-004	6th tray temperature
x_6	TI-036	Bottom temperature 1
x_7	TI-037	Bottom temperature 2

Table 2: Statistical results for butane content prediction.

	MLP	NMI-MLP	LSTM	NMI-LSTM
MS	40	12	40	8
PMSE	0.0720	0.0673	0.0683	0.0421
R^2	0.9379	0.9524	0.9502	0.9801

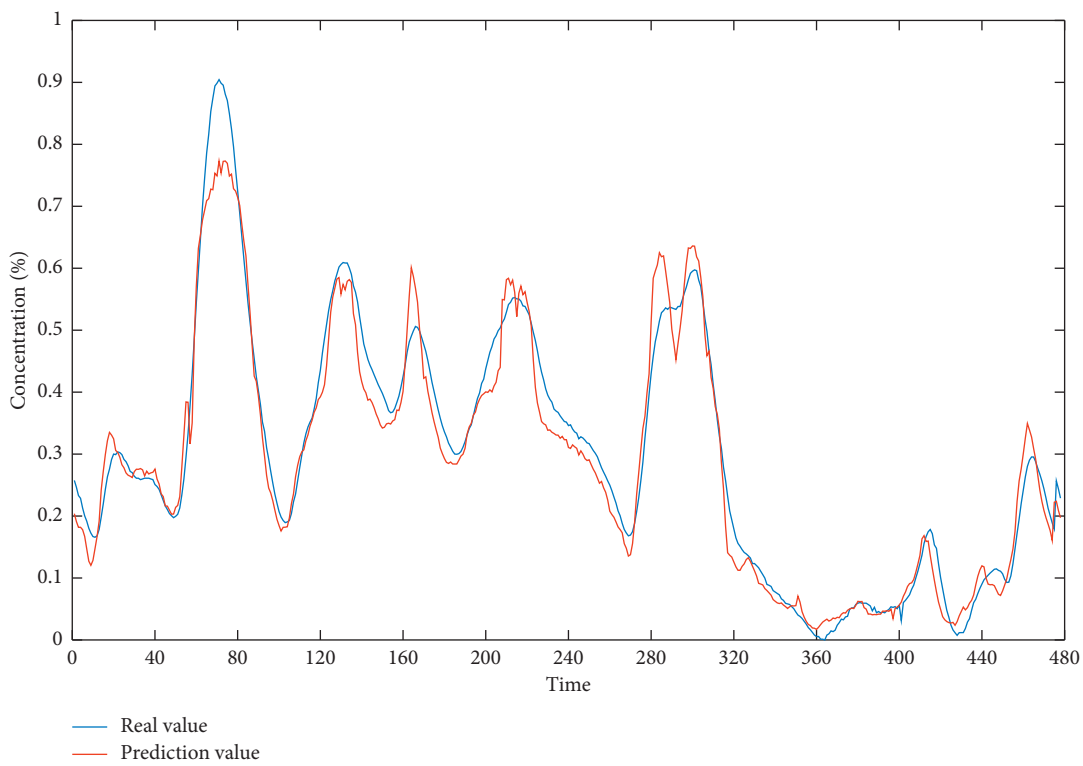

Figure 6: Measured and predicted content of butane.

are detached in the column after the treatment under normal circumstances, which makes the natural gas almost pure methane.

In this case, the content of butane is very important to ensure the product quality during the process. However, this variable is very hard to measure in real time. Hence, a compatible online soft sensing model was proposed to forecast the content. Seven practical sensors were installed in the process, marked as yellow circles in the brief diagram [35], as displayed in Figure 5. All of these candidate variables are listed in Table 1.

2394 data samples were presented at intervals of 15 minutes. The dataset was separated into two parts: the dataset of the first 80% applied for training and the others for testing. On the basis of plant experts guidance [22], the time delay of the process was probably 20–60 minutes. Based on this advice, we extended the input variables to $x = \{x_1(t), ..., x_p(t), x_1(t-1), ..., x_p(t-1), \ldots, x_1(t-4), ..., x_p(t-4)\}$, in which $x_i(t-j)$ means the value of x_i at time $t-j$. In addition, we added a guided value of $(y\text{–}t)$ in each group to enhance the accuracy of modelling. The number of candidate variables was raised from 7 to 40, which resulted in additional complexity of the process.

Table 2 presents the experimental results with these four algorithms. The table shows that the NMI-LSTM algorithm has obvious advantage over others in model

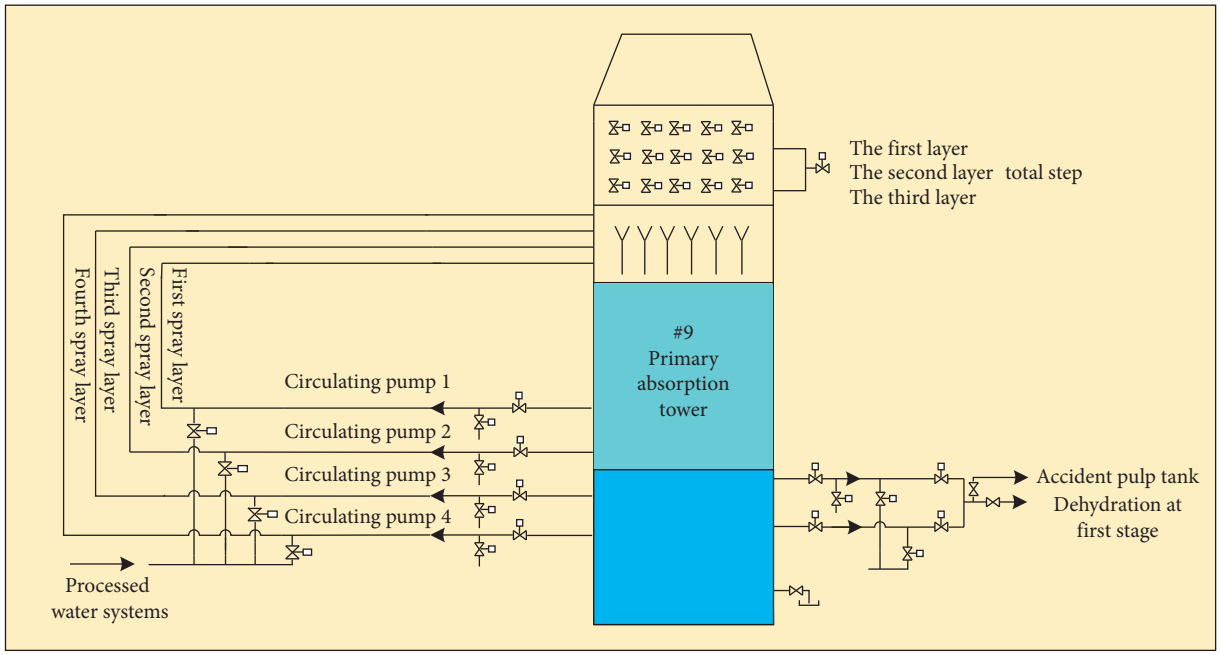

Figure 7: Process flow diagram of primary absorption tower.

Table 3: Candidate input variables of flue gas desulfurization system.

Variable	Description	Unit
1	Generator power	kW
2	#9 furnace original flue gas SO_2	mg/m^3
3	#9-1 absorption tower export flue gas SO_2	mg/m^3
4	#9 absorption tower gypsum slurry pH	
5	Limestone slurry to #9 absorption tower stream	m^3/h
6	#9-2 absorption tower pH 1	
7	#9-2 absorption tower feed flow	m^3/h
8	#9-1 circulating slurry pump current	A
9	#9-3 circulating slurry pump current	A
10	#9 absorption tower entrance flue gas temperature	°C
11	The sum of air flow	CMH
12	The sum of coal	t
13	#9 absorption tower export flue gas temperature 1	°C
14	#9 absorption tower export flue gas temperature 2	°C
15	#9 absorption tower export flue gas temperature 3	°C
16	#9 furnace chimney entrance net flue gas flow	Nm^3/h
17	#9 furnace chimney entrance net flue gas pressure	Pa
18	#9 furnace raw flue gas NOx	mg/m^3
19	#9 furnace raw flue gas O_2	mg/m^3
20	Median value of desulfurization productivity of unit 9	%
21	#9-2 absorption tower export temperature 1	°C
22	#9-2 absorption tower export pressure	Pa
23	#9-1 absorption tower export flue gas O_2	mg/m^3
24	#9 absorption tower level value	m
25	#9-2 absorber tower level	m
26	Water circulation vacuum pump	kW
27	Gypsum slurry outflow pump a current	A
28	#9 gypsum slurry cyclone entrance pressure	Pa
29	Dewatering machine power	kW
30	Gypsum filter cake height	m

accuracy. The simulation performance presents that NMI-LSTM shows a tighter and higher accurate model than other methods.

Figure 6 shows the real values and prediction values of target variable by applying the NMIFS-LSTM model. The fitted graph clearly illustrates that our approach can follow

Table 4: Comparison of prediction results of flue gas SO_2 with different algorithms.

	MLP	NMI-MLP	LSTM	NMI-LSTM
MS	30	11	30	8
PMSE	5.9569	3.3295	3.2419	2.1233
R^2	0.3392	0.7765	0.7524	0.9023

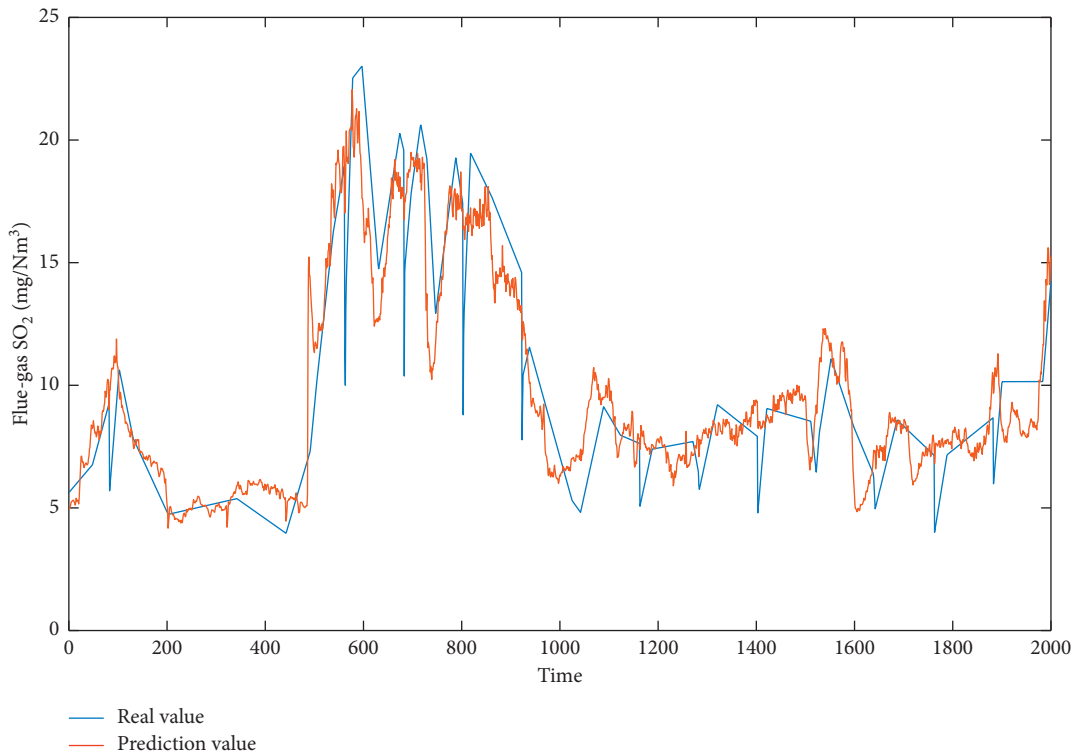

Figure 8: Prediction curve of flue gas SO_2 concentration by NMI-LSTM algorithm.

the variations of the butane content successfully, which further verifies its efficacy.

4.2. Application to Power Plant Desulfurization Technology. The flue gas desulfurization system and industrial process parameters are basically collected from unit 9 of a thermal power plant, which achieves limestone-gypsum wet flue gas desulfurization technology with twin towers. The system's SO_2 is absorbed by lime or limestone with chemical reaction. Compared to the single tower, these twin towers can carry out secondary reaction of transmitted flue gas and eliminate SO_2 in the flue gas more successfully. The flue gas desulfurization process includes SO_2 absorption system, flue gas system, mist eliminator system, absorption tower overflow device, slurry mixing system of absorption tower, oxidizing blower, etc. These twin towers have an absorption area of 12 meters in diameter and a height of 32.6 meters. The flue gas containing SO_2 moves from bottom to top where the bottom of the primary absorption tower (PAT) and encounters a liquid suspension from the spray layer. SO_2 chemically reacts with the alkaline suspension through the gas film and the liquid film in a molecular diffusion manner. The PAT includes four spray layers that are dominated by circulating pumps, shown in Figure 7.

This paper collects the data sample of desulfurization index parameters of unit 9 of a thermal power plant as the research object. The dataset includes 30 input variables and a target output variable flue gas SO_2 concentration. All candidate variables are given in Table 3. The time span is from July 1, 2019, to July 7, 2019, with a time interval of 1 min and a total of 10000 samples. The first 8000 samples are used as the training data and the others are used as the testing data. In the practical simulation experiment, redundant variables in the pool of candidate variables can lead to unsuitable modelling. Consequently, IVFS technique is very important for building a suitable and stable soft measurement model.

Table 4 presents the statistics of data-driven models with different algorithms. Experimental results present that NMI-LSTM has better performance with fewer input variables than other approaches. R^2 of NMI-LSTM is higher than 90%, representing that the proposed soft sensor can precisely forecast the actual values.

Figure 8 shows the prediction curve of SO_2 concentration by NMI-LSTM algorithm. Obviously, NMI-LSTM can

track the dynamic change of target variable effectively, which shows that our algorithm is very effective.

5. Conclusion

In this paper, a novel soft sensor was designed to model complex and dynamic industrial processes with time series characteristics. The LSTM network is trained by datasets taken from actual processes, and NMI is applied to select the variables related to the target variable. The proposed algorithm deletes one irrelevant variable at every step until all the variables are removed. After that, the path of variable selection appears and the algorithm takes the segment with the lowest prediction error. The proposed soft sensor was applied to two practical industrial processes. The simulation and comparison with other algorithms demonstrate the effectiveness and excellence of our approach. The developed soft sensor provides an additional and reliable monitoring tool for pivotal variables and can be further applied to the design of model predictive control systems.

The proposed soft sensor algorithm is easy to implement, and the related program can be preserved as a subroutine in the industrial computer of the DCS. By calling the subroutine, the soft sensor could be periodically retrained and updated with the new production data. The disadvantage of model degradation can be completely eliminated with this technique.

Data Availability

The data used to support the findings of this study are available from the corresponding author upon request.

Conflicts of Interest

The authors declare that there are no conflicts of interest regarding the publication of this paper.

Authors' Contributions

Dongfeng Li and Zhirui Li contributed equally to this article.

Acknowledgments

The authors acknowledge the Yau Mathematical Sciences Center and Huangtai Power Plant for data gathering and experiment. This work was partially supported by the Major Science and Technology Innovation Projects of Shandong Province (Grant no. 2019JZZY010731), the Key Research and Development Program of Shandong Province (Grant no. 2019GGX104037), the S.-T. Yau High School Science Award (Computer), and the National Natural Science Foundation of China (Grant no. 51874300).

References

[1] Z. Ujevic, I. Mohler, and N. Bolf, "Soft sensors for splitter product property estimation in CDU," *Chemical Engineering Communications*, vol. 198, pp. 1566–1578, 2011.

[2] K. Sun, J. Liu, J.-L. Kang, S.-S. Jang, D. S.-H. Wong, and D.-S. Chen, "Development of a variable selection method for soft sensor using artificial neural network and nonnegative garrote," *Journal of Process Control*, vol. 24, pp. 1068–1075, 2014.

[3] S. Gao, J. Yang, and J. Wang, "D-FNN based modeling and BP neural network decoupling control of PVC stripping process," *Mathematical Problems in Engineering*, vol. 2014, Article ID 681259, 13 pages, 2014.

[4] A. Nawaz, A. S. Arora, C. M. Yun, H. Cho, S. You, and M. Lee, "Data authorization and forecasting by a proactive soft sensing tool-anammox based process," *Industrial & Engineering Chemistry Research*, vol. 58, no. 22, pp. 9552–9563, 2019.

[5] S. Zhang, X. Chen, and Y. Yin, "An ELM based online soft sensing approach for alumina concentration detection," *Mathematical Problems in Engineering*, vol. 2015, Article ID 268132, 8 pages, 2015.

[6] K. Sun, X. Wu, J. Xue, and F. Ma, "Development of a new multi-layer perceptron based soft sensor for SO_2 emissions in power plant," *Journal of Process Control*, vol. 84, pp. 182–191, 2019.

[7] E. Heidari, M. A. Sobati, and S. Movahedirad, "Accurate prediction of nanofluid viscosity using a multilayer perceptron artificial neural network (MLP-ANN)," *Chemometrics and Intelligent Laboratory Systems*, vol. 155, pp. 73–85, 2016.

[8] K. G. Sheela and S. N. Deepa, "Neural network based hybrid computing model for wind speed prediction," *Neurocomputing*, vol. 122, pp. 425–429, 2013.

[9] Y. He, Y. Xu, Z. Geng, and Q. Zhu, "Soft sensor of chemical processes with large numbers of input parameters using auto-associative hierarchical neural network," *Chinese Journal of Chemical Engineering*, vol. 23, no. 1, pp. 138–145, 2015.

[10] M. Zabadaj, K. Chreptowicz, J. Mierzejewska, and P. Ciosek, "Two-dimensional fluorescence as soft sensor in the monitoring of biotransformation performed by yeast," *Biotechnology Progress*, vol. 33, no. 2, pp. 299–307, 2017.

[11] J. Rehrla, A. P. Karttunenb, N. Nicolaïc, T. Hörmanne, and M. Hornd, "Control of three different continuous pharmaceutical manufacturing processes: use of soft sensors," *International Journal of Pharmaceutics*, vol. 543, no. 1-2, pp. 60–72, 2018.

[12] Z. Ge, "Supervised latent factor analysis for process data regression modeling and soft sensor application," *IEEE Transactions on Control Systems Technology*, vol. 24, no. 3, pp. 1004–1011, 2015.

[13] G. Hussain, M. Jabbar, J.-D. Cho, and S. Bae, "Indoor positioning system: a new approach based on LSTM and two stage activity classification," *Electronics*, vol. 8, no. 4, p. 375, 2019.

[14] L. Yang, Y. Li, J. Wang, and Z. Tang, "Post text processing of Chinese speech recognition based on bidirectional LSTM networks and CRF," *Electronics*, vol. 8, no. 11, p. 1248, 2019.

[15] J. Chen, Q. Jin, and J. Chao, "Design of deep belief networks for short-term prediction of drought index using data in the Huaihe river basin," *Mathematical Problems in Engineering*, vol. 2012, Article ID 235929, 16 pages, 2012.

[16] S. Xingjian, Z. Chen, H. Wang et al., "Convolutional LSTM network: a machine learning approach for precipitation nowcasting," in *Proceedings of Advances in Neural Information Processing Systems*, Montreal, Canada, pp. 802–810.

[17] Z. Zhao, W. Chen, X. Wu, P. C. Y. Chen, and J. Liu, "LSTM network: a deep learning approach for short-term traffic forecast," *IET Intelligent Transport Systems*, vol. 11, no. 2, pp. 68–75, 2017.

[18] J. Liu, A. Shahroudy, D. Xu et al., "Spatio-temporal lstm with trust gates for 3d human action recognition," in *Proceedings of*

European Conference on Computer Vision, Amsterdam, Netherlands, pp. 816–833.

[19] X. Yuan, L. Li, and Y. Wang, "Nonlinear dynamic soft sensor modeling with supervised long short-term memory network," *IEEE Transactions on Industrial Informatics*, vol. 16, no. 5, pp. 3168–3176, 2019.

[20] Q. Sun and Z. Ge, "Probabilistic sequential network for deep learning of complex process data and soft sensor application," *IEEE Transactions on Industrial Informatics*, vol. 15, pp. 2700–2709, 2018.

[21] S. Greenland, "Modeling and variable selection in epidemiologic analysis," *American Journal of Public Health*, vol. 79, no. 3, pp. 340–349, 1989.

[22] Z. Hui and T. A. Hastie, "Regularization and variable selection via the elastic net," *Journal of the Royal Statistical Society*, vol. 67, p. 768, 2005.

[23] J. Wang, J. Zhang, and X. Wang, "A data driven cycle time prediction with feature selection in a semiconductor wafer fabrication system," *IEEE Transactions on Semiconductor Manufacturing*, vol. 31, no. 1, pp. 173–182, 2018.

[24] K. Sun, P. Tian, H. Qi, F. Ma, and G. Yang, "An improved normalized mutual information variable selection algorithm for neural network-based soft sensors," *Sensors*, vol. 19, no. 24, p. 5368, 2019.

[25] P. Hanchuan, L. Fuhui, and D. Chris, "Feature selection based on mutual information: criteria of max-dependency, max-relevance, and min-redundancy," *IEEE Transactions on Pattern Analysis & Machine Intelligence*, vol. 27, pp. 1226–1238, 2005.

[26] P. A. Estevez, M. Tesmer, C. A. Perez, and J. M. Zurada, "Normalized mutual information feature selection," *IEEE Transactions on Neural Networks*, vol. 20, no. 2, pp. 189–201, 2009.

[27] H. Hirschmuller, "Stereo processing by semiglobal matching and mutual information," *IEEE Transactions on Pattern Analysis and Machine Intelligence*, vol. 30, no. 2, pp. 328–341, 2007.

[28] M. Bennasar, Y. Hicks, and R. Setchi, "Feature selection using joint mutual information maximisation," *Expert Systems with Applications*, vol. 42, no. 22, pp. 8520–8532, 2015.

[29] J. Novovicová, P. Somol, M. Haindl, and P. Pudil, "Conditional mutual information based feature selection for classification task," in *Proceedings of the Iberoamerican Congress on Pattern Recognition*, pp. 417–426, Valparaíso, Chile, November 2007.

[30] A. Dame and E. Marchand, "Mutual information-based visual servoing," *IEEE Transactions on Robotics*, vol. 27, no. 5, pp. 958–969, 2011.

[31] S. Hochreiter and J. Schmidhuber, "Long short-term memory," *Neural Computation*, vol. 9, no. 8, pp. 1735–1780, 1997.

[32] Z. Yu, G. Chen, Y. Dong et al., "Highway long short-term memory RNNS for distant speech recognition," in *Proceedings of IEEE International Conference on Acoustics*, Shanghai, China, March 2016.

[33] R. Battiti, "Using mutual information for selecting features in supervised neural net learning," *IEEE Transactions on Neural Networks*, vol. 5, no. 4, pp. 537–550, 1994.

[34] N. Kwak and C.-H. Chong-Ho Choi, "Input feature selection for classification problems," *IEEE Transactions on Neural Networks*, vol. 13, no. 1, pp. 143–159, 2002.

[35] L. Fortuna, S. Graziani, and M. G. Xibilia, "Soft sensors for product quality monitoring in debutanizer distillation columns," *Control Engineering Practice*, vol. 13, no. 4, pp. 499–508, 2005.

Hindawi
Mathematical Problems in Engineering
Volume 2020, Article ID 3518180, 8 pages
https://doi.org/10.1155/2020/3518180

Research Article

Two Types of Synchronization Problems in a New 5D Hyperchaotic System

Bin Li,[1] **Xue Yang**,[1] **Qixing Liang**,[1] **and Zhi Li**[2]

[1]*School of Mathematics and Statistics, Qilu University of Technology, Shandong Academy of Sciences, Jinan 250353, China*
[2]*School of Electrical Engineering and Automation, Qilu University of Technology, Shandong Academy of Sciences, Jinan 250353, China*

Correspondence should be addressed to Bin Li; ribbenlee@126.com

Received 22 February 2020; Accepted 26 March 2020; Published 22 April 2020

Guest Editor: Yi Qi

This paper investigates the synchronization problem in a new 5D hyperchaotic system. Firstly, the existence of two types of synchronization problems in the new 5D hyperchaotic system is proved. Then, by the dynamic feedback control method, one complete synchronization problem and three coexistence of complete synchronization and antisynchronization problems in such system are realized. Finally, numerical simulations are used to verify the validity and effectiveness of the theoretical results.

1. Introduction

Since Lorenz proposed the first chaotic system in 1963, many researchers are stimulated to investigate this chaotic phenomena. Then, lots of chaotic systems and hyperchaotic systems are proposed. Since the OGY method [1] and PC method [2] were first observed for chaos control and chaos synchronization in 1990, respectively, the control problems and synchronization problems of those chaotic systems have become hot topics, see References [13–15] and the references therein. However, there are still some important questions need to be solved completely. For example, the existence of the synchronization problem in a given chaotic or hyperchaotic system, which is a fundamental theoretical base to design a physical controller. Furthermore, how to design a not only simple but also physical controller to realize the synchronization problem is also a question which needs to be solved. For the realization of such synchronization problems, there are many methods to use, linear feedback control method, dynamic feedback control method, sliding mode control method, and so on. Among those methods, the dynamic feedback control method has been applied often in applications, which is also used in this paper.

The new 5D hyperchaotic system was firstly presented in [16], and it has complex dynamics. There are eight parameters to control with only one equilibrium point. This new dynamics can generate four-wing hyperchaotic and chaotic attractors for some specific parameters and initial conditions. One remarkable feature of the new system is that it can generate double-wing and four-wing smooth chaotic attractors with special appearance. However, the synchronization problem in this system has not been solved. Moreover, for the new 5D hyperchaotic system, the existence of the synchronization problems in such system is a fundamental question, but it still not be solved. Therefore, investigating the synchronization problems in the new 5D hyperchaotic system is very important in both theory and applications, which motivates our work in this paper.

Motivated by the abovementioned conclusions, the synchronization problem in the new 5D chaotic system is studied by the dynamic feedback control method. The main contributions of this paper are given as follows:

(1) The existence of two types of synchronization problems in the new 5D system is proved

(2) These two types of synchronization problems in the new 5D system are realized by the dynamic feedback control method

2. Problem Formulation

According to [16], the new 5D hyperchaotic system is given as

$$\dot{x} = f(x), \tag{1}$$

where $x \in R^5$ is the state and

$$f(x) = \begin{pmatrix} f_1(x) \\ f_2(x) \\ f_3(x) \\ f_4(x) \\ f_5(x) \end{pmatrix} = \begin{pmatrix} -10x_1 + x_2x_3 \\ -60x_2 + x_5 \\ -20x_3 + 50x_4 + x_1x_2 \\ 15x_4 - 10x_3 \\ 40x_5 - x_1^2x_2 \end{pmatrix}. \tag{2}$$

Let system (1) be the master system, then the controlled slave system is described as follows:

$$\dot{y} = f(y) + Bu, \tag{3}$$

where $y \in R^5$ is the state,

$$B = \begin{pmatrix} 0 & 0 & 0 \\ 0 & 0 & 0 \\ 1 & 0 & 0 \\ 0 & 1 & 0 \\ 0 & 0 & 1 \end{pmatrix}, \tag{4}$$

and $u \in R^3$ is the controller to be designed.

This paper investigates the synchronization problem of the master system (1) and the slave system (3) and presents some new results.

For the development of this paper, the dynamic feedback control method is introduced in the next.

3. Preliminary

Consider the following controlled chaotic system:

$$\dot{z} = F(z) + Bu, \tag{5}$$

where $z \in R^n$ is the state, $F(z) \in R^n$ is continuous vector function with $F(0) = 0$, $B \in R^{n\times r}$ is a constant matrix, and u is the designed controller.

Lemma 1 (see [17]). *Consider system (5), if $(F(z), B)$ can be stabilized; then, the controller u is designed as follows:*

$$u = K(t)z, \tag{6}$$

where $K = k(t)B^T$, and the feedback gain $k(t)$ is updated by the following equation:

$$\dot{k}(t) = -z^Tz = -\|z\|^2. \tag{7}$$

4. Main Results

4.1. The Existence of Synchronization Problems in the New 5D Hyperchaotic System. According to the results in [17], the existence of synchronization problems in the 5D hyperchaotic system (1) is proved by the following condition:

$$f(\alpha x) \equiv \alpha f(x), \tag{8}$$

where $\alpha = \mathrm{Diag}\{\alpha_1, \alpha_2, \ldots, \alpha_5\}$, $\alpha_i \neq 0$, $i = 1, 2, \ldots, 5$,

$$\begin{cases} f_1(\alpha x) - \alpha_1 f_1(x) = (\alpha_2\alpha_3 - \alpha_1)x_2x_3 \equiv 0, \\ f_2(\alpha x) - \alpha_2 f_2(x) = (\alpha_2 - \alpha_5)x_5 \equiv 0, \\ f_3(\alpha x) - \alpha_3 f_3(x) = 50(\alpha_3 - \alpha_4)x_4 + (\alpha_1\alpha_2 - \alpha_3)x_1x_2 \equiv 0, \\ f_4(\alpha x) - \alpha_4 f_4(x) = -10(\alpha_3 - \alpha_4)x_3 \equiv 0, \\ f_5(\alpha x) - \alpha_4 f_4(x) = -(\alpha_1^2\alpha_2 - \alpha_5)x_1 \equiv 0. \end{cases} \tag{9}$$

It results in

$$\begin{cases} \alpha_2\alpha_3 = \alpha_1, \\ \alpha_2 = \alpha_5, \\ \alpha_1\alpha_2 = \alpha_3, \\ \alpha_3 = \alpha_4, \\ \alpha_1^2\alpha_2 = \alpha_5. \end{cases} \tag{10}$$

Solving equation (10), we obtain

(I) $\alpha_1 = \alpha_2 = \alpha_3 = \alpha_4 = \alpha_5 = 1$, which implies the complete synchronization problem exists

(II) $\alpha_1 = \alpha_2 = \alpha_5 = -1$ and $\alpha_3 = \alpha_4 = 1$, which implies the coexistence of complete synchronization and antisynchronization problem exists

(III) $\alpha_2 = \alpha_3 = \alpha_4 = \alpha_5 = -1$ and $\alpha_1 = 1$, which implies the coexistence of complete synchronization and antisynchronization problem exists

(IV) $\alpha_1 = \alpha_3 = \alpha_4 = -1$ and $\alpha_2 = \alpha_5 = 1$, which implies the coexistence of complete synchronization and antisynchronization problem exists

4.2. Complete Synchronization in the New 5D Hyperchaotic System. For the master system (1) and the slave system (3), let $e = y - x$, and the error system is given as

$$\dot{e} = f(y) - f(x) + Bu = g(x, e) + Bu, \tag{11}$$

where

$$g(x,e) = \begin{pmatrix} g_1(x,e) \\ g_2(x,e) \\ g_3(x,e) \\ g_4(x,e) \\ g_5(x,e) \end{pmatrix} = \begin{pmatrix} -10e_1 + x_2e_3 + x_3e_2 + e_2e_3 \\ -60e_2 + e_5 \\ -20e_3 + 50e_4 + x_1e_2 + x_2e_1 + e_1e_2 \\ 15e_4 - 10e_3 \\ 40e_5 - 2x_1x_2e_1 - 2x_1e_2e_1 - x_2e_1^2 - e_1^2e_2 \end{pmatrix}, \tag{12}$$

and B is given in (4).

According to Lemma 1, we propose the following conclusion.

Theorem 1. *Consider the error system (11). If the controller u is designed as follows*

$$u = Ke, \tag{13}$$

where $K = k(t)B^T$, B is given in (4), and $k(t)$ is updated by the following update law:

$$\dot{k} = -\|e\|^2. \tag{14}$$

Then, the master system (1) and the slave system (3) reach complete synchronization.

Proof. For the error system (11) with $u = 0$, if $e_3 = e_4 = e_5 = 0$, then the following subsystem

$$\begin{aligned} \dot{e}_1 &= -10e_1 + x_3 e_2, \\ \dot{e}_2 &= -60e_2, \end{aligned} \tag{15}$$

is asymptotically stable.

Thus, $(g(x,e), B)$ can be stabilized. According to Lemma 1, the error system (11) is stabilized by the abovementioned controller u given in (13), which completes the proof. □

In the following, numerical simulation is carried out with the initial conditions: $x_1(0) = 1, x_2(0) = -2, x_3(0) = 3, x_4(0) = -4$, $y_1(0) = 5, y_2(0) = -6, y_3(0) = 7, y_4(0) = -8$, and $k(0) = -1$. Figure 1 shows e_1, e_2, and e_3 are asymptotically stable, Figure 2 shows e_4 and e_5 are asymptotically stable, and Figure 3 shows that the feedback gain $k(t)$ tends to constant.

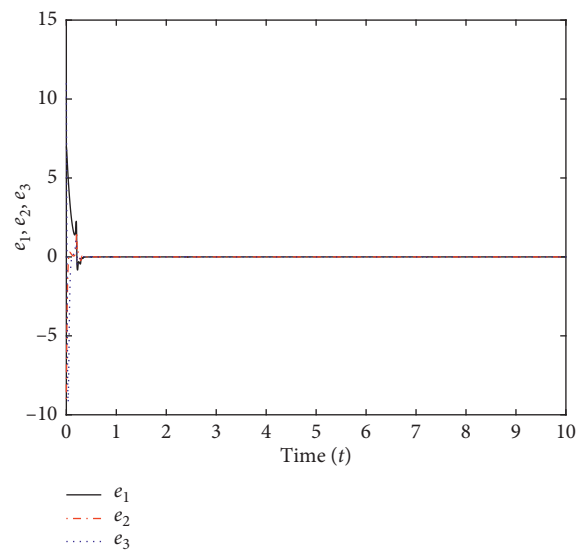

Figure 1: e_1, e_2, and e_3 are asymptotically stable.

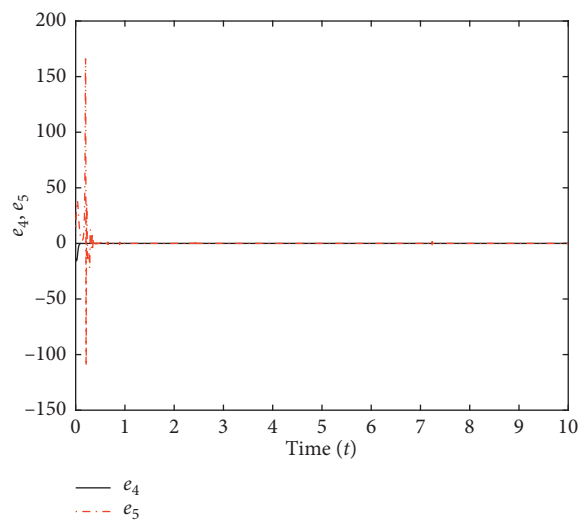

Figure 2: e_4 and e_5 are asymptotically stable.

4.3. Coexistence of Synchronization and Antisynchronization in the New 5D Hyperchaotic System

Case 1. $\alpha_1 = \alpha_2 = \alpha_5 = -1$ and $\alpha_3 = \alpha_4 = 1$.

Let $E_i = x_i + y_i, i = 1, 2, 5$, and $e_i = y_i - x_i, i = 3, 4$; then, the sum and error system is described as follows:

$$\begin{pmatrix} \dot{E} \\ \dot{e} \end{pmatrix} = \begin{pmatrix} \dot{E}_1 \\ \dot{E}_2 \\ \dot{E}_5 \\ \dot{e}_3 \\ \dot{e}_4 \end{pmatrix} = \begin{pmatrix} f_1(y) + f_1(x) \\ f_2(y) + f_2(x) \\ f_5(y) + f_5(x) \\ f_3(y) - f_3(x) \\ f_4(y) - f_4(x) \end{pmatrix} + Bu = G(x, E, e) + Bu, \tag{16}$$

where

$$G(x,E,e) = \begin{pmatrix} G_1(x,E,e) \\ G_2(x,E,e) \\ G_5(x,E,e) \\ G_3(x,E,e) \\ G_4(x,E,e) \end{pmatrix} = \begin{pmatrix} -10E_1 - x_2 e_3 - x_3 E_2 + E_2 e_3 \\ -60E_2 + E_5 \\ 40e_5 - 2x_1 x_2 E_1 + 2x_1 E_2 E_1 + x_2 E_1^2 - E_1^2 E_2 \\ -20e_3 + 50e_4 - x_1 E_2 - x_2 E_1 + E_1 E_2 \\ 15e_4 - 10e_3 \end{pmatrix}, \tag{17}$$

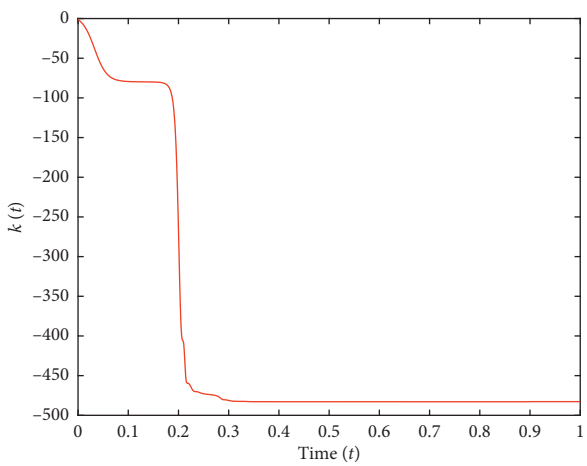

FIGURE 3: The feedback gain $k(t)$ tends to constant.

and B is given in (4).

According to Lemma 1, we propose the following conclusion.

Theorem 2. *Consider the sum and error system (16). If controller u is designed as follows*

$$u = K\begin{pmatrix} E \\ e \end{pmatrix}, \tag{18}$$

where $K = k(t)B^T$, B is given as (4), and $k(t)$ is updated by the following update law:

$$\dot{k} = -\left(\|e\|^2 + \|E\|^2\right). \tag{19}$$

Then, the master system (1) and the slave system (3) realize the coexistence of complete synchronization and antisynchronization.

Proof. For the sum and error system (16) with $u = 0$, if $e_3 = e_4 = E_5 = 0$, then the following subsystem

$$\begin{aligned} \dot{E}_1 &= -10E_1 - x_3E_2, \\ \dot{E}_2 &= -60E_2, \end{aligned} \tag{20}$$

is asymptotically stable.

Thus, $(G(x, E, e), B)$ can be stabilized. According to Lemma 1, the sum and the error system (16) is stabilized by the abovementioned controller u given in (18), which completes the proof. □

In the following, numerical simulation is carried out with the initial conditions: $x_1(0) = 1, x_2(0) = -2, x_3(0) = 3, x_4(0) = -4, \quad y_1(0) = 5, y_2(0) = -6, y_3(0) = 7, y_4(0) = -8$, and $k(0) = -1$. Figure 4 shows E_1, E_2, and e_3 are asymptotically stable, Figure 5 shows e_4 and E_5 are asymptotically stable, and Figure 6 shows that the feedback gain $k(t)$ tends to constant.

Case 2. $\alpha_2 = \alpha_3 = \alpha_4 = \alpha_5 = -1$ and $\alpha_1 = 1$.

Let $E_i = x_i + y_i, i = 2, 3, 4, 5$, and $e_1 = y_1 - x_1$, and then the sum and error system is described as follows:

$$\begin{pmatrix} \dot{E} \\ \dot{e} \end{pmatrix} = \begin{pmatrix} \dot{E}_2 \\ \dot{E}_3 \\ \dot{E}_4 \\ \dot{E}_5 \\ \dot{e}_1 \end{pmatrix} = \begin{pmatrix} f_2(y) + f_2(x) \\ f_3(y) + f_3(x) \\ f_4(y) + f_4(x) \\ f_5(y) + f_5(x) \\ f_1(y) - f_1(x) \end{pmatrix} + B^*u = G^*(x, E, e) + B^*u, \tag{21}$$

where

$$G^*(x, E, e) = \begin{pmatrix} G_2^*(x, E, e) \\ G_3^*(x, E, e) \\ G_4^*(x, E, e) \\ G_5^*(x, E, e) \\ G_1^*(x, E, e) \end{pmatrix} = \begin{pmatrix} -60E_2 + E_5 \\ -20E_3 + 50E_4 + x_1E_2 - x_2e_1 + e_1E_2 \\ 15E_4 - 10E_3 \\ 40E_5 - 2x_1x_2e_1 - 2x_1E_2e_1 + x_2e_1^2 - e_1^2E_2 \\ -10e_1 + x_2E_3 + x_3E_2 + E_2E_3 \end{pmatrix}, \tag{22}$$

and

$$B^* = \begin{pmatrix} 0 & 0 & 0 \\ 1 & 0 & 0 \\ 0 & 1 & 0 \\ 0 & 0 & 1 \\ 0 & 0 & 0 \end{pmatrix}. \tag{23}$$

According to Lemma 1, we propose the following conclusion.

Theorem 3. *Consider the controlled sum and error system (21). If controller u is designed as follows*

$$u = K\begin{pmatrix} E \\ e \end{pmatrix}, \tag{24}$$

where $K = k(t)B^{*T}$, B^* is given in (23), and $k(t)$ is updated by the following update law:

$$\dot{k} = -\left(\|e\|^2 + \|E\|^2\right). \tag{25}$$

Then, the master system (1) and the slave system (3) realize the coexistence of complete synchronization and antisynchronization.

Proof. For the sum and error system (21) with $u = 0$, if $E_3 = E_4 = E_5 = 0$, then the following subsystem

$$\begin{aligned} \dot{e}_1 &= -10e_1 + x_3E_2, \\ \dot{E}_2 &= -60E_2, \end{aligned} \tag{26}$$

is asymptotically stable.

Thus, $(G(x, E, e), B)$ can be stabilized. According to Lemma 1, the sum and the error system (21) is stabilized by the abovementioned controller u given in (24), which completes the proof. □

In the following, numerical simulation is carried out with the initial conditions: $x_1(0) = 1, x_2(0) = -2, x_3(0) = 3, x_4(0) = -4, \quad y_1(0) = 5, y_2(0) = -6, y_3(0) = 7, y_4(0) = -8$, and $k(0) = -1$. Figure 7 shows e_1, E_2, and E_3 are asymptotically stable, Figure 8 shows E_4 and E_5 are asymptotically stable, and Figure 9 shows that the feedback gain $k(t)$ tends to constant.

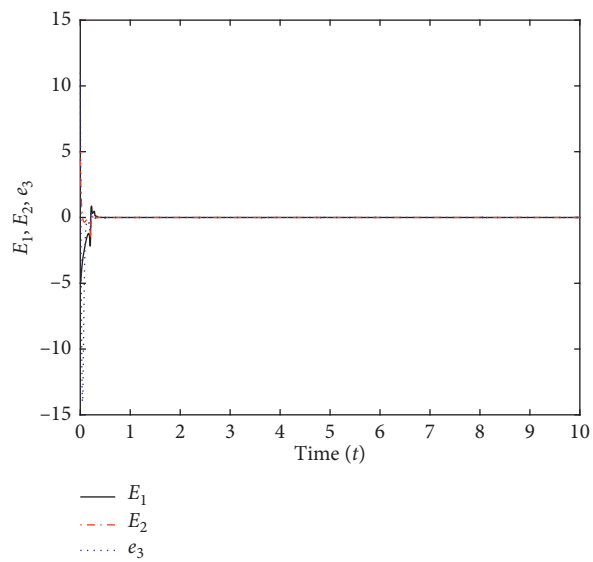

FIGURE 4: E_1, E_2, and e_3 are asymptotically stable.

Case 3. $\alpha_1 = \alpha_3 = \alpha_4 = -1$ and $\alpha_2 = \alpha_5 = 1$.

Let $E_i = x_i + y_i$, $i = 1, 3, 4$, and $e_i = y_i - x_i$, $i = 2, 5$, and then the sum and error system is described as follows:

$$\begin{pmatrix} \dot{E} \\ \dot{e} \end{pmatrix} = \begin{pmatrix} \dot{E}_1 \\ \dot{E}_3 \\ \dot{E}_4 \\ \dot{e}_2 \\ \dot{e}_5 \end{pmatrix} = \begin{pmatrix} f_1(y) + f_1(x) \\ f_3(y) + f_3(x) \\ f_4(y) + f_4(x) \\ f_2(y) - f_2(x) \\ f_5(y) - f_5(x) \end{pmatrix} + B^{**}u = G^{**}(x, E, e) + B^{**}u, \tag{27}$$

where

$$G^{**}(x, E, e) = \begin{pmatrix} G_1^{**}(x, E, e) \\ G_3^{**}(x, E, e) \\ G_4^{**}(x, E, e) \\ G_2^{**}(x, E, e) \\ G_5^{**}(x, E, e) \end{pmatrix} = \begin{pmatrix} -10E_1 + x_2E_3 - x_3e_2 + e_2E_3 \\ -20E_3 + 50E_4 - x_1e_2 + x_2E_1 + E_1e_2 \\ 15E_4 - 10E_3 \\ -60e_2 + e_5 \\ 40e_5 + 2x_1x_2E_1 + 2x_1e_2E_1 - x_2E_1^2 - E_1^2e_2 \end{pmatrix} \tag{28}$$

and

$$B^{**} = \begin{pmatrix} 0 & 0 & 0 \\ 1 & 0 & 0 \\ 0 & 1 & 0 \\ 0 & 0 & 0 \\ 0 & 0 & 1 \end{pmatrix}. \tag{29}$$

According to Lemma 1, we propose the following conclusion.

Theorem 4. *Consider the controlled sum and error system (27). If controller u is designed as follows:*

$$u = K\begin{pmatrix} E \\ e \end{pmatrix}, \tag{30}$$

where $K = k(t)B^{**T}$, B^{**} is given in (29), and $k(t)$ is updated by the following update law:

$$\dot{k} = -\left(\|e\|^2 + \|E\|^2\right). \tag{31}$$

Then, the master system (1) and the slave system (3) realize the coexistence of complete synchronization and antisynchronization.

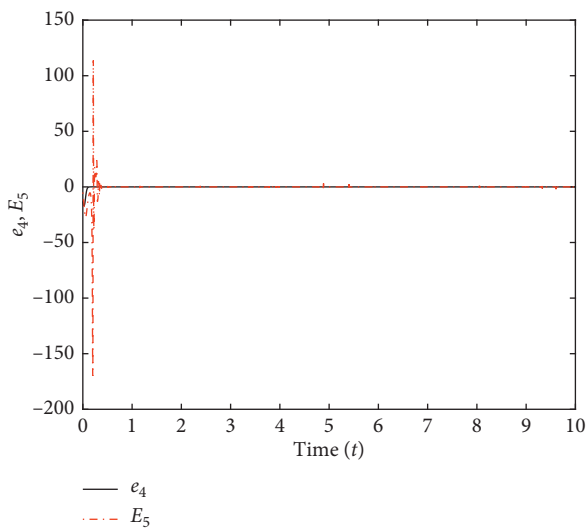

FIGURE 5: e_4, and E_5 are asymptotically stable.

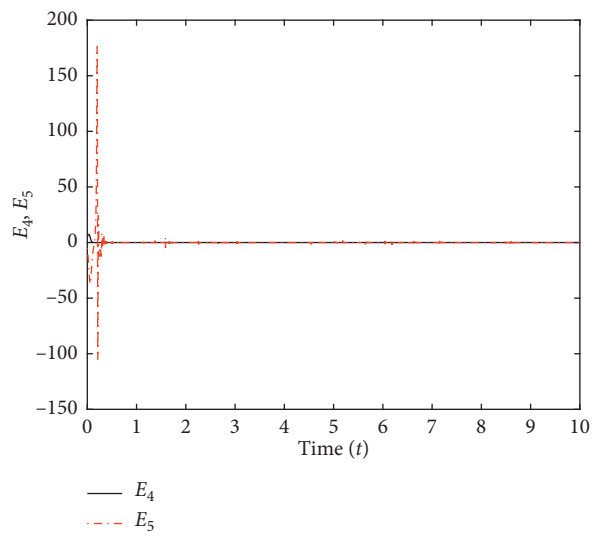

FIGURE 8: E_4 and E_5 are asymptotically stable.

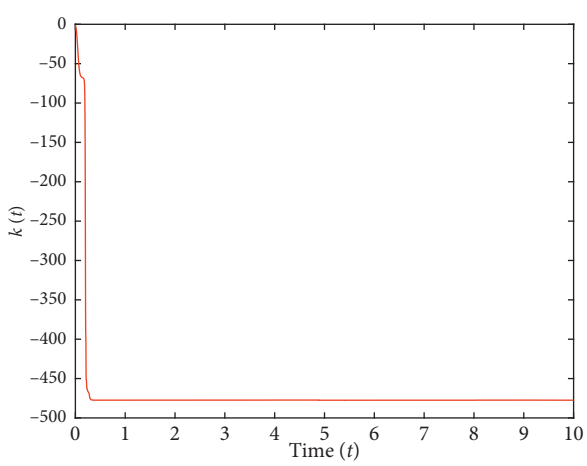

FIGURE 6: The feedback gain $k(t)$ tends to constant.

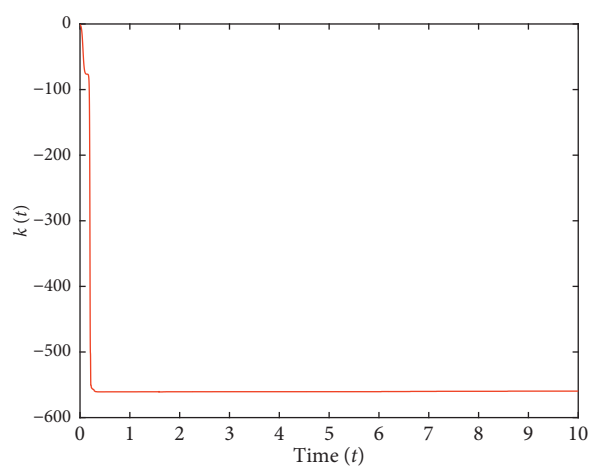

FIGURE 9: The feedback gain $k(t)$ tends to constant.

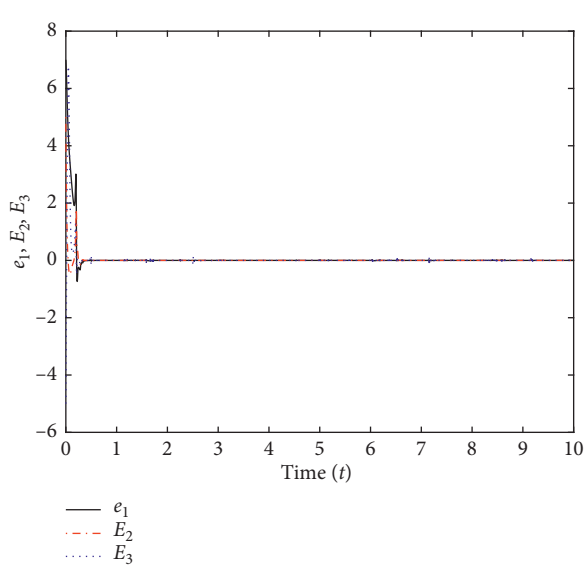

FIGURE 7: e_1, E_2, and E_3 are asymptotically stable.

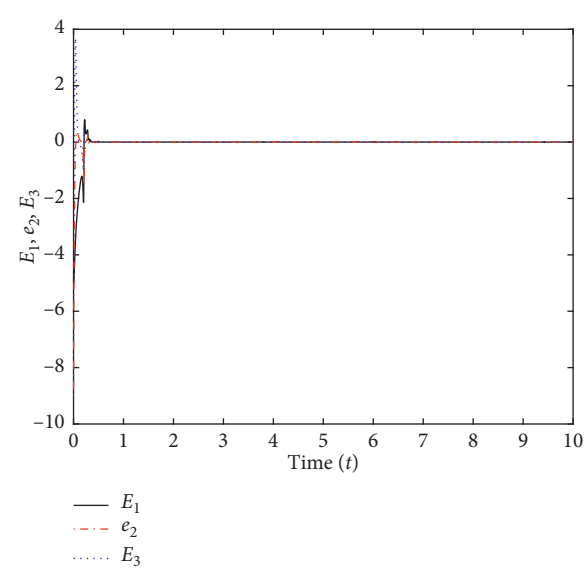

FIGURE 10: E_1, e_2, and E_3 are asymptotically stable.

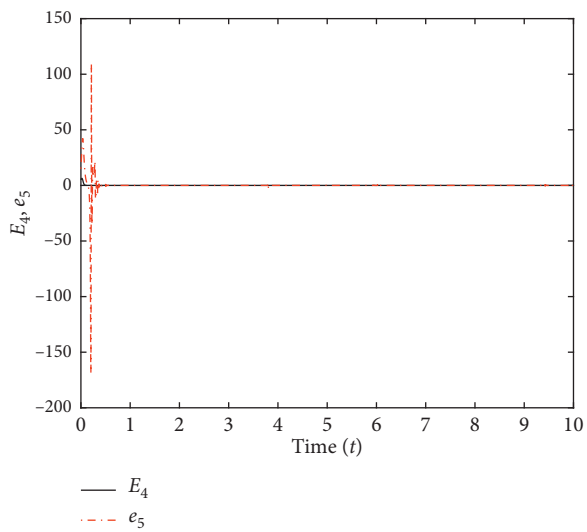

Figure 11: E_4 and E_5 are asymptotically stable.

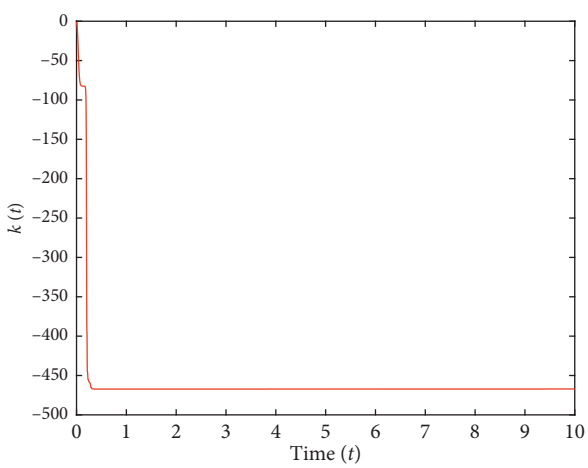

Figure 12: The feedback gain $k(t)$ tends to constant.

Proof. For the sum and error system (27) with $u = 0$, if $E_3 = E_4 = E_5 = 0$, then the following subsystem

$$\begin{aligned} \dot{E}_1 &= -10e_1 - x_3 e_2, \\ \dot{e}_2 &= -60e_2, \end{aligned} \tag{32}$$

is asymptotically stable.

Thus, $(G^{**}(x, E, e), B^{**})$ can be stabilized. According to Lemma 1, the sum and the error system (27) is stabilized by the abovementioned controller u given in (30), which completes the proof. □

In the following, numerical simulation is carried out with the initial conditions: $x_1(0) = 1, x_2(0) = -2, x_3(0) = 3, x_4(0) = -4, \quad y_1(0) = 5, y_2(0) = -6, y_3(0) = 7, y_4(0) = -8$, and $k(0) = -1$. Figure 10 shows E_1, e_2, and E_3 are asymptotically stable, Figure 11 E_4 and E_5 are asymptotically stable, Figure 12 shows that the feedback gain $k(t)$ tends to constant.

5. Conclusions

In conclusion, two types of synchronization problems in the new 5D hyperchaotic system have been investigated. Firstly, the existence of these synchronization problems in such system has been proven. Secondly, those synchronization problems have been realized by the dynamic feedback control method. Finally, numerical simulations have been used to verify the validity and effectiveness of the proposed results.

Data Availability

In our paper, we only used MATLAB for simulation. Therefore, we could only provide simulation programming which can be obtained from the corresponding author upon request.

Conflicts of Interest

The authors declare that there are no conflicts of interest regarding the publication of this paper.

Acknowledgments

This work was supported by the National Natural Science Foundation of China (Grant no. 61973185), Natural Science Foundation of Shandong Province (Grant no. ZR2018MF016), Development Plan of Young Innovation Team in Colleges and universities of Shandong Province (Grant no. 2019KJN011), Shandong Province Key Research and Development Program (Grant no. 2018GGX103054), and Young Doctor Cooperation Foundation of Qilu University of Technology (Shandong Academy of Sciences) (Grant no. 2018BSHZ2008).

References

[1] E. Ott, C. Grebogi, and J. A. Yorke, "Controlling chaos," *Physical Review Letters*, vol. 64, no. 11, pp. 1196–1199, 1990.

[2] L. M. Pecora and T. L. Carroll, "Synchronization in chaotic systems," *Physical Review Letters*, vol. 64, no. 8, pp. 821–824, 1990.

[3] H. Nijmeijer, "A dynamical control view on synchronization," *Physica D: Nonlinear Phenomena*, vol. 154, no. 3-4, pp. 219–228, 2001.

[4] R. Guo, "A simple adaptive controller for chaos and hyperchaos synchronization," *Physics Letters A*, vol. 372, no. 34, pp. 5593–5597, 2008.

[5] A. Yang, L. Li, Z. Wang, and R. Guo, "Tracking control of a class of chaotic systems," *Symmetry*, vol. 11, no. 4, p. 568, 2019.

[6] R. W. Guo, "Simultaneous synchronization and anti-synchronization of two identical new 4D chaotic systems," *Chinese Physics Letter*, vol. 28, pp. 040205–040209, 2011.

[7] Z. Wang and R. Guo, "Hybrid synchronization problem of a class of chaotic systems by an universal control method," *Symmetry*, vol. 10, no. 11, p. 552, 2018.

[8] R. Xu and F. Zhang, "ϵ-Nash mean-field games for general linear-quadratic systems with applications," *Automatica*, vol. 114, pp. 1–6, 2020.

[9] L. Ren and R. Guo, "Synchronization and antisynchronization for a class of chaotic systems by a simple adaptive controller,"

Mathematical Problems in Engineering, vol. 2015, Article ID 434651, 7 pages, 2015.

[10] L. Ren, R. Guo, and U. E. Vincent, "Coexistence of synchronization and anti-synchronization in chaotic systems," *Archives of Control Sciences*, vol. 26, no. 1, pp. 69–79, 2016.

[11] G. Fu and Z. Li, "Robust adaptive anti-synchronization of two different hyperchaotic systems with external uncertainties," *Communications in Nonlinear Science and Numerical Simulation*, vol. 16, no. 1, pp. 395–401, 2011.

[12] S. Hammam, M. Benrejeb, M. Feki, and P. Borne, "Feedback control design for Rössler and Chen chaotic systems anti-synchronization," *Physics Letters A*, vol. 374, pp. 2835–2840, 2010.

[13] C. Huang and J. Cao, "Active control strategy for synchronization and anti-synchronization of a fractional chaotic financial system," *Physica A: Statistical Mechanics and Its Applications*, vol. 473, no. 5, pp. 262–275, 2017.

[14] X. F. Yi, R. W. Guo, and Y. Qi, "Stabilization of chaotic systems with both uncertainty and disturbance by the UDE-based control method," *IEEE Access*, vol. 8, no. 1, pp. 62471–62477, 2020.

[15] W. Yu, Y. Yong, G. Guan, Y. Huang, W. Su, and C. Cui, "Valuing guaranteed minimum death benefits by cosine series expansion," *Mathematics*, vol. 7, no. 9, p. 835, 2019.

[16] A. Zarei, "Complex dynamics in a 5-D hyper-chaotic attractor with four-wing, one equilibrium and multiple chaotic attractors," *Nonlinear Dynamics*, vol. 81, no. 3, pp. 585–605, 2015.

[17] R. Guo, "Projective synchronization of a class of chaotic systems by dynamic feedback control method," *Nonlinear Dynamics*, vol. 90, no. 1, pp. 53–64, 2017.

Hindawi
Mathematical Problems in Engineering
Volume 2020, Article ID 2087169, 6 pages
https://doi.org/10.1155/2020/2087169

Research Article

Antisynchronization of the Hyperchaotic Systems with Uncertainty and Disturbance Using the UDE-Based Control Method

Zuoxun Wang,[1,2] **Xiaotong Yu**,[1,2] **and Guijuan Wang**[1,2]

[1]*School of Electrical Engineering and Automation, Qilu University of Technology (Shandong Academy of Sciences), Jinan 250353, China*
[2]*School of Electrical Engineering and Automation, Shandong Jianzhu University, Jinan 250101, China*

Correspondence should be addressed to Guijuan Wang; wangguijuan2012@163.com

Received 27 February 2020; Accepted 26 March 2020; Published 21 April 2020

Guest Editor: Yi Qi

In this paper, we investigate the antisynchronization problem of a class of hyperchaotic systems with both model uncertainty and external disturbance. Firstly, combining the dynamic feedback control method and the uncertainty and disturbance estimation (UDE)-based control method, we propose a new UDE-based dynamic feedback control method. Secondly, we take the 4D hyperchaotic system as an example and realize the antisynchronization problem of such system. Finally, the effectiveness and correctness of the proposed method is verified by numerical simulation.

1. Introduction

Chaotic behavior has been extensively analyzed in many fields, e.g., engineering, medicine, ecology, biology, and economics, even in social science. In 1990, Pecora and Carroll first discovered the phenomenon of chaotic synchronization [1]. Many types of synchronization problems have been proposed successively, including complete synchronization, generalized synchronization, phase synchronization, lag synchronization, and projective synchronization, see References [2–8]. Later, antisynchronization or antiphase synchronization [9] was proposed. So far, many methods have been proposed to realize chaotic antisynchronization, such as active control, adaptive control, linear feedback control, sliding mode control, and time-delay feedback approach, see References [10–22] and the references therein. Among them, the dynamic feedback control method [19] has a wide range of applications because of its simple design and easy implementation. Thus, this dynamic feedback control method is used in this paper.

It should be pointed out that among the abovementioned chaotic and hyperchaotic systems, model uncertainty and external disturbance are not considered. Unfortunately, this is not the case in practice. The UDE-based control method [23] is a good method to deal with the model uncertainty and external disturbance, and it has the following two advantages: one is that the system model or a disturbance model is not known completely; the other is that both structured (or unstructured) uncertainties and external disturbances are robust against. Being an effective robust control strategy, the UDE-based control has found widespread applications in various systems. Naturally, it is of interest to apply the UDE-based control to chaotic and hyperchaotic systems with both model uncertainty and external disturbance. However, to the best of the authors' knowledge, this problem has not been addressed in the existing literature. Therefore, the main goal of this paper is to develop a new UDE-based dynamic feedback control method to realize the antisynchronization problem of the chaotic and hyperchaotic systems.

This paper mainly studies the antisynchronization problem of chaotic and hyperchaotic systems with both model uncertainty and external disturbance. Combining the dynamic dynamic feedback control method and the UDE-based control method, a new UDE-based dynamic feedback control method is proposed. Then, by the obtained new method, the antisynchronization problem of the 4D

hyperchaotic system is realized and the effectiveness of the method is verified by the numerical simulation.

2. Preliminary

2.1. Dynamic Feedback Control Method for Antisynchronization. Consider the following hyperchaotic system:

$$\dot{w} = G(w), \tag{1}$$

where $w \in R^n$ is the state and $G(w) \in R^n$ is a continuous vector function.

Let system (1) be the master system; then, the corresponding slave system with v is given as

$$\dot{v} = G(v) + bu, \tag{2}$$

where $v \in \mathrm{R}^n$ is the state, $G(v) \in R^n$ is a continuous vector function, $b \in R^{n\times s}$ is a constant matrix, and $u \in R^s$ is the designed controller, $s \geq 1$.

Set $E = w + v$; then, the sum system is described as

$$\dot{E} = G(w) + G(v) + bu, \tag{3}$$

where $E \in R^n$ is the state and b and u are given in (2).

Definition 1. Consider the sum system (3). If $\lim_{t\longrightarrow\infty} \|E(t)\| = 0$; then, we call the master system (1) and slave system (2) achieve antisynchronization.

Remark 1. According to the results in [21], the antisynchronization of system (1) exists only and only if $G(-w) = -G(w)$.

At present, there are many methods for the antisynchronization problem. Among them, the dynamic feedback control method has a wide range of applications because of its simple design and easy implementation. Here is a brief introduction.

According to the existing result in [19–22], we present the following conclusion.

Lemma 1. *Consider system (3), where $b = (b_{ij})_{n\times r}$ and $b_{ij} = 0$ or $b_{ij} = 1$, $i = 1, 2, \ldots, n$, $j = 1, 2, \ldots r$, where $(E(t), b)$ is controllable; then, the dynamic feedback controller is designed as follows:*

$$u = KE, \tag{4}$$

where $K = k(t)b^T$, $K \in R^{n\times n}$, and the feedback gain $k(t)$ is updated by the following law:

$$\dot{k}(t) = -\|E(t)\|^2. \tag{5}$$

2.2. UDE-Based Control Method. Consider the following controlled systems with model uncertainty and disturbance:

$$\dot{p} = H(p) + \Delta H(p) + bu + d(t), \tag{6}$$

where $p \in R^n$ is the state, $H(p)$ is a continuous vector function, $b \in R^{n\times s}$, $s \geq 1$, $\Delta H(p) \in R^n$ represents the model uncertainty, $d(t) \in R^n$ is the external disturbance vector, u is the controller to be designed, and $(H(x), b)$ is assumed controllable.

The stable linear reference model is presented as follows:

$$\dot{p}_m = A_m p_m + B_m C, \tag{7}$$

where $p_m \in R^n$ is the reference state, $A_m \in R^{n\times n}$ is a Hurwitz constant matrix, $B_m \in R^{n\times s}$ is a vector, and $C \in R^s$ is a command.

According to the existing results in [23], the UDE-based control method is presented as follows.

Lemma 2 (see [23]). *Consider system (6) and the reference system (7). If the designed filter $g_f(t)$ satisfies the following condition,*

$$\widetilde{u}_d = \widehat{u}_d - u_d, \tag{8}$$

where $\widehat{u}_d = (\dot{x} - H(p) - bu) * g_f(t)$ and $u_d = \triangle H(x) + d(t)$, then UDE-based controller u is expressed as follows:

$$u = b^+\left\{-H(p) + \ell^{-1}\left[\frac{1}{1 - G_f(s)}\right] * \left(A_m p + B_m C - Kq\right)\right\} - b^+\left\{\ell^{-1}\left[\frac{sG_f(s)}{1 - G_f(s)}\right] * p(t)\right\}, \tag{9}$$

where $q = p - p_m$, $b^+ = (b^T b)^{-1} b^T$, ℓ^{-1} is the inverse Laplace transform operator, $*$ is the convolution operator, and $G_f(s) = \ell[g_f(t)]$.

Remark 2. Since controller in equation (9) cancels $H(p)$ in system (6) directly, thus this controller is too complex to be used in actual chaotic antisynchronization system.

Remark 3. According to the existing result in [23], two kinds of filters are introduced. One is the first-order low-pass filter:

$$G_f(s) = \frac{1}{\tau s + 1}, \tag{10}$$

in general, $\tau = 0.001$.

The other is the secondary filter:

$$G_f(s) = \frac{as + b - w_0^2}{s^2 + as + b}, \tag{11}$$

where $w_0 = 4\pi$, $a = 10w_0$, and $b = 100w_0$.

3. Problem Formulation

Consider the following hyperchaotic system with both model uncertainty and external disturbance:

$$\dot{x} = f(x) + \Delta f(x) + d(t), \tag{12}$$

where $x \in R^n$ is the state, $f(x) \in R^n$ is a continuous vector function, $\Delta f(x) \in R^n$ denotes system model uncertainty, and $d(t) \in R^n$ stands for the external disturbance.

Let system (12) be the master system; then, the slave system with y is given as

$$\dot{y} = f(y) + Bu, \tag{13}$$

where $x \in R^n$ is the state, $B \in R^{n\times r}$ is a constant matrix, and $u \in R^r$, $r \geq 1$ is the controller to be designed, and it is assumed that $(f(y) + f(x), B)$ is controllable.

Let $e = x + y$, then the sum system is described as follows:

$$\dot{e} = f(x) + f(y) + +\Delta f(x) + d(t) + Bu. \tag{14}$$

The main goal of this paper is to design a controller u to meet the following condition:

$$\lim_{t\longrightarrow\infty} e(t) = \lim_{t\longrightarrow\infty} [y(t) + x(t)] = 0. \tag{15}$$

4. Main Results

In this section, we investigate the antisynchronization problem of the hyperchaotic systems with both uncertainty and external disturbance and present the following result.

Theorem 1 Consider system (14). *If a filter $g_f(t)$ is designed to satisfy the following condition,*

$$\tilde{u}_d = \hat{u}_d - u_d \longrightarrow 0, \tag{16}$$

where $\hat{u}_d = (\dot{x} - f(x)) * g_f(t)$ and $u_d = \Delta f(x) + d(t)$, then the dynamic feedback UDE-based controller u is designed as follows:

$$u = u_s + u_{\text{ude}}, \tag{17}$$

where

$$u_s = K(t)e = k(t)B^T e, \tag{18}$$

$k(t)$ is updated by the update law (5), and

$$u_{\text{ude}} = B^+\left[-u_d * g_f(t)\right] = B^+\left[-(\dot{x} - f(x)) * g_f(t)\right], \tag{19}$$

where $B^+ = (B^T B)^{-1} B^T$ and $*$ stands for the convolution operator.

Proof. Substituting controller (17) into system (14), we obtain

$$\begin{aligned}\dot{e} &= f(x) + f(y) + Bu_s + Bu_{\text{ude}} + \Delta f(x) + d(t)\\ &= F(x) + Bu_{\text{ude}} + u_d,\end{aligned} \tag{20}$$

where $F(x) = f(x) + f(y) + Bu_s$ and $u_d = \Delta f(x) + d(t)$.

According to Lemma 1, the system $\dot{e} = F(x)$ is globally asymptotically stable. Noting condition (16), we can obtain

$$Bu_{\text{ude}} = -\hat{u}_d. \tag{21}$$

Thus, system (20) is rewritten as

$$\dot{x} = F(x) + \tilde{u}_d, \tag{22}$$

and this system is globally asymptotically stable, which completes the proof.

5. An Illustrative Example with Numerical Simulation

In this section, we take the new 4D hyperchaotic system as an example to apply our theoretical results.

Example 1. The new 4D hyperchaotic system with uncertainty and disturbance is given as follows:

$$\dot{x} = f(x) + \Delta f(x) + d(t), \tag{23}$$

where $x \in R^4$, $f(x) \in R^4$ is a continuous vector function, $\Delta f(x) \in R^4$ is the model uncertainty, and $d(t) \in R^4$ is the external disturbance, i.e.,

$$\begin{aligned} f(x) &= \begin{pmatrix} f_1(x)\\ f_2(x)\\ f_3(x)\\ f_4(x)\end{pmatrix} = \begin{pmatrix} 35(x_2 - x_1) + x_2x_3x_4\\ 10(x_1 + x_2) - x_1x_3x_4\\ -x_3 + x_1x_2x_4\\ -10x_4 + x_1x_2x_3\end{pmatrix},\\ \Delta f(x) &= \begin{pmatrix} 0\\ -0.1x_1^2\\ 0\\ 0\end{pmatrix},\\ d(t) &= \begin{pmatrix} 0\\ 0.1\ \sin(t)\\ 0\\ 0\end{pmatrix}.\end{aligned} \tag{24}$$

Obviously, $f(-x) = -f(x)$. Thus, the antisynchronization problem of the system $\dot{x} = f(x)$ exists.

Let system (23) be the master system, then the corresponding slave system with y is described as

$$\dot{y} = f(y) + Bu, \tag{25}$$

where $y \in R^4$, $u = u_s + u_{\text{ude}}$ is the controller to be designed, and

$$\begin{aligned} f(y) &= \begin{pmatrix} f_1(y)\\ f_2(y)\\ f_3(y)\\ f_4(y)\end{pmatrix} = \begin{pmatrix} 35(y_2 - y_1) + y_2y_3y_4\\ 10(y_1 + y_2) - y_1y_3y_4\\ -y_3 + y_1y_2y_4\\ -10y_4 + y_1y_2y_3\end{pmatrix},\\ B &= \begin{pmatrix} 0 & 0\\ 1 & 0\\ 0 & 1\\ 0 & 0\end{pmatrix}.\end{aligned} \tag{26}$$

Set $e = x + y$, then the sum system is given as follows:

$$\dot{e} = f(x) + f(y) + Bu + \Delta f(x) + d(t), \tag{27}$$

where $e \in R^4$.

The controlled sum system without model uncertainty and external disturbance is presented as

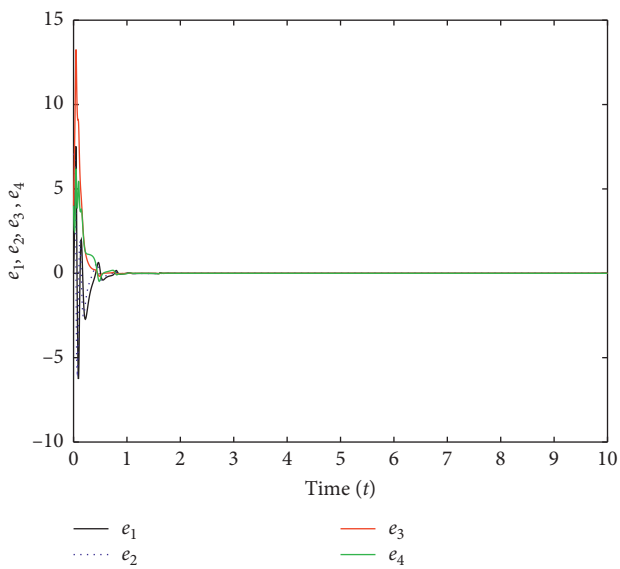

FIGURE 1: The sum system is asymptotically stable.

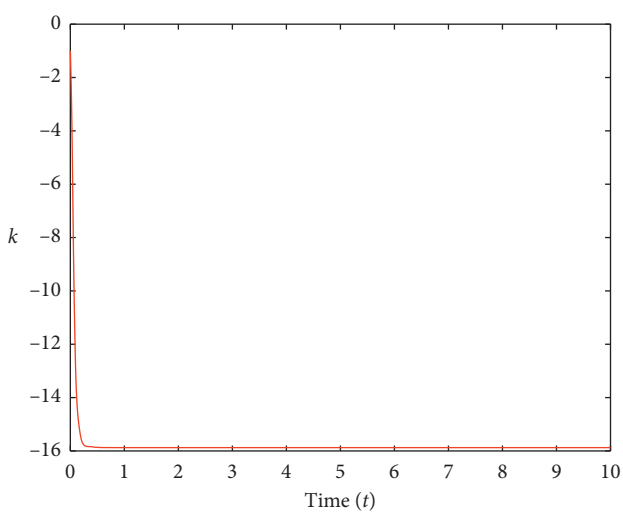

FIGURE 2: $k(t)$ tends to a constant.

$$\dot{e} = f(x) + f(y) + Bu. \tag{28}$$

Our goal is to design a controller $u = u_s + u_{\text{ude}}$. to stabilize the system (27), i.e., $\lim_{t\longrightarrow\infty} \|e(t)\| = 0$.

The first step is to design controller u_s.

For system (28), it is obvious that if $e_2 = 0$ and $e_3 = 0$, we can get that the following two-dimensional system

$$\begin{aligned} \dot{e}_1 &= -35e_1 + x_2x_3e_4, \\ \dot{e}_4 &= -e_4 + x_2x_3e_1, \end{aligned} \tag{29}$$

is globally asymptotically stable.

From Lemma 1, we can design controller u_s as follows:

$$u_s = k(t)B^T e = k(t)\begin{pmatrix} 0 & 1 & 0 & 0 \\ 0 & 0 & 0 & 1 \end{pmatrix} e, \tag{30}$$

where $k(t)$ is updated by the update law (5).

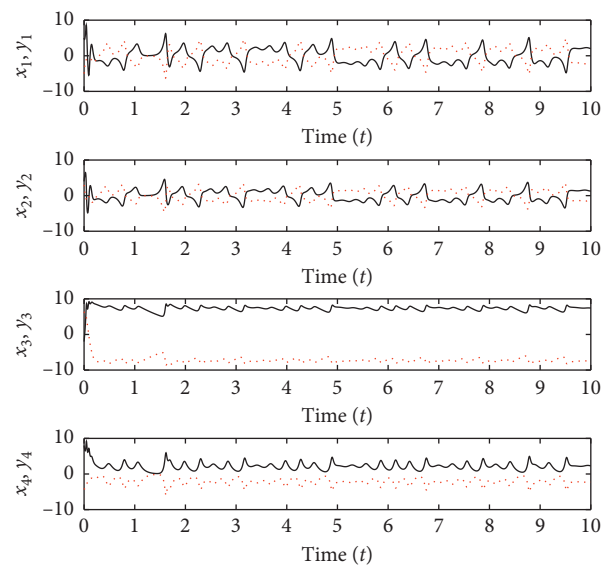

FIGURE 3: x_1, x_2, x_3, and x_4 antisynchronizes y_1, y_2, y_3, and y_4, respectively.

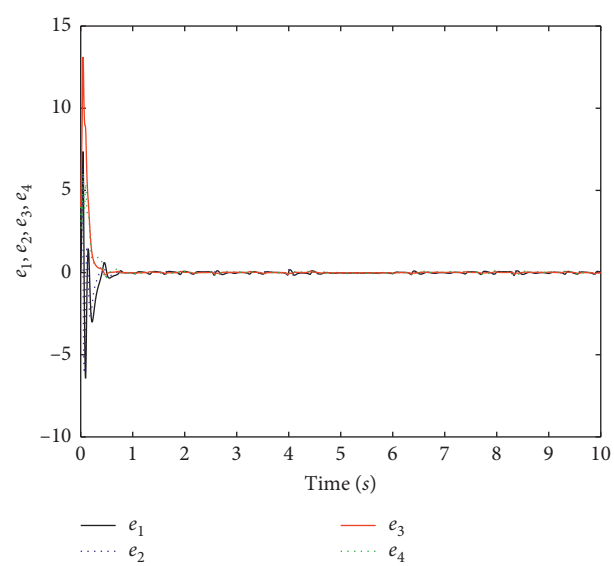

FIGURE 4: The sum system is also asymptotically stable.

For system (28), the numerical simulation is carried out with the initial conditions: $x(0) = [5, 4, -2, 8]$, $y(0) = [-5, 3, 6, -4]$, $k(0) = -1$. Figure 1 shows that under the abovementioned controller, the sum system is asymptotically stable, i.e., the master-slave system achieves antisynchronization. Figure 2 shows that the feedback gain converges to an appropriate constant. Figure 3 shows that states of the master system: x_1, x_2, x_3, and x_4, antisynchronize, the states of the slave system: y_1, y_2, y_3, and y_4, respectively.

The second step is to design the UDE controller u_{ude}.

Let $u_d = \Delta f(x) + d(t)$ and $F(x) = f(x) + f(y) + Bu_s$; the system (27) is rewritten as

$$\dot{e} = F(x) + Bu_{\text{ude}} + u_d. \tag{31}$$

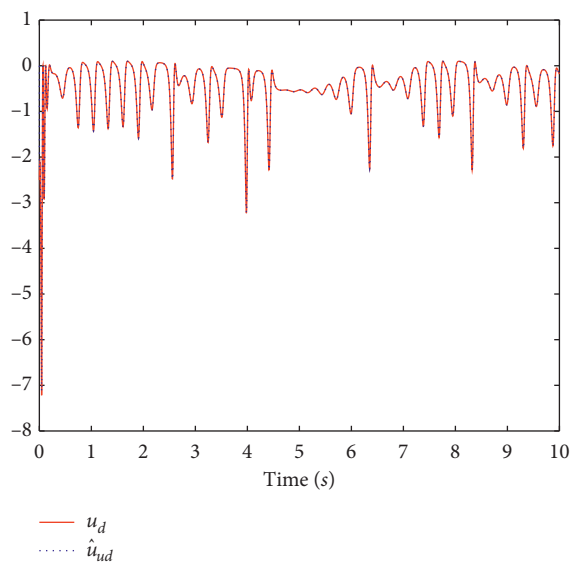

FIGURE 5: $\hat{u}_d$ tends to u_d.

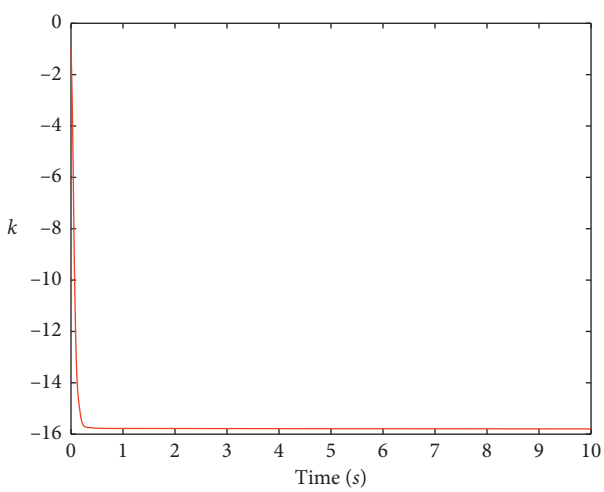

FIGURE 6: $k(t)$ also tends to a constant.

According to Theorem 1, the controller u_{ude} is designed as

$$u_{\text{ude}} = B^{+}\left(-(\dot{x} - f(x)) * g_f(t)\right), \tag{32}$$

where $B^{+} = (B^T B)^{-1} B^T$ and $*$ stands for the convolution operator.

Thus, $u = u_s + u_{\text{ude}}$ is obtained.

For system (27), the numerical simulation is carried out with the initial conditions: $x(0) = [5, 4, -2, 8]$, $y(0) = [-5, 3, 6, -4]$, and $k(0) = -1$. Figure 3 shows that under the abovementioned controller, the error system is asymptotically stable. Figure 4 shows that u_d and $\hat{u}_d$ after a certain time tend to the same constant. Figure 5 shows that the feedback gain $k(t)$ converges to an appropriate constant. Figure 6 shows that the system achieves antisynchronization. The numerical simulation results show that the new 4D hyperchaotic system achieves antisynchronization under the abovementioned controller. Figure 7 shows that states of the master system: x_1, x_2, x_3, and x_4 also antisynchronize the states of the slave system: y_1, y_2, y_3, and y_4, respectively.

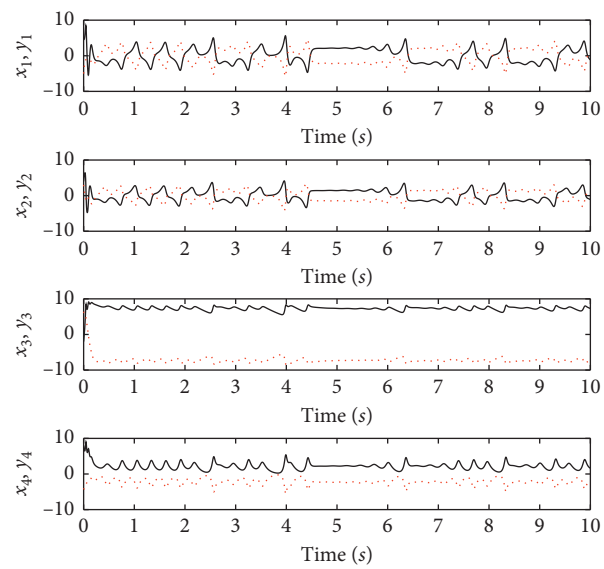

FIGURE 7: x_1, x_2, x_3, and x_4 also antisynchronizes y_1, y_2, y_3, and y_4, respectively.

6. Conclusion

In this paper, the antisynchronization problem of the hyperchaotic systems has been investigated. A new UDE-based dynamic feedback control method has been proposed, and the antisynchronization of the new 4D hyperchaotic system has been realized by the obtained control method. The correctness and effectiveness of the abovementioned theoretical methods have been verified by numerical simulation.

Data Availability

All figures are made by Matlab.

Conflicts of Interest

The authors declare that there are no conflicts of interest regarding the publication of the article.

Acknowledgments

This work was supported by the Natural Science Foundation of Shandong Province (ZR2018MF016).

Supplementary Materials

The supplementary file supplied includes MATLAB Programs. (*Supplementary Materials*)

References

[1] L. M. Pecora and T. L. Carroll, "Synchronization in chaotic systems," *Physical Review Letters*, vol. 64, no. 8, pp. 821–824, 1990.

[2] S. Bowong, "Stability analysis for the synchronization of chaotic systems with different order: application to secure communications," *Physics Letter A*, vol. 326, no. 1-2, pp. 102–113, 2004.

[3] J. García-Ojalvo and R. Roy, "Spatiotemporal communication with synchronized optical chaos," *Physical Review Letter*, vol. 86, no. 22, pp. 5204–5207, 2001.

[4] K. Murali and M. Lakshmanan, "Impulsive stabilization for control and synchronization of chaotic systems: theory and application to secure communication," *Physical Review E*, vol. 44, no. 10, pp. 976–988, 1997.

[5] D. B. Huang, "Synchronization-based estimation of all parameters of chaotic systems from time series," *Physical Review E*, vol. 69, no. 6, Article ID 067201, 2004.

[6] D. B. Huang, "Adaptive-feedback control algorithm," *Physical Review E*, vol. 73, no. 6, Article ID 066204, 2006.

[7] D. B. Huang, "Simple adaptive-feedback controller for identical chaos synchronization," *Physical Review E*, vol. 71, no. 3, p. 37203, 2005.

[8] R. M. Xu and F. Zhang, ".ε-Nash mean-field games for general linear-quadratic systems with applications," *Automatica*, vol. 114, pp. 1–6, 2020.

[9] Z.-L. Wang and X.-R. Shi, "Anti-synchronization of Liu system and Lorenz system with known or unknown parameters," *Nonlinear Dynamics*, vol. 57, no. 3, pp. 425–430, 2009.

[10] S. Hammami, M. Benrejeb, M. Feki, and P. Borne, "Feedback control design for Rössler and Chen chaotic systems anti-synchronization," *Physics Letters A*, vol. 374, no. 28, pp. 2835–2840, 2010.

[11] X.-F. Li, A. C.-S. Leung, X.-P. Han, X.-J. Liu, and Y.-D. Chu, "Complete (anti-)synchronization of chaotic systems with fully uncertain parameters by adaptive control," *Nonlinear Dynamics*, vol. 63, no. 1-2, pp. 263–275, 2011.

[12] H.-L. Li, Y.-L. Jiang, and Z.-L. Wang, "Anti-synchronization and intermittent anti-synchronization of two identical hyperchaotic Chua systems via impulsive control," *Nonlinear Dynamics*, vol. 79, no. 2, pp. 919–925, 2015.

[13] D. Liu, S. Zhu, and K. Sun, "Anti-synchronization of complex-valued memristor-based delayed neural networks," *Neural Networks*, vol. 105, no. 9, pp. 1–13, 2018.

[14] L. Wang and T. Chen, "Finite-time anti-synchronization of neural networks with time-varying delays," *Neurocomputing*, vol. 275, no. 1, pp. 1595–1600, 2018.

[15] E. E. Mahmoud and S. M. Abo-Dahab, "Dynamical properties and complex anti synchronization with applications to secure communications for a novel chaotic complex nonlinear model," *Chaos, Solitons & Fractals*, vol. 106, no. 1, pp. 273–284, 2018.

[16] B. Jia, Y. Wu, D. He, B. Guo, and L. Xue, "Dynamics of transitions from anti-phase to multiple in-phase synchronizations in inhibitory coupled bursting neurons," *Nonlinear Dynamics*, vol. 93, no. 3, pp. 1599–1618, 2018.

[17] X. Zhang, P. Niu, X. Hu, Y. Ma, and G. Li, "Global quasi-synchronization and global anti-synchronization of delayed neural networks with discontinuous activations via non-fragile control strategy," *Neurocomputing*, vol. 361, no. 10, pp. 1–9, 2019.

[18] Y. Huang, J. Hou, and E. Yang, "General decay lag anti-synchronization of multi-weighted delayed coupled neural networks with reaction-diffusion terms," *Information Sciences*, vol. 511, no. 2, pp. 36–57, 2020.

[19] R. W. Guo, "A simple adaptive controller for chaos and hyperchaos synchronization," *Physics Letter A*, vol. 372, no. 34, pp. 5593–5597, 2008.

[20] Z. Wang and R. Guo, "Hybrid synchronization problem of a class of chaotic systems by an universal control method," *Symmetry*, vol. 10, no. 11, p. 552, 2018.

[21] R. Guo, "Projective synchronization of a class of chaotic systems by dynamic feedback control method," *Nonlinear Dynamics*, vol. 90, no. 1, pp. 53–64, 2017.

[22] L. Liu and R. W. Guo, "Control problems of Chen–Lee system by adaptive control method," *Nonlinear Dynamics*, vol. 87, no. 1, pp. 503–510, 2017.

[23] B. Ren, Q.-C. Zhong, and J. Chen, "Robust control for a class of nonaffine nonlinear systems based on the uncertainty and disturbance estimator," *IEEE Transactions on Industrial Electronics*, vol. 62, no. 9, pp. 5881–5888, 2015.

Hindawi
Mathematical Problems in Engineering
Volume 2020, Article ID 4792183, 9 pages
https://doi.org/10.1155/2020/4792183

Research Article

Practical Stability and Integral Stability for Singular Differential Systems with Maxima

Junyan Bao, Peiguang Wang, and Yanjun Li

College of Mathematics and Information Science, Hebei University, Baoding 071002, China

Correspondence should be addressed to Peiguang Wang; pgwang@hbu.edu.cn

Received 17 February 2020; Accepted 14 March 2020; Published 14 April 2020

Guest Editor: Rongwei Guo

In this paper, we introduce various definitions of practical stability and integral stability for nonlinear singular differential systems with maxima and give criteria of stability for such systems via the Lyapunov method and comparison principle.

1. Introduction and Preliminaries

Differential equations with maxima are a special type of differential equations that contain the maximum of the unknown function over a previous interval, of which many examples are found in the fields of application such as automatic control, population dynamics, disease control, and so on. Recently, the research interest in differential equations with maxima has increased exponentially. Some stability results for such equations can be found in the monographs [1, 2], the papers [3–9], and references cited therein.

In practical applications, many problems can be described by singular system models, such as optimal control problems and constrained control problems, which can be found in the monographs of Campbell [10] and Dai [11]. Singular system is a type of dynamic system which is more complicated than the ordinary one. Owing to its complicated structure and many other factors, the study of stability for singular systems involves greater difficulty than that of nonsingular systems. Till now, various types of stability for singular systems have been investigated via Lyapunov functions. However, most previous studies focused on the singular systems described by ordinary differential equations [10–13], difference equations [14–17], and delay differential equations [18–20], and there are a few results for singular differential systems with maxima. In addition, differential equations with maxima have some different properties from the well-known differential equations and delay differential equations.

The purpose of this paper is to integrate these two areas and analyze the practical stability and integral stability of nonlinear singular systems with maxima. To extend Lyapunov's stability and support the specific needs of singular systems, we introduce the function $q(t,x)$ and obtain some different types of stability criteria by using the Lyapunov function method and comparison principle.

2. Practical Stability

The practical stability, being quite different from the stability in the sense of Lyapunov, is neither weaker nor stronger than the usual stability. It is significant from the perspective of engineering application (see [21–25]). In this section, by using Lyapunov functions and the comparison principle, we study some practical stability for the following singular differential systems.

Consider the singular differential systems with maxima

$$\begin{cases} E\dot{x} = f\left(t, x, \max\limits_{s\in[t-\tau,t]} x(s)\right), & \text{for } t \geq t_0 \geq 0, \\ x_{t_0} = \varphi(t), & t \in [-\tau, 0], \end{cases} \tag{1}$$

where $E \in R^{n\times n}$ with rank $(E) < n$ is a singular constant matrix, $x \in R^n$, $f \in C(R_+ \times R^n \times R^n, R^n)$, $f(t,0,0) \equiv 0$, $\tau > 0$ is a constant, and $\varphi \in C([-\tau, 0], R^n)$.

Firstly, we introduce the following notations and sets for convenience.

Let $T_k = [0, t_k)$, where $0 < t_k \leq +\infty$; $q(t,x) \in C^1(J \times R^n, R^m)$, $q(t,0) \equiv 0$, $J \subseteq R_+$. $S_k(t_0)$ is a set of all consistent initial functions at initial time t_0. Then, for any $\varphi \in S_k(t_0)$, there exists at least one continuous solution of systems (1) in $[t_0 - \tau, +\infty)$ through (t_0, φ) (see [20]).

$K = \{a(t) \in C(T_k, R_+) \mid a(t);$
is strictly increasing and $a(0) = 0\}$

$K^* = \{a(t_0, r) \in C(T_k \times R_+, R_+) \mid a(t_0, r);$
is strictly increasing in r and $a(t_0, 0) = 0\}$

$Q(\varepsilon) = \{x \in R^n \mid \|q(t,x)\| < \varepsilon, t \in T_k, \varepsilon > 0$ is a constant$\}$

$D(A) = \{x \in R^n \mid \|q(t,x)\| < A, A > 0$ is a constant$\}$

$\Lambda = \{V \mid V \in C(R \times D(A), R_+)$ and
V islocallyLipschitzianin $x\}$

$G \Longrightarrow H$ means that G implies H

We denote by $x(t) \equiv x(t; t_0, \varphi)$ the solution of the initial value problems (1).

Definition 1. Let $V \in \Lambda, t \in T_k$, and we define the derivative of the function $V(t; x)$ along the trajectory of solution of the singular systems (1) as follows:

$$D^+_{(2.1)} V(t, x(t)) = \limsup_{h \longrightarrow 0} \frac{1}{h} \left\{ V\left(t + h, x(t) + h f\left(t, x(t), \max_{s \in [-\tau, 0]} x(t+s) \right) \right) - V(t, x(t)) \right\}. \tag{2}$$

Definition 2. Let $\varphi \in S_k(t_0)$. The singular systems (1) is said to be

(S_1) stable with respect to $(q(t,x), T_k)$ if for any $\varepsilon > 0$, and some $t_0 \in T_k$, there exists $\delta(t_0, \varepsilon) > 0$, such that

$$\max_{s \in [-\tau, 0]} \|\varphi(s)\| < \delta(t_0, \varepsilon) \Longrightarrow \left\| q(t, x(t; t_0, \varphi)) \right\| < \varepsilon, \quad \text{for } t \geq t_0. \tag{3}$$

Definition 3. Let $\varphi \in S_k(t_0)$. The singular systems (1) is said to be (PS_1) practically stable for given (λ, A) with $0 < \lambda < A$ and some $t_0 \in T_k$, such that

$$\max_{s \in [-\tau, 0]} \|\varphi(s)\| < \lambda \Longrightarrow \left\| q(t, x(t; t_0, \varphi)) \right\| < A, \quad \text{for } t \geq t_0, \tag{4}$$

(PS_2) uniformly practically stable if (PS_1) holds for all $t_0 \in T_k$

(PS_3) practically quasistable for given (λ, B, T) with $\lambda, B, T > 0$, and some $t_0 \in T_k$, we have

$$\max_{s \in [-\tau, 0]} \|\varphi(s)\| < \lambda \Longrightarrow \left\| q(t, x(t; t_0, \varphi)) \right\| < B, \quad \text{for } t \geq t_0 + T, \tag{5}$$

(PS_4) uniformly practically quasistable if (PS_1) holds for all $t_0 \in T_k$

(PS_5) strongly practically stable if (PS_1) and (PS_3) hold simultaneously

(PS_6) strongly uniformly practically stable if (PS_2) and (PS_4) hold simultaneously

Remark 1. If $q(t,x) = x, t_k = +\infty$, and $S_k(t_0, t_k) = C([-\tau, 0], R^n)$, then Definitions 2 and 3 reduce to the concepts of classic Lyapunov stability.

It is well known that the comparison principle plays an important role in the development of stability theory. By the comparison principle, we can reduce the study of a given complicated differential system to that of a relatively simpler differential equation. For this purpose, we give the following lemma and definition.

Lemma 1 (See [1]). *Assume that the following conditions hold*

(A_1) $m(t) \in C(R_+, R_+)$, $g(t,u) \in C(R_+ \times R_+, R)$ *and for any* $t \in T_k$ *such that* $m(t) > m(t+s)$ *for* $s \in [-\tau, 0)$, *the inequality*

$$D^+ m(t) \leq g(t, m(t)), \tag{6}$$

holds, where $D^+ m(t) = \limsup_{h \longrightarrow 0^+} (1/h)[m(t+h) - m(t)]$, $g(t, 0) \equiv 0$

(A_2) *the maximal solution* $r(t) \equiv r(t; t_0, u_0)$ *of the scalar equation*

$$\dot{u} = g(t, u), u(t_0) = u_0, \tag{7}$$

exists, on $[t_0, +\infty)$. *Then,* $m(t) \leq r(t), t \geq t_0$, *provided* $\max_{s \in [-\tau, 0]} m(t_0 + s) \leq u_0$.

Definition 4. Comparison equation (7) is said to be (PS_7) practically stable if for given (λ, A) with $0 < \lambda < A$ and some $t_0 \in R_+$, we have $u_0 < \lambda$ implies $u(t) < A$, for $t \geq t_0$

(PS_8) uniformly practically stable if (PS_7) holds for all $t_0 \in R_+$

(PS_9) practically quasistable if for given (λ, B, T) with $0 < \lambda < A$, $B > 0$, $T > 0$, and some $t_0 \in R_+$, we have that $u_0 < \lambda$ implies $u(t) < B$, for $t \geq t_0 + T$

(PS_{10}) uniformly practically quasistable if (PS_9) holds for all $t_0 \in R_+$

Theorem 1. *Assume that the following conditions hold*

(A_3) $(q(t,x), T_k, \lambda, A)$ *with* $0<\lambda<A$ *are given*

(A_4) *there exists a function* $V \in C(T_k \times D(A), R_+)$ *and* $V \in \Lambda$ *such that*

(i) for any $t>t_0$, $V(t,x(t)) > V(t+s, x(t+s))$, $s \in [-\tau, 0)$, *the inequality*

$$D^+_{(2.1)} V(t,x(t)) \le g(t, V(t,x(t))), \tag{8}$$

holds, where $g \in C(T_k \times R_+, R)$ *and* $g(t,0) \equiv 0$

(ii) $b(\|q(t,x)\|) \le V(t,x) \le a(\|x\|)$, *where* $a(\cdot)$, $b(\cdot) \in K$ *and* $a(\lambda) < b(A)$

Then, equation (7) is (uniformly) practically stable with respect to $(a(\lambda), b(A))$ *implies that system (1) is (uniformly) practically stable with respect to* $(q(t,x), T_k, \lambda, A)$.

Proof. Assume that $u(t;t_0,u_0)$ is a solution of the equation (7), and is practically stable with respect to $(a(\lambda), b(A))$ for given $0<\lambda<A$. Let $m(t) = V(t,x(t))$, where $x(t)$ is a solution of the systems (1). From the condition (i) of (A_4), it follows that $D^+m(t) \le g(t, m(t))$, for $t \ge t_0$. Let

$$u(t_0) = \max_{s\in[-\tau,0]} V(t_0+s, \varphi(s)) = \max_{s\in[-\tau,0]} m(t_0+s). \tag{9}$$

By Lemma 1, we know that the inequality $V(t,x(t)) = m(t) \le r(t)$, for $t \ge t_0$, holds, where $r(t)$ is the maximal solution of comparison equation (7) existing on T_k. Assume that $\max_{s\in[-\tau,0]}\|\varphi(s)\| < \lambda$, then, we have

$$\begin{aligned} u(t_0) &= \max_{s\in[-\tau,0]} V(t_0+s, \varphi(s)) \le \max_{s\in[-\tau,0]} a(\|\varphi(s)\|) \\ &= a\left(\max_{s\in[-\tau,0]} \|\varphi(s)\|\right) < a(\lambda). \end{aligned} \tag{10}$$

Furthermore, from the condition (ii) of (A_4) and Lemma 1, we get $b(\|q(t,x)\|) \le V(t,x) = m(t) \le r(t) < b(A)$. Thus, $\max_{s\in[-\tau,0]}\|\varphi(s)\| < \lambda$ implies $\|q(t,x)\| < A$, $t \ge t_0$, that is, system (1) is practically stable with respect to $(q(t,x), T_k, \lambda, A)$.

Similarly, we can prove that equation (7) is uniformly practically stable with respect to $(a(\lambda), b(A))$ implies that the systems (1) is uniformly practically stable with respect to $(q(t,x), T_k, \lambda, A)$. The proof is completed.

By Theorem 1, we can obtain the following corollaries. □

Corollary 1. *Assume that the conditions* (A_3) *and (ii) of* (A_4) *hold in Theorem 1, and*

(A_5) *there exists a function* $V \in C(T_k \times D(A), R_+)$ *and* $V \in \Lambda$ *such that for any* $t>t_0$, $V(t,x(t)) > V(t+s, x(t+s))$, $s \in [-\tau, 0)$, *the inequality*

$$D^+_{(2.1)} V \le 0 \tag{11}$$

holds. Then, system (1) is uniformly practically stable with respect to $(q(t,x), T_k, \lambda, A)$.

The conclusion of Corollary 1 can be obtained by considering the case of $g(t,u) \equiv 0$ and $\dot{u} = 0$ is uniformly practically stable with respect to $(a(\lambda), b(A))$ for given $0<\lambda<A$.

Corollary 2. *Assume that the conditions* (A_3) *and (ii) of* (A_4) *hold in Theorem 1, and*

(A_6) *there exists a function* $V(t,x) \in C(T_k \times D(A), R_+)$ *and* $V \in \Lambda$ *such that for any* $t>t_0$, $V(t,x(t)) > V(t+s, x(t+s))$, $s \in [-\tau, 0)$, *the inequality*

$$D^+_{(2.1)} V \le \alpha(t) F(V(t,x)), \tag{12}$$

holds, where $F \in C(R_+, R_+)$ *and* $0 < F(V) \le V$

(A_7) *the inequalities*

$$\int_{t_0}^{t} \alpha(t)\mathrm{d}t \le M < +\infty, \quad M \le \ln\frac{b(A)}{a(\lambda)}, t \in [t_0, +\infty), \tag{13}$$

hold

Then, system (1) is uniformly practically stable with respect to $(q(t,x), T_k, \lambda, A)$.

Proof. By Theorem 1, we only prove that the system $\dot{u} = (\alpha(t)F(u))$ is uniformly practically stable with respect to $(a(\lambda), b(A))$. In fact, let $u(t_0) = u(t_0;t_0,u_0) = \max_{s\in[-\tau,0]} V(t_0+s, \varphi(s))$. Assume that $\max_{s\in[-\tau,0]}\|\varphi(s)\| < \lambda$, it follows from the condition (ii) of (A_4) that

$$u(t_0;t_0,u_0) \le \max_{s\in[-\tau,0]} a(\|\varphi(s)\|) = a\left(\max_{s\in[-\tau,0]} \|\varphi(s)\|\right) < a(\lambda). \tag{14}$$

Furthermore, by condition (A_7), the inequality

$$u(t;t_0,u_0) \le u_0 \exp\left\{\int_{t_0}^{t} \alpha(s)\mathrm{d}s\right\} < a(\lambda)e^M < b(A), \tag{15}$$

holds. Then, system (1) is uniformly practically stable with respect to $(q(t,x), T_k, \lambda, A)$. The proof is completed. □

Corollary 3. *Assume that the conditions* (A_3) *and (ii) of* (A_4) *hold in Theorem 1, and*

(A_8) *there exists a function* $V \in C(T_k \times D(A), R_+)$ *and* $V \in \Lambda$ *such that for any* $t>t_0$, $V(t,x(t)) > V(t+s, x(t+s))$ *for* $s \in [-\tau, 0)$, *the inequality*

$$D^{+}_{(2.1)}V \leq -\alpha F(V(t,x)) + \beta, \tag{16}$$

holds, in which α and β are positive constants, $0 < F(V) \leq V$

(A_9) the inequalities

$$\begin{gathered} a(\lambda) < b(A), \\ a(\lambda) + \frac{\beta}{\alpha} \leq b(A), \end{gathered} \tag{17}$$

hold

Then, system (1) is uniformly practically stable with respect to $(q(t,x), T_k, \lambda, A)$.

Proof. In fact, we only need to prove that the system $\dot{u} = -\alpha F(u) + \beta$ is uniformly practically stable with respect to $(a(\lambda), b(A))$. Let $u(t_0) = u(t_0; t_0, u_0) = \max_{s\in[-\tau,0]} V(t_0 + s, \varphi(s))$; then, we have

$$u(t_0; t_0, u_0) \leq \max_{s\in[-\tau,0]} a(\|\varphi(s)\|) = a\left(\max_{s\in[-\tau,0]} \|\varphi(s)\|\right) < a(\lambda). \tag{18}$$

Furthermore, by condition (A_8), the inequality

$$u(t; t_0, u_0) \leq u_0 e^{-\alpha(t-t_0)} + \frac{\beta}{\alpha} < a(\lambda) + \frac{\beta}{\alpha} \leq b(A) \tag{19}$$

holds. Then, system (1) is uniformly practically stable with respect to $(q(t,x), T_k, \lambda, A)$. □

Theorem 2. *Assume that the conditions (A_3) and (ii) of (A_4) hold in Theorem 1, and (iii) $V(t,x) \geq b(\|q(t,x)\|)$, $V(t_0, x) \leq a(t_0, \|x\|)$, where $b(\cdot) \in K, a(t_0, \cdot) \in K^*$.*

Then, equation (7) is (uniformly) practically stable with respect to $(a(t_0, \lambda), b(A))$ implies that the systems (1) is (uniformly) practically stable with respect to $(q(t,x), T_k, \lambda, A)$.

Proof. In fact, by the condition (iii) of (A_4), we have

$$\begin{aligned} u(t_0) &= \max_{s\in[-\tau,0]} V(t_0 + s, \varphi(s)) \leq \max_{s\in[-\tau,0]} a(t_0, \|\varphi(s)\|) \\ &= a\left(t_0, \max_{s\in[-\tau,0]} \|\varphi(s)\|\right). \end{aligned} \tag{20}$$

Then, we can get the result by using a method similar to Theorem 1. We omit its details. □

Theorem 3. *Assume that the following conditions hold*

(A_{10}) $(q(t,x), T_k, \lambda, A, B, T)$ with $0 < \lambda < A$, $0 < B < A$ and $T > 0$ are given

(A_4) there exists a function $V \in C(T_k \times D(A), R_+)$ and $V \in \Lambda$ such that

(i) for any $t > t_0$, $V(t, x(t)) > V(t+s, x(t+s))$, $s \in [-\tau, 0)$, the inequality

$$D^{+}_{(2.1)}V(t, x(t)) \leq g(t, V(t, x(t))), \tag{21}$$

holds, where $g \in C(T_k \times R_+, R)$, $g(t, 0) \equiv 0$

(ii) $b(\|q(t,x)\|) \leq V(t,x) \leq a(\|x\|)$, where $a(\cdot), b(\cdot) \in K$ and $a(\lambda) < b(A)$

Then, equation (7) is (uniformly) practically quasistable with respect to $(a(\lambda), b(B), T)$ implies that system (1) is (uniformly) practically quasistable with respect to $(q(t,x), T_k, \lambda, B, T)$.

Proof. Assume that $u(t; t_0, u_0)$ is a solution of equation (7) and is practically quasistable with respect to $(a(\lambda), b(B), T)$ for given $0 < \lambda < A$, $0 < B < A$ and $T > 0$. Let $m(t) = V(t, x(t))$, where $x(t)$ is a solution of system (1). It follows from the condition (A_4) that

$$D^{+}m(t) \leq g(t, m(t)), \quad \text{for } t \geq t_0. \tag{22}$$

Let $u(t_0) = \max_{s\in[-\tau,0]} V(t_0 + s, \varphi(s)) = \max_{s\in[-\tau,0]} m(t_0 + s)$. Then, by Lemma 1, we know that the inequality

$$V(t,x) = m(t) \leq r(t), \quad \text{for } t \geq t_0, \tag{23}$$

holds, where $r(t)$ is the maximal solution of comparison equation (7) existing on T_k. Assume that $\varphi(s) \in C([-\tau, 0], R^n)$ and $\max_{s\in[-\tau,0]} \|\varphi(s)\| < \lambda$. Then, we obtain

$$\begin{aligned} u(t_0) &= \max_{s\in[-\tau,0]} V(t_0 + s, \varphi(s)) \leq \max_{s\in[-\tau,0]} a(\|\varphi(s)\|) \\ &= a\left(\max_{s\in[-\tau,0]} \|\varphi(s)\|\right) < a(\lambda). \end{aligned} \tag{24}$$

Furthermore, by comparison equation (7) which is practically quasistable with respect to $(a(\lambda), b(B), T)$, the condition (A_4), and Lemma 1, we get

$$b(\|q(t,x)\|) \leq V(t,x) = m(t) \leq r(t) < b(B), \quad \text{for } t \geq t_0 + T. \tag{25}$$

Thus, $\max_{s\in[-\tau,0]} \|\varphi(s)\| < \lambda$ implies $\|q(t,x)\| < B$, $t \geq t_0 + T$, that is, system (1) is practically quasistable with respect to $(q(t,x), T_k, \lambda, B, T)$.

Similarly, we can prove that equation (7) is uniformly practically stable with respect to $(a(\lambda), b(B), T)$ implies that the systems (1) is uniformly practically stable with respect to $(q(t,x), T_k, \lambda, B, T)$. □

Theorem 4. *Assume that the conditions (A_{10}) and (i) of (A_4) hold in Theorem 3, and the condition (ii) of (A_4) is replaced by*

(iv) $V(t,x) \geq b(\|q(t,x)\|)$, $V(t_0, x) \leq a(t_0, \|x\|)$, where $b(\cdot) \in K, a(t_0, \cdot) \in K^*$

Then, equation (7) is (uniformly) practically quasistable with respect to $(a(\lambda), b(B), T)$ implies that the systems (1) is (uniformly) practically quasistable with respect to $(q(t,x), T_k, \lambda, B, T)$.

The proof of Theorem 4 is similar to that of Theorem 3, so we omit its details.

3. Integral Stability

The concept of integral stability, which was introduced for ordinary differential equations by Vrhoc in 1959 [26] and Lakshmikantham in 1969 [27], enlarges the collection of dynamical properties of solutions which can be investigated by the direct Lyapunov method. The integral stability theory has been rapidly developed recently. For example, Martynyuk [28], Salvadori and Visentin [29], Soliman and Abdalla [30] obtained the integral stability criteria for nonlinear differential equations, respectively; Hristova [31] obtained the integral stability in terms of two measures for impulsive differential equations; and Sood and Srivastava [32] gave the φ_0-integral stability criteria for impulsive differential equations. The main purpose of this section is to discuss the integral stability of singular differential systems with maxima and its perturbed systems.

Consider singular differential system (1) and its perturbed systems

$$\begin{cases} E\dot{x} = f\left(t, x, \max\limits_{s\in[t-\tau,t]} x(s)\right) + h\left(t, x, \max\limits_{s\in[t-\tau,t]} x(s)\right), & \text{for } t \geq t_0 \geq 0, \\ x_{t_0} = \varphi(t), & t \in [-\tau, 0], \end{cases} \tag{26}$$

where $h \in C(R_+ \times R^n \times R^n, R^n)$, $h(t, 0, 0) \equiv 0$.

Let $S_{pk}(t_0)$ be a set of all consistent initial functions of (1) and (26) in $[t_0, t_k)$ through (t_0, φ). For any $\varphi \in S_{pk}(t_0)$, assume that there exists a continuous solution of (1) and (26) in $[t_0, t_k)$ through (t_0, φ) at least.

$$B(\varphi, \delta) = \left\{\psi \in C\left([-\tau, 0], R^n\right) \middle| \max_{s\in[-\tau,0]} \|\psi(s) - \varphi(s)\| < \delta, \varphi \in C\left([-\tau, 0], R^n\right), \delta \in R_+\right\}. \tag{27}$$

Definition 5. Let $\varphi \in S_{pk}(t_0)$. Singular system (1) is said to be

(IS_1) equi-integrally stable on $\{q(t, x), T_k\}$, if for given $\alpha \geq 0$ and $t_0 \in T_k$, there exists a positive function $\beta = \beta(t_0, \alpha)$, which is continuous in t_0 for each α and $\beta \in K$, such that, for every solution $x(t; t_0, \varphi)$ of the perturbed systems (26),

$$q(t, x) \in D(\beta), \quad t \geq t_0, \tag{28}$$

holds, provided that $\varphi \in B(0, \alpha) \cap S_{pk}(t_0)$ and

$$\int_{t_0}^{t_0+T} \sup_{\|q(t,x)\|\leq\beta} \left\| h\left(s, x, \max_{u\in[s-\tau,s]} x(u)\right)\right\| \mathrm{d}s \leq \alpha, \quad \text{for } T > 0; \tag{29}$$

(IS_2) uniformly integrally stable on $\{q(t, x), T_k\}$, if the β in (IS_1) is independent of t_0

(IS_3) equiasymptotically integrally stable on $\{q(t, x), T_k\}$, if (IS_1) holds and for every $\epsilon > 0$, $\alpha \geq 0$ and $t_0 \in T_k (t_k = +\infty)$, there exist positive functions $T = T(t_0, \alpha, \epsilon)$ and $\gamma = \gamma(t_0, \alpha, \epsilon)$, which are continuous in t_0 for each α and ϵ, and for every solution $x(t; t_0, \varphi)$ of the perturbed systems (26),

$$q(t, x) \in D(\epsilon), \quad t \geq t_0 + T, \tag{30}$$

holds, provided that $\varphi \in B(0, \alpha) \cap S_p(t_0)$, and

$$\int_{t_0}^{+\infty} \sup_{\|q(t,x)\|\leq\beta} \left\| h\left(s, x, \max_{u\in[s-\tau,s]} x(u)\right)\right\| \mathrm{d}s \leq \gamma, \tag{31}$$

(IS_4) uniformly asymptotically integrally stable on $\{q(t, x), T_k\}$ if the T and γ in (IS_3) are independent of t_0 and (IS_2) holds

Now, we consider comparison scalar differential equation (7) and its perturbed equation

$$\dot{u} = g(t, u) + p(t), \quad u(t_0) = u_0, \tag{32}$$

where $g(t, 0) \equiv 0$, $g \in C[T_k \times R_+, R]$, $p(t) \in C[T_k, R_+]$.

Definition 6. Equation (7) is said to be equi-integrally stable, if for given $\alpha_1 \geq 0$, $t_0 \in T_k$, there exists a positive function $\beta_1 = \beta_1(t_0, \alpha_1)$ that is continuous in t_0 for each α_1 and $\beta_1 \in K$, such that, for every solution $u(t; t_0, u_0)$ of the perturbed differential equation (32), the inequality

$$\left|u(t; t_0, u_0)\right| < \beta_1, \tag{33}$$

holds, provided that $|u_0| \leq \alpha_1$ and $\int_{t_0}^{t_0+T} p(s)\mathrm{d}s \leq \alpha_1$ for every $T > 0$.

Remark 2. Similar to Definition 5, we can give the corresponding concepts of stability of equation (7).

Next, we investigate the integral stability of system (1) via the Lyapunov function method and comparison principle.

Theorem 5. *Assume that the condition (i) of (A_4) holds in Theorem 1, and condition (ii) of (A_4) is replaced by*

$$(A_4')\, b(\|q(t, x)\|) \leq V(t, x), \quad t \geq t_0, \text{where } b \in K, \text{ and } b(r) \longrightarrow +\infty \text{ as } r \longrightarrow +\infty. \tag{34}$$

Then, equation (7) which is equi-integrally stable implies that system (1) is equi-integrally stable on $\{q(t, x), T_k\}$.

Proof. Let $\varphi \in B(0, \alpha) \cap S_{pk}(t_0)$ for every $\alpha \geq 0$, $t_0 \in T_k$. Since $V(t, x)$ is Lipschitzian in x, we have

$$|V(t, x) - V(t, y)| \leq L\|x - y\|, \quad L > 0 \text{ is a constant}, \quad \max_{s\in[-\tau,0]} V(t_0 + s, \varphi(s)) \leq L \max_{s\in[-\tau,0]} \|\varphi(s)\| \leq L\alpha = \alpha_1. \tag{35}$$

Let $x(t) = x(t; t_0, \varphi)$ be any solution of (26). Thus, by the condition (i) of (A_4) and (29), we get

$$D^+_{(21)} V(t, x) \leq g(t, V(t, x)) + L\left\| h\left(t, x, \max_{s\in[t-\tau,t]} x(s)\right)\right\|. \tag{36}$$

Defining $p(t) = L\|h(t, x, \max_{s\in[t-\tau,t]} x(s))\|$ and choosing $u_0 = \max_{s\in[-\tau,0]} V(t_0 + s, \varphi(s))$, by Lemma 1, we have

$$V(t, x) \le r(t; t_0, u_0), \tag{37}$$

where $r(t; t_0, u_0)$ is the maximal solution of (32).

If equation (7) is equi-integrally stable, then for $\alpha_1 \ge 0$ and $t_0 \in T_k$, there exists a $\beta_1 = \beta_1(t_0, \alpha_1)$, which is continuous in t_0 for each α_1 and $\beta_1 \in K$, such that, for every solution $u(t; t_0, u_0)$ of (32), the inequality

$$u(t; t_0, u_0) < \beta_1, \quad t \ge t_0 \tag{38}$$

holds, whenever $u_0 \le \alpha_1$ and $\int_{t_0}^{t_0+T} p(s)\mathrm{d}s \le \alpha_1$ for any $T > 0$.

By the condition (A_4'), it is possible to choose a $\beta = \beta(t_0, \alpha)$ satisfying

$$b(\beta) \ge \beta_1. \tag{39}$$

It is easily shown that β is continuous in t_0 for each α and $\beta \in K$ for each $t_0 \in T_k$. Moreover, we claim that system (1) is equi-integrally stable on $\{q(t, x), T_k\}$. In fact, if this is not true, there exists a $t_1 > t_0$ such that

$$\|q(t_1, x)\| = \beta, \text{ and } \|q(t, x)\| < \beta,\ t \in [t_0, t_1). \tag{40}$$

From (37)–(40), we have

$$\beta_1 \le b(\beta) \le V(t_1, x(t_1; t_0, \varphi)) \le r(t_1; t_0, u_0) < \beta_1, \tag{41}$$

which is a contradiction. Thus, system (1) is equi-integrally stable on $\{q(t, x), T_k\}$. □

Corollary 4. *Assume that the conditions of Theorem 5 hold. Then, equation (7) which is uniformly integrally stable implies that system (1) is uniformly integrally stable on {q(t; x); T_k}.*

The detailed proof of Corollary 4 is similar to the proof in Theorem 5, so we omit it.

Theorem 6. *Assume that the conditions of Theorem 5 hold and $t_k = +\infty$ Then, equation (7) which is equiasymptotically integrally stable implies that system (1) is equiasymptotically integrally stable on {q(t. x), R_+}.*

Proof. It can be known from the proof of Theorem 5 that system (1) is equi-integrally stable on $\{q(t, x), R_+\}$. Let $\varphi \in B(0, \alpha) \cap S_p(t_0, +\infty)$ and $\alpha_1 = L\alpha$, for given $\alpha \ge 0$ and $t_0 \in [0, +\infty)$. For given .., $\alpha_1 \ge 0$ and $t_0 \in R_+$, there exist $\gamma_1 = \gamma_1(t_0, \alpha_1, \varepsilon)$ and $T = T(t_0, \alpha_1, \varepsilon)$, such that for every solution $u(t; t_0, u_0)$ of (32),

$$u(t; t_0, u_0) < b(\varepsilon),\ t \ge t_0 + T, \tag{42}$$

holds, whenever $u_0 = \max_{s\in[-\tau,0]} V(t_0 + s, \varphi(s)) \le \alpha_1$ and $\int_{t_0}^{\infty} p(s)\mathrm{d}s < \gamma_1$.

Choosing a positive number $\gamma = \gamma(t_0, \alpha, \epsilon)$ such that $L\gamma = \gamma_1$, for given γ and T, system (1) satisfies (IS_3) of Definition 5. In fact, suppose that the conclusion is not true, then $q(t, x) \in D(\epsilon)$, $t \ge t_0 + T$ cannot be satisfied when

$$\begin{aligned} &\varphi \in B(0, \alpha) \cap S_p(t_0, +\infty) \\ &\text{and } \int_{t_0}^{+\infty} \sup_{\|q(t,x)\|\le\beta} \left\| h\left(s, x, \max_{u\in[s-\tau,s]} x(u)\right)\right\| \mathrm{d}s \le \gamma. \end{aligned} \tag{43}$$

Let $\{t_k\}$ be a sequence such that $t_k \ge t_0 + T$ and $\lim_{k\longrightarrow+\infty tk} = +\infty$. Suppose that there is a solution $x(t) = x(t; t_0, \varphi)$ of system (26), such that for every k,

$$\|q(t_k, x(t_k; t_0, \varphi))\| \ge \varepsilon. \tag{44}$$

By the condition (A_4') and (44), we obtain

$$b(\varepsilon) \le b(\|q(t_k, x(t_k; t_0, \varphi))\|) \le V(t_k, x(t_k; t_0, \varphi)). \tag{45}$$

Furthermore, by the equiasymptotical integral stability of equations (7), (37), and (42)–(59), we can get

$$b(\epsilon) \le V(t_k, x(t_k; t_0, \varphi)) \le r(t_k; t_0, u_0) < b(\epsilon). \tag{46}$$

which is a contradiction. Thus, system (1) is equi-asymptotically integrally stable on $\{q(t, x), [0, +\infty)\}$. □

Corollary 5. *Assume that the conditions of Theorem 6 hold. Then, equation (7) which is uniformly asymptotically integrally stable implies that system (1) is uniformly asymptotically integrally stable on {q(t; x); T_k}.*

In fact, we can show that the positive numbers T and γ_1 in proof of Theorem 6 are independent of t_0; therefore, (44) implies that γ is independent of t_0. The rest of the proof is similar to that of Theorem 6, so we omit the details here.

For the comparison equation (7), if we suppose that the function $g(t, u)$ is nonincreasing in u for $t \in [t_0, +\infty)$; then, we can get the uniform asymptotic integral stability of system (1) by the uniform asymptotic stability of the comparison equation (7). Therefore, we firstly give the following definition and Lemmas, which can be found in [27].

Definition 7. Comparison equation (7) is said to be

(S_1) equistable, if for each $\epsilon > 0$, $t_0 \in R_+$, there exists a positive function $\delta = \delta(t_0, \epsilon)$, such that

$$|u_0| \le \delta \Longrightarrow |u(t; t_0, u_0)| < \varepsilon, \quad \text{for } t \ge t_0, \tag{47}$$

(S_2) uniformly stable if δ in (S_1) is independent of t_0

(S_3) equiasymptotically stable, if it is equistable and for each $\epsilon > 0$, $t_0 \in R_+$, there exists a positive function $\delta_0 = \delta_0(t_0)$, $T = T(t_0, \epsilon)$, such that

$$|u_0| \le \delta_0 \Longrightarrow |u(t; t_0, u_0)| < \epsilon, \text{for } t \ge t_0 + T, \tag{48}$$

(S_4) uniformly asymptotically stable if (S_2) holds and the numbers δ_0 and T in (S_3) are independent of t_0

Lemma 2 (see [27]). *Equation (7) is uniformly stable if and only if there exists a function $a(r) \in K$, such that*

$$|u_0| \le \delta \Longrightarrow |u(t; t_0, u_0)| \le a(|u_0|), \quad \text{for } t \ge t_0. \tag{49}$$

Lemma 3 (see [27]). *Equation (7) is uniformly asymptotically stable if and only if there exist functions $a(r) \in K$ and $\sigma(r) \in \mathcal{S}$, such that*

$$|u_0| \le \delta \Longrightarrow |u(t;t_0,u_0)| \le a(|u_0|)\sigma(t-t_0), \quad \text{for } t \ge t_0, \tag{50}$$

where $\mathcal{F} = \{\sigma(r) \in C[R_+, R_+]\sigma(r)$ is monotone decreasing in r, and $\sigma(r) \longrightarrow 0$ as $r \longrightarrow +\infty\}$.

Theorem 7. *Assume that the conditions of Theorem 6 hold, the function $g(t;u)$ be nonincreasing in u for any $t \in [t_0, +\infty)$, and*

$$V(t,x(t)) > V(t+s, x(t+s)) - L\int_t^{t+s}\left\|h\left(v, x, \max_{u\in[v-\tau,v]} x(u)\right)\right\|\mathrm{d}v, \quad \text{for } s \in [-\tau, 0). \tag{51}$$

Then, equation (7) which is uniformly asymptotically stable implies that system (1) is uniformly asymptotically integrally stable on $\{q(t,x), T_k\}$.

Proof. Firstly, we prove system (1) is uniformly integrally stable. Because equation (7) is uniformly stable, by Lemma 2, there exists a function $\beta_1 \in K$, such that

$$0 < u_0 \le \alpha_1 \text{ implies } u(t;t_0,u_0) < \beta_1(u_0), \quad t \ge t_0. \tag{52}$$

For given $\alpha > 0$ and $t_0 \in T_k$, where $L\alpha = \alpha_1$, let $\varphi \in B(0,\alpha) \cap S_p(t_0)$. Since $V(t,x)$ is Lipschitzian in x, we have

$$\max_{s\in[-\tau,0]} V(t_0+s, \varphi(s)) \le L \max_{s\in[-\tau,0]} \|\varphi(s)\| \le L\alpha = \alpha_1. \tag{53}$$

Let $x(t) = x(t;t_0,\varphi)$ be any solution of (26) with $\varphi \in B(0,\alpha) \cap S_p(t_0)$, and

$$V(t, x(t;t_0,\varphi)) \equiv m(t) + p(t), \tag{54}$$

where $p(t) = L\int_{t_0}^t \|h(s,x,\max_{u\in[s-\tau,s]} x(u))\|\mathrm{d}s$. According to the condition (i) of (A_4), we get

$$\begin{aligned} D^+m(t) &\le D^+_{(3.1)}V(t,x(t)) - L\left\|h\left(t, x, \max_{s\in[t-\tau,t]} x(s)\right)\right\| \\ &\le D^+_{(2.1)}V(t,x(t)) \le g(t, m(t)). \end{aligned} \tag{55}$$

By (51) and Lemma 1, we have

$$m(t) \le r(t;t_0,u_0), \tag{56}$$

where $r(t;t_0,u_0)$ is the maximal solution of (7) with $u_0 = \max_{s\in[-\tau,0]} m(t_0+s)$.

We choosing $\beta > 0$, such that

$$b(\beta) > \beta_1(L\alpha) + L\alpha. \tag{57}$$

In view of the condition $b(r) \longrightarrow +\infty$ as $r \longrightarrow +\infty$, the choice of β is reasonable. It is obvious that $\beta = \beta(\alpha)$ and $\beta \in K$. At the same time, we can claim that system (1) is uniformly integrally stable. In other words, the solution of system (26) satisfies $q(t,x) \in D(\beta)$, $t \ge t_0$, whenever $\varphi \in B(0,\alpha) \cap S_p(t_0)$, and

$$\int_{t_0}^{t_0+T} \sup_{\|q(t,x)\|\le\beta} \left\|h\left(s, x, \max_{u\in[s-\tau,s]} x(u)\right)\right\|\mathrm{d}s \le \alpha, \quad \text{for } T > 0. \tag{58}$$

Suppose that this is not true; there exists a $t_1 > t_0$ such that

$$\|q(t_1, x(t_1))\| = \beta \text{ and } \|q(t,x(t))\| \le \beta,\ t \in [t_0, t_1]. \tag{59}$$

From the condition (A_4') and (54)–(58), we get

$$\begin{aligned} b(\beta) &\le V(t_1, x(t_1)) \le r(t_1;t_0,u_0) + p(t_1) \\ &\le \beta_1(L\alpha) + L\int_{t_0}^{t_1} \sup_{\|q(t,x)\|\le\beta} \left\|h\left(s, x, \max_{u\in[s-\tau,s]} x(u)\right)\right\|\mathrm{d}s \\ &\le \beta_1(L\alpha) + L\alpha < b(\beta). \end{aligned} \tag{60}$$

This is a contradiction, and then system (1) is uniformly integrally stable.

Secondly, we prove that system (1) is uniformly asymptotically integrally stable. By the uniform asymptotic stability of equation (7) and Lemma 3, we have

$$u(t;t_0,u_0) \le \beta_1(u_0)\sigma(t-t_0), \quad t \ge t_0, \tag{61}$$

where $\beta_1 \in K$ and $\sigma \in \mathcal{F}$. For given $\epsilon > 0$, $\alpha \ge 0$ and $t_0 \in T_k$, let $\varphi \in B(0,\alpha) \cap S_p(t_0)$, and

$$L\int_{t_0}^{+\infty} \sup_{\|q(t,x)\|\le\beta} \left\|h\left(s, x, \max_{u\in[s-\tau,s]} x(u)\right)\right\|\mathrm{d}s \le L\gamma_1 < b(\varepsilon), \tag{62}$$

where $\gamma = \min(\gamma_1, \alpha)$. For any solution $x(t) = x(t;t_0,\varphi)$ of (26) and (56), holds whenever $u_0 = \max_{s\in[-\tau,0]} V(t_0+s, \varphi(s))$. By (54), (56), and (61), together with (A_4'), we can obtain the inequality

$$\begin{aligned} b(\|q(t,x(t))\|) &\le V(t,x(t)) \le r(t;t_0,u_0) \\ &\quad + L\int_{t_0}^t \left\|h\left(s, x, \max_{u\in[s-\tau,s]} x(u)\right)\mathrm{d}s\right\| \\ &\le \beta_1(L\alpha)\sigma(t-t_0) \\ &\quad + L\int_{t_0}^t \sup_{\|q(t,x)\|\le\beta} \left\|h\left(s, x, \max_{u\in[s-\tau,s]} x(u)\right)\right\|\mathrm{d}s \\ &< \beta_1(L\alpha)\sigma(t-t_0) + L\gamma. \end{aligned} \tag{63}$$

Since $\sigma \in \mathcal{F}$, then there exists a $T = T(\alpha, \epsilon)$, such that

$$\sigma(t-t_0) < \frac{b(\epsilon) - L\gamma}{\beta_1(L\alpha)}, \quad t \ge t_0 + T. \tag{64}$$

Furthermore, we have

$$b(\|q(t,x(t))\|) < b(\epsilon), \quad t \ge t_0 + T, \tag{65}$$

which implies that

$$\|q(t, x(t))\| < \epsilon, \quad t \geq t_0 + T, \tag{66}$$

provided $\varphi \in B(0, \alpha) \cap S_p(t_0)$, and (62) is satisfied. Therefore, system (1) is uniformly asymptotically integrally stable. □

4. Conclusion

This paper discussed a class of nonlinear singular differential systems with maxima. Some notions of practical stability and integral stability for such systems were introduced, and various stability criteria were obtained by using the Lyapunov method and comparison principle.

Data Availability

Data sharing is not applicable to this article as no data sets were generated or analyzed during the current study.

Conflicts of Interest

The authors declare that they have no conflicts of interest.

Authors' Contributions

All authors read and approved the final manuscript.

Acknowledgments

This paper was supported by the National Natural Science Foundation of China (11771115 and 11271106).

References

[1] D. Bainov and S. Hristova, *Differential Equations with Maxima*, CRC Press, New York, NY, USA, 2011.

[2] E. Popov, *Automatic Regulation and Control*, Elsevier, Amsterdam, Netherlands, in Russian, 1996.

[3] N. Bantsur and E. Trofimchuk, "On the existence and stability of the periodic and almost periodic solutions of quasilinear systems with maxima," *Ukrainian Mathematical Journal*, vol. 6, pp. 747–754, 1998, in Ukrainian.

[4] M. Bohner, A. Atanaska, and S. G. Hristova, "Nonlinear differential equations with "maxima": parametric stability in terms of two measures," *Applied Mathematics & Information Sciences*, vol. 7, no. 1, pp. 41–48, 2013.

[5] T. Donchev, N. Kitanov, and D. Kolev, "Stability for the solutions of parabolic equations with maxima," *PanAmerican Mathematical Journal*, vol. 20, no. 2, pp. 1–19, 2010.

[6] S. Hristova, "Stability in terms of two measures for impulsive differential equations with supremum," *Nonlinear Studies*, vol. 17, no. 4, pp. 299–308, 2010.

[7] S. Hristova and S. Gluhcheva, "Lipschitz stability in terms of two measures for differential equations with maxima," *International Journal of Pure and Applied Mathematics*, vol. 2, no. 2, pp. 1–12, 2010.

[8] S. G. Hristova and A. Georgieva, "Practical stability in terms of two measures for impulsive differential equations with supremum," *International Journal of Differential Equations*, vol. 2011, Article ID 703189, 13 pages, 2011.

[9] P. Wang, Q. Xu, and X. Liu, "Integral stability in terms of two measures for nonlinear differential systems with maxima," *Abstract and Applied Analysis*, vol. 2014, Article ID 656290, 7 pages, 2014.

[10] S. L. Campbell, *Singular Systems of Differential Equations*, Pitman Advanced Publishing Program (I), London, UK, 1980.

[11] L. Dai, *Singular Control Systems*, Springer-Verlag, New York, NY, USA, 1989.

[12] S. L. Campbell, *Singular Systems of Differential Equations*, Pitman Advanced Publishing Program (II), London, UK, 1982.

[13] M. Mirko and B. Vladimir, "Stability analysis of singular systems," *Circuits Systems and Signal Processing*, vol. 8, no. 3, pp. 267–287, 1989.

[14] P. Anh and D. Hoang, "Stability of a class of singular difference equations," *IJDE, International Journal of Difference Equations*, vol. 1, pp. 181–193, 2006.

[15] K. Takaba, N. Morihira, and T. Katayama, "A generalized Lyapunov theorem for descriptor system," *Systems & Control Letters*, vol. 24, no. 1, pp. 49–51, 1995.

[16] P. Wang, M. Wu, and Y. Wu, "On ϕ_0-stability of a class of singular difference equations," *Advances in Difference Equations*, vol. 1, pp. 1–10, 2013.

[17] L. Zhang, J. Lam, and Q. Zhang, "New Lyapunov and Riccati equations for discrete time descriptor systems," *IEEE-Transactions on Automatic Control Author Information*, vol. 44, no. 11, pp. 2134–2139, 1999.

[18] Y. Li and Y. Liu, "Stability of solutions of singular systems with delay," *Control Theory & Applications*, vol. 15, pp. 542–550, 1998.

[19] P. Wang and J. Zhang, "Stability of solutions for nonlinear singular systems with delay," *Applied Mathematics Letters*, vol. 25, no. 2, pp. 1291–1295, 2012.

[20] C. Yang, Q. Zhang, and L. Zhou, "Practical stability of descriptor systems with time delays in terms of two measurements," *Journal of the Franklin Institute*, vol. 343, no. 6, pp. 635–646, 2006.

[21] S. Hristova, "Practical stability and cone valued Lyapunov functions for differential equations with maxima," *International Journal of Pure and Applied Mathematics*, vol. 57, no. 3, pp. 313–324, 2009.

[22] V. Lakshmikantham, S. Leela, and A. Martynyuk, *Practical Stability of Nonlinear Systems*, World Scientific, Singapore, 1990.

[23] P. Mahajan, S. K. Srivastava, and R. Dogra, "Uniform practical stability of perturbed impulsive differential system in terms of two measures," *Malaya Journal of Matematik*, vol. 7, no. 2, pp. 142–146, 2019.

[24] A. Martynyuk, G. Stamov, and I. Stamova, "Practical stability analysis with respect to manifolds and boundedness of differential equations with fractional-like derivatives," *Rocky Mountain Journal of Mathematics*, vol. 49, no. 1, pp. 211–233, 2019.

[25] Y. Zhang and J. Sun, "Eventual practical stability of impulsive differential equations with time delay in terms of two measurements," *Journal of Computational and Applied Mathematics*, vol. 176, no. 1, pp. 223–229, 2005.

[26] I. Vrhoc, "Integral stability," *Czechoslovak Mathematical Journal*, vol. 9, pp. 71–129, 1959.

[27] V. Lakshmikantham and S. Leela, *Differential and Integral Inequalities*, Vol. 1, Academic Press, New York, NY, USA, 1969.

[28] A. A. Martynyuk, "On integral stability and Lipschitz stability of motion," *Ukrainian Mathematical Journal*, vol. 49, no. 1, pp. 84–92, 1997.

[29] L. Salvadori and F. Visentin, "Non-asymptotic stability and integral stability trough a reduction principle," *Ricerche di Matematica*, vol. 63, no. 2, pp. 335–345, 2014.
[30] A. A. Soliman and M. H. Abdalla, "Integral stability criteria of nonlinear differential systems," *Mathematical and Computer Modelling*, vol. 48, no. 1-2, pp. 258–267, 2008.
[31] S. G. Hristova, "Integral stability in terms of two measures for impulsive functional differential equations," *Mathematical and Computer Modelling*, vol. 51, no. 1-2, pp. 100–108, 2010.
[32] A. Sood and S. K. Srivastava, "Integral Φ_0-stability of impulsive differential equations," *Open Journal of Applied Sciences*, vol. 5, no. 10, pp. 651–660, 2015.

Hindawi
Mathematical Problems in Engineering
Volume 2020, Article ID 1381095, 7 pages
https://doi.org/10.1155/2020/1381095

Research Article

Turing Instability and Amplitude Equation of Reaction-Diffusion System with Multivariable

Qianqian Zheng[1] and Jianwei Shen[2]

[1]*School of Mathematics and Statistics, Xuchang University, Xuchang, Henan 461000, China*
[2]*School of Mathematics and Statistics, North China University of Water Resources and Electric Power, Zhengzhou 450046, China*

Correspondence should be addressed to Jianwei Shen; xcjwshen@gmail.com

Received 3 February 2020; Accepted 29 February 2020; Published 29 March 2020

Guest Editor: Rongwei Guo

In this paper, we investigate pattern dynamics with multivariable by using the method of matrix analysis and obtain a condition under which the system loses stability and Turing bifurcation occurs. In addition, we also derive the amplitude equation with multivariable. This is an effective tool to investigate multivariate pattern dynamics. The example and simulation used in this paper validate our theoretical results. The method presented is a novel approach to the investigation of specific real systems based on the model developed in this paper.

1. Introduction

The pattern formation was first investigated and interpreted by Alan Turing 60 years ago [1]. In general, Turing model contains two reactants: activator and inhibitor, which engage in diffusion. Recently, the study of Turing bifurcation, amplitude equation, and secondary bifurcation have paid more attention on the pattern formation [2–4], and Lee and Cho found that dynamical parameters and external periodic forcing play an important role in the shape and type of pattern formation [5]. And the robustness problem is also investigated [6]. The effects of cross-diffusion, the phenomenon in which a gradient in the concentration of one species induces other species, on pattern formation in reaction-diffusion systems have been discussed in many theoretical papers [7–14]. Regarding noise, noise is a ubiquitous phenomenon in nature and always deemed to play a very important role in the natural synthetic system [15]. Viney and Reece [16] treated noise as adaptive and suggested that applying evolutionary rigour to the study of noise is necessary to fully understand organismal phenotypes, and Shen considered the Lévy noise in the gene network [17, 18].

Recently, the pattern formation with three or four variables has been investigated, and it obtains promising results [19, 20], and Xu et al. made a concrete analysis with three variables [21]. As we all know that amplitude equation is a promising tool to investigate the pattern dynamics of the reaction-diffusion system [2, 22], however, the amplitude equation is a complex process [3], and the researcher often chose the amplitude equation [23–26] to investigate the reaction-diffusion system. In conclusion, spatial patterns in reaction-diffusion systems have attracted the interest of experimentalists and theorists during the last few decades. But, these previous works did not give a general method to define Turing instability and derive the amplitude equation with n variables.

Besides, the study of patterns can offer useful information on the underlying processes causing possible changes in the system. In order to better understand the reaction-diffusion model, first, we propose to study the Turing instability with n variables by matrix theory [27]. In addition, we also derive the amplitude equation by using the standard multiple scale analysis [28, 29] which provides a way to investigate the mechanism of pattern formation.

The paper is organized as follows. In Section 2, we give the general reaction diffusion with multivariable and derive

the condition of Turing instability. In Section 3, we derive the amplitude equation from the reaction-diffusion system with multivariable. In Section 4, we utilize an example to illustrate the application of these ideas. The simulation validates our theoretical results. Finally, we summarize our results and conclusion.

2. Turing Instability with Multivariate

For a multivariate reaction-diffusion system, we have

$$\frac{\partial \mathbf{u}}{\partial t} = \mathbf{f}(\mathbf{u}) + \mathbf{D}\nabla^2\mathbf{u}, \quad \mathbf{u} = (u_{11}, \ldots, u_{nn}), \tag{1}$$

where the function $\mathbf{f}(\mathbf{u})$ specifies dynamics of the interaction of the species and $\mathbf{D}$ is the diffusion parameter diagonal matrix.

Also, we can obtain the following linear system at equilibrium $\mathbf{u} = \mathbf{0}$ from (1):

$$\frac{\partial \mathbf{u}}{\partial t} = \mathbf{A}\mathbf{u} + \mathbf{D}\nabla^2\mathbf{u}, \tag{2}$$

where A is the Jacobian matrix.

As we all know that the stability of a system depends on the sign of the real part of eigenvalue [23], for coefficient matrix $\mathbf{A}$, there is a nonsingular matrix $\mathbf{P}$ subject to $\mathbf{A} = \mathbf{P}^{-1}\mathbf{J}\mathbf{P}$, and $\mathbf{J}$ is a Jordan form [27]. Also, we have

$$\begin{aligned} |\lambda\mathbf{I} - \mathbf{A}| = |\lambda\mathbf{I} - \mathbf{J}| &= \begin{vmatrix} \lambda - \mathbf{J}_1 & 0 & 0 & 0 \\ 0 & \lambda - \mathbf{J}_2 & 0 & \vdots \\ 0 & 0 & \lambda - \mathbf{J}_3 & 0 \\ 0 & \cdots & \cdots & \lambda - \mathbf{J}_n \end{vmatrix} \\ &= (\lambda + \lambda_1)(\lambda + \lambda_2)\cdots(\lambda + \lambda_n) = 0, \end{aligned} \tag{3}$$

where

$$\mathbf{J} = \begin{pmatrix} \mathbf{J}_1 & 0 & \vdots \\ 0 & \mathbf{J}_2 & \vdots \\ \cdots & \cdots & \mathbf{J}_i \end{pmatrix}, \tag{4}$$

where

$$\mathbf{J}_k = \begin{pmatrix} \lambda_k & 1 & 0 & 0 \\ 0 & \lambda_k & 1 & \vdots \\ 0 & 0 & \lambda_k & 1 \\ 0 & \cdots & \cdots & \lambda_k \end{pmatrix}, \tag{5}$$

where $-\lambda_i$ is the eigenvalue and has a negative real part which means stable without diffusion. In addition, we can get the condition of stability by Routh–Hurwitz criteria.

In the standard way, we assume that $\mathbf{u}$ takes the form

$$\mathbf{u} = \mathbf{c}e^{\lambda_k t + ikr}, \tag{6}$$

and obtains the characteristic equation from system (1.2) as follows:

$$\left|\lambda\mathbf{I} - \mathbf{A} + \mathbf{D}k^2\right| = \left|\lambda\mathbf{I} - \mathbf{J} - \mathbf{D}k^2\right| = \lambda^n + a_1\lambda^{n-1} + \cdots + a_{n-1}\lambda + a_n = 0, \tag{7}$$

and there is at least $\lambda > 0$ which exists when $a_n < 0$ based on Routh–Hurwitz criteria.

Now, we obtain the definition of Turing instability with n variables.

Theorem 1. *Turing instability occurs when $a_n < 0$.*

In addition, we obtain the critical condition of Turing instability. Assume $x = k^2$ and $p(x) = x^n + p_1x^{n-1} + \cdots + p_n$, $p'(x) = 0$ has $n-1$ roots, and $x_i, i = 1, \ldots, n-1$ and can get the minimum value $p(x_c > 0)$ [30]. We can obtain the critical condition of Turing instability from $a_n(k_c^2) = 0$.

3. Amplitude Equation with Multivariable

In this paper, we continue to study the system with n variables. In the following, we use multiple scale analysis to derive the amplitude equations.

The solutions of systems can be expanded as

$$c = c_0 + Z_i e^{ik_i r} + c.c., \quad i = 1, 2, 3. \tag{8}$$

And system (1) can be written as

$$\frac{\partial \mathbf{c}}{\partial t} = \mathbf{L}\mathbf{c} + N(\mathbf{c}, \mathbf{c}), \tag{9}$$

where $\mathbf{c} = \mathbf{u}$ is the variable, $\mathbf{L} = \mathbf{A} + \mathbf{D}\nabla^2$ is the linear operator, $N = N_1\mathbf{u}^2 + N_2\mathbf{u}^3$ is the nonlinear term, $N_1\mathbf{u}^2$ is all the twice term, and $N_2\mathbf{u}^3$ is all the triple term.

We need to investigate the dynamical behavior when γ is close to γ_c, and then we expand γ as

$$\gamma_c - \gamma = \varepsilon\gamma_1 + \varepsilon^2\gamma_2 + \cdots, \tag{10}$$

where γ_c is the critical value and ε is a small enough parameter.

We expand $\mathbf{c}$ and N as the series form of ε:

$$\begin{aligned} \mathbf{c} &= \mathbf{u}_1\varepsilon + \mathbf{u}_2\varepsilon^2 + \cdots, \\ N &= N_1\mathbf{u}_1^2\varepsilon^2 + \left(N_1\mathbf{u}_1\mathbf{u}_2 + N_2\mathbf{u}_1^3\right)\varepsilon^3 + o\left(\varepsilon^4\right). \end{aligned} \tag{11}$$

Linear operator L can be expanded as

$$\mathbf{L} = \mathbf{L}_c + (\gamma_c - \gamma)M. \tag{12}$$

Let

$$\begin{aligned} T_0 &= t, \\ T_1 &= \varepsilon t, \\ T_2 &= \varepsilon^2 t, \ldots. \end{aligned} \tag{13}$$

T_i is a dependent variable, and amplitude is a slow variable. For the derivation of time, we have that

$$\frac{\partial W}{\partial t} = \varepsilon\frac{\partial W}{\partial T_1} + \varepsilon^2\frac{\partial W}{\partial T_2} + \cdots. \tag{14}$$

Substituting the above equations into (1) and expanding (1) according to different orders of ε, we can obtain three equations as follows:

$$\begin{aligned}
&\varepsilon : \mathbf{L}_c\mathbf{u}_1 = 0,\\
&\varepsilon^2 : \mathbf{L}_c\mathbf{u}_2 = \frac{\partial}{\partial T_1}\mathbf{u}_1 - \gamma_1 M\mathbf{u}_1 - N_1\mathbf{u}_1^2,\\
&\varepsilon^3 : \mathbf{L}_c\mathbf{u}_3 = \frac{\partial}{\partial T_1}\mathbf{u}_2 + \frac{\partial}{\partial T_2}\mathbf{u}_1 - \gamma_1 M\mathbf{u}_2 - \gamma_2 M\mathbf{u}_1 - N_1\mathbf{u}_1\mathbf{u}_2 - N_2\mathbf{u}_1^3.
\end{aligned} \tag{15}$$

We first consider the case of the first order of ε. Since L_c is the linear operator of the system close to the onset, $\mathbf{u}_1$ is the linear combination of the eigenvectors that corresponds to the eigenvalue zero. Since that

$$\mathbf{u}_1 = \mathbf{b}W_i e^{ik_i r} + c.c, \tag{16}$$

where $\mathbf{L}_c\mathbf{b} = 0$, nonzero root exists [27].

Now, we consider the case of ε^2 and the zero eigenvectors of operator $\mathbf{L}_c^+$, $\exists\mathbf{b}^+$ s.t.:

$$\mathbf{L}_c^+\mathbf{b}^+ = 0. \tag{17}$$

By investigating $e^{ik_1 r}$ only in the following, another case we can get is by changing subscript which is not described in detail here. It can be obtained from the orthogonality condition that

$$\mathbf{b}^{+T}\mathbf{b}\frac{\partial}{\partial T_1}W_1 = \mathbf{b}^{+T}M\mathbf{b}W_1 + \left(\mathbf{b}^{+T}\mathbf{b}^2\right)N_1\overline{W_2W_3}. \tag{18}$$

By using the same methods, one has

$$\begin{aligned}
\mathbf{u}_2 = {} & a_0 + a_i Z_i e^{ik_i r} + a_{ii}Z_{ii}e^{i2k_i r} + a_{12}Z_{12}e^{i(k_1-k_2)r}\\
& + a_{23}Z_{23}e^{i(k_2-k_3)r} + a_{31}Z_{31}e^{i(k_3-k_1)r} + c.c.
\end{aligned} \tag{19}$$

For the case of ε^3, we have that

$$\mathbf{L}_c\mathbf{u}_2 = 0. \tag{20}$$

We can obtain all the coefficients and $a_i = \mathbf{b}$.

Using the Fredholm solubility condition again, we can obtain

$$\begin{aligned}
\left(\mathbf{b}^{+T}\mathbf{b}\right)\frac{\partial Z}{\partial T_1} + \left(\mathbf{b}^{+T}\mathbf{b}\right)\frac{\partial Z}{\partial T_2} = {} & \gamma_1\mathbf{b}^{+T}M\mathbf{b}Z_1 + \gamma_2\mathbf{b}^{+T}M\mathbf{b}W_1\\
& + \mathbf{b}^{+T}\mathbf{b}^2N_1\left(\overline{Z_2W_3} + \overline{Z_3W_2}\right)\\
& + \mathbf{b}^{+T}\mathbf{b}^3N_2\left(|W|_1^2 + |W_2|^2 + |W_3|^2\right)W_1,
\end{aligned} \tag{21}$$

and then we substitute systems (18) and (21) into (14) for simplification, in which we can obtain

$$\begin{aligned}
\left(\mathbf{b}^{+T}\mathbf{b}\right)\frac{\partial W_1}{\partial t} = {} & (\gamma_c - \gamma)W_1 + \mathbf{b}^{+T}\mathbf{b}^2N_1\overline{W_2W_3}\\
& + \mathbf{b}^{+T}\mathbf{b}^3N_2\left(|W|_1^2 + |W_2|^2 + |W_3|^2\right)W_1.
\end{aligned} \tag{22}$$

4. Method

In the following, we consider the Turing instability of a system with 3 variables:

$$\begin{aligned}
\frac{\partial u}{\partial t} &= \frac{k_0 u}{1 + k_0 u} - \mu u + d_1\nabla^2 u,\\
\frac{\partial v}{\partial t} &= \frac{k_1 u + k_2 v}{1 + k_1 u + k_2 v} - \mu v + d_2\nabla^2 v,\\
\frac{\partial w}{\partial t} &= \frac{k_3 u + k_4 v + k_5 w}{1 + k_3 u + k_4 v + k_5 w} - \mu w + d_3\nabla^2 w,
\end{aligned} \tag{23}$$

and we obtain the Jacobian matrix at equilibrium $(u_0, v_0, w_0) = (0, 0, 0)$:

$$A = \begin{pmatrix} k_0 - \mu & 0 & 0\\ k_1 & k_2 - \mu & 0\\ k_3 & k_4 & k_5 - \mu \end{pmatrix}. \tag{24}$$

The characteristic equation is

$$|\lambda I - A| = (\lambda - k_0 + \mu)(\lambda - k_2 + \mu)(\lambda - k_5 + \mu) = 0. \tag{25}$$

The system is stable without diffusion when $\mu - k_0 < 0, \mu - k_2 < 0$ and $\mu - k_5 < 0$, that is to say it is stable when $\mu < min(k_0, k_2, k_5)$.

Then, the Jacobian matrix with diffusion is given as follows:

$$B = \begin{pmatrix} k_0 - \mu - d_1k^2 & 0 & 0\\ k_1 & k_2 - \mu - d_2k^2 & 0\\ k_3 & k_4 & k_5 - \mu - d_3k^2 \end{pmatrix}. \tag{26}$$

The characteristic equation is

$$|\lambda I - B| = \lambda^3 + a\lambda^2 + b\lambda + c = 0, \tag{27}$$

where

$$\begin{aligned}
a &= (d_3 + d_1 + d_2)k^2 - k_0 - k_5 + 3\mu - k_2,\\
b &= (d_2d_3 + d_1d_3 + d_1d_2)k^4 + (-d_1k_2 - k_0d_3 + 2\mu d_3 + 2\mu d_2\\
&\quad - k_0d_2 - k_2d_3 - d_2k_5 - d_1k_5 + 2d_1\mu)k^2\\
&\quad - 2\mu k_2 + 3\mu^2 - 2\mu k_5 - 2k_0\mu + k_0k_2 + k_2k_5 + k_0k_5,\\
c &= a_5k^6 + b_5k^4 + c_5k^2 + d_5,
\end{aligned} \tag{28}$$

where

$$\begin{aligned}
a_5 &= d_1d_2d_3,\\
b_5 &= \mu d_2d_3 - k_0d_2d_3 - d_1k_2d_3 + d_1\mu d_3 - d_1d_2k_5 + d_1d_2\mu,\\
c_5 &= -\mu d_2k_5 - d_1\mu k_5 + \mu^2d_2 - k_0d_2\mu - d_1k_2\mu - \mu k_2d_3\\
&\quad + k_0d_2k_5 + d_1\mu^2 + d_1k_2k_5 + \mu^2d_3 + k_0k_2d_3 - k_0\mu d_3,\\
d_5 &= -\mu^2k_5 + k_0\mu k_5 + \mu k_2k_5 + \mu^3 + k_0k_2\mu - k_0k_2k_5 - \mu^2k_2 - k_0\mu^2.
\end{aligned} \tag{29}$$

For convenience, we assume $x = k^2$, and then $f(x) = a_5x^3 + b_5x^2 + c_5x + d_5$ and $f'(x) = 3a_5x^2 + 2b_5x + c_5$ which have two roots $x_{12} = -b_5 \pm \sqrt{b_5^2 - 3a_5c_5}$. We know $f(x) \geq f(x_1)$, $k_c^2 = x_1 = -b_5 + \sqrt{b_5^2 - 3a_5c_5}$, and the critical value is $f(x_1) = 0$.

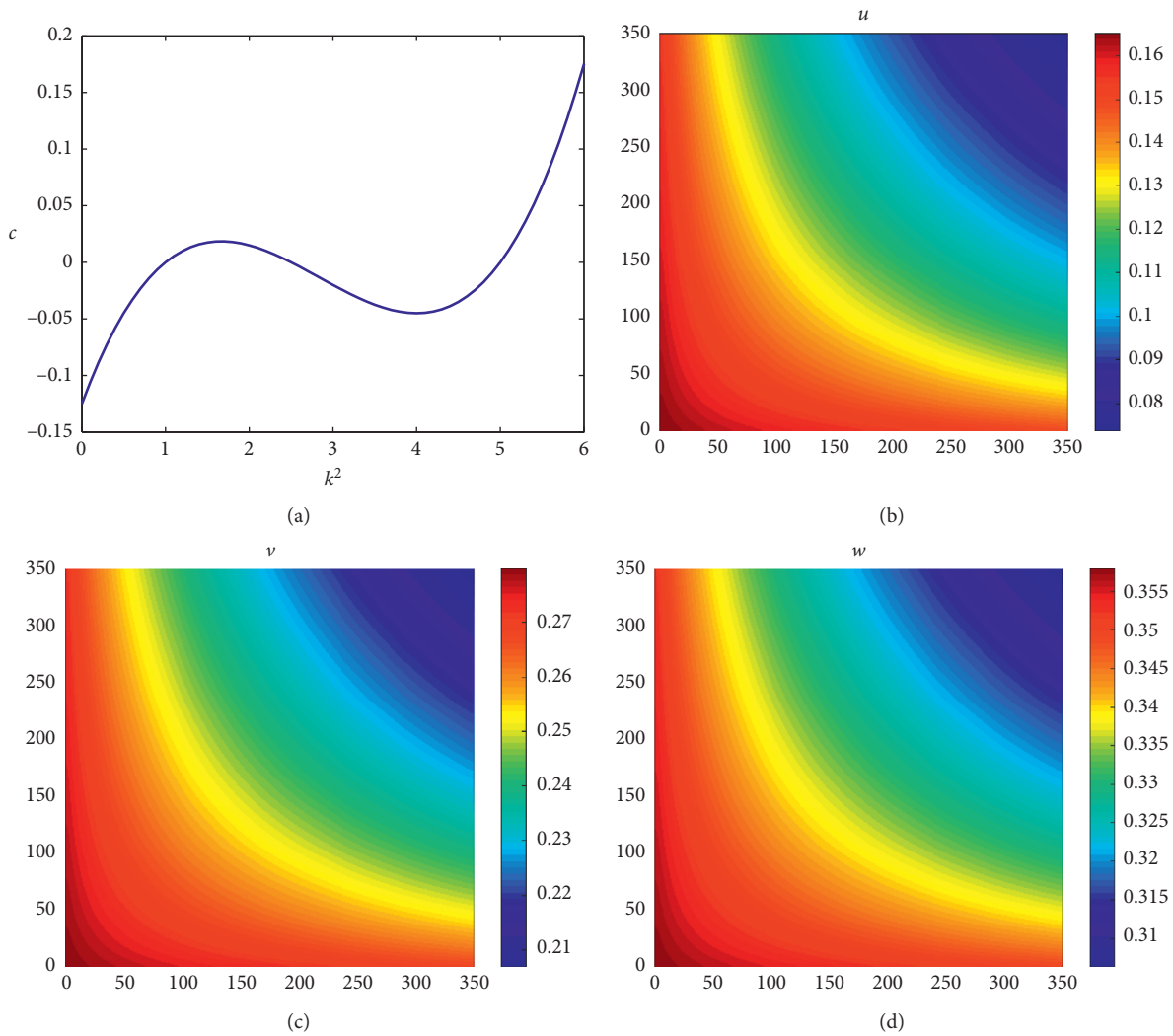

Figure 1: Dispersion curve and rainbow pattern.

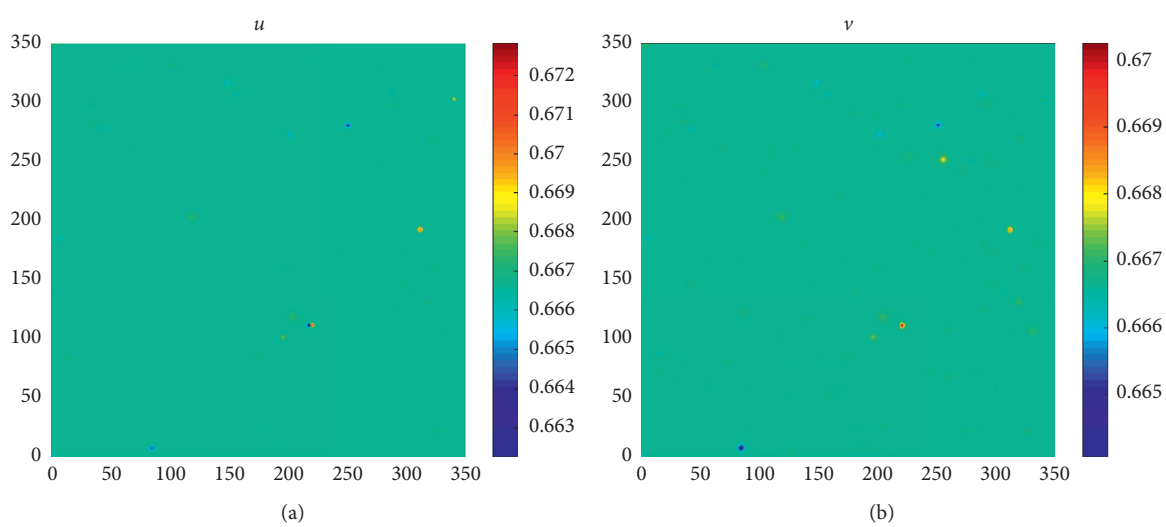

Figure 2: Continued.

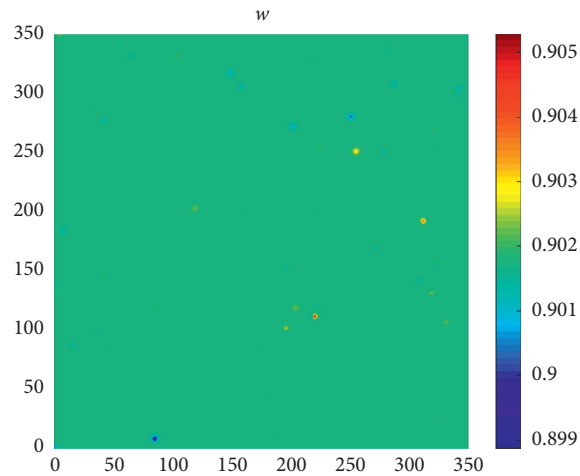

(c)

Figure 2: Spot pattern occurs.

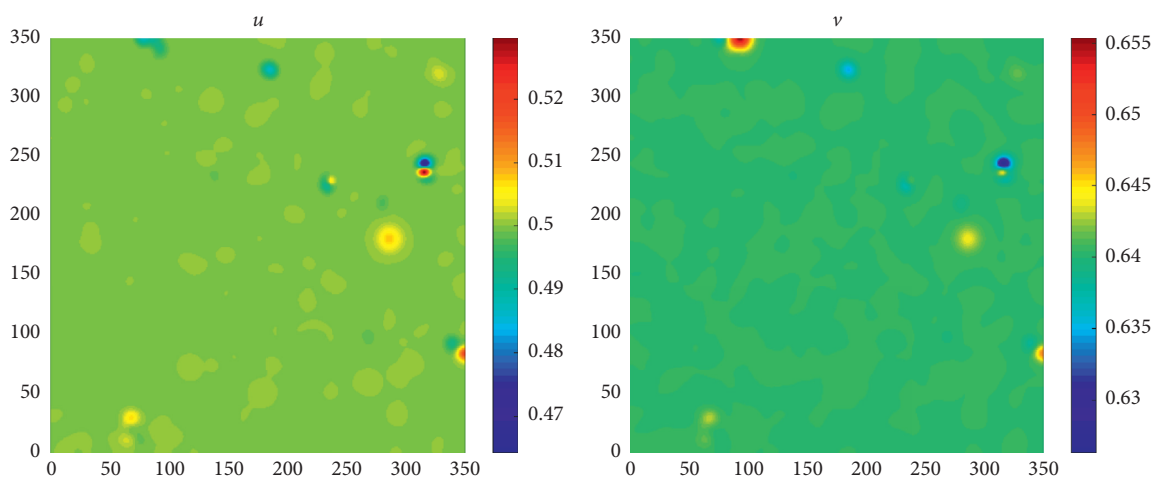

(a) (b)

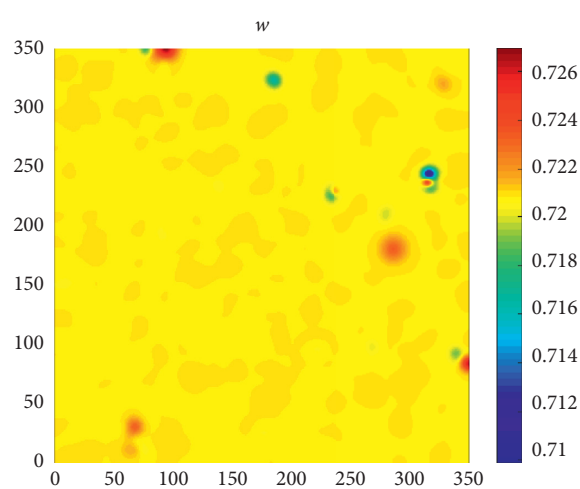

(c)

Figure 3: Nebulous pattern occurs.

We get $k_c^2 = 0.12$, $c = -0.1022$ when $k_0 = 2$, $k_1 = 1$, $k_2 = 2$, $k_3 = 1$, $k_4 = 1$, $k_5 = 2$, $d_1 = 0.1$, $d_2 = 0.2$, $d_3 = 0.5$, and $\mu = 1.5$ with the perturbation $1/((X+10)(Y+20))$ which means Turing instability, and then the rainbow stripe pattern (Figures 1(b)–1(d)) and dispersion curve occur (Figure 1(a)). In addition, spot pattern occurs (Figure 2) when $k_0 = 3, k_1 = 1, k_2 = 2, k_3 = 3, k_4 = 4, k_5 = 5, d_1 = 0.1$, $d_2 = 0.2, d_3 = 0.3, \mu = 1$ with the perturbation $\sin(X^2 + Y^2)$, and nebulous pattern occurs (Figure 3) when $k_0 = 2, k_1 = 1$, $k_2 = 2, k_3 = 1, k_4 = 1, k_5 = 2$, $d_1 = 1$, $d_2 = 2$, $d_3 = 1$, $\mu = 1$ with the perturbation $\sin(X^2 + Y^2)$.

5. Conclusion

In this article, we present the theoretical analysis and numerical simulation of the Turing instability with multivariable. It is found that the reaction-diffusion systems with multivariable have rich spatial dynamics by performing a series of numerical simulations. We also give a general method to derive the amplitude equation with multivariable in theory which can be used to solve some problems about pattern formation with multiple variables in the further study. In addition, the mechanism of pattern formation with multiple variables is on the way and can be derived based on the above theory in this paper; however, it is a very complex process, and we will investigate it in the future.

Data Availability

No data were used to support this study.

Conflicts of Interest

The authors declare that there are no conflicts of interest.

Acknowledgments

This work was supported by the National Natural Science Foundation of China (11772291), Young Talent Support Project of Henan Province (2020HYTP012), and Key Program of Xuchang University (2020ZD012).

References

[1] A. Turing, "The chemical basis of morphogenesis," *Philosophical Transactions of the Royal Society B*, vol. 237, pp. 37–72, 1952.

[2] H. Liu and W. Wang, "The amplitude equations of an epidemic model," *Science Technology and Engineering*, vol. 10, no. 8, pp. 1929–1933, 2010.

[3] A. K. Dutt, "Amplitude equation for a diffusion-reaction system: the reversible Sel'kov model," *AIP Advances*, vol. 2, no. 4, Article ID 042125, 2012.

[4] Q. Zheng and J. Shen, "Dynamics and pattern formation in a cancer network with diffusion," *Communications in Nonlinear Science and Numerical Simulation*, vol. 27, no. 1–3, pp. 93–109, 2015.

[5] I. Lee and U. I. Cho, "Pattern formations with turing and hopf oscillating pattern," *Bulletin of the Korean Chemical Society*, vol. 21, no. 12, pp. 1213–1216, 2000.

[6] P. K. Maini, T. E. Woolley, R. E. Baker et al., "Turing's model for biological pattern formation and the robustness problem," *Interface Focus*, vol. 2, no. 4, pp. 487–496, 2012.

[7] V. K. Gaffney, "Epstein IR, cross-diffusion and pattern formation in reaction-diffusion systems," *Physical Chemistry Chemical Physics*, vol. 11, pp. 897–912, 2008.

[8] D. Fanelli, C. Cianci, and F. D. Patti, "Turing instabilities in reaction-diffusion systems with cross diffusion," *The European Physical Journal B*, vol. 86, no. 4, pp. 1–8, 2013.

[9] J. Shi, Z. Xie, and K. Little, "Cross-diffusion induced instability and stability in reaction-diffusion systems," *Journal of Applied Analysis and Computation*, vol. 1, no. 1, pp. 95–119, 2011.

[10] Z. Liu, J. Shen, S. Cai, and F. Yan, *MicroRNA Regulatory Network: Structure and Function*, Springer, Berlin, Germany, 2018.

[11] Q. Zheng, J. Shen, and Z. Wang, "Pattern formation and oscillations in reaction-diffusion model with p53-Mdm2 feedback loop," *International Journal of Bifurcation and Chaos*, vol. 29, no. 14, Article ID 1930040, 2019.

[12] Q. Zheng, J. Shen, and Z. Wang, "Pattern dynamics of the reaction-diffusion immune system," *PLoS One*, vol. 13, no. 1, Article ID e0190176, 2018.

[13] Q. Zheng, Z. Wang, and J. Shen, "Pattern dynamics of network-organized system with cross-diffusion," *Chinese Physics B*, vol. 26, no. 2, Article ID 020501, 2017.

[14] Q. Zheng, Z. Wang, J. Shen, and H. M. Iqbal, "Turing bifurcation and pattern formation of stochastic reaction-diffusion system," *Advances in Mathematical Physics*, vol. 2017, Article ID 9648538, 9 pages, 2017.

[15] M. Thattai and A. Van Oudenaarden, "Intrinsic noise in gene regulatory networks," *Proceedings of the National Academy of Sciences*, vol. 98, no. 15, pp. 8614–8619, 2001.

[16] M. Viney and S. E. Reece, "Adaptive noise," *Proceedings of the Royal Society B: Biological Sciences*, vol. 280, no. 1767, Article ID 20131104, 2013.

[17] Y. Ding, J. Shen, J. Lu, and J. Kurths, "Stochastic resonance in genetic regulatory networks under Lévy noise," *EPL (Europhysics Letters)*, vol. 127, no. 5, p. 50003, 2019.

[18] Q. H. Zhu, J. W. Shen, and J. C. Ji, "Internal signal stochastic resonance of a two-component gene regulatory network under Lévy noise," *Nonlinear Dynamics*, pp. 1–4, 2020.

[19] K. Uriu and Y. Iwasa, "Turing pattern formation with two kinds of cells and a diffusive chemical," *Bulletin of Mathematical Biology*, vol. 69, no. 8, pp. 2515–2536, 2007.

[20] Z. Li and W. Chen, "Two dimension spatial pattern formation in a coupled autocatalysis system," *Applied Mathematical Modelling*, vol. 39, no. 1, pp. 50–69, 2015.

[21] J. Xu, G. X. Yang, H. G. Xi, and J. Z. Su, "Pattern dynamics of a predator-prey reaction-diffusion model with spatiotemporal delay," *Nonlinear Dynamics*, vol. 81, Article ID 2155C2163, 2015.

[22] L. Guan and J. Shen, "Self-organized pattern dynamics of somitogenesis model in embryos," *Physica A: Statistical Mechanics and Its Applications*, vol. 506, pp. 587–601, 2018.

[23] Q. Ouyang, *Introduction to Nonlinear Science and Pattern Dynamics*, Peking University Press, Beijing, China, 2010.

[24] C. Mayol, R. Toral, and C. R. Mirasso, "Derivation of amplitude equations for nonlinear oscillators subject to arbitrary forcing," *Physical Review E*, vol. 69, no. 6, Article ID 066141, 2004.

[25] J. Murray, *Mathematical Biology: I. An Introduction*, Springer, Berlin, Germany, 2007.

[26] Y. Kuramoto, *Chemical Oscillations, Waves and Turbulence*, Dover Publications, Mineola, NY, USA, 2003.

[27] D. Serre, *Matrices: Theory and Applications*, Springer, Berlin, Germany, 2002.
[28] G. H. Gunaratne, Q. Ouyang, and H. L. Swinney, "Pattern formation in the presence of symmetries," *Physical Review E*, vol. 50, no. 4, pp. 2802–2820, 1994.
[29] B. Pena and C. Perez-Garcia, "Stability of turing patterns in the brusselator model," *Physical Review E*, vol. 64, no. 5, Article ID 056213, 2001.
[30] V. A. Zorich, *Mathematical Analysis*, Springer, Berlin, Germany, 2004.